STRUCTURAL DYNAMICS

RECENT ADVANCES

PROCEEDINGS OF THE 6TH INTERNATIONAL CONFERENCE

EDITED BY:
N. S. FERGUSON
H. F. WOLFE
C. MEI

STRUCTURAL DYNAMICS: RECENT ADVANCES

Proceedings of the 6th International Conference

Volume II

Proceedings of the Sixth International Conference on Recent Advances in Structural Dynamics, held at the Institute of Sound and Vibration Research, University of Southampton, England, from 14th to 17th July, 1997, co-sponsored by the US Airforce European Office of Aerospace Research and Development and the Wright Laboratories, Wright Patterson Air Force Base.

Edited by

N.S. FERGUSON

Institute of Sound and Vibration Research,
University of Southampton, Southampton, UK.

H.F. WOLFE

Wright Laboratory,
Wright Patterson Air Force Base, Ohio, USA.

and

C. MEI

Department of Aerospace Engineering,
Old Dominion University, Norfolk, Virginia, USA.

ISBN no. 0-85432-6375

PREFACE

The papers contained herein were presented at the Sixth International Conference on Recent Advances in Structural Dynamics held at the Institute of Sound and Vibration Research, University of Southampton, England in July 1997. The conference was organised and sponsored by the Institute of Sound and Vibration Research and co-sponsored by the Wright Laboratories, Wright Patterson Air Force Base. We wish to also thank the following for their contribution to the success of the conference: the United States Air Force European Office of Aerospace Research and Development. The conference follows equally successful conferences on the same topic held at Southampton in 1980, 1984,1988,1991 and 1994.

There are over one hundred papers written by authors from approximately 20 different countries, making it a truly international forum. Many authors have attended more than one conference in the series whilst others attended for the first time.

It is interesting to note the change in emphasis of the topics covered. Analytical and numerical methods have featured strongly in all the conferences. This time, system identification and power flow techniques are covered by even more papers than previously. Also, there are many contributions in the field of passive and active vibration control. Papers dealing with nonlinear aspects of vibration continue to increase. These observations seem to reflect the trend in current research in structural dynamics. We therefore hope that the present series of International Conferences will play a part in disseminating knowledge in this area.

We would like to thank the authors, paper reviewers and session chairmen for the part they played in making it a successful conference.

My personal thanks go to the following individuals who willingly and enthusiastically contributed to the organisation of the event:

Dr. H.F. Wolfe	Wright Laboratories, WPAFB, USA
Dr. C. Mei	Old Dominion University, USA
Mrs. M.Z. Strickland	ISVR, University of Southampton, UK

Grateful thanks are also due to many other members of ISVR who contributed to the success of the event.

N.S. Ferguson

Sixth International Conference on Recent Advances in Structural Dynamics

Volume II

Contents

SYSTEM IDENTIFICATION II

POWER FLOW TECHNIQUES II

PASSIVE AND ACTIVE CONTROL III

ANALYTICAL METHODS II

NONLINEAR VIBRATION III

ANALYTICAL METHODS III

RANDOM VIBRATION I

RANDOM VIBRATION II

SIGNAL PROCESSING I

SYSTEM IDENTIFICATION III

INVITED PAPERS

ON RANDOM VIBRATION, PROBABILITY, AND FATIGUE

R. D. Blevins
Rohr Inc., Mail Stop 107X
850 Lagoon Drive
Chula Vista, California 91910

ABSTRACT

Analysis is made to determine the properties of a random process consisting of the sum of a series of sine waves with deterministic amplitudes and independent, random phase angles. The probability density of the series and its peaks are found for an arbitrary number of terms. These probability distributions are non-Gaussian. The fatigue resulting from the random vibration is found as a function of the peak-to-rms ratio.

1. INTRODUCTION

Vibration spectra of aircraft components often are dominated by a relatively small number of nearly sinusoidal peaks as shown in Figure 1. The time history of this process, shown in Figure 2, is irregular but bounded. The probability density of the time history, shown in figure 3 only roughly approximates a Gaussian distribution and it does not exceed 2.5 standard deviations.

The time history of displacement or stress of these processes over a flight or a take off time can be expressed as a Fourier series of a finite number of terms over the finite sampling period T.

$$Y = \sum_{n=1}^{N} a_n cos(\omega_n t_n + \phi_n), \quad 0 \leq t_n \leq T, \quad a_n \geq 0 \tag{1}$$

Each frequency ω_n is a positive, non-zero integer multiple of $2\pi/T$. The following model is used for the nature of the Fourier series: 1) the amplitudes a_n are positive and deterministic in the sense that they do not vary much from sample to sample, 2) the phases ϕ_n are random in the sense that they vary from sample to sample, they are equally likely to occur over the range $-\infty < \phi_n < \infty$. This last condition implies that the terms on the right hand side of equation (1) are statistically independent of each other.

We can generate an ensemble of values of the dependent variable Y by randomly choosing M sets of N phase angles $(\{\phi_n\}, n = 1, 2..N)$, computing Y at some fixed time from equation (1), choosing another set of phases, computing a second value of Y and so

on until we have a statistically significant sample of M $Y's$. This random phase approach, introduced by Rayleigh (1880), models a multi-frequency processes where each frequency component is independent and whose power spectral density (PSD) is known.

The maximum possible (peak) value of equation (1) is the sum of the amplitude of each term (recall $a_n \geq 0$). The mean square of the sum of independent sine waves is the sum of the mean squares of the terms.

$$Y_{peak} = \sum_{n=1}^{N} a_n \tag{2a}$$

$$= Na, \quad for\ a_1 = a_2 = a_n = a \tag{2b}$$

$$Y_{rms}^2 = \frac{1}{T}\int_0^T [\sum_{n=1}^{N} a_n cos(2\pi t_n/T + \phi_n)]^2 dt_n = \frac{1}{2}\sum_{n=1}^{N} a_n^2 \tag{3a}$$

$$= \frac{1}{2}Na^2, \quad for\ a_1 = a_2 = a_n = a \tag{3b}$$

The peak-to-rms ratio of the sum of N mutually independent sine waves thus is,

$$\frac{Y_{peak}}{Y_{rms}} = 2^{1/2}\sum_{n=1}^{N} a_n \Big/ \Big(\sum_{n=1}^{N} a_n^2\Big)^{1/2}, \tag{4a}$$

$$= (2N)^{1/2}, \quad for\ a_1 = a_2 = a_n = a. \tag{4b}$$

Equation (4b) shows that the peak-to-rms ratio for an equal amplitude series increases from $2^{1/2}$ for a single term (N=1) and approaches infinity as the number of terms N approaches infinity, as shown in Figure 4. The probability of Y is zero beyond the peak value. For example, there is no chance that the sum of any four ($N = 4$) independent sinusoidal terms will be greater than $8^{1/2} = 2.828$ times the overall rms value.

2. PROBABILITY DENSITY OF A SINE WAVE

The probability density $p_Y(y)$ of the random variable Y is probability that the random variable Y has values within the small range between y and $y + dy$, divided by dy. $p(Y)$ has the units of $1/Y$. Consider single a sine wave of amplitude a_n, circular frequency ω_n, and phase ϕ_n.

$$Y = a_n\ cos(\omega_n t_n + \phi_n), \quad 0 \leq \phi_n < 2\pi. \tag{5}$$

Y is the dependent random variable. The independent random variables are t_n or ϕ_n. The probability density of a sine wave for equal likely phases $p(\phi_n) = 1/(2\pi)$, or equally likely times, $p(t_n) = 1/T$, is (Bennett, 1944; Rice 1944, art. 3.10),

$$p_Y(y) = \begin{cases} \pi^{-1}(a_n^2 - y^2)^{-1/2}, & \text{if } -a_n < y < a_n; \\ 0, & \text{if } |y| \geq a_n. \end{cases} \tag{6}$$

The probability density of the sine wave is symmetric about $y = 0$, i.e., $p_Y(y) = p_Y(-y)$, it is singular at $y = a_n$, and it falls to zero for $|y|$ greater than a_n as shown in Figure 5.

The characteristic function of a random variable x is the expected value of $e^{j2\pi fx}$,

$$C(f) = \int_{-\infty}^{\infty} e^{j2\pi fx} p(x) dx, \tag{7}$$

and it is also the Fourier transform of the probability density function (Cramer, 1970, pp. 24-35; Sveshnikov, 1965; with notation of Bendat, 1958). $j = \sqrt{-1}$ is the imaginary constant. The characteristic function of the sine wave is found using equations (13) and (14) and integrating over the range $0 \leq X \leq a_n$ (Gradshteyn, Ryzhik, Jeffrey, 1994, article 3.753).

$$C_n(f) = 2(\pi a_n)^{-1} \int_0^{a_n} cos(2\pi fY))[1 - (Y/a_n)^2]^{-1/2} dY = J_0(2\pi f a_n), \tag{8}$$

The characteristic function of a sine wave is a Bessel function of the first kind and zero order (Rice, 1944, art. 3.16). Equations (6) and (8) are starting points for determining the probability density of the Fourier series.

3. PROBABILITY DENSITY OF THE SUM OF N SINE WAVES

It is possible to generate an expression for the probability density of Fourier series (equation 1) with 1,2,3,to any number of terms provided the sine wave terms are mutually independent. This is done with characteristic functions. The characteristic function of the sum of N mutually independent random variables ($Y = X_1 + X_2 + .. + X_N$) is the product of their characteristic functions (Weiss, 1990, p.22; Sveshnikov, pp. 124-129),

$$\begin{aligned} C(f) &= \int_{-\infty}^{\infty} .. \int_{-\infty}^{\infty} e^{j2\pi f(X_1+X_2+..+X_N)} p(X_1)p(X_2)..p(X_N) dX_1 dX_2 .. dX_N, \\ &= \prod_{n=1}^{N} \int_{-\infty}^{\infty} e^{j2\pi f X_n} p(X_n) dX_n = \prod_{n=1}^{N} C_n(f). \end{aligned} \tag{9}$$

The symbol Π denotes product of terms. The characteristic function for the sum of N independent sine waves is found from equations (8) and (9).

$$C(f) = \begin{cases} \prod_{n=1}^{N} J_0(2\pi f a_n), & \text{unequal } a_n \\ [J_0(2\pi f a)]^N, & a_1 = a_2 = a_n = a \end{cases} \tag{10}$$

The probability density of Y is the inverse Fourier transform of its characteristic function (Sveshnikov, 1968, p. 129).

$$p_Y(y) = \int_{-\infty}^{\infty} e^{-j2\pi fy} C(f) df \tag{11}$$

By substituting equation (10) into equation (11) we obtain an integral equation for the probability density of a N-term finite Fourier series of independent sine waves (Barakat, 1974).

$$p_Y(y) = 2\int_0^\infty cos(2\pi yf)\ \{\ \prod_{n=1}^{N} J_0(2\pi f a_n)\ \}\ df, \quad N = 1, 2, 3... \tag{12}$$

If all N terms of the Fourier series have equal amplitudes $a = a_1 = a_2 = a_n = a_N$, then this simplifies,

$$p_Y(y) = 2\int_0^\infty cos(2\pi yf)[J_0(2\pi fa)]^N df, \quad N = 1, 2, 3... \tag{13}$$

These distributions are symmetric about $y = 0$ as are all zero mean, sum-of-sine-wave distributions. Figures 5 and 6 show results of numerically integrating equations (45) and (46) over interval $f = 0$ to $f = 15a$ using Mathematica (Wolfram, 1995).

Barakat (1974, also see Weiss, 1994, p. 25) found a Fourier series solution to equation (45). He expanded the probability density of the N term sum in a Fourier series over the finite interval $-L_Y < Y < L_Y$ where $L_Y = a_1 + a_2 + .. + a_N$. The result for unequal amplitudes is ,

$$p_Y(y) = \frac{1}{2L_Y} + \frac{1}{L_Y}\sum_{i=1}^{\infty}\{\prod_{n=1}^{N} J_0(\frac{i\pi a_n}{L_Y})\}cos(\frac{i\pi y}{L_Y}), \qquad |y| \le L_Y. \tag{14}$$

For equal amplitudes, $a_1 = a_2 = a_n = a$, $L_Y = Na$, and

$$p_Y(y) = \frac{1}{2Na} + \frac{1}{Na}\sum_{i=1}^{\infty}[J_0(\frac{i\pi}{N})]^N cos(\frac{i\pi y}{Na}), \qquad |y| \le Na. \tag{15}$$

Figure 6 shows that the Fourier series solution (equation 15) carried to 20 terms to be virtually identical to numerical integration of equation (13) and it compares well with the approximate solution. Note that theory requires $p_Y(|y7| > L_Y) = 0$.

A power series solution for equation (13) can be found with a technique used by Rice (1944, art. 16) for shot noise and by Cramer (1970) who called it an Edgeworth series. The Bessel function term in equation (13) is expressed as an exponent of a logarithm which is then expanded in a power series.

$$\begin{aligned}[J_o(2\pi fa)]^N &= exp(N\ ln[J_0(2\pi af)]), \qquad (16)\\ &= exp(-N\pi^2a^2f^2 - (1/4)N\pi^4a^4f^4 - (1/9)N\pi^6a^6f^6 + (11/192)N\pi^8a^8f^8...),\\ &= [exp(-N\pi^2a^2f^2)][1 - \frac{1}{4}N\pi^4a^4f^4 - \frac{1}{9}N\pi^6a^6f^6 - (\frac{11N}{192} - \frac{N^2}{32})\pi^8a^8f^8 + ...]\end{aligned}$$

Substituting this expansion into equation (13) and rearranging gives a series of integrals, which are then solved (Gradshteyn, Ryzhik, Jeffrey, 1994, arts. 3.896, 3.952) to give a

power series for the probability density of the equal-amplitude N-term Fourier series sum.

$$p_Y(y) = \frac{e^{-y^2/(2Y_{rms}^2)}}{\sqrt{2\pi}Y_{rms}}\Big(1 - \frac{\Gamma(5/2)}{4\pi^{1/2}N}{}_1F_1[-2,1/2,y^2/(2Y_{rms}^2)] - \frac{\Gamma(7/2)}{9\pi^{1/2}N^2}{}_1F_1[-3,1/2,y^2/(2Y_{rms}^2)] - (\frac{11}{192N^3} - \frac{1}{32N^2})\frac{\Gamma(9/2)}{\pi^{1/2}}{}_1F_1[-4,1/2,Y^2/(2Y_{rms}^2)] + ..), \quad |y| < Na \tag{17}$$

$p_Y(|y| > Na) = 0$ and Y_{rms} is given by equation (3b). There are two special functions in equation (17), the gamma function Γ and the confluent hypergeometric function ${}_1F_1[n,\gamma,z]$. These are defined by Gradshteyn, Ryzhik, and Jeffrey (1994).

As N approaches infinity, the peak-to-rms (equation 4b) ratio approaches infinity, and equation (51) approaches the normal distribution,

$$\lim_{N\to\infty} p_Y(y) = \frac{1}{\sqrt{2\pi}Y_{rms}} e^{-y^2/(2Y_{rms}^2)} \tag{18}$$

as predicted by the central limit theorem (Cramer, 1970; Lin, 1976).

4. PROBABILITY DENSITY OF PEAKS

Theories for calculating the fatigue damage from a time history process generally require knowledge of the peaks and troughs in the time history. This task is made simpler if we assume that the time history is narrow band. If $Y(t)$ is *narrow band* that is, that each trajectory of $Y(t)$ which crosses zero has only a single peak before crossing the axis again, then (1) the number of peaks equals the number of times the time history crosses the axis with positive slope, and (2) only positive peaks occur for $Y(t) > 0$ and they are located at points of zero slope, $dY(t)/dt = 0$. Lin (1967, p. 304) gives expressions for the expected number of zero crossings with positive slope (peaks above the axis) per unit time for a general, not necessarily narrow band, process,

$$E[N_{0+}] = \int_0^\infty \dot{y} p_{Y\dot{Y}}(0,\dot{y}) d\dot{y} \tag{19}$$

and the probability density of the peaks for a narrow band process.

$$p_A(A) = -\frac{1}{E[N_{0+}]}\frac{d}{dA}\int_0^\infty \dot{y} p_{Y\dot{Y}}(A,\dot{y}) d\dot{y} \tag{20}$$

In order to apply these expressions, the joint probability distribution of Y and $\dot{Y}$ must be established. The joint probability density function $p_{Y\dot{Y}}(y,\dot{y})$ of the two random variable Y and $\dot{Y}$ is the probability that Y falls in the range between y and $y+dy$ and $\dot{y}$ falls in the range between $\dot{y}$ and $\dot{y}+d\dot{y}$, divided by $dyd\dot{y}$. The derivative of the sine wave Y (equation 12) with respect to time can be expressed in terms of Y,

$$dY/dt = \dot{Y} = -a_n\omega_n \, sin(\omega_n t + \phi_n) = \pm\omega_n\sqrt{a_n^2 - Y^2}, \quad |Y| \le a_n. \tag{21}$$

The joint probability density is the inverse Fourier transform of its characteristic function.

$$p_{Y\dot{Y}}(y,\dot{y}) = \int_{-\infty}^{\infty}\int_{-\infty}^{\infty} e^{-j2\pi(f_1 y + f_2 \dot{y})} C(f_1, f_2) df_1 df_2 \tag{30}$$

The proof of equations (28), (29), and (30) can be found in Chandrasekhar (1943), Willie (1987), Weiss and Shmueli (1987), and Weiss (1994, pp. 21-26).

Since the probability is symmetric about $y = \dot{y} = 0$, $p_{Y\dot{Y}}(y,\dot{y}) = p_{Y\dot{Y}}(-y,-\dot{y})$, only symmetric terms survive the integration. Substituting, equation (29) into equation (30) and expanding gives and integral expression for the joint probability of y and $\dot{Y}$.

$$p_{Y\dot{Y}}(y,\dot{y}) = \int_{-\infty}^{\infty}\int_{-\infty}^{\infty} \{\prod_{n=1}^{N} J_0(2\pi a_n \sqrt{f_1^2 + f_2^2\omega_n^2})\} cos(2\pi f_1 y) cos(2\pi f_2 \dot{y}) df_1 df_2 \tag{31}$$

It is also possible to expand the joint probability of Y and $\dot{Y}$ in as double finite Fourier series. The result is:

$$p_{Y\dot{Y}}(y,\dot{y}) = \frac{1}{L_Y L_{\dot{Y}}} \sum_{i=0}^{\infty}\sum_{k=0}^{\infty} \alpha_{ik} \{\prod_{n=1}^{N} J_0\Big(\pi a_n \sqrt{(\frac{i}{L_Y})^2 + (\frac{k\omega_n}{L_{\dot{Y}}})^2}\Big)\} cos(i\pi y/L_Y) cos(k\pi \dot{Y}/L_{\dot{y}}) \tag{32}$$

$$\alpha_{ik} = 1,\ i,k > 0; 1/2,\ i = 0\ or\ k = 0; 1/4,\ i = k = 0 \tag{33}$$

The expected number of peaks per unit time and the probability distribution of the narrow band peaks is obtained by substituting this equation into equations (19) and (20) and integrating. The results are:

$$E[N_{0+}] = \frac{L_{\dot{Y}}}{L_Y} \sum_{i=0}^{\infty}\sum_{k=0}^{\infty} \gamma_{ik} \{\prod_{n=1}^{N} J_0\Big(\pi a_n \sqrt{(\frac{i}{L_Y})^2 + (\frac{k\omega_n}{L_{\dot{Y}}})^2}\Big)\} \tag{34}$$

$$p_A(A) = \frac{\pi L_{\dot{Y}}}{L_Y^2 E[N_p]} \sum_{i=0}^{\infty}\sum_{k=0}^{\infty} i\gamma_{ik} \{\prod_{n=1}^{N} J_0(\pi a_n \sqrt{(\frac{i}{L_Y})^2 + (\frac{k\omega_n}{L_{\dot{Y}}})^2})\} sin(i\pi A/L_Y) \tag{35}$$

where

$$\gamma_{ik} = \begin{cases} 1/8, & i = k = 0, \\ 1/4, & i > 0, k = 0 \\ (1/2)[(-1)^k - 1]/(k\pi)^2, & i = 0, k > 0, \\ [(-1)^k - 1]/(k\pi)^2, & i > 0, k > 0. \end{cases} \tag{36}$$

If the frequencies are closely spaced so $\omega_n \approx \omega$ and hence $L_{\dot{Y}} \approx \omega L_Y$, then one positive peak is expected once per cycle,

$$E[N_{0+}] = \omega/(2\pi) \tag{37}$$

and the probability density of narrow band peaks becomes,

$$p_A(A) = \frac{2\pi^2}{L_Y} \sum_{i=0}^{\infty} \sum_{k=0}^{\infty} i\gamma_{ik} \{ \prod_{n=1}^{N} J_0(\frac{\pi a_n}{L_Y} \sqrt{i^2 + k^2}) \} sin(\frac{i\pi A}{L_Y}). \tag{38}$$

Figure 7 shows probability density of narrow band peaks for N=2,3, and 4 equal amplitude ($a_i = 1$) equal frequency series using equation (38). Each sum in equation (38) was carried to 40 terms.

A power series solution for equation (20) can be found if all N terms in the series have equal amplitude and frequency. The result is

$$p_A(A) = \frac{Ae^{-A^2/(2Y_{rms}^2)}}{Y_{rms}^2} \left(1 - \frac{1}{4N} + \frac{1}{4N} \frac{A^2}{Y_{rms}^2} - \frac{1}{32N} \frac{A^4}{Y_{rms}^4} + ...\right) \tag{39}$$

In the limit as N becomes infinite these equations become,

$$p_{Y\dot{Y}}(y, \dot{y}) = \frac{e^{-(1/2)(y^2/Y_{rms}^2 + \dot{y}^2/\dot{Y}_{rms}^2)}}{2\pi Y_{rms} \dot{Y}_{rms}} \tag{40}$$

$$p_A(A) = \frac{Ae^{-A^2/(2Y_{rms}^2)}}{Y_{rms}^2} \tag{41}$$

Equation (40) is in agreement with an expression given by Crandall and Mark (1963, p. 47) and equation (41)is the Rayleigh distribution.

Equations (20), (35), (38), and (41) are conservative when applied to non-narrow band processes in the sense that any troughs above the axis (points with $Y > 0$ and $dY/dt = 0$ but $d^2Y/dt^2 > 0$) are counted as peaks (Lin, 1967, p. 304; Powell, 1958; Broch, 1963).

Equations (35), (38) and (41) can provide probability distributions for peaks of narrow band processes as a function of the number of sine waves from one to infinity and thus they model random processes with peak-to-rms ratios from $2^{1/2}$ to infinity.

5. FATIGUE UNDER RANDOM LOADING

Fatigue tests are most often made with constant-amplitude sinusoidal loading. The number of cycles to failure is plotted versus the stress that produced failure and the data is often fitted with an empirical expression. MIL-HDBK-5G (1994) uses the following empirical expression to fit fatigue data,

$$log\ N_f = B_1 + B_2 log(S_{eq} - B_4), \quad S_{eq} = S(1 - R)^{B_3}. \tag{42}$$

Here N_f is the cycles to failure during sinusoidal loading that has maximum stress S per cycle. R is the ratio of maximum to minimum stress during a cycle. $R = -1$ is fully

reversed stress cycling. B_1 though B_4 are fitted parameters. With a little work, we can put this expression in the form used by Crandall and Mark (1963, p. 113).

$$N = cS_d^{-b} \tag{43}$$

where $S_d = S(1-R)^{B_3} - B_4$, $c = 10^{B_1}$, and $b = -B_2$. For cycling in a time history that has non constant amplitude, Miner-Palmgren proposed that the accumulated damage is the sum of the ratios of the number of cycles at each amplitude to the allowing number of cycles to failure at that amplitude (equations 42 and 43).

$$D = \sum_i n(S_i)/N_f(S_i) \tag{44}$$

where $n(S_i)$ is the number of cycle accumulated at stress amplitude S_i and N_f is the number of stress cycles at this amplitude which would cause failure.

Following Miles(1954) and Crandall and Mark(1963), the expected fractional damage for a random stress cycling in system with dominant cycling at frequency f in time t_f, is

$$E[D[t_f)] = ft_f \int_0^\infty \frac{p_A(S)}{N_f(S)} dS \tag{45}$$

where $p_A(S)$ is the probability density of a stress cycle having amplitude S and $N_f(S)$ is the number of allowable cycles to failure at this stress. Failure under random loading is expected when the expected damage is unity. Setting $E[D[t_d)] = 1$ at time t_d such that $ft_d = N_d$, the inverse of the expected number of random vibration cycles to failure is

$$(N_d)^{-1} = \int_0^\infty \frac{p_A(S)}{N_f(S)} dS \tag{46}$$

This expression can be used to create a fatigue curve for random cycling given the probability density of the random stress cycle amplitudes ($p_A(S)$) and a fatigue curve (equation 42 with parameters B_1 though B_4 and R) for sinusoidal cycling.

Substituting the probability density expression for narrow band amplitude (equation 35) and for the fatigue curve(equations 42 or 43) into equation (46) and integrating, we obtain an expression for the expected number of cycles to failure as a function of the number of sine waves and their amplitudes. For N equal amplitude sine waves this is,

$$(N_d)^{-1} = \frac{2\pi^2}{c(1-R)^{B_3}L_y} \sum_{i=0}^{\infty} \Big(\sum_{k=0}^{\infty} i\gamma_{ik} [J_0(\frac{\pi}{N}\sqrt{i^2+k^2}]^N \Big) \tag{47}$$

$$\Big(\frac{i\pi(L_y(1-R)^{B_3} - B_4)^{2+b}}{(2+b)L_y(1-R)^{B_3}} cos[\frac{i\pi B_4}{(1-R)^{B_3}L_y}]_pF_q[\{1+\frac{b}{2}\},\{\frac{3}{2},2+\frac{b}{2}\},-\frac{i^2\pi^2(L_y(1-R)^{B_3}-B_4)^2}{4L_y^2(1-R)^{2B_3}}]$$

$$+ \frac{(L_y(1-R)^{B_3} - B_4)^{1+b}}{1+b} sin[\frac{i\pi B_4}{(1-R)^{B_3}L_y}]_pF_q[\{\frac{1}{2}+\frac{b}{2}\},\{\frac{1}{2},\frac{3}{2}+\frac{b}{2}\},-\frac{i^2\pi^2(L_y(1-R)^{B_3}-B_4)^2}{4L_y^2(1-R)^{2B_3}}$$

Recall that for this case $L_y = Na$, the rms value is $Y_{rms}^2 = (1/2)Na$ and the peak-to-rms ratio is $Peak/Yrms = \sqrt{2N}$ (equations 2 though 4). ${}_pF_q[..]$ is the generalized hypergeometric function which is a series of polynomials. It is described by Gradshteyn, Ryzhik, and Jeffrey (1994).

It is also possible to establish the fatigue curve using the Rayleigh distribution (equation 18) and the MIL-HDBK-5 fatigue curve (equation 42). The result is

$$(N_d)^{-1} = \frac{2^{(b-1)/2}}{c(1-R)^{2B_3}Y_{rms}^2} exp[-B_4^2/(2Y_{rms}^2(1-R)^{2B_3}]((1-R)^{2B_3}Y_{rms}^2)^{b/2} \quad (48)$$
$$\Big(2^{1/2}\Gamma[1+\frac{b}{2}]((1-R)^{2B_3}Y_{rms}^2{}_1F_1[1+\frac{b}{2},\frac{1}{2},\frac{B_4^2}{2Y_{rms}^2(1-R)^{2B_3}}]$$
$$-B_4^2{}_1F_1[1+\frac{b}{2},\frac{3}{2},\frac{B_4^2}{2Y_{rms}^2(1-R)^{2B_3}}])$$

$$+B_4(1-R)^{B_3}Y_{rms}(\Gamma[\frac{1}{2}+\frac{b}{2}]{}_1F_1[\frac{1}{2}+\frac{b}{2},\frac{1}{2},\frac{B_4^2}{2Y_{rms}^2(1-R)^{2B_3}}]$$
$$-2\Gamma[\frac{3}{2}+\frac{b}{2}]{}_1F_1[\frac{3}{2}+\frac{b}{2},\frac{3}{2},\frac{B_4^2}{2Y_{rms}^2(1-R)^{2B_3}}])\Big)$$

${}_1F_1[..]$ is the confluent hypergeometric function which is described by Gradshteyn, Ryzhik, and Jeffrey (1994).

Much of the complexity of these last two equations arises from the term B_4 which is associated with an endurance limit in the fatigue equation. That is, equation (42)predicts that sinusoidal stress cycling with stress less than $B_4/(1-R)^{B_3}$ produces no fatigue damage. If we set $B_4 = 0$ to set the endurance limit to zero, then equation (48) simplifies to,

$$N_d = \frac{c}{2^{b/2}\Gamma[1+b/2]}\left(Y_{rms}(1-R)^{B_3}\right)^{-b} \quad (49)$$

This result for cycles to failure under Gaussian loading without an endurance limit is also given by Crandall and Mark (1963, p. 117).

Equations (47), (48) and (49) allow us to compute the fatigue curves of a material under random loading from a fatigue curve generated under sinusoidal loading (equation 43) for narrow band random processes with any peak-to-rms ratio from $2^{1/2}$ to infinity.

6. APPLICATION

Figure 8 is the MIL-HDBK-5G fatigue curve for aluminum 2024-T3 with a notch factor of Kt=4 under sinusoidal loading with various R values. The fitted curve shown in the figure, gives the following parameters for equation (42).

$$B_1 = 8.3, \quad B_2 = -3.30, \quad B_3 = 0.66, \quad B_4 = 8.4$$

The B_2 and B_3 are dimensionless. B_4 has the units of ksi, that is thousands of psi, and 10^{B_1} has units of $(ksi)^{-B_2}$. These B_1,..B_4 are substituted into equations (43), (47), (48), and (49).

The fatigue curves under random loading are computed as follows, 1) the number of sine waves N is chosen and this fixes the peak-to-rms ratio from equation (3b), 2) set of values of rms stresses are chosen and for each the corresponding sine waves amplitudes are computed using equation (3b), $a = S_{rms}\sqrt{2/N}$ (note that the peak stress much exceed B_4=8.5 ksi), and 3)the cycles to failure are calculated from equation (47) for finite peak-to-rms ratios and equation (48) for Gaussian loading (infinite peak-to-rms).

For single sine wave, the peak-to-rms ratio is $2^{1/2}$, equation 4b, and the fatigue curve interms of rms stress is adapted from the empirical data fit (equations 42, 43) by substituting $2^{1/2}S_{rms}$ for the stress amplitude.

$$N_d = c(2^{1/2}S_{rms}(1-R)^{B_3} - B_4)^{-b} \tag{50}$$

where $b = -B_2$ and $c = 10^{B_1}$. Some results are shown in Figure 9 for R=-1.

7. CONCLUSIONS

Analysis has been made to determine the properties of a random process consisting of the sum of a series of sine waves with deterministic amplitudes and random phase angles. The joint probability density of the sum and its first two derivatives is determined. The probability density of the sum and narrow band peaks have been found for an arbitrary number of statistically independent sine wave terms. The fatigue cycles-to-failure resulting from these processes has been found.

1. The peak-to-rms ratio of the sum of mutually independent terms exceeds unity. If all terms have the same peak and rms values then the peak-to-rms ratio of the series sum increases with the square root of the number of terms in the series. The probability of the series sum is zero beyond a maximum value, equal to the sum of the series amplitudes, and below the minimum value. Hence, he probability densities of the finite series, their peaks, and their envelope are non Gaussian.

3. The formulas allow the direct calculation of the probability density of the series and its peaks from its power spectra density (PSD) under the assumption that each spectral component is statistically independent.

4. The fatigue curves of a material under random loading with any peak-to-rms ratio from $2^{1/2}$ to infinity can be computed directly from the fatigue curve of the material under sinusoidal loading.

REFERENCES

Abramowitz, M. and I.A. Stegun 1964 *Handbook of Mathematical Functions*, National Bureau of Standards, U.S. Government Printing Office, Washington D.C. Reprinted by Dover.

Bennett, W.R., 1944 *Acoustical Society of America* **15**, 165. Response of a Linear Rectifier to Signal and Noise.

Bendat, J.S., 1958 *Principles and Applications of Random Noise Theory*, Wiley, N.Y.

Chandrasekhar, S., 1943,*Reviews of Modern Physics*, **15**, 2-74. Also available in Wax, N. (ed) *Selected Papers on Noise and Stochastic Processes*, Dover, N.Y., 1954.

Cramer, H., 1970 *Random Variables and Probability Distributions*, Cambridge at the University Press.

Crandall, S.H., and C. H. Mark 1963 *Random Vibrations in Mechanical Systems*, Academic Press, N.Y.

Department of Defense, 1994 *Metallic Materials and Elements for Aerospace Vehicle Structures*, MIL-HDBK-5G.

Gradshteyn, I.S., I.M. Ryzhik, and A. Jeffrey 1994 *Table of Integrals, Series, and Products* 5th Ed., Academic Press, Boston.

Lin, P.K., 1976 *Probabilistic Theory of Structural Dynamics*, Krieger, reprint of 1967 edition with corrections.

Mathematica, 1995 Ver 2.2, Wolfram Research, Champaign, Illiinois.

Miles, J., 1954 *Journal of Aeronautical Sciences* **21**, 753-762. On Structural Fatigue under Random Loading.

Powell, A., 1958 *Journal of the Acoustical Society of America* **30** No. 12, 1130-1135. On the Fatigue Failure of Structure due to Vibrations Excited by Random Pressure Fields.

Rayleigh, J.W.S. 1880 *Philosophical Magazine* **X** 73-78. On the Resultant of a Large Number of Vibrations of the Same Pitch and Arbitrary Phase. Also see *Theory of Sound*, Vol 10, art. 42a, reprinted 1945 by Dover, N.Y.. and *Scientific Papers*, Dover, N.Y., 1964, Vol. I, pp. 491-496.

Rice, S.O., 1944 *The Bell System Technical Journal* **23** 282-332. Continued in 1945 **24** , 46-156. Mathematical Analysis of Random Noise. Also available in Wax, N. (ed) *Selected Papers on Noise and Stochastic Processes*, Dover, N.Y., 1954.

Shmulei, U. and G.H. Weiss 1990 *Journal of the American Statistical Association* **85** 6-19. Probabilistic Methods in Crystal Structure Analysis.

Sveshnikov, A.A. 1968 *Problems in Probability Theory, Mathematical Statistics and Theory of Random Functions* Dover, N.Y., translation of 1965 edition. pp. 74, 116.

Tolstov, G.P., 1962 *Fourier Series*, Dover, N.Y., pp. 173-177. Reprint of 1962 edition.

Weiss, G.H., 1994 *Aspects and Applications of the Random Walk*, North-Holland, Amsterdam.

Weiss, S.H. and U. Shmulei, 1987 *Physica* **146A** 641-649. Joint Densities for Random Walks in the Plane.

Willie, L.T., 1987 *Physica* **141A** 509-523. Joint Distribution Function for position and Rotation angle in Plane Random Walks.

Wirsching, P.H., T.L. Paez, and K. Ortiz 1995 *Random Vibrations, Theory and Practice*, Wiley-Interscience, N.Y., pp. 162-166.

NOMENCLATURE

A	amplitude, peak, or envelope
a_n	amplitude of the nth sine wave, $a_n \geq 0$
B_n	fitted parameter in equation (42)
$C(f)$	characteristic function with parameter f
$C(f_1, f_2)$	joint characteristic function with parameters f_1 and f_2
$E[N_p]$	expected number of positive peaks per unit time
$E[N_{0+}]$	expected number of zero crossing with positive slope per unit time
${}_1F_1$	confluent hypergeometric function (Gradshteyn, Ryzhik, Jeffrey, 1994, art. 9.210)
${}_pF_q$	generalized hypergeometric function (Gradshteyn, Ryzhik, Jeffrey, 1994, art. 9.210)
f	parameter in Fourier transform
i	integer index
j	imaginary constant, $\sqrt{-1}$
J_0	Bessel function of first kind and zero order
k	integer index
K	complete elliptic integral of first kind, equation (33a)
L_Y	$a_1 + a_2 + .. + a_N$, sum of amplitudes
$L_{\dot{Y}}$	$\omega_1 a_1 + \omega_2 a_2 + .. + \omega_N a_N$, sum of velocity amplitudes
m	integer index
N	number of terms in series
N_f	cycles to failure
n	integer index, n=1,2,..N
$P_Y(y)$	cumulative probability, the integral of $p_Y(x)$ from x=$-\infty$ to y
$p_Y(x)$	probability density of random parameter Y evaluated at $Y = x$
$p_{XY}(x, y)$	joint probability density of X and Y evaluated at $Y = y$ and $X = x$
S	stress
t	time, $0 \leq t < T$
T	length of time interval
Y	sum of N modes or terms, $-L_Y \leq Y \leq L_Y$
$\dot{Y}$	first derivative with respect to time of Y, $-L_{\dot{Y}} \leq Y \leq L_{\dot{Y}}$
X	a random variable
α_{ij}	dimensionless coefficient, equation (33)
Γ	gamma function, $\Gamma[(2n+1)/2] = \pi^{1/2} 2^{-n} (2n-1)!!$
γ_{ij}	dimensionless coefficient, equation (36)
δ	Dirac delta function
π	3.1415926..
$\Pi_{n=1}^{N} x_n$	$x_1 x_2 .. x_N$, product of terms
ϕ_n	phase angle of the nth sine wave, a uniformly distributed independent random variable
ω	circular frequency, a positive (non zero) real number
ω_n	circular frequency of the nth term, a non zero integer multiple of $2\pi/T$

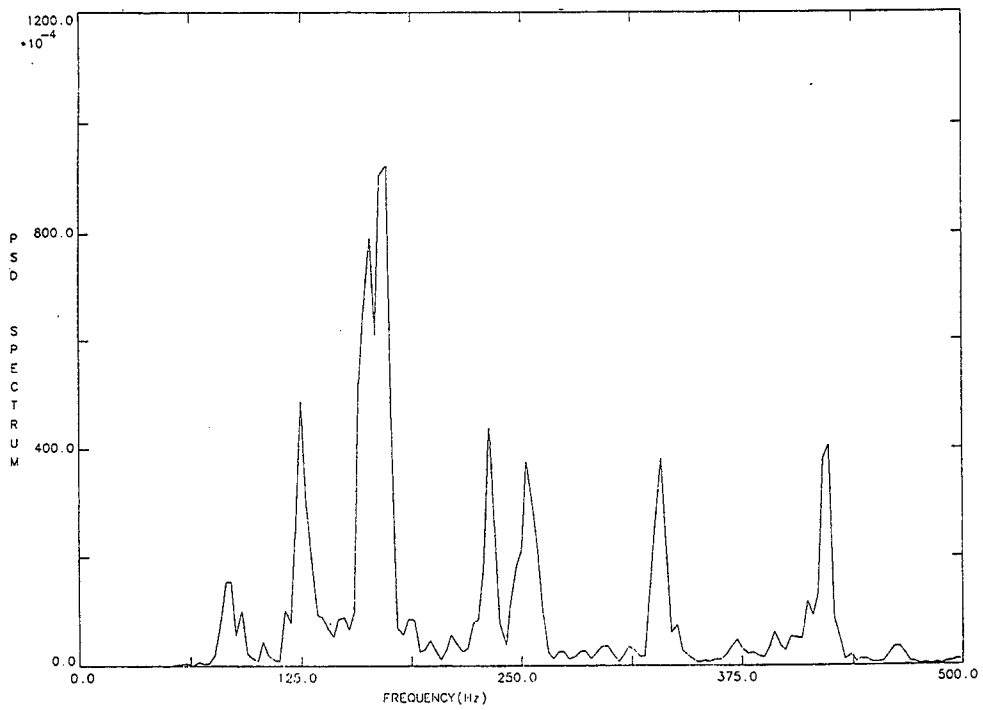

Figure 1 Spectrum of vibration of a component on a turbojet engine cowling. Note the finite number of distinct peaks.

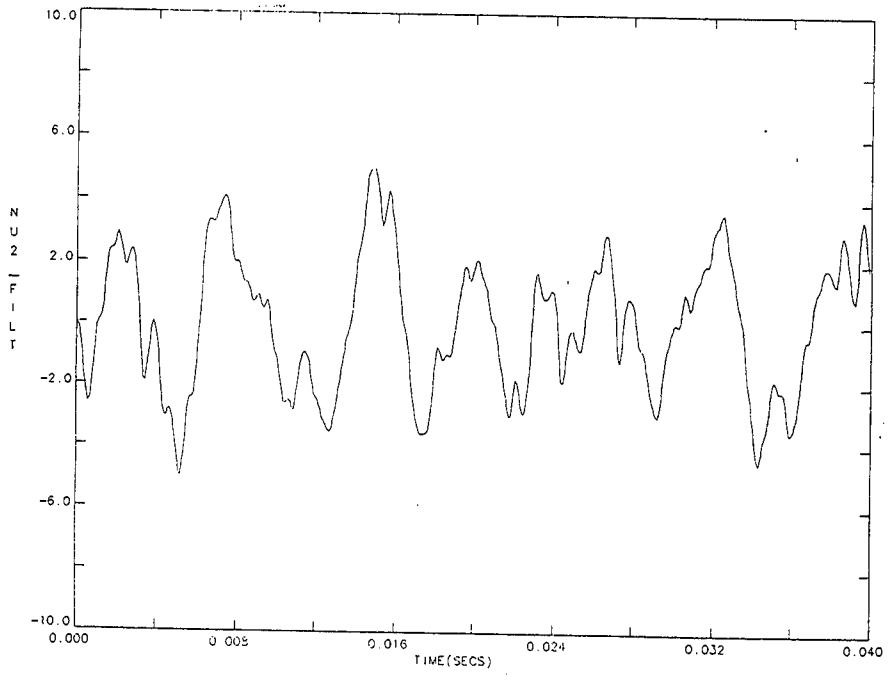

Figure 2 Sample of the time history associated with the spectrum of Figure 1. Note the signal is bounded, irregular and quasi sinusoidal.

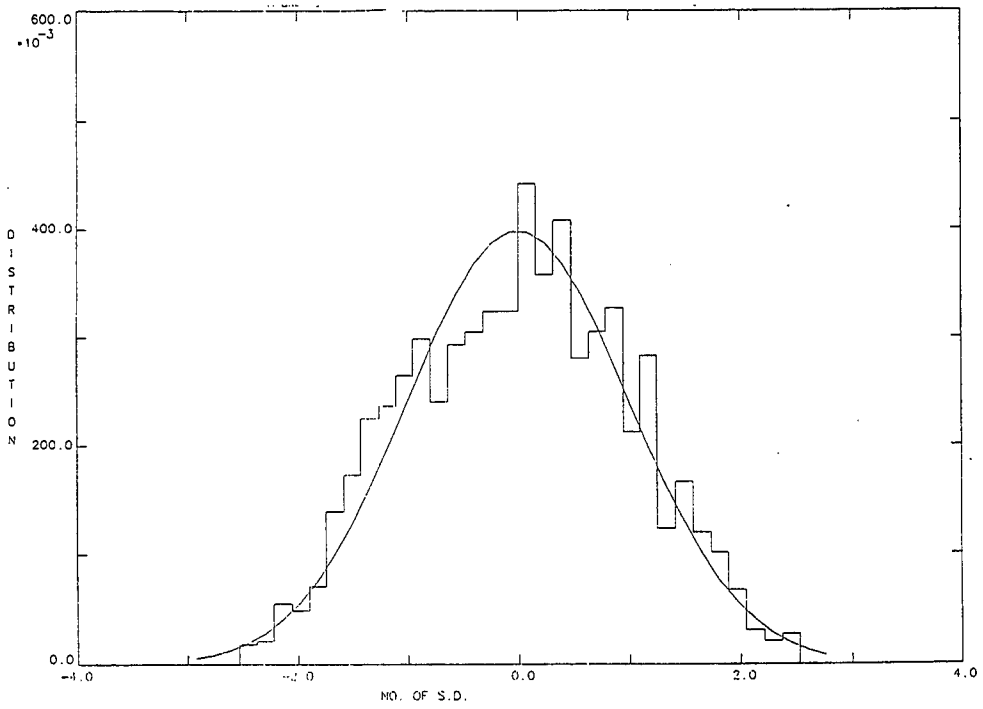

Figure 3 Probability density of the time history of Figures 1 and 2. Note that the maximum values do not exceed plus or minus 2.5 standard deviations.

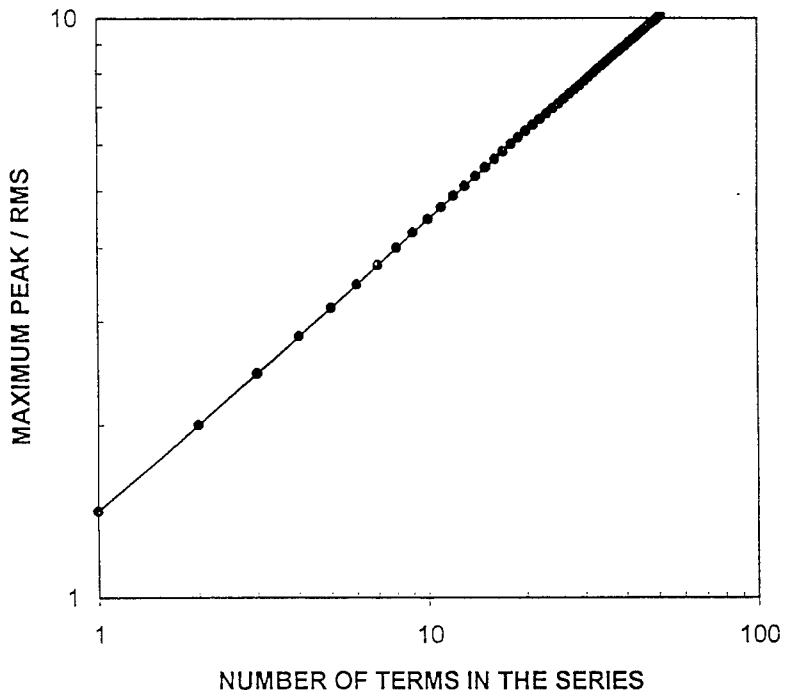

Figure 4 Ratio of the peak to the root-mean-square value of a Fourier series of N equal amplitude terms (equation 4b)

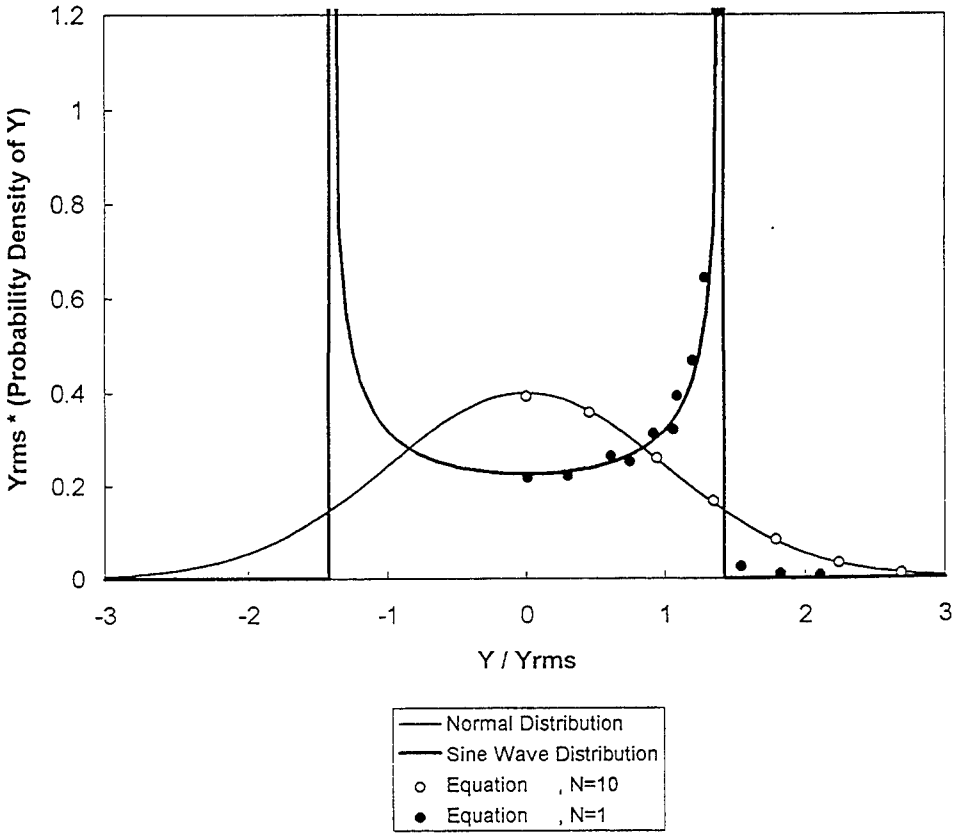

Figure 5 Normal probability density (equation 18) and sine wave probability density (equation 6) in comparison with results of numerical integration of equation (13) for N=1 and N=10.

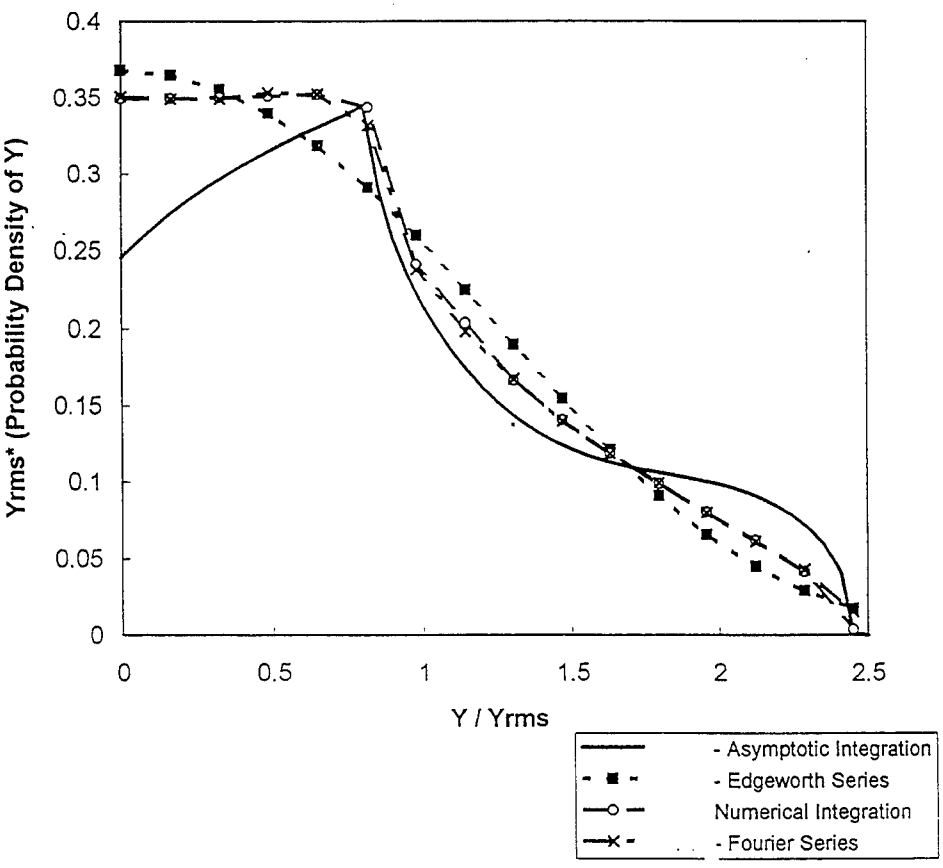

Figure 6 Probability density of the sum of three equal-amplitude sine waves computed by various techniques.

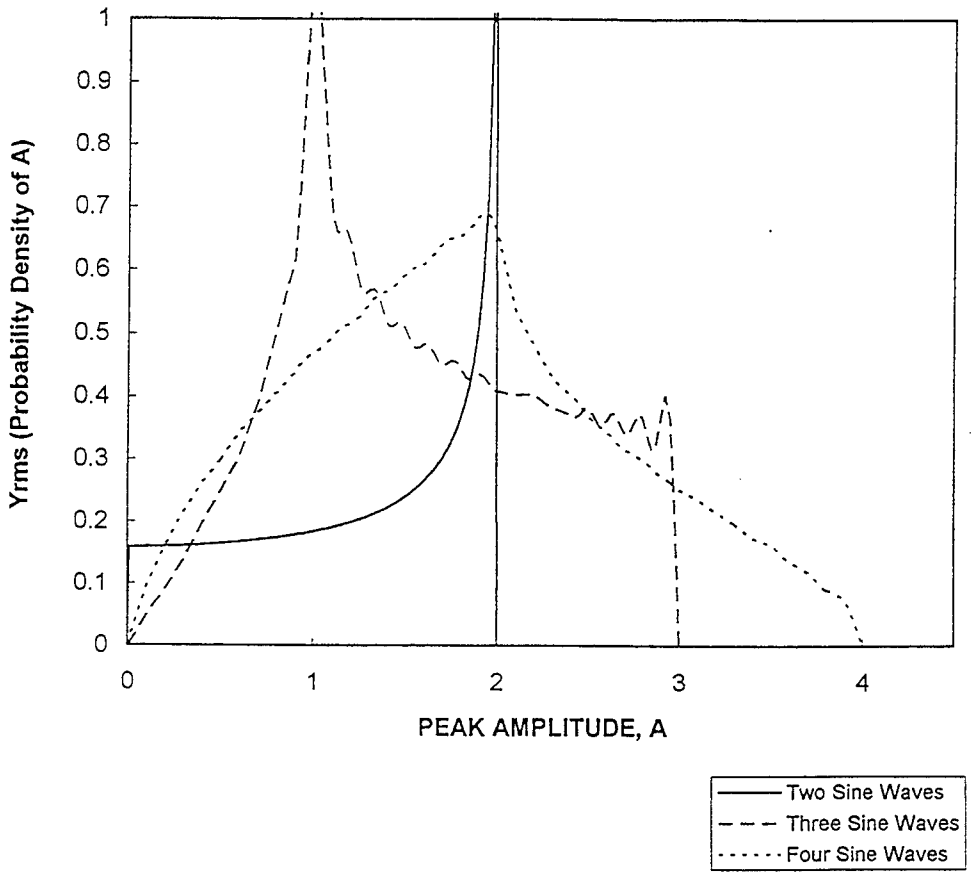

Figure 7 Probability density of peaks in narrow band series with equal amplitudes ($a_1 = a_2.. = 1$) and frequencies.

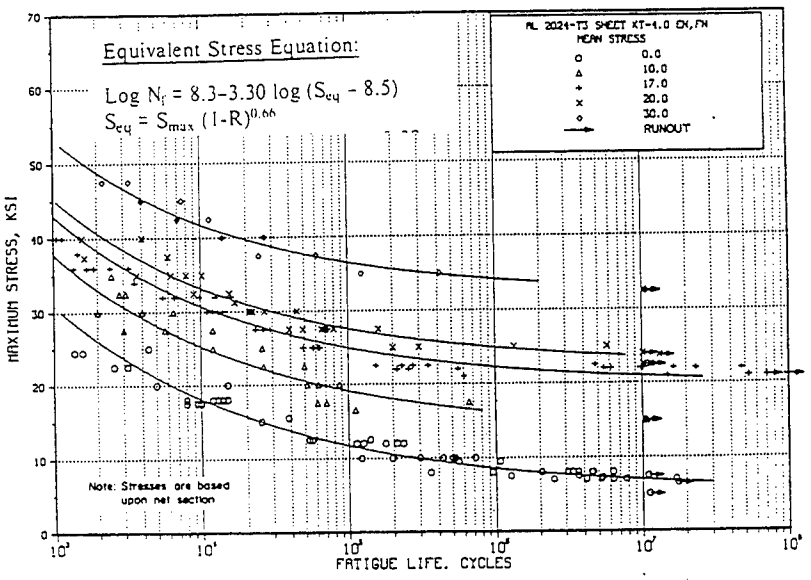

FIGURE 3.2.3.1.8(h). *Best-fit S/N curves for notched, K_t = 4.0 of 2024-T3 aluminum alloy sheet, longitudinal direction.*

Figure 8 Fatigue curves for notched 2024-T3 aluminum alloy with Kt=4. MIl-HDBK-5G (1994, p. 3-115)

ACOUSTIC FATIGUE I

Strain Power Spectra of a Thermally Buckled Plate in Random Vibration

Jon Lee and Ken R. Wentz
Wright Laboratory (FIB)
Wright-Patterson AFB, OH 45433, USA

Abstract

Several years ago, Ng and Wentz reported strain power spectra measured at the mid-point of a buckled aluminum plate which is randomly excited by an electrodynamic shaker attached to the clamped-plate boundary fixture. We attempt to explain the peculiar features in strain power spectra by generating the corresponding power spectra by the numerical simulation of a single-mode equation of motion. This is possible because the essential dynamics takes place in the frequency range just around and below the primary resonance frequency.

1. Introduction

For high performance military aircraft and future high-speed civil transport planes, certain structural skin components are subjected to very large acoustic loads in an elevated thermal environment [1]. This is because high-speed flights call for a very powerful propulsion system and thereby engendering acoustic loads in the anticipated range of 135–175 dB. More importantly, because of the aerodynamic heating in hypersonic flights and the modern trend in integrating propulsion sub-systems into the overall vehicular configuration, some structural components must operate at high temperatures reaching up to 1300°F. Hence, the dual effect of thermal and acoustic loading has given rise to the so-called *thermal-acoustic structural fatigue* [2,3].

Generally, raising the plate temperature uniformly but with an immovable edge boundary constraint would result in thermal buckling, just as one observes flexural buckling as the inplane stress along plate edges is increased beyond a certain critical value. This equivalence has been recognized [4,5] and exploited in previous analytical and experimental investigations of the thermal-acoustic structural fatigue [6,7,8]. An experimental facility for thermal-acoustic fatigue, termed the Thermal Acoustic Fatigue Apparatus, was constructed at the NASA Langley Research Center in the late 80's. Under the acoustic loading of 140–160 dB, Ng and Clevenson [9] obtained some strain measurements of root-mean-square value and power spectral density (PSD) on an aluminum plate heated up to 250°F. Later, Ng and Wentz [10] have repeated the heated Aluminum plate experiment but by randomly exciting the clamped-plate boundary fixture by a shaker, and thereby recovering similar strain measurements.

It should be noted that Ng and his colleagues [7,9,10] were the first to achieve sufficient plate heating to induce thermal buckling and thus observe the *erratic* snap-through under the acoustic or shaker excitations. Here, by erratic

we mean that a snap-through from one static buckled position to another takes place in an unpredictable fashion. We reserve the adjective *chaotic* for a snap-through occurring under the deterministic single-frequency forcing [11,12]. It has already been observed that certain of the buckled plate experiment can be explained, at least qualitatively, by a single-mode model of plate equations. This is also validated by a theoretical analysis. Indeed, we showed that a single-mode Fokker-Planck formulation can predict the high-temperature moment behavior and displacement and strain histograms of thermally buckled plates, metallic and composite [13,14].

In retrospect, a single-mode model has proven more useful than originally intended. That is, the single-mode Fokker-Planck formulation of an isotropic plate lends itself to predicting certain statistics of composite plates which are simulated by multimode equations or tested experimentally by multimode excitations. For a refined and more quantitative comparison, one must inject more realism into dynamical models by including the multimode interactions. However, before giving up the single-mode plate equation, there is an important problem that this simple model is well suited for investigation. That is, prediction of the strain PSD measurement by Ng and Wentz [10]. As we shall see in Sec. 4, the strain PSD of a thermally buckled plate exhibits a strong spectral energy transfer toward zero frequency, and thereby saturating frequency range well below the primary resonance frequency. This downward spectral energy transfer can be modeled quite adequately by the single-mode plate equation without necessitating multimode interactions.

2. Equation of motion for the aluminum plate experiment

By the Galerkin procedure, the von Karman-Chu-Herrmann type of large-deflection plate equations give rise to infinitely coupled modal equations [15]. However, much has been learned from a prototype single-mode equation for displacement q [13,14].

$$\ddot{q} + \beta \dot{q} + k_o(1 - s)\, q + \alpha q^3 = g_o + g(t), \tag{1}$$

where the overhead dot denotes d/dt and the viscous damping coefficient is $\beta = 2\xi\sqrt{k_o}$ with damping ratio ξ. For the clamped plate, we have

$$\begin{aligned}
k_o &= \tfrac{16}{3}(\gamma^4 + 2\gamma^2/3 + 1), \\
s &= T_o\,[1 + (1-\mu)\,\delta_v(1 + \gamma^2(\gamma^2+1)^{-2})/6], \\
\alpha &= \tfrac{32\gamma^2}{3}\{(\gamma^2 + \gamma^{-2} + 2\mu) + \tfrac{4}{9}(1-\mu^2)[\tfrac{17}{8}(\gamma^2+\gamma^{-2}) + 4(\gamma+\gamma^{-1})^{-2} \\
&\qquad + (\gamma+4\gamma^{-1})^{-2} + (4\gamma+\gamma^{-1})^{-2}]\}, \\
g_o &= (\gamma^4 + 2\gamma^2/3 + 1)\,\delta_g T_o/6.
\end{aligned}$$

Note that the expressions for s and g_o are specific to the typical temperature

variation and gradient profiles assumed in Ref. [15]. Here, $\gamma = b/a$ is the aspect ratio of plate sides a and b, and μ is Poisson's ratio. The uniform plate temperature T_o is measured in units of the critical buckling temperature. The maximum temperature variation on the mid-plate plane is denoted by $T_o\delta_v$, and $T_o\delta_g$ is the maximum magnitude of temperature gradient across the plate thickness, where δ_v and δ_g are scale factors. Hence, $\delta_v = 0$ signifies no temperature variation over the mid-plate plane, and $\delta_g = 0$ zero temperature gradient across the plate thickness. Finally, $g(t)$ denotes the external forcing.

The parameter s represents thermal expansion due to both the uniform plate temperature rise above room temperature and temperature variation over the mid-plate uniform temperature. The combined stiffness $k_o(1-s)q$ consists of the structural stiffness k_oq and thermal stiffness $-sk_oq$, which cancel each other due to the sign difference. It is positive for $s<1$, then Eq. (1) has the form of Duffing oscillator with a cubic term multiplied by α, which represents geometric nonlinearity of membrane stretching. For $s>1$ Eq. (1) reduces to the so-called *buckled-beam* equation of Holmes [11] with a negative combined stiffness. In contrast, g_o denotes thermal moment induced by a temperature gradient across the plate thickness; hence, it appears in the right-hand side of Eq. (1) as an additional forcing. The interplay of the terms involving s, α, and g_o can best be illustrated by the potential energy [15]

$$U(q) = -g_o q + k_o(1-s)q^2/2 + \alpha q^4/4. \tag{2}$$

Fig. 1 shows that $U(q)$ is symmetric when $g_o = 0$. For $s<1$ it has a single well which splits into a double well as s exceeds unity. Note that the distance between the twin wells increases as $\sqrt{s}$ for large s (Fig. 1(b)). This interpretation is valid approximately for $g_o > 0$. That is, a positive g_o lowers the positive side potential ($q>0$) and raises the negative side potential ($q<0$), and thereby rendering the potential energy asymmetric.

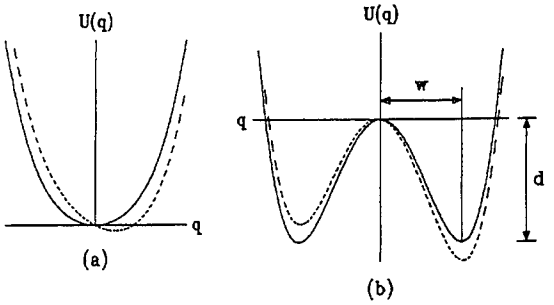

Fig. 1 Potential energy. (a) $s<1$; (b) $s>1$, $w = \sqrt{k_o(s-1)/\alpha}$, $d = -(k_o(s-1))^2/4\alpha$.
(——— $g_o = 0$; – – – $g_o > 0$)

It must be pointed out that Eq. (1) is dimensionless and involves explicitly only γ and μ. For the aluminum plate experiment [10], γ=10 in./8 in. and $\mu=\sqrt{0.1}$, so that k_o=23.91 and α=85.33. If we further assume $\delta_v=\delta_g=0$ for simplicity, the thermal parameter reduces to $s=T_o$. Previously, Eq. (1) was used for the investigation of stationary Fokker-Planck distribution which involves only the ratio β/F, where F is the constant power input [13,14]. Hence, nondimensionalization has indeed spared us from specifying in detail other plate parameters. Things are however different in numerical simulation because we must know the characteristic scales to correctly interpret time-dependent solutions. By retracing the derivation, we find that the dimensionless quantities in Eq. (1) are (Eq. (IV.1) in Ref. [1])

$$q=\bar{q}/h, \quad t=\bar{t}/t^*, \quad g=\bar{g}/g^*, \tag{3}$$

where the overhead bar denotes the physical quantity. Here, the plate thickness h, $t^*=(b/\pi)^2\sqrt{\rho h/D}$, and $g^*=\rho(h/t^*)^2$ are the characteristic length, time, and force, respectively (ρ = mass density, $D=Eh^3/12(1-\mu^2)$, E= Young's modulus of elasticity), as listed in Table I. We now rewrite Eq. (1) with the numerical coefficients (Table I).

$$\ddot{q}+0.0978\dot{q}+23.91(1-s)\,q+85.33q^3=\frac{\bar{g}(t)}{0.058psi}, \tag{4}$$

where $\bar{g}(t)$ has the unit of psi.

Table I. Parameter values for the aluminum plate experiment

γ, μ, ξ, k_o, α	10 in./8 in., $\sqrt{0.1}$, 0.01, 23.910, 85.332
s, δ_v, δ_g	T_o, 0, 0
h, t^*, g^*	0.05 in., $3.305\ 10^{-3}$sec.$^+$, $5.806\ 10^{-2}$ psi$^+$

(+) ρ = 0.098 lb/in^3 and E =1.03 10^7 psi.

3. Monte-Carlo simulation

Because of δ_g=0, Eq. (4) has the standard form of Duffing (s<1) and Holmes (s>1) oscillators. In stead of a single frequency for forcing $\bar{g}(t)$ [11, 12], in Monte-Carlo simulation all forcing frequencies are introduced up to a preassigned maximum f_{max} so that forcing represents a plausible physical realization. Of course, particular interest here is a constant PSD. We shall begin with generation of a time-series for random processes with such a PSD.

3.1 Random forcing time-series

We adopt here the procedure for generating a time-series of Shinozuka and Jan [16], which has been used for a oscillator study [17] and extensively for structural simulation applications by Vaicaitis [18,19]. Since it relies heavily on the discrete fast Fourier transforms, such as FFTCF and FFTCB subroutines of the IMSL library, it is more expedient to describe the procedure operationally rather than by presenting somewhat terse formulas. Let us

introduce N_f frequency coordinates which are equally spaced in $[0, f_{\max}]$ with the band width $\Delta f = f_{\max}/N_f$. Now, the task is to generate a time-series of total time T that can resolve up to $f_{\max}$. Assume T is also divided into N_t time coordinates with the equal time interval $\Delta t = T/N_t$. From the time-frequency relation $T = 1/\Delta f$, we find $f_{\max} = N_f/N_t\Delta t$. If we choose

$$N_f = \frac{N_t}{2}, \tag{5}$$

$f_{\max}$ is the Nyquist frequency, consistent with our original definition of the upper frequency limit of resolution.

A random time-series with a constant PSD can be generated in the following roundabout way. We begin by assuming that we already have a forcing power spectrum $\Phi_g(f)$ of constant magnitude over $[0, f_{\max}]$. Such a PSD may be represented by a complex array $A_n = \sqrt{C}\exp(-2\pi i\theta_n)$ (n = 1, ..., N_f), where θ_n takes a random value distributed uniformly in [0, 1]. Clearly the magnitudes of A_n are C, hence $\Phi_g(f) = C$. We then enlarge the complex array A_n by padding with zeros for $n = N_f+1$, ..., N_t, and Fourier transform it to obtain a complex array B_n (n = 1, ..., N_t). The random time-series for $\bar{g}_n$ is now given by the real part of B_n

$$\bar{g}_n = \text{Real part of } B_n. \ (n = 1, ..., N_t) \tag{6}$$

As it turns out, when $\bar{g}_n$ is padded with zeros for the imaginary components and Fourier transformed, we recover the original array A_n (n=1, ..., N_f) with $\Phi_g(f) = C$. Since the spectrum area $Cf_{\max}$ is nothing but total forcing power $\langle\bar{g}^2\rangle$ (say, in psi^2), we can relate C with the variance $\langle\bar{g}^2\rangle$ of pressure fluctuations, which is often expressed by the sound pressure level (SPL) in dB, according to SPL=10 log$\langle\bar{g}^2\rangle/p_o^2$, where p_o=2.9 10^{-9} psi. Hence,

$$C = \frac{p_o^2\, 10^{SPL/10}}{f_{\max}}. \tag{7}$$

Here, Eqs. (6) and (7) defined heuristically are meant to explain the corresponding formulas (2) and (12) in Ref. [18].

For the numerical simulation we first note that the resonance frequency of Eq. (1) is $f_r = \sqrt{k_o}/2\pi \approx 0.778$ for s = 0. This gives the dimensional resonance frequency $f_r/t^* \approx 235.5$ Hz which is somewhat larger than the experimental 217.7 Hz (Fig. 3(a)). As shown in Table II, we assign $f_{\max}$=7 (~9f_r) because the electrodynamic shaker used in the experiment [10] has the upper frequency limit 2000 Hz.

Table II. Dimensionless parameter values for the numerical simulation

$f_{\max}$, N_t, N_f	7, 8192, 4096
Δt, T	0.071, 585

3.2 Displacement power spectrum

Under a random $\bar{g}_n$, time integration of Eq. (4) yields a time-series for q_n. We first comment on the time integration. Although there are special solvers [17,20] proposed for stochastic ordinary differential equations (ODEs), we shall use here the Adams-Bashforth-Moulton scheme of Shampine and Gordon [21], which has been implemented in DEABM subroutine of the SLATEK library. Although DEABM has been developed for nonstochastic ODEs, its use for the present stochastic problem may be justified in part by that one recovers linearized frequency response functions by the numerical simulation (Sec. 3.4). Obviously, this does not say anything about the strongly nonlinear problem in hand, and it should be addressed as a separate issue. In any event, DEABM requires the absolute and relative error tolerances, both of which are set at no larger than 10^{-5} under the single-precision algorithm for time integration. Note that actual integration time steps are chosen by the subroutine itself, commensurate with the error tolerances requested. Recall that $\bar{g}_n$ is updated at every time interval Δt, and we linearly interpolate the forcing value within Δt.

We begin time integration of Eq. (4) from the initial configuration at the bottom of the single-well potential, $q(0)=p(0)=0$, for $s<1$ and the positive side double-well potential, $q(0)=\sqrt{k_o(s-1)/\alpha}$ and $p(0)=0$, for $s>1$. And we continue the integration up to T. By Fourier transforming time-series q_n, we obtain displacement power spectrum $\Phi_x(f)$. This process of integrating and transforming is repeated over three contiguous time ranges of T, and the successive PSDs are compared for stationarity. Since it is roughly stationary after three repetitions, we report here only the PSD of the third repetition. From the stationary input–output relation [22] $\Phi_x(f)=|H_x(f)|^2\Phi_g(f)$, where $|H_x(f)|$ is the magnitude of system frequency response function, we write

$$|H_x(f)|^2 = \frac{\Phi_x(f)}{\Phi_g(f)}. \tag{8}$$

Since $\Phi_g(f)=C$, the $|H_x(f)|^2$ and $\Phi_x(f)$ would have a similar functional dependence upon f. Hence, we call them both the displacement PSD.

3.3 Strain power spectrum

Although displacement is the direct output of numerical simulation, one measures strain rather than the displacement in plate experiment. At the present level of plate equation formulation, the strain ε ($\equiv\varepsilon_x b^2/\pi^2 h^2$) is given by the quadratic relation

$$\varepsilon = C_o + C_1 q + C_2 q^2, \tag{9}$$

where C_i are given at the middle ($x/a = y/b = 1/2$) of a clamped plate as follows (Appendix D of Ref. [13])

$$C_o = \frac{(\gamma^4+2\gamma^2/3+1)T_o\delta_v}{3(1+\mu)(\gamma^2+1)}\left\{1-\frac{1}{4}\left[(1-\mu)-\frac{1-\mu\gamma^2}{\gamma^2+1}\right]\right\}, \quad C_1 = \frac{8\gamma^2}{3},$$

$$C_2 = \frac{32}{9}\left\{\frac{\gamma^2}{2}-\frac{5\mu}{16}+\frac{(1-\mu\gamma^2)}{2(\gamma+\gamma^{-1})^2}+\frac{(1-\mu\gamma^2/4)}{(\gamma+4\gamma^{-1})^2}+\frac{(\frac{1}{4}-\mu\gamma^2)}{(4\gamma+\gamma^{-1})^2}\right\}.$$

For δ_v=0 we have C_o=0, C_1=4.17, and C_2=2.77 (Table I). Hence, Eq. (9) engenders only the linear and quadratic transformations, but no translation. In any event, translation has no effect on the spectral energy contents. By Fourier transforming time-series ε_n (n=1, ..., N_t), we obtain strain power spectrum $\Phi_\varepsilon(f)$. Although the forcing PSD is not constant, one computes the forcing spectrum ratio as in Eq. (8) and call it the magnitude square of strain frequency response function $H_\varepsilon(f)$, for the lack of a better terminology.

3.4 The linear oscillators

For the pre-buckled (s <1) linear oscillator ($\alpha = 0$) we rewrite Eq. (4) in standard form

$$\ddot{q} + 2\xi\omega_o\dot{q} + \omega_o^2(1-s)\,q = \frac{\overline{g}(t)}{g^*}, \tag{10}$$

where ω_o^2=k_o, and obtain

$$|H_x(f)|^2 = [(\omega_o^2(1-s) - 4\pi^2 f^2)^2 + (4\pi\xi\omega_o f)^2]^{-1}. \tag{11}$$

As shown in Fig. 2(a), the numerical simulation of Eq. (10) recovers $|H_x(f)|^2$ as given by Eq. (11) over the entire frequency range. Although the simulation of Fig. 2(a) was carried out with SPL=130 dB, it does not depend on SPL since Eq. (10) is linear. Physically speaking, Eq. (10) oscillates in a single-well potential (Fig. 1(a)). Since the potential energy has two wells (Fig. 1(b)) for s >1, we linearize Eq. (1) around the positive side potential well by the transformation $q=q'+\sqrt{k_o(s-1)/\alpha}$. Hence, the corresponding linear oscillator is

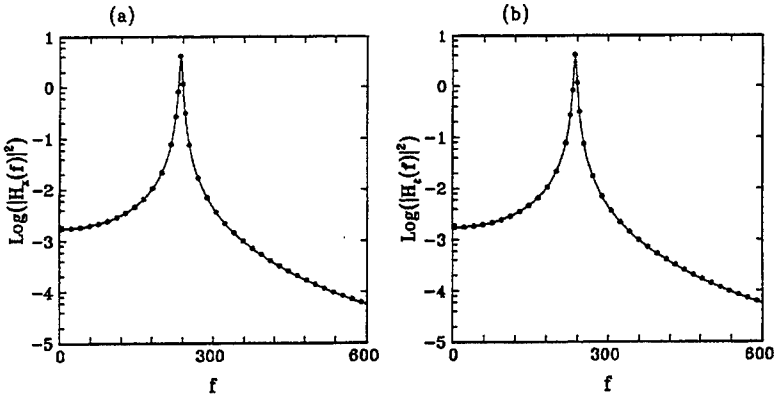

Fig. 2 Linear frequency response functions. (a) Displacement; (b) Strain (s = 0; ——— Numerical simulation; • Eq. (11))

$$\ddot{q}' + 2\xi\omega_o \dot{q}' + 2\omega_o^2(s-1)\,q' = \frac{\overline{g}(t)}{g^*}. \tag{12}$$

In parallel to Eq. (11), the frequency response function of a post-buckled plate is

$$|H_x(f)|^2 = [(2\omega_o^2(s-1) - 4\pi^2 f^2)^2 + (4\pi\xi\omega_o f)^2]^{-1}. \tag{13}$$

The resonance frequency $f_r = \omega_o\sqrt{2(s-1)}\,/2\pi$ of a post-buckled ($s>1$) plate should be compared with $f_r = \omega_o\sqrt{2(1-s)}\,/2\pi$ of the pre-buckled ($s<1$) plate.

Now, for the linear oscillators we see that $|H_\varepsilon(f)|^2$ is also given by Eq. (11) and (13) for $s<1$ and >1, respectively (Fig. 2(b)). This is because the spectral energy distribution is not at all affected by a linear transformation.

4. Displacement and strain power spectra

As we shall see in Sec 4.1, the experimental strain PSD exhibits downward spectral energy transfer toward zero frequency, so that there is a considerable spectral energy buildup below the resonance frequence as SPL is raised. Moreover, it also involves an upward spectral energy transfer which then contributes to both the increased resonance frequency and broadened resonance frequency peak. Since spectral energy transfers take place around and below the primary resonance frequency, it is possible to depict the downward and upward spectral energy transfers by the numerical simulation of Eq. (4) without necessitating multimode interactions. We shall first discuss the characteristic features of experimental strain PSDs.

4.1 Experimental strain PSD

Of the spectra reported in Ref. [10], we consider the following two sets. One is the nonthermal set (s=0) consisting of two PSDs of small and large SPLs. The other is the post-buckled set (s=1.7) of four PSDs. For the convenience of readers, we have reproduced in Figs. 3 and 4 the selected PSDs from Ref. [10] by limiting the upper frequency to 600 Hz, and the pertinent data are summarized in Table III.

Table III. Strain power spectra of experiment and numerical simulation

			s=0		
	Experiment			Numerical simulation	
PSD	Ref. [11]	$a/31.6g$	SPL(dB)*	SPL(dB)	Results
Fig. 3(a)	Fig. 4a	0.16	138.6	130	Fig. 5
Fig. 3(b)	Fig. 4c	0.59	149.9	138	Fig. 6
			s=1.7		
Fig. 4(a)	Fig. 6a	0.06	130.1	129	Fig. 7
Fig. 4(b)	Fig. 6b	0.24	142.0	138	Fig. 8
Fig. 4(c)	Fig. 6c	0.70	151.5	143	Fig. 9
Fig. 4(d)	Fig. 6d	1.02	154.6	146	Fig. 10

(*) Computed from the acceleration a measured in units of g.

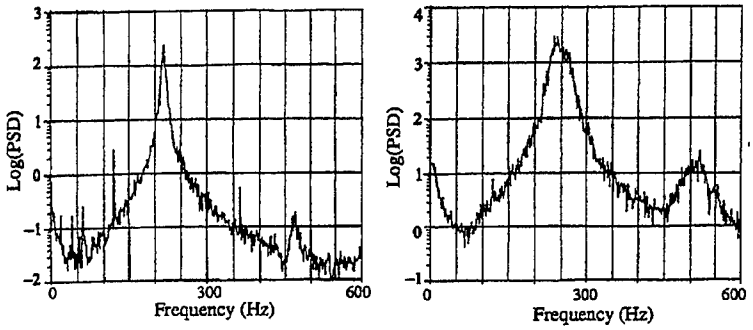

Fig. 3 Experimental strain PSD (s =0). (a) 138.6 dB; (b) 149.9 dB

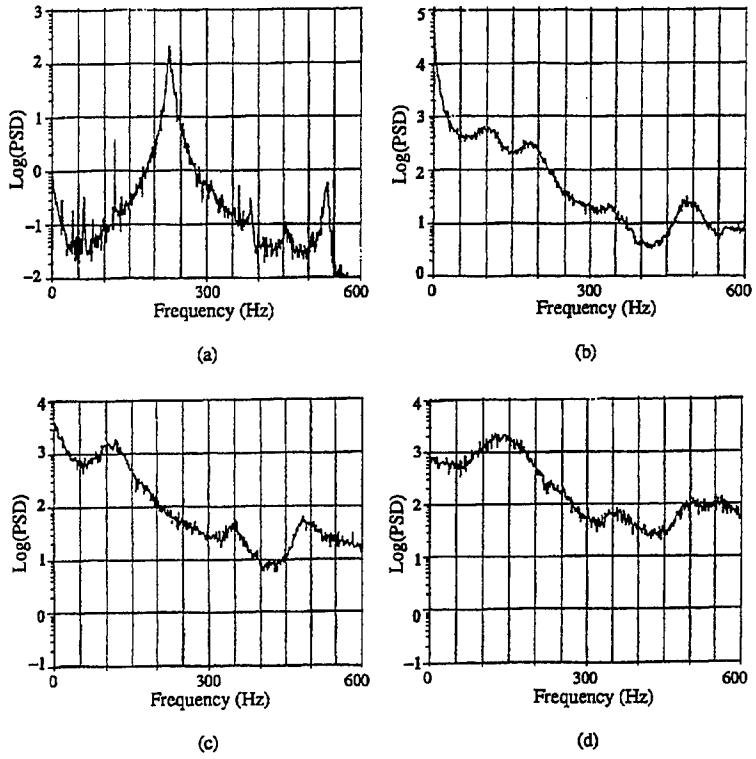

Fig. 4 Experimental strain PSD (s =1.7). (a) 130.1dB; (b) 142dB; (c) 151.5dB; (d) 154.6dB

The following observations are drawn from the experimental PSDs. First, for the nonthermal plate

Figure 3(a): Compare the measured strain f_r=217 Hz with the theoretical displacement f_r= 235 Hz of Eq. (4). Note that a small spectral energy peak is found at 467 Hz which is about twice (~2.15) the strain f_r value.

Figure 3(b): With SPL~150 dB the strain f_r increases to 240 Hz and the spectral width at the half resonance peak has nearly doubled. The spectral energy buildups at zero and 515 Hz are more noticeable than in Fig. 3(a). Again, 515 Hz is about twice (~2.15) the primary strain f_r.

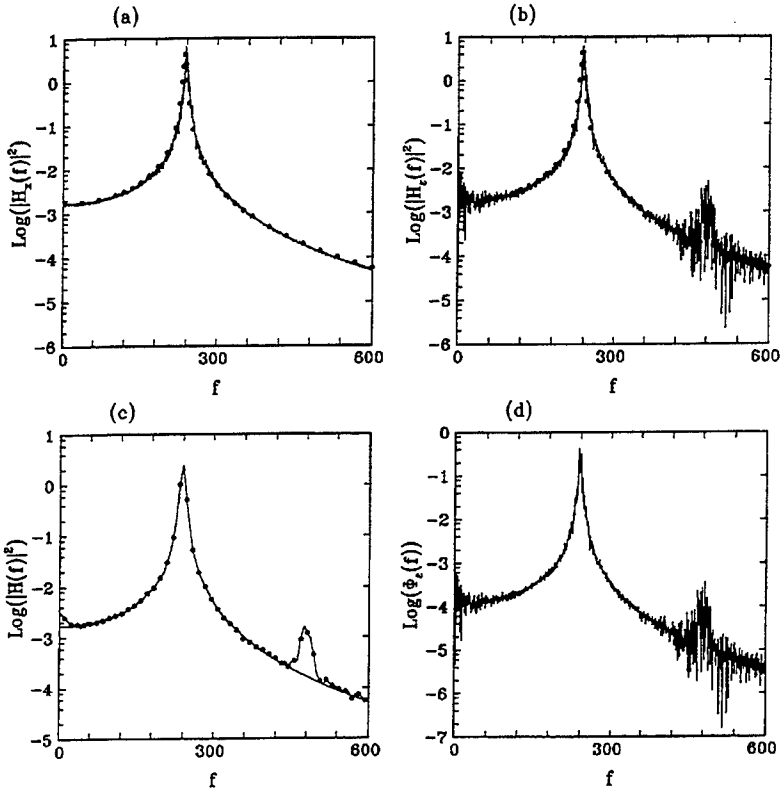

Fig. 5 Numerical simulation results under s=0 and SPL=130 dB.
(a) Displacement (—— simulation, ● Eq. (11)); (b) Strain (—— simulation, ● Eq. (11));
(c) PSD averaged over 12 frequency intervals (—— displacement, —●— strain);
(d) Strain PSD.

Next, for the thermally buckled plate

Figure 4(a): The primary strain f_r=227 Hz should be compared with the theoretical displacement f_r=279 Hz of Eq. (13). A second spectral energy peak is found at 537 Hz, much larger than twice (~2.37) the primary strain f_r.

Figure 4(b): Here, the spectral energy buildup is most significant at zero frequency. Besides, there appear two spectral energy humps at 100 and 183 Hz, below the primary strain f_r = 227 Hz of Fig. 4(a). Discounting the zero-frequency spectral peak, PSD may be approximated by a straight line in the semi-log plot, hence it is of an exponential form up to 400 Hz.

Figure 4(c): The zero-frequency peak is followed by a single spectral energy hump at 115 Hz. Again, PSD can be approximated by a straight line and its slope is roughly the same as in Fig. 4(b).
Figure 4(d): A major spectral energy peak emerges at 130 Hz, followed by a minor one at 350 Hz. Theoverall spectral energy level is raised so that the magnitude of PSD ranges over only two decades in the figure.

In Figs. 4(b)–(d) we have ignored the spectral energy peaks at around 500 Hz, for they are not related to the first plate mode under consideration. This is further supported by the simulation evidence to be discussed presently.

4.2 Numerical simulation results

After choosing s = 0 or 1.7, we are left with SPL yet to be specified. Ideally, one would like to carry out the numerical simulation of Eq. (4) by using SPL of the plate experiment (Table III) and thus generate strain PSDs which are in agreement with Figs. 3 and 4. Not surprisingly, the reality is less than ideal. An obvious reason that this cannot be done is that the forcing energy input is fed into all plate modes being excited in experiment, whereas the forcing energy excites only one mode in the numerical simulation. Consequently, SPL for the numerical simulation should be less than the experimental SPL, but we do not know *a priori* how much less. We therefore choose a SPL to bring about qualitative agreements between the single-mode simulation and multimode experiment. As anticipated, the simulation SPLs (Table III) are consistently smaller than the experimental values.

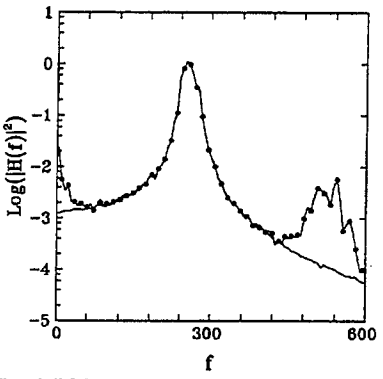

Fig. 6 PSD averaged over 12 frequency intervals (s=0, SPL=138 dB)
—— displacement; —●— strain

The numerical simulation results are shown in Figs. 5–6 for s = 0 and Figs. 7–10 for s =1.7. Actually each figure has four frames, denoted by (a)–(d). First, frames (a) and (b) depict $|H_x(f)|^2$ and $|H_\varepsilon(f)|^2$. Since they are very jagged at large SPLs, we average the spectral energy over 12 frequency intervals and present both of the smoothed-out frequency response functions in the same frame (c). Lastly, frame (d) shows $\Phi_\varepsilon(f)$ itself. Since there is no qualitative difference between $\Phi_\varepsilon(f)$ and $|H_\varepsilon(f)|^2$, we shall call them both the strain PSD. We present all four frames (a)–(d) of Figs. 5 and 7, but only the frame (c) of Figs. 6, 8, 9 and 10 here for the lack of space.

First, for the nonthermal plate

Figure 5: The simulated $|H_x(f)|^2$ is closely approximated by Eq. (11) with f_r= 236 Hz. Note that $|H_\varepsilon(f)|^2$ is also approximated by Eq. (11) for all frequencies

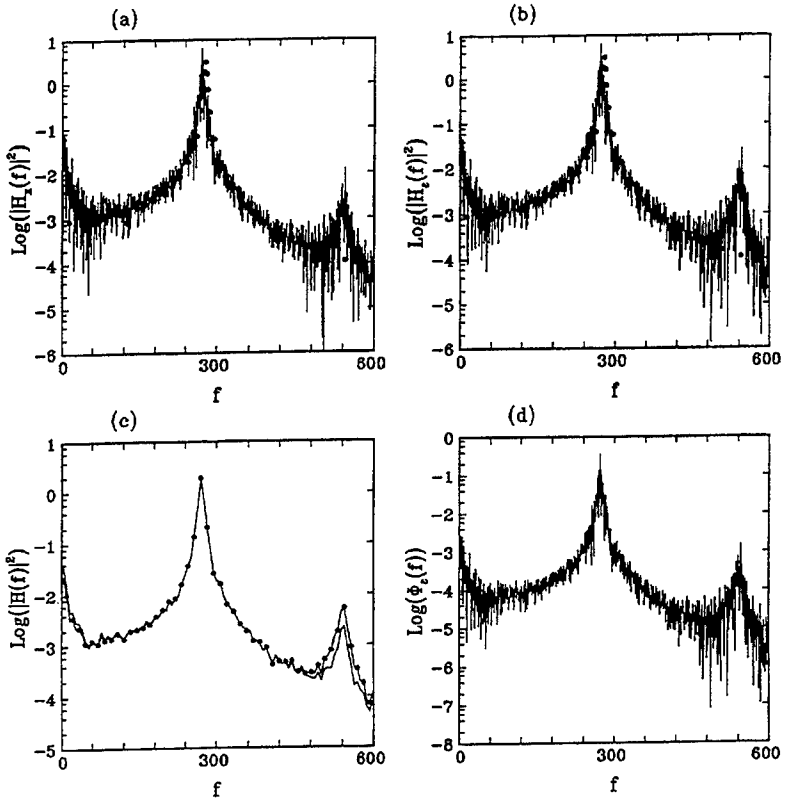

Fig. 7 Numerical simulation results under s=1.7 and SPL=129 dB.
(a) Displacement (—— simulation, • Eq. (13)); (b) Strain (—— simulation, • Eq. (13));
(c) PSD averaged over 12 frequency intervals (—— displacement, —•— strain);
(d) Strain PSD.

but zero and 476 Hz, where the strain spectral energy piles up due to the quadratic transformation (9). Since 476 Hz is nearly twice (~2.02) the primary f_r, strain spectral energy buildups are due to the sum and difference of two nearly equal frequencies, $f_1 \pm f_2$, where $f_1 \approx f_2 \approx f_r$.

Figure 6: The primary strain f_r is shifted slightly upward to 253 Hz and the spectral width at half resonance peak is 50% wider than that of Fig. 5(c). The spectral energy builds up at 525 Hz which is roughly twice (~2.08) the f_r. At SPL=138 dB we find that the strain spectral energy hump at 525 Hz is about 2 decades below the resonance frequency peak, as was in Fig. 3(b).

Now, for the thermally buckled plate

Figure 7: The simulated $|H_x(f)|^2$ and $|H_\varepsilon(f)|^2$ are well approximated by Eq. (13) around f_r=270 Hz which is a little below the linearized f_r=279 Hz. Unlike in Fig. 5 for s=0, both $|H_x(f)|^2$ and $|H_\varepsilon(f)|^2$ show spectral energy building up significantly near zero and 543 Hz which is twice (~2.01) the f_r.

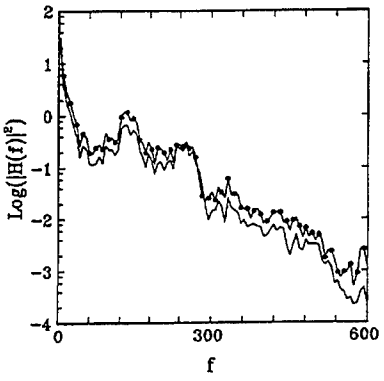

Fig. 8 PSD averaged over 12 frequency intervals (s =1.7, SPL=138 dB)
—— displacement; —●— strain

Note that in Fig. 7(a) the spectral energy hump at 543 Hz is about 3 decades below the primary frequency peak, as was in Fig. 4(a).

Figure 8: After a large zero-frequency peak, two spectral energy humps appear at 131 Hz and 236 Hz. Note that the ratios of these frequencies to the f_r (131/279 ~0.47 and 236/279 ~ 0.85) are comparable with the same ratios (100/227 ~0.44 and 183/227 ~ 0.81) found in Fig. 4(b). Excluding the zero-frequency peak, the overall strain PSD is a straight line, hence of an exponential form, as in Fig. 4(b).

Figure 9: The zero-frequency spectral peak is followed by a single major energy hump at 154 Hz. The ratio of this to the f_r (154/279 ~0.56) is somewhat larger than the ratio (115/227 ~0.51) in Fig. 4(c). The strain PSD can also be approximated by a straight line over the entire frequency range, and Figs. 8 and 9 seem to have the same slope when fitted by straight lines.

Figure 10: The spectral magnitude of $|H_\varepsilon(f)|^2$ is larger than that of $|H_x(f)|^2$ in the frequency range above 300 Hz. The choice of SPL=146 dB was based on that the PSD magnitude around 300 Hz is about 2 decades below the main spectral peak magnitude at 180 Hz, thus emulating Fig. 4(d).

All in all, by numerical simulations we have successfully reproduced the peculiar features in the two sets of strain PSDs observed experimentally under s = 0 and 1.7.

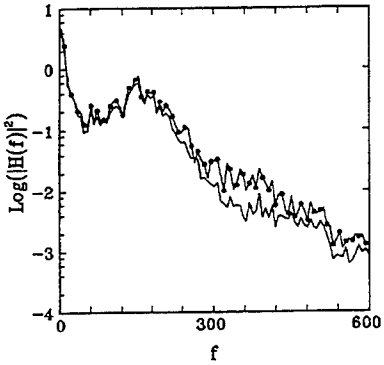

Fig. 9 PSD averaged over 12 frequency intervals (s =1.7, SPL=143 dB)
—— displacement; —●— strain

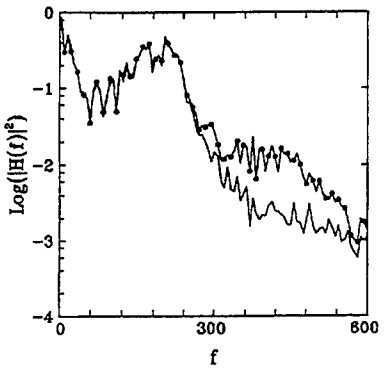

Fig. 10 PSD averaged over 12 frequency intervals (s =1.7, SPL=146 dB)
—— displacement; —●— strain

5. Concluding remarks

At low SPL the nonthermal (s= 0) and post-buckled (s=1.7) plates appear to have a similar PSD. However, this appearance is quite deceptive in that the nonthermal plate motion is in a single-well potential, so that PSD does not change qualitatively as SPL is raised. On the other hand, the trajectory of a post-buckled plate is in one of the two potential energy wells when SPL is very small. However, as we raise SPL such a plate motion can no longer be contained in a potential well, and hence it encircles either one or both of the potential wells in an erratic manner. This is why the experimentally observed and numerically simulated strain PSDs of a post-buckled plate exhibit qualitative changes with the increasing SPL, and thereby reflect the erratic snap-through plate motion. A quantitative analysis of snap-through dynamics will be presented elsewhere.

Lastly, we wish to point out that a PSD of straigh-line form in the semi-log plot was observed in a Holmes oscillator when trajectories are superposed randomly near the figure-eight separatrix [23].

Acknowledgments

Correspondence and conversations with Chung Fi Ng, Chuh Mei, Rimas Vaicaitis, and Jay Robinson are sincerely appreciated. We also wish to thank the referees for their helpful suggestions to improve the readability of this paper.

References

1. Lee, J., *Large-Amplitude Plate Vibration in an Elevated Thermal Environment*, WL-TR-92-3049, Wright Lab., Wright-Patterson AFB, OH, June, 1992.
2. Jacobson, M.J. and Maurer, O.F., Oil canning of metallic panels in thermal-acoustic environment, AIAA Paper 74-982, Aug., 1974.
3. Jacobson, M.J., Sonic fatigue of advanced composite panels in thermal environments, *J. Aircraft*, 1983, **20**, 282-288.
4. Bisplinghoff, R.L. and Pian, T.H.H., On the vibrations of thermally buckled bars and plates, in Proc. 9th Inter. Congr. of Appl. Mech., Brussels, 1957, **7**, 307-318.
5. Tseng, W.-Y., *Nonlinear vibration of straight and buckled beams under harmonic excitation*, AFOSR 69-2157TR, Air Force Office of Scientific Research, Arlington, VA, Nov., 1969.
6. Seide, P. and Adami, C., *Dynamic stability of beams in a combined thermal-acoustic environment,* AFWAL-TR-83-3072, Flight Dynamics Lab., Wright-Patterson AFB, OH, Oct., 1983.
7. Ng, C.F., Nonlinear and snap-through responses of curved panels to intense acoustic excitation, *J. Aircraft*, 1989, **26**, 281-288.
8. Robinson, J.H. and Brown, S.A., Chaotic structural acoustic response of a milled aluminum panel, 36th Structures, Structural Dynamics, and

Material Conference, AIAA-95-1301-CP, New Orleans, LA, 1240-1250, Apr. 10-13, 1995.
9. Ng, C.F. and Clevenson, S.A., High-intensity acoustic tests of a thermally stressed plate, *J. Aircraft*, 1991, **28**, 275-281..
10. Ng, C.F. and Wentz, K.R., The prediction and measurement of thermo-acoustic response of plate structures, 31st Structures, Structural Dynamics, and Material Conference, AIAA-90-0988-CP, Long Beach, CA, 1832-1838, Apr. 2-4, 1990.
11. Holmes, P., A nonlinear oscillator with a strange attractor, *Phil. Trans., Roy. Soc. of London*, 1979, **292A**, 419-448.
12. Dowell, E.H. and Pezeski, C., On the understanding of chaos in Duffings equation including a comparison with experiment, *J. Appl. Mech.*, 1986, **53**, 5-9.
13. Lee, J., Random vibration of thermally buckled plates: I Zero temperature gradient across the plate thickness, in Progress in Aeronautics and Astronautics, **168**, *Aerospace Thermal Structures and Materials for a New Era*, Ed. E.A. Thornton, AIAA, Washington, DC, 1995. 41-67.
14. Lee, J., Random vibration of thermally buckled plates: II Nonzero temperature gradient across the plate thickness, to appear in *J. Vib. and Control*, 1997.
15. Lee, J., Large-amplitude plate vibration in an elevated thermal environment, *Appl. Mech. Rev.*, 1993, **46**, S242-254.
16. Shinozuka, M. and Jan, C.-M., Digital simulation of random processes and its applications, *J. Sound and Vib.*1972, **25**, 111-128.
17. Chiu, H.M. and Hsu, C.S., A cell mapping method for nonlinear deterministic and stochastic systems – Part II: Examples of application, *J. Appl. Mech.*, 1986, **53**, 702-710.
18. Vaicaitis, R., Nonlinear response and sonic fatigue of national aerospace space plane surface panels, *J. Aircraft*, 1994, **31**, 10-18.
19. Vaicaitis, R., *Response of Composite Panels Under Severe Thermo-Acoustic Loads*, Report TR-94-05, Aerospace Structures Information and Analysis Center, Wright-Patterson AFB, OH, Feb., 1994.
20. Kasdin, N.J., Runge-Kutta algorithms for the numerical integration of stochastic differential equations, *J. Guidance, Control, and Dynamics*, 1995, **18**, 114-120.
21. Shampine, L.F. and Gordon, M.K., *Computer solution of ordinary differential equations*, 1975, Freeman, San Francisco.
22. Lin, Y.K., *Probabilistic theory of structural dynamics*, Robert E. Krieger Publishing, 1976, Huntington, NY.
23. Brunsden, V., Cortell, J. and Holmes, P.J., Power spectra of chaotic vibrations of a buckled beam, *J. Sound and Vib.*, 1989, **130**, 1-25.

ENHANCED CAPABILITIES OF THE NASA LANGLEY THERMAL ACOUSTIC FATIGUE APPARATUS

Stephen A. Rizzi and Travis L. Turner
Structural Acoustics Branch
NASA Langley Research Center
Hampton, VA 23681-0001

ABSTRACT

This paper presents newly enhanced acoustic capabilities of the Thermal Acoustic Fatigue Apparatus at the NASA Langley Research Center. The facility is a progressive wave tube used for sonic fatigue testing of aerospace structures. Acoustic measurements for each of the six facility configurations are shown and comparisons with projected performance are made.

INTRODUCTION

The design of supersonic and hypersonic vehicle structures presents a significant challenge to the airframe analyst because of the wide variety and severity of environmental conditions. One of the more demanding of these is the high intensity noise produced by the propulsion system and turbulent boundary layer [1]. Complicating effects include aero-thermal loads due to boundary layer and local shock interactions, static mechanical preloads, and panel flutter. Because of the difficulty in accurately predicting the dynamic response and fatigue of structures subject to these conditions, experimental testing is often the only means of design validation. One of the more common means of simulating the thermal-vibro-acoustic environment is through the use of a progressive wave tube. The progressive wave tube facility at NASA Langley Research Center, known as the Thermal Acoustic Fatigue Apparatus (TAFA), has been used in the past to support development of the thermal protection system for the Space Shuttle and National Aerospace Plane [2]. It is presently being used for sonic fatigue studies of the wing strake subcomponents on the High Speed Civil Transport [3].

The capabilities of the TAFA were previously documented by Clevenson and Daniels [4]. The system was driven by two Wyle WAS 3000 airstream modulators which provided an overall sound pressure level range of between 125 and 165 dB and a useful frequency range of 50-200 Hz. A 360 kW quartz lamp bank provided radiant heat with a peak heat flux of 54 W/cm^2. A schematic of the facility is shown in Figure 1. Representative spectra and coherence plots are shown in Figures 2 and 3. Since that time, the facility has undergone significant enhancements designed to improve its acoustic capabilities; the heating capabilities were not changed. The objectives of the enhancements were to increase the maximum overall sound pressure level (OASPL) to 178 dB, increase the frequency bandwidth to 500 Hz and improve the uniformity of the sound pressure field in the test section. This paper

documents the new capabilities of the TAFA and makes comparisons with the projected performance.

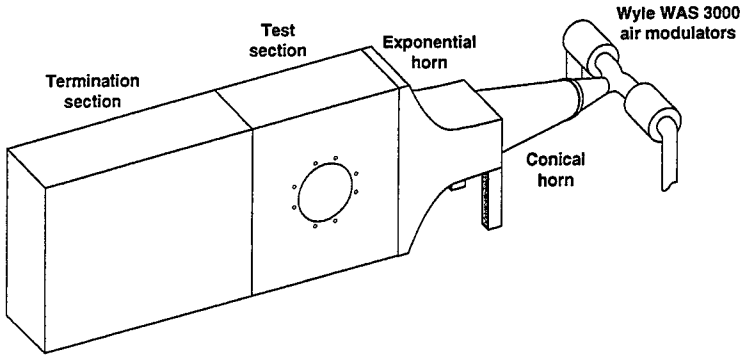

Figure 1: Schematic of the old TAFA facility.

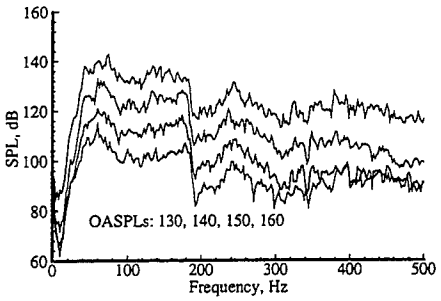

Figure 2: Test section spectra of the old TAFA facility.

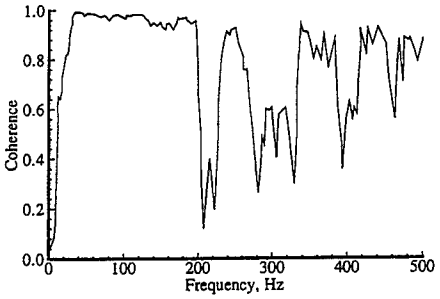

Figure 3: Test section coherence of the old TAFA facility.

FACILITY DESCRIPTION

In order to meet the design objectives, extensive modifications were made to the sound generation system and to the wave tube itself. A theoretical increase of 6 dB OASPL was projected by designing the system to utilize eight WAS 3000 air modulators compared to the two used in the previous system. A further increase of nearly 5 dB was expected by designing the test section to accommodate removable water-cooled insert channels which reduced its cross-sectional area from 1.9m x 0.33m to 0.66m x 0.33m. The frequency range was increased through the use of a longer horn design with a lower (15 Hz vs. 27 Hz in the old facility) cut-off frequency, use of insert channels in the test section to shift the frequency of significant standing waves above 500 Hz, and design of facility sidewall structures with resonances above 1000 Hz. The uniformity of the sound pressure field in the test section was improved through several means. A new, smooth exponential horn was designed to avoid the impedance mismatches of the old design. To minimize the effect of uncorrelated, broadband noise (which develops as a byproduct of the sound

generation system), a unique design was adopted which allows for the use of either two-, four-, or eight-modulators. When testing at the lower excitation levels for example, a two-modulator configuration might be used to achieve a lower background level over that of the four- or eight-modulator configurations. In doing so, the dynamic range is extended. Lastly, a catenoidal design for the termination section was used to smoothly expand from the test section.

Schematics of the facility in the three full test section configurations are shown in Figures 4-6. In the two-modulator configuration, the 2 x 4 transition cart acts to block all but two of the eight modulators. The facility is converted from the two- to four-modulator configuration by the removal of the 2 x 4 transition cart and connection of two additional modulators. In doing so, the modulator transition cart slides forward and thereby maintains the continuous exponential expansion of the duct. In the four-modulator configuration, the 4 x 8 transition cart acts to block the two upper and two lower modulators. Removal of this component and connection of the four additional modulators converts the facility to the eight-modulator configuration. Again, the continuous exponential expansion is maintained as the modulator transition cart slides forward.

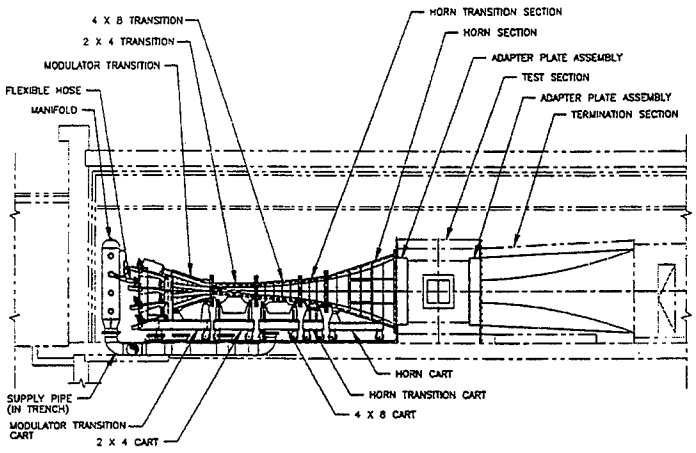

Figure 4: Two-modulator full test section configuration.

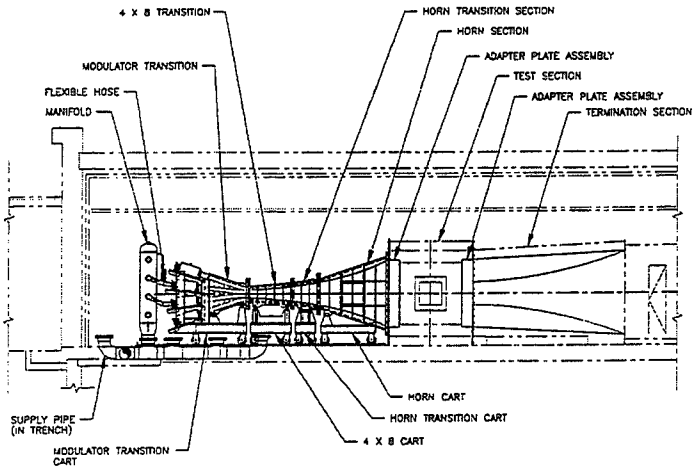

Figure 5: Four-modulator full test section configuration.

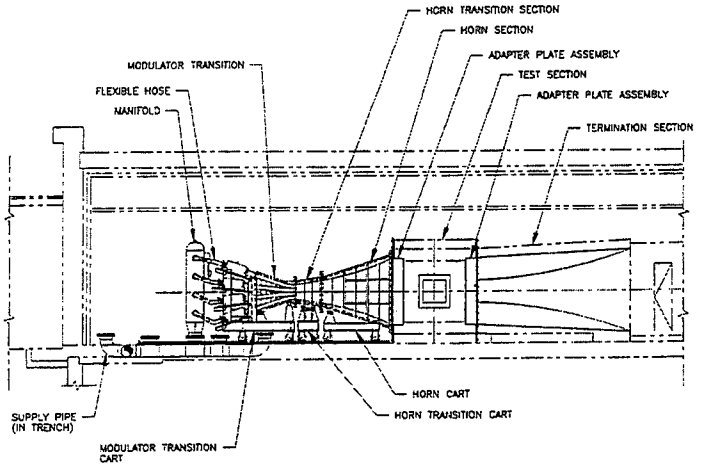

Figure 6: Eight-modulator full test section configuration.

Schematics of the three reduced test section configurations are shown in Figures 7-9. In these configurations, the horn cart is discarded and the horn transition cart mates directly to the test section. Water-cooled inserts are used in the test section to reduce its cross-sectional area. Upper and lower inserts in the termination section are used to smoothly transition the duct area to the full dimension at the exit. Conversion from the two- to the four-modular configuration and from the four- to the eight-modulator configuration is again accomplished through removal of the 2 x 4 and 4 x 8 transition carts, respectively.

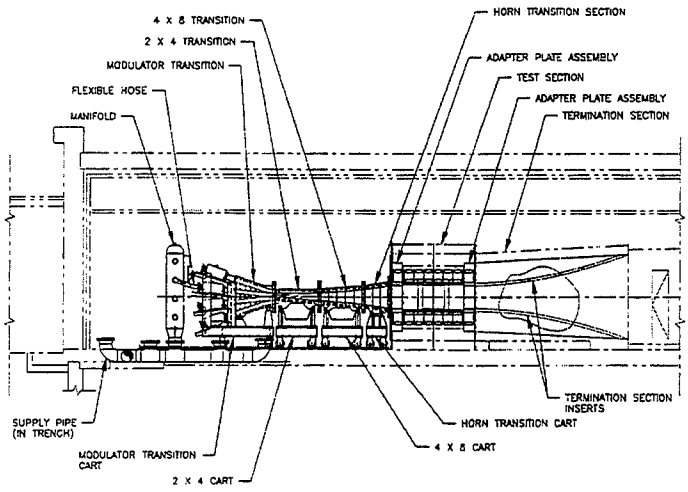

Figure 7: Two-modulator reduced test section configuration.

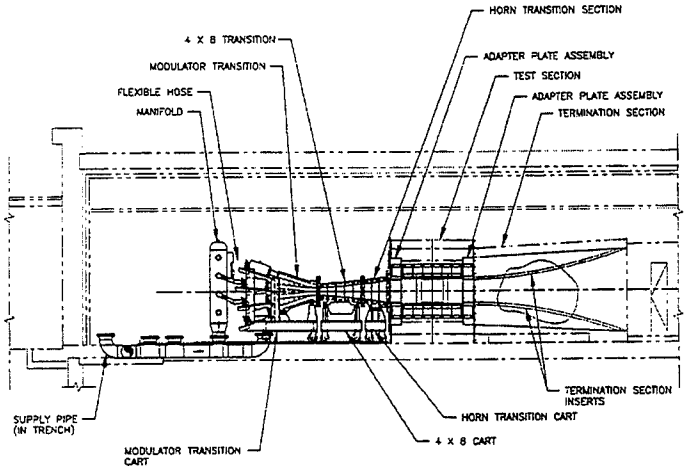

Figure 8: Four-modulator reduced test section configuration.

TEST PROCEDURE

Measurements were taken for several conditions in each of the six facility configurations. Each modulator was supplied with air at a pressure of 207 kPa (mass flow rate of approximately 8.4 kg/s) and was electrically driven with the same broadband (40-500 Hz) signal. Acoustic pressures were measured at several locations along the length of the progressive wave tube using B&K model 4136 microphones and Kulite model MIC-190-HT pressure transducers, see Table 1. The positive x-direction is defined in the two-modulator full configuration (from the modulator exit) along the direction of the duct. The positive y-direction is taken vertically from the horizontal centerline of the

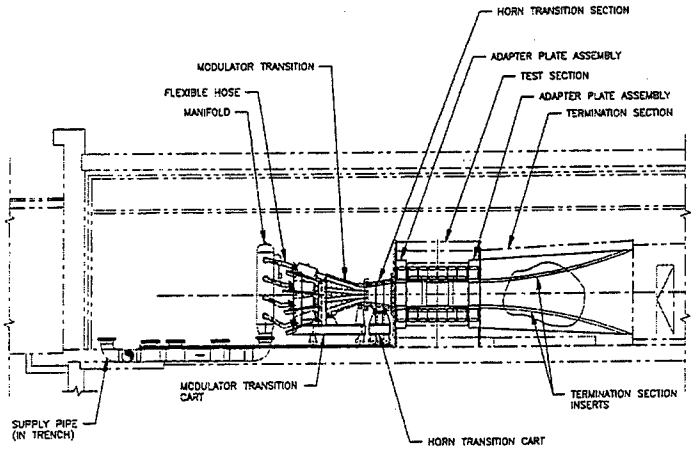

Figure 9: Eight-modulator reduced test section configuration.

duct and the positive z-direction is defined from the left sidewall of the duct as one looks downstream.

Table 1: Kulite (K) and microphone (M) locations of acoustic measurements.

Loc.	Description	Type	Coordinate (m)
1	Test Sect. Horizontal Centerline Upstream	K	7.75, 0, 0
2	Test Sect. Horizontal Centerline Downstream	K	8.71, 0, 0
5	Test Sect. Vertical Centerline Top	M	8.23, 0.3, 0
15	Test Sect. Horizontal/Vertical Centerline	K	8.23, 0, 0
25	Test Sect. Vertical Centerline Bottom	M	8.23, -0.3, 0
28	2x4 Horizontal/Vertical Centerline	M	2.19, 0, 0
29	4x8 Horizontal Centerline, ¾ Downstream	M	3.66, 0, 0
30	Horn Tran, Hor. Centerline, ¾ Downstream	M	4.75, 0, 0
35	Termination Horizontal/Vertical Centerline	M	12.46, 0, 0.17

The acoustic pressure at location 1 was used as a reference measurement for shaping the input spectrum and for establishing the nominal overall sound pressure level for each test condition. For each configuration, the input spectrum to the air modulators was manually shaped through frequency equalization to produce a nearly flat spectrum at the reference pressure transducer. Data was acquired at the noise floor level (flow noise only) and at overall levels above the noise floor in 6 dB increments (as measured at the reference location) up to the maximum achievable. Thirty-two seconds of time data were collected at a sampling rate of 4096 samples/s for each transducer in each test condition. Post-processing of the time data was performed to generate averaged spectra and coherence functions with a 1-Hz frequency resolution.

RESULTS

For each facility configuration, plots of the following quantities are presented: normalized input spectrum to the air modulators, minimum to maximum sound pressure levels at the reference location, maximum sound pressure levels in the test section, maximum sound pressure levels upstream and downstream of the test section, and vertical and horizontal coherence in the test section. The minimum levels in each case correspond to the background noise produced by the airflow through the modulators.

Normalized input voltage spectra to each modulator for each configuration are shown in Figures 10, 15, 20, 25 and 30. These spectra were generated to achieve as flat an output spectrum as possible at the reference location for the frequency range of interest (40-200 Hz for the full section, 40-500 Hz for the reduced section). As expected, the significant difference between the full and reduced configurations is seen in the high (>200 Hz) frequency content.

Figure 11 shows a background noise level of 126 dB (the lowest of all configurations) for the two-modulator full test section configuration. Nearly flat spectra are observed below 210 Hz for levels above 130 dB, giving a dynamic range of about 32 dB. The flat spectrum shape is a significant improvement over the performance of the old configuration as shown in Figure 2. Standing waves are evident at frequencies of 210, 340 and 480 Hz. For this reason, the full section operation is limited to less than 210 Hz or to the 220-330 and 370-480 Hz frequency bands. The effect of standing waves are explored in further depth in the next section. The spectra in Figure 12 indicate a nearly uniform distribution in the x-direction throughout the test section. It is interesting to note that Figure 13 shows no sign of standing waves upstream of the test section, confirming that the cause is associated with the test section. Lastly, a near perfect coherence between upstream and downstream, and upper and lower test section locations is shown in Figure 14 for frequencies between 40 and 210 Hz. Again, this is a significant improvement over the performance of the old configuration (Figure 3).

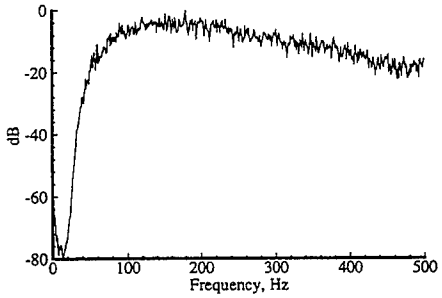

Figure 10: Normalized input spectrum (2-modulator full).

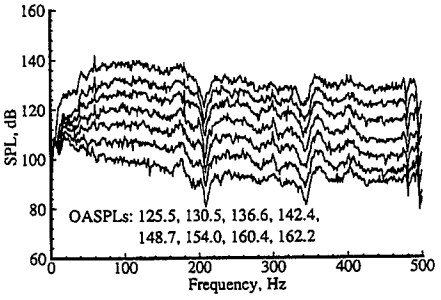

Figure 11: Min to max SPL at location 1 (2-modulator full).

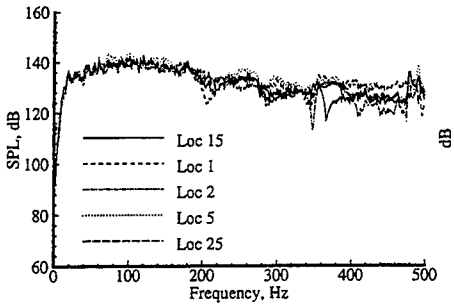

Figure 12: SPL in test section at max level (2-modulator full).

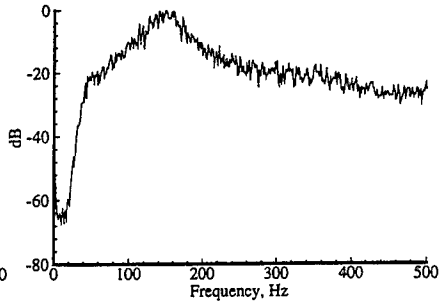

Figure 15: Normalized input spectrum (4-modulator full).

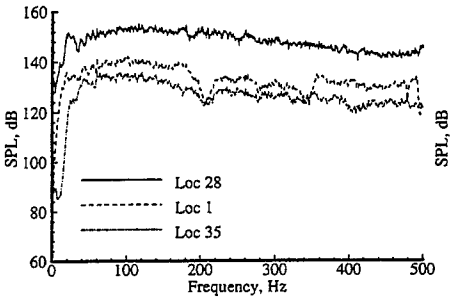

Figure 13: SPL along length of TAFA (2-modulator full).

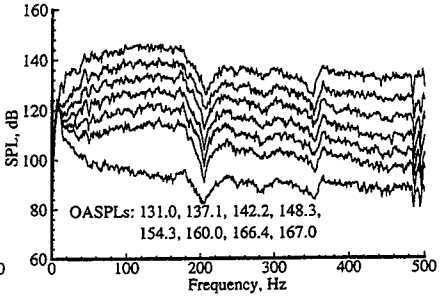

Figure 16: Min to max SPL at location 1 (4-modulator full).

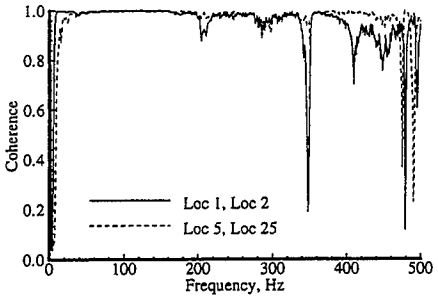

Figure 14: Test section coherence (2-modulator full).

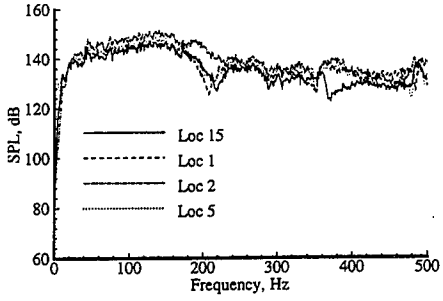

Figure 17: SPL in test section at max level (4-modulator full).

The four-modulator full configuration exhibits similar behavior as the two-modulator full configuration as seen in Figures 16-19. The lowest level at which a uniform spectrum is achieved is 137 dB, giving a dynamic range of roughly 30 dB in this configuration. Lastly, the eight-modulator full

configuration results, shown in Figures 21-24, indicate a noise floor of about 142 dB and dynamic range of 22 dB.

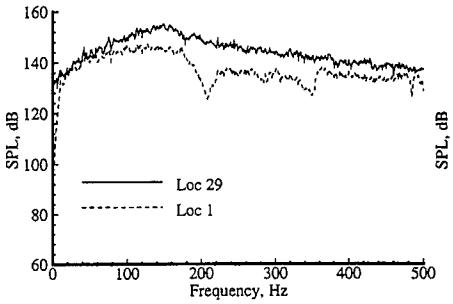

Figure 18: SPL along length of TAFA (4-modulator full).

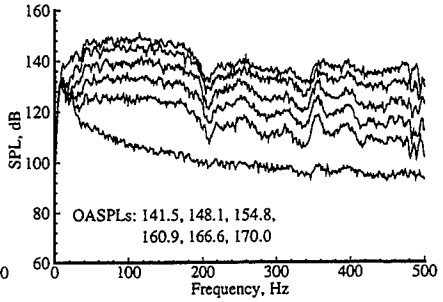

Figure 21: Min to max SPL at location 1 (8-modulator full).

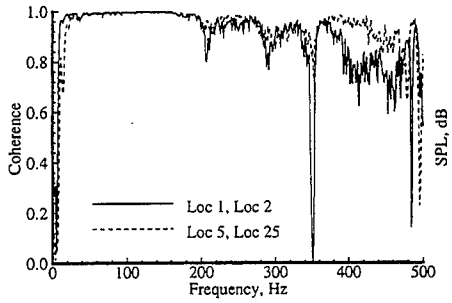

Figure 19: Test section coherence (4-modulator full).

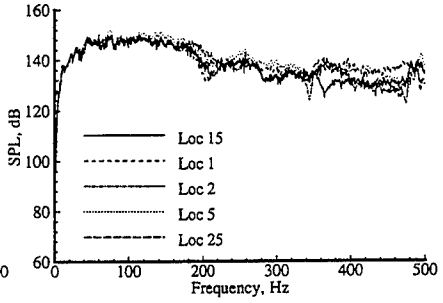

Figure 22: SPL in test section at max level (8-modulator full).

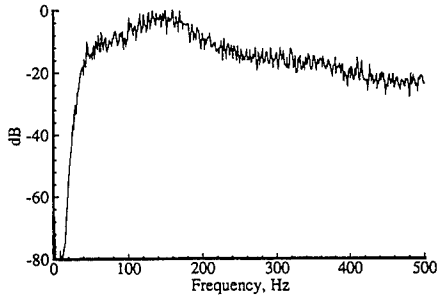

Figure 20: Normalized input spectrum (8-modulator full).

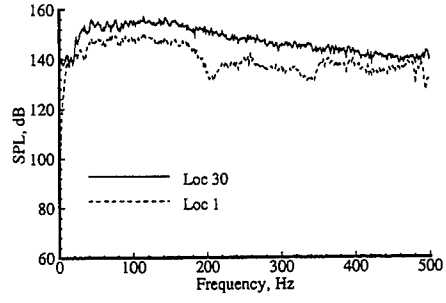

Figure 23: SPL along length of TAFA (8-modulator full).

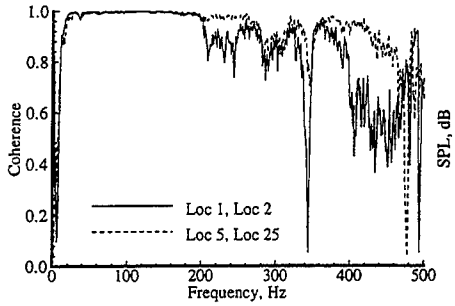

Figure 24: Test section coherence (8-modulator full).

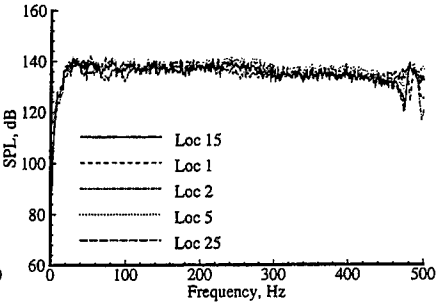

Figure 27: SPL in test section at max level (2-modulator reduced).

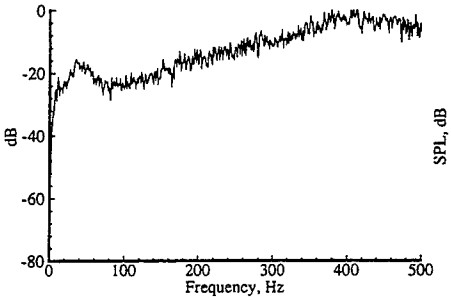

Figure 25: Normalized input spectrum (2-modulator reduced).

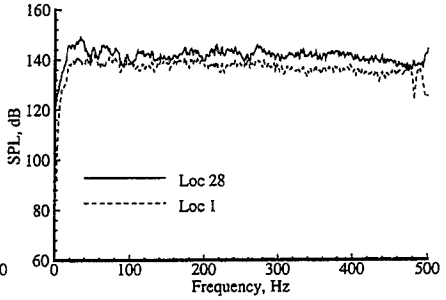

Figure 28: SPL along length of TAFA (2-modulator reduced).

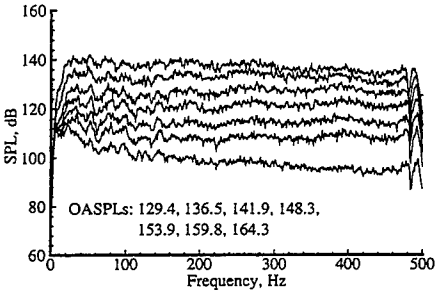

Figure 26: Min to max SPL at location 1 (2-modulator reduced).

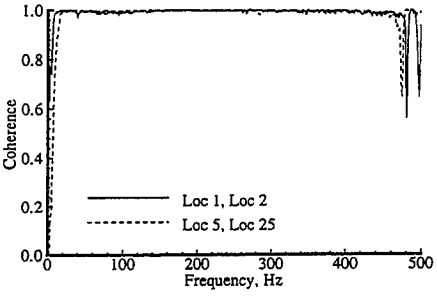

Figure 29: Test section coherence (2-modulator reduced).

The reduced test section configurations are used to increase the frequency range and maximum sound pressure level in the test section. Results for the two-modulator reduced configuration, shown in Figures 26-29, indicate a nearly flat spectrum between 40 and 480 Hz, a noise floor of 129 dB and a dynamic range of about 28 dB. Coherence in the test section is nearly unity

over this frequency range. This represents a significant improvement over the old facility configuration. Results of similar quality indicate a dynamic range of roughly 26 and 29 dB for the four- (Figures 31-34) and eight-modulator (Figures 36-39) configurations, respectively. Note that the coherence for these configurations is slightly reduced at the high frequencies, but is still very good out to 480 Hz.

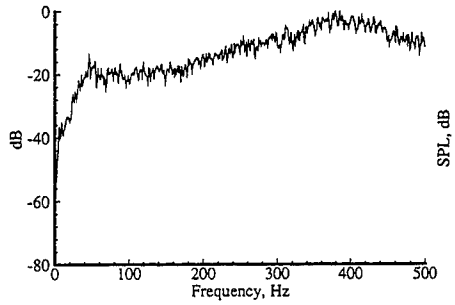

Figure 30: Normalized input spectrum (4-modulator reduced).

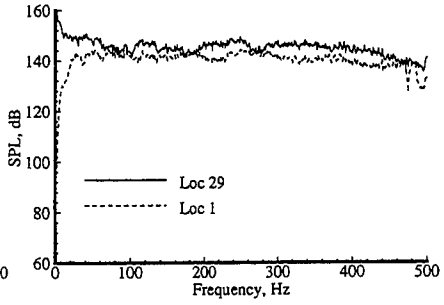

Figure 33: SPL along length of TAFA (4-modulator reduced).

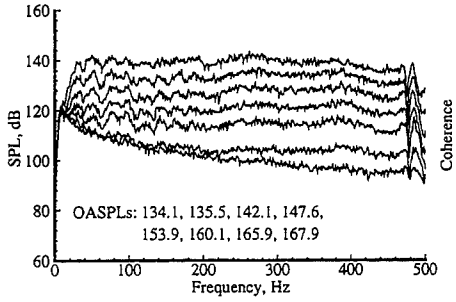

Figure 31: Min to max SPL at location 1 (4-modulator reduced).

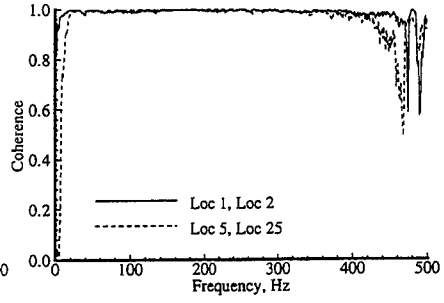

Figure 34: Test section coherence (4-modulator reduced).

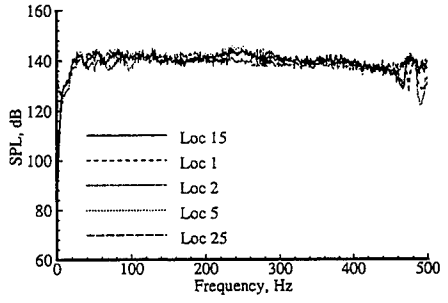

Figure 32: SPL in test section at max level (4-modulator reduced).

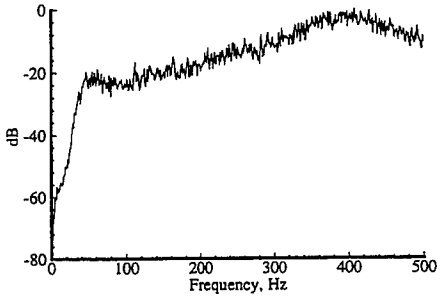

Figure 35: Normalized input spectrum (8-modulator reduced).

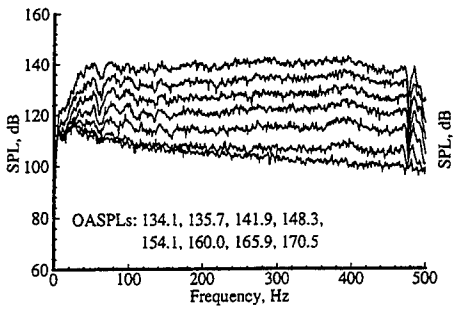

Figure 36: Min to max SPL at location 1 (8-modulator reduced).

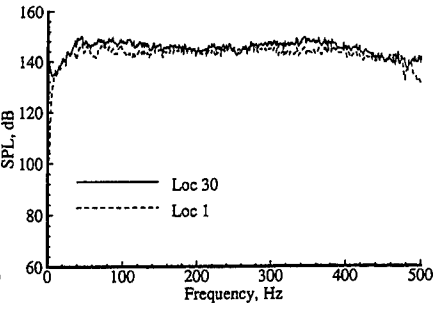

Figure 38: SPL along length of TAFA (8-modulator reduced).

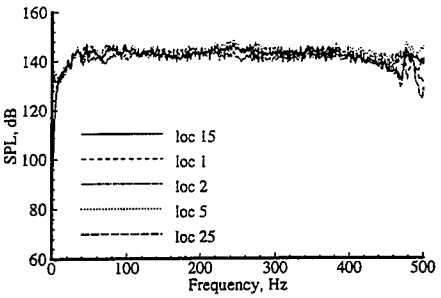

Figure 37: SPL in test section at max level (8-modulator reduced).

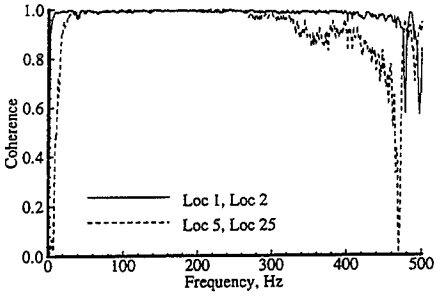

Figure 39: Test section coherence (8-modulator reduced).

Table 2 presents a summary of the maximum average OASPL for each facility configuration. In each case, the number of active modulators were run at maximum power as an independent group (independently for the single modulator case) and the results averaged. For example, results for one active modulator were obtained by running each modulator individually and averaging the resulting pressures.

Table 2: Summary of maximum average overall sound pressure levels (dB).

	Number of Active Modulators			
Configuration	1	2	4	8
2-Modulator Red.	160.4	164.3		
2-Modulator Full	156.7	162.2		
4-Modulator Red.	159.1	—	167.9	
4-Modulator Full	155.6	161.2	167.0	
8-Modulator Red.	158.4	—	—	171.7*
8-Modulator Full	153.0	158.4	164.5	170.0

*Pressure scaled by $^{8}/_{7}$ from 7-modulator run

DISCUSSION

In this section, limiting behaviors of the full and reduced test section configurations are explored and the effect of test section inserts, modulator coupling and wave tube performance are discussed.

Limiting Behaviors

The auto-spectra from the full test section configurations exhibit sharp reductions in level at approximately 210, 340, and 480 Hz. This behavior corresponds to measurements near nodes of vertical (height) standing waves in the test section portion of the wave tube. Table 3 summarizes theoretical, resonant frequencies and corresponding modal indices of the test section duct resonances within the excitation bandwidth. The modal indices m and n correspond to half wavelengths in the vertical and transverse (width) directions of the cross section, respectively. There are several resonances that may be excited below 500 Hz, but only three of these appear to be significant at the test section transducer locations (about the horizontal centerline). Because of the presence of air flow in the facility and lack of measurements in the cross section, it is difficult to correlate the experimental and theoretical modes. Measurements of the acoustic pressure at several locations in a cross-section of the duct will be necessary to fully characterize the resonant behavior. It is sufficient to say that the usable frequency range in the full test section configurations is approximately 40-210 Hz near the horizontal centerline.

Acoustic pressure auto-spectra from the reduced test section configurations are essentially flat to almost 500 Hz. This is due to the fact that only two resonances are within the excitation bandwidth for this configuration, see Table 3. A sharp reduction is noted in the vicinity of 480 Hz. Although the (m=1, n=0) resonance does not appear to be significant, close inspection of the data (not shown) indicates its presence. Therefore, the usable frequency range for the reduced test section configurations is approximately 40-500 Hz.

Table 3: Theoretical resonant frequencies of test section duct modes in Hz.

Trans.	Vertical Index (m)					
Index (n)	0	1	2	3	4	5
	Full Test Section (1.9m x 0.33m)					
0	0.0	84.62	169.24	253.86	338.48	423.10
1	465.41	473.04	495.23	530.14		
	Reduced Test Section (0.66m x 0.33m)					
0	0.0	250.61	501.21			
1	465.41	528.59				

Performance of Test Section Configurations

For constant input acoustic power, the change from full to reduced test section configurations should theoretically result in a 4.7 dB increase in OASPL. However, Table 2 shows that increases of only 2.1 (e.g. 164.3-162.2), 0.9, and 1.7 dB were realized for the two-, four- and eight-modulator configurations. The system efficiency (actual/expected mean-square pressure) of the two-, four- and eight-modulator reduced configurations is 38, 40 and 44 percent, respectively, compared with 51, 63 and 62 percent for the two-, four- and eight-modulator full configurations. The expected pressure is calculated based upon a input-scaled value of the rated acoustic power of the WAS 3000 modulator assuming incoherent sources (3 dB per doubling). In general, the full section efficiency is greater than the corresponding reduced section efficiency. While the reason for this phenomena is not known, it is conjectured that the lack of expansion in the reduced configurations limits the development of plane waves. Therefore, phase and amplitude mismatches between acoustic sources may be accentuated.

Modulator Coupling Performance

A simplified waveguide analysis for coherent, phase-matched sources predicts increases in OASPL as shown in Table 4. Measured performance gains were less than predicted because of the assumptions of the waveguide analysis (inactive source area treated as hard wall), and possible reductions due to phase differences between modulators and non-parallel wave fronts at the exit of the modulator cart, see Figures 4-9. The latter effect is due to different angles of inclination of the sources relative to the axis of the wave tube. The greater gains achieved in the full test section configurations support the above contention that they are more efficient than the reduced configurations in combining the acoustic sources.

Table 4: Change in SPL (dB) from 1 to max. number of active modulators.

Configuration	Δ SPL from 1 Active Mod. (Meas/Pred)
2-Modulator Red. (2 active mods.)	3.9 / 6.53
2-Modulator Full (2 active mods.)	5.5 / 6.53
4-Modulator Red. (4 active mods.)	8.8 / 13.98
4-Modulator Full (4 active mods.)	11.4 / 13.98
8-Modulator Red. (8 active mods.)	13.3 / 22.10
8-Modulator Full (8 active mods.)	17.0 / 22.10

Wave Tube Performance

A change in configuration from the two- to the four-modulator configurations, and from the four- to the eight-modulator configurations, will result in an incremental increase of 3 dB in OASPL if the individual sources are phase-matched. This is due to a pure doubling of the power without any change in the radiation impedance of the individual sources. For the reduced configurations, a 3.6 and 3.8 dB increase are observed, respectively. A 4.8 and

3.0 dB increase are observed for the full configurations, respectively. Note that a greater than 3 dB increase is possible when the higher modulator configuration (for example, the four-modulator reduced configuration) is less susceptible than the lower modulator configuration (the two-modulator reduced configuration) to phase mismatches between modulators. This seems plausible because any such mismatches are averaged over a larger number of sources.

SUMMARY

Modifications to the NASA Langley TAFA facility resulted in significant improvements in the quality and magnitude of the acoustic excitation over the previous facility. The maximum OASPL was increased by over 6 dB (vs the previous 165 dB) with a nearly flat spectrum between 40-210 and 40-480 Hz for the full and reduced test section configurations, respectively. In addition, the coherence over the test section was excellent. These improvements, however, did not meet the objective for a maximum OASPL of 178 dB.

There are several reasons why the maximum OASPL did not meet the objectives, including a lack of expansion in the reduced configurations and phase differences between modulators. A detailed computational analysis would be desirable to indicate the source of the inefficiencies and to help identify possible means of increasing the overall system performance.

ACKNOWLEDGEMENTS

The authors wish to thank Mr. H. Stanley Hogge and Mr. George A. Parker for their support in configuring and running the facility. We wish to also thank Mr. James D. Johnston, Jr. of NASA Johnson Space Center for loan of four Wyle air modulators.

REFERENCES

1. Maestrello, L., Radiation from a Panel Response to a Supersonic Turbulent Boundary Layer, *Journal of Sound and Vibration,* 1969, **10**(2), pp. 261-295.
2. Pozefsky, P., Blevins, R.D., and Langanelli, A.L., Thermal-Vibro-Acoustic Loads and Fatigue of Hypersonic Flight Vehicle Structure, AFWAL-TR-89-3014,
3. Williams, L.J., HSCT Research Gathers Speed, *Aerospace America,* April 1995, pp. 32-37.
4. Clevenson, S.A. and Daniels, E.F., Capabilities of the Thermal Acoustic Fatigue Apparatus, NASA TM 104106, February 1992.

"SONIC FATIGUE CHARACTERISTICS OF HIGH TEMPERATURE MATERIALS AND STRUCTURES FOR HYPERSONIC FLIGHT VEHICLE APPLICATIONS"

Dr. I. Holehouse, Staff Specialist,
Rohr Inc., Chula Vista, California

1. INTRODUCTION SUMMARY

A combined analytical and experimental program was conducted to investigate thermal-acoustic loads, structural response, and fatigue characteristics of skin panels for a generic hypersonic flight vehicle. Aerothermal and aeroacoustic loads were analytically quantified by extrapolating existing data to high Mach number vehicle ascent trajectories. Finite-element thermal and sonic fatigue analyses were performed on critically affected skin panels. High temperature random fatigue shaker tests were performed on candidate material coupons and skin-stiffener joint subelements to determine their random-fatigue strength at high temperatures. These were followed by high temperature sonic fatigue tests of stiffened-skin panels in a progressive wave tube. The primary materials investigated were carbon-carbon and silicon-carbide refractory composites, titanium metal matrix composites and advanced titanium alloys. This paper reports on the experimental work and compares measured frequencies and acoustically induced response levels with analytically predicted values.

The coupon shaker test data were used to generate material random fatigue "S-N" curves at temperatures up to 980°C. The joint subelements provided data to determine the effects on fatigue life of skin-stiffener joining methods. The PWT sonic fatigue panel tests generated response and fatigue life data on representative built-up skin panel design configurations at temperatures up to 925°C and sound pressure levels up to 165 dB. These data are used in determining the response strains and frequencies of skin panel designs when subjected to combined thermal-acoustic loading and to identify modes of failure and weaknesses in design details that affect sonic fatigue life. Sonic fatigue analyses of selected test panel design configurations using finite-element techniques were also performed and related to the experimental results. Acoustically induced random stresses were analytically determined on a mode-by-mode basis using finite element generated mode shapes and an analytical procedure that extends Miles' approach to include multi-modal effects and the spatial characteristics of both the structural modes and the impinging sound field.

The paper also describes the instrumentation development work performed in order to obtain reliable strain measurements at temperatures in excess of conventional strain gauge capabilities. This work focused primarily on the use of recently developed high temperature (350°C to 1000°C) strain gauges, laser Doppler vibrometers, high temperature capacitance displacement probes, and the determination of strain-displacement relationships to facilitate the use of double integrated accelerometer data to derive strain levels.

This work was funded by the USAF Flight Dynamics Laboratory (Kenneth R. Wentz, Project Engineer). The complete program report is contained in References 1 and 2.

2. HIGH TEMPERATURE STRAIN MEASUREMENTS

Conventional adhesively bonded strain gauge installations are temperature limited to approximately 350°C. In order to achieve strain measurements at higher temperatures, up to 980°C, ceramic layers and coatings were used to both attach strain gauges and to thermally protect them. However, such strain gauge installations are very sensitive to process parameters which often need varying depending upon the test specimen material. Coated carbon-carbon is a particularly difficult material to adhere to due to its material characteristics and relatively rough surface texture. Carbon-carbon also has a near zero coefficient of thermal expansion which presents attachment and fixturing problems in a high temperature environment.

When high test temperatures either preclude or make problematic the use of strain gauges, an alternative technique for obtaining strain levels is to measure displacements and then determine strain levels using strain-displacement ratios. Strain is directly proportional to displacement for a given deflected shape, or mode shape, regardless of changes in the elastic modulus of the specimen material as it is heated. Consequently, if the deflected shape does not change significantly with temperature, high temperature test strain levels can be determined from room temperature strain and displacement measurements in combination with displacement measurements made at the test temperature.

This measurement technique facilitates the use of non-contacting transducers which can be located away from the heated area, such as capacitance displacement probes or Laser Doppler Vibrometers (LDV). LDVs actually measure surface velocity but their signal outputs can be readily integrated and displayed as displacement. Accelerometers can also be used to measure displacement by double integrating their signal output. However, since accelerometers require surface contact they have to either withstand, or be protected from, the thermal environment. When this is not readily achievable, it is sometimes possible to install an accelerometer at a location on the test specimen or fixturing where the temperature is within its operating range, providing the displacement response at the point of measurement is fully coherent with the strain response at the required location.

The displacement range limitations of the LDV and capacitance probes available to the program resulted in having to use double-integrated accelerometer outputs to measure displacements at room temperature and at the test temperature. Conventional strain gauges were used to measure strains at room temperature. In order to confirm that the strain-displacement ratios were unaffected by temperature, limited high temperature strains were measured at temperatures up to 980°C. Once the strain-displacement ratio for a given specimen type was determined, air-cooled accelerometers were used to determine high temperature test strain levels. The level of measurement accuracy of this technique was estimated to be within 10 percent.

The most successful strain measurements made at 980°C utilized a ceramic flame spray installation of an HFN type free filament gauge. This gauge installation included the use of silicon-carbide (SiC) cement as a base coat for the gage, applied over a 1-inch square area of a lightly sanded carbon-carbon surface substrate. Lead wire attachments to the gauge were made with standard Nichrome ribbon wire anchored to the specimen with SiC cement. With this gauge installation, it was possible to make dynamic strain measurements for short periods of time at 980°C.

3. RANDOM FATIGUE SHAKER TESTS

The instrumented test specimens were mounted in a duckbill fixture and the specimen/fixture assembly then enclosed in a furnace. An opening in the furnace allows the specimen tip to protrude out in order to accommodate the air-cooled tip accelerometer. Figure 1 shows strain gauge locations and fixturing for material coupon and joint subelement specimens.

The test procedure comprised a room temperature sine-sweep in order to identify the fundamental mode and its natural frequency, one-third octave random loading at room temperature centered around the fundamental natural frequency and one-third octave random endurance testing at the required test temperature and load level.

Twelve inhibited carbon-carbon material coupons generated usable S-N data, eleven at 980°C and one at 650°C. S-N data points were also generated at 980°C for two integral joint and two mechanically fastened joint subelements. Fixturing problems and specimen availability limited the number of S-N data points generated. Figure 2 shows the random fatigue S-N data points with joint subelement data points superimposed. The random fatigue endurance level for the material coupons, extrapolated from 10^7 to 10^9 cycles, is approximately 320 microstrain rms. The integral joint subelements did not fail at the strain gauge locations; consequently, the actual maximum strain levels were higher than those shown on Figure 2. Taking this into account, it appears that the integral joints have a fatigue endurance level of greater than one-half of that for the material coupons. The mechanically fastened joint subelements exhibited fatigue strength comparable to that of the material coupons. These results indicate that carbon-carbon joints and attachments methods are not critically limiting factors in the structural applications of inhibited carbon-carbon. Figure 3 shows a representative example of the strain amplitude and peak strain amplitude probability density functions at room temperature for a material coupon specimen. The "peak" function can be seen to approximate a Rayleigh distribution, as it should for a Gaussian random process.

Random fatigue S-N data were also generated for enhanced silicon-carbide composites (SiC/SiC) including thermally exposed specimens (160 hours at 980°C), titanium metal matrix composites (TMC) utilizing Ti 15-3 and Beta 21S titanium matrix materials, titanium aluminide (super alpha two), titanium 6-2-4-2, titanium 6-2-4-2-Si (including thermally exposed specimens) and Ti-1100. The fatigue endurance levels are shown in Table 1. Also shown in Table 1 are S-N data points for uninhibited carbon-carbon generated on a previous program (Reference 3).

TABLE 1. SUMMARY OF RANDOM FATIGUE ENDURANCE LEVELS.

MATERIAL		TEMPERATURE	ENDURANCE LEVEL CORRESPONDING TO 10^9 CYCLES: OVERALL RMS STRAIN (MICROSTRAIN)	
			MATERIAL COUPONS	SUBELEMENTS
INHIBITED CARBON-CARBON		1800°F (980°C)	320	INTEGRAL JOINTS > 160 BOLTED JOINTS ≅ 320
UNINHIBITED CARBON-CARBON	5 PLY	1800°F (980°C)	100	-
	18 PLY	1800°F (980°C)	150	-
	5 PLY	1000°F (540°C)	100	-
	18 PLY	1000°F (540°C)	450	-
	5 PLY	ROOM TEMPERATURE	550	-
	18 PLY	ROOM TEMPERATURE	450	-
ENHANCED SiC/SiC	NON-EXPOSED	1800°F (980°C)	450	-
	THERMALLY EXPOSED	1800°F (980°C)	300	-
Ti 15-3 TMC		1000°F (540°C)	520	DIFFUSION-BONDED HAT-STIFFENED = 520
		ROOM TEMPERATURE	2250	-
BETA 21S TMC		1500°F (815°C)	200	-
		1200°F (650°C)	510	-
TITANIUM ALUMINIDE (SUPER ALPHA TWO)		ROOM TEMPERATURE	410	-
Ti-6242-Si	NON-EXPOSED	1150°F (620°C)	735	WELDED JOINT = 650
		1150°F (620°C)	-	LID BONDED HONEYCOMB BEAM = 388
	THERMALLY EXPOSED (CASE 4)	1200°F (650°C)	480	WELDED JOINT = 400
Ti 1100		1150°F (620°C)	700	-
Ti 6-2-4-2		ROOM TEMPERATURE	675	-

866MISC/039-T1.IH
12-02-96

Figure 4 shows random fatigue S-N curves for the materials tested superimposed on one graph for comparison purposes. The Ti 15-3 TMC data are not shown since this was a concept demonstrator material utilizing a Ti 15-3 matrix material for producibility reasons. Ti 15-3 does not have the temperature capability for hypersonic vehicle applications. Titanium aluminide data are not shown due to its brittle material characteristics making it unsuitable for sonic fatigue design critical structures. Ti-1100 S-N data were very similar to the non-exposed Ti 6-2-4-2-Si and are not shown. Ti 6-2-4-2 coupons were only tested at room temperature before being replaced by Ti 6-2-4-2-Si, which has higher structural temperature capabilities.

The fatigue curves in Figure 4 show inhibited carbon-carbon to have higher fatigue strength at 980°C than does its uninhibited counterpart. Inhibited carbon-carbon also has greater resistance to oxidation at high temperatures.

Although unexposed enhanced SiC/SiC had greater random fatigue strength at 980°C than did inhibited carbon-carbon, the two materials exhibited similar strength at temperature after allowing for thermal exposure. However, SiC/SiC has a maximum temperature capability of 1100 to 1200°C compared to 1700 to 1900°C for carbon-carbon.

The Beta 21S TMC material demonstrated resonable fatigue strength at 815°C and the Ti 6-2-4-2-Si specimens exhibited high fatigue strength at 620°C to 650°C.

4. SONIC FATIGUE PANEL TESTS

These tests were performed in Rohr's high temperature progressive-wave tube (PWT) test facility. The facility is capable of generating overall sound pressure levels of 165 to 168 dB at temperatures up to 925°C to 980°C, depending upon the test panel configuration and material.

Three rib-stiffened carbon-carbon panels and a monolithic hat-stiffened Beta 21S TMC panel were subjected to sonic fatigue testing. Response strains were measured on the four panels over a range of incrementally increasing sound pressure levels (140 to 165 dB) at room temperature. One carbon-carbon panel was subjected to sonic fatigue testing at room temperature and the other two tested at 925°C. The TMC panel was endurance tested at 815°C. Figures 5 and 6 show a carbon-carbon panel and its fixturing installed in the PWT. The panels were attached to the fixture via flexures in order to allow for differences in the thermal expansion of the panel and fixture materials. Structural details of the panels and instrumentation locations are given in References 1 and 2.

The three carbon-carbon panel configurations encompassed two skin thicknesses and two stiffener spacings as follows:

Panel 1: 3 skin bays, 6 in. by 20 in. by 0.11 in. thick
Panel 2: 2 skin bays, 9 in. by 20 in. by 0.11 in. thick
Panel 3: 3 skin bays, 6 in. by 20 in. by 0.17 in. thick

Table 2 summarizes the measured room temperature frequencies and strain response levels:

TABLE 2. ROOM TEMPERATURE RESPONSE OF TEST PANELS.

TEST PANEL	FREQUENCY OF IN-PHASE MODE (Hz)	OASPL (dB)	OVERALL RMS STRAINS (MICROSTRAIN)	
			EDGE OF SKIN BAY	CENTER OF SKIN BAY
CARBON-CARBON NO. 1	267	165	305	149
CARBON-CARBON NO. 2	155 & 171	145 150 165	126 191 558*	39 59 173*
CARBON-CARBON NO. 3	423	165	69	127
BETA 21S TMC	241	165	HIGHEST STRAIN = 287 AT PANEL CENTER ON STIFFENER CAP	

*** EXTRAPOLATED ON THE BASIS OF THE STRAIN RESPONSE WITH SPL FOR PANELS 1 AND 3.**

Panel 1 was subjected to 165 dB at room temperature for 10 hours at which point cracks developed at the ends of the stiffeners. The frequency dropped slightly during the ten hour test resulting in the number of cycles to failure being approximately 9 million.

Panel 2 was endurance tested at 925°C at 150, 155 and 160 dB for 3-1/2 hours at each level, followed by one hour at 165 dB. At this point, cracks were observed at the ends of the stiffeners, similar to the cracks in Panel 1.

Panel 3 was endurance tested at 925°C and 165 dB for 10 hours without any damage to the panel.

The TMC panel was endurance tested at 815°C and 165 dB for 3-1/2 hours at which time cracks were observed in two stiffener caps at the panel center.

The high test temperatures for Panels 2 and 3 and the TMC panel precluded attaching an accelerometer directly to the panel surface, even with air cooling. This prevented the direct measurement of panel displacements at 925°C. In order to attempt to estimate the high temperature endurance test strain levels, a temperature survey was performed on the panel fixturing with Panel 3 installed in order to determine an acceptable location for an accelerometer. An accelerometer at the selected fixture location tracked linearly with the highest reading strain gauges during a room temperature response survey. The coherence between the fixture accelerometer and the panel strain gauges was 0.9 in the frequency range of panel response.

Having established a coherent strain displacement relationship at room temperature, the temperature was increased progressively with increasing acoustic loading, generating accelerometer and microphone data at 480°C and 140 dB, 650°C and 155 dB, 860°C and 155 dB, and 925°C at 165 dB. It was clear from the data at the higher temperatures and load levels that the full spectrum overall rms displacement levels obtained by double integrating the accelerometer output signals could not be used to determine high temperature strain levels due to high amplitude, low frequency displacements (displacement being inversely proportional to frequency squared for a given "g" level) that were well below the panel response frequency range and therefore would not be proportional to panel strain levels. It is important to remember here that since the accelerometer is mounted on the panel fixture, it is measuring fixture response, some of which is not related to panel response.

After reviewing the various frequency spectra, it was decided to re-analyze the data to generate overall rms levels over selected frequency bandwidths that would encompass a high percentage of the full-spectrum overall rms strains and eliminate the low frequency displacements. If a consistent strain-displacement relationship could be established at room temperature within a frequency bandwidth such that the strains could be related to the full-spectrum overall rms strains, and if the same bandwidth could be used to generate displacements at temperatures that were sufficiently consistent to relate to strain response, then it would be possible to at least make a reasonable estimate of the test temperature strain level. It was determined that band-passed response data in the 300 to 600 Hz frequency range gave consistent strain-displacement ratios at room temperature. Double-integrated band-passed accelerometer outputs (displacements) were consistent with increasing sound pressure levels at incrementally increasing test temperatures up to the 925°C/165 dB endurance test conditions. Table 3 summarizes the high temperature test panel results.

TABLE 3. HIGH TEMPERATURE TEST PANEL RESULTS.

TEST PANEL	TEST TEMPERATURE (°F)	TEST TEMPERATURE (°C)	OVERALL SOUND PRESSURE LEVEL (dB)	HIGHEST ESTIMATED OVERALL RMS STRAIN (MICROSTRAIN)	EXPOSURE TIME, ESTIMATED FATIGUE CYCLES AND COMMENTS
BETA 21S TMC PANEL	1500	815	165	NOT ESTIMATED	3 1/2 HRS, $3x10^6$ CYCLES, STIFFENERS CRACKED AT MID-SPAN
CARBON-CARBON PANEL NO. 2	1700	925	150	155	3 1/2 HRS, $2.3x10^6$ CYCLES, NO FAILURE
			155	219	3 1/2 HRS, $2.3x10^6$ CYCLES, NO FAILURE
			160	316	3 1/2 HRS, $2.3x10^6$ CYCLES, NO FAILURE
			165	453	1 HR, $6.4x10^5$ CYCLES, CRACKS AT STIFFENER ENDS
CARBON-CARBON PANEL NO. 3	1700	925	165	103	10 HRS, $1.7x10^7$ CYCLES, NO FAILURE

It should be noted that carbon-carbon panels 1 and 2 exhibited cracks at the stiffener ends, whereas the maximum measured strains were at the edges of skin bays. Consequently, the actual strain levels at the crack locations were either higher than the measured levels or there were significant stress concentrations at the stiffener terminations.

5. COMPARISON OF ANALYTICAL AND TEST RESULTS FOR CARBON-CARBON PANELS

MSC NASTRAN was used to perform finite element analyses on the three carbon-carbon panels that were subjected to the sonic fatigue testing described in Section 4. The oxidation resistant coating was modeled as a non-structural mass, which is compatible with the panel test results. Natural frequencies, mode shapes and acoustically induced random strain levels were analytically determined for room-temperature conditions and compared to the room-temperature panel test results.

Acoustically induced random stresses were analytically determined on a mode-by-mode basis using the finite element generated mode shapes and a Rohr computer code based on an analytical procedure presented in Reference 4. This procedure extends Miles' approach (Reference 5) to include multi-modal effects and the spatial characteristics of both the structural modes and the impinging sound field.

Table 4 shows the calculated and measured frequencies, overall rms strain levels and the strain spectrum levels for the in-phase stiffener bending mode for the carbon-carbon panels at room temperature.

TABLE 4. CALCULATED AND MEASURED RESPONSE FREQUENCIES AND STRAIN LEVELS FOR CARBON-CARBON PANELS AT ROOM TEMPERATURE.

	NATURAL FREQUENCY OF IN-PHASE MODE (Hz)		STRAIN LEVELS AT EDGE OF SKIN BAY			
			OVERALL RMS STRAIN (MICROSTRAIN)		STRAIN SPECTRUM LEVEL IN-PHASE MODE (MICROSTRAIN/Hz)	
	FE ANALYSIS	MEASURED	FE ANALYSIS	MEASURED	FE ANALYSIS	MEASURED
PANEL 1 (165 dB)	305	267	510	305	84	60
PANEL 2 (145 dB)	190	155 & 171	133	126	40	41
PANEL 3 (165 dB)	460	423	77	69	16	16

The above results show good agreement between the finite element generated values and those measured. The level of agreement is particularly good for the strain spectrum levels, which are typically more difficult to accurately predict. Figure 7 shows the finite-element frequency solution for Panel 3. The in-phase mode shape can be seen to have an overall modal characteristic due to the relatively low bending stiffness of the stiffeners for the skin thickness used. Figure 8 shows the measured and finite-element generated strain frequency spectra for Panel 3.

Details of the finite-element analyses and models are contained in References 1 and 2.

6. CONCLUSIONS AND RECOMMENDATIONS

1. The high temperature testing techniques and strain measuring procedures successfully generated usable random fatigue S-N curves and panel response data. The use of strain-displacement ratios were shown to be an effective alternative to high temperature strain gauge measurements.

2. In general, the materials and structural concepts tested demonstrated their suitability for hypersonic flight vehicle skin panel applications. The major exception was Titanium-Aluminide Super Alpha Two which was determined to be too brittle.

3. Inhibited carbon-carbon exhibited significantly higher random fatigue strength at 980°C than did the uninhibited carbon-carbon -- two to three times the random fatigue endurance strain level.

4. Thermally exposed enhanced SiC/SiC had comparable fatigue strength to that of inhibited carbon-carbon at 980°C.

5. The TMC specimens usefully demonstrated the fatigue strength of the TMC concept and the need to develop the concept to incorporate higher temperature capability titanium matrix materials.

6. Titanium 6-2-4-2-Si exhibited high fatigue strength in the 590°C to 650°C temperature range and also demonstrated the need for TMC materials to utilize higher temperature matrix materials in order to be cost effective against the newer titanium alloys.

7. The level of agreement between the finite element analysis results for the carbon-carbon panels and the progressive-wave tube test data demonstrated the effectiveness of the analytical procedure used. The analysis of structures utilizing materials such as carbon-carbon clearly presents no special difficulties providing the material properties can be well defined.

8. It is recommended that further tests be conducted similar to those performed in this program but with greater emphasis on testing panels having dimensional variations in order to develop design criteria and life prediction techniques. Such testing should be performed on those structural materials and design concepts that emerge as the major candidates for flight vehicle applications as materials development and manufacturing techniques progress.

REFERENCES

1. R. D. Blevins and I. Holehouse, "Thermo-Vibro Acoustic Loads and Fatigue of Hypersonic Flight Vehicle Structure," Rohr, Inc. Engineering Report RHR 96-008, February 1996.

2. United States Air Force Systems Command, Flight Dynamics Laboratory Final Technical Report, Contract No. F33615-87-C-3327, to be published.

3. R. D. Blevins, "Fatigue Testing of Carbon-Carbon Acoustic Shaker Table Test Coupons," Rohr, Inc. Engineering Report RHR 91-087, September 1991.

4. R. D. Blevins, "An Approximate Method for Sonic Fatigue Analysis of Plates and Shells," Journal of Sound and Vibration, Vol. 129, 51-71, 1989.

5. J. W. Miles, "On Structural Fatigue Under Random Loading," Journal of Aeronautical Sciences, Vol. 21, November 1954.

A. Test Configuration for Material Coupons

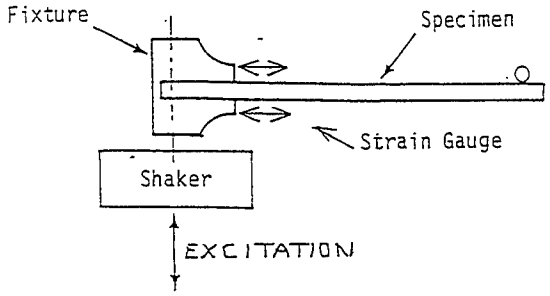

B. Test Configuration for Carbon-Carbon Integral Stiffener Specimens

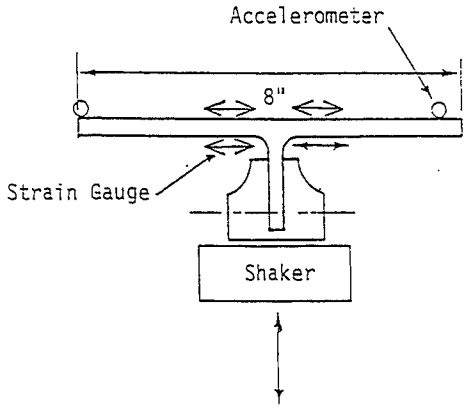

C. Test Configuration For Carbon-Carbon Mechanically Fastened Stiffener and All Titanium Diffusion Bonded Joint Specimens

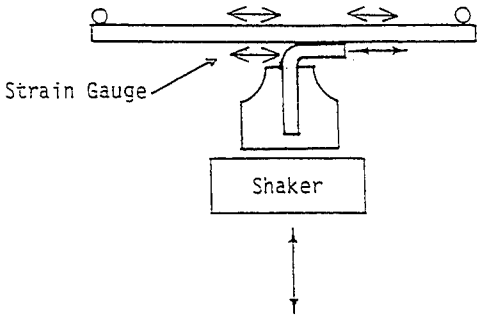

FIGURE 1 Typical Strain Gauge Locations and Test Configurations for Material Coupon and Joint Subelement Shaker Test Specimens

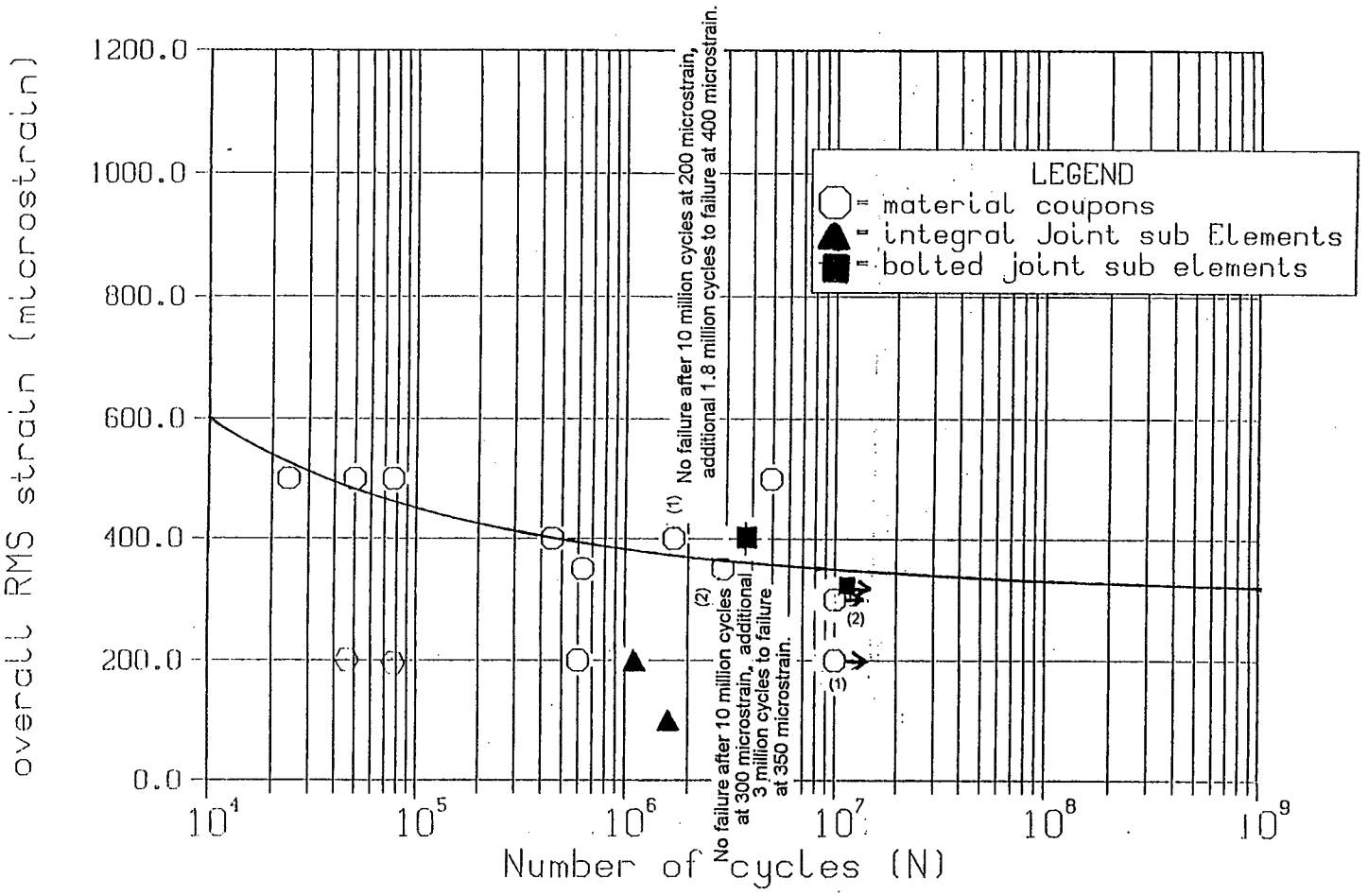

FIGURE 2 Random Fatigue S-N Curve for Inhibited Carbon-Carbon Coupons and S-N Data Points for Joint-Subelements

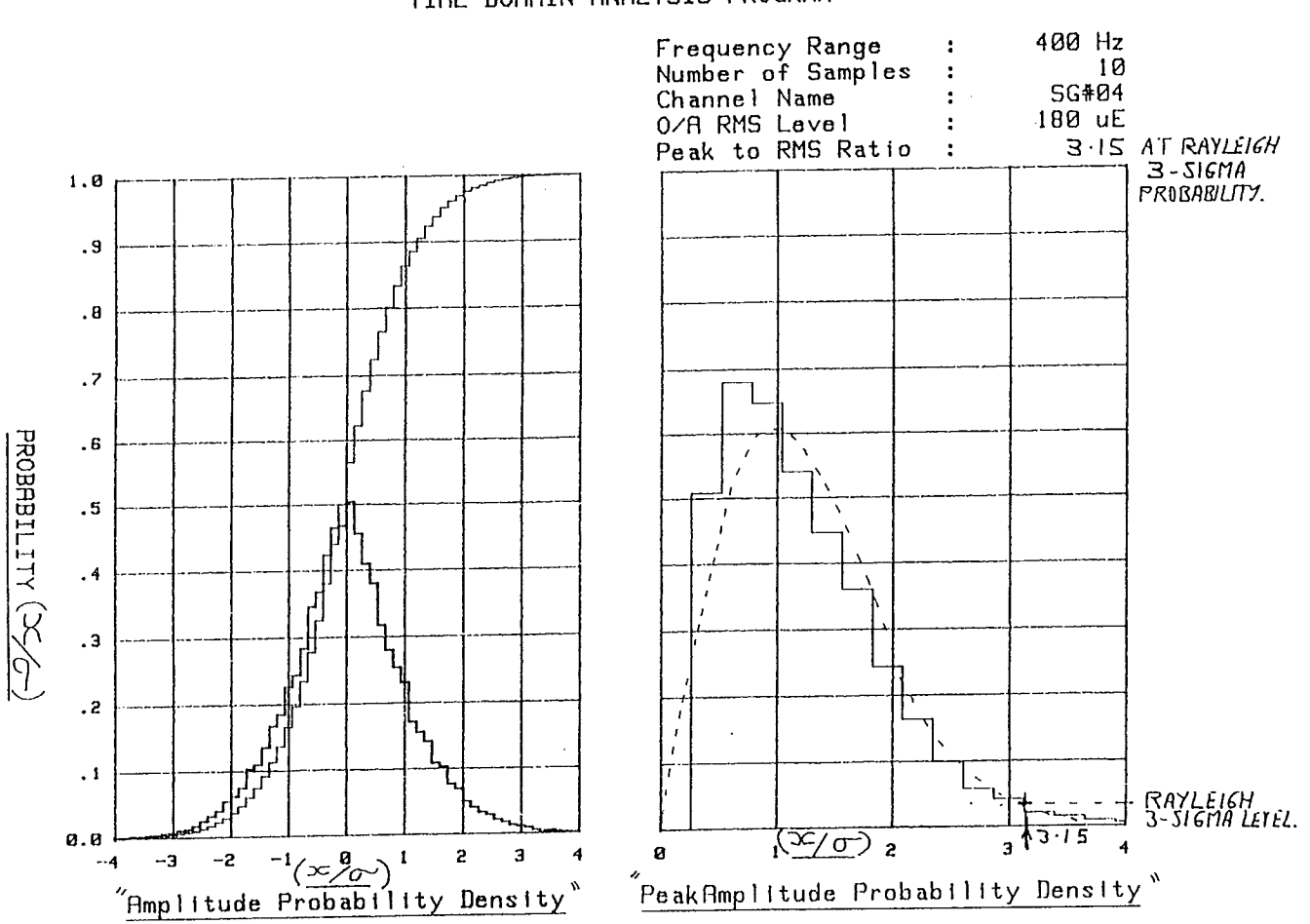

FIGURE 3 Strain Amplitude and Peak Amplitude Probability Density Functions for Carbon-Carbon Shaker Test Specimen at Room Temperature

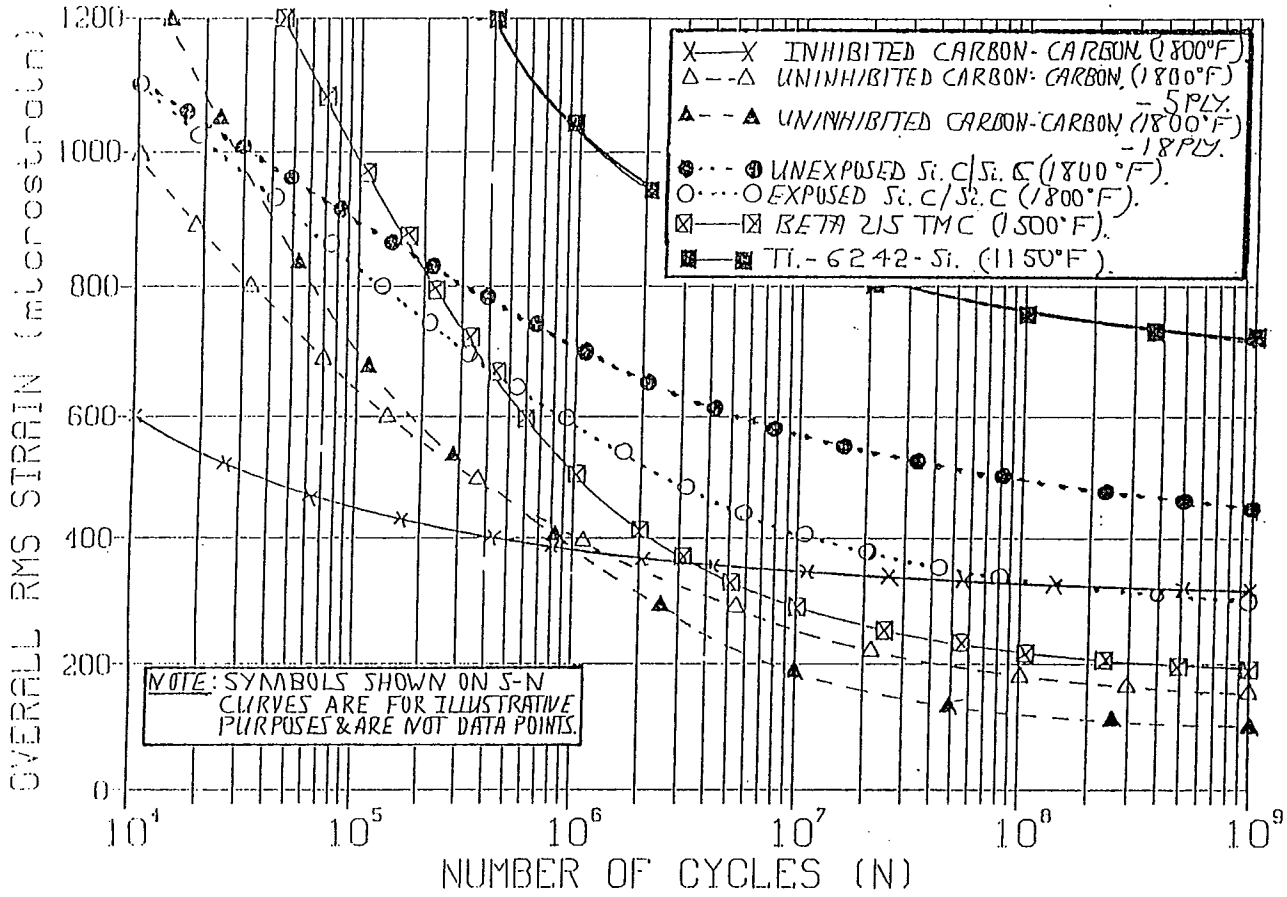

FIGURE 4 Random Fatigue S-N Curves for Materials Tested Shown Superimposed for Comparison Purposes

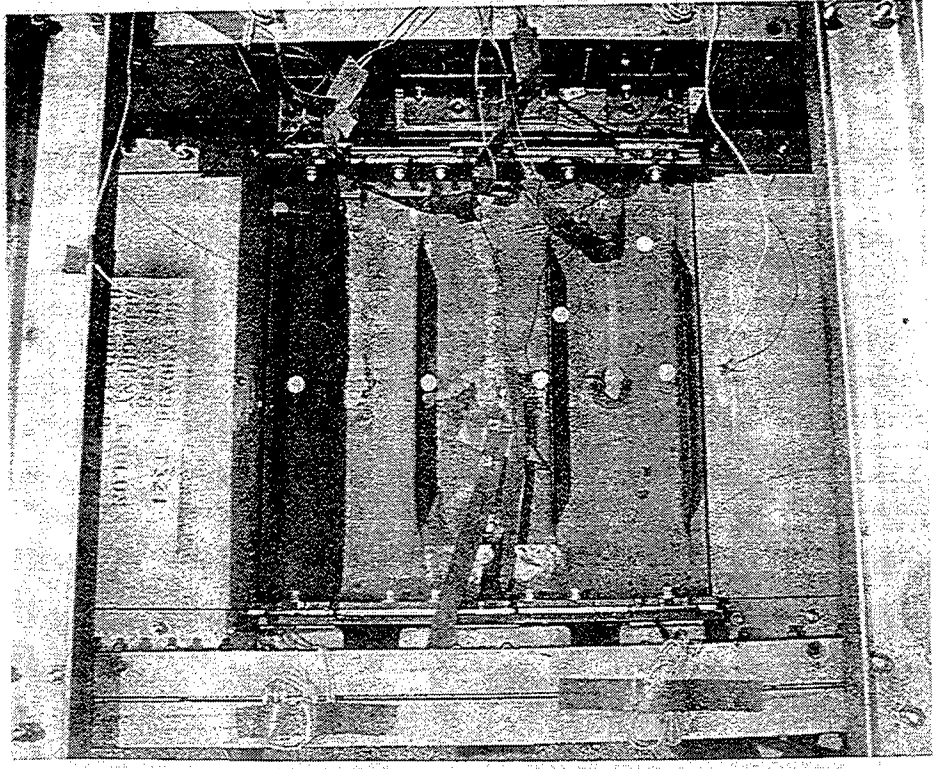

Figure 5 Carbon-Carbon Sonic Fatigue Test Panel and High Temperature Fixture Installed in Progressive-Wave Tube

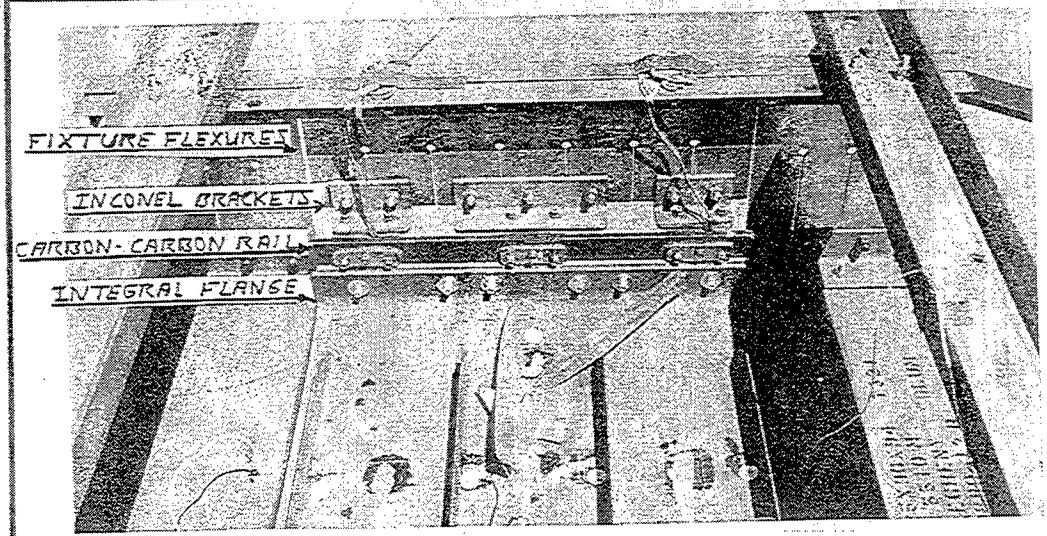

Figure 6 Close-up View of Carbon-Carbon Panel Attachments to High Temperature Fixture

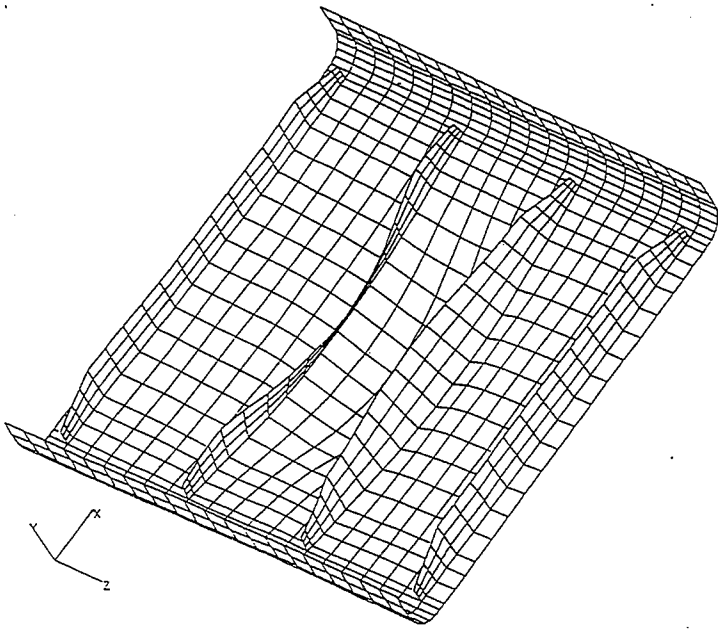

FREQUENCY = 460 Hz.

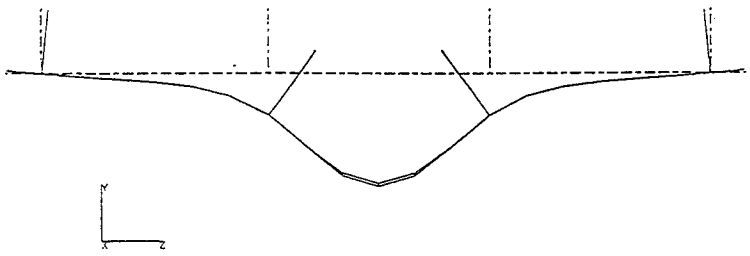

FIGURE 7 Finite Element Solution for In-Phase Overall Mode -- Carbon-Carbon Panel, Concept 3

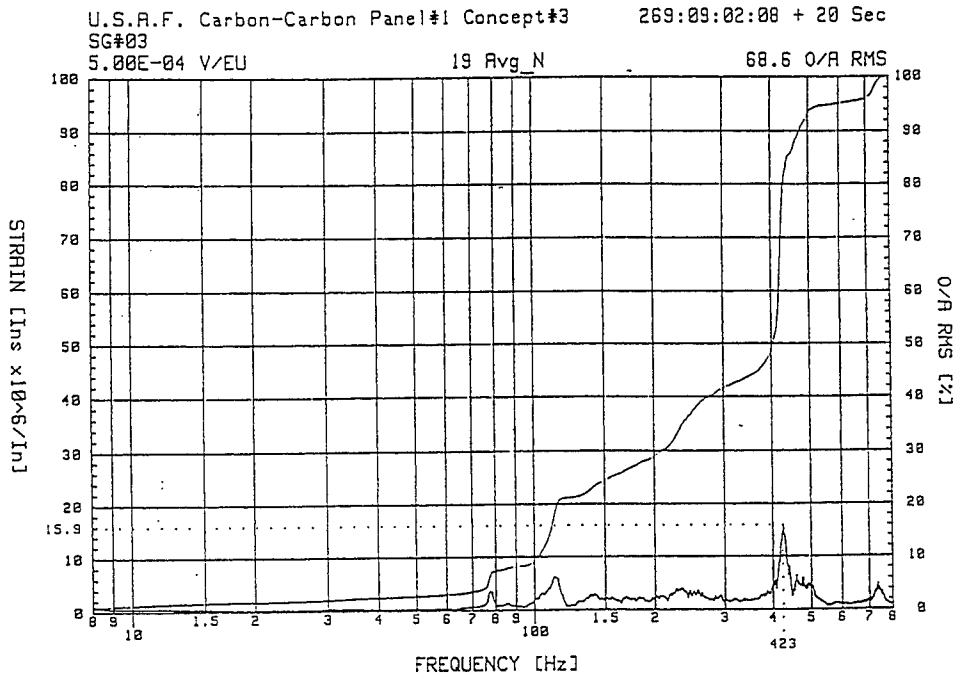

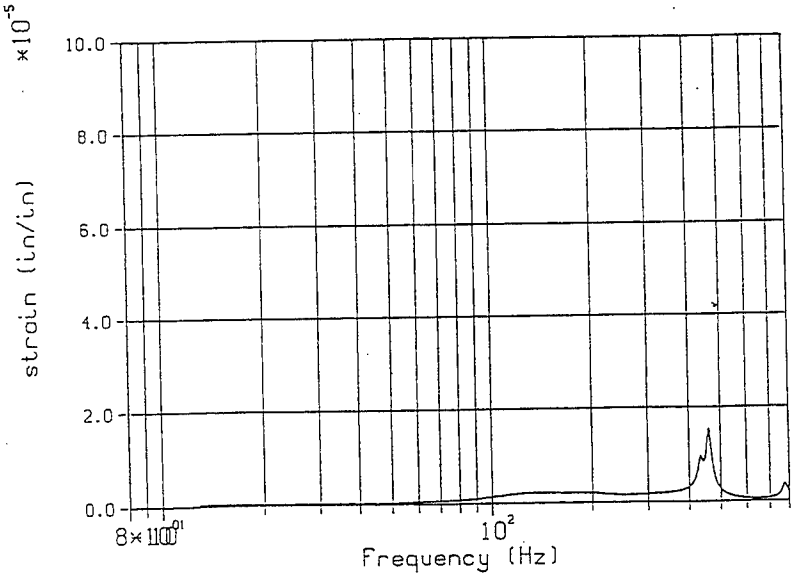

FIGURE 8 MEASURED AND CALCULATED STRAIN FREQUENCY SPECTRA
CARBON-CARBON PANEL 3, STRAIN GAUGE 3

SCALING CONCEPTS IN RANDOM ACOUSTIC FATIGUE

BY

Marty Ferman* and Howard Wolfe**

ABSTRACT

Concepts are given for scaling acoustic fatigue predictions for application to extreme environmental levels based on testing " scaled" structures at existing, lesser environmental levels. This approach is based on scaling a test structure to fit within the capabilities of an existing test facility to attain fatigue results, and then using analytical extrapolation methods for predicting the full scale case to achieve accurate design results. The basic idea is to utilize an existing acoustic fatigue facility to test a structure which has been designed (scaled) to fatigue within that facility's limits, employing the appropriate structural properties (such as thinning the skins, etc.). Then, the fatigue life of the actual structure is determined by analytically scaling the test results to apply to the full scale case (thicker) at higher noise levels for example. Examples are given to illustrate the approach with limits suggested, and with the recognition that more work is needed to broaden the idea.

BACKGROUND

While it is important to continually expand the capability of acoustic test facilities , it is perhaps equally important to be able to work with existing facilities at any time. That is, facility expansions, enhancements , and modernization's should always be sought from time to time, so long as practical and affordable from cost effective considerations. Limits should be pushed to accommodate larger sizes of test specimens with higher noise levels with wider ranges of frequencies, with wider ranges of temperatures, and with better capabilities for applying pressures along with any one of several types of preloads. These are costly considerations and require considerable time to accomplish. Facility rental can be used in some cases to bolster one's testing facilities, however if the application suggests a situation beyond any available facility for the required design proof, then an alternate is needed. Thus the scaling concept suggested here is a viable and useable possibility.

The Author's basis for the approach stems from their extensive, collective, experience in Structural Dynamics, especially work in Acoustic Fatigue, Fluid-Structure Interaction, Buffet , and Aeroelasticity/Flutter , and particularly from experience with flutter model testing, in which it is quite common to ratio test results from a model size to full scale for valid

---

* Assoc. Prof., Aerospace and Mech. Engr. Dept, Parks College, St. Louis Univ., Cahokia, IL, 62206, USA

** Aerospace Engineer, Wright Laboratory, Wright Patterson AFB, OH, 45433, USA

predictions . Flutter is a well recognized area where model data is commonly used in nondimensional form to establish design margins of safety, as typified in Ref (1-2). Flutter can be nondimensionalized quite broadly as pointed out in many works, and is clearly done for a wide range of general cases using the "so-called" Simplified Flutter Concept, Ref (3) . The degree of the use of the flutter model scaling rules varies considerably today, because some people are testing as much or more than ever, while others are testing less and relying more heavily on advanced theories such as Computational Fluid Dynamics, CFD. However, the basic ideas in flutter model scaling are still POWERFUL! In fact, this concept **has fueled** the Author's desires to develop the "acoustical scaling" used in the approach presented. Moreover, when starting to write this paper, the Authors realized that this type of scaling is also common to many related areas of structural dynamics, and thus chose to include some examples of those areas to emphasize the main point here!

For example, experience in fluid-structure interaction and fatigue of fuel tank skins, a related work area, serves as another example of scaling structures to demonstrate accurate predictions with widely varied environmental levels, and a multitude of configurations. Scaling and nondimensional results were used extensively in Ref (4 -13), and are cited here because of the immense data base accumulated. The work at that time did not necessarily define scaling as used here , but hindsight now suggests that there is a clear relation.

It is becoming well recognized that Buffet is easily scaled , and many engineers and investigators are now employing scaling of pressures from model to full size applications, and are also using scaled model response to predict full scale cases . Some of the earliest and some of the more modern results clearly show this aspect. For example, Ref (14 -16) are typical, quite convincing, and pace setting regarding scaled data. Buffet models which are much more frail that the full-scale cases are used to develop data for full scale applications, and besides giving full sized results, provide a guide to safe flight testing as has been done more extensively with flutter testing.

Obviously, acoustical response and fatigue phenomenon are also nondimensionalizable and scaleable, Ref (17 -18), for example. This point is being taken further here; that is , scaling will be used to take better advantage of limited facility testing capability to predict more severe situations, as is used in the case of flutter model testing where a larger specimen is predicted from tests of a smaller structure using similarity rules. Here in the acoustic application, a thinner , or otherwise more responsive specimen, is tested and then analytical means are used to make the prediction for the nominal case.

APPROACH

The method is shown here is basically an extension of the flutter model scaling idea, as applied to acoustical fatigue testing with a particular emphasis on random applications. The technique will also work for sine type testing in

acoustical fatigue, and perhaps it will be even more accurate there, but most of today's applications are with random testing, notably in the aircraft field. Thus it is in this area where the method should find more application . The Authors have a combined professional work experience of some 70+ years and thus have tried to focus this extensive background on an area where gains can be made to help reduce some costs while making successful designs, by using lesser testing capability than might be more ideally used. It is believed that the best testing for random acoustic fatigue, is of course, with (a) the most highly representative structure, and as large a piece as can be tested, both practically and economically, (b) the most representative environmental levels in both spectrum shape and frequency content, (c) test times to represent true or scaled time, as commonly accepted, (d) temperatures should be applied both statically and dynamically, and finally (e) preloading from pressures, vibration, and from boundary loading of adjacent structure. Frequently, testing is done to accomplish some goal using a portion of these factors, and the remainder is estimated . Thus the Authors believed that there is a high potential to extend the flutter model approach to acoustical applications.

Recall that in the flutter model approach , the full scale flutter speed is predicted by the rule

$$((V_F)_A)_P = [((V_F)_M)_E / ((V_F)_M)_C] \times [((V_F)_A)_C] \qquad (1)$$

where V_F is flutter speed, the subscripts M and A refer to model and aircraft respectively, the subscript C refers to calculated, and the subscript P refers to predicted. Thus the equation suggests that the full scale predicted flutter speed is obtained by taking the ratio of experimental to calculated flutter speed for the model and then multiplying by a calculated speed for the airplane. These flutter model scaling ideas are covered in any number of References, i.e. Ref (1-3), for example.

The same concept can be utilized in acoustic fatigue, i.e. the strain at fatigue failure relation, (ε,N) can be scaled from model structure tested at one level and then adjusted for structural sizing and environmental levels. This relation can be addressed as done for the flutter case:

$$((\varepsilon,N)_A)_P = [((\varepsilon,N)_M)_E / ((\varepsilon,N)_M)_C] \times [((\varepsilon,N)_A)_C] \qquad (2)$$

where ε is strain, and N is the number of cycles at failure, where as above in Eq (1) , the subscripts M and A refer respectively to Model and Full Scale for parallelism, while the subscripts E, C, and P have the same connotation again, namely, experimental, calculated, and predicted. Thus the full scale case is

predicted from a subscale case by using the ratio of experimental to theoretical model results as adjusted by a full scale calculation. Flutter model scaling depends upon matching several nondimensional parameters to allow the scaling steps to be valid. While these same parameters are, of course, not necessarily valid for the acoustic relationships, other parameters unique to this acoustical application must be considered, and will be discussed. Accurate predictions for the method relies on extensive experience with the topic of Acoustic Fatigue in general, because concern is usually directed towards the thinner structure such as: panels, panels and stiffeners, and panels and frames, bays (a group of panels), or other sub-structure supporting the panels. These structures are difficult to predict and are quite sensitive to edge conditions, fastening methods, damping, combination of static and dynamic loading, and temperature effects. Panel response prediction is difficult , and the fatigue properties of the basic material in the presence of these complex loadings is difficult. However, the experienced Acoustic Fatigue Engineer is aware of the limits, and normally accounts for these concerns. Thus the method here will show that these same concerns can be accounted for with the scaling approach through careful considerations.

The Authors believe that the method is best explained by reviewing the standard approach to acoustic fatigue, especially when facility limits are of major concern. Fig (1) was prepared to illustrate these points of that approach. Here it is seen that key panels for detail design are selected from a configuration where the combination of the largest, thinnest, and most severely loaded panels at the worst temperature extremes and exposure times are considered. These can be selected by many means ranging from empirical methods, computational means, and the various Government guides, Ref (17-18), for example. Then detailed vibration studies are run using Finite elements , Rayleigh methods, Finite Difference methods, etc. to determine the modal frequencies and shapes, and frequently linearity is assessed. Then acoustical strain response of the structure is determined for sine, narrowband, and broadband random input to assess fatigue life based on environmental exposure times in an aircraft lifetime of usage. These theoretical studies are then followed by tests of the worst cases, where vibration tests are conducted to verify modal frequencies, shapes, and damping, and linearity is checked again for the principal modes. This is followed by acoustical strain response tests where the strain growth versus noise levels is checked, again employing sine, narrowband and broadband random excitation. Note the figure suggests that data from the vibration tests are fed back to the theoretical arena where measured data are used to update studies and to correlate with predictions, especially the effect of damping on response and fatigue, and of course, the representation of nonlinearity. Also, the measured strain response is again used to update fatigue predictions. These updates to theory are made before the fatigue tests are run to insure that nothing is missed. However, in this

case, the required sound presssure level SPL in (dB) is assumed to exceed the test chamber's capability. Thus , as shown in the sketch in Fig (2) the key strain response curve, ε vs dB, is extrapolated to the required dB level. This data is merged with the strain-to-failure curve at the right to establish the cycle count, N, giving the (ε, N) point for this case. The extrapolated data provides some measure of the estimated life, but again is heavily dependent upon the accuracy of the basic strain response curve, and is especially dependent on whether high confidence exists at the higher strains. Linear theory is also shown in this case, indicating it overpredicts the test strain response and hence shows a shortened fatigue life compared to test data, as is generally the case in today's extreme noise levels. This illustration is highly simplified, because experienced designers readily know that it is difficult to predict even simple panels accurately at all times, let alone complex and built-up structure consisting of bays (multi-panel); this will addressed again later in the paper.

The new concept of scaled acoustic fatigue structures is shown on the sketch of Fig (3) where the standard method is again shown, but smaller in size, to refocus the thrust of the new idea. The scaling process parallels the standard approach, and actually complements that approach, so that the two can be run simultaneously to save time, costs, and manpower. Here the panel selection process recognizes that the design application requires environments far in excess of available facility capability. Thus the scaling is invoked in the beginning of the design cycle. As the nominal panels (bays) are selected and analyzed for vibration, response and fatigue, scaled structures are defined to provide better response within the existing chamber ranges so that they can be fatigued and then the results can be rescaled to the nominal case. In this manner, appropriate designs can be established to meet safety margins with more confidence, and will avoid costly redesign and retrofitting at downstream stages where added costs can occur and where down times are difficult to tolerate. The concept is further illustrated in the sketch of Fig (4). Here the strain response curve of the nominal case and that of the scaled version are combined with strain to failure data (coupon tests) to show fatigue results. Note the strain response for the nominal case at the highest dB level available gives the fatigue value at point A, while the extrapolated data for this curve gives point B. The scaled model being more responsive gives the point C, and when rescaled gives the point D which differs slightly from the extrapolated point B as it most likely will, realistically. More faith should be placed on data from an actual fatigue point than a point based on the projected strain response curve. Note, Fig (5) illustrates the winning virtue of the scaleable design. The figure shows a hypothetical set of test data for the (ε ,N) for a structure for various SPLs for the nominal case, open circles, and for the fatigue results of the scaled model , closed squares. The scaled model was assumed to be thinner here for example, and that the scaled data is also

rescaled to fit the nominal curve here. The most interesting aspect is shown by the two clusters of data , denoted as **A** and **B** where there are rough circles about drawn about the clusters. Here the emphasis is that tests of the scaled model (and rescaled data) are used to find the higher strain conditions which cannot be found from the nominal case. In both cases at the highest strain levels, the facility is used to its limits, but with enough testing with the thinner case, adequate data is available to make the prediction more accurate using Eq (2) for the final correlation as shown here. The statistical scattering of the scaled data will be an accurate measure for the nominal case, particularly when compared to estimates based on extrapolation of the strain response for the nominal case. There are many cautions to be noted with this approach as there are with all acoustic fatigue methods, and of course, tests. First, the linearity of the modes, either in unimodal sine excitation, multi-mode sine, narrow band or broadband random must be carefully handled. The strain response of individual locations throughout the structure must be carefully monitored in calculations and tests so that strain response is truly understood and used to define fatigue life carefully. This is difficult to do in many applications where widely varying conditions and durations require some type of Miner Rule combination to provide a true measure of fatigue. Similarly, strain risers at fasteners, discontinuities, holes, frames, stiffeners, material changes along with temperature gradients, temperature transients, require final "tweeks" to predictions, regardless. Nonlinearity , especially in the multi -mode case, is one of the most formidable foes to conquer for any application.

APPLICATIONS AND EXAMPLES

The tests of an Aluminum panel of size 10x20 in. and with a thickness of 0.063 thickness , Ref (19), will be used to illustrate the technique. The panel has approximately fixed-fixed edge conditions, and is quite nonlinear in terms of strain response, Ref (19). The measured strain response for the panel is shown in Fig (6) along with an estimated response curve for a thinner panel (0.040 in) based on the test data. For this case it is assumed that data were needed at 175 dB, while the facility could only achieve 164 dB. The strain response for the thinner case was estimated using the classical equation for the amplitude of response, δ ;

$$\delta = \frac{\left[\iint \phi^2 dxdy\right]\left[PSD_P(f)\right]}{M\omega^{3/2}(8\zeta)^{1/2}} \qquad (3)$$

where M is the generalized mass, ω is the natural frequency, ξ is the viscous damping factor , ϕ is mode shape, PSD_P is the pressure Power Spectral Density, and x,y are the positional coordinates along the plate. Since strain , ε, is proportional to the amplitude,

$$\varepsilon = (t/2)(\partial\phi^2/\partial x^2)\,\delta \qquad (4)$$

Combining Eq (3 and 4) shows that the strain response curves are proportional to the thickness factor, as given by:

$$\varepsilon_2 = \varepsilon_1 (t_1/t_2)^{3/2} \qquad (5)$$

However, it must be noted that this case is nonlinear, and thus, this result is not exactly correct, but simply used for an illustration here. The actual data for the 0.063 thickness is extrapolated to a required 175 dB, showing a strain of 1000 micro in/in. The estimated curve for the thickness of 0.040 in. shows ,of course, a greater response at all dB levels as it should, and moreover shows that only 150 dB are needed to achieve the 1000 micro - strain condition. Moreover, the thinner panel will exhibit large enough strains at the lower SPLs to improve the fatigue curve where the thicker panel is insensitive. Taking the example a step further, the fatigue point of the nominal case is shown on a strain to failure plot in Fig (7) , employing beam coupon tests of Ref (11), which were shown to be excellent correlators with panel fatigue in the collection of work in Ref (6-13). The fatigue point for the 164 dB excitation, 800 micro-strain, is shown as a triangle, while the extrapolated data for 175 dB is shown as the flagged triangle. One test point exists for the nominal case, Ref (20) , and is shown by a star symbol. Data for the thinner panel are shown as circles at the various strain to cycle count cases for the various SPLs corresponding to the beam curve. Notably, these points can be seen to produce shorter fatigue cases as they should due to increased strains, but note that they are also at lower frequencies which would give a longer test time than if they were the nominal thickness. The scaled model is seen to produce the same point as the extrapolated case in this hypothetical case for the 1000 microstrain case (again, at two different dB levels for two thicknesses). A SPL of 150 dB, rather benign, is seen to be quite effective. The actual fatigue point at 164 dB for the nominal case required 3 hours and was predicted to be 2.8 hrs. The estimated fatigue for the extrapolated case of 175 dB was estimated to be 1.7 hrs, while the scaled point from the thinner panel was estimated to be 2.2 hours which is slightly off, but the Authors have had to rely on log plots for much of the data and thus lack someaccuracy. Because of lack of actual data , the scatter from the estimate vs the test of the nominal case was used to scatter the estimate for the 1000 microstrain case, flagged dark circle, as if the use of Eq (2) had been employed directly. One must be careful here, because there can be a vast difference between theory and test, and this can mislead inexperienced persons applying these methods. As noted earlier, related work in fluid-structure and buffet , actually demonstrate this type of scaling. To illustrate, several figures are republished

here to make this point rather clear. Fig (8) of Ref (8) shows the dynamic bending strains in the bottom panel of an otherwise rigid fuel tank which is being excited vertically with moving base input. The vertical axis is strain while the abscissa is the number of g's input. Three panel thicknesses and four depths of fluid (water in this case) were used. Note the sharp nonlinear effect in the response, rather than linear response growth as force increases. Interestingly, the data was nondimensionalized into the curve of Fig (9), Ref (8), which was originally intended for a design chart to aid in developing strain response characteristics for use in fatigue. This curve displays a parameter of response as the ordinate vs an excitation parameter on the abscissa. Here, E is Young's modulus, ρ is density, t is thickness, a is the panel length of the short side, h is fluid depth, and the subscripts, p and F refer to panel and fluid, respectively. A point not realized previously is that the scaling shows that the thinner case can be used to represent the thicker panel under the appropriate conditions and when nonlinearity is carefully considered. More data with the thinner panels at the extreme conditions were unfortunately not taken in several cases of strain response because of concern with accumulating too many cycles before running the actual fatigue tests; else the thinner cases could have shown even more dramatically the scale effect.

Buffet has been of more interest in the past 15 years because of high angle of attack operation of several modern USAF fighters. Much effort was placed upon research with accurately scaled models to determine if these could be employed as in prior flutter work. The answer was YES! Several figures were taken from Ref (16) to illustrate scaling of data from a model of , a fraction of the size of a fighter, to the full scale quantity. Fig (10) shows the correlation between scaled-up model data, flight test, and two sets of calculations over a wide range of aircraft angle of attack for the F/A-18 stabilator. The data is for inboard bending and torsion moment coefficients produced by buffeting loads. The scaled model data correlates well, the calculations using Doublet Lattice (DLM) aerodynamics is close, while the strip theory is not as accurate. Fig (11) shows similar type of data for the F/A-18 Vertical Tail for outboard bending moment coefficients. Here a wider range of angle of attack was considered, and again scaled model data and calculations are close to aircraft values. Both cases suggest that model data can be used to supplement full scale work and that when combined with theory , are a powerful aid to full scale analysis and tests. These tests can be used early in the aircraft design cycle to insure full scale success.

CONCLUSIONS AND RECOMMENDATIONS

An attempt was made to employ a view of acoustical scaling different from that usually taken. The idea is to develop data for a model that fits within a test facility's capability and then by using analytical methods, adjust these results to the nominal case using factors from the test based on the ratio of

experimental to calculated data. This is analogous to the flutter model approach. One example is offered, and similar results from related scaling in fluid -structure and buffet work were shown to further the point. While more work is needed to fully display the concept, enough has been done to inspire others to dig-in and more fully evaluate the approach. The Writers intend to do more research, since they fully appreciate this difficult task.

REFERENCES

1.Scanlon , R.H., and Rosenbaum, R., " Introduction to The Study of Aircraft Vibration and Flutter", The MacMillian Company, New York, 1951

2. Bisplinghoff, R.L., Ashley , H. and , Halfman, R. L., "Aeroelasticity", Addision-Wesley Publishing Co., NY, Nov. 1955, pp. 695-787

3. Ferman, M. A., "Conceptual Flutter Analysis Techniques - Final Report" Navy BuWeps Contract NO w 64-0298-c, McDonnell Report F322, 10 Feb. 1967

4. Ferman, M.A. and Unger, W. H., "Fluid-Structure Interaction Dynamics in Fuel Cells", 17th Aerospace Sciences Meeting, New Orleans, La. Jan 1979

5. Ferman, M.A. and Unger, W. H. , "Fluid-Structure Interaction Dynamics in Aircraft Fuel Cells", AIAA Journal of Aircraft, Dec. 1979

6. Ferman, M.A. , et al , " Fuel Tank Durability with Fluid-Structure Interaction Dynamics ," USAF AFWAL TR-83-3066, Sept. 1982

7. Ferman, M..A., Unger, W. H., Saff, C.R., and Richardson, M.D., "A New Approach to Durability Predictions For Fuel Tank Skins" , 26th SDM, Orlando, FL, 15-17 April 1985

8. Ferman, M. A. , Unger, W. H., Saff, C.R., and Richardson, M.D. , " A New Approach to Durability Prediction For Fuel Tank Skins", Journal of Aircraft, Vol 23, No. 5, May 1986

9. Saff, C.R., and Ferman, M.A., "Fatigue Life Analysis of Fuel Tank Skins Under Combined Loads", ASTM Symposium of Fracture Mechanics , Charleston, SC, 21 March 1985

10. Ferman, M.A., Healey, M.D., Unger, W.H., and Richardson, M.D., "Durability Prediction of Parallel Fuel Tank Skins with Fluid-Structure Interaction Dynamics", 27th SDM, San Antonio, TX, 19-21 May 1986

11. Ferman, M.A., and Healey, M.D., "Analysis of Fuel Tank Dynamics for Complex Configurations, AFWAL TR -87-3066, Wright-Patterson AFB, OH, Nov 1987

12. Ferman, M.A., Healey, M.D. and Richardson, M.D.," Durability Prediction of Complex Panels With Fluid-Structure Interaction", 29th SDM, Williamsburg, VA, 18-20 April 1988

13. Ferman, M.A., Healey, M.D., and Richardson, M.D., "A Dynamicist's View of Fuel Tank Skin Durability, AGARD/NATO 68th SMP, Ottawa, Canada, 23-28 April 1989

14. Zimmerman, N.H. and Ferman, M.A., "Prediction of Tail Buffet Loads for Design Applications, USN Report, NADC 88043-30, July 1987

15. Zimmerman, N.H., Ferman, M.A., Yurkovich, R.N, "Prediction of Tail Buffet Loads For Design Applications", 30th SDM, Mobil, AL , 3-5 April 1989
16. Ferman, M.A., Patel, S.R., Zimmerman, N.H., and Gersternkorn, G., " A Unified Approach To Buffet Response Response of Fighters",AGARD/NATO 70th SMP, Sorrento, Italy, 2-4 April 1990
17. Cote, M.J. et al, "Structural Design for Acoustic Fatigue", USAF ASD-TR-63-820, Oct 1963
18. Rudder, F.F., and Plumblee, H.E., Sonic Fatigue Guide for Military Aircraft" AFFDL-TR-74-112, Wright-Patterson AFB, OH, May 1975
19. Jacobs, J.H., and Ferman, M.A. , Acoustic Fatigue Characteristics of Advanced Materials and Structures, " AGARD/NATO SMP , Lillehammer, Norway, 4-6 May 1994
20. McDonnell Douglas Lab Report, Tech. Memo 253.4415, Acoustic Fatigue Tests of Four Aluminum Panels, Two With Polyurethene Sprayon", 27 June 1984

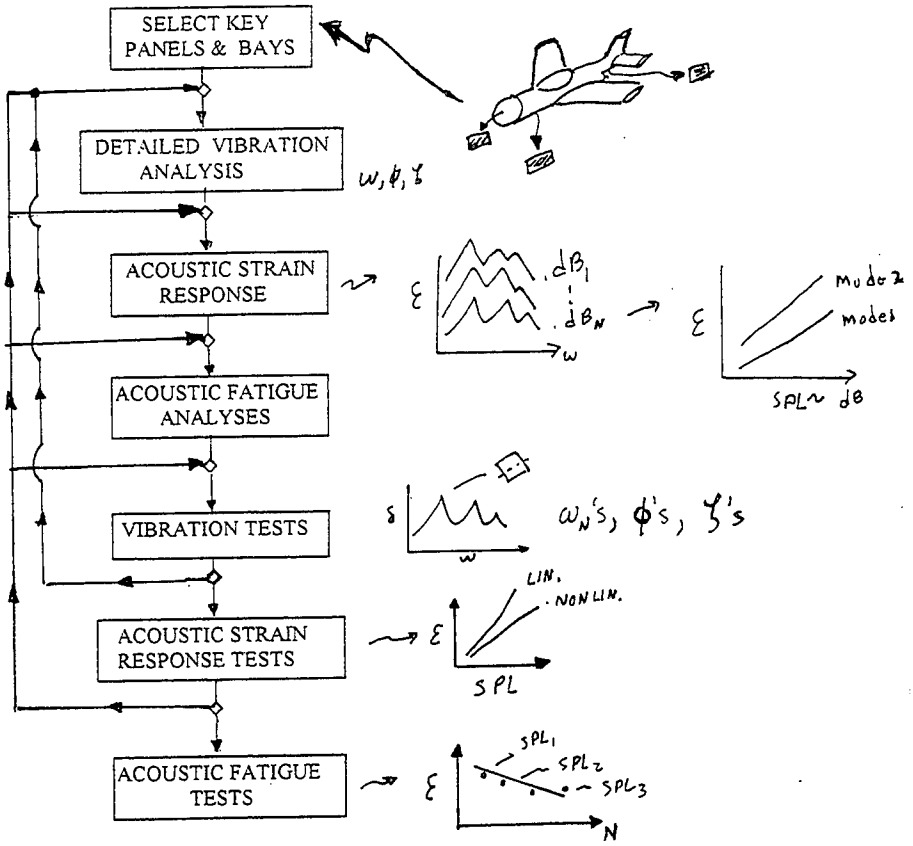

Figure 1 - Standard Acoustic Fatigue Design Method

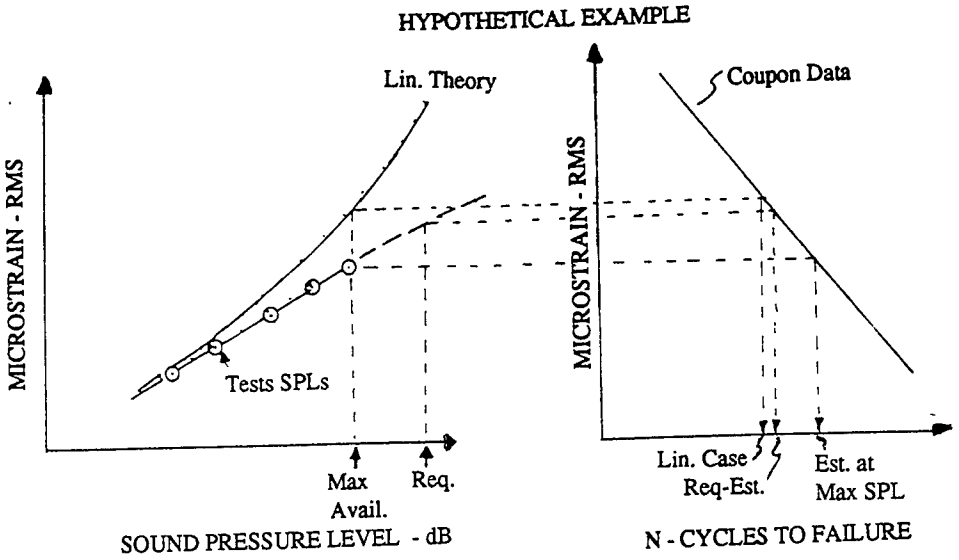

Figure 2 - General Method for Estimating Fatigue Life at SPL above Test Facility Capability

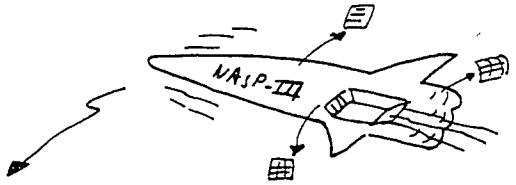

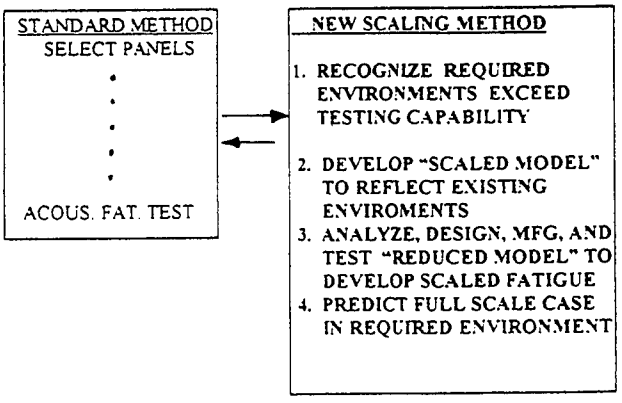

Figure 3 - Scaling Method Fits-in with General Design Cycle for Acoustic Fatigue

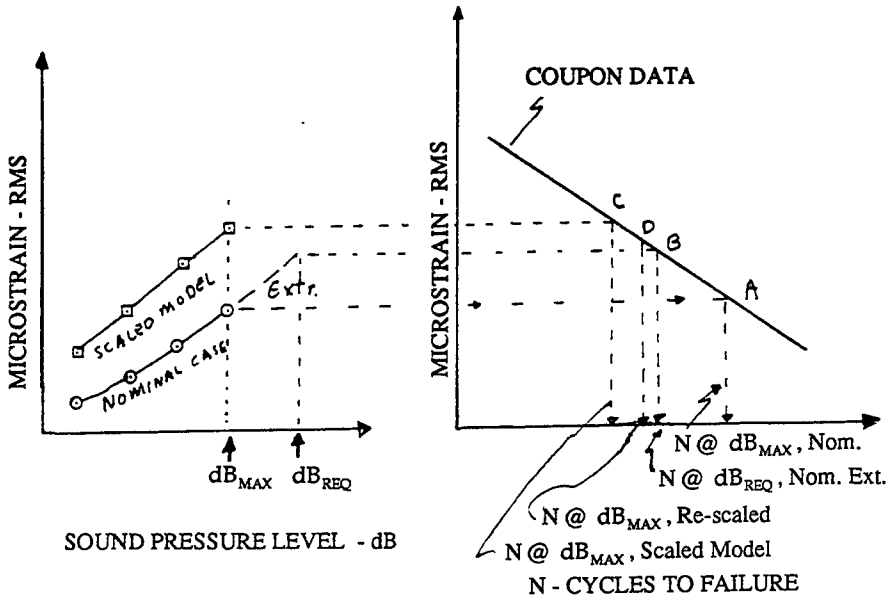

Figure 4 - Hypothetical Examples of Acoustic Scaling to Tests at Higher SPLs

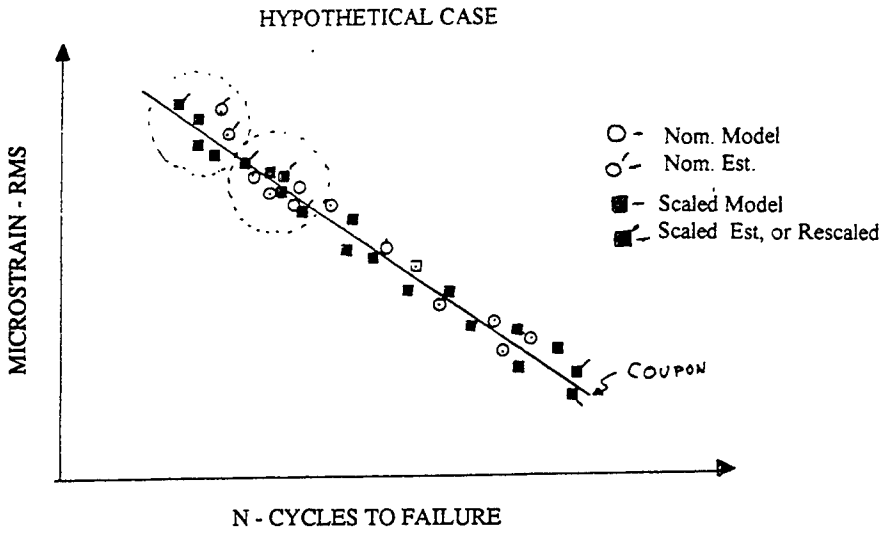

Figure 5 - Statistical Aspects of Scaling

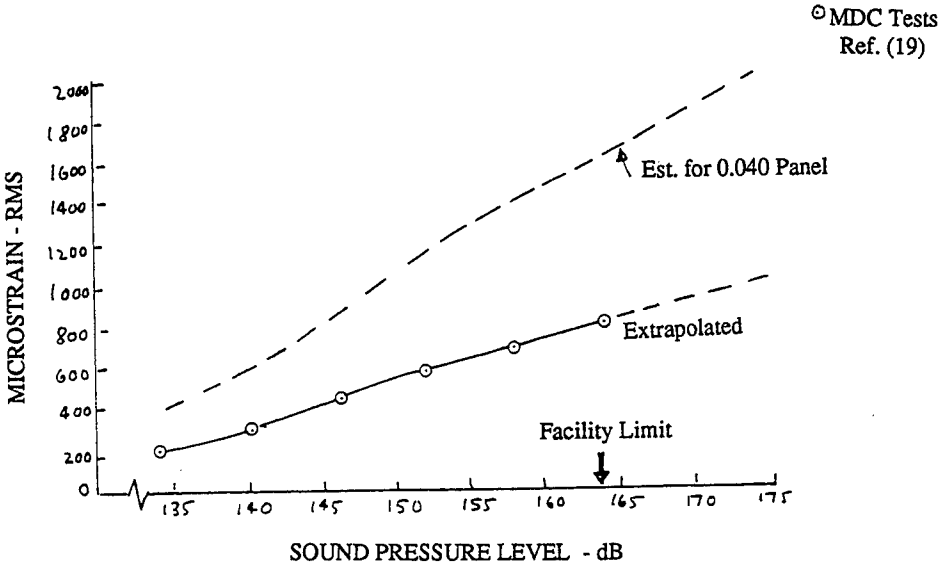

Figure 6 - Strain Response of an Aluminum Panel
(10 x 20 x 0.063 in. 7075 T6) Narrowband Random

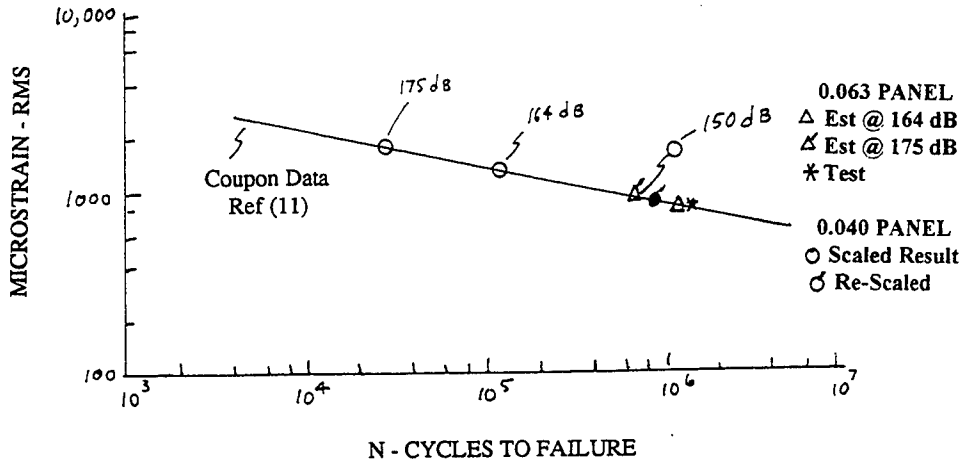

Figure 7 - Example of scaled Model of the 10 x 20 in.
Aluminum Panel

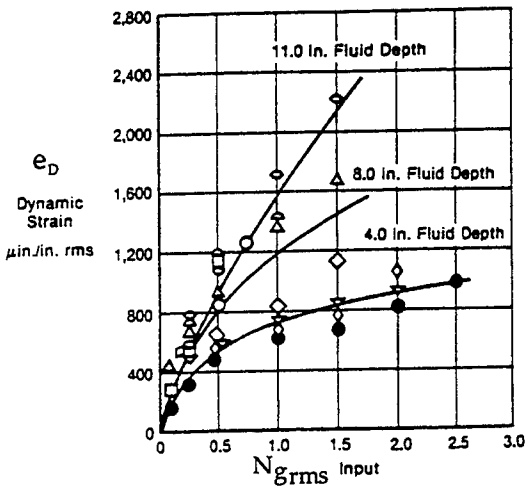

Symbol	Panel Thickness (in.)	Fluid Depth (in.)
□	0.032	11.0
○	0.040	11.0
⬭	0.063	11.0
◇	0.032	8.0
△	0.040	8.0
▰	0.063	8.0
◇	0.032	4.0
△	0.040	4.0
●	0.063	4.0

Figure 8 - Dynamic Strain vs Excitation Level - Sine

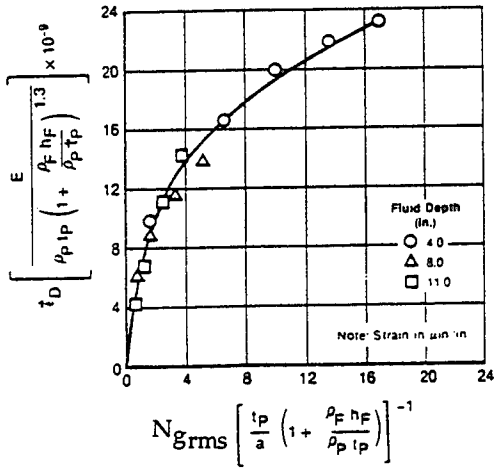

Figure 9 - Dynamic Strain Parameter vs Input $N_{g_{rms}}$ Parameter
Mean Strain at Fluid Depth

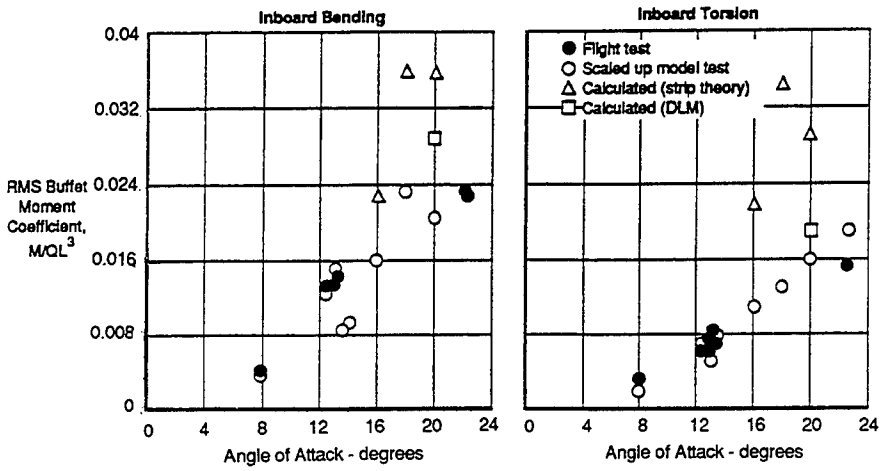

Figure 10 - F/A-18 Stabilator Buffet Correlation Study

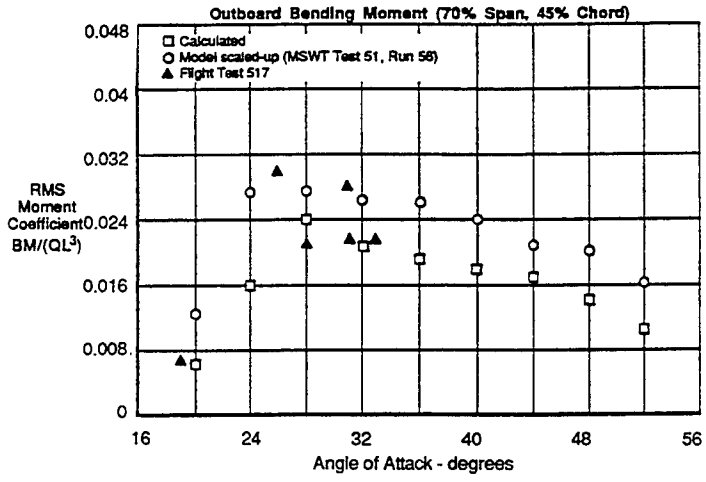

Figure 11 - F-18 Vertical Tail Buffet Response Moment Coefficients for Angle-of-attack Variations

ACOUSTIC FATIGUE II

THE DEVELOPMENT AND EVALUATION OF A NEW MULTIMODAL ACOUSTIC FATIGUE DAMAGE MODEL

Howard F. Wolfe
WL/FIBG Bldg 24C
2145 Fifth St Ste2
Wright-Patterson AFB, OH
45433-7006
USA

Robert G. White
Head of Department
Department of Aeronautics and Astronautics
University of Southampton
Southampton, S017 1BJ
UK

ABSTRACT

A multimodal fatigue model has been developed for flat beams and plates. The model was compared with experimental bending resonant fatigue lifetimes under random loading. The method was accurate in predicting cantilevered beam fatigue lifetimes, but under predicted clamped- clamped beam test results. For the clamped plate tests, one calculation was accurate and the other predicted about half the test lifetimes. The comparisons and the parameters affecting them are presented.

INTRODUCTION

While the single mode acoustic fatigue theory is satisfactory for sound pressure levels around 158 dB overall and below, there is evidence in the literature [1, 2, and 3] that above this level the accuracy of the simple response prediction method decreases with increasing sound pressure levels. The purpose of the paper is two fold, first to develop a multimodal acoustic fatigue life prediction model and secondly, to evaluate its accuracy in estimating the fatigue life theoretically by comparing predictions with experimental results.

FATIGUE MODEL DEVELOPMENT

Many fatigue models are found in the literature. The Miner single mode model used by Bennouna and White [4] and Rudder and Plumblee [5] was selected to develop a multimodal nonlinear model. The fundamental formulation is given by,

$$N_t = \left[\sum \frac{P(\varepsilon)}{N}\right]^{-1} \qquad (1)$$

where N_t is the total number of cycles to failure, $P(\varepsilon)$ is the peak strain probability density. N is the total number of cycles to failure at incremental constant amplitude strain levels derived from a sinusoidal strain versus cycles to failure curve. To calculate the fatigue life in hour, Eq (1) can be expressed as,

$$t\,(\text{hours}) = \left[\sum \frac{P_p(sd)}{N_c} 3600 x f_c\right]^{-1} \qquad (2)$$

where t is time, $P_p(sd)$ is the peak standard deviation probability density, N_c is the total number of cycles to failure at a specified strain level and f_c is the cyclic frequency. When the mean value is <u>not</u> zero, which is the case with axial strain in the beam or plate, the rms value is <u>not</u> the standard deviation. The standard deviation is usually employed to compute the time to failure. Most of the S-N curves or ε-N curves are approximated as a straight line on a logarithmic graph. The relationship between the surface strain and the cycles to failure is then,

$$\varepsilon = \left[\frac{K}{N_c}\right]^{\alpha} \qquad (3)$$

where K is a constant and α the slope of a straight line on a log-log graph. The cyclic frequency f_c for a single mode case is taken as the frequency of the associated resonance. Two types of peak probability density techniques were investigated from multimodal nonlinear strain responses [3]. These were called major peaks and minor peaks. The major peaks were counted for the largest peaks between zero crossings. The minor peaks were counted for all stress reversals or a positive slope in the time history followed by any negative slope. The effective cyclic frequency is much lower for the major peak count than the minor peak count. However, the peak probability density functions or PPDFs compared for these two cases were almost the same. The major peak method was selected for further study.

Given a particular peak probability density curve from a measured response in an experiment, the number of peaks and the sampling time t_s can be used to determine the effective multimodal cyclic frequency,

$$f_{cm} = \text{number of peaks} / t_s \qquad (4)$$

where f_{cm} is the effective multimodal cyclic frequency. Substituting the multimodal cyclic frequency into Eq (4),

$$t\ (\text{hours}) = \left\{ \left[\sum \frac{P_p(sd)}{K / (\varepsilon)^{1/\alpha}} \right] 3600 x f_{cm} \right\}^{-1} \qquad (5)$$

This model accounts for the effects of axial strains which cause the mean value not to be zero, nonlinear response and multimodal effects. If the mean value is zero, then the standard deviation is equal to the rms value and Eq (5) reduces to Eq (2).

FATIGUE MODEL COMPARISON WITH EXPERIMENTAL RESULTS

The peak probability density function (PPDF) is needed or preferably the time history from strain or dynamic response measurements to evaluate the fatigue model developed. Also needed are sinusoidal ε-N curves for the structure, and knowledge of its boundary conditions and the equivalent multimodal cyclic frequency.

Two types of peak probability density techniques were investigated from multimodal nonlinear strain responses [3]. These were called major peaks and minor peaks. The major peaks were counted for the largest peaks between zero crossings. The minor peaks were counted for all stress reversals or a positive slope in the time history followed by any negative slope. The effective cyclic frequency is much lower for the major peak count than the minor peak count. However, the peak probability density functions or PPDFs compared for these two cases were almost the same. The major peak method was selected for further study.

Comparison with Beam Data:

The K and α terms were calculated from ε-N and S-N data, where S is stress, using Eq (3). Selecting two values of strain and their corresponding cycles to failure, yields two simultaneous equations which were solved for K and α. Two sinusoidal ε-N curves for BS1470-NS3 aluminum alloy which has a relatively low tensile strength were obtained from Bennouna and White [4 Fig 8]. These were for a cantilevered beam and a clamped-clamped (C-C) beam as shown in Fig 1. The K and α terms calculated were used to compute the cycles to failure, N_c, for each strain level. Table I shown is the same as Table I in reference [4] except N_c was calculated from Eq (3) to sum the damages.

Delta is the sample size. The cyclic frequency was for one mode the one resonant response frequency. The time to failure in hours using Eq (2) for the cantilevered beam was 16.6 hours compared with 16.2 predicted theoretically [4], 15.3 and 15.9 obtained experimentally [4]. Both theoretical results were essentially equal, but slightly higher than the test results. The time to failure from Eq (2) for the (C-C) beam was 3.04 hours compared with 2.53 theoretically [4] and 5.25 and 5.92 experimentally [4]. Both theoretical results were about one half of the test results. The K and α terms, the theoretical fatigue life times and the experimental fatigue life times are listed in Table II. The table contains three sections: lifetimes calculated using a strain gauge PPDF, a displacement PPDF and the Gaussian and Rayleigh PDFs. As noted in reference [4], failure occurred much earlier for the C-C beam than the cantilevered beam for the same strain level. This was attributed to the influence of a large axial strain in the clamped- clamped beam.

Comparison with Plate Data:

Two fatigue tests were conducted to provide some additional limited data for comparison with the fatigue model developed. These tests used the base excitation method with a 1.09×10^5 N ($20{,}000\,lb_f$) electrodynamic shaker. The clamping fixture consisted of a flat aluminum alloy 6061-T6 plate 19 mm thick and four clamping bars of equal thickness. The radius of curvature of the clamping edges was 4.76 mm to prevent early fatigue failure. A four bar clamping arrangement was selected to prevent buckling of the plate while torquing the clamping bolts. The unclamped size was 254 x 203 x 1.30 mm which results in a 1.25 aspect ratio. Strain gauges were bonded along the center of the larger dimension (SG 2) and at the center of the plate (SG 3). Displacements were measured with a scanning laser vibrometer at the center of the plate. An accelerometer was mounted on the shaker head to determine the acceleration imparted to the clamped plate. A flat acceleration spectral density was used between 100-1500 Hz. Recordings were taken at increasing levels of excitation up to the fatigue test level. The time to detecting the first fatigue crack was recorded for each plate.

The constants K and α were calculated from random single mode S-N data for 7075-T6 aluminum alloy [5 p 489] shown in Fig 1, with $K = 1.01 \times 10^{23}$ and $\alpha = -0.175$. The rms stress (S_{rms}) was changed to rms strain, $S_{rms} = E\varepsilon_{rms}$, where E is Young's modulus. The stress was measured half way between two rivets along the center line between the rivets on the test specimen. The strain gauge location, stress concentrations, and the boundary conditions greatly affect the strain

level measured. Correction factors are needed for a different set of conditions and to convert random data to sinusoidal data. Sinusoidal ε-N bending coupon curves for 7075-T6 aluminum alloy were difficult to find. S-N curves were found for an aerospace material with both sinusoidal and random excitations. These curves were nearly parallel. The sinusoidal strain was 1.38 times larger than the random strain for 10^5 cycles. Multiplying the constant K for the 7075-T6 material by 1.38 resulted in $K = 1.40 \times 10^{23}$.

Early strain gauge failures prevented strain measurement above 500 microstrain with 20.7 g rms shaker excitation. The fatigue test level was 115 g rms and the response contained at least six frequency response peaks. The major peak strain PPDFs were determined for 5.32 g rms and 20.7 g rms as shown in Fig 2 with the Gaussian PDF. Compared with the Gaussian distribution, an increased number of peaks occurred greater than 1 sigma and smaller than -1 sigma. Also a larger number of peaks occurred around zero. The PPDF determined from the 20.7g rms test case was used to predict fatigue life, but a new strain estimate was needed since the excitation level increased 5.6 times. The displacement is directly related to the strain at each excitation level. Displacement measurements at the fatigue test level were used to estimate the strain level shown in Fig 3. The estimated strain from the figure was 770 microstrain for SG 2. The scale of the displacement measurements was adjusted to coincide with strain measurements at increasing increments of shaker excitation.

The equivalent cyclic multimodal frequency is needed to predict the fatigue life. Prediction of the linear modal frequencies is carried out by a variety of methods. Usually the first mode prediction is the most accurate. The cyclic multimodal nonlinear frequencies have been studied for two clamped beams and two clamped plates [3]. These were based upon the peak probability density functions (PPDFs) where the peaks were counted for a specific time interval, from which the nonlinear cyclic multimodal frequencies were calculated. Generally the resonant frequencies increased with increasing excitation levels. Those for the two beams increased more rapidly than those for the two plates. Very little change was noted for the plates. The equivalent cyclic multimodal frequency determined via Eq (4) from the SG 2 PPDF was 348 Hz.

The time to failure in hours predicted using Eq (5) and the parameter mentioned above for the clamped plate was 0.706 hours compared with 1.17 and 0.92 shown in Table II. The predicted result was slightly lower

than the test results. A ε_{rms}-N curve was calculated with the test lifetimes available, by determining a new constant K, assuming the slope was the same as for the riveted coupon and applying the sinusoidal correction factor. The time to failure in hours predicted using Eq 5 and the calculated ε-N curve for the clamped plate was 0.274 hours compared with 1.17 and 0.92 shown in Table II. The cyclic multimodal frequency used was the same at that determined from SG 2 and the same strain was used. This prediction was about 1/3 of the test results. This method incorporates the failure data at two points.

The displacement PPDF shown in Fig 4 was used to predict fatigue life. The number of displacement peaks increased significantly above the strain PPDF around 1 sigma and -1 sigma. The large number of peaks around zero was similar to the characteristics observed in the strain PPDF. The equivalent cyclic multimodal frequency was 375 Hz, slightly higher than that determined from the strain PPDF. However, the same frequency (348 Hz) was used to predict fatigue life. The time to failure in hours using Eq (5) for the clamped plate was 1.15 hours with the riveted ε-N curve and 0.446 with the calculated ε-N curve shown in Table II. This PPDF improved considerably the prediction. The Gaussian and Rayleigh PDFs were used to predict the time to failure with the same parameters as those used with the riveted ε-N curve. The lifetime using the displacement PPDF was 1.15 hours, using the Gaussian PDF, 0.600 hours and using the Rayleigh PDF, 0.237 hours, as shown in Table II. The Gaussian PDF under predicts by a factor of 2. The Rayleigh PDF under predicts by a factor of 5.

The spread sheets containing PPDF / N_{cm} data for various sigma values were used to determine damage accumulation shown in Fig 5. Almost 55% of the normalized damage occurs between -2 and -1 sigma and 38% of the damage between 1 and 2 sigma using the displacement PPDF. However, the damage is spread more evenly using the available strain gauge PPDF. The strain gauge PPDF was recorded at a much lower level than the displacement PPDF. The damage accumulation compared more closely to Gaussian PDF than the Rayleigh function.

Damage Model with a Specific Function Describing the PPDF:

A curve-fitting routine was used to determine a mathematical function for a high level strain gauge PPDF for the clamped shaker plate. The most important part of the fit is outside the range of -1 to 1 sigma, since most of the damage accumulation occurs outside this range. The highest ranking function was a tenth order polynomial followed by

ninth and eighth order polynomial fits. The goodness of fit in order from 1 to 14 ranges from 0.9775 to 0.9625, which are very close statistically. The tenth order polynomial is,

$$y = a + bx + cx^2 + dx^3 + ex^4 + fx^5 + gx^6 + hx^7 + ix^8 + jx^9 + kx^{10} \quad (6)$$

where a=0.346, b=-0.0148, c=-0.137, d=-0.054, e=0.090, f=0.043, g=-0.0400, h=-0.00976, i= 0.00722, $j=6.85\times10^{-4}$, $k=-4.36\times10^{-4}$. Ranked fourteenth is a natural logarithmic function. The function and its coefficients are,

$$\ln y = a + bx + cx^2 + dx^3 + ex^4 + fx^5 \quad (7)$$

where a=-1.088, b=-0.1191, c=-0.1.302, d=0.0104, e=-0.0653, and f=0.0079. The function fits the test data similar to the tenth order polynomial and may be easier to use. Ranked forty-first is a Gaussian function. The function and its coefficients are,

$$y = a + b\exp\left\{0.5[(x-c)/d]^2\right\} \quad (8)$$

where a=-0.0968, b=0.4485, c=-0.050 and d=1.45. The function fits better for sigma values of 2 or greater than those of -2 sigma and greater. A constant coefficient is used to fit the Gaussian function to permit shifting the function to fit the test data. This equation can be used in the PPDF in Eq (5),

$$N_t = \left\{\left[\sum \frac{a + b\exp\{-0.5[(x-c)/d]^2\}}{[K/(\varepsilon)]^{1/\alpha}}\right] 3600 f_{cm}\right\}^{-1} \quad (9)$$

where a=-0.0968, b=0.4485, c=-0.050 and d=1.45.

CONCLUSIONS

The prediction of multimodal fatigue life is primarily dependent upon the peak probability density function (PPDF) which changes shape with increasing excitation levels. The next in order of importance is the sinusoidal ε-N bending fatigue curve and finally the effective multimodal cyclic frequency.

A multimodal fatigue model was developed with the PPDF estimated from a form of the Gaussian function being useful especially in the

range of cycles to failure from $10^6 - 10^8$. The lifetime predication calculations for the clamped-clamed beam was about one half the experimental value. For the plate, the calculations was about one half the experimental value. Using riveted coupon fatigue data, the calculation was accurate.

REFERENCES

1. B.L. Clarkson, April 1994, "Review of sonic fatigue technology", NASA contractor report 4587, NASA Langley Research Center, Hampton, Virginia.
2. R.G. White, October 1978, "A comparison of some statistical properties of the responses of aluminium alloy and CFRP plates to acoustic excitation", *Composites* 9(4), 125-258.
3. H.F. Wolfe, October 1995, "An experimental investigation of nonlinear behaviour of beams and plates excited to high levels of dynamic response", PhD Thesis, University of Southampton.
4. M. M. Bennouna, and R. G. White, 1984, "The effects of large vibration amplitudes on the dynamic strain response of a clamped-clamped beam with consideration on fatigue life", *Journal of Sound and Vibration*, 96 (3), 281-308.
5. J. R. Ballentine, F. F. Rudder, J. T. Mathis and H.E. Plumblee, 1968, "Refinement of sonic fatigue structural design criteria", AFFDL TR 67-156, AD831118, Wright-Patterson AFB, Ohio.

TABLE I

FATIGUE CALCULATIONS USING EQUATION 5.9
CANTILEVERED BEAM BS 1470-NS3 (REF 4 FIG 8)

ε/sd	sd $\mu\varepsilon$	ε $\mu\varepsilon$	Nc=(2.172 x10^{11}/sd)$^{-0.560}$	PPDF x Δ	PPDF x Δ/Nc	t hours
0.5	425	213	15079045.41	0.213	1.41256E-07	
1	425	425	4390936.857	0.310	7.06000E-07	
1.5	425	638	2125446.064	0.240	1.12917E-06	
2	425	850	1273261.536	0.138	1.08383E-06	
2.5	425	1063	854026.6252	0.060	7.02554E-07	
3	425	1275	617189.6449	0.018	2.91645E-07	
3.5	425	1488	468372.0662	0.005	1.06753E-07	
TOTAL				0.984	4.16121E-06	16.7

TABLE II
SUMMARY OF FATIGUE CALCULATIONS

BOUNDARY CONDITIONS	ε -N DATA SOURCE	ALUMINUM ALLOY	K SINE (ε -N curve) CONSTANT	alpha (ε -N) slope	METHOD OF EXCITATION	μ STRAIN RMS	t hours	t (note 1) hours	t (note 2) hours	t (note 3) hours
PPDF SG										
CANT	Ref 4	BS1470-NS3	2.17E+11	-0.56	RAND	425	16.69	16.15	15.25	
BEAM	Fig 8				one mode		pos		15.91	
CANT	Ref 5	DTD 5070	7.17E+20	-0.203	RAND	425	15.3			
BEAM	p 488				one mode		pos & neg			
C-C	Ref 4	BS1470-NS3	9.61E+14	-0.3187	RAND	427	3.04	2.53	5.25	
BEAM	Table 1				one mode		pos		5.92	
C-C-C-C	Ref 5 riveted	7075-T6	1.40E+23	-0.175	RAND	770	0.706			1.17
PLATE	p 488				multimodal		pos & neg			0.92
C-C-C-C	Calculated	7075-T6	5.44E+22	-0.175	RAND	770	0.274			
PLATE					multimodal		pos & neg			
PPDF DISPL	Calculated	7075-T6	5.44E+22	-0.175	RAND	770	0.446			
PLATE					multimodal		pos & neg			
C-C-C-C	Ref 5 riveted	7075-T6	1.40E+23	-0.175	RAND	770	1.15			
PLATE					multimodal		pos & neg			
PPDF theory	Gaussian	7075-T6	1.40E+23	-0.175	RAND	770	0.6			
PLATE					multimodal		pos & neg			
C-C-C-C	Rayleigh	7075-T6	1.40E+23	-0.175	RAND	770	0.237			
PLATE					multimodal		pos & neg			

Note 1 Theoretical results from reference 4 Note 2 Test results from reference 4 Note 3 Current test results

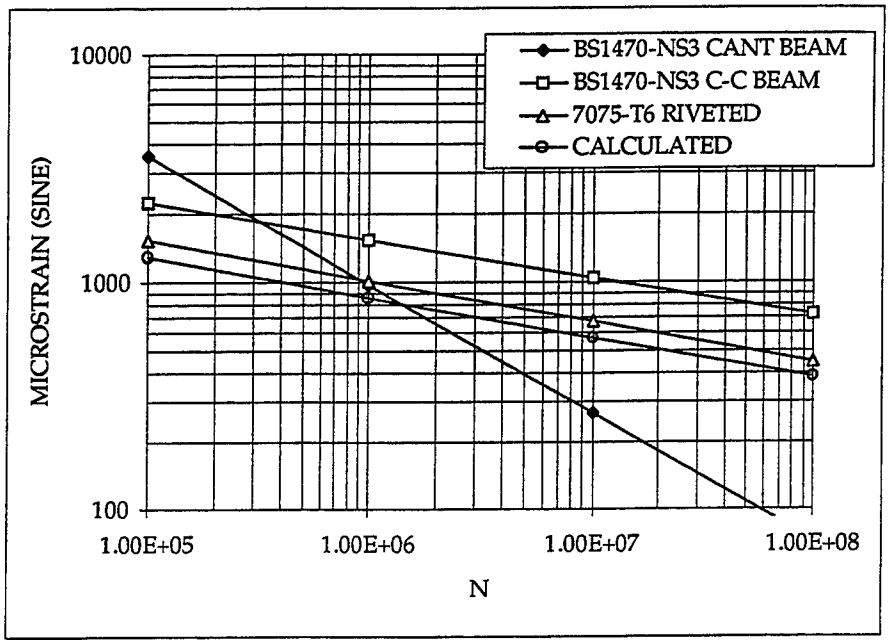

Figure 1 ε-N curves for aluminum alloys tested.

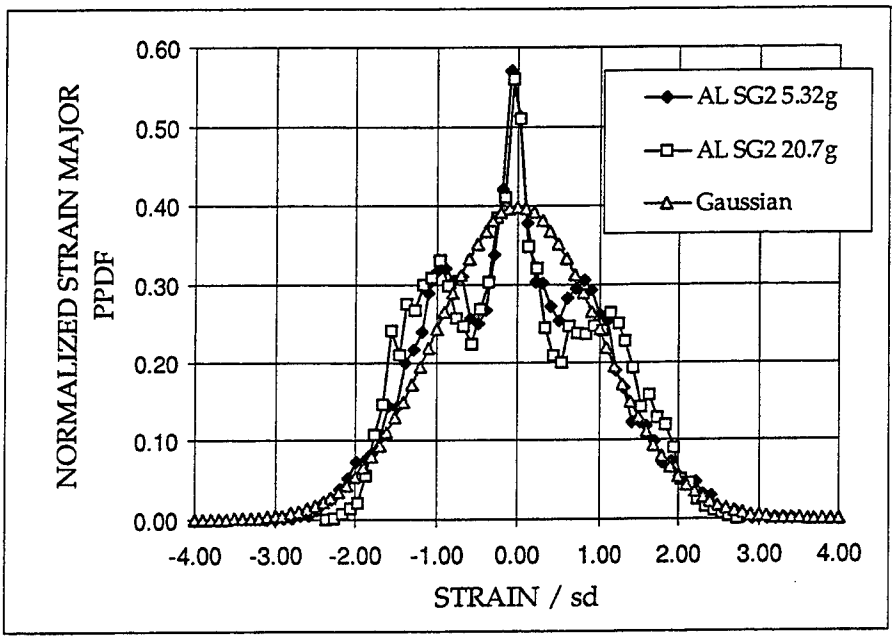

Figure 2 Normalized strain PPDF comparison with a Gaussian PDF.

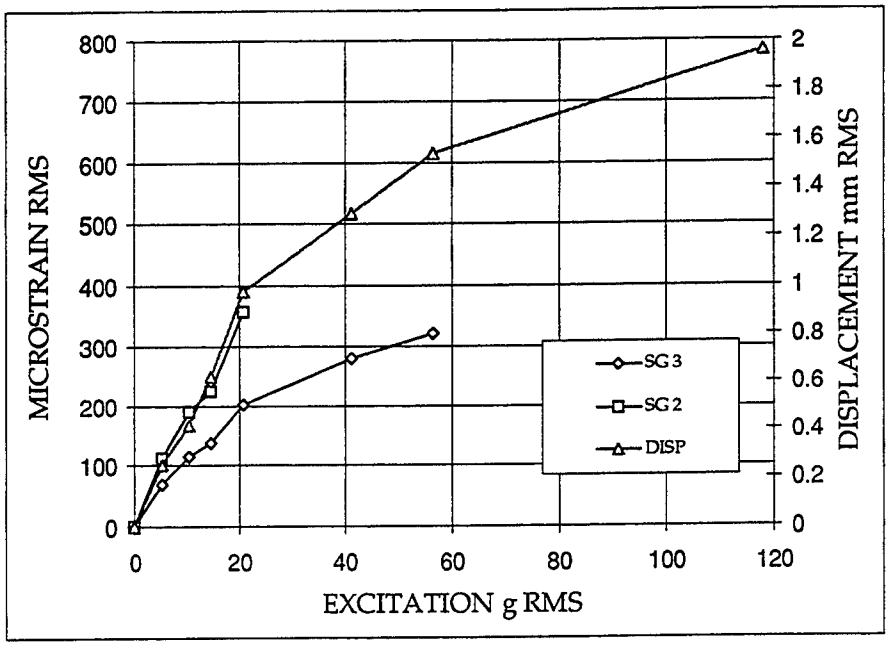

Figure 3 Strain and displacement as a function of excitation.

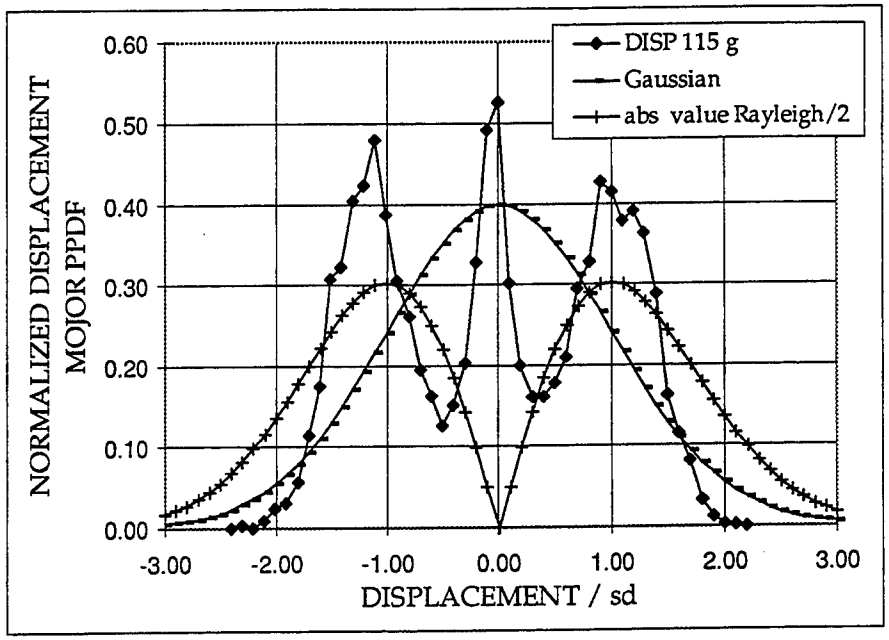

Figure 4 Normalized displacement PPDF comparisons.

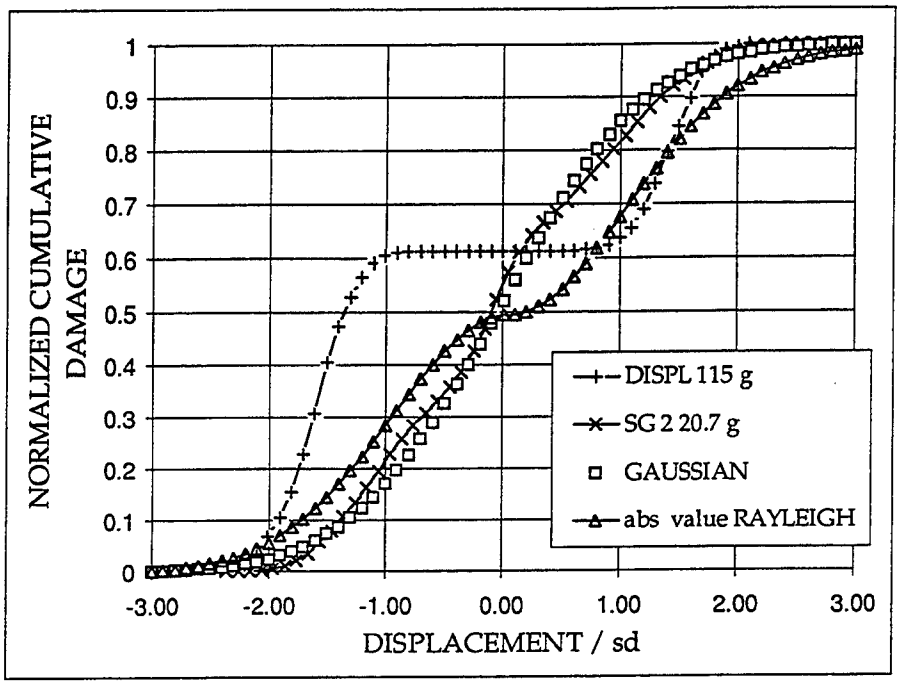

Figure 5 Damage accumulation for SG 2, displacement, Gaussian and Rayleigh distributions.

ACOUSTIC FATIGUE AND DAMPING TECHNOLOGY IN COMPOSITE MATERIALS

By B. Benchekchou and R.G. White

Abstract

Considerable interest is being shown in the use of composite materials in aerospace structures. Important areas include development of a stiff, lightweight composite material with a highly damped, high temperature polymer matrix material. The study described in this paper concerns the application of such material in the form used in thin skin panels of aircraft and investigation of its fatigue properties at room and high temperature. For this purpose, flexural fatigue tests have been carried out at two different temperatures and harmonic three–dimensional FE analyses were performed in order to understand the dynamic behaviour of plates. Random acoustic excitation tests using a progressive wave tube, up to an overall sound pressure level of 162 dB, at room temperature and high temperatures were also performed in order to investigate the dynamic behaviour of panels made of the materials. Various methods for including damping in the structure were examined when parameter studies were carried out, and conclusions have been drawn concerning optimal incorporation of a highly damped matrix material into a high performance structure.

1–Introduction

Significant areas of primary and secondary structures in military aircraft operate at high temperature and are subjected to high levels of random acoustic loading, because of their closeness to jet effluxes. There is then a need to develop a carbon fibre reinforced plastic material with a high temperature polymer matrix and high fatigue resistance. Highly damped composite structures should be developed in order to better resist dynamic loading and to have an enhanced fatigue life. Work previously carried out on improving the damping in fibre reinforced plastic (FRP) composites as well as the number of approaches which can be taken to improve the damping properties of polymeric composites have been summarised in [1]. The aim of the research described here was to study lightweight composite materials with a highly damped, high temperature polymer matrix material, by

investigating its mechanical and acoustic fatigue properties, the latter investigation being carried out using thin, multilayered plates.

2–Experimental work

For this type of study, two adequate prepregs were highlighted after investigation: SE300 and PMR15. The SE300 material was carbon fibre reinforced prepreg of ($0^o/90^o$) woven form, 0.25 mm thick and had 60% fibre volume fraction, with no suitable data available on the material properties. Dynamic mechanical thermal analyser (DMTA) analyses carried out on four specimens (20 mm long and 12 mm wide) with different lay–ups i.e. $(0^o/90^o)_4$, $(+45^o/-45^o)_4$, $(0^o/90^o, 45^o/45^o)_s$ and $(45^o/45^o;0^o/90^o)_s$, allowed to get provided the material properties. Results from DMTA analyses are shown in Table 1.a where the loss factor and the Young's modulus values at 40^oC and at the glass transition temperature Tg are presented. The loss factor values varied from 0.0097 to 0.085 for a range of temperature from 40^oC to 300^oC.

The PMR15 prepreg was also of ($0^o/90^o$) woven carbon form and had 58% volume fraction. Six DMTA specimens having the following lay–ups: $(0^o/90^o)_4$, $(0^o/90^o)_8$, $(+45^o/-45^o)_4$, $(+45^o/-45^o)_8$, $(0^o/90^o; 45^o/45^o)_s$ and $(45^o/45^o;0^o/90^o)_s$ were made. Results from DMTA analyses showed that the loss factor values varied from 0.0129 to 0.0857 for a range of temperature from 40^oC to 400^oC, with a value of loss factor of 0.1293 at 375^oC, the maximum temperature for normal use being 352^oC. The loss factor and Young's modulus values at 40^oC and Tg are given in Table 1.b.

Mechanical behaviour of the selected materials

The fatigue characteristics of these new materials were investigated and results were compared with those of well established structural materials. Mechanical fatigue tests of SE300 and PMR15 samples using "sinusoidal" loading at a chosen maximum strain level, i.e. 8000 μS were carried out and performances compared to that of an XAS/914 sample. A mechanical (flexural) fatigue rig was used for this purpose to test specimens in a cantilevered configuration. Details of the rig are available in [2]. The particular clamp used was designed by Drew [3] to induce damage in the centre of the specimen instead of having edge damage, i.e. peeling while flexural tests are carried out. In order to investigate the performance of these new materials at high temperature, fatigue tests were also carried out on samples, at 210^oC . This was achieved by using a heating system which consisted of two air

blowers (electronically regulated hot–air guns) positioned at 40 mm above and below the specimens, which allowed specimens to be tested at a uniform temperature of 210±5°C. The aim of the mechanical fatigue test was to determine the number of loading cycles needed for damage to occur and its subsequent growth rate in cyclically loaded composite specimens of SE300 and PMR15 matrix materials . The samples were 140 mm long, 70 mm wide and 2 mm thick. Fatigue tests of SE300 (S3 and S4) and PMR15 (P1 and P2) specimens, at room temperature and at 210°C respectively, at a level of 8000 μS, located by the peak of the half–sine clamp, have been carried out. Ultrasonic scans of specimens S3 and S4 before any loading cycles and after 100, 500, 1000, 2000, 5000, 10000, 20000 and 50000 loading cycles are shown respectively in Figures 1.a–h and Figures 2.a–h. A small delamination, indicated by lighter areas in the scans, starts to show in both specimens S3 and S4 after applying 500 loading cycles and increases substantially after 5000 loading cycles. After 5000 loading cycles, the damage area increased more for specimen S4 than specimen S3, which shows that the latter is slightly more fatigue resistant. In other words, when increasing the temperature from 25°C to 210°C, the resistance to fatigue slightly decreases. Figures 3.a–h and Figures 4.a–h show the ultrasonic scans for PMR15 specimens P1 and P2 before and after several loading cycles. For both specimens P1 and P2, damage starts after 500 loading cycles and increases substantially after 20000 loading cycles. At this stage, delamination areas are similar for both specimens P1 and P2 and just a little more pronounced in specimen P2, which shows that the latter is slightly less fatigue resistant. Hence, an increase in temperature leads to a decrease in the fatigue resistance properties of the specimens. From Figures 1, 2, 3 and 4, one can conclude that the PMR15 specimens tested were slightly more fatigue resistant than the SE300 specimens. In fact, damage in specimens was generally more defined, clearer and spread more rapidly in the SE300 samples than was the case for the PMR15 samples. Figure 5 shows damage propagation occuring in an XAS/914 sample (X1), with $(0°/\pm45°/0°)_s$ stacking sequence, tested at 8000 μS level and at room temperature, from [3]. Note that substantial damage existed after 1000 loading cycles in this specimen, which shows that both SE300 and PMR15 are more fatigue resistant than XAS/914 at room temperature.

Acoustic fatigue behaviour of panels of the selected materials

Investigations were carried out by installing the CFRP plates in an acoustic progressive wave tunnel, (APWT) in order to determine the response of CFRP plates under broadband acoustic excitation simulating jet noise. The plate was fully clamped around its boundaries on to a vertical steel frame fixed to one side of the APWT, so that it formed one of the vertical walls of the test section of the APWT.

Overall sound pressure levels (OSPL) up to 165 dB of broadband noise in the test section of the tunnel was generated by a Wyle Laboratories WAS 3000 siren. A heater panel capable of heating and maintaining the temperature of test plates up to 300°C while mounted on the tunnel was designed and built. Temperatures were monitored and controlled via thermocouples on the panel. Plates were excited by broadband excitation in the frequency range 80–800 Hz. A B&K type 4136 microphone mounted at the centre of the test section of the tunnel adjacent to the mid–point of the plate were used for sound pressure measurements. Eight strain gauges, four on each side of the plate were attached in order to monitor the strain distribution in the panel while the rig was running; more details of the experiment may be found in [1]. Acoustic tests were run, at various temperatures and OSPL. Since plates were excited in the frequency range 80–800 Hz, spectral analyses would not include the first natural frequency. The natural fundamental frequency of an SE300 clamped panel was found to be 49.02 Hz analytically. The second and third resonance frequencies were 149.5 and 198.5 Hz, as calculated from strain spectral densities, from tests carried out with an OSPL of 156 dB and a temperature of 162°C. At 162 dB, results showed that the second resonance frequency was 113 Hz at 150°C and 106.5 Hz at 195°C, which shows that when the temperature and the OSPL increased, the resonance frequencies of the plates decreased. Also, it was found that the damping increased at elevated temperatures. The overall modal viscous damping ratios, for the second mode, were calculated from strain spectral densities, for an SE300 panel driven at an OSPL of 162 dB and at 195°C, and was found to be 8.91%; this value is similar to that calculated from analytical simulations, for the first mode, which is 8.50% at 242°C, (see the analytical section below). A typical strain spectral density obtained from recorded results is presented in Figure 6 for an SE300 specimen, at an OSPL = 156 dB and at 162°C, from a strain gauge in the centre of the specimen. Maximum RMS strain values recorded from experimental tests, at a strain gauge in the centre of the specimen were, at an OPSL =156 dB, 1300 μS, 1800 μS and 2800 μS at room temperature and at 90°C and 162°C respectively. These results clearly indicate a trend for significant increase in dynamic response with increasing temperature.

Experiments were also carried out on a PMR15 panel at various OSPL and temperatures. Results from tests run at 159 dB and at room temperature show that the second and third resonance frequencies were indicated as 112 and 182.5 Hz. When the OSPL increased to 162 dB, the second and third resonance frequencies decreased to 110.5 Hz and 176.5 Hz. At the same OSPL (162dB) and when temperature increased to 281°C, the third resonance frequency became 139 Hz. This

shows that, for PMR15 plates, when the temperature and the OSPL increased, the resonance frequencies of the plates decreased. It was also clear that modal damping increased with increasing temperature. In fact, the overall viscous damping reached 20%, for the second mode, at an OSPL=162 dB and at 281°C. It must be stated here, however, that apparent damping trends could include nonlinear effects which influence bandwidths of resonances. Maximum RMS strain values recorded at room temperature, by a strain gauge in the centre of the plate were found to be: 2700 μS at 153 dB, 2800 μS at 157.9 dB and 2900 μS at 159 dB.

It is clear from these values that increasing the OSPL obviously leads to an increase of the strain in the plate. Similar results were observed when the temperature was increased. In fact, at an OSPL of 162 dB, the maximum strain values recorded by a strain gauge in the centre of the specimen were 3000 μS, 3400 μS and 5000 μS at 105°C, 165°C and 281°C respectively, which clearly indicates the effects of temperature. It was observed that both the PMR15 and SE300 panels behaved in a non linear manner.

Attempts to acoustically fatigue a PMR15 panel were made at 162 dB. No signs of fatigue damage were shown in an ultrasonic scan of the panel after 1389 minutes of running time.

3–Analytical work

In order to examine various methods for including damping in a structure, parametric studies were carried out using the finite element FE method. ANSYS software has been used. A three–dimensional, 3D layered element, SOLID46 was used to build theoretical models. The element is defined by eight nodal points, average layer thickness, layer material direction angles and orthotropic material properties, [4]. Meshes were built in order to carry out modal and harmonic analyses of multilayered composite plates (410 mm, 280 mm, 2 mm). The plates were fully clamped along all edges, in order to simulate the panels tested in the APWT. Natural frequencies were first determined from free vibration analyses and compared to resonance frequency values derived from experimental data. Then, the plate was driven by harmonic loading at one point of application. The forcing frequency varied from 0 to 400 Hz. The amplitude of the load was 50 N. Results for displacements and response phase angles relative to the force for a chosen position on the plate as a function of frequency were obtained. The approach was then to carry out parameter studies in order to examine various methods for including damping in the structure, i.e. to use highly damped matrix material throughout the whole structure or possible

incorporation in a few layers. Structural damping was included, allowing models to run with different damping values in each ply of the panel. Structural damping is inherent in the structure and depends on the natural frequency; details on structural damping modeling may be found in [1]. Analyses were performed considering structural damping for the first mode. The structural damping was then varied for plies with the same orientation for a viscous damping ratio $\xi = 0.01, 0.02, 0.05, 0.10$ and 0.20.

Simulations with SE300

Models were built up with the following stacking sequence $((45^o/45^o),(0^o/90^o))_s$, lay–up used for the experimental plates. Table 2 gives the first three modal frequencies of the panel obtained from free vibration analyses results. Harmonic simulations were carried out and the overall damping value was calculated for each case with results given in Table 3. As can be seen, if high overall damping is needed for a structure composed of the SE300 material, increasing the damping value of the $(45^o/45^o)$ orientation plies most significantly increases the overall damping value of the panel. In fact, putting a damping value of 20% in the $(45^o/45^o)$ orientation plies leads to an overall viscous damping value of 14.52%, which is better than including a 10% damping value in all of the plies of the structure.

Harmonic analyses of fully clamped plates were also performed with the values of material properties taken at several temperatures. Simulations were carried out with material properties at 242°C and 300°C. Free vibration analyses permitted calculation of the modal frequencies of the panels at the temperatures mentioned above. Table 2 also lists the first three modal frequencies from analyses with material properties at 242°C and 300°C. The overall viscous damping values, obtained from FE simulations, are given for each temperature in Table 4. Again, the damping value has been varied through the layers and the overall damping value was calculated in order to see which of the plies contributes the most to heavily damp the plate. It was found that putting a damping value of 20% in the $(45^o/45^o)$ orientation plies, the first mode viscous damping ratios were 14.62% and 14.55% at 242°C and 300°C respectively. This shows that this material is more highly damped at high temperature and presents better damping properties of the two materials at 242°C.

Simulations with PMR15

Free vibration analyses of models built up with the following stacking sequence $((45^o/45^o),(0^o/90^o))_s$ were carried out and the first three modal frequencies of the panel are shown in Table 5. Harmonic analyses were run and the overall damping

value was calculated for each simulation with results given in Table 6. If high overall damping is needed for a structure composed of the PMR15 material, increasing the damping value of the ($45^o/45^o$) orientation plies most significantly increases the overall damping value of the panel. In fact, putting a damping value of 20% in the ($45^o/45^o$) orientation plies leads to an overall viscous damping value of 14.39%, while if ($0^o/90^o$) orientation plies have a 20% damping value, the overall damping is 7.42%.

Harmonic analyses of fully clamped plates were also carried out with the values of material properties taken at several temperatures. Simulations were carried out using material properties at 375°C and 400°C. Free vibration analyses permitted calculation of the modal frequencies of the panels at the temperatures mentioned above. Table 5 lists the first three modal frequencies from analyses with material properties at 375°C and 400°C. The overall viscous damping values, obtained from FE simulations, are given for each temperature in Table 7. Again, the damping value has been varied through the layers and the overall damping value was calculated in order to see which of the plies contributes the most to heavily damp the plate. It was found that putting a damping value of 20% in the ($45^o/45^o$) orientation plies, the first mode viscous damping ratios were 18.39% and 16.94% at 375°C and 400°C respectively. This shows that this material is more highly damped at high temperature and presents better damping properties of the two materials at 375°C.

4–Conclusions

Two matrix materials, SE300 and PMR15, with potential for use in aircraft structures in a severe environment, i.e. temperatures up to 300°C were selected for this study. Material properties were determined using DMTA techniques and results show that these materials have high damping abilities at high temperature. Dynamic loading tests, performed in flexure at room and high temperature showed that the carbon fibre reinforced PMR15 material is more fatigue resistant than SE300 and XAS/914 based composites. Acoustic tests using a progressive wave tunnel, up to a random acoustic OSPL of 162 dB, at room temperature and elevated temperatures up to 281°C were also performed. When increasing the excitation level and the temperature higher strain values in the centre of the panels were recorded. Free vibration and harmonic FE analyses permitted determination of the natural frequencies and the overall viscous damping values. Resonance frequencies determined from results obtained from acoustic tests were similar to

natural frequencies obtained from FE simulations. Overall viscous damping values obtained from experimental results agreed well with those obtained from the FE analyses for SE300 panels. Results obtained for PMR15 panels, from tests, were higher than those calculated analytically. Both tests and simulations showed that SE300 and PMR15 present higher damping capabilies at high temperatures. Conclusions, via parameter studies including material damping, have been drawn concerning optimal incorporation of a highly damped matrix material into a high performance structure.

5–Acknowlegments

The authors wish to thank the Minister of Defence for sponsorship of the programme of research under which the work was carried out. Thanks are also due to Dr M. Nash of the DRA, Farnborough for many helpful discussions throughout the project.

6–References

1– Benchekchou, B. and White, R.G., Acoustic fatigue and damping technology in FRP composites, submitted to Composite Structures.

2– Benchekchou, B. and White, R.G., Stresses around fasteners in composite structures in flexure and effects on fatigue damage initiation: I–Cheese–head bolts. Composite structures, 33(2), pp. 95–108, November 1995.

3– Drew, R.C. and White, R.G., An experimental investigation into damage propagation and its effects upon dynamic properties in CFRP composite material . Proceedings of the Fourth International Conference on Composite Structures, Paisley College of Technology, July 1987.

4– ANSYS theoretical manual, Swanson Analysis Systems Inc, December 1992.

Table 1.a: Loss factor and Young's modulus values at 40°C and at Tg for SE300 samples analysed by the DMTA.

	stacking sequences			
	$(+45/-45)_4$	$(-45/+45)_4$	(45/45;0/90)s	$(0/90)_4$
Tg (°C)	242	242	240.3	238.71
η at Tg	0.085	0.085	0.081	0.061
η at 40°C	0.012	0.014	0.010	0.0097
Log E' at 40°C	9.870	9.840	9.970	10.097

Table 1.b: Loss factor and Young's modulus values at 40°C and at Tg for PMR15 samples analysed by the DMTA.

	stacking sequences			
	$(+45/-45)_4$	$(0/90;45/45)_s$	$(45/45;0/90)_s$	$(0/90)_4$
Tg (°C)	372	375	375	375
η at Tg	0.117	0.124	0.121	0.129
η at 40°C	0.0110	0.0138	0.0086	0.0117
Log E' at 40°C	9.583	9.944	9.972	9.875

Table 2: The first three modal frequencies for SE300 panel; FE analyses carried out with material propert ies at room temperature, at 242°C and at 300°C.

Room temperature	242°C	300°C
49.02Hz	44.72Hz	43.61Hz
155.80Hz	143.27Hz	140.17Hz
212.04Hz	194.19Hz	189.68Hz

Table 3: Overall viscous damping values of SE300 panel. Values are calculated from results obtained from harmonic analyses; the material damping being considered for the first mode.

Simulation with damping of	(45°/45°)orientation plies	(0°/90°)orientation plies
5%	3.81%	2.51%
10%	7.06%	3.92%
20%	14.52%	11.57%

Table 4: Overall viscous damping values of SE300 panel, for the first mode.

Temperature (°C)	Overall viscous damping ξ
25	1.20%
242	8.50%
300	5.45%

Table 5: The first three modal frequencies for PMR15 panel; FE analyses carried out with material properties at room temperature, 375°C and 400°C.

Room temperature	375°C	400°C
43.43Hz	32.68Hz	25.54Hz
130.35Hz	99.65Hz	78.83Hz
183.96Hz	139.04Hz	109.11Hz

Table 6: Overall viscous damping values of PMR15 panel. Values are calculated from results obtained from harmonic analyses; the material damping being considered for the first mode..

Simulation with damping of	(45°/45°)orientation plies	(0°/90°)orientation plies
5%	3.76%	2.44%
10%	7.26%	4.10%
20%	14.39%	7.42%

Table 7: Overall viscous damping values of PMR15 panel, for the first mode..

Temperature (°C)	Overall viscous damping ξ
25	1.33%
275	13.24%
400	8.6%

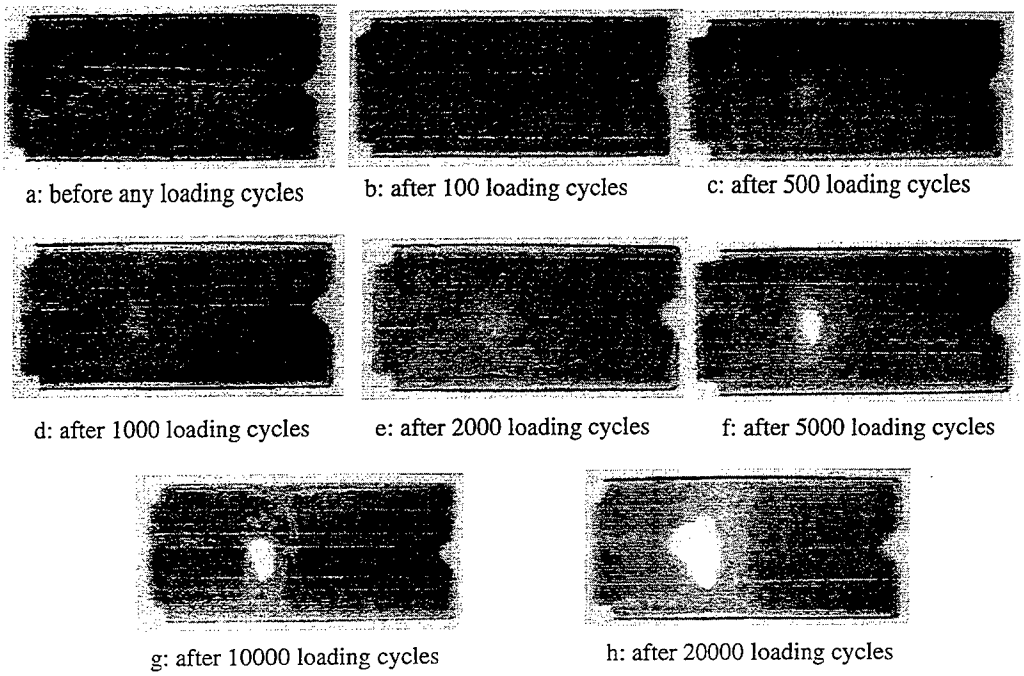

Figure 1. Ultrasonic scans of specimen S3 after applying different numbers of loading cycles. (SE 300 material, ambient temperature)

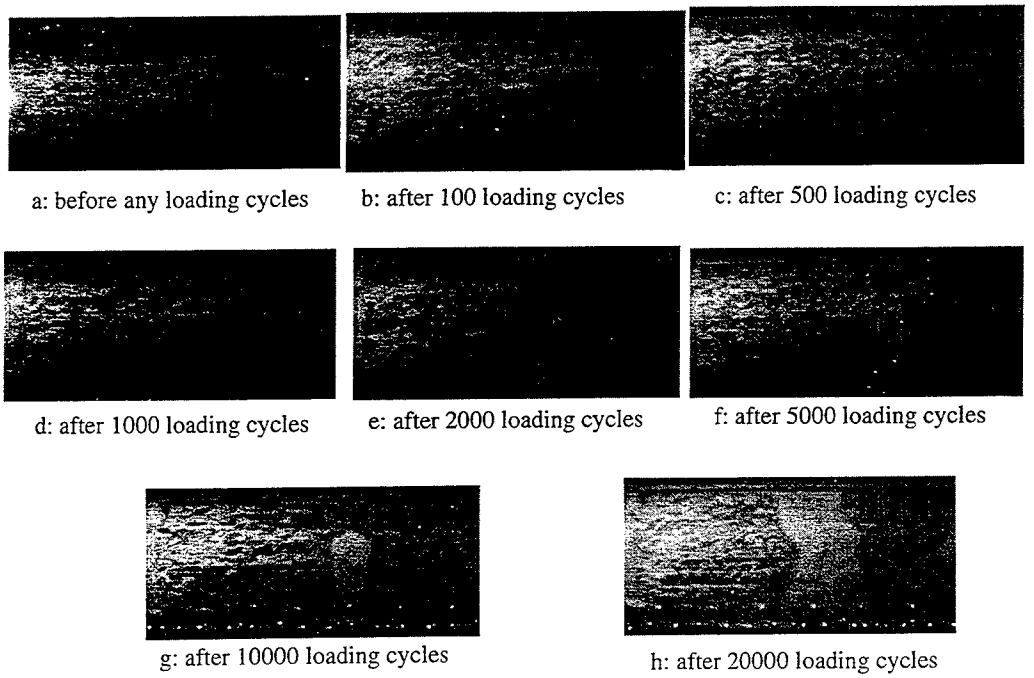

Figure 2. Ultrasonic scans of specimen S4 after applying different numbers of loading cycles. (SE300 material, 210°C)

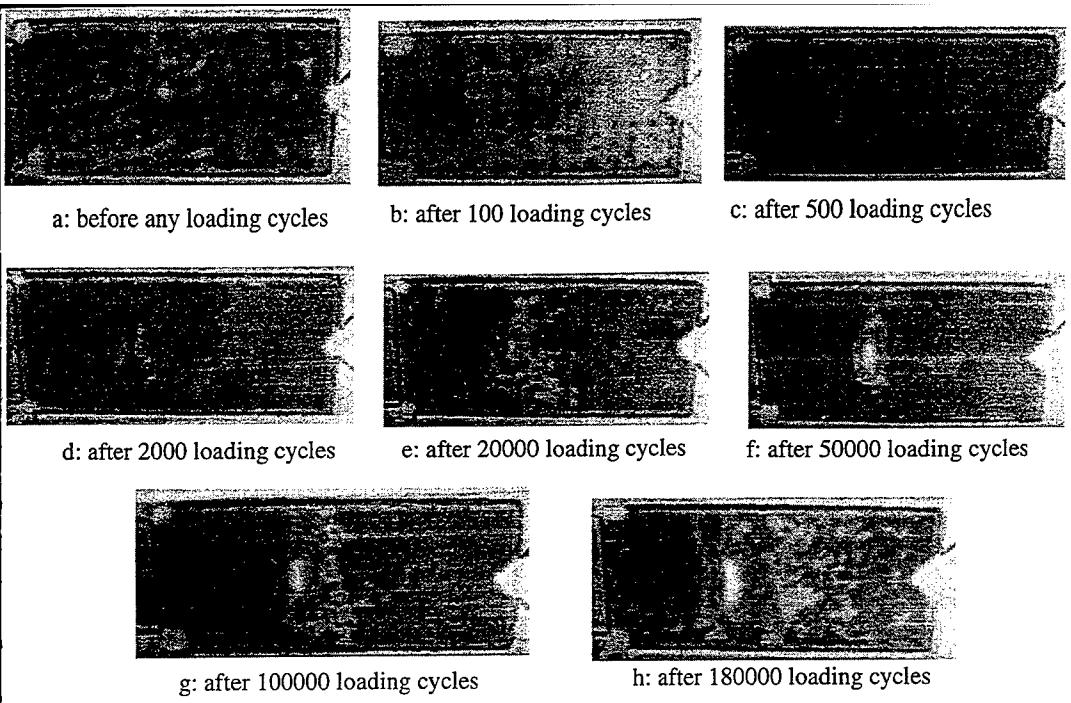

Figure 3. Ultrasonic scans of specimen P1 after applying different numbers of loading cycles. (PMR15 material, ambient temperature, 8000μS)

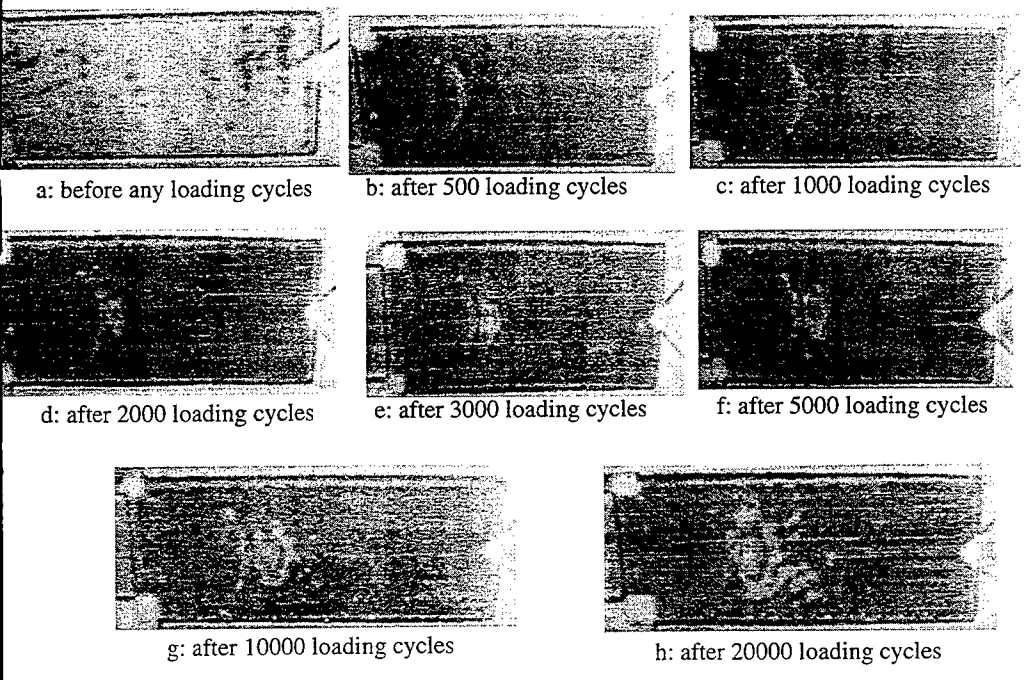

Figure 4. Ultrasonic scans of specimen P2 after applying different numbers of loading cycles. (PMR15 material, 210°C, 8000μS)

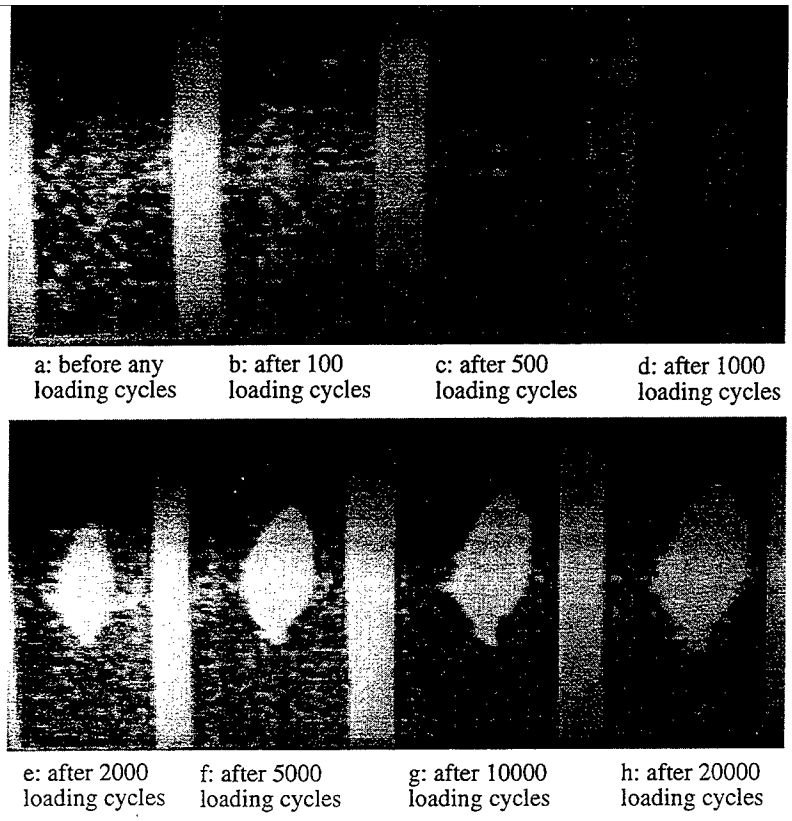

Figure 5. Ultrasonic scans of an XAS/914 specimen fatigued at a level of 8000 μS showing the damage propagation; the lay–up is (0/±45/90)s, [3].

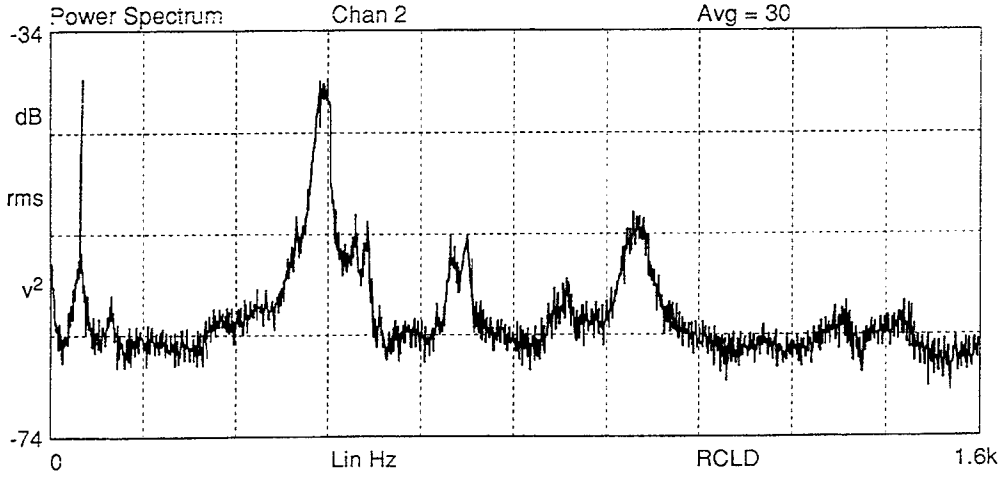

Figure 6: SE300 specimen S1 strain spectral density, recorded from strain gauge ST2, OSPL =156 dB, temperature = 162°C.

THE BEHAVIOUR OF LIGHT WEIGHT HONEYCOMB SANDWICH PANELS UNDER ACOUSTIC LOADING

David Millar
Senior Stress Engineer
Short Bros. PLC
Airport Road
Belfast
Northern Ireland

SUMMARY

This paper discusses the results of a progressive wave tube test on a carbon composite honeycomb sandwich panel. A comparison was made with the test panel failure and the failure of panels of similar construction used in the intake ducts of jet engine nacelles. The measured panel response is compared with traditional analytical methods and finite element techniques.

Nomenclature

S_{rms} = Overall rms stress (psi) or strain ($\mu\varepsilon$).
π = 3.14159
f_n = Fundamental frequency (Hz).
δ = Critical damping ratio ($\approx$0.017).
$L_{ps}(f_n)$ = Spectrum level of acoustic pressure (- expressed as a fluctuating rms pressure in psi in a 1 Hz band).
j_r = Joint acceptance function (non dimensional).
P_{ic} = Characteristic modal pressure (psi)
ρh = Mass per unit area (lb/in^2)
S_{ic} = Modal stress (psi) or modal strain ($\mu\varepsilon$).
w_{ic} = Modal displacement (in).
a = Panel length (in).
b = Panel width (in).
x,y,z = Co-ordinate axes.

1.0 Introduction

Honeycomb sandwich panels have been used for some time in the aircraft industry as structural members which offer a high bending stiffness relative to their weight. In particular, they have proved very attractive in the construction of jet engine nacelle intake ducts where, in addition to their load carrying ability, they have been used for noise attenuation.

2.0 Acoustic Fatigue

The intake duct of a jet engine nacelle can experience a severe acoustic environment and as such the integrity of the nacelle must be assessed with regard to acoustic fatigue [1]. Acoustic fatigue characterises the behaviour of structures subject to acoustic loading, in which the fluctuating sound pressure levels can lead to a fatigue failure of the structure. The traditional approach to acoustic fatigue analysis has assumed fundamental mode response and given that aircraft panels will in general, have fundamental frequencies of the order of several hundred hertz, it is clear that the potential to accumulate several thousand fatigue cycles per flight can exist.

Techniques for analysing the response of structures to acoustic loads were developed originally by Miles [2] and Powell [3]. Other significant contributions are listed in References 4 - 7. Design guides such as AGARD [8] and the Engineering Sciences Data Unit (ESDU) series of data sheets on vibration and acoustic fatigue [9], have proved useful in the early stages of design.

Note - further details on the general subject of acoustic fatigue can be found in Ref. 10, while a more detailed review of the subject up to more recent times is presented in Ref. 11.

3.0 In Service Failures

In recent years a number of failures have been experienced involving intake barrel honeycomb sandwich panels. Failures have been experienced with panels which had both aluminium facing and backing skins and carbon composite panels. The metal intake liner was observed to have skin cracking and also core failure, while the composite panel was only observed to have core failure.

With regard to the metal panels, flight testing was carried out and the predominant response frequency was observed to be at the fan blade passing frequency - much higher than the fundamental frequency of the intake barrel; this went some way to explaining why the traditional approach in estimating the response did not indicate a cause for concern. The response of the panel was also very narrow band - almost a pure sinusoid (again differing from the traditional approach of broad band/random load and response), and the subsequent analysis of the results was based on a mechanical fatigue approach [12]. Subsequent fleet inspections revealed that core failure was observed prior to skin failure and it was assumed that the skin failure was in fact caused by a breakdown in the sandwich panel construction. The core was replaced with a higher density variety, with higher shear strength and moduli. This modification has been in service for several years with no reported failures. The modification represented only a moderate weight increase of the panel, without recourse to changing skin thickness, which would have proved very expensive and resulted in a substantial weight penalty.

As mentioned above, another intake duct, of carbon composite construction, also began to suffer from core failure. The panels of this duct had a carbon backing skin while the facing skin had a wire mesh bonded to an open weave carbon sheet. The only similarity was the use of the same density of honeycomb core (although of different cell size and depth). For other reasons this core had been replaced by a heavier variety, prior to the discovery of the core failures and the impact of the failures was minimised.

Limited data is available on similar failures and only 2 other cases, regarding nacelle intake barrels, appear to have been documented [13 & 14], however neither case involved sandwich panels.

A number of theories had been put forward as to the cause of the failures. These included neighbouring cells resonating out of phase, cell walls resonating or possibly the panel vibrating as a 2 degree of freedom system (the facing and backing skins acting as the masses, with the core as the spring) - this phenomenon had originally been investigated by Mead [15].

4.0 Physical Testing

A number of tests were carried out with "beam" type high cycle fatigue specimens and also small segments of intake barrel. None of these tests were able to reproduce the failures observed in service (Figure 1.0) which further served to reinforce the belief that the failures were attributed to an acoustic mechanism as opposed to a mechanical vibration mechanism, however in an attempt to cover all aspects it was decided to carry out a progressive wave tube (PWT) test on an abbreviated panel.

For simplicity it was decided to test a flat sandwich panel of overall dimensions 36"x21" (Figure 2.0). The panel was instrumented with 12 strain gauges and 2 accelerometers. Two pressure transducers were also mounted in the fixture surrounding the specimen.

Testing was carried out by the Consultancy Service at the Institute of Sound and Vibration Research (ISVR) at the University of Southampton.

4.1 PWT Results

The panel was first subject to a sine sweep from 50 to 1000 Hz in order to identify its resonant frequencies. The response of a strain gauge at the centre of the panel has been included in Figure 3.0. On completion of the sine sweeps, the linearity tests were carried out.. As only 8 channels could be accommodated at one time, it had been decided to arrange the parameters into 5 groups, with each group containing 4 strain gauges, 2 accelerometers, 1 pressure transducer on the fixture and 1 pressure transducer in the PWT (this was required by the facility for the feedback loop).

The initial tests were carried out with a power spectral density of the applied loading constant over the 100 Hz to 500 Hz range, however when using this bandwidth only 155 dB overall, could be achieved. In an attempt to increase the strain levels it was decided to reduce the bandwidth to 200 Hz. The bandwidth (BW) was subsequently reduced to 100 Hz and finally 1/3 octave centred on the predominant response frequency of the panel. When failure occurred a dramatic change in response was observed. The failure mechanism was that of core failure as shown in Figure 4.0. There was no indication of facing or backing skin distress.

5.0 Comparison With Theoretical Predictions

5.1 Fundamental Frequency

From the strain gauge readings the panel was seen to be vibrating with simply supported edge conditions. Soovere [7] suggests that "effective" dimensions (essentially from the start of the pan down) be used to determine the fundamental frequency which is given by;

$$f_n = \frac{\pi}{2}[h+t]\left[\left(\frac{m}{a}\right)^2 + \left(\frac{n}{b}\right)^2\right]\left[\frac{Et}{2(1-\upsilon^2)M}\right]^{1/2} \quad (1)$$

This equation is applicable to simply supported panels with isotropic facing and backing skins, thus for the purpose of applying the above equation, the actual section was approximated to a symmetric (isotropic) section. The predicted fundamental frequency is given below. It was observed however, that if the panel dimensions are taken relative to mid way between the staggered pitch of the fasteners a significant improvement was achieved (see "Soovere (2)" in table 1). Alternative frequency estimations using an FE model and an ESDU data item [16] are summarised in the following table;

Method	Freq.(Hz)	% Error
Measured	228	-
Soovere	274.3	+20.3
Soovere (2)	213.3	-6.4
FE	239.04	+4.8
ESDU	193	-15.3

Table 1 - Comparison of calculated frequencies for simply supported sandwich panel.

Note; the percentage error is based on the actual measured response frequency of the panel in the PWT.

Given that the excitation bandwidth extended (at least initially) up to 500 Hz, modes up to 500 Hz were obtained from the FE model. In actual fact 2 FE models were used, the first was a basic model with 380 elements, however a more detailed model, shown in Figure 5.0, (with essentially each element split into 4) was used for the results presented in this paper. The predicted modes from the FE model were as follows;

Mode No.	Frequency (Hz)	Mode No. in x direction (m)	Mode No. in y direction (n)	Figure No.
1	239.04	1	1	6
2	334.0	2	1	7
3	430.02	1	2	8
4	461.37	3	1	9

Table 2 - Finite Element Model Predicted Frequencies.

5.2 rms Strain

The predicted strains were calculated using Blevins' normal mode method (NMM) [5], with a joint acceptance of unity for the fundamental mode of vibration, using the following expression;

$$S_{rms} = \left(\frac{\pi f_n}{4\delta}\right)^{1/2} . L_{ps}(f_n) . \frac{S_{ic}}{P_{ic}} \qquad (2)$$

In an attempt to improve the estimated response, the rms strain was calculated for each mode within the bandwidth of excitation. The joint accetptance for each mode was calculated using equation 3 and the calculated strains for each mode were then factored by the relevant joint acceltance term. The overall strain was then calculated for all the relevant modes. A comparison with ESDU [16] has also been included, however the ESDU method does not provide an indication of shear stress in the core.

Soovere presents a simple expression for the joint acceptance function for a simply supported panel excited by an (acoustic) progressive wave, for the case where n is odd;

$$j^2 = \frac{8}{\pi^4 m^2 n^2} . \frac{(1-\mathrm{Cos}(m\pi)\mathrm{Cos}(\omega_r a/c)}{(1-(\omega_r a/m\pi c)^2)} \qquad (3)$$

Note, when n is even the joint acceptance is zero.

Given that the bandwidth varied for the applied loading, the overall SPLs were expressed as spectrum levels for the purpose of comparison in the linearity results, the results (both measured and predicted) have been summarised in table 3, (SG1 results have been plotted in Figure 10.0). The results from the ESDU data item [16] have been included in table 4 for comparison.

Note - due to recorder channel limitations SG1 & SG2 were not connected at the time of failure and no results were available at the highest sound pressure levels.

OASPL (dB)	Spectrum Level SPL (dB)	Measured Strains(με)		Calculated (με) j=1		Calculated (Multi Mode)	
		SG1	SG2	SG1	SG2	SG1 (με)	SG2
130	107	7	7	8.7	9.2	2.5	2.6
140	117	20	19	27.5	29.1	8.0	8.1
150	127	55	60	87.0	92.0	25.4	25.8
155	132	100	100	154.7	163.7	45.1	45.8
157	134	130	130	194.8	206.0	56.8	57.6
163	140	-	-	388.7	411.1	202.5	162.7
164	141	-	-	436.1	461.2	312.0	250.7

Table 3 - Comparison of Measured & Predicted rms Strains for the Panel Centre, Facing & Backing Skin Gauges.

OASPL (dB)	Spectrum Level SPL (dB)	Measured Strains (με)		ESDU Strains (με)	
		SG1	SG2	SG1	SG2
130	107	7	7	10.1	29
140	117	20	19	31.9	91.7
150	127	55	60	101	290
155	132	100	100	179.5	515.7
157	134	130	130	253.6	728.5
163	140	-	-	637	1830
164	141	-	-	1010	2900

Table 4 - Comparison of Measured & ESDU Predictions of the rms Strains for the Panel Centre, Facing & Backing Skin Gauges.

There is a considerable difference in the calculated response from using a joint acceptance of unity for the fundamental mode and that when estimating the joint acceptance for each mode and calculating the overall response for several modes, however it was observed that if the average value from both methods is used the response compares favourably with that measured (-at least for the cases under consideration). The average value has been included on the linearity plot for SG1, shown in Figure 10.0).In general, the level of agreement between theory and practice was considered adequate and it was decided to apply the theory to estimating the shear stresses in the core (Table 5);

OASPL (dB)	Spectrum Level SPL (dB)	Core Shear Stress (j=1) (rms psi)	Core Shear Stress (Multi Mode) (rms psi)	Average Core Shear Stress (rms psi)	Peak Core Shear Stress (psi)
130	107	0.3	0.09	0.19	0.58
140	117	0.94	0.28	0.61	1.84
150	127	2.99	0.88	1.93	5.8
155	132	5.31	1.57	3.44	10.32
157	134	6.69	1.97	4.33	13.0
163	140	13.35	5.57	9.46	**28.38**
164	141	14.98	8.59	11.78	35.34

Table 5 - Predicted Core Shear Stress.

6.0 Discussion & Recommendations

The ESDU method proved very conservative and will thus give a degree of confidence when used in the early stages of the design process. Blevins Normal Mode Method was observed to give reasonable accuracy in predicting the highest strains in the panel and would merit use when designs have been fixed to some degree; at which stage FE models become available.

For panels whose predominant response is in the fundamental mode it is accepted that the contribution from shear to overall deformation is very small. The main concern when designing a honeycomb sandwich panel which is subject to "severe" acoustic

loads has tended to focus on skin strains and to some degree the properties of the core material have been ignored. The fact that low skin strains are observed has the effect of giving an impression that there is no cause for concern, however when the properties of the core material are low or unknown, some caution is required. There is unfortunately no available S-N data for the type of honeycomb used in the construction of the panel, however the allowable ultimate strength for the core material is of the order of 26 psi, so clearly the 163 dB level was sufficient to cause a static failure while the lower SPLs can be assumed to the have contributed to initiating fatigue damage. On cutting up the test panel, a large disbond was observed however it did not extend to the panel edge where cracking had occurred (the mid point of the long edge being the location of maximum shear for a simply supported panel) and it was the opinion of the materials department that the failure had not initiated in the disbond.

The SPLs used in the test were not excessively high and were comparable to service environments (an example of which is given in Table 6). It should be noted that while the levels in Table 5 are 1/3 octave bandwidths, the actual spectrum is not generally flat within each band for engine intakes, but is rather made up of tones (Figure 11). These tones or spectrum levels can thus essentially be the band level and thus some caution should be exercised when converting intake band levels to spectrum levels using the traditional approach [17].

1/3 Octave Centre Frequency (Hz)	Sound Pressure Level (dB)
100	141
125	133
160	140
200	142
250	140
315	139

Table 6 - Typical Acoustic Service Environment.

Note; Overall levels may reach 160 - 170 dB, however they tend to be influenced by SPLs at blade passing frequencies, which are much higher than panel fundamental frequencies.

7.0 Conclusion

It has been shown that although moderate levels of acoustic excitation produce quite low overall rms strains in the skins of honeycomb sandwich panels, it is still possible, when using very light weight cores, to generate core shear stresses of a similar order of magnitude to the allowable ultimate strength of the material.

Acknowledgements

The author acknowledges the support of Short Bros. PLC in the course of preparing this paper and also the assistance of Mr Neil McWilliam with regard to the FE modelling.

References

1.0 Air worthiness Requirements (JAR/FAR) Section 25.571.d.

2.0 Miles, J.W., "On Structural Fatigue Under Random Loading," Journal of the Aeronautical Sciences, (1954),Vol.21, p753 - 762.

3.0 Powell, A., "On the Fatigue Failure of Structures due to Vibrations Excited by Random Pressure Fields," Journal of the Acoustical Society of America, (1958), Vol.30, No.12, p1130 - 1135.

4.0 Clarkson, B.L., "Stresses in Skin Panels Subjected to Random Acoustic Loading," Journal of the Royal Aeronautical Society, (1968), Vol.72, p1000- 1010.

5.0 Blevins, R.D., "An Approximate Method for Sonic Fatigue Analysis of Plates & Shells," Journal of Sound & Vibration, (1989), Vol.129, No.1, p51-71.

6.0 Holehouse, I., "Sonic Fatigue Design Techniques for Advanced Composite Aircraft Structures," AFWAL TR 80-3019,(1980).

7.0 Soovere, J., "Random Vibration Analysis of Stiffened Honeycomb Panels with Beveled Edges," Journal of Aircraft, (1986), Vol.23, No.6, p537-544.

8.0 Acoustic Fatigue Design Data (Part 1), AGARD-AG-162-72, (1972).

9.0 ESDU International, London, Series on Vibration & Acoustic Fatigue.

10.0 Richards, E.J., Mead, D.J.,"Noise and Acoustic Fatigue in Aeronautics," John Wiley & Sons, New York, (1968).

11.0 Clarkson, B.L., "A Review of Sonic Fatigue Technology," NASA CR 4587, (1995).

12.0 Millar, D., "Analysis of a Honeycomb Sandwich Panel Failure," M.Sc. Thesis, University of Sheffield, (1995).

13.0 Holehouse, I., "Sonic Fatigue of Aircraft Structures due to Jet Engine Fan Noise," Journal of Sound & Vibration, (1971), Vol.17, No.3, p287-298.

14.0 Soovere, J., "Correlation of Sonic Fatigue Failures in Large Fan Engine Ducts with Simplified Theory," AGARD CP113 (Symposium on Acoustic Fatigue), (1972), p11-1 - 11-13.

15.0 Mead, D.J., "Bond Stresses in a Randomly Vibrating Sandwich Plate: Single Mode Theory," Journal of Sound & Vibration, (1964), Vol.1, No.3, p258-269.

16.0 ESDU Data Item 86024 (ESDUpac A8624), "Estimation of RMS Strain in Laminated Face Plates of Simply Supported Sandwich Panels Subjected to Random Acoustic Loading," Vol. 3 of Vibration & Acoustic Fatigue Series.

17.0 ESDU Data Item 66016, "Bandwidth Correction," Vol. 1 of Vibration & Acoustic Fatigue Series.

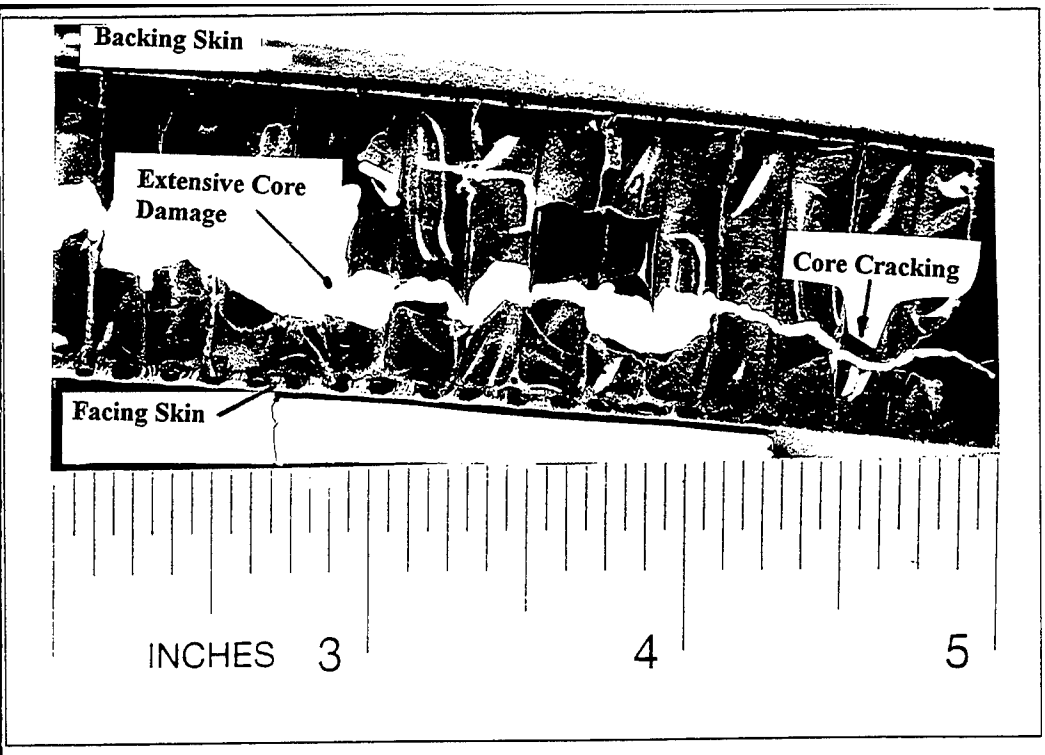

Figure 1.0 - Typical Example of Observed In-Service Failure.

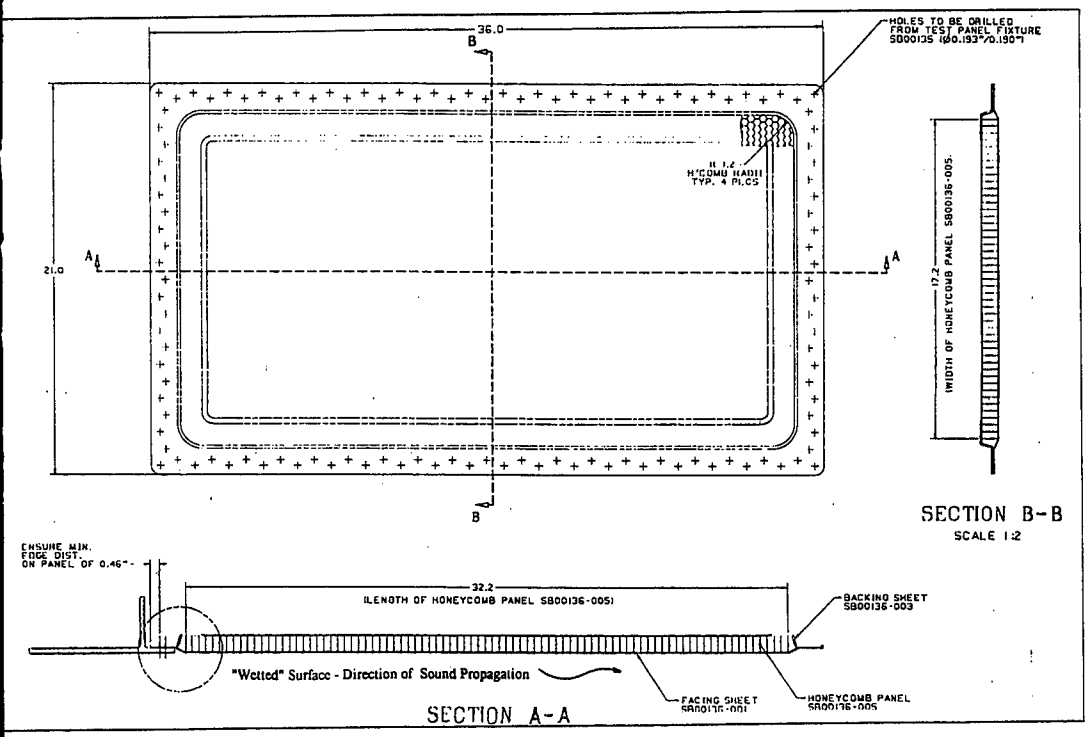

Figure 2.0 - PWT Test Specimen.

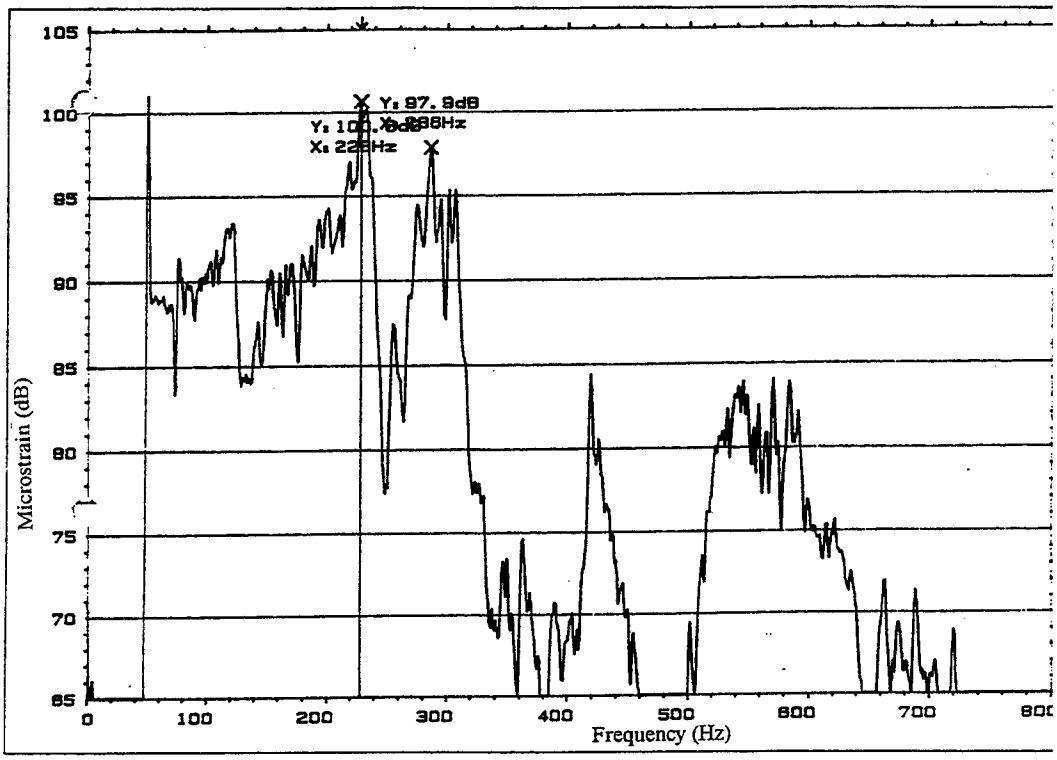

Figure 3.0 - Response of Strain Gauge SG1 During Sine Sweep.

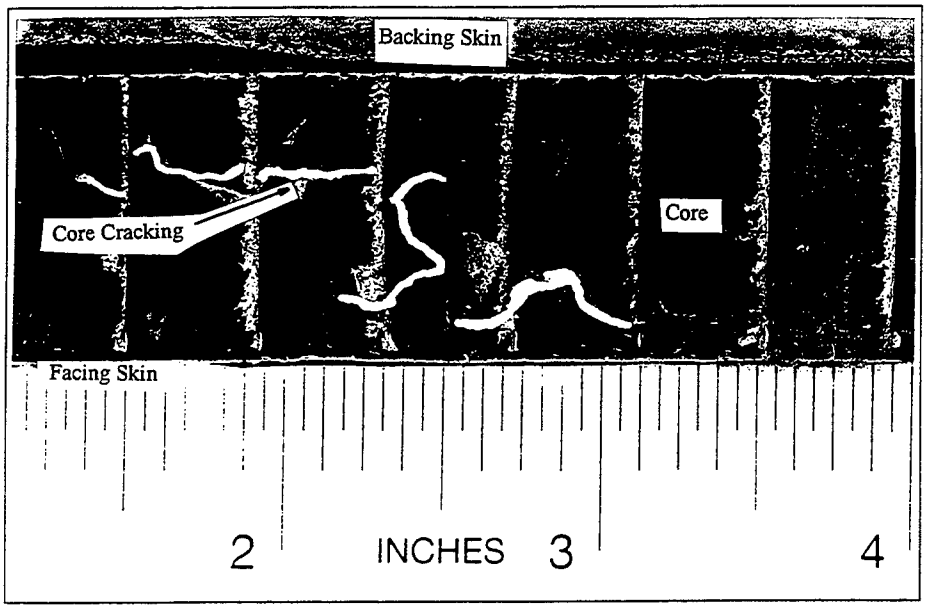

Figure 4.0 - Section Through Failure Region in PWT Panel.

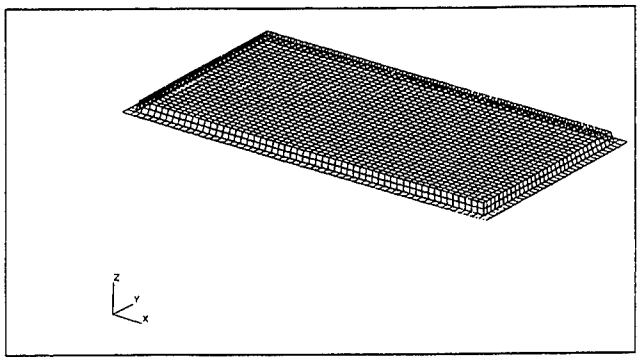

Figure 5.0 - PWT Panel Finite Element Model.

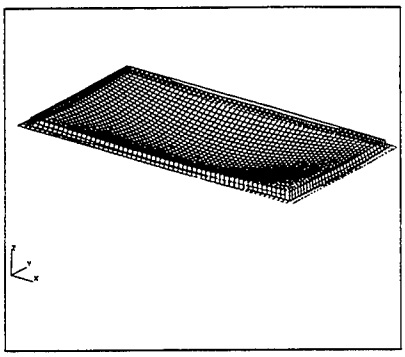

Figure 6.0 - FE Mode 1 (m=1, n=1)

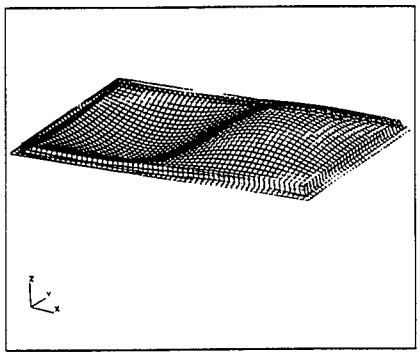

Figure 7.0 - FE Mode 2 (m=2, n=1)

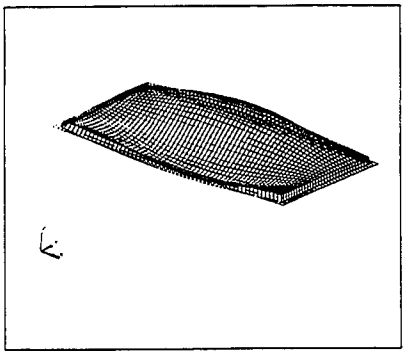

Figure 8.0 - FE Mode 1 (m=1, n=2)

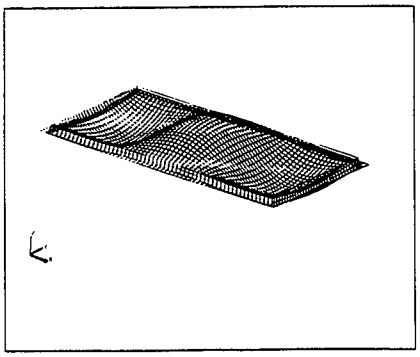

Figure 9.0 - FE Mode 2 (m=3, n=1)

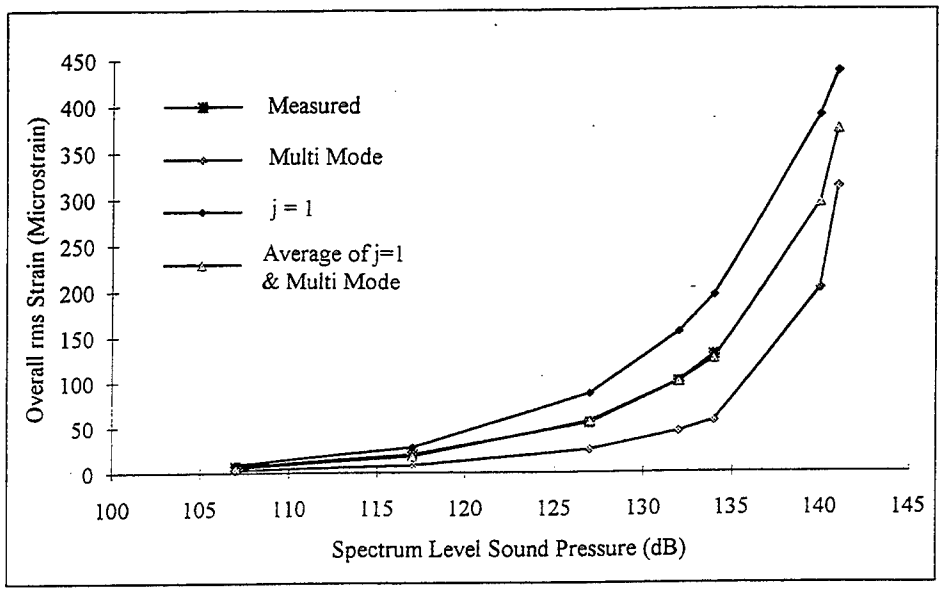

Figure 10.0 - Linearity Plot for SG1 (Measured & NMM Prediction).

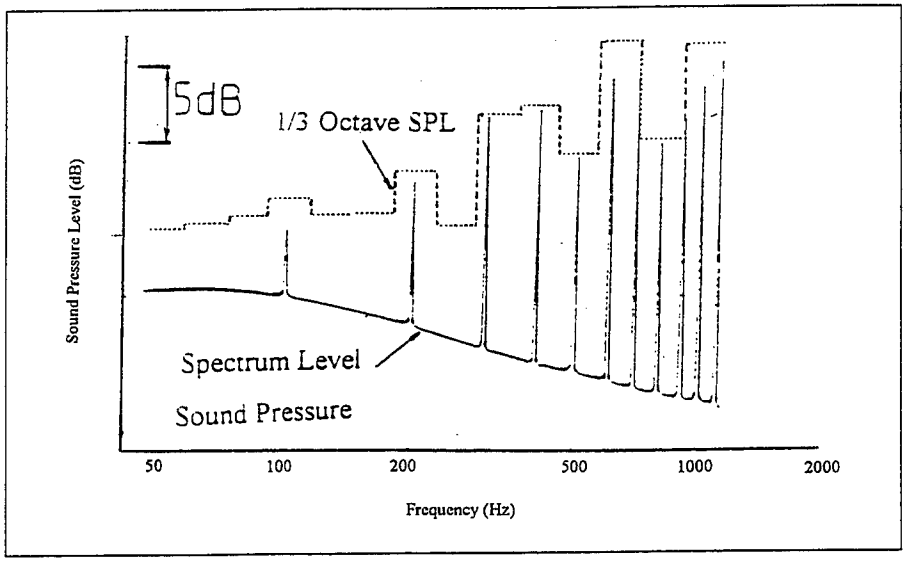

Figure 11.0 - Typical Spectral Content of Intake Duct Sound Pressures with Equivalent 1/3 Octave Levels Superimposed.

Time Domain Dynamic Finite Element Modelling in Acoustic Fatigue Design

Authors:

P. D. Green
Military Aircraft
British Aerospace
Warton

A. Killey
Sowerby Research Centre
British Aerospace
Filton

Summary

Advanced Aircraft are expected to fly in increasingly severe and varied acoustic environments. Improvements are needed in the methods used to design aircraft against acoustic fatigue. Since fatigue life depends strongly on the magnitude of the cyclic stress and the mean stress, it is important to be able to the predict the dynamic stress response of an aircraft to random acoustic loading as accurately as possible.

The established method of determining fatigue life relies on linear vibration theory and assumes that the acoustic pressure is fully spatially correlated across the whole structure. The technique becomes increasingly unsatisfactory when geometric non-linearities start to occur at high noise levels and/or when the structure is significantly curved. Also the excitation is generally not in phase across the whole structure because of complex aerodynamic effects.

Recent advances in finite element modelling, combined with the general availability of extremely fast supercomputers, have made it practical to carry out non-linear random vibration response predictions using time stepping finite element (FE) codes.

Using the time domain Monte Carlo (TDMC) technique it is possible to model multi-modal vibrations of stiffened aircraft panels without making the simplifying assumptions concerning the linearity of the response and the characteristics of the noise excitation.

The technique has been developed initially using a simple flat plate model. This paper presents some of the results obtained during the course of this work. Also described are the results of a study of the "snap-through" behaviour of the flat plate, using time domain finite element analysis. For simplicity, it was assumed that the dynamic loading was fully in phase across the plate.

Introduction

Aircraft structures basically consist of thin, generally curved, plates attached to a supporting framework. During flight these stiffened panels are subjected to a combination of static and dynamic aerodynamic loads. On some aircraft there may be additional quasi-static thermal loads due to the impingement of jet effluxes in some areas. Parts of advanced short take of and landing (ASTOVL) aircraft may be required to withstand noise levels up to 175dB and temperatures up to 200deg C. Under these conditions the established methods of dynamic stress analysis for acoustic fatigue design are inappropriate and cannot be employed.

British Aerospace (BAe), Sowerby Research Centre (SRC) and Military Aircraft (MA) have been developing a method to predict the stress/strain response of aircraft structures in these extreme loading situations. The primary consideration has been the requirement to create an acoustic fatigue design tool for dealing with combined static and dynamic loads, including thermally generated "quasi-static" loads.

The resonant response of thin aircraft structures to aeroacoustic loading is generally in a frequency range which implies that, if defects form, they will quickly grow. Hence to be conservative, it is generally assumed that a component has reached its life when it is possible to find quite small defects by non-destructive evaluation techniques. Several different materials and construction methods are used in modern aircraft and so there are a number of possible failure criteria. In the case of metals, it is the presence of cracks larger than a certain size. For composites it can be the occurrence of either cracking or delamination. Degradation due to the presence of microcracks may be monitored by measuring the level of stiffness reduction which has taken place.

This philosophy simplifies the type of stress analysis needed, because it is not necessary to model structures with defects present. Materials can be assumed to have simple elastic properties which remain unchanged throughout their lives. In consequence, it is necessary to know the fatigue behaviour in terms of a direct relationship between number of cycles to failure and the magnitude of the "nominal" cyclic stress, or strain, at a reference location.

If considered important and capable of satisfactory treatment, the relationship can be modified to take into account material property changes due to the development of very small defects at points of stress concentration. For example, metal plasticity in the region of a small crack, could be included in an analysis of the stress distribution around a fastener hole. It is well known that plasticity reduces the peaks of stress which are predicted at defects by analysis which assumes perfectly elastic material behaviour.

The technique developed at BAe for modelling high acoustic loads combined with possible thermal buckling uses the time domain Monte Carlo (TDMC) technique together with finite element analysis by proprietary FE codes. Response characteristics are predicted directly in the time domain using simulated random acoustic loadings. These may then be used in fatigue life estimations which employ cycle counting methods such as Rainflow counting. It is now practical to predict the vibrational response of stiffened aircraft panels without the necessity to assume a linear response, and without simplifying the spatial and temporal representation of the noise excitation.

Since the technique uses proprietary finite element codes, quite large and complex models of aircraft structure can be analysed in a single run. Standard pre- and post-processor techniques are available to speed up generation of the finite element mesh and to display the stress/strain results.

The initial development work was carried out by modelling the random vibration of a flat plate. For fully in-phase random loading at low noise levels the predicted response is predominantly single mode and at the frequency calculated by linear theory. However, as the decibel level is increased, the frequency of the fundamental rises due to geometrically non-linear stiffening. At very high dB levels the predicted response becomes multi-modal; the resonance peaks move to higher and higher frequencies and broaden.

The effect of static loading on the response has been studied as part of these investigations to assist in the validation of the methodology being developed.

Thermal Effects

In some flight conditions it is possible for a panel to be buckled due to constrained thermal expansion and also be subjected to very noise levels at the same time. An example is when a ASTOVL aircraft hovers close to the ground for an extended period, panels which are initially curved, or thermally buckled panels may possibly be snapped through from one side to the other by a large increase in dynamic pressure.

"Snap-through" can be potentially damaging to the structure of an aircraft if it occurs persistently, because the process is associated with a large change in the cyclic bending stress present at the edge of a stiffened panel. High performance aircraft must therefore be designed so that snap-through never occurs in practice.

The dynamic response of curved panels or buckled flat plates is difficult to predict theoretically because of non-linear effects. The established acoustic fatigue design techniques, which are based on linear vibration theory, are only able to provide approximate predictions of the loading regimes in which particular panels might be expected to undergo snap-through.

The TDMC method can be used to model non-linear multi-modal vibrations of stiffened aircraft panels which are also subject to quasi-static stress. In particular calculations may be carried out in the post-buckling regime.

With this technique simulated random dynamic pressure loading, with measured or otherwise known spectral characteristics is applied to a curved, or post-buckled panel and the time domain response calculated. The magnitude of the dynamic loading may then be increased until persistent snap-through is observed in the predicted response. This gives the designer the ability to design out the potential problem by systematically altering the most important parameters in order to identify the critical regime.

Fatigue Life Estimation

Although acoustic fatigue is a complex phenomenon, it has been established that the life of a component mainly depends on its stress/strain history. The most important factors in this regard are the magnitude and frequency of the cyclic strain and the mean level of stress at the likely failure points. On this basis fatigue life can be estimated by carrying out the three stage operation illustrated in Figure 1.

Stage 1: Determine Loads

A determination of static design loads is relatively straightforward compared to a calculation of the full temporal and spatial dependence of the aeroacoustic pressure on a military jet in flight. This is an enormous task in computational fluid dynamics (CFD). Designers have to rely on experimental data which can come from measurements on existing aircraft or from scale model tests of jets, for example. Existing databases can be extrapolated if the circumstances are similar. Experimental noise data is usually in the form of power spectral density curves as opposed to time series fluctuating pressures, but either can be used, depending on the circumstances.

Stage 2: Calculate Stresses

The technique chosen to obtain the stresses clearly depends on how much knowledge there is about the expected loads. In the early stages of design analytic techniques would be used to establish approximate sizes and stress levels. However, later on when the design is nearly completion, finite element (FE) stress analysis can be used to model the effect of random acoustic loading on the parts of the skin which are likely to be severely affected. These calculations would, of course, be done including the effect of attached substructure.

The established method of designing against acoustic fatigue uses a frequency domain technique which relies on the validity of linear vibration theory. The method forms the basis of a number of methodology documents published by the Engineering Sciences Data Unit (ESDU). Whenever there are large out-of-plane deflections the frequency domain method cannot be used because of the "geometric non-linearity". From a strictly theoretical point of view such analyses have to be carried out in the time domain, although approximate methods are applied with some success.

The established technique produces inaccurate results for curved panels, buckled panels and for panels under high amplitude vibration. Geometric non-linearity usually stiffens a structure in bending so there is a tendency to overestimate the stress levels using the frequency domain technique. This conservatism is clearly useful from the point of view of safety, but it can lead to possible "over-design". Unfortunately this is not always the case when there are compressive static stresses present. The established method also fails if the phase of the noise varies significantly over the surface of the structure, which is the case in a number of aeroacoustic problems. The techniques under development are designed to overcome these problems.

Stage 3: Estimate Fatigue Life

In cases of random acoustic loading it is customary to assume that damage accumulates according to the linear Miner's rule. Fatigue life is determined from experimental data in the form of stress (or strain amplitude), S, versus number of cycles to failure, N. If a number of cycles, n, of stress/strain, S, occur at a level of stress/strain where N(S) cycles would cause failure then the fractional damage done by the n(S) cycles is n(S)/N(S).

Various methods have been developed for obtaining n(S) from the stress (strain) response. If the excitation is stationary, ergodic and the response is narrow band random then the function n(S) can be shown to be in the form of a Rayleigh distribution and the damage sum can be evaluated from plots of root mean square stress (or strain) against number of cycles to failure. If the statistics of the response are not Gaussian then it is necessary to count the numbers of stress cycles from the time domain response and use constant amplitude S/N curves. It is now widely accepted that the best way of counting the cycles is to use the Rainflow method, [1].

The Loading Regime

The loads on an aircraft may be conveniently divided into static and dynamic.

Loads which vary only slowly are:

a) Steady Aerodynamic Pressure Loading,
b) In-Plane Loads transferred from "external structure", and
c) Thermal Loads due to Constrained Expansions.

The rapidly varying loads are, of course, the aeroacoustic pressure fluctuations which originate from any form of unstable gas or air flow.

This division is central to the methodology which has been developed because it enables the modelling to be carried out in two distinct phases. The, so called, static loads do vary, of course, but the idea is to separate effects which occur on a time scale of seconds from the more rapidly varying acoustic phenomena. The aim is to split the loads so that the quasi-static effects can be calculated in an initial static analysis which does not depend on a particular dynamic loading regime. Any aerodynamic pressure may be divided into a steady part and a fluctuating part. The natural place to make the cut-off is at 1Hz which means that epoch times for TDMC simulations are then of the order of a second. The epoch time must not be too short because of statistical errors, and it cannot be too long because this would invalidate the assumption of constant quasi-static loads. In practice, there is another constraint on the epoch time. The number of finite elements in the model coupled with the premium on cpu time places an obvious limit on the epoch time.

Comparison of the Time and Frequency Domain Methods

A flow chart comparing the two methods is given as Figure 2. The main difference between the two techniques lies in the representation of the dynamic loads. The FD method uses rms loadings and spectral characteristics, whereas the TD method uses the full time series loadings. Gaussian statistics are, de facto, assumed by the FD method, but this is not necessarily the case with the TD technique.

Application of the frequency domain method requires that the response is dominated either by a single mode or a small number of modes. To determine whether or not this is the case in practice, a normal modes analysis must be followed by a determination of the amount of coupling between the excitation and each mode. This can be determined quite accurately even if there is a certain amount of potential non-linearity by computing the joint acceptances for each mode, which are overlap integrals of the mode shape functions with the spatial characteristics of the excitation. Normally these quantities will be dominated by a few of the low order modes. If there is significant coupling into more than one mode then it will be necessary to use the TD method instead.

With the time domain technique it is possible to represent the dynamic loads in a way which models the convection of the noise field across the structure. Very complicated loadings can be applied to large

models but in consequence it can be difficult to validate the results obtained, because they cannot be checked against anything other than test data which is itself subject to confidence levels. In addition it must be remembered that the TDMC results themselves are subject to statistical variability. Finally it should be noted that TDMC data must be used in conjunction with constant amplitude endurance data. Rms fatigue data can only be used with frequency domain results.

Time Domain Finite Element Modelling

Until recently, the majority of finite element analyses were applied to static loading conditions or "low frequency normal modes analysis". The method involves the use of an implicit code to invert in one operation, a single stiffness matrix, which can be very large. The general availability of extremely fast super-computers has now made it possible to carry out large scale non-linear dynamic finite element modelling using explicit FE codes. These codes use very similar types of element formulation to the implicit ones, e.g. shells, solids and bars, but the solution is advanced in time using a central difference scheme.

One potentially very useful capability of time domain modelling is the application of acoustic pressure loadings which vary both in the time and spatial domains. If the spectral characteristics are known, either from test or from other modelling it is possible to generate samples of random acoustic noise and apply these directly to the finite element model as a series of "load curves".

The technique for determining time series noise was developed by Rice [2] and Shinozuka [3]. They showed that homogeneous Gaussian random noise can be generated from the power spectral density as a sum of cosine functions with different frequencies and random phase. Noise can be temporally and spatially correlated noise by deriving phase differences from cross spectral functions if they are known.

The TDMC method can be quite costly in terms of central processor unit (cpu) time because the solution must be recalculated at each point in time. To reduce execution times, the explicit codes employ reduced numbers of volume integration points in the finite element formulations. However in this work cpu times are extended because long epoch times are required to ensure adequate statistics. It can take more than 24hrs to obtain a solution over a half second epoch if there are a few thousand elements in the model.

Hence there is always a practical limit to the size of a particular time domain finite element analysis, (TDFEA). If the loading and geometry are not too complicated, the frequency domain method of analysis can be tried initially to gain more understanding of the nature of the response in an approximate way. In some cases the vibrational response regime must be considered carefully to decide whether TDFEA is really necessary. These may be situations where the non-linear effects are only moderate.

It would be ideal if the full dynamic response of an aircraft could be determined with a fine mesh model in one huge operation, but experience has shown that this requires too many elements. It is possible to construct full models with reduced stiffness using superelements, enabling flutter and buffet to be studied, because these are essentially low frequency phenomena. However, in time domain analysis it has been found that models containing a large amount of detail, such as fasteners and individual composite material plys, require a great deal of cpu time. To progress we must devise some strategies to overcome this situation. Since a full TDFEA can only handle a part of the aircraft structure, it is very important that loads external to the area under consideration are properly taken into account. This is crucial to the success of this type of modelling as it is to all finite element modelling.

The most important parameter in any time series analysis is the time step. This is determined by the velocity of sound waves in the structural material, and is generally of the order of a/v where a is the shortest element dimension and v is the velocity of longitudinal sound. A small time step is therefore required when the elements are small and the velocity of sound is large. For an aluminium model with 10mm square elements the time step is about 1.6μs. Hence a TDMC run with a half second epoch time needs about a half a million steps. A simple 5000 shell element calculation on a Cray C94 would take approximately 10 hours.

Dynamic FE models of aircraft structure can be constructed in many ways, using shell elements, beam elements and/or solid elements. Special elements exist for damping and for sliding interfaces. Joints can be modelled with sliding interfaces, or with short beams, or just with tied nodes. Fasteners can be modelled with small solid elements, with short beams or with tied nodes, also. Unfortunately, however short beams and small solid elements cause a dramatic lowering of the time step. For example, if the smallest fastener dimension is, say 3mm, the time step will have to be reduced to about 0.5μs if solid elements are used in the model. The effect on cpu time is such as to make the calculations impractical. Sliding interfaces are an efficient way to model skin/substructure contact in explicit analyses, but it is important to choose the algorithm carefully because some techniques can consume large amounts of cpu time.

The best practical way of representing stiffened aircraft panels for TDMC analyses is considered to be with four noded shell elements simply tied together at their edges. A number of efficient shell formulations are avail-able and meshes can be rapidly produced from the design geometry. Of course, such models cannot be expected to produce highly accurate stress data in the region of small features but this aspect has to be sacrificed in the interests of achieving statistically significant amounts of time series data. To improve the accuracy of stress predictions in the neighbourhood of stiffeners etc., it will be necessary to couple TDMC analyses with fine mesh static analyses.

The Generation of Time Series Data

A number of factors must be borne in mind when generating time series data for TDMC calculations. It is important to consider carefully the frequency range and number of points which define the load spectrum in conjunction with the epoch time and number of points on the time series.

The Nyquist Criterion [4] states that the time increment must be less than or equal to one over twice the upper frequency on the power spectral density curve. For the sake of argument, take the upper frequency to be 1kHz. This means that the time increment must be less than 500μs. A more conservative time increment is based on the requirement to represent the dynamic response of the structure as accurately as possible over a full cycle. Assuming a resonant frequency of 500Hz, which is perhaps near the limit in practice, and 10 points per cycle which is more than sufficient, the lower limit on the time step works out at about 200μs. Taking all these factors into consideration, the number of points on the spectrum curve should be of the order of 1000 and there should be between 1000 and 5000 on the time series. Longer epoch times can be used but for reasons of practicality and statistics it is better to run more than one short epoch simulation rather than one long simulation.

Explicit FE modelling frequently requires that the time step be smaller than 200μs. In the example given above the time step required by the explicit code was 1.6μs. Under these circumstances the random noise could be defined with a smaller time increment, but going to this level of effort has been found to produce no measurable change to the calculated response.

Static Initialisation

There are two possible ways of dealing with the effect of static loads in TDMC modelling. Firstly the complete analysis can be carried out using the explicit code. To do this it is necessary to apply only the static loads to the model and run the code until equilibrium is reached. By introducing a high level of artificial damping the stresses created can be relaxed in a relatively short period of time. The time required depends on the lowest resonant frequency of the structure and the size of the smallest element in the model. This facility is termed "dynamic relaxation".

The alternative is to make use of another facility in the explicit code called "static initialisation". The deformed shape and stress state of the structure with just the static loads applied are first obtained very quickly using an implicit code. The solution for the stressed state is then initialised into the explicit code prior to the application of the dynamic loads. Dynamic relaxation may be used to smooth out any differences between the models.

Damping Representation

Vibrating aircraft structures are damped by several mechanisms, for example friction at joints, re-radiation of acoustic waves, and energy loss in viscoelastic materials It is difficult to generalise about the relative importance of each damping process in practice. Also reliable quantitative data is not available in sufficient detail to justify the inclusion of complex models of damping into the TDMC analyses. Test results on vibrating stiffened aluminium panels tend to show that the damping is best approximated by a combination of mass and stiffness proportional coefficients. There is a range of frequencies in which the damping ratio can be considered to be roughly constant. Until more detailed experimental data are available the most expedient approach is to assume a nominal value for the global damping ratio which does not change with frequency. Over the years it has become standard practice to assume a damping ratio of about 2% for fastened aluminium structures.

Equivalent Linearisation

There are some loading regimes in which the non-linear response to high levels of random acoustic loading can be approximately found using a linearisation technique combined with a frequency domain analysis. The basic idea is to replace the non-linear stiffness term in the general vibration equation by a linear term such that the difference between the rms response of the two equations is minimised with respect to a shifted fundamental resonance frequency. If an approximate equation for the non-linear stiffness is known then it is possible to derive an expression for the shifted "non-linear" resonance frequency. The rms response to random acoustic loading may then be found by combining the Miles/Clarkson equation with some form of static geometrically non-linear analysis. References to this technique are Blevins [5], Mei [6] and Roberts & Spanos [7]. Where the geometry is complex the most appropriate form of analysis is clearly finite element analysis.

Implementation and Validation Studies

The stress analysis work described in this paper has been undertaken using MSC-NASTRAN and LLNL-DYNA.

NASTRAN is a well known implicit finite element code which is capable of handling very large numbers of elements. It has been developed very much with aerospace structural analysis in mind. It is basically a linear analysis code, although there are a large number of adaptations to deal with non-linear problems. It can also function as a dynamic code, but is much slower than DYNA in this mode because it basically needs to solve the complete problem at each time step. The non-linear features which are most relevant to the type of stress analysis being discussed here are those concerned with geometric non-linearity. Geometric non-linearity is treated by dividing the load into a series of steps, obtaining the solution incrementally. In this work, the code has been used for linear and non-linear static analyses and for normal modes analyses.

DYNA is an explicit finite element code originally developed for the calculation of the non-linear transient response of three dimensional structures. The code has shell, beam and solid element models and there are a large number of non-linear and/or anisotropic material models available. DYNA was developed primarily for the modelling of impact and there is no limit, as far as the code is concerned, on the size of finite element model which can be analysed. Many of its advanced features relate to impact modelling and are not required for this work. One useful feature, however is the laminated composite material model based on the equivalent single layer approximation. This code has been used for the TDMC calculations presented in this paper.

Finite element models for the stress analyses were produced using MSC-PATRAN. It has a wide range of geometry and mesh generation tools and now has built in interfaces for both NASTRAN and DYNA. The element definitions are compatible with both codes and it is a simple matter to toggle between the two codes by changing the analysis preference. Not all the features of DYNA are supported and some of the parameters must be set by editing the DYNA bulk data produced by PATRAN.

NASTRAN results were post-processed using PATRAN. DYNA results were post processed using TAURUS, which is faster and easier to use than PATRAN for this task. Some special in-house codes have been written to generate random acoustic noise from power spectral densities, as described above,

and to post process time series output from TAURUS. One of the codes incorporates a fast Fourier transform (FFT) routine to determine spectral responses from the DYNA time series predictions. These codes are covered under the generic title "NEW-DYNAMIC".

TDMC Calculations on a Simple Flat Plate

Calculations have been performed on a very simple model to implement the TDMC technique and develop the in-house software referred to above. A PATRAN database was constructed representing a simple flat plate, 350mm x 280mm x 1.2mm thick as an array of shell elements 34x28. For simplicity the boundary conditions were taken either as simply supported or clamped. There are a number of alternative shell element formulations available in DYNA, [8]. The Hughes-Liu shell was used initially because of its good reputation for accuracy, but later a switch was made to a similar, but slightly faster shell element, called the YASE. It was found that equally satisfactory results could be obtained more quickly using this element.

Analyses without Static Loads

A series of DYNA calculations were carried out with a fully correlated random acoustic pressure load with a flat noise spectrum between 0Hz and 1024Hz. Investigations were carried out into the effect of varying the sound pressure level, the epoch time, the mesh resolution, the damping coefficient and the stochastic function.

Figure 3 shows the displacement response of the central node of the model for a sound pressure level of 115dB (about 12Pa rms), simply supported edges and mass proportional damping set so that the damping ratio was equal to 2% at the fundamental (1,1) resonance of the plate. The corresponding spectral response is shown in Figure 4. shows a sharp resonance peak at a frequency of 61.0Hz which is very close to the theoretical frequency of the (1,1) mode for the simply supported plate. The in-phase loading means that only the modes with odd numbered indices are excited. The peaks corresponding to the (3,1) and (1,3) modes are, however, not visible on the plot because they are too small. It may be concluded from these results that the behaviour of the plate at these pressure level is well within the linear regime.

An investigation into the behaviour of the rms displacement response as a function of SPL was carried out by increasing the loading incrementally from 75dB (0.12Pa rms) to 175dB (12kPa rms). The results are shown in Figure 5. Also shown are theoretical predictions obtained using the Miles/Clarkson formula with NASTRAN linear and non-linear analyses as explained above, see below for discussion.

The statistical variation of the results was investigated by repeating a half second epoch TDMC run ten times with different samples of flat spectrum noise. It was found that the standard error of the rms response was about 16%. A second set of ten repeats were carried out with the epoch increased to 2.5s. In this case the standard error reduced to roughly 8%. From the theory of stochastic processes, it can be shown that the standard error is inversely proportional to the square root of the epoch time. On this basis therefore the ratio between the standard errors should be equal to the square root of five, or 2.23. From the analyses this ratio is about 2. Further runs established that these results are not affected by the vibration amplitude, even when the response becomes non-linear.

Cautiously therefore, it can be concluded that the variance of the TDMC results is unaffected by non-linearity of the response. This is an important finding because it builds confidence in the technique. In many practical situations it may be necessary to rely on just one simulation and an appropriate factor of safety. It can be quite time consuming to carry out a large number of repeat TDMC simulations. The level of variance would be first established by repeating one load case a number of times, before confidently applying it to the results of other load cases.

Comparisons with Linearised Theory

The linear theory of plate bending, [9], leads to relationships between the central deflection, w, of a rectangular plate and a uniform static pressure load, p_{stat} which take the following form.

$$p_{stat}\, a\, b = k_{eff}\, w \qquad (1)$$

where a and b are the length and breadth of the plate, and k_{eff} is an effective stiffness parameter which is a function of the modulus of rigidity of the plate and the edge boundary conditions. For the plate studied k_{eff} is about 30N/mm for the case of simply supported edges and 100N/mm for clamped edges. The above equation only holds, however, at very low amplitudes, as can be seen from Figure 6. This compares geometrically non-linear NASTRAN predictions with the linear theory. Curves are shown for both simply supported and clamped boundary conditions. The finite element results show the characteristic hardening spring type of non-linearity.

At higher amplitudes the dynamic behaviour may be approximately predicted using "equivalent linearisation" theory, which assumes that the response remains predominantly single mode, but with a resonant frequency which rises as the stiffness of the structure increases. When the deflection is large the static force-deflection relationship can be written as the sum of a linear stiffness term and a cubic non-linear term:

$$p_{stat}\, a\, b = k\, w\, (1+\mu w^2) \qquad (2)$$

where p_{stat} a b is the force, k is the linear stiffness. The equation is written with the leading term factored out to emphasis the point that μ is a constant which is small compared to the rms deflection. In the limit of small w we can expect the μw^2 term in the brackets to be negligible compared to one, which means that the k in this equation must be the same as k_{eff} above.

Equation 2 was fitted to the NASTRAN results shown in Figure 6 to find the best fit values of k and μ. Table 1 shows the results compared with the effective stiffness calculated from linear plate bending theory. It can be seen that the theoretical stiffness is almost identical to the best fit k from the non-linear finite element analysis.

With reference to the results in Figure 5, it is obvious that the nature of the response is strongly dependent on the amplitude of the vibrations. For rms displacements up to about 4% of the plate thickness the behaviour was completely linear. For displacements between 4% and 150% of plate thickness, the response was essentially single mode dominated but the level could not be predicted by the Miles/Clarkson approach. The "equivalently linear" solution does, however, agree with the DYNA result up to a displacement of about 1.8mm. The linearisation approach cannot be expected to be correct for displacements above about 1.5 times plate thickness. Above this point the response predicted by DYNA was multi-modal and strongly non-linear. The equivalently linear predictions departed considerably from the DYNA results when the vibration amplitude was very high.

It was also observed that the frequency response peaks became increasingly noisy for higher pressures, representing the increased level of non-linearity in the plate vibrations. The increase in the frequency of the fundamental mode with acoustic pressure, as calculated by DYNA, is shown in Figure 7. Predictions from equivalent linearisation theory and from the theory of Duffing's equation are also included, see Nayfeh & Mook [10].

$$f_{nl} = f\,(1 + 3\mu w_{rms}^{2})^{0.5} \qquad \text{Equiv. Lin. Pred.} \qquad (3)$$

$$f_{nl} = f\,(1 + (3/8) w_{rms}^{2}) \qquad \text{Duffing's Eq. Pred.} \qquad (4)$$

The DYNA results lie mostly between the two theoretical curves, agreeing particularly well with the results of equivalent linearisation theory up to around 700Pa (151dB rms). The level of agreement obtained shows that the frequency response behaviour of the DYNA model is similar the theoretical predictions, providing an independent check on the results. As might be expected, at around 700Pa the agreement begins to breakdown, since the linearisation theories are not valid for deflections which are significantly greater than the plate thickness. It may be concluded, however, that the effect of geometric non-linearity at high amplitudes is being computed by DYNA in a reasonably accurate manner. A detailed comparison with experimental data is needed to determine the accuracy of the DYNA response predictions themselves.

Due to the increasingly irregular shape of the frequency response functions derived from the DYNA time series predictions at high acoustic loads, it was not possible to calculate very accurate peak widths for pressures above approximately 135dB (120Pa rms). Figure 8 shows that the width of the peak increased with increasing acoustic pressure, but not in a regular manner. When the damping is mass proportional, equivalently linear theory predicts that the width of the peak should remain unchanged as the pressure rises. This is because the geometric stiffening effect of rising acoustic pressure exactly cancels the effect of a smaller damping ratio at the higher resonant frequency. This graph shows this as a horizontal straight line at 2.44Hz. The DYNA result is closer to the type of behaviour observed experimentally where the width of the peak generally increases with increasing the sound pressure level.

Analyses with Combined Loads

Further work was conducted with static loads superimposed on different levels of random acoustic loading. These calculations were done using the coupled NASTRAN-DYNA approach outlined earlier. That is to say the deformed geometry was obtained by applying the static loads to a NASTRAN model, with the results being initialised into DYNA and dynamically relaxed before the dynamic loading was applied. Calculations were performed with compressive in-plane loading, static pressure loading and thermal loading. With the exception of the thermal runs, the boundary conditions used in these runs were identical to clamped, except that symmetrical in-plane movement of the edges was permitted. We have called these conditions "semi-clamped". It has been found that the fundamental resonant frequency of the plate without static loading is only reduced by a very small amount if the appropriate in-plane degrees of freedom are released, see Figure 9. These boundary conditions are actually closer to those which exist in reality when a panel in built into a larger structure.

Figures 10-14 show results of some of the analyses which have been carried out. They give time series data along with spectra responses calculated by the in-house post-processing code. Numerical data derived from these results are summarised in Tables 3-5.

A series of analyses have been carried out with compressive in-plane loads equal to one third of the theoretical buckling loads in compression. For the plate used, the forces per unit side length were -3.46N/mm in the x-direction and -5.46N/mm in the y-direction. The results of one analysis are shown in Figure 10. It has been found that the response remains dominated by the fundamental (1,1) mode as long as the plate is unbuckled and the SPL is low. The softening effect of the compressive loads on the frequency agreed quite well with Rayleigh-Ritz predictions, [5], up to an SPL of ?dB. At higher sound pressure levels, the DYNA results reflected stiffness changes which were greater than those predicted by the theory. The same was found in the case of tensile loading. It is believed that these differences are due to approximations built into both the Rayleigh-Ritz theory and the DYNA code.

Figure 11 shows the results of a calculation with a superimposed normal pressure. The magnitude of the pressure, 700Pa, was chosen so as to provide an example of "post-buckled" analysis. This size of pressure causes the plate to bow out in the centre by about 0.6mm. It is well known that in the post-buckling regime the random response of a plate depends upon the magnitudes of both the static and dynamic loads. In this case the static loading was large compared to the applied dynamic loads and "snap-through" did not occur. The plate simply vibrated about its statically deflected position in the fundamental mode with a slightly increased frequency.

To provide a test of the DYNA thermal stressing capability, and to carry out an investigation into "snap-through", several analyses were carried out with a uniform temperature rise of 10deg C applied to the plate with clamped edges. This is quite sufficient to cause buckling because the resulting compressive biaxial stress, σ, is well above the buckling level, σ_b. If f is the frequency of the fundamental and J is a constant equal to 1.248 because of the clamped boundary condition, the two stresses can be determined approximately from

$$\sigma = E \alpha T / (1-\nu^2) \qquad (5)$$

&

$$\sigma_b = 4 \rho a^2 f^2 / J \qquad (6)$$

where E, α, v and ρ are Young's modulus, coefficient of thermal expansion, Poisson's ratio, and density respectively. Using these formulae we find $\sigma = 24MPa$ and $\sigma_b = 14MPa$.

Analyses were carried out with several different levels of dynamic load. The results of three of the calculations are shown in Figures 12,13 and 14. It was found that the threshold for snap-through occurred at an acoustic load of about 1kPa, see Table 4. Below this level the mean deflection, w, is a function of the static load alone, equal to about 2.8mm (the negative sign indicates that the plate has bowed in direction of negative z). At higher SPLs the mean deflection reduces because the plate snaps backwards and forwards between positive and negative z. The calculated response spectra for these higher level runs, show an additional peak at a very low frequency, ie less than 10Hz. This is an artifact caused by the snap-through since the fundamental resonance of the clamped plate is at 113Hz.

Figures 10-14 all show probability density functions derived from the time series data. The fluctuations on these plots are caused by the smallness of the epoch time. In all cases, except for the thermal calculations with the two largest acoustic loads, it can be seen that the functions are basically Gaussian in shape. It may therefore be concluded that it is reasonable to assume that the response of a plate in the post-buckled region is Gaussian unless there is a large amount of snap-through.

Discussion

The work described is the starting point for investigations and validations using more complex FE models. Further work has been carried out using models including curvature, sub-structure and detailed features. It is difficult to validate the predictions obtained from such models by comparing with test data because the results themselves are open to interpretation. It has been found that the predicted stress levels are closer to the test results when the chosen location is away from any small features. The lack of good agreement in the neighbourhood of the features can be explained by the relatively coarse mesh used in the dynamic models. The overall level agreement was much better than that between predictions based on linear or equivalently linear theory and test. On the basis of experience, the latter tend to over-predict by upwards of factors of two and three. From this work it has been found that the DYNA predictions tend to be greater than test by amounts which vary but are generally much less. The average over-prediction was about 40% with a significant change as a function of location.

TDMC runs can take a significant amount of computer time to carry out and it is believed that to make further improvements the technique should be combined with detailed stressing using static finite element analysis. Inaccurate results can be obtained if the boundaries of the part of the structure under analysis are not properly restrained. In the case of models of aircraft panels this may significantly affect the resonant frequencies which in turn affects the level of calculated dynamic stress. In-plane loads on a panel, perhaps due to thermal stressing, can alter the fundamental by as much as 100-200Hz. Looked at from a theoretical point of view, the only way to solve this problem is to construct a second, coarse model of the component, along with some of its surrounding structure. An initial calculation can then be carried out with this model in order to obtain the loads and boundary conditions for subsequent application to the original model.

The dynamic phenomenon of "snap-through" cannot be modelled using existing methods and so the TDMC / finite element technique offers the engineer a way to determine where the likely regions of unstable vibration are located in circumstances where the structure is complicated by attachments etc.

Conclusions

This paper has sought to explain how time domain finite element modelling can be used to assist in the design of aircraft against acoustic fatigue. Although the technique is computationally intensive, it does have a place in the effort to understand complex vibrations, such as the response of structures to spatially correlated jet noise excitations, or interactions between high sound pressure levels and thermal loads.

The work at BAe is continuing in an attempt to provide the analyst with a greater ability to determine dynamic stress levels in advanced structures with complex loadings.

References

1. Dowling N. E. , Fatigue Prediction for Complicated Stress Strain Histories, J Materials 1, 71 (1972).

2. Rice, In Selected Papers on Noise and Stochastic Processes, Ed N Wax pp180, Dover New York (1954).

3. Shinozuka M. , Computers and Structures, 2, 855, (1972).

4. Bendat J. S. and Piersol A.G. , Engineering Applications of Correlation and Spectral Analysis, Wiley (1990).

5. Blevins R.D. , An approximate method for sonic fatigue analysis of plates and shells, J Sound and Vibration, 129, 1, 51 (1989).

6. Mei C. and Paul D.B. , Non Linear multi-modal response of a clamped rectangular plates to Acoustic Loading, AIAA Journal, 24, 634, (1986).

7. Roberts J. B. & Spanos P.D , Random Vibration and Statistical Linearisation, Wiley, (1990).

8. Whirley R.G. and Engelmann B.E. , DYNA3D: A Nonlinear, Explicit, Three Dimensional Finite Element Code for Solid and Structural Mechanics --- User Manual, Lawrence Livermore National Laboratory, UCRL-MA-107254 Rev. 1, (Nov 1993).

9. Szilard R. , Theory and Analysis of Plates, Prentice Hall, New Jersey.

10. Nayfeh A.H. & Mook D.T. , Non Linear Oscillations, Wiley (1979).

Parameter	Stiffness k (N.mm^{-1})	Stiffness k (N.mm^{-1})	'Non-Lin Stiff' μ (mm^{-2})
	Linear Theory	NASTRAN	NASTRAN
Simply Supported	30.0	30.7	1.09
Clamped	104.	101.	0.266

Table 1: Values of Parameters fitted to NASTRAN results compared with the linear theory values.

Static Loads		Acoustic Load	Theory		DYNA	
N_x (N.mm^{-1})	N_y (N.mm^{-1})	P_{rms} (Pa/dB)	Freq (Hz)	w_{rms} (mm)	Freq (Hz)	w_{rms} (mm)
None	None	1.2 (95.6)	113.6	0.00290	114	0.01.2
	-3.46	**1.2 (95.6)**	**93.72**	**0.00316**	**94.1**	**0.00313**
	-3.46	**643.5 (150.1)**	**93.72**	**1.69**	**115**	**1.08**
-5.41	**-3.46**	**1.2 (95.6)**	**68.33**	**0.00359**	**68.1**	**0.00368**
-5.41	**-3.46**	**700 (150.9)**	**68.33**	**2.09**	**103**	**1.42**

Table 2: Summary of results of calculations with random acoustic loading superimposed on compressive in-plane loads.

Static Load	Acoustic Load	DYNA		
p (Pa)	P_{rms} (Pa / dB)	Freq (Hz)	$\overline{w}$ (mm)	w_{rms} (mm)
None	1.2 (95.6)	114	0.0000	0.01.2
700	None	—	-0.646	—
700	**12 (115.6)**	**115**	**-0.655**	**0.0189**
700	**700 (150.9)**	**134**	**-0.477**	**1.28**
5 k	None	—	-2.89	—
5 k	**12 (115.6)**	**179**	**-2.93**	**0.0152**
5 k	**700 (150.9)**	**173**	**-2.70**	**0.999**

Table 3: Summary of results of calculations with random acoustic loading superimposed on static pressure loads.

Temperature	Acoustic Load	DYNA		
T (°C)	P_{rms} (Pa / dB)	Freq (Hz)	$\overline{w}$ (mm)	w_{rms} (mm)
None	**1.2 (95.6)**	**114**	**0.0000**	**0.00256**
10	**None**	**—**	**-2.85**	**—**
10	**1.2 (95.6)**	**234**	**-2.86**	**0.0140**
10	**700 (150.9)**	**219**	**-2.80**	**0.197**
10	**1k (154.0)**	**9.01**	**2.47**	**1.02**
10	**1.2k (155.6)**	**5.01**	**-0.717**	**2.24**
10	**1.5k (157.5)**	**3.00**	**-0.376**	**2.20**
10	**2k (160.0)**	**92.2**	**0.0185**	**1.95**
10	**4k (166.0)**	**195**	**0.0568**	**2.08**

Table 4: Summary of results of calculations with random acoustic loading superimposed on a thermal load.

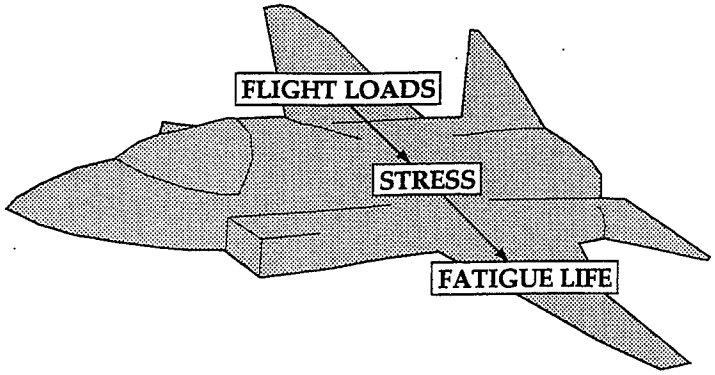

Figure 1: Illustrating the Process of Fatigue Life Estimation.

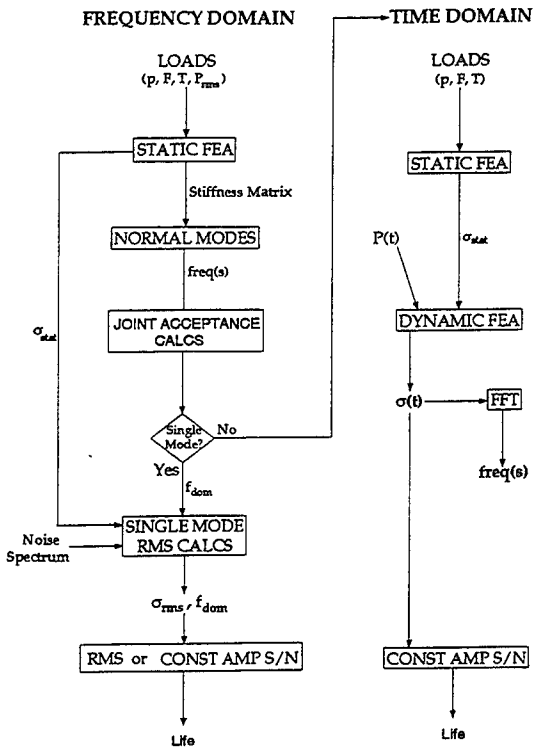

Figure 2: Flowchart Illustrating the Frequency and Time Domain Techniques.

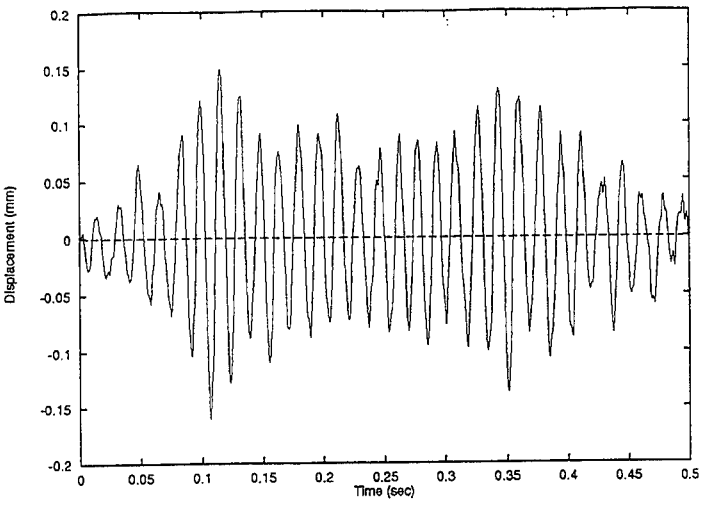

Figure 3: Displacement of central node for 12Pa rms acoustic pressure, DYNA calculation.

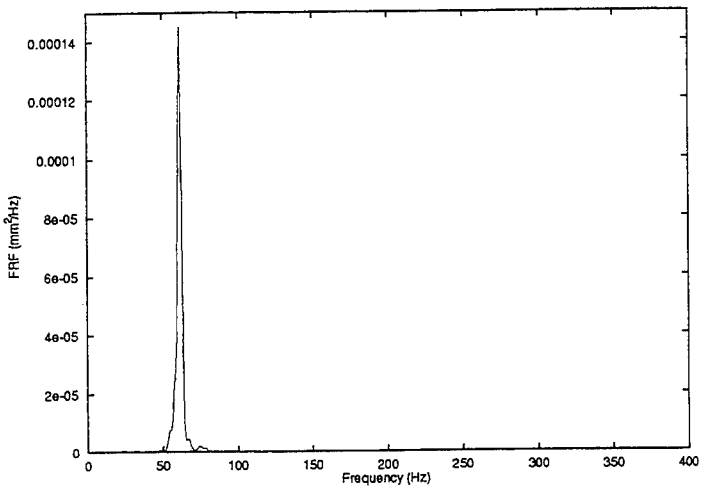

Figure 4: Spectral Response of the flat plate corresponding to Fig 3. Central Node for 12Pa rms pressure, DYNA calculation.

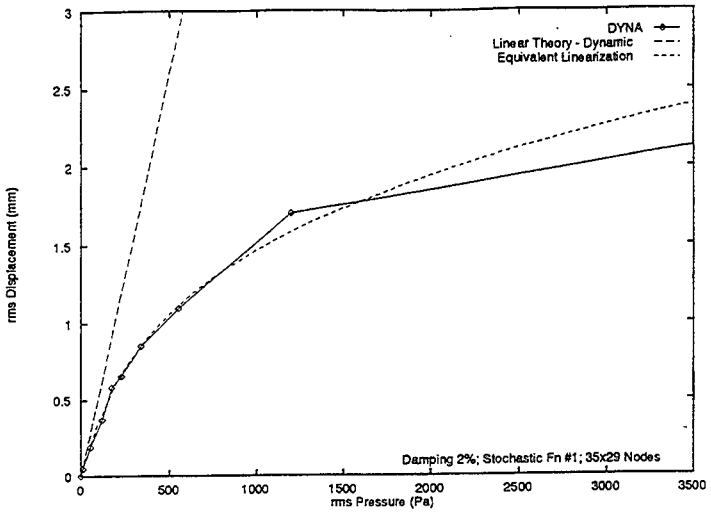

Figure 5: Rms Central Deflection of the plate versus sound pressure level. Comparison between DYNA results and linear theory.

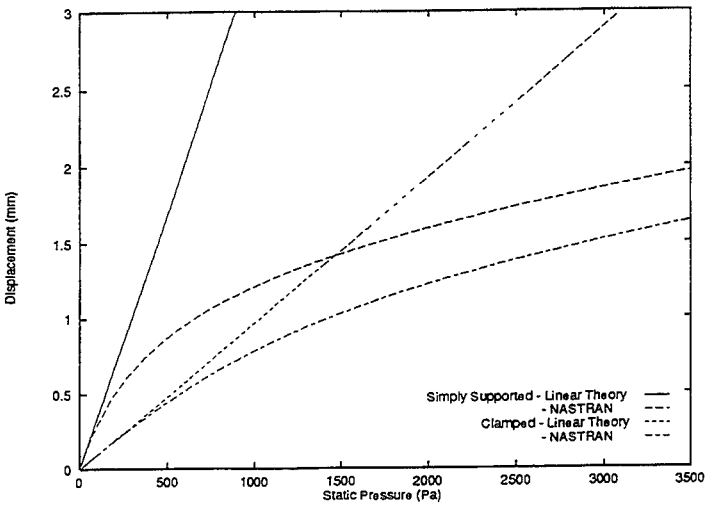

Figure 6: Central deflection of the plate versus pressure, NASTRAN calculations compared to linear theory.

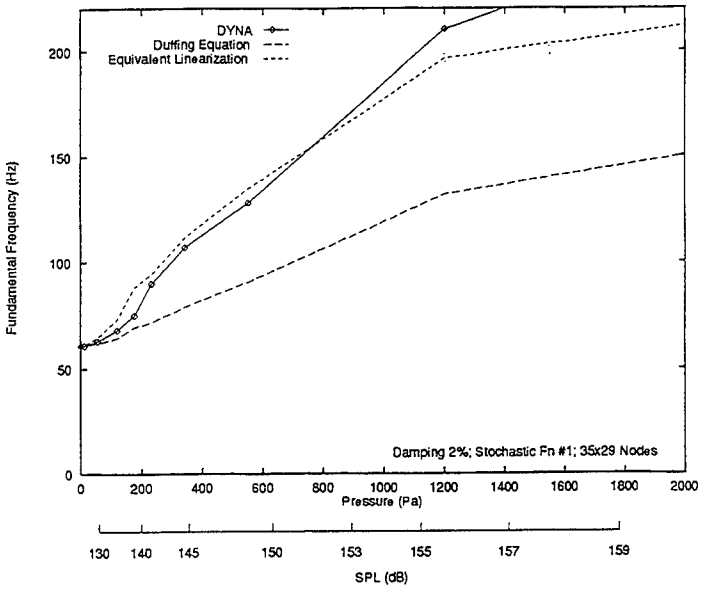

Figure 7: Variation of fundamental frequency of the (1,1) mode with rms pressure, Comparison between DYNA and theory.

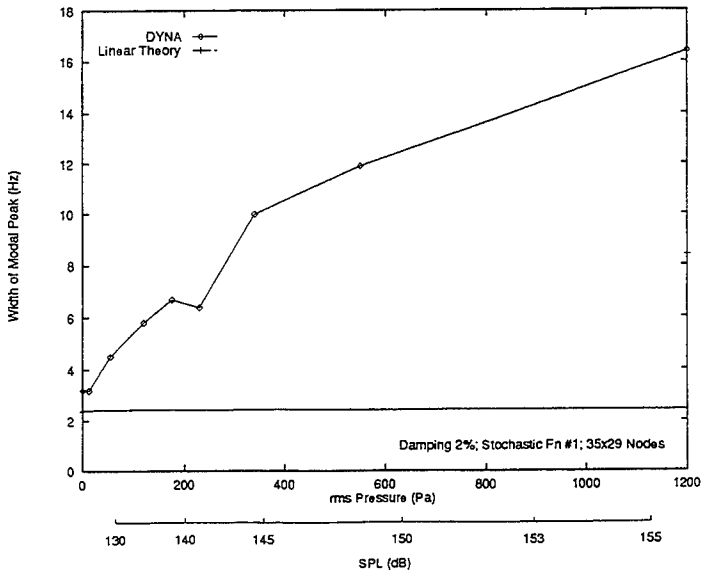

Figure 8: Variation of width of the (1,1) mode resonance peak with rms pressure, Comparison between DYNA and theory.

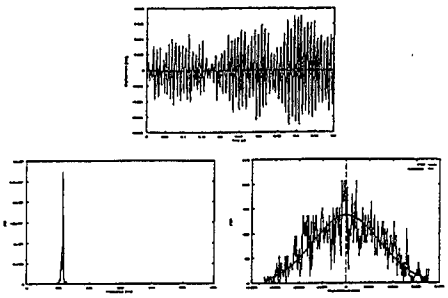

Figure 9: DYNA model predictions for random vibration of the plate with semi-clamped boundary conditions.

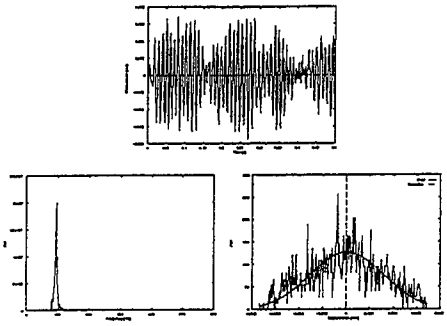

Figure 10: Random Vibration results with compressive load in the y-direction of -3.46N/mm and SPL of 1.0Pa.

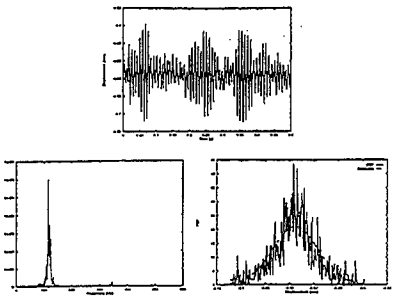

Figure 11: Random Acoustic Loading of SPL=12Pa superimposed on a static pressure of 700Pa.

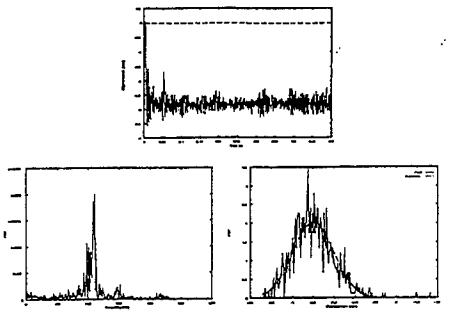

Figure 12: Random acoustic loading of SPL=700Pa superimposed on a thermal load of 10 deg, clamped edges. — No Snap Through

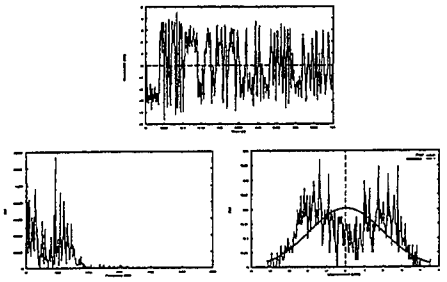

Figure 13: Random acoustic loading of SPL=2kPa superimposed on a thermal load of 10 deg, clamped edges. —Nearly continuous snap-through.

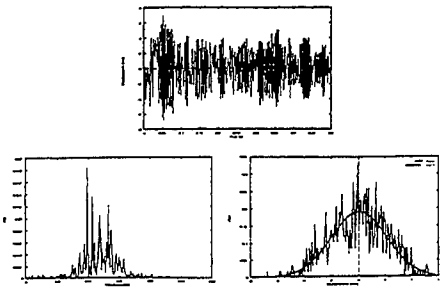

Figure 14: Random acoustic loading of SPL=4kPa superimposed on a thermal load of 10 deg, clamped edges. —Dominant acoustic load.

SYSTEM IDENTIFICATION II

ROBUST SUBSYSTEM ESTIMATION USING ARMA-MODELLING IN THE FREQUENCY DOMAIN

by U. Prells, A. W. Lees, M. I. Friswell and M. G. Smart,
Department of Mechanical Engineering of the University of Wales Swansea,
Singleton Park, Swansea SA2 8PP, United Kingdom

ABSTRACT

This paper reflects early results of the research on modelling the influence of the foundation on the dynamics of the rotor. The foundation is connected to the rotor via journal bearings. Dynamic models exist for the subsystems of the rotor and of the bearings; the first is reliable but the latter is uncertain. The foundation model is unknown and has to be estimated using rundown data.These are measured responses of the foundation at the bearings due to unbalance forces of the rotor which are assumed to be known. Uncertainties in the bearing model will be transfered to the estimated foundation parameters. The main scope of this paper is to introduce a method which enables the decoupling of the problem of model estimation and the problem of the influence of the bearing model uncertainty.

The influence of changes in the model of the bearings on the estimation of the foundation model is mainly due to the sensitivity of the computed forces applied to the foundation at the bearings. These are used together with the associated measured responses to estimate the foundation model in the frequency domain. Using an ARMA model in the frequency domain it is possible to estimate a filtered foundation model rather than the foundation model itself. The filter is defined in such a way that the resulting force has minimum sensitivity with respect to deviations in the model of the bearings. This leads to a robust estimation of the filtered model of the foundation. Since the filter can be defined in terms of the models of the rotor and of the bearings only, the problems of estimating the foundation's influence and of the sensitivity of the estimates with respect to the model of the bearings are decoupled.

The method is demonstrated by a simple example of a single-shaft rotor. Even if the errors in the bearing model are about 50 % the relative input and output errors of the filtered foundation model are of the same magnitude as the round-off and truncating errors.

1 INTRODUCTION

An important part of a machine monitoring system for fault diagnostics of

a turbo generator is a reliable mathematical model. This model includes the subsystems of the rotor, the bearings and the foundation. The model of the rotor represents the most reliable knowledge, the model of the journal bearings is uncertain, and despite of intensive research it is not yet possible to define a model for the foundation which reflects the dynamical contribution to the rotor with sufficient accuracy. The first step to determine the contribution of the foundation on the rotor's dynamic performance is the estimation of a reliable foundation model.

Rundown data are available, i.e. displacements $u_{FB}(\omega) \in \mathbb{C}^{4m}$ of the foundation at the bearings which are due to an unbalance force $f_U(\omega) \in \mathbb{C}^{2m}$ of the m-shaft rotor, given at discrete frequencies $\omega \in \Omega := \{\omega_1, \cdots, \omega_M\}$, and this data may be used to estimate the foundation model. A common method ([1],[2],[3],[4],[5]) is to estimate the unknown dynamic stiffness matrix $F(\omega) \in \mathbb{C}^{4m \times 4m}$ of the foundation at the bearings using the input/output equation

$$F(\omega) u_{FB}(\omega) = f_{FB}(\omega), \tag{1}$$

where the force f_{FB} of the foundation at the bearings can be expressed by dynamic condensation in terms of the data u_{FB}, f_U and in terms of the dynamic stiffness matrices A_R, B of the rotor and the bearings respectively yielding

$$f_{FB} = -B u_{FB} + [0, B] A_{RB}^{-1} \begin{pmatrix} f_{RI} \\ u_{FB} \end{pmatrix}. \tag{2}$$

Here the dynamic stiffness matrix A_{RB} of the rotor mounted on the bearings is partitioned with respect to the n inner degrees-of-freedom (dof) of the rotor and to the $4m$ connecting (interface) dof

$$A_{RB} = \begin{bmatrix} A_{RII} & A_{RIB} \\ A_{RBI} & A_{RBB} + B \end{bmatrix} \in \mathbb{C}^{(n+4m)\times(n+4m)} \tag{3}$$

The non-zero components of the force $f_{RI} \in \mathbb{C}^n$ in eq. (2) of the inner part of the rotor are the components of the unbalance force f_U, i.e. introducing the control matrix $S_U \in \mathbb{R}^{n \times 2m}$ then $f_{RI} = S_U f_U$. The dynamic stiffness matrix A_R of the rotor is given in terms of the matrices of inertia and stiffness which are defined by modal analysis and by its physical data given by the manufacturer. Each of the m shafts of the rotor is connected to the foundation usually via 2 journal bearings. Since the dynamic stiffness matrix B of the journal bearings represents a model for the oil film it consists of connecting dof only. It can be shown that B is block diagonal

$$B = \begin{bmatrix} B_1 & & 0 \\ & \ddots & \\ 0 & & B_m \end{bmatrix} \tag{4}$$

containing the dynamic stiffness matrices $B_i = K_i + j\omega D_i, i = 1, \cdots, m$, of the m bearings. K_i, D_i are the matrices of stiffness and damping respectively

which result from linearisation and are in general non-symmetric and non-singular. Eq. (1) is then used to estimate the foundation transfer function $F(\omega)$. This has been discussed in several papers ([1],[2],[3],[4],[5]). Lees et al. [3] pointed out that f_{FB} is sensitive with respect to deviations in the model of the bearings over part of the frequency range. This sensitivity is transfered to the model estimates.

In this paper a method is introduced which enables the decoupling of the two problems of model estimation and of sensitivity of the foundation model with respect to the model of the bearings. The basic idea of this method is to estimate a transfer function $H(\omega)$ which maps the displacements $u_{FB}(\omega)$ to a force $f_H(\omega)$ rather than the force $f_{FB}(\omega)$, i.e.

$$H(\omega)u_{FB}(\omega) = f_H(\omega). \tag{5}$$

In extension of the earlier method the force $f_H(\omega)$ can be chosen to be of minimum sensitivity with respect to the model of the bearings. This robust estimated transfer function $H(\omega)$ is related to that of the foundation $F(\omega)$ by a transformation $P(\omega)$

$$H(\omega) = P(\omega)F(\omega), \tag{6}$$

which of course retains the sensitivity with respect to the model of the bearings. But since $P(\omega)$ only depends on the models of the rotor and the bearings in the case of a modification within the model of the bearings no new model estimation has to be performed because this has been done robustly with respect to such model changes.

2 THE OPTIMUM CHOICE OF THE FORCE VECTOR

As stated in Lees et al. [3] the sensitivity of the force f_{FB} with respect to B is mainly due to the inversion of the matrix A_{RB} in eq. (2). It can be shown that the condensation method of estimating the force f_{FB} results from the special case of eliminating the last $4m$ rows of the matrix

$$W := \begin{bmatrix} A_{RII} & A_{RIB} \\ A_{RBI} & A_{RBB} + B \\ 0 & -B \end{bmatrix} \in \mathbb{C}^{(n+8m)\times(n+4m)}, \tag{7}$$

which can be written as $A_{RB} = T^\top W \in \mathbb{C}^{(n+4m)\times(n+4m)}$ by defining the selecting matrix of the master dof as

$$T := [e_1, \cdots, e_{n+4m}] \in \mathbb{R}^{(n+8n)\times(n+4m)}, \tag{8}$$

where in general e_n denotes a unit vector of appropriate dimension containing zeros everywhere but in the nth place. In extension to the force f_{FB} defined in eq. (2) for an arbitrary selecting matrix $T \in \mathbb{R}^{(n+8m)\times(n+4m)}$ the condensation leads to a force f_H given by

$$\begin{aligned} f_H &:= T^{\perp\top}\left[I_{n+8m} - W\left(T^\top W\right)^{-1}T^\top\right]\begin{pmatrix} f_{RI} \\ Bu_{FB} \\ -Bu_{FB} \end{pmatrix} \\ &= \underbrace{T^{\perp\top}\left[I_{n+8m} - W\left(T^\top W\right)^{-1}T^\top\right]\begin{pmatrix} 0 \\ 0 \\ I_{4m} \end{pmatrix}}_{=:P} f_{FB}. \end{aligned} \tag{9}$$

Here $T^\perp \in \mathbb{R}^{(n+8m)\times(4m)}$ denotes the matrix which selects the slave dof, and in general I_n denotes the unit matrix of dimension n. Indeed, inserting the special choice of T from eq. (8) into eq. (9) leads to the sensitive force $f_H = f_{FB}$ as defined in eq. (2).

The reason for the sensitivity of f_{FB} is that the subsystem of the rotor has low damping. Near the resonance frequencies of A_{RB} its large condition number depends sensitively on B. Thus the sensitivity of f_{FB} with respect to B is due to a large condition number of A_{RB}. Let $\mathcal{T}$ denote the set of all possible selecting matrices, i.e.

$$\begin{aligned} \mathcal{T} := \big\{ &[e_{i_1}, \cdots, e_{i_{n+4m}}] : e_{i_k} \in \mathbb{R}^{n+8m}, \\ &1 \le i_k \le n+8m, \quad \forall \quad k = 1, \cdots, n+4m\big\}. \end{aligned} \tag{10}$$

One criterion for an optimum choice of the force f_H may be formulated as the following minimisation problem:

Criterion 1:
The optimum choice is the solution of

$$\min_{T\in\mathcal{T}} \operatorname{cond}(T^\top W), \tag{11}$$

where W is defined in eq. (7).

A low condition number is necessary but not sufficient in order to provide a low sensitivity of the force f_H. Therefore a numerical test can be applied using stochastic deviations in the bearing model. Let $\Delta K_i, \Delta D_i$ consist of uniform distributed non-correlated random numbers with zero mean values and variances equal to $1/3$ for all $i \in 1, \cdots, 2m$. Define

$$\Delta B_i \equiv \Delta B_i(s_i, r_i) := s_i \Delta K_i + j\omega r_i \Delta D_i, \tag{12}$$

where the positive scalars s_i, r_i control the magnitude of the random error of the i-th bearing model. Thus, the error $\Delta B \equiv \Delta B(s, r)$ of the bearing model is well defined for $s := (s_1, \cdots, s_{2m})^\top$ and $r := (r_1, \cdots, r_{2m})^\top$.

Regard the force $f_H = f(\omega, T, \Delta B)$ as a function of the selecting matrix T and the bearing model error ΔB. For l random samples $\Delta B(k) = \Delta B(r(k), s(k)), k = 1, \cdots, l$, calculate for each frequency $\omega \in \Omega$ the upper and lower bounds for the real and imaginary part of each component f_i, $i = 1, \cdots, 4m$ of the force vector f, i.e.:

$$f^R_{i\max}(\omega, T) := \max_{k=1,\cdots,l} \mathrm{Re}\{f_i(\omega, T, \Delta B(k))\}, \tag{13}$$

$$f^R_{i\min}(\omega, T) := \min_{k=1,\cdots,l} \mathrm{Re}\{f_i(\omega, T, \Delta B(k))\}, \tag{14}$$

$$f^I_{i\max}(\omega, T) := \max_{k=1,\cdots,l} \mathrm{Im}\{f_i(\omega, T, \Delta B(k))\}, \tag{15}$$

$$f^I_{i\min}(\omega, T) := \min_{k=1,\cdots,l} \mathrm{Im}\{f_i(\omega, T, \Delta B(k))\}. \tag{16}$$

Defining the force vectors

$$f_{\max}(\omega, T) := f^R_{\max}(\omega, T) + j \cdot f^I_{\max}(\omega, T), \tag{17}$$

$$f_{\min}(\omega, T) := f^R_{\min}(\omega, T) + j \cdot f^I_{\min}(\omega, T), \tag{18}$$

the second criterion can be formulated as a minimax problem:

Criterion 2:
The optimum selection is obtained from

$$\min_{T \in \mathcal{T}} \max_{\omega \in \Omega} \sum_{i=1}^{4m} |f_{i\max}(\omega, T) - f_{i\min}(\omega, T)|. \tag{19}$$

Before the method outlined is demonstrated by an example some aspects of the mathematical model of the foundation and methods for its estimation based on the input/output equation (5) will now be considered.

3 ESTIMATION OF THE FOUNDATION MODEL

The purpose of this section is to estimate the unknown foundation model represented by the matrix

$$F(\omega) = A_{FBB}(\omega) - A_{FBI}(\omega) A^{-1}_{FII}(\omega) A_{FIB}(\omega). \tag{20}$$

This expression results from dynamic condensation of the dynamic stiffness matrix of the foundation

$$A_F = \begin{bmatrix} A_{FBB} & A_{FIB} \\ A_{FIB} & A_{FII} \end{bmatrix} \tag{21}$$

which is partitioned with respect to its inner dof (index I) and those dof coupled to the bearings (index B). For viscous damped linear elastomechanical models the dynamic stiffness matrix $A_F(\omega)$ of the foundation is given by

$$A_F(\omega) := \sum_{i=0}^{2} (j\omega)^i A_i \in \mathbb{C}^{(k+4m)\times(k+4m)}. \tag{22}$$

The matrices A_i are real valued and represent the contributions of stiffness, damping and inertia for $i = 0, 1, 2$ respectively. In this case the identification of the foundation model requires the estimation of the three matrices A_i which are parameterised by introducing dimensionless adjustment parameters $a_{ik} \in \mathbb{R}$, for all $k = 1, \cdots, N_i, i = 0, 1, 2$ (see for instance [6] or [7]). Those parameters are related to given real-valued matrices S_{ik} by

$$A_i(a_i) := \sum_{k=1}^{N_i} S_{ik} a_{ik}, \tag{23}$$

Writing the adjustment parameters as one vector $a^\top := (a_0^\top, a_1^\top, a_2^\top) \in \mathbb{R}^p$, $p := N_0 + N_1 + N_2$, the estimation of the foundation model is equivalent to the estimation of the parameter vector a. The dynamic stiffness matrix of the foundation becomes a nonlinear function of this parameter vector

$$F(\omega) \equiv F(\omega, a) = A_{FBB}(\omega, a) - A_{FBI}(\omega, a) A_{FII}^{-1}(\omega, a) A_{FIB}(\omega, a). \tag{24}$$

Substituting the measured quantities for u_{FB} and f_U into eqs. (5) and (9) the parameter vector a is usually estimated by minimising some norm of the difference between measured and calculated quantities, called residuals [8]. Using equation (5) is equivalent to the input residual method. Defining the ith partial input residual as

$$v_I(i) := f(\omega_i, a) - f_H(\omega_i) \in \mathbb{C}^{4m}, \tag{25}$$

where the dependency on the model parameters a of the input vector is defined by

$$f(\omega, a) := P(\omega) F(\omega, a) u_{FB}(\omega), \tag{26}$$

the cost function to be minimised is given by

$$J_I(a) := \sum_{i=1}^{M} v_I^\dagger(i) W_I(i) v_I(i), \tag{27}$$

where $W_I(i)$ represents a weighting matrix for the ith partial residual and the superscript $\dagger$ denotes the conjugate-transpose. The inverse problem (27) is nonlinear with respect to the parameters to be estimated. Thus, there is no advantage relative to the output residual method. Defining the ith partial output residual as

$$v_O(i) := u(\omega_i, a) - u_{FB}(\omega_i), \tag{28}$$

where the model output is defined by

$$u(\omega, a) := [0, 0, I_{2(m+1)}, 0] A^{-1}(\omega, a) \begin{bmatrix} S_U \\ 0 \\ 0 \\ 0 \end{bmatrix} f_U(\omega), \tag{29}$$

with the dynamic stiffness matrix A of the entire model

$$A(\omega, a) = \begin{bmatrix} A_{RII}(\omega) & A_{RIB}(\omega) & 0 & 0 \\ A_{RBI}(\omega) & A_{RBB}(\omega) + B(\omega) & -B(\omega) & 0 \\ 0 & -B(\omega) & B(\omega) + A_{FBB}(\omega, a) & A_{FBI}(\omega, a) \\ 0 & 0 & A_{FIB}(\omega, a) & A_{FII}(\omega, a) \end{bmatrix}, \tag{30}$$

the cost function to be minimised is

$$J_O(a) := \sum_{i=1}^{M} v_O^{\dagger}(i) W_O(i) v_O(i). \tag{31}$$

$W_O(i)$ denotes a weighting matrix for the ith partial output residual.

Mathematical modelling is always purpose orientated [9]. In the case discussed in this paper the purpose is to estimate the influence of the foundation on the dynamics of the rotor. For this purpose, no physically interpretable model is necessary in order to model this influence. In the next section an alternative mathematical model is introduced which leads to a linear inverse problem.

3.1 ARMA MODELLING IN THE FREQUENCY DOMAIN: THE FILTER MODEL

Auto Regressive Moving Average models are well developed (see for instance [10],[7]) in order to simulate dynamic system behaviour. ARMA models are defined in the time domain by

$$\sum_{i=0}^{n_o} A_i u(t - i\Delta t) = \sum_{i=0}^{n_i} B_i f(t - i\Delta t), \tag{32}$$

where the present output (state or displacement) $u(t)$ due to the present input $f(t)$ depends on n_o past outputs and on n_i past inputs.

In the frequency domain eq. (32) leads to a (frequency-) filter model [7]. With reference to eq. (5) it has the form

$$\underbrace{\left(\sum_{i=0}^{n_o} (j\omega)^i A_i\right)}_{=: \tilde{A}(\omega)} u_{FB}(\omega) = \underbrace{\left(\sum_{k=0}^{n_i} (j\omega)^k B_k\right)}_{=: \tilde{B}(\omega)} f_H(\omega) \tag{33}$$

The output and input powers n_o, n_i respectively, and the matrices $(A_i)_{i=0,\cdots,n_o}, (B_k)_{k=0,\cdots,n_i}$ are called *filter parameters* and have to be estimated. Of course the minimum of $\det[\tilde{A}(\omega)]$ and of $\det[\tilde{B}(\omega)]$ correspond to the resonance and anti-resonance frequencies of the subsystem of the foundation respectively.

For an optimum choice of P (see eq. (9)) the estimation of $\tilde{A}$ and $\tilde{B}$ can be considered to be **independent** of the precise values of the model of the bearings. Thus, the problem of the uncertainty in the bearing models and the problem of model estimation are **decoupled**. If $\tilde{A}$ and $\tilde{B}$ are estimated refering to eq. (5) then

$$\tilde{B}^{-1}\tilde{A} = H. \tag{34}$$

The estimation of the filter parameters is robust with respect to deviations in the bearings model. Thus, the uncertainty of the estimation of the foundation model F is due to the inversion of the matrix P only

$$F = P^{-1}H = P^{-1}\tilde{B}^{-1}\tilde{A}, \tag{35}$$

which represents a problem *a priori* and which occurs only in the calculation of the force of the foundation at the bearings

$$f_{FB} = P^{-1}\tilde{B}^{-1}\tilde{A}u_{FB}. \tag{36}$$

Of course the force vector f_{FB} is sensitive to changes in the bearings model but only due to corresponding changes in P. The estimated part $\tilde{B}^{-1}\tilde{A}$ is robust with respect to changes in the bearings model.

In order to calculate the response u_{FB} no explicit calculation of the inverse of P is necessary,

$$u_{FB} = \tilde{A}^{-1}\tilde{B}f_H. \tag{37}$$

Since the estimated model and the force f_H are insensitive with respect to the bearings model the estimation of u_{FB} is robust in this sense.

Of course the influence of errors in u_{FB} and f_U have not yet been taken into account. Accordingly the model powers n_o, n_i, must be estimated as well as the matrices A_i, B_k. The estimation method is outlined in the following section.

3.2 ESTIMATION OF THE FILTER PARAMETERS

In order to estimate the filter parameters the least squares method can be applied to minimise the equation error in eq. (33). Defining the ith partial equation residual as

$$v_E(i) := \tilde{A}(\omega_i)u_{FB}(\omega_i) - \tilde{B}(\omega_i)f_H(\omega_i) \tag{38}$$

the cost function to be minimized is given by

$$J_E := \sum_{i=1}^{M} v_E^{\dagger}(i) W_E(i) v_E(i), \tag{39}$$

where $W_E(i)$ denotes a weighting matrix for the ith equation residual. Assuming $W_E(i) = I_{4m}$ for all $i = 1, \cdots, M$, the filter equation (33) can be extended for M excitation frequencies as

$$\left(\sum_{i=0}^{n_o} A_i U \Lambda^i \right) = \left(\sum_{k=0}^{n_i} B_i Z \Lambda^k \right), \tag{40}$$

where U, Z and Λ are defined by

$$U := [u_{FB}(\omega_1), \cdots, u_{FB}(\omega_M)], \tag{41}$$

$$Z := [f_H(\omega_1), \cdots, f_H(\omega_M)], \tag{42}$$

$$\Lambda := j \begin{bmatrix} \omega_1 & & 0 \\ & \ddots & \\ 0 & & \omega_M \end{bmatrix}. \tag{43}$$

The solution of the minimisation problem (39) is equivalent to the normal solution of eq. (40) which can be rewritten as

$$\underbrace{[A_{n_o}, \cdots, A_0, -B_{n_i}, \cdots, -B_0]}_{=: V} \underbrace{\begin{bmatrix} U\Lambda^{n_o} \\ \vdots \\ U \\ Z\Lambda^{n_i} \\ \vdots \\ Z \end{bmatrix}}_{=: Y} = 0 \tag{44}$$

Because the filter parameters represented by the matrix $V \in \mathbb{R}^{4m \times 4m(n_o+n_i+2)}$ are real-valued, equation (44) must be satisfied for the real and imaginary parts of the matrix $Y \in \mathbb{C}^{4m(n_o+n_i+2) \times M}$, which finally yields

$$V[\mathrm{Re}\{Y\}, \mathrm{Im}\{Y\}] =: VX = 0. \tag{45}$$

This problem does not lead to a unique solution for the filter parameters. Indeed, for any arbitrary non-singular matrix C

$$C\tilde{A}u_{FB} = C\tilde{B}f_H \tag{46}$$

is also a solution. But since one is interested (see eq. (34)) in the product $\tilde{B}^{-1}\tilde{A}$ (or its inverse) only this final result is of interest and this product is unique.

As a necessary and a sufficient condition for a full-rank solution V of eq. (45) the matrix $X \in \mathbb{R}^{4m(n_o+n_i+2)\times 2M}$ has to have a rank deficiency of $4m$, i.e.

$$\operatorname{rank}(X) = 4m(n_o + n_i + 1). \tag{47}$$

Of course this problem has to be treated numerically. The rank decision is usually made by looking to the singular values $\gamma(n_o, n_i) \in \mathbb{R}^{4m(n_o+n_i+2)}$ of the matrix $X = X(n_o, n_i)$. Because one cannot expect to achieve zero rather than relative small singular values one has to define a cut-off limit. This is due to the fact that the equation error (39) can be made arbitrary small by increasing the degree $p := n_o + n_i$ of the filter model. The same situation occurs if one looks at the maximum relative input error

$$e_I := \max_{i=1,\cdots,M} \frac{\|\tilde{B}^{-1}(\omega_i)\tilde{A}(\omega_i)u_{FB}(\omega_i) - f_H(\omega_i)\|}{\|f_H(\omega_i)\|}, \tag{48}$$

or to the maximum relative output error

$$e_O := \max_{i=1,\cdots,M} \frac{\|\tilde{A}^{-1}(\omega_i)\tilde{B}(\omega_i)f_H(\omega_i) - u_{FB}(\omega_i)\|}{\|u_{FB}(\omega_i)\|}. \tag{49}$$

With increasing degree p the errors e_I and e_O can be made arbitrary small.

This is a typical expression for an ill-posed problem which can be turned into an well-posed problem by applying regularisation methods [11]. To choose an appropriate regularisation method needs further investigation and is beyond the scope of this paper. In the next section the method of choosing the optimum force vector f_H is demonstrated by a simple example.

4 A SIMPLE EXAMPLE

The test model is depicted in Fig. 1. The one-shaft-rotor is simulated by an Euler-Bernoulli beam which is spatially discretised with 10 dof. According to the partition with respect to inner points and interface points (see eq. (3)) the number n of inner rotor dof is 8 and the number of connecting dof is 2. Only one translation dof of the rotor is connected to each bearing which are modelled by massless springs with stiffnesses $k_1 = 1.77 \cdot 10^8$ and $k_2 = 3.54 \cdot 10^8$ N/m respectively. The foundation is modelled by an unconnected pair of masses $m_1 = 90, m_2 = 135$ kg and springs with stiffnesses $k_{f1} = k_{f2} = 1.77 \cdot 10^8$ N/m. The force f_U due to an unbalance $b = 0.01$ kg·m is given by $f_U(\omega) := b\omega^2 \in \mathbb{R}$. The force vector $f_{RI} \in \mathbb{R}^8$ is assumed to have one non-zero component only, i.e. $f_{RI} := f_U e_4$. The frequency range between 0 and 250 Hz is discretised with equally spaced stepsize of 0.5 Hz. The selecting matrix $T \in \mathbb{R}^{12\times 2}$ of the master dof is assumed to consist of the unit vector e_4 in order to select out the unbalance force f_U because this

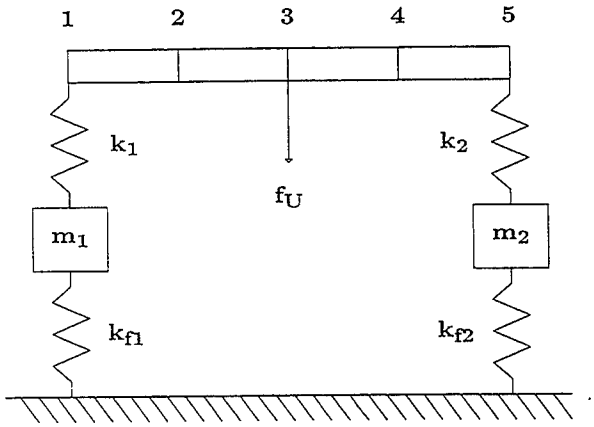

Figure 1: The simple test model

excitation is independent of the model of the bearings and therefore of minimum sensitivity. Thus the remaining redundancy consists in eliminating one row of the matrix

$$G := [e_1, e_2, e_3, e_5, \cdots, e_{12}]^\top W \in \mathbb{R}^{11\times 10}. \tag{50}$$

The result of the first criterion are depicted in Fig. 2. It shows the frequency dependent condition numbers for the elimination of each row of the matrix G in turn. This leads to an optimum choice by eliminating the 4-th row of G. Thus, the optimum choice of the master dof is given by $T^\perp = [e_4, e_5]$. This result is confirmed by applying the second optimisation criterion.

For this purpose a uniform distributed uncorrelated random error with zero mean value is added to the stiffnesses of the bearings simulating a model variation of 50 per cent, i.e. $k_i \longrightarrow k_i + \Delta k_i k_i/2$, where $\Delta k_i, i = 1, 2$, are uncorrelated random numbers with expectation value $E\{\Delta k_i\} = 0$ and with variance $E\{\Delta k_i \Delta k_j\} = (1/3)\delta_{ij}$. For a size of $l = 500$ random samples, the upper and lower bounds $f_{\max}, f_{\min}$ and $f_{H\max}, f_{H\min}$ of the force $f_{FB} = f_{FB}(\omega, \Delta B)$ and of the force $f_H = f(\omega, T, \Delta B)$ respectively with the selecting matrix $T = [e_4, e_5]$, have been calculated. In contrast to the maximum difference of upper and lower bounds of the force f_{FB} of ~ 20, that of the force f_H is of the order of the computational accuracy $\sim 10^{-7}$, and is therefore negligible. In a first step the force f_{FB} is used to estimate the filter parameters of the model F of the foundation. Solving the singular value decomposition for all input and output powers $(n_i, n_o) \in [0, 5]^2 \subset \mathbb{Z}^2$ the calculation of the maximum relative input and of the maximum output errors as defined by eqs. (48) and (49) with $f_H = f_{FB}$ leads to the results

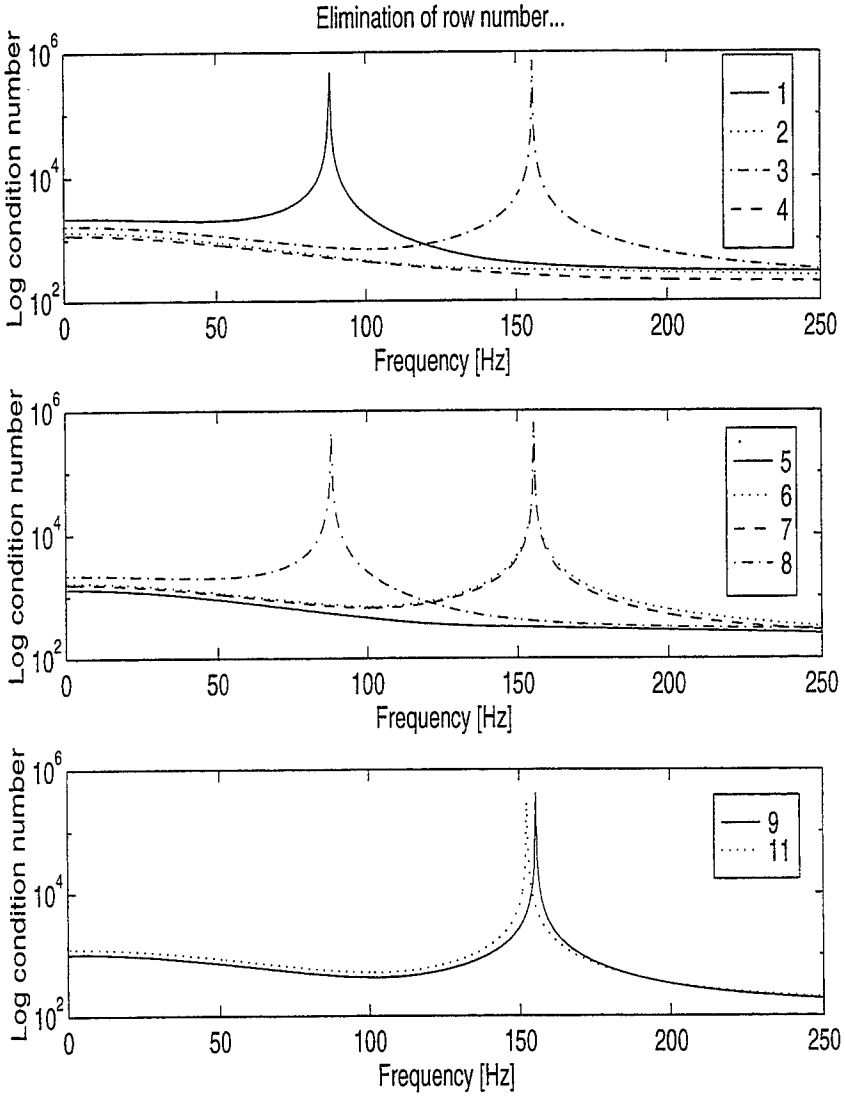

Figure 2: Frequency dependent condition numbers

depicted in Fig. 3. For a model realisation with $(n_i, n_o) = (0, 2)$ the values of the maximum relative errors are approximately $e_I \approx 7.1 \cdot 10^{-7}$ and $e_O \approx 9.0 \cdot 10^{-7}$ which corresponds to the computational accuracy. Using this model the estimates of the filter matrices correspond within the computational accuracy to those of the 'true' foundation model.

Using variations of the force f_{FB} between the bounds $f_{\max}, f_{\min}$ from the second criterion the associated upper and lower bounds of the relative input and output error have been calculated. The influence of the variation

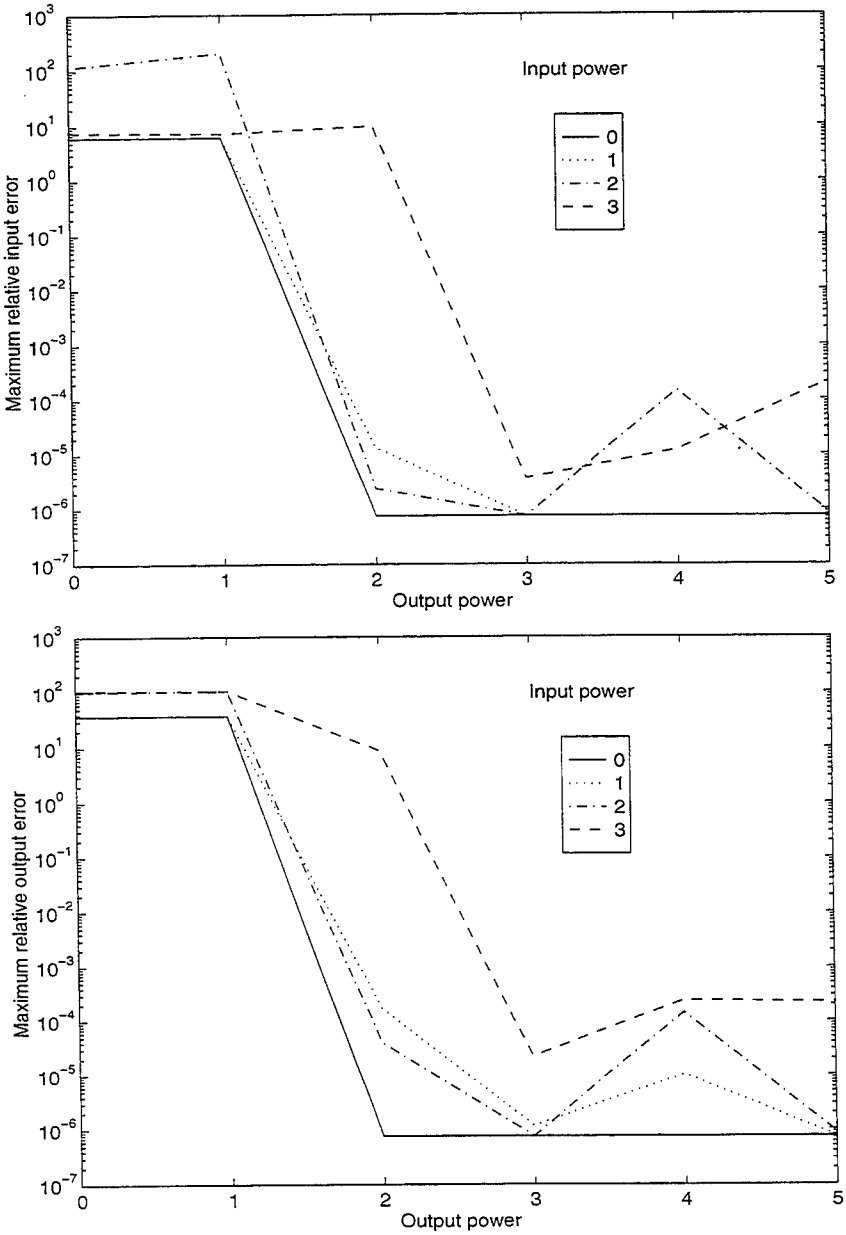

Firgure 3: Maximum relative input and output error for different input powers n_i and output powers n_o using the force vector f_{FB}

of the bearing stiffness of 50% leads via the associated variation of the force f_{FB} to drastic variations of the relative input and output errors. The difference of upper and lower bound of the maximum relative input error is

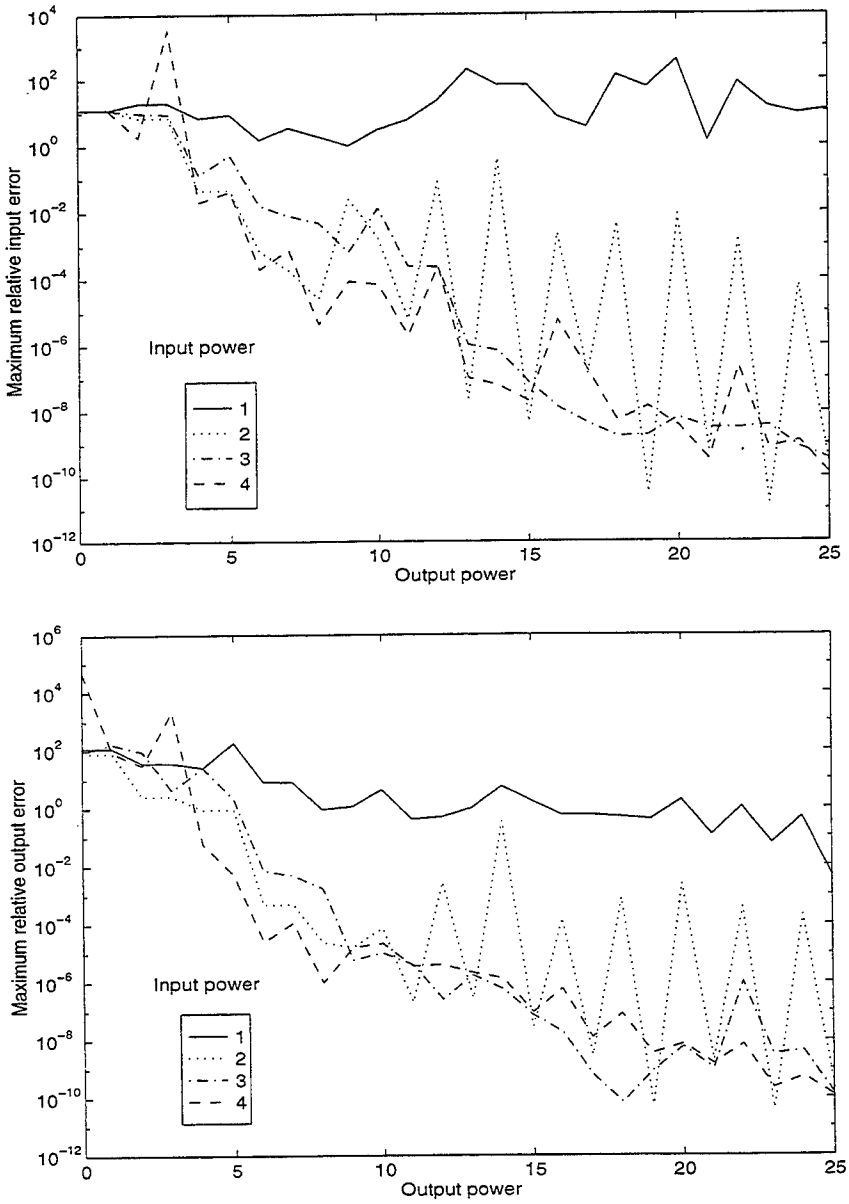

Figure 4: Maximum relative input and output error for different input powers n_i and output powers n_o using the optimised force vector f_H

of order 100 and that of the maximum relative output error is approximately 10^4.

The situation is different using the optimised force f_H in order to estimate the filter parameters of the model H. For each input and output power $(n_i, n_o) \in [0, 25]^2 \subset \mathbb{Z}^2$ the maximum relative input error and the maximum relative output error have been calculated. The result is shown in Fig. 4. For a maximum relative input error $e_I \approx 6.5 \cdot 10^{-5}$ a filter model of degree 12 is available with the powers $(n_i, n_o) = (4, 8)$. This model produces a maximum relative output error $e_O \approx 10^{-6}$.

Analogous to the robustness investigations for f_{FB} now for the force f_H the upper and lower bounds of the relative input and of the relative output error due to the random variation in the bearing models have been calculated. For the chosen model with powers $(n_i, n_o) = (4, 8)$ the difference of upper and lower bound of the relative input error as well that of the relative output error are of about the same order $\approx 10^{-4}$. Thus, compared with the order of variation 100 and 10^4 of the direct foundation model estimate the estimate of H is robust with respect to changes in the bearing model.

5 CONCLUSION

In this paper a method is introduced which enables the decoupling of the two problems of model estimation and of sensitivity of the foundation model with respect to the model of the bearings. The method produces an optimised choice of the input/output equation which provides a transfer function estimation that is robust with respect to deviations in the model of the bearings. For the foundation model estimation a filter model is introduced. This modelling strategy has the advantage of leading to a linear inverse problem. The disadvantage is that with increasing model degree the equation error can be made arbitrarily small. Because this error should not become smaller than the accuracy of the data, a cut-off limit has to be determined *a priori*. Further investigations should allow the cut-off limit to be related to the data errors.

REFERENCES

1. Feng, N.S. and Hahn, E.J., Including Foundation Effects on the Vibration Behaviour of Rotating Machinery. *Mechanical Systems and Signal Processing*, 1995 Vol. 9, No. 3, pp. 243-256.

2. Friswell, M.I., Lees, A.W. and Smart, M.G., Model Updating Techniques Applied to Turbo-Generators Mounted on Flexible Foundations. *NAFEMS Second International Conference: Structural Dynamics Modelling Test, Analysis and Correlation*, Glasgow: NAFEMS, 1996 pp. 461-472.

3. Lees, A.W. and Friswell, M.I., Estimation of Forces Exerted on Machine Foundations. *Identification in Engineering Systems*, Wiltshire: The Cromwell Press Ltd., 1996, pp. 793-803.

4. Smart, M.G., Friswell, M.I., Lees, A.W. and Prells, U., Errors in estimating turbo-generator foundation parameters. In *Proceedings ISMA21 - Noise and Vibration Engineering*, ed. P. Sas, Katholieke Universiteit Leuven, Belgium, 1996, Vol. II, pp. 1225-1235

5. Zanetta, G.A., Identification Methods in the Dynamics of Turbogenerator Rotors. *The International Conference on Vibrations in Rotating Machinery*, IMechE, C432/092, 1992, pp. 173-181.

6. Friswell, M.I. and Mottershead, J.E., *Finite Element Model Updating in Structural Dynamics*. Dordrecht, Boston, London: Kluwer Academic Publishers, 1995.

7. Natke, H.G., *Einführung in die Theorie und Praxis der Zeitreihen- und Modalanalyse - Identifikation schwingungsfähiger elastomechanischer Systeme*. Braunschweig, Wiesbaden: Friedrich Vieweg & Sohn, 1993.

8. Natke, H.G., Lallement, G., Cottin, N. and Prells, U., Properties of Various Residuals within Updating of Mathematical Models. *Inverse Problems in Engineering, Vol. 1*, 1995, pp. 329-348.

9. Natke, H.G., What is a true mathematical model? - A discussion of system and model definitions. *Inverse Problems in Engineering*, 1995, Vol. 1, pp. 267-272.

10. Gawronski, W. and Natke, H.G., On ARMA Models for Vibrating Systems. *Probabilistic Engineering Mechanics*, 1986, Vol. 1, No. 3, pp. 150-156.

11. Baumeister,J., *Stable Solution of Inverse Problems*. Braunschweig, Wiesbaden: Friedrich Vieweg & Sohn, 1987.

ACKNOWLEDGEMENTS

The authors are indebted to Nuclear Electric Ltd and Magnox Plc for funding the research project BB/G/40068/A to develop methods which enables the estimation of the influence of the foundation on the dynamics of the rotor. Dr. Friswell gratefully acknowledges the support of the Engineering and Physical Sciences Research Council through the award of an Advanced Fellowship.

MATHEMATICAL HYSTERESIS MODELS AND THEIR APPLICATION TO NONLINEAR ISOLATION SYSTEMS

Y.Q. Ni, J.M. Ko and C.W. Wong

Department of Civil and Structural Engineering
The Hong Kong Polytechnic University, Hong, Kong

Abstract

Two mathematical hysteresis models, the Duhem-Madelung (DM) model and the Preisach model, are introduced to represent the hysteretic behavior inherent in nonlinear damping devices. The DM model generates the hysteresis with local memory. Making use of the Duhem operator, the constitutive relation can be described by single-valued functions with two variables in transformed state variable spaces. This makes it feasible to apply the force-surface nonparametric identification technique to hysteretic systems. The Preisach model can represent the hysteresis with nonlocal memory. It is particularly suitable for describing the selective-memory hysteresis which appears in some friction-type isolators. An accurate frequency-domain method is developed for analyzing the periodic forced vibration of hysteretic isolation systems defined by these models. A case study of wire-cable vibration isolator is illustrated.

1. Introduction

The dynamic response of a structure is highly dependent on the ability of its members and connections to dissipate energy by means of hysteretic behavior. The assessment of this behavior can be done by means of experimental tests and the use of analytical models that take into account the main characteristics of this nonlinear mechanism. Although a variety of hysteresis models have been proposed in the past decades, many structural systems exhibit more complicated hysteretic performance (mainly due to stiffness or/and strength degrading) which the models in existence are reluctant and even inapplicable to depict [1,2]. On the other hand, nonlinear vibration isolation has recently been recognized as one of effective vibration control techniques. In

particular, hysteretic isolation devices have got wide applications owing to their good dry friction damping performance. These hysteretic isolators may exhibit very complicated features such as asymmetric hysteresis, soft-hardening hysteresis, nonlocal selective-memory hysteresis [3-5]. None of the models available currently in structural and mechanical areas can represent all these hysteresis characteristics. Other more elaborate hysteresis models need to be established for this purpose.

In reality, hysteresis phenomenon occurs in many different areas of science, and has been attracting the attention of many investigators for a long time. However, the true meaning of hysteresis varies from one area to another due to lack of a stringent mathematical definition of hysteresis. Fortunately, because of the applicative interest and obvious importance of hysteresis phenomenon, Russian mathematicians in 1970's and the Western mathematicians in 1980's, began to study hysteresis systematically as a new field of mathematical research [6,7]. They also deal with the hysteresis models proposed by physicists and engineers in various areas, but they separate these models from their physical meanings and formulate them in a purely mathematical form by introducing the concept of *hysteresis operators*. Such mathematical exposition and treatment can generalize a specific model from a particular area as a general mathematical model which is applicable to the description of hysteresis in other areas. In this paper, two mathematical hysteresis models are introduced and the related problems such as identification and response analysis encountered in their application to nonlinear isolation systems are addressed.

2. Definition of Hysteresis

Hysteresis loops give the most direct indication of hysteresis phenomena. But it is intended here to introduce a mathematical definition of hysteresis. Let us consider a constitutive law: $u \mapsto r$, which relates an input variable $u(t)$ and an output variable $r(t)$. For a structural or mechanical system, $u(t)$ denotes displacement (strain); $r(t)$ represents restoring force (stress); t is time. We can define hysteresis as a special type of memory-based relation

between $u(t)$ and $r(t)$. It appears when the output $r(t)$ is not uniquely determined by the input $u(t)$ at the same instant t, but instead $r(t)$ depends on the evolution of u in the interval $[0, t]$ and possibly also on the initial value r_0, i.e.

$$r(t) = \Re[u(\cdot), r_0](t) \tag{1}$$

where the memory-based functional $\Re[u(\cdot), r_0](t)$ is referred to as *hysteresis operator*. In order to exclude viscosity-type memory such as those represented by time convolution, we require that $\Re$ is *rate-independent*, i.e. that $r(t)$ depends just on the range of u in $[0, t]$ and on the order in which values have been attained, not on its velocity. In reality, memory effects may be not purely rate independent as hysteresis is coupled with viscosity-type effects. However, as shown later, in most cases the rate independent feature of hysteresis is consistent with experimental findings, especially when evolution (variation in time) is not too fast.

3. Duhem-Madelung (DM) Model

3.1 Formulation

The DM model can be defined with or without referring to a confined hysteresis region. For the structural or mechanical hysteretic systems, it is not necessary to introduce the notion of bounded curves because there exists neither the saturation state nor the major loop. In this instance, the DM model establishes a mapping (named *Duhem operator*) $\Re$: $(u, r_0) \mapsto r$ by postulating the following Cauchy problem [7,8]

$$\dot{r}(t) = g_1(u,r) \cdot \dot{u}_+(t) - g_2(u,r) \cdot \dot{u}_-(t) \tag{2a}$$

$$r(0) = r_0 \tag{2b}$$

where an overdot denotes the derivative with respect to t; $g_1(u,r)$ and $g_2(u,r)$ are referred to as ascending and descending functions (curves) respectively; and

$$\dot{u}_+(t) = \max[0, \dot{u}(t)] = \frac{1}{2}[|\dot{u}(t)| + \dot{u}(t)] \tag{3a}$$

$$\dot{u}_-(t) = \min[0, \dot{u}(t)] = \frac{1}{2}[|\dot{u}(t)| - \dot{u}(t)] \tag{3b}$$

Eq. (2a) can be rewritten as

$$\dot{r}(t) = g[u, r, \mathrm{sgn}(\dot{u})] \cdot \dot{u}(t) \tag{4}$$

in which the describing function has the form

$$g[u,r,\mathrm{sgn}(\dot{u})] = \begin{cases} g(u,r,1) = g_1(u,r) & \dot{u} > 0 \\ g(u,r,-1) = g_2(u,r) & \dot{u} < 0 \end{cases} \tag{5}$$

It is obvious that the DM model is rate independent. In addition, it is specially noted that in this constitutive law the output $r(t)$ is not directly dependent on the entire history of $u(t)$ through $[0,t]$; but instead depends only on the local history covered since the last change of $\mathrm{sgn}(\dot{u})$ and on the value of the output at this switching instant. It means that the output can only change its character when the input changes direction. As a consequence, the DM model usually represents the hysteresis with local memory except that the functions $g_1(u,r)$ and $g_2(u,r)$ are re-specified as hysteresis operators.

Within the framework of DM formulation, the ascending and descending functions $g_1(u,r)$ and $g_2(u,r)$ are just required to fulfill suitable regularity conditions and need not to be specified in specific expressions, so both the form and parameters of the functions can be fine-tuned to match experimental findings. On the other hand, the DM formulation can deduce a wide kind of differential-type hysteresis models such as Bouc-Wen model, Ozdemir's model, Yar-Hammond bilinear model and Dahl's frictional model. For the Bouc-Wen model

$$r(t) = \kappa u(t) + z(t) \tag{6a}$$

$$\dot{z}(t) = \alpha\dot{u}(t) - \beta|\dot{u}(t)|z(t)|z(t)|^{n-1} - \gamma\dot{u}(t)|z(t)|^n \tag{6b}$$

it corresponds to the DM model with the specific ascending and descending functions as

$$g_1(u,r) = \alpha + \kappa - [\gamma + \beta\,\mathrm{sgn}(r - \kappa u)]|r - \kappa u|^n \tag{7a}$$

$$g_2(u,r) = \alpha + \kappa - [\gamma - \beta\,\mathrm{sgn}(r - \kappa u)]|r - \kappa u|^n \tag{7b}$$

and for the Yar-Hammond bilinear model

$$\dot{r}(t) = \{\alpha - \gamma\,\mathrm{sgn}(\dot{u})\,\mathrm{sgn}[r - \beta\,\mathrm{sgn}(\dot{u})]\}\dot{u} \tag{8}$$

its describing function is independent of $u(t)$ as follows

$$g[u,r,\mathrm{sgn}(\dot{u})] = g[r,\mathrm{sgn}(\dot{u})] = \alpha - \gamma\,\mathrm{sgn}(\dot{u})\,\mathrm{sgn}[r - \beta\,\mathrm{sgn}(\dot{u})] \tag{9}$$

Hence, the Duhem operator also provides an accessible way to construct novel hysteresis models by prescribing specific

expressions of the ascending and descending functions. Following this approach, it is possible to formulate some models which allow the description of special hysteretic characteristics observed in experiments, such as soft-hardening hysteresis, hardening hysteresis with overlapping loading envelope, and asymmetric hysteresis [5].

3.2 Identification

System identification techniques are classified as parametric and nonparametric procedures. The parametric identification requires that the structure of system model is *a priori* known. The advantage of nonparametric identification methods is that they do not require *a priori* the knowledge of system model. The most used nonparametric procedure for nonlinear systems is the *force mapping* (or called *force surface*) method [9]. This method is based on the use of polynomial approximation of nonlinear restoring force in terms of two variables—the displacement $u(t)$ and the velocity $\dot{u}(t)$. For nonlinear hysteretic systems, however, the hysteretic restoring force appears as a multivalued function with respect to the variables $u(t)$ and $\dot{u}(t)$ due to its history-dependent and non-holonomic nature. This renders the force mapping method inapplicable to hysteretic systems, although some efforts have been made to reduce the multivaluedness of the force surface [10,11].

One of the appealing virtues of the DM model is that it can circumvent this difficulty. Making use of the Duhem operator, the hysteretic constitutive relation of Eq.(1) is described by two continuous, single-valued functions $g_1(u,r)$ and $g_2(u,r)$ in terms of the displacement $u(t)$ and the restoring force $r(t)$. Thus, single-valued "force" surfaces $g_1(u,r)$ and $g_2(u,r)$ can be formulated in the subspaces of the state variables (u,r,g_1) and (u,r,g_2), and can be identified by using the force mapping technique. Following this formulation, a nonparametric identification method is developed by the authors [12]. In this method, the functions $g_1(u,r)$ and $g_2(u,r)$ are expressed in terms of shifted generalized orthogonal polynomials with respect to u and r as follows

$$g_1(u,r) = \sum_{i=1}^{m}\sum_{j=1}^{n}\phi_i(r)g_{ij}^{(1)}\phi_j(u) = \Phi^T(u)\mathbf{G}^{(1)}\Phi(r) \qquad (10a)$$

$$g_2(u,r) = \sum_{i=1}^{m}\sum_{j=1}^{n}\phi_i(r)g_{ij}^{(2)}\phi_j(u) = \Phi^T(u)\mathbf{G}^{(2)}\Phi(r) \qquad (10b)$$

where $\mathbf{G}^{(1)} = [g_{ij}^{(1)}]_{m\times n}$ and $\mathbf{G}^{(2)} = [g_{ij}^{(2)}]_{m\times n}$ are called the expansion-coefficient matrices of $g_1(u,r)$ and $g_2(u,r)$. Some algorithms have been proposed to estimate the values of these coefficient matrices based on experimentally observed input and output data. It should be noted that here the vectors $\Phi(u)$ and $\Phi(r)$ are shifted generalized orthogonal polynomials [13]. They are formulated on the basis of common recurrence relations and orthogonal rule, and cover all kinds of individual orthogonal polynomials as well as non-orthogonal Taylor series. Consequently, they can obtain specific polynomial-approximation solutions of the same problem in terms of Chebyshev, Legendre, Laguerre, Jacobi, Hermite and Ultraspherical polynomials and Taylor series as special cases.

4. Preisach Model

4.1 Formulation

The intent of introducing the Preisach model is to supply the lack of a suitable hysteresis model in structural and mechanical areas, which is both capable of representing nonlocal hysteresis and mathematically tractable. Experiments revealed that the hysteretic restoring force of some cable-type vibration isolators relates mainly to the peak displacements incurred by them in the past deformation [3]. It will be shown that the Preisach model is especially effective in representing such nonlocal but selective-memory hysteresis, in which only some past input extrema (not the entire input variations) leave their marks upon future states of hysteresis nonlinearities.

The Preisach model is constructed as a superposition of a continuous family of elementary rectangular loops, called *relay hysteresis operators* as shown in Fig.1. That is [7,14],

$$r(t) = \Re[u(\cdot)](t) = \iint_{\alpha\geq\beta}\mu(\alpha,\beta)\gamma_{\alpha,\beta}[u(t)]d\alpha d\beta \qquad (11)$$

where $\mu(\alpha,\beta) \geq 0$ is a weight function, usually with support on a bounded set in the (α,β)-plane, named *Preisach plane*; $\gamma_{\alpha,\beta}[u(t)]$ is the relay hysteresis operator with thresholds $\alpha \geq \beta$. Outputs of

these simplest hysteresis operators have only two values +1 and −1, so can be interpreted as two-position relays with "up" and "down" positions corresponding to $\gamma_{\alpha,\beta}[u(t)]=+1$ and $\gamma_{\alpha,\beta}[u(t)]=-1$.

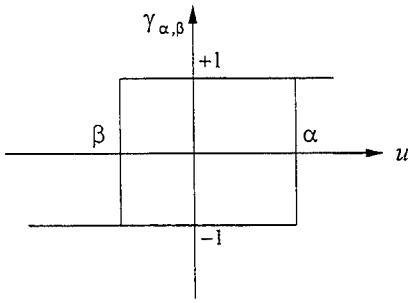

Fig. 1 Relay Hysteresis Operator

Hence, the Preisach model of Eq.(11) can be interpreted as a spectral decomposition of the complicated hysteresis operator $\Re$, that usually has nonlocal memory, into the simplest hysteresis operators $\gamma_{\alpha,\beta}$ with local memory. In the following, we illustrate how the model depicts the nonlocal selective-memory feature.

Consider a triangle T in the half-plane $\alpha \geq \beta$ as shown in Fig.2. It is assumed that the weight function $\mu(\alpha,\beta)$ is confined in the triangle T, i.e. $\mu(\alpha,\beta)$ is equal to zero outside T. Following the Preisach formulation, at any time instant t, the triangle T can be subdivided into two sets: $S^+(t)$ consisting of points (α,β) for which the corresponding $\gamma_{\alpha,\beta}$-operators are in the "up" position; and $S^-(t)$ consisting of points (α,β) for which the corresponding $\gamma_{\alpha,\beta}$-operators are in the "down" position. The interface $L(t)$ between $S^+(t)$ and $S^-(t)$ is a staircase line whose vertices have α and β coordinates coinciding respectively with local maxima and minima of input at previous instants of time. The nonlocal selective-memory is stored in this way. Thus, the output $r(t)$ at any instant t can be expressed equivalently as [14]

$$r(t) = \iint_{S^+(t)} \mu(\alpha,\beta)d\alpha d\beta - \iint_{S^-(t)} \mu(\alpha,\beta)d\alpha d\beta \qquad (12)$$

It should be noted that the Preisach model does not accumulate all past extremum values of input. Some of them can be wiped out by sequent input variations following the *wiping-out property* (*deletion rule*): each local input maximum wipes out the

vertices of $L(t)$ whose α-coordinates are below this maximum, and each local minimum wipes out the vertices whose β-coordinates are above this minimum. In other words, only the alternating series of *dominant* input extrema are stored by the Preisach model; all other input extrema are erased.

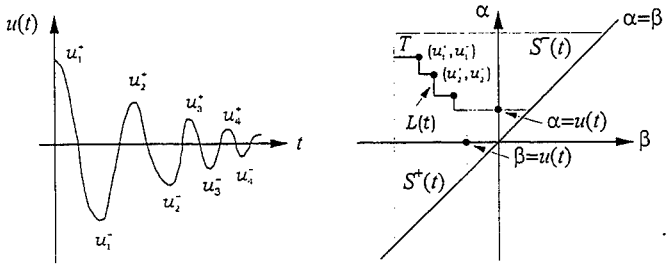

Fig. 2 Input Sequence and Preisach Plane

4.2 Identification

It is seen from Eq.(11) that the Preisach model is governed by the weight function $\mu(\alpha,\beta)$ after determining $L(t)$ which depends on the input sequence. $\mu(\alpha,\beta)$ is a single-valued function with respect to two variables α and β. Hence, the aforementioned nonparametric identification method can be also implemented to identify $\mu(\alpha,\beta)$ by expanding it in a similar expression to Eq.(10). An alternating approach is to define the following function

$$H(\alpha',\beta') = \iint_{T(\alpha',\beta')} \mu(\alpha,\beta)d\alpha d\beta = \int_{\beta'}^{\alpha'} \left[\int_{\beta}^{\alpha'} \mu(\alpha,\beta)d\alpha\right]d\beta \tag{13}$$

where $T(\alpha',\beta')$ is the triangle formed by the intersection of the line $\alpha = \alpha'$, $\beta = \beta'$ and $\alpha = \beta$. Differentiating Eq.(13) yields

$$\mu(\alpha',\beta') = -\frac{\partial^2 H(\alpha',\beta')}{\partial\alpha'\partial\beta'} \tag{14}$$

Thus, the force mapping identification technique can be applied to determine $H(\alpha,\beta)$ consistent with the experimental data, and then $\mu(\alpha,\beta)$ is obtained by Eq.(14).

5. Steady-State Response Analysis

Hysteretic systems are strongly nonlinear. A study of the steady-state oscillation is one of the classical problems of

nonlinear systems. Usually, the dynamic behavior of a nonlinear system is represented by its resonant frequency and frequency response characteristics. In the following, an accurate frequency-domain method accommodating multiple harmonics is developed to analyze the periodically forced response of hysteretic systems defined by mathematical hysteresis models.

Fig.3 shows a single-degree-of-freedom hysteretic oscillator with mass m, viscous damping coefficient c, and linear stiffness k, subjected to an external excitation $F(t)$, for which the governing equation of motion is

$$m \cdot \ddot{u}(t) + c \cdot \dot{u}(t) + k \cdot u(t) + r(t) = F(t) \qquad (15)$$

where the hysteretic restoring force $r(t)$ is represented by the DM model as Eq.(4). It is worth noting that for the kinetic equation Eq.(15), the excitation is $F(t)$ and the response is $u(t)$; and for the hysteretic constitutive law Eq.(4), $u(t)$ is input and $r(t)$ is output. The causal relationship is different.

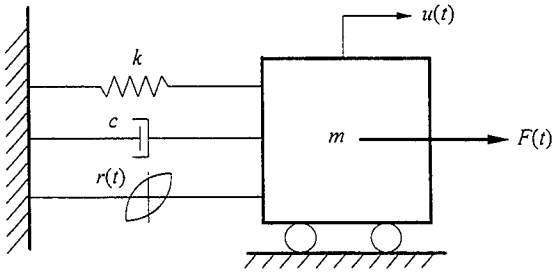

Fig. 3 Single-Degree-of-Freedom Hysteretic System

Due to the hereditary nature of the hysteresis model, it is difficult to directly solve the kinetic equation Eq.(15) by iteration. Here, Eq.(15) is only used to establish the relation between the harmonic components of $u(t)$ and $r(t)$. Suppose that the system is subjected to a general periodic excitation $F(t)$ with known harmonic components $\boldsymbol{F}=\{F_0\ F_1\ F_2\ \cdots\ F_N\ F_1^*\ F_2^*\ \cdots\ F_N^*\}^T$. The multi-harmonic steady-state response can be expressed as

$$u(t) = \frac{a_o}{2} + \sum_{j=1}^{N} a_j \cos j\omega t + \sum_{j=1}^{N} a_j^* \sin j\omega t \qquad (16)$$

in which $\boldsymbol{a}=\{a_0\ a_1\ a_2\ \cdots\ a_N\ a_1^*\ a_2^*\ \cdots\ a_N^*\}^T$ is the unknown vector containing the harmonic components of $u(t)$. Introducing Eq.(16) into Eq.(15) and using the Galerkin method provide

$$r_0 = F_0 - k \cdot a_0 \tag{17a}$$

$$r_j = F_j - (k - m \cdot \omega^2 j^2) \cdot a_j - c \cdot \omega j \cdot a_j^* \quad (j = 1, 2, \cdots, N) \tag{17b}$$

$$r_j^* = F_j^* + c \cdot \omega j \cdot a_j - (k - m \cdot \omega^2 j^2) \cdot a_j^* \quad (j = 1, 2, \cdots, N) \tag{17c}$$

where $\boldsymbol{r}=\{r_0\ r_1\ r_2\ \cdots\ r_N\ r_1^*\ r_2^*\ \cdots\ r_N^*\}^T$ is the harmonic vector of the hysteretic restoring force $r(t)$. Referring to the hysteretic constitutive law, we define the determining equation as

$$D(t) = \dot{r}(t) - g[u, r, \mathrm{sgn}(\dot{u})] \cdot \dot{u}(t) \tag{18}$$

When $\boldsymbol{a}$ is the solution of $u(t)$, applying the Galerkin method into Eq.(18) and considering Eq.(17) achieve

$$\boldsymbol{d}(\boldsymbol{a}) = \boldsymbol{0} \tag{19}$$

where the vector $\boldsymbol{d}(\boldsymbol{a})=\{d_0\ d_1\ d_2 \cdots d_N\ d_1^*\ d_2^* \cdots d_N^*\}^T$ is comprised of the harmonic components of $D(t)$ corresponding to $\boldsymbol{a}$. An efficient procedure to seek the solution of Eq.(19) is the Levenberg-Marquardt algorithm with the iteration formula

$$\boldsymbol{a}^{(k+1)} = \boldsymbol{a}^{(k)} - \{\boldsymbol{J}[\boldsymbol{a}^{(k)}]^T \cdot \boldsymbol{J}[\boldsymbol{a}^{(k)}] + \varphi_k \boldsymbol{I}\}^{-1} \cdot \boldsymbol{J}[\boldsymbol{a}^{(k)}]^T \cdot \boldsymbol{d}[\boldsymbol{a}^{(k)}] \tag{20}$$

where the Jacobian matrix $\boldsymbol{J}[\boldsymbol{a}^{(k)}] = \partial \boldsymbol{d}(\boldsymbol{a}) / \partial \boldsymbol{a} | \boldsymbol{a}=\boldsymbol{a}^{(k)}$; φ_k is the Levenberg-Marquardt parameter and $\boldsymbol{I}$ is identity matrix.

At each iteration, the function vector $\boldsymbol{d}[\boldsymbol{a}^{(k)}]$ and Jacobian matrix $\boldsymbol{J}[\boldsymbol{a}^{(k)}]$ should be recalculated with updated values of $\boldsymbol{a}^{(k)}$. Here, a frequency/time domain alternation scheme by FFT is introduced to evaluate the values of $\boldsymbol{d}(\boldsymbol{a})$ and $\boldsymbol{J}(\boldsymbol{a})$ at $\boldsymbol{a}=\boldsymbol{a}^{(k)}$. $\boldsymbol{d}(\boldsymbol{a})$ and $\partial \boldsymbol{d}(\boldsymbol{a}) / \partial \boldsymbol{a}$ are known to be the Fourier expansion coefficients of $D(t)$ and $\partial D(t) / \partial \boldsymbol{a}$ respectively. For a given $\boldsymbol{a}^{(k)}$ and known $\boldsymbol{F}$, the corresponding $\boldsymbol{r}[\boldsymbol{a}^{(k)}]$ is obtained from Eq.(17), and the inverse FFT is implemented for $\boldsymbol{a}^{(k)}$ and $\boldsymbol{r}[\boldsymbol{a}^{(k)}]$ to obtain all the time domain discrete values of $u(t)$, $\dot{u}(t)$, $r(t)$ and $\dot{r}(t)$ over an integral period. Then the time domain discrete values of the function $D(u, \dot{u}, r, \dot{r}, t)$, corresponding to $\boldsymbol{a}=\boldsymbol{a}^{(k)}$, are evaluated from Eq.(18). Making use of forward FFT to these time domain discrete values of $D(u, \dot{u}, r, \dot{r}, t)$, the values of function vector $\boldsymbol{d}[\boldsymbol{a}^{(k)}]$ are obtained.

Similarly, the partial differential $\partial D(t) / \partial \boldsymbol{\alpha}$ can be analytically evaluated in the time domain. Forward FFT to the time domain values of $\partial D(t) / \partial \boldsymbol{\alpha}$ at $\boldsymbol{\alpha}=\boldsymbol{\alpha}^{(k)}$ gives rise to $\partial \boldsymbol{d}[\boldsymbol{\alpha}^{(k)}]/\partial \boldsymbol{\alpha}$.

6. Case Study

Wire-cable vibration isolators are typical hysteretic damping devices. Dynamic tests show that their hysteresis behaviors are almost independent of the frequency in the tested frequency range [4,15]. Experimental study and parametric modelling of a wire-cable isolator have been carried out [5]. Fig.4 shows the experimental hysteresis loops in shear mode. It is seen that for relatively small deformations, the isolator exhibits softening hysteresis loops. When large displacements are imposed, the stiffness of the loops becomes smoothly hard. This nature is referred to as soft-hardening hysteresis. Based on the Bouc-Wen model, a parametric identification was performed to model these hysteresis loops, but the result is unsatisfactory. This is due to the fact that the Bouc-Wen model cannot represent such soft-hardening nature of hysteresis.

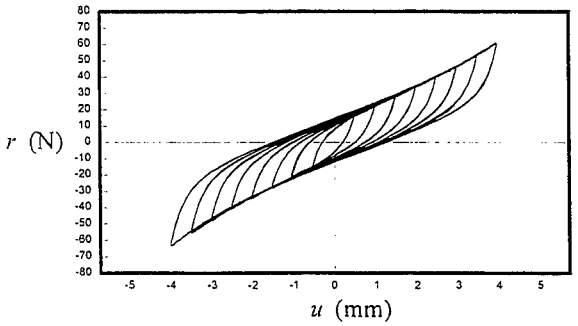

Fig. 4 Experimental Hysteresis Loops

We now use the DM model to represent these hysteresis loops, and perform a nonparametric identification to determine the functions $g_1(u,r)$ and $g_2(u,r)$. The simplest Taylor series are adopted, i.e. $\phi_i(r) = (r / r_0)^{i-1}$ and $\phi_j(u) = (u / u_0)^{j-1}$ (r_0 = 20.0 and u_0 = 2.0). Fig.5 shows the identified "force" surfaces of $g_1(u,r)$ and $g_2(u,r)$ by taking m=n=8. Fig.6 presents the theoretical hysteresis

loops generated by the DM model using the identified $g_1(u,\dot{r})$ and $g_2(u,\dot{r})$. It is seen that the modeled hysteresis loops are agreeable to the observed loops. In particular, the soft-hardening nature is reflected in the modeled hysteresis loops.

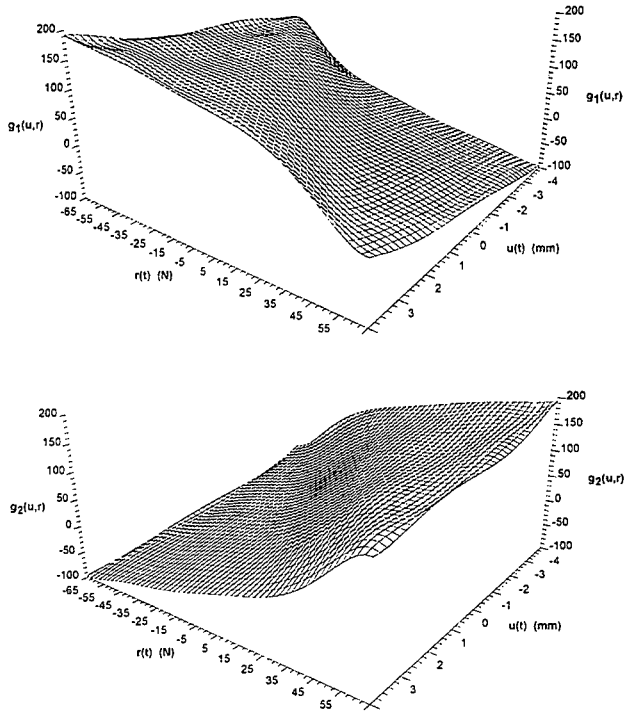

Fig. 5 Identified "Force" Surfaces of $g_1(u,\dot{r})$ and $g_2(u,\dot{r})$

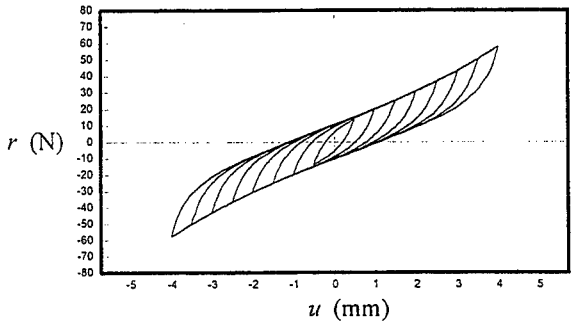

Fig. 6 Modeled Hysteresis Loops by DM Model

After performing the modelling of hysteretic behavior, the dynamic responses of hysteretic systems can be predicted by the developed method. Fig.7 shows a vibration isolation system installed with wire-cable isolators in shear mode. It is subjected to harmonic ground acceleration excitation $\ddot{x}_g(t)=A\cos 2\pi ft$. The equation of motion of the system is expressed as

$$m \cdot \ddot{u}(t) + K \cdot r(t) = -m \cdot \ddot{x}_g(t) \tag{21}$$

where m is the mass of the system; K is number of the isolators installed. $u(t)$ is the displacement of the system relative to the ground. $r(t)$ is the restoring force of each isolator and has been determined from nonparametric identification.

Fig.8 illustrates the predicted frequency-response curves of the relative displacement when m=6kg and K=2. The excitation amplitude A is taken as 0.25g, 0.30g, 0.35g, 0.40g and 0.45g respectively. The frequency-response curves show clearly the nonlinear nature of the wire-cable isolation system.

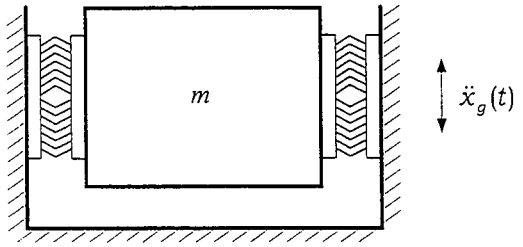

Fig. 7 Vibration Isolation System with Wire-Cable Isolators

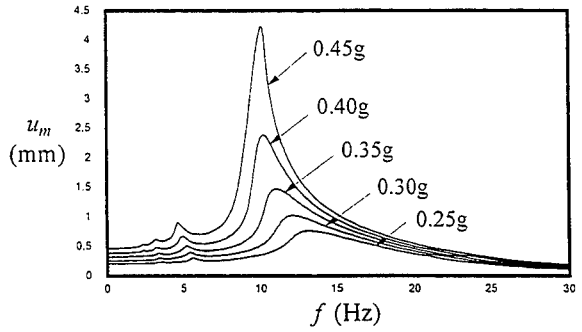

Fig. 8 Frequency Response Curves of Relative Displacement

7. Concluding Remarks

This paper reports a preliminary work of introducing the mathematical hysteresis models in structural and mechanical areas. It is shown that a wide kind of differential hysteresis models, which are extensively used at present, can be derived from the Duhem-Madelung (DM) model. Thus, the mathematical properties concerning the DM model are also possessed by these models. Two potential advantages appear when the DM formulation is used. Firstly, it allows to apply the force mapping technique to hysteretic systems. Secondly, it provides an approach to construct novel differential models which reflect some special hysteretic characteristics. The Preisach model is shown to be capable of representing nonlocal hysteresis and mathematically tractable. It offers a more accurate description of several observed hysteretic phenomena. Emphasis is placed on demonstrating the selective-memory nature of this hysteresis model. The case study based on experimental data of a wire-cable isolator has shown the applicability of the mathematical hysteresis model, and the validity of the steady-state response analysis method proposed in the present paper.

Acknowledgment: This study was supported in part by the Hong Kong Research Grants Council (RGC) and partly by The Hong Kong Polytechnic University. These supports are gratefully acknowledged.

References

1. Azevedo, J. and Calado, L., "Hysteretic behaviour of steel members: analytical models and experimental tests", *J. Construct. Steel Research*, 1994, 29, 71-94.
2. Kayvani, K. and Barzegar, F., "Hysteretic modelling of tubular members and offshore platforms", *Eng. Struct.*, 1996, 18, 93-101.
3. Lo, H.R., Hammond, J.K. and Sainsbury, M.G., "Nonlinear system identification and modelling with application to an isolator with hysteresis", *Proc. 6th Int. modal Anal. Conf.*, Kissimmee, Florida, 1988, Vol.II, 1453-1459.

4. Demetriades, G.F., Constantinou, M.C. and Reinhorn, A.M., "Study of wire rope systems for seismic protection of equipment in buildings", *Eng. Struct.*, 1993, 15, 321-334.
5. Ni, Y.Q., "Dynamic response and system identification of nonlinear hysteretic systems", *PhD Dissertation*, The Hong Kong Polytechnic University, Hong, Kong, November 1996.
6. Krasnosel'skii, M.A. and Pokrovskii, A.V., *Systems with Hysteresis*, translated from the Russian by M. Niezgódka, Springer-Verlag, Berlin, 1989.
7. Visintin, A., *Differential Models of Hysteresis*, Springer-Verlag, Berlin, 1994.
8. Macki, J.W., Nistri, P. and Zecca, P., "Mathematical models for hysteresis", *SIAM Review*, 1993, 35, 94-123.
9. Masri, S.F. and Caughey, T.K., "A nonparametric identification technique for nonlinear dynamic problems", *J. Appl. Mech.*, ASME, 1979, 46, 433-447.
10. Lo, H.R. and Hammond, J.K., "Nonlinear system identification using the surface of nonlinearity form: discussion on parameter estimation and some related problems", *Proc. 3rd Int. Conf. Recent Adv. Struct. Dyn.*, Southampton, UK, 1988, 339-348.
11. Benedettini, F., Capecchi, D. and Vestroni, F., "Identification of hysteretic oscillators under earthquake loading by nonparametric models", *J. Eng. Mech.*, ASCE, 1995, 121, 606-612.
12. Ni, Y.Q., Ko, J.M. and Wong, C.W., "Modelling and identification of nonlinear hysteretic vibration isolators", Accepted to *SPIE's 4th Annual Symposium on Smart Structures and Materials : Passive Damping and Isolation*, 3-6 March 1997, San Diego, USA.
13. Ni, Y.Q., Wong, C.W. and Ko, J.M., "The generalized orthogonal polynomial (GOP) method for the stability analysis of periodic systems", *Proc. Int. Conf. Comput. Methods Struct. Geotech. Eng.*, Hong Kong, 1994, Vol.II, 464-469.
14. Mayergoyz, I.D., *Mathematical Models of Hysteresis*, Springer-Verlag, New York, 1991.
15. Ko, J.M., Ni, Y.Q. and Tian, Q.L., "Hysteretic behavior and empirical modeling of a wire-cable vibration isolator", *Int. J. Anal. Exp. Modal Anal.*, 1992, 7, 111-127.

The identification of turbogenerator foundation models from run-down data

M Smart, M I Friswell, A W Lees, U Prells
Department of Mechanical Engineering
University of Wales Swansea, Swansea SA2 8PP UK
email: m.smart@swansea.ac.uk

ABSTRACT

The trend of placing turbines in modern power stations on flexible steel foundations means that the foundations exert a considerable influence on the dynamics of the system. In general, the complexity of the foundations means that models are not available *a priori*, but rather need to be identified. One way of doing this is to use the measured responses of the foundation at the bearings to the synchronous excitation obtained when the rotor is run down. This paper discusses the implementation of such an estimation technique, based on an accurate model of the rotor and state of unbalance, and some knowledge of the dynamics of the bearings. The effect of errors in the bearing model and response measurements on the identified parameters is considered, and the instrumental variable method is suggested as one means of correcting them.

1 INTRODUCTION

The cost of failure of a typical turbine in a modern power station is very high, and therefore development of condition monitoring techniques for such machines is an active area of research. Condition monitoring relies on measuring machine vibrations and using them to locate and quantify faults, which obviously requires an accurate dynamic model of the machine. Although the dynamic characteristics of rotors are generally well understood, the foundations on which they rest are not. Since the foundations are often quite flexible, they can contribute considerably to the rotor's dynamic behaviour.

Finite element modelling has been attempted but the complexity of the foundations, and the fact that they often differ substantially from the original drawings rendered the technique generally unsuccessful[1]. Experimental modal analysis is another possible solution, but this requires that the rotor be removed from the foundation, and that all casings remain in place, which is not practical for existing power plant. However, maintenance procedures require that rotors are run down at regular intervals and this procedure provides forcing to the foundation over the frequency range

of operation. By measuring the response at the bearing pedestals (which is already performed for condition monitoring purposes) an input-output relation for the foundation may be obtained.

Lees[2] developed a least-squares method to calculate the foundation parameters by assuming that an accurate model exists for the rotor, that the state of unbalance is known from balancing runs, and that the dynamic stiffness matrices of the bearings can be calculated. Although bearing models are not in fact well characterised, Lees and Friswell[3] showed that the parameter estimates are only sensitive to the bearing stiffnesses over limited frequency ranges, which can be calculated.

Feng and Hahn[4] followed a similar approach but added extra information by measuring the displacements of the shaft. Zanetta[5] also measured the shaft displacements but included the bearing characteristics as parameters to be estimated. Although any extra information is desirable in a parameter estimation routine the equipment necessary to measure these quantities only exists in the newer power stations, and it was desired to make the method applicable to older plant as well. In the analysis presented here, the measured data consists of the motion of the bearing pedestals in the horizontal and vertical directions, although not necessarily in both directions at every bearing.

2 THEORY

2.1 Force estimation

If $\boldsymbol{D}$ is the dynamic stiffness matrix of a structure defined as

$$\boldsymbol{D}(\omega) = \boldsymbol{K} + \omega\boldsymbol{C} - \omega^2\boldsymbol{M} \tag{1}$$

where $\boldsymbol{M}, \boldsymbol{C}, \boldsymbol{K}$ are the mass, damping and stiffness matrices then

$$\boldsymbol{D}\boldsymbol{x} = \boldsymbol{f} \tag{2}$$

where $\boldsymbol{x}$ is response and $\boldsymbol{f}$ force. Referring to figure 1 it is seen that the rotor is connected to the foundation via the bearings. It is assumed that good models exist for both rotor and bearings, and that the state of unbalance is known. The implications of these assumptions will be discussed later.

The dynamic stiffness equation for the whole system may be written as

$$\begin{pmatrix} \boldsymbol{D}_r & 0 \\ 0 & \boldsymbol{D}_f \end{pmatrix} \begin{pmatrix} \boldsymbol{x}_r \\ \boldsymbol{x}_f \end{pmatrix} = \begin{pmatrix} \boldsymbol{f}_r \\ \boldsymbol{f}_f \end{pmatrix} = \begin{pmatrix} \boldsymbol{f}_{ur} \\ 0 \end{pmatrix} - \begin{pmatrix} \boldsymbol{f}_{br} \\ \boldsymbol{f}_{bf} \end{pmatrix} \tag{3}$$

The subscripts r and f refer to the rotor and foundation degrees-of-freedom respectively, u refers to the unbalance forces and b to the bearing forces.

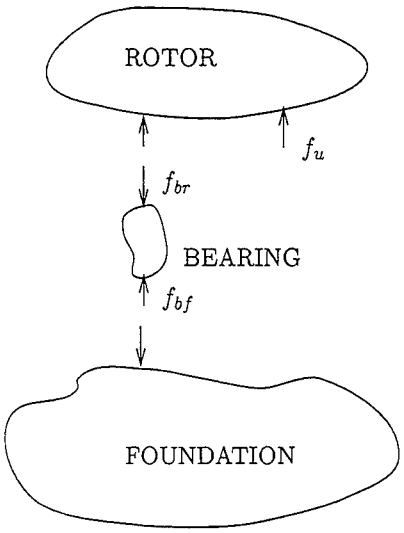

Figure 1: Rotor-bearing system

There is a negative sign before the bearing forces $\boldsymbol{f_b}$ since they refer to the forces acting on the bearings. The foundation d.o.f are those where the responses are measured, in other words no internal d.o.f are represented. $\boldsymbol{D_f}$ therefore represents a reduced dynamic stiffness matrix. The response measurements will not be the total vibration level at the bearings but rather the vibrations at once-per-revolution and it is assumed that no dynamic forces at this frequency will be transmitted to the foundation via the substructure onto which it is fixed.

The equation for the bearings in the global coordinate system is

$$\begin{pmatrix} \boldsymbol{D}_{brr} & \boldsymbol{D}_{brf} \\ \boldsymbol{D}_{bfr} & \boldsymbol{D}_{bff} \end{pmatrix} \begin{pmatrix} \boldsymbol{x}_r \\ \boldsymbol{x}_f \end{pmatrix} = \begin{pmatrix} \boldsymbol{f}_{br} \\ \boldsymbol{f}_{bf} \end{pmatrix} \tag{4}$$

This assumes that the bearings behave as complex springs, in other words they have negligible inertia and no internal d.o.f. Substituting (4) into (3) we have

$$\begin{pmatrix} \boldsymbol{D}_{trr} & \boldsymbol{D}_{trf} \\ \boldsymbol{D}_{tfr} & \boldsymbol{D}_{tff} \end{pmatrix} \begin{pmatrix} \boldsymbol{x}_r \\ \boldsymbol{x}_f \end{pmatrix} = \begin{pmatrix} \boldsymbol{f}_{ur} \\ \boldsymbol{0} \end{pmatrix} \tag{5}$$

where

$$\begin{pmatrix} \boldsymbol{D}_{trr} & \boldsymbol{D}_{trf} \\ \boldsymbol{D}_{tfr} & \boldsymbol{D}_{tff} \end{pmatrix} = \left(\begin{pmatrix} \boldsymbol{D}_r & \boldsymbol{0} \\ \boldsymbol{0} & \boldsymbol{D}_f \end{pmatrix} + \begin{pmatrix} \boldsymbol{D}_{brr} & \boldsymbol{D}_{brf} \\ \boldsymbol{D}_{bfr} & \boldsymbol{D}_{bff} \end{pmatrix} \right) \tag{6}$$

and where subscript t refers to the total model. Solving equation (5) for $\boldsymbol{x}_r$ leads to

$$\boldsymbol{x}_r = \boldsymbol{D}_{t_{rr}}^{-1}(\boldsymbol{f}_{u_r} - \boldsymbol{D}_{t_{rf}}\boldsymbol{x}_f) \tag{7}$$

and solving equation (4) for $\boldsymbol{f}_{b_f}$ yields

$$\boldsymbol{f}_{b_f} = -\boldsymbol{f}_{b_r} = -\boldsymbol{D}_{b_{rr}}\boldsymbol{x}_r - \boldsymbol{D}_{b_{rf}}\boldsymbol{x}_f \tag{8}$$

All quantities in equation (8) are known either from assumed models ($\boldsymbol{D}_r$, $\boldsymbol{D}_b$) or experiment ($\boldsymbol{x}_f$, $\boldsymbol{f}_{u_r}$). This calculated force $\boldsymbol{f}_{b_f}$ may then be used together with the measured responses to estimate the foundation parameters.

2.2 Foundation parameter estimation

Once the forces have been estimated, the foundation parameters must be derived. The dynamic stiffness equation for the foundation is

$$\boldsymbol{D}_f\boldsymbol{x}_f = \boldsymbol{f}_{b_f} \tag{9}$$

Although $\boldsymbol{D}_f$ is a reduced stiffness matrix it is assumed that it has the form of equation (1). Therefore equation (9) may be written as

$$\boldsymbol{W}(\omega)\boldsymbol{v} = \boldsymbol{f}_{b_f} \tag{10}$$

where $\boldsymbol{v}$ is a column vector formed from the elements of $\boldsymbol{M}$, $\boldsymbol{C}$ and $\boldsymbol{K}$ and $\boldsymbol{W}$ is a matrix formed from the response vector which depends explicitly on ω. Clearly this is an under-determined set of equations, but by taking measurements at many frequencies it may be made over-determined, and thus solvable in a least squares sense. Since the magnitude of the mass, damping and stiffness elements normally differ by several orders-of-magnitude, it was found expedient to scale the mass parameters by $\overline{\omega}^2$, and the damping parameters by $\overline{\omega}$, where $\overline{\omega}$ is the mean value of the frequency.

2.3 Errors in estimates

It is necessary now to examine the effect of errors on the parameter estimates. Equation (10) is of the form $\boldsymbol{A}\boldsymbol{x} = \boldsymbol{b}$, where $\boldsymbol{A}$ has dimension $m \times n$. In this particular case, $\boldsymbol{A}$ depends on the measured response $\boldsymbol{x}_f$, whilst $\boldsymbol{b}$ depends on the measured response, applied unbalance, and assumed rotor and bearing models. Therefore the estimated parameters will be sensitive to the following errors:

1. Errors in the rotor model
2. Errors in the bearing model
3. Errors in the state of unbalance

4. Errors in the measured foundation response

The rotor model is generally well known, as is the state of unbalance, so the main source of error in the estimates is due to measurement noise and bearing uncertainty. If the least squares problem is formulated as

$$\boldsymbol{A}\boldsymbol{x} = \boldsymbol{b} \tag{11}$$

then

$$(\boldsymbol{A}_0 + \boldsymbol{A}_N)\boldsymbol{x} = \boldsymbol{b}_0 + \boldsymbol{b}_N \tag{12}$$

where the subscript N refers to noise and 0 to data which is noise-free. The least-squares estimate is given by

$$\hat{\boldsymbol{x}} = (\boldsymbol{A}_0^T\boldsymbol{A}_0 + \boldsymbol{A}_N^T\boldsymbol{A}_N + \boldsymbol{A}_0^T\boldsymbol{A}_N + \boldsymbol{A}_N^T\boldsymbol{A}_0)^{-1}(\boldsymbol{A}_0 + \boldsymbol{A}_N)^T(\boldsymbol{b}_0 + \boldsymbol{b}_N) \tag{13}$$

Even if the noise on the outputs is uncorrelated with the noise on the inputs the expected value of $\boldsymbol{x}$ does not equal that of its estimate:

$$E[\boldsymbol{x}] - E[\hat{\boldsymbol{x}}] \neq 0 \tag{14}$$

In other words the estimate $\hat{\boldsymbol{x}}$ is biased[6]. In order to reduce the bias of the estimates, the instrumental variables method can be used. Essentially, it requires the use of a matrix that is uncorrelated with the noise on the outputs, but which is strongly correlated with the noise-free measurements themselves. If $\boldsymbol{W}$ is the instrumental variable matrix, then

$$\boldsymbol{W}^T\boldsymbol{A}\boldsymbol{x} = \boldsymbol{W}^T\boldsymbol{b} \tag{15}$$

Expanding

$$\hat{\boldsymbol{x}} = (\boldsymbol{W}^T\boldsymbol{A}_0 + \boldsymbol{W}^T\boldsymbol{A}_N)^{-1}(\boldsymbol{W})^T(\boldsymbol{b}_0 + \boldsymbol{b}_N) \tag{16}$$

This means that $E[\hat{\boldsymbol{x}}] = \boldsymbol{x}$, in other words unbiased estimates result. Fritzen[7] suggested an iterative method for solving for the parameters. Initially, equation (10) is solved in a least-squares sense, and the values of the estimated parameters are used to calculate outputs for the model. These outputs are then used to create $\boldsymbol{W}$ in the same way as the original outputs were used to create $\boldsymbol{A}$, new estimates are obtained, and if necessary the process is repeated. Experience seems to suggest good convergence properties[7].

3 SIMULATION

The method under discussion in this paper was tested on a model of a small test rig located at Aston University, Birmingham. This consists of a steel shaft approximately 1.1m long, with nominal diameter 38mm. The shaft is supported at either end by a journal bearing of diameter 100mm,

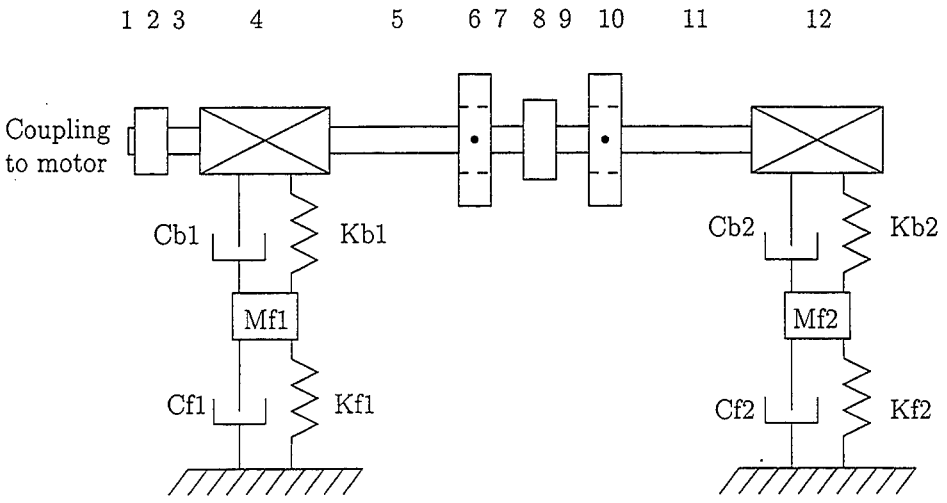

Figure 2: Rotor-bearing system

L/D ratio of 0.3 and clearance of 25μm. There are two shrink-fitted balancing discs for balancing runs. Each bearing is supported on a flexible pedestal to simulate the flexible foundations encountered in power station turbines. At present these pedestals are bolted onto a massive lathe bed. The rotor is powered by a DC motor attached via a belt to a driving pulley, which is in turn attached via a flexible coupling to the main rotor shaft.

A schematic of the rig is shown in figure 2. Dimensions of each station and material properties are given in table 1. A finite element model of the rotor with 23 elements was created and short bearing theory was used to obtain values for the bearing stiffness and damping[8].

The pedestals themselves consist of two rectangular steel plates, 600mm $\times$ 150mm which have two channels cut into them, and which are supported on knife-edges (figure 3). The vertical stiffness arises from the hinge effect of the channels, whilst the horizontal stiffness is as a result of the shaft centre tilting under an applied load. Treating the supports as beams, the theoretical stiffnesses are:

$$K_y = 0.55MN/m \qquad K_x = 1.5MN/m$$

where x and y refer to the horizontal and vertical directions respectively. The masses and damping factors were taken as:

$$M_x = M_y = 50kg \qquad C_x = C_y = 150N \cdot s/m$$

The estimation theory was tested using this model. The finite element model was used to generate responses at the bearings for frequencies from

Table 1: Table of rotor rig properties

Shaft Properties				
Station	Length (mm)	Diameter (mm)	E (GPa)	ρ (kg/m^3)
1	6.35	38.1	200	7850
2	25.4	77.57	200	7850
3	50.8	38.1	200	7850
4	203.2	100	200	7850
5	177.8	38.1	200	7850
6	50.8	116.8	200	7850
7	76.2	38.1	200	7850
8	76.2	109.7	200	7850
9	76.2	38.1	200	7850
10	50.8	102.9	200	7850
11	177.8	38.1	200	7850
12	203.2	100	200	7850
Balancing discs				
Station	Length (mm)	Diameter (mm)	Unbalance (kg · m)	
6	25.4	203.2	0.001	
10	25.4	203.2	0.001	

0 to 30 Hz with a spacing of 0.1 Hz. The responses were corrupted by normally distributed random noise with zero mean and standard deviation of 0.1% of the maximum response amplitude (applied to both real and imaginary parts of the response). At each frequency the bearing static forces were disturbed by noise drawn from a uniform distribution spanning an interval of 20% of the force magnitude, to introduce uncertainty into the bearing parameters. The unbalance was assumed to be exactly known. A series of 30 runs was performed, foundation parameter estimates calculated and the mean and standard deviations of these estimates obtained.

The magnitudes of the responses at both bearings are given in figure 4, which show that there are four critical speeds in the frequency range under consideration. A sample of true and estimated forces in the bearings are shown in figures 5 and 6.

The means (μ) and standard deviations (σ) of the least-square (LS) and instrumental variable (IV) estimates for the foundation parameters are shown in table 2.

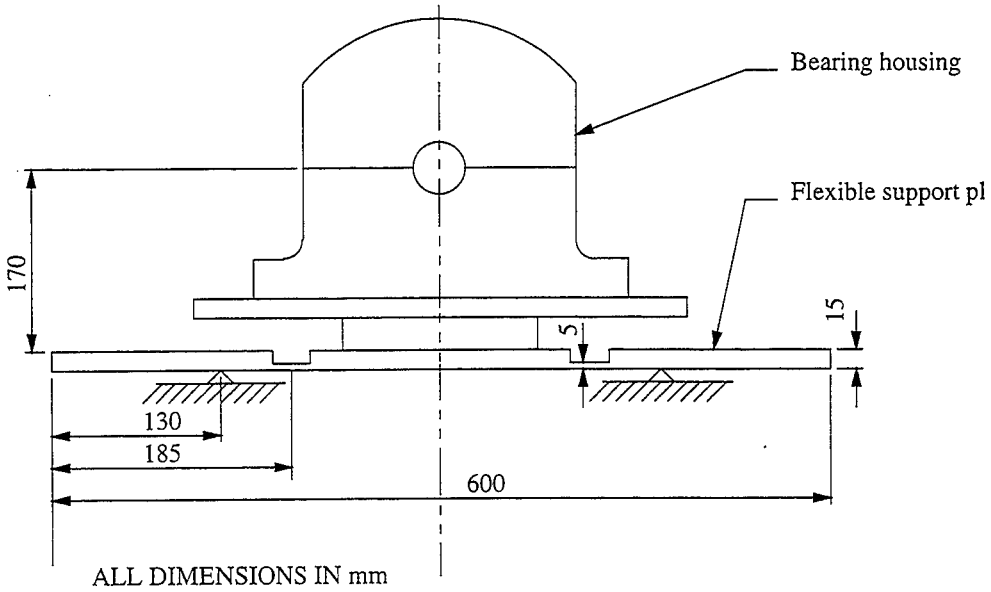

Figure 3: Flexible bearing supports

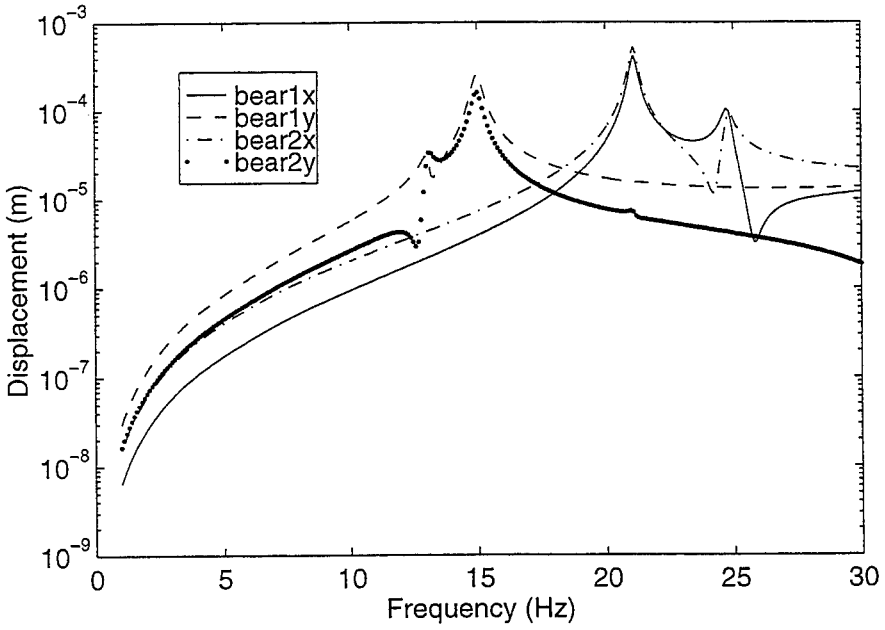

Figure 4: Magnitudes of responses at bearings

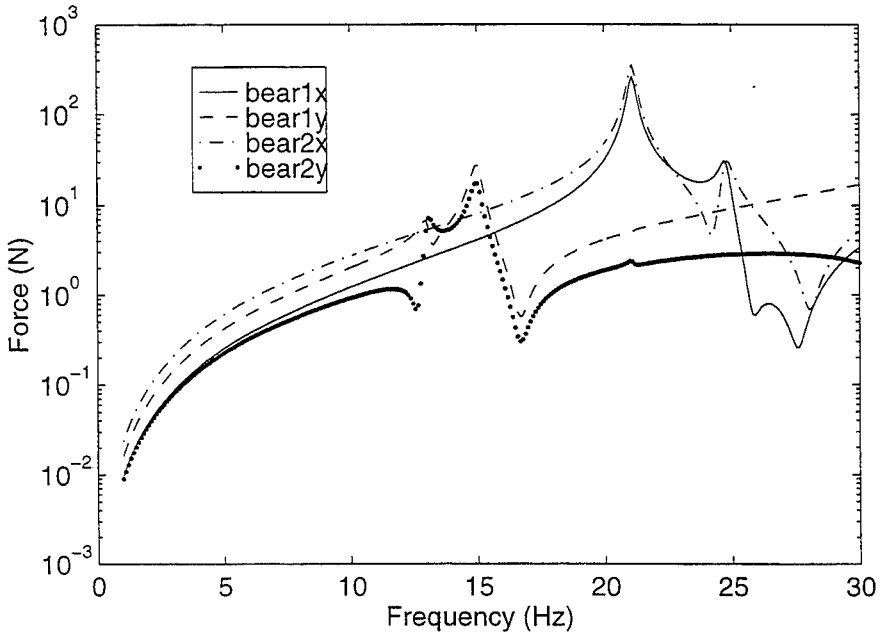

Figure 5: Magnitude of forces at bearings

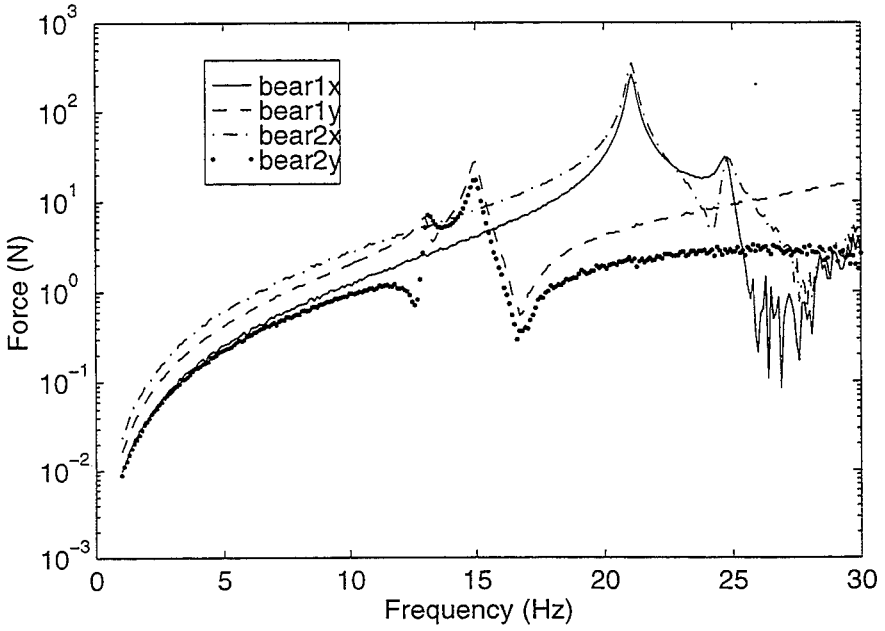

Figure 6: Magnitude of estimated forces at bearings

Table 2: Parameter estimates for foundations showing uncertainty

	Structural parameters (assumed symmetry)									
Parameter	m_{11}	m_{12}	m_{13}	m_{14}	m_{22}	m_{23}	m_{24}	m_{33}	m_{34}	m_{44}
Value (kg)	50	0	0	0	50	0	0	50	0	50
LS μ (kg)	29.78	1.41	0.00	0.00	47.13	1.14	0.00	40.96	1.66	53.01
LS σ (kg)	7.53	0.76	0.00	0.00	0.81	0.67	0.00	3.30	0.52	2.42
IV μ (kg)	51.53	0.19	0.00	0.00	50.03	-0.07	0.00	51.51	-0.11	50.28
IV σ (kg)	1.05	0.11	0.00	0.00	0.46	0.64	0.00	1.21	0.99	3.52
Parameter	c_{11}	c_{12}	c_{13}	c_{14}	c_{22}	c_{23}	c_{24}	c_{33}	c_{34}	c_{44}
Value (Ns/m)	150	0	0	0	150	0	0	150	0	150
LS μ (Ns/m)	128.12	0.00	0.00	0.00	145.94	0.00	0.00	162.76	0.00	161.12
LS σ (Ns/m)	4.48	0.00	0.00	0.00	1.69	0.00	0.00	3.86	0.00	6.09
IV μ (Ns/m)	143.35	0.00	0.00	0.00	152.29	0.00	0.00	147.01	0.00	132.36
IV σ (Ns/m)	8.86	0.00	0.00	0.00	18.51	0.00	0.00	9.45	0.00	38.98
Parameter	k_{11}	k_{12}	k_{13}	k_{14}	k_{22}	k_{23}	k_{24}	k_{33}	k_{34}	k_{44}
Value (MN/m)	1.55	0	0	0	0.55	0	0	1.55	0	0.55
LS μ (MN/m)	1.07	0.01	0.06	0.00	0.52	0.02	0.00	1.34	0.03	0.57
LS σ (MN/m)	0.16	0.01	0.02	0.00	0.01	0.01	0.00	0.07	0.01	0.02
IV μ (MN/m)	1.53	0.00	0.00	0.00	0.55	0.00	0.00	1.58	0.00	0.55
IV σ (MN/m)	0.02	0.00	0.00	0.00	0.00	0.01	0.00	0.03	0.02	0.03

4 DISCUSSION

The results in table 2 show a clear improvement in parameter estimates when the instrumental variable method is used. There is a clear bias in the least-squares estimates which is significantly less when the instrumental variable method is employed. Also, despite the fact that the bearing parameters are assumed to be seriously in error, the estimates appear to be insensitive to them. This will be true provided that the bearings are much stiffer than the foundation (a reasonable assumption in practice). It does appear however that in some cases the standard deviation of the instrumental variable estimate is larger than that of the least-squares estimate, a fact which warrants further investigation.

As far as the rotor model is concerned, impact tests, which are performed on rotors prior to them entering service, normally give experimental frequencies which are within a few percent of the theoretical ones. Thus the assumption that the rotor model is accurately known would appear to be reasonable.

The state of unbalance may in theory be established from a balancing run. If two successive run-downs are performed, one due to the unknown system unbalance and one with known balance weights attached, then provided the system is linear the response measurements may be vectorially subtracted to give the response due to the known balance weights alone. In order to ascertain the effect of unbalance uncertainty on the parameter estimates, one run was performed assuming no error in the unbalance. It should be noted that this assumes that the system is linear.

5 CONCLUSIONS

A method of estimating turbogenerator foundation parameters from potentially noisy measurement data is demonstrated. It is shown that making use of the instrumental variable method reduces the bias in the estimates and improves them quite significantly.

6 ACKNOWLEDGEMENT

The authors wish to acknowledge the support and funding of Nuclear Electric Ltd and Magnox Electric Plc. Dr Friswell wishes to acknowledge the support of the Engineering and Physical Sciences Research Council through the award of an advanced fellowship.

REFERENCES

[1] A. W. Lees and I. C. Simpson. The dynamics of turbo-alternator foundations: Paper C6/83. In *Conference on steam and gas turbine foundations and shaft alignment*, Bury St Edmunds, 1983, IMechE, pp37-44.

[2] A. W. Lees. The least squares method applied to identify rotor/foundation parameters: Paper C306/88. In *Proceedings of the International Conference on Vibrations in Rotating Machinery*, Edinburgh, 1988, IMechE, pp209-216.

[3] M. I. Friswell and A. W. Lees. Estimation of forces exerted on machine foundations. In M. I. Friswell and J. E. Mottershead, editors, *International Conference on Identification in Engineering Systems*, Swansea, 1996, pp793-803.

[4] N. S. Feng and E. J. Hahn. Including foundation effects on the vibration behaviour of rotating machinery. *Mechanical Systems and Signal Processing*, 1995, **9**, pp243–256.

[5] G. A. Zanetta. Identification methods in the dynamics of turbogenerator rotors: Paper C432/092. In *IMechE Conference on Vibrations in rotating machinery*, Bath, 1992. IMechE, pp173-181.

[6] J. Schoukens and R. Pintelon. *Identification of linear systems.* Pergamon Press, 1991.

[7] C. P. Fritzen. Identification of mass, damping and stiffness matrices of mechanical systems. *Journal of Vibration, Acoustics, Stress and Reliability if Design*, 1986 **108**, pp9-17.

[8] D. M. Smith. *Journal bearings in Turbomachinery.* Chapman and Hall, 1969.

SHELL MODE NOISE IN RECIPROCATING REFRIGERATION COMPRESSORS

Cüneyt Öztürk and Aydın Bahadır
Türk Elektrik Endüstrisi A.Ş
R&D Department
Davutpaşa, Litros Yolu, Topkapı -34020, İstanbul, Turkey

ABSTRACT

This study describes the successful endeavor to understand the causes of noise that appear on the shell modes of the reciprocating refrigeration compressors. The compressor shell is generally considered as the acoustic enclosure that reflects the acoustic energy back into the compressor cavity but also as the transmitter and radiator of the transmitted acoustic energy that could be radiated into the air or transmitted to the structure. Vibrations of the compressor shell can easily be characterized in terms of the modal parameters that consist of the natural frequencies, mode shapes and damping coefficients. The noise source harmonics and the shell resonances couple to produce the shell noise and vibration. The harmonic spacing is equal to the basic pumping frequency. Results of the studies indicate that important natural frequencies of the compressor shell usually stay between 2000-6000 Hz interval. The important natural frequencies are first natural frequencies in the lower range with the longer wavelengths that radiate well.

INTRODUCTION

Compressor noise sources are those processes where certain portions are separated from the desired energy flow and transmitted through the internal components of compressor to the hermetic shell where it is radiated from the shell as airborne noise on vibration of supporting structure will eventually radiate noise from some portion of the structure. Noise sources of the reciprocating refrigeration compressors can be classified as motor noise, compression process noise and valve port flow noise.

In reciprocating compressors there is very high density of noise harmonics even though they decay in amplitude at high frequencies. Generally, these noise source harmonics and the shell resonances couple to produce shell noise and vibration

NOISE GENERATION MECHANISM OF THE RECIPROCATING REFRIGERATION COMPRESSORS

Significance of the problem

The results of the sound radiation characteristics shown at figure 1 indicated that certain high amplitude frequency components had very distinctive sound radiation patterns. It was suspected these frequencies correspond to excitation of either structural resonances of the compressor shell or acoustic resonances of the interior cavity space. Resonances those amplify the noise and vibration caused by pumping harmonics of a compressor and thus can be the cause of significant noise problems.

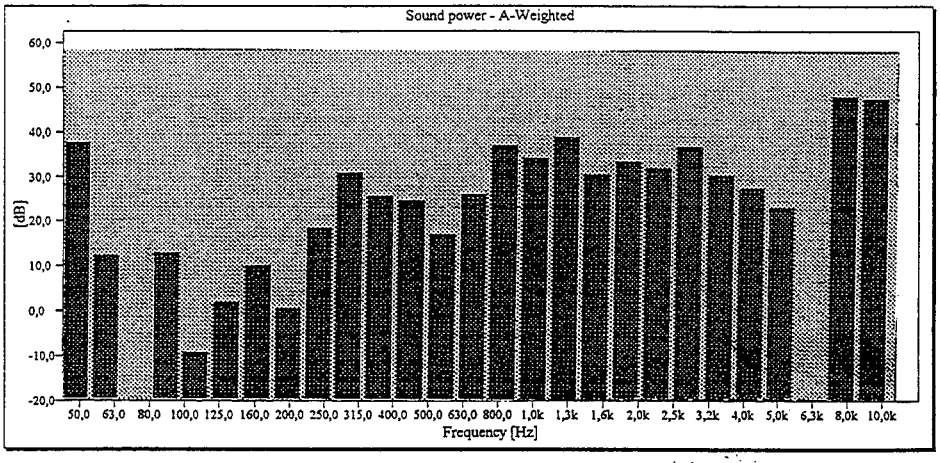

Figure 1, Noise Radiation Characteristics of Reciprocating Refrigeration Compressor.

Noise sources

Noise in a compressor is generated during cyclic compression, discharge, expansion and suction process. The character of noise sources is harmonic due to periodic nature of the compression process. These harmonics are present in the compression chamber, pressure time history and loading of the compressor through drive system. The motor can not provide immediate response to load harmonics and load balance is obtained at the expense of acceleration and

deceleration of the motor drive system. Harmonic vibrations of the motor drive system can then excite the resonant response in the compressor components that can transmit the acoustic energy in very efficient way. The rest of the noise sources are, turbulent nature of flow depending to passage through valve ports, valve impacts on their seats and possible amplification when matched with mechanical resonances.

MECHANICAL FEATURES OF SHELL

Mechanical features of the compressor

The hermetically sealed motor compressor comprises in general a motor compressor unit including a motor assembly mounted with a frame and a sealed housing within which the compressor is supported by means of plurality of coil springs each having one end spring with the frame and the other end connected with the interior of the housing.

The refrigerant gas as it is compressed in the cylinder is discharged through the discharge chamber in the cylinder head into the discharge muffler. The discharge muffler is generally mounted on the cylinder head attached in covering relation to an end face of the cylinder. Where the sealed casing is spherical in shape for better noise suppression, an upper end of the cylinder head tends to interfere with an inner wall surface of the casing, a disadvantage that can only be eliminated by increasing the size of scaled casing for providing a desired hermetically sealed motor.

Compressor Shell

The shell is easily be characterized with the modal parameters. The ideal shell should be designed in a way that keep all the excitation frequencies at the mass controlled region of all its modes. But, depending on the very tight constraints that come with the gas dynamics and motor locations, it is not allowed to be flexible during the design of shell. As a consequence of the existing design limitations natural frequencies of the shell usually fall between 1000-5000 Hz.

SHELL RADIATION

Figure 1 illustrates how the sound pressure level of a pumping harmonic can increase as it nears a resonant frequency. The sound pressure level of the pumping harmonic increases around the shell resonances. The resonance generally radiates primarily from the large flat sides of the compressor. There are three major acoustic cavity resonances 400, 500 and 630 Hz and four major structural resonances of the compressor shell: around 1.6 K, 2 K, 2.5 and 3.2 K. Hz at which noise radiates well in certain directions.

SHELL RESONANCES

Figures 2, 3 and 4 illustrate the frequency responses of the compressor shell when measured with the impact hammer method. Figure 2 is the response to the excitation in x direction, figure 3 is for the excitation direction and figure 4 is for the excitation in z direction.

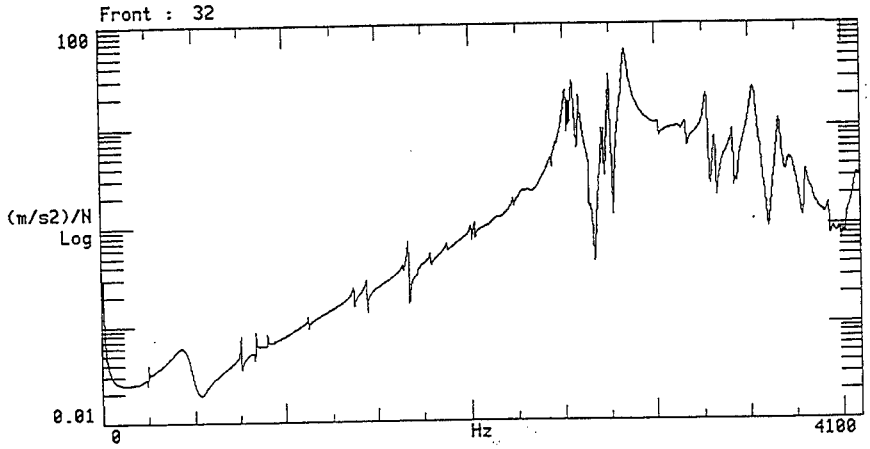

Figure 2, Frequency response of the compressor shell when excited in X direction.

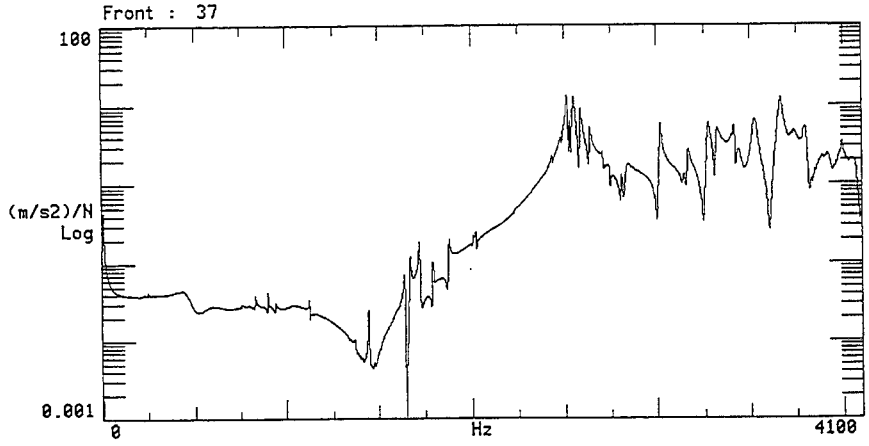

Figure 3, Frequency response of the compressor shell when excited in Y direction.

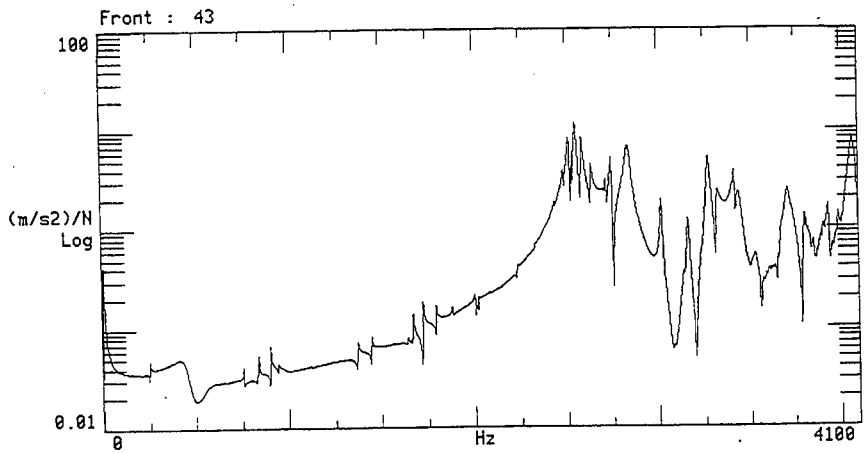

Figure 4, Frequency response of the compressor shell when excited in Z direction.

To verify the hypothesis that resonances were contributing to some of the noise problems of the reciprocating piston compressor, a modal analysis of the shell and interior cavity was performed.

For the shell modal analysis, the accelerometer to measure the response remained stationary, while the impact location was moved. The test was performed in this manner for convenience since it was easier to fix the accelerometer in one location and strike the compressor with force hammer at each grid point to obtain transfer function for each measurement location. Identical results are obtained if impact occurred at a single point and the response was measured at each measurement location. Preliminary test were performed initially to identify an appropriate measurement location at which all important natural frequencies of shell are detectable. Several force input and response locations were evaluated to determine the best location to mount accelerometer to measure the shell response.

The shell resonances are also calculated by using the Structural FEM analysis. Table-1 lists the natural frequencies predicted in these studies. During the finite element analysis, the models of the compressor were built, based on the CAD models. The shell consists of 7500 elements. The mesh densities are quite adequate for the structural analysis in the frequency range of interest. In order to investigate the possible influence of the crank mechanism on the natural frequencies of the shell, a simple model of the crank mechanism was introduced to the FE model. During the calculations, the crank mechanism was simplified as a rigid block with certain mass and rotary inertia and modeled with solid elements. The shell and the crank mechanism have been suspended with the

springs from 3 positions and in all 6 transitional and rotational directions. Depending on the negligible spring effect on the longitudinal direction, estimated values have been used in 5 directions. The FE model has been assumed to be free-free.

Mode #	Frequency Hz	Mode #	Frequency Hz
1	1997	21	4716
2	2027	22	4925
3	2293	23	4994
4	2418	24	5110
5	2605	25	5159
6	2754	26	5454
7	2889	27	5476
8	3258	28	5738
9	3332	29	5761
10	3336	30	5783
11	3376	31	5936
12	3551	32	5999
13	3577	33	6035
14	3606	34	6055
15	3788	35	6183
16	3958	36	6237
17	4383	37	6314
18	4481	38	6318
19	4644	39	6670
20	4702	40	6701

Table-1, Calculated Natural Frequencies of the Shell

Figures 5, 6, 7 and 8 illustrate how the mode shapes of the shell vary at the mode frequencies of 2754, 3332, 3551 and 3788 Hz . These figures indicate that the shell vibrates predominantly along the large flat sides of the compressor at points where the suspension springs are attached to the shell wall at these natural frequencies. When referred to figure 1 of the noise radiation this frequency range is also the range where the noise radiates efficiently from the large flat sides of the compressor. Thus, there is good correlation between the acoustic data and structural data for these frequencies. The slight discrepancies in the structural natural frequencies and the acoustic data. Acoustic data have been picked up at the shell temperature of the reciprocating piston compressor that could reach up to 110^{0} C.

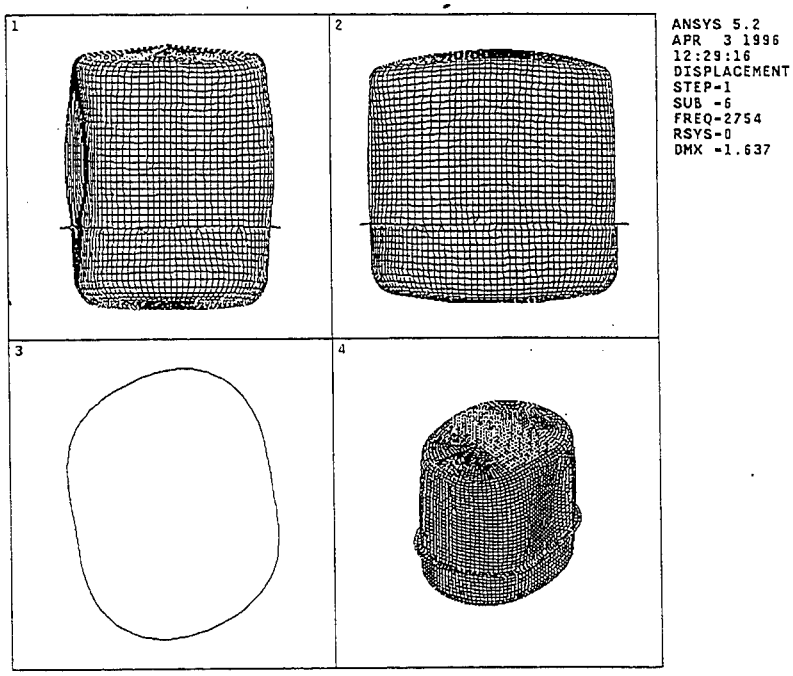

Figure 5, Predicted mode shape at 2754 Hz.

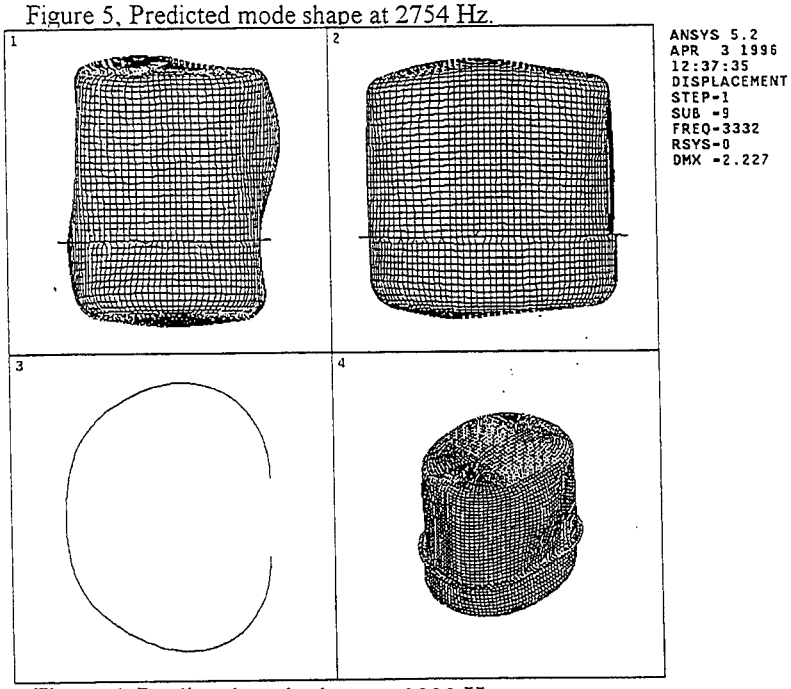

Figure 6, Predicted mode shape at 3332 Hz.

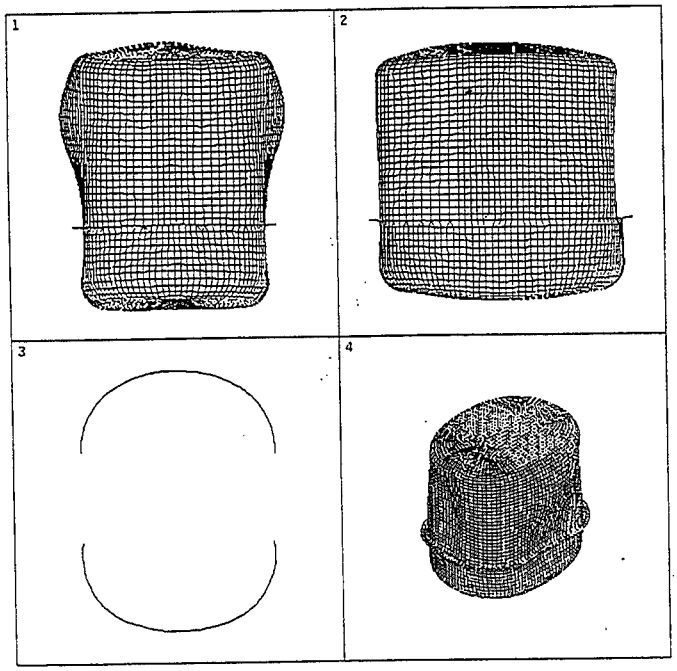

Figure 7, Predicted mode shape at 3551 Hz.

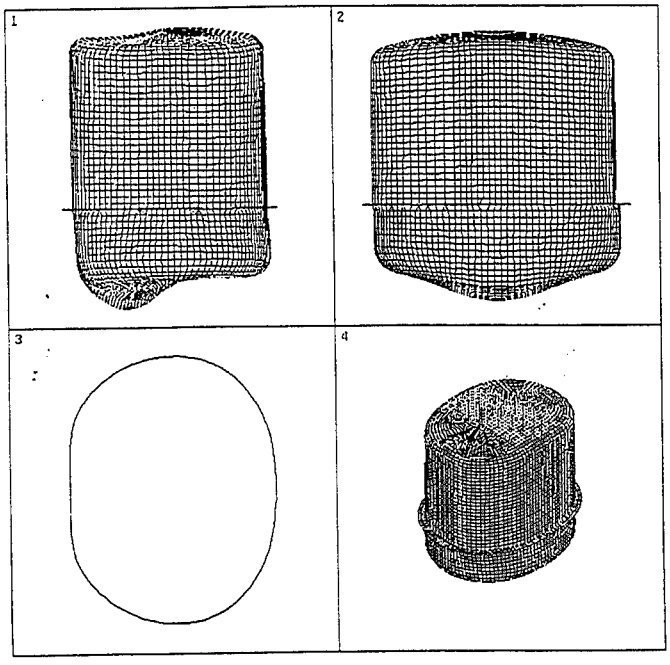

Figure 8, Predicted mode shape at 3788 Hz

The modal analysis results also indicate that the compressor suspension springs are attached to a point on the shell where the shell is comparatively compliant. Thus, the vibrational energy transmitted through the springs to the compressor shell can and did effectively excite the shell vibrations. Also, significant shell vibrations occur along the large flat sides of the compressor shell indicating the curvature of the shell needs to be increased to add stiffness to the shell.

Based on the results of the shell modal analysis, it is recommended the suspension springs moved away from the compliant side walls of the shell. A four spring arrangement at the bottom of the shell near corners where the curvature is sharp would reduce the amount of vibration energy transferred to the shell because of the reduced input mobility of the shell at these locations.

It is also believed increasing the stiffness of the shell by increasing the curvature will provide noise reduction benefits. The greater shell stiffness lowers the amplitude of the shell vibrations. Figure 9, illustrate the third octave change in compressor noise with the same compressor in the new shell. An over all noise level of 5 dBA has been obtained.

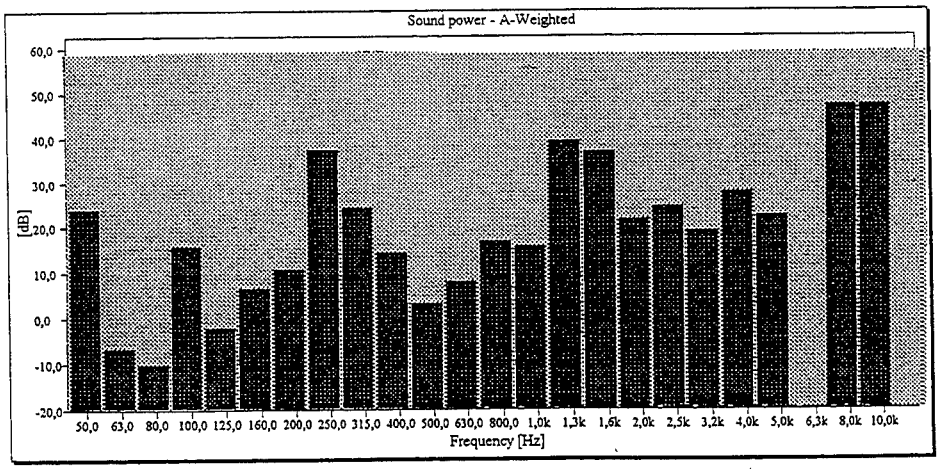

Figure 9 Compressor noise level improvement after the shell modification.

The increased shell stiffness also raises the natural frequencies of the shell where there is less energy for transfer function response. However, there is a possible disadvantage to increasing stiffness of the shell. The higher natural frequency lowers critical frequency of the shell thus reducing transmission loss of the shell.

Damping treatments can also have obvious benefits in vibration and noise reduction. Visco elastic and Acoustic dampings are considered to avoid the shell excitations. The application of dampers can also provide up to 5 dBA reductions when appropriately located on the shell.

CONCLUSION

The results of studies indicate that structural resonances of the shell are indeed amplifying the noise due to the pumping harmonics of the reciprocating refrigeration compressor to cause significant noise radiation outside of compressor.

In order to tackle with this noise problem, within the scope of these studies two different effective shell noise control are considered based on the results of numerical and experimental structural analysis and acoustic features of the reciprocating compressor. First, shell noise control method is the redesign of the shell with increased stiffness by replacing all the abrupt changes in the curvature with the smooth continuous changes. It is apparent that change in the shell configuration can shift the first shell resonance from 1750 Hz to nearly 3200 Hz. The results of the redesign effects can reach up to 3-5 dBA reduction on third octave noise levels. Second treatment that could be applied against the excitation of shell resonances are considered as the acoustic and viscoelastic dampers. These dampers can be chosen to operate efficiently at the shell resonant frequencies. These two applications can also provide up to 2-5 dBA reduction on the third octave band of the noise emission but the long term endurance and temperature dependence of these materials can always be a question mark when considered from the manufacturer point of view.

REFERENCES

1. J FROBATTA and J D.JONES 1991, *Purdue University, School of Mechanical Engineering, The Ray Herrick Laboratories,* Report no: 1912-1 HL 91-9P, 73-84, Investigation of Noise Generation Mechanisms and Transmission Paths of Fractional Horsepower Reciprocating Piston and Rolling Piston Compressors
2. HAMILTON J F 1988, *Purdue University , School of Mechanical Engineering, The Ray Herrick Laboratories,* 207-213 Measurement and Control of Compressor Noise
3. C ÖZTÜRK, A AÇIKGÖZ and J L MIGEOT 1996, *International Compressor Engineering Conference at Purdue, Conference Proeceeding , Volume II,* 697-703, Radiation Analysis of the Reciprocating Refrigeration Compressor Casing

A COMPARATIVE STUDY OF MOVING FORCE IDENTIFICATION

T.H.T. Chan, S.S. Law, T.H. Yung
Department of Civil & Structural Engineering,
The Hong Kong Polytechnic University, Hung Hom, Kowloon, Hong Kong

ABSTRACT

Traditional ways to acquire truck axle and gross weight information are expensive and subject to bias, and this has led to the development of Weigh-in-Motion (WIM) techniques. Most of the existing WIM systems have been developed to measure only the static axle loads. However dynamic axle loads are also important. Some systems use instrumented vehicles to measure dynamic axle loads, but are subject to bias. These all prompt the need to develop a system to measure the dynamic axle loads using an unbiased random sample of vehicles. This paper aims to introduce four methods in determining such dynamic forces from bridge responses. The four methods are compared with one another based on maximum number of forces to be identified, minimum number of sensors, sensitivity towards noise and the computation time. It is concluded that acceptable estimates could be obtained by all the four methods. Further work includes merging the four methods into a Moving Force Identification System (MFIS).

INTRODUCTION

The truck axle and gross weight information have application in areas such as the structural and maintenance requirements of bridges and pavements. However, the traditional ways to acquire that are expensive and subject to bias, and this has led to the development of Weigh-in-Motion (WIM) techniques. Some systems are road-surface systems which make use of piezo-electric (pressure electricity) or capacitive properties to develop a plastic mat or capacitive sensors to measure axle weight [1]. Another kind of WIM system is the under-structure systems in which sensors are installed under a bridge or a culvert and the axle loads are computed from the measured responses e.g. AXWAY [2] and CULWAY [3]. All the above mentioned systems can only give the equivalent static axle loads. However dynamic axle loads are also important as they may increase road surface damage by a factor of 2 to 4 over that caused by static loads [4]. Some systems use instrumented vehicles to measure dynamic axle loads [5], but are subject to bias. These all prompt the need to develop a system to measure the dynamic axle loads using unbiased random samples of vehicles. Four methods are developed to determine such

dynamic forces from bridge responses which include bending moments or accelerations.

EQUATION OF MOTIONS FOR MOVING LOADS

The moving force identification methods described in this paper are the inverse problems of an predictive analysis which is defined by O'Connor and Chan [6] as an analysis to simulate the structural response caused by a set of time-varying forces running across a bridge. Two models can be used for this kind of analysis.

A. Beam-Elements Model

O'Connor and Chan [6] model the bridge as an assembly of lumped masses interconnected by massless elastic beam elements as shown in Figure 1, and the nodal responses for displacement or bending moments at any instant are given by Equations (1) and (2) respectively.

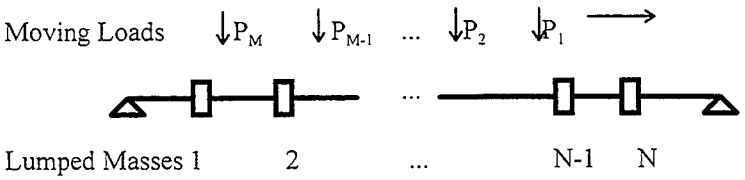

Figure 1 - Beam-Elements Model

$$\{Y\} = [Y_A]\{P\} - [Y_I][\Delta m]\{\ddot{Y}\} - [Y_I][C]\{\dot{Y}\} \quad (1)$$

$$\{BM\} = [BM_A]\{P\} - [BM_I][\Delta m]\{\ddot{Y}\} - [BM_I][C]\{\dot{Y}\} \quad (2)$$

where $[P]$ is a vector of wheel loads, $[\Delta m]$ is a diagonal matrix containing values of lumped mass, [C] is the damping matrix, $BM, Y, \dot{Y}, \ddot{Y}$ are the nodal bending moments, displacements, velocities and accelerations respectively, $[R_A]$ ('R' can be Y or BM) is an m x n matrix with the ith column representing the nodal responses caused by a unit load acting at the position of the ith wheel load and $[R_I]$ ('R' can be Y or BM) is an n x n matrix with the ith column representing the nodal responses caused by a unit load acting at the position of ith internal node.

B. Continuous Beam Model

Assuming the beam is of constant cross-section with constant mass per unit length, having linear, viscous proportional damping and with small deflections, neglecting the effects of shear deformation and rotary inertia (Bernoulli-Euler's beam), and the force is moving from left to right at a constant speed c, as shown in Figure 2, then the equation of motion can be written as

$$\rho\frac{\partial^2 v(x,t)}{\partial t^2} + C\frac{\partial v(x,t)}{\partial t} + EI\frac{\partial^4 v(x,t)}{\partial x^4} = \delta(x-ct)f(t) \tag{3}$$

where $v(x,t)$ is the beam deflection at point x and time t; ρ is mass per unit length; C is viscous damping parameter; E is Young's modulus of material; I is the second moment of inertia of the beam cross-section; $f(t)$ is the time-varying force moving at a constant speed of c, and $\delta(t)$ is Dirac delta function.

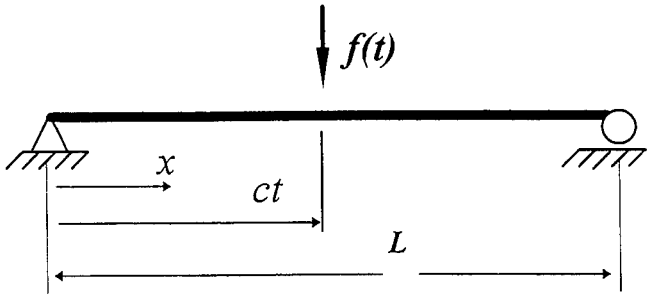

Figure 2 - Simply supported beam subjected to a moving force $f(t)$

Based on modal superposition, the dynamic deflection $v(x,t)$ can be described as follows:

$$v(x,t) = \sum_{n=1}^{\infty} \Phi_n(x) q_n(t) \tag{4}$$

where n is the mode number; $\Phi_n(x)$ is the mode shape function of the n-th mode and $q_n(t)$ is the n-th modal amplitudes.

Based on the above mentioned predictive analyses, four Moving Force Identification Methods (MFIM) are developed.

FIRST MOVING FORCE IDENTIFICATION METHOD INTERPRETIVE METHOD I - BEAM-ELEMENTS MODEL (IMI)

It is an inverse problem of the predictive analysis using beam-elements model. From Equation (1), it can be seen that if Y is known at all times for all interior nodes, then $\dot{Y}$ and $\ddot{Y}$ can be obtained by numerical differentiation. Equation (1) becomes an overdetermined set of linear simultaneous equations in which the P may be solved for them. However a particular difficulty arises if measured BM are used as input data. Remembering that the moving loads P are not normally at the nodes, the relation between nodal displacements and nodal bending moments is

$$\{Y\} = [Y_B]\{BM\} + [Y_C]\{P\} \tag{5}$$

where $[Y_C]\{P\}$ allows for the deflections due to the additional triangular bending moment diagrams that occur within elements carrying one or more point loads P. $[Y_c]$ can be calculated from the known locations of the loads. $[Y_B]$ and $\{BM\}$ are known, but $\{Y\}$ cannot be determined without a knowledge of $\{P\}$. O'Connor and Chan [6] describe a solution uses values of $\{P\}$ assumed from the previous time steps.

SECOND MOVING FORCE IDENTIFICATION METHOD INTERPRETIVE METHOD II - CONTINUOUS BEAM MODEL (IMII)

From the predictive analysis using continuous beam model, if the ith-mode shape function of the simply supported Euler's beam is $\sin\frac{i\pi x}{L}$, then the solution of Equation (3) takes the form

$$v = \sum_{i=1}^{\infty} \sin\frac{i\pi x}{L} V_i(t) \tag{6}$$

where $V_i(t)$, $(i = 1, 2, \cdots)$ are the modal displacements.

Substitute Equation (6) into Equation (3), and multiply each term of Equation (3) by the mode shape function $\sin(j\pi x / L)$, and then integrate the resultant equation with respect to x between 0 and L and use the boundary conditions and the properties of Dirac function. Consequently, the following equation can be obtained

$$\ddot{V}_j(t) + 2\zeta_j \omega_{(j)} \dot{V}_j(t) + \omega_{(j)}^2 V_j(t) = \frac{2P}{\mu L} \sin j\omega t \qquad j = 1,2,\cdots \qquad (7)$$

where $\omega_{(j)}^2 = \dfrac{j^4\pi^4}{L^4}\dfrac{EI}{\mu}$ $\qquad \zeta_{(j)} = \dfrac{C}{2\mu\omega_{(j)}}$ at the j-th mode.

If there are more than one moving loads on the beam, Equation (7) can be written as

$$\begin{bmatrix} \ddot{V}_1 \\ \ddot{V}_2 \\ \vdots \\ \ddot{V}_n \end{bmatrix} + \begin{bmatrix} 2\zeta_1\omega_1\dot{V}_1 \\ 2\zeta_2\omega_2\dot{V}_2 \\ \vdots \\ 2\zeta_n\omega_n\dot{V}_n \end{bmatrix} + \begin{bmatrix} \omega_1^2 V_1 \\ \omega_2^2 V_2 \\ \vdots \\ \omega_n^2 V_n \end{bmatrix} = \frac{2}{\mu l} \begin{bmatrix} \sin\dfrac{\pi(ct-\hat{x}_1)}{L} & \sin\dfrac{\pi(ct-\hat{x}_2)}{L} & \cdots & \sin\dfrac{\pi(ct-\hat{x}_k)}{L} \\ \sin\dfrac{2\pi(ct-\hat{x}_1)}{L} & \sin\dfrac{2\pi(ct-\hat{x}_2)}{L} & \cdots & \sin\dfrac{2\pi(ct-\hat{x}_k)}{L} \\ \vdots & \vdots & \vdots & \vdots \\ \sin\dfrac{n\pi(ct-\hat{x}_1)}{L} & \sin\dfrac{n\pi(ct-\hat{x}_2)}{L} & \cdots & \sin\dfrac{n\pi(ct-\hat{x}_k)}{L} \end{bmatrix} \begin{bmatrix} P_1 \\ P_2 \\ \vdots \\ P_k \end{bmatrix} \qquad (8)$$

in which $\hat{x}_k$ is the distance between the k-th load and the first load and $\hat{x}_1 = 0$.

If $P_1, P_2, \ldots, P_k$ are constants, the closed form solution of Equation (3) is

$$v(x,t) = \frac{l^3}{48EI} \sum_{i=1}^{k} P_i \sum_{j=1}^{\infty} \frac{1}{j^2(j^2-\alpha^2)} \sin\frac{j\pi x}{L} \left(\sin\frac{j\pi(ct-\hat{x}_i)}{L} - \frac{\alpha}{j} \sin\omega_{(j)}(t-\hat{x}_i/c) \right) \qquad (9)$$

in which $\alpha = \dfrac{\pi c}{L\omega}$.

If we know the displacements of the beam at $x_1, x_2, \cdots, x_l$, the moving loads on the beam are given by

$$\{v\} = [S_{vp}]\{P\} \qquad (10)$$

in which $\{v\} = [v_1 \quad v_2 \quad \cdots \quad v_l]^T \qquad \{P\} = [P_1 \quad P_2 \quad \cdots \quad P_k]$

$$[S_{vp}] = \begin{bmatrix} s_{11} & \cdots & \cdots & \cdots & s_{1k} \\ \vdots & \ddots & & & \vdots \\ s_{m1} & & s_{mi} & & s_{mk} \\ \vdots & & & \ddots & \vdots \\ s_{l1} & \cdots & \cdots & \cdots & s_{lk} \end{bmatrix}, \quad \text{where}$$

$$s_{mi} = \frac{L^3}{48EI} \sum_{j=1}^{\infty} \frac{1}{j^2(j^2-\alpha^2)} \sin\frac{j\pi x_m}{L} \left(\sin\frac{j\pi(ct-\hat{x}_i)}{L} - \frac{\alpha}{j} \sin\omega_{(j)}(t-\hat{x}_i/c) \right)$$

If $l \geq k$, that means the number of nodal displacements is larger than or equal to the number of axle loads, then according to the least squares method, the equivalent static axle load can be given by

$$\{P\} = \left(\left[S_{vP}\right]^T \left[S_{vP}\right]\right)^{-1} \left[S_{vP}\right]^T \{v\} \tag{11}$$

If the loads are not constant with time, then central difference is used to proceed from modal displacements to modal velocities and accelerations. Equation (8) becomes a set of linear equations in which P_k for any instant can be solved by least squares method. Similar sets of equations could be obtained for using bending moments to identify the moving loads.

THIRD MOVING FORCE IDENTIFICATION METHOD TIME DOMAIN METHOD (TDM)

This method is based on the system identification theory [7]. Substituting Equation (4) into Equation (3), and multiplying each term by $\Phi_j(x)$, integrating with respect to x between 0 and L, and applying the orthogonality conditions, then

$$\frac{\mathrm{d}^2 q_n(t)}{\mathrm{d}t^2} + 2\xi_n \omega_n \frac{\mathrm{d}q_n(t)}{\mathrm{d}t} + \omega_n^2 q_n(t) = \frac{1}{M_n} p_n(t) \tag{12}$$

where ω_n is the modal frequency of the n-th mode; ξ_n is the damping ratio of the n-th mode; M_n is the modal mass of the n-th mode, $p_n(t)$ is the modal force and the mode shape function can be assumed as $\Phi_n(x) = \sin(n\pi x / L)$.

Equation (12) can be solved in the time domain by the convolution integral, and yields

$$q_n(t) = \frac{1}{M_n} \int_0^t h_n(t-\tau) p(\tau) \mathrm{d}\tau \tag{13}$$

$$\text{where } h_n(t) = \frac{1}{\omega_n'} \mathrm{e}^{-\xi_n \omega_n t} \sin(\omega_n' t), \qquad t \geq 0 \tag{14}$$

$$\text{and } \omega_n' = \omega_n \sqrt{1-\xi_n^2} \tag{15}$$

Substituting Equation (13) into Equation (4), the dynamic deflection of the beam at point x and time t can be found as

$$v(x,t) = \sum_{n=1}^{\infty} \frac{2}{\rho L \omega_n'} \sin\frac{n\pi x}{L} \int_0^t \mathrm{e}^{-\xi_n \omega_n (t-\tau)} \sin\omega_n'(t-\tau) \sin\frac{n\pi c \tau}{L} f(\tau) \mathrm{d}\tau \tag{16}$$

A. Force Identification from Bending Moments

The bending moment of the beam at point x and time t is

$$m(x,t) = -EI\frac{\partial^2 v(x,t)}{\partial x^2} \tag{17}$$

Substituting Equation (16) into Equation (17), and assuming the force $f(t)$ is a step function in a small time interval and $f(t)$ =0 at the entry and exit, then let

$$C_{xn} = \frac{2EI\pi^2}{\rho L^3}\frac{n^2}{\omega_n^{'}}\sin\frac{n\pi x}{L}\Delta t, \tag{18}$$

$$\begin{aligned} &\mathrm{E_n}^{\mathrm{k}} = \mathrm{e}^{-\xi_n\omega_n\Delta tk}, \\ &S_1(k) = \sin(\omega_n^{'}\Delta tk), \\ &S_2(k) = \sin(\frac{n\pi c\Delta t}{L}k) \\ &N_B = \frac{L}{c\Delta t} \end{aligned} \tag{19}$$

Equation (17) can be expressed as

$$\begin{Bmatrix} m(2) \\ m(3) \\ \vdots \\ m(N) \end{Bmatrix} = \sum_{n=1}^{\infty} C_{xn} \begin{bmatrix} E_n^1 S_1(1)S_2(1) & 0 & \cdots & 0 \\ E_n^2 S_1(2)S_2(1) & E_n^1 S_1(1)S_2(2) & \cdots & 0 \\ \vdots & \vdots & \vdots & \vdots \\ E_n^{N-1} S_1(N-1)S_2(1) & E_n^{N-2} S_1(N-2)S_2(2) & \cdots & b_{cc} \end{bmatrix} \begin{Bmatrix} f(1) \\ f(2) \\ \vdots \\ f(N_B-1) \end{Bmatrix} \tag{20}$$

where Δt is the sample interval and $N+1$ is the number of sample points, and

$$b_{cc} = E_n^{N-N_B+1} S_1(N-N_B+1)S_2(N_B-1)$$

Equation (20) can be simplified as

$$\underset{(N-1)\times(N_B-1)}{\mathbf{B}} \quad \underset{(N_B-1)\times 1}{\mathbf{f}} = \underset{(N-1)\times 1}{\mathbf{m}} \tag{21}$$

If $N = N_B$, matrix **B** is a lower triangular matrix. We can directly find the force vector **f** by solving Equation (21). If $N > N_B$, and/or N_l bending moments ($N_l > 1$) are measured, least squares method can be used to find the force vector **f** from

$$\begin{bmatrix} \mathbf{B}_1 \\ \mathbf{B}_2 \\ \vdots \\ \mathbf{B}_{N_t} \end{bmatrix} \mathbf{f} = \begin{Bmatrix} \mathbf{m}_1 \\ \mathbf{m}_2 \\ \vdots \\ \mathbf{m}_{N_t} \end{Bmatrix} \tag{22}$$

The above procedure is derived for single force identification. Equation (21) can be modified for two-forces identification using the linear superposition principle as

$$\begin{bmatrix} \mathbf{B}_a & \mathbf{0} \\ \mathbf{B}_b & \mathbf{B}_a \\ \mathbf{B}_c & \mathbf{B}_b \end{bmatrix} \begin{Bmatrix} \mathbf{f}_1 \\ \mathbf{f}_2 \end{Bmatrix} = \mathbf{m} \tag{23}$$

where $\mathbf{B}_a$ $[N_s \times (N_B - 1)]$, $\mathbf{B}_b$ $[(N - 1 - 2N_s) \times (N_B - 1)]$, and $\mathbf{B}_c$ $[N_s \times (N_B - 1)]$ are sub-matrices of matrix **B.** The first row of sub-matrices in the first matrix describes the state having the first force on beam after its entry. The second and third rows of sub-matrices describe the states having two-forces on beam and one force on beam after the exit of the first force.

B. Identification from Bending Moments and Accelerations

Similarly the acceleration response of the beam can be expressed as

$$\underset{N \times (N_B - 1)(N_B - 1) \times 1}{\mathbf{A}} \quad \underset{}{\mathbf{f}} = \underset{N \times 1}{\ddot{\mathbf{v}}} \tag{24}$$

The force can also be found from the measured acceleration from Equation (24). If the bending moments and accelerations responses are measured at the same time, both of them can be used together to identify the moving force. The vector **m** in Equation (21) and $\ddot{\mathbf{v}}$ in Equation (24) should be scaled to have dimensionless unit, and the two equations are then combined together to give

$$\begin{bmatrix} \mathbf{B} / \|\mathbf{m}\| \\ \mathbf{A} / \|\ddot{\mathbf{v}}\| \end{bmatrix} \mathbf{f} = \begin{Bmatrix} \mathbf{m} / \|\mathbf{m}\| \\ \ddot{\mathbf{v}} / \|\ddot{\mathbf{v}}\| \end{Bmatrix} \tag{25}$$

where $\|\bullet\|$ is the norm of the vector.

FOURTH MOVING FORCE IDENTIFICATION METHOD FREQUENCY DOMAIN METHOD (FDM)

Equation (12) can also be solved in the Frequency Domain. Performing the Fourier Transform for Equation (12),

$$Q_n(\omega) = \frac{1}{\omega_n^2 - \omega^2 + 2\xi_n \omega_n \omega} \frac{1}{M_n} P_n(\omega) \tag{26}$$

where

$$P_n(\omega) = \frac{1}{2\pi} \int_{-\infty}^{\infty} p_n(t) e^{-i\omega t} dt \tag{27}$$

$$Q_n(\omega) = \frac{1}{2\pi} \int_{-\infty}^{\infty} q_n(t) e^{-i\omega t} dt \tag{28}$$

Let $$H_n(\omega) = \frac{1}{\omega_n^2 - \omega^2 + 2\xi_n \omega_n \omega} \tag{29}$$

$H_n(\omega)$ is the frequency response function of the n-th mode. Performing the Fourier Transform of Equation (4), and substituting Equations (26) and (29) into the resultant equation, the Fourier Transform of the dynamic deflection $v(x,t)$ is obtained as

$$V(x,\omega) = \sum_{n=1}^{\infty} \frac{1}{M_n} \Phi_n(x) H_n(\omega) P_n(\omega) \tag{30}$$

A. Force Identification from Accelerations

Based on Equation (30), the Fourier Transform of the acceleration of the beam at point x and time t can be written as

$$\ddot{V}(x,\omega) = -\omega^2 \sum_{n=1}^{\infty} \frac{1}{M_n} \Phi_n(x) H_n(\omega) P_n(\omega) \tag{31}$$

Considering the periodic property of the Discrete Fourier Transform (DFT), and let

$$\overline{H}_{xn}(m) = -\frac{\Delta f^3 m^2}{M_n} \Phi_n(x) H_n(m) \tag{32}$$

Equation (32) can be rewritten as

$$\ddot{V}(m) = \sum_{n=1}^{\infty} \overline{H}_{xn}(m)\Psi_n(m)\left[F_R(0) + \mathrm{i}F_I(0)\right]$$
$$+ \sum_{k=1}^{N/2-1} \sum_{n=1}^{\infty} \overline{H}_{xn}(m)[\Psi_n(m-k) + \Psi_n(m+k-N)]F_R(k)$$
$$+\mathrm{i} \sum_{k=1}^{N/2-1} \sum_{n=1}^{\infty} \overline{H}_{xn}(m)[\Psi_n(m-k) - \Psi_n(m+k-N)]F_I(k) \qquad , m = 0,1, \ldots, N\text{-}1 \quad (33)$$
$$+\sum_{n=1}^{\infty} \overline{H}_{xn}(m)\Psi_n(m-N/2)\left[F_R(N/2) - \mathrm{i}F_I(N/2)\right]$$

where Ψ_n is the Fourier Transform of the n-th mode shape, and F is the Fourier Transform of the moving force.

Writing Equation (33) into matrix form and dividing F and $\ddot{\mathrm{V}}$ into real and imaginary parts, it yields

$$\underset{(N+2)\times 1}{\begin{Bmatrix} \ddot{\mathbf{V}}_{\mathbf{R}} \\ \ddot{\mathbf{V}}_{\mathbf{I}} \end{Bmatrix}} = \underset{(N+2)\times(N+2)}{\begin{bmatrix} \mathbf{A}_{\mathbf{RR}} & -\mathbf{A}_{\mathbf{II}} \\ \mathbf{A}_{\mathbf{RI}} & \mathbf{A}_{\mathbf{IR}} \end{bmatrix}} \underset{(N+2)\times 1}{\begin{Bmatrix} \mathbf{F}_{\mathbf{R}} \\ \mathbf{F}_{\mathbf{I}} \end{Bmatrix}} \qquad (34)$$

Because $F_I(0) = 0, F_I(N/2) = 0, \ddot{V}_I(0) = 0, \ddot{V}_I(N/2) = 0$, Equation (34) can be condensed into a set of N order simultaneously equations as

$$\ddot{\mathbf{V}}_{\mathbf{RI}} = \mathbf{A}_{\mathbf{D}}\mathbf{F}_{\mathbf{RI}} \qquad (35)$$

$\mathbf{F}_{\mathbf{R}}$ and $\mathbf{F}_{\mathbf{I}}$ can be found from Equation (35) by solving the *Nth* order linear equation. The time history of the moving force *f(t)* can then be obtained by performing the inverse Fourier Transformation.

If the DFTs are expressed in matrix form, the Fourier Transform of the force vector **f** can be written as follows if the terms in **f** are real [8].

$$\mathbf{F} = \frac{1}{N}\mathbf{W}\mathbf{f} \qquad (36)$$

$$\text{where } \mathbf{W} = e^{-\mathrm{i}2\mathbf{k}\pi/N} \qquad (37)$$

$$\mathbf{k} = \begin{bmatrix} 0 & 0 & 0 & \cdots & 0 & 0 \\ 0 & 1 & 2 & \cdots & -2 & -1 \\ 0 & 2 & 4 & \cdots & -4 & -2 \\ \vdots & \vdots & \vdots & & \vdots & \vdots \\ 0 & -2 & -4 & \cdots & 4 & 2 \\ 0 & -1 & -2 & \cdots & 2 & 1 \end{bmatrix}_{N \times N}$$

The matrix **W** is an unitary matrix, which means

$$\mathbf{W}^{-1} = (\mathbf{W}^{*})^{T} \tag{38}$$

where **W*** is a conjugate of **W**. Substituting Equation (36) into Equation (35),

$$\ddot{\mathbf{V}} = \frac{1}{N}\mathbf{A}\begin{bmatrix} \underset{N \times N_B}{\mathbf{W_B}} & \mathbf{0} \end{bmatrix}\begin{Bmatrix} \mathbf{f_B} \\ \mathbf{0} \end{Bmatrix} \tag{39}$$

or

$$\underset{N \times 1}{\ddot{\mathbf{V}}} = \frac{1}{N}\underset{N \times N}{\mathbf{A}}\ \underset{N \times N_B}{\mathbf{W_B}}\ \underset{N_B \times 1}{\mathbf{f_B}} \tag{40}$$

linking the Fourier Transform of acceleration $\ddot{V}$ with the force vector $\mathbf{f_B}$ of the moving forces in the time domain. $\mathbf{W_B}$ is the sub-matrix of **W**. If $N = N_B$, $\mathbf{f_B}$ can be found by solving the Nth order linear equations. If $N > N_B$ or more than one accelerations are measured, the least squares method can be used to find the time history of the moving force $f(t)$.

Equation (40) can be rewritten as follows

$$\underset{N \times 1}{\ddot{\mathbf{v}}} = \left(\underset{N \times N}{\mathbf{W}^{*}}\right)^{T}\underset{N \times N}{\mathbf{A}}\ \underset{N \times N_B}{\mathbf{W_B}}\ \underset{N_B \times 1}{\mathbf{f_B}} \tag{41}$$

relating the accelerations and force vectors in the time domain. Also if $N = N_B$, $\mathbf{f_B}$ can be found by solving the Nth order linear equation. If $N > N_B$ or more than one acceleration are measured, the least squares method can be used to find the time history of the moving force $f(t)$.

If only N_C ($N_C \leq N$) response data points of the beam are used, the equations for these data points in Equation (41) are extracted, and described as

$$\underset{N_C \times 1}{\ddot{\mathbf{v}}_{\mathbf{C}}} = \left(\underset{N_C \times N}{\mathbf{W}_{\mathbf{B}}^{*}}\right)^{T}\underset{N \times N}{\mathbf{A}}\ \underset{N \times N_B}{\mathbf{W_B}}\ \underset{N_B \times 1}{\mathbf{f_B}} \tag{42}$$

In usual cases $N_C > N_B$, so the least squares method is used to find the time history of the moving force *f(t)*. More than one acceleration measurements at different locations can be used together to identify a single moving force for higher accuracy.

B. Identification from Bending Moments and Accelerations

Similarly, the relationships between bending moment **m** (and M) and the moving force **f** can be described as follows,

$$\underset{N\times 1}{\mathbf{M}} = \frac{1}{N} \underset{N\times N}{\mathbf{B}} \underset{N\times N_B}{\mathbf{W}} \underset{N_B\times 1}{\mathbf{f}_B} \tag{43}$$

$$\underset{N\times 1}{\mathbf{m}} = \underset{N\times N}{\left(\mathbf{W}^*\right)^T} \underset{N\times N}{\mathbf{B}} \underset{N\times N_B}{\mathbf{W}_B} \underset{N_B\times 1}{\mathbf{f}_B} \tag{44}$$

$$\underset{N_C\times 1}{\mathbf{m}_B} = \underset{N_C\times N}{\left(\mathbf{W}^*\right)^T} \underset{N\times N}{\mathbf{B}} \underset{N\times N_B}{\mathbf{W}_B} \underset{N_B\times 1}{\mathbf{f}_B} \tag{45}$$

The force vector $\mathbf{f}_B$ can be obtained from the above three sets of equations. Furthermore, these equations can be combined with Equations (40), (41) and (42) to construct overdetermined equations before the equations are scaled. Two forces identification are developed using the similar procedure as that for the Time Domain Method.

COMPARATIVE STUDY

The first moving force identification method is implemented in a computer program using FORTRAN, while the other three methods are implemented under the environment of a high performance numerical computation and visualization software. The predictive analysis using beam-elements model is used to generate the theoretical bridge responses and the four moving force identification methods then use these responses to recover the original dynamic loads. In this study, if at least 80% of the identified forces at any instant of any load lie within ± 10% of the original input force, the method is considered acceptable. It is found that all the four methods can give acceptable results.

It is decided to carry out a preliminary comparative study on the four methods in order to study the merits and limitations of each method so as to consider the future development of each method and devise a plan to develop a

moving force identification system which can make use of the benefits of all the four methods.

A. Maximum Number of Forces

This is to examine the maximum number of axle loads that can be identified by each method. Theoretically, provided that sufficient number of nodal sensors are installed, IMI and IMII can be used to identify as many loads as the system allows. Basically, the number of axle loads cannot be larger than the number of nodal sensors. Regarding TDM and FDM, as the formulation of the governing equation is derived for two moving forces, the maximum number of axle loads that can be identified is two.

B. Minimum Number of Sensors

Based on a study of common axle spacings of vehicles currently operating on Australian roads, and the cases with zero nodal responses, O'Connor and Chan [6] state the relationships of the minimum number of sensors used for IMI and the span length of a bridge as follows:

Using bending moment, for span length $L \geq 4.8$m,

$$\text{Min. number of nodal moments required} = INT\left(\frac{L-4.8}{1.7}\right)+4 \qquad (46)$$

Using displacements, for span length $L \geq 13.8$m,

$$\text{Min. number of nodal displacement required} = INT\left(\frac{L-13.8}{3.7}\right)+6 \qquad (47)$$

and for span length $L < 13.8$m,

$$\text{Min. number of nodal displacement required} = INT\left(\frac{L}{2.3}\right)-1 \qquad (48)$$

For IMII, it is found that the number of sensors required are generally less than that for IMI. Regarding TDM and FDM, the programs are not as flexible as that for IMI and IMII and it is not easy to change the number of sensors. Meanwhile the sensors are fixed to be at 1/4, 1/2 and 3/4 of the span.

C. Sensitivity towards Noise

In general, all the four methods can compute the identified forces exactly the same as those given to the predictive analysis to generate the corresponding responses. It is decided to add white noise to the calculated responses to simulate polluted measurements and to check their sensitivity towards noise. The polluted measurements are generated by the following

equations:

$$\mathbf{m} = \mathbf{m}_{\text{calculated}} + Ep \times \left\|\mathbf{m}_{\text{calculated}}\right\| \times \mathbf{N}_{\text{oise}} \tag{49}$$

where Ep is a specified error level; N_{oise} is a standard normal distribution vector (with zero mean value and unity standard deviation).

Several cases are studied using Ep =1%, 3%, 5% and 10%. It is found that when using bending moments for IMI and IMII, and if Ep is less than 3%, acceptable results can be obtained. For noise which is greater than 3%, a smoothing scheme should be adopted to smooth the simulated data. Acceptable results cannot be obtained for Ep > 10%. Besides, both IMI and IMII cannot give acceptable results when using displacements.

Both TDM and FDM cannot give acceptable results when using displacements only, accelerations only or bending moments only. In general TDM and FDM are less sensitive to noise when comparing to IMI and IMII. They can give acceptable results for Ep up to 5 % without any smoothing of the polluted simulated data.

D. Computation Time

In general, the computer program for IMI only takes few seconds to identify moving forces. In order to compare the computation time, IMI is implemented in the same environment as the other three methods. It is found that IMI and IMII take about 2-3 minutes to give the identified forces for a case of two axle loads using a 80486 computer. However, under the same working conditions, TDM and FDM almost take a whole day for any one of them to identify two moving forces. It is due to the fact that both of them require to set up an huge parametric matrix.

CONCLUSIONS

Four methods are developed to identify moving time-varying force and they all can produce acceptable results. From a preliminary comparative study of the methods, it is found that IMI and IMII have a wider applicability as the locations of sensors are not fixed and it can identify more than two moving forces. However, TDM and FDM are less sensitive to noise and require less number of sensors. It is decided to further improve the four methods and then a more detailed and systematic comparison can be carried out afterwards. The possible development of the methods are described as follows.

Both the IMI and IMII are developed to work with one kind of responses, e.g. either displacements or bending moments. It is suggested to modify the programs to use mixed input parameter, e.g. use bending moments as well as accelerations as that for TDM or FDM. Regarding the TDM and FDM, as the basic formulations are based on two-axle moving forces, so it is necessary to modify the governing equations for multi-axle. In addition, the computation time for TDM or FDM under the environment of the high performance numerical computation and visualization software used is unbearable. It is expected that the time will be significantly reduced if the methods are implemented in programs using standard programming languages like FORTRAN 90 or C. Then the four methods can be combined together and merged into a Moving Force Identification System (MFIS) so that it can automatically select the best solution routines for the identification.

ACKNOWLEDGMENT

The present project is funded by the Hong Kong Research Grants Council.

REFERENCES

1. Davis, P. and Sommerville, F., Low-Cost Axle Load Determination, Proceedings, 13th ARRB & 5th REAAA Combined Conference, 1986, Part 6, p 142-149.
2. Peters, R.J., AXWAY - a System to Obtain Vehicle Axle Weights, Proceedings, 12th ARRB Conference, 1984, 12 (2), p 10-18.
3. Peters, R.J., CULWAY - an Unmanned and Undetectable Highway Speed Vehicle Weighing System, Proceedings, 13th ARRB & 5th REAAA Combined Conference, 1986, Part 6, p 70-83.
4. Cebon, D. Assessment of the Dynamic Wheel Forces Generated by Heavy Vehicle Road Vehicles. Symposium on Heavy Vehicle Suspension Characteristics, ARRB, 1987.
5. Cantineni, R., Dynamic Behaviour of Highway Bridges Under The Passage of Heavy Vehicles. Swiss Federal Laboratories for Materials Testing and Research (EMPA) Report No. 220, 1992, 240p.
6. O'Connor, C. and Chan, T.H.T., Dynamic Wheel Loads from Bridge Strains. *Structural Engineering ASCE*, 114 (ST8), 1988, p.1703-1723.
7. Briggs, J.C. and Tse, M.K. Impact Force Identification using Extracted Modal Parameters and Pattern Matching, *International Journal of Impact Engineering*, 1992, Vol. 12, p361-372.
8. Bendat, J.S. and Piersol, J.S., *Engineering Application of Correlation and Spectral Analysis*. John Wiley & Sons, Inc. Second Edition, 1993.

ESTIMATING THE BEHAVIOUR OF A NONLINEAR EXPERIMENTAL MULTI DEGREE OF FREEDOM SYSTEM USING A FORCE APPROPRIATION APPROACH

P.A. Atkins & J.R.Wright
Dynamics and Control Research Group
School of Engineering, Simon Building, University of Manchester,
Oxford Road, Manchester. M13 9PL

ABSTRACT

The identification of nonlinear multi degree of freedom systems involves a significant number of nonlinear cross coupling terms, whether the identification is carried out in spatial or modal domains. One possible approach to reducing the order of each identification required is to use a suitable pattern of forces to drive any mode of interest. For a linear system, the force pattern required to drive a single mode is derived using a Force Appropriation method. This paper presents a method for determining the force pattern necessary to drive a mode of interest of a nonlinear system into the nonlinear region whilst the response is controlled to remain in proportion to the linear mode shape. Such an approach then allows the direct nonlinear modal terms for that mode to be identified using the Restoring Force method. The method for determining the relevant force patterns is discussed. The implementation of the method for experimental systems is considered and experimental results from a two degree of freedom 'benchmark structure' are presented.

INTRODUCTION

Force Appropriation [1] is used in the analysis of linear systems to determine the force patterns which will induce single mode behaviour when applied at the relevant natural frequency. This technique is used in the aerospace industry during Ground Vibration Tests: each normal mode of

a structure is excited using the derived force pattern and thus identified in isolation. Current practice, when the presence of nonlinearity is suspected, is to increase input force levels and monitor the variation of tuned frequencies. Some information about the type of nonlinearity present may be found, but no analytical model can be derived. Thus predictions for behaviour at higher levels of excitation are not possible.

A number of techniques for identifying nonlinearity, for example the Restoring Force method [2], have been demonstrated on systems with low numbers of degrees of freedom. Unfortunately, in practice, structures have a large number of degrees of freedom, often with a high modal density. A classical Restoring Force approach to the identification of such systems could involve a prohibitive number of cross coupling terms. The ability to treat each mode separately, by eliminating the effects of the cross coupling terms, would thus be advantageous. Subsequent tests could then evaluate the cross coupling terms.

For these reasons it would be useful to extend Force Appropriation to the identification of nonlinear systems. An approach has been developed [6] that allows an input force pattern to be derived that will result in a nonlinear response in the linear mode shape of interest. This force pattern is derived using an optimisation approach. The mode of interest can then be identified using a single degree of freedom nonlinear identification method. In this work the Restoring Force method is used to examine the nonlinear response of a particular linear mode and an application of this approach to a two degree of freedom experimental system is presented.

THEORY

The theoretical approach is demonstrated for the two degree of freedom system with spring grounded nonlinearity shown in figure 1. The equations of motion for this system in physical space are:

$$\begin{bmatrix} m & 0 \\ 0 & m \end{bmatrix} \begin{Bmatrix} \ddot{x}_1 \\ \ddot{x}_2 \end{Bmatrix} + \begin{bmatrix} (1+a)c & -ac \\ -ac & (1+a)c \end{bmatrix} \begin{Bmatrix} \dot{x}_1 \\ \dot{x}_2 \end{Bmatrix} + \begin{bmatrix} (1+a)k & -ak \\ -ak & (1+a)k \end{bmatrix} \begin{Bmatrix} x_1 \\ x_2 \end{Bmatrix} + \begin{bmatrix} \beta x_1^3 \\ 0 \end{bmatrix} = \begin{Bmatrix} f_1 \\ f_2 \end{Bmatrix} \quad (1)$$

where β is the cubic stiffness coefficient and a is a constant that allows the frequency spacing of the natural frequencies to be varied. These equations can be transformed to linear modal space using the transformation:

$$\{x\} = [\phi]\{u\} \quad (2)$$

where $[\phi]$ is the modal matrix of the underlying linear system and the vector $\{u\}$ defines the modal displacements. For this symmetrical system

the modal matrix is

$$[\phi] = \begin{bmatrix} 1 & 1 \\ 1 & -1 \end{bmatrix} \tag{3}$$

The equations of motion transformed to linear modal space using the normalised modal matrix are:

$$\begin{bmatrix} m & 0 \\ 0 & m \end{bmatrix} \begin{Bmatrix} \ddot{u}_1 \\ \ddot{u}_2 \end{Bmatrix} + \begin{bmatrix} c & 0 \\ 0 & (1+2a)c \end{bmatrix} \begin{Bmatrix} \dot{u}_1 \\ \dot{u}_2 \end{Bmatrix} + \begin{bmatrix} k & 0 \\ 0 & (1+2a)k \end{bmatrix} \begin{Bmatrix} u_1 \\ u_2 \end{Bmatrix} + \begin{bmatrix} \beta(u_1-u_2)^3/4 \\ \beta(u_1-u_2)^3/4 \end{bmatrix} = \begin{Bmatrix} p_1 \\ p_2 \end{Bmatrix} \tag{4}$$

where $\{p\}$ is the modal input vector. It can be seen from the above equations that the cubic nonlinearity couples the modes in linear modal space; in fact there are a significant number of terms for a single nonlinearity. The proposed method aims to determine the force pattern that will reduce the response of this system to that of a single mode.

It was shown in a previous paper [3] that this can be achieved by seeking a force vector that will cause motion only in the target mode, by eliminating motion in the coupled mode. In practice, physical data from transducers are available. Any subsequent transformations would be time consuming. It is shown below that causing motion in one mode to be zero is equivalent to forcing motion in a linear mode shape, mode one in this example. Consider the coordinate transformation $\{x\} = [\phi]\{u\}$ or more explicitly for the two degree of freedom system in Figure 1:

$$\begin{Bmatrix} x_1 \\ x_2 \end{Bmatrix} = \begin{bmatrix} 1 & -1 \\ 1 & 1 \end{bmatrix} \begin{Bmatrix} u_1 \\ u_2 \end{Bmatrix} \tag{5}$$

Thus

$$\begin{Bmatrix} u_1 \\ u_2 \end{Bmatrix} = \frac{1}{2} \begin{bmatrix} 1 & -1 \\ 1 & 1 \end{bmatrix} \begin{Bmatrix} x_1 \\ x_2 \end{Bmatrix} \tag{6}$$

and enforcing the first mode shape $(1,1)$ in physical space should give a second modal displacement of zero.

$$\frac{1}{2} \begin{bmatrix} 1 & -1 \\ 1 & 1 \end{bmatrix} \begin{Bmatrix} 1 \\ 1 \end{Bmatrix} = \begin{Bmatrix} 1 \\ 0 \end{Bmatrix} = \begin{Bmatrix} u_1 \\ u_2 \end{Bmatrix} \tag{7}$$

So if an excitation is applied which causes the nonlinear system to vibrate in its first linear mode shape, the response will be composed only of u_1 and the influence of the coupled mode, u_2, will then have been eliminated.

The method must therefore derive a force pattern which will cause the system to vibrate in one of its linear mode shapes. It has been shown

in a previous paper [3] that if the response contains harmonics then the force pattern must also contain harmonics in order to control the harmonic content of the response. In theory, the responses will be an infinite series of harmonics, but this series is truncated in this case of a cubic stiffness nonlinearity to include only the fundamental and third harmonic terms.

The physical input forces will thus be of the form:

$$f_1(t) = F_{11}\cos(\omega_{ex}t + \phi_{11}) + F_{13}\cos(\omega_{ex}t + \phi_{13}) \quad (8)$$

$$f_2(t) = F_{21}\cos(\omega_{ex}t + \phi_{21}) + F_{23}\cos(\omega_{ex}t + \phi_{23}) \quad (9)$$

where ω_{ex} is the excitation frequency. Parameters for these force patterns may then be chosen such that only mode one is excited.

OPTIMISATION APPROACH

In general, no a priori model of the system exists so an optimisation routine is used to determine the force pattern parameters required to maximise the contribution of the mode of interest. The objective function, the quantity that the optimisation routine seeks to minimise, must be representative of the deviation of the response from the target linear mode shape. The objective function, F, that was chosen in this case was based on the vector norm [4] of the two physical responses, x_1 and x_2, and is shown below:

$$F = \frac{\sqrt{\sum_{i=1}^{npts}\left(\frac{x_{1i}}{\phi_1} - \frac{x_{2i}}{\phi_2}\right)^2}}{npts} \quad (10)$$

where ϕ_1 and ϕ_2 are elements of the mode shape vector for the target mode. This summation is carried out over one cycle of the fundamental response. The number of data points per cycle is $npts$ and x_{ki} the kth response at the ith sample. This objective function allows the response to contain harmonics and can be extended to more degrees of freedom by choosing a reference displacement and subtracting further displacements from it. The Variable Metric optimisation method [5] was used in this work as it has been found to produce the best results for simulated data. The application of this method to a two degree of freedom system such as that shown in figure 1 is detailed in [6]. Optimised force patterns are obtained at several levels of input amplitude. These force patterns are then applied and the Restoring Force method is used to curve fit the resulting modal displacement and velocity time histories to give the direct linear and nonlinear coefficients for the mode of interest.

EXPERIMENTAL IMPLEMENTATION

The simulated application of this method assumed that certain parameters were known. In order to carry out an identification of an experimental structure, these parameters must be measured or calculated. Some processing of experimental data is necessary in order to apply the Restoring Force method. The restoring force of a system can be expressed for a single degree of freedom system as:

$$h(x, \dot{x}) = f(t) - m\ddot{x} \tag{11}$$

where $h(x, \dot{x})$ is the restoring force and $f(t)$ the input force. A similar expression applies to the modal restoring force for an isolated mode. Thus the input force, acceleration, velocity and displacement must be calculated at the each time instant. A similar expression applies to the modal restoring force for an isolated mode. In the experimental case it is usual to measure acceleration and input force; the remaining two states must therefore be obtained by integration of the acceleration time history. Frequency domain integration [7] was used for this purpose. High pass filtering was used to remove any low frequency noise which can be amplified by this type of integration. Several methods have been suggested for estimating modal mass, but in this study a method developed by Worden and Tomlinson [8] was used. An estimate for the modal mass is obtained and then an error term is included in the curve fit which will iteratively yield a more accurate estimate of the mass. Generally the mass value will converge after one iteration.

The objective function used in the simulations was calculated from the displacement time histories. In the experimental case, acceleration was used rather than displacement as it was considered that using 'raw' data would be quicker and give less opportunity for error. In the simulated case, the system parameters were known a priori so the modal matrix of the underlying linear system could be calculated. For most types of nonlinearity the response of the system at low input force levels will be dominated by linear terms. Normal mode tuning [1] was therefore applied at low force levels to yield an approximation to the modal matrix of the underlying linear system.

A quality indicator to give some idea of the effectiveness of the optimisation performed would be advantageous. Results corrupted by background noise, for example, could then be discarded. A perfect optimisation will occur when the ratio of measured accelerations exactly matches the mode shape ratio specified for the mode of interest. Thus a least squares fit of the sampled accelerations was carried out over a cycle of the fundamental frequency and the percentage error of the measured mode shape to the

required mode shape was calculated. This percentage error will indicate whether the optimisation has been successful.

To assess the accuracy of the parameters estimated using this method, an identification was carried out using a conventional Restoring Force approach in physical space. A band limited random excitation was used, and the physical data processed and curve fitted. The physical parameters were then transformed to modal space. The direct linear and nonlinear parameters for modes one and two are shown in table 1. It should be noted that although this conventional Restoring Force approach is possible for this two degree of freedom system, it will not generally be possible since the number of terms in the curve fit increases dramatically when different types of nonlinearity and more degrees of freedom are included. It is carried out in this case as a means of validating the proposed method.

EXPERIMENTAL SETUP

The rig constructed consisted of two masses on thin legs connected in series by a linear spring, each mass being driven by a shaker. A cubic nonlinearity was introduced between the first mass and ground using a clamped-clamped beam attached at the centre which will yield a cubic stiffness for large deflections [9]. A schematic diagram of the rig is shown in figure 2. The force input by each shaker was measured using a force gauge and the acceleration of each mass was measured using an accelerometer in the positions also shown in figure 2. Acceleration and force data were acquired using a multiple channel acquisition system, the optimisation routine was carried out on line.

RESULTS

Normal mode tuning of the rig gave natural frequencies of 20.67 Hz and 24.27 Hz and a modal matrix of:

$$\begin{bmatrix} 3.87 & 5.03 \\ 5.52 & -3.27 \end{bmatrix} \tag{12}$$

The excitation frequency was chosen to be slightly lower than the natural frequency of the mode of interest in order to avoid the problems associated with force drop out which are worst at the natural frequency. For each mode optimisation was performed at three input force levels, the highest level was as high as possible so as to excite the nonlinearity strongly. The optimisation routine was carried out using the voltage input into the signal generator as the variable. The force input into the structure was measured

for use in the Restoring Force identification but was not used in the optimisation as it is not directly controllable. The details of the optimisation for each force level are presented in table 2. The optimised forces and resulting accelerations for mode one are shown in figure 3 and figure 4. The acceleration data for the optimised force patterns were then integrated and the modal restoring force for the mode of interest calculated. The initial estimate of modal mass for the calculation of the modal restoring force was taken from a previous paper [10] in which the rig was identified using a using a physical parameter identification method. The mass was estimated in this paper to be 2.62 kg, this physical mass will then be equal to the modal mass since the modal matrix was normalised to be orthonormal. The restoring force data was then transformed to modal space. The modal restoring force surface obtained using optimised force inputs for mode one is shown in figure 5 and a stiffness section through this surface is shown in figure 6. The restoring force time histories were then curve fitted against modal velocity and displacement.

The estimated parameters for mode one are shown in table 3. It can be seen that they do not compare very well with those estimates obtained using the band limited random excitation. It was suspected that at lower excitation levels the estimates were being distorted by linear dependence [11]. Linear dependence is a problem which occurs when curve fitting a harmonic response from a linear system; the equations of motion may be identically satisfied by mass and stiffness terms modified by an arbitrary constant. This condition is avoided by the harmonic terms introduced into the response by nonlinearity. The curve fit was thus repeated using only the data obtained from the highest level of excitation; the estimates obtained are shown in table 4. It can be seen that the linear parameter estimates now agree well with the band limited random results. The estimates for the cubic stiffness coefficient do not appear to agree so well. The standard deviation on the cubic stiffness derived from the band limited random excitation is approximately a third of the value of the parameter itself. The uncertainty on this parameter occurs because the nonlinearity is not very strongly excited by this type of excitation. A stiffness section through the restoring force surface, figure 7, shows little evidence of a cubic stiffness component. If a higher level of excitation were possible then a better estimate may be achieved.

The identification was repeated for mode two. The restoring force surface obtained and a stiffness section through it are shown in figure 8 and figure 9. It can be seen from the stiffness section that the nonlinearity is not very strongly excited. The estimated direct modal parameters are shown in table 5. It can be seen that these results agree quite well with those obtained using band limited random excitation. It is considered that the discrepancy between the two sets of results, in particular the mass and

stiffness estimates, is again due to linear dependence.

CONCLUSIONS

An extension of the force appropriation method has been proposed for nonlinear systems. In this method, an optimisation routine is used to determine the force patterns which will excite a single mode nonlinear response . The direct linear and nonlinear modal parameters can then be estimated from a curve fit of the modal restoring force surface. The method was applied to an experimental two degree of freedom system whose modes were coupled in linear modal space by a spring grounded nonlinearity. A conventional restoring force identification was performed using a band limited random signal for comparison. The parameters estimated from the single mode responses were found to agree quite well with those from the band limited random tests.

REFERENCES

1. Holmes P., *Advanced Applications of Normal Mode Testing*, PhD Thesis, University of Manchester 1996.

2. Hadid M.A. and Wright J.R., Application of Force State Mapping to the Identification of Nonlinear Systems *Mechanical Systems and Signal Processing*, 1990, **4(6)**, 463-482

3. Atkins P.A., Wright J.R., Worden K., Manson G.M. and Tomlinson G.R., Dimensional Reduction for Multi Degree of Freedom Nonlinear Systems, *International Conference on Identification in Engineering Systems* 1996, 712-721

4. Kreyszig E., *Advanced Engineering Mathematics*, Wiley, 6th Edition

5. Press W.H., Teukolsky S.A., Vettering W.T. and Flannery B.P., *Numerical Recipes in Fortran* Cambridge University Press, 6th Edition

6. Atkins P.A. and Wright J.R., An Extension of Force Appropriation for Nonlinear Systems *Noise and Vibration Engineering*, Proceedings of ISMA21(2), 915-926, 1996

7. Worden K., Data Processing and Experiment Design for the Restoring Force Method, Part I: Integration and Differentiation of Measured Time Data, *Mechanical Systems and Signal Processing*, 4(4) 295-319, 1990

8. Ajjan Al-Hadid M., *Identification of Nonlinear Dynamic Systems using the Force State Mapping Technique*, PhD Thesis, Queen Mary College, University of London, 1989

9. Storer D.M., *Dynamic Analysis of Nonlinear Structures Using Higher Order Frequency Response Function*, PhD Thesis, University of Manchester, 1991

10. Atkins P. and Worden K., Identification of a Multi Degree of Freedom Nonlinear System, *Proc. of IMAC XV*, 1997

ACKNOWLEDGEMENTS

This work was supported by E.P.S.R.C. under research grant number GR/J48238 at the University of Manchester

Modal parameter	Mode one	Mode two
k (N/m)	4.87×10^4	6.49×10^4
c (Nm/s)	10.11	9.49
β(N/m^3)	3.83×10^8	8.90×10^8
m (kg)	2.60	3.06

Table 1: Direct modal parameters estimated from curve fit of band limited random data

	Low forcing	Medium forcing	High forcing
F_{11} (Volts)	1.0	2.0	3.0
F_{21} (Volts)	1.0	2.0	3.0
ω_{ex} (Hz)	20.0	20.0	20.0
initial mode shape ratio	0.72	0.68	0.65
final mode shape ratio	0.70	0.70	0.70
target mode shape ratio	0.70	0.70	0.70
percentage error	0.14	0.03	0.71

Table 2: Details of optimisation for mode one

Model parameter	Estimated parameter
k (N/m)	3.99×10^4
c (Nm/s)	8.60
β(N/m^3)	5.59×10^8
m (kg)	2.36

Table 3: Direct modal parameters estimated from optimised responses

Model parameter	Estimated parameter
k (N/m)	4.57×10^4
c (Nm/s)	8.62
β(N/m^3)	6.81×10^8
m (kg)	2.75

Table 4: Direct modal parameters estimated using high force level only

Model parameter	Estimated parameter
k (N/m)	5.37×10^4
c (Nm/s)	10.16
β(N/m^3)	2.45×10^9
m (kg)	2.29

Table 5: Direct modal parameters estimated for mode two

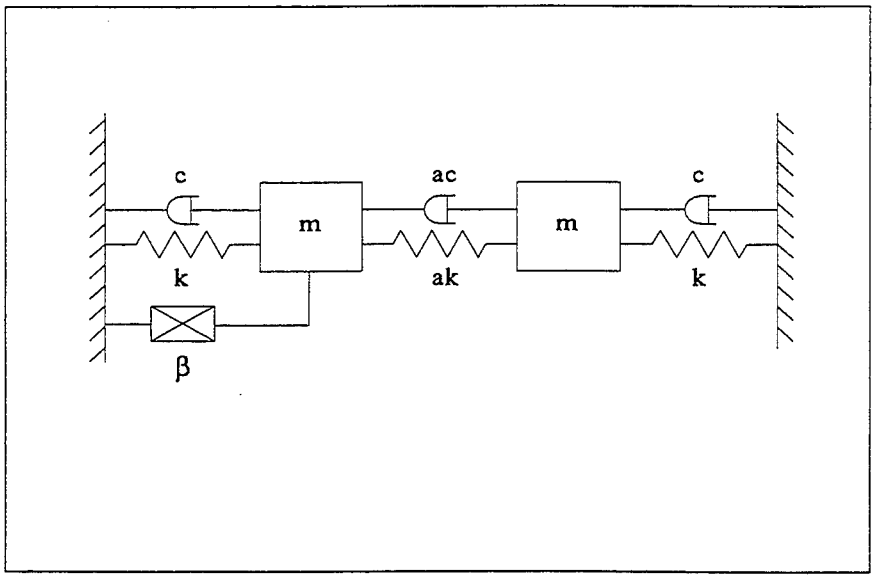

Figure 1: Two degree of freedom system

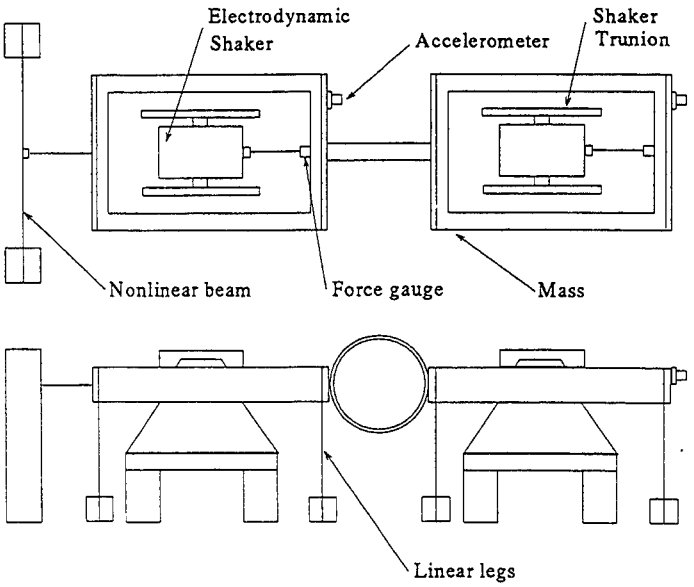

Figure 2: Experimental Rig

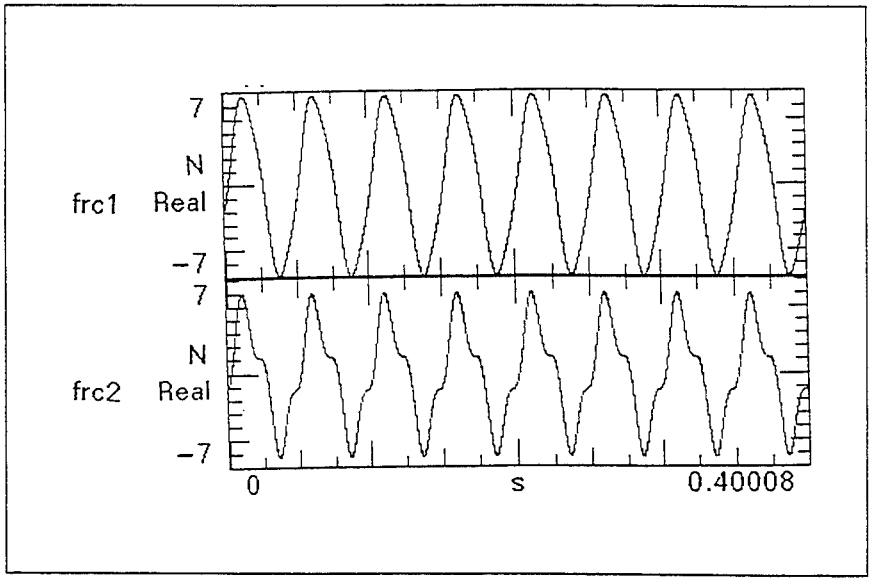

Figure 3: Optimised forces for mode one at a high force level

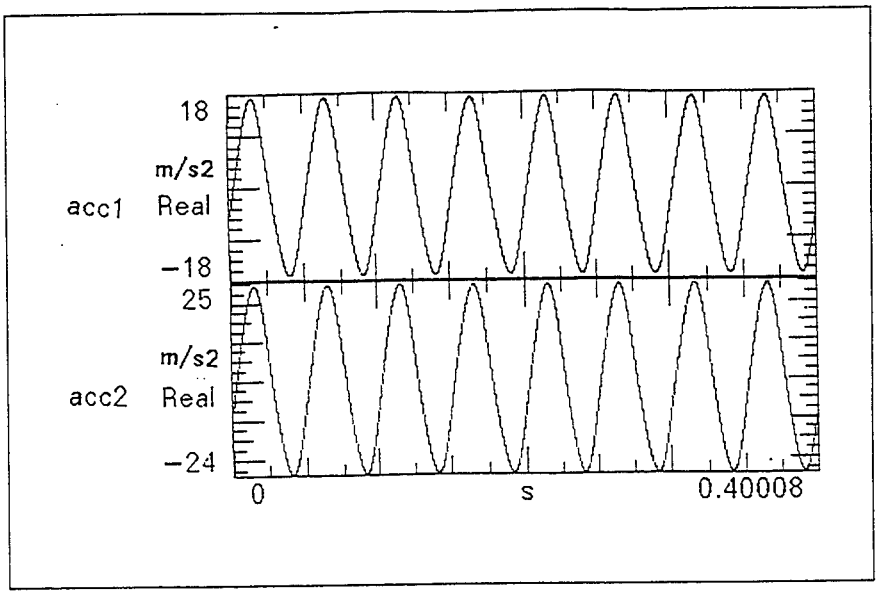

Figure 4: Accelerations responses to optimised forces

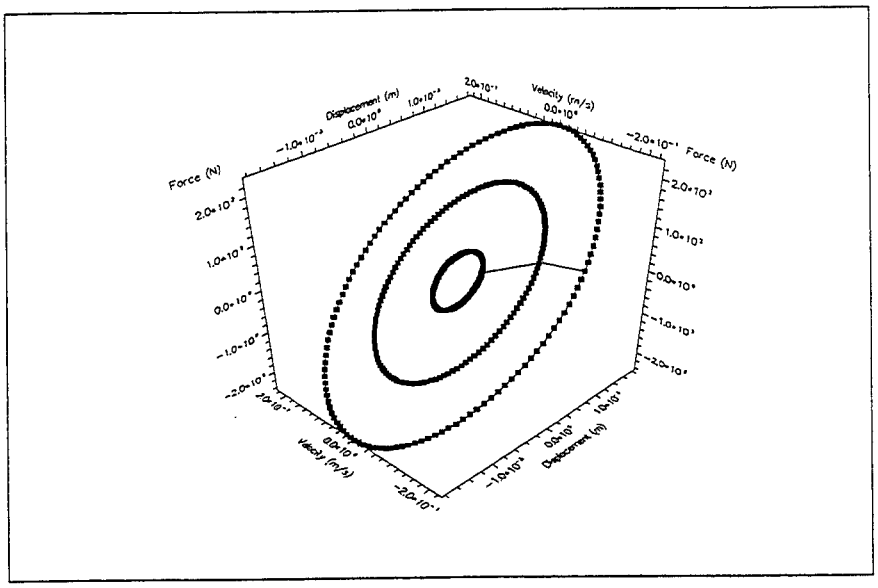

Figure 5: Modal restoring force surface for mode one

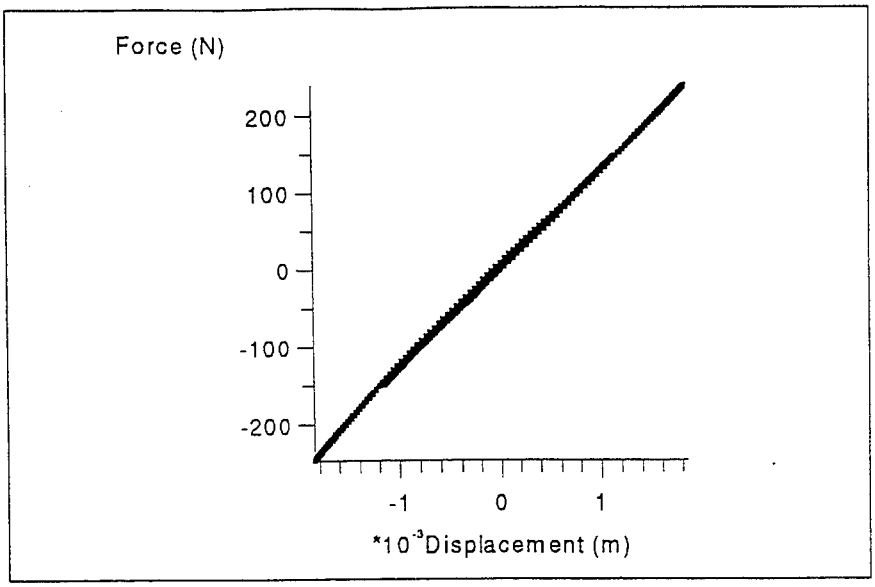

Figure 6: Stiffness section through modal restoring force surface for mode one

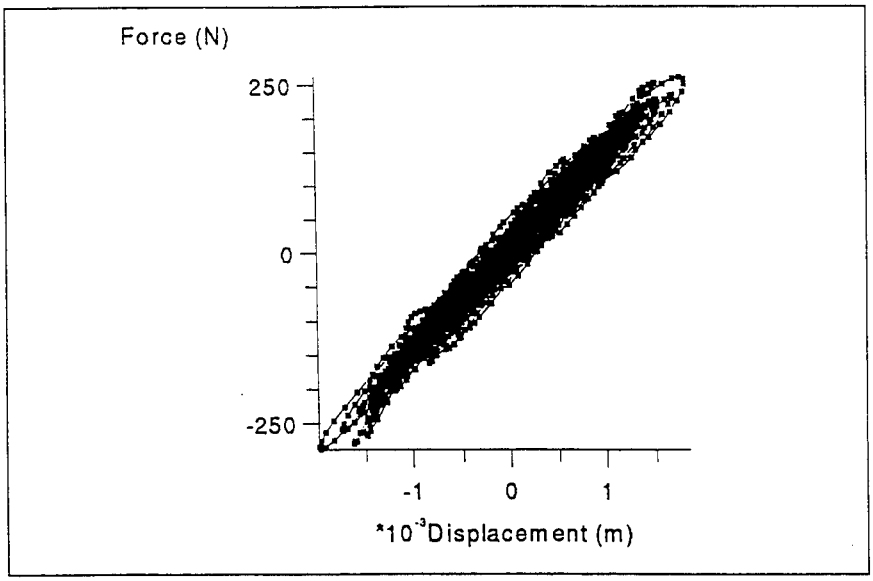

Figure 7: Stiffness section through modal restoring force derived from random excitation for mode one

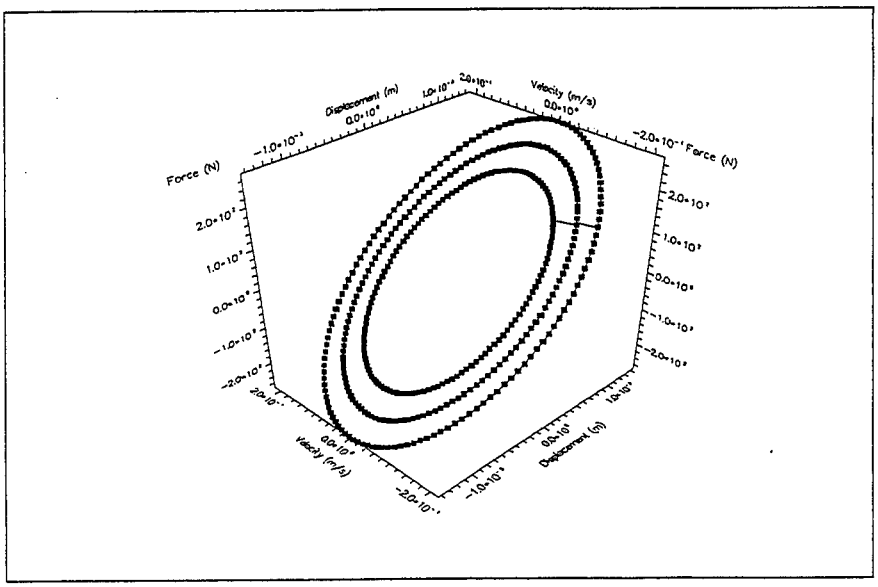

Figure 8: Modal restoring force surface for mode two

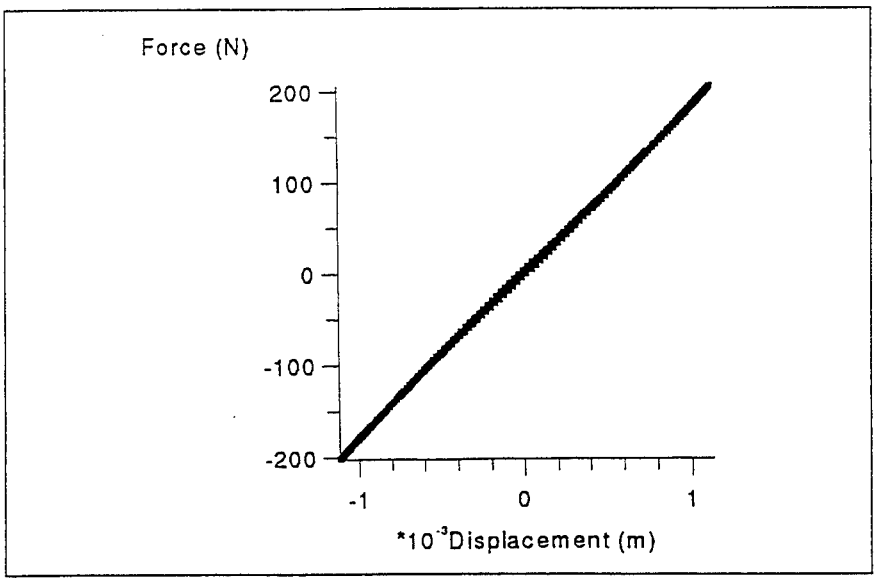

Figure 9: Stiffness section through modal restoring force for mode two

POWER FLOW TECHNIQUES II

THE OPTIMAL DESIGN OF NEAR-PERIODIC STRUCTURES TO MINIMISE NOISE AND VIBRATION TRANSMISSION

R.S. Langley, N.S. Bardell, and P.M. Loasby
Department of Aeronautics and Astronautics
University of Southampton
Southampton SO17 1BJ, UK

1. INTRODUCTION

An engineering structure is said to be of "periodic" construction if a basic structural unit is repeated in a regular pattern . A beam which rests on regularly spaced supports is one example of a one-dimensional periodic structure, while an orthogonally stiffened cylinder is an example of a two-dimensional periodic structure. It has long been known that perfectly periodic structures have very distinctive vibration properties, in the sense that "pass bands" and "stop bands" arise: these are frequency bands over which elastic wave motion respectively can and cannot propagate through the structure [1,2]. If the excitation frequency lies within a stop band then the structural response tends to be localised to the immediate vicinity of the excitation source. Conversely, if the excitation frequency lies within a pass band then strong vibration transmission can occur, and it is generally the case that the resonant frequencies of the structure lie within the pass bands.

Much recent work has been performed concerning the effect of random disorder on a nominally periodic structure (see for example [3-5]). It has been found that disorder can lead to localisation of the response even for excitation which lies within a pass band, and this reduces the propensity of the structure to transmit vibration. This raises the possibility of *designing* disorder into a structure in order to reduce vibration transmission, and this possibility was briefly investigated in reference [6] for a one-dimensional periodic waveguide which was embedded in an otherwise infinite homogeneous system. The present work extends the work reported in reference [6] to the case of a finite near-periodic beam system, which more closely resembles the type of optimisation problem which is likely to occur in engineering practice. The beam is taken to have N bays, and the design parameters are taken to be the individual bay lengths. Both single frequency and band-limited excitation are considered, and two objective functions are investigated: (i) the response in a bay which is distant from the applied loading (minimisation of vibration transmission), and (ii) the maximum response in the structure (minimisation of maximum stress levels). In each case the optimal configuration is found by employing a quasi-Newton algorithm, and the physical features of the resulting design are discussed in order to suggest general design guidelines.

2. ANALYTICAL MODEL OF THE NEAR-PERIODIC BEAM

2.1 Calculation of the Forced Response

A schematic of an N bay near-periodic beam structure is shown in Figure 1. The structure is subjected to dynamic loading, and the aim of the present work is to find the optimal design which will minimise a prescribed measure of the vibration response. No matter what type of optimisation algorithm is employed, this type of study requires repeated computation of the system dynamic response as the design parameters are varied, and it is therefore important to employ an efficient analysis procedure. In the present work the *h-p* version of the finite element method (FEM) is employed: with this approach the structure is modelled as an assembly of elements which have both nodal and internal degrees of freedom. Each element has two nodes and the nodal degrees of freedom consist of the beam displacement and slope; the internal degrees of freedom are generalised coordinates which are associated with a hierarchy of shape functions which contribute only to the internal displacement field of the element. The internal shape functions used here are the K-orthogonal Legendre polynomials of order four onwards - full details of the present modelling approach are given in reference [7].

For harmonic excitation of frequency ω the equations of motion of the complete beam structure can be written in the form

$$[-\omega^2 \boldsymbol{M}+(1+i\eta)\boldsymbol{K}]\boldsymbol{q}=\boldsymbol{F}, \tag{1}$$

where $\boldsymbol{M}$ and $\boldsymbol{K}$ are the global mass and stiffness matrices (assembled from the individual element matrices taking into account the presence of any mass or spring elements and allowing for constraints), $\boldsymbol{q}$ contains the system generalized coordinates, $\boldsymbol{F}$ is the generalized force vector, and η is the loss factor, which in the present study is taken to be uniform throughout the structure.

Equation (1) can readily be solved to yield the system response $\boldsymbol{q}$. In the present work it is convenient to use the time averaged kinetic and strain energies of each of the N bays as a measure of the response - for the nth bay these quantities can be written as T_n and U_n say, where

$$T_n=(\omega^2/4)\boldsymbol{q}_n^{*T}\boldsymbol{M}_n\boldsymbol{q}_n, \quad U_n=(1/4)\boldsymbol{q}_n^{*T}\boldsymbol{K}_n\boldsymbol{q}_n. \tag{2,3}$$

Here $\boldsymbol{M}_n$ and $\boldsymbol{K}_n$ are the mass and stiffness matrices of the nth bay, and $\boldsymbol{q}_n$ is the vector of generalized coordinates for this bay.

Many of the physical features of the forced response of a near-periodic structure can be explained in terms of the free vibration behaviour of the

associated perfectly periodic structure. The following section outlines how the present finite element modelling approach can be used to study the pass bands and stop bands exhibited by a perfect periodic structure.

2.2 Periodic Structure Analysis

The finite element method described in section 2.1 can be applied to a *single bay* of a perfectly periodic structure to yield an equation of motion in the form

$$\boldsymbol{D}\boldsymbol{q}=\boldsymbol{F}, \quad \boldsymbol{D}=-\omega^2\boldsymbol{M}+(1+i\eta)\boldsymbol{K}, \tag{4,5}$$

where the matrix $\boldsymbol{D}$ is referred to as the dynamic stiffness matrix. In order to study wave motion through the periodic system it is convenient to partition $\boldsymbol{D}$, $\boldsymbol{q}$ and $\boldsymbol{F}$ as follows

$$\boldsymbol{D}=\begin{pmatrix} \boldsymbol{D}_{LL} & \boldsymbol{D}_{LI} & \boldsymbol{D}_{LR} \\ \boldsymbol{D}_{IL} & \boldsymbol{D}_{II} & \boldsymbol{D}_{IR} \\ \boldsymbol{D}_{RL} & \boldsymbol{D}_{RI} & \boldsymbol{D}_{RR} \end{pmatrix}, \quad \boldsymbol{q}=\begin{pmatrix} \boldsymbol{q}_L \\ \boldsymbol{q}_I \\ \boldsymbol{q}_R \end{pmatrix}, \quad \boldsymbol{F}=\begin{pmatrix} \boldsymbol{F}_L \\ \boldsymbol{0} \\ \boldsymbol{F}_R \end{pmatrix}, \tag{6-8}$$

where L relates to the coordinates at the left most node, R relates to those at the right most node, and I relates to the remaining "internal" coordinates. Equations (4-8) can be used to derive the following transfer matrix relation between the displacements and forces at the left and right hand nodes

$$\boldsymbol{T}\begin{pmatrix} \boldsymbol{q}_L \\ \boldsymbol{F}_L \end{pmatrix}=\begin{pmatrix} \boldsymbol{q}_R \\ -\boldsymbol{F}_R \end{pmatrix}, \quad \boldsymbol{T}=\begin{pmatrix} \boldsymbol{D}_{LL}-\boldsymbol{D}_L\boldsymbol{D}_{II}^{-1}\boldsymbol{D}_{IL} & \boldsymbol{D}_{LR}-\boldsymbol{D}_L\boldsymbol{D}_{II}^{-1}\boldsymbol{D}_{IR} \\ \boldsymbol{D}_{RL}-\boldsymbol{D}_R\boldsymbol{D}_{II}^{-1}\boldsymbol{D}_{IL} & \boldsymbol{D}_{RR}-\boldsymbol{D}_R\boldsymbol{D}_{II}^{-1}\boldsymbol{D}_{IR} \end{pmatrix}, \tag{9,10}$$

Equation (9) can now be used to analyze wave motion through the periodic system: such motion is governed by Bloch's Theorem, which states that $(\boldsymbol{q}_L \ \boldsymbol{F}_L)=\exp(-i\varepsilon-\delta)(\boldsymbol{q}_R \ -\boldsymbol{F}_R)$ where ε and δ are known respectively as the phase and attenuation constants. A pass band is defined as a frequency band over which $\delta=0$, so that wave motion can propagate down the structure without attenuation. It follows from equation (9) that

$$(\boldsymbol{T}-\boldsymbol{I}e^{-i\varepsilon-\delta})\begin{pmatrix} \boldsymbol{q}_L \\ \boldsymbol{F}_L \end{pmatrix}=\begin{pmatrix} \boldsymbol{0} \\ \boldsymbol{0} \end{pmatrix}, \tag{11}$$

so that ε and δ can be computed from the eigenvalues of $\boldsymbol{T}$, thus enabling the pass bands and stop bands to be identified.

2.3 Optimisation Procedure

Equations (1)-(3) enable the forced response of the system to be calculated for any prescribed set of system properties. The aim of the present analysis is to compute the *optimal* set of system properties for a prescribed design objective, and in order to achieve this equations (1)-(3) are evaluated repeatedly as part of an optimisation algorithm. As an example, it might be required to minimise the kinetic energy of bay N by changing the various bay lengths. In this case equations (1)-(3) provide the route via which the objective function (the kinetic energy in bay N) is related to the design parameters (the bay lengths), and the optimisation algorithm must adjust the design parameters so as to minimise the objective function. The optimisation process has been performed here by using the NAg library routine E04JAF [8], which employs a quasi-Newton algorithm. This type of algorithm locates a minimum in the objective function, although there is no indication whether this minimum is the global minimum or a less optimal local minimum. The probability of locating the global minimum can be increased significantly by repeated application of the NAg routine using random starts, i.e. random initial values of the design parameters. Numerical investigations have led to the use of 30 random starts in the present work.

3. NUMERICAL RESULTS

3.1 The System Considered

The foregoing analysis has been applied to a beam of flexural rigidity EI, mass per unit length m, and loss factor $\eta=0.015$, which rests on $N+1$ simple supports, thus giving an N-bay near-periodic system. The design parameters are taken to be the bay lengths (i.e. the separation of the simple supports), and the design is constrained so that the length L_n of any bay lies within the range $0.9L_r \le L_n \le 1.1L_r$ where L_r is a reference length. A non-dimensional frequency Ω is introduced such that $\Omega=\omega L_r^2\sqrt{(m/EI)}$, and the non-dimensional kinetic and strain energies of a bay are defined as $T_n'=T_n(EI/L_r^3|F|^2)$ and $U_n'=U_n(EI/L_r^3|F|^2)$ where F is the applied point load. As discussed in the following subsections, two objective functions are considered corresponding to minimum vibration transmission and minimum overall response. In all cases the excitation consists of a point load applied to the first bay and the response is averaged over 11 equally spaced point load locations within the bay. For reference, the propagation constants for a periodic system in which all the bay lengths are equal to L_r are shown in Figure 2 - the present study is focused on excitation frequencies which lie in the range $23 \le \Omega \le 61$, which covers the second stop band and the second pass band of the periodic system.

3.2 Design for Minimum Vibration Transmission

In this case the objective function is taken to be the kinetic energy in bay N, so that the aim is to minimise the vibration transmitted along the structure. Three types of loading are considered: (i) single frequency loading with $\Omega=50$,

which lies within the second pass band of the ordered structure; (ii) band-limited loading with $40 \leq \Omega \leq 60$, which covers the whole of the second pass band; (iii) band-limited loading with $23 \leq \Omega \leq 61$, which covers the whole of the second stop band and the second pass band.

Results for the optimal design under single frequency loading are shown in Table 1; in all cases it was found that the bay lengths were placed against either the upper bound ($U=1.1L_r$) or the lower bound ($L=0.9L_r$), and significant reductions in the energy level of bay N were achieved. In this regard it should be noted that the dB reduction quoted on Table 1 is defined as $-10\log(T_N/T_{Nr})$ where T_{Nr} is the kinetic energy in the final bay of the ordered system. The optimal designs shown in Table 1 all tend to consist of a bi-periodic structure in which the basic unit consists of two bays in the configuration LU. The pass bands and stop bands for this configuration are shown in Figure 3, and further, T_N for the optimal 12 bay system is shown in Figure 4 over the frequency range $0 \leq \Omega \leq 250$. By comparing Figures 3 and 4 it is clear why the selected design is optimal - the new bi-periodic system has a stop band centred on the specified excitation frequency $\Omega=50$. It can be seen from Figure 4 that the improvement in the response at the specified frequency $\Omega=50$ is accompanied by a worsening of the response at some other frequencies.

Results for the optimal design under band-limited excitation over the range $40 \leq \Omega \leq 60$ are shown in Table 2. In some cases two results are shown for the optimised "Final Energy": in such cases the first result has been obtained by forcing each bay length onto either the upper (U) or lower (L) bound, while the second result has been obtained by using the NAg optimisation routine. If only one result is shown then the two methods yield the same optimal design. The "bound" result is easily obtained by computing the response under each possible combination of U and L bay lengths - this requires 2^N response calculations, which normally takes much less CPU time than the NAg optimisation routine. It is clear from Table 2 that the additional improvement in the response yielded by the full optimisation routine is minimal for this case. The response curve for the 12-bay system is shown in Figure 5, where it is clear that a significantly reduced response is achieved over the specified frequency range; as would be expected an increase in the response can occur at other frequencies. It is interesting to note that most of the optimal designs shown in Table 2 lack symmetry - however, it follows from the principle of reciprocity that a design which minimises vibration transmission from left to right will also minimise transmission from right to left. It should therefore be possible to "reverse" the designs without changing the transmitted vibration levels. This hypothesis is tested in Figure 6 for a 12 bay structure - the figure shows the energy distribution for the optimal design UUULUULLLLLU and for the reversed design ULLLLLUULUUU. Although the detailed distribution of energy varies between the two designs, the energy levels achieved in bay

12 are identical, as expected.

Results for the optimal design under wide-band excitation $23 \leq \Omega \leq 61$ are shown in Table 3, and the response curve for the 12-bay optimised system is shown in Figure 7. The form of optimal design achieved is similar to that obtained for the narrower excitation band $40 \leq \Omega \leq 60$, although there are detailed differences between the two sets of results. In each case there is a tendency for a group of lower bound bays (L) to occur in the mid region of the structure, and a group of upper bound bays (U) to occur at either end. This creates an "impedance mismatch" between the two sets of bays, which promotes wave reflection and thus reduces vibration transmission along the structure. By comparing Tables 1-3, it is clear that the achievable reduction in vibration transmission reduces as the bandwidth of the excitation is increased.

3.3 Design for Minimum "Maximum" Strain Energy

In this case the strain energy U_n of each bay is computed and the objective function is taken to be the maximum value of U_n. As a design objective, this procedure can be likened to minimising the maximum stress in the structure. As in the previous section the three frequency ranges $\Omega=50$, $40 \leq \Omega \leq 60$, and $23 \leq \Omega \leq 61$ are considered, and the present study is limited to systems having 9,10, 11, or 12 bays; the optimal designs achieved are shown in Table 4.

Considering the single frequency results ($\Omega=50$) shown in Table 4, it is clear that a large dB reduction is achieved only for those systems which have an even number of bays; furthermore, the optimal energy obtained has the same value (0.0297) in all cases. This can be explained by noting that for an odd number of bays the frequency $\Omega=50$ lies near to an anti-resonance of the ordered structure, whereas a resonance is excited for an even number of bays - this feature is illustrated in Figure 8 for the 12 bay structure. The repeated occurrence of the optimal energy 0.0297 arises from the fact that the initial bay pattern ULLLUUU occurs in all four designs - it has been found that this pattern causes a vibration reduction of over 20dB from bay 1 to bay 8, so that the response in bay 1 (the maximum response) is insensitive to the nature of structure from bay 8 onwards.

The optimal "bounded" designs arising for band-limited excitation either tend to be of the "UL" bi-periodic type or else nearly all the bays are assigned the same length. However it should be noted that in all cases the design produced by the NAg optimisation routine offers an improvement over the "bounded" design, particularly for the wide-band case ($23 \leq \Omega \leq 61$). It is clear from Table 4 that the achieved reduction in strain energy reduces as the bandwidth of the excitation is increased.

4. CONCLUSIONS

The present work has considered the optimal design of a near-periodic beam system to minimise vibration transmission and also maximum stress levels. With regard to vibration transmission it has been found that very significant reductions in transmission are achievable with relatively minor design changes. The optimum design normally involves placing the design parameters (the bay lengths) on the permissible bounds, and this means that a simple design search routine can be used in preference to a full optimisation algorithm. With regard to minimum stress levels, it has been found that the optimal design for wide-band excitation is not normally a "bounded" design, and thus use of a full optimisation algorithm is preferable for this case. For both vibration transmission and maximum stress levels, the benefits obtained from an optimal design decrease with increasing excitation bandwidth, but nonetheless very significant reductions can be obtained for wide-band excitation.

REFERENCES

1. S.S. MESTER and H. BENAROYA 1995 *Shock and Vibration* **2**, 69-95. Periodic and near-periodic structures.
2. D.J. MEAD 1996 *Journal of Sound and Vibration* **190**, 495-524. Wave propagation in continuous periodic structures: research contributions from Southampton 1964-1995.
3. C.H. HODGES 1982 *Journal of Sound and Vibration* **82**, 411-424. Confinement of vibration by structural irregularity.
4. D. BOUZIT and C. PIERRE 1992 *Journal of Vibration and Acoustics* **114**, 521-530. Vibration confinement phenomena in disordered, mono-coupled, multi-span beams.
5. R.S. LANGLEY 1996 *Journal of Sound and Vibration* **189**, 421-441. The statistics of wave transmission through disordered periodic waveguides.
6. R.S. LANGLEY 1995 *Journal of Sound and Vibration* **188**, 717-743. Wave transmission through one-dimensional near periodic structures: optimum and random disorder.
7. N.S. BARDELL, R.S. LANGLEY, J.M. DUNSDON and T. KLEIN 1996 *Journal of Sound and Vibration* **197**, 427-446. The effect of period asymmetry on wave propagation in periodic beams.
8. ANON 1986 *The NAg Fortran Workshop Library Handbook - Release 1*. Oxford: NAg Ltd.

TABLE 1

Optimal design of 1-D beam structure, to minimise energy transmission, Ω=50.

Original Energy: Non-dimensional kinetic energy in bay N of the periodic structure.
Final Energy: Non-dimensional kinetic energy in bay N of the optimised structure.

No. of Bays, N	Optimal Pattern	Original Energy	Final Energy	Reduction (dB)
4	UULU	0.276E 1	0.804E-3	35.348
5	ULULU	0.609E-1	0.179E-3	25.304
8	UULULULU	0.674E 0	0.613E-5	50.408
9	ULULULULU	0.564E-1	0.135E-5	46.216
10	UULULULULU	0.424E 0	0.532E-6	59.017
11	ULULULULULU	0.535E-1	0.117E-6	56.604
12	UULULULULULU	0.289E 0	0.461E-7	67.966
13	ULULULULULULU	0.502E-1	0.101E-7	66.950
16	UULULULULULULULU	0.154E 0	0.346E-9	86.484
17	ULULULULULULULULU	0.431E-1	0.761E-10	87.529

TABLE 2

Optimal design of 1-D beam structure, to minimise energy transmission, $40 \leq \Omega \leq 60$.

Original Energy: Non-dimensional kinetic energy in bay N of the periodic structure.
Final Energy: Non-dimensional kinetic energy in bay N of the optimised structure.

No. of Bays, N	Optimal pattern	Original Energy	Final Energy	Reduction (dB)
4	ULLU	0.670E 0	0.103E-1	18.112
5	ULLLU	0.631E 0	0.735E-2	19.338
			0.711E-2	19.482
6	UULLLU	0.384E 0	0.221E-2	22.407
7	ULLUULU	0.463E 0	0.171E-2	24.335
8	UULLLLLU	0.430E 0	0.966E-3	26.487
			0.914E-3	26.725
9	UUULLLLLU	0.444E 0	0.341E-3	31.142
10	UUUULLLLLU	0.449E 0	0.192E-3	33.681
			0.189E-3	33.758
11	ULLUUUULLLU	0.291E 0	0.821E-4	35.504
12	UUULUULLLLLU	0.201E 0	0.352E-4	37.558
13	ULUUUUULLLLLU	0.199E 0	0.153E-4	41.148

TABLE 3

Optimal design of 1-D beam structure, to minimise energy transmission, $23 \leq \Omega \leq 61$.

Original Energy: Non-dimensional kinetic energy in bay N of the periodic structure.
Final Energy: Non-dimensional kinetic energy in bay N of the optimised structure.

No of Bays, N	Optimal pattern	Original Energy	Final Energy	Reduction (dB)
4	LLUU	0.536E 0	0.581E-1	9.650
			0.383E-1	11.460
5	LLLUU	0.340E 0	0.180E-1	12.762
			0.138E-1	13.916
6	LLLLUU	0.494E 0	0.648E-2	18.821
7	LLLULUU	0.183E 0	0.246E-2	18.715
8	LLLLLUUU	0.175E 0	0.180E-2	19.878
9	ULLLLLLUU	0.139E 0	0.904E-3	21.868
10	UUULLLLLUU	0.105E 0	0.277E-3	25.787
11	UUULLLLLLUU	0.105E 0	0.776E-4	31.313
12	UUULLLLLLLUU	0.166E 0	0.526E-4	34.991
13	UUULLLLLLULUU	0.973E-1	0.282E-4	35.379
14	UUUULLLLLLULUU	0.581E-1	0.122E-4	36.778

TABLE 4

Optimal design of 1-D beam structure, to minimise "maximum" strain energy.

Bay No.: Bay in which the optimal minimum "maximum" non-dimensional strain energy occurs
Original Energy: Initial "maximum" non-dimensional bay strain energy of the periodic structure.
Final Energy: Non-dimensional strain energy in bay N' of the optimised structure.

No of Bays, N	Optimal Pattern	Original Energy	Final Energy	Bay No., N'	Reduction (dB)
$\Omega=50$					
9	ULLLUUUUL	0.667E-1	0.297E-1	1	3.514
			0.296E-1	1	3.528
10	ULLLUUUULU	0.540E 0	0.297E-1	1	12.596
			0.296E-1	1	12.611
11	ULLLUUUULUU	0.691E-1	0.297E-1	1	3.667
			0.296E-1	1	3.682
12	ULLLUUUULULU	0.404E 0	0.297E-1	1	11.336
			0.296E-1	1	11.351
$40\leq\Omega\leq60$					
9	UUUUULULU	0.486E 0	0.710E-1	1	8.354
			0.449E-1	1-2	10.344
10	ULULULULLL	0.606E 0	0.643E-1	1	9.743
			0.451E-1	1-2	11.283
11	ULULULULLUU	0.456E 0	0.682E-1	1	8.252
			0.425E-1	1-2	10.306
12	UUUUUUUUUUUL	0.332E 0	0.550E-1	2	7.808
			0.412E-1	1-2	9.062
$23\leq\Omega\leq61$					
9	LLLLLLLLL	0.234E 0	0.203E 0	1	0.617
			0.979E-1	1	3.784
10	LLLLLLLLLL	0.200E 0	0.178E 0	1	0.506
			0.951E-1	1-2	3.228
11	UUUUUUUUULL	0.198E 0	0.193E 0	1	0.111
			0.910E-1	1-2	3.376
12	UUUUUUUUULUU	0.314E 0	0.182E 0	1	2.369
			0.803E-1	1-2	5.922

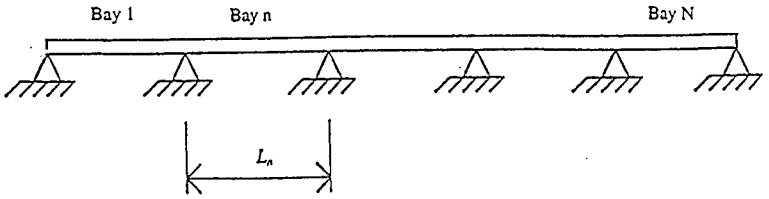

Figure 1: A simply supported periodic beam.

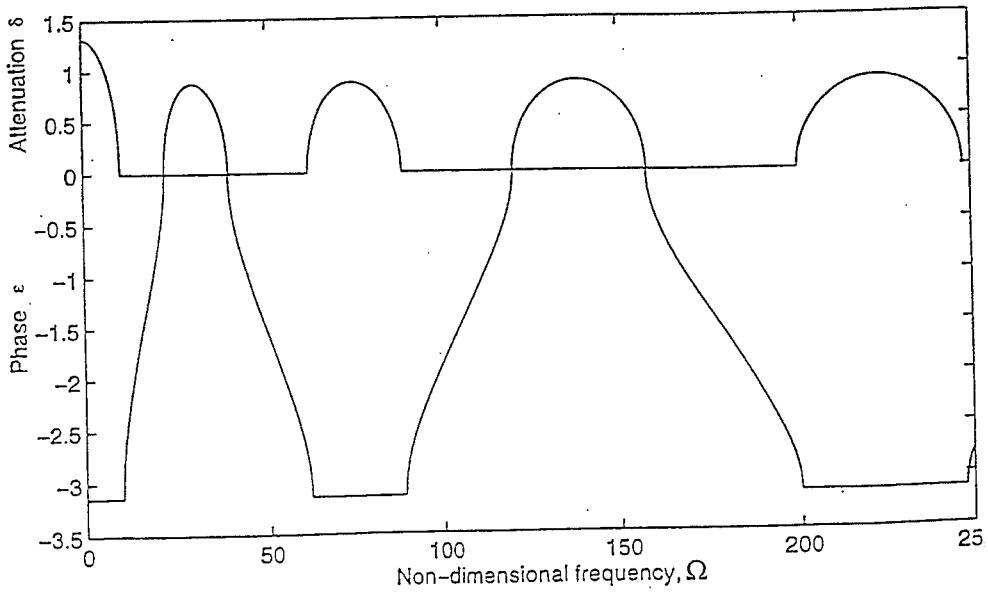

Figure 2: Propagation constants for a simply supported beam, bay lengths equal to L_r.

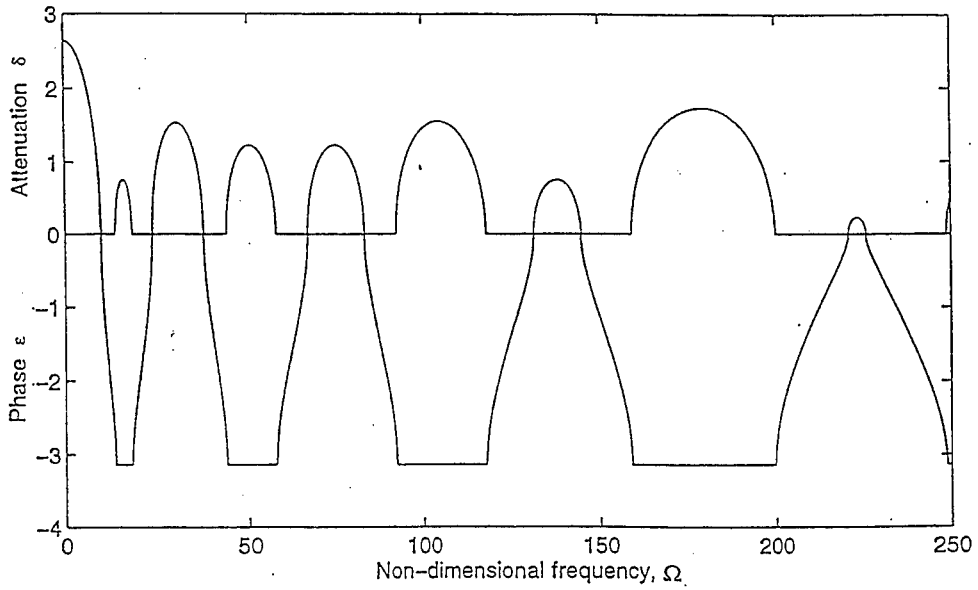

Figure 3: Propagation constants for a bi-periodic simply supported beam, with configuration LU.

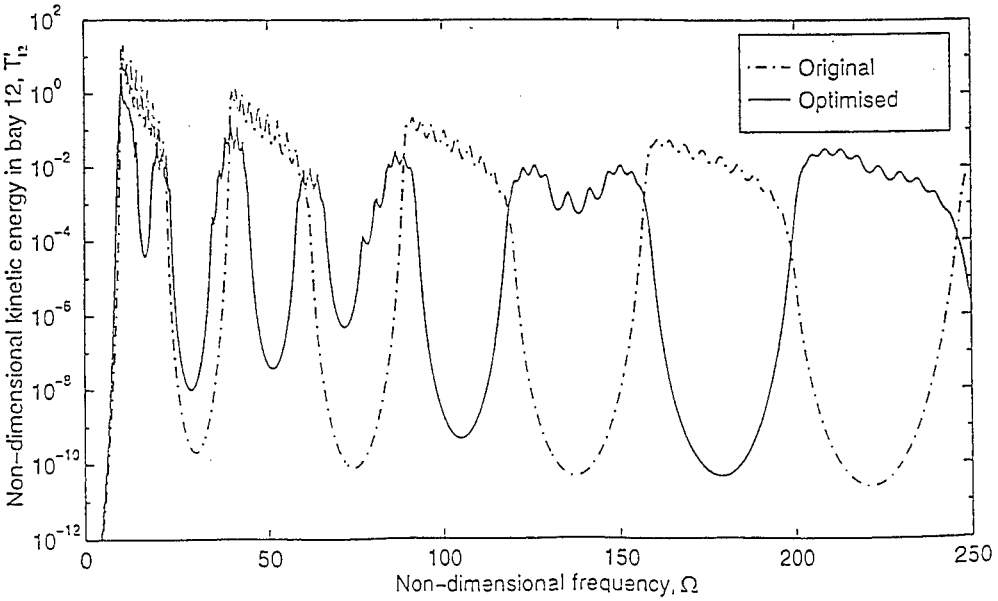

Figure 4: Frequency response of a 12 bay structure; — kinetic energy in bay 12, optimised for Ω=50.

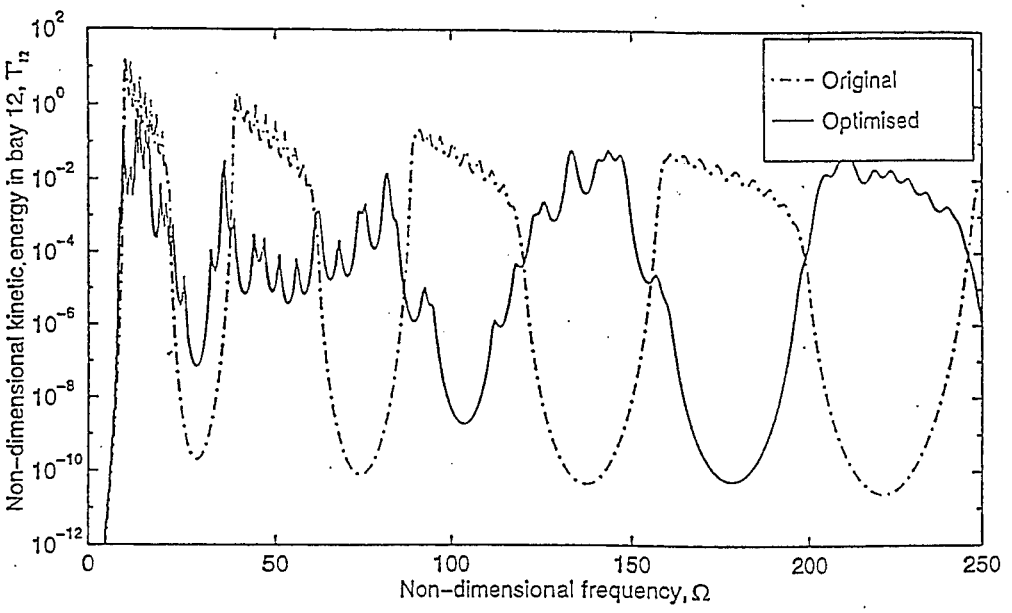

Figure 5: Frequency response of a 12 bay structure; —. kinetic energy in bay 12, optimised for $40 \leq \Omega \leq 60$.

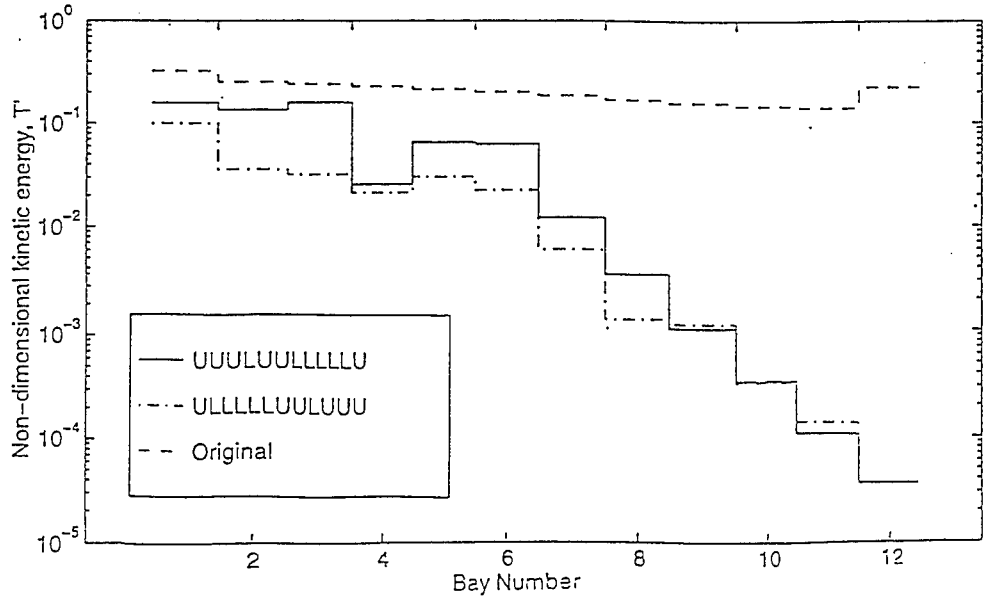

Figure 6: Distribution of kinetic energy within a 12 bay structure, showing reciprocity. Also shown is the kinetic energy within the original structure.

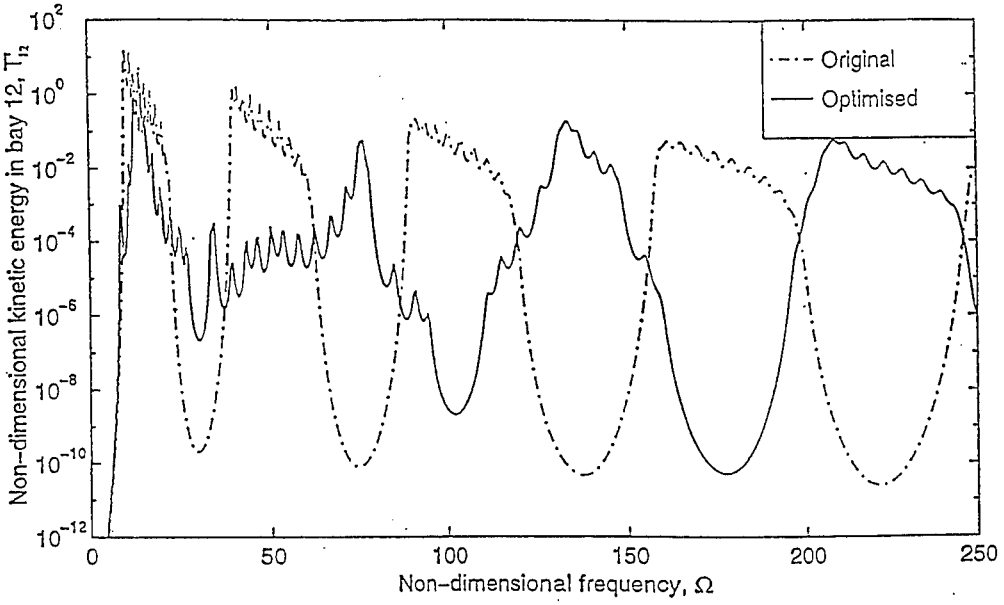

Figure 7: Frequency response of a 12 bay structure; — kinetic energy in bay 12, optimised for $23 \leq \Omega \leq 61$.

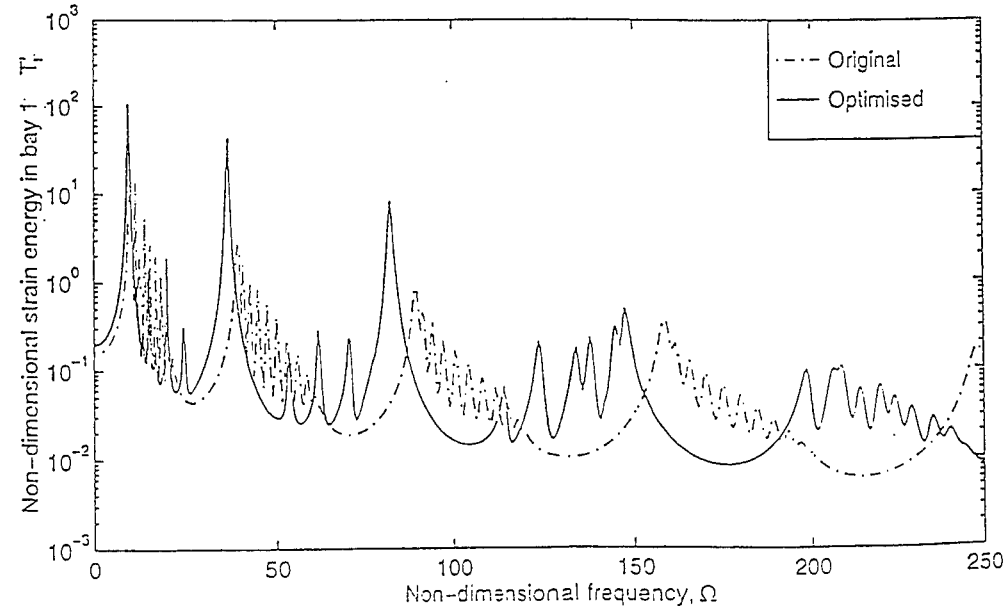

Figure 8: Frequency response of a 12 bay structure; — minimum "maximum" strain energy, optimised for $\Omega=50$.

EFFECTS OF GEOMETRIC ASYMMETRY ON VIBRATIONAL POWER TRANSMISSION IN FRAMEWORKS

J L Horner
Department of Aeronautical and Automotive Engineering
and Transport Studies, Loughborough University
Loughborough, Leics , LE11 3TU, UK

ABSTRACT

Many sources, such as machines, are installed on supports, or frameworks, constructed from beam-like members. It is desirable to be able to predict which wave types will be present at particular points in the support structure. By using the concept of vibrational power it is possible to compare the contributions from each wave type. Wave motion techniques are used to determine the expressions for vibrational power for each of the various wave types present. The results from the analysis show the amount of vibrational power carried by each wave type and the direction of propagation. Consideration is given to the effect on the vibrational power transmission of introducing misalignment of junctions in previously symmetric framework structures. By splitting a four beam junction in to, say, a pair of three beam junctions separated by a small distance, it is possible to establish the effects of separating the junctions on the various transmission paths. Unlike other techniques using vibrational power to analysis frameworks, the model keeps the contributions from each of the various wave types separate. This allows decisions to be made on the correct vibrational control techniques to be applied to the structure.

INTRODUCTION

When attempting to control vibration levels transmitted from a machine through the various connections to the structure upon which it is mounted, it is desirable to be able to identify and quantify the vibration paths in the structure. Often large machinery installations are installed on frameworks consisting of beam like members. These frameworks are then isolated from the main structure. Simple framework models are also used in the initial design stages of automotive body shell structures to determine dynamic responses.

If the dominant transmission path in the framework is identified it is possible to reduce vibration levels by absorbing the mechanical energy along the propagation path in some convenient manner. By utilising the concept of vibrational power it is possible to quantitatively compare the wave type contributions to each transmission path. In order to predict vibrational power transmission in a framework, it is necessary to identify the wave amplitude reflection and transmission coefficients for each joint in the structure. Lee and Kolsky [1] investigated the effects of longitudinal wave impingement on a junction of arbitrary angle between two rods. Similarly Doyle and Kamle [2] examined the wave amplitudes resulting from a flexural wave impinging on the junction between two beams. By using the reflection and transmission coefficients for different joints, it is possible to predict the vibrational power associated with flexural and longitudinal waves in each section of the

framework. Previous investigations [3,4] have considered the effects of bends and junctions in infinite beams. This work was extended to consider the finite members which constitute frameworks [5]. Unlike other techniques [6, 7] utilising energy techniques to analyse frame-works, the technique produces power distributions for each wave type present in the structure. By comparing the results for each wave type, it is possible to apply the correct methods of vibration control.

The technique is used to investigate the effect of geometric asymmetry on the vibration transmission, due to steady state sinosodial excitation, in a framework structure similar to, say, those used in the automotive industry (figure 1). By splitting a four beam junction into a pair of three beam junctions separated by a known distance, it is possible to establish the effect of junction separation on the dominant transmission paths. The investigation presented is limited to one dimensional bending waves and compressive waves only propagating in the structure. To consider the addition of other wave types ie. torsional waves and bending waves in the other plane, the analysis presented here for the junctions should be extended as indicated by Gibbs and Tattersall [3].

TRANSMITTED POWER IN A UNIFORM BEAM

For flexural wave motion, consider a section of a uniform beam carrying a propagating flexural wave. Two loads act on this beam element, the shear force and the bending moment. It is assumed that the flexural wave can be described by using Euler-Bernoulli beam theory, so that the displacement can be expressed as

$$W(x,t) = A_f \sin(\omega t - k_f x),$$

the shear force acting on a section as

$$S = EI\,\partial^3 W/\partial x^3,$$

and the bending moment on the section as

$$B = EI\,\partial^2 W/\partial x^2.$$

Then the instantaneous rate of working X at the cross-section is given by the sum of two terms (negative sign merely due to sign convention).

$$X = S\frac{\partial W}{\partial t} - B\frac{\partial^2 W}{\partial x\,\partial t} = EI\frac{\partial^3 W}{\partial x^3}\frac{\partial W}{\partial t} - EI\frac{\partial^2 W}{\partial x^2}\frac{\partial^2 W}{\partial x\,\partial t}$$

The time averaged power

$$\langle P\rangle_f = (1/T)\int_0^T X\,dt \text{ then is given by } \langle P\rangle_f = EIk_f^3\omega A_f^2 \qquad (1)$$

For longitudinal wave motion consider a section of a uniform beam with a longitudinal wave propagating through the beam

$$U(x,t) = A_1 \sin(\omega t - k_1 x)$$

The instantaneous rate of working X is then

$$X = -EA\,(\partial u/\partial x)\,\dot{u}$$

and the time averaged power is

$$\langle P\rangle_l = \frac{1}{T}\int_0^T X\,dt = \frac{1}{2}EA\omega k_l A_l^2 \qquad (2)$$

If dissipation is present in the structure, the modulus of elasticity may be considered to be a complex quantity

$$E^* = E(1 + i\eta)$$

where η represents the loss factor of the material, present due to inherent material damping.
The displacement of a beam at a distance x from the source, due to flexural wave motion may now be considered to be, assuming that material damping is small.

$$W = A_f\, e^{-k\eta\frac{x}{4}} \sin(\omega t - k_f x)$$

and the resulting time averaged power is given by

$$\langle P\rangle_f = EI\omega k_f^3\, e^{-k_f\eta\frac{x}{2}} A_f^2 \qquad (3)$$

The above reduces to equation (1) at the source.
Similarly, the displacement of beam, due to longitudinal wave motion may be considered to be

$$U = A_l e^{-k_l\eta\frac{x}{2}} \sin(\omega t - k_l x)$$

and the resulting time averaged longitudinal power may be rewritten as

$$\langle P\rangle_l = \frac{1}{2}EA\omega k_l\, e^{-k_l\eta x} A_l^2 \qquad (4)$$

WAVE TRANSMISSION THROUGH A MULTI BRANCH JUNCTION

Consider a four branch junction as shown in figure 2. Assuming only flexural and longitudinal waves propagating in the structure, the displacements of Arm 1 will be, where A_4 represents the impinging flexural wave arriving from infinity.

$$W_1(x,t) = \left(A_1 e^{k_{f1}x} + A_3 e^{ik_{f1}x} + A_4 e^{-ik_{f1}x}\right) e^{i\omega t} \qquad (5)$$

$$U_1(x,t) = \left(A_a e^{ik_{l1}x}\right) e^{i\omega t} \tag{6}$$

Similarly for arms 2 to 4 the displacement will be,
where $\psi_n = x \cos \theta_n$ and n is the beam number

$$W_n(\psi_n,t) = \left(B_{2n} e^{-k_{fn}\psi_n} + B_{4n} e^{-ik_{fn}\psi_n}\right) e^{i\omega t} \tag{7}$$

$$U_n(\psi_n,t) = \left(B_{bn} e^{-ik_{ln}\psi_n}\right) e^{i\omega t} \tag{8}$$

Here A_3, A_4, B_{4n} are travelling flexural wave amplitudes, A_1 and B_{2n} are near field wave amplitudes and A_a and B_{bn} are travelling longitudinal wave amplitudes.

In previous work [2] in this field a theoretical model was used in which it was assumed that the junction between the beams was a rigid mass. The mass or joint is modelled here as a section of a cylinder. This represents the physical shape of most joints in practical systems. It has been shown [4] that the joint mass has an insignificant effect on the reflected and transmitted power for the range of values used in this work.

The joint mass $M_j = \rho_j \pi L^2 J_w / 4$, and the moment of inertia of the joint is $I_j = M_j L^2 / 8$.

By considering the conditions for continuity and equilibrium at the beam junction the following expressions may be written.

For each arm

For continuity of longitudinal displacement

$$U_1 = U_n \cos\theta_n - W_n \sin\theta_n + \frac{L}{2}\frac{\partial W_n}{\partial \psi_n}\sin\theta_n$$

For continuity of flexural displacement

$$W_1 = U_n \sin\theta_n + W_n \cos\theta_n - \frac{L}{2}\frac{\partial W_n}{\partial \psi_n}(1+\cos\theta_n)$$

For continuity of slope

$$\frac{\partial W_1}{\partial \psi} = \frac{\partial W_n}{\partial \psi_n}$$

For the junction

Equilibrium of forces

$$E_1 I_1 \frac{\partial^2 W_1}{\partial x^2} + \frac{L}{2} E_1 I_1 \frac{\partial^3 W_1}{\partial x^3} + I_j \frac{\partial W_1}{\partial x}$$

$$= \sum_1^n \left(E_n I_n \left(\frac{\partial^2 W_n}{\partial \psi_n^2} - \frac{L}{2} \frac{\partial^3 W_n}{\partial \psi_n^3} \right) \right)$$

$$E_1 A_1 \frac{\partial U_1}{\partial x} + M_j \frac{\partial^2 U_1}{dt^2} = \sum_1^n \left(E_n A_n \frac{\partial U_n}{\partial \psi_n} \cos\theta_n + E_n I_n \frac{\partial^3 W_n}{\partial \psi_n^3} \sin\theta_n \right)$$

$$E_1 I_1 \frac{\partial^3 W_1}{\partial x^3} + M_j \frac{\partial}{dt^2} \left[W_1 - \frac{L}{2} \frac{\partial W_1}{\partial x} \right]$$

$$= \sum_1^n \left(E_n A_n \frac{\partial U_n}{\partial \psi_n} \sin\theta_n - E_n I_n \frac{\partial^3 W_n}{\partial \psi_n^3} \cos\theta_n \right)$$

WAVE MOTION AT A FORCED OR FREE END

As indicated in figure 1, the framework has one forced end and one free end. Assuming the structure is only excited by a transverse harmonic force, the boundary conditions are as follows:

at the forced end

$$EI \frac{\partial^3 W}{\partial x^3} = P e^{i\omega t}$$

$$EI \frac{\partial^2 W}{\partial x^2} = 0 \qquad EA \frac{\partial^2 U}{\partial x^2} = 0$$

Similarly at the free end the above boundary conditions apply with the exception that

$$EI \frac{\partial^3 W}{\partial x^3} = 0$$

POWER TRANSMISSION THROUGH A FRAMEWORK

The structure shown in figure 1 consits of one four-beam junction, two three-beam junctions and four two-beam junctions. From the equations detailed in the above two sections, it is possible to construct matrices of continuity and equilibrium equations for sub structures. These may be combined to obtain the overall matrix for the system. For the framework shown in figure 1, the size of the overall matrix is 60x60. This matrix may be solved to obtain the sixty unknown wave amplitude coefficients from which time averaged transmitted power for each beam may be calculated using equations (3) and (4).

Normalised nett vibrational power is then calculated at the centre of each beam constituting the structure. Nett vibrational power may be considered to be the difference between power flowing in the positive direction and power flowing in the negative direction for each wave type. Normalised nett power is considered to be nett power divided by total input power. The input power to a structure may be calculated from the following expression [8]

$$\text{Input Power} = \frac{1}{2} |F| |V| \cos\phi$$

where ø is the phase angle between the applied force and the velocity of the structure at the forcing position.

Figures 3-6 show the nett normalised power in each arm of a framework structure over the frequency range 0-1kHz excited by 1N force, whose material and geometric properties are given in Appendix 2. For the results shown, angle 1 is 45° and angle x is 40° (or the ratio $\theta_x/\theta_1 = 0.89$) and L = y = 0.1m. Using these parameters the ratio of the length of beam No.6 to beam No.4 is 0.12. The predicted flexural power is shown in figures 3 and 4 and from these it can be seen that the dominant transmission paths are arms 1 and 5, the forced and free arms. The transmitted power in arm 10 is next dominant and comparable to arm 5 in the region 0-600Hz.

The response for all other arms are small, typically less than 5% of input power, with, as would be expected, arms 2 and 9 being approximately identical in transmission properties.

Figures 5 and 6 show the nett normalised power for the longitudinal waves in the structure. As the frequency range of interest corresponds to a flexural Helmoltz number of 1 to 5 with L being the reference length, the conversion of power from flexural to longitudinal waves is minimal. From the figures it can be seen that beams 1, 5, 6 and 10 have identical transmission characteristics, which would be expected at such large longitudinal wavelengths. Significant longitudinal power is only observed in arms 3 and 8 in the frequency region 200-300Hz. This frequency region coincides with a drop in the flexural power due to the structure being at resonance in that region. It should be noted that power transmitted through arms 3 and 8 has travelled through two junctions.

EFFECT OF GEOMETRIC ASYMMETRY

By altering the ratio of angle θ_1 to angle θ_x it is possible to alter the length of beam 6 and hence move a pair of three arm junctions further or closer apart. From the discussion in the previous section, it was seen, for the structure under investigation, that the dominant flexural path, not surprisingly, is through the centre of the structure, whilst the peaks in longitudinal power occur in beams 3 and 8. Thus θ_x was varied and the effect on transmission in the dominant paths noted.

Figures 7-9 show flexural power for arms 5 and 10 and longitudinal power for arm 8 for four values of θ_x. The values chosen were 36°, 38.25°, 40° and 42.75° which are equivalent respectively to θ_x over θ_1 ratios of 80%, 85%, 90% and 95%. Thus as θ_x increases, the structure moves to being symmetrical in nature. From figure 7, the increase in junction separation decreases power in the frequency region 0-500Hz and increases it in the region 500-1kHz. In beam 10 (figure 10) the effect on the flexural power is reversed with increase in junction separation leading to increased power below 500Hz and decreased power above 500Hz. It should also be noted that increased junction separation has little effect on the power below 250Hz. The effect was also noted on all other beams which had both ends connected to a joint. It may be concluded that at long flexural wavelengths the junction separation has little effect with the impedance mis-match at the junctions being the important criteria to effect transmission. It should also be noted that increasing power in one arm ie. 5, causes a decrease in arms ie. 10, connected to it. An example of the effect of junction separation on longitudinal power is shown in figure 9. This shows nett normalised longitudinal power for arm 8 for the same variation in θ_x. Again minimal effect is seen at low frequencies, with increased junction separation having different effects in different frequency region. Increasing junction separation has little effect on the region between 200 and 300Hz when the longitudinal power was dominant. This would be caused by the junction separation having little effect on the structures flexural natural frequencies. Only by shifting those would the peaks in longitudinal power by shifted in frequency.

CONCLUSIONS

Results are presented for normalised nett time average vibrational power for a framework structure. The geometric symmetry of the structure is broken by allowing one angle to decrease in value. The effects of varying the angle change by up to 20% of its original value are investigated. Although the results presented are for one example only, highlighted are the fact that decreases in power in one part of the structure result in increases in power in another part. Also shown was the effect of splitting a junction in to a pair of junctions is minimal at low frequencies, or long wavelengths. From the results of the analysis it is possible to establish frequencies and positions for minimum power on the structure. Other configurations of framework structure may be analysed by applying the equations presented.

REFERENCES

1. J. P. LEE. and H. KOLSKY 1972 Journal of Applied Mechanics 39, 809-813. The generation of stress pulses at the junction of two non-collinear rods.
2. J. F. DOYLE and S. KAMLE 1987 Journal of Applied Mechanics 54, 136-140. An experimental study of the reflection and transmission of flexural waves at an arbitrary T-Joint.
3. B. M. GIBBS and J. D. TATTERSALL 1987 Journal of Vibration, Acoustics, Stress and Reliability in Design, 109, 348-355. Vibrational energy transmission and mode conversion at a corner junction of square section rods.
4. J. L. HORNER and R. G. WHITE 1991 Journal of Sound and Vibration 147, 87-103. Prediction of vibrational power transmission through bends and joints in beam-like structures.
5. J. L. HORNER 1994 Proceedings of the 5th International Conference on Recent Advances in Structural Dynamics, SOUTHAMPTON UK, 450-459. Analysis of vibrational power transmission in framework structures.
6. P. E. CHO and R. J. BERNHARD 1993 Proceedings of the 4th International Congress on Intensity Techniques, SENLIS, France, 347-354. A simple method for predicting energy flow distributions in frame structures.
7. M. BESHARA and A. J. KEANE 1996 Proceedings of Inter-Noise '96, LIVERPOOL, UK 2957-2962. Energy flows in beam networks with complient joints.
8. R.J.PINNINGTON and R.G.WHITE 1981 Journal of Sound and Vibration 75, 179-197. Power flow through machine isolators to resonant and non-resonant beams.

APPENDIX 1 - NOTATION

A - Cross sectional area
A_f - Amplitude of flexural wave
A_l - Amplitude of longitudinal wave
B - Bending moment
E - Young's modulus
E^* - Complex Young's modulus
F - Excitation force
I - Moment of inertia
I_j - Moment of inertia of joint
J_w - Joint width
k_f - Flexural wave number
k_l - Longitudinal wave number
L - Joint length
M_j - Joint mass
n - Beam number
P - Transverse force
Q - Axial force
S - Shear force
T - Time period
t - Time
U - Displacement due to longitudinal wave motion
V - Velocity
W - Displacement due to flexural wave motion
X - Instantaneous rate of working
x - Distance
η - Loss factor
θ_n - Angle of Arm n
ρ_j - Joint density
M - Moment force
ϕ - Phase angle
ψ_n - Distance along Arm n

$\langle P \rangle_f$ - Time averaged flexural power ω - Frequency (rad/s)

$\langle P \rangle_l$ - Time averaged longitudinal power

APPENDIX 2 - MODEL PROPERTIES

Beam Breadth	=	33mm
Beam Depth	=	6mm
Youngs Modulus	=	5GN/m2
Density	=	1180kg/m3
Loss factor	=	0.001

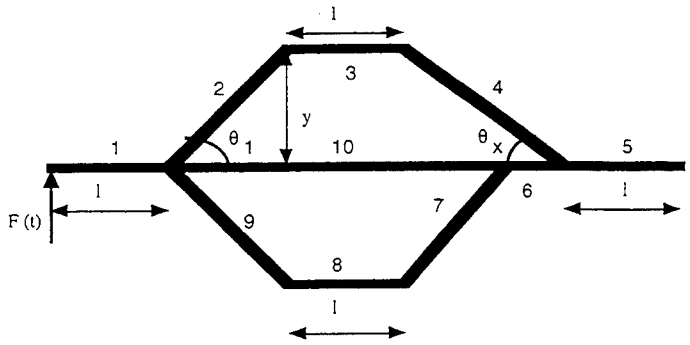

Figure 1: Framework Structure

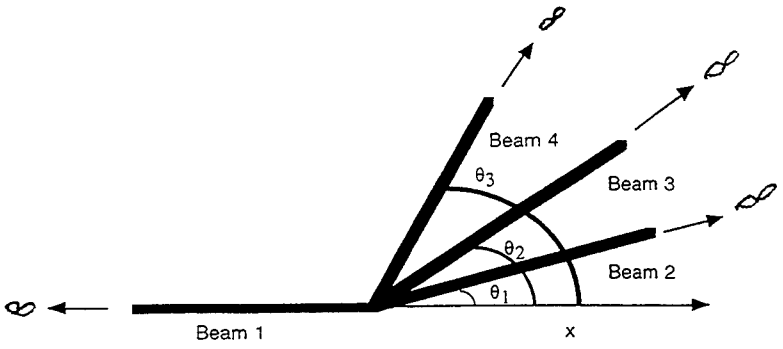

Figure 2: Four Beam Junction

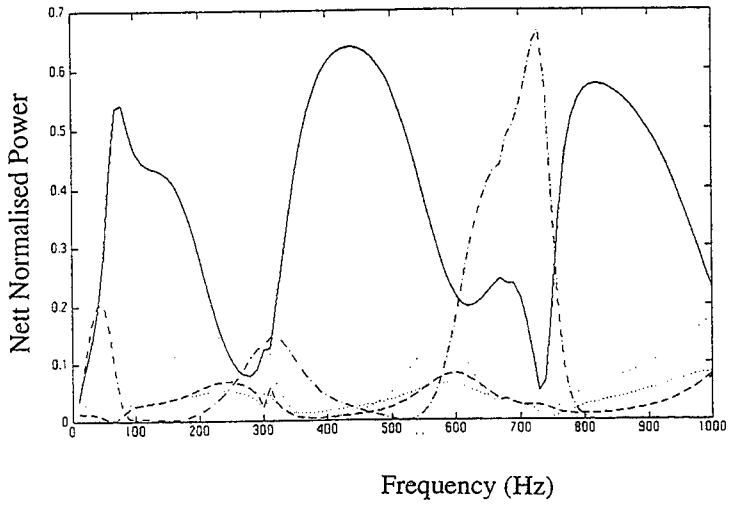

Figure 3: Flexural Power - Beams 1-5

(Beam 1-----, Beam 2 ....., Beam 3 . . ., Beam 4- - -, Beam 5 -.-.-)

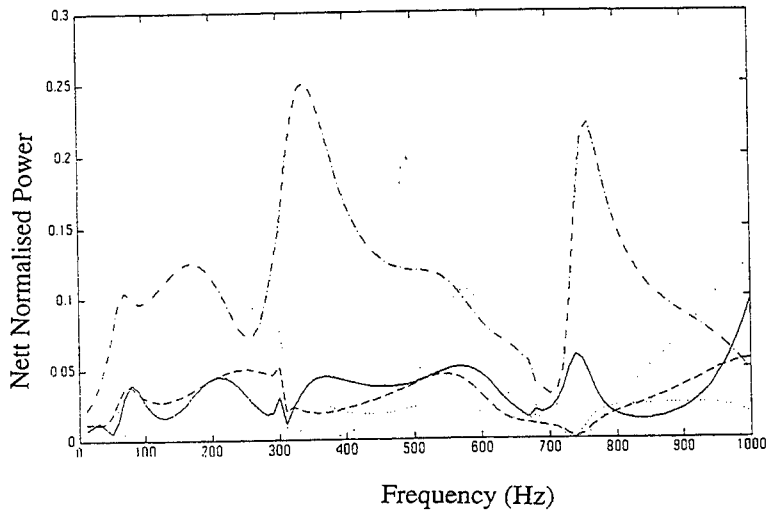

Figure 4: Flexural Power - Beams 6-10

(Beam 6-----, Beam 7 ....., Beam 8 . . ., Beam 9- - -, Beam 10 -.-.-)

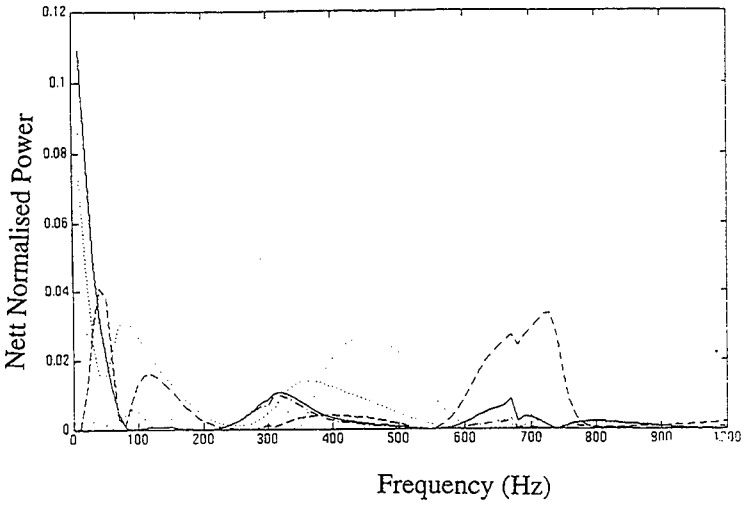

Figure 5: Longitudinal Power - Beams 1-5

(Beam 1-----, Beam 2 ....., Beam 3 . . ., Beam 4- - -, Beam 5 -.-.-)

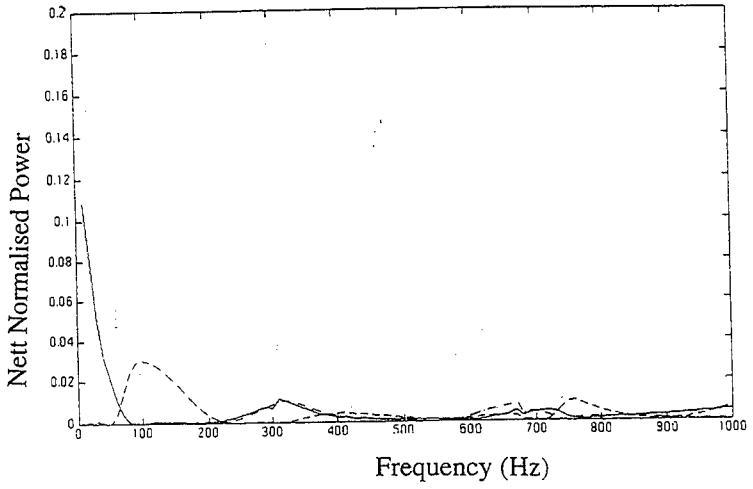

Figure 6: Longitudinal Power - Beams 6-10

(Beam 6-----, Beam 7 ....., Beam 8 . . ., Beam 9- - -, Beam 10 -.-.-)

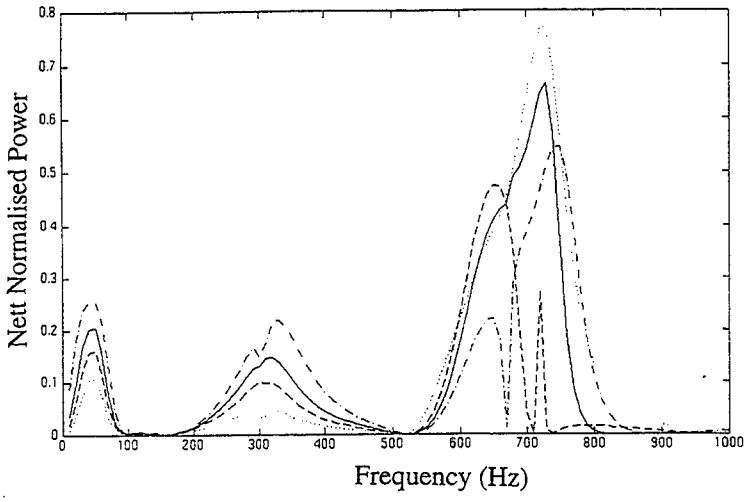

Figure 7: Flexural Power - Beam 5

(36 deg ..... , 38.25 deg - - -, 40 deg ----- , 42.75 deg -.-.-)

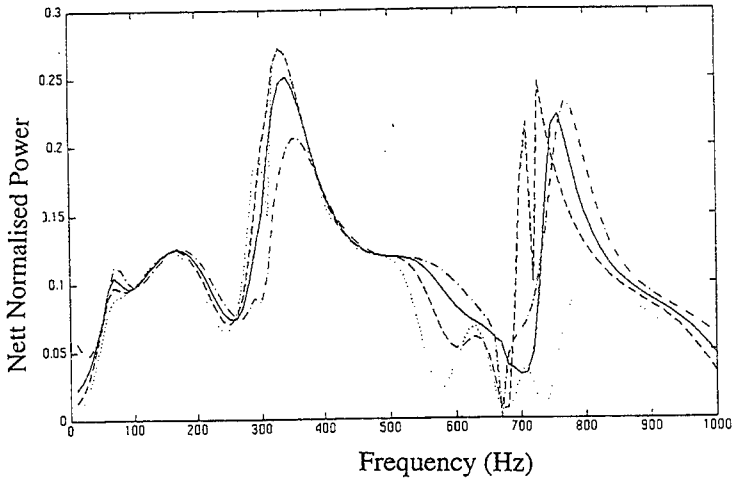

Figure 8: Flexural Power - Beam 10

(36 deg ..... , 38.25 deg - - -, 40 deg ----- , 42.75 deg -.-.-)

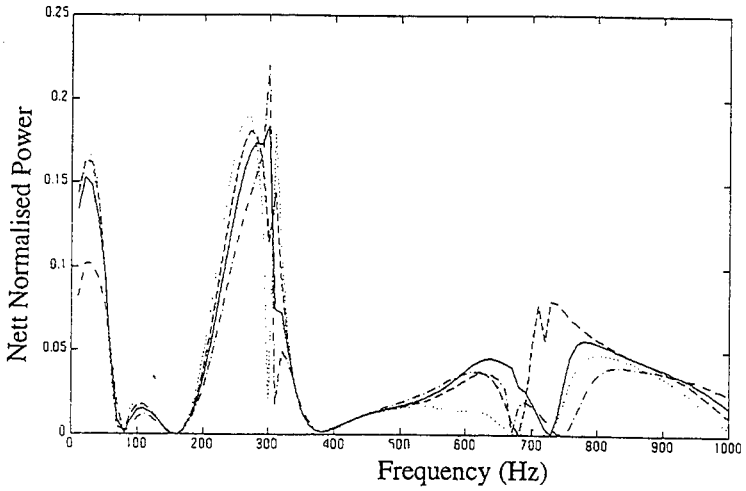

Figure 9: Longitudinal Power - Beam 8

(36 deg ..... , 38.25 deg - - -, 40 deg ----- , 42.75 deg -.-.-)

THE INFLUENCE OF THE DISSIPATION LAYER ON ENERGY FLOW IN PLATE CONNECTIONS

Marek Iwaniec, Ryszard Panuszka

Technical University of Mining and Metallurgy,
Structural Acoustics and Intelligent Materials Group
30-059 Cracow, al. Mickiewicza 30, Poland

1. Introduction

Dynamic behaviour of mechanical structures may be modelled on the basis of and with the help of mathematical apparatus used in Statistical Energy Analysis (SEA) [5]. The method is especially useful to calculate the statistical approach vibroacoustical energy flow in middle and high frequency range. With the help of a few parameters, such as: modal density, damping loss factor, coupling loss factor and the value of input power, building linear equations set it is possible to describe the flow of vibroacoustical energy in a complicated structure. There is also a possibility of quick estimation of the influence of construction method on the vibroacoustical parameters of the whole set. In the following work an exemplary application of one of the most frequently used software for calculating the flow of acoustic energy has been presented: AutoSEA programme [1]. The aim of the work is practical modelling of vibroacoustical energy flows through screw-connection of two plates and comparing quantity results with experimental (outcome) measurements. Equivalent coupling loss factor has been calculated for a group of mutually combined elements constituting a construction fragment. A comparison between the measured results and the value of coupling loss factor in linear joint (e.g. in welded one) has also been made. Using the method of finite elements, the influence of rubber separator thickness on the value of the first several frequencies of free vibrations has been computed as well.

2. Physical model of plate connection

A connection of two perpendicular plates has been chosen for modelling the flow of vibroacoustical energy in mechanical joints. Connection diagram is presented in Figure 1. On the length of common edge the plates has been joined with anglesteel by screws. A rubber separator (4) has been placed between the excited plate and the anglesteel leg (3).

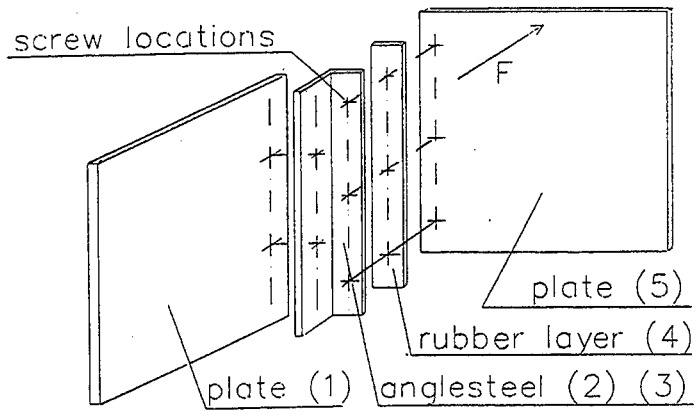

Fig.1. Modelled structure

3. SEA model

In order to carry out the vibroacoustical analysis of the system using Statistical Energy Analysis a model of the examined structure has been built. It has been assumed that in every element of the construction only flexural waves propagate. Every plate and the rubber layer have been modelled with just one appropriately chosen subsystem. The anglesteel, however, has been modelled as a continuous connection of two plates having the dimensions which correspond to the anglesteel legs, the plates themself being set at the right angle.

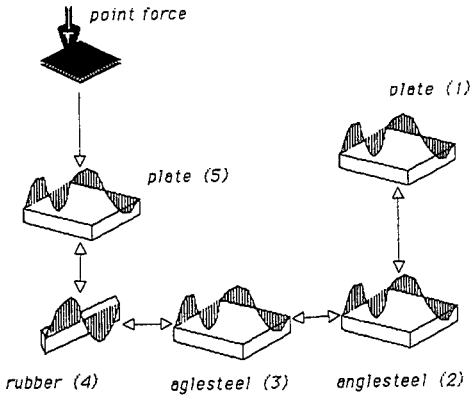

Fig. 2. SEA model of a system

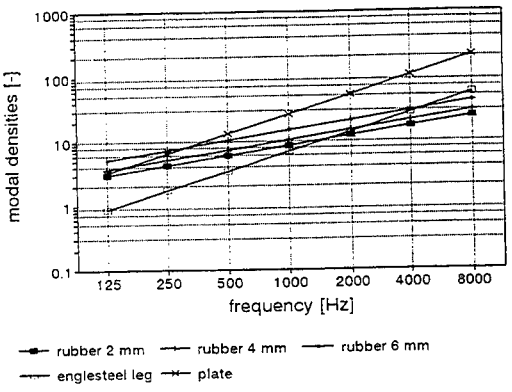

Fig. 3. Modal densities of the subsystems

Using the SEA method we are able to describe the flow of the vibroacoustical energy in middle and high frequencies with an algebraic equation set. The examined system consists of five simple subsystems, of which only one is exited to vibration with applied force. The flow of vibroacoustical energy in the model presented is depicted with the following equation:

$$\begin{bmatrix} \eta_{1\,tot} & -\eta_{21} & 0 & 0 & 0 \\ -\eta_{12} & \eta_{2\,tot} & -\eta_{32} & 0 & 0 \\ 0 & -\eta_{23} & \eta_{3\,tot} & -\eta_{43} & 0 \\ 0 & 0 & -\eta_{34} & \eta_{4\,tot} & -\eta_{54} \\ 0 & 0 & 0 & -\eta_{45} & \eta_{5\,tot} \end{bmatrix} \cdot \begin{vmatrix} E_{1\,tot} \\ E_{2\,tot} \\ E_{3\,tot} \\ E_{4\,tot} \\ E_{5\,tot} \end{vmatrix} = \begin{vmatrix} \frac{W_1}{\omega} \\ 0 \\ 0 \\ 0 \\ 0 \end{vmatrix} \qquad (1)$$

where:
$\eta_{i,tot} = \eta_i + \Sigma\, \eta_{ij}$ is a total coefficient of energy loss for every subsystem,
η_i - internal loss factor of the subsystem,
η_{ij} - coupling loss factor between subsystems,
$E_{i,tot}$ - the mean vibrational energy in Δf frequency band in i-subsystem,
W_{in} - the input power carried into i-subsystem from outside.

To determine the elements of the coefficients matrix in eq.1 it is necessary to know [1,4,6] coupling loss factors (CLF) between structural subsystems and damping loss factors (DLF).

In the SEA model in question transmission of the acoustic energy occurs in two types of connections between:
- the plate and the beam (the point joint of the beam which is parallel to the edge of the plate. (transfers flexural waves),
- two plates (linear connections and point joints transferring flexural waves).

The coupling loss factor between the plate and the beam which vibrate in the flexural way (in the case of the point joint), is defined with following equation [1].

$$\eta = \frac{1.75 c_l^2}{\omega_i A_l} \tau_{2i} Q \qquad (2)$$

where:
c - is the speed of flexural wave,
τ - transmission factor,
Q - the number of point connections,
ω - angular frequency,
A - the surface of the plate.

The speed of the flexural wave in the first plate c_{1i} can be calculated in the following way:

$$c_{p1} = \sqrt{\omega_i}\left[\frac{h_1 E_1}{12\rho_1(1-\nu_1^2)}\right]^{\frac{1}{4}} \tag{3}$$

In the model under examination formula (2) defines coupling loss factors between the anglesteel leg (2) and the beam (4) - (factors η_{34} and η_{43}) or the beam (4) and the plate (5) - η_{45} and η_{54}.

The flow of energy between two plates (which are connected at the right angle and which vibrate in flexural way) is defined with the following formula in the case of linear connection:

$$\eta_i = \frac{2}{\Pi}\frac{c_{1i}\, l}{\omega_i A_1}\tau_{12i} \tag{4}$$

where:
l - is the length of the connection.
With above formula it is possible to describe the flow of energy through correctly made welded joints of plates or, for example, through bent plates. In the system presented the factor determines the flow of energy between anglesteel legs (2) and (3).

The coupling loss factor between two plates with a point joint is described by the following formula:

$$\eta_i = \frac{1}{3}\frac{h_1 c_{1i}}{\omega_i A_1}\tau_{12i} Q \tag{5}$$

This type of connection occurs between the plate representing the anglesteel leg and the plate (5).

After defining the value of factors matrix in the first equation it is possible to specify the ratio of the vibroacoustical energy gathered in plate (1) and (5).

$$\frac{E_1}{E_5} = \frac{(\eta_{2tot}\eta_{3tot}-\eta_{24}\eta_{32})(\eta_{4tot}\eta_{5tot}-\eta_{54}\eta_{45})-\eta_{34}\eta_{43}\eta_{5tot}}{\eta_{21}\eta_{32}\eta_{43}\eta_{54}} \tag{6}$$

The damping loss factor is important parameter of every subsystem. For steel plates used in the experiment the value of the damping loss factor have been measured experimentally with the decay method. The results of the measurements have been presented in figure 4. The frequency characteristic of rubber damping has been shown in figure 5.

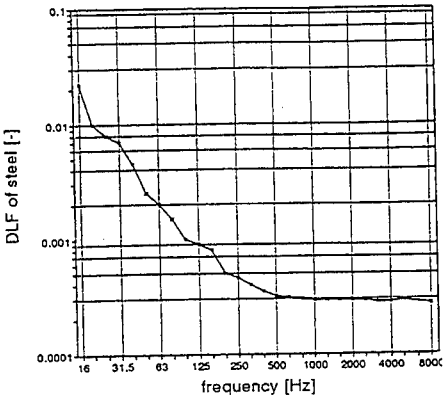

Fig. 4. Damping loss factor of steel

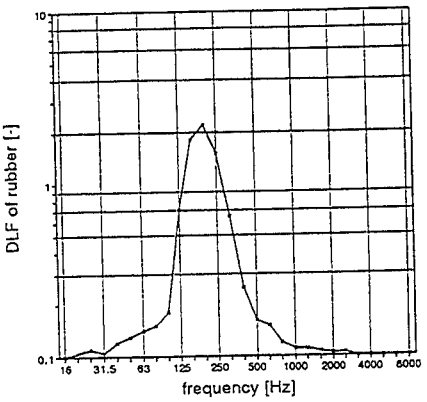

Fig. 5. Damping loss factor of rubber

4. Experimental research

Experimental investigations have been carried out for connections made with the use of rubber separator (elastic layer) of 50° Shore hardness. The connection was build up of two identical, perpendicular plates connected each to another using the anglesteel and the elastic rubber layer. These are the properties and material parameters of individual elements:

plates:
- material: constructional steel (St3);
- dimensions: 500 * 500 * 2.2 mm;
- Young modulus: $2{,}1\ 10^{11}$ Pa.

anglesteel:
- material: constructional steel (St3);
- dimensions: L 40 * 40 * 2.2 mm;
- Young modulus: $2{,}1\ 10^{11}$ Pa

elastic layer:
- material: rubber 50° Shore
- dimensions: 500 * 40 mm
- thickness: 2, 3, 4, 5, 6 mm

To avoid the loss of mechanical energy in the environment, during measurements the construction was suspended to the supporting frame with three weightless strings in such way that only rigid body motions in the plane perpendicular to the plate surface can occur. The excitation of the wide-band type with constant power spectral density was applied in the symmetry axis of the plate (5) about 20 mm below the upper edge (Figure 1). During the experiment the distribution of vibrating velocities on the plate surface was obtain by non contact method using laser-vibrometry.

5. FEM model

Vibration of modelled structure in low frequency has been analyzed by the Finite Element Method (FEM). Several FEM models, was build in order to consider the valid thickness of the rubber layer. The rubber thickness has been changed from 0 mm to 6 mm. The dimensions and material parameters of the plates and the anglesteel was constant. The structure was fixed in four corners. Calculations were made for a division of the structure into 608 elements of type BRICK8. The influence of the rubber thickness on the eigenfrequencies was remarkable. The results for first 15 eigenfrequencies are presented in the table 1. In fig. was shown also the changes of the value of natural frequencies in comparison with the natural frequencies of structure without applying the rubber layer.

table 1. Natural frequencies of connection

Natural frequencies [Hz] for various rubber layer thickness				
0 mm	2 mm	3 mm	4 mm	5 mm
127.8	123.1	121.5	119.4	117.5
297.5	235.8	224.6	212.6	204.6
507.6	432.5	391.3	357.1	330.0
1003.2	566.9	525.7	503.7	491.9
1282.3	807.1	768.9	733.5	712.2
1900.5	1185.2	1169.4	1123.2	1070.2
2386.7	1570.2	1483.6	1376.2	1304.6
3272.3	1851.6	1634.2	1531.6	1490.8
3603.4	2303.1	2263.4	2167.8	2147.3
4263.3	2611.2	2539.5	2496.9	2463.7
4759.5	3192.7	3515	3110.1	2913.2
5438.4	3926.7	3874.6	3626.4	2937.0
7627.4	4110.1	4105.5	3639.9	3026.6
7691.6	5070.7	5137.0	3670.5	3111.2
11543.2	5547.1	5503.9	3721.9	3181.2

The decreasing of the absolute values of the natural frequencies is observed according to increasing of the thickness of the rubber layer. Beginning from the third mode of vibrations of the system the decrease of the natural frequencies is almost constant for the rubber layer 2 mm or 3 mm and is continuously decreasing for rubber layer 4-6 mm (See fig.6).

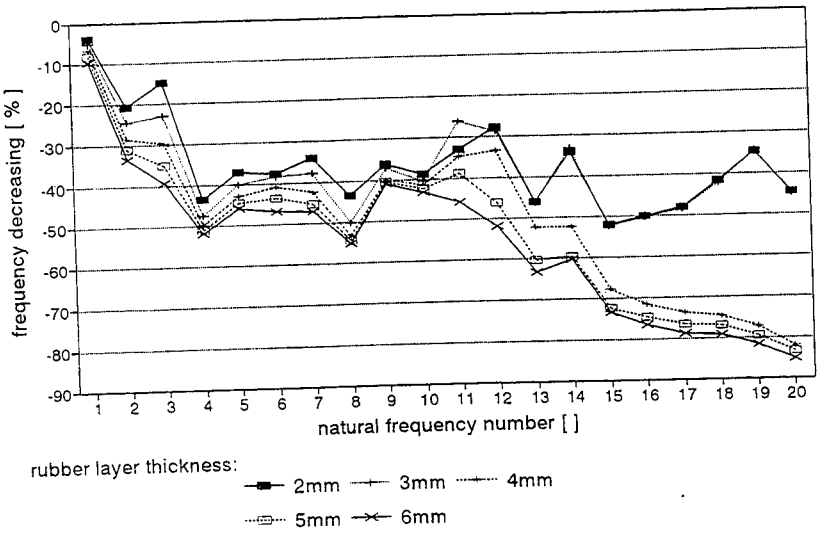

Fig. 6. Changes of natural frequencies

6. Comparison with experimental results

The equivalent coupling loss factor defining the energy flow between the plates has been determined experimentally [3] for a model consisting of two subsystems: two plates. The coupling loss factor in such two element model may be specified by the following equation:

$$\eta_{zast.} = \frac{\eta_2}{\frac{N_2}{N_1}\frac{E_{1tot}}{E_{2tot}} - 1} \qquad (7)$$

The quotient of plate energies E_1/E_2 in a two-element model is relevant to the quotient of energy in the first and fifth subsystem (E_1/E_5) in the five element model presented in figure 2 the value of these quotient is defined with the equation (6)

In the picture we have presented the values of the equivalent coupling loss factor in the connection. Individual points in the diagram show the results obtained experimentally. The values received in computer simulation have been presented as a continuous diagram. The upper curve shows the values of the coupling loss factor in the joint before the application of the rubber layer.

In the frequency range above ca. 125 Hz we have received a very good comparison of experimental results and computer simulation results performed with the AutoSEA software. At the frequency of about 200Hz there occurs a local minimum of the equivalent coupling loss factor between the plates. The value of the minimum is essentially influenced by the value of the rubber damping loss factor. The frequency (with the minimum CLF) is strongly influenced by the peak frequency of the rubber damping curve.

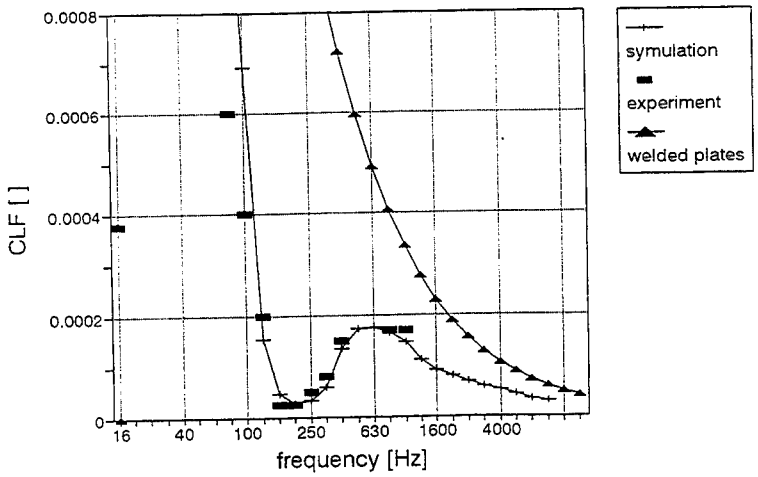

Fig.7 Equivalent CLF factor in the joint

7. Conclusion

A way of modelling the vibroacoustical energy flow with the help of SEA method has been presented in the work. We have examined the screw connection of two plates, where a rubber elastic layer has been applied. A comparison has also been made between the results of computer simulation of the mechanical energy flow with SEA method and the experimental results, and thus we have noticed the good correlation, especially as far as middle frequencies are concerned.

The joint modification through introduction of the rubber separator has a remarkable impact on the acoustic energy flow:

- The application of the elastic layer in the joint in question lowers the value of equivalent coupling loss factor in the whole frequency range.
- the value of rubber damping factor has most significant influence on the acoustic energy flow through connection in middle frequencies range:
  * The minimum value of the equivalent coupling loss factor in a joint is essentially influenced by the rubber separator damping loss factor.
  * The frequency of minimum CLF occurrence is strongly influenced by the peak frequency of the rubber damping curve.

The increasing thickness of the rubber layer produces on decreasing natural frequencies of the structure.

8. Bibliography:

[1] AutoSEA - User Guide Vibro-Acoustic Sciences Limited 1992.
[2] Fahy F.J. Sound and Structural Vibration: Radiation, Transmission and Response Academic Pres 1985.
[3] Fortuin J. Smals N. Panuszka R. "Method of estimating the coupling loss factor for a set of plates" Mechanic, Technical University of Mining and Metallurgy, Cracow, 10, 1991.
[4] Lalor, N.: The evaluation of SEA Coupling Loss Factors. Proc. V School "Energy Methods in Vibroacoustics" - Supplement, Kraków-Zakopane 1996.
[5] Lyon R., DeJong R.: Theory and Application of Statistical Energy Analysis. Butterworth-Heinemann, Boston, 1995.

Variation Analysis on Coupling Loss Factor due to the Third Coupled Subsystem in Statistical Energy Analysis

Hongbing Du Fook Fah Yap
School of Mechanical & Production Engineering
Nanyang Technological University
Singapore 639798

Abstract

Statistical Energy Analysis (SEA) is potentially a powerful method for analyzing vibration problems of complex systems, especially at high frequencies. An important parameter in SEA modeling is the coupling loss factor which is usually obtained analytically based on a system with only two coupled elements. Whether the coupling loss factor obtained in the classical way is applicable to a practical problem, which normally comprises of more than two elements, is of importance to the success of SEA. In this paper, the variation of coupling loss factor between two subsystems due to the presence of a third coupled subsystem is investigated. It is shown that the degree to which the coupling loss factor is affected depends on how strong the third subsystem is coupled. It also depends on the distribution of the modes in the coupled subsystems. This kind of effect will diminish when the damping is high, subsystems are reverberant, or ensemble-average is considered, but not for individual cases.

1 Introduction

SEA is potentially a powerful method for analyzing vibration and acoustic problems of complex systems, especially at high frequencies, because of the simplicity of its equations compared to other deterministic analysis techniques. SEA models a system in terms of interconnected subsystems. The coupling parameter between any two subsystems is characterized by a coupling loss factor. If the coupling loss factors and internal (damping) loss factors of all subsystems are known, the power balance equation (e.g., see [1]) for each subsystem can be established. From this set of equations, SEA predicts the system response (due to certain types of excitation) in terms of the average energy of every subsystem. The energy can in turn be related to other response quantities such as mean velocity or strain.

Historically, the SEA power balance equations were initially derived from an analysis of two coupled oscillators [2, 3]. It has been shown that the energy flow between them is directly proportional to the difference in their uncoupled modal energies. The theory has then been extended to systems with multi-coupled subsystems (e.g., [4]). Strictly this extension is only applicable if certain assumptions are justified [4, 5]. Also the new concept of indirect coupling loss factor, which is used to represent the energy flow proportionality between the indirectly coupled subsystems, is also introduced.

In practice, the indirect coupling loss factors are normally ignored in SEA applications because they are very difficult to determine analytically. Only coupling loss factors between directly coupled substructures are considered. Some analyses [6–8] have shown that this approximation may lead to significant errors in the predicted results if certain conditions are not met in the system. These conditions include not only the well known requirement of weak coupling between subsystems (e.g., see [6]), but also others, such as given by Langley that the response in each element must be reverberant [7]; and by Kean that there should be no dominant modes (peaks) inside the frequency-averaging band [8]. However, it is usually difficult to know whether these conditions are satisfied for a particular system. In fact the above mentioned conditions do not always hold for practical engineering cases. On this point of view, the importance of a coupling loss factor for describing the coupling between indirectly coupled subsystems are to be further examined.

A related question is whether the coupling loss factors obtained from the system with only two subsystems can still be applied when other subsystems are present. Generally, the coupling loss factor is sensitive to the amount of overlap between the modes of the two coupled subsystems. When additional subsystems are coupled to the original two-subsystem model, the mode distributions of the originally coupled two subsystems will be affected. The change of mode distributions will further affect the modal overlap between the coupled two subsystems and finally the coupling loss factor between them. However, general estimation methods for coupling loss factor assume that the coupling parameters between two subsystems are not affected much by the presence of the other subsystems. Therefore the conventional approaches of deriving coupling loss factor are mostly based on consideration of a two-subsystem model only. One method is the wave approach, by which the coupling loss factor used in the SEA applications are derived analytically from averaged transmission factors of waves that are transmitted through a junction between semi-infinite subsystems. This method only takes into account local properties at the joints and sometimes may be inaccurate. Recent research [1, 7, 9–11] based on the model with two-coupled subsystems has shown that the coupling parameter does depend on other system properties, such as damping loss factor, etc. It can be argued that, if there is a third coupled subsystem, the coupling parameters between the first two subsystems will also depend on the energy flow to the third subsystem. Therefore, from a practical point of view, the coupling loss factor estimated for two-coupled subsystems, ignoring the indirectly coupled subsystems, can only be of approximate value.

In this paper, the variation of coupling loss factor between two subsystems due to the presence of a third coupled subsystem is studied. In the following sections, the coupling loss factor is firstly expressed in terms of global mobility functions. The exact solution of mobility functions is only for simple structures. However, for general structures, it can be obtained by Finite Element Analysis (FEA) [10, 11]. The coupling loss factors obtained respectively in the cases with and without the third subsystem in the model are compared for two particular system configurations, respectively. The system used in this investigation is one-dimensional simply supported beams coupled in series by rotational springs. By varying the spring stiffness, the strength of the coupling between the second and the third subsystems can be changed. It is shown that the effect of the third coupled subsystem on the coupling loss factor between the first two coupled subsystems depends on how strong the third subsystem is coupled. For each individual case, it is also shown that this kind of effect may be positive or negative, depending on the distribution of modes in the coupled subsystems.

2 Coupling Loss Factor by Global Modal Approach

In this section, a modal method is used to derive coupling loss factor in a system with any number of coupled subsystems. The result is then simplified for two cases: (1) a three-subsystem model; (2) a two-subsystem model which is simply substructured from the previous three-subsystem model by disconnected the third subsystem.

For a linear system which consists of N coupled subsystems, if "rain-on-the-roof" excitation [10] is assumed to be applied to each subsystem in turn, the corresponding response energy can be expressed as

$$E_{ij} = m_i S_j \int_{\Omega} \int_{subsystem\,i} \int_{subsystem\,j} |H(r,s,\omega)|^2 \, dr \, ds \, d\omega \qquad (1)$$

where E_{ij} is the total time-averaged response energy of the subsystem i due to the excitation on the subsystem j, $H(r,s,\omega)$ is the transfer mobility function between the response points r and the excitation point s, Ω is the averaging range of frequency, ω, m and S are the mass density and the power spectral density of excitation. The input power due to the excitation is given by

$$\Pi_j = S_j \int_{\Omega} \int_{subsystem\,j} Re\left[H(s,s,\omega)\right] \, ds \, d\omega \qquad (2)$$

where $Re[H(s,s,\omega)]$ is the real part of the point mobility at the position s. For simplicity, two terms, a_{ij} and b_j, are defined as

$$a_{ij} = \frac{E_{ij}}{m_i S_j} = \int_{\Omega} \int_{subsystem\,i} \int_{subsystem\,j} |H(r,s,\omega)|^2 \, dr \, ds \, d\omega \qquad (3)$$

$$b_j = \frac{\Pi_j}{S_j} = \int_{\Omega} \int_{subsystem\,j} Re\left[H(s,s,\omega)\right] \, ds \, d\omega \qquad (4)$$

The mobility function, $H(r,s,\omega)$, is to be expressed in terms of the global modes of the system, which can be obtained by Finite Element Analysis (FEA). By the principle of reciprocity of the mobility function, the relation of $a_{ij} = a_{ji}$ always holds regardless of the strength of coupling and the magnitude of input power if the excitation is "rain-on-the-roof". Theoretically applying the Power Injection Method [12] we can obtain the SEA equation as

$$\mathbf{\Pi} = [\eta]\mathbf{E} \tag{5}$$

where $\mathbf{\Pi} = \{\Pi_1, \Pi_2, \ldots, \Pi_N\}^T$ and $\mathbf{E} = \{E_1, E_2, \ldots, E_N\}^T$. The SEA loss factor matrix $[\eta]$ is

$$[\eta] = \begin{bmatrix} (\eta_1 + \sum_{i\neq 1}^{N}\eta_{1i}) & -\eta_{21} & \cdots & -\eta_{N1} \\ -\eta_{12} & (\eta_2 + \sum_{i\neq 2}^{N}\eta_{2i}) & \cdots & -\eta_{N2} \\ \vdots & \vdots & \ddots & \vdots \\ -\eta_{1N} & -\eta_{2N} & \cdots & (\eta_N + \sum_{i\neq N}^{N}\eta_{Ni}) \end{bmatrix}$$

$$= \frac{1}{\omega_c}\begin{bmatrix} \frac{m_1 a_{11}}{b_1} & \frac{m_1 a_{12}}{b_2} & \cdots & \frac{m_1 a_{1N}}{b_N} \\ \frac{m_2 a_{21}}{b_1} & \frac{m_2 a_{22}}{b_2} & \cdots & \frac{m_2 a_{2N}}{b_N} \\ \vdots & \vdots & \ddots & \vdots \\ \frac{m_N a_{N1}}{b_1} & \frac{m_N a_{N2}}{b_2} & \cdots & \frac{m_N a_{NN}}{b_N} \end{bmatrix}^{-1} = \frac{1}{\omega_c}\mathbf{B}\,\mathbf{A}^{-1}\,\mathbf{M}^{-1} \tag{6}$$

where, η_i is the internal loss factor for subsystem i, η_{ij} is the coupling loss factor from subsystem i to subsystem j, ω_c is the central frequency of the averaging band Ω,

$$\mathbf{B} = \begin{bmatrix} \ddots & & \\ & b_i & \\ & & \ddots \end{bmatrix}, \quad \mathbf{M} = \begin{bmatrix} \ddots & & \\ & m_i & \\ & & \ddots \end{bmatrix} \quad \mathbf{A} = [a_{ij}]$$

From equation (6), the reciprocity principle of the coupling loss factors can be easily seen, due to $a_{ij} = a_{ji}$,

$$\frac{\eta_{ij}}{\eta_{ji}} = \frac{m_j b_j}{m_i b_i} = \frac{m_j b_j/(\omega_c \pi/2)}{m_i b_i/(\omega_c \pi/2)} \tag{7}$$

Where, $(m_i b_i)/(\omega_c \pi/2)$ is the averaged real part of point mobility [4] and can be regarded as the generalized modal density of the subsystem i. Assuming weak coupling and light damping, it approximately equals to the classical definition of modal density [13]. Therefore, the relation given by equation (7) also reduces to the classical reciprocity principle.

2.1 Substructured two-subsystem model

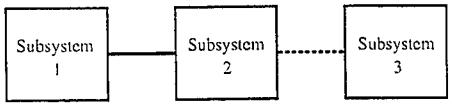

Figure 1: A general SEA model with three coupled subsystems in series

Consider a whole system with three substructures coupled in series as shown in Figure 1. If subsystem 3 is removed, the coupling loss factors between subsystems 1 and 2 are given in the equation

$$\begin{bmatrix} \eta_1+\eta_{12} & -\eta_{21} \\ -\eta_{12} & \eta_2+\eta_{21} \end{bmatrix} = \frac{1}{\omega_c} \begin{bmatrix} \dfrac{b_1 a_{22}}{m_1(a_{11}a_{22}-a_{12}a_{21})} & -\dfrac{b_1 a_{12}}{m_2(a_{11}a_{22}-a_{12}a_{21})} \\ -\dfrac{b_2 a_{21}}{m_1(a_{11}a_{22}-a_{12}a_{21})} & \dfrac{b_2 a_{11}}{m_2(a_{11}a_{22}-a_{12}a_{21})} \end{bmatrix}$$

$$\approx \frac{1}{\omega_c} \begin{bmatrix} \dfrac{b_1}{m_1 a_{11}} & -\dfrac{b_1 a_{12}}{m_2 a_{11} a_{22}} \\ -\dfrac{b_2 a_{21}}{m_1 a_{11} a_{22}} & \dfrac{b_2}{m_2 a_{22}} \end{bmatrix} \tag{8}$$

The approximation in the above equation is due to $a_{11}a_{22} \gg a_{12}a_{21}$ when the coupling is weak. Manipulating equation (8) with or without using the approximation both can work out the coupling loss factors η_{12} and η_{21} as

$$\eta_{12} = \frac{1}{m_1 b_1} \frac{(m_1 b_1)(m_2 b_2)\left[\dfrac{b_1}{\omega_c m_1 a_{11}}\eta_2 - \dfrac{b_2}{\omega_c m_2 a_{22}}\eta_1\right]}{m_2 b_2 \dfrac{b_2}{\omega_c m_2 a_{22}} - m_1 b_1 \dfrac{b_1}{\omega_c m_1 a_{11}}} \tag{9}$$

$$\eta_{21} = \frac{1}{m_2 b_2} \frac{(m_1 b_1)(m_2 b_2)\left[\dfrac{b_1}{\omega_c m_1 a_{11}}\eta_2 - \dfrac{b_2}{\omega_c m_2 a_{22}}\eta_1\right]}{m_2 b_2 \dfrac{b_2}{\omega_c m_2 a_{22}} - m_1 b_1 \dfrac{b_1}{\omega_c m_1 a_{11}}} \tag{10}$$

The equations are true regardless of the strength of the coupling. It can be seen that η_{12} and η_{21} depend on the values of the three terms $m_i b_i$, η_i and $b_i/(\omega_c m_i a_{ii})$. The first two are the generalized modal density and the internal loss factor, or in combination equivalent to modal overlap factor. The third one, by noting the definitions of b_i and a_{ii}, is the ratio of input power to response energy for the directly excited subsystem, i.e., the total loss factor of subsystem i. From equation (8), this term can be approximately expressed as

$$\begin{matrix}\text{Total loss factor} \\ \text{of subsystem } \ i\end{matrix} = \eta_{total,i} = \frac{b_i}{m_i \omega_c a_{ii}} \approx \eta_i + \sum_{j \neq i} \eta_{ij} \tag{11}$$

In the classical wave approach, where semi-infinite subsystems are assumed, the total internal loss factors becomes

$$\eta_{total,1} = \eta_1 + \eta_{12}^{\infty} \quad \text{and} \quad \eta_{total,2} = \eta_2 + \eta_{21}^{\infty} \tag{12}$$

where η_{ij}^{∞} is the classical coupling loss factor. Substituting equation (12) into equations (9) and (10), η_{ij} reduces to the classical η_{ij}^{∞}, which only depends on the local properties at the joints rather than other properties of the system, such as damping. If the subsystem modal parameters are used to evaluate the term, $b_i/(\omega_c m_i a_{ii})$, then the total loss factor is just the internal loss factor of the subsystem and the coupling loss factor is equal to zero. This is reasonable because using the uncoupled modal parameters instead of the coupled modal parameters is actually equivalent to removing the coupling between two subsystems.

However, for finite system where the assumption of semi-infinity is not justified, there will be no immediate simplication for equations (9) and (10). Numerically, FEA can be employed to obtain the global modes and then the coupling loss factor can be calculated [10, 11].

2.2 Full three-subsystem model

Instead of substructuring, consider the three-subsystem model as a whole system, shown in figure 1. Now the order of equation (6) is reduced to 3. With the global modal parameters obtained from FEA, the coupling loss factors can be directly evaluated. However, when the coupling between subsystems is weak, the order-reduced equation (6) is still able to be simplified. Matrix $\mathbf{A}$ may be alternatively expressed in the form of

$$\mathbf{A} = \begin{bmatrix} a_{11} & 0 & 0 \\ 0 & a_{22} & 0 \\ 0 & 0 & a_{33} \end{bmatrix} + \begin{bmatrix} 0 & a_{12} & 0 \\ a_{12} & 0 & a_{23} \\ 0 & a_{23} & 0 \end{bmatrix} + \begin{bmatrix} 0 & 0 & a_{13} \\ 0 & 0 & 0 \\ a_{13} & 0 & 0 \end{bmatrix} \tag{13}$$

where the terms on the right side are sequentially defined as $\mathbf{A_1}$, $\mathbf{A_2}$ and $\mathbf{A_3}$. Under the assumption of weak coupling, the non-zero entries in $\mathbf{A_1}$, $\mathbf{A_2}$ and $\mathbf{A_3}$ will be of the order $O(\varepsilon^0)$, $O(\varepsilon^1)$ and $O(\varepsilon^3)$, respectively [14]. The inverse of matrix $\mathbf{A}$ may be approximately written as

$$\mathbf{A}^{-1} = \mathbf{A_1}^{-1} - \mathbf{A_1}^{-1}\mathbf{A_2}\mathbf{A_1}^{-1} - \mathbf{A_1}^{-1}\mathbf{A_3}\mathbf{A_1}^{-1} + \mathbf{A_1}^{-1}\mathbf{A_2}\mathbf{A_1}^{-1}\mathbf{A_2}\mathbf{A_1}^{-1} + \cdots \tag{14}$$

As an approximation, substituting only the first three terms in equation (14) into equation (6) gives

$$[\eta] \approx 1/\omega_c \begin{bmatrix} \dfrac{b_1}{m_1 a_{11}} & -\dfrac{b_1 a_{12}}{m_2 a_{11} a_{22}} & -\dfrac{b_1 a_{13}}{m_3 a_{11} a_{33}} \\ -\dfrac{b_2 a_{12}}{m_1 a_{11} a_{22}} & \dfrac{b_2}{m_2 a_{22}} & -\dfrac{b_2 a_{23}}{m_3 a_{22} a_{33}} \\ -\dfrac{b_3 a_{13}}{m_1 a_{11} a_{13}} & -\dfrac{b_3 a_{23}}{m_2 a_{22} a_{33}} & \dfrac{b_3}{m_3 a_{33}} \end{bmatrix} \tag{15}$$

Generally, under the condition of weak coupling, the indirect coupling loss factors, η_{13} and η_{31}, are much smaller than the direct coupling loss factors and the internal loss factors [5,7,15]. The diagonal elements in $[\eta]$ can therefore be approximated to the sum of internal loss factor and direct loss factor. It can be shown from equation (15) that equation (11) remains valid for three coupled subsystems. But in the three-subsystem case, the term, $b_i/(\omega_c m_i a_{ii})$, is to be evaluated by using the global modes of the three-subsystem model.

3 Numerical Examples and Variation Analysis

In this section, two examples with different configurations are used to show the variation of coupling loss factor due to the presence of a third coupled subsystem. The coupling loss factor of the two-subsystem model is evaluated by using equations (9) and (10). For the three-subsystem model, equations (6) and (15) are used. It can be shown that both equations (6) and (15) give the same results as the couplings are weak.

3.1 Structural details and SEA model

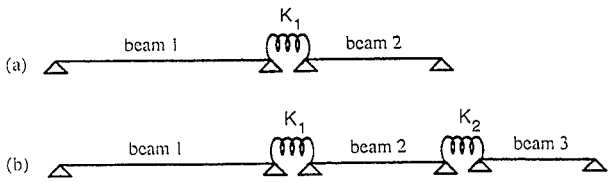

Figure 2: A structural model comprising of three beams

To begin example calculations, consider initially a two-subsystem model (figure 2(a)) which is two thin beams coupled through a rotational spring. The group of flexural vibration modes of each beam are taken as a SEA subsystem. The spring provides weak coupling between them where only rotational moment is transmitted. When beam 3 is connected at the free end of beam 2 to the original two-beam model, a three-subsystem model is formed (figure 2(b)). The specifications for the three beams are given in table 1. The spring stiffness, K_2, is adjustable in order to look into the significance of the effect of the third subsystem. There are two cases where the length of beam 2 is: (i) $L_2 = 1.0m$; (ii) $L_2 = 1.1m$. The spring constants at the joints are chosen to be weak enough to ensure that:(a) the coupling loss factor is much smaller than the internal loss factor; (b) the indirect coupling loss factor is much smaller than the direct coupling loss factor.

In the global modal approach (see section 2), the modes of two-subsystem model and three-subsystem model are obtained from FEA. In numerical simulation, the

Table 1: The specifications of the three beams

BEAM	1	2	3
length (m)	2.0	1.0 & 1.1	0.7
width (mm)	4		
Thickness (mm)	2		
Density (Kg/m^3)	7890		
Young's Modulus (N/m^2)	196E+9		
Poisson Ratio	0.29		
spring constant, K_1 (Nm/rad)	1.0		

central frequency is 200Hz and the averaging band is selected as $100 \sim 300$Hz. In order to take into account the contribution from the modes out of the band, all the modes up to 500Hz are extracted for evaluating the mobility functions in averaging. The modal loss factor is assumed to be the same for each modes used in averaging. This means that the internal loss factor is the same for each subsystem and is equal to the modal loss factor [11]. The results given are plotted against the modal loss factor in order to show the damping effect at the same time.

3.2 Results and discussion

Figure 3 shows the identified coupling loss factor η_{12} for the case (i) ($L_2 = 1.0m$) with different stiffness of K_2. The case of $K_2 = 0$ means that the third subsystem

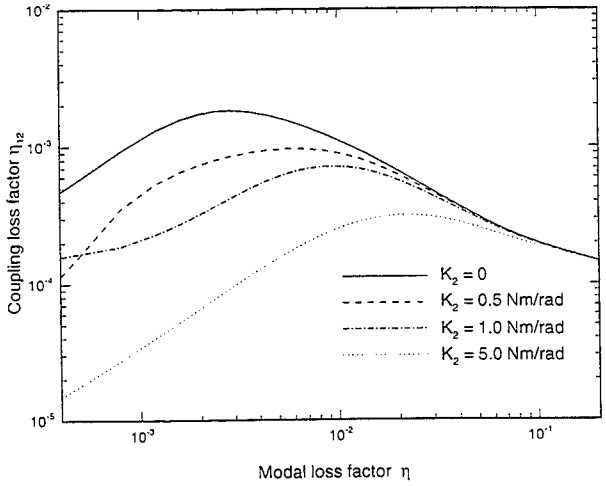

Figure 3: η_{12} is negatively affected in three-subsystem model

is not present. It can be seen that the coupling loss factor η_{12} is decreased in the low

range of damping while the strength of the coupling between subsystem 2 and 3 is increased. The stronger the coupling, the more η_{12} is decreased.

On the other hand, for the case (ii) where $L_2 = 1.1m$, the different results are shown in figure 4 where the presence of the third subsystem would mainly increase η_{12} in the low range of damping. The increasing magnitude is also dependent on the strength of coupling between subsystem 2 and 3. The explanation for the different variation trends of η_{12} due to the third coupled subsystem between figure 3 and 4 will be given later.

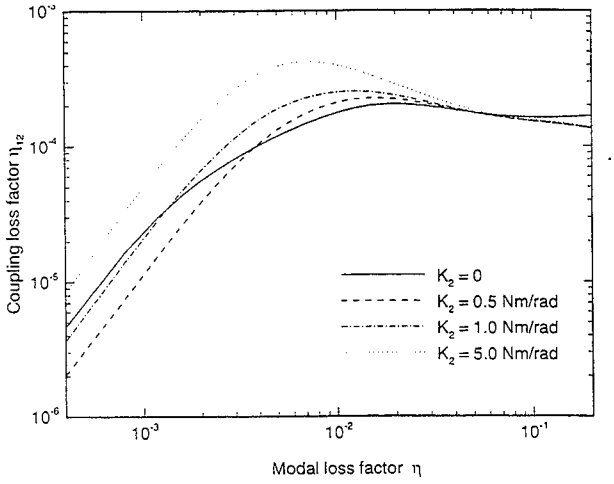

Figure 4: η_{12} is positively affected in three-subsystem model

From figure 3 and 4, the effect of damping on the coupling loss factor can also be observed. In the low damping region, increasing damping would increase coupling loss factor. After a certain turnover point, increasing damping would make the coupling loss factor decrease and finally η_{12} becomes convergent to a value. This agrees with the conclusions drawn in [10, 11]. It is shown that, even though the length of beam 2 has a slight difference in figure 3 and 4, the converged values are still very close. Thus, the converged value seems not to depend on the variation of coupling strength at K_2 and the structural details, although, with the third subsystem existing in the system, the convergent speed is faster. Therefore, it is reasonable to believe that the converged coupling loss factor at sufficiently high damping only depends on the property of the joint rather than other system properties. This joint-dependent property of coupling loss factor in the high range of damping accords with the assumption in the wave approach. Here, it is convenient to define the convergent region in the figure 3 and 4 as the "joint-dependent zone".

However, before the "joint-dependent zone", coupling loss factor seems very sensitive to the variation of damping loss factor as well as the strength of coupling between subsystem 2 and 3. It is because in the low damping region the system

modal properties have been playing a major role in determining coupling loss factor [10, 11]. In general, the coupling loss factor represents the ability of energy transmitted between subsystems. It depends not only on the physical strength of the coupling (e.g., spring stiffness in the examples), but also on the amount of overlap between the modes of two connected subsystems. The higher modal overlap between the modes of two connected subsystem, the more energy is transmitted between the subsystems. As a result, the coupling loss factor will be higher even though the physical strength at the joint is unchanged. If the modes in one subsystem are distributed exactly the same as those in one another(for instance, two exactly same structures are coupled together), the coupling loss factor would be varied to the maximum, and vice versa. Therefore, this region could be likely defined as "modal-sensitive zone".

In the "modal-sensitive-zone", the dependence of coupling loss factor on the amount of overlap between the modes of two connected subsystems has been clearly shown in figures 3 and 4. For the case (i) illustrated in figure 3, the length of beam 2 is half of beam 1. Due to the characteristic of mode distribution in beam structure, the amount of overlap between the modes of subsystem 1 and 2 is more than that in the case (ii) shown in figure 4, where beam 1 is 2 meters and beam 2 is 1.1 meters. Therefore, case (i) has higher coupling loss factor than case (ii) in "modal-sensitive zone". When the third beam is coupled, the induced variation of coupling loss factor depends on how the amount of overlap between the modes of subsystems 1 and 2 is affected. It can be increased or decreased and thus the coupling loss factor between subsystems 1 and 2 can also be increased or decreased due to the third coupled subsystem. For example, the amount of such overlap in case (i) is decreased after the third subsystem is coupled. As a result, the coupling loss factor, η_{12}, becomes decreased.

The above discussed variability of coupling loss factor due to the third coupled subsystem has been shown for individual cases. On the other hand, if an ensemble of similar structures are considered, this sensitivity may be reduced (as it is sometimes positive or negative depending on each special situation). However, such a variability obtained from two typical examples is nevertheless very useful when one individual case is studied in SEA or SEA-like problems. The ignorance of such effect of the other coupled subsystems on the coupling loss factor may become one of the possible error sources causing SEA failure.

4 Conclusions

The variation of coupling loss factor due to the third coupled subsystem is studied in this paper. The effect of a third coupled subsystem on the coupling loss factor between the first two coupled subsystems depends on how strong the third subsystem is coupled. Roughly, along with the damping in the subsystems, "joint-dependent zone" and "modal-sensitive zone" are defined according to the different variation properties of coupling loss factor. In the "modal-sensitive zone", the ef-

fect of a third coupled subsystem on the coupling loss factor could be positive or negative. It depends on how the amount of overlap between the modes of two connected subsystems is affected. This "modal-sensitive" effect may be averaged out for an ensemble of structures, but it is important when SEA is applied to individual cases. In the "joint-dependent zone", the coupling loss factor is insensitive to the strength of the coupling between the second and third subsystems. Since the two different zones are allocated according to the system damping (which is equivalent to modal overlap factor when the central frequency and modal density are fixed), it shows the importance of reverberance in subsystems when the classical SEA is applied [7, 8]. How to take into account the effect of the other coupled subsystems in evaluating coupling loss factor, especially when the system damping is low and when an individual case is considered, definitely needs to be further investigated.

References

[1] Richard H. Lyon and Richard G. DeJong. *Theory and Application of Statistical Energy Analysis*. Butterworth-Heinemann, second edition, 1995.

[2] Richard H. Lyon and G. Maidanik. Power flow between linearly coupled oscillators. *Journal of the Acoustic Society of America*, 34:623–639, 1962.

[3] Eric E. Ungar. Statistical energy analysis of vibrating systems. *Transactions of the ASME, Journal of Engineering for Industry*, pages 626–632, November 1967.

[4] F. J. Fahy. Statistical energy analysis. In R. G. White and J. G. Walker, editors, *Noise and Vibration*, chapter 7, pages 165–186. Chichester, Ellis Horwood, 1982.

[5] J. M. Cuschieri and J. C. Sun. Use of statistical energy analysis for rotating machinery, part II: Coupling loss factors between indirectly coupled substructures. *Journal of Sound and Vibration*, 170(2):191–201, 1994.

[6] P. W. Smith. Statistical models of coupled dynamical systems and the transition from weak to strong coupling. *Journal of the Acoustic Society of America*, 65:695–698, 1979.

[7] S. Finnveden. Ensemble averaged vibration energy flows in a three-element structure. *Journal of Sound and Vibration*, 187(3):495–529, 1995.

[8] A. J. Keane. A note on modal summations and averaging methods as applied to statistical energy analysis (SEA). *Journal of Sound and Vibration*, 164(1):143–156, 1993.

[9] B. R. Mace. The statistical energy analysis of two continuous one-dimensional subsystems. *Journal of Sound and Vibration*, 166(3):429–461, 1993.

[10] Hongbing Du and Fook Fah Yap. A study of damping effects on coupling loss factor used in statistical energy analysis. In *Proceedings of the Fourth International Congress on Sound and Vibration*, pages 265–272, St. Petersburge, Russia, June 1996.

[11] Fook Fah Yap and J. Woodhouse. Investigation of damping effects on statistical energy analysis of coupled structures. *Journal of Sound and Vibration*, 197(3):351–371, 1996.

[12] D. A. Bies and S. Hamid. In situ determination of loss and coupling loss factors by the power injection method. *Journal of Sound and Vibration*, 70(2):187–204, 1980.

[13] L. Cremer, M. Heckl, et al. *Structure-Borne Sound: Structural Vibrations and Sound Radiation at Audio Frequencies*. Springer-Verlag, second edition, 1987.

[14] R. S. Langley. A derivation of the coupling loss factors used in statistical energy analysis. *Journal of Sound and Vibration*, 141(2):207–219, 1990.

[15] J. C. Sun, C. Wang, et al. Power flow between three series coupled oscillators. *Journal of Sound and Vibration*, 189(2):215–229, 1996.

THE EFFECT OF CURVATURE UPON VIBRATIONAL POWER TRANSMISSION IN BEAMS

S.J. Walsh[1] and R.G.White[2]

(1) Department of Aeronautical and Automotive Engineering and Transport Studies
Loughborough University

(2) Department of Aeronautics and Astronautics
University of Southampton

ABSTRACT

Previous research into structural vibration transmission paths has shown that it is possible to predict vibrational power transmission in simple beam and plate structures. However, in many practical structures transmission paths are composed of more complex curved elements; therefore, there is a need to extend vibrational power transmission analyses to this class of structure. In this paper, expressions are derived which describe the vibrational power transmission due to flexural, extensional and shear types of travelling wave in a curved beam which has a constant radius of curvature. By assuming sinusoidal wave motion, expressions are developed which relate the time-averaged power transmission to the travelling wave amplitudes. The results of numerical studies are presented which show the effect upon power transmission along a curved beam of: (i) the degree of curvature; and (ii) various simplifying assumptions made about the beam deformation.

1. INTRODUCTION

Previous research into structural transmission paths has shown it is possible to predict vibrational power transmission in simple beam and plate structures. More recently, transmission through pipes with bends, branches and discontinuities has been studied, which has led to useful design rules concerning the position and size of pipe supports for minimum power transmission[1]. However, in many practical structures transmission paths are composed of more complex curved elements. Therefore, there is a need to extend power transmission analyses to this class of structure.

Wave motion in a curved beam with a constant radius of curvature has been considered by Love [2] who assumed that the centre-line remains unextended during flexural motion, whilst flexural behaviour is ignored when considering extensional motion. Using these assumptions the vibrational behaviour of complete or incomplete rings has been considered by many researchers who are interested in the low frequency behaviour of arches and reinforcing rings. In reference [2] Love also presented equations for thin shells which include the effects of extension of the mid-surface during bending motion. Soedel [3] reduced these equations and made them applicable to a curved beam of constant radius of curvature. In an alternative approach Graff [4] derived these equations from first principles and also constructed frequency verses wavenumber and wavespeed versus wavenumber graphs. Philipson [5] derived a set of equations of motion which included extension of the central line in the flexural wave motion, and also rotary inertia effects. In a development analogous to that of Timoshenko for straight beams, Morley [6] introduced a correction for radial shear when considering the vibration of curved beams. Graff later presented frequency versus wave number and wave speed versus wave number data for wave motion in a curved beam, when higher order effects are included [7].

In this paper, expressions for vibrational power transmission in a curved beam are derived from first principles. In the next section two sets of governing equations for wave motion in a curved beam are presented both of which include coupled extensional-flexural motion. The first set is based upon a reduction of Love's thin shell equations mentioned above. The second set is based upon a reduction of Flügge's thin shell equations [8]. In section three, the expressions for stresses and displacements presented in section two are used to derive formulae for vibrational power transmission in terms of centre-line displacements. By assuming sinusoidal wave motion, expressions are developed which relate the time-averaged power transmission to the extensional and flexural travelling wave amplitudes. In section four, corrections for rotary inertia and shear deformation are introduced. The results of numerical studies of these expressions are presented which show the effect upon wave motion and power transmission of (i) the degree of curvature, and (ii) the various simplifying assumptions made about the beam deformation.

2. WAVE MOTION IN CURVED BEAMS

In this section the governing relations between displacements, strains, stresses and force resultants in a curved beam are presented. The centre-line of the beam lies in a plane and forms a constant radius of curvature. The cross-section of the beam is uniform and symmetrical about the plane and it is assumed that there is no motion perpendicular to the plane. It is also assumed that the beam material is linearly elastic, homogeneous, isotropic and continuous.

Consider a portion of the curved beam, as shown in Figure 1. The circumferential coordinate measured around the centre-line is s, while the outward pointing normal coordinate from the centre-line is z, and the general radial coordinate is r. A complete list of notation is given in the appendix. For small displacements of thin beams the assumptions, known as "Love's first approximation" in classical shell theory, can be made [8]. This imposes the following linear relationships between the tangential and radial displacements of a material point and components of displacement at the undeformed centre-line:

$$U(r, s, t) = u(R, s, t) + z\,\phi\ (s, t) \tag{1}$$

$$W(r, s, t) = w(R, s, t) \tag{2}$$

where u and w are the components of displacement at the centre-line in the tangential and radial directions, respectively, ϕ is the rotation of the normal to the centre-line during deformation:

$$\phi = \underbrace{\frac{u}{R}}_{\left(\begin{smallmatrix}\text{angle of}\\ \text{curvature}\end{smallmatrix}\right)} - \underbrace{\frac{\partial w}{\partial s}}_{\left(\begin{smallmatrix}\text{rotational displacement}\\ \text{of straight beam}\end{smallmatrix}\right)} \tag{3}$$

and W is independent of z and is completely defined by the centre-line component w.

Circumferential strain consists of both an extensional strain and bending strain component. Expressions for these are listed in table 1. The strain-displacement expressions of the Love and Flügge based equations are identical. However, in the total circumferential strain of the Love based theory, the term z/R in the denominator has been neglected with respect to unity. Assuming the material to be linearly elastic, the circumferential stress-strain relationship is given by Hooke's Law, whilst the shear strain, γ_{sr}, and shear stress, σ_{sr}, are assumed to be zero. Assuming the material

to be homogeneous and isotropic, the material properties E, G and ν can be treated as constants. Thus, by integrating the stresses over the beam thickness, force and moment resultants can be obtained, which are listed in table 2. The adopted sign convention is shown in Figure 2.

Equations of motion for a curved beam are presented in [4]. These equations are derived in terms of the radian parameter θ. By applying the substitution, $s = R\theta$, the equations of motion can be expressed in terms of the circumferential length, s. These equations are listed in [9] along with the Flügge based equations of motion which have been obtained by a reduction of the equations of motion for a circular cylindrical shell presented in [8]. An harmonic solution of the equations of motion can be obtained by assuming that extensional and flexural sinusoidal waves propagate in the circumferential direction. The harmonic form of the equations of motion are also listed in [9].

3. VIBRATIONAL POWER TRANSMISSION IN CURVED BEAMS

In this section the expressions for displacements and stresses presented in section two are used to derive the structural intensity and power transmission due to flexural and extensional travelling waves in a curved beam. The structural intensity expressions are formulated in terms of displacements at the centre-line. By assuming sinusoidal wave motion, expressions are developed which relate the time-averaged power transmission to the flexural and extensional travelling wave amplitudes.

Structural Intensity in the circumferential direction of a curved beam is given by [10]:

$$I_s = \underbrace{\left(-\sigma_s \frac{\partial U}{\partial t}\right)}_{\left(\begin{array}{c}\text{intensity due to}\\ \text{circumferential stress}\end{array}\right)} + \underbrace{\left(-\sigma_{sr} \frac{\partial W}{\partial t}\right)}_{\left(\begin{array}{c}\text{intensity due to}\\ \text{radial shear stress}\end{array}\right)} \qquad (4)$$

By integrating across the beam thickness power transmission per unit length in the circumferential direction is obtained:

$$P_s = \int_{-h/2}^{h/2} I_s \, dz \qquad (5)$$

Substituting the Love based circumferential stress-strain relation and strain-displacement expression into equation (5) the power transmission due to circumferential stress is obtained. (A full derivation is given in [9].) By analogy to power transmission in a straight beam [1] this can be expressed in terms of an extensional component, P_e, and a bending moment component, P_{bm}. Although the transverse shear stress σ_{sr} is negligible under Love's first approximation, the power transmission due to transverse shear stress can be evaluated from the non-vanishing shear force, Q, because the radial displacement W does not vary across the beam thickness. Again, by analogy to power transmission in a straight beam [1] this is expressed as a shear force component. Thus, the total power transmission in the circumferential direction is given by the sum of the extensional, bending moment and shear force components. These equations are listed in table 3 along with Flügge based power transmission equations which are also listed in table 3. Substituting harmonic wave expressions into the Love and Flügge based power transmission equations gives expressions for the power transmission in the circumferential direction in terms of travelling wave amplitudes A and B. For sinusoidal wave motion it is useful to develop time-averaged power transmission defined by [1]:

$$\langle P_s \rangle_t = \frac{1}{T} \int_{-T/2}^{T/2} P_s\,(s,t)\,dt \qquad (6)$$

where T is the period of the signal. Time averaged Love and Flügge based power transmission equations are given in table 4.

4. THE EFFECT OF ROTARY INERTIA AND SHEAR DEFORMATION

It is known that shear deformation and rotary inertia effects become significant for straight beams as the wave length approaches the same size as the thickness of the beam, and for cylindrical shells as the shell radius decreases [8]. Thus, the objective in this section is to establish more complete equations for power transmission in a curved beam and to show under what conditions these specialise to the simple bending equations presented in section three.

Rotary inertia effects are included by considering each element of the beam to have rotary inertia in addition to translational inertia. Equations of motion for a curved beam which include the

effect of rotary inertia are presented in [7]. These equations are listed in [9] in terms of the circumferential distance parameter, s. Equations for vibrational power transmission can be derived in the same manner as described in section three. These equations are listed in tables 3 and 4 where it can be seen that the extensional and bending moment components when including rotary inertia effects are identical to the corresponding Flügge based expressions. However, the shear force component now contains an additional rotary inertia term.

If shear deformation is included then Kirchoff's hypothesis is no longer valid, and the rotation of the normal to the centre-line during bending, ϕ, is no longer defined by equation (3) but is now another independent variable related to the shear angle, γ. However, unlike simple bending theory, where the transverse shear strain, γ_{sr}, is negligible, the transverse shear strain is now related to the shear angle, γ which is expressed in terms of displacements u, w and ϕ. The circumferential force, bending moment, and shear force obtained from [8] are given in table 2. A set of equations of motion for a curved beam which includes the effect of shear deformation is presented in [9]. Power transmission equations in the circumferential direction can be obtained in a manner analogous to that used for Love and Flügge based theories. As before, the power transmission due to circumferential stress can be identified as consisting of extensional and bending moment components. The contribution to the power transmission from the transverse shear stress is obtained from the product of the shear force resultant and the radial velocity which gives the shear force component of power transmission.

5. NUMERICAL STUDY

For a given real wavenumber, k, the harmonic equations of motion were solved to find the corresponding circular frequency, ω, and complex wave amplitude ratio. The simulated beam was chosen to have the physical dimensions and material properties of typical mild steel beams used for laboratory experiments. Four different radii of curvature were investigated, which were represented in terms of the non-dimensional thickness to radius of curvature ratio, h/R. These ratios were $1/10$, $1/100$, $1/1000$ and $1/10000$.

Using the Love equations of motion, Figure 3 shows the relationship between wave number and frequency for a beam with a

thickness to radius of curvature ratio of $^1/_{10}$. The frequency range is represented in terms of the non-dimensional frequency parameter $\Omega = \omega R/c_o$, where c_o is the phase velocity of extensional waves in a straight bar and the wave number range is represented in terms of the non-dimensional wave number, kR. It can be seen that two types of elastic wave exist: one involving predominantly flexural motion; the other predominantly extensional motion. However, for wave numbers less than kR = 1, the predominantly flexural wave exhibits greater extensional than flexural motion.

Solution of the shear deformation equations of motion for a curved beam shows that three types of elastic wave exist. These are the predominantly flexural and predominantly extensional waves of simple bending theory and additionally a predominantly rotational wave related to the shear angle. The relationship between wave number and frequency for these three wave types is shown in Figure 4.

A numerical investigation of the power transmission equations was undertaken using simulated beams with the same dimensions and material properties as those used in the previous study of wave motion. Figure 5 shows the relationship between transmitted power ratio and frequency. For the predominantly flexural wave the time-averaged transmitted power ratio is calculated by dividing the time-averaged power transmitted along a curved beam by a predominantly flexural wave by the time-averaged power transmitted by a pure flexural wave travelling in a straight Euler-Bernoulli beam. i.e. the ratio $(\langle P_e \rangle_t + \langle P_{bm} \rangle_t + \langle P_{sf} \rangle_t)/EI\omega k_f^3 A_f^2$. For the predominantly extensional wave the transmitted power ratio is calculated by dividing the time-averaged power transmitted along a curved beam by a predominantly extensional wave by the time-averaged power transmitted by a pure extensional wave in a straight rod. i.e. the ratio $(\langle P_e \rangle_t + \langle P_{bn} \rangle_t + \langle P_{sf} \rangle_t)/ES\omega k_{ex} B^2_{ex}$

6. SUMMARY AND CONCLUSIONS

In this paper, starting from first principles, expressions for vibrational power transmission in a curved beam have been derived using four different theories. Love's generalised shell equations include extension of the centre-line during bending motion were the first set of equations considered. Flügge's equations also include centre-line extensions and were the second set of equations used. Corrections for rotary inertia and shear deformation produced the third and fourth sets of governing

equations, respectively. By letting the radius of curvature, R, tend to infinity these equations reduce to the corresponding straight beam expressions presented in [1].

Using the governing equations for each theory, expressions were then developed which related time-averaged power transmission to the amplitudes of the extensional, flexural and rotational displacements. For each theory the effects of curvature upon the resulting wave motion and power transmission were then investigated using beams with different degrees of curvature. From the results of this study it can be seen that vibrational power transmission in curved beams can be classified into three different frequency regions:

(i) below the ring frequency, $\Omega = 1$, curvature effects are important;
(ii) above the ring frequency but below the shear wave cut-on frequency, $\omega K/c_s = 1$ the curved beam behaves essentially as a straight beam;
(iii) above the shear wave cut-on frequency, higher order effects are important.

ACKNOWLEDGEMENT

The analytical work presented in this paper was carried out while both authors were at the Institute of Sound and Vibration Research, University of Southampton. The financial support of the Marine Technology Directorate Limited and the Science and Engineering Research Council is gratefully acknowledged.

REFERENCES

1. J.L. HORNER 1990 *PhD thesis, University of Southampton* Vibrational power transmission through beam like structures.
2. A.E.H. LOVE 1940 *Dover, New-York.* A treatise on the mathematical theory of elasticity.
3. W. SOEDEL 1985 *Dekker, New York.* Vibrations of shells and plates
4. K.F. GRAFF 1975 *Clarenden Press, Oxford.* Wave motion in elastic solids
5. L.L. PHILIPSON 1956 *Journal of Applied Mechanics* **23**, 364-366. On the role of extension in the flexural vibrations of rings.
6. L.S.D. MORLEY 1961 *Quarterly Journal of Mechanics and Applied Mathematics* **14**, (2), 155-172. Elastic waves in a naturally curved rod.

7. K.F. GRAFF 1970 *IEEE Transactions on Sonics and Ultrasonics,* SU-17 (1), 1-6. Elastic wave propagation in a curved sonic transmission line.
8. A.W. LEISSA 1977 *NASA SP-288, Washington DC* Vibrations of shells.
9. S.J. WALSH 1996 *PhD thesis, University of Southampton.* Vibrational power transmission in curved and stiffened structures.
10. A.J. ROMANO, P.B. ABRAHAM, E.G. WILLIAMS 1990 *Journal of the Acoustical Society of America* **87**. A Poynting vector formulation for thin shells and plates, its application to structural intensity analysis and source localization. Part I: Theory.

APPENDIX: NOTATION

A	flexural wave amplitude
A_f	amplitude of a purely flexural wave
B	extensional wave amplitude
B_{ex}	amplitude of a purely extensional wave
C	rotation wave amplitude
E	Young's modulus
G	shear modulus
I	second moment of area of cross-section of beam
I_s	structural intensity in circumferential direction
K	radius of gyration
M	bending moment on cross-section of beam
N	circumferential force on cross-section of beam
P	transmitted power
Q	shear force on cross-section of beam
R	radius of curvature
S	cross-sectional area of beam
T	period of wave
U	displacement in circumferential direction
W	displacement in radial direction
c_o	wavespeed of extensional waves in a straight bar
c_s	wavespeed of shear waves in a straight bar
d_s	length of elemental slice of curved beam
e_s	total circumferential strain
h	thickness of beam
k	wavenumber
k_{ex}	wavenumber of a purely extensional wave
k_f	wavenumber of a purely flexural wave
r	coordinate in radial direction

s	coordinate in circumferential direction
u	displacement at centre-line in circumferential direction
w	displacement at centre-line in radial direction
z	coordinate of outward pointing normal
Ω	non-dimensional frequency
β_s	bending strain
γ	shear angle
γ_{sr}	transverse shear strain
ε_r	radial strain
ε_s	circumferential strain
θ_A	phase angle of flexural wave
θ_C	phase angle of rotational wave
κ	Timoshenko shear coefficient
λ_{ex}	wave length of extensional waves in a straight bar
ν	Poisson's ratio
σ_r	radial stress
σ_s	circumferential stress
σ_{sr}	transverse shear stress
ϕ	change in slope of normal to centre-line
ω	radian frequency

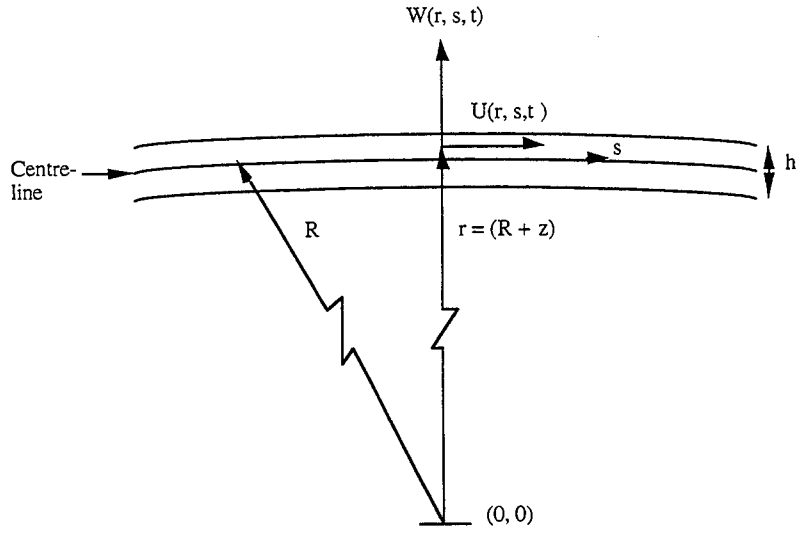

Figure 1: Geometry of a curved beam

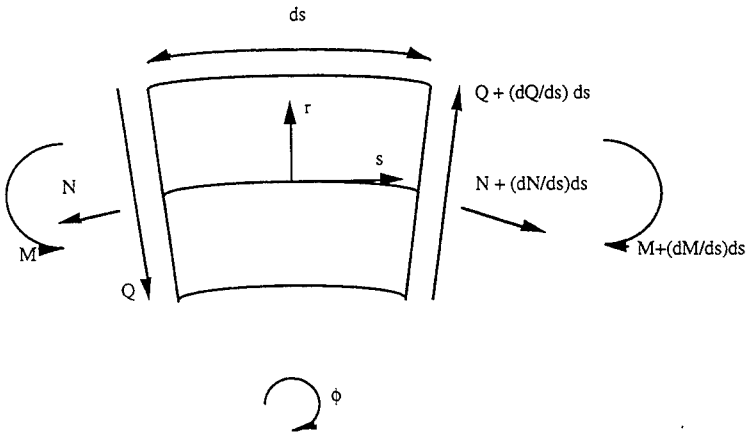

Figure 2: Sign convention and force resultants on an elemental slice of curved beam

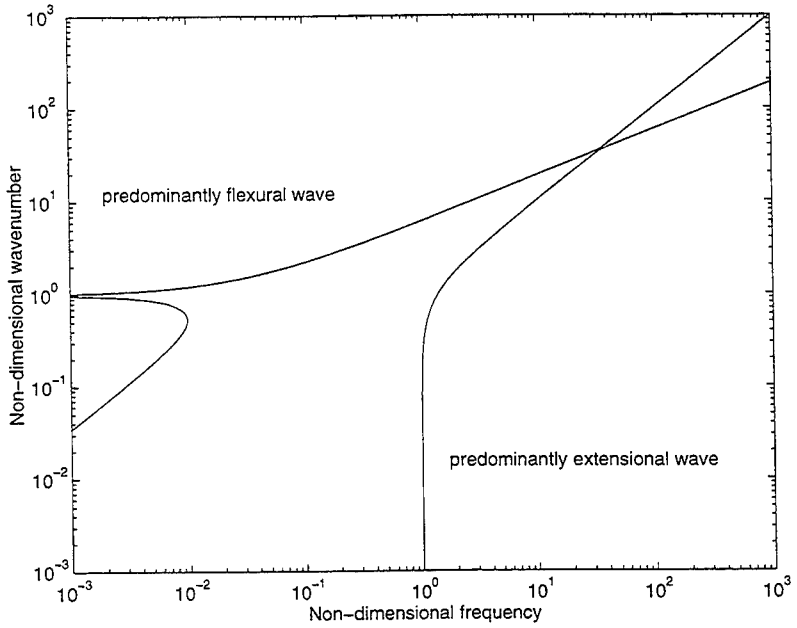

Figure 3: Wave number v. frequency relationship for a curved beam predicted using Love theory

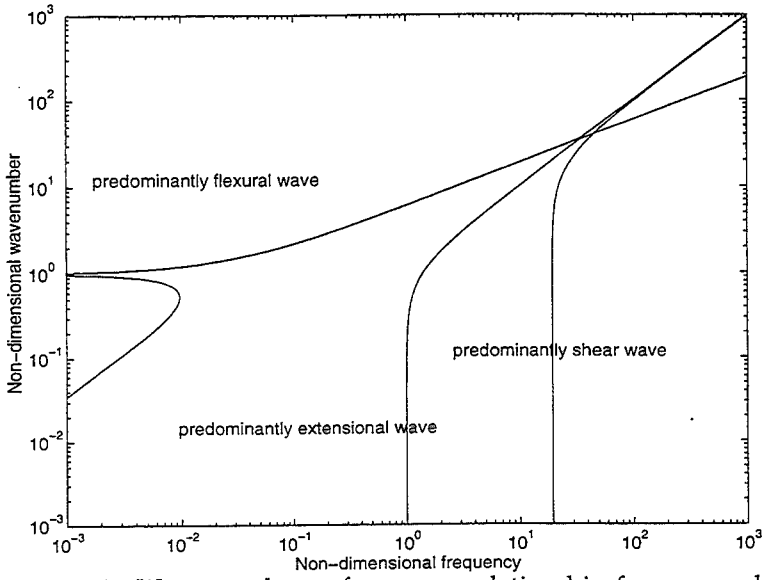

Figure 4: Wave number v. frequency relationship for a curved beam predicted using shear theory

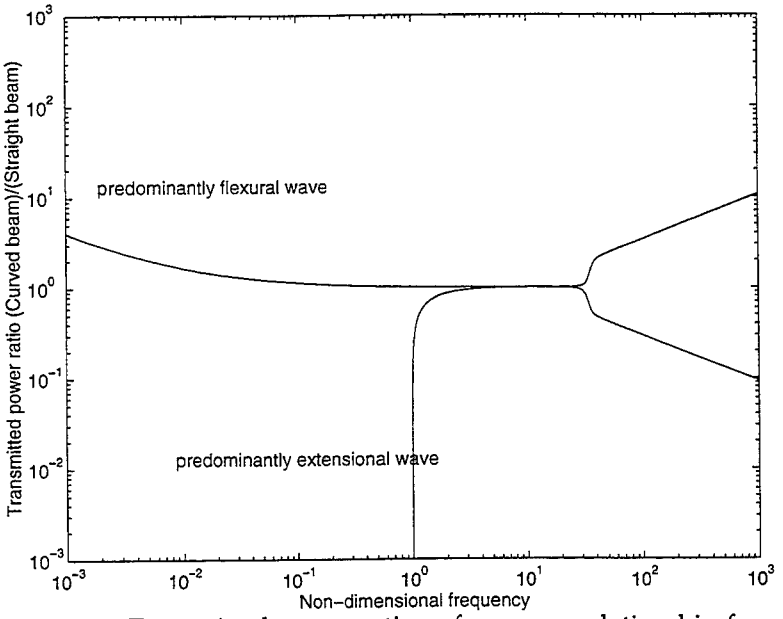

Figure 5: Transmitted power ratio v. frequency relationship for a curved beam predicted using Love theory

Table 1: Displacement, strain-displacement and stress-strain equations for a curved beam.

Quantity	Love based equations	Flügge based equations	Including rotary inertia	Including shear deformation
Displacements relative to centre-line	$U = u + z\phi$ $W = w$	$U = u + z\phi$ $W = w$	$U = u + z\phi$ $W = w$	$U = u + z\phi$ $W = w$
Rotation of normal to centre-line	$\phi = \frac{u}{R} - \frac{\partial w}{\partial s}$	$\phi = \frac{u}{R} - \frac{\partial w}{\partial s}$	$\phi = \frac{u}{R} - \frac{\partial w}{\partial s}$	ϕ = independent variable related to shear angle
Extensional strain-displacement	$\varepsilon_s = \frac{w}{R} + \frac{\partial u}{\partial s}$	$\varepsilon_s = \frac{w}{R} + \frac{\partial u}{\partial s}$	$\varepsilon_s = \frac{w}{R} + \frac{\partial u}{\partial s}$	$\varepsilon_s = \frac{w}{R} + \frac{\partial u}{\partial s}$
Bending strain-displacement	$\beta_s = \frac{\partial}{\partial s}\phi$	$\beta_s = \frac{\partial}{\partial s}\phi$	$\beta_s = \frac{\partial}{\partial s}\phi$	$\beta_s = \frac{\partial}{\partial s}\phi$
Total circumferential strain	$e_s = \varepsilon_s + z\beta_s$	$e_s = \frac{1}{\left(1 + \frac{z}{R}\right)}\left(\varepsilon_s + z\beta_s\right)$	$e_s = \frac{1}{\left(1 + \frac{z}{R}\right)}\left(\varepsilon_s + z\beta_s\right)$	$e_s = \frac{1}{\left(1 + \frac{z}{R}\right)}\left(\varepsilon_s + z\beta_s\right)$
Circumferential stress-strain	$\sigma_s = Ee_s$	$\sigma_s = Ee_s$	$\sigma_s = Ee_s$	$\sigma_s = Ee_s$
Radial strain-displacement	$\gamma_{sr} = 0$	$\gamma_{sr} = 0$	$\gamma_{sr} = 0$	$\gamma_{sr} = \frac{\gamma}{\left(1 + \frac{z}{R}\right)}$
Transverse shear stress	$\sigma_{sr} = 0$	$\sigma_{sr} = 0$	$\sigma_{sr} = 0$	$\sigma_s = G\gamma_{sr}$

Table 2: Force resultants for a curved beam.

Quantity	Love based equations	Flügge based equations	Including rotary inertia	Including shear deformation
Circumferential force	$N = SE\left(\frac{w}{R} + \frac{\partial u}{\partial s}\right)$	$N = SE\left(\frac{w}{R} + \frac{\partial u}{\partial s}\right) + \frac{EI}{R}\left(\frac{w}{R^2} + \frac{\partial^2 w}{\partial s^2}\right)$	$N = SE\left(\frac{w}{R} + \frac{\partial u}{\partial s}\right) + \frac{EI}{R}\left(\frac{w}{R^2} + \frac{\partial^2 w}{\partial s^2}\right)$	$N = SE\left(\frac{w}{R} + \frac{\partial u}{\partial s}\right) + \frac{EI}{R}\left(\frac{w}{R^2} + \frac{1}{R}\frac{\partial u}{\partial s} - \frac{\partial \phi}{\partial s}\right)$
Bending moment	$M = EI\frac{\partial}{\partial s}\left(\frac{u}{R} - \frac{\partial w}{\partial s}\right)$	$M = -EI\left(\frac{w}{R^2} + \frac{\partial^2 w}{\partial s^2}\right)$	$M = -EI\left(\frac{w}{R^2} + \frac{\partial^2 w}{\partial s^2}\right)$	$M = -EI\left(\frac{w}{R^2} + \frac{1}{R}\frac{\partial u}{\partial s} - \frac{\partial \phi}{\partial s}\right)$
Shear force	$Q = EI\frac{\partial^2}{\partial s^2}\left(\frac{u}{R} - \frac{\partial w}{\partial s}\right)$	$Q = -EI\frac{\partial}{\partial s}\left(\frac{w}{R^2} + \frac{\partial^2 w}{\partial s^2}\right)$	$Q = -EI\frac{\partial}{\partial s}\left(\frac{w}{R^2} + \frac{\partial^2 w}{\partial s^2}\right) - \rho I\frac{\partial^2}{\partial t^2}\left(\frac{2u}{R} - \frac{\partial w}{\partial s}\right)$	$Q = \kappa G\left(S + \frac{I}{R^2}\right)\left[\phi - \left(\frac{u}{R} - \frac{\partial w}{\partial s}\right)\right]$

Table 3: Power transmission for a curved beam.

Quantity	Love based equations	Flügge based equations	Including rotary inertia	Including shear deformation
Extensional component	$P_e = -ES\left[\frac{w}{R} + \frac{\partial u}{\partial s}\right]\frac{\partial u}{\partial t}$	$P_e = -\left[ES\left(\frac{w}{R} + \frac{\partial u}{\partial s}\right) + \frac{EI}{R}\left(\frac{w}{R^2} + \frac{\partial^2 w}{\partial s^2}\right)\right]\frac{\partial u}{\partial t}$	$P_e = -\left[ES\left(\frac{w}{R} + \frac{\partial u}{\partial s}\right) + \frac{EI}{R}\left(\frac{w}{R^2} + \frac{\partial^2 w}{\partial s^2}\right)\right]\frac{\partial u}{\partial t}$	$P_e = -\left[ES\left(\frac{w}{R} + \frac{\partial u}{\partial s}\right) + \frac{EI}{R}\left(\frac{w}{R^2} + \frac{1}{R}\frac{\partial u}{\partial s} - \frac{\partial \phi}{\partial s}\right)\right]\frac{\partial u}{\partial t}$
Bending moment component	$P_{bm} = -EI\left[\frac{\partial}{\partial s}\left(\frac{u}{R} - \frac{\partial w}{\partial s}\right)\right] \times \left[\frac{\partial}{\partial t}\left(\frac{u}{R} - \frac{\partial w}{\partial s}\right)\right]$	$P_{bm} = EI\left[\frac{w}{R^2} + \frac{\partial^2 w}{\partial s^2}\right] \times \left[\frac{\partial}{\partial t}\left(\frac{u}{R} - \frac{\partial w}{\partial s}\right)\right]$	$P_{bm} = EI\left[\frac{w}{R^2} + \frac{\partial^2 w}{\partial s^2}\right] \times \left[\frac{\partial}{\partial t}\left(\frac{u}{R} - \frac{\partial w}{\partial s}\right)\right]$	$P_{bm} = EI\left[\frac{w}{R^2} + \frac{1}{R}\frac{\partial u}{\partial s} - \frac{\partial \phi}{\partial s}\right]\frac{\partial \phi}{\partial t}$
Shear force component	$P_{sf} = -EI\left[\frac{\partial^2}{\partial s^2}\left(\frac{u}{R} - \frac{\partial w}{\partial s}\right)\right] \times \frac{\partial w}{\partial t}$	$P_{sf} = EI\left[\frac{\partial}{\partial s}\left(\frac{w}{R^2} + \frac{\partial^2 w}{\partial s^2}\right)\right] \times \frac{\partial w}{\partial t}$	$P_{sf} = \left[EI\frac{\partial}{\partial s}\left(\frac{w}{R^2} + \frac{\partial^2 w}{\partial s^2}\right) + \rho I\frac{\partial^2}{\partial t^2}\left(\frac{2u}{R} - \frac{\partial w}{\partial s}\right)\right]\frac{\partial w}{\partial t}$	$P_{sf} = -\kappa G\left(S + \frac{I}{R^2}\right) \times \left[\phi - \left(\frac{u}{R} - \frac{\partial w}{\partial s}\right)\right]\frac{\partial w}{\partial t}$

Table 4: Time-averaged power transmission by a single harmonic wave

Quantity	Love based equations	Flügge based equations	Including rotary inertia	Including shear deformation
Extensional component	$\langle P_e \rangle_t = \frac{ES\omega}{2} \left[kB^2 - \frac{BA}{R} \sin [\theta_A] \right]$	$\langle P_e \rangle_t = \frac{ES\omega}{2} \left[kB^2 - \frac{BA}{R} \sin [\theta_A] \right]$	$\langle P_e \rangle_t = \frac{ES\omega}{2} \left[kB^2 - \frac{BA}{R} \sin [\theta_A] \right]$	$\langle P_e \rangle_t = \frac{E\omega}{2} \left(S + \frac{I}{R^2} \right) \times \left[kB^2 - \frac{BA}{R} \sin [\theta_A] \right] - \frac{EI\ \omega\ k\ B\ C}{2R} \cos [\theta_C]$
Bending moment component	$\langle P_{bm} \rangle_t = EI \left[\frac{\omega\ k\ B^2}{2R^2} + \frac{\omega\ k^3\ A^2}{2} - \frac{\omega\ k^2\ BA}{R} \sin [\theta_A] \right]$	$\langle P_{bm} \rangle_t = \frac{EI\ \omega\ k\ A^2}{2} \times \left(k^2 - \frac{1}{R^2} \right)$	$\langle P_{bm} \rangle_t = \frac{EI\ \omega\ k\ A^2}{2} \times \left(k^2 - \frac{1}{R^2} \right)$	$\langle P_{bm} \rangle_t = \frac{EI\ \omega\ k\ C^2}{2} - \frac{EI\ \omega\ k\ B\ C}{2R} \cos [\theta_C] - \frac{EI\ \omega\ AC}{2R^2} \sin [\theta_C - \theta_A]$
Shear force component	$\langle P_{sf} \rangle_t = \frac{EI\ k^3\ \omega\ A^2}{2} - \frac{EI\ \omega\ k^2\ BA}{2R} \sin [\theta_A]$	$\langle P_{sf} \rangle_t = \frac{EI\ \omega\ k\ A^2}{2} \times \left(k^2 - \frac{1}{R^2} \right)$	$\langle P_{sf} \rangle_t = \frac{EI\ \omega\ k\ A^2}{2} \times \left(k^2 - \frac{1}{R^2} \right) - \frac{\rho I \omega^3 k A^2}{2} + \frac{\rho\ I\ \omega^3\ BA}{R} \sin [\theta_A]$	$\langle P_{sf} \rangle_t = \frac{\kappa\ G\ \omega}{2} \times \left(S + \frac{I}{R^2} \right) \left[kA^2 - \frac{B\ A}{R} \sin [\theta_A] + A\ C \sin [\theta_A - \theta_C] \right]$

A Parameter-based Statistical Energy Method for Mid-frequency Vibration Transmission Analysis

Sungbae Choi, Graduate Student Research Assistant
Matthew P. Castanier, Assistant Research Scientist
Christophe Pierre, Associate Professor
Department of Mechanical Engineering and Applied Mechanics
The University of Michigan
Ann Arbor, MI 48109-2125, USA

Abstract

Vibration transmission between two multi-mode substructures connected by a spring is investigated. A classical Statistical Energy Analysis (SEA) approach is reviewed, and it is seen that some typical assumptions which are valid at high frequencies lose accuracy in the mid-frequency range. One assumption considered here is that of an identical probability density function (pdf) for each resonant frequency. This study proposes a Parameter-based Statistical Energy Method (PSEM) which considers individual modal information. The results of PSEM have good agreement with those of a Monte Carlo technique for an example system.

Nomenclature

$E[\ \ ]$	expected value
$\Pi_{ik}(\omega)$	power transmitted between substructure i and k
$\Pi_k(\omega)$	total power transmitted to substructure k
P_i	power input to substructure i
η_{ik}	coupling loss factor (CLF)
$\overline{f}_{1_j}$	modal driving force for mode j of substructure 1
ω	frequency [rad/sec]
$_{1,1_i,1_j,01}$	subscripts for decoupled Bar 1
$_{2,2_r,2_s,02}$	subscripts for decoupled Bar 2
E_1, E_2	blocked energy
E_{01}, E_{02}	Young's modulus
ρ_1, ρ_2	density
m_1, m_2	mass per unit length
M_1, M_2	total mass
ζ_1, ζ_2	viscous damping ratio
A_1, A_2	cross-sectional area
L_{01}, L_{02}	nominal length

L_1, L_2	disordered length
ϵ_1, ϵ_2	ratio of disorder to nominal length
k	coupling stiffness
R_1, R_2	coupling ratio
x_1, x_2	position coordinate
a_1, a_2	point-coupling connection position
w_1, w_2	deflection
W_{1_i}, W_{2_r}	modal amplitude
Ψ_{1_i}, Ψ_{2_r}	mode shape function
N_1, N_2	number of resonant frequencies
$\omega_{1_i}, \omega_{2_r}$	resonant frequencies
$\omega_{1_{i_l}}, \omega_{2_{r_l}}$	lower limit of resonant frequencies
$\omega_{1_{i_u}}, \omega_{2_{r_u}}$	upper limit of resonant frequencies
σ_1, σ_2	standard deviation of disorder

1 Introduction

Vibration transmission analysis between connected substructures in the mid-frequency range is often a daunting prospect. Since the analysis at high frequencies requires greater model discretization, the size and computational cost of a full structure model (e.g., a Finite Element model) can become prohibitive. Also, as the wavelengths approach the scale of the structural variations, uncertainties (tolerances, defects, etc.) can significantly affect the dynamics of the structure. Starting at what may be called the mid-frequency range, deterministic models fail to predict the response of a representative structure with uncertainties.

Therefore, in the mid-frequency range, a statistical analysis of vibration transmission may be more appropriate. This approach is taken in the procedure known as Statistical Energy Analysis (SEA) [1]. In SEA, a structure is divided into coupled substructures. It is assumed that each substructure exhibits strong modal overlap which makes it difficult to distinguish individual resonances. Therefore, the resonant frequencies are treated as random variables, each with an identical, uniform probability density function (pdf) in the frequency range of interest. This assumption greatly simplifies the evaluation of the expected value of transmitted vibration energy. A simple linear relation of vibration transmission between each pair of substructures is retrieved. The power transmitted is proportional to the difference in the average modal energies of the substructures. This relation is analogous to Fourier's law of heat transfer [1-4].

In the low- to mid-frequency region, the modal responses are not strongly overlapped. In this case, two typical SEA assumptions are less accurate: an identical pdf for all resonant frequencies, and identical (ensemble-averaged)

values of the associated mode shape functions at connection positions. In this paper, these two assumptions are relaxed. A distinct uniform pdf is applied for each resonant frequency, and a piecewise evaluation of the transmitted power is performed. This is called a Parameter-based Statistical Energy Method (PSEM) because it considers the statistical characteristics of individual system parameters. This solution can accurately capture peaks of transmitted power while maintaining the SEA advantage of efficiency.

This paper is organized as follows. In section 2, we briefly review SEA along with the associated assumptions and limitations. In section 3, the power transmitted between two spring-coupled multi-mode substructures is investigated by applying several SEA assumptions. A Monte Carlo solution is used for comparison. In section 4, the PSEM approach is presented and the results are shown. Finally, section 5 draws conclusions from this study.

2 Overview of SEA

In Statistical Energy Analysis, the primary variable is the time-averaged total energy of each substructure. This is called the blocked energy, where blocked means an assumed coupling condition. The assumed coupling condition may be the actual coupling, a clamped condition at the substructure junctions, or a decoupled condition [2, 5].

In order to predict the average power transmitted between two directly-coupled substructures, a few simplifying assumptions are applied. Some of the essential SEA assumptions are summarized by Hodges and Woodhouse in Ref. [3]:

- Modal incoherence: the responses of two different modal coordinates are uncorrelated over a long time interval
- Equipartition of modal energy: all modes within the system have the same kinetic energy

The above conditions make it possible to treat all modal responses as statistically identical. The first assumption implies a broad band, distributed driving force (often called "rain on the roof") which leads to uncorrelated modal driving forces. The second assumption implies that the substructures have strong modal overlap, or that the parameter uncertainties are sufficiently large that the modes are equally excited in an ensemble average sense. Thus, the resonant frequencies are treated as random variables with identical, uniform probability density functions (pdfs) for the frequency range of interest.

The SEA relation for the expected value of power transmitted from

substructure i to substructure k, $E[\Pi_{ik}(\omega)]$, may be expressed as

$$E[\Pi_{ik}(\omega)] = \omega\eta_{ik}N_i(\frac{E_i}{N_i} - \frac{E_k}{N_k}) = \omega(\eta_{ik}E_i - \eta_{ki}E_k) \tag{1}$$

where ω is the frequency, η_{ik} is the coupling loss factor, E_i is the blocked energy of substructure i, and N_i is the number of participating modes of substructure i for the frequency range of interest. The power dissipated by substructure i is expressed as

$$\Pi_{i,diss} = \omega\eta_i E_i \tag{2}$$

where η_i is the damping loss factor. Using Eqs.(1) and (2), the equation of power balance for substructure i at steady state [1, 2, 5, 6] is

$$P_i = \sum_{\substack{j=1 \\ j\neq i}}^{N} E[\Pi_{ij}] + \omega\eta_i E_i = \omega\sum_{\substack{j=1 \\ j\neq i}}^{N}(\eta_{ij}E_i - \eta_{ji}E_j) + \omega\eta_i E_i \tag{3}$$

where P_i is the power input to substructure i from external sources. Note that the first term on the right-hand side is the power transmitted through direct coupling between substructures.

3 Vibration Transmission in a Two-Bar System

The longitudinal vibration of the structure shown in Fig.1 is considered in this study. The structure consists of two uniform bars with viscous damping which are coupled by a linear spring of stiffness k. The spring is connected at intermediate points on the bars, $x_1 = a_1$ and $x_2 = a_2$. Bar i has nominal length L_{0i}. A parameter uncertainty may be introduced by allowing the length to vary by a small random factor ϵ_i, which is referred to as disorder. The length of a disordered bar is $L_i = L_{0i}(1+\epsilon_i)$. The ratio of the connection position to the length, a_i/L_i, is held constant. Bar 1 is excited by a distributed force $F_1(x_1, t)$.

3.1 Nominal transmitted power

The power transmitted from Bar 1 to Bar 2 for the nominal system (no disorder) is briefly presented here. A more detailed derivation is shown in the Appendix (see also Refs. [7] and [8]). The equations of motion are

$$\begin{aligned}
&\left(E_{01}A_1\tfrac{\partial^2}{\partial x_1^2} + m_1\tfrac{\partial^2}{\partial t^2}\right)\mathrm{w}_1(x_1,t) + \tfrac{\partial}{\partial t}C_1(\mathrm{w}_1(x_1,t)) = F_1(x_1,t) + \\
&\qquad\qquad k[\mathrm{w}_2(a_2,t) - \mathrm{w}_1(a_1,t)]\delta(x_1 - a_1) \\
&\left(E_{02}A_2\tfrac{\partial^2}{\partial x_2^2} + m_2\tfrac{\partial^2}{\partial t^2}\right)\mathrm{w}_2(x_2,t) + \tfrac{\partial}{\partial t}C_2(\mathrm{w}_2(x_2,t)) = \\
&\qquad\qquad k[\mathrm{w}_1(a_1,t) - \mathrm{w}_2(a_2,t)]\delta(x_2 - a_2)
\end{aligned} \tag{4}$$

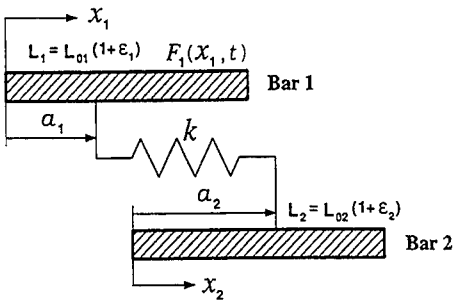

Fig. 1: Two-bar system

where δ is a Dirac delta function, and (for Bar i) E_{0i} is Young's modulus, A_i is the cross-sectional area, m_i is the mass per unit length, C_i is the viscous damping operator, and $\mathrm{w}_i(x_i, t)$ is the deflection. The deflections of the two bars can be expressed by a summation of modes:

$$\mathrm{w}_1(x_1, t) = \sum_{i=0}^{\infty} W_{1_i}(t)\Psi_{1_i}(x_1), \quad \mathrm{w}_2(x_2, t) = \sum_{r=0}^{\infty} W_{2_r}(t)\Psi_{2_r}(x_2) \tag{5}$$

where $W_{1_i}(t)$ and $W_{2_r}(t)$ are modal amplitudes, and $\Psi_{1_i}(x_1)$ and $\Psi_{2_r}(x_2)$ are mode shape functions of the decoupled bars. These mode shape functions are normalized so that each modal mass is equal to the total mass of the bar, M_i. Applying modal analysis and taking a Fourier transform, the following equations are obtained:

$$\begin{aligned} M_1\phi_{1_j}\overline{W}_{1_j} &= \overline{f}_{1_j} + k\Psi_{1_j}(a_1)[\sum_{r=0}^{\infty}\overline{W}_{2_r}\Psi_{2_r}(a_2) - \sum_{i=0}^{\infty}\overline{W}_{1_i}\Psi_{1_i}(a_1)] \\ M_2\phi_{2_s}\overline{W}_{2_s} &= k\Psi_{2_s}(a_2)[\sum_{i=0}^{\infty}\overline{W}_{1_i}\Psi_{1_i}(a_1) - \sum_{r=0}^{\infty}\overline{W}_{2_r}\Psi_{2_r}(a_2)] \end{aligned} \tag{6}$$

$$\begin{aligned} \phi_{1_j} &= (\omega_{1_j}^2 - \omega^2 + \sqrt{-1}\cdot 2\zeta_1\omega_{1_j}\omega)(2 - \mathrm{sgn}(j)) \\ \phi_{2_s} &= (\omega_{2_s}^2 - \omega^2 + \sqrt{-1}\cdot 2\zeta_2\omega_{2_s}\omega)(2 - \mathrm{sgn}(s)) \\ \mathrm{sgn}(i) &= \begin{cases} 1 & \text{for } i > 0 \\ 0 & \text{for } i = 0 \end{cases} \end{aligned}$$

where an over-bar ($\bar{}$) denotes a Fourier transform, ω_{1_j} and ω_{2_s} are resonant frequencies, ζ_1 and ζ_2 are damping ratios, and f_{1_j} is a modal driving force. Mode 0 is a rigid body mode, which is why the $\mathrm{sgn}(i)$ term is present. Note that the damping ratio of each bar is assumed to be the same for all modes.

Next, the modal driving forces are assumed to be incoherent, and each spectral density function is assumed to be constant (white noise) over a finite range of frequency [2]. After some algebra, the power transmitted

from Bar 1 to Bar 2, $\Pi_{12}(\omega)$, is found as:

$$\Pi_{12}(\omega) = \frac{2\omega^2 k^2 \zeta_2 S_{p_1 p_1}}{M_1^2 M_2 |\Delta|^2} \sum_{i=0}^{\infty} \frac{\Psi_{1_i}^2(a_1)}{|\phi_{1_i}|^2} \sum_{r=0}^{\infty} \frac{\Psi_{2_r}^2(a_2)\omega_{2_r}}{|\phi_{2_r}|^2} \tag{7}$$

$$\Delta = 1 + \frac{k}{M_1} \sum_{i=0}^{\infty} \frac{\Psi_{1_i}^2(a_1)}{\phi_{1_i}} + \frac{k}{M_2} \sum_{r=0}^{\infty} \frac{\Psi_{2_r}^2(a_2)}{\phi_{2_r}}$$

where $S_{p_1 p_1}$ is the same uniform spectral density function for each modal driving force on Bar 1.

3.2 Monte Carlo Energy Method (MCEM)

The disordered case is now considered, where each bar has a random length. The ensemble-averaged transmitted power for a population of disordered two-bar systems is found by taking the expected value of Eq. (7):

$$E[\Pi_{12}] \approx E\left[\frac{2\omega^2 k^2 \zeta_2 S_{p_1 p_1}}{M_1^2 M_2 |\Delta|^2} \sum_{i=1}^{N_1} \frac{\Psi_{1_i}^2(a_1)}{|\phi_{1_i}|^2} \sum_{r=1}^{N_2} \frac{\Psi_{2_r}^2(a_2)\omega_{2_r}}{|\phi_{2_r}|^2}\right]. \tag{8}$$

where N_i is the number of modes taken for Bar i (this is an arbitrary set of modes that have been aliased to the numbers 1,2,$\cdots$,N_i). Since a truncated set of modes is used, Eq. (8) is an approximation. The random variables in Eq. (8) are the resonant frequencies of the bars (which are present in the terms ϕ_{1_i}, ϕ_{2_r}, and Δ).

Equation (8) may be solved numerically using a Monte Carlo method: the random variables are assigned with a pseudo-random number generator for each realization of a disordered system, and the transmitted power is averaged for many realizations. This is called a Monte Carlo Energy Method (MCEM) here. It may be used as a benchmark for comparing the accuracy of other approximate methods.

Note that the resonant frequencies of a bar may be found directly from the disordered length. Therefore, for the MCEM results in this study, the actual number of random variables in Eq. (8) is taken to be one for each decoupled bar. That is, the two random lengths are assigned for each realization, and then the natural frequencies are found for each bar in order to calculate the transmitted power. If such a relation were not known, each resonant frequency could be treated as an independent random variable.

3.3 SEA-equivalent Transmitted Power

An SEA approximation of the transmitted power may be obtained by applying several typical SEA assumptions to Eq. (8). (Since Eq. (1) is not used directly, this might be called an SEA-equivalent transmitted power.) These assumptions were summarized in Ref. [8]: the coupling between

substructures is weak, the modal responses are uncorrelated, the expected value of the square of mode shape functions at connection positions is unity, and the pdfs of the resonant frequencies are uniform and identical.

The assumption of weak coupling means that the value of $|\Delta|$ in Eq. (8) is approximately one. Applying the second and third assumptions then yields

$$E[\Pi_{12}] \approx \frac{2\omega^2 k^2 \zeta_2 S_{p_1 p_1}}{M_1^2 M_2} \left(\sum_{i=1}^{N_1} E\left[\frac{1}{|\phi_{1_i}|^2}\right] \right) \left(\sum_{r=1}^{N_2} E\left[\frac{\omega_{2_r}}{|\phi_{2_r}|^2}\right] \right) \tag{9}$$

Since the pdf of each resonant frequency is assumed to be uniform, the expected values in Eq. (9) are

$$E[\frac{1}{|\phi_{1_i}|^2}] = \frac{1/4\omega^3}{\omega_{1_{i_u}} - \omega_{1_{i_l}}} \left[\frac{1}{2cos\frac{\alpha}{2}} log \frac{\omega_{1_i}^2 + 2\omega\omega_{1_i} \cdot cos\frac{\alpha}{2} + \omega^2}{\omega_{1_i}^2 - 2\omega\omega_{1_i} \cdot cos\frac{\alpha}{2} + \omega^2} + \frac{1}{sin\frac{\alpha}{2}} tan^{-1} \frac{2\omega\omega_{1_i} \cdot sin\frac{\alpha}{2}}{\omega^2 - \omega_{1_i}^2} \right] \Bigg|_{\omega_{1_i}=\omega_{1_{i_l}}}^{\omega_{1_i}=\omega_{1_{i_u}}} \tag{10}$$

$$E[\frac{\omega_{2_r}}{|\phi_{2_r}|^2}] = \frac{1/4\omega^2 \zeta_2 \sqrt{1-\zeta_2^2}}{\omega_{2_{r_u}} - \omega_{2_{r_l}}} tan^{-1} \frac{2\omega_{2_r}^2 + 2\omega^2(2\zeta_2^2 - 1)}{4\omega^2 \zeta_2 \sqrt{1-\zeta_2^2}} \Bigg|_{\omega_{2_r}=\omega_{2_{r_l}}}^{\omega_{2_r}=\omega_{2_{r_u}}} \tag{11}$$

where $\alpha = cos^{-1}(1 - 2\zeta_1^2)$, subject to the restrictions $(1 - 2\zeta_1^2)^2 < 1$ and $(1 - 2\zeta_2^2)^2 < 1$. Finally, since the pdfs of the resonant frequencies are taken to be identical, the frequency limits do not depend on the individual modes ($\omega_{1_{i_l}} = \omega_{2_{r_l}} = \omega_l$ and $\omega_{1_{i_u}} = \omega_{2_{r_u}} = \omega_u$). Therefore, each sum in Eq. (9) simplifies to the product of the expected value and the number of modes in the frequency range of interest:

$$E[\Pi_{12}] \approx \frac{2\zeta_2 k^2 \omega^2 N_1 N_2 S_{p_1 p_1}}{M_1^2 M_2} E[\frac{1}{|\phi_{1_i}|^2}] \; E[\frac{\omega_{2_r}}{|\phi_{2_r}|^2}] \tag{12}$$

Equation (12) is the SEA approximation used in this study.

3.4 Example

The three formulations of the transmitted power presented thus far — the nominal transmitted power in Eq. (7), the MCEM transmitted power in Eq. (8), and the SEA-equivalent transmitted power in Eq. (12) — are now compared for a two-bar system with the parameters shown in Table 1. For the MCEM results, the disorder (ϵ_1 and ϵ_2) was taken to be uniformly distributed with mean zero and standard deviation $\sigma_1 = \sigma_2 = 10\%$.

As a measure of the coupling strength, the coupling ratio, R_i, is defined as the ratio of coupling stiffness to the equivalent stiffness of a bar at the

Table 1: Material properties and dimensions of two bars

M_1/M_2	21.53/21.53	[Kg]	L_{01}/L_{02}	10.58/8.817	[m]
E_{01}/E_{02}	200 $\times 10^9$/200 $\times 10^9$	[N/m^2]	a_1/a_2	2.116/7.053	[m]
ρ_1/ρ_2	7,800/7,800	[Kg/m^3]	$S_{p_1p_1}$	1	[N^2]
ζ_1/ζ_2	0.005/0.005		k	4.868 $\times 10^5$	[N/m]

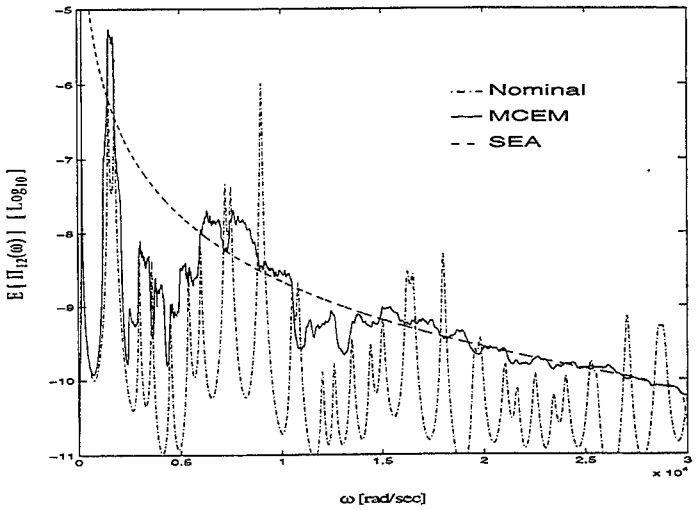

Fig. 2: Comparison of the nominal transmitted power, the MCEM results (20,000 realizations with $\sigma_1 = \sigma_2 = 10\%$), and the SEA approximation.

fundamental resonant frequency, $R_i = \frac{k}{\pi^2 E_{0i} M_i / \rho_i L_{0i}^2}$. The case of weak coupling is considered here such that $R_1 = 0.01$.

The nominal transmitted power, the MCEM results, and the SEA approximation are shown in Fig.2. The transmitted power calculated for the nominal system exhibits distinct resonances. This is due to the low modal overlap of the bars in this frequency range. The MCEM results show distinct peaks for $\omega < 15{,}000$ rad/s, but they become smooth as the frequency increases. The SEA approximation does not capture individual resonances. However, at the higher frequencies where the disorder effects are stronger, the SEA approximation agrees well with the MCEM results. The frequency range between where the MCEM results are close to the nominal results and where they are close to the SEA results (approximately 2,500 $\sim$ 15,000 rad/s for this case) is considered to be the mid-frequency range here. This range will vary depending on the system

parameters and the disorder strength. In the next section, an efficient approximation of the transmitted power is presented which compares well with MCEM in the mid-frequency range.

4 Parameter-based Statistical Energy Method (PSEM)

The SEA approximation presented in the previous section does not capture the resonances in the transmitted power because of two assumptions: the resonant frequencies all have the same uniform pdf, and the values of the square of mode shape functions at the connection positions are taken to be the ensemble-averaged value. Keane proposed an alternate pdf of resonant frequencies in order to apply SEA to the case of two coupled nearly periodic structures [9]. This pdf is shown in Fig.3(a). It accounts for the fact that

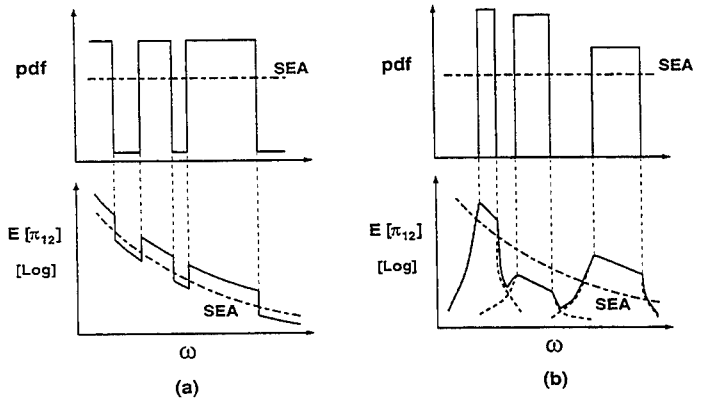

Fig. 3: (a) The pdf of the natural frequencies and the resultant transmitted power from Ref. [9]. (b) The pdfs of three natural frequencies, and a schematic representation of the piecewise evaluation of transmitted power for PSEM. The individual modal contributions are extrapolated (- - -) and summed to calculate the total transmitted power (—).

the natural frequencies of a nearly periodic structure tend to be grouped in several distinct frequency bands. Thus the pdf has a large constant value for those frequency bands, and a small constant value elsewhere. The SEA approximation of transmitted power is then modified by simply adding a positive value or negative value on a logarithmic scale, as demonstrated in Fig. 3(a). This solution thus captures some of the resonant behavior of the transmitted power.

Here, a more general approach is taken for approximating the power transmitted between two substructures in a frequency range in which they have low or intermediate modal overlap. Each resonant frequency is assigned a uniform pdf. However, the frequency range of each pdf is different; it corresponds to the range in which that resonant frequency is most likely to be found. (The concept of using "confidence bands" as one-dimensional pdfs was suggested but not pursued in Ref. [8].) An example is shown in Fig. 3(b) for three resonant frequencies. Furthermore, it is assumed that the values of the square of the mode shape functions at the connection positions are known. Thus, applying only the first two SEA assumptions along with those noted above, Eq. (8) becomes:

$$E[\Pi_{12}] \approx \frac{2\zeta_2 k^2 \omega^2 S_{p_1 p_1}}{M_1^2 M_2} \left(\sum_{i=1}^{N_1} \Psi_{1_i}^2(a_1) E\left[\frac{1}{|\phi_{1_i}|^2}\right] \right) \left(\sum_{r=1}^{N_2} \Psi_{2_r}^2(a_2) E\left[\frac{\omega_{2_r}}{|\phi_{2_r}|^2}\right] \right) \tag{13}$$

This is called a Parameter-based Statistical Energy Method (PSEM) because it employs information for individual modal parameters.

Since each modal pdf is uniform, Eqs. (10) and (11) still hold for the expected values in Eq. (13). However, unlike the SEA approximation, each expected value is different, because the corresponding frequency bounds are unique. Furthermore, note that the pdfs do not cover the entire frequency range of interest. The results for each mode are therefore extrapolated outside the frequency range of that modal pdf before the individual modal contributions are summed. This is shown schematically in Fig. 3(b). PSEM is therefore a piecewise evaluation of the expected value of transmitted power.

The PSEM approximation is now applied to the two-bar system of Table 1, with the standard deviation of disorder $\sigma_1 = \sigma_2 = 10\%$. The pdfs of the resonant frequencies of Bar 1 and Bar 2 are shown in Fig. 4(a) and (b), respectively. For this system, the bounds for each resonant frequency may be found directly from the variation of the uncertain parameter. It can be seen that the spread of each natural frequency pdf due to disorder increases with increasing frequency.

The MCEM, PSEM, and SEA approximations for the transmitted power are shown in Fig. 4(c). There were 20,000 realizations taken for the MCEM results at each sampled frequency. This took about 10 hours of computation time. In contrast, the PSEM results only required 3 seconds of computation time, and the SEA results only required about 1 second. Note that the PSEM results show excellent agreement with the much more expensive MCEM results. The difference at very low frequencies comes from the fact that for the PSEM approximation, the value of the term $|\Delta|$ was assumed to be one due to weak coupling. This assumption breaks down as the frequency approaches zero. However, the match between the MCEM and

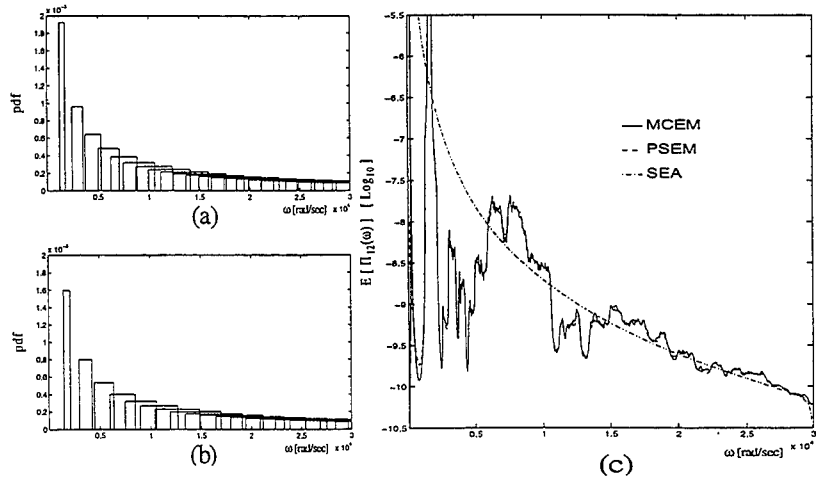

Fig. 4: (a) Natural frequency pdfs for Bar 1. (b) Natural frequency pdfs for Bar 2. (c) Transmitted powers obtained by MCEM, PSEM, and SEA for $\sigma_1 = \sigma_2 = 10\%$.

PSEM results in the mid-frequency range is excellent. Again, it is noted that the SEA results converge to those of MCEM (and PSEM) as the frequency increases. Now it can be seen that the assumption of identical pdfs for all modes becomes better with increasing frequency.

Next, the example system is considered with smaller disorder, $\sigma_1 = \sigma_2 = 1\%$. Fig. 5 shows the results for this case for what might be called the mid-frequency range. Note that even though this is a higher frequency range than that considered for the previous case, the pdfs of the resonant frequencies shown in Fig. 5(a) and (b) are not as strongly overlapped. Thus, several peaks are seen in the transmitted power in Fig. 5(c). Again, the PSEM approximation agrees well with the MCEM results, although there is more discrepancy for this case. The SEA approximation follows the global trend, but does not capture the resonances or anti-resonances. The SEA results drop off at the edges because only modes within this frequency range are considered to contribute to the transmitted power.

In addition to PSEM, another piecewise evaluation of the transmitted power is considered here. For this approximation, wherever the individual mode pdfs overlap, they are superposed to form a pdf for all the modes in that "section" of the frequency range. This superposition is demonstrated in Fig. 6. Also, if the number of modes in a section is above a certain cutoff number, N_c, then it is assumed that their mode shape function values at the connection positions are unknown, so that the ensemble-averaged value must be used. This is called a multiple mode approximation. The purpose

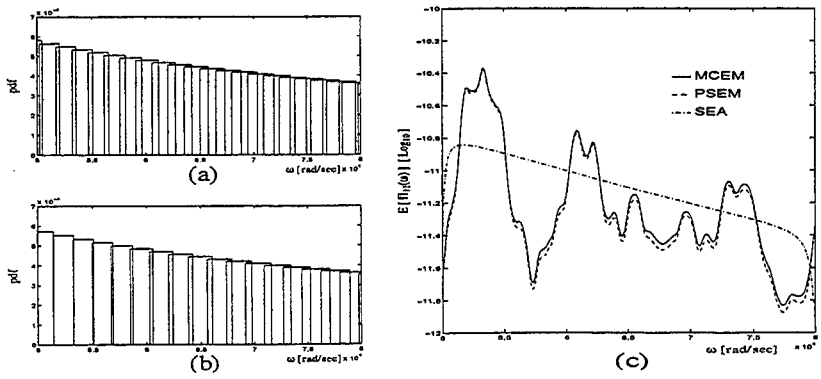

Fig. 5: (a) Natural frequency pdfs for Bar 1. (b) Natural frequency pdfs for Bar 2. (c) Transmitted power obtained by MCEM, PSEM, and SEA for $\sigma_1 = \sigma_2 = 1\%$.

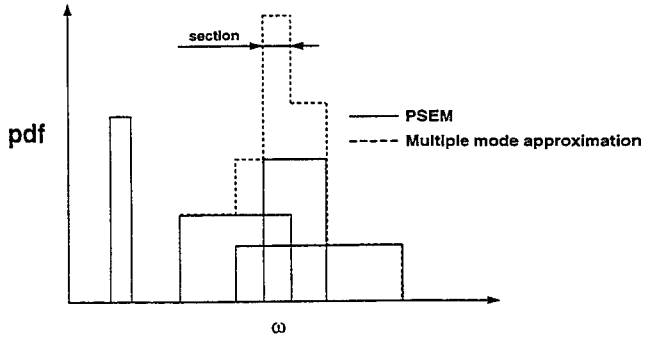

Fig. 6: Resonant frequency pdfs for PSEM and for the multiple mode approximation.

of formulating this approach is to investigate what happens as information about the individual modes is lost.

The multiple mode approximation is applied to the example system with $\sigma_1 = \sigma_2 = 10\%$ in Fig.7. For $N_c = 2$, this approximation has good agreement with MCEM. The match is especially good for $\omega < 10,000$. Above this frequency, the number of overlapped resonant frequencies in each pdf section is greater than N_c, and the loss of mode shape information affects the results slightly. For $N_c = 0$, the values of the mode shape functions are taken to be one for the entire frequency range, just as in the SEA approximation. As can be seen in Fig. 7, the piecewise construction of the pdf roughly captures the frequency ranges of the resonances and anti-resonances. However, the mode shape effect is more pronounced in

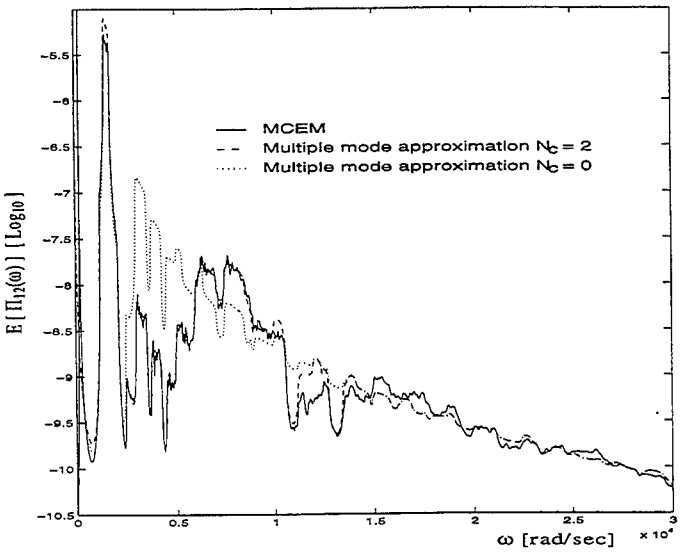

Fig. 7: Transmitted power obtained from MCEM and the multiple mode approximation for $\sigma_1 = \sigma_2 = 10\%$

the mid-frequency range. The peak values are now similar to the SEA approximation.

5 Conclusions

In this study, the power transmitted between two multi-mode substructures coupled by a spring was considered. A Monte Carlo Energy Method (MCEM) was used to calculate the ensemble average of the transmitted power for the system with parameter uncertainties. A classical Statistical Energy Analysis (SEA) approximation matched the Monte Carlo results in the high-frequency range, but did not capture the resonant behavior of the transmitted power in the mid-frequency range where the substructures have weak modal overlap.

A Parameter-based Statistical Energy Method (PSEM) was presented which uses a distinct pdf for each natural frequency as well as some individual mode shape information. A piecewise evaluation of the transmitted power was performed, and then the modal contributions were extrapolated and superposed. The PSEM approximation compared very well with the much more expensive Monte Carlo results, including in the mid-frequency

range.

References

1 R. H. Lyon. *Statistical Energy Analysis of Dynamical Systems: Theory and Applications.* M.I.T. Press, 1st edition, 1975.

2 R. H. Lyon. *Theory and Application of Statistical Energy Analysis.* Butterworth-Heinemann, 2nd edition, 1995.

3 C. H. Hodges and J. Woodhouse. Theories of noise and vibration transmission in complex structures. *Rep.Prog.Physics*, 49:107–170, 1986.

4 J. Woodhouse. An approach to the theoretical background of statistical energy analysis applied to structural vibration. *Journal of the Acoustical Society of America*, 69(6):1695–1709, 1981.

5 M. P. Norton. *Fundamentals of Noise and Vibration Analysis for Engineers.* Cambridge University Press, 1st edition, 1989.

6 N. Lalor. Statistical energy analysis and its use as an nvh analysis tool. *Sound and Vibration*, 30(1):16–20, 1996.

7 Huw G. Davies. Power flow between two coupled beams. *Journal of the Acoustical Society of America*, 51(1):393–401, 1972.

8 A. J. Keane and W. G. Price. Statistical energy analysis of strongly coupled systems. *Journal of Sound and Vibration*, 117(2):363–386, 1987.

9 A. J. Keane. *Statistical Energy Analysis of Engineering Structures (Ph.D Dissertation).* Brunel University (England), 1988.

Appendix

In this appendix, the nominal transmitted power in Eq. (7) for the mono-coupled two-bar system is derived. The procedure follows that of Refs [7, 8].

Plugging Eq. (5) into Eq. (4),

$$\left(E_{01}A_1\frac{d^2}{dx_1^2}+m_1\frac{d^2}{dt^2}\right)\sum_{i=0}^{\infty}W_{1_i}(t)\Psi_{1_i}(x_1)+\frac{d}{dt}C_1(\sum_{i=0}^{\infty}W_{1_i}(t)\Psi_{1_i}(x_1))=$$

$$F_1(x_1,t)+k\Big[\sum_{r=0}^{\infty}W_{2_r}(t)\Psi_{2_r}(a_2)-\sum_{i=0}^{\infty}W_{1_i}(t)\Psi_{1_i}(a_1)\Big]\delta(x_1-a_1) \quad \text{(A.1)}$$

$$\Big(E_{02}A_2\frac{d^2}{dx_2^2}+m_2\frac{d^2}{dt^2}\Big)\sum_{r=0}^{\infty}W_{2_r}(t)\Psi_{2_r}(x_2)+\frac{d}{dt}C_2(\sum_{r=0}^{\infty}W_{2_r}(t)\Psi_{2_r}(x_2))=$$
$$k\Big[\sum_{i=0}^{\infty}W_{1_i}(t)\Psi_{1_i}(a_1)-\sum_{r=0}^{\infty}W_{2_r}(t)\Psi_{2_r}(a_2)\Big]\delta(x_2-a_2) \qquad \text{(A.2)}$$

Multiplying Eq. (A.1) by $\Psi_{1_j}(x_1)$, and integrating with respect to x_1 for $[0,\ L_1]$ yields

$$M_1(\omega_{1_j}^2+\frac{d^2}{dt^2})W_{1_j}(t)+2\zeta_{1_j}\omega_{1_j}M_1\frac{d}{dt}W_{1_j}(t)= \qquad \text{(A.3)}$$
$$f_{1_j}+k\Psi_{1_j}(a_1)M_1\Big[\sum_{r=0}^{\infty}W_{2_r}(t)\Psi_{2_r}(a_2)-\sum_{i=0}^{\infty}W_{1_i}(t)\Psi_{1_i}(a_1)\Big]$$

where

$$2\zeta_{1j}\omega_{1_j}M_1=\int_0^{L_1}C_1(\Psi_{1_j}(x_1))\Psi_{1_j}(x_1)dx_1\quad,\quad f_{1_j}=\int_0^{L_1}F_1(x_1,t)\Psi_{1_j}(x_1)dx_1$$

and ω_{1j} is the jth resonant frequency of decoupled Bar 1. The damping ratio in Eq. (A.3) is now assumed to be the same (ζ_1) for all modes, since the differences in the ratio are usually small and this simplifies the equation. Taking the Fourier transform of Eq. (A.3) with zero initial conditions leads to the following

$$\begin{aligned}M_1\phi_{1_j}\overline{W}_{1_j} &= \overline{f}_{1_j}+k\Psi_{1_j}(a_1)\Big[\sum_{r=0}^{\infty}\overline{W}_{2_r}\Psi_{2_r}(a_2)-\sum_{i=0}^{\infty}\overline{W}_{1_i}\Psi_{1_i}(a_1)\Big]\\ \phi_{1_j} &= (\omega_{1_j}^2-\omega^2+\sqrt{-1}\cdot 2\zeta_1\omega_{1_j}\omega)(2-\mathrm{sgn}(j))\\ \mathrm{sgn}(j) &= \begin{cases}1 & \text{for } j>0\\ 0 & \text{for } j=0\end{cases}\end{aligned} \qquad \text{(A.4)}$$

where $(\bar{\ })$ denotes a Fourier transform. Similarly, applying the previous procedure to Eq. (A.2),

$$\begin{aligned}M_2\phi_{2_s}\overline{W}_{2_s} &= k\Psi_{2_s}(a_2)\Big[\sum_{i=0}^{\infty}\overline{W}_{1_i}\Psi_{1_i}(a_1)-\sum_{r=0}^{\infty}\overline{W}_{2_r}\Psi_{2_r}(a_2)\Big] \qquad \text{(A.5)}\\ \phi_{2_s} &= (\omega_{2_s}^2-\omega^2+\sqrt{-1}\cdot 2\zeta_2\omega_{2_s}\omega)(2-\mathrm{sgn}(s)).\end{aligned}$$

Solving for $\overline{W}_{2_s}$ from Eq. (A.4) and (A.5),

$$\overline{W}_{2_s}=\frac{1}{(1+\alpha_1)M_2\phi_{2_s}}[\overline{F}_{2_s}-k\Psi_{2_s}(a_2)\sum_{r=0}^{\infty}\overline{W}_{2_r}\Psi_{2_r}(a_2)] \qquad \text{(A.6)}$$

where

$$\overline{F}_{2_s}=\frac{k\Psi_{2_s}(a_2)}{M_1}\sum_{i=0}^{\infty}\frac{\overline{f}_{1_i}\Psi_{1_i}(a_1)}{\phi_{1_i}}\qquad \alpha_1=\frac{k}{M_1}\sum_{i=0}^{\infty}\frac{\Psi_{1_i}^2(a_1)}{\phi_{1_i}}.$$

Calculating the second term in brackets in Eq. (A.6),

$$k\Psi_{2_s}(a_2)\sum_{r=0}^{\infty}\overline{W}_{2_r}\Psi_{2_r}(a_2)=\frac{k\Psi_{2_s}(a_2)}{M_2(1+\alpha_1+\alpha_2)}\sum_{r=0}^{\infty}\frac{\Psi_{2_r}(a_2)\overline{F}_{2_r}}{\phi_{2_r}} \qquad (A.7)$$

where

$$\alpha_2=\frac{k}{M_2}\sum_{r=0}^{\infty}\frac{\Psi_{2_r}^2(a_2)}{\phi_{2_r}}.$$

Plugging Eq. (A.7) into Eq. (A.6),

$$\overline{W}_{2_s}=\frac{1}{M_2\phi_{2_s}}\underbrace{\frac{k\Psi_{2_s}(a_2)}{1+\alpha_1+\alpha_2}\sum_{i=0}^{\infty}\frac{\overline{f}_{1_i}\Psi_{1_i}(a_1)}{M_1\phi_{1_i}}}_{\text{Coupling force } P_s}. \qquad (A.8)$$

Using the definition of transmitted power in Ref. [7], $\Pi_{12}(\omega)$ is

$$\begin{aligned}\Pi_{12} &= Re\Big[-\sqrt{-1}\omega\sum_{s=0}^{\infty}E[P_s\overline{W}_{2_s}^*(\omega)]\Big]\\ &= Re\Big[-\sqrt{-1}\omega k\frac{1+\alpha_2^*}{|\underbrace{1+\alpha_1+\alpha_2}_{\Delta}|^2}\sum_{i=0}^{\infty}\sum_{j=0}^{\infty}\frac{\Psi_{1_i}(a_1)\Psi_{1_j}(a_1)\overbrace{E[\overline{f}_{1_i}\overline{f}_{1_j}^*]}^{S_{l_il_j}}}{M_1^2\phi_{1_i}\phi_{1_j}^*}\Big]\\ &= \frac{2\zeta_2k^2\omega^2}{M_1^2M_2|\Delta|^2}\sum_{r=0}^{\infty}\frac{\Psi_{2_r}^2(a_2)\omega_{2_r}}{|\phi_{2_r}|^2}\sum_{i=0}^{\infty}\sum_{j=0}^{\infty}\frac{S_{l_il_j}\Psi_{1_i}(a_1)\Psi_{1_j}(a_1)}{\phi_{1_i}\phi_{1_j}^*} \qquad (A.9)\end{aligned}$$

where $Re[\cdot]$ denotes the real part of the argument, * is a complex conjugate, and

$$S_{l_il_j}(\omega)=E[\overline{f}_{1_i}\overline{f}_{1_j}^*]$$

Finally, it is assumed that the modal driving forces, $\overline{f}_{1_j}$, are uncorrelated. Also, the spectral density function of each modal driving force is assumed to be constant for the finite frequency range of interest:

$$S_{l_il_j}(\omega)=\begin{bmatrix}S_{p_1p_1} & \text{for} \quad i=j\\ 0 & \text{for} \quad i\neq j.\end{bmatrix} \qquad (A.10)$$

Therefore, Eq. (A.9) becomes

$$\Pi_{12}=\frac{2\zeta_2k^2\omega^2S_{p_1p_1}}{M_1^2M_2|\Delta|^2}\sum_{i=0}^{\infty}\frac{\Psi_{1_i}^2(a_1)}{|\phi_{1_i}|^2}\sum_{r=0}^{\infty}\frac{\Psi_{2_r}^2(a_2)\omega_{2_r}}{|\phi_{2_r}|^2}. \qquad (A.11)$$

PASSIVE AND ACTIVE CONTROL III

Research on Control Law of Active Suspension of a Seven Degree of Freedom Vehicle Model

Dr&Prof. Yucheng Lei Lifen Chen
Automobile Engineering Dept.,Tong Ji University ,Shang Hai,P.R.of China

Abstract

In the paper , control law of active suspension is presented , which involves 7-DOF vehicle model for improving control accuracy .The control law involve vehicle running velocity , road power spectrum , suspension stiffness and damping .The control law can be applied to multi-DOF control of active suspension of vehicle .

Keywords: Active suspension , control law , Game theory , Modeling , 7 — DOF Vehicle Model .

1 . Introduction

An individual control system for each wheel by applying the optimum regulation method for the two degrees of freedom is showed in [3] . [4] and [5] also introduce two-DOF feedback control method of active suspension .It is difficult for two-DOF control method to coordinate multi-DOF kinematic distances of entire car . Muti-DOF active control can improve coordination control accuracy of entire car , but high speed of CPU is asked for control and calculation while control law of multi-DOF is got by real-time calculation . And, ride performance and handling performance is inconsistent . For resolving the problem ,the paper holds a new calculation method for optimizing the law that can be programmed for real-time control by table-lookup and not by real-time calculation .So the method and law can not only improve coordination control accuracy ,but also develop control speed .

2 . Mathematical Model

Vehicle is simplified to turn into 7 DOF model . 7-DOF vibration motion equation can be written as follow

$$[M]\ddot{Z}+[C]\dot{Z}+[K]Z=[C_t]\dot{Q}+[K_t]Q \qquad (1)$$

Where $[M]$ is mass matrix , $[C]$ is suspension damping matrix , $[K]$ is suspension stiffness matrix , $[C_t]$ is tyre damping matrix , $[K_t]$ is tyre stiffness matrix , $\ddot{Z}$ is acceleration matrix , $\dot{Z}$ is velocity matrix , Z is 7-DOF displacement matrix , $\dot{Q}$ is road surface input velocity matrix , Q is road surface input displacement matrix .

$$\ddot{Z} = \left(\ddot{Z}_1, \ddot{Z}_2 \bullet\bullet\bullet, \ddot{Z}_7 \right)^T \qquad (2)$$

Where $\ddot{Z}_1$ is vehicle vertical acceleration, $\ddot{Z}_2$ is roll acceleration , $\ddot{Z}_3$ is pitch acceleration , $\ddot{Z}_i \quad (i = 4,\bullet\bullet\bullet,7)$ is four tyres vertical acceleration .

3 General Optimization Method of Control Law

Objective function of optimization of control law can generally got by calculating weighted sum of 7-DOF mean square root of acceleration , dynamic deflection and dynamic load .it can be written as follows

$$J = \sum_{i=1}^{7} \alpha_i \cdot \sigma^2_{\ddot{Z}_i} + \sum_{j=1}^{4} \beta_i \cdot \sigma^2_{fd_j} + \sum_{k=1}^{4} \gamma_k \cdot \sigma^2_{F_{dk}/G_k} \qquad (3)$$

Where $\alpha_i (i = 1,\bullet\bullet\bullet,7), \beta_j (j = 1,\bullet\bullet\bullet,4), \gamma_k (k = 1,\bullet\bullet\bullet,4)$ is weighted ratio . Where $\sigma_{\ddot{Z}_i}$ (i=1, · · · ,7) is 7-DOF mean square root of acceleration , σ_{fd_j} (j=1, · · ·,4) is 7-DOF mean square root of dynamic deflection , $\sigma_{F_{dk}/G}$ (k=1, · · · ,4) is 7-DOF mean square root of relative dynamic load . $\sigma_{\ddot{Z}_i}$, $\sigma_{fd_j}, \sigma_{F_{dk}/G}$ can be calculated by resolving (1) using numerical method .

4 Result of General Optimization Method of Control Law

Optimization result of control law of a truck is got using above method as figure 1 and 2 , its main parameters as follows .

Wheel distance is 1.4 meter , axle distance is 2.297 meter , mass is 1121.3 kg , front tyre and axle' s mass is 22.8 kg , rear tyre and axle' s mass is 35.0 kg , X axis' rotational

inertia is 307.4 $kg \cdot m^2$, Y axis' rotational inertia is 1276.5 $kg \cdot m^2$.

In fig. 1 and 2 , C1 of RMSMIN and C3 of RMSMIN are respectively front and rear suspension damping of getting minimization of above objective function , it is changing while road surface rough coefficient C_{sp} and automobile velocity V is changing . C1 and C3 also rise when velocity V rises . This is called control law of general optimization method of active suspension in the paper . The result in fig. 1 and fig. 2 has been verified by road test .

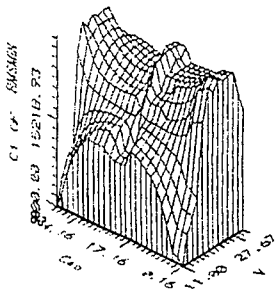

Fig. 1 front suspension optimization damping

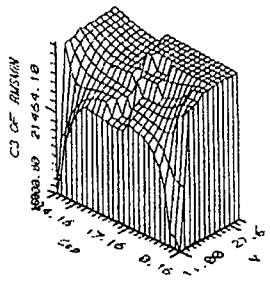

Fig. 2 rear suspension optimization damping

Simulation result can also verify that ride performance' s increasing (suspension stiffness reducing) will make handling performace reduce . So selecting perfect $\alpha_i (i = 1,\bullet\bullet\bullet,7), \beta_j (j = 1,\bullet\bullet\bullet,4), \gamma_k (k = 1,\bullet\bullet\bullet,4)$ is very difficult and inconsistent .The paper advances next game method to try to resolve the inconsistent problem .

5 Game Optimization Method of Control Law

Because to select weighted ratio of general optimization method is difficult , the paper advances a new method of optimization of control law — Game Balance Optimization Method ,it is discussed as follows .

Game theory method of two countermeasure aspect can be expressed as follows :

$$\begin{cases} \sum_{i=1}^{m_1} r_i = 1 \quad , \quad r_i \geq 0 \quad , i = 1, \quad 2, \quad , \cdots, m_1 \\ \sum_{j=1}^{m_2} h_j = 1 \quad , \quad h_j \geq 0 \quad , j = 1, \quad 2, \cdots, m_2 \end{cases} \tag{4}$$

where $r_1, r_2, \cdots\cdots r_{m_1}$ is probability of selecting $R_1, R_2, \cdots\cdots, R_{m_1}$ of countermeasure R (where R is acceleration mean square root) , and $h_1, h_2, \cdots\cdots, h_{m_2}$ is probability of selecting H_1, H_2, ……, H_{m_2} of countermeasure H (where H is mean square root of deflection or handling and satiability) .

It is called hybrid game method while these probability is leaded into the method . Countermeasure R selects r_i in order to get maximization of minimization paying expected value of column vector of paying matrix , and countermeasure H selects h_j in order to get minimization of maximization paying expected value of row vector of paying matrix .

If rank of paying matrix is $m_1 \times m_2$,R should select r_i as follows.

$$MAX\left\{ MIN\left(\sum_{i=1}^{m_1} a_{i1} r_i, \sum_{i=1}^{m_1} a_{i2} r_i, \cdots, \sum_{i=1}^{m_1} a_{im_2} r_i \right) \right\} \tag{5}$$

relative r_i

And H should select h_j as follows :

$$MAX\left\{ MIN\left(\sum_{j=1}^{m_2} a_{1j} h_j, \sum_{j=1}^{m_2} a_{2j} h_j, \cdots, \sum_{j=1}^{m_2} a_{m_1 j} h_j \right) \right\} \tag{6}$$

relative h_j

a_{ij} $(i = 1, \cdots\cdots, m_1 \quad , j = 1, \cdots\cdots, m_2)$ in (5) and (6) is element value of paying matrix , basing vehicle theory it can be got as follows :

$$a_{ij} = C_1 / \sigma_{\ddot{z}} + C_2 \sigma_{fd} \tag{7}$$

Where C_1, C_2 in (7) is coefficient of paying matrix (The paper orders they is 1 as an example , as C_1, C_2 ' s real value about very much condition is related to some privacy

problem it can' t be introduced.) . (5),(6) called respectively minimization maximization expected value and maximization minimization expected value can be abbreviated as $MAX\{MIN(\sum)\}$ and $MIN\{MAX(\sum)\}$. if $r_i and h_j$ is got as optimization of countermeasure , it can be written as follows :

$$MAX\{MIN(\sum)\} \le Optimization\ \ Countermeasure\ \ Expected\ \ Value \le MIN\{MAX(\sum)\} \quad (8)$$

A probability association (r_i^*, h_j^*) can be content with optimization expected value as follows :

Optimization Countermeasure Expected

$$\text{Value}=\sum_{i=1}^{m_1}\sum_{j=1}^{m_2} a_{ij} \bullet r_i^* \bullet h_j^* \quad (9)$$

Writer advances reformation simplex algorithm for resolving the game problem as reference [1] . In the paper the writer selects only an example to introduce calculation results as follows because the paper has limited space .

6 Results of Game Optimization Method of Control Law

Paying matrix as fig. 3 and fig. 4 , optimization result of control law of a truck is got using above game method as figure 5 and 6 , calculated truck' s main parameters as follows .

Wheel distance is 1.23 meter , axle distance is 3.6 meter , mass is 13880.0 kg , front tyre and axle' s mass is 280.0 kg , rear tyre and axle' s mass is 280.0 kg , X axis' rotational inertia is 1935 $kg \cdot m^2$, Y axis' rotational inertia is 710 $kg \cdot m^2$.

In fig. 3 and 4 ,B(I,J) is paying matrix value a_{ij} $(i = 1,\cdots\cdots, m_1$ $, j = 1,\cdots\cdots, m_2)$. In fig. 5 and fig. 6 , K1 of RMSMIN and K3 of RMSMIN are respectively front and rear suspension stiffness of getting optimization countermeasure expected value of above game method , it is changing while road surface rough coefficient C_{sp} and automobile velocity V is changing . K1 and K3 also rise

when velocity V rises . This is called control law of active suspension . The result in fig. 5 and fig. 6 has been verified by road test .

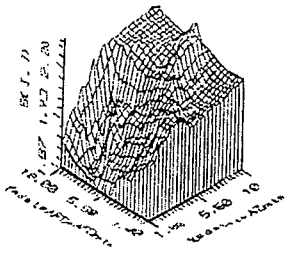

Fig. 3 paying matrix

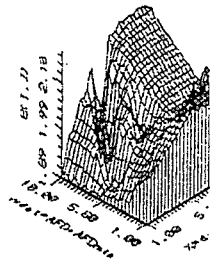

Fig. 4 paying matrix

7 Conclusion

The paper introduces two method to get optimization control

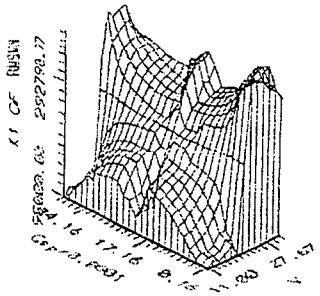

Fig. 5 front suspension optimization stiffness

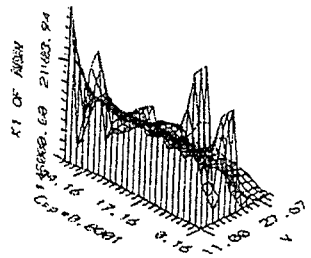

Fig. 6 rear suspension optimization stiffness

law of active suspension , and the control law is verified to ability to be applied to real control of active suspension . This will develop control accuracy and speed of active suspension .Off course , it need being researched further .

8 reference

1 Lei Yucheng , Theory and Engineering Realization of Semi — Active Control of Vehicle Vibration ,Dr. paper , Harbin Institute of Technology ,China ,1995 6 .

2 Thompson A.G. , A Suspension Proc. Int of Mechanical

Engr. Vol 185 No.36,970 — 990,553 — 563 .
3 Lei , S. , Fasuda , E. and Hayashi , Y. : "An Experimental Study of Optimal Vibration Adjustment Using Adaptive Control Methods ", Proc . IMechE Int . Conf . Advanced Suspensions , London , England , (1988) , C433/88 , 119-124.
4 Karnopp D. ,Active Damping in Road Vehicle Systems , VSD , 12(1983) , 291-316 .
5 Karnopp D . C ., Grosby M. J. & Harword R. ,Vibration Control Using Semi-Active Force , Generator , Trans . ASME, J . Eng . for Ind . Vol . 96 Ser . B , No .2 , (1974) , 619-626 .

Designing Heavy Truck Suspensions for Reduced Road Damage

Mehdi Ahmadian
Edward C. Mosch Jr.

Department of Mechanical Engineering
Virginia Polytechnic Institute and State University
Blacksburg, Virginia 24061-0238; USA
(540) 231-4920/-9100(fax)
ahmadian@vt.edu

ABSTRACT

The role of semiactive dampers in reducing tire dynamic loading is examined. An alternative to the well-known skyhook control policy, called "groundhook," is introduced. Using the dynamic model of a single suspension, it is shown that groundhook semiactive dampers can reduce tire dynamic loading, and potentially lessen road damage, for heavy trucks.

INTRODUCTION

The main intent of this work is to determine, analytically, the role of semiactive suspension systems in reducing tire dynamic loading, and road and bridge damage. Although primary suspension systems with semiactive dampers have been implemented in some vehicles for improving ride and handling, their impact on other aspects of the vehicle remain relatively unknown. Specifically, it is not yet known if implementing semiactive dampers in heavy truck suspension systems can reduce the tire dynamic forces that are transferred by the vehicle to the road. Reducing dynamic forces will result in reducing pavement loading, and possibly road and bridge damage.

The idea of semiactive dampers has been in existence for more than two decades. Introduced by Karnopp and Crosby in the early 70's [1-2], semiactive dampers have most often been studied and used for vehicle primary suspension systems. A semiactive damper draws small amounts of energy to operate a valve to adjust the damping level and reduce the amount of energy that is transmitted from the source of vibration energy (e.g., the axle) to the suspended body (e.g., the vehicle structure). Therefore, the force generated by a semiactive damper is directly proportional to the relative velocity across the damper (just like a passive damper). Another class of dampers that is usually considered for vibration control is fully active dampers. Active dampers draw

relatively substantial amounts of energy to produce forces that are not necessarily in direct relationship to the relative velocity across the damper.

The virtues of active and semiactive dampers versus passive dampers have been addressed in many studies [3-10]. Using various analytical and experimental methods, these studies have concluded that in nearly all cases semiactive dampers reduce vibration transmission across the damper and better control the suspended (or sprung) body, in comparison to passive dampers. Further, they have shown that, for vehicle primary suspension systems, semiactive dampers can lower the vibration transmission nearly as much as fully active dampers; without the inherent cost and complications associated with active dampers. This has led to the prototype application, and production, of semiactive dampers for primary suspensions of a wide variety of vehicles, ranging from motorcycles, to passenger cars, to bus and trucks, and to military tanks, in favor of fully active systems.

Although there is abundant research on the utility of semiactive dampers for improving vehicle ride and handling, their potential for reducing dynamic forces transmitted to the pavement remains relatively unexplored. This is because most suspension designers and researchers are mainly concerned with the role of suspension systems from the vehicle design perspective. Another perspective, however, is the effect of suspension systems on transmitting dynamic loads to the pavement.

ROAD DAMAGE STUDIES

Dynamic tire forces, that are heavily influenced by the suspension, are believed to be an important cause of road damage. Cole and Cebon [11] studied the design of a passive suspension that causes minimum road damage by reducing the tire force. They propose that there is a stronger correlation between the forth power of the tire force and road damage than the dynamic load coefficient (DLC) and road damage.

A simple measure of road damage, introduced by Cebon in [12], is the aggregate fourth power force A_k^4 defined as

$$A_k^4 = \sum_{j=1}^{Na} P_{jk}^4 \qquad \text{k} = 1,2,3 \ldots \text{ns} \tag{1}$$

where Pjk = force applied by tire j to point k along the wheel path,

n_a = number of axles on vehicle, and

n_s = number of points along the road..

DLC is a popular measurement frequently used to characterize dynamic loading and is defined as the root mean square (RMS) of the tire force divided by the mean tire force, which is typically the static weight of the vehicle. The equation takes the form:

$$DLC = \frac{RMS\ Dynamic\ Tire\ Force}{Static\ Tire\ Force} \tag{2}$$

This study shows that minimum road damage, for a two degree-of-freedom model, is achieved by a passive system with a stiffness of about one fifth of current air suspensions and a damping of about twice that typically provided. In practice, however, reducing the suspension stiffness can severely limit the static load carrying capacity of the suspension and cause difficulties in vehicle operation. Further, higher damping can substantially increase vibration transmission to the body and worsen the ride.

In another study by Cole and Cebon [13] a two-dimensional articulated vehicle simulation is validated with measurements from a test vehicle. The effect of modifications to a trailer suspension on dynamic tire forces are investigated. The RMS of dynamic loads generated by the trailer are predicted to decrease by 31 per cent, resulting in a predicted decrease in theoretical road damage of about 13 per cent.

Yi and Hedrick compared the effect of continuous semiactive and active suspensions and their effect on road damage using the vehicle simulation software VESYM [14]. A control strategy based on the tire forces in a heavy truck model is used to show that active and semiactive control can potentially reduce pavement loading. They, however, mention that measuring the tire forces poses serious limitation in practice.

The primary purpose of this paper is to extend past studies on semiactive suspension systems for reducing road damage. An alternative semiactive control policy, called "groundhook," is developed such that it can be easily applied in practice, using existing hardware for semiactive suspensions. A simulation model representing a single primary suspension is used to illustrate the system effectiveness. The simulation results show that groundhook control can reduce the dynamic load coefficient and fourth power of tire force substantially, without any substantial increase in body acceleration.

MATHEMATICAL FORMULATION

We consider a model representing the dynamics of a single primary suspension in a heavy truck, as shown in Figure 1.

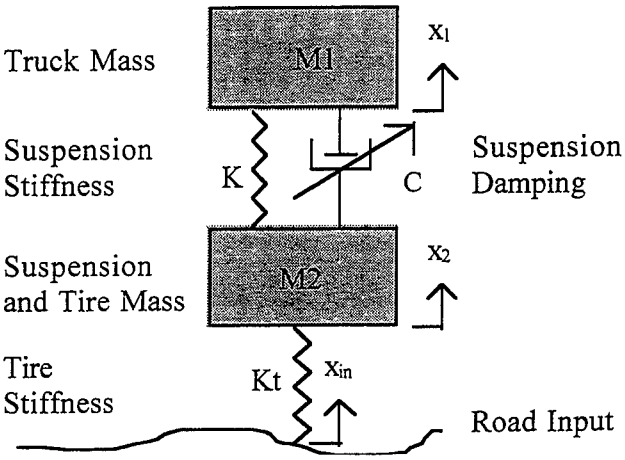

Figure 1. Primary Suspension Model

This model has been widely used in the past for automobile applications, due to its effectiveness in analyzing various issues relating to suspensions. Although it does not include the interaction between the axles and the truck frame dynamics, the model still can serve as an effective first step in studying fundamental issues relating to truck suspensions. Follow up modeling and testing, using a full vehicle, is needed to make a more accurate assessment.

The dynamic equations for the model in Figure 1 are:

$$M_1\ddot{x}_1 + C(\dot{x}_1 - \dot{x}_2) + K(x_1 - x_2) = 0 \tag{3a}$$

$$M_2\ddot{x}_2 - C(\dot{x}_1 - \dot{x}_2) - K(x_1 - x_2) + K_t x_{in} = 0 \tag{3b}$$

The variables x_1 and x_2 represent the body and axle vertical displacement, respectively. The variable x_{in} indicates road input, that is assumed to be a random input with a low-pass (0 - 25 Hz) filter. The amplitude for x_{in} is adjusted such that it creates vehicle and suspension dynamics that resembles field measurements. Such a function has proven to sufficiently represent actual road input to the vehicle tires.

Table 1 includes the model parameters, that are selected to represent a typical laden truck used in the U.S. The suspension is assumed to have a linear stiffness in its operating range. The damper characteristics are modeled as a non-linear function, as shown in Figure 2.

Table 1. Model Parameters

Description	Symbol	Value
Body Mass	M1	287 kg
Axle Mass	M2	34 kg
Suspension Stiffness	K1	196,142 N/m
Tire Stiffness	Kt	1,304,694 N/m
Suspension Damping	C	See Table 2

The bilinear function in Figure 2 represents the force-velocity characteristics of an actual truck damper. The parameters selected for both passive and semiactive dampers are shown in Table 2. These parameters are selected based on truck dampers commonly used in the U.S. Although we examined the effect of damper tuning on dynamic loading, if falls outside the scope of this paper. Instead, we concentrate here on comparing different semiactive dampers with a passive damper, using the baseline parameters shown in Table 2. The semiactive and passive damper characteristics used for this study are further shown in Figure 3.

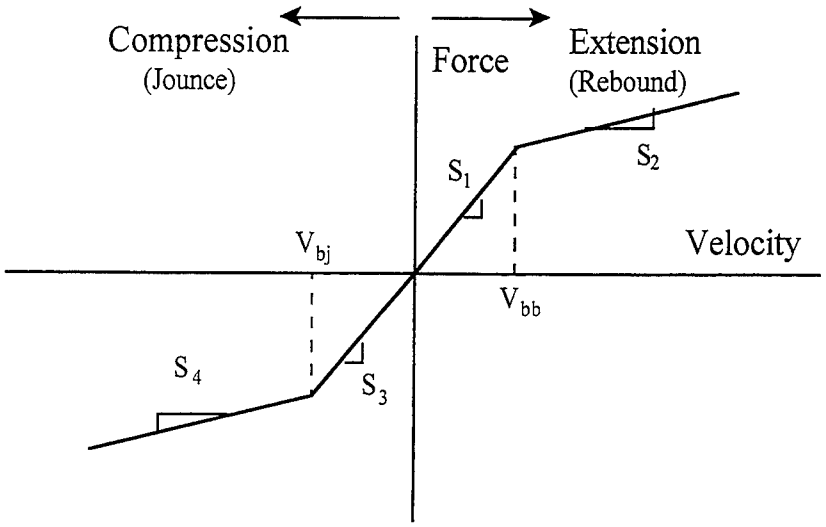

Figure 2. Nonlinear Damper Characteristics

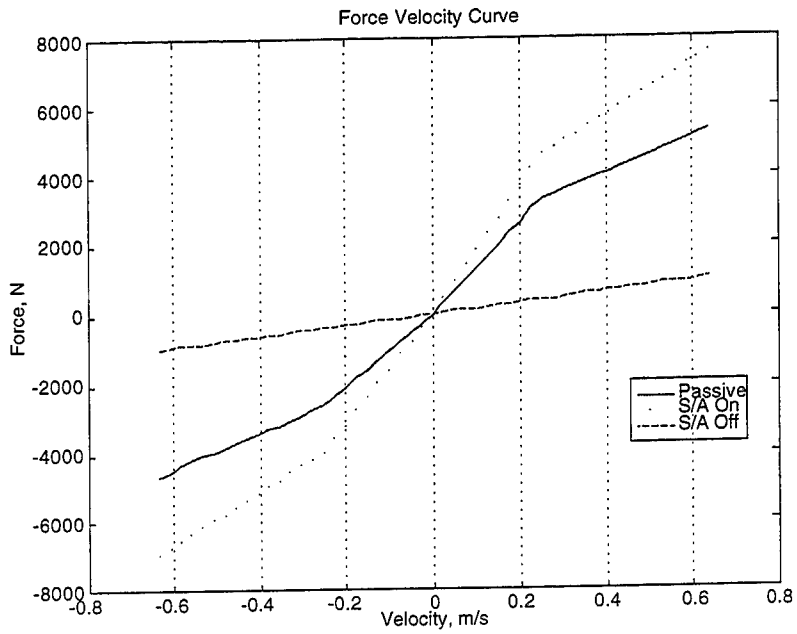

Figure 3. Passive and Semiactive Damper Characteristics

SKYHOOK CONTROL POLICY

As mentioned earlier, the development of semiactive dampers dates back to early 70's when Karnopp and Crosby introduced the skyhook control policy. For the system shown in Figure 1, skyhook control implies

$$\dot{x}_1(\dot{x}_1 - \dot{x}_2) \geq 0 \qquad C = C_{on} \tag{4a}$$

$$\dot{x}_1(\dot{x}_1 - \dot{x}_2) < 0 \qquad C = C_{off} \tag{4b}$$

Where $\dot{x}_1$ and $\dot{x}_2$ represents the velocities of M_1 (vehicle body) and M_2 (axle), respectively. The parameters C_{on} and C_{off} represent the on- and off-state of the damper, respectively, as it is assumed that the damper has two damping levels. In practice, this is achieved by equipping the hydraulic damper with an orifice that can be driven by a solenoid. Closing the orifice increases damping level and achieves C_{on}, whereas opening it gives C_{off}.

Table 2. Damper Parameters

	Passive	Semiactive On-State	Semiactive Off-State
S_1	0.25	0.35	0.03
S_2	0.10	0.15	0.03
V_{bb}	0.254 m/sec	0.254 m/sec	0.254 m/sec
S_3	0.20	0.30	0.03
S_4	0.10	0.15	0.03
V_{bj}	0.254 m/sec	0.254 m/sec	0.254 m/sec

The switching between the two damper states, shown in Eq. (4), is arranged such that when the damper is opposing the motion of the sprung mass (vehicle body), it is on the on-state. This will dampen the vehicle body motion. When the damper is pushing into the body, it is switched to the off-state to lower the amount of force it adds to the body. Therefore, a semiactive damper combines the performance of a stiff damper at the resonance frequency, and a soft damper at the higher frequencies, as shown in Figure 4.

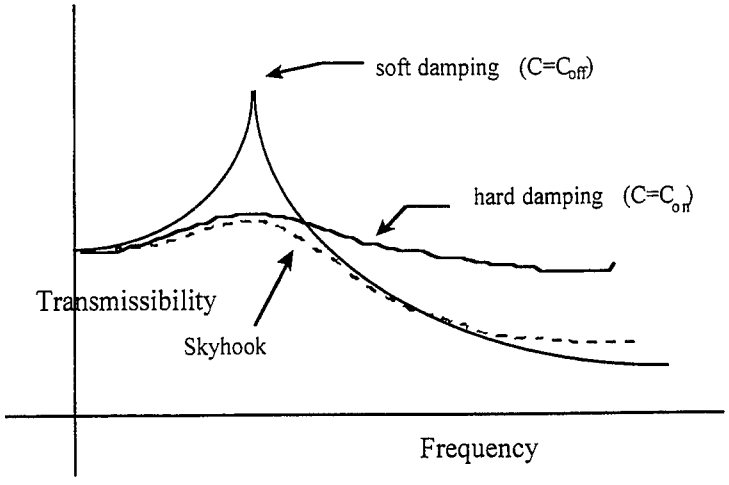

Figure 4. Transmissibility Characteristics for Passive and Semiactive Dampers

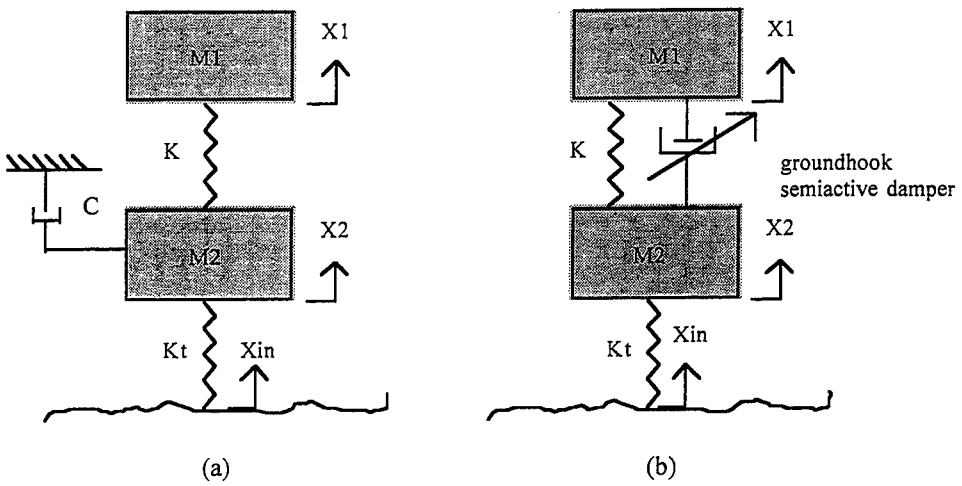

Figure 5. Groundhook Damper Configurations: a) optimal groundhook damper configuration, b) semiactive groundhook damper configuration.

This feature allows for a better control of the vehicle body, as has been discussed in numerous past studies. The skyhook control policy in Eq. (4), however, works such that it increases axle displacement, x_2, (commonly called wheel hop). Because the tire dynamic loading can be defined as

$$DL = K_t x_2 \tag{5}$$

The skyhook control actually increases dynamic loading. As mentioned earlier the development of skyhook policy was for improving ride comfort of the vehicle, without losing vehicle handling. Therefore, the dynamic loading of the tires was not a factor in the control development.

GROUNDHOOK CONTROL POLICY

To apply semiactive dampers to reducing tire dynamic loading, we propose an alternative control policy that can be implemented in practice using the same hardware needed for the skyhook policy. To control the wheel hop, this policy, called "groundhook," implies:

$$\dot{x}_2(\dot{x}_1 - \dot{x}_2) \le 0 \quad C = C_{on} \tag{6a}$$

$$\dot{x}_2(\dot{x}_1 - \dot{x}_2) > 0 \quad C = C_{off} \tag{6b}$$

As shown in Figure 5, the above attempts to optimize the damping force on the axle, similar to placing a damper between the axle and a fictitious ground (thus, the name "groundhook"). The groundhook semiactive damper maximizes the damping level (i.e., $C = C_{on}$) when the damper force is opposing

the motion of the axle; otherwise, it minimizes the damping level (i.e., C = C_{off}). The damper hardware needed to implement groundhook semiactive is exactly the same as

the skyhook semiactive, except for the control policy programmed into the controller.

SIMULATION RESULTS

The model shown in Figure 1 is used to evaluate the benefits of groundhook dampers versus passive and skyhook dampers. A non-linear damper model was considered for the simulations, as discussed earlier. The road input was adjusted such that the dynamic parameters for the passive damper resembles actual field measurements. Five different measures were selected for comparing the dampers:

- Dynamic Load Coefficient (DLC)
- Fourth Power of the tire dynamic load
- Sprung mass acceleration
- Rattle Space (relative displacement across the suspension)
- Axle Displacement, relative to the road

Dynamic load coefficient and fourth power of tire force are measures of pavement dynamic loading and are commonly used for assessing road damage. They are both considered here because there is no clear consensus on which one is a better estimate of road damage. Axle displacement, relative to the road, indicates wheel hop and is directly related to DLC and tire force, therefore it is yet another measure of road damage. Sprung mass acceleration is a measure of ride comfort. Our experience, however, has shown that for trucks this may not be a reliable measure of the vibrations the driver feels in the truck. The relative displacement across the dampers relates to the rattle space, that is an important design parameter in suspension systems, particularly for cars. For each of the above measures, the data was evaluated in both time (Figures 6 - 7) and frequency domain (Figures 8 - 10). In time domain, the root mean square (RMS) and maximum of the data for a five-second simulation are compared. In frequency domain, the transfer function between each of the measures and road displacement is plotted vs. frequency. The frequency plots highlight the effect of each damper on the body and axle resonance frequency.

Figures 6 and 7 show bar charts of root mean square (RMS) and maximum time data, respectively. In each case the data is normalized with respect to the performance of passive dampers commonly used in trucks. Therefore, values below line 1.0 can be interpreted as an improvement over the existing dampers. As Figures 6 and 7 show, groundhook dampers significantly

improve pavement loading, particularly as related to the fourth power of tire force. Furthermore, the rattle space is improved slightly over passive dampers, indicating that groundhook dampers do not impose any additional burden on the suspension designers.

One measure that has increased due to groundhook dampers is body acceleration. As mentioned earlier, in automobiles this measure is used as an indicator of ride comfort. In our past testing, however, we have found that for trucks it is a far less accurate measure of ride comfort. This is mainly due to the complex dynamics of the truck frame and the truck secondary suspension. A more accurate measure of ride comfort is acceleration at the B-Post (the post

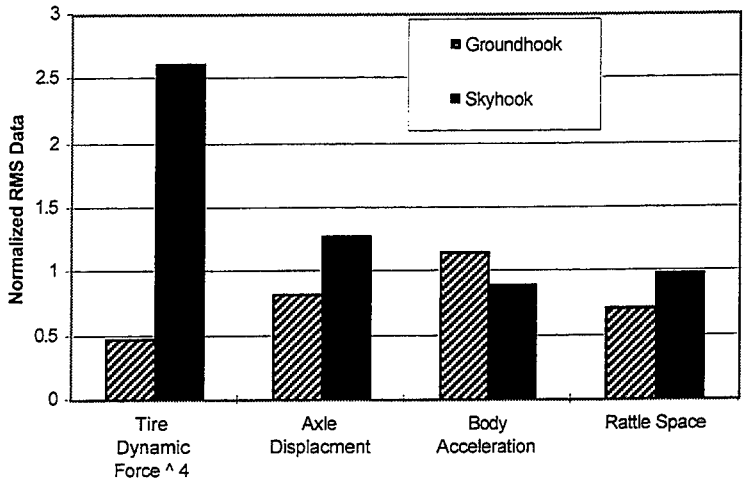

Figure 6. RMS Time Data Normalized with respect to Passive Damper

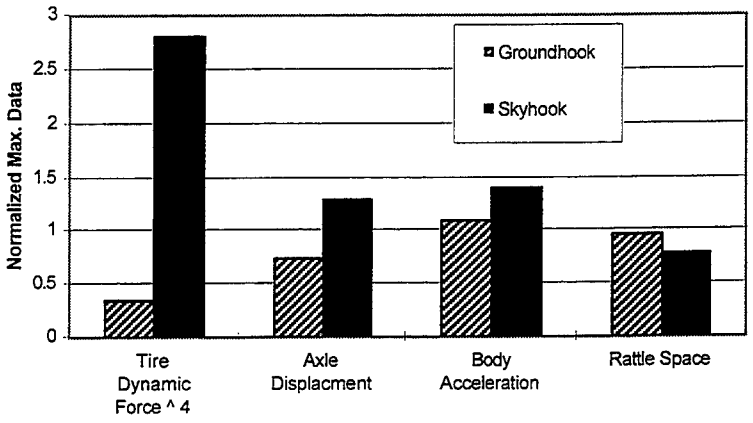

Figure 7. Max. Time Data Normalized with respect to Passive Damper

behind the driver), which cannot be evaluated from the single suspension model considered here. Nonetheless, the body acceleration is included for the sake of completeness of data.

The model shows that skyhook dampers actually increase the measures associated with pavement loading, while improving body acceleration. This agrees with the purpose of skyhook dampers that are designed solely for improving the compromise between ride comfort and vehicle handling. The improvement in ride comfort occurs at the expense of increased pavement loading.

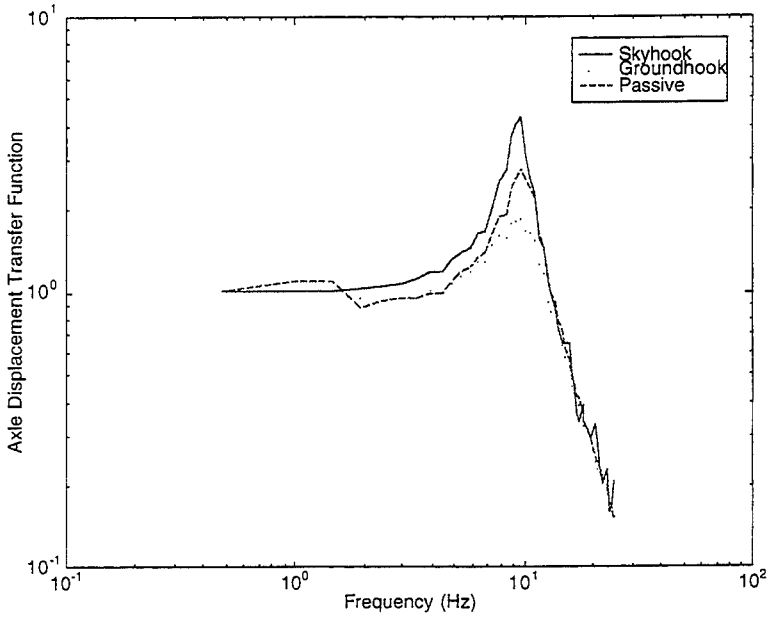

Figure 8. Transfer Function between Axle Displacement and Road Input

Figures 8 - 10 show the frequency response of the system due to each damper. In each figure, the transfer function between one of the measures and input displacement is plotted vs. frequency. These plots highlight the impact of skyhook and groundhook on the body and wheel hop resonance, relative to existing passive dampers. The frequency plots indicate that the

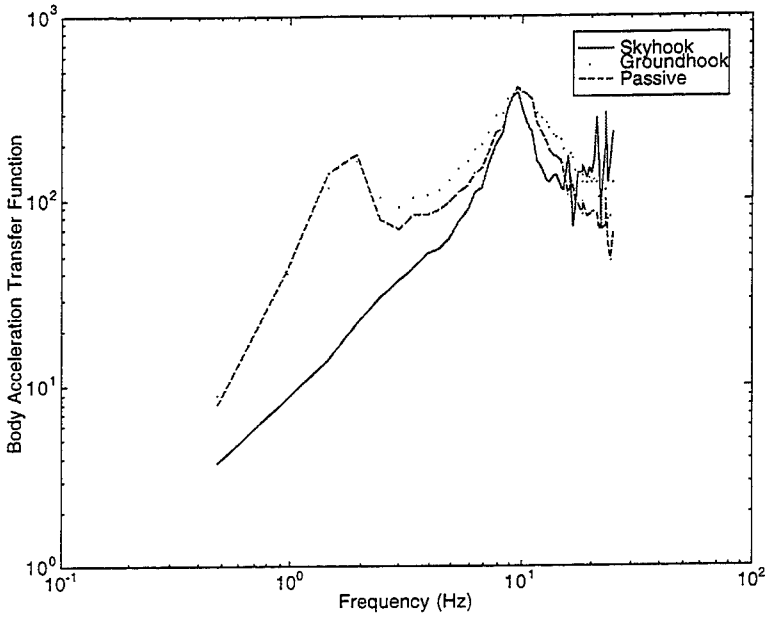

Figure 9. Transfer Function between Body Acceleration and Road Input

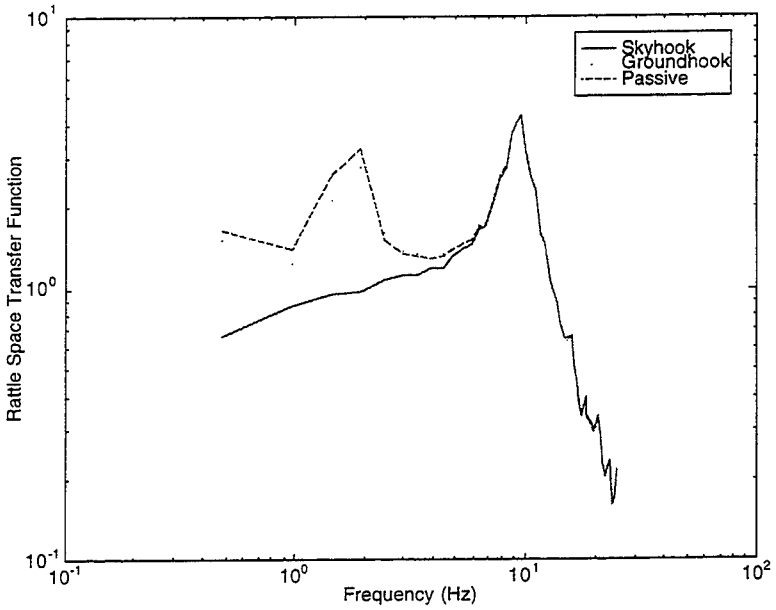

Figure 10. Transfer Function between Rattle Space and Road Input

groundhook dampers reduce axle displacement and fourth power of tire dynamic force at wheel hop frequency. At body resonance frequency, groundhook dampers do not offer any benefits over passive dampers. The

frequency results for body acceleration and rattle space are similar to those discussed earlier for the time domain results. The frequency plots show that the skyhook dampers offer benefits over passive dampers at frequencies close to the body resonance frequencies. At the higher frequencies, associated with wheel hop, skyhook dampers result in a larger peak than either passive or groundhook dampers. This indicates that skyhook dampers are not suitable for reducing tire dynamic loading.

CONCLUSIONS

An alternative to skyhook control policy for semiactive dampers was developed. This policy, called "groundhook," significantly improves both dynamic load coefficient (DLC), and fourth power of tire dynamic load, therefore holding a great promise for reducing road damage to heavy trucks. The dynamic model used for assessing the benefits of groundhook dampers represented a single suspension system. Although the results presented here show groundhook dampers can be effective in reducing tire dynamic loading and pavement damage, more complete models and road testing are necessary for more accurately assessing the benefits.

REFERENCES

1. Crosby, M. J., and Karnopp, D. C., "The Active Damper," The Shock and Vibration Bulletin 43, Naval Research Laboratory, Washington, D.C., 1973.

2. Karnopp, D. C., and Crosby, M. J., "System for Controlling the Transmission of Energy Between Spaced Members," U.S. Patent 3,807,678, April 1974.

3. Ahmadian, M. and Marjoram, R. H., "Effects of Passive and Semi-active Suspensions on Body and Wheelhop Control," Journal of Commercial Vehicles, Vol. 98, 1989, pp. 596-604.

4. Ahmadian, M. and Marjoram, R. H., "On the Development of a Simulation Model for Tractor Semitrailer Systems with Semiactive Suspensions," Proceedings of the Special Joint Symposium on Advanced Technologies, 1989 ASME Winter Annual Meeting, San Francisco, California, December 1989 (DSC-Vol. 13).

5. Hedrick, J. K., "Some Optimal Control Techniques Applicable to Suspension System Design," American Society of Mechanical Engineers, Publication No. 73-ICT-55, 1973.

6. Hac, A., "Suspension Optimization of a 2-DOF Vehicle Model Using Stochastic Optimal Control Technique," Journal of Sound and Vibration, 1985.

7. Thompson, A. G., "Optimal and Suboptimal Linear Active Suspensions for Road Vehicles," Vehicle System Dynamics, Vol. 13, 1984.

8. Karnopp, D., Crosby, M. J., and Harwood, R. A., "Vibration Control Using Semiactive Force Generators," American Society of Mechanical Engineers, Journal of Engineering for Industry, May 1974, pp. 619-626.

9. Krasnicki, E. J., "Comparison of Analytical and Experimental Results for a Semiactive Vibration Isolator," Shock and Vibration Bulletin, Vol. 50, September 1980.

10. Chalasani, R.M., "Ride Performance Potential of Active Suspension Systems-Part 1: Simplified Analysis Based on a Quarter-Car Model," proceedings of 1986 ASME Winter Annual Meeting, Los Angeles, CA, December 1986.

11. Cole, D. J. and Cebon, D., "Truck Suspension Design to Minimize Road Damage," Proceedings of the Institution of Mechanical Engineers, Vol. 210, D06894, 1996, pp. 95-107.

12. Cebon, D., "Assessment of the Dynamic Forces Generated by Heavy Road Vehicles," ARRB/FORS Symposium on Heavy Vehicle Suspension Characteristics, Canberra, Australia, 1987.

13. Cole, D. J. and Cebon, D., "Modification of a Heavy Vehicle Suspension to Reduce Road Damage," Proceedings of the Institution of Mechanical Engineers, Vol. 209, D03594, 1995.

14. Yi, K. and Hedrick, J. K., "Active and Semi-Active Heavy Truck Suspensions to Reduce Pavement Damage," SAE SP-802, paper 892486, 1989.

Active Vibration Control of Isotropic Plates Using Piezoelectric Actuators

A. M. Sadri*, J. R., Wright† and A. S. Cherry‡
The Manchester School of Engineering, Manchester M13 9PL, UK

and

R. J. Wynne§
Sheffield Hallam University, School of Engineering, Sheffield, UK

Abstract: Theoretical modelling of the vibration of plate components of a space structure excited by piezoelectric actuators is presented. The equations governing the dynamics of the plate, relating the strains in the piezoelectric elements to the strain induced in the system, are derived for isotropic plates using the Rayleigh-Ritz method. The developed model was used for a simply supported plate. The results show that the model can predict natural frequencies and mode shapes of the plate very accurately. The open loop frequency response of the plate when excited by the patch of piezoelectric material was also obtained. This model was used to predict the closed loop frequency response of the plate for active vibration control studies with suitable location of sensor-actuators.

Introduction

Vibration suppression of space structures is very important because they are lightly damped due to the material used and the absence of air damping. Thus the modes of the structure must be known very accurately in order to be affected by the controller while avoiding spillover. This problem increases the difficulty of predicting the behaviour of the structure and consequently it might cause unexpected on-orbit behaviour.

These difficulties have motivated researchers to use the actuation strain concept. One of the mechanisms included in the actuation strain concept is the piezoelectric effect whereby the strain induced through a piezoelectric actuator is used to control the

*Research Student, Dynamics & Control Research Group.
† Professor , Dynamics & Control Research Group.
‡ Former Lecturer, Dynamics & Control Research Group.
§ Professor of Mechanical and Control Engineering.

deformation of the structure [1]. It can be envisaged that using this concept in conjunction with control algorithms can enhance the ability to suppress modes of vibration of flexible structures.

Theoretical and experimental results of the control of a flexible ribbed antenna using piezoelectric materials has been investigated in [2]. An active vibration damper for a cantilever beam using a piezoelectric polymer has been designed in [3]. In this study, Lyapunov's second or direct method for distributed-parameter systems was used to design control algorithms and the ability of the algorithms was verified experimentally. These works have clearly shown the ability of piezoelectric actuators for vibration suppression. However, they have been limited to one dimensional systems. Obviously, there is a need to understand the behaviour of piezoelectric actuators in two dimensional systems such as plates.

Vibration excitation of a thin plate by patches of piezoelectric material has been investigated in [4]. Their work was basically an extension of the one dimensional theory derived in [1] to show the potential of piezoelectric actuators in two dimensions. In their studies, it was assumed that the piezoelectric actuator doesn't significantly change the inertia, mass or effective stiffness of the plate. This assumption is not guaranteed due to the size, weight and stiffness of the actuator. Based on this assumption, their model can not predict the natural frequencies of the plate accurately after bonding piezoelectric actuators. Therefore, it is essential to have a more general model of a plate and bonded piezoelectric actuators with various boundary conditions. The model should be able to predict frequency responses because this is fundamental to the understanding of the behaviour of the system for control design purposes. It is the objective of the current study to develop such a modelling capability.

Previous work [5, 6, 7] has concentrated on the modelling and control of a cantilever beam. The method used involved bonding piezoelectric material to a stiff constraining layer, which was bonded to the beam by a thin viscoelastic layer in order to obtain both active and passive damping. Then a Rayleigh-Ritz model was developed and used to derive a linearized control model so as to study different control strategies. In the work described in this paper, the method has been extended to the more complex plate problem. The paper introduces a modelling approach based on the Rayleigh-Ritz assumed mode shape method to predict the behaviour of a thin plate excited by a patch of piezoelectric material bonded to the surface of the plate. The model includes the added inertia and stiffness of the actuator and has been used to predict the frequency response of the plate. Suggestions for future work are also included.

Theoretical Modelling

In developing the Rayleigh-Ritz model of a plate excited by a patch of piezoelectric material bonded to the surface of the plate, a number of assumptions must be made. The patch of piezoelectric material is assumed to be perfectly bonded to the surface of the plate. The magnitude of the strains induced by the piezoelectric element is a linear function of the applied voltage that can be expressed by

$$\varepsilon'_x = \varepsilon'_y = \frac{d_{31}}{t_{pe}} V_{33}. \tag{1}$$

Here d_{31} is the piezoelectric strain constant, t_{pe} is the piezoelectric layer thickness and V_{33} is the applied voltage. The index 31 shows that the induced strain in the '1' direction is perpendicular to the direction of poling '3' and hence the applied field. The piezoelectric element thickness is assumed to be small compared to the plate thickness. The displacements of the plate middle surface are assumed to be normal to it due to the bending affects.

Figure 1 shows the configuration of the bonded piezoelectric material relative to the surface of the plate.

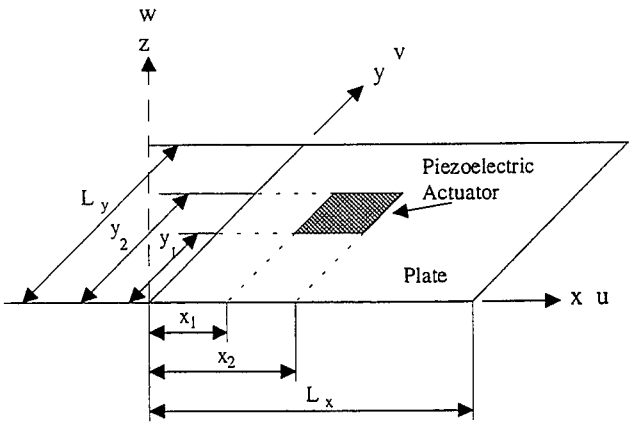

Figure 1. Configuration of the bonded piezoelectric actuator on the surface of the plate.

In figure 1, L_x and L_y are the dimensions of the plate, x_1, x_2, y_1 and y_2 are the boundaries of the piezoelectric element and u, v and w are the displacements in the x, y and z direction, respectively.

To derive the equations of motion of the plate based on the Rayleigh-Ritz method, both the strain energy U and kinetic energy T of the plate and the piezoelectric element must be determined. The strain

and kinetic energy result from the deformation produced by the applied strain which is induced by exciting the piezoelectric element. The deformations can be expressed by the combination of the midplane displacement and the deformations resulting from the bending of the plate.

Strain Energy

The strain energy of the plate and piezoelectric material can be calculated by

$$U = \frac{1}{2}\int_{v_p} (\sigma_x \varepsilon_x + \sigma_y \varepsilon_y + \tau_{xy} \gamma_{xy})\, dV_p + \frac{1}{2}\int_{v_{pe}} (\sigma_x \varepsilon_x + \sigma_y \varepsilon_y + \tau_{xy} \gamma_{xy})\, dV_{pe} \qquad (2)$$

where ε is the inplane direct strain, σ is the inplane direct stress, τ is the inplane shear stress and γ is shear strain. dV shows volume differential and indices p and pe refer to the plate and piezoelectric actuator, respectively. The strains ε_x , ε_y and γ_{xy} can be shown to be

For the Plate :

$$\begin{aligned} \varepsilon_x &= \frac{\partial u}{\partial x} - z\frac{\partial^2 w}{\partial x^2} \\ \varepsilon_y &= \frac{\partial v}{\partial x} - z\frac{\partial^2 w}{\partial y^2} \\ \gamma_{xy} &= \frac{\partial u}{\partial y} + \frac{\partial v}{\partial x} - 2z\frac{\partial^2 w}{\partial x \partial y} \end{aligned} \qquad (3)$$

For the Piezoelectric actuator :

$$\begin{aligned} \varepsilon_x &= \frac{\partial u}{\partial x} - z\frac{\partial^2 w}{\partial x^2} - \frac{d_{31}}{t_{pe}} V_{33} = \underline{\varepsilon_x} - \mu V_{33} \\ \varepsilon_y &= \frac{\partial v}{\partial y} - z\frac{\partial^2 w}{\partial y^2} - \frac{d_{31}}{t_{pe}} V_{33} = \underline{\varepsilon_y} - \mu V_{33} \\ \gamma_{xy} &= \frac{\partial u}{\partial y} + \frac{\partial v}{\partial x} - 2z\frac{\partial^2 w}{\partial x \partial y} = \underline{\gamma_{xy}} \end{aligned} \qquad (4)$$

where $\underline{\ }$ refers to the strains due to the deformation. The stresses σ_x , σ_y , γ_{xy} can be expressed as

For the Plate :

$$\begin{bmatrix}\sigma_x\\ \sigma_y\\ \gamma_{xy}\end{bmatrix}=\frac{E_p}{1-\upsilon_p^2}\begin{bmatrix}1 & \upsilon_p & 0\\ \upsilon_p & 1 & 0\\ 0 & 0 & \frac{1-\upsilon_p}{2}\end{bmatrix}\begin{bmatrix}\varepsilon_x\\ \varepsilon_y\\ \gamma_{xy}\end{bmatrix} \tag{5}$$

For the Piezoelectric actuator :

$$\begin{bmatrix}\sigma_x\\ \sigma_y\\ \gamma_{xy}\end{bmatrix}=\frac{E_{pe}}{1-\upsilon_{pe}^2}\begin{bmatrix}1 & \upsilon_{pe} & 0\\ \upsilon_{pe} & 1 & 0\\ 0 & 0 & \frac{1-\upsilon_{pe}}{2}\end{bmatrix}\begin{bmatrix}\underline{\varepsilon_x}-\mu V_{33}\\ \underline{\varepsilon_y}-\mu V_{33}\\ \underline{\gamma_{xy}}\end{bmatrix} \tag{6}$$

where E is Young modulus and υ is Poisson's ratio for the assumed isotropic material. Substituting equations 3, 4, 5 and 6 into 2 yields the strain energy of the plate and piezoelectric actuator,

$$U=\frac{1}{2}\int_{V_p}\frac{E_p}{1-\upsilon_p^2}\left[\varepsilon_x^{\,2}+2\,\upsilon_p\varepsilon_x\varepsilon_y+\varepsilon_x^2+\frac{1}{2}(1-\upsilon_p)\,\gamma_{xy}^2\right]dV_p$$
$$+\frac{1}{2}\int_{V_{pe}}\frac{E_{pe}}{1-\upsilon_{pe}^2}\left[(\underline{\varepsilon_x}-\mu V_{33})^2+2\upsilon_{pe}(\underline{\varepsilon_x}-\mu V_{33})(\underline{\varepsilon_y}-\mu V_{33})^2+\underline{\gamma_{xy}}^2\frac{1-\upsilon_{pe}}{2}\right]dV_{pe}. \tag{7}$$

Kinetic Energy

To obtain the kinetic energy, the velocity components in x, y and z directions are needed. The velocity components can be calculated by differentiating the displacement components which are

$$\begin{aligned}\underline{u}&=u-z\frac{\partial w}{\partial x}\\ \underline{v}&=v-z\frac{\partial w}{\partial y}\\ \underline{w}&=w.\end{aligned} \tag{8}$$

Differentiating equations 8 yields

$$\underline{\dot{u}} = \dot{u} - z\frac{\partial \dot{w}}{\partial x}$$
$$\underline{\dot{v}} = \dot{v} - z\frac{\partial \dot{w}}{\partial y} \qquad (9)$$
$$\underline{\dot{w}} = \dot{w}$$

where $\underline{\dot{u}}$, $\underline{\dot{v}}$ and $\underline{\dot{w}}$ are the velocity components in the x, y and z directions respectively. Using these velocity components, the kinetic energies of the plate and piezoelectric actuator are obtained as

$$T = \frac{1}{2}\int_{V_p} \rho_p[\dot{w}^2 + (\dot{u} - z\frac{\partial \dot{w}}{\partial x})^2 + (\dot{v} - z\frac{\partial \dot{w}}{\partial y})^2]dV_p$$
$$+\frac{1}{2}\int_{V_{pe}} \rho_{pe}[\dot{w}^2 + (\dot{u} - z\frac{\partial \dot{w}}{\partial x})^2 + (\dot{v} - z\frac{\partial \dot{w}}{\partial y})^2]dV_{pe} \qquad (10)$$

where ρ is the mass density.

Equation of Motion

The static or dynamic response of the plate excited by the piezoelectric actuator can be calculated by substituting the strain and kinetic energy into Lagrange's equation

$$\frac{d}{dt}(\frac{\partial T}{\partial \dot{q}_i}) - \frac{\partial T}{\partial q_i} + \frac{\partial U}{\partial q_i} = Q_i \qquad (11)$$

where q_i represents the ith generalised coordinate and Q_i is the ith generalised force. As there are no external forces (the force applied by the piezoelectric element is included as an applied strain) or gyroscopic terms and there is no added damping, Lagrange's equation reduces to :

$$\frac{d}{dt}(\frac{\partial T}{\partial \dot{q}_i}) + \frac{\partial U}{\partial q_i} = 0. \qquad (12)$$

Now the equation of motion can be obtained by using the expression obtained for the strain and kinetic energy, and the assumed shape functions for flexural and longitudinal motion

$$u(x,y,t) = \{\psi(x,y)\}^T \{h(t)\}$$
$$v(x,y,t) = \{\xi(x,y)\}^T \{f(t)\} \quad (13)$$
$$w(x,y,t) = \{\phi(x,y)\}^T \{g(t)\}.$$

Here ψ , ξ and ϕ are the assumed displacement shape and h , f and g are generalised coordinate of the plate response in x, y and z directions. Using the shape functions expressed in equations 13, substituting equations 7 and 10 into equation 12, and including Rayleigh damping yields the equation of motion of the plate in the form

$$[M]\{\ddot{q}\} + [C]\{\dot{q}\} + [K]\{q\} = \{P\}V \quad (14)$$

where M, C and K are mass, damping and stiffness matrices and P is the voltage-to-force transformation vector. Vector q represents the plate response modal amplitudes and V is the applied voltage.

State-Space Equations

A model of a structure found via finite element or Rayliegh-Ritz methods results in second-order differential equations of the form

$$[M]\{\ddot{q}\} + [C]\{\dot{q}\} + [K]\{q\} = \{P\}V \quad (15)$$

Choosing state variables $x_2 = q$ and $x_2 = \dot{x}_1$, equation 1 may be reduced to a state-space representation as follows :

$$\dot{q} = \dot{x}_1 = x_2$$
$$\ddot{q} = \dot{x}_2 = -M^{-1}Kq - M^{-1}C\dot{q} + M^{-1}PV. \quad (16)$$

Equations 15 can then be rewritten as

$$\begin{bmatrix} \dot{x}_1 \\ \dot{x}_2 \end{bmatrix} = \begin{bmatrix} 0 & I \\ -M^{-1}K & -M^{-1}C \end{bmatrix} \begin{bmatrix} x_1 \\ x_2 \end{bmatrix} + \begin{bmatrix} 0 \\ M^{-1}P \end{bmatrix} V$$
$$[q] = [I \quad 0] \begin{bmatrix} x_1 \\ x_2 \end{bmatrix} \quad (17)$$

where [ ], { } are ignored. It should be noted that the vector q must be multiplied by the shape functions to produce the actual displacement.

Results

The model was used to investigate the response of a simply supported plate. In order to maintain symmetry of the geometric structure a piezoelectric actuator is assumed to be bonded to both the top and bottom surfaces of the plate. So The symmetry of the elements causes no extension of the plate midplane and the plate deforms in pure bending. In this case the shape functions are assumed to be :

$$\begin{aligned} &\psi(x,y) = 0 \\ &\xi(x,y) = 0 \\ &\phi(x,y) = sin(\frac{m\pi}{L_x}x)sin(\frac{n\pi}{L_y}y) \end{aligned} \tag{18}$$

where m and n are the number of half waves in the x and y directions.

The properties of the plate are given in Table 1 and its dimensions are $L_x = 0.38\,m$, $L_y = 0.30\,m$ and $t_p = 1.5876\,mm$. Tables 2 and 3 show the natural frequencies of the bare plate obtained by the thin plate theory and the RR model, respectively. Since the shape functions used in this example express the exact shape of the simply supported plate, the natural frequencies included in Tables 2 and 3 are very close.

In order to excite the plate, a piezoelectric actuator with configuration $x_1 = 0.32\,m$, $x_2 = 0.36\,m$, $y_1 = 0.04\,m$ and $y_2 = 0.26\,m$ is used above and below. The natural frequencies of the plate after bonding the piezoelectric actuator to the surface are given in Table 4. The results show an increase in natural frequencies, showing that the added stifness is more important than the added inertia.

Table 1 : Properties of the plate

$E_p(\times 10^9\,N/m^2)$	$\rho_p(kg/m^3)$	υ_p
207	7870	.292

Table 2 : Plate natural frequencies (rad / s) , Thin Plate Theory

n/m	1	2	3	4
1	437.5	1246.0	2593.5	4480.0
2	941.4	1749.9	3097.4	4983.9
3	1781.2	2589.7	3937.2	5823.7
4	2957.0	3765.5	5113.0	6999.5

Table 3 : Plate natural frequencies (rad / s) , RR Model

n/m	1	2	3	4
1	437.5	1245.9	2593.2	4479.1
2	941.3	1749.7	3097.0	4982.8
3	1781.1	2589.4	3936.6	5822.3
4	2956.7	3764.9	5111.9	6997.4

Table 4 : Plate-Piezo natural frequencies (rad / s)

n/m	1	2	3	4
1	444.0	1257.1	2611.3	4502.8
2	957.2	1775.6	3182.1	5076.7
3	1854.6	2642.5	4072.3	6029.6
4	3076.6	3933.8	5224.6	7277.2

Initially, the piezoelectric actuator was excited by a constant DC voltage. The result of this action is shown in figure 2 which shows the dominant out of plane displacement around the location of the piezoelectric actuator bonded to the surface of the plate. To show the modes of vibration, the piezoelectric actuator was excited by a voltage with frequencies near to the natural frequencies of modes (2,2) and (1,3). The response in figures 3 , 4 show that the piezoelectric actuator excited both of these modes.

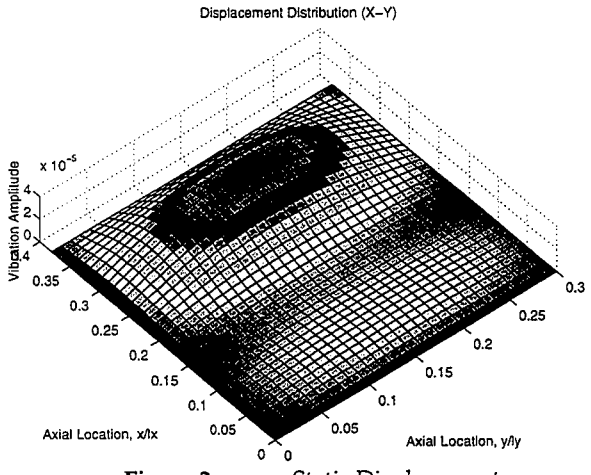

Figure 2. Static Displacement

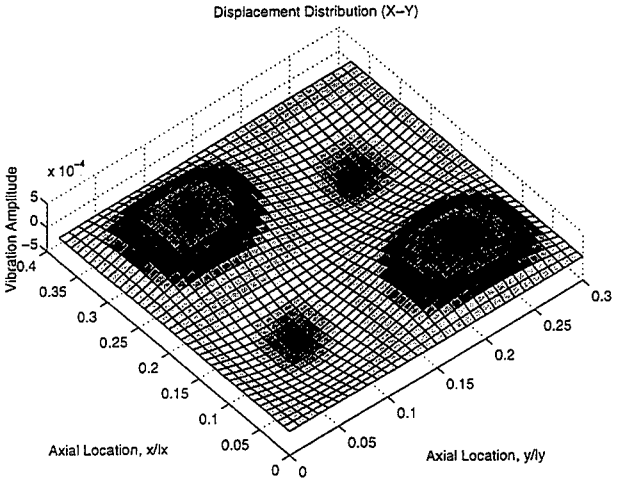

Figure 3. Vibration of the plate, mode (2,2)

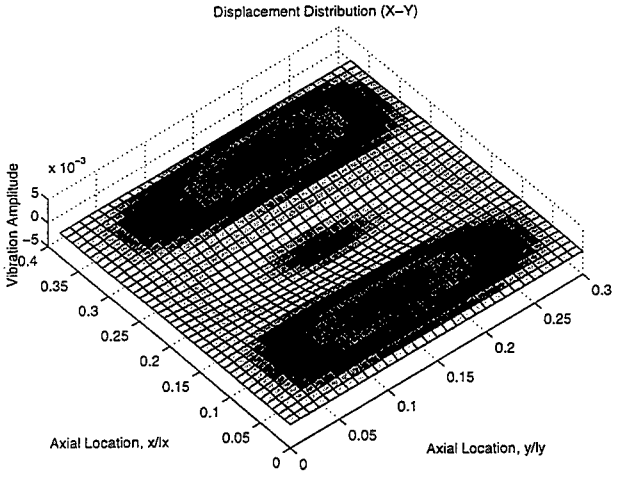

Figure 4. Vibration of the plate, mode (3,1)

The frequency response of the plate at the centre was obtained by exciting the piezoelectric actuator at a range of frequencies between 0 and 4000 rad/s. Figure 5 shows the frequency response of the plate at its centre. The frequency response of the plate at $y = 0.5L_x$ along the x-direction is shown in figure 6. It can be seen that the amplitude of vibration of some modes are very high compared to that of the other modes. Special attention must be given for the suppression of vibration of these modes.

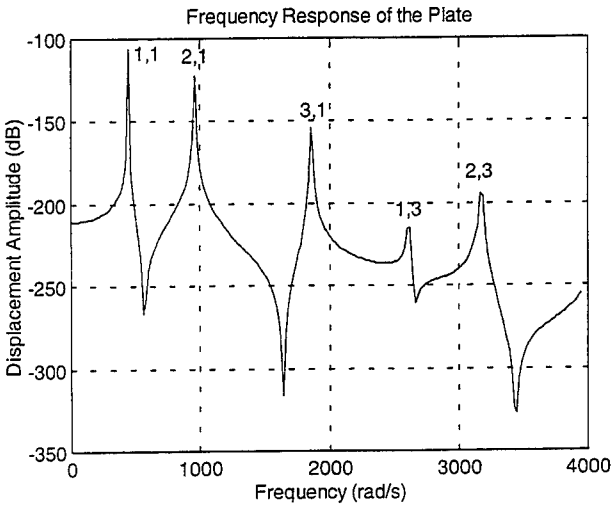

Figure 5. Frequency response of the plate at the centre

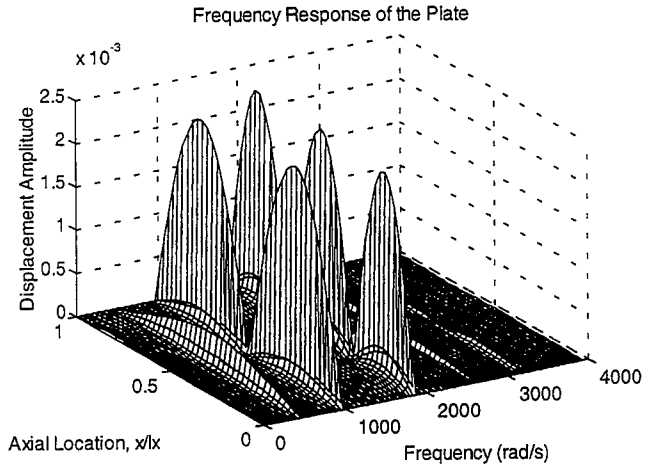

Figure 6. Frequency response of the plate along x-direction

The results show that it is possible to predict the frequency response of a plate when it is excited by a patch of piezoelectric material. Consequently, a sensor model can be also added to the model and a signal proportional to velocity fed back to the piezoelectric patch. As a result, the closed loop frequency response of the plate can be obtained theoretically which is very important for active vibration control studies. This also permits the investigation of the optimal

location of the actuators and the study of control algorithms for the best possible vibration suppression before using any costly experimental equipment.

For this purpose, two patches of piezoelectric (10cm×8cm and 5cm×4cm), whose specifications are listed in table 5, were bonded to the surface of the plate in different locations and then the plate was excited by a point force marked by "D" in the figure 7. In figure 7 the dash lines are showing the nodal lines of a simply supported plate up to mode (3, 3).

Table 5 : Properties of the actuator

t_{pc} (mm)	$E_{pc}(\times 10^{10}\ N/m^2)$	$\rho_{pc}(kg/m^3)$	$d_{31}(\times 10^{-12} m/v)$	ν_{pc}
.2	6.25	7700	-180	.3

An actuator is most effective for control of a particular mode if the sign of the strain due to the modal deflection shape is the same over the entire actuator. Consequently, as can be seen from figure 7, the actuators are placed between the nodal lines and at the points of maximum curvature in order to obtain good damping effect on the modes of interest. Then two accelerometers were located at the center of the location of the actuators, marked by "S" in figure 7, in order to have collocated sensor-actuators. The signals obtained by the accelerometers are integrated and fed back to the actuators separately. Therefore rate feedback was used in this configuration. This leads to the feedback control law

$$V = k\dot{q} \tag{19}$$

where k is an amplification factor or feedback gain. Substituting equation 19 into equation 17 the closed-loop state-space representation of the system can then be obtained as

$$\begin{bmatrix} \dot{x}_1 \\ \dot{x}_2 \end{bmatrix} = \begin{bmatrix} 0 & I \\ -M^{-1}K & -M^{-1}(C - kP) \end{bmatrix} \begin{bmatrix} x_1 \\ x_2 \end{bmatrix}$$
$$[q] = [I \quad 0] \begin{bmatrix} x_1 \\ x_2 \end{bmatrix}. \tag{20}$$

Then the effects of the actuators on vibration suppression were investigated. At first, only the actuator near to the center of the plate was used to suppress the vibration. The effect of this is shown in figure 8. As can be seen, damping in some modes are improved and some modes are untouched.

The second actuator was added to the model to see its effect on modes of vibration.

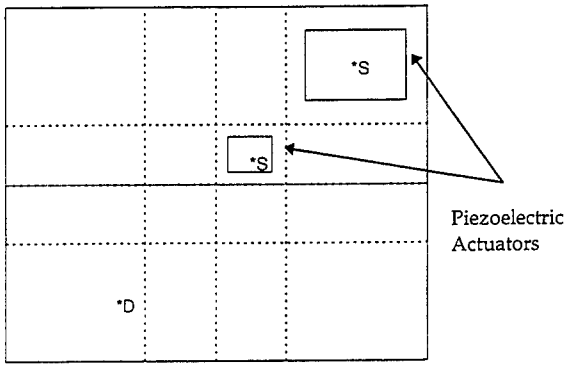

Figure 7. Plate with Bonded Piezoelectric Actuators

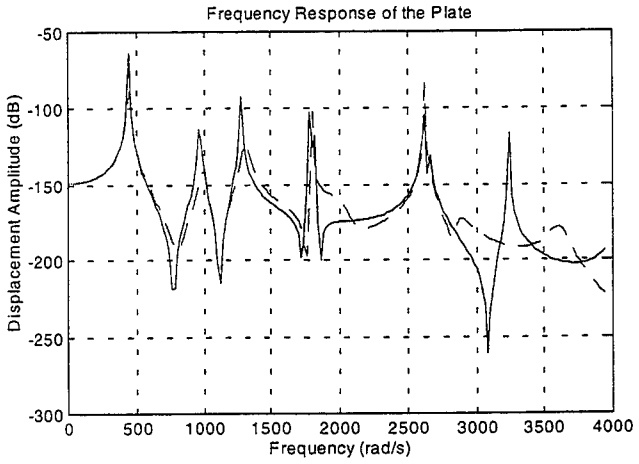

Figure 8. Open and Closed loop Frequency Response of the plate
solid line : open loop, dash line : closed loop

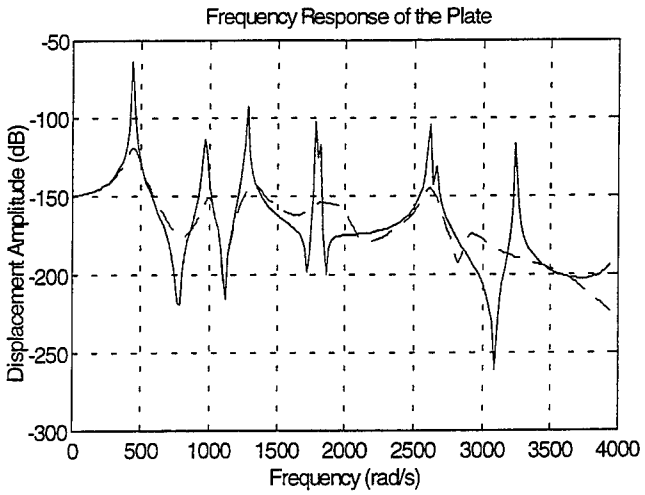

Figure 9. Open and Closed Loop Frequency Response of The Plate
solid line : open loop, dash line : closed loop

The open and closed loop frequency response of the plate when excited by the point force and controlled by two actuators is shown in figure 9. As can be seen, significant vibration suppression was obtained in both lower and higher modes. Also, it shows that the place of actuators was successfully chosen. This analysis showed that obtaining reasonable but not necessarily optimal placement of actuators in structures is very important in order to obtain a high level of damping in the modes of interest. Obviously, bonding more than one piezoelectric actuator in suitable locations helps to successfully suppress vibration of the plate.

Conclusions

A model of an active structure is fundamental to the design of control strategies. It can be used to analyse the system and investigate optimal control strategies without using costly experimental equipment.

A Rayleigh-Ritz model has been developed to analyse the behaviour of a thin plate excited by a patch of piezoelectric material. The model has been used for a simply supported plate. It has been shown that the model can predict natural frequencies of the plate alone very accurately. The obtained mode shapes also correspond to the actual mode shapes. The frequency response of the plate can be obtained to show the suitability of the model for control design studies. This study allowed the behaviour of the system in open and closed loop form for active vibration control purposes to be investigated. Two piezoelectric actuators were used to investigate their effectiveness on vibration

suppression of the plate. The analysis showed that the location of two actuators was very important to increase the level of damping in both lower and higher frequency modes. The future work will be to extend the model to analyse a plate with more than two patches of piezoelectric material with optimal configuration, obtained by controllability theory, and independent controller for vibration suppression, and experimental verification of the theoretical analysis.

References

1. Crawley, E. F. and de Luis, J., Use of Piezoelectric Actuators as Elements of Intelligent Structures, *AIAA Journal*, Vol. 25, No. 10, 1987, p. 1373.
2. Dosch, J., Leo, D. and Inman, D., Modelling and control for Vibration Suppression of a Flexible Active structure, *AIAA Journal of Guidance, Control and Dynamics*, Vol. 18, No. 2, 1995, p.340.
3. Bailey, T. and Hubbard J. E. Jr., Distributed Piezoelectric Polymer Active Vibration Control of a Cantilever Beam, *AIAA Journal of Guidance, Control and Dynamics*, Vol. 8, No. 4, 1985, p.605.
4. Dimitriadis, E. K., Fuller, C. R., Rogers C. A., Piezoelectric Actuators for Distributed Vibration Excitation of Thin Plates, *Journal of Vibration and Acoustics*, Vol. 113, No. 1, 1991, p. 100.
5. Azvine, B., Tomlinson, G. R. and Wynne, R. J., Use of Active Constrained Layer Damping for Controlling Resonant, *Journal of Smart Materials and Structures*, No. 4, 1995.
6. Rongong, J. A., Wright, J. R., Wynne, R. J. and Tomlinson, G. R., Modelling of a Hybrid Constrained Layer/Piezoceramic Approach to Active Damping, *Journal of Vibration and Acoustics*, To appear.
7. Sadri, A. M., Wynne, R. J. and Cherry, A. S., Modelling and Control of Active Damping for Vibration Suppression, *UKACC International Conference on Control' 96*, 2-5 September 1996.
8. Bathe, K., *Finite Element Procedures in Engineering Analysis*, Prentice-Hall, Inc., 1982.
9. Blevins, R. D., *Formulas for Natural Frequency and Mode Shapes*, Van Nostrand Reinhold, NY 1979.
10. Thomson, W. T., *Theory of Vibration with Applications*, Prentice-Hall, Inc., 1988.

Active control of sound transmission into a rectangular enclosure using both structural and acoustic actuators

S.M. Kim and M.J. Brennan
ISVR, University of Southampton, Highfield, Southampton, SO17 1BJ, UK

ABSTRACT

This paper presents an analytical investigation into the active control of sound transmission in a 'weakly coupled' structural-acoustic system. The system under consideration is a rectangular enclosure having one flexible plate through which external noise is transmitted. Three active control systems classified by the type of actuators are discussed. They are; i) a single force actuator, ii) a single acoustic piston source, and iii) simultaneous use of both the force actuator *and* the acoustic piston source. For all three control systems the acoustic potential energy inside the enclosure is adopted as the cost function to minimise, and perfect knowledge of the acoustic field is assumed. The results obtained demonstrate that a single point force actuator is effective in controlling well separated plate-controlled modes, whereas, a single acoustic piston source is effective in controlling well separated cavity-controlled modes provided the discrete actuators are properly located. Using the hybrid approach with both structural and acoustic actuators, improved control effects on the plate vibration together with a further reduction in transmitted noise and reduced control effort can be achieved. Because the acoustic behaviour is governed by both plate *and* cavity-controlled modes in a 'weakly coupled' structural-acoustic system, the hybrid approach is desirable in this system.

1. INTRODUCTION

Analytical studies of vibro-acoustic systems have been conducted by many investigators to achieve physical insight so that effective active control systems can be designed. It is well established that a single point force actuator and a single acoustic piston source can be used to control well separated vibration modes in structures and well separated acoustic modes in cavities, respectively, provided that the actuators are positioned to excite these modes[1,2]. Active control is also applied to structural-acoustic coupled systems for example, the control of sound radiation from a plate[3-6] and the sound transmission into a rectangular enclosure[7-8]. Meirovitch and

Thangjitham[6], who discussed the active control of sound radiation from a plate, concluded that more control actuators resulted in better control effects. Pan *et al*[8] used a point force actuator to control sound transmission into an enclosure, and discussed the control mechanism in terms of plate *and* cavity-controlled modes.

This paper is concerned with the active control of sound transmission into a 'weakly coupled' structural-acoustic system using both structural and acoustic actuators. After a general formulation of active control theory for structural-acoustic coupled systems, it is applied to a rectangular enclosure having one flexible plate through which external noise is transmitted. Three active control systems classified by the type of actuators are compared using computer simulations. They are; i) a single force actuator, ii) a single acoustic piston source, and iii) simultaneous use of both the force actuator *and* the acoustic piston source. For all three control systems the acoustic potential energy inside the enclosure is adopted as the cost function to minimise, and perfect knowledge of the acoustic field is assumed. The effects of each system are discussed and compared, and a desirable control system is suggested.

2. THEORY

2.1 Assumptions and co-ordinate systems

Consider an arbitrary shaped enclosure surrounded by a flexible structure and a acoustically rigid wall as shown in **Figure 1.** A plane wave is assumed to be incident on the flexible structure, and wave interference outside the enclosure between the incident and radiated waves by structural vibration is neglected. Three separate sets of co-ordinates systems are used; Co-ordinate **x** is used for the acoustic field in the cavity, co-ordinate **y** is used for the vibration of the structure, and co-ordinate **r** is used for the sound field outside the enclosure. The cavity acoustic field and the flexible structure are governed by the linear Helmholtz equation and the isotropic thin plate theory[9], respectively. The sign of the force distribution function and normal vibration velocity are set to be positive when they direct inward to the cavity so that the structural contribution to acoustic pressure has the same sign as the acoustic source contribution to acoustic pressure.

Weak coupling rather than full coupling is assumed between the structural vibration system and the cavity acoustic system. Thus, the acoustic reaction force on the strucural vibration under structural excitation *and* the structural induced source effect on the cavity acoustic field under acoustic excitation is neglected. This assumption is generally accepted when the enclosure consists of a heavy structure and a big volume cavity. It is also assumed that the coupled response of the system can be described by finites summations of the

uncoupled acoustic and structural modes. The uncoupled modes are the *rigid-walled* acoustic modes of the cavity and the *in vacuo* structural modes of the structure. The acoustic pressure and structural vibration velocity normal to the vibrating surface are chosen to represent the responses of the coupled system.

2.2 Structural-acoustic coupled response

The acoustic potential energy in the cavity is adopted as the cost function for the global sound control, which is given by[2]

$$E_p = \frac{1}{4\rho_o c_o^2}\int_V |p(\mathbf{x},\omega)|^2 dV \tag{1}$$

where, ρ_o and c_o respectively denote the density and the speed of sound in air, and $p(\mathbf{x},\omega)$ is the sound pressure inside the enclosure.

The vibrational kinetic energy of the flexible structure, which will be used to judge the control effect on structural vibration, is given by[1]

$$E_k = \frac{\rho_p h}{2}\int_{S_f} |u(\mathbf{y},\omega)|^2 dS \tag{2}$$

where, ρ_s is the density of the plate material, h is the thickness of the plate.

If the acoustic pressure and the structural vibration are assumed to be described by a summation of N and M modes, respectively, then the acoustic pressure at position $\mathbf{x}$ inside the enclosure and the structural vibration velocity at position $\mathbf{y}$ are given by

$$p(\mathbf{x},\omega) = \sum_{n=1}^{N} \psi_n(\mathbf{x}) a_n(\omega) = \Psi^T \mathbf{a} \tag{3}$$

$$u(\mathbf{y},\omega) = \sum_{m=1}^{M} \phi_m(\mathbf{y}) b_m(\omega) = \Phi^T \mathbf{b} \tag{4}$$

where, the N length column vectors Ψ and $\mathbf{a}$ consist of the array of uncoupled acoustic mode shape functions $\psi_n(\mathbf{x})$ and the complex amplitude of the acoustic pressure modes $a_n(\omega)$ respectively. Likewise the M length column vectors Φ and $\mathbf{b}$ consist of the array of uncoupled vibration mode shape functions $\phi_m(\mathbf{y})$ and the complex amplitude of the vibration velocity modes $b_m(\omega)$ respectively.

The mode shape functions $\psi_n(\mathbf{x})$ and $\phi_m(\mathbf{y})$ satisfy the orthogonal property in each uncoupled system, and can be normalised as follows.

$$V = \int_V \psi_n^2(\mathbf{x})\, dV \tag{5}$$

$$S_f = \int_{S_f} \phi_m^2(\mathbf{y}) dS \tag{6}$$

where, V and S_f are the volume of the enclosure and the area of the flexible structure, respectively. Since mode shape functions are normalised as given by (Eq. 5), the acoustic potential energy can be written as

$$E_p = \frac{V}{4\rho_o c_o^2}\mathbf{a}^{\mathbf{H}}\mathbf{a} \tag{7}$$

Similarly from (Eq. 2) and (Eq. 6), the vibrational kinetic energy can be written as

$$E_k = \frac{\rho_p h S_f}{2}\mathbf{b}^{\mathbf{H}}\mathbf{b} \tag{8}$$

Where superscript **H** denotes the Hermitian transpose.
For the global control of sound transmission, it is required to have knowledge of the complex amplitude of acoustic pressure vector **a** for various excitations.

The complex amplitude of the n-th acoustic mode under structural and acoustic excitation is given by[9,10]

$$a_n(\omega) = \frac{\rho_o c_o^2}{V} A_n(\omega)\left(\int_V \psi_n(\mathbf{x}) s(\mathbf{x},\omega) dV + \int_{S_f} \psi_n(\mathbf{y}) u(\mathbf{y},\omega) dS\right) \tag{9}$$

where, $s(\mathbf{x},\omega)$ denotes the acoustic source strength density function in the cavity volume V, and $u(\mathbf{y},\omega)$ denotes the normal velocity of the surrounding flexible structure on surface S_f. The two integrals inside the brackets represent the nth acoustic modal source strength contributed from $s(\mathbf{x},\omega)$ and $u(\mathbf{y},\omega)$, respectively. The acoustic mode resonance term $A_n(\omega)$ is given by

$$A_n(\omega) = \frac{j\omega}{\omega_n^2 - \omega^2 + j2\zeta_n\omega_n\omega} \tag{10}$$

where ω_n and ζ_n are the natural frequency and damping ratio of the nth acoustic mode, respectively.
Substituting (Eq. 4) into (Eq. 9) and introducing the modal source strength $q_n = \int_V \psi_n(\mathbf{x}) s(\mathbf{x},\omega) dV$, then we get

$$a_n(\omega) = \frac{\rho_o c_o^2}{V} A_n(\omega)\left(q_n(\omega) + \sum_{m=1}^{M} C_{n,m} \cdot b_m(\omega)\right) \tag{11}$$

where, $C_{n,m}$ represents the geometric coupling relationship between the uncoupled structural and acoustic mode shape functions on the surface of the vibrating structure S_f and is given by[11]

$$C_{n,m} = \int_{S_f} \psi_n(\mathbf{y}) \phi_m(\mathbf{y},\omega) dS \tag{12}$$

If we use L independent acoustic control sources, q_n can be written as

$$q_n(\omega) = \sum_{l=1}^{L} \frac{1}{S_{q,l}} \int_V \psi_n(\mathbf{x}_{c,l}) dV q_{c,l}(\omega) = \sum_{l=1}^{L} D_{q,nl} q_{c,l}(\omega) \tag{13}$$

where $D_{q,nl} = \frac{1}{S_{q,l}} \int_V \psi_n(\mathbf{x}_{c,l}) dV$, and the *l-th* control source strength $q_{c,l}(\omega)$ having an area of $S_{q,l}$ is defined at $\mathbf{x}_{c,l}$.

Thus, the complex amplitude of acoustic modal pressure vector **a** can be expressed as

$$\mathbf{a} = \mathbf{Z}_a\left(\mathbf{D}_q\mathbf{q}_c + \mathbf{Cb}\right) \tag{14}$$

where $\mathbf{Z}_a = \frac{\rho_o c_o^2}{V}\mathbf{A}$.

The matrix **A** is a *(N×N)* diagonal matrix in which each *(n,n)* diagonal term consists of A_n, the *(N×M)* matrix **C** is the structural-acoustic mode shape coupling matrix, the *(N×L)* matrix $\mathbf{D_q}$ determines coupling between the L acoustic source locations and the N acoustic modes, the L length vector $\mathbf{q_c}$ is the complex strength vector of acoustic control sources, and **b** is the complex vibrational modal amplitude vector. The *(N×N)* diagonal matrix $\mathbf{Z_a}$ can be defined as *the uncoupled acoustic modal impedance matrix* which determines the relationship between the acoustic source excitation and the resultant acoustic pressure in modal co-ordinates of the uncoupled acoustic system. Generally the impedance matrix is symmetric *but* non-diagonal in physical co-ordinates, however the uncoupled modal impedance matrix is diagonal because of the orthogonal property of uncoupled modes in modal co-ordinates.

Since the flexible structure in **Figure 1** is assumed to be governed by the isotropic thin plate theory, the complex vibrational velocity amplitude of the *m*th mode can be expressed as[10]

$$b_m(\omega) = \frac{1}{\rho_s h S_f} B_m(\omega)\left(\int_{S_f} \phi_m(\mathbf{y})\left(f(\mathbf{y},\omega) + p^{ext}(\mathbf{y},\omega) - p^{\text{int}}(\mathbf{y},\omega)\right)dS\right) \tag{15}$$

where, again ρ_s is the density of the plate material, h is the thickness of the plate, S_f is the area of flexible structure. Inside the integral $f(\mathbf{y},\omega)$, $p^{ext}(\mathbf{y},\omega)$, and $p^{\text{int}}(\mathbf{y},\omega)$ denote the force distribution function, and the exterior and interior sides of acoustic pressure distribution on the surface S_f, respectively. Because of the sign convention used, there is a minus sign in front of $p^{\text{int}}(\mathbf{y},\omega)$. The structural mode resonance term $B_m(\omega)$ can be expressed as

$$B_m(\omega) = \frac{j\omega}{\omega_m^2 - \omega^2 + j2\zeta_m\omega_m\omega} \tag{16}$$

where ω_m and ζ_m are the natural frequency and the damping ratio of *m*-th mode, respectively. Substituting (Eq. 3) into (Eq. 15), then we get

$$b_m(\omega) = \frac{1}{\rho_s h S_f} B_m(\omega)\left(g_{c,m}(\omega) + g_{p,m}(\omega) - \sum_{n=1}^{N} C_{n,m}^T \cdot a_n(\omega)\right) \tag{17}$$

where, $g_{c,m}(\omega) = \int_{S_f} \phi_m(\mathbf{y}) f(\mathbf{y},\omega) dS$, $g_{p,m}(\omega) = \int_{S_f} \phi_m(\mathbf{y}) p^{ext}(\mathbf{y},\omega) dS$,

and $C^T_{n,m} = C_{m,n}$.

If we use K independent point force actuators, the *m-th* mode generalised force due to control forces, $g_{c,m}$, can be written by

$$g_{c,m}(\omega) = \sum_{k=1}^{K} \int_{S_f} \phi_m(\mathbf{y}) \delta(\mathbf{y} - \mathbf{y}_{c,k}) dS f_{c,k}(\omega) = \sum_{k=1}^{K} D_{f,mk} f_{c,k}(\omega) \tag{18}$$

where $D_{f,mk} = \int_{S_f} \phi_m(\mathbf{y}) \delta(\mathbf{y} - \mathbf{y}_{c,k}) dS$, and the *k-th* control point force $f_{c,k}(\omega)$ is located at $\mathbf{y}_{c,k}$.

Thus the modal vibrational amplitude vector $\mathbf{b}$ can be expressed as

$$\mathbf{b} = \mathbf{Y}_s\left(\mathbf{g}_p + \mathbf{D}_f\mathbf{f}_c - \mathbf{C}^T\mathbf{a}\right) \tag{19}$$

where $\mathbf{Y}_s = \dfrac{1}{\rho_s h S_f}\mathbf{B}$.

The matrix $\mathbf{B}$ is a $(M \times M)$ diagonal matrix in which each (m,m) diagonal term consists of B_m, $\mathbf{C}^T$ is the transpose matrix of $\mathbf{C}$, the $(N \times K)$ matrix $\mathbf{D}_f$ determines coupling between the K point force locations and the M structural modes, $\mathbf{g}_p$ is the generalised modal force vector due to the primary plane wave excitation, the K length vector $\mathbf{f}_c$ is the complex vector of structural control point forces, and $\mathbf{a}$ is the complex acoustic modal amplitude vector. The $(M \times M)$ diagonal matrix $\mathbf{Y}_s$ can be defined as *the uncoupled structural modal mobility matrix* which determines the relationship between structural excitation and the resultant structural velocity response in modal co-ordinates of the uncoupled structural system. As with the uncoupled acoustic impedance matrix $\mathbf{Z}_a$, note that $\mathbf{Y}_s$ is a diagonal matrix.

From (Eq. 14) and (Eq. 19), we get

$$\mathbf{a} = \left(\mathbf{I} + \mathbf{Z}_a\mathbf{C}\mathbf{Y}_s\mathbf{C}^T\right)^{-1}\mathbf{Z}_a\left(\mathbf{D}_q\mathbf{q}_c + \mathbf{C}\mathbf{Y}_s\mathbf{g}_p + \mathbf{C}\mathbf{Y}_s\mathbf{D}_f\mathbf{f}_c\right) \tag{20}$$

$$\mathbf{b} = \left(\mathbf{I} + \mathbf{Y}_s\mathbf{C}^T\mathbf{Z}_a\mathbf{C}\right)^{-1}\mathbf{Y}_s\left(\mathbf{g}_p + \mathbf{D}_f\mathbf{f}_c - \mathbf{C}^T\mathbf{Z}_a\mathbf{D}_q\mathbf{q}_c\right) \tag{21}$$

Since weakly coupling is assumed i.e. $\mathbf{Z}_a\mathbf{C}\mathbf{Y}_s\mathbf{C}^T \cong \mathbf{0}$ and $\mathbf{Y}_s\mathbf{C}^T\mathbf{Z}_a\mathbf{C} \cong \mathbf{0}$, then we get

$$\mathbf{a} = \mathbf{Z}_a\left(\mathbf{D}_q\mathbf{q}_c + \mathbf{C}\mathbf{Y}_s\mathbf{g}_p + \mathbf{C}\mathbf{Y}_s\mathbf{D}_f\mathbf{f}_c\right) \tag{22}$$

$$\mathbf{b} = \mathbf{Y}_s\left(\mathbf{g}_p + \mathbf{D}_f\mathbf{f}_c - \mathbf{C}^T\mathbf{Z}_a\mathbf{D}_q\mathbf{q}_c\right) \tag{23}$$

Although the formulation developed above covers fully coupled systems, weak coupling is assumed hereafter for the convenience of analysis.

In order to minimise the sound transmission into the cavity, two kinds of actuators are used: a single point force actuator for controlling the structural vibration of the plate and a single rectangular type acoustic piston source for controlling the cavity acoustic pressure. The rectangular piston source is centred at (1.85,0.15,0) with the area of 0.15m by 0.15m. This location was chosen because the sound pressure of each mode in a rectangular cavity is a maximum at the corners, and thus the control source is placed away from the acoustic nodal planes[2]. For a similar reason, the point force actuator is located at ($9/20L_1$, $L_2/2$) on the plate, at which there are no nodal lines within the frequency range of interest. **Table 2** shows the natural frequencies of each uncoupled systems and their geometric mode shape coupling coefficients which are normalised by their maximum value. Some of natural frequencies which are not excited by the given incident angle($\varphi = 0°$) were omitted. The (m_1, m_2) and (n_1, n_2, n_3) indicate the indices of the m-th plate mode and the nth cavity mode, and corresponding the uncoupled natural frequencies of the plate and the cavity are listed. A total 15 structural and 10 acoustic modes were used for the analysis under 300 Hz, and no significant difference was noticed in simulations with more modes.

3.2 Active minimisation of the acoustic potential energy

This section considers an analytical investigation into the active control of the sound transmission into the rectangular enclosure in **Figure 2**. Three active control strategies classified by the type of actuators are considered. They are; i) a single force actuator, ii) a single acoustic piston source, and iii) simultaneous use of both the force actuator *and* the acoustic piston source. Although the formulation developed in this paper is not restricted to a single actuator, each single actuator was used to simplify problems so that the control mechanisms could be understood and effective guidelines for practical implementation could be established.

3.2.1 control using a single force actuator

A point force actuator indicated in **Figure 2** is used as a structural actuator and the optimal control strength of the point force actuator can be calculated using (Eq. 26). **Figure 3(a)** shows the acoustic potential energy of the cavity with and without the control force. To show how this control system affects the vibration of the plate, the vibration kinetic energy of the plate obtained from (Eq. 8) is also plotted in **Figure 3(b).** On each graph, natural frequencies of the plate and the cavity are marked '*' and 'o' at the frequencies, respectively. It can be seen that the acoustic response of uncontrolled state has peaks at both

plate and cavity resonances, and the vibration response of uncontrolled state is governed by the plate resonances only because of 'weak coupling'.
Examining **Figure 3(a,b)** it can be seen that at the 1st, 2nd, 4th, and 5th plate modes corresponding to 52 Hz, 64 Hz, 115 Hz, and 154 Hz, respectively there is a large reduction of the acoustic potential energy. This is because the sound field at these frequencies is governed by the plate vibration modes, and a single structural actuator is able to control the corresponding vibration mode to minimise sound transmission.
The structural actuator reduces sound at cavity-controlled modes as well(especially the 2nd and 3rd cavity modes corresponding respectively to 85 Hz and 170 Hz), however it has to increase plate vibration significantly. It shows that minimisation of the acoustic potential energy does not always bring the reduction of structural vibration, and *vice versa*. Since a cavity-controlled mode is generally well coupled with several structural modes, a single structural actuator is not able to deal with several vibration modes because of '*control spillover*'[4]. This is the reason why a single acoustic piston source used in the next section was introduced. However, it is clear that a single point force actuator is effective in controlling a well separated plate-controlled mode provided the actuator is not located close to the nodal line.

3.2.2 control using a single piston force source

A single acoustic piston source indicated in **Figure 2** is used for controlling the acoustic sound field directly. The optimal control source strength of the acoustic piston source can be determined using (Eq. 26). **Figure 4** shows the acoustic potential energy of the cavity and the vibrational kinetic energy of the plate with and without the control actuators.
Since a plate-controlled mode is generally coupled with several cavity modes, the control effect of the acoustic source is not effective at plate-controlled modes (e.g. 52 Hz, 64 Hz, 115 Hz etc.). Whereas, it is more able to reduce transmitted sound at the cavity-controlled modes (e.g. 0 Hz, 85 Hz, 170 Hz and 189 Hz) than the structural actuator. As can be noticed from (Eq. 22), the external incident wave and force excitation have the same sound transmission mechanism, which is vibrating the plate and transmitting sound through the geometric mode shape coupling matrix **C**. Thus, it can be said that the structural actuator is generally effective in controlling sound transmission. At cavity controlled modes, however, several vibration modes are coupled with an acoustic mode. It means that a single acoustic source is more effective than a single structural actuator since a single actuator is generally able to control only one mode. From the results, it is clear that a single acoustic piston source is effective in controlling well separated cavity-controlled modes. It is interesting that there is not much difference in the vibrational kinetic energy

with and without control state. It means that the acoustic actuator is able to reduce sound field globally without increasing plate vibration.

3.2.3 control using both the piston source and the structural actuator

In this section, a hybrid approach, simultaneous use of both the point force actuator and the acoustic piston source, is applied. The optimal strength of the force actuator and the piston source can be obtained from Eq. (26). **Figure 5** shows the acoustic potential energy of the cavity and the vibrational kinetic energy of the plate with and without the control actuators. Even at the cavity-controlled modes, it can be seen that a large reduction in the acoustic potential energy is achieved without significantly increasing the structural vibration. In general, more control actuators result in better control effects[6]. However, the hybrid approach with both structural and acoustic actuators in the system does not merely mean an increase in the number of actuators. As demonstrated in the last two sections, a single structural actuator is effective in controlling well separated plate-controlled modes and a single acoustic actuator is effective for controlling well separated cavity-controlled modes. Since the acoustic response is governed by both plate-controlled and cavity-controlled modes, the hybrid control approach can be desirable for controlling sound transmission in a 'weakly-coupled' structural acoustic system.
To investigate the control efforts of each control system, the amplitude of the force actuator and the source strength of the piston source are plotted in **Figure 6**. There is a large decrease of the force amplitude at the well separated cavity-controlled modes, e.g. 85 Hz and 170 Hz, by using the both actuators. This trend can also be seen in the case of the piston source strength, especially at the 1st and 2nd structural natural frequency (52 Hz, 64 Hz). By using the hybrid approach, simultaneous use of both actuators, better control effects on the vibration of the plate, the transmission noise reduction and the control efforts of the actuators can be achieved.

4. Conclusion

The active control of the sound transmission into a 'weakly coupled' structural-acoustic system has been considered. The results obtained demonstrates that a single point force actuator is effective in controlling well separated plate-controlled modes, whereas, a single acoustic piston source is effective in controlling well separated cavity-controlled modes.
By using the hybrid approach with both structural and acoustic actuators, improved control effects on the plate vibration, further reduction in sound

transmission, and reduced control efforts of the actuators can be achieved. Since the acoustic behaviour is governed by both plate and cavity resonances, the hybrid control approach can be desirable in controlling sound transmission in a 'weakly coupled' structural-acoustic system.

References

1. C.R. FULLER, S.J. ELLIOTT and P.A. NELSON*Active control of vibration,* Academic Press Limited, 1996
2. P.A. NELSON and S.J. ELLIOTT *Active control of sound,* Academic Press Limited, 1992
3. B.-T. WANG, C.R. FULLER and K. DIMITRIADIS Active control of noise transmission through rectangular plates using multiple piezoelectric or point force actuators *Journal of the Acoustical Society of America,* 1991, **90**(5), 2820-2830.
4. M.E. JOHNSON and S. J. ELLIOTT Active control of sound radiation using volume velocity cancellation, *Journal of the Acoustical Society of America,* 1995, **98**(4), 2174-2186.
5. C.R. FULLER, C.H. HANSEN and S.D. SNYDER Active control of sound radiation from a vibrating rectangular panel by sound sources and vibration inputs: an experimental comparison, *Journal of Sound and Vibration,* 1991, **145**(2), 195-215.
6. L. MEIROVITCH and S. THANGJITHAM Active control of sound radiation pressure, *Trans. of the ASME Journal of Vibration and Acoustics,* 1990, **112**, 237-244.
7. S.D. SNYDER and N. TANAKA On feedforward active control of sound and vibration using vibration error signals, *Journal of the Acoustical Society of America,* 1993, **94**(4), 2181-2193.
8. J. PAN C.H. HANSEN and D. A. BIES Active control of noise transmission through a panel into a cavity : I. analytical study, *Journal of the Acoustical Society of America,* 1990, **87**(5), 2098-2108.
9. P.M. MORSE and K.U. INGARD *Theoretical Acoustics,* McGraw-Hill, 1968
10. E.H. DOWELL, G.F. GORMAN III, and D.A. SMITH Acoustoelasticity : general theory, acoustic modes and forced response to sinusoidal excitation, including comparisons with experiment, *Journal of Sound and Vibration,* 1977, **52**(4), 519-542.
11. F. FAHY *Sound and Structural Vibration, Radiation, Transmission and Response,* Academic Press Limited, 1985

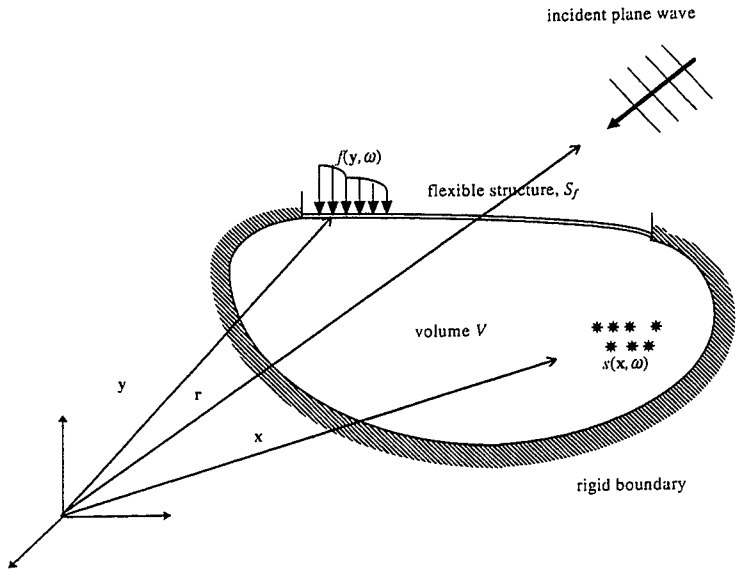

Figure 1 A structural acoustic coupled system with the volume V and its flexible boundary surface S_f.

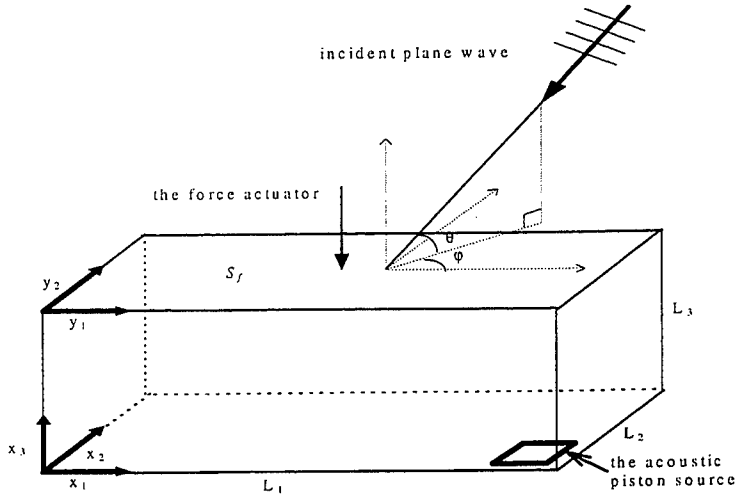

Figure 2 The rectangular enclosure with one simply supported plate on the surface S_f on which external plane wave is incident with the angles of ($\varphi = 0°$) and ($\theta=45°$).

Table 1 Material properties

Material	Density (kg/m^3)	Phase speed (m/s)	Young's modulus (N/m^2)	Poisson's ratio (v)	Damping ratio (ζ)
Air	1.21	340	-	-	0.01
Steel	7870	-	207×10^9	0.292	0.01

Table 2 The natural frequencies and geometric mode shape coupling coefficients of each uncoupled system

Order		Plate	1	2	3	4	5	7	10
	Type		(1,1)	(2,1)	(3,1)	(4,1)	(5,1)	(6,1)	(7,1)
Cavity		Freq.	52 Hz	64 Hz	86 Hz	115 Hz	154 Hz	200 Hz	256 Hz
1	(0,0,0)	0 Hz	0.71	0	0.24	0	0.14	0	0.10
2	(1,0,0)	85 Hz	0	0.67	0	0.27	0	0.17	0
3	(2,0,0)	170 Hz	-0.33	0	0.60	0	0.24	0	0.16
4	(0,0,1)	189 Hz	-1.00	0	-0.33	0	-0.20	0	-0.14
5	(1,0,1)	207 Hz	0	-0.94	0	-0.38	0	-0.24	0
6	(2,0,1)	254 Hz	0.47	0	-0.85	0	-0.34	0	-0.22
7	(3,0,0)	255 Hz	0	-0.40	0	0.57	0	0.22	0

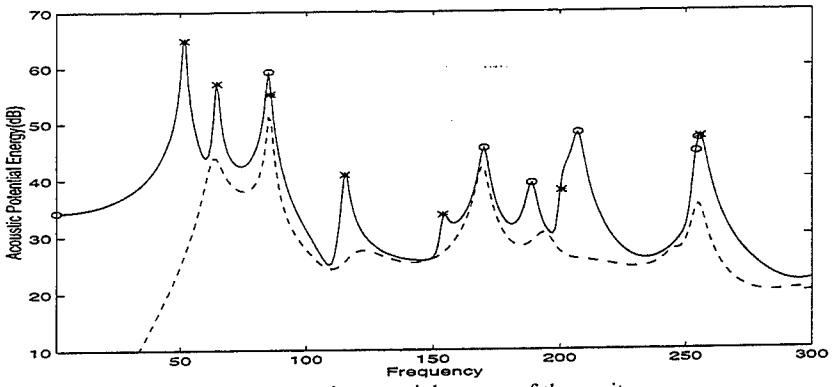

(a) the acoustic potential energy of the cavity

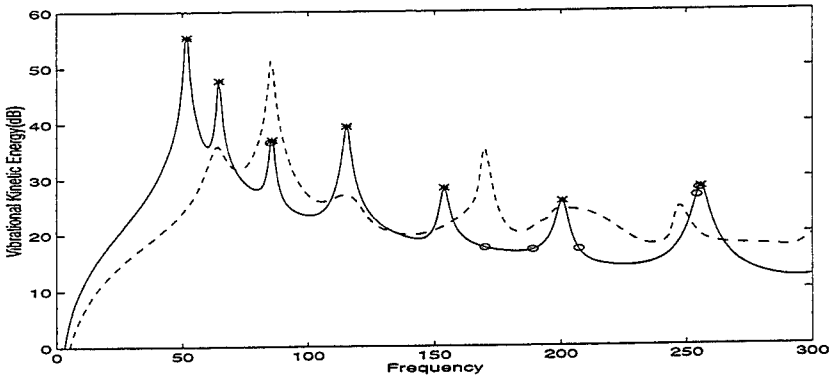

(b) the vibrational kinetic energy of the plate(dB ref.=10^{-9} J)

Figure 3 Effects of minimising the acoustic potential energy using a point force actuator (solid line : without control, dashed line : with control), where '*' and 'o' are at uncoupled plate and cavity natural frequencies, respectively.

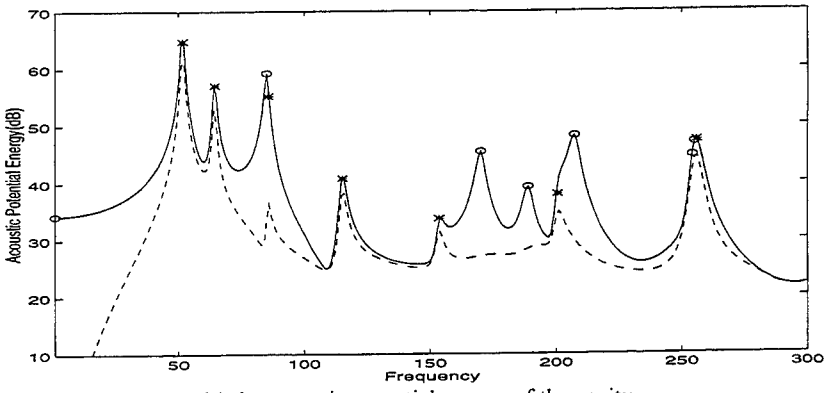

(a) the acoustic potential energy of the cavity

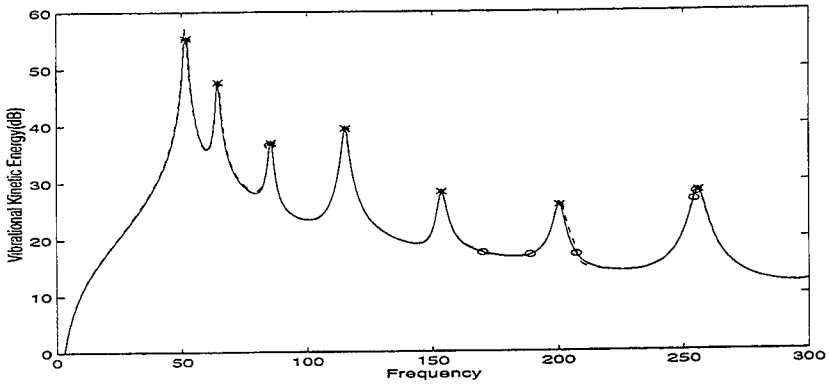

(b) the vibrational kinetic energy of the plate(dB ref.=10^{-9} J)

Figure 4 Effects of minimising the acoustic potential energy using an acoustic piston source (solid line : without control, dashed line : with control), where '*' and 'o' are at uncoupled plate and cavity natural frequencies, respectively.

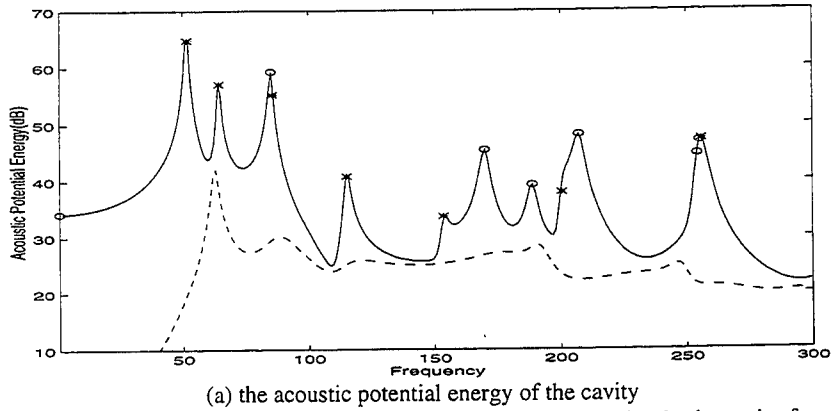

(a) the acoustic potential energy of the cavity

Figure 5 Effects of minimising the acoustic potential energy using both a point force actuator and an acoustic piston source - continued

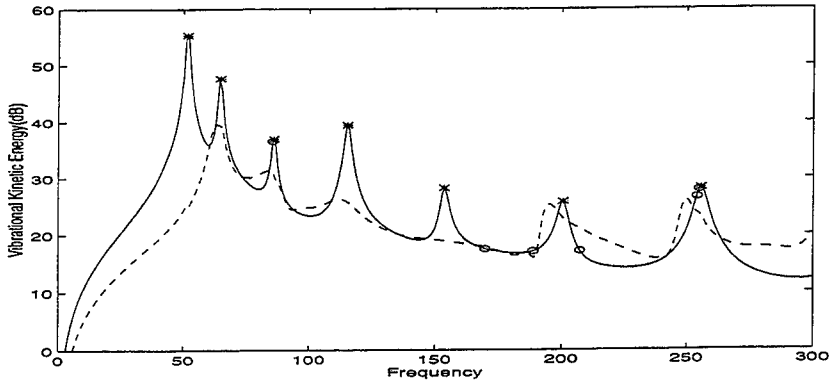

(b) the vibrational kinetic energy of the plate(dB ref.=10^{-9} J)

Figure 5 Effects of minimising the acoustic potential energy using both a point force actuator and an acoustic piston source (solid line : without control, dashed line: with control), where '*' and 'o' are at uncoupled plate and cavity natural frequencies, respectively.

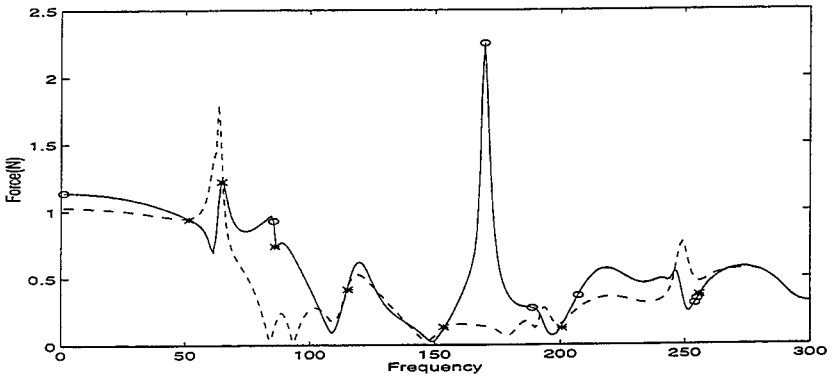

(a) the strength of the force actuator

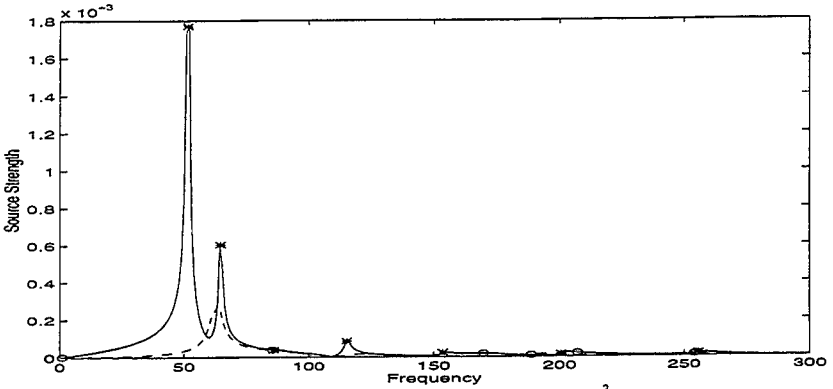

(b) the strength of the piston source(unit: m^3/sec)

Figure 6 Comparison of control efforts of the three control strategies; using each actuator separately (solid line) and using both the force actuator and the piston source (dashed line) , where '*' and 'o' are at uncoupled plate and cavity natural frequencies, respectively.

A DISTRIBUTED ACTUATOR FOR THE ACTIVE CONTROL OF SOUND TRANSMISSION THROUGH A PARTITION

T.J. Sutton, M.E. Johnson and S.J. Elliott

Institute of Sound and Vibration Research
University of Southampton, Southampton SO17 1BJ

ABSTRACT

The paper considers the problem of active control of sound transmission through a partition using a single distributed actuator. The use of shaped, distributed actuators rather than point sources or locally-acting piezoceramic elements offers the possibility of controlling the volume velocity of a plate without giving rise to control spillover and avoids an increase in the sound radiated by uncontrolled structural modes. Specifically, a form of distributed piezoelectric actuator is described in which the electrode takes the form of a set of quadratic strips and serves to apply a roughly uniform normal force over its surface.

INTRODUCTION

The strong piezoelectric properties of the polymer polyvinylidene fluoride (PVDF) were discovered in 1969 [1]. The material is lightweight, flexible, inexpensive and can be integrated into engineering structures for strain sensing and to apply distributed forces and moments for the active control of vibration and sound transmission. Such 'smart' materials offer the possibility of providing lightweight sound-insulating barriers for application to aircraft, ground-based transport and in buildings.

Lee [2] has set out the underlying theory of active laminated structures in which one or more layers of flexible piezoelectric material are attached to a plate. Practical sensors using PVDF material have been implemented by Clark and Fuller [3], Johnson and Elliott [4-6], and others. In these cases thin PVDF films were attached to the structure to sense integrated strain over a defined area. In [4] for example a distributed sensor was developed whose output is proportional to the integrated volume velocity over the surface of a plate.

A number of studies have been carried out in which distributed piezoelectric *actuators* form a layer of a laminated system. In [7] the shape of a distributed piezoelectric actuator was chosen to be orthogonal to all but one of the natural modeshapes of the cylindrical shell system under control. Using this approach a set of actuators could be matched to the modes of the system under control, avoiding control spillover (*i.e.* the excitation of uncontrolled structural modes).

In the present paper a single shaped PVDF actuator is applied to a thin plate to control the noise transmission through it. The shape of the actuator is chosen specifically to apply an approximately uniform force to the plate. Such an actuator can be used to cancel the total volume velocity of the plate and therefore substantially to reduce the radiated sound power. (If volume velocity is measured at the plate surface there is no requirement for a remote error microphone.) As noted by Johnson and Elliott [6], the sound power radiated by a plate which is small compared with an acoustic wavelength depends mainly on the volume velocity of the plate. The simulations in [6] show that provided the plate is no larger than half an acoustic wavelength, a single actuator used to cancel volume velocity will achieve similar results to a strategy in which radiated power is minimised. It is possible to envisage a large partition made up of a number of active plate elements designed on this basis.

CALCULATION OF NORMAL FORCES IN THE PLATE

In this section the equation of motion of the plate and attached PVDF layers is set out. The film thickness is assumed to be 0.5 mm. The analysis broadly follows that of Dimitriadis, Fuller and Rogers [8], but the individual piezoelectric coefficients d_{31} and d_{32} are included separately as is appropriate for PVDF and a sensitivity function is included to account for variations in electrode shape. In addition the bending stiffness of the piezoelectric film is included (it is not negligible as the whole plate is covered). The nomenclature matches that used by Fuller, Elliott and Nelson [9] but here the analysis leads to the inhomogeneous wave equation for the plate-actuator system.

We consider an aluminium plate of thickness $2h_b$ as shown in Figure 1. The plate is covered on its upper and lower surfaces with a piezoelectric film of sensitivity $\phi(x,y)d_{ip}$ in which d_{ip} is the strain/electric field matrix of the material (3x6 array) and $\phi(x,y)$ is a spatially-varying sensitivity function ($0 \le \phi(x,y) \le 1$). The two piezoelectric films are assumed to be identical but the same drive voltage is applied with opposite polarity to the lower film. As a result of this antisymmetric arrangement, the plate is subject to pure bending with no straining of the plate midplane.

In line with other similar calculations [2,9] it is assumed that any line perpendicular to the midplane before deformation will remain perpendicular to it when the plate/PVDF assembly is deformed. As a result, the strain at any point in the assembly is proportional to distance z through it. (z=0 is defined to be on the midplane of the plate as indicated in Figure 1.) The direct and shear strains throughout the whole assembly (ε_x, ε_y, ε_{xy}) are then given by [10]:

$$\varepsilon_x = -z\frac{\partial^2 w}{\partial x^2}$$
$$\varepsilon_y = -z\frac{\partial^2 w}{\partial y^2} \qquad (1\text{-}3)$$
$$\varepsilon_{xy} = -2z\frac{\partial^2 w}{\partial x \partial y}$$

in which w is the displacement of the midplane in the z direction.

The corresponding stresses in the plate (only) follow from Hooke's law as in the standard development for thin plates:

$$\sigma_x^p = \frac{E_p}{1-\nu_p^2}(\varepsilon_x + \nu_p \varepsilon_y)$$
$$\sigma_y^p = \frac{E_p}{1-\nu_p^2}(\varepsilon_y + \nu_p \varepsilon_x) \qquad (4\text{-}6)$$
$$\sigma_{xy}^p = \frac{E_p}{2(1+\nu_p)}\varepsilon_{xy}$$

in which E_p is the Young's modulus and ν_p is Poisson's ratio for the plate material. Stress in the piezoelectric film follows from the constitutive equations for the material [2]. The direct and shear stresses for the upper piezo film are designated $\sigma_x^{pe(1)}, \sigma_y^{pe(1)}$ and $\sigma_{xy}^{pe(1)}$ respectively:

$$\begin{bmatrix} \sigma_x^{pe(1)} \\ \sigma_y^{pe(1)} \\ \sigma_{xy}^{pe(1)} \end{bmatrix} = \mathbf{C} \left\{ \begin{bmatrix} \varepsilon_x \\ \varepsilon_y \\ \varepsilon_{xy} \end{bmatrix} - \phi(x,y) \begin{bmatrix} d_{31} \\ d_{32} \\ d_{36} \end{bmatrix} \frac{V_3}{h_a} \right\} \qquad (7)$$

in which V_3 is the voltage applied across the actuator film (thickness h_a) and d_{31}, d_{32} and d_{36} are the strain/field coefficients for the material. For PVDF d_{36} = 0, but it is included in the analysis for completeness. As in [2], the stiffness matrix **C** is given by:

$$\mathbf{C} = \begin{bmatrix} \dfrac{E_{pe}}{1-\nu_{pe}^2} & \dfrac{\nu_{pe}E_{pe}}{1-\nu_{pe}^2} & 0 \\ \dfrac{\nu_{pe}E_{pe}}{1-\nu_{pe}^2} & \dfrac{E_{pe}}{1-\nu_{pe}^2} & 0 \\ 0 & 0 & \dfrac{E_{pe}}{2(1+\nu_{pe})} \end{bmatrix} \tag{8}$$

The stresses in the lower piezoelectric layer are designated $\sigma_x^{pe(2)}, \sigma_y^{pe(2)}$ and $\sigma_{xy}^{pe(2)}$, and the form of the expression is similar to the upper layer except that the voltage is applied with reversed polarity:

$$\begin{bmatrix} \sigma_x^{pe(2)} \\ \sigma_y^{pe(2)} \\ \sigma_{xy}^{pe(2)} \end{bmatrix} = \mathbf{C} \left\{ \begin{bmatrix} \varepsilon_x \\ \varepsilon_y \\ \varepsilon_{xy} \end{bmatrix} + \phi(x,y) \begin{bmatrix} d_{31} \\ d_{32} \\ d_{36} \end{bmatrix} \frac{V_3}{h_a} \right\} \tag{9}$$

Summing moments about the x and y axes for a small element $\delta x \delta y$ of the plate yields the moment per unit length M_x about the y-axis and M_y about the x-axis; also the corresponding twisting moments per unit length, M_{yx} and M_{xy}.

$$M_x = \int_{-h_b}^{h_b} \sigma_x^p z dz + \int_{-h_b-h_a}^{-h_b} \sigma_x^{pe(2)} z dz + \int_{h_b}^{h_b+h_a} \sigma_x^{pe(1)} z dz \tag{10}$$

$$M_y = \int_{-h_b}^{h_b} \sigma_y^p z dz + \int_{-h_b-h_a}^{-h_b} \sigma_y^{pe(2)} z dz + \int_{h_b}^{h_b+h_a} \sigma_y^{pe(1)} z dz \tag{11}$$

$$M_{xy} = \int_{-h_b}^{h_b} \sigma_{xy}^p z dz + \int_{-h_b-h_a}^{-h_b} \sigma_{xy}^{pe(2)} z dz + \int_{h_b}^{h_b+h_a} \sigma_{xy}^{pe(1)} z dz \tag{12}$$

and $M_{yx} = M_{xy}$.

The vertical acceleration at each point of the plate $\partial^2 w / \partial t^2$ is obtained by taking moments about the x and y axes for a small element $\delta x \delta y$ and resolving vertical forces as in standard thin plate theory. If the plate is acted on by some external force per unit area $p(x,y)f(t)$ then the vertical motion of the plate is described by:

$$\frac{\partial^2 M_x}{\partial x^2} + 2\frac{\partial^2 M_{xy}}{\partial x \partial y} + \frac{\partial^2 M_y}{\partial y^2} - m\frac{\partial^2 w}{\partial t^2} = -p(x,y)f(t) \tag{13}$$

in which m is the mass/area of the plate-film assembly.

The equation of motion of the plate complete with attached piezoelectric film is obtained by combining the above equations. For convenience the following constants are defined:

$$D_p = \frac{2E_p h_b^3}{3(1-\nu_p^2)} \qquad \text{(bending stiffness of plate, thickness } 2h_b\text{)} \quad (14)$$

$$D_{pe} = \frac{2E_{pe}(h_a^3 + 3h_a h_b^2 + 3h_a^2 h_b)}{3(1-\nu_{pe}^2)} \qquad \text{(bending stiffness due to PVDF)} \quad (15)$$

$$C_{pe} = \frac{E_{pe}(h_a + 2h_b)}{1-\nu_{pe}^2} \qquad (16)$$

The equation of motion of the plate assembly including upper and lower piezoelectric layers is then given by:

$$(D_p + D_{pe})\left\{\frac{\partial^4 w}{\partial x^4} + 2\frac{\partial^4 w}{\partial x^2 \partial y^2} + \frac{\partial^4 w}{\partial y^4}\right\} + m\frac{\partial^2 w}{\partial t^2} = p(x,y)f(t) -$$

$$C_{pe}V_3\left\{(d_{31} + \nu_{pe}d_{32})\frac{\partial^2 \phi(x,y)}{\partial x^2} + (d_{32} + \nu_{pe}d_{31})\frac{\partial^2 \phi(x,y)}{\partial y^2} + d_{36}(1-\nu_{pe})\frac{\partial^2 \phi(x,y)}{\partial x \partial y}\right\} \quad (17)$$

The left-hand side of this equation determines the free response of the plate-film assembly and is recognised as the standard form for a thin plate. The first term on the right-hand side is the assumed externally applied normal force per unit area. The second term on the right-hand side gives the effective normal force per unit area applied to the plate due to the two piezoelectric films driven by a voltage V_3 . It is clear that this force depends on the spatially-varying sensitivity which has been assumed for the piezoelectric material.

An examination of Eqns. (16) and (17) shows that the normal force applied by the piezoelectric film depends on the sum of the plate thickness and the thickness of one of the film layers. If the film is much thinner than the plate ($h_a << h_b$) then the applied force becomes *independent of the film thickness* and depends only on the *plate* thickness, the applied voltage, the electrode pattern and the material constants. Eqn. (17) also shows that the normal force is applied locally at all points on the plate. No integration is involved, and so in contrast with a volume velocity sensor designed using quadratic strips [5], the force does not depend on the plate boundary conditions in any way. Furthermore, there is no need to use two films oriented at 90 degrees to cancel

the cross-sensitivity d_{32}. It is also worth noting that no assumption has been made about the modeshapes on the plate.

We can create a *uniform force* actuator by choosing:

$$\frac{\partial^2 \phi(x,y)}{\partial x^2} = \text{constant, and} \tag{18}$$

$$\frac{\partial^2 \phi(x,y)}{\partial y^2} = 0 \tag{19}$$

This can approximately be achieved by depositing electrodes in the form of narrow strips whose width varies quadratically in the x-direction. (Note that the x-direction is defined as the direction of rolling of the PVDF material, *i.e.* the direction of d_{31} for maximum sensitivity.) The form of the electrodes is as shown in Figure 2. With this pattern the sensitivity function takes the form:

$$\phi(x,y) = \frac{4}{L_x^2}(L_x x - x^2) \tag{20}$$

where L_x is the length of the strip. Thus $\phi(x,y) = 0$ at $x = 0$ and $x = L_x$ (no electrode), while $\phi(x,y) = 1$ halfway along at $x = L_x/2$ (electrode fully covers the film).

APPLICATION TO A THIN ALUMINIUM PLATE

If a plane wave of sound pressure level 94 dB (say) is normally incident on a hard surface, it will exert a pressure of 2 Pa rms on that surface. If this incident pressure is counterbalanced by a uniform force actuator applied to a plate, then the plate could in principle be brought to rest. Thus for active control of everyday noise levels the uniform force actuator will need to be able to generate a normal force/area of a few pascal over the surface of the plate. (When the incident wave impinges on the plate at an oblique angle, many natural modes of the plate will be excited and it will not be possible to bring it perfectly to rest with a single actuator; however it will remain possible to cancel the plate volume velocity as explained earlier.)

By way of example an aluminium plate of thickness 1 mm will be assumed, with a free surface measuring 300 x 400 mm. Attached to each side is a PVDF film of thickness 0.5 mm. One electrode of each panel would be masked to give quadratic strips of length 300 mm as shown in Figure 2. (The width of the strips is unimportant, but should be significantly smaller than the structural wavelength of modes of interest on the plate.) In this case it turns out that

$D_p = 6.64$ for the plate, and

D_{pe} = 1.27 for the PVDF film.

The piezoelectric constants for the film are typically

d_{31} = 23 x 10^{-12} m/V and
d_{32} = 3 x 10^{-12} m/V, giving
C_{pe} = 3.28 x 10^{6}

Finally the double derivative of the sensitivity function turns out to be

$$\frac{\partial^2 \phi}{\partial x^2} = 88.9 \qquad \text{(300 mm strip length)}$$

The bending stiffness of the 1 mm aluminium plate is increased by 20% due to the addition of two layers of PVDF film of thickness 0.5 mm each. The force per unit area due to the actuator is obtained from Eqn. (17):

$$\text{force/area} = C_{pe}(d_{31} + \nu_{pe} d_{32}) \frac{\partial^2 \phi}{\partial x^2} V_3$$

$$= 6.96 \times 10^{-3}\ V_3 \qquad \text{Pa}$$

Thus 1000 volt rms would yield a uniform force/area of close to 7 Pa. This is not an impracticable voltage level, but previous experience at ISVR suggests that care would need to be taken to avoid electrical breakdown through the air between electrodes, or over damp surfaces.

ACTIVE CONTROL OF SOUND TRANSMISSION

In reference [6] Johnson and Elliott have presented simulations of the active control of harmonic sound transmitted through a plate using a uniform force actuator. Their actuator might be realised along the lines described in this paper. In the simulations presented in [6] the uniform force actuator is used with a matched volume velocity sensor having the same electrode shape [4]. The advantage of this configuration is that the actuator can be used to drive the net volume velocity of the plate to zero without exciting high order structural modes in the process (control spillover). Simulations of a 300x380x1 mm aluminium plate showed that reductions in transmitted sound power of around 10 dB were achievable in principle up to 600 Hz using this matched actuator-sensor arrangement.

A further advantage of the distributed matched actuator-sensor pair is that the secondary path through the plate (for active control) is minimum phase [6], giving good stability characteristics if a feedback control loop is implemented to control random incident sound for which no reference signal is available.

CONCLUSION

A design of distributed piezoelectric actuator has been presented which generates a roughly uniform force over the surface of a plate. An example calculation shows that the design is capable of controlling realistic sound pressure levels. When used in combination with a matched volume velocity sensor, the actuator-sensor pair will have minimum-phase characteristics and will offer the possiblity of feedback control in which neither a reference signal nor a remote error sensor will be required.

ACKNOWLEDGEMENT

The financial support of the European Community under the Framework IV programme is gratefully acknowledged. (Project reference: BRPR-CT96-0154)

REFERENCES

[1] G.M. Sessler (1981) *J Acoust Soc Am* **70**(6) Dec 1981 1596-1608 Piezoelectricity in polyvinylidene fluoride
[2] C.K. Lee (1990) *J Acoust Soc Am* **87**(3) Mar 1990 1144-1158 Theory of laminated piezoelectric plates for the design of distributed sensors/actuators. Part I: Governing equations and reciprocal relationships
[3] R.L. Clark and C.R. Fuller (1992) *J Acoust Soc Am* **91**(6) June 1992 3321-3329 Modal sensing of efficient acoustic radiators with polyvinylidene fluoride distributed sensors in active structural acoustic control approaches
[4] M.E. Johnson, S.J. Elliott and J.A. Rex (1993) *ISVR Technical Memorandum 723*. Volume Velocity Sensors for Active Control of Acoustic Radiation
[5] M.E. Johnson and S.J. Elliott (1995) *Proceedings of the Conference on Smart Structures and Materials* 27 Feb-3 Mar 1995, San Diego, Calif. SPIE Vol 2443. Experiments on the active control of sound radiation using a volume velocity sensor
[6] M.E. Johnson and S.J. Elliott (1995) *J Acoust Soc Am* **98**(4) Oct 1995 2174-2186. Active control of sound radiation using volume velocity cancellation
[7] H.S. Tzou, J.P. Zhong and J.J. Hollkamp (1994) *Journal of Sound and Vibration* **177**(3) 363-378 Spatially distributed orthogonal piezoelectric shell actuators: theory and applications
[8] E.K. Dimitriadis, C.R. Fuller and C.A. Rogers (1991) *Transactions of the ASME, Journal of Vibration and Acoustics* **113** 100-107 Piezoelectric actuators for distributed vibration excitation of thin plates
[9] C.R. Fuller, S.J. Elliott and P.A. Nelson (1996) Active Control of Vibration. Academic Press, London.
[10] G.B. Warburton (1976) *The Dynamical Behaviour of Structures*, 2nd Edition. Pergamon Press, Oxford.

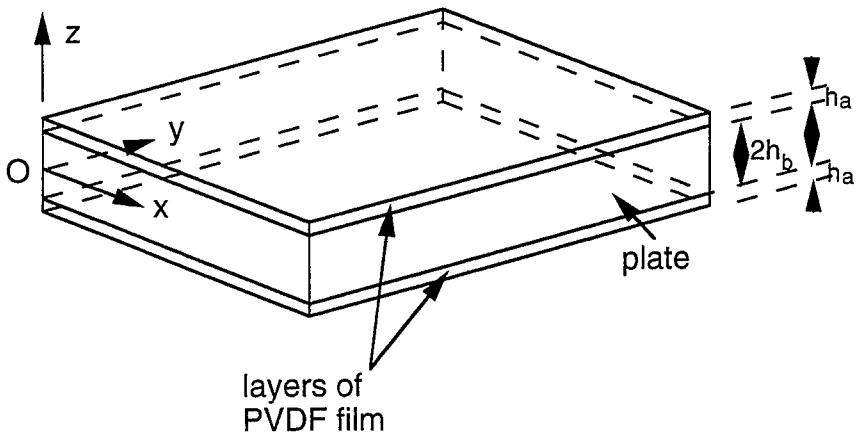

Figure 1: Schematic diagram of thin plate covered on both sides with a layer of PVDF film

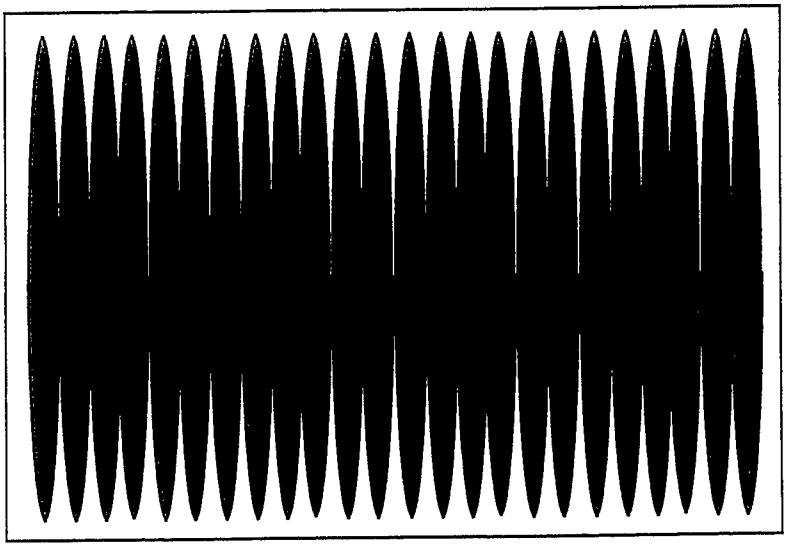

Figure 2: Electrode pattern of quadratic strips for uniform-force actuator

CONTROL OF SOUND RADIATION FROM A FLUID-LOADED PLATE USING ACTIVE CONSTRAINING LAYER DAMPING

J. Ro, A. Al-Ali and A. Baz

Mechanical Engineering Department
The Catholic University of America
Washington D. C. 20064

Abstract

Sound radiation from a vibrating flat plate, with one side subjected to fluid-loading, is controlled using patches of Active Constrained Layer Damping (ACLD). The fluid-structure-controller interaction is modeled using the finite element method. The damping characteristics of the ACLD/plate/fluid system are determined and compared with the damping characteristics of plate/fluid system controlled with conventional Active Control (AC) and/or Passive Constrained Layer Damping (PCLD) treatments. Such comparisons are essential in quantifying the individual contribution of the active and passive damping components to the overall damping characteristics, when each operates separately and when both are combined to interact in unison as in the ACLD treatments.

I. INTRODUCTION

When a structure is in contact with or immersed in a fluid, its vibration energy radiates into the fluid domain. As a result, there is an observable increase in the kinetic energy of the structure due to the fluid loading. Because of this kinetic energy increase, the natural frequencies of structures which are subjected to fluid-loading decrease significantly compared to the natural frequencies of structures in vacuo. Therefore, through understanding of the interaction between the elastic plate structures and the fluid loading has been essential to the effective design of complex structures like ships and submarine hulls. Lindholm *et al.* [1] used a chordwise hydrodynamic strip theory approach to study the added mass factor for cantilever rectangular plates vibrating in still water. Fu *et al.* [2] studied the dry and wet dynamic characteristics of vertical and horizontal cantilever square plates immersed in fluid using linear hydroelasticity theory. Ettouney *et al.* [3] studied the dynamics of submerged structures using expansion vectors, called wet modes which are finite series of complex eigenvectors of the fluid-structure system. Recently Kwak [4] presented an approximate formula to estimate the natural frequencies in water from the natural frequencies in vacuo.

When the structure and the fluid domains become rather complex, solutions of fluid-structure coupled system can be obtained by finite element

methods. Marcus [5], Chowdhury [6], Muthuveerappan *et al.* [7] and Rao *et al.* [8] have successfully implemented the finite element method to predict the dynamic characteristics of elastic plates in water. Everstine [9] used both finite and boundary element methods to calculate the added mass matrices of fully-coupled fluid-structure systems.

The above investigations formed the bases necessary to devising passive and active means for controlling the vibration of as well as the sound radiation from fluid-loaded plates. Passive Constrained Layer Damping (PCLD) treatments have been used extensively and have proven to be effective in suppressing structural vibration as reported, for example, by Jones and Salerno [10], Sandman [11] and Dubbelday [12]. Recently, Gu and Fuller [13] used feed-forward control algorithm which relied in its operation on point forces to actively control the sound radiation from a simply-supported rectangular fluid-loaded plate.

In the present study, the new class of Active Constrained Layer Damping (ACLD) treatment is utilized as a viable alternative to the conventional PCLD treatment and Active Constrained (AC) with PCLD treatment (AC/PCLD). The ACLD treatment proposed combines the attractive attributes of both active and passive damping in order to provide high energy dissipation-to-weight characteristics as compared to the PCLD treatment. Such surface treatment has been successfully employed to control the vibration of various structural members as reported, for example, by Shen [14] and Baz and Ro [15]. In this paper, the use of the ACLD is extended to the control of sound radiation from fluid-loaded plates. Finite element modeling of the dynamics and sound radiation of fluid-loaded plates is developed and validated experimentally. Particular focus is placed on demonstrating the effectiveness of the ACLD treatment in suppressing the structural vibration and attenuating the sound radiation as compared to conventional PCLD and AC/PCLD.

This paper is organized in five sections. In Section 1, a brief introduction is given. In Section 2., the concepts of the PCLD, ACLD and AC/PCLD treatments are presented. In Section 3, the dynamical and fluid finite element models are developed to describe the interaction between the plate, ACLD and the contacting fluid. Experimental validation of the models are given in Section 4. Comparisons between the theoretical and experimental performance are also presented in Section 4 for different active and passive damping treatments. Section 5, summarizes the conclusions of the present study.

2. CONCEPTS OF PCLD, ACLD AND AC/PCLD TREATMENTS

Figures (1-a), (1-b) and (1-c) show schematic drawings of the PCLD, ACLD and AC/PCLD treatments respectively. In Figure (1-a), the plate is treated

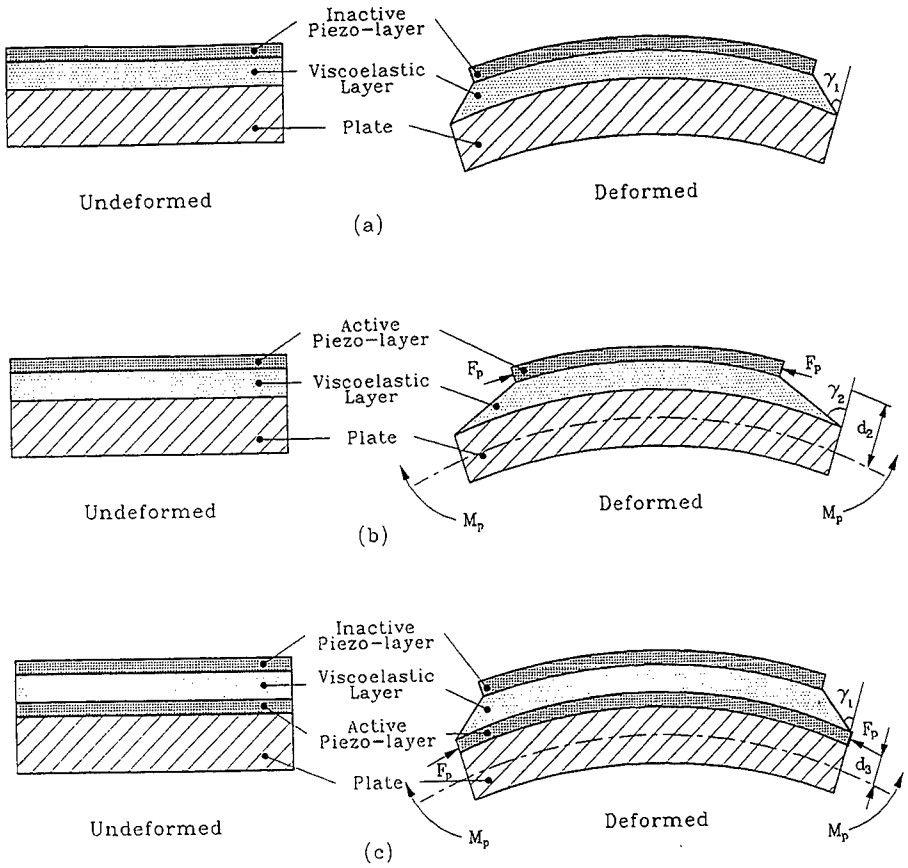

Figure (1) - Schematic drawing of different surface treatments (a) PCLD, (b) ACLD and (c) AC/PCLD.

with a viscoelastic layer which is bonded directly to the plate. The outer surface of the viscoelastic layer is constrained by an inactive piezo-electric layer in order to generate shear strain γ_1 which results in dissipation of the vibrational energy of the plate. Activating the constraining layer electrically, generates a control force F_p by virtue of the piezo-electric effect as shown in Figure (1-b) for the ACLD treatment . Such control action increases the shear strain to γ_2 which in turn enhances the energy dissipation characteristics of the treatment. Also, a restoring moment $M_p=d_2F_p$ is developed which attempts bring the plate back to its undeformed position. In the case of AC/PCLD treatment, shown in Figure (1-c), two piezo-films are used. One film is active and is bonded directly to the plate to control its vibration by generating active control (AC) force F_p and moment $M_p=d_3F_p$. The other film is inactive and used to restrain the motion of the

viscoelastic layer in a manner similar to the PCLD treatment of Figure (1-a). In this way, the AC action operates separately from the PCLD action. This is unlike the ACLD configuration where the active and passive control actions operate in unison. Note that in the ACLD configuration, larger shear strains are obtained hence larger energy dissipation is achieved. Furthermore, larger restoring moments are generated in the ACLD treatments as compared to the AC/PCLD treatments as the moment arm d_2 in the former case is larger than the moment arm d_3 of the latter case. This results in effective damping of the structural vibrations and consequently effective attenuation of sound radiation can be obtained.

3. FINITE ELEMENT MODELING

3.1 Overview

A finite element model is presented in this section, to describe the behavior of fluid-loaded thin plates which are treated with ACLD, PCLD and AC/PCLD treatments.

3.2 Finite Element Model of Treated Plates

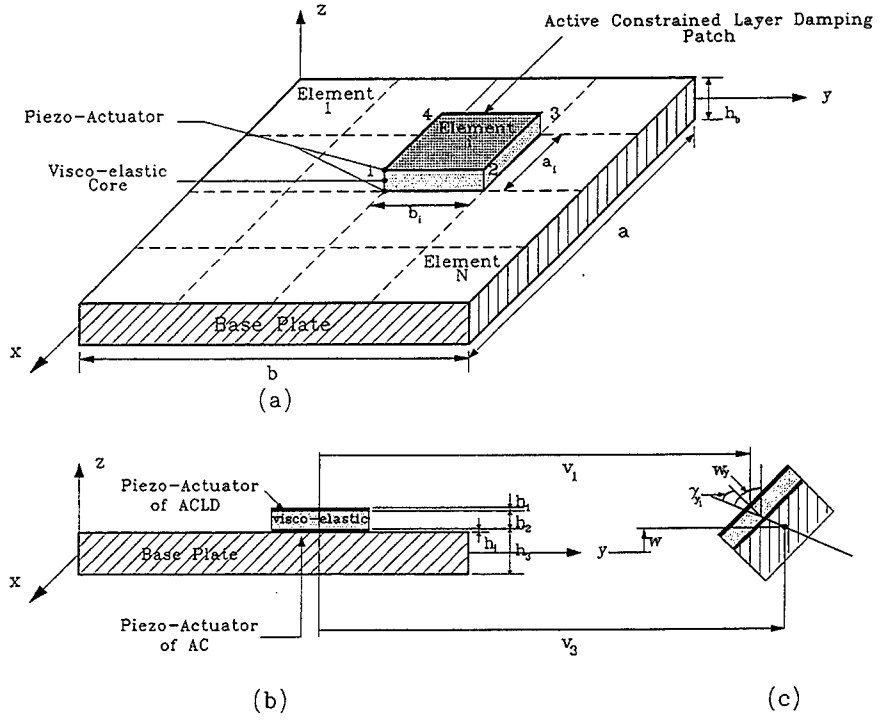

Figure (2) - Schematic drawing of plate with ACLD/AC/PCLD patches.

Figure (2) shows a schematic drawing of the ACLD and AC/PCLD treatments of the sandwiched plate which is divided into N finite elements. It is assumed that the shear strains in the piezo-electric layers and in the base plate are negligible. The transverse displacement w of all points on any cross section of the sandwiched plate are considered to be the same. The damping layers are assumed to be linearly viscoelastic with their constitutive equations described by the complex shear modulus approach such that $G=G^*(1+\eta i)$. In addition, the bottom piezo-electric layer (AC) and the base plate are considered to be perfectly bonded together and so are the viscoelastic layer and the top piezo-electric layer.

The treated plate elements considered are two-dimensional elements bounded by four nodal points. Each node has seven degrees of freedom to describe the longitudinal displacements u_1 and v_1 of the constraining layer, u_3 and v_3 of the base plate, the transverse displacement w and the slopes $w_{,x}$ and $w_{,y}$ of the deflection line. The deflection vector $\{\delta\}$ can be written as:

$$\begin{aligned}\{\delta\} &= \{u_1, v_1, u_3, v_3, w, w_{,x}, w_{,y}\}^T \\ &= \left[\{N_1\} \ \{N_2\} \ \{N_3\} \ \{N_4\} \ \{N_5\} \ \{N_5\}_{,x} \ \{N_5\}_{,y}\right]^T \{\delta^e\}\end{aligned} \tag{1}$$

where $\{\delta^e\}$ is the nodal deflection vector, $\{N_1\}$, $\{N_2\}$, $\{N_3\}$, $\{N_4\}$, $\{N_5\}$, $\{N_5\}_{,x}$, and $\{N_5\}_{,y}$ are the spatial interpolating vectors corresponding to u_1, v_1, u_3, v_3, w, $w_{,x}$, and $w_{,y}$ respectively. Subscripts ,x and ,y denote spatial derivatives with respect to x and y.

Consider the following energy functional Π_p for the treated plate/fluid system:

$$\Pi_p = \int_V \left(U - T_K + W_e - W_p + W_c\right) dV, \tag{2}$$

where U is the strain energy, T_K is the kinetic energy, W_e is work done by external forces, W_p is work done by the back pressure inside the fluid domain, W_c is work done by the control forces and moments and V is the volume of the plate. These energies are expressed as follows

$$\int_V U dV = \sum_{i=1}^{3} \frac{E_i h_i}{2(1-\nu_i^2)} \int_0^a \int_0^b \left[\left(\frac{\partial u_i}{\partial x}\right)^2 + 2\nu_i \left(\frac{\partial u_i}{\partial x}\right)\left(\frac{\partial v_i}{\partial y}\right) + \left(\frac{\partial v_i}{\partial y}\right)^2 + \frac{1-\nu_i}{2}\left(\frac{\partial u_i}{\partial y} + \frac{\partial v_i}{\partial x}\right)^2 \right] dxdy$$

$$+ \sum_{i=1}^{3} \frac{E_i h_i^3}{24(1-\nu_i^2)} \int_0^a \int_0^b \left[\left(\frac{\partial^2 w}{\partial x^2}\right)^2 + 2\nu_i \left(\frac{\partial^2 w}{\partial x^2}\right)\left(\frac{\partial^2 w}{\partial y^2}\right) + \left(\frac{\partial^2 w}{\partial y^2}\right)^2 + 2(1-\nu_i)\left(\frac{\partial^2 w}{\partial x \partial y}\right)^2 \right] dxdy$$

$$+\frac{G_2 h_2}{2}\int_0^a\int_0^b\left(\gamma_{x_2}^2+\gamma_{y_2}^2\right)dxdy \qquad =\frac{1}{2}\{\delta^e\}^T[K_p]\{\delta^e\}, \tag{3}$$

$$\int_V T_k dV=\sum_{i=1}^{3}\frac{\rho_i h_i}{2}\int_0^a\int_0^b\left(\dot{w}^2+\dot{u}_i^{\,2}+\dot{v}_i^{\,2}\right)dxdy=\frac{1}{2}\{\dot{\delta}^e\}^T[M_p]\{\dot{\delta}^e\}, \tag{4}$$

$$\int_V W_e dV=\frac{1}{2}\{\delta^e\}^T\{F\}, \tag{5}$$

$$\int_V W_e dV=\frac{E_i h_i}{2(1-\nu_i^2)}\int_0^a\int_0^b\left[\left(\frac{d_{31}}{h_i}+\frac{d_{32}}{h_i}\nu_i\right)V_a\frac{\partial u_i}{\partial x}+\left(\frac{d_{31}}{h_i}\nu_i+\frac{d_{32}}{h_i}\right)V_a\frac{\partial v_i}{\partial y}\right]dxdy$$

$$+\frac{E_i h_i^3}{24(1-\nu_i^2)}\int_0^a\int_0^b\left[\left(\frac{d_{31}}{h_i}+\frac{d_{32}}{h_i}\nu_i\right)V_a\frac{\partial^2 w}{\partial x^2}+\left(\frac{d_{31}}{h_i}\nu_i+\frac{d_{32}}{h_i}\right)V_a\frac{\partial^2 w}{\partial y^2}\right]dxdy$$

$$=\{\delta^e\}^T[K_c]\{\delta^e\} \qquad \text{where i=1 for ACLD control or i=3 for AC control} \tag{6}$$

and $$\int_V W_p dV=\{\delta^e\}^T[\Omega]\{p^e\}. \tag{7}$$

where $\{p^e\}$ is the nodal pressure vector of the fluid element. In the above equation $[K_p]$, $[M_p]$, $\{F\}$, $[K_c]$ and $[\Omega]$ are the plate stiffness matrix, mass matrix, external forces vector, piezo-electric forces and moments matrix and plate/fluid coupling matrix as given in the appendix. In equation (6), $d_{31,32}$ are the piezo-strain constants in directions 1 and 2 due to voltage V_a applied in direction 3. The voltage V_a is generated by feeding back the derivative of the displacement δ at critical nodes such that $V_a=-K_d C\{\dot{\delta}^e\}$ where K_d is the derivative feedback gain matrix and C is the measurement matrix defining the location of sensors.

Minimizing the plate energy functional using classical variational methods such that $\{\partial\Pi_p/\partial\{\delta^e\}\}=0$ leads to the following finite element equation:

$$([K]-\omega^2[M_p])\{\delta^e\}-[\Omega]\{p^e\}=\{F\} \tag{8}$$

where ω is the frequency and $[K]=[K_p]+[K_c]$ is overall stiffness matrix.

3.3 Finite Element Model of the Fluid

The fluid model uses solid rectangular tri-linear elements to calculate the sound pressure distribution inside the fluid domain and the associated structural coupling effects. The fluid domain is divided into N_a fluid elements. Each of

these elements has eight nodes with one degree of freedom per node. The pressure vector is expressed by $p = [N_f]\{p^e\}$ and $[N_f]$ is pressure shape function and $\{p^e\}$ is nodal pressure vector.

Considering the following functional Π_f of fluid domain Craggs [16]

$$\Pi_f = \frac{1}{2}\{p^e\}^T[K_f]\{p^e\} - \frac{1}{2}\omega^2\{p^e\}^T[M_f]\{p^e\} - \omega^2\{p^e\}^T[\Omega]^T\{\delta^e\}, \tag{9}$$

where $[K_f]$ and $[M_f]$ are the fluid stiffness and mass matrices as given in the appendix. Minimization of equation (9) such that $\{\partial\Pi_f/\partial\{p^e\}\} = 0$ yields the fluid dynamics as coupled with the structural vibration:

$$([K_f] - \omega^2[M_f])\{p^e\} - \omega^2[\Omega]^T\{\delta^e\} = \{0\} \tag{10}$$

The boundary conditions involved are of the form

$\partial p / \partial n = 0$, at a rigid boundary

$\partial p / \partial n = -\rho_f \partial^2\delta / \partial t^2$, at a vibrating boundary

and $p = 0$. at a free surface

where ρ_f is fluid density.

3.4. Solutions of the Coupled Plate/Fluid System

Combining equations (8) and (10) gives

$$\begin{bmatrix} [K] - \omega^2[M_p] & -[\Omega] \\ -\omega^2[\Omega]^T & [K_f] - \omega^2[M_f] \end{bmatrix} \begin{bmatrix} \delta^e \\ p^e \end{bmatrix} = \begin{bmatrix} F \\ 0 \end{bmatrix} \tag{11}$$

At low frequencies, the fluid pressure is in phase with the structural acceleration, i.e. the fluid appears to the structure like an added mass. However, as the frequency increases the added mass effect diminishes and the damping effect, i.e. the pressure proportional to velocity, increases. For an incompressible fluid, the speed of sound c approaches ∞, thus the mass matrix of the fluid $[M_f]$ vanishes, and equation (11) can be simplified to

$$\begin{bmatrix} [K] - \omega^2[M_p] & -[\Omega] \\ -\omega^2[\Omega]^T & [K_f] \end{bmatrix} \begin{bmatrix} \delta^e \\ p^e \end{bmatrix} = \begin{bmatrix} F \\ 0 \end{bmatrix} \tag{12}$$

If the fluid-structure coupled system has free boundary surface, then $[K_f]$ is non-singular [Everstin, 1991] and the nodal pressure vector $\{p^e\}$ can be eliminated from equation (12) as follows:

$$\{p^e\} = -\omega^2[K_f]^{-1}[\Omega]^T\{\delta^e\} \tag{13}$$

Hence, equation (12) yields

$$\left(\left[K\right]-\omega^2\left(\left[M_p\right]+\left[M_a\right]\right)\right)\left\{\delta^e\right\}=\left\{F\right\} \tag{14}$$

where $[M_a]$ is added virtual mass matrix defined by [Muthuveerappan, 1979]

$$\left[M_a\right]=\left[\Omega\right]\left[K_r\right]^{-1}\left[\Omega\right]^T \tag{15}$$

Equation (14) only involves the unknown nodal deflection vector $\{\delta^e\}$ of the structure. When $\{F\}=0$, equation (14) becomes an eigenvalue problem, the solution of which yields the eigenvalues and eigenvectors. The nodal pressures can then be obtained from equation (13) when the nodal displacements are determined for any particular loading on plate.

4. PERFORMANCE OF PARTIALLY TREATED PLATES WITH FLUID LOADING

In this section, comparisons are presented between the numerical predictions and experimental results of the natural frequencies and damping ratios of a fluid-loaded plate treated with ACLD, PCLD and AC/PCLD. The effect of the Active Control, Passive Constrained Layer Damping and Active Constrained Layer Damping on the resonant frequency, damping ratio, attenuation of vibration amplitude and sound radiation are investigated experimentally. The vibration and sound radiation attenuation characteristics of the fluid-structure coupled system are determined when the plate is excited acoustically with broadband frequency excitation while the piezo-electric layers are controlled with various control gains. The experimental results are compared with the theoretical predictions.

4.1 Experimental Set-up

Figures (3-a) and (3-b) show a schematic drawing and finite element mesh of the experimental set-up along with the boundary conditions used to describe the fluid-structure system. The finite element mesh includes: 24 plate-elements and 560 fluid-elements. The coupled system has a total of 815 active degree of freedoms. The aluminum base plate is 0.3m long, 0.2m wide and 0.4mm thick mounted with all its edges in a clamped arrangement in a large aluminum base. The aluminum base with mounting frame sits on top of a water tank. One side of the base plate is partially treated with the ACLD/AC/PCLD and the other side is in contact with water. The material properties and thickness of piezo-electric material and the viscoelastic layer listed in Table (1). The size of the combined piezo-electric and viscoelastic patch occupied one-third of the surface area of the base plate and it is placed in the middle of plate as shown in Figure (3-b). A laser

sensor is used to measure the vibration of the treated plate at node 27 as shown in Figure (3-b). The sensor signal is sent to a spectrum analyzer to determine the frequency content and the amplitude of vibration. The signal is also sent via analog power amplifiers to the piezo-electric layers to actively control the sound radiation and structural vibration. The radiated sound pressure level into the tank is monitored by a hydrophone located at 5.0 cm below the plate center. This position is chosen to measure the plate mode (1, 1) which dominates the sound radiation. The hydrophone signal is sent also to the spectrum analyzer to determine its frequency content and the associated sound pressure levels.

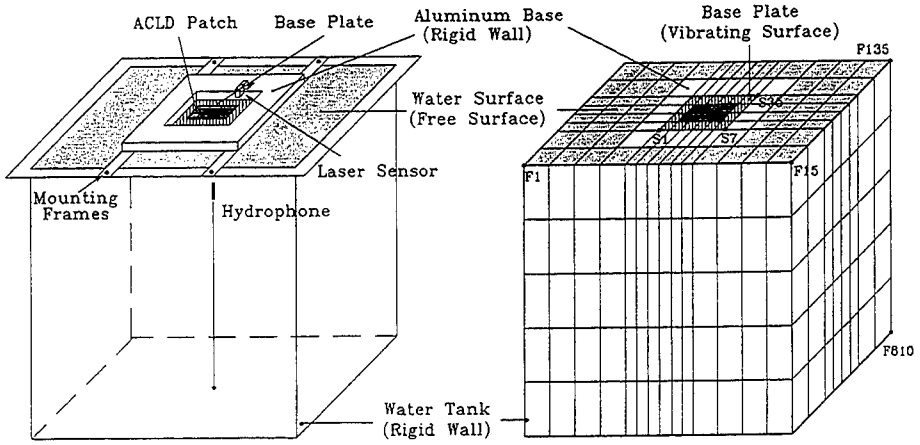

Figure (3) - The experimental set-up, (a) schematic drawing, (b) finite element meshes.

Table (1) - Physical and geometrical properties of the ACLD treatment

Layer	Thickness(m)	Density(Kg/m^3)	Modulus(MPa)
viscoelastic	5.08×10^{-4}	1104	30**
piezoelectric	28×10^{-6}	1780	2500*

* Young's modulus ** Shear modulus

4.2 Experimental Results

Experimental validation of the dynamic finite element model of the ACLD/plate system in air has been presented by Baz and Ro [15] in detail. Close agreement was obtained between the theoretical predictions and the experimental

measurements. The dynamic finite element model is therefore valid to provide accurate predictions.

For the uncontrolled treated plate/fluid system, considered in this study, the experimental results indicate that coupling the plate with the fluid loading results in decreasing the first mode of vibration from 59.475Hz to 10.52Hz. The coupled finite element model predicts the first mode of vibration to decrease from 57.91Hz to 10.24Hz. The results obtained indicate close agreement between the theory and experiments.

Figure (4-a) shows a plot of the normalized experimental vibration amplitudes for the fluid-loaded plate with the ACLD treatment using different derivative feedback control gains. According to Figure (4-a), the experimental results obtained by using the ACLD treatment indicate that amplitude attenuations of 11.36%, 48.25% and 75.69% are obtained, for control gains of 2500, 5000, and 13500, respectively. The reported attenuations are normalized with respect to the amplitude of vibration of uncontrolled plate, i.e. the plate with PCLD treatment. Figures (4-b) display the vibration amplitudes of the plate/fluid system with AC/PCLD treatment at different derivative feedback control gains. The corresponding experimental attenuations of the vibration amplitude obtained are 4.6%, 20.29%, 54.04% respectively.

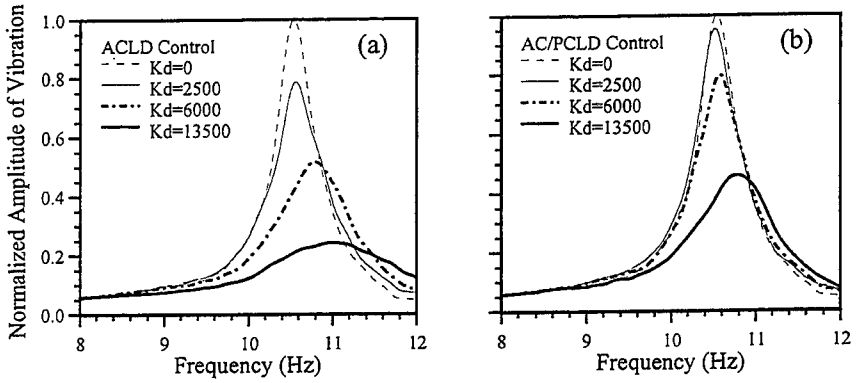

Figure (4) - Effect of control gain on normalized amplitude of vibration of the treated plate. (a) ACLD control and (b) AC/PCLD control.

Figures (5-a) and (5-b) show the associated normalized experimental sound pressure levels (SPL) using ACLD and AC/PCLD controllers, respectively. The normalized experimental SPL attenuations obtained using the ACLD controller are 26.29%, 50.8% and 76.13% compared to 10.02%, 24.52% and 53.49% with the AC/PCLD controller for the considered control gains. Table (2)

lists the maximum control voltages for the ACLD and AC/PCLD controllers for the different control gains.

It is clear that increasing the control gain has resulted in improving the attenuations of the plate vibration and the sound radiation into the fluid domain. It is evident that the ACLD treatment has produced significant vibration and sound pressure level attenuation as compared to the attenuations developed by the AC/PCLD or PCLD treatments. It is also worth emphasizing that the ACLD treatment requires less control energy than the conventional AC/PCLD treatments to control the sound radiation from the plate.

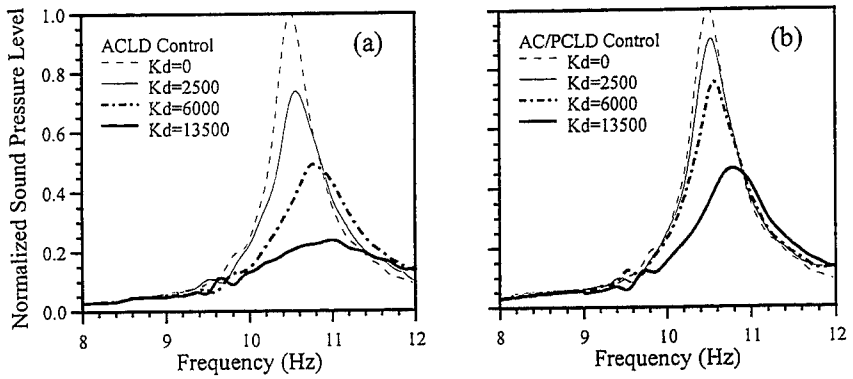

Figure (5) - Effect of control gain on normalized sound pressure level radiated from the treated plate. (a) ACLD control and (b) AC/PCLD control.

Table (2) - Maximum control voltage for the ACLD/AC/plate system

K_d	0(PCLD)	2500	5000	13500
ACLD	0	21.75V	31.20V	39.60V
AC	0	26.50V	50.40V	76.38V

Figure (6) shows the mode shapes of the first four modes of the treated plate with and without fluid-loading as obtained experimentally using STARMODAL package. Figure (7) shows the corresponding theoretical predictions of the first four mode shapes. Close agreement is found between experimental measurement and theoretical predictions.

Figure (8) presents comparisons between the theoretical and experimental natural frequencies and the loss factor of a plate treated with the ACLD and AC/PCLD for different control gains. Close agreement between theory and

experiment is evident. Note also that increasing the control gain has resulted in increasing the damping ratio for both ACLD and AC/PCLD treatments. The comparisons emphasize the effectiveness of the ACLD treatment in acquiring the large damping ratio to attenuate the structural vibration and sound radiation.

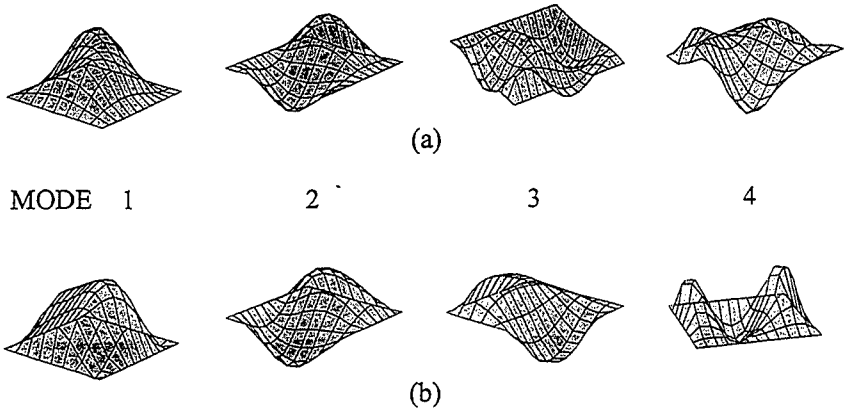

Figure (6) - Experimental results of first four mode shapes of treated plate (a) without fluid loading and (b) with fluid loading.

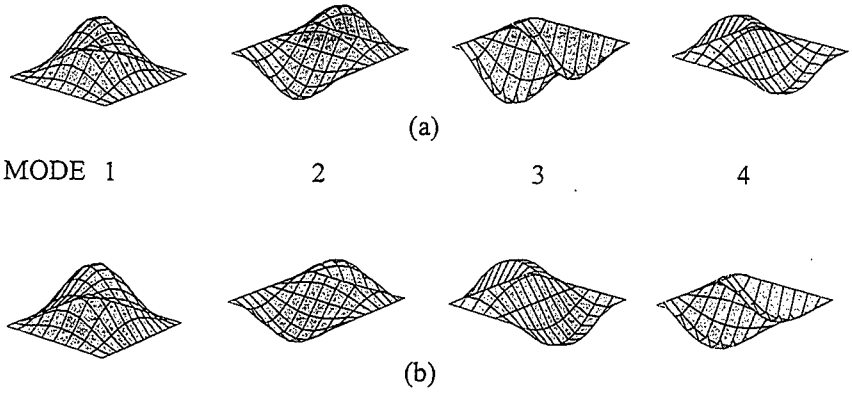

Figure (7) - Theoretical predictions of first four mode shapes of treated plate (a) without fluid loading and (b) with fluid loading.

5. SUMMARY

This paper has presented theoretical and experimental comparisons between the damping characteristics of plates treated with ACLD and

conventional AC with PCLD treatments. The dynamic characteristics of the treated plates when subjected to fluid loading is determined for different derivative control gains. The fundamental issues governing the performance of this class of smart structures have been introduced and modeled using finite element method. The accuracy of the developed finite element model has been validated experimentally. The effectiveness of the ACLD treatment in attenuating structural vibration of the plates as well as the sound radiated from these plates into fluid domain has also been clearly demonstrated. The results obtained indicate that the ACLD treatments have produced significant attenuation of the structural vibration and sound radiation when compared to PCLD and to AC with PCLD. Such favorable characteristics are achieved with control voltages that are much lower than those used with conventional AC systems. The developed theoretical and experimental techniques present invaluable tools for designing and predicting the performance of the plates with different damping treatments and coupled with fluid loading that can be used in many engineering applications.

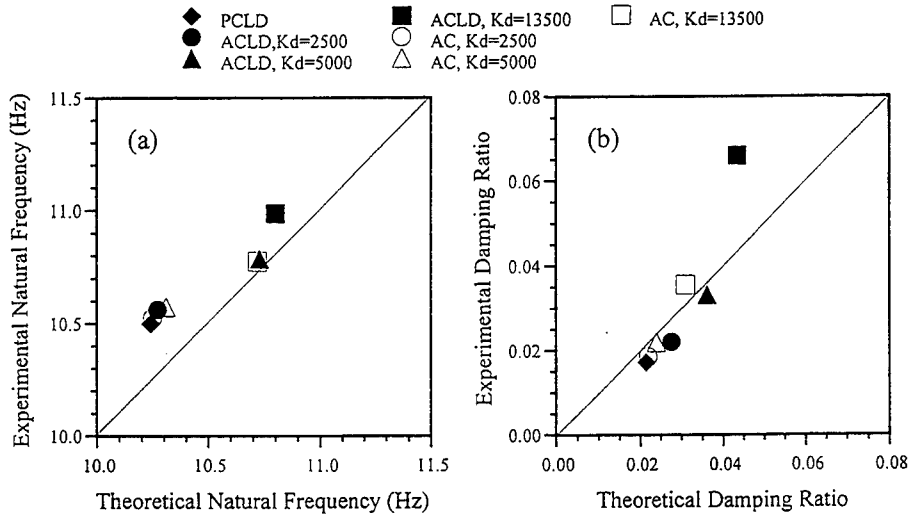

Figure (8) - Comparison between theoretical predictions and experimental results, (a) natural frequency, (b) damping ratio.

ACKNOWLEDGMENTS

This work is funded by The U.S. Army Research Office (Grant number DAAH-04-93-G-0202). Special thanks are due to Dr. Gary Anderson, the technical monitor, for his invaluable technical inputs.

REFERENCES

1. Lindholm U. S., Kana, D. D., Chu, W. H. and Abramson, H. N., Elastic vibration characteristics of cantilever plates in water. *Journal of Ship Research*, 1965, **9**, 11-22.
2. Fu, Y. and Price, W. G., Interactions between a partially or totally immersed vibrating cantilever plate and the surrounding fluid. *Journal of Sound and Vibration*, 1987, **118**(3), 495-513.
3. Ettouney, M. M., Daddazio, R. P. and Dimaggio, F. L., Wet modes of submerged structures - part 1:theory. *Trans. of ASME, Journal of Vibration and Acoustics*, 1992, **114**(4), 433-439.
4. Kwak, M. K., Hydroelastic vibration of rectangular plates. *Trans. of ASME Journal of Applied mechanics*, 1996, **63**(1), 110-115.
5. Marcus, M. S., A finite-element method applied to the vibration of submerged plates. *Journal of Ship Research*, 1978, **22**, 94-99.
6. Chowdury, P. C., Fluid finite elements for added mass calculations. *International Ship Building Progress*, 1972, **19**, 302-309.
7. Muthuveerappan G., Ganesan, N. and Veluswami, M. A., A note on vibration of a cantilever plate immersed in water. *Journal of Sound and Vibration*, 1979, **63**(3), 385-391.
8. Rao, S. N. and Ganesan, N., Vibration of plates immersed in hot fluids. *Computers and structures*, 1985, **21**(4), 777-787.
9. Everstine G. C., Prediction of low frequency vibrational frequencies of submerged structures. *Trans. of ASME, Journal of Vibration and Acoustics*, 1991, **113**(2), 187-191.
10. Jones, I. W. and Salerno, V. L., The vibration of an internally damped sandwich plate radiating into a fluid medium. *Trans. of ASME, Journal of Engineering for Industry*, 1965, 379-384.
11. Sandman B. E., Motion of a three-layered elastic-viscoelastic plate under fluid loading. *J. of Acoustical Society of America*, 1975, **57**(5), 1097-1107.
12. Dubbelday, P. S., Constrained-layer damping analysis for flexural waves in infinite fluid-loaded plates. *Journal of Acoustical Society of America*, 1991, (3), 1475-1487.
13. Gu, Y. and Fuller, C. R., Active control of sound radiation from a fluid-loaded rectangular uniform plate. *Journal of Acoustical Society of America*, 1993, **93**(1), 337-345.
14. Shen, I. Y., Bending vibration control of composite plate structures through intelligent constrained layer treatments. *Proc. of Smart Structures and Materials Conference on Passive Damping* ed. C. Johnson, 1994, Vol. **2193**, 115-122, Orlando, FL.

15. Baz, A. and Ro, J., Vibration control of plates with active constrained layer damping. *Journal of Smart Materials and Structures*, 1996, **5**, 272-280.
16. Craggs, A., The transient response of a coupled plate-acoustic system using plate and acoustic finite elements. *Journal of Sound and Vibration*, 1971, **15**(4), 509-528.

APPENDIX

1. Stiffness Matrix of the Treated Plate Element

The stiffness matrix $[K_p]_i$ of the ith element of the plate/ACLD system is given by Baz and Ro [15]:

$$\left[K_p\right]_i = \left[K_{ip}\right]_i + \left[K_s\right]_i + \left[K_b\right]_i \tag{A-1}$$

where $[K_{ip}]_i$, $[K_s]_i$ and $[K_b]_i$ denote the in-plane, shear and bending stiffnesses of the ith element. These stiffness matrices are given by:

$$\left[K_{ip}\right]_i = h_j \int_{a_i}\int_{b_i}\left[B_{jp}\right]^T\left[D_{jp}\right]\left[B_{jp}\right]dxdy, \quad j = \text{layer 1, 2, and 3} \tag{A-2}$$

$$\left[K_s\right]_i = G_2 h_2 \int_{a_i}\int_{b_i}\left[B_s\right]^T\left[B_s\right]dxdy, \tag{A-3}$$

$$\text{and } \left[K_b\right]_i = \int_{a_i}\int_{b_i}\left[B_b\right]^T\left[D_{jb}\right]\left[B_b\right]dxdy. \qquad j = \text{layer 1, 2 and 3} \tag{A-4}$$

with G_2 denoting the shear modulus of the viscoelastic layer and the matrices $[B_s]$, $[B_b]$, $[B_{jp}]$, $[D_{jp}]$, and $[D_{jb}]$ are given by

$$\left[B_s\right] = \frac{d}{h_2}\begin{bmatrix}\left(\{N_1\}-\{N_3\}\right)/d + \{N_5\}_{,x}\\ \left(\{N_2\}-\{N_4\}\right)/d + \{N_5\}_{,y}\end{bmatrix}, \qquad \left[B_b\right] = \begin{bmatrix}\{N_5\}_{,xx}\\ \{N_5\}_{,yy}\\ 2\{N_5\}_{,xy}\end{bmatrix},$$

$$\left[B_{1p}\right] = \begin{bmatrix}\{N_1\}_{,x}\\ \{N_2\}_{,y}\\ \{N_1\}_{,y}+\{N_2\}_{,x}\end{bmatrix}, \qquad \left[B_{3p}\right] = \begin{bmatrix}\{N_3\}_{,x}\\ \{N_4\}_{,y}\\ \{N_3\}_{,y}+\{N_4\}_{,x}\end{bmatrix},$$

$$\left[B_{2p}\right] = \begin{bmatrix}\{N_1\}_{,x}+\{N_3\}_{,x}+h\{N_5\}_{,xx}\\ \{N_2\}_{,y}+\{N_4\}_{,y}+h\{N_5\}_{,yy}\\ \{N_1\}_{,y}+\{N_3\}_{,y}+h\{N_5\}_{,yx}+\{N_2\}_{,x}+\{N_4\}_{,x}+h\{N_5\}_{,xy}\end{bmatrix},$$

$$\left[D_{jp}\right]=\frac{E_j}{1-\nu_j^2}\begin{bmatrix}1 & \nu_j & 0\\ \nu_j & 1 & 0\\ 0 & 0 & \frac{1-\nu_j}{2}\end{bmatrix} \text{ and } \left[D_{jb}\right]=\frac{E_jI_j}{1-\nu_j^2}\begin{bmatrix}1 & \nu_j & 0\\ \nu_j & 1 & 0\\ 0 & 0 & \frac{1-\nu_j}{2}\end{bmatrix}. \quad j=1, 2 \text{ and } 3 \quad \text{(A-5)}$$

where $h = (h_1-h_3)/2$ and $d = (h_2+h_1/2+D)$ with D denoting the distance from the mid-plane of the plate to the interface with the viscoelastic layer. Also, I_j represent the area moment of inertia of the jth layer.

2. Mass Matrix of the Treated Plate Element

The mass matrix $[M_p]_i$ of the ith element of the plate/ACLD system is given by:

$$\left[M_p\right]_i=\left[M_{ip}\right]_i+\left[M_b\right]_i \quad \text{(A-6)}$$

where $[M_{ip}]_i$ and $[M_b]_i$ denote the mass matrices due to extension and bending of the ith element. These matrices are given by

$$\left[M_{ip}\right]_i=\rho_1h_1\int_{a_i}\int_{b_i}\left(\{N_1\}^T\{N_1\}+\{N_2\}^T\{N_2\}\right)dxdy+\rho_3h_3\int_{a_i}\int_{b_i}\left(\{N_3\}^T\{N_3\}+\{N_4\}^T\{N_4\}\right)dxdy$$
$$+\tfrac{1}{4}\rho_2h_2\int_{a_i}\int_{b_i}\left(\{N_6\}^T\{N_6\}+\{N_7\}^T\{N_7\}\right)dxdy$$

$$\text{and } \left[M_b\right]_i=\left(\rho_1h_1+\rho_2h_2+\rho_3h_3\right)\int_{a_i}\int_{b_i}\left[N_5\right]^T\left[N_5\right]dxdy \quad \text{(A-7)}$$

where $\{N_6\} = \{N_1\}+\{N_3\}+h\{N_5\}_{,x}$ and $\{N_7\} = \{N_2\}+\{N_4\}+h\{N_5\}_{,y}$

3. Control Forces and Moments Generated by the Piezo-electric Layer

3.1 The in-plane piezo-electric forces

The work done by the in-plane piezo-electric forces $\{F_p\}_i$ of the ith element is given by:

$$\tfrac{1}{2}\left\{\delta^e\right\}_i^T\left\{F_p\right\}_i=h_j\int_{a_i}\int_{b_i}\sigma_{jp}\varepsilon_{jp}dxdy \quad \text{(A-8)}$$

where j=1 for ACLD control or j=3 for AC control. Also, σ_{jp} and ε_{jp} are the in-plane stresses and strains induced in the piezo-electric layers. Equation (A-8) reduces to:

$$\begin{Bmatrix} F_{pxk} \\ F_{pyk} \\ F_{pxyk} \end{Bmatrix}_i = V_a \int_{a_i} \int_{b_i} [B_{jp}]^T [D_{jp}] \begin{bmatrix} d_{31} \\ d_{32} \\ 0 \end{bmatrix} dxdy \qquad \text{for k=1, .., 4} \qquad \text{(A-9)}$$

3.2 The piezo-electric moments

The work done by the piezo-electric moments $\{M_p\}_i$ due to the bending of the piezo-electric layer of the ith element is given by:

$$\tfrac{1}{2}\{\delta^e\}_i^T \{M_p\}_i = h_j \int_{a_i} \int_{b_i} \sigma_{jb} \varepsilon_{jb} dxdy \qquad \text{(A-10)}$$

Where σ_{jb} and ε_{jb} are the bending stresses and strains induced in the piezo-electric layers. Equation (A-10) reduces to:

$$\begin{Bmatrix} M_{pxk} \\ M_{pyk} \\ M_{pxyk} \end{Bmatrix}_i = V_a \int_{a_i} \int_{b_i} [B_b]^T [D_{jb}] \begin{bmatrix} d_{31} \\ d_{32} \\ 0 \end{bmatrix} dxdy \qquad \text{for k=1, .., 4} \qquad \text{(A-11)}$$

4. Stiffness and Mass Matrices of the Fluid Element

The stiffness matrix $[K_f]_i$ and mass matrix $[M_f]_i$ of the ith element of the fluid system are given by:

$$[K_f]_i = \frac{1}{\rho_f} \int_{V_i} [B_f]^T [B_f] dv \qquad \text{(A-12)}$$

and $$[M_f]_i = \frac{1}{\rho_f c^2} \int_{V_i} [N_f]^T [N_f] dv \qquad \text{(A-13)}$$

where $[B_f] = [[N_f]_x \quad [N_f]_y \quad [N_f]_z]^T$ and c is the sound speed.

5. Coupling matrix of the Treated Plate/Fluid System

The coupling matrix $[\Omega]$ of the interface element of the structure/fluid system can be presented by:

$$[\Omega] = \int_a \int_b \{N_s\}^T [N_f] dxdy \qquad \text{(A-14)}$$

ANALYTICAL METHODS II

DYNAMIC RESPONSE OF SINGLE-LINK FLEXIBLE MANIPULATORS

E. Manoach[1] G. de Paz[2] K. Kostadinov[1] and F. Montoya[2]

[1] Bulgarian Academy of Sciences, Institute of Mechanics
Acad. G. Bonchev St. Bl. 4; 1113 Sofia, Bulgaria

[2] Universidad de Valladolid, E.T.S.I.I. Dpto. IMEIM.
C/Paseo del Cauce, s/n 47011- Valladolid, Spain

1. INTRODUCTION

The flexible-link manipulators have many advantages over the traditional stiff ones. The requirements for light-weight and energy efficient robotic arms could be naturally satisfied by using flexible manipulators. On the other hand the application of the robotic arm in such activities as positioning in electronic microscopes and disc-drivers, hammering a nail into a board or playing tennis, also forces the modeling and control of the dynamic behavior of flexible link manipulators.

In most cases the elastic vibrations which arise during the motion must be avoided when positioning the end point of a robotic arm. These are a part of the reasons that cause a great increase of the publications in this topic in recent years.

In most papers the flexible robotic arms are modeled as thin linear elastic beams. In [1-3] (and many others) the Bernouli-Euiler beam theory, combined with finite-element technique for discretization with respect to the space variables is used for modeling and control of single-link flexible manipulators. The same beam theory, combined with mode superposition technique is used in [4]. Geometrically nonlinear beam theories are used in [5,6] for the modeling of a single-link and multi-link flexible robotic manipulators, correspondingly.

Taking into account the fact that robotic arms are usually not very thin and that the transverse shear could play an important role for dynamically loaded structures [7] the application of the Bernouli-Euiler beam theory could lead to a discrepancy between the robotic arm behavior and that one described by the model.

The aim of this work is to model the dynamic behavior of a single link flexible robotic arm employing the Timoshenko beam theory, which considers the transverse shear and rotary inertia. The arm is subjected to a dynamic loading. As in [3], the viscous friction is included into the model and slip-stick boundary conditions of the rotating hub are introduced. Besides that, the possibility of the rise of a contact interaction between the robotic arm and the stop (limiting support) is included into the model. The beam stress state is checked for plastic yielding during the whole process of deformation and the plastic strains (if they arise) are taken into account in the model. The numerical results are provided in order to clarify the influence of the different parameters of the model on the response of the robotic arm.

2. BASIC EQUATIONS

2.1. Formulation of the problem

The robotic arm - flexible beam is attached to a rotor that has friction and inertia. The beam is considered to be clamped to a rotating hub and its motion consists of two components: "rigid-body" component and a component describing the elastic deflection of the beam (see Figure 1). The motion of the flexible beam is accomplished in the horizontal plane and gravity is assumed to be negligible.

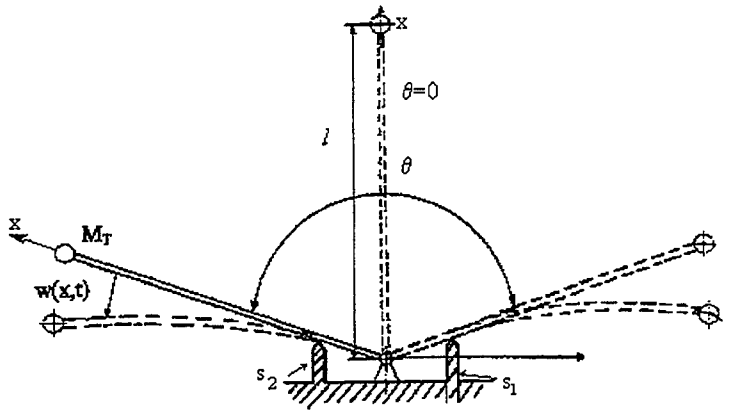

Figure 1. Model of one-link flexible manipulator.

Tip of the beam (with attached tip-mass) is subjected to an impulse loading. Stick-slip boundary conditions due to Coulomb friction of the hub are introduced when describing the motion of the beam. In other words, if the bending moment, about the hub axis, due to the impact is lower than the static friction torque threshold then the hub is considered clamped and the beam elastic motion is considered only. When the bending moment exceeds friction torque threshold this boundary condition is removed, allowing rotation of the hub and the arm. When the hub speed and kinetic energy of the beam become again beneath the torque threshold, the hub clamps again.

The possibility of the rise of a contact interaction between the robotic and the stop is envisaged. In this case, if the hub angle exceeds the limit value, the robotic arm clamps and a part of the beam goes in a contact with the stop, which is modeled as an elastic foundation of a Vinkler type.

In view of the fact that the impact loading and contact interactions are included in the investigations, it is expedient to be considered the rise of plastic strains in the beam.

2.2. Deriving the equations of motion.

The total kinetic and potential energy of the rotating hub with the attached beam (described by the Timoshenko beam theory) and a lumped mass at it's tip can be expressed as follow:

$$E_K = \frac{1}{2}\int_0^l \rho A\left[\dot{u}(x,t)\right]^2 dx + \frac{1}{2} J_H\left[\dot{\theta}(t)\right]^2 + \frac{1}{2} M_T\left[\dot{u}(l,t)\right]^2 + \frac{1}{2}\int_0^l EI\left[\dot{\varphi}(x,t)\right]^2 dx$$

$$E_P = \frac{1}{2}\int_0^l \left[EI\left(\frac{\partial \varphi}{\partial x}\right)^2 + kGA\left(\frac{\partial w}{\partial x} - \varphi\right)^2 \right] dx \qquad (1\ a,b)$$

In these equation u(x,t) is the total displacement

$$u(x,t) = w(x,t) + x\theta(t) \qquad (2)$$

and w is the transverse displacement of the beam, φ is the angular rotation, θ is the hub angle, E is the Young modulus, G is the shear modulus, k is a shear correction factor, ρ is the material density, J_H is the inertia moment of the hub, $A=b*h$ is the beam cross-section area, h is the thickness, b is the width, $I=bh^3/12$, l is the length of the beam, M_T is the tip mass, t is the time.

Denoting the work of external forces (applied actuating torque T(t) and the beam loading p(x,t)) by

$$W=T(t)\theta(t)+\int_0^l p(x,t)w(x,t)dx \tag{3}$$

the Hamilton's principle can be applied:

$$\int_{t_1}^{t_2}\delta(E_k-E_p)dt+\int_{t_1}^{t_2}\delta W dt=0 \tag{4}$$

Substituting eqns (1)-(3) into eqn (4) after integrating and including damping of the beam material, the viscous friction of the hub and the reaction force of the elastic foundation the following equations of motion can be obtained:

$$(J+J_H+M_Tl^2)\frac{d^2\theta}{dt^2}+d_1\frac{d\theta}{dt}+M_Tl\frac{\partial^2 w(l,t)}{dt^2}+\int_0^l \rho Ax\frac{\partial^2 w(x,t)}{dt^2}dx=T(t)$$

$$EI\frac{\partial^2\varphi}{\partial x^2}+kGA\left(\frac{\partial w}{\partial x}-\varphi\right)-d_2\frac{\partial w}{\partial t}-\rho I\frac{\partial^2\varphi}{\partial t^2}=0,\qquad 0<x<l\,,\ t>0 \tag{5a-c}$$

$$kGA\left(\frac{\partial^2 w}{\partial x^2}-\frac{\partial\varphi}{\partial x}\right)-d_3\frac{\partial w}{\partial t}-\rho A\left(\frac{\partial^2 w}{\partial t^2}+x\frac{\partial^2\theta}{\partial t^2}\right)-R(x,t)=p(x,t)$$

The boundary conditions are:

$$w(0,t)=\varphi(0,t)=0$$

$$\frac{\partial\varphi(l,t)}{\partial x}=0,\quad kGA\left(\frac{\partial w(l,t)}{\partial x}-\varphi(l,t)\right)=-M_T\left(\frac{\partial^2 w(l,t)}{\partial t^2}+l\frac{\partial^2\theta}{\partial t^2}\right) \tag{6a-c}$$

and the initial conditions are:

$$w(x,0)=w^0(x),\ \dot{w}(x,0)=\dot{w}^0(x),\ \varphi(x,0)=\varphi^0(x),\ \dot{\varphi}(x,0)=\dot{\varphi}^0(x) \tag{7a-d}$$

$$\theta(t)=\dot{\theta}(t)=0,\quad t<t_{slip} \tag{7 e,f}$$

$$or\ \theta(t)=\theta_{boundary}, \tag{7 e)'}$$

when $|\dot{\theta}(t)|$ and kinetic energy of the beam falls simultaneously under the Coulomb friction thresholds.

In eqns (5) the viscous friction coefficient of the hub is denoted by d_1, d_2 and d_3 are damping coefficients of the beam material, J is the moment of inertia of the beam about the motor axis and R(x,t) is the reaction force of the stop disposed from x_1 to x_2 ($x_1<x_2<l$) and modeled as an elastic foundation with Vinkler constant r:

$$R(x,t)=\begin{cases} r[w(x,t)-w_{stop}(x)] & \text{for} \quad x_1 \le x \le x_2; \quad |\theta| \ge \theta_{stop} \\ 0 & \text{for} \quad 0<x<x_1, x_2<x<l; \quad |\theta|<\theta_{stop} \end{cases} \tag{8}$$

The time when the bending moment about the hub axis exceeds the friction torque threshold is denoted by t_{slip}. When $t>t_{slip}$ this condition is removed (allowing rotation of the hub and the beam) until the moment when the beam clamps again.

2.3. Elastic-plastic relationships

The beam stress-strain state is usually expressed in terms of generalized stresses and strains which are function of x coordinate only. As a unique yield criterion in terms of moments and the transverse shear force does not exist according to Drucker [8], the beam cross-section is divided into N_z layers and for each of them the stress state has to be checked for yielding.

The relation between the stress vector $\mathbf{S}=\{\sigma_x,\sigma_{xz}\}^T$ and the strain vector $\varepsilon=\left\{-z\frac{\partial\varphi}{\partial x}, f(z)\left(\frac{\partial w}{\partial x}-\varphi\right)\right\}^T$, can be generally presented as

$$\mathbf{S}=[D]\,\varepsilon, \tag{9}$$

where in the case of an elastic material $[D]=[D^e]=\begin{bmatrix} E & 0 \\ 0 & G \end{bmatrix}$ is the elastic matrix and f(z) is a function describing the distribution of the shear strains along the thickness.

On the basis of the von Mises yield criterion, the yield surface is expressed as:

$$\phi(\mathbf{S})=\left\{\sigma_x^2+3\sigma_{xz}^2\right\}^{1/2}-\sigma_p \ge 0, \tag{10}$$

After yielding during infinitesimal increment of the stresses, the changes of strains are assumed to be divisible into elastic and plastic parts

$$\Delta\varepsilon=\Delta\varepsilon^e+\Delta\varepsilon^p \tag{11}$$

where

$$\Delta\varepsilon^e=\left[D^e\right]^{-1}\Delta\mathbf{S} \tag{12}$$

By using eqns (10), (11) and the associated flow rule [9], following Yamada and others [10], the following explicit relationship between the increments of stresses and strains is obtained

$$\Delta \mathbf{S} = \left[D^{ep} \right] \Delta \varepsilon \tag{13}$$

where $\left[D^{ep} \right]$ is the elastic-plastic matrix:

$$\left[D^{ep} \right] = \left[D^{e} \right] - \left[D^{e} \right] \left\{ \frac{\partial \phi}{\partial \mathrm{S}} \right\} \left\{ \frac{\partial \phi}{\partial \mathrm{S}} \right\}^{T} \left[D^{e} \right] \left[H + \left\{ \frac{\partial \phi}{\partial \mathrm{S}} \right\}^{T} \left[D^{e} \right] \left\{ \frac{\partial \phi}{\partial \mathrm{S}} \right\} \right]^{-1} \tag{14}$$

In this equation H is a function of the hardening parameter. For ideal plasticity H is equal to zero, while for a wholly elastic material $\mathrm{H} \to \infty$.

3. Use of mode superposition.

3.1. Rearrangement of the equation of motion.

Let the total time interval T on which the dynamic behavior of the structures is investigated, be divided into sequence of time increments $[t_i, t_{i+1}]$.

In the numerical calculations the following dimensionless variables are used:

$\bar{x} = x / l, \quad \bar{w} = w / l, \quad \bar{t} = tl / c \quad c = \sqrt{E / \rho}$

and then omitting the bars, and after some algebra, the governing equations can be written in the following form:

$$\frac{\mathrm{d}^2\theta}{\mathrm{d}t^2} + \mathrm{c}_1 \frac{\mathrm{d}\theta}{\mathrm{d}t} - \mathrm{c}_2 \left(\mathrm{w}(1,\mathrm{t}) - \int_0^1 \varphi(\mathrm{x},\mathrm{t})\, \mathrm{dx} \right) = \mathrm{c}_3 \left(\mathrm{T}(\mathrm{t}) + \int_0^1 \mathrm{xp}(\mathrm{x},\mathrm{t})\, \mathrm{dx} \right)$$

$$\frac{\partial^2 \varphi}{\partial t^2} + \mathrm{c}_4 \frac{\partial \varphi}{\partial t} - \frac{\partial^2 \varphi}{\partial x^2} - \alpha\beta \left(\frac{\partial \mathrm{w}}{\partial \mathrm{x}} - \varphi \right) = -\mathrm{G}_1^{\mathrm{p}}, \tag{15 a-c}$$

$$\frac{\partial^2 w}{\partial t^2} + c_5 \frac{\partial w}{\partial t} - \beta \left(\frac{\partial^2 w}{\partial x^2} - \frac{\partial \varphi}{\partial x} \right) = -\bar{p} - G_2^p - G^r$$

where $\alpha = 12l^2/h^2$, $\beta = kG/E$, $\bar{p} = pl/(EA)$, $c_1 = d_1 l/(cJ_H)$, $c_2 = \mathrm{Al}^3\rho/(\mathrm{J_H}\rho)$ $c_3 = l^2/(c^2 J_H)$, $c_4 = d_4 l^2/EI$, $c_5 = d_5 l/EA$, $k^2 = 5/6$. The nonlinear force due to the reaction of the foundation is denoted by G^r = R(x,t).l/EA and G_1^P and G_2^P are the components of the so-called non-linear force vector $\mathbf{G}_\mathrm{P}(G_1^P, G_2^P)$ which is due to the inelastic strains. It has the presentation (see [7]):

$$\mathbf{G}_p(x,t_{i+1}) = \sum_{j=0}^{i} \int_{-h/2}^{h/2} \Delta\mathbf{G}_p^{j+1,j}\, dz, \qquad (16\ \text{a-c})$$

$$\Delta\mathbf{G}_p^{j+1,j} = \mathbf{L}([D^e]\Delta\varepsilon^{j+1,j}) - \mathbf{L}([D^{ep}]\Delta\varepsilon^{j+1,j})$$

where $\Delta\varepsilon^{i+1,i} = \varepsilon(r,t_{i+1}) - \varepsilon(r,t_i)$, etc. a by $\mathbf{L}$ the following differential operator is denoted $\mathbf{L} = \begin{pmatrix} -\partial/\partial x & 1 \\ 0 & \partial/\partial x \end{pmatrix}$.

Boundary condition (6 c) is transformed in

$$\left(\frac{\partial w(1,t)}{\partial x} - \varphi(1,t)\right) = -\lambda\left(\frac{\partial^2 w(1,t)}{\partial t^2} + \frac{\partial^2 \theta}{\partial t^2}\right) \qquad \lambda = M_T/(\rho Al) \qquad (6\ c)'$$

3.2 Mode superposition method

The l.h.s. of eqns (15 b,c) is a linear form and therefore the mode superposition method can be used for its solution. As the eigen frequencies and the normal modes of vibrations of an elastic beam do not correspond to the real nonlinear system, these modes are called "pseudo-normal" modes.

Thus, the generalized displacements vector $\mathbf{v} = \{\alpha^{-1}\varphi, w\}^T$ is expanded as a sum of the product of the vectors of pseudo-normal modes v_n and the time dependent functions $q_n(t)$ as

$$\mathbf{v}(r,t) = \sum_n \mathbf{v}_n(r) q_n(t). \qquad (17)$$

The analytically obtained eigen functions of the elastic Timoshenko beam are chosen as basis functions (see APPENDIX). When the tip mass is attached to the beam the eigen functions of the system used in the mode superposition method are preliminary orthogonalized by standard orthogonalization procedure as it is mentioned in the APPENDIX.

Substituting eqn (17) into (15 b,c), multiplying by $\mathbf{v}_m(x)$, integrating the product over the beam length, invoking the orthogonality condition (see (A9)) and assuming a proportional damping for the beam material $\left(\int_0^1 (c_4\varphi_n^2 + c_5 w_n^2) r dr = 2\xi_n\omega_n\right)$ the following system of ordinary differential equations (ODE) for $\theta(t)$ and $q_n(t)$ is obtained:

$$\ddot{\theta}(t) + c_1\dot{\theta}(t) = c_2\left(\sum_n [w_n(1) - \gamma_n]q_n(t)\right) + c_3(T(t) + P(t)) \qquad (18a,b)$$

$$\ddot{q}_n(t) + 2\xi_n\omega_n\dot{q}_n(t) + \omega_n^2 q_n(t) = -\delta_n - \kappa_n\ddot{\theta}(t) + g_n^p - g_n^r$$

In this equations

$$\gamma_n = \int_0^1 \varphi_n(x)dx,\ \delta_n = \int_0^1 p(x,t)w_n(x)dx,\ \kappa_n = \int_0^1 xw_n(x)dx, \quad P(t) = \int_0^1 xp(x,t)\,dx,$$

$$g_n^p(t) = \int_0^1 G^p(x,t)v_n(x)dx, \quad g_n^r(t) = \int_0^1 G^r(x,t)w_n(x)dx, \quad \omega_n \text{ are the eigen}$$

frequencies of the elastic clamped beam and ξ_n are the modal damping parameters.

The initial conditions defined by eqns (7 a-d) are transformed also in terms of $q_n(0)$, and $\dot{q}_n(0)$

$$q_n(0) = q_n^0, \quad \dot{q}_n(0) = \dot{q}_n^0,$$

$$q_n^0 = \int_0^1 (w^0 w_n + \alpha^{-1}\varphi^0\varphi_n)dx, \quad \dot{q}_n^0 = \int_0^1 (\dot{w}^0 w_n + \alpha^{-1}\dot{\varphi}^0\varphi_n)dx, \qquad (19a\text{-}d)$$

The obtained system of nonlinear ordinary differential equations is a stiff one and it is solved numerically by the backward differential formula method, also called the Gear's method [11].

The rise of plastic strains is taking into account by using an iterative procedure based on the "initial stresses" numerical approach [7].

4. RESULTS AND DISCUSSION

Numerical results were performed for the robotic-arm with the same material and geometrical characteristic as these given in [3] in order to make some comparisons. Model parameters are: $E=6.5\times10^{10}$ Pa ,$\nu=0.2$, $\sigma_p=2.6\times10^8$ Pa, $l=0.7652$, $b=0.00642$ m, $h=0.016$ m, $\rho=2590$ kg/m^3 , $M_T=0.153$ kg, $J_H=0.285$ kgm^2 (J_H is not defined in [3].)

The aim of the computations is to show and clarify the influence of the elastic or elastic-plastic deformation on the motion of the robotic-arm, to demonstrate the effect of the hub friction, slip-stick boundary conditions and the contact interaction between the beam and the stop.

Only impact loading on the beam is considered in this work, i.e. dynamic load p(x,t) and applied torque T(t) are equal to zero. The impact loading is expressed as an initial velocity applied to the tip of the beam $0.95 < \bar{x} < 1$.

Nine modes are used in expansion (15) but the results obtained with number of modes greater than nine are practically indistinguishable from these shown here.

For all calculations the material damping is equal to 8% of the critical damping.

The results for the rotation of the hub of the flexible manipulator with an attached mass at its tip -1 and without an attached mass -2 are shown in Figure 2. The hub friction is not considered. The beam is subjected to an impact loading with initial velocity $\dot{w}^0$ =-1.95 m/s. As can be expected, the hub angle increases much faster in the case of the beam with an attached mass. The corresponding beam deflections are presented in Figure 3. The results obtained are very close to these obtained in [3] (Fig. 7 and 8 in [3]). The frequencies of forced vibrations obtained in [3], however, correspond to the beam without an attached mass.

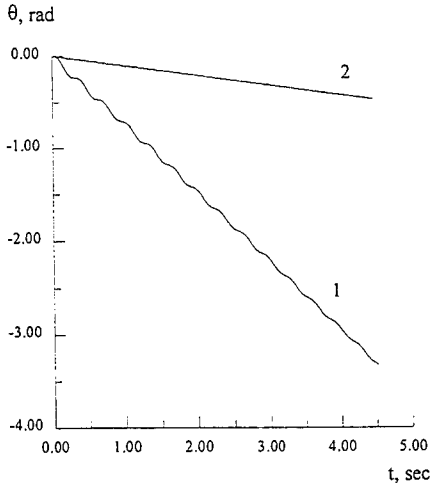

Figure 2. Hub response without viscous friction. 1 - beam with an attached mass; 2- without an attached mass

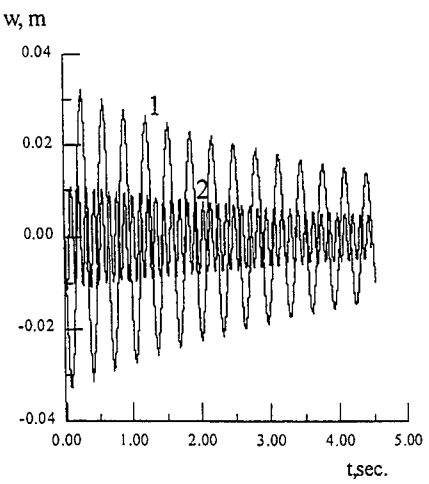

Figure 3. Deflection of the tip of the beam without viscous friction of the hub. 1 - beam with an attached mass; 2 - without an attached mass

The influence of the hub friction on the flexible manipulator response can be seen in Figure 4. The viscous friction is set d_1=0.1 Nms, the static Coulomb friction threshold is equal to 0.06 Nm and three cases of the hub slip-stick threshold are tested: $|\dot{\theta}|_{stick}$ = 0.005 rad.s^{-1} - 1, $|\dot{\theta}|_{stick}$ = 0.0085 rad.s^{-1} , $|\dot{\theta}|_{stick}$ = 0.01 rad.s^{-1}. For this initial velocity ($\dot{w}^0$ =-1.95m/s) the hub slips very fast from the initial clamped state and the beam begins to rotate. As can be expected, the consideration of the viscous friction of the hub leads to a decrease of the angle of rotation of the beam and changes the linear variation of θ with time. The results show also that the value of the hub speed threshold $|\dot{\theta}|_{stick}$ exercises an essential influence on the motion of the rotating system.

When $|\dot{\theta}|_{stick}$ =0.005 rad.s^{-1} the beam sticks at t = 2.602 s after that the hub periodically slips and sticks which also leads to damping of the motion. When $|\dot{\theta}|_{stick}$ = 0.0085 rad.s^{-1} the start of sticking occurs at t = 1.7207 s and after t=2.417 s the hub clamps with short interruptions till t=3.4 s when due to the elastic vibrations it snaps in the direction opposite to $\dot{w}^0$, clamps again at 3.679s, slip at 4.5s, and finally clamps at t=4.5s. When $|\dot{\theta}|_{stick}$ =0.0085 rad.s^{-1} the sticking begins at t=1.0525s and very fast (at t≈2 s) the beam clamps with θ=-0.587 rad.

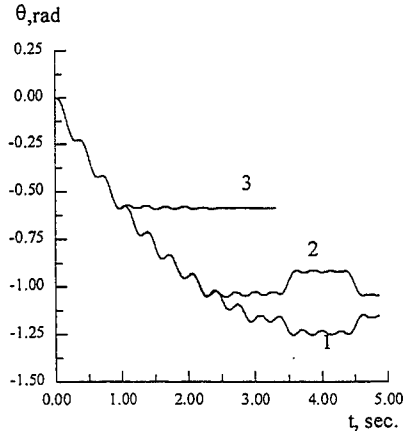

Figure 4. Hub response in time with d_1=0.1 Nms. 1- $|\dot{\theta}|_{stick}$=0.005rad.s^{-1}, 2 - $|\dot{\theta}|_{stick}$= 0.0085 rad s^{-1} ; 3- $|\dot{\theta}|_{stick}$= 0.01s^{-1}

In order to observe the occurrence of the plastic deformation the beam was subjected to impulse loading having larger values of initial velocities. In addition, the contact interaction between the beam and the stop was considered.

The beam-tip deflection in the presence of a contact with the stop disposed at $\bar{x} \in [0.16, 0.263]$ and initial velocity $\dot{w}^0$=-15.95 m/s is shown in Fig. 5.

In order to reduce the computational time the limit value of θ was chosen θ_{stop}=0.0025 rad. When this value was reached the problem was automatically resolved with new initial conditions θ=0, w^o=$w(x_{stop},t_{stop})$, etc.

As can be seen, the presence of the contact interaction during the process of motion of the beam due to the elastic support for $\bar{x} \in [0.16, 0.263]$ leads to a decrease of the amplitudes of vibrations in the direction of the stop in comparison with the amplitudes in the opposite direction. The variation of the beam displacements along the beam length for the first 0.8 s of motion is shown in Fig. 6. It must be noted that in this case of loading a plastic yielding occurs. It is assumed that beam material is characterized by an isotropic linear strain hardening and H=0.5. The plastic yielding occurs simultaneously with the contact interaction at t=0.01366 s at the clamped end of the beam. At t=0.0186 s the plastic zone spreads to $\bar{x}$ = 0.158 and at t=0.08767 it covers the length to $\bar{x}$ =0.31. The last points that yields are $\bar{x}$ =0.55, 0.61 at t=1.119 s.

Seven layers along the beam thickness, symmetrically disposed about the beam axis was checked for yielding (N_z=7) but the plastic zone has reached the second and 6th layers only at the clamped end of the beam ($\bar{x}$ =0). In all other point along beam length the plastic yielding occurs only at the upper and lower surface of the beam. The plastic strains are small and the response of the beam is not very different from the wholly elastic response. Nevertheless, the appearance of such kind of plastic deformations in the structures used for the precise operations must be taken into account in the manipulator self calibration procedure.

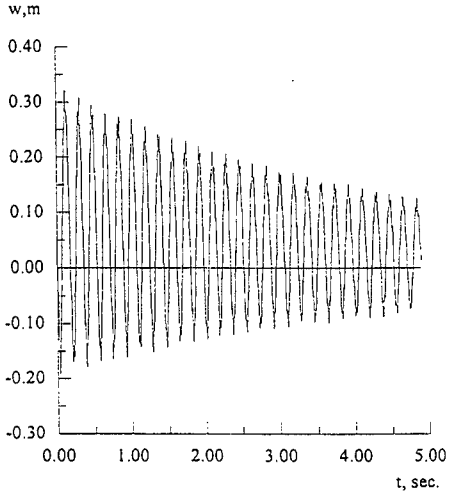

Figure 5. Deflection of the tip of the beam with time in the case of a contact with the stop. r=5.5x10^5 Pa

5. CONCLUSIONS

In this work a model describing dynamic behavior of a deformable beam attached to a rotating hub that has friction and inertia is developed. The Timoshenko beam theory is used to model the elastic deformation of the beam.

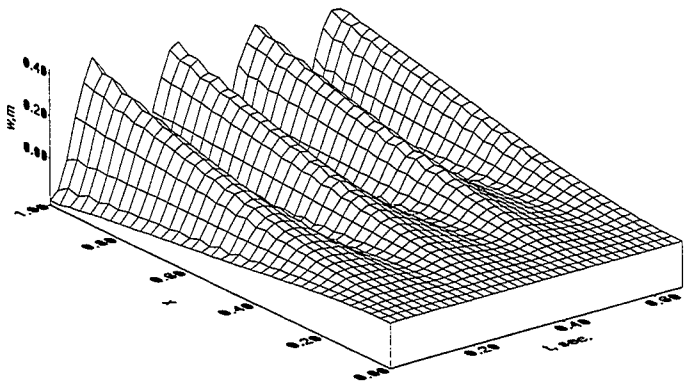

Figure 6. Variation of the elastic-plastic beam displacement along the beam length with time in the case of a contact with the stop.

The slip-stick boundary conditions are also incorporated into the model.
The possibility of the rise of undesired plastic deformations in the case of a high velocity impact on the clamped robotic arm, or in the case of a contact with limiting support (stop) is included into the model.
The analytically obtained eigen functions of the elastic Timoshenko beam vibrations are used to transform the partial differential equations into a set of ODE by using the mode superposition method. This approach minimizes the number of ODE which have to be solved in comparison with another numerical discretization techniques (finite elements or finite difference methods).
The results obtained show the essential influence of elasticity on the robotic-arm motion.
The model will be used to synthesise a control of one link flexible manipulators and for a self calibration procedure when plastic deformation would occur.

Acknowledgments
The authors gratefully acknowledge the financial support from EC Copernicus Program under the Project ROQUAL CIPA CT 94 0109.
The first author wishes to thank the National Research Fund for the partial financial support on this study through Contract MM-517/95.

REFERENCES

1. Bayo, E. A finite-element approach to control the end-point motion of a single -link flexible Robert. *J. Robotic System, 1987, **4,, 63-75***
2. Bayo, E. and Moulin, H., An efficient computation of the inverse dynamics of flexible manipulators in the time domain. *IEEE Proc Int. Conf. on Robotics and Automations, 1989, 710-15.*
3. Chapnik, B.V., Heppler, G.R., and Aplevich, J.D. Modeling impact on a one-link flexible robotic arm. *IEEE Transaction on Robotics and Automation,* 1991, 7, 479-88.
4. Liu, L. and Hac, A., Optimal control of a single link flexible manipulator. *Advances in Robotics, Mechatronics, and Haptic Interfaces*, 1993, DCS-**49**, 303-13.
5. Wen, J.T., Repko, M. and Buche, R., Modeling and control of a rotating flexible beam on a translatable base, *Dynamics of Flexible Multibody Systems*: Theory and Experiment, 1992, DCS-**37**, 39-45.
6. Sharan, A.M. and Karla, P., Dynamic Response of robotic manipulators using modal analysis. *Mech. Mach. Theory*, 1994, **29**, 1233-49.
7. Manoach, E. and Karagiozova, D. Dynamic response of thick elastic-plastic beams. *International Journal of Mechanical Sciences*, 1993, **35**, 909-19
8. Drucker, D.C. Effect of shear on plastic bending of beams. *J. of Applied Mechanics*, 1956, **23**, 515-21
9. Hill, R. *Mathematical Theory of Plasticity,* 1950, Oxford University Press, London.
10. Yamada, Y., Yoshimura, N. and Sakurai T., Plastic stress-strain matrix and its application for the solution of elastic-plastic problems by the finite elements, *Int. J. of Mechanical Sciences* , 1968, **10**, 343-54
11. Gear, C.W., *Numerical initial value problem in ordinary differential equations*, 1971, Prentice-Hall, Englewood Cliffs, NJ.
12. Abramovich, H. Elishakoff, I. Influence of shear deformation and rotary inertia on vibration frequencies via Love's equations. *J. Sound Vibr.*, 1990, **137,** 516-22.

APPENDIX: NORMAL MODES OF FREE VIBRATIONS OF A CLAMPED TIMOSHENKO BEAM WITH AN ATTACHED MASS.

Equations (5 b,c) can be decoupled, transforming them into two fourth order equations [12] as regards φ and w.

Solving this equations (with p=0 and R=0) and using the boundary conditions (6) (with θ=0) , the equations of the frequencies and forms of vibrations of the beam are obtained.

Introducing following denotations

$$s_{1n} = \left\{-\omega_n^2(1+\beta) + [\omega_n^4(1+\beta)^2 + 4\omega_n^2(\alpha - \beta\omega_n^2)]^{1/2}\right\}^{1/2} / 2,$$
$$s_{2n} = \left\{\omega_n^2(1+\beta) + [\omega_n^4(1+\beta)^2 + 4\omega_n^2(\alpha - \beta\omega_n^2)]^{1/2}\right\}^{1/2} / 2, \qquad \text{(A1 a-e)}$$
$$f_{1n} = (s_{1n}^2 + \omega_n^2\beta) / s_{1n}, \quad f_{2n} = (s_{2n}^2 - \omega_n^2\beta) / s_{2n}, \quad f_{3n} = (s_{1n}^2 - \omega_n^2\beta) / s_{1n},$$

the frequencies of free vibrations are determined as roots of equation:

a) <u>In the case</u> $s_{1n}^2 > 0$ i.e. $\omega_n^2 < \alpha / \beta$ the frequencies equation is:

$$b_{11}b_{22} - b_{12}b_{21} = 0 , \qquad \text{(A2)}$$

where

$$b_{11} = f_{1n}s_{1n}\mathrm{ch}(s_{1n}) + f_{2n}s_{2n}\cos(s_{2n}) \quad b_{12} = s_{1n}f_{2n}\mathrm{sh}(s_{1n}) + f_{2n}s_{2n}\sin(s_{2n})$$
$$b_{21} = -f_{1n}\mathrm{sh}(s_{1n}) - f_{2n}\sin(s_{2n}) + s_{1n}\mathrm{sh}(s_{1n}) + s_{2n}\sin(s_{2n}) + \qquad \text{(A3 a-d)}$$
$$\lambda[s_{1n}^2\mathrm{ch}(s_{1n}) + s_{2n}^2\cos(s_{2n})]$$
$$b_{22} = f_{2n}[\cos(s_{2n}) - \mathrm{ch}(s_{1n})] + \frac{f_{2n}}{f_{1n}}s_{1n}\mathrm{ch}(s_{1n}) - s_{2n}\cos(s_{2n}) +$$
$$\lambda[\frac{f_{2n}}{f_{1n}}s_{1n}^2\mathrm{sh}(s_{1n}) + s_{2n}^2\sin(s_{2n})]$$

and the modes of vibrations are:

$$w_n(x) = B_n\left[\frac{b_{12}}{b_{11}}\left(\mathrm{ch}(s_{1n}x) - \cos(s_{2n}x)\right) + \sin(s_{2n}x) - \frac{f_{2n}}{f_{1n}}\mathrm{sh}(s_{1n}x)\right] \qquad \text{(A4 a,b)}$$
$$\varphi_n(x) = B_n\left[\frac{b_{12}}{b_{11}}\left(f_{1n}\mathrm{sh}(s_{1n}x) + f_{2n}\sin(s_{2n}x)\right) + f_{2n}(\cos(s_{2n}x) - \mathrm{ch}(s_{1n}x)\right]$$

<u>b) In the case</u> $s_{1n}^2 < 0$ i.e. $\omega_n^2 > \alpha / \beta$ the eigen frequency equation (A2) has the following presentation:

$$b_{11} = f_{1n}\bar{s}_{1n}cos(\bar{s}_{1n}) + f_{2n}s_{2n}\cos(s_{2n})$$
$$b_{12} = \bar{s}_{1n}f_{2n}\sin(\bar{s}_{1n}) - f_{2n}s_{2n}\sin(s_{2n})$$
$$b_{21} = f_{3n}\sin(\bar{s}_{1n}) - f_{2n}\sin(s_{2n}) - \bar{s}_{1n}\sin(\bar{s}_{1n}) + s_{2n}\sin(s_{2n}) - \lambda[\bar{s}_{1n}^2\cos(\bar{s}_{1n}) - s_{2n}^2\cos(s_{2n})] \quad \text{(A5 a-e)}$$
$$b_{22} = f_{2n}[\cos(s_{2n}) - \cos(\bar{s}_{1n})] - \frac{f_{2n}}{f_{1n}}\bar{s}_{1n}\cos(\bar{s}_{1n}) + s_{2n}\cos(s_{2n}) - \lambda[\frac{f_{2n}}{f_{1n}}\bar{s}_{1n}^2\sin(s_{1n}) - s_{2n}^2\sin(s_{2n})]$$
$$\bar{s}_{1n}^2 = -s_{1n}^2$$

and the of vibrations are:

$$w_n(x) = B_n\left[\sin(s_{2n}x) - \frac{f_{2n}}{f_{1n}}\sin(\bar{s}_{1n}x) - \frac{b_{12}}{b_{11}}\left(\cos(s_{2n}x) - \cos(\bar{s}_{1n}x)\right)\right] \quad \text{(A6a-b)}$$
$$\varphi_n(x) = B_n\left[f_{2n}(\cos(s_{2n}x) - \cos(\bar{s}_{1n}x)) - \frac{b_{12}}{b_{11}}\left(f_{3n}\sin(\bar{s}_{1n}x) - f_{2n}\sin(s_{2n}x)\right)\right]$$

When a mass is not attached at the beam tip the following orthogonality condition is fulfilled:

$$\int_0^1(\alpha^{-1}\varphi_n\varphi_m + w_n w_m)dx = \begin{cases}0, & n \neq m;\\ 1, & n = m.\end{cases} \quad \text{(A7)}$$

and when an attached mass is considered the modes are orthogonalized by standard orthogonalization procedure.

The constants B_n are obtained from condition (A7).

Wave Reflection and Transmission in an Axially Strained, Rotating Timoshenko Shaft

B. Kang [1] and C. A. Tan [2]
Department of Mechanical Engineering
Wayne State University
Detroit, Michigan 48202, U. S. A.

Abstract

In this paper, the wave reflection and transmission characteristics of an axially strained, rotating Timoshenko shaft under general support and boundary conditions, and with geometric discontinuities are examined. The static axial deformation due to an axial force is also included in the model. The reflection and transmission matrices for incident waves upon these point supports and discontinuities are derived. These matrices are combined, with the aid of the transfer matrix method, to provide a concise and systematic approach for the free vibration analysis of multi-span rotating shafts with general boundary conditions. Results on the wave reflection and transmission coefficients are presented for both the Timoshenko and the simple Euler-Bernoulli models to investigate the effects of the axial strain, shaft rotation speed, shear and rotary inertia.

[1] Graduate Research Assistant, Tel: +1-313-577-6823, Fax: +1-313-577-8789, E-mail: kang@feedback.eng.wayne.edu
[2] Associate professor (Corresponding Author), Tel: +1-313-577-3888, Fax:+1-313-577-8789, E-mail: tan@tan.eng.wayne.edu

Submitted to: *Sixth International Conference on Recent Advances in Structural Dynamics*, Institute of Sound and Vibration, Southampton, England, July, 1997

NOMENCLATURE

A_s	Area of shaft cross section [m^2]
a_0	Diameter of shaft cross section [m]
C	Generalized coordinate of an incident wave [m]
c_{dt} (c_t)	Translational damping coefficient [N·sec/m]
c_{dr} (c_r)	Rotational damping coefficient [N·m·sec/rad]
c_o	Bar velocity [m/sec]
c_s	Shear velocity [m/sec]
D	Generalized coordinate of a transmitted wave [m]
E , G	Young's and shear modulus [N/m^2], respectively
I	Lateral moment of inertia of shaft [m^4]
J_M (J_m)	mass moment of inertia of a rotor mass [$kg·m^4$]
K	Timoshenko shear coefficient
K_R (k_r)	Rotational spring [N/rad]
K_T (k_t)	Translational spring [N/m]
ℓ	Length of shaft [m]
M (m)	Mass of rotor [kg]
P	Axial force [N]
r_{ij} , t_{ij}	Reflection and transmission coefficients, respectively. i = 1 positive traveling wave; i = 2 negative traveling wave; j = 1 propagating wave for *Cases II* and *IV*; j = 2 attenuating wave for *Cases II* and *IV*. Both j =1, 2 for propagating wave for *Case I*
U (u)	Transverse displacement [m]
X-Y-Z (x-y-z)	Reference frame coordinates [m]
α	$(K·G)/E$
β	Rotation parameter, see Eqn. (1d)
ε	$P/(E·A)$, axial strain
ε'	Non-dimensional axial load parameter, see Eqn. (13b)
$\overline{\Gamma}$, $\bar{\gamma}$ (Γ, γ)	Wavenumber [m^{-1}]
$\overline{\eta}$, (η)	See Eqns. (20a, b), (22a, b) and (24a, b)
ρ	Mass density of shaft [kg/m^3]
σ	Diameter ratio between two shaft elements
$\overline{\omega}$, (ω)	System natural frequency for Timoshenko model [rad/sec]
$\tilde{\omega}$	System natural frequency for Euler-Bernoulli model [rad/sec]
Ω	Rotation speed of shaft [rad/sec]
$\overline{\Psi}$ (ψ)	Bending angle of the shaft cross-section [rad]
subscript l, r	The left and right side of a discontinuity, respectively.
superscript −,+	Negative and positive traveling waves, respectively, when used in C and D. Otherwise denotes quantities on the left and right side of a discontinuity, respectively

Note: Symbols in parenthesis are the corresponding non-dimensional parameters.

1. INTRODUCTION

The vibrations of elastic structures such as strings, beams, and plates can be described in terms of waves propagating and attenuating in waveguides. Although the subject of wave motions has been considered much more extensively in the field of acoustics in fluids and solids than mechanical vibrations of elastic structures, wave analysis techniques have been employed to reveal important, physical characteristics associated with vibrations of structures. One advantage of the wave technique is its compact and systematic approach to analyze complex structures such as trusses, aircraft panels with periodic supports, and beams on multiple supports [1]. Previous works based on wave propagation techniques have been well documented in several books [2-4]. Recently, Mead [5] applied the phase-closure principle to determine the natural frequencies of Euler-Bernoulli beam models. A systematic approach including both the propagating and near-field waves was employed to study the free vibrations of Euler-Bernoulli beams [6].

High speed rotating shafts are commonly employed in precision manufacturing and power transmission. Despite the usefulness of the wave propagation method in structural vibrations, applications of this technique to study the dynamics and vibrations of a flexible shaft rotating about its longitudinal axis have seldom been considered. The purpose of this paper is to examine the wave reflection and transmission [6] in an axially strained, rotating Timoshenko shaft under various support and boundary conditions. The effect of the axial load is included by considering the axial static deformations in the equations of motion. This paper is a sequel to another paper in which the authors discuss the basic wave motions in the infinitely long shaft model [7].

Although there have been numerous studies on the dynamics and vibration of rotating shafts, none has examined the effects of axial strains (which cannot be neglected in many applications) on the vibration characteristics of a Timoshenko shaft under multiple supports. Modal analysis technique has been applied to study the vibration of a rotating Timoshenko shaft with general boundary conditions [8, 9], and subject to a moving load [10]. Recently, the distributed transfer function method was applied to a rotating shaft system with multiple, geometric discontinuities [11]. The wave propagation in a rotating Timoshenko shaft was considered in Ref. [12]. Other major works on the dynamics of rotating shafts have been well documented in Refs. [13-15].

This manuscript is organized as follows. Governing equations of motion [16] and basic wave solutions for the Timoshenko shaft are outlined in Section 2. Each wave solution consists of four wave components: positive and negative, propagating and attenuating waves. In Section 3, the wave reflection and transmission matrices are derived for the shaft under various point supports and boundary conditions. The supports may include translational and rotational springs and dampers, and rotor mass. Results are presented for both the Timoshenko and the simple Euler-Bernoulli models to assess the effects of axial strain, shaft rotation, shear and rotary inertia. The wave propagation across a shaft with geometric discontinuities such as a change in the cross-section is examined in Section 4, and the wave reflection at a boundary with arbitrary support conditions is considered in Section 5.

With the wave reflection and transmission matrices as the main analytical tools, it is shown in Section 6 how to apply the current results together with the transfer matrix method to analyze the

free vibration of a rotating, multi-span Timoshenko shaft system in a systematic manner. The proposed approach is then demonstrated by considering the free vibration of a two-span beam with an intermediate support.

2. FORMULATION AND WAVE SOLUTIONS

Consider a rotating shaft subjected to axial loads and with multiple intermediate supports and arbitrary boundary conditions, as shown in Fig. 1. Including the effects of rotary inertia, shear deformations, and axial deformations due to the axial loads, the uncoupled equations of motion governing the transverse displacement u and the slope ψ due to bending can be derived in the following non-dimensional form

$$\frac{\partial^4 u}{\partial z^4}-(1+\alpha)\frac{\partial^4 u}{\partial z^2\partial t^2}+2i\beta\frac{\partial^3 u}{\partial z^2\partial t}-2i\beta\frac{\partial^3 u}{\partial t^3}+\alpha\frac{\partial^4 u}{\partial t^4}-16\varepsilon(1+\varepsilon-\frac{\varepsilon}{\alpha})\frac{\partial^2 u}{\partial z^2}$$
$$+16\alpha(1+\varepsilon)(1+\varepsilon-\frac{\varepsilon}{\alpha})\frac{\partial^2 u}{\partial t^2}=0\,, \tag{1a}$$

$$\frac{\partial^4 \psi}{\partial z^4}-(1+\alpha)\frac{\partial^4 \psi}{\partial z^2\partial t^2}+2i\beta\frac{\partial^3 \psi}{\partial z^2\partial t}-2i\beta\frac{\partial^3 \psi}{\partial t^3}+\alpha\frac{\partial^4 \psi}{\partial t^4}-16\varepsilon(1+\varepsilon-\frac{\varepsilon}{\alpha})\frac{\partial^2 \psi}{\partial z^2}$$
$$+16\alpha(1+\varepsilon)(1+\varepsilon-\frac{\varepsilon}{\alpha})\frac{\partial^2 \psi}{\partial t^2}=0\,, \tag{1b}$$

where,

$$u=\frac{U}{a_0},\quad z=\frac{Z}{a_0},\quad t=\frac{T}{T_0},\quad T_0=\sqrt{\frac{\rho a_0^2}{KG}}\;; \tag{1c}$$

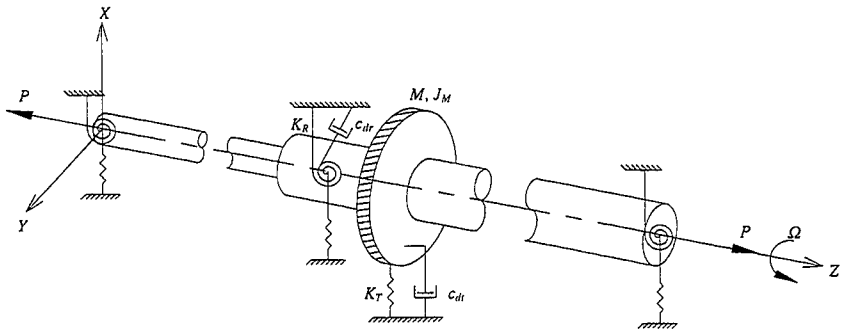

Figure 1. A rotating Timoshenko shaft model subject to axial loads and with general boundary conditions.

$$\alpha = \frac{KG}{E},\ \beta = \frac{\rho a_0^2}{ET_0}\Omega = \frac{\rho a_0 c_s}{E}\Omega,\ \varepsilon = \frac{P}{EA_s} \tag{1d}$$

Note that u and ψ are the measurements in the complex plane, that is $u=u_x+iu_y$ and $\psi=\psi_x+i\psi_y$. E denotes the Young's modulus, ρ the mass density, A_s the area of the cross section, a_0 the diameter of shaft, K the Timoshenko shear coefficient, G the shear modulus and Ω the constant angular velocity of the shaft. Details of deriving these equations of motion are found in Ref. [16].

Assuming and substituting the following wave solutions into Eqns. (1a) and (1b)

$$u(z,t) = C_u e^{i(\bar{\gamma}z+\bar{\omega}t)}, \tag{2a}$$

$$\psi(z,t) = C_\psi e^{i(\bar{\gamma}z+\bar{\omega}t)}, \tag{2b}$$

and defining the non-dimensionalized wavenumber $\bar{\gamma}$ and system natural frequency $\bar{\omega}$ gives the frequency equation, Eqn. (3a); see Ref. [7],

$$\bar{\gamma} = \gamma a_0, \tag{2c}$$

$$\bar{\omega} = \frac{\omega a_0}{c_s}\ \left(c_s = \sqrt{\frac{KG}{\rho}}\ \text{is known as the } \textit{shear velocity}\right). \tag{2d}$$

$$\bar{\gamma}^4 - A\bar{\gamma}^2 + B = 0, \tag{3a}$$

where,

$$A = (1+\alpha)\bar{\omega}^2 - 2\beta\,\bar{\omega} - 16\varepsilon\left(1+\varepsilon-\frac{\varepsilon}{\alpha}\right), \tag{3b}$$

$$B = \bar{\omega}^2\left[\alpha\,\bar{\omega}^2 - 2\beta\,\bar{\omega} - 16\alpha(1+\varepsilon)\left(1+\varepsilon-\frac{\varepsilon}{\alpha}\right)\right]. \tag{3c}$$

The four roots of Eqn. (3a) are

$$\bar{\gamma} = \pm\frac{1}{\sqrt{2}}\left(A \pm \sqrt{A^2-4B}\right)^{\frac{1}{2}}. \tag{4}$$

In general, $\bar{\gamma}$ is complex. Let $\bar{\omega}$ be real. It can be shown that, with $\alpha > 0$ and ε the axial strain of the elastic solid, the discriminant A^2-4B is positive semi-definite for most engineering applications. Hence, it is possible to classify the wave solutions into four distinct cases. Note that one may study the wave propagation by considering only a single general form of the wave solution. However, the classification procedure identifies the coupled modes of vibration of the

Timoshenko shaft model and provides a better understanding on how each wave solution governs the wave motions [7]. Based on the algebraic relationships between A and B, the four valid wave solutions are obtained as follows.

Case I ($A > 0$ and $B > 0$):

$$u(z,t) = (C_{u1}^{+}e^{-i\bar{\gamma}_1 z} + C_{u1}^{-}e^{i\bar{\gamma}_1 z} + C_{u2}^{+}e^{-i\bar{\gamma}_2 z} + C_{u2}^{-}e^{i\bar{\gamma}_2 z})e^{i\bar{\omega}t} \tag{5a}$$

$$\psi(z,t) = (C_{\psi 1}^{+}e^{-i\bar{\gamma}_1 z} + C_{\psi 1}^{-}e^{i\bar{\gamma}_1 z} + C_{\psi 2}^{+}e^{-i\bar{\gamma}_2 z} + C_{\psi 2}^{-}e^{i\bar{\gamma}_2 z})e^{i\bar{\omega}t} \tag{5b}$$

Case II ($A > 0$ and $B < 0$):

$$u(z,t) = (C_{u1}^{+}e^{-i\bar{\Gamma}_1 z} + C_{u1}^{-}e^{i\bar{\Gamma}_1 z} + C_{u2}^{+}e^{-\bar{\Gamma}_2 z} + C_{u2}^{-}e^{\bar{\Gamma}_2 z})e^{i\bar{\omega}t} \tag{6a}$$

$$\psi(z,t) = (C_{\psi 1}^{+}e^{-i\bar{\Gamma}_1 z} + C_{\psi 1}^{-}e^{i\bar{\Gamma}_1 z} + C_{\psi 2}^{+}e^{-\bar{\Gamma}_2 z} + C_{\psi 2}^{-}e^{\bar{\Gamma}_2 z})e^{i\bar{\omega}t} \tag{6b}$$

Case III ($A < 0$ and $B > 0$):

$$u(z,t) = (C_{u1}^{+}e^{-\bar{\gamma}_1 z} + C_{u1}^{-}e^{\bar{\gamma}_1 z} + C_{u2}^{+}e^{-\bar{\gamma}_2 z} + C_{u2}^{-}e^{\bar{\gamma}_2 z})e^{i\bar{\omega}t} \tag{7a}$$

$$\psi(z,t) = (C_{\psi 1}^{+}e^{-\bar{\gamma}_1 z} + C_{\psi 1}^{-}e^{\bar{\gamma}_1 z} + C_{\psi 2}^{+}e^{-\bar{\gamma}_2 z} + C_{\psi 2}^{-}e^{\bar{\gamma}_2 z})e^{i\bar{\omega}x} \tag{7b}$$

Case IV ($A < 0$ and $B < 0$):

$$u(z,t) = (C_{u1}^{+}e^{-\bar{\Gamma}_1 z} + C_{u1}^{-}e^{\bar{\Gamma}_1 z} + C_{u2}^{+}e^{-i\bar{\Gamma}_2 z} + C_{u2}^{-}e^{i\bar{\Gamma}_2 z})e^{i\bar{\omega}t} \tag{8a}$$

$$\psi(z,t) = (C_{\psi 1}^{+}e^{-\bar{\Gamma}_1 z} + C_{\psi 1}^{-}e^{\bar{\Gamma}_1 z} + C_{\psi 2}^{+}e^{-i\bar{\Gamma}_2 z} + C_{\psi 2}^{-}e^{i\bar{\Gamma}_2 z})e^{i\bar{\omega}t} \tag{8b}$$

where,

$$\bar{\gamma}_1 = \frac{1}{\sqrt{2}}\left(|A| + \sqrt{A^2 - 4|B|}\right)^{\frac{1}{2}},\ \bar{\gamma}_2 = \frac{1}{\sqrt{2}}\left(|A| - \sqrt{A^2 - 4|B|}\right)^{\frac{1}{2}}, \tag{9a, b}$$

$$\bar{\Gamma}_1 = \frac{1}{\sqrt{2}}\left(\sqrt{A^2 + 4|B|} + |A|\right)^{\frac{1}{2}},\ \bar{\Gamma}_2 = \frac{1}{\sqrt{2}}\left(\sqrt{A^2 + 4|B|} - |A|\right)^{\frac{1}{2}}, \tag{9c, d}$$

and the coefficients C^{+} and C^{-} denote positive- and negative-travelling waves from the origin of disturbance, respectively. Important remarks on the basic wave propagation characteristics are summarized from [7]. First, the wave solution of *Case III* does not exist in the real frequency space since this type of solution represents a situation in which none of the wave components can propagate along the waveguide. Therefore the study of *Case III* is excluded in the present paper. Second, the vibrating motion of the shaft model in *Case I* is predominately pure shear [17] which

is unique for the Timoshenko shaft model, while in *Case II* and *Case IV* the flexural mode and the simple shearing mode, which are corrected by including the rotary inertia and shearing effects in the formulation, dominate. Third, when the shaft rotates at a very high speed and/or the shaft is axially strained by tensile loads, the wave solution of *Case IV* governs the vibrating motion of the shaft model in the low frequency range.

For comparison, the parameters A and B in the simple Euler-Bernoulli beam model are

$$A = -2\beta\,\tilde{\omega} - 16\varepsilon, \tag{10a}$$

$$B = -16\tilde{\omega}^2, \tag{10b}$$

where, the non-dimensionalized natural frequency $\tilde{\omega}$ is defined as

$$\tilde{\omega} = \frac{\omega a_0}{c_0} \quad \left(c_0 = \sqrt{\frac{E}{\rho}} \text{ is known as the } \textit{bar velocity}\right). \tag{10c}$$

Note that, because B is negative, wave solutions of *Case I* and *Case III* do not exist.

In general the displacement and the rotation of an infinitesimal shaft element consist of four wave components as shown by Eqns. (5a-8b). Once the displacement and the bending slope are known, the moment M and shear force V at a cross section can be determined from

$$M = EI\frac{\partial \psi}{\partial z}, \tag{11}$$

$$V = KAG\left(\frac{\partial u}{\partial z} + i\psi\right). \tag{12}$$

Moreover, the kinematic relationship between the transverse displacement and the slope due to bending is

$$\frac{\partial^2 u}{\partial t^2} = \frac{\partial^2 u}{\partial z^2} + i\varepsilon'\frac{\partial \psi}{\partial z}, \tag{13a}$$

where ε' denotes the effects of the axial force and is defined as

$$\varepsilon' = 1 + \varepsilon - \frac{\varepsilon}{\alpha}. \tag{13b}$$

3. WAVE REFLECTION AND TRANSMISSION AT SUPPORTS

When a wave is incident upon a discontinuity, it is transmitted and reflected at different rates depending on the properties of the discontinuity. Consider a rotating Timoshenko shaft model supported at $z = 0$; see Fig. 2. The support simulates a bearing modelled by linear, translational and rotational springs, dampers, and a rotor mass which typically represents a gear transmitting a torque. Based on Eqns. (5a-8b), group the four wave components into 2×1 vectors of positive-travelling waves $\mathbf{C}^+$ and negative-travelling waves $\mathbf{C}^-$, i. e.,

$$\mathbf{C}^+ = \begin{Bmatrix} C_1^+ \\ C_2^+ \end{Bmatrix} ; \ \mathbf{C}^- = \begin{Bmatrix} C_1^- \\ C_2^- \end{Bmatrix} \tag{14a, b}$$

Recall that, depending on the system parameters, the rotating Timoshenko shaft model has four (practically three) different wave solutions in the entire frequency region as described in Eqns. (5a-8b). Thus C_1 and C_2 in the above expression do not always correspond to propagating and attenuating wave components, respectively. When a set of positive-travelling waves $\mathbf{C}^+$ is incident upon the support, it gives rise to a set of reflected waves $\mathbf{C}^-$ and transmitted waves $\mathbf{D}^+$. These waves are related by

$$\mathbf{C}^- = \mathbf{r}\mathbf{C}^+ \tag{15}$$

and

$$\mathbf{D}^+ = \mathbf{t}\mathbf{C}^+, \tag{16}$$

where $\mathbf{r}$ and $\mathbf{t}$ are the 2×2 reflection and transmission matrices respectively and are expressed as

$$\mathbf{r} = \begin{bmatrix} r_{11} & r_{12} \\ r_{21} & r_{22} \end{bmatrix}, \tag{17}$$

$$\mathbf{t} = \begin{bmatrix} t_{11} & t_{12} \\ t_{21} & t_{22} \end{bmatrix}. \tag{18}$$

From Eqns. (5a-8b), suppressing $e^{i\omega t}$ term and excluding *Case III*, the displacements u^- and u^+ and the bending slopes ψ^- and ψ^+ at the left and right of $z = 0$, respectively, can be expressed in terms of the wave amplitudes of the displacement. For convenience, the over-bar ($\bar{\bullet}$) on the wavenumbers is dropped hereafter.

Case I ($A > 0$ and $B > 0$):

$$u^-(z) = C_{u1}^+ e^{-i\gamma_1 z} + C_{u1}^- e^{i\gamma_1 z} + C_{u2}^+ e^{-i\gamma_2 z} + C_{u2}^- e^{i\gamma_2 z}, \tag{19a}$$

$$\psi^-(z) = \eta_1 C_{u1}^+ e^{-i\gamma_1 z} - \eta_1 C_{u1}^- e^{i\gamma_1 z} + \eta_2 C_{u2}^+ e^{-i\gamma_2 z} - \eta_2 C_{u2}^- e^{i\gamma_2 z}, \tag{19b}$$

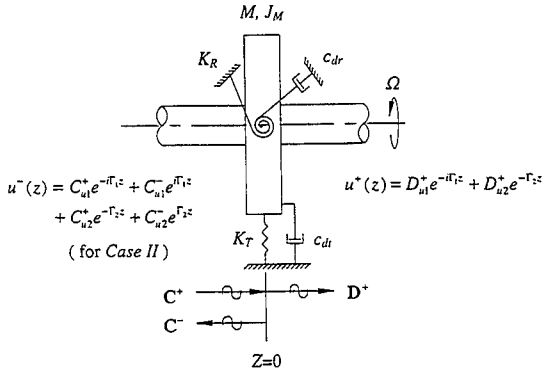

Figure 2. Wave motion at a general support (the disk may be considered as a gear transmitting a torque).

$$u^+(z) = D_{u1}^+ e^{-i\gamma_1 z} + D_{u2}^+ e^{-i\gamma_2 z}, \tag{19c}$$

$$\psi^+(z) = \eta_1 D_{u1}^+ e^{-i\gamma_1 z} + \eta_2 D_{u2}^+ e^{-i\gamma_2 z}, \tag{19d}$$

where,

$$\eta_1 = \frac{\gamma_1^2 - \omega^2}{\gamma_1 \varepsilon'}, \quad \eta_2 = \frac{\gamma_2^2 - \omega^2}{\gamma_2 \varepsilon'}. \tag{20a, b}$$

Case II ($A > 0$ and $B < 0$):

$$u^-(z) = C_{u1}^+ e^{-i\Gamma_1 z} + C_{u1}^- e^{i\Gamma_1 z} + C_{u2}^+ e^{-\Gamma_2 z} + C_{u2}^- e^{\Gamma_2 z}, \tag{21a}$$

$$\psi^-(z) = \eta_1 C_{u1}^+ e^{-i\Gamma_1 z} - \eta_1 C_{u1}^- e^{i\Gamma_1 z} + \eta_2 C_{u2}^+ e^{-\Gamma_2 z} - \eta_2 C_{u2}^- e^{\Gamma_2 z}, \tag{21b}$$

$$u^+(z) = D_{u1}^+ e^{-i\Gamma_1 z} + D_{u2}^+ e^{-\Gamma_2 z}, \tag{21c}$$

$$\psi^+(z) = \eta_1 D_{u1}^+ e^{-i\Gamma_1 z} + \eta_2 D_{u2}^+ e^{-\Gamma_2 z}, \tag{21d}$$

where

$$\eta_1 = \frac{\Gamma_1^2 - \omega^2}{\Gamma_1 \varepsilon'}, \quad \eta_2 = \frac{\Gamma_2^2 + \omega^2}{i\Gamma_2 \varepsilon'}. \tag{22a, b}$$

Case IV ($A < 0$ and $B < 0$):

$$u^-(z) = C_{u1}^+ e^{-\Gamma_1 z} + C_{u1}^- e^{\Gamma_1 z} + C_{u2}^+ e^{-i\Gamma_2 z} + C_{u2}^- e^{i\Gamma_2 z}, \tag{23a}$$

$$\psi^-(z) = \eta_1 C_{u1}^+ e^{-\Gamma_1 z} - \eta_1 C_{u1}^- e^{\Gamma_1 z} + \eta_2 C_{u2}^+ e^{-i\Gamma_2 z} - \eta_2 C_{u2}^- e^{i\Gamma_2 z}, \tag{23b}$$

$$u^+(z) = D_{u1}^+ e^{-\Gamma_1 z} + D_{u2}^+ e^{-i\Gamma_2 z}, \tag{23c}$$

$$\psi^+(z) = \eta_1 D_{u1}^+ e^{-\Gamma_1 z} + \eta_2 D_{u2}^+ e^{-i\Gamma_2 z}. \tag{23d}$$

where,

$$\eta_1 = \frac{\Gamma_1^2 + \omega^2}{i\Gamma_1 \varepsilon'}, \quad \eta_2 = \frac{\Gamma_2^2 - \omega^2}{\Gamma_2 \varepsilon'}. \tag{24a, b}$$

Introducing the following non-dimensional parameters

$$k_t = \frac{K_t a_0}{KAG}, \; k_r = \frac{K_r a_0}{EI}, \; c_t = \frac{c_{dt} c_s}{KAG}, \; c_r = \frac{c_{dr} c_s}{EI}, \; m = \frac{M}{\rho A a_0}, \text{ and } J_m \doteq \frac{J_M c_s^2}{EI}, \tag{25}$$

and by imposing the geometric continuity

$$u^-(0) = u^+(0), \quad \psi^-(0) = \psi^+(0) \tag{26a, b}$$

and the moment and force balance conditions at the support

$$M^- - M^+ = k_r \psi + c_r \dot{\psi} + J_m \frac{\partial \ddot{\psi}}{\partial z}, \tag{27a}$$

$$V^+ - V^- = k_t u + c_t \dot{u} + m\ddot{u}, \tag{27b}$$

the following set of matrix equations can be established for each *Case*.

Case I ($A > 0$ and $B > 0$):

$$\begin{bmatrix} 1 & 1 \\ \eta_1 & \eta_2 \end{bmatrix} \mathbf{C}^+ + \begin{bmatrix} 1 & 1 \\ -\eta_1 & -\eta_2 \end{bmatrix} \mathbf{r}\mathbf{C}^+ = \begin{bmatrix} 1 & 1 \\ \eta_1 & \eta_2 \end{bmatrix} \mathbf{t}\mathbf{C}^+, \tag{28a}$$

$$\begin{bmatrix} -i\gamma_1\eta_1 & -i\gamma_2\eta_2 \\ i(\gamma_1 - \eta_1) & i(\gamma_2 - \eta_2) \end{bmatrix} \mathbf{C}^+ + \begin{bmatrix} -i\gamma_1\eta_1 & -i\gamma_2\eta_2 \\ -i(\gamma_1 - \eta_1) & -i(\gamma_2 - \eta_2) \end{bmatrix} \mathbf{r}\mathbf{C}^+$$

$$= \begin{bmatrix} \eta_1(k_r - J_m\omega^2) + i\eta_1(c_r\omega - \gamma_1) & \eta_2(k_r - J_m\omega^2) + i\eta_2(c_r\omega - \gamma_2) \\ (k_t - m\omega^2) + i(c_t\omega + \gamma_1 - \eta_1) & (k_t - m\omega^2) + i(c_t\omega + \gamma_2 - \eta_2) \end{bmatrix} \mathbf{t}\mathbf{C}^+, \tag{28b}$$

Case II ($A > 0$ and $B < 0$):

$$\begin{bmatrix} 1 & 1 \\ \eta_1 & \eta_2 \end{bmatrix} \mathbf{C}^+ + \begin{bmatrix} 1 & 1 \\ -\eta_1 & -\eta_2 \end{bmatrix} \mathbf{r}\mathbf{C}^+ = \begin{bmatrix} 1 & 1 \\ \eta_1 & \eta_2 \end{bmatrix} \mathbf{t}\mathbf{C}^+, \tag{29a}$$

$$\begin{bmatrix} -i\Gamma_1\eta_1 & -\Gamma_2\eta_2 \\ i(\Gamma_1 - \eta_1) & \Gamma_2 - i\eta_2 \end{bmatrix} \mathbf{C}^+ + \begin{bmatrix} -i\Gamma_1\eta_1 & -\Gamma_2\eta_2 \\ -i(\Gamma_1 - \eta_1) & -(\Gamma_2 - i\eta_2) \end{bmatrix} \mathbf{r}\mathbf{C}^+$$

$$= \begin{bmatrix} \eta_1(k_r - J_m\omega^2) + i\eta_1(c_r\omega - \gamma_1) & \eta_2(k_r - J_m\omega^2 - \gamma_2) + i\eta_2 c_r\omega \\ (k_t - m\omega^2) + i(c_t\omega + \Gamma_1 - \eta_1) & (k_t - m\omega^2 + \Gamma_2) + i(c_t\omega - \eta_2) \end{bmatrix} \mathbf{t}\mathbf{C}^+, \tag{29b}$$

Case IV ($A < 0$ and $B < 0$):

$$\begin{bmatrix} 1 & 1 \\ \eta_2 & \eta_1 \end{bmatrix} \mathbf{C}^+ + \begin{bmatrix} 1 & 1 \\ -\eta_2 & -\eta_1 \end{bmatrix} \mathbf{r}\mathbf{C}^+ = \begin{bmatrix} 1 & 1 \\ \eta_2 & \eta_1 \end{bmatrix} \mathbf{t}\mathbf{C}^+, \tag{30a}$$

$$\begin{bmatrix} -i\Gamma_2\eta_2 & -i\Gamma_1\eta_1 \\ i(\Gamma_2 - \eta_2) & \Gamma_1 - i\eta_1 \end{bmatrix} \mathbf{C}^+ + \begin{bmatrix} -i\Gamma_2\eta_2 & -i\Gamma_1\eta_1 \\ -i(\Gamma_2 - \eta_2) & -(\Gamma_1 - i\eta_1) \end{bmatrix} \mathbf{r}\mathbf{C}^+$$

$$= \begin{bmatrix} \eta_2(k_r - J_m\omega^2) + i\eta_2(c_r\omega - \gamma_2) & \eta_1(k_r - J_m\omega^2 - \gamma_1) + i\eta_1 c_r\omega \\ (k_t - m\omega^2) + i(c_t\omega + \Gamma_2 - \eta_2) & (k_t - m\omega^2 + \Gamma_1) + i(c_t\omega - \eta_1) \end{bmatrix} \mathbf{t}\mathbf{C}^+, \tag{30b}$$

where Eqns. (15) and (16) have been applied in all *Cases*. Note that in Eqn. (27a), it is assumed that the rotational spring at the support is attached to the cross section of a shaft element such that the rotational spring responds only to the slope change due to rotation of the cross section and not the total slope change of the neutral axis of the shaft model. This assumption allows the shearing motion of the shaft element at the support. Note also that the effect of axial loads on the shear force at the support is neglected since the contribution of axial loads to the shear force at the support or boundary is small compared to the shear force due to the flexural motion of the shaft element. Exact moment and force balance conditions at boundaries for a rotating Timoshenko shaft element subjected to axial loads can be found in Ref. [16].

The corresponding matrix equations for the simple Euler-Bernoulli shaft model are shown in Appendix I. Solving the set of matrix equations simultaneously for **r** and **t** gives the elements of the reflection and transmission matrices for each *Case*. The general forms of solutions to these sets of equations for each *Case* is not presented in this paper due to space limitation. However one can obtain the solutions in either closed-form or numerically. Note that in *Case II* and *Case IV*, the first columns of **r** and **t** are the reflection and transmission coefficients due to incident propagating wave components, and the second columns are due to an incident attenuating wave component which is generally termed as *near-field* since this type of wave decays exponentially with distance. When the distance between the origin of disturbance and the discontinuity is very

large, these attenuating wave components can be neglected. However, as mentioned by many authors, for example Graff [2], attenuating waves play an important role in wave motions by contributing a significant amount of energy to the propagating wave components when a set of propagating and attenuating waves are incident at a discontinuity and, in particular, when the distances between the discontinuities are relatively small, as in the case of closely-spaced multi-span beams. In this paper, near-field components are included. In what follows, the effects of the point supports on the reflection and transmission of an incident wave are studied. For comparison, the results are obtained for both the Timoshenko and the simple Euler-Bernoulli models, which hereafter, for brevity, are denoted by TM and EB, respectively. The system parameters used in the numerical results are taken from Ref. [10]; a_0 = 0.0955 m, ρ = 7700 kg/m^3, K = 0.9, $E = 207\times10^9$ N/m^2, $G = 77.7\times10^9$ N/m^2.

3.1. Wave reflection and transmission at rigid supports

Consider two cases: the simple support and the clamped support. The **r** and **t** are solved and shown as follows.

- Simple support ($k_t = \infty$, $k_r = m = c_t = c_r = J_m = 0$)

Case I ($A > 0$ and $B > 0$):

$$\mathbf{r} = \frac{1}{(\gamma_2-\gamma_1)(\gamma_1\gamma_2+\omega^2)}\begin{bmatrix}\gamma_1(\omega^2-\gamma_2^2) & \gamma_1(\omega^2-\gamma_2^2)\\ \gamma_2(\gamma_1^2-\omega^2) & \gamma_2(\gamma_1^2-\omega^2)\end{bmatrix}, \tag{31a}$$

$$\mathbf{t} = \frac{1}{(\gamma_2-\gamma_1)(\gamma_1\gamma_2+\omega^2)}\begin{bmatrix}\gamma_2(\omega^2-\gamma_1^2) & \gamma_1(\omega^2-\gamma_2^2)\\ \gamma_2(\gamma_1^2-\omega^2) & \gamma_1(\gamma_2^2-\omega^2)\end{bmatrix}, \tag{31b}$$

Case II ($A > 0$ and $B < 0$):

$$\mathbf{r} = \frac{1}{(i\Gamma_1-\Gamma_2)(\Gamma_1\Gamma_2-i\omega^2)}\begin{bmatrix}\Gamma_1(\Gamma_2^2+\omega^2) & \Gamma_1(\Gamma_2^2+\omega^2)\\ -i\Gamma_2(\Gamma_1^2-\omega^2) & -i\Gamma_2(\Gamma_1^2-\omega^2)\end{bmatrix}, \tag{32a}$$

$$\mathbf{t} = \frac{1}{(i\Gamma_1-\Gamma_2)(\Gamma_1\Gamma_2-i\omega^2)}\begin{bmatrix}i\Gamma_2(\Gamma_1^2-\omega^2) & \Gamma_1(\Gamma_2^2+\omega^2)\\ -i\Gamma_2(\Gamma_1^2-\omega^2) & -\Gamma_1(\Gamma_2^2+\omega^2)\end{bmatrix}, \tag{32b}$$

Case IV ($A < 0$ and $B < 0$):

$$\mathbf{r} = \frac{1}{(\Gamma_1-i\Gamma_2)(\Gamma_1\Gamma_2+i\omega^2)}\begin{bmatrix}\Gamma_2(\Gamma_1^2+\omega^2) & \Gamma_2(\Gamma_1^2+\omega^2)\\ -i\Gamma_1(\Gamma_2^2-\omega^2) & -i\Gamma_1(\Gamma_2^2-\omega^2)\end{bmatrix}, \tag{33a}$$

$$\mathbf{t} = \frac{1}{(\Gamma_1 - i\Gamma_2)(\Gamma_1\Gamma_2 + i\omega^2)}\begin{bmatrix} i\Gamma_1(\Gamma_2^2 - \omega^2) & \Gamma_2(\Gamma_1^2 + \omega^2) \\ -i\Gamma_1(\Gamma_2^2 - \omega^2) & -\Gamma_2(\Gamma_1^2 + \omega^2) \end{bmatrix}, \tag{33b}$$

- Clamped support ($k_t = \infty$, $k_r = \infty$, $m = c_t = c_r = J_m = 0$); $\mathbf{t} = 0$ for all *Cases* because no wave can be transmitted through the rigid constraints.

Case I ($A > 0$ and $B > 0$):

$$\mathbf{r} = \frac{1}{(\gamma_1 - \gamma_2)(\gamma_1\gamma_2 + \omega^2)}\begin{bmatrix} (\gamma_1 + \gamma_2)(\gamma_1\gamma_2 - \omega^2) & 2\gamma_1(\gamma_2^2 - \omega^2) \\ -2\gamma_2(\gamma_1^2 - \omega^2) & -(\gamma_1 + \gamma_2)(\gamma_1\gamma_2 - \omega^2) \end{bmatrix}, \tag{34}$$

Case II ($A > 0$ and $B < 0$):

$$\mathbf{r} = \frac{1}{(\Gamma_1 + i\Gamma_2)(\Gamma_1\Gamma_2 + i\omega^2)}\begin{bmatrix} (\Gamma_1 - i\Gamma_2)(\Gamma_1\Gamma_2 - i\omega^2) & -2i\Gamma_1(\Gamma_2^2 + \omega^2) \\ -2\Gamma_2(\Gamma_1^2 - \omega^2) & (\Gamma_1 - i\Gamma_2)(\omega^2 - \Gamma_1\Gamma_2) \end{bmatrix}, \tag{35}$$

Case IV ($A < 0$ and $B < 0$):

$$\mathbf{r} = \frac{1}{(\Gamma_1 - i\Gamma_2)(\Gamma_1\Gamma_2 + i\omega^2)}\begin{bmatrix} (\Gamma_1 + i\Gamma_2)(i\omega^2 - \Gamma_1\Gamma_2) & -2\Gamma_2(\Gamma_1^2 + \omega^2) \\ 2i\Gamma_1(\Gamma_2^2 - \omega^2) & (\Gamma_1 + i\Gamma_2)(\Gamma_1\Gamma_2 - i\omega^2) \end{bmatrix}, \tag{36}$$

The corresponding reflection and transmission matrices for the EB model are listed in App. I.

Figures 3 and 4 plot the moduli (magnitudes) of the reflection and transmission coefficients for the simple and clamped supports. The finite cutoff frequencies, above which all waves propagate, are also marked in the figures. Thus, for the TM model, the wave motions change from *Case II* to *Case I* when $\omega > \omega_c$ ($\omega_c \cong 4$ in Fig. 3, $\omega_c \cong 4.24$ in Fig. 4; ω_c is slightly altered by rotation speed and axial load). The results show that, at low frequencies ($\omega < 0.1 = 3156$ rad/sec), the wave reflection and transmission coefficients of the TM model agree well with those of the EB model for both support conditions. However, as the frequency increases, the wave propagation characteristics of the TM model differ significantly from those of the EB model. These differences can be explained by examining the different modes of vibration. When $\omega > \omega_c$ (in the regime of *Case I*), the vibrating motion of the TM model is dominated by the pure shearing motion [7, 17], and hence the EB model, which neglects the rotary inertia and pure shear effects, become inaccurate at high frequency. As discussed in Ref. [7], at the finite cutoff frequency, the TM shaft experiences no transverse displacement, and the cross-section of the shaft simply rotates back and forth in unison

In Figs. 3(d)-(f) and 4(d)-(f), for $\beta = 0$ and $\varepsilon = 0$, the reflection and transmission coefficients of the EB model are independent of the frequency. This is because from Eqn. (10a), $A = 0$, and Eqns. (9c,d) lead to a single wavenumber $\Gamma_1 = \Gamma_2$. From Appendix I, Eqns. (32*-36*), the $\mathbf{r}$ and $\mathbf{t}$ are thus constant matrices. It is also seen that the wave reflection and transmission coefficients

for both shaft models are basically independent of the rotation speed over the entire frequency range, even at high rotation speed $\beta = 0.05 \cong 44{,}600$ rpm. In Ref. [7], it is also found that β has negligible effects on the system frequency spectrum, phase velocity and group velocity. On the other hand, the effects of the axial load are significant for both propagating and attenuating waves in the regime of *Case II*, see Figs. 3(b)-(c) and 4(b)-(c). For both shaft models under simple support and compressive loads (Figs. 3(b, e)), the reflection coefficient r_{11} of the incident propagating wave is reduced significantly in the regime of *Case II*, while the transmission coefficient t_{11} of the propagating wave component increases to balance the energy carried in the wave. However, the attenuating wave component t_{12} which does not carry any energy loses its transmissibility in the same amount as the reflection coefficient r_{12}. Thus, in the presence of a compressive load, most of the transmitted wave energy in *Case II* comes from the propagating component of the incident wave. Note that axial tensile loads have the reverse effects on these wave components. In the clamped support case, the positive propagating wave component r_{11} is constant over the regime of *Case II* under any loading conditions for the both shaft models, as seen in Fig. 4.

Since there is no damping at the support, the incident power (Π_{inc}), reflected power (Π_{refl}) and transmitted power (Π_{tran}) in *Cases II* and *IV* are related by $\Pi_{inc} = \Pi_{refl}+\Pi_{tran} = (|r_{11}|^2+|t_{11}|^2)\ \Pi_{inc}$, or $|r_{11}|^2+|t_{11}|^2 = 1$. This relationship is confirmed by the plots shown in Figs. 3 and 4, where for both shaft models, $|r_{11}|$ and $|t_{11}|$ cannot exceed one. However in the regime of *Case I*, in which all wave components propagate, the energy balance is $\Pi_{inc} = (|r_{11}+r_{21}|^2+|t_{11}+t_{21}|^2)\ \Pi_{inc}$, or $\Pi_{inc} = (|r_{12}+r_{22}|^2+|t_{12}+t_{22}|^2)\ \Pi_{inc}$. Together with the plots on the phase of these coefficients (not shown to minimize the size of this manuscript), the above relationships can also be verified for wave motion of *Case I*.

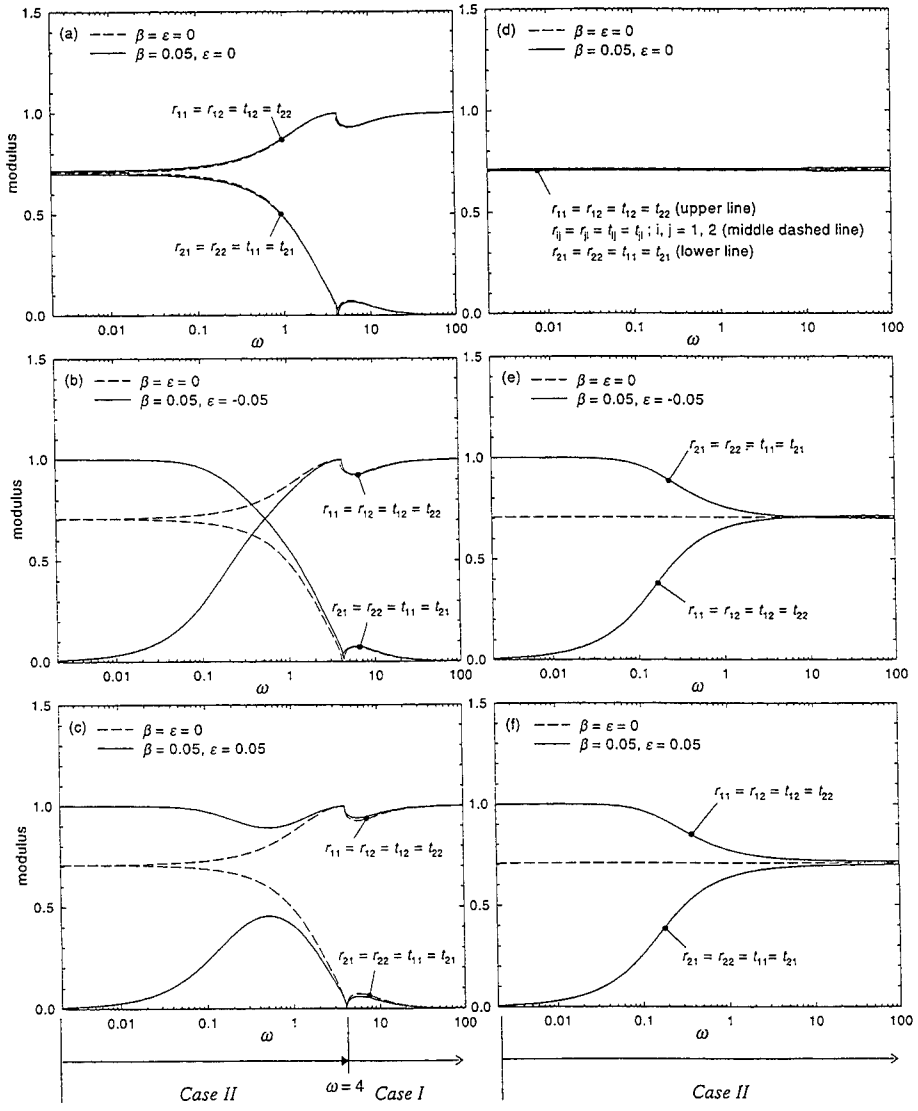

Figure 3. Wave reflection and transmission coefficients at a simple support ($k_t = \infty$ and $k_r = c_t = c_r = m = J_m = 0$) as a function of frequency. (a)-(c) and (d)-(f) are the results for the Timoshenko and Euler-Bernoulli shaft models, respectively. The transition from one type of wave motion to another is marked for the case $\beta = \varepsilon = 0$.

support without "resistance". The impedance mismatching ($r_{11} = 1$, $t_{11} = 0$) frequency at which the propagating wave component is completely reflected without being transmitted can also be determined from Figs. 4(b, d) for the two shaft models. This impedance mismatching frequency is located in the regime of *Case II* for the TM model where the transverse mode dominates the vibrating motion of the shaft. Numerical results show that, as the spring constant increases, this impedance mismatching frequency increases, but is limited to within the regime of *Case II* and can never be found in the regime of *Case I* where the pure shearing mode dominates the vibrating motion of the shaft (refer to Fig. 3 for the transition of types of wave motion).

Figure 6 shows the reflection and transmission coefficients for waves incident upon a support having both translational and rotational constraints. Since both flexural and shearing modes of vibration are constrained at this support, the maximum of the reflection coefficient is expected to be higher than the previous case. Figures 6(a-b) and (c-d) are the results for the TM and EB models, respectively. The translational and rotational spring constants used in the simulations are $k_{t0} = 10^9$ N/m and $k_{r0} = 10^9$ Nm/rad, respectively. It is noted that in the regime of *Case II*, i.e.,

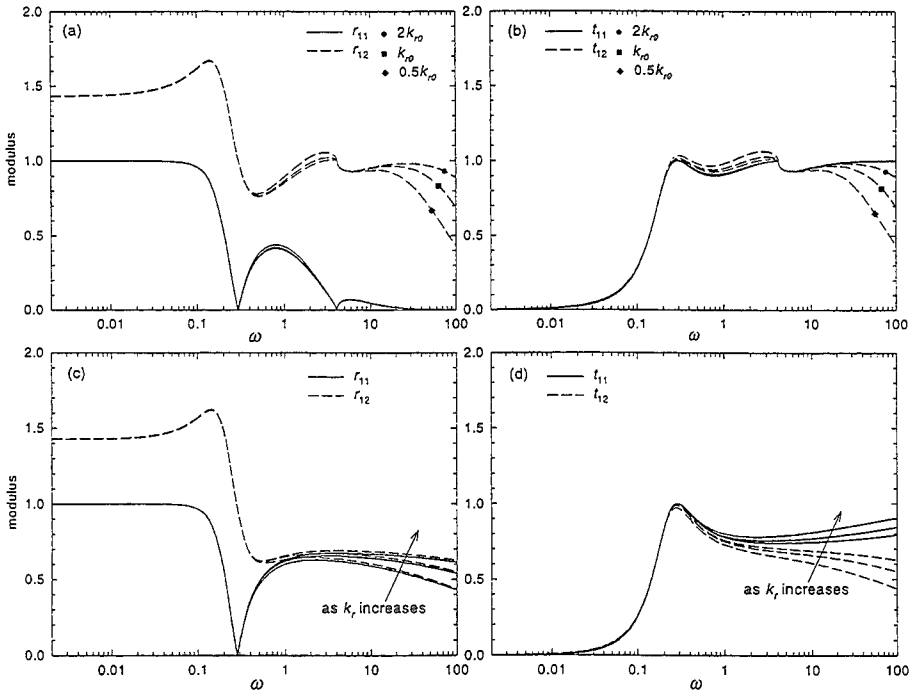

Figure 6. Wave reflection and transmission coefficients at an elastic support with translational and rotational springs ($k_t = k_{t0}$, $k_r \neq 0$, $c_t = c_r = m = J_m = 0$) as a function of frequency, $\beta = 0.05$ and $\varepsilon = 0$. (a-b) and (c-d) are results for the Timoshenko and Euler-Bernoulli shaft models, respectively.

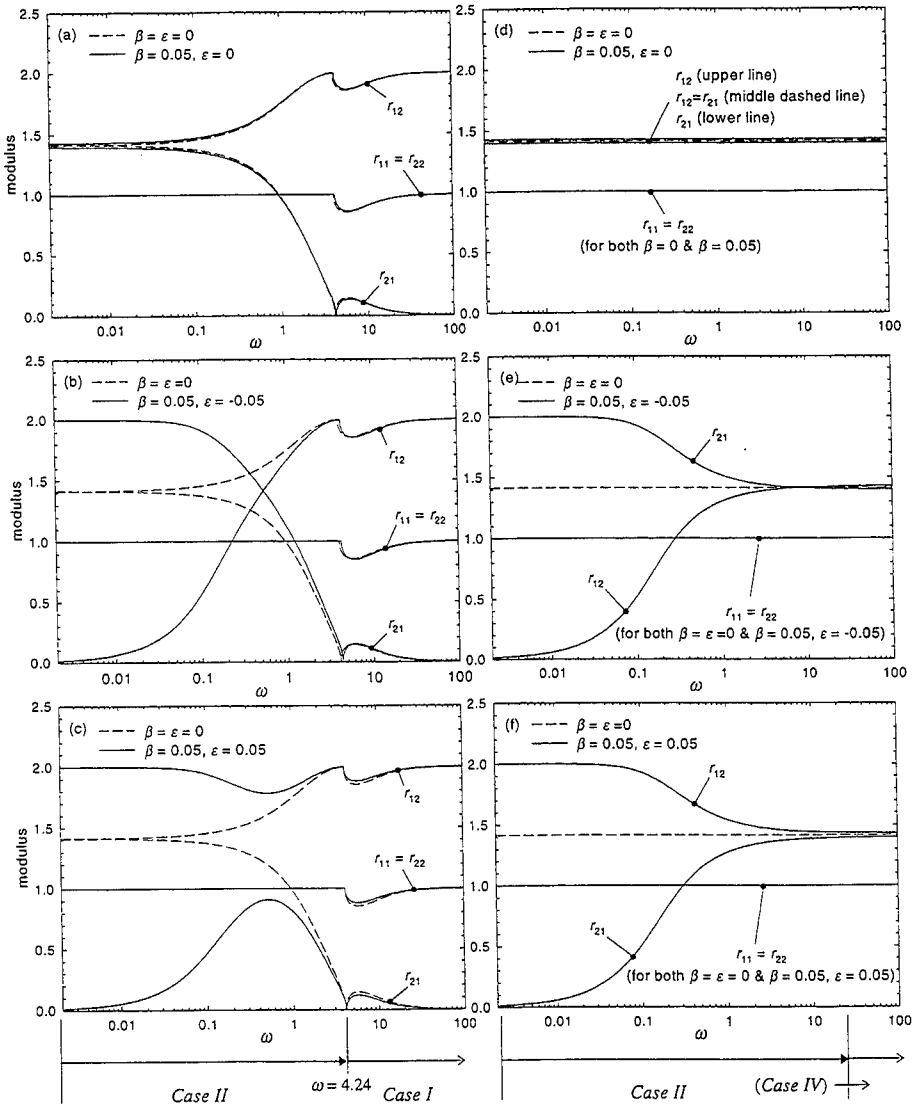

Figure 4. Wave reflection coefficients at a clamped support ($k_t = k_r = \infty$ and $c_t = c_r = m = J_m = 0$) as a function of frequency. (a)-(c) and (d)-(f) are the results for the Timoshenko and Euler-Bernoulli shaft models, respectively. The transition from one type of wave motion to another is marked for the case $\beta = 0.05$, $\varepsilon = -0.05$.

3.2. Wave reflection and transmission at elastic supports

Figure 5 shows the reflection and transmission coefficients for waves incident upon a support with a finite translational spring for three different spring constants. Figures 5(a)-(b) and (c)-(d) are results for the TM and EB models, respectively. The spring constant used, $k_{t0} = 10^9$ N/m, is a typical bearing spring constant value for turbine generators. The plots show that there is no significant difference in the moduli between the two shaft models. This is because the incident wave does not experience any rotational constraint at the support, and hence the additional rotary inertia factor in the TM model has only a small contribution to the wave motions. As the support spring constant increases, the curves for both the reflection and transmission coefficients are shifted to the right and, as the spring constant approaches infinity, these curves eventually become asymptotic to those shown in Fig. 3. Note that an impedance matching ($\mathbf{r} = 0$, $\mathbf{t} = \mathbf{I}$), where all wave components are transmitted without being reflected, is found in the high frequency region for both shaft models. Thus, as the frequency increases, the characteristics of waves travelling along the shaft remain unchanged such that waves propagate through this elastic

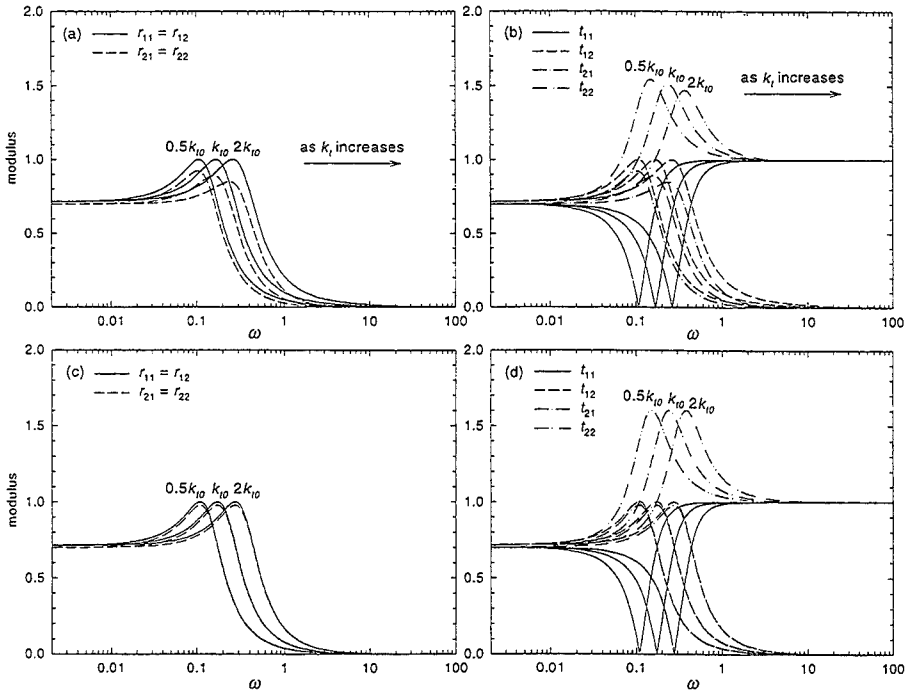

Figure 5. Wave reflection and transmission coefficients at an elastic support with a translational spring ($k_t \neq 0$, $k_r = c_t = c_r = m = J_m = 0$) as a function of frequency, $\beta = 0.05$ and $\varepsilon = 0$. (a-b) and (c-d) are results for the Timoshenko and Euler-Bernoulli shaft models, respectively.

in the low frequency range, both shaft models have similar reflection characteristics, and both the reflection and transmission coefficients are not significantly affected by the rotational spring. However, as the frequency increases, the effect of the rotational constraint on the wave motion becomes eminent, particularly for the TM model. As seen in Figs. 6(a) and 6(c), the reflection of the attenuating wave components are significantly higher than those of the propagating wave components. Hence, when a rotating shaft has a clamped support(s) such as a journal bearing, contributions from the attenuating wave components should be included in the formulation since a significant amount of energy in the propagating component arises from the incident attenuating wave component. It is noted that the impedance matching regions seen in Figs 5(a, c) disappear when the rotational constraint is added. Moreover, the impedance mismatching frequency shown in Figs. 5(b, d), which is found in the regime of *Case II*, also does not occur. At low frequency in Figs. 6 (b, d), there appears to be a mismatching region, but t_{11} is not exactly equal to zero. From Figs. 6(a, c), it is seen that there is a frequency at which the positive propagating wave component r_{11} is zero (this frequency is slightly different for the two models). This frequency does not correspond to an impedance matching, though the propagating wave is not reflected at all but is only transmitted ($t_{11} = 1$). Based on other research results [18], this phenomenon likely indicates a structural *mode delocalization* in bi-coupled systems, in which vibrations on both sides of the support become strongly coupled. Further research on the vibrations of rotating shafts with intermediate supports is being pursued to confirm the mode delocalization.

Figure 7 plots the effects of axial compressive loads on the wave reflection and transmission upon a support with finite spring constant for the Timoshenko shaft model. As seen in Fig. 7(a), the reflection coefficient for the incident propagating wave component r_{11} is substantially reduced in the low frequency range while the reflection coefficient for the incident attenuating wave component increases significantly. However, Fig. 7(b) shows the reversed effects on the transmission coefficient. It can therefore be concluded that, when the shaft is axially strained by

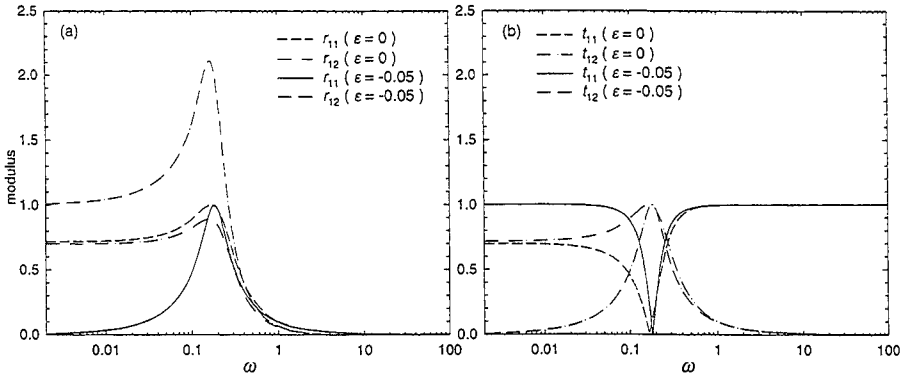

Figure 7. Wave reflection and transmission coefficients at an elastic support ($k_t = k_{t0}$ and $k_r = c_t = c_r = m = J_m = 0$) for the Timoshenko shaft model with and without the compressive load. (a) reflection coefficients, (b) transmission coefficients.

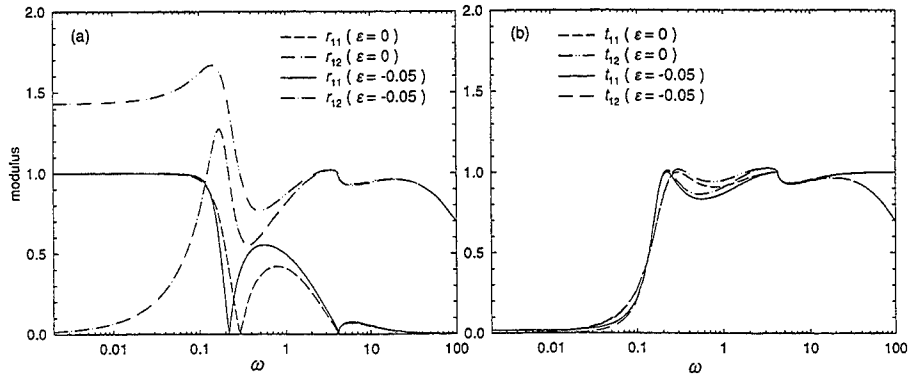

Figure 8. Wave reflection and transmission coefficients at an elastic support ($k_t = k_{t0}$, $k_r = k_{r0}$ and $c_t = c_r = m = J_m = 0$) for the Timoshenko shaft model with and without the compressive load. (a) reflection coefficients, (b) transmission coefficients.

compressive loads, the energy contribution from the incident attenuating wave component to the energy in the reflected propagating wave is more significant than the strain-free situation in the low frequency range, while most of the energy in the transmitted wave derives from the incident propagating wave component.

Figure 8 plots the wave reflection and transmission coefficients along an axially compressed Timoshenko shaft model at a support with finite translational and rotational spring constants. Similar results to the previous example can be observed in terms of energy contribution from the incident attenuating wave component in the low frequency range. However, the effects of the axial compressive load on both the reflection and transmission coefficients for the propagating wave component (r_{11} and t_{11}) are significantly reduced when compared to Fig. 7.

3.3. Wave reflection and transmission at damped supports

Figure 9 shows the effects of both translational and rotational dampers at a support with finite translational and rotational spring constants. Figures 9(a, b) and (c, d) are results for the TM and EB models, respectively. The translational and rotational damping constants used in this study are $c_{dt0} = 2\times10^5$ Ns/m and $c_{dr0} = 64\times10^5$ N-m-s/rad, typical values for bearings in turbine generators. The curves with symbols (● and ◆) are the results when the rotational damping factor is also included in the formulation. It can be seen that $|t_{11}|$ and $|t_{12}|$ for both shaft models are significantly lowered due to the presence of damping. Note that, because of the damping, the frequency at which $|r_{11}| = 0$ (compare with Figs. 6(a, c)) no longer exists for both shaft models. It can also be seen that the effect of the rotational damping factor on the wave reflection and transmission is not significant over the entire frequency range for both shaft models. For TM model, the contribution of the rotational damping to both $|r_{11}|$ and $|t_{11}|$ is almost negligible. The

support condition considered in this particular example is simulated as an actual bearing support adopted in turbine generators. Hence for this particular type of bearing support, the effect of the rotational damping on wave reflection and transmission is not considerable. Other numerical results (not shown in this paper) show that the wave propagation at the damped support is characterized by translational damping rather than rotational damping. Note that similar results have been presented for the support without damping (see Fig. 6).

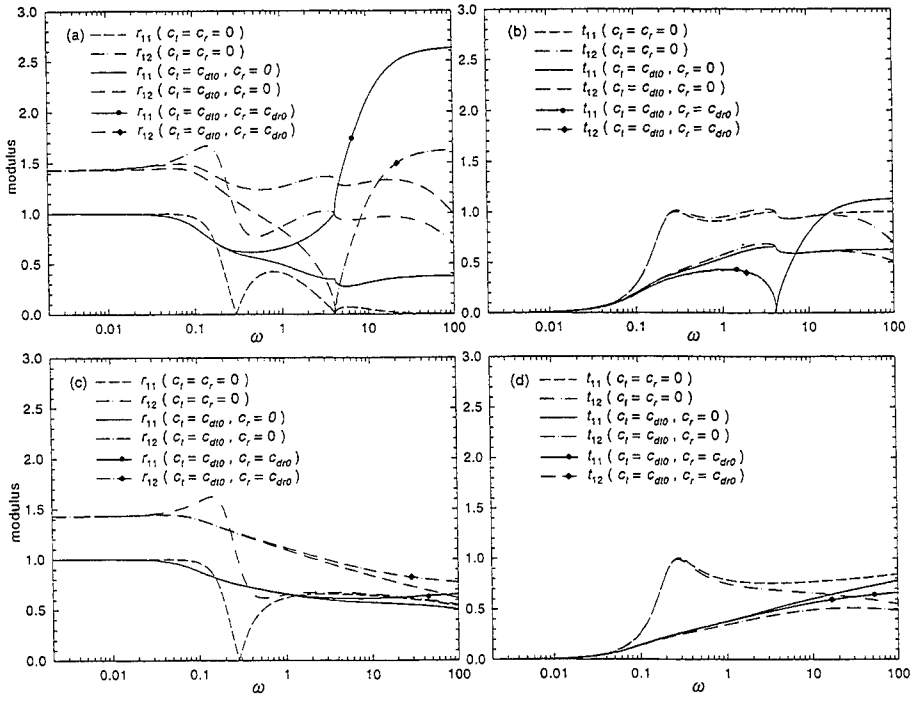

Figure 9. Wave reflection and transmission coefficients at an elastic support with damping ($k_t = k_{t0}$, $k_r = k_{r0}$, $c_t = c_{dt0}$, $c_r = c_{dr0}$ and $m = J_m = 0$) as a function of frequency for $\beta = 0.05$ and $\varepsilon = 0$. (a-b) and (c-d) are results for the Timoshenko and Euler-Bernoulli shaft models, respectively.

3.4. Wave reflection and transmission at a rotor mass

Consider a gear rigidly assembled to a rotating shaft. The gear is assumed to be perfectly balanced and its thickness is sufficiently small such that wave reflection and transmission due to the geometric discontinuity between the shaft and the gear can be neglected. However the gear does resist the translational and rotational motions of the cross-sectional element of the shaft.

Figure 10 shows the reflection and transmission upon the gear when the mass m_0 and mass moment of inertia J_{m0} of the gear are 4 and 16 times of the shaft, respectively. Not shown in Figs. 10 (b, d) is that $r_{ij} = 0$, $t_{12} = 0$ when $m = J_m = 0$. Like some previous support conditions discussed, the effects of the rotor mass are much more significant in the high frequency region for both models (particularly around and beyond the cutoff frequency for the TM model). In general, the rotor mass decreases the transmission and increases the reflection of the wave. At very high frequency, there is basically no wave transmission. Note that, since the geometric discontinuity between the shaft and the gear is neglected in this model, one may expect that the actual reflection for both the propagating and attenuating wave components would be higher.

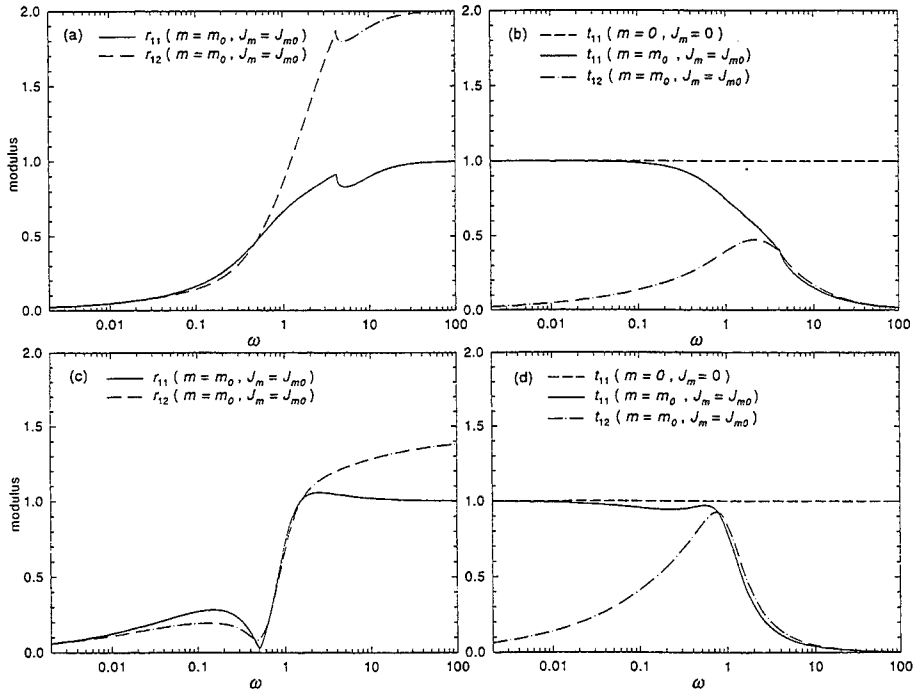

Figure 10. Wave reflection and transmission at a rotor mass assembled to a rotating shaft ($k_t = 0 = k_r = c_t = c_r = 0$, and $m = m_0$, and $J_m = J_{m0}$) as a function of frequency when $\beta = 0.05$ and $\varepsilon = 0$. (a-b) and (c-d) are results for the Timoshenko and Euler-Bernoulli shaft models, respectively.

4. WAVE REFLECTION AND TRANSMISSION AT A GEOMETRIC DISCONTINUITY

It is common for a rotating shaft element to have changes in cross-section, or to be joined to

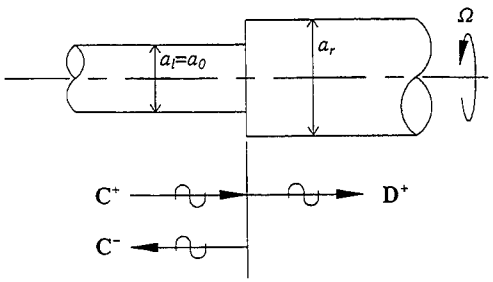

Case I, II, or *IV*

$$A_l = (1+\alpha)\omega^2 - 2\beta\omega - 16\varepsilon\,(1+\varepsilon-\frac{\varepsilon}{\alpha})$$

$$B_l = \omega^2\left[\alpha\,\omega^2 - 2\beta\omega - 16\alpha\,(1+\varepsilon)(1+\varepsilon-\frac{\varepsilon}{\alpha})\right]$$

Case I, II, or *IV*

$$A_r = (1+\alpha)\omega^2 - 2\beta\omega - \frac{16\varepsilon_r}{\sigma^2}\,(1+\varepsilon_r-\frac{\varepsilon_r}{\alpha})$$

$$B_r = \omega^2\left[\alpha\,\omega^2 - 2\beta\omega - \frac{16\alpha}{\sigma^2}\,(1+\varepsilon_r)(1+\varepsilon_r-\frac{\varepsilon_r}{\alpha})\right]$$

Figure 11. Wave reflection and transmission at a geometric discontinuity.

another shaft element by a coupling. Figure 11 shows a typical example of a discontinuous shaft model in which two shafts of differing wavenumber and diameter are joined at $z=0$. The subscripts l and r denote $z=0^-$ and $z=0^+$ regions, respectively. It is known that when a wave encounters a junction or a discontinuity, its wavenumber is changed. It is therefore possible that a wave on the left side of the junction can be propagating, while after crossing the junction to the right side, the wave becomes attenuating. Therefore, for a Timoshenko shaft, when a wave propagates through the junction, there are mathematically nine possible different combinations of wave motions to be considered depending on the values of the functions A and B on each side of the junction, as depicted in Fig. 12.

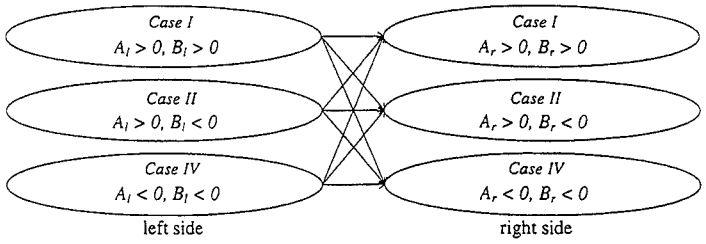

Figure 12. Nine possible combinations of wave motions at a geometric discontinuity of the cross section for the Timoshenko shaft model. Subscripts l and r denote the left and the right side of the discontinuity, respectively.

For simplicity, assume that material properties such as ρ, E, and G are the same for both sides of shaft element. The displacement continuity, moment and force equilibrium conditions are applied at the junction to determine the wave refection and transmission matrices. Results for the three most commonly encountered possibilities in the low frequency regime are listed as follows.

Case II ($A_l > 0$, $B_l < 0$) – *Case I* ($A_r > 0$, $B_r > 0$):

$$\begin{bmatrix} 1 & 1 \\ \eta_{1l} & \eta_{2l} \end{bmatrix}\mathbf{C}^+ + \begin{bmatrix} 1 & 1 \\ -\eta_{1l} & -\eta_{2l} \end{bmatrix}\mathbf{rC}^+ = \begin{bmatrix} 1 & 1 \\ \eta_{1r} & \eta_{2r} \end{bmatrix}\mathbf{tC}^+, \tag{37a}$$

$$\begin{bmatrix} -i\Gamma_{1l}\eta_{1l} & -\Gamma_{2l}\eta_{2l} \\ i(\Gamma_{1l}-\eta_{1l}) & \Gamma_{2l}-i\eta_{2l} \end{bmatrix}\mathbf{C}^+ + \begin{bmatrix} -i\Gamma_{1l}\eta_{1l} & -\Gamma_{2l}\eta_{2l} \\ -i(\Gamma_{1l}-\eta_{1l}) & -(\Gamma_{2l}-i\eta_{2l}) \end{bmatrix}\mathbf{rC}^+$$

$$= \begin{bmatrix} -i\sigma^4\gamma_{1r}\eta_{1r} & -i\sigma^4\gamma_{2r}\eta_{2r} \\ -i\sigma^2(\gamma_{1r}-\eta_{1r}) & -i\sigma^2(\gamma_{2r}-\eta_{2r}) \end{bmatrix}\mathbf{tC}^+, \tag{37b}$$

Case II ($A_l > 0$, $B_l < 0$) – *Case II* ($A_r > 0$, $B_r < 0$):

$$\begin{bmatrix} 1 & 1 \\ \eta_{1l} & \eta_{2l} \end{bmatrix}\mathbf{C}^+ + \begin{bmatrix} 1 & 1 \\ -\eta_{1l} & -\eta_{2l} \end{bmatrix}\mathbf{rC}^+ = \begin{bmatrix} 1 & 1 \\ \eta_{1r} & \eta_{2r} \end{bmatrix}\mathbf{tC}^+, \tag{38a}$$

$$\begin{bmatrix} -i\Gamma_{1l}\eta_{1l} & -\Gamma_{2l}\eta_{2l} \\ i(\Gamma_{1l}-\eta_{1l}) & \Gamma_{2l}-i\eta_{2l} \end{bmatrix}\mathbf{C}^+ + \begin{bmatrix} -i\Gamma_{1l}\eta_{1l} & -\Gamma_{2l}\eta_{2l} \\ -i(\Gamma_{1l}-\eta_{1l}) & -(\Gamma_{2l}-i\eta_{2l}) \end{bmatrix}\mathbf{rC}^+$$

$$= \begin{bmatrix} -i\sigma^4\Gamma_{1r}\eta_{1r} & -\sigma^4\Gamma_{2r}\eta_{2r} \\ -i\sigma^2(\Gamma_{1r}-\eta_{1r}) & -\sigma^2(\Gamma_{2r}-\eta_{2r}) \end{bmatrix}\mathbf{tC}^+, \tag{38b}$$

Case II ($A_l > 0$, $B_l < 0$) – *Case IV* ($A_r < 0$, $B_r < 0$):

$$\begin{bmatrix} 1 & 1 \\ \eta_{1l} & \eta_{2l} \end{bmatrix}\mathbf{C}^+ + \begin{bmatrix} 1 & 1 \\ -\eta_{1l} & -\eta_{2l} \end{bmatrix}\mathbf{rC}^+ = \begin{bmatrix} 1 & 1 \\ \eta_{2r} & \eta_{1r} \end{bmatrix}\mathbf{tC}^+, \tag{39a}$$

$$\begin{bmatrix} -i\Gamma_{1l}\eta_{1l} & -\Gamma_{2l}\eta_{2l} \\ i(\Gamma_{1l}-\eta_{1l}) & \Gamma_{2l}-i\eta_{2l} \end{bmatrix}\mathbf{C}^+ + \begin{bmatrix} -i\Gamma_{1l}\eta_{1l} & -\Gamma_{2l}\eta_{2l} \\ -i(\Gamma_{1l}-\eta_{1l}) & -(\Gamma_{2l}-i\eta_{2l}) \end{bmatrix}\mathbf{rC}^+$$

$$= \begin{bmatrix} -i\sigma^4\Gamma_{2r}\eta_{2r} & -\sigma^4\Gamma_{1r}\eta_{1r} \\ -i\sigma^2(\Gamma_{2r}-\eta_{2r}) & -\sigma^2(\Gamma_{1r}-\eta_{1r}) \end{bmatrix}\mathbf{tC}^+. \tag{39b}$$

where σ is the diameter ratio between the shaft elements, defined as

$$\sigma = \frac{a_r}{a_l}. \tag{40}$$

Note that η_l's in Eqns. (37a-39b) are given by Eqns. (20a, b), (22a, b), and (24a, b) according to the type of wave motion, and η_r's on the right side of the geometric discontinuity are modified as follows.

$$\eta_{1r} = \frac{\gamma_{1r}^2 - \omega^2}{\gamma_{1r}\varepsilon_r'}, \ \eta_{2r} = \frac{\gamma_{2r}^2 - \omega^2}{\gamma_{2r}\varepsilon_r'} \text{ for } \textit{Case I}, \tag{41a, b}$$

$$\eta_{1r} = \frac{\Gamma_{1r}^2 - \omega^2}{\Gamma_{1r}\varepsilon_r'}, \ \eta_{2r} = \frac{\Gamma_{2r}^2 + \omega^2}{i\Gamma_{2r}\varepsilon_r'} \text{ for } \textit{Case II}, \tag{42a, b}$$

$$\eta_{1r} = \frac{\Gamma_{1r}^2 + \omega^2}{i\Gamma_{1r}\varepsilon_r'}, \ \eta_{2r} = \frac{\Gamma_{2r}^2 - \omega^2}{\Gamma_{2r}\varepsilon_r'} \text{ for } \textit{Case IV}, \tag{43a, b}$$

where

$$\varepsilon_r' = 1 + \varepsilon_r - \frac{\varepsilon_r}{\alpha}, \text{ and } \varepsilon_r = \frac{\varepsilon}{\sigma^2}. \tag{44}$$

Moreover, the wavenumbers, A and B of the shaft element on the right side of the junction are modified as follows.

$$\gamma_{1r} = \frac{1}{\sqrt{2}}\left(A_r + \sqrt{A_r^2 - 4B_r}\right)^{\frac{1}{2}}, \ \gamma_{2r} = \frac{1}{\sqrt{2}}\left(A_r - \sqrt{A_r^2 - 4B_r}\right)^{\frac{1}{2}}, \tag{45a, b}$$

$$\Gamma_{1r} = \frac{1}{\sqrt{2}}\left(\sqrt{A_r^2 + 4|B_r|} + |A_r^2|\right)^{\frac{1}{2}}, \ \Gamma_{2r} = \frac{1}{\sqrt{2}}\left(\sqrt{A_r^2 + 4|B_r|} - |A_r^2|\right)^{\frac{1}{2}}, \tag{45c, d}$$

where,

$$A_r = (1+\alpha)\omega^2 - 2\beta\omega - \frac{16\varepsilon_r}{\sigma^2}(1 + \varepsilon_r - \frac{\varepsilon_r}{\alpha}), \tag{46a}$$

$$B_r = \omega^2\left[\alpha\,\overline{\omega}^2 - 2\beta\,\overline{\omega} - \frac{16\alpha}{\sigma^2}(1+\varepsilon_r)(1 + \varepsilon_r - \frac{\varepsilon_r}{\alpha})\right], \tag{46b}$$

Corresponding results for the simple Euler-Bernoulli shaft model are listed in Appendix II.

Figures 13 to 16 show some representative examples of wave reflection and transmission upon the geometric discontinuity. In Figs. 13 and 14, the thick and thin curves represent results

for the TM and EB models, respectively. The second graph in each figure shows the changes of A_l, B_l, A_r and B_r, and how wave solutions on both sides of the discontinuity change as the frequency increases for the TM model. In general, the wave reflection and transmission for the EB model are frequency independent except when the shaft is axially strained, while the wave propagation characteristics for the TM model are strongly dependent on the frequency.

Comparing Figs. 13 and 14, it is noted that, for both shaft models, the average reflection and transmission rates for $\sigma = 0.8$ are higher than those for $\sigma = 1.2$, especially for the attenuating wave components. These results imply that incident attenuating waves contribute more energy to propagating waves at the discontinuity when the waves travel from a smaller to a larger cross-section. In particular, it is noted that the transmissibility of the attenuating wave t_{12} has a strong dependency on the direction of propagation. Note also that the differences between the two shaft models are more pronounced when $\sigma = 0.8$. It is clearly seen from the figures that when B_l and B_r change from negative to positive, both reflection and transmission coefficients experience a sharp jump or drop at the finite cutoff frequencies, due to changes in the types of wave motion. In the frequency region ($B_l > 0$ and $B_r < 0$) located between the two cutoff frequencies in Fig.

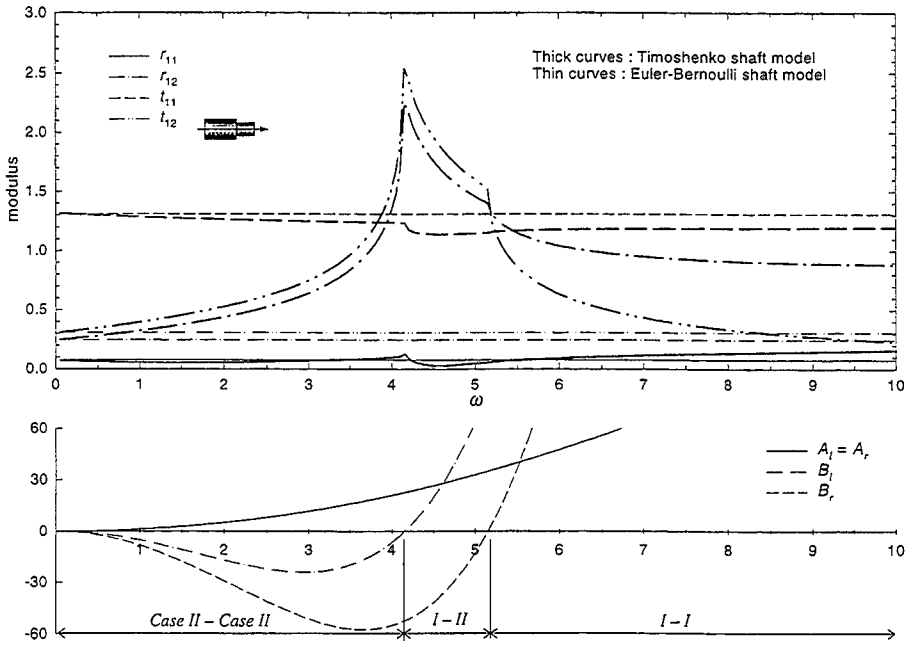

Figure 13. Reflection and transmission of waves incident upon a change in the cross-section, $\sigma = 0.8$, $\beta = 0.05$, and $\varepsilon = 0$. Thick and thin curves are results for the Timoshenko and Euler-Bernoulli shaft models, respectively. Note that the ordinates in the lower graphs keep increasing with frequency (abscissa).

13, the wave motion on the left side of the junction is governed by the wave solution of *Case I* since all wave components are propagating at a frequency larger than the cutoff frequency, while the wave motion on the right side of the junction is governed by the wave solution of *Case II*. Thus, for $\sigma = 0.8$, some of the propagating wave components on the left side of the shaft element cannot propagate as they pass the discontinuity, and become attenuating. A similar, but converse conclusion can be drawn for the frequency region ($B_r > 0$, $B_l < 0$) when $\sigma = 1.2$, as shown in Fig. 14. The results of Figs. 13 and 14 show that, for different system parameters σ, β, and ε and at any given frequency, the types of wave motion on each side of the discontinuity can be different, as depicted in Fig. 12.

From Eqns. (41a-43b), it is seen that when the Timoshenko shaft is axially strained and ω is not sufficiently large, the wavenumber (hence wave propagation characteristics) depends strongly on the cross-section ratio σ. Figure 15 shows the effects of the axial load on the wave reflection and transmission, which are mostly limited to the relatively low frequency region. In Figs. 15(a-b), when the shaft is axially compressed ($\varepsilon = -0.05$), the reflection and transmission due to the incident attenuating wave component decrease for both $\sigma < 1$ (plot (a)) and $\sigma > 1$ (plot (b)). However, the transmission t_{11} due to an incident propagating wave decreases significantly for

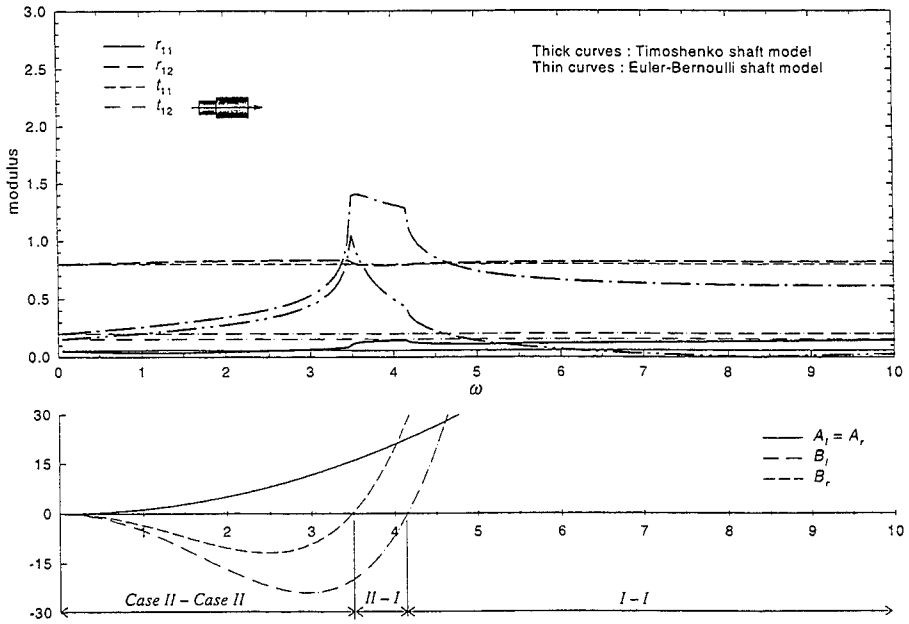

Figure 14. Reflection and transmission of waves incident upon a change in the cross-section, $\sigma = 1.2$, $\beta = 0.05$, and $\varepsilon = 0$. Thick and thin curves are results for the Timoshenko and Euler-Bernoulli shaft models, respectively. Note that the ordinates in the lower graphs keep increasing with frequency (abscissa).

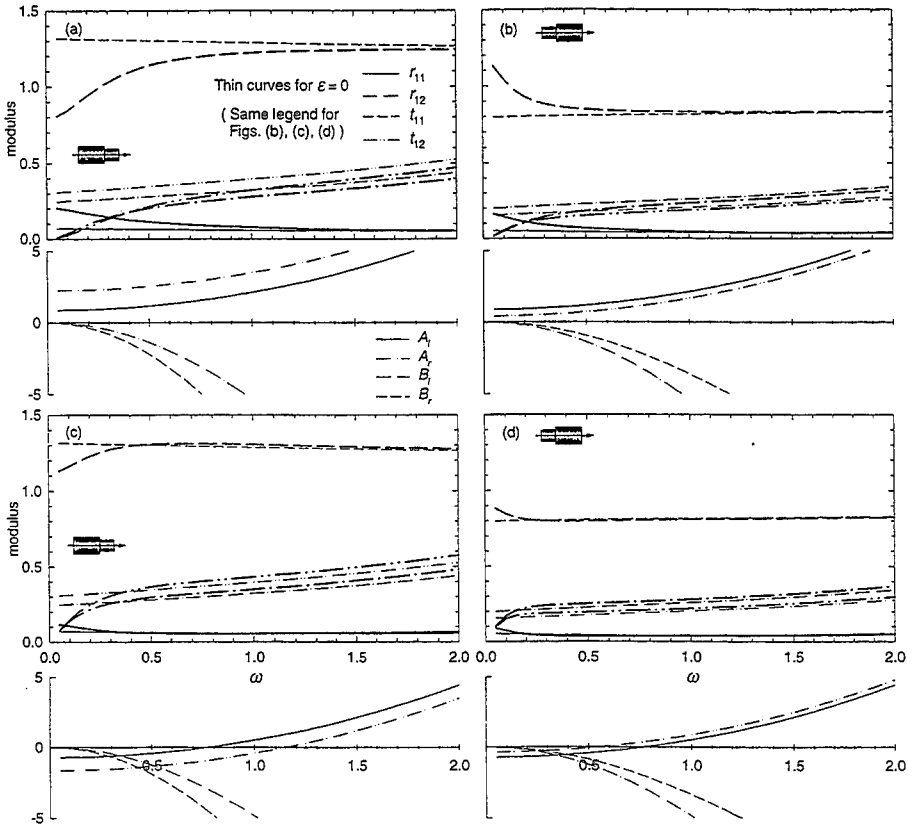

Figure 15. Reflection and transmission of waves upon a change in the cross-section when β = 0.05 for the Timoshenko shaft model. (a) $\sigma = 0.8$ and $\varepsilon = -0.05$. (b) $\sigma = 1.2$ and $\varepsilon = -0.05$. (c) $\sigma = 0.8$ and $\varepsilon = 0.05$. (d) $\sigma = 1.2$ and $\varepsilon = 0.05$. Thin and thick curves show the results when the shaft is strain-free ($\varepsilon = 0$) and strained, respectively.

$\sigma = 0.8$ and increases for $\sigma = 1.2$ at low frequency.

Effects of the axial load on the wave reflection and transmission are more significant when the shaft is compressed (Figs. 15(a-b)) than when it is under tension (Figs. 15(c-d)). This is because the wavenumbers of both the propagating and attenuating wave components are only slightly changed. It is also noted that, in the low frequency range, the wave solution of *Case IV* governs the wave motions on both sides of the discontinuity, and the wave components which have large wavenumber (Γ_1) attenuate, while wave components with small wavenumber (Γ_2) propagate along the waveguide as long as A remains negative.

5. WAVE REFLECTION AT BOUNDARIES

When a wave is incident upon a boundary, it is only reflected because no waveguide exists beyond the boundary. Consider an arbitrary boundary condition with translational and rotational spring constraints, dampers, and a rotor mass, as shown in Fig. 16. The reflection matrix at the boundary is derived for each *Case*. Applying the same non-dimensional parameters employed in Section 3, and by imposing the force and moment balances at the boundary, which can be deduced by eliminating M^+ and V^+ in Eqns. (27a, b),

$$M^- = k_r\psi + c_r\dot{\psi} + J_m\ddot{\psi}\,, \tag{47a}$$

$$-V^- = k_t u + c_t\dot{u} + m\ddot{u}\,, \tag{47b}$$

the reflection matrix for each *Case* is determined.

Case I ($A>0$, $B>0$):

$$\mathbf{r} = \begin{bmatrix} \eta_1(i\gamma_1 - \Sigma_m) & \eta_2(i\gamma_2 - \Sigma_m) \\ i(\gamma_1 - \eta_1) + \Sigma_s & i(\gamma_2 - \eta_2) + \Sigma_s \end{bmatrix}^{-1} \begin{bmatrix} -\eta_1(i\gamma_1 + \Sigma_m) & -\eta_2(i\gamma_2 + \Sigma_m) \\ i(\gamma_1 - \eta_1) - \Sigma_s & i(\gamma_2 - \eta_2) - \Sigma_s \end{bmatrix}, \tag{48}$$

Case II ($A>0$, $B<0$):

$$\mathbf{r} = \begin{bmatrix} \eta_1(i\Gamma_1 - \Sigma_m) & \eta_2(\Gamma_2 - \Sigma_m) \\ i(\Gamma_1 - \eta_1) + \Sigma_s & (\Gamma_2 - i\eta_2) + \Sigma_s \end{bmatrix}^{-1} \begin{bmatrix} -\eta_1(i\Gamma_1 + \Sigma_m) & -\eta_2(\Gamma_2 + \Sigma_m) \\ i(\Gamma_1 - \eta_1) - \Sigma_s & (\Gamma_2 - i\eta_2) - \Sigma_s \end{bmatrix}, \tag{49}$$

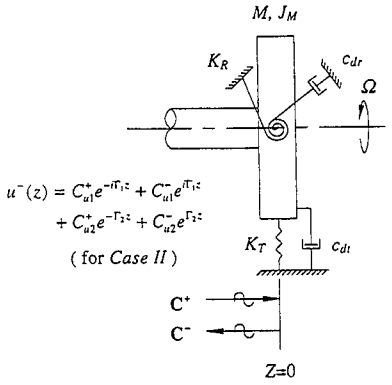

Figure 16. Wave reflection upon a general boundary.

Case IV ($A<0$, $B<0$):

$$\mathbf{r}=\begin{bmatrix} \eta_2(i\Gamma_2-\Sigma_m) & \eta_1(\Gamma_1-\Sigma_m) \\ i(\Gamma_2-\eta_2)+\Sigma_s & (\Gamma_1-i\eta_1)+\Sigma_s \end{bmatrix}^{-1}\begin{bmatrix} -\eta_2(i\Gamma_2+\Sigma_m) & -\eta_1(\Gamma_1+\Sigma_m) \\ i(\Gamma_2-\eta_2)-\Sigma_s & (\Gamma_1-i\eta_1)-\Sigma_s \end{bmatrix}, \tag{50}$$

where η's in above equations have been defined in Eqns. (20a, b), (22a, b) and (24a, b), and

$$\Sigma_m = k_r + ic_r\omega - J_m\omega^2 \text{, and } \Sigma_s = k_t + ic_t\omega - m\omega^2 \text{ ,} \tag{51a, b}$$

The corresponding results for the simple Euler-Bernoulli shaft model are listed in the Appendix III. By specifying the parameters in the reflection matrix **r**, results for three typical boundary conditions (simple support, clamped support, and free end) can be obtained.

- Simple support ($k_t=\infty$, $k_r=m=c_t=c_r=J_m=0$)

$$\mathbf{r}=\begin{bmatrix} -1 & 0 \\ 0 & -1 \end{bmatrix} \text{ for } \textit{Case I, II, and IV,} \tag{52}$$

- Clamped support ($k_t=\infty$, $k_r=\infty$, $m=c_t=c_r=J_m=0$)

$$\mathbf{r}=\frac{1}{\eta_1-\eta_2}\begin{bmatrix} \eta_1+\eta_2 & 2\eta_2 \\ -2\eta_1 & -(\eta_1+\eta_2) \end{bmatrix} \text{ for } \textit{Case I,} \tag{53a}$$

$$\mathbf{r}=\frac{1}{\eta_1-\eta_2}\begin{bmatrix} \eta_1+\eta_2 & 2\eta_2 \\ -2\eta_1 & -(\eta_1+\eta_2) \end{bmatrix} \text{ for } \textit{Case II,} \tag{53b}$$

$$\mathbf{r}=\frac{1}{\eta_1-\eta_2}\begin{bmatrix} -(\eta_1+\eta_2) & -2\eta_2 \\ 2\eta_1 & (\eta_1+\eta_2) \end{bmatrix} \text{ for } \textit{Case IV,} \tag{53c}$$

- Free end ($k_t=k_r=m=c_t=c_r=J_m=0$, and $\varepsilon=0$)

$$\mathbf{r}=\frac{1}{\Delta_I}\begin{bmatrix} \eta_1\eta_2(\gamma_1+\gamma_2)-\gamma_1\gamma_2(\eta_1+\eta_2) & 2\eta_2\gamma_2(\eta_2-\gamma_2) \\ -2\eta_1\gamma_1(\eta_1-\gamma_1) & -\eta_1\eta_2(\gamma_1+\gamma_2)+\gamma_1\gamma_2(\eta_1+\eta_2) \end{bmatrix} \tag{54a}$$

where, $\Delta_I=\eta_1\eta_2(\gamma_2-\gamma_1)+\gamma_1\gamma_2(\eta_1-\eta_2)$ for *Case I,*

$$\mathbf{r}=\frac{1}{\Delta_{II}}\begin{bmatrix} -\eta_1\eta_2(i\gamma_1+\gamma_2)+\gamma_1\gamma_2(\eta_1+\eta_2) & 2i\eta_2\gamma_2(i\eta_2-\gamma_2) \\ 2i\eta_1\gamma_1(\eta_1-\gamma_1) & \eta_1\eta_2(i\gamma_1+\gamma_2)-\gamma_1\gamma_2(\eta_1+\eta_2) \end{bmatrix} \tag{54b}$$

where, $\Delta_{II}=\eta_1\eta_2(i\gamma_1-\gamma_2)-\gamma_1\gamma_2(\eta_1-\eta_2)$ for *Case II,*

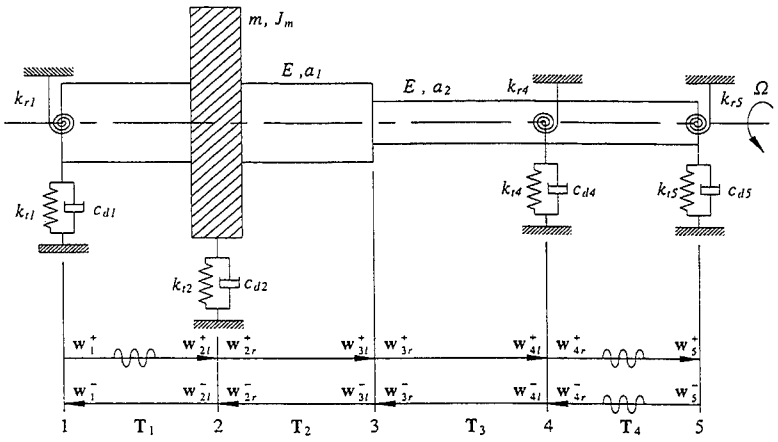

Figure 17. An example of a rotating shaft with multiple supports and discontinuities.

$$\mathbf{r} = \frac{1}{\Delta_{IV}} \begin{bmatrix} \eta_1\eta_2(\gamma_1 + i\gamma_2) - \gamma_1\gamma_2(\eta_1 + \eta_2) & 2\eta_1\gamma_1(\eta_1 + i\gamma_1) \\ -2i\eta_2\gamma_2(\eta_2 - \gamma_2) & -\eta_1\eta_2(\gamma_1 + i\gamma_2) + \gamma_1\gamma_2(\eta_1 + \eta_2) \end{bmatrix} \tag{54c}$$

where, $\Delta_{IV} = \eta_1\eta_2(\gamma_1 - i\gamma_2) - \gamma_1\gamma_2(\eta_1 - \eta_2)$ for *Case IV*.

6. APPLICATIONS

The reflection and transmission matrices for waves incident upon a general point support or a change in cross-section can be combined with the transfer matrix method to analyze the free vibration of a rotating Timoshenko shaft with multiple supports and discontinuities, and general boundary conditions. The basic idea of this technique has been shown in Ref. [6]. However, due to the complex wave motions in the Timoshenko shaft model, such as the frequency dependency of the wave reflection and transmission at a cross-section change, it is important to apply the proper reflection and transmission matrices consistent with the values of A and B on both sides of the discontinuity, particularly when numerical calculations are performed. Consider for example the free vibration problem of the rotating Timoshenko shaft model shown in Fig. 17. Denoting $\mathbf{R}$ as a reflection matrix which relates the amplitudes of negative and positive travelling waves at a discontinuity, and defining $\mathbf{T}_i$ as the field transfer matrix which relates the wave amplitudes by

$$\mathbf{C}^+(z_0 + z) = \mathbf{T}\mathbf{C}^+(z_0), \quad \mathbf{C}^-(z_0 + z) = \mathbf{T}^{-1}\mathbf{C}^-(z_0), \tag{55}$$

the following relations can be found.

$$\mathbf{w}_5^- = \mathbf{R}_5 \mathbf{w}_5^+, \qquad (\mathbf{R}_5 = \mathbf{r}_5), \tag{56a}$$

$$\mathbf{w}_{i\mu}^- = \mathbf{R}_{i\mu} \mathbf{w}_{i\mu}^+, \qquad \begin{matrix} i = 2,3,4 \text{ (station number)}, \\ \mu = \text{left } (l) \text{ or right } (r) \end{matrix} \tag{56b}$$

$$\mathbf{w}_1^- = \mathbf{T}_1 \mathbf{w}_{2l}^-, \tag{56c}$$

$$\mathbf{w}_1^+ = \mathbf{r}_1 \mathbf{w}_1^-, \tag{56d}$$

$$\mathbf{w}_{2l}^+ = \mathbf{T}_1 \mathbf{w}_1^+, \tag{56e}$$

where in Eqn. (56b),

$$\mathbf{R}_{ir} = \mathbf{T}_i \mathbf{R}_{i+1,l} \mathbf{T}_i, \quad \mathbf{R}_{il} = \mathbf{r}_i + \mathbf{t}_i (\mathbf{R}_{ir}^{-1} - \mathbf{r}_i)^{-1} \mathbf{t}_i \tag{56f}$$

Solving the above matrix equations gives

$$(\mathbf{r}_1 \mathbf{T}_1 \mathbf{R}_{2l} \mathbf{T}_4 - \mathbf{I}) \mathbf{w}_1^+ = 0, \tag{57}$$

where each element of the matrix is a function of two different wavenumbers and the frequency ω. For non-trivial solutions, the natural frequencies are obtained from the characteristic equation

$$\text{Det}\,[(\mathbf{r}_1 \mathbf{T}_1 \mathbf{R}_{2l} \mathbf{T}_4 - \mathbf{I})] = 0. \tag{58}$$

The proposed method is applied to an example of a two-span rotating shaft, simply supported at the ends and with an intermediate support consisting of translational and rotational springs, as shown in Fig. 18. Numerical computations were performed by a PC-based *Mathematica*®. The values of the spring constants K_T and K_R are those introduced in Section 3.2, with $\ell = 1$ m and the rotation parameter $\beta = 0.05$.

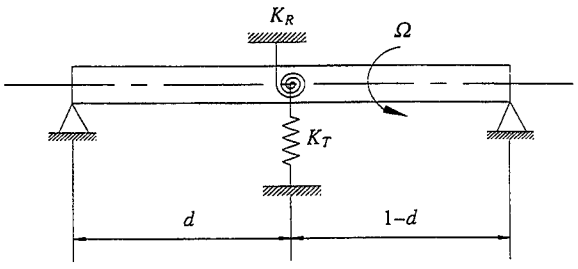

Figure 18. A simply-simply supported, rotating two-span shaft with intermediate supports.

Figure 19 shows the first eight natural frequencies of the vibrating shaft for both the TM and EB models for a classical simple intermediate fixed support ($K_T \to \infty$, $K_R = 0$) placed at various locations. The results confirm the well-known fact that the Timoshenko model leads to smaller eigenvalues. Figure 20 shows the first eight natural frequencies of the Timoshenko shaft for an elastic intermediate support with three different translational spring constants. It can be seen that the effect of the translational spring diminishes for higher modes. The proposed wave analysis technique can also be applied effectively to the study of structural mode localizations in mistuned, rotating systems. Dynamics of such systems will be addressed in another paper.

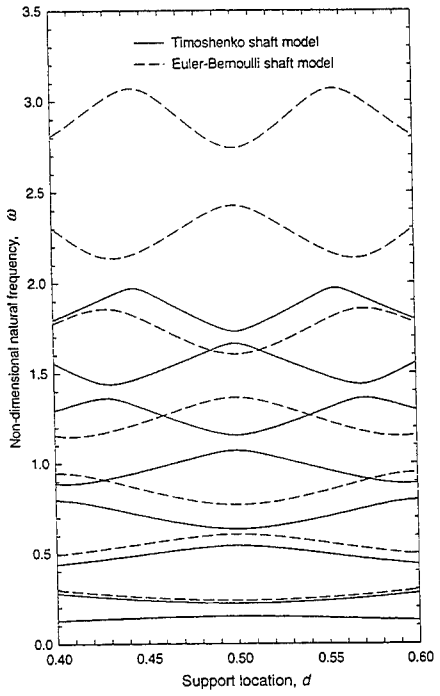

Figure 19. Natural frequencies of a two-span, rotating shaft as a function of the support location; intermediate support is fixed.

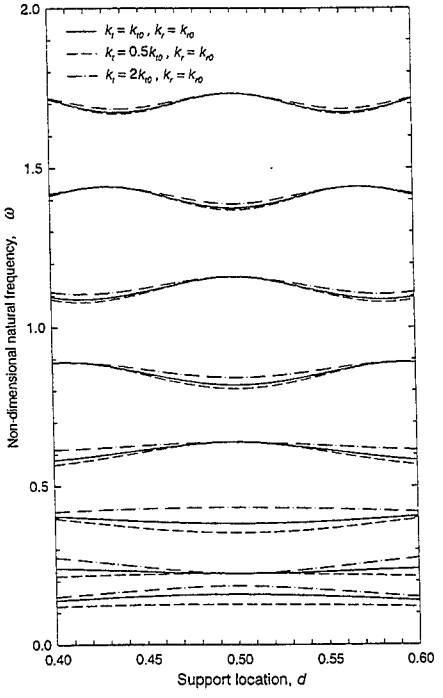

Figure 20. Natural frequencies of a two-span rotating Timoshenko shaft as a function of the support location; intermediate support consists of k_t and k_r.

7. SUMMARY AND CONCLUSIONS

In modern high speed rotating shaft applications, it is common that the shaft has multiple intermediate supports and discontinuities such as bearings, rotor masses, and changes in cross-

sections. In many cases, the ratio of the shaft diameter to its length between consecutive supports is large, and the Timoshenko model (TM) is needed to accurately account for the shear and rotary inertia effects. In this paper, the wave propagation in a rotating, axially strained Timoshenko shaft model with multiple discontinuities is examined. The effect of the static axial deformation due to an axial load is also included in the model. Based on results from Ref. [7], there are four possible types of wave motions (*Cases I, II, III* and *IV*) in the Timoshenko shaft, as shown by Eqns. (5a-8b). In practice, *Case III* does not occur and is excluded in the analysis. For each *Case*, the wave reflection and transmission matrices are derived for a shaft under various support and boundary conditions. Results are compared with those obtained by using the simple Euler-Bernoulli model (EB) and are summarized as follows.

1) In general, the two shaft models show good agreement in the low frequency range where the wave motion is governed by *Case II* and *Case IV*. However, at high frequencies, the types of wave motions and propagation characteristics for the TM and EB models are very different.
2) The effects of shaft rotation on the wave reflection and transmission are negligible over the entire frequency range and even at high speed (up to 44,600 rpm). While the effects of the axial load are significant, especially in the low frequency range.
3) When waves are incident at supports with only translational springs, differences in the results between the TM and EB models are small, and there exists frequency regions of impedance matching and an impedance mismatching frequency (limited to within the regime of *Case II*). The impedance matching and mismatching disappear when a rotational spring is added to the support. Instead, there is a frequency at which $|r_{11}| = 0$ and $|t_{11}| = 1$, and vibrations on both sides of the support become strongly coupled. This (delocalization) phenomenon suggests further research on the vibrations of constrained multi-span beams. When there is damping at the support, the frequency at which $|r_{11}| = 0$ does not occur. Moreover, effects of translational damping on the wave propagation are more significant at high frequency, especially for the TM model, however effects of rotational damping is not significant over the entire frequency range.
4) Contributions of attenuating wave components to the energy in the reflected and transmitted waves are significant when the shaft is axially strained and when the support has a rotational constraint. Thus attenuating waves should be included in the formulation.
5) Unlike the spring supports, in which waves are easily transmitted at high frequency, the rotor mass support diminishes the wave transmission as the frequency increases.
6) When waves are incident at a geometric discontinuity such as a change in the cross-section, there are nine possible combinations of wave motions on both sides of the discontinuity. It is shown that differences of the results between the TM and EB models depend on the diameter ratio (and hence the direction of the wave incidence). Moreover, incident attenuating waves contribute more energy to propagating waves at the discontinuity when the waves travel from a smaller to a larger cross-section. When the shaft is axially strained, the effects of the load on the wave propagation are primarily limited to the low frequency range.

The reflection and transmission matrices are combined with the transfer matrix method to provide a systematic solution method to analyze the free vibration of a multi-span, rotating shaft. Since the procedure involves only 2×2 matrices (while including the near-field effects already), strenuous computations associated with large-order matrices are eliminated.

ACKNOWLEDGMENTS

The authors wish to acknowledge the support of the National Science Foundation and the Institute of Manufacturing Research of Wayne State University for this research work.

REFERENCES

1. Lin, Y.K., Free Vibrations of a Continuous Beam on Elastic Supports. *International Journal of Mechanical Sciences*, 1962, **4**, pp. 409-423.
2. Graff, K.F., *Wave Motion in Elastic Solids*, Ohio State University Press, 1975.
3. Cremer, L., Heckl, M. and Ungar E.E., *Structure-Borne Sound*, Springer-Verlag, Berlin, 1973.
4. Fahy, F., *Sound and Structural Vibration*, Academic Press, 1985.
5. Mead, D.J., Waves and Modes in Finite Beams: Application of the Phase-Closure Principle. *Journal of Sound and Vibration*, 1994, **171**, pp. 695-702.
6. Mace, B.R., Wave Reflection and Transmission in Beams. *Journal of Sound and Vibration*, 1984, **97**, pp. 237-246.
7. Kang, B. and Tan, C.A., Elastic Wave Motions in an Axially Strained, Infinitely Long Rotating Timoshenko Shaft. *Journal of Sound and Vibration* (submitted), 1997.
8. Han, R.P.S. and Zu, J.W.-Z., Modal Analysis of Rotating Shafts: A Body-Fixed Axis Formulation Approach. *Journal of Sound and Vibration*, 1992, **156**, pp. 1-16.
9. Zu, J.W.-Z. and Han, R.P.S., Natural Frequencies and Normal Modes of a Spinning Timoshenko Beam With General Boundary Conditions. *Transactions of the American Society of Mechanical Engineers, Journal of Applied Mechanics*, 1992, **59**, pp. 197-204.
10. Katz, R., Lee, C.W., Ulsoy, A.G. and Scott, R.A., The Dynamic Response of a Rotating Shaft Subject to a Moving Load. *Journal of Sound and Vibration*, 1988, **122**, pp. 131-148.
11. Tan, C.A. and Kuang, W., Vibration of a Rotating Discontinuous Shaft by the Distributed Transfer Function Method. *Journal of Sound and Vibration*, 1995, **183**, pp. 451-474.
12. Argento, A. and Scott, R.A., Elastic Wave Propagation in a Timoshenko Beam Spinning about Its Longitudinal Axis. *Wave Motion*, 1995, **21**, pp. 67-74.
13. Dimentberg, F.M., *Flexural Vibrations of Rotating Shafts*, Butterworth, London, 1961.
14. Dimarogonas, A.D. and Paipeties, S.A., *Analytical Method in Rotor Dynamics*, Applied Science, New York, 1983.
15. Lee, C.W., *Vibration Analysis of Rotors*, Kluwer Academic Publishers, 1993.
16. Choi, S.H., Pierre, C. and Ulsoy, A.G., Consistent Modeling of Rotating Timoshenko Shafts Subject to Axial Loads. *Journal of Vibration and Acoustics*, 1992, **114**, pp. 249-259.
17. Bhashyam, G.R. and Prathap, G., The Second Frequency Spectrum of Timoshenko Beams.

Journal of Sound and Vibration, 1981, **76**, pp. 407-420.

18. Riedel, C.H. and Tan, C. A., Mode Localization and Delocalization of Constrained Strings and Beams. *Proceedings of ASME Biennial Conference on Mechanical Vibration and Noise* (submitted), 1997

APPENDIX I

The reflection and transmission matrices for a wave incident upon a generalized support for the simple Euler-Bernoulli shaft model can be obtained by solving the following sets of matrix equations. Asterisks in the equation numbering denote correspondence to the equations for the Timoshenko model.

Case II ($A > 0$, $B < 0$):

$$\begin{bmatrix} 1 & 1 \\ -i\Gamma_1 & -\Gamma_2 \end{bmatrix}\mathbf{C}^+ + \begin{bmatrix} 1 & 1 \\ i\Gamma_1 & \Gamma_2 \end{bmatrix}\mathbf{r}\mathbf{C}^+ = \begin{bmatrix} 1 & 1 \\ -i\Gamma_1 & -\Gamma_2 \end{bmatrix}\mathbf{t}\mathbf{C}^+, \tag{29a*}$$

$$\begin{bmatrix} -\Gamma_1^2 & \Gamma_2^2 \\ i\Gamma_1^3 & -\Gamma_2^3 \end{bmatrix}\mathbf{C}^+ + \begin{bmatrix} -\Gamma_1^2 & \Gamma_2^2 \\ -i\Gamma_1^3 & \Gamma_2^3 \end{bmatrix}\mathbf{r}\mathbf{C}^+$$

$$= \begin{bmatrix} -\Gamma_1^2 + i\Gamma_1(k_r + ic_r\omega - J_m\omega^2) & \Gamma_2^2 + \Gamma_2(k_r + ic_r\omega - J_m\omega^2) \\ (k_t - m\omega^2) + i(c_t\omega + \Gamma_1^3) & (k_t - m\omega^2 - \Gamma_2^3) + ic_t\omega \end{bmatrix}\mathbf{t}\mathbf{C}^+, \tag{29b*}$$

Case IV ($A < 0$, $B < 0$):

$$\begin{bmatrix} 1 & 1 \\ -i\Gamma_2 & -\Gamma_1 \end{bmatrix}\mathbf{C}^+ + \begin{bmatrix} 1 & 1 \\ i\Gamma_2 & \Gamma_1 \end{bmatrix}\mathbf{r}\mathbf{C}^+ = \begin{bmatrix} 1 & 1 \\ -i\Gamma_2 & -\Gamma_1 \end{bmatrix}\mathbf{t}\mathbf{C}^+, \tag{30a*}$$

$$\begin{bmatrix} -\Gamma_2^2 & \Gamma_1^2 \\ i\Gamma_2^3 & -\Gamma_1^3 \end{bmatrix}\mathbf{C}^+ + \begin{bmatrix} -\Gamma_2^2 & \Gamma_1^2 \\ -i\Gamma_2^3 & \Gamma_1^3 \end{bmatrix}\mathbf{r}\mathbf{C}^+$$

$$= \begin{bmatrix} -\Gamma_2^2 + i\Gamma_2(k_r + ic_r\omega - J_m\omega^2) & \Gamma_1^2 + \Gamma_1(k_r + ic_r\omega - J_m\omega^2) \\ (k_t - m\omega^2) + i(c_t\omega + \Gamma_2^3) & (k_t - m\omega^2 - \Gamma_1^3) + ic_t\omega \end{bmatrix}\mathbf{t}\mathbf{C}^+, \tag{30b*}$$

where, the following non-dimensional parameters are employed.

$$k_t = \frac{K_t a_0^3}{EI},\ k_r = \frac{K_r a_0}{EI},\ c_t = \frac{c_{dt} c_0 a_0^2}{EI},\ c_r = \frac{c_{dr} c_0}{EI},\ m = \frac{M a_0}{\rho I},\ J_m = \frac{J_M c_0^2}{EI}, \text{ and } c_0 = \sqrt{\frac{E}{\rho}} \tag{25*}$$

For simple and clamped supports, the reflection and transmission matrices are listed as follows.

- Simple support ($k_t = \infty,\ k_r = m = c_t = c_r = J_m = 0$)

Case II ($A > 0,\ B < 0$):

$$\mathbf{r} = \frac{1}{i\Gamma_1 - \Gamma_2}\begin{bmatrix} \Gamma_2 & \Gamma_2 \\ -i\Gamma_1 & -i\Gamma_1 \end{bmatrix}, \quad \mathbf{t} = \frac{1}{i\Gamma_1 - \Gamma_2}\begin{bmatrix} i\Gamma_1 & \Gamma_2 \\ -i\Gamma_1 & -\Gamma_2 \end{bmatrix}, \tag{32a*, b*}$$

Case IV ($A < 0,\ B < 0$):

$$\mathbf{r} = \frac{1}{i\Gamma_1 + \Gamma_2}\begin{bmatrix} -i\Gamma_1 & -i\Gamma_1 \\ -\Gamma_2 & -\Gamma_2 \end{bmatrix}, \quad \mathbf{t} = \frac{1}{i\Gamma_1 + \Gamma_2}\begin{bmatrix} \Gamma_2 & -i\Gamma_1 \\ -\Gamma_2 & i\Gamma_1 \end{bmatrix}, \tag{33a*, b*}$$

- Clamped support ($k_t = \infty,\ k_r = \infty,\ m = c_t = c_r = J_m = 0$); $\mathbf{t} = 0$.

Case II ($A > 0,\ B < 0$):

$$\mathbf{r} = \frac{1}{i\Gamma_1 - \Gamma_2}\begin{bmatrix} i\Gamma_1 + \Gamma_2 & 2\Gamma_2 \\ -2i\Gamma_1 & -(i\Gamma_1 + \Gamma_2) \end{bmatrix}, \tag{35*}$$

Case IV ($A < 0,\ B < 0$):

$$\mathbf{r} = \frac{1}{i\Gamma_1 + \Gamma_2}\begin{bmatrix} -(i\Gamma_1 - \Gamma_2) & -2i\Gamma_1 \\ -2\Gamma_2 & i\Gamma_1 - \Gamma_2 \end{bmatrix}. \tag{36*}$$

APPENDIX II

The reflection and transmission matrices for a wave incident upon a cross-sectional change for the simple Euler-Bernoulli shaft model can be determined by solving the following sets of matrix equations. Only two representative combinations are shown.

Case II ($A_l > 0,\ B_l < 0$) – *Case II* ($A_r > 0,\ B_r < 0$):

$$\begin{bmatrix} 1 & 1 \\ -i\Gamma_{1l} & -\Gamma_{2l} \end{bmatrix}\mathbf{C}^+ + \begin{bmatrix} 1 & 1 \\ i\Gamma_{1l} & \Gamma_{2l} \end{bmatrix}\mathbf{r}\mathbf{C}^+ = \begin{bmatrix} 1 & 1 \\ -i\Gamma_{1r} & -\Gamma_{2r} \end{bmatrix}\mathbf{t}\mathbf{C}^+, \tag{38a*}$$

$$\begin{bmatrix} -\Gamma_{1l}^2 & \Gamma_{2l}^2 \\ i\Gamma_{1l}^3 & -\Gamma_{2l}^3 \end{bmatrix}\mathbf{C}^+ + \begin{bmatrix} -\Gamma_{1l}^2 & \Gamma_{2l}^2 \\ -i\Gamma_{1l}^3 & \Gamma_{2l}^3 \end{bmatrix}\mathbf{r}\mathbf{C}^+ = \begin{bmatrix} -\sigma^4\Gamma_{1r}^2 & \sigma^4\Gamma_{2r}^2 \\ i\sigma^4\Gamma_{1r}^3 & -\sigma^4\Gamma_{2r}^3 \end{bmatrix}\mathbf{t}\mathbf{C}^+ \tag{38b*}$$

Case II ($A_l > 0$, $B_l < 0$) – *Case IV* ($A_r < 0$, $B_r < 0$):

$$\begin{bmatrix} 1 & 1 \\ -i\Gamma_{1l} & -\Gamma_{2l} \end{bmatrix}\mathbf{C}^+ + \begin{bmatrix} 1 & 1 \\ i\Gamma_{1l} & \Gamma_{2l} \end{bmatrix}\mathbf{r}\mathbf{C}^+ = \begin{bmatrix} 1 & 1 \\ -i\Gamma_{2r} & -\Gamma_{1r} \end{bmatrix}\mathbf{t}\mathbf{C}^+, \tag{39a*}$$

$$\begin{bmatrix} -\Gamma_{1l}^2 & \Gamma_{2l}^2 \\ i\Gamma_{1l}^3 & -\Gamma_{2l}^3 \end{bmatrix}\mathbf{C}^+ + \begin{bmatrix} -\Gamma_{1l}^2 & \Gamma_{2l}^2 \\ -i\Gamma_{1l}^3 & \Gamma_{2l}^3 \end{bmatrix}\mathbf{r}\mathbf{C}^+ = \begin{bmatrix} -\sigma^4\Gamma_{2r}^2 & \sigma^4\Gamma_{1r}^2 \\ i\sigma^4\Gamma_{2r}^3 & -\sigma^4\Gamma_{1r}^3 \end{bmatrix}\mathbf{t}\mathbf{C}^+, \tag{39b*}$$

where, Γ_{1r} and Γ_{2r} have been defined in Eqns. (45c, d), and A_r and B_r are given by

$$A_r = -2\beta\tilde{\omega} - 16\frac{\varepsilon_r}{\sigma^2}, \tag{46a*}$$

$$B_r = -16\frac{\tilde{\omega}^2}{\sigma^2}. \tag{46b*}$$

APPENDIX III

The reflection matrices for a group of waves incident upon a general boundary for the Euler-Bernoulli shaft model are listed as follows.

Case II ($A > 0$, $B < 0$):

$$\mathbf{r} = \begin{bmatrix} -\Gamma_1(\Gamma_1 + \Sigma_m) & \Gamma_2(\Gamma_2 - \Sigma_m) \\ \Sigma_s - i\Gamma_1^3 & \Sigma_s + \Gamma_2^3 \end{bmatrix}^{-1}\begin{bmatrix} \Gamma_1(\Gamma_1 - i\Sigma_m) & -\Gamma_2(\Gamma_2 + \Sigma_m) \\ -\Sigma_s - i\Gamma_1^3 & \Sigma_s + \Gamma_2^3 \end{bmatrix}, \tag{49*}$$

Case IV ($A < 0$, $B < 0$):

$$\mathbf{r} = \begin{bmatrix} -\Gamma_2(\Gamma_2 + \Sigma_m) & \Gamma_1(\Gamma_1 - \Sigma_m) \\ \Sigma_s - i\Gamma_2^3 & \Sigma_s + \Gamma_1^3 \end{bmatrix}^{-1}\begin{bmatrix} \Gamma_2(\Gamma_2 - i\Sigma_m) & -\Gamma_1(\Gamma_1 + \Sigma_m) \\ -\Sigma_s - i\Gamma_2^3 & \Sigma_s + \Gamma_1^3 \end{bmatrix}, \tag{50*}$$

where,

$$\Sigma_m = J_m\tilde{\omega}^2 - k_r - ic_r\omega, \text{ and } \Sigma_s = k_t - m\tilde{\omega}^2 + ic_t\tilde{\omega}. \tag{51a*, b*}$$

If the rotating shaft is strain-free, then $\mathbf{r}$ can be reduced to simple forms representing typical boundary conditions such as simple support, clamped support, and free end as shown in Ref. [6]. Note that for those supports in the strain-free case, the reflection matrices are constant.

ANALYTICAL MODELLING OF COUPLED VIBRATIONS OF ELASTICALLY SUPPORTED CHANNELS

Yavuz YAMAN
Department of Aeronautical Engineering, Middle East Technical University
06531 Ankara, Turkey

An exact analytical method is presented for the analysis of forced vibrations of uniform thickness, open-section channels which are elastically supported at their ends. The centroids and the shear centers of the channel cross-sections do not coincide; hence the flexural and the torsional vibrations are coupled. Ends of the channels are constrained with springs which provide finite transverse, rotational and torsional stiffnesses. During the analysis, excitation is taken in the form of a point harmonic force and the channels are assumed to be of type Euler-Bernoulli beam with St.Venant torsion and torsional warping stiffness. The study uses the wave propagation approach in constructing the analytical model. Both uncoupled and double coupling analyses are performed. Various response and mode shape curves are presented.

1. INTRODUCTION

Open-section channels are widely used in aeronautical structures as stiffeners. These are usually made of beams in which the centroids of the cross-section and the shear centers do not coincide. This, inevitably leads to the coupling of possible flexural and torsional vibrations. If the channels are symmetric with respect to an axis, the flexural vibrations in one direction and the torsional vibrations are coupled. The flexural vibrations in mutually perpendicular direction occur independently. In the context of this study, this type of coupling is referred to as double-coupling. If there is no cross-sectional symmetry, all the flexural and torsional vibrations are coupled. This is called as triple-coupling. The coupling mechanism alters the otherwise uncoupled response characteristics of the structure to a great extent.

This problem have intrigued the scientists for long time. Gere *et al* [1], Lin [2], Dokumacı [3] and Bishop *et al* [4] developed exact analytical models for the determination of coupled vibration characteristics. All those works, though pioneering in nature, basically aimed to determine the free vibration characteristics of open-section channels.

The method proposed by Cremer *et al* [5] allowed the determination of forced vibration characteristics, provided that the structure is uniform in cross-section. The use of that method was found to be extremely useful when the responses of uniform structures to point harmonic forces or line harmonic loads were calculated. Mead and Yaman presented analytical models for the

analysis of forced vibrations of Euler-Bernoulli beams [6]. In that they considered finite length beams , being periodic or non-periodic, and studied the effects of various classical or non-classical boundary conditions on the flexural response. Yaman in [7] developed mathematical models for the analysis of the infinite and periodic beams, periodic or non-periodic Kirchoff plates and three-layered, highly damped sandwich plates.

Yaman in [8] also developed analytical models for the coupled vibration analysis of doubly and triply coupled channels having classical end boundary conditions. In that the coupled vibration characteristics are expressed in terms of the coupled wave numbers of the structures. The structures are first assumed to be infinite in length, and hence the displacements due to external forcing(s) are formulated. The displacements due to the waves reflected from the ends of the finite structure are also separately determined. Through the superposition of these two, a displacement field is proposed. The application of the end boundary conditions gives the unknowns of the model. The analytical method yields a matrix equation of unknowns which is to be solved numerically. The order of the matrix equation varies depending on the number of coupled waves. If the cross-section is symmetric with respect to an axis (double-coupling) and if the warping constraint is neglected, the order is six. If there is no cross-sectional symmetry (triple-coupling) and if one also includes the effects of warping constraint, the order then becomes twelve. This order is independent of the number of externally applied point forces. Although the method is basically intended to calculate the forced response characteristics, it conveniently allows the computation of free vibration characteristics as well. The velocity or acceleration of a point can easily be found. The mode shapes can also be determined. Both undamped and damped analyses can be undertaken.

This study is based on the models developed in reference [8] and aims to analyze the effects of non-classical end boundary conditions on the coupled vibratory responses. If the ends are elastically supported (which may also have inertial properties) the problem becomes so tedious to tackle through the means of classical analytical approaches. The current method alleviates the difficulties encountered in the consideration of complex end boundary conditions.

In this study a typical channel, assumed to be of type Euler-Bernoulli beam, is analyzed. It represents the double-coupling. Effects of the elastic end boundary conditions on the resonance frequencies, response levels and mode shapes are analyzed. Characteristics of otherwise uncoupled vibrations are also shown.

2. THEORY

2.1 Flexural Wave Propagation in Uniform Euler-Bernoulli Beams

Consider a uniform Euler-Bernoulli beam of length L which is subjected to a harmonically varying point force $F_o e^{i\omega t}$ acting at $x=x_f$. The total flexural displacement of the beam at any x_r ($0 \le x_r \le L$) can be found to be [5-8],

$$w(x_r,t) = \left(\sum_{n=1}^{4} A_n e^{k_n x_r} + F_o \sum_{n=1}^{2} a_n e^{-k_n |x_r - x_f|} \right) e^{i\omega t} \qquad (1)$$

The first series of the equation represents the effects of four waves which are being reflected from the ends of the finite beam. They are called *free-waves*. The second series accounts for the waves which are being created by the application of the external force $F_o e^{i\omega t}$ on the infinite beam. Those waves are known as *forced-waves*. k_n is the n'th wave number of the beam and $k_n = (m\omega^2/EI)^{1/4}$ where m= Mass per unit length of the beam, ω= Angular frequency, EI= Flexural rigidity of the beam. a_n values are the complex coefficients which are to be found by satisfying the relevant compatibiliy and continuity conditions at the point of application of the harmonic force [6,7]. A_n values, on the other hand are the complex amplitudes of the free waves and are found by satisfying the required boundary conditions at the ends of the beam. Once determined, their substitution to equation (1) yields the flexural displacement at any point on the finite beam due to a transversely applied point harmonic force. More comprehensive information can be found in [7].

2.2 Torsional Wave Propagation in Uniform Bars

If one requires to determine the torsional displacements generated by a point, harmonically varying torque, a similar approach to the one given in Section 2.1 can be used. In that case, the total torsional displacement can be written as:

$$\phi(x_r,t) = \left(\sum_{n=1}^{2} B_n e^{k_n x_r} + T_o b\, e^{-k |x_r - x_t|} \right) e^{i\omega t} \qquad (2)$$

k is the wave number of the purely torsional wave and is known to be $k=(-\rho I_o \omega^2/GJ)^{1/2}$. $k_2 = -k_1$ and GJ=Torsional rigidity of the beam, ρ=Material density, I_o=Polar second moment of area of the cross-section with respect to the shear centre. $T_o e^{i\omega t}$ is the external harmonic torque applied at $x=x_t$ and $b=1/(2kGJ)$. B_n values are the complex amplitudes of the torsional free-waves and are found by satisfying the appropriate end torsional boundary conditions.

The consideration of the warping constraint Γ_o modifies equation (2) to the following form.

$$\phi(x_r,t) = \left(\sum_{n=1}^{4} C_n e^{k_n x_r} + T_o \sum_{n=1}^{2} c_n e^{-k_n |x_r - x_t|} \right) e^{i\omega t} \qquad (3)$$

Now k_n are the roots of

$$E\Gamma_o k_n^4 - GJ k_n^2 - \rho I_o \omega^2 = 0 \qquad (4)$$

c_n values are found by satisfying the necessary equilibrium and compatibility conditions at the point of application of the point harmonic torque acting on an infinite bar [8]. C_n values are determined from the end torsional boundary conditions of the finite bar.

2.3 End Boundary Conditions for Uncoupled Vibrations

2.3.1 Purely Flexural Vibrations

Consider an Euler-Bernoulli beam of length L which is supported by springs at its ends. The springs provide finite transverse and rotational constraints K_t and K_r respectively. The elastic end boundary conditions can be found to be:

$$\begin{aligned} EI\, w''(0) - K_{r,l}\, w'(0) &= 0 \qquad & EI\, w'''(0) + K_{t,l}\, w(0) &= 0 \\ EI\, w''(L) + K_{r,r}\, w'(L) &= 0 \qquad & EI\, w'''(L) - K_{t,r} w(L) &= 0 \end{aligned} \qquad (5)$$

Here $w' = \frac{d\,w(x)}{dx}$, $w'' = \frac{d^2 w(x)}{dx^2}$ and $w''' = \frac{d^3 w(x)}{dx^3}$. $w(x)$ is the spatially dependent part of equation (1) and second subscripts l and r allows one to use different stiffnesses for left and right ends. A more comprehensive study on these aspects can be found in references [6,7].

2.3.2 Purely Torsional Vibrations

Now consider a bar of length L which is supported by torsional springs, having finite K_{tor}, at its ends. The elastic end boundary conditions requires that,

$$\text{Torque}(0) - K_{tor,l}\, \phi(0) = 0 \text{ and } \text{Torque}(L) + K_{tor,r}\, \phi(L) = 0 \qquad (6)$$

Depending on the consideration of the warping constraint Γ_o, the torque has the following forms

$$\text{Torque}(x) = GJ \frac{d\phi(x)}{dx} \text{ or } \text{Torque}(x) = GJ \frac{d\phi(x)}{dx} - E\Gamma_o \frac{d^3\phi(x)}{dx^3} \qquad (7)$$

$\phi(x)$ in equation (7) should be obtained either from equation (2) or equation (3) depending on the warping constraint Γ_o.

2.4 Doubly-Coupled Vibrations

Now, consider Figure 1 . It defines a typical open cross-section which is symmetric with respect to y axis

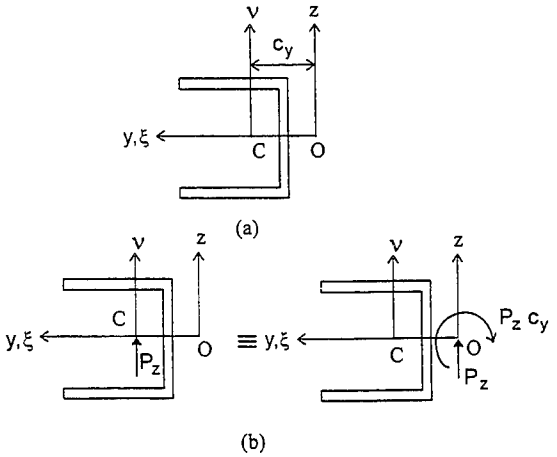

Figure 1 : A Typical Cross-section of Double-coupling
(a. Coordinate System, b. Real and Effective Loadings
C: Centroid, O: Shear Centre)

A transverse load applied through C results in a transverse load through O and a twisting torque about O. In this case the flexural vibrations in z direction are coupled with the torsional vibrations whereas the flexural vibrations in y direction occur independently. The motion equation of the coupled vibrations is known to be [1,2].

$$EI_\xi \frac{\partial^4 w}{\partial x^4} + m\frac{\partial^2 w}{\partial t^2} + c_y m\frac{\partial^2 \phi}{\partial t^2} = 0$$

$$E\Gamma_o \frac{\partial^4 \phi}{\partial x^4} - GJ\frac{\partial^2 \phi}{\partial x^2} + c_y m\frac{\partial^2 w}{\partial t^2} + \rho I_o \frac{\partial^2 \phi}{\partial t^2} = 0 \qquad (8)$$

If one assumes that,

$$w(x,t) = w_n e^{k_n x} e^{i\omega t}$$

$$\phi(x,t) = \phi_n e^{k_n x} e^{i\omega t} \qquad (9)$$

Then, it can be found that, a load P_z through the centroid will create the following displacements at any x ($0 \leq x \leq L$) along the length of the channel [8],

$$w(x,t) = (\sum_{n=1}^{2j} A_n e^{k_n x} + P_z \sum_{n=1}^{j} a_n e^{-k_n |x-x_f|}) e^{i\omega t}$$

$$\phi(x,t) = (\sum_{n=1}^{2j} \Psi_n A_n e^{k_n x} + P_z \sum_{n=1}^{j} \Psi_n a_n e^{-k_n |x-x_f|}) e^{i\omega t} \quad (10)$$

Now k_n values are the coupled wave numbers, A_n values are the complex amplitudes of the coupled free waves, a_n values are the complex coefficients which are to be found by satisfying the required compatibility and continuity conditions and $\Psi_n = ((EI_\xi k_n^4 - m\omega^2) / (c_y m\omega^2))$ [8].

If required, the warping displacement u(x,t) can be found from $\phi(x,t)$ as

$$u(x,t) = -2A_s \frac{\partial \phi(x,t)}{\partial x} \quad (11)$$

where A_s is the swept area.

Here 2j gives the order of the motion equation. j=3 defines the case in which the effects of warping constraint are neglected and j=4 represents the case which includes the warping effects.

A_n values are found by satisfying the necessary 2j end boundary conditions. If warping constraint is neglected, the required six boundary conditions have the general forms given in equations (5) and (6). But the forms of w(x) and $\phi(x)$ are now those given by equations (10) with j=3. If the warping constraint is included in the analysis the boundary conditions become eight. The six of those are again found by considering equations (10) with j=4 and substituting the resultant forms into equations (5) and (6). The remaining two can be found by evaluating equation (11) at both ends.

When the flexural and torsional displacement expressions are substituted into the relevant equations, a set of equations is obtained. For the case of a load P_z and no warping constraint, the following equations can be found for j=3.

$$EI_\xi w'''(0) + K_{t,l} w(0) = 0$$

$$EI_\xi (\sum_{n=1}^{2j} k_n^3 A_n + (-1) P_z \sum_{n=1}^{j} - k_n^3 a_n e^{-k_n |x_f|}) + K_{t,l} (\sum_{n=1}^{2j} A_n + P_z \sum_{n=1}^{j} a_n e^{-k_n |x_f|}) = 0 \quad (12)$$

$EI_\xi\, w''(0) - K_{r,l}\, w'(0) = 0$:

$$EI_\xi \Big(\sum_{n=1}^{2j} k_n^2 A_n + P_z \sum_{n=1}^{j} k_n^2 a_n e^{-k_n |x_f|} \Big)$$
$$- K_{r,l} \Big(\sum_{n=1}^{2j} k_n A_n + P_z \sum_{n=1}^{j} - k_n a_n e^{-k_n |x_f|} \Big) = 0 \qquad (13)$$

$$GJ \frac{d\phi(x)}{dx}\Big|_{x=0} - K_{tor,l}\, \phi(0) = 0 :$$

$$GJ \Big(\sum_{n=1}^{2j} k_n \Psi_n A_n + (-1)(P_z c_y) \sum_{n=1}^{j} -k_n \Psi_n a_n e^{-k_n |x_f|} \Big)$$
$$- K_{tor,l} \Big(\sum_{n=1}^{2j} \Psi_n A_n + (P_z c_y) \sum_{n=1}^{j} \Psi_n a_n e^{-k_n |x_f|} \Big) = 0 \qquad (14)$$

$$GJ \frac{d\phi(x)}{dx}\Big|_{x=L} + K_{tor,r}\, \phi(L) = 0 :$$

$$GJ \Big(\sum_{n=1}^{2j} k_n \Psi_n A_n e^{k_n L} + (P_z c_y) \sum_{n=1}^{j} -k_n \Psi_n a_n e^{-k_n |L - x_f|} \Big)$$
$$+ K_{tor,r} \Big(\sum_{n=1}^{2j} \Psi_n A_n e^{k_n L} + (P_z c_y) \sum_{n=1}^{j} \Psi_n a_n e^{-k_n |L - x_f|} \Big) = 0 \qquad (15)$$

$$EI_\xi\, w''(L) + K_{r,r}\, w'(L) = 0 :$$

$$EI_\xi \Big(\sum_{n=1}^{2j} k_n^2 A_n e^{k_n L} + (P_z) \sum_{n=1}^{j} k_n^2 a_n e^{-k_n |L - x_f|} \Big)$$
$$+ K_{r,r} \Big(\sum_{n=1}^{2j} k_n A_n e^{k_n L} + (P_z) \sum_{n=1}^{j} - k_n a_n e^{-k_n |L - x_f|} \Big) = 0 \qquad (16)$$

$$EI_\xi\, w'''(L) - K_{t,r} w(L) = 0 :$$

$$EI_\xi \Big(\sum_{n=1}^{2j} k_n^3 A_n e^{k_n L} + (P_z) \sum_{n=1}^{j} - k_n^3 a_n e^{-k_n |L - x_f|} \Big)$$
$$- K_{t,l} \Big(\sum_{n=1}^{2j} A_n e^{k_n L} + (P_z) \sum_{n=1}^{j} a_n e^{-k_n |L - x_f|} \Big) = 0 \qquad (17)$$

Here (-1) multipliers are included due to the symmetry and anti-symmetry effects.

Those equations can be cast into the following matrix form.

$$\begin{bmatrix} & & & & & \\ & & & & & \\ & & & & & \\ & & & & & \\ & & & & & \\ & & & & & \end{bmatrix} \begin{Bmatrix} A_1 \\ A_2 \\ A_3 \\ A_4 \\ A_5 \\ A_6 \end{Bmatrix} = -\{\text{Terms containing } P_z\} \qquad (18)$$

An eighth order equation represents the necessary matrix equation for the determination of A_n values if the warping constraint is included in the analysis. In that case, equations (12), (13), (16) and (17) are valid with j=4. On the other hand equations (14) and (15) should be replaced by,

$$\left(GJ\frac{d\phi(x)}{dx} - E\Gamma_o\frac{d^3\phi(x)}{dx^3}\right)\Big|_{x=0} - K_{tor,l}\,\phi(0) = 0 :$$
$$\left(GJ\left(\sum_{n=1}^{2j} k_n \Psi_n A_n + (-1)(P_z c_y)\sum_{n=1}^{j} -k_n \Psi_n a_n e^{-k_n|x_f|}\right) -\right.$$
$$E\Gamma_o\left(\sum_{n=1}^{2j} k_n^3 \Psi_n A_n + (-1)(P_z c_y)\sum_{n=1}^{j} -k_n^3 \Psi_n a_n e^{-k_n|x_f|}\right)\Big)$$
$$-K_{tor,l}\left(\sum_{n=1}^{2j} \Psi_n A_n + (P_z c_y)\sum_{n=1}^{j} \Psi_n a_n e^{-k_n|x_f|}\right)=0 \qquad (19)$$

$$\left(GJ\frac{d\phi(x)}{dx} - E\Gamma_o\frac{d^3\phi(x)}{dx^3}\right)\Big|_{x=L} + K_{tor,r}\,\phi(L) = 0 :$$
$$\left(GJ\left(\sum_{n=1}^{2j} k_n \Psi_n A_n e^{k_n L} + (P_z c_y)\sum_{n=1}^{j} -k_n \Psi_n a_n e^{-k_n|L-x_f|}\right)-\right.$$
$$E\Gamma_o\left(\sum_{n=1}^{2j} k_n^3 \Psi_n A_n e^{k_n L} + (P_z c_y)\sum_{n=1}^{j} -k_n^3 \Psi_n a_n e^{-k_n|L-x_f|}\right)\Big)$$
$$+ K_{tor,r}\left(\sum_{n=1}^{2j} \Psi_n A_n e^{k_n L} + (P_z c_y)\sum_{n=1}^{j} \Psi_n a_n e^{-k_n|L-x_f|}\right)=0 \qquad (20)$$

where j=4. The remaining two equations are found by considering the warping of the extreme ends. If the ends are free to warp the axial stress is zero, if the ends are not to warp the axial displacements are zero at both ends. No elastic constraints are imposed on end warping. If the left end is free to warp and the right end is not to warp, the required boundary conditions can be shown to be:

$$u'(0)=0 : \left(\sum_{n=1}^{2j} k_n^2 \Psi_n A_n + P_z \sum_{n=1}^{j} \Psi_n a_n k_n^2 e^{-k_n|x_f|}\right) = 0 \qquad (21)$$

$$u(L)=0 : \left(\sum_{n=1}^{2j} k_n e^{k_n L} \Psi_n A_n + P_z \sum_{n=1}^{j} \Psi_n a_n (-k_n) e^{-k_n|L-x_f|}\right) = 0 \qquad (22)$$

All the equations can be put into the following matrix form

$$\begin{bmatrix} & & \\ & & \\ & & \end{bmatrix}\begin{Bmatrix} A_1 \\ A_2 \\ A_3 \\ A_4 \\ A_5 \\ A_6 \\ A_7 \\ A_8 \end{Bmatrix} = -\{\text{Terms containing } P_z\} \qquad (23)$$

Required A_n values are numerically found from equations (18) or (23). Their substitution to the appropriate forms of equations (10) and (11) yield the required responses at any point on the beam.

3.RESULTS AND DISCUSSION

The theoretical model used in the study is shown in Figure 1 and has the following geometric and material properties:

$L = 1$ (m), $A = 1.0*10^{-4}$ (m^2), $h = 5.0*10^{-2}$ (m), $I_\xi = 4.17*10^{-8}$ (m^4), $c_y = 15.625*10^{-3}$ (m), $J = 3.33*10^{-11}$ (m^3), $I_o = 7.26*10^{-8}$ (m^4), $\rho = 2700$ (kg/m^3), $\Gamma_o = 2.85*10^{-12}$ (m^6), $E = 7*10^{10}$ (N/m^2), $G = 2.6*10^{10}$ (N/m^2).

Structural damping for torsional vibrations is included through complex torsional rigidity as $GJ^*=GJ(1+i\beta)$. For coupled vibrations, it is also included through the complex flexural rigidity as $EI_\xi^* = EI_\xi(1+i\eta)$.

First presented are the results for purely torsional vibrations. A bar assumed to have the given L, ρ, I_o, G and J values is considered. The bar is then restrained at both ends by springs having the same torsional stiffness K_{tor}. A very low damping, $\beta=10^{-6}$, is assigned and the resonance frequencies are precisely determined. It is found that, the introduction of a small K_{tor} introduces a very low valued resonance frequency. That fundamental frequency increases with increasing K_{tor} and as torsional constraint reaches to very high values, it approaches to the fundamental natural frequency of torsionally fixed-fixed beam. Table 1 gives the fundamental frequencies for a range of K_{tor} values and Figure 2 represents the fundamental mode shapes for selected K_{tor} values.

Table 1: Uncoupled Fundamental Torsional Resonance Frequencies ($\beta=10^{-6}$,No Warping Constraint)

K_{tor} [N]	Frequency [Hz]
0	0.
10^{-2}	1.606
10^{-1}	5.035
10^{0}	14.683
10^{1}	28.407
10^{2}	32.678
10^{3}	33.187
10^{4}	33.239
10^{20}	33.245

Figure 6 on the other hand represents the low frequency torsional receptances of the case in which the warping constraint is taken into consideration and the ends are free to warp. This graph is included in order to show the variation of fundamental torsional resonance frequencies for a range of K_{tor} values.

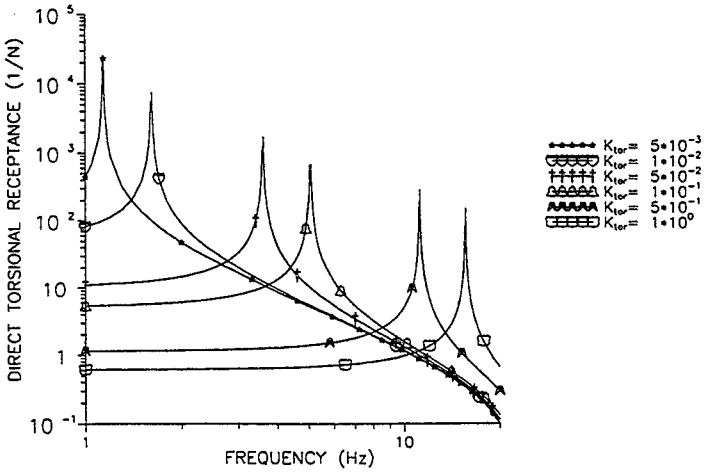

Figure 6. Fundamental Frequencies of Purely Torsional Vibrations
(β=0.01, x =0.13579[m], Warping Constraint Included, Ends are Free to Warp)

The second part of the study investigates the characteristics of doubly-coupled vibrations. Now, the effects of each constraint are separately considered. A channel having the given parameters is supported at its ends by springs K_t, K_r, and K_{tor}. Warping constraint is included in the analysis and the ends are assumed to warp freely. First analyzed is the effects of K_{tor}. For this $K_t = 10^{20}$ [N/m] and $K_r = 10^{20}$ [N] are assigned at both ends of the channel and kept fixed throughout the study. K_{tor} is varied and the frequencies are shown in Table 2.

Table 2. Effects of K_{tor} in Doubly-coupled Vibrations
($K_t = 10^{20}$ [N/m] and $K_r = 10^{20}$ [N], Warping Constraint Included)
A: First Torsion Dominated Frequency [Hz]
B: First Flexure Dominated Frequency [Hz]

K_{tor} [N]	A	B
10^{-2}	1.607	134.603
10^{-1}	5.069	134.936
10^{0}	15.620	138.258
10^{1}	39.725	169.247
10^{2}	56.691	318.423
10^{3}	59.528	422.061
10^{4}	59.828	430.642

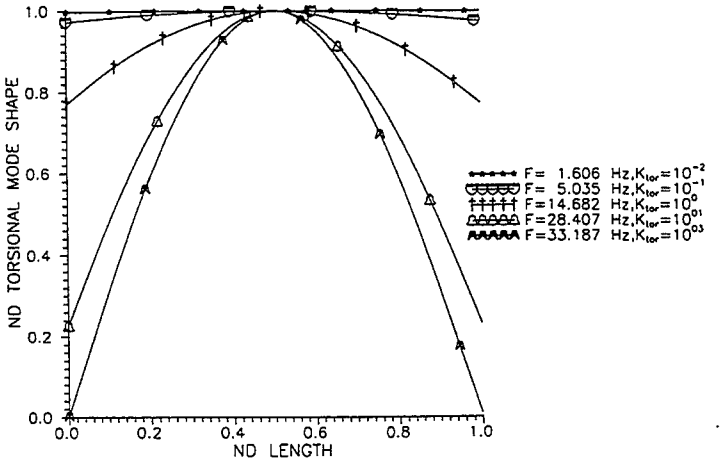

Figure 2. Fundamental Mode Shapes of Purely Torsional Vibrations
(β=0, No Warping Constraint)

Then, the warping constraint Γ_o is included in the analysis and the results of purely torsional vibrations are presented again. The beam had the same K_{tor} values at both ends and the numerical values of the relevant parameters are taken to be those previously defined. Figure 3 represents the fundamental mode shapes for which the ends are free to warp, whereas Figure 4 shows the mode shapes of the case in which there is no warping at the ends.

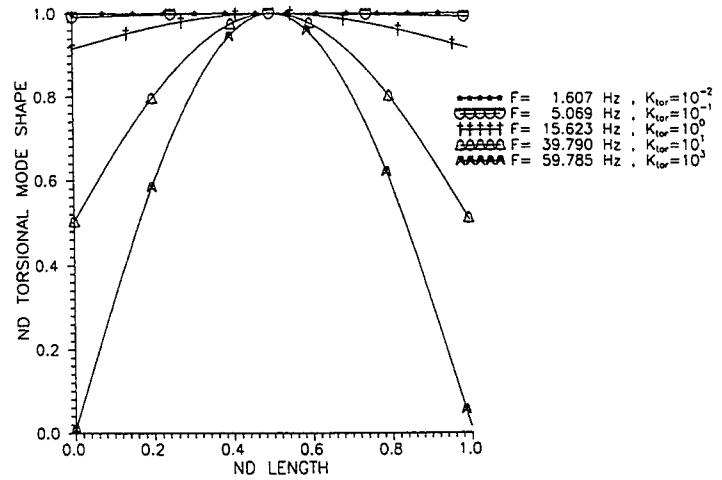

Figure 3. Fundamental Mode Shapes of Purely Torsional Vibrations
(β=0, Warping Constraint Included, Ends are Free to Warp)

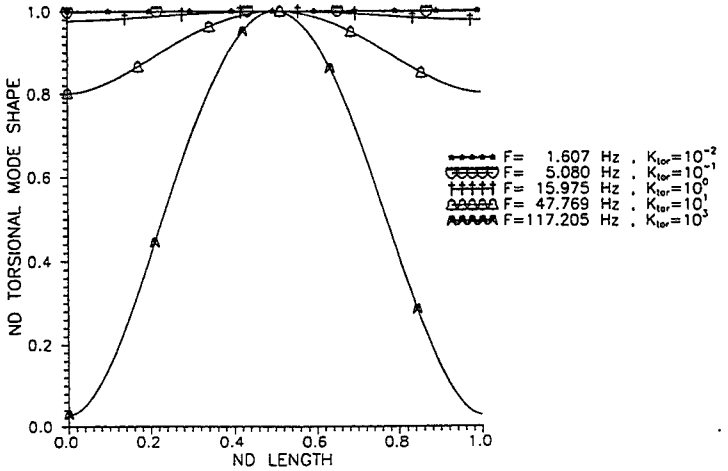

Figure 4. Fundamental Mode Shapes of Purely Torsional Vibrations
(β=0, Warping Constraint Included, Ends Can Not Warp)

Figure 5 is drawn to highlight the effects of end warping. Both ends of the channel are restrained with $K_{tor}=1*10^{1}$ [N] and all the other parameters of the study are kept fixed. Figure 5 represents the direct torsional receptances of two cases in which the ends of the channel are allowed to warp and not to warp in turn. It can be seen that the prevention of end warping increases the resonant frequencies.

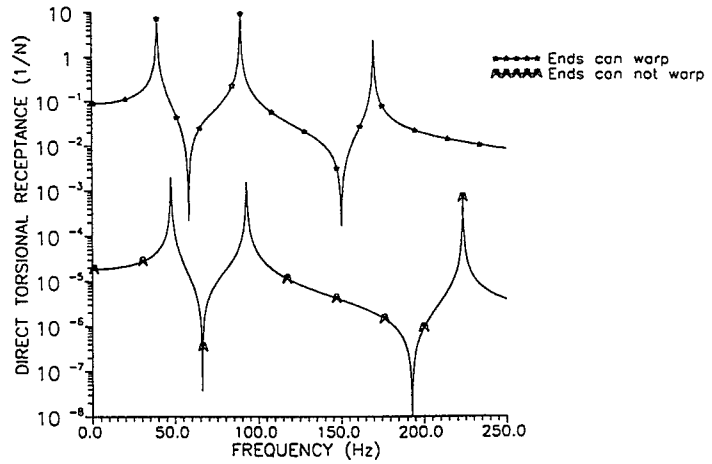

Figure 5. Frequency Response of Purely Torsional Vibrations
(β=0.01, x=0.13579 [m], $K_{tor}=1*10^{1}$ [N], Warping Constraint Included)

It can be seen that, when it has lower values K_{tor} is more effective on the torsion dominated resonance frequencies. For the higher K_{tor} values, the effects are more apparent on the flexure dominated frequencies.

Figure 7 represents the direct flexural receptance of the channel for a set of selected end stiffnesses. Torsion dominated resonances at 59.528 [Hz], 206.071 [Hz] and 476.649 [Hz] appear as spikes. The flexure dominated resonance occurs at 422.061 Hz.

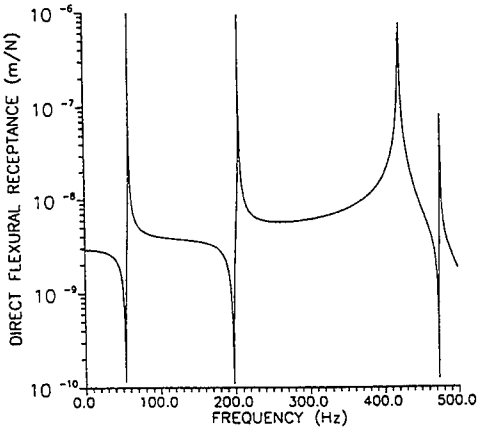

Figure 7. Frequency Response of Doubly-coupled Vibrations
(η=0.001, β=0.001, x=0.13579[m], Warping Constraint Included,
Ends are free to warp, $K_r=1.10^{20}$[N], $K_t=1.10^{20}$ [N/m], $K_{tor}=1.10^{3}$ [N])

Then the effects of the rotational spring, K_r, are considered. The ends of the channel are assumed to be restrained with $K_t=10^{20}$ [N/m] and $K_{tor}=10^{20}$ [N]. The resulting frequencies are given in Table 3 for a range of K_r values.

Table 3. Effects of K_r in Doubly-coupled Vibrations
($K_t=10^{20}$ [N/m] and $K_{tor}=10^{20}$ [N], Warping Constraint Included)
A: First Torsion Dominated Frequency [Hz]
B: First Flexure Dominated Frequency [Hz]

K_r [N]	A	B
10^{-2}	58.678	205.344
10^{0}	58.679	205.358
10^{2}	58.699	206.688
10^{3}	58.858	218.055
10^{4}	59.437	289.738
10^{5}	59.799	405.667
10^{6}	59.855	429.345

It is seen that K_r is not effective on torsion dominated resonance frequencies, but plays significant role for flexure dominated resonance frequencies.

Finally considered the effects of the transverse spring K_t. Again, the channel is assumed to have very high K_r and K_{tor} values at both ends and K_t values are varied. Table 4 shows the resonance frequencies.

Table 4. Effects of K_t in Doubly-coupled Vibrations
($K_r=10^{20}$ [N] and $K_{tor}=10^{20}$ [N], Warping Constraint Included)
A: First Torsion Dominated Frequency [Hz]
B: First Flexure Dominated Frequency [Hz]

K_t [N/m]	A	B
10^1	1.369	70.455
10^2	4.328	70.501
10^3	13.592	70.973
10^4	39.282	77.379
10^5	58.095	159.665
10^6	59.699	361.255
10^8	59.860	431.215

It can be seen that the transverse stiffness, like torsional stiffness, effects both flexure and torsion dominated frequencies.

4.CONCLUSIONS

In this study, a new analytical method is presented for the analysis of forced vibrations of open section channels in which the flexible supports provide the end constraints. The dynamic response of open section channels is a coupled problem and their analysis requires the simultaneous consideration of all the possible vibratory motions. The wave propagation approach is an efficient tool for this complicated problem and the developed method is based on that.

The current method analyzes the forced, coupled vibrations of open section channels. The channels, taken as Euler-Bernoulli beams, have uniform cross-section and a single symmetry axis. That consecutively leads to the coupling of flexural vibrations in one direction and torsional vibrations. The excitation is assumed to be in the form of a harmonic point force, acting at the centroid.

Various frequency response curves of uncoupled and coupled vibrations are presented for a variety of different elastic end boundary conditions(which may also have the inertial properties). The developed method, although aimed at determining the forced vibration characteristics, is also capable of determining the free vibration properties. This is also demonstrated by presenting various mode shape graphs. It has been determined that the transverse and the torsional stiffnesses play more significant role as compared to the rotational stifness.

The method can be used in analyzing the effects of multi point and/or distributed loadings. This can simply be achieved by modifying the terms of the forcing vector without increasing the order of the relevant matrix equation. The developed method can also be used in the analysis of elastically supported, triply-coupled vibrations of uniform channels. Results of that study will be the subject of another paper.

REFERENCES

1. Gere, J.M. and Lin, Y.K., Coupled Vibrations of Thin-Walled Beams of Open Cross-Section. *J. Applied Mech. Trans.ASME.*, 1958, **80**, 373-8.
2. Lin, Y.K., Coupled Vibrations of Restrained Thin-Walled Beams. *J. Applied Mech. Trans.ASME.*, 1960, **82**, 739-40.
3. Dokumacı, E., An Exact Solution for Coupled Bending and Torsional Vibrations of Uniform Beams Having Single Cross-Sectional Symmetry. *J.Sound and Vib.*,1987, **119**, 443-9.
4. Bishop, R.E.D, Cannon, S.M. and Miao, S., On Coupled Bending and Torsional Vibration of Uniform Beams. *J.Sound and Vib.*,1989,**131**,457-64.
5. Cremer, L. and Heckl, M.,*Structure- Borne Sound,* Springer-Verlag,1988.
6. Mead, D.J. and Yaman, Y., The Harmonic Response of Uniform Beams on Multiple Linear Supports: A Flexural Wave Analysis. *J. Sound and Vib,* 1990, **141**, 465-84
7. Yaman, Y. Wave Receptance Analysis of Vibrating Beams and Stiffened Plates. *Ph.D. Thesis,* University of Southampton, 1989.
8 Yaman, Y., Vibrations of Open-Section Channels: A Coupled Flexural and Torsional Wave Analysis. (*J. Sound and Vib*, Accepted for publication)

THE RESPONSE OF TWO-DIMENSIONAL PERIODIC STRUCTURES TO HARMONIC AND IMPULSIVE POINT LOADING

R.S. Langley
Department of Aeronautics and Astronautics
University of Southampton
Southampton SO17 1BJ

ABSTRACT

Much previous work has appeared on the response of a two-dimensional periodic structure to distributed loading, such as that arising from a harmonic pressure wave. In contrast the present work is concerned with the response of a periodic structure to localised forcing, and specifically the response of the system to both harmonic and impulsive point loading is considered by employing the method of stationary phase. It is shown that the response can display a complex spatial pattern which could potentially be exploited to reduce the level of vibration transmitted to sensitive equipment.

1. INTRODUCTION

Many types of engineering structure are of a repetitive or periodic construction, in the sense that the basic design consists of a structural unit which is repeated in a regular pattern, at least over certain regions of the structure. An orthogonally stiffened plate or shell forms one example of an ideal two-dimensional periodic structure in which the fundamental structural unit is an edge stiffened panel. Although a completely periodic structure is unlikely to occur in practice, much can be ascertained regarding the structural dynamic properties of a real structure by considering the behaviour of a suitable periodic idealization. For this reason, much previous work has been performed on the dynamic behaviour of two-dimensional periodic structures, with particular emphasis on free vibration and the response to pressure wave excitation [1,2]. However, no results have yet been appeared regarding the response of two-dimensional periodic structures to point loading (as might arise from equipment mounts), and this topic forms the subject of the present work. A general method of computing the response to both harmonic and impulsive loading is presented, and this is then applied to an example system.

Initially the response of a two-dimensional periodic structure to harmonic point loading is considered, and it is shown that the far-field response can be expressed very simply in terms of the "phase constant" surfaces which describe the propagation of plane waves. It is further shown that for

excitation within a pass band two distinct forms of response can occur: in the first case the amplitude of the response has a fairly smooth spatial distribution, whereas in the second case a very uneven distribution is obtained and "shadow zones" of very low response are obtained. The second form of behaviour is related to the occurrence of caustics (defined in section 3.3), and the distinctive nature of the response suggests that a periodic structure might be designed to act as a spatial filter to isolate sensitive equipment from an excitation source.

Attention is then turned to the impulse response of a two-dimensional periodic structure. It is again shown that the response can be expressed in terms of the phase constant surfaces which describe the propagation of plane waves. The application of the method of stationary phase to this problem has a number of interesting features, the most notable being the fact that four or more stationary points can arise. It is found that a surface plot of the maximum response amplitude against spatial position reveals features which resemble the "caustic" distributions obtained under harmonic loading.

2. RESPONSE TO A HARMONIC POINT LOAD

2.1 Modal Formulation and Extension to the Infinite System

A two-dimensional periodic structure consists of a basic unit which is repeated in two directions to form a regular pattern, as shown schematically in Figure 1. Each unit shown in this figure might represent for example an edge stiffened curved panel in an aircraft fuselage structure, a three-dimensional beam assembly in a roof truss structure, or a pair of strings in the form of a "+" in a cable net structure. The displacement w of the system can be written in the form $w(n,x)$, where $n=(n_1\ n_2)$ identifies a particular unit and $x=(x_1\ x_2\ x_3)$ identifies a particular point within the unit. The coordinate system x is taken to be local to each unit, and the precise dimension of both x and the response vector w will depend on the details of the system under consideration.

The present section is concerned with the response of a two-dimensional periodic structure to harmonic point loading of frequency ω. In the case of a system of finite dimension, the response at location (n,x) to a harmonic force F applied at $(0,x_o)$ can be expressed in the standard form [3]

$$w(n,x)=\sum_p \sum_q \frac{\phi_{pq}(n,x)F^T\phi_{pq}(0,x_o)}{\omega_{pq}^2(1+i\eta)-\omega^2}, \qquad (1)$$

where η is the loss factor, $\phi_{pq}(n,x)$ are the modes of vibration of the system and ω_{pq} are the associated natural frequencies. The modes ϕ_{pq} which appear in equation (1) are scaled to unit generalized mass, so that

$$\sum_{n_1}\sum_{n_2}\int_V \rho(\boldsymbol{x})\boldsymbol{\phi}_{pq}^T(\boldsymbol{n},\boldsymbol{x})\boldsymbol{\phi}_{pq}(\boldsymbol{n},\boldsymbol{x})d\boldsymbol{x}=1, \qquad (2)$$

where V represents the volume (or equivalent) of a unit and $\rho(\boldsymbol{x})$ is the mass density. The present concern is with the response of an infinite system, or equivalently the response of a large finite system in which the vibration decays to a negligible level before reaching the system boundaries. In this case the response is independent of the system boundary conditions, and it follows that any analytically convenient set of modes can be employed in equation (1). As explained in reference [4], it is expedient to consider the Born-Von Kármán (or "periodic") boundary conditions, as in this case the modes of vibration can be expressed very simply in terms of propagating plane wave components. In this regard it can be noted from periodic structure theory [5] that a propagating plane wave of frequency ω has the general form

$$w(\boldsymbol{n},\boldsymbol{x})=Re\{\boldsymbol{g}(\boldsymbol{x})\exp(i\epsilon_1 n_1+i\epsilon_2 n_2+i\omega t)\}, \qquad (3)$$

where ϵ_1 and ϵ_2 are known as the propagation constants of the wave (with $-\pi<\epsilon_1\leq\pi$ and $-\pi<\epsilon_2\leq\pi$ for uniqueness), and $\boldsymbol{g}(\boldsymbol{x})$ is a complex amplitude function. By considering the dynamics of a single unit of the system and applying Bloch's Theorem [5], it is possible to derive a dispersion equation which must be satisfied by the triad $(\omega,\epsilon_1,\epsilon_2)$ - by specifying ϵ_1 and ϵ_2 this equation can be solved to yield the admissible propagation frequencies ω. By way of example, solutions yielded by this procedure for a plate which rests on a grillage of simple supports are shown in Figure 2 (after reference [6]). It is clear that the solutions form surfaces above the ϵ_1-ϵ_2 plane - these surfaces are usually referred to as "phase constant" surfaces, and a single surface will be represented here by the equation $\omega=\Omega(\epsilon_1,\epsilon_2)$. The phase constant surfaces always have cyclic symmetry of order two, so that $\Omega(\epsilon_1,\epsilon_2)=\Omega(-\epsilon_1,-\epsilon_2)$; for an orthotropic system the surfaces also have cyclic symmetry of order four, and therefore only the first quadrant of the ϵ_1-ϵ_2 plane need be considered explicitly, as in Figure 2.

The key point about the Born-Von Kármán boundary conditions is that a single propagating wave can fully satisfy these conditions providing ϵ_1 and ϵ_2 are chosen appropriately. The conditions state that the left hand edge of the system is contiguous with the right hand edge, and similarly the top edge is contiguous with the bottom edge, so that the system behaves as if it were topologically equivalent to a torus. If the system is comprised of $N_1\times N_2$ units, then a propagating wave will satisfy these conditions if $\epsilon_1 N_1=2\pi p$ and $\epsilon_2 N_2=2\pi q$ for any integers p and q. Following equation (3), the displacement associated with such a wave can be written in the form

$$w_{pq}(\boldsymbol{n},\boldsymbol{x})=Re\{g_{pq}(\boldsymbol{x})\exp(i\epsilon_{1p}n_1+i\epsilon_{2q}n_2+i\omega_{pq}t)\}, \tag{4}$$

where ϵ_{1p} and ϵ_{2q} are the appropriate values of the phase constants, and $\omega_{pq}=\Omega(\epsilon_{1p},\epsilon_{2q})$. Now since $\Omega(\epsilon_{1p},\epsilon_{2q})=\Omega(-\epsilon_{1p},-\epsilon_{2q})$ it follows that a wave of frequency ω_{pq} travelling in the opposite direction to w_{pq} will also satisfy the boundary conditions. This wave (w_{pq}' say) will have the form

$$w'_{pq}(\boldsymbol{n},\boldsymbol{x})=Re\{g^*_{pq}(\boldsymbol{x})\exp(-i\epsilon_{1p}n_1-i\epsilon_{2q}n_2+i\omega_{pq}t)\}, \tag{5}$$

where it has been noted from periodic structure theory that reversing the direction of a wave leads to the conjugate of the complex amplitude function $g(x)$. The two waves represented by equations (4) and (5) can be combined with the appropriate phase to produce two modes of vibration of the system in the form

$$\begin{Bmatrix}\phi_{1pq}(\boldsymbol{n},\boldsymbol{x})\\ \phi_{2pq}(\boldsymbol{n},\boldsymbol{x})\end{Bmatrix}=\begin{Bmatrix}Re\\ Im\end{Bmatrix}2g_{pq}(\boldsymbol{x})\exp(i\epsilon_{1p}n_1+i\epsilon_{2q}n_2). \tag{6}$$

By adopting this set of modes it can be shown [4] that equation (1) can be re-expressed as

$$w(\boldsymbol{n},\boldsymbol{x})=\sum_{p=1-N_1/2}^{N_1/2}\sum_{q=1-N_2/2}^{N_2/2}\frac{2g^*_{pq}(\boldsymbol{x})\boldsymbol{F}^Tg_{pq}(\boldsymbol{x}_o)\exp(-i\epsilon_{1p}n_1-i\epsilon_{2q}n_2)}{\omega^2_{pq}(1+i\eta)-\omega^2}, \tag{7}$$

where N_1 and N_2 have been taken to be even, and the amplitude function g_{pq} is scaled so that

$$g_{pq}=[2\rho(\boldsymbol{x})VN_1N_2]^{-1/2}f_{pq}(\boldsymbol{x}),\quad (1/V)\int_V f^T_{pq}(\boldsymbol{x})f^*_{pq}(\boldsymbol{x})d\boldsymbol{x}=1, \tag{8,9}$$

where the normalized amplitude function f_{pq} is defined accordingly. The summation which appears in equation (7) includes only those modes associated with a single phase constant surface $\Omega(\epsilon_1,\epsilon_2)$; if more than one surface occurs then the equation should be summed over the complete set of surfaces. The summation will include N_1N_2 modes for each surface, which is consistent with known results for the modal density of a two-dimensional periodic structure.

Equation (7) yields the response of a finite system of dimension $N_1\times N_2$ to a harmonic point load - this response is identical to that of an infinite system if the vibration decays to a negligible amount before meeting the system boundaries. If the system size is allowed to tend to infinity in equation

(7) then neighbouring values of the phase constants ϵ_{1p} and ϵ_{2q} become closely spaced (since $d\epsilon_{1p}=\epsilon_{1,p+1}-\epsilon_{1p}=2\pi/N_1$ and $d\epsilon_{2q}=\epsilon_{2,q+1}-\epsilon_{2q}=2\pi/N_2$), and in this case the summations can be replaced by integrals over the phase constants to yield

$$w(n,x)=(N_1N_2/2\pi^2)\int_{-\pi}^{\pi}\int_{-\pi}^{\pi}\frac{g^*(x)F^Tg(x_o)\exp(-i\epsilon_1n_1-i\epsilon_2n_2)d\epsilon_1d\epsilon_2}{[\Omega(\epsilon_1,\epsilon_2)]^2(1+i\eta)-\omega^2}, \qquad (10)$$

where $\omega=\Omega(\epsilon_1,\epsilon_2)$ and $g(x)$ is the complex amplitude associated with the wave $(\omega,\epsilon_1,\epsilon_2)$. The evaluation of the integrals which appear in equation (10) is discussed in the following sub-sections.

2.2 Integration over ϵ_1

The integral over ϵ_1 which appears in equation (10) can be evaluated by using contour integration techniques. Two possible contours in the complex ϵ_1 plane are shown in Figure 3; to ensure a zero contribution from the segment $\mathrm{Im}(\epsilon_1)=\pm\infty$, the upper contour is appropriate for $n_1<0$ while the lower contour should be used for $n_2>0$. For each contour the contributions from the segments $\epsilon_{1R}=-\pi$ and $\epsilon_{1R}=\pi$ cancel, since the integrand which appears in equation (10) is unchanged by an increment of 2π in the real part of ϵ_1. The only non-zero contribution to the integral around either contour therefore arises from the segment which lies along the real axis. The poles of the integrand occur at the ϵ_1 solutions of the equation

$$[\Omega(\epsilon_1,\epsilon_2)]^2(1+i\eta)-\omega^2=0, \qquad (11)$$

for specified ϵ_2 and ω. By definition there will be two real solutions[1] in the absence of damping ($\eta=0$) providing the frequency range covered by the phase constant surface includes ω. Any complex solutions to equation (11) in the absence of damping will correspond physically to "evanescent" waves which decay rapidly away from the applied load. The present analysis is concerned primarily with the response of the system in the far field (that is, at points remote from the excitation source), and for this reason attention is focused solely on those roots to equation (11) which are real when $\eta=0$. The effect of damping on these roots can readily be deduced: if η is small then it follows from equation (11) that a real solution ϵ_1 will be modified to become $\epsilon_1-i(\omega/2)(\partial\Omega/\partial\epsilon_1)^{-1}$, and hence the real pole for which $\partial\Omega/\partial\epsilon_1<0$ is moved to the upper half plane, while that for which $\partial\Omega/\partial\epsilon_1>0$ is moved to the lower half plane. Given that the residue at such a pole is proportional to $(\partial\Omega/\partial\epsilon_1)^{-1}$,

[1]One positive and one negative. These solutions will have the form $\pm\epsilon_1$ for an orthotropic system.

it follows that the sign of the residue which arises from the contour integral is determined by the integration path selected, and hence by the sign of n_1. These considerations lead to the result

$$w(\boldsymbol{n},\boldsymbol{x})=\frac{-iN_1N_2}{2\pi}\int_{-\pi}^{\pi}\frac{\boldsymbol{g}^*\boldsymbol{F}^T\boldsymbol{g}_o\exp(-i\epsilon_1 n_1-i\epsilon_2 n_2)\mathrm{d}\epsilon_2}{\Omega\,|\partial\Omega/\partial\epsilon_1|\,(1+i\eta)}, \tag{12}$$

where $\epsilon_1(\epsilon_2,\omega)$ is the appropriate solution to equation (11). The evaluation of the integral over ϵ_2 is discussed in the following section.

3.3 Integration over ϵ_2

Since the present concern is with the response of the system at some distance from the excitation point, the integral over ϵ_2 which appears in equation (12) can be evaluated to an acceptable degree of accuracy by using the method of steepest descent [7]. With this approach it is first necessary to identify the value of ϵ_2 for which the exponent $-i(\epsilon_1 n_1+\epsilon_2 n_2)$ is stationary. The condition for this is

$$(\partial\epsilon_1/\partial\epsilon_2)n_1+n_2=0. \tag{13}$$

Now ϵ_1 and ϵ_2 satisfy the dispersion relation, equation (11), and thus equation (13) can be re-expressed in the form

$$(\partial\Omega/\partial\epsilon_2)n_1-(\partial\Omega/\partial\epsilon_1)n_2=0, \tag{14}$$

where it has been noted from equation (11) that, for fixed ω, $\partial\epsilon_1/\partial\epsilon_2=-(\partial\Omega/\partial\epsilon_2)/(\partial\Omega/\partial\epsilon_1)$. In the absence of damping the wave group velocity lies in the direction $(\partial\Omega/\partial\epsilon_1\ \partial\Omega/\partial\epsilon_2)$, and in this case it follows from equation (14) that the group velocity associated with the required value of ϵ_2 is along $(n_1\ n_2)$. For light damping this result will be substantially unaltered, although damping *will* have an important effect on the value of the exponent $-i(\epsilon_1 n_1+\epsilon_2 n_2)$ at the stationary point. This effect can be investigated by noting initially that

$$\partial(\epsilon_1 n_1+\epsilon_2 n_2)/\partial\eta=(\partial\epsilon_1/\partial\eta\ \ \partial\epsilon_2/\partial\eta).(n_1\ \ n_2). \tag{15}$$

Now it follows from equation (11) that for light damping ($\eta\ll 1$)

$$(\partial\Omega/\partial\epsilon_1\ \ \partial\Omega/\partial\epsilon_2).(\partial\epsilon_1/\partial\eta\ \ \partial\epsilon_2/\partial\eta)=-i\omega/2, \tag{16}$$

and hence equations (14)-(16) can be combined to yield the following result at the stationary point

$$\partial(\epsilon_1 n_1+\epsilon_2 n_2)/\partial\eta=-i\omega n/2c_g. \tag{17}$$

Here $c_g=\sqrt{[(\partial\Omega/\partial\epsilon_1)^2+(\partial\Omega/\partial\epsilon_2)^2]}$ is the resultant group velocity and $n=\sqrt{[n_1^2+n_2^2]}$ is the radial distance (in units) from the excitation point to the unit under consideration. It follows that in the immediate vicinity of the stationary point the exponent $-i(\epsilon_1 n_1+\epsilon_2 n_2)$ can be expanded in the form

$$-i(\epsilon_1 n_1+\epsilon_2 n_2)=-i(\epsilon_1 n_1+\epsilon_2 n_2)_0-(\omega\eta n/2c_g)_0-in_1(\partial^2\epsilon_1/\partial\epsilon_2^2)_0[\epsilon_2-(\epsilon_2)_0]^2/2, \tag{18}$$

where the subscript 0 indicates that the term is to be evaluated at the stationary point under the condition $\eta=0$; for ease of notation, this subscript is omitted in the following analysis. The method of steepest descent proceeds by substituting equation (18) into equation (12) and assuming that: (i) the main contribution to the integral arises from values of ϵ_2 in the immediate vicinity of the stationary point; (ii) the integrand is effectively constant in this vicinity, other than through variation of the term ϵ_2-$(\epsilon_2)_0$ which appears in equation (18); (iii) under conditions (i) and (ii) the integration range can be extended to an infinite path without significantly altering the result. The method then yields [7]

$$w(\boldsymbol{n},\boldsymbol{x})=-if^{*}F^{T}f_0\left[2\Omega V|\partial\Omega/\partial\epsilon_1|\sqrt{2\pi\rho(\boldsymbol{x})\rho(\boldsymbol{x}_0)|n_1(\partial^2\epsilon_1/\partial\epsilon_2^2)|}\right]^{-1}\cdots\cdots$$
$$\times\exp\left[-i\epsilon_1 n_1-i\epsilon_2 n_2-\omega\eta n/2c_g-i(\pi/4)sgn\{n_1(\partial^2\epsilon_1/\partial\epsilon_2^2)\}\right], \tag{19}$$

where $\boldsymbol{f}$ is the normalized complex wave amplitude which appears in equation (9), and all terms are to be evaluated at the stationary point.

The stationary point associated with equation (19) is that point for which the group velocity is in the $(n_1\ n_2)$ direction. Geometrically, this is the point at which the normal to the curve $\omega=\Omega(\epsilon_1,\ \epsilon_2)$ in the ϵ_1-ϵ_2 plane lies in the $(n_1\ n_2)$ direction. Three such curves are shown schematically in Figure 4, together with a specified $(n_1\ n_2)$ direction. For the frequencies ω_1 and ω_3 the situation is straight forward, in the sense that a unique stationary point exists for any $(n_1\ n_2)$ direction. For the frequency ω_2 the situation is more complex, since: (i) two stationary points occur for the $(n_1\ n_2)$ direction shown, and (ii) no stationary point exists if the $(n_1\ n_2)$ direction lies beyond the heading θ shown in the figure (the dashed arrow represents the normal with maximum inclination to the ϵ_1 axis). In case (i) equation (19) should be summed over the two stationary points, while in case (ii) the method of steepest descent predicts that $w(\boldsymbol{n},\boldsymbol{x})$ will be approximately zero, leading to a region of very low vibrational response. If the direction $(n_1\ n_2)$ coincides with the dashed arrow, then equation (19) breaks down, since it can be shown that $\partial^2\epsilon_1/\partial\epsilon_2^2=0$ at this point. The heading indicated by the dashed arrow represents a *caustic* [7], and the theory given in the present section must be modified for headings

(n_1 n_2) which are in the immediate vicinity of the caustic - full details of the appropriate modifications are given in reference [4]. An example which illustrates the application of equation (19) is given in section 4.

3. RESPONSE TO AN IMPULSIVE POINT LOAD

If the system is subjected to an impulsive (i.e. a delta function applied at $t=0$), rather than harmonic, point load, then equation (10) becomes [8]

$$w(\boldsymbol{n},\boldsymbol{x},t)=(N_1N_2/2\pi^2)\int_{-\pi}^{\pi}\int_{-\pi}^{\pi} \boldsymbol{g}^*(\boldsymbol{x})\boldsymbol{F}^T\boldsymbol{g}(\boldsymbol{x}_o)\exp(-i\epsilon_1 n_1-i\epsilon_2 n_2)\,(1/\omega)\sin\omega t\, d\epsilon_1 d\epsilon_2, \tag{20}$$

where $\omega=\Omega(\epsilon_1,\epsilon_2)$. The method of stationary phase can be applied to this expression to yield [8]

$$w(\boldsymbol{n},\boldsymbol{x},t)=(1/2V\pi)[\rho(\boldsymbol{x})\rho(\boldsymbol{x}_o)|J|]^{-1/2}Re\{-(i/\Omega t)\boldsymbol{f}^*(\boldsymbol{x})\boldsymbol{F}^T\boldsymbol{f}(\boldsymbol{x}_o)\ldots$$
$$\exp(-i\epsilon_1 n_1-i\epsilon_2 n_2+i\Omega t+i\delta)\}, \tag{21}$$

where all terms are evaluated at the stationary point, and J and δ are defined as

$$J=(\partial^2\Omega/\partial\epsilon_1^2)(\partial^2\Omega/\partial\epsilon_2^2)-(\partial^2\Omega/\partial\epsilon_1\partial\epsilon_2)^2, \quad \delta=(\pi/4)\mathrm{sgn}(\partial^2\Omega/\partial\epsilon_1^2)\{1+\mathrm{sgn}(J)\}. \tag{22,23}$$

In this case the stationary point is given by the solution to the equations

$$n_1=(\partial\Omega/\partial\epsilon_1)t, \quad n_2=(\partial\Omega/\partial\epsilon_2)t. \tag{24,25}$$

In practice equations (24) and (25) may yield multiple solutions (stationary points), in which case equation (21) should be summed over all such points. Furthermore, stationary points having $J=0$ indicate the occurrence of a caustic, and equation (21) must be modified in the immediate vicinity of such points as detailed in reference [8]. An example of the application of equation (21) is given in the following section.

4. EXAMPLE APPLICATION

4.1 The System Considered

The foregoing analysis is applied in this section to a two-dimensional periodic structure which consists of a rectangular grid of lumped masses m which are coupled through horizontal and vertical shear springs of stiffness k_1 and k_2 respectively. Each mass has a single degree of freedom consisting of the out-of-plane displacement w, and a linear spring of stiffness k is attached between each mass and a fixed base. It is readily shown that the system has a single phase constant surface of the form

$$\Omega^2(\epsilon_1,\epsilon_2)=\mu_1(1-\cos\epsilon_1)+\mu_2(1-\cos\epsilon_2)+\omega_n^2, \tag{26}$$

where $\mu_1=2k_1/m$, $\mu_2=2k_2/m$, and $\omega_n^2=k/m$. The function Ω can be used in conjunction with the analysis of the previous sections to yield the response of the system to harmonic and impulsive point loading; in this regard it can be noted that for the present case $\rho(x)=m$, $V=1$, and $f(x)=1$.

4.2 Response to Harmonic Loading

The surface $\Omega(\epsilon_1,\epsilon_2)$ is shown as a contour plot in Figure 5 for the case $m=1.0$, $\omega_n=0$, $\mu_1=1.0$, $\mu_2=0.57$. Results for the forced harmonic response of this system at the two frequencies $\omega=1.003$ and $\omega=1.181$ are shown in Figures 6 and 7. In each case the response of a 40×40 array of point masses is shown; a unit harmonic point load is applied to mass (21,21) and the loss factor is taken to be $\eta=0.05$. Two sets of contours are shown in each Figure: the smooth contours have been calculated by using equation (19) while the more irregular contours have been obtained by a direct solution of the equations of motion of the finite 1600 degree-of-freedom system. By considering the results shown in Figure 6, it can be concluded that: (i) for the present level of damping the finite system effectively behaves like an infinite system, and (ii) the analytical result yielded by equation (19) provides a very good quantitative estimate of the far field response. It can be noted from Figure 5 that no caustic occurs for $\omega=1.003$, in the sense that equation (14) yields only one stationary point which contributes to equation (19). In contrast, a caustic does occur for the case $\omega=1.181$, and this leads to the very irregular spatial distribution of response shown in Figure 7. Two stationary points contribute to equation (19), and constructive and destructive interference between these contributions is responsible for the rapid fluctuations in the response amplitude. It is clear that the response exhibits a "dead zone" for points which lie beyond the caustic heading (in this case 30.25° to the n_1-axis), as predicted by the analysis presented in section 2.

4.3 Response to Impulsive Loading

The impulse response of a system having $m=1.0$, $\mu_1=1.0$, $\mu_2=0.57$, and

$\omega_n^2=0.25$ has been computed. The impulse was taken to act at the location $n_1=n_2=0$ and the time history of the motion of each mass in the region $-10\leq(n_1,n_2)\leq 10$ was found by using equations (21)-(23). For each mass the maximum response $|w|$ was recorded, and the results obtained are shown as a contour plot in Figure 8. In accordance with Fourier's Theorem, the impulse response of the system contains contributions from all frequencies, and therefore the spatial distribution of $|w|$ can be expected to lie somewhere between the two extreme forms of harmonic response exhibited in Figures 6 and 7. This is in fact the case, and the response shown in Figure 8 retains a distinctive spatial pattern. As discussed in reference [8], the results shown in Figure 8 are in good agreement with direct simulation of the impulse response of the system.

5. CONCLUSIONS

This paper has considered the response of a two-dimensional periodic structure to both harmonic and impulsive point loading. With regard to harmonic loading, it has been shown that the spatial pattern of the response is strongly dependent on the occurrence of a caustic: if no caustic occurs then the response has a fairly smooth spatial distribution, whereas the presence of a caustic leads to an irregular spatial distribution and a "dead zone" of very low response. This type of feature is also exhibited, although to a lesser degree, in the spatial distribution of the response to an impulsive point load. This behaviour could possibly be exploited to reduce vibration transmission along a specified path, although the practicality of this approach for a complex system has yet to be investigated. The present analytical approach can be applied to all types of two-dimensional periodic structure - the information required consists of the phase constant surface(s) $\Omega(\epsilon_1,\epsilon_2)$ and the associated wave form(s) $f(x)$, both of which are yielded by standard techniques for the analysis of free wave motion in periodic structures [1,2].

REFERENCES

1. S.S. MESTER and H. BENAROYA 1995 *Shock and Vibration* **2**, 69-95. Periodic and near-periodic structures.
2. D.J. MEAD 1996 *Journal of Sound and Vibration* **190**, 495-524. Wave propagation in continuous periodic structures: research contributions from Southampton 1964-1995.
3. L. MEIROVITCH 1986 *Elements of Vibration Analysis, Second Edition*. New York: McGraw-Hill Book Company.
4. R.S. LANGLEY 1996 *Journal of Sound and Vibration* (to appear). The response of two-dimensional periodic structures to point harmonic forcing.

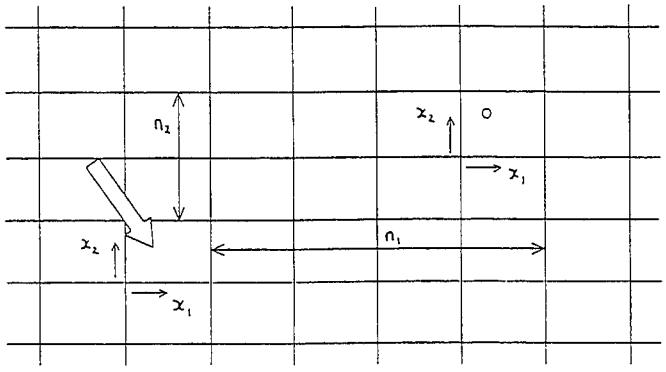

Figure 1. Schematic of a two-dimensional periodic structure. The arrow indicates the reference unit (with $n=0$) while the circle represents a general point (n,x). The structure may have a third spatial coordinate x_3, which for convenience is not shown in the figure. The point load considered in section 3 is applied at the location of the arrow.

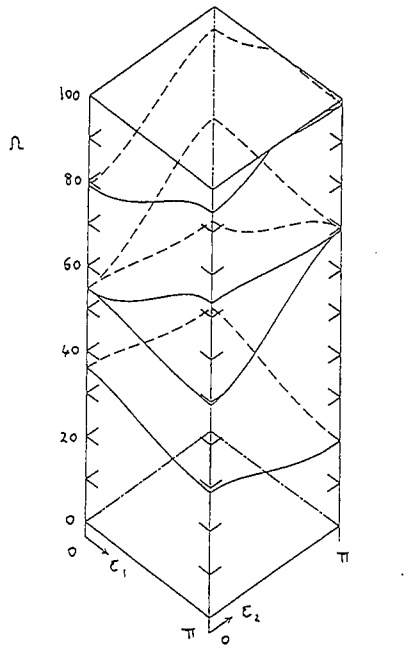

Figure 2. Phase constant surfaces for a plate which rests on a square grillage of simple supports. Ω is a non-dimensional frequency which is defined as $\Omega=\omega L^2\sqrt{(m/D)}$, where m and D are respectively the mass per unit area and the flexural rigidity of the plate, and L is the support spacing.

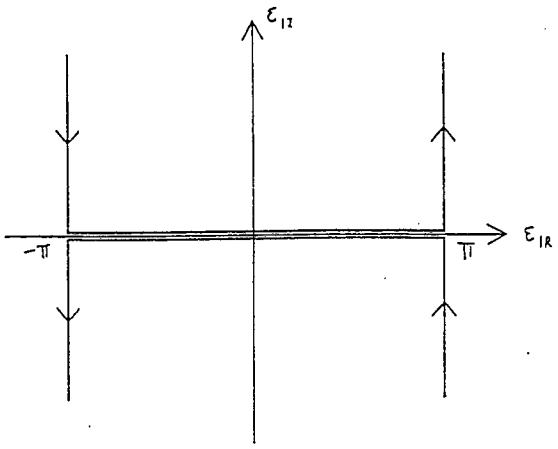

Figure 3. Integration paths in the complex ϵ_1 plane.

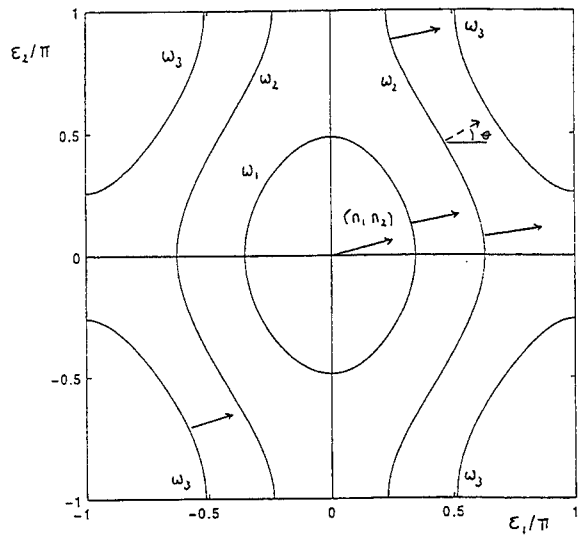

Figure 4. Schematic of three constant frequency contours in the ϵ_1-ϵ_2 plane. The arrows indicate normals to the contours which are aligned to a fied direction (n_1, n_2). The dashed arrow indicates the caustic heading in the first quadrant for the case ω_2.

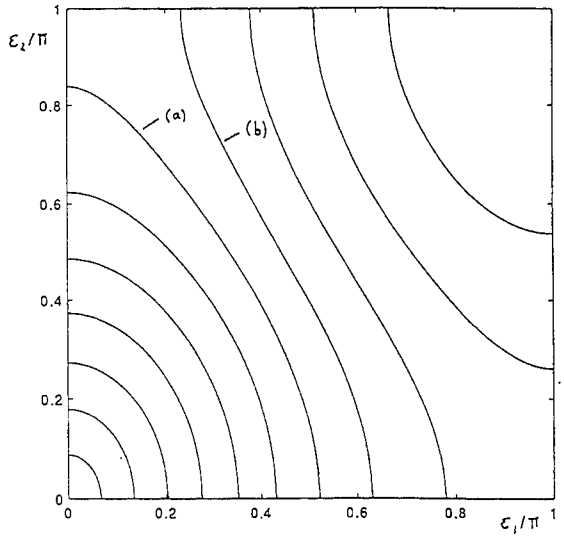

Figure 5. Contour plot of the phase constant surface for the case $\mu_1=1.0$, $\mu_2=0.57$. The contours are separated by an increment $\Delta\omega=0.1477$. The two contours considered in section 4.2 are indicated as follows: (a) $\omega=1.033$; (b) $\omega=1.181$.

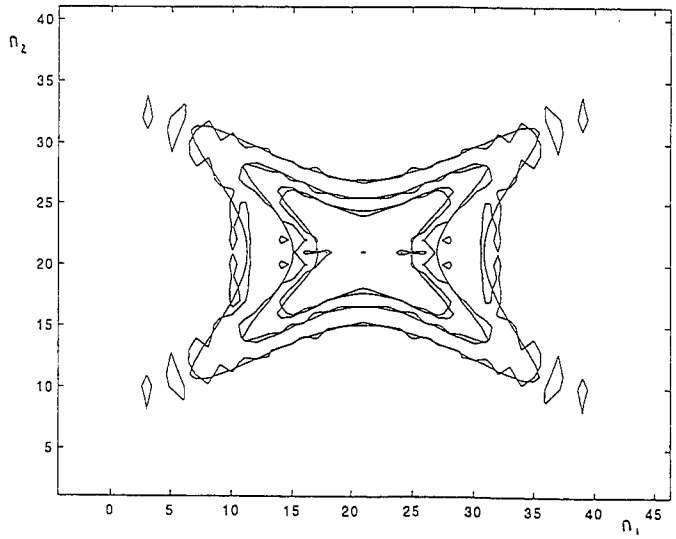

Figure 6. Response $|w(n,x)|^2$ of the 40×40 mass/spring system to a unit harmonic force of frequency $\omega=1.033$ applied at the location $i=j=21$. The contours correspond to the response levels $|w(n,x)|^2=0.01$, 0.02, and 0.05.

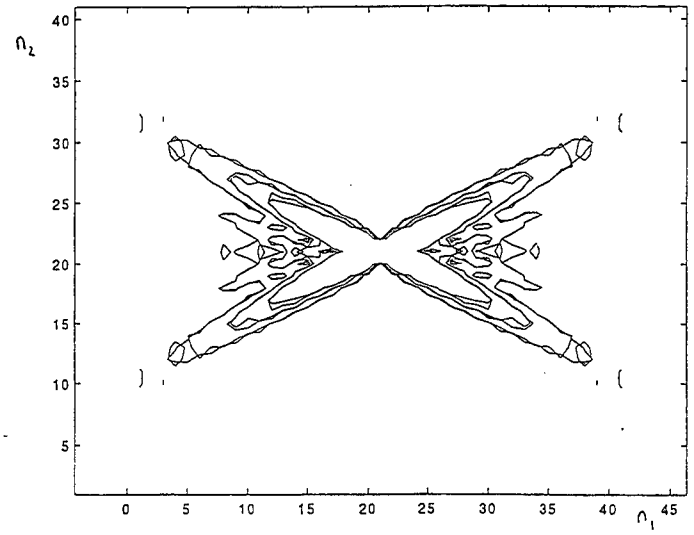

Figure 7. Response $|w(n,x)|^2$ of the 40×40 mass/spring system to a unit harmonic force of frequency $\omega=1.181$ applied at the location $i=j=21$. The contours correspond to the response levels $|w(n,x)|^2=0.01$, 0.025, and 0.05.

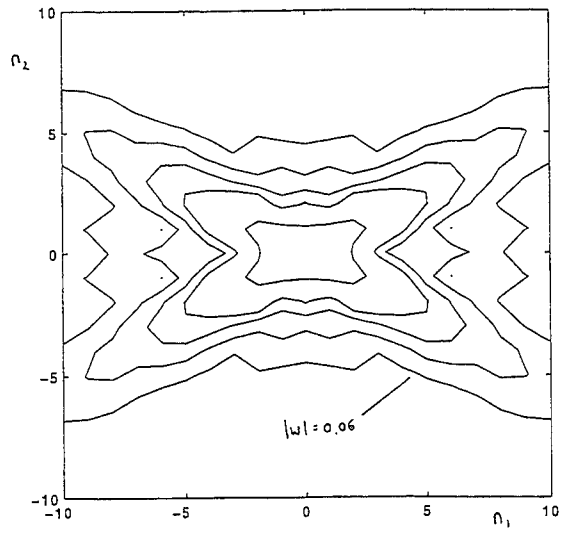

Figure 8. Contours of the maximum response $|w|$; the levels shown are 0.06, 0.08, 0.1, 0.12, and 0.2.

NONLINEAR VIBRATION III

STICK-SLIP MOTION OF AN ELASTIC SLIDER SYSTEM ON A VIBRATING DISC

H Ouyang J E Mottershead M P Cartmell [1] M I Friswell [2]

Department of Mechanical Engineering, University of Liverpool

[1] Department of Mechanical Engineering, University of Edinburgh

[2] Department of Mechanical Engineering, University of Wales Swansea

ABSTRACT

The in-plane vibration of a slider-mass which is driven around the surface of a flexible disc, and the transverse vibration of the disc, are investigated. The disc is taken to be an elastic annular plate and the slider has flexibility in the circumferential (in-plane) and transverse directions. The static friction coefficient is assumed to be higher than the kinetic friction. As a result of the friction force acting between the disc and the slider system, the slider will oscillate in the stick-slip mode in the plane of the disc. The transverse vibration induced by the slider will change the normal force of the slider system acting on the disc, which in turn will change the in-plane oscillation of the slider. For different values of system parameters, the coupled in-plane oscillation of the slider and transverse vibration of the disc will exhibit quasi-periodic as well as chaotic behaviour. Rich patterns of chaotic vibration of the slider system are presented in graphs to illustrate the special behaviour of this non-smooth nonlinear dynamical system. The motivation of this work is to analyse and understand the instability and/or squeal of physical systems such as car brake discs where there are vibrations induced by non-smooth dry-friction forces.

NOMENCLATURE

a, b inner and outer radii of the annular disc

c damping coefficient of the slider in in-plane direction

h thickness of the disc

$\mathrm{i} = \sqrt{-1}$

k, k_p transverse and in-plane stiffness of the slider system

m mass of the slider

r radial co-ordinate in cylindrical co-ordinate system

r_0 radial position of the slider

q_{kl} modal co-ordinate for k nodal circles and l nodal diameters

t time

t_{stick} the time of the onset of sticking

u, u_0 transverse displacement of the slider mass and its initial value

w, w_0 transverse displacement of the disc and its initial value

D flexural rigidity of the disc

D^* Kelvin-type damping coefficient

E Young's modulus

N initial normal load on the disc from the slider system

P total normal force on the disc from the slider system

R_{kl} combination of Bessel functions representing mode shape in radial direction

θ circumferential co-ordinate of cylindrical co-ordinate system

μ_k, μ_s kinetic and static dry fiction coefficient between the slider and the disc

ν Poisson's ratio

ξ damping ratio of the disc

ρ specific density of the disc

φ absolute circumferential position of the slider

φ_{stick} absolute circumferential position of the slider when it sticks to the disc

ψ circumferential position of the slider relative to the drive point

ψ_{kl} mode function for the transverse vibration of the disc corresponding to q_{kl}

ω_{kl} natural (circular) frequency corresponding to q_{kl}

Ω constant rotating speed of the drive point around the disc in radians per second

INTRODUCTION

There exists a whole class of mechanical systems which involve discs rotating relative to stationery parts, such as car brake discs, clutches, saws, computer discs and so on. In these systems, dry-friction induced vibration plays a crucial role in system performance. If the vibration becomes excessive, the system might fail, or cease to perform properly, or make offensive noises. In this paper, we investigate the vibration of an in-plane slider system, with a transverse mass-spring-damper, attached through an in-plane spring to a drive point which rotates at constant speed around an elastic disc, and the vibrations of the disc. Dry friction acts between the slider system and the disc.

Dry-friction induced vibration has been studied extensively [1-4]. For car brake vibration and squeal, see the review papers [5,6]. The stick-slip phenomenon of dry-friction induced vibration is studied in the context of chaotic vibration [7-10]. Popp and Stelter [7] studied such motion of one and two degrees of freedom system and found chaos and bifurcation. They also conducted experiments on a beam and a circular plate (infinite number of degrees of freedom). These theoretical works are about systems of less than three degrees of freedom, and the carrier which activates the friction is assumed to be rigid. In this paper, we consider an elastic disc so that the transverse vibrations of the disc are important. As a result of including the transverse vibrations of the disc, rich patterns of chaos, which have not been reported previously are found. If there is only sliding present at constant speed, the problem is reduced to a linear parametric analysis which was carried out for a pin-on-disc system in [11] and for a pad-on-disc system in [12,13].

IN-PLANE OSCILLATION OF THE SLIDER SYSTEM

As the drive point, which is connected to the slider-mass through an in-plane, elastic spring, is rotated at constant angular speed around the disc, the driven slider will undergo stick-slip oscillations. The whole system of the slider and the disc is shown in Figure 1.

The equation of the in-plane motion of the slider system relative to the rotating drive point, in the sliding phase, is,

$$r_0(m\ddot{\psi} + k_p\psi) = -\mu_k \mathrm{Sgn}(\dot{\varphi})P, \tag{1}$$

while in sticking, the equation of the motion becomes,

$$\psi = -\Omega(t - t_{\mathrm{stick}}). \tag{2}$$

The relationship between the relative motion of the slider system to the drive point and its absolute motion (relative to the stationary disc) is

$$\varphi = \Omega t + \psi, \qquad \dot{\varphi} = \Omega + \dot{\psi}. \tag{3}$$

We consider the following initial conditions which are intended to simulate what happens in a disc brake. The slider system is at rest and there is no normal loading on the disc from the slider. Then a constant normal load is applied which causes transverse vibrations in the disc. At the same time, the drive point is given a constant angular velocity. Other initial conditions are possible, so that there is no loss of generality.

First, sliding from the initial sticking phase occurs when,

$$k_p r_0 \psi \geq \mu_s P. \tag{4}$$

The slider will stick to the disc again when,

$$\dot{\psi} = -\Omega, \quad \left|k_p r_0 \psi\right| \leq \mu_s P \quad \text{(during sliding)}, \tag{5}$$

or it will begin to slide again if,

$$\dot{\psi} = -\Omega, \quad \left|k_p r_0 \psi\right| \geq \mu_s P \quad \text{(during sticking)}. \tag{6}$$

Consequently, the slider system will stick and slide consecutively on the disc surface.

TRANSVERSE VIBRATION OF THE ANNULAR DISC

The equation of motion of the disc under the slider system is,

$$\rho h \frac{\partial^2 w}{\partial t^2} + D^* \nabla^4 \dot{w} + D\nabla^4 w = -\frac{1}{r}\delta(r - r_0)\delta(\theta - \varphi)P. \tag{7}$$

The total force P is the summation of initial normal load N and the resultant of the transverse motion u of the slider. Its expression is,

$$P = N + m\ddot{u} + c\dot{u} + k(u - u_0). \tag{8}$$

Since it is assumed that the slider system is always in perfect contact with the disc, then,

$$u(t) = w(r_0, \varphi(t), t)\,. \tag{9}$$

Substitution of equations (8) and (9) into (7) leads to,

$$\rho h\frac{\partial^2 w}{\partial t^2} + D^*\nabla^4\frac{\partial w}{\partial t} + D\nabla^4 w = -\frac{1}{r}\delta(r-r_0)\delta(\theta-\varphi)[N + m(\ddot{\varphi}\frac{\partial w}{\partial \theta} + \dot{\varphi}^2\frac{\partial^2 w}{\partial \theta^2} + 2\dot{\varphi}\frac{\partial^2 w}{\partial \theta \partial t} + \frac{\partial^2 w}{\partial t^2}) + c(\dot{\varphi}\frac{\partial w}{\partial \theta} + \frac{\partial w}{\partial t}) + k(w - w_0)]. \tag{10}$$

Note that equation (10) is valid whether the slider system is sticking or sliding. When the slider sticks to the disc, equation (10) reduces to,

$$\rho h\frac{\partial^2 w}{\partial t^2} + D^*\nabla^4\frac{\partial w}{\partial t} + D\nabla^4 w = -\frac{1}{r}\delta(r-r_0)\delta(\theta-\varphi)\times [N + m\frac{\partial^2 w}{\partial t^2} + c\frac{\partial w}{\partial t} + k(w - w_0)]. \tag{11}$$

COUPLED VIBRATIONS OF THE SLIDER AND THE DISC

Assume that the transverse motion of the disc can be represented by,

$$w(r,\theta,t) = \sum_{k=0}^{\infty}\sum_{l=-\infty}^{\infty}\psi_{kl}(r,\theta)q_{kl}(t)\,, \tag{12}$$

and,

$$\psi_{kl}(r,\theta) = \frac{1}{\sqrt{\rho h b^2}}R_{kl}(r)\exp(il\theta)\,, \tag{13}$$

where $R_{rs}(r)$ is a combination of Bessel functions satisfying the boundary conditions in radial direction at the inner radius and outer radius of the disc. The modal functions satisfy the ortho-normality conditions of,

$$\int_a^b \rho h\overline{\psi}_{kl}\psi_{rs}r\,dr\,d\theta = \delta_{kr}\delta_{ls}\,,$$
$$\int_a^b D\overline{\psi}_{kl}\nabla^4\psi_{rs}r\,dr\,d\theta = \omega_{rs}^2\delta_{kr}\delta_{ls}\,. \tag{14}$$

Equations (10) and (11) can be simplified by being written in terms of the modal co-ordinates from equation (12).

During sticking, the motion of the whole system of the slider and the disc can be represented by,

$$\ddot{q}_{kl} + 2\xi\omega_{kl}\dot{q}_{kl} + \omega_{kl}^2 q_{kl} = -\frac{N}{\sqrt{\rho h b^2}} R_{kl}(r_0)\exp(-\mathrm{i}l\varphi) - \frac{1}{\rho h b^2}\sum_{r=0}^{\infty}\sum_{s=-\infty}^{\infty} R_{rs}(r_0)R_{kl}(r_0)\exp[\mathrm{i}(s-l)\varphi]\times \{m\ddot{q}_{rs} + c\dot{q}_{rs} + k[q_{rs} - q_{rs}(0)]\}, \tag{15}$$

and,

$$\varphi = \varphi_{\text{stick}}, \qquad \psi = -\Omega(t - t_{\text{stick}}). \tag{16}$$

The sticking phase can be maintained if,

$$r_0 k_{\text{p}}|\psi| < \mu_{\text{s}}[N + \frac{1}{\sqrt{\rho h b^2}}\sum_{k=0}^{\infty}\sum_{l=-\infty}^{\infty} R_{kl}(r)\exp(\mathrm{i}l\varphi)\times \{m\ddot{q}_{rs} + c\dot{q}_{rs} + k[q_{rs} - q_{rs}(0)]\}]. \tag{17}$$

While in sliding, the motion of the whole system can be represented by,

$$\ddot{q}_{kl} + 2\xi\omega_{kl}\dot{q}_{kl} + \omega_{kl}^2 q_{kl} = -\frac{N}{\sqrt{\rho h b^2}} R_{kl}(r_0)\exp(-\mathrm{i}l\varphi) - \frac{1}{\rho h b^2}\sum_{r=0}^{\infty}\sum_{s=-\infty}^{\infty} R_{rs}(r_0)R_{kl}(r_0)\exp[\mathrm{i}(s-l)\varphi]\times \{m[\ddot{q}_{rs} + \mathrm{i}2s\dot{\varphi}\dot{q}_{rs} + (\mathrm{i}s\ddot{\varphi} - s^2\dot{\varphi}^2)q_{rs}] + c(\dot{q}_{rs} + \mathrm{i}s\dot{\varphi}q_{rs}) + k[q_{rs} - q_{rs}(0)]\}, \tag{18}$$

and,

$$r_0(m\ddot{\psi} + k_{\text{p}}\psi) = -\mu_{\text{k}}\text{Sign}(\dot{\varphi})[N + \frac{1}{\sqrt{\rho h b^2}}\sum_{r=0}^{\infty}\sum_{s=-\infty}^{\infty} R_{rs}(r_0)\times \exp(\mathrm{i}s\varphi)\{m[\ddot{q}_{rs} + \mathrm{i}2s\dot{\varphi}\dot{q}_{rs} + (\mathrm{i}s\ddot{\varphi} - s^2\dot{\varphi}^2)q_{rs}] + c(\dot{q}_{rs} + \mathrm{i}s\dot{\varphi}q_{rs}) + k[q_{rs} - q_{rs}(0)]\}]. \tag{19}$$

The sliding phase can be maintained if,

$$\left|k_p r_0 \psi\right| < \mu_s [N + \frac{1}{\sqrt{\rho h b^2}} \sum_{r=0}^{\infty} \sum_{s=-\infty}^{\infty} R_{rs}(r_0) \exp(\mathrm{i}s\varphi) \times$$

$$\{m[\ddot{q}_{rs} + \mathrm{i}2s\dot{\varphi}\dot{q}_{rs} + (\mathrm{i}s\ddot{\varphi} - s^2\dot{\varphi}^2)q_{rs}] + \quad (20)$$

$$c(\dot{q}_{rs} + \mathrm{i}s\dot{\varphi}q_{rs}) + k[q_{rs} - q_{rs}(0)]\}],$$

when,

$$\dot{\psi} = -\Omega \quad \text{or} \quad \dot{\varphi} = 0. \quad (21)$$

COMPUTING PROCESS

As the slider system sticks and slides consecutively, the governing equations of the coupled motions of the whole system switch repeatedly from equations (15), (16) and (17) to equation (18), (19) and (20). The system is not smooth. Since the condition which controls the phases of the slider system itself depends on the motions, it is also a nonlinear system, whether μ_k is a constant or a function of relative speed $\dot{\varphi}$. In order to get modal co-ordinates, we have to truncate the infinite series in equation (12) to finite terms. Then numerical integration is used to solve equations (15), (18) and (19). Here a fourth order Runge-Kutta method is used for second order simultaneous ordinary differential equations.

Since equation (18) has time-dependent coefficients, time step length has to be very small. Constant time step lengths are chosen when the in-plane slider motion is well within the sticking phase or the sliding phase in the numerical integration. As it is imperative that the time step should be chosen such that at the end of some time intervals the slider happens to be on the sticking-sliding interfaces, we use a prediction criterion to choose next time step length when approaching these interfaces. Therefore, at the sticking-sliding interfaces, the time step length is variable (actually smaller than it is while well within sticking or sliding). Nevertheless, the interfaces equations (equation (17) or equations (20-21)) are only approximately satisfied [10].

When transverse motion of the slider system becomes so violent that the total normal force P in it becomes negative or becomes several times larger than the initial normal load N, we describe the system as being unstable. Then the motion begins to diverge. But this instability should be distinguished from a chaotic motion which is bounded but never converge to a point.

NUMERICAL EXAMPLES

The following data are used in the computation of numerical examples: $a = 0.065\text{m}$, $b = 0.12\text{m}$, $r_0 = 0.1\text{m}$, $h = 0.001\text{m}$; $E = 120\text{GPa}$, $\nu = 0.35$, $D^* = 0.00004$; $\mu_s = 0.4$, $\mu_k = 0.24$, $k = 1000\text{N/m}$, $k_p = 100\text{N/m}$, $m = 0.1\text{kg}$, $\rho = 7000\text{kg/m}^3$. The disc is clamped at inner radius and free at outer radius. Note that in these numerical examples, the disc thickness is deliberately taken to be very small in order to reduce the amount of computing work. However, this will not affect the qualitative features of the results or conclusion drawn from the results thus obtained. The first five natural (circular) frequencies are 451.29, 462.73, 426.73, 508.23, 508.23. We will concentrate on the vibration solutions at different levels of initial normal load. But occasionally solutions at different rotating speed or different damping ratios are investigated. Unless specified expressly, the Poincare sections are for the in-plane vibration of the slider system.

First of all, we study the effect of the normal load N. Take Ω=10 and $\Delta t = \dfrac{2\pi}{20\omega_{0v}}$. When N is very small, the Poincare section is a perfect ellipse which indicate the in-plane vibration of the slider system is quasi-periodic, as the transverse vibration of the disc is too small to affect total normal force P. A typical plot of such motion is shown in Figure 2 for N=0.5kPa. As N increases, the sticking period gets longer, the bottom part of the ellipse evolves into a straight line, indicating phase points within the sticking phase. One of such plots is given in Figure 3 for N=3kPa. A further increase of N not only lengthens the straight line part of the Poincare section, but also creates an increasingly ragged outline in the arch part of the plot. The curve is no longer smooth and it seems that the in-plane motion begins to enter a chaotic state from the quasi-periodic state. Figure 4 presents the Poincare section plot for N=7.5kPa. There is a transition period from quasi-periodic motion to chaotic motion, extending from N=6kPa up to N=9kPa. Chaos becomes detectable at N=10kPa, whose Poincare section is shown in Figure 5. Then chaotic vibration follows. When N=15kPa, the arch part of the Poincare section becomes so fuzzy and thick that it should no longer be considered as a curve, but rather a narrow (fractal) area. A 'blow-up' view of the arch part reveals that phase points are distributed across the arch. Both plots are shown in Figure 6. Between N=17.1kPa and 18.325kPa, the vibration of the slider enters a new stage, with Poincare sections looking like star clusters as illustrated in Figures 7 and 8. This kind of motions are rather extraordinary and

have not been reported in other works on stick-slip motions with a rigid carrier. Afterwards, the 'arch-door' like Poincare sections come back (see Figure 9). The difference from previous Poincare sections of lower N is that the new Poincare sections look like overlapping of earlier Poincare sections, which indicates a clear layered structure, as shown in Figure 10 and more obviously in the left hand side of Figure 11. At this stage, the vibration is very chaotic. To give the reader a better picture, the Poincare section of a fixed point on the disc at ($r_0 = 0.1$m and $\theta = 0$), is also shown in the right hand side of Figure 11. The Poincare sections of the slider-mass and a point on the disc are also given in Figures 12-15. In Figure 12 for N=30.5kPa, the vibration goes unstable. Here again, the Poincare sections have not been reported elsewhere.

If disc damping is increased, vibration will become more regular, as shown in Figure 13. Comparing Figures 11 with 13, we see that increase of disc damping makes the vibration more concentrated though not always smaller. Unstable vibration can be stabilised with more disc damping, as seen from Figure 14.

If there is no damping at all, the resulting vibration due to dry friction will be unstable, even at very small normal load N. In Figure 15, the motion of the slider tends to run away in the tangential direction from the normal ellipse attractor, while the motion of the disc goes unbounded.

Increasing the speed of the drive point seems to make vibration more chaotic and more unstable, as shown in Figures 16-18. At this stage, however, we are unable to make a definite conclusion on rotating speed as there might be intervals of regular motions and intervals of chaotic motion for Ω. More numerical examples must be computed to draw a positive conclusion on this parameter.

The correlation dimension is not a good measure of the vibration for the current problem because its values fluctuate in some numerical examples. This failure was perhaps first discovered in [7]. The reason can be either that the system is non-smooth, or that the system has multiple degrees of freedom, or both. Therefore, the correlation dimension or any other fractal dimensions is not presented in this paper.

CONCLUSIONS

In this paper, we studied the in-plane stick-slip vibration of a slider system with a transverse mass-spring-damper driven around an elastic disc through a spring from a constant speed drive point, and transverse vibrations of the disc. The

whole system had been reduced to six degrees of freedom after simplification. From numerical examples computed so far, we can conclude that:

1. Both vibrations are very complex as this is a multi-degree of freedom, non-smooth system. Rich patterns of chaotic vibration are found. Some have not been reported elsewhere.

2. For the normal pressure parameter, smaller values allow quasi-periodic solutions. Greater pressures result in chaotic motions. At certain large pressures, the vibrations become unstable.

3. Disc damping makes vibration more concentrated to smaller areas and when sufficiently large it can stabilise otherwise unstable vibration.

4. An increase in the rotating speed can make the vibration more chaotic or more unstable.

5. Correlation dimension is not a good measure of the vibration of this multi-degree of freedom, non-smooth dynamical system.

6. Much more investigation needs to be carried out in understanding and characterising the vibration of multi-degree of freedom, non-smooth dynamical systems.

ACKNOWLEDGEMENT

This research is supported by the Engineering and Physical Sciences Research Council (grant number J35177) and BBA Friction Ltd.

REFERENCES

1. Nakai, M., Chiba, Y. and Yokoi, M., Railway wheel squeal. *Bulletin of JSME*, 1984, **27**, 301-8
2. Lin, Y-Q and Wang Y-H, Stick-slip vibration of drill strings. *J.Eng.Ind., Trans.ASME*, 1991, **113**, 38-43
3. Ferri, A.A. and Bindemann, A.C., Damping and vibration of beams with various types of frictional support conditions. *J.Vib.Acoust., Trans.ASME*, 1992, **114**, 289-96
4. Lee, A.C., Study of disc brake noise using multi-body mechanism with friction interface. In *Friction-Induced Vibration, Chatter, Squeal, and Chaos*, Ed. Ibrahim, R.A. and Soom, A., DE-Vol. 49, ASME 1992, pp.99-105

5. Ibrahim, R.A., Friction-induced vibration, chatter, squeal, and chaos. In *Friction-Induced Vibration, Chatter, Squeal, and Chaos*, Ed. Ibrahim, R.A. and Soom, A., DE-Vol. 49, ASME 1992, pp.107-38
6. Yang, S. and Gibson, R.F., Brake vibration and noise: reviews ,comments, and proposed considerations. *Proceedings of the 14th Modal Analysis Conference*, The Society of Experimental Mechanics, Inc., 1996, pp.1342-9
7. Popp, K. and Stelter, P., Stick-slip vibration and chaos. *Phil. Trans. R. Soc. Lond.* A(1990), **332**, 89-106
8. Pfeiffer, F. and Majek, M., Stick-slip motion of turbine blade dampers. *Phil. Trans. R. Soc. Lond.* A(1992), **338**, 503-18
9. Wojewoda, J., Kapitaniak, T., Barron, R. and Brindley, J., Complex behaviour of a quasiperiodically forced experimental system with dry friction. *Chaos, Solitons and Fractals*, 1993, **3**, 35-46
10. Wiercigroch, M., A note on the switch function for the stick-slip phenomenon. *J.Sound.Vib.*, 1994, **175**, 700-4
11. Chan, S.N., Mottershead, J.E. and Cartmell, M.P., Parametric resonances at subcritical speeds in discs with rotating frictional loads. *Proc. Instn. Mech. Engrs*, 1994, **208**, 417-25
12. Mottershead, J.E., Ouyang, H., Cartmell, M.P. and Friswell, M.I., Parametric Resonances in an annular disc, with a rotating system of distributed mass and elasticity; and the effects of friction and damping. *Proc. Royal Soc. Lond. A.*, 1997, **453**, 1-19
13. Ouyang, H., Mottershead, J.E., Friswell, M.I. and Cartmell, M.P., On the prediction of squeal in automotive brakes. *Proceedings of the 14th Modal Analysis Conference*, The Society of Experimental Mechanics, Inc., 1996, pp.1009-16

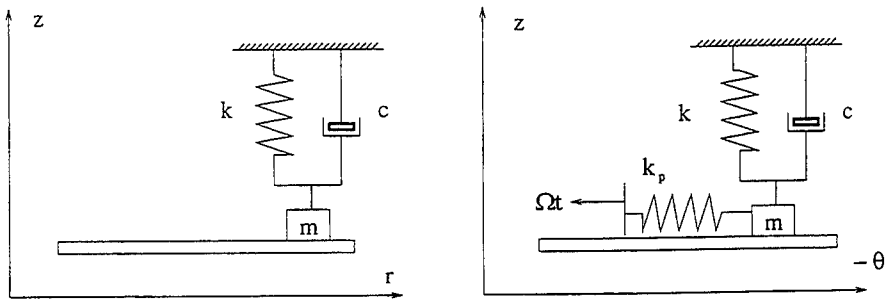

Figure 1. Slider system and disc in cylindrical co-ordinate system

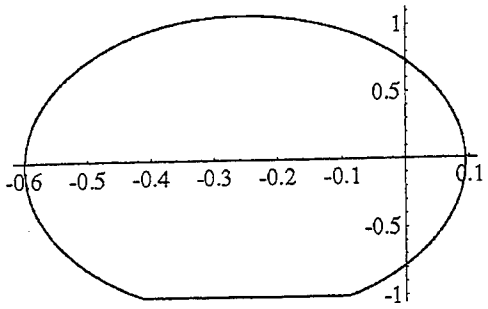

Figure 3. N=3kPa

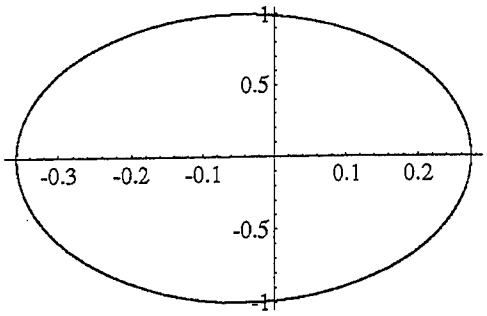

Figure 2. N=0.5kPa

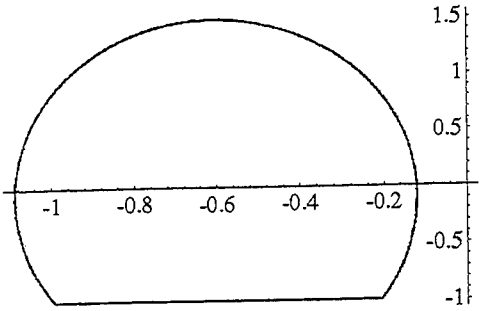

Figure 4. N=7.5kPa

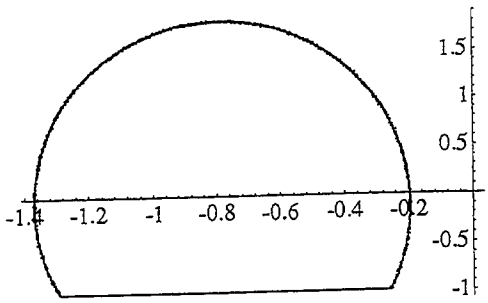

Figure 5. N=10kPa

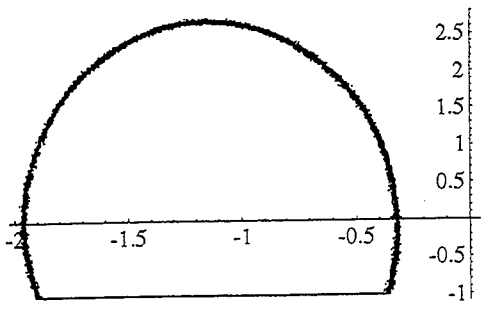

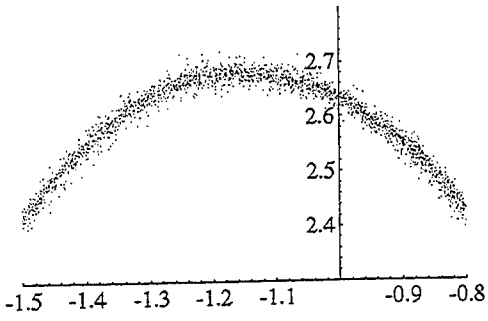

Figure 6. N=15kPa

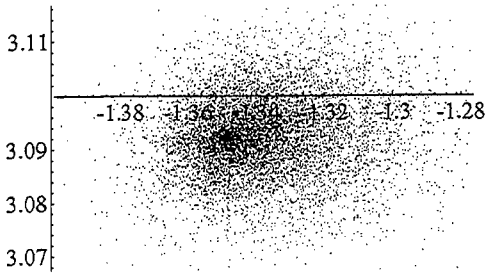

Figure 7. N=17.25kPa

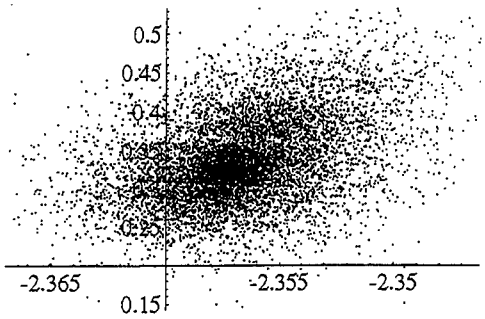

Figure 8. N=18kPa

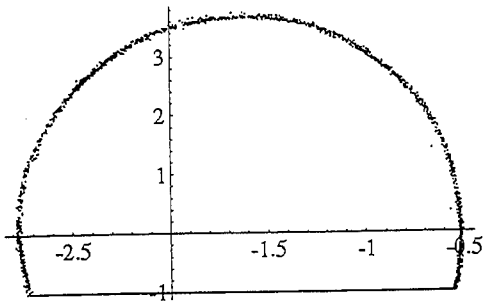

Figure 9. N=21kPa

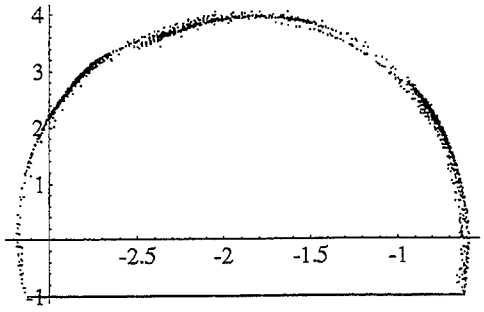

Figure 10. N=24kPa

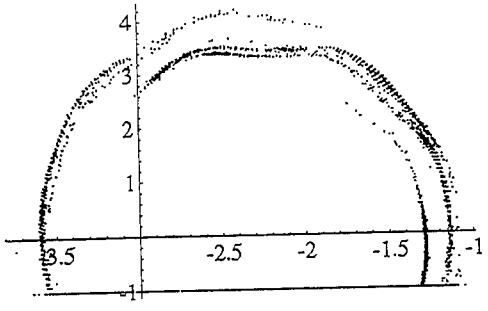

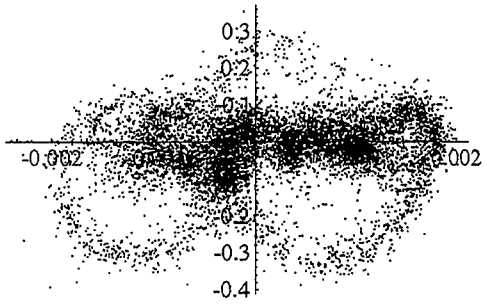

Figure 11. N=30.4kPa

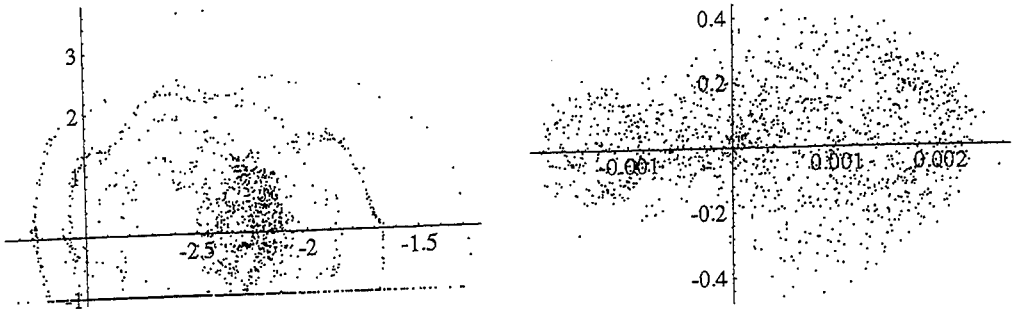

Figure 12. N=30.5kPa D^*=0.0004

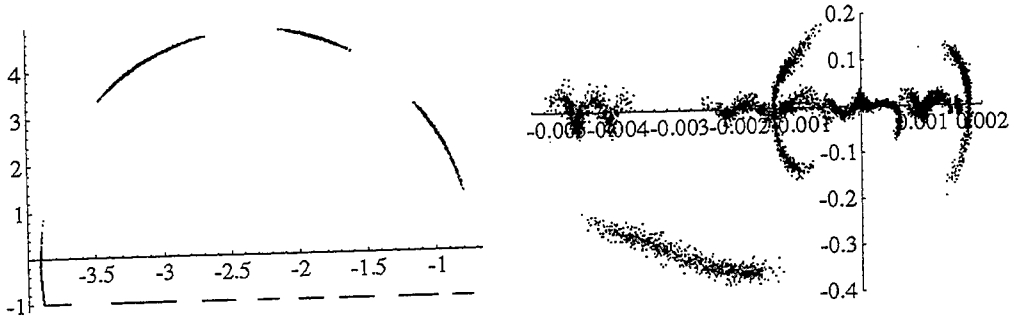

Figure 13. N=30.4kPa D^*=0.0004

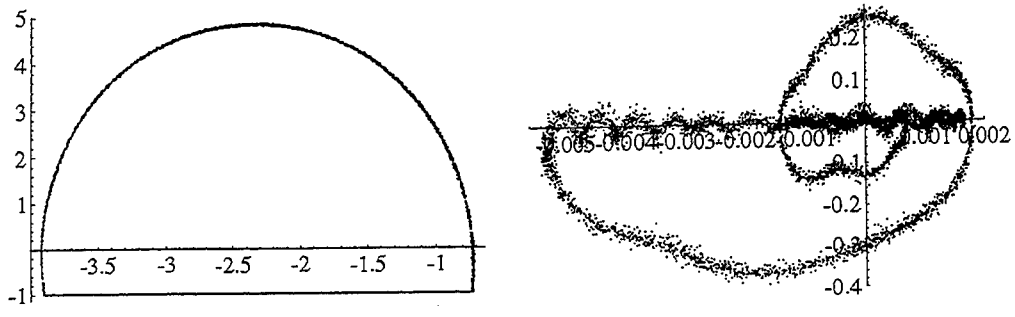

Figure 14. N=30.5kPa D^*=0.00004

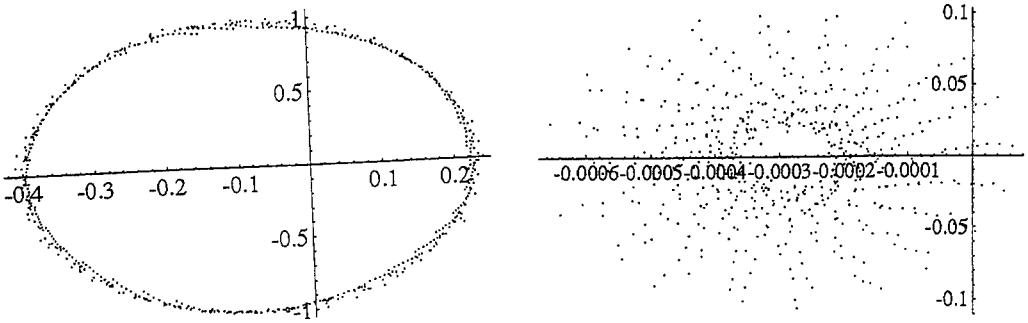

Figure 15. Unstable solution N=1kPa D^{*}=0

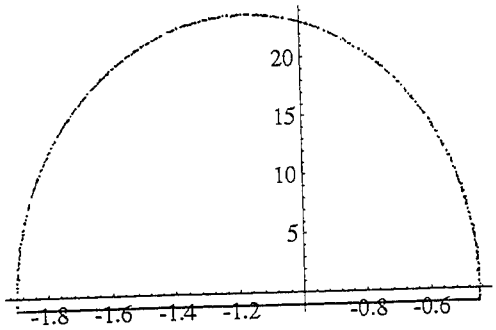

Figure 16. N=15kPa Ω=1rad/sec

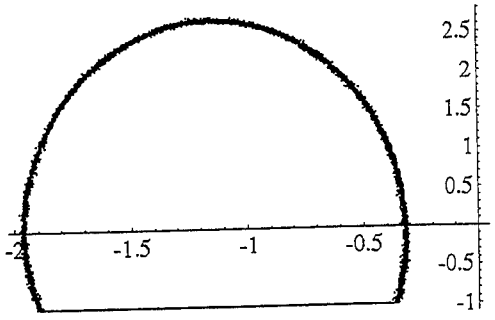

Figure 17. N=15kPa Ω=10rad/sec

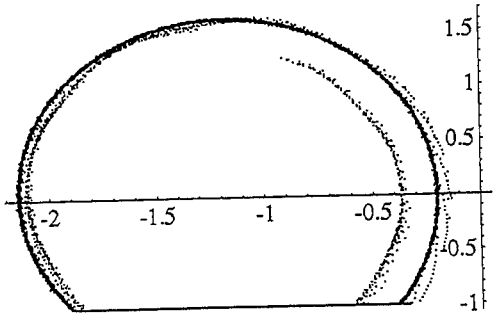

Figure 18. N=15kPa Ω=20rad/sec

A Finite Element Time Domain Multi-Mode Method For Large Amplitude Free Vibration of Composite Plates

Raymond Y. Y. Lee, Yucheng Shi and Chuh Mei
Department of Aerospace Engineering
Old Dominion University, Norfolk, VA 23529-0247

Abstract

This paper presents a time-domain modal formulation using the finite element method for large-amplitude free vibrations of generally laminated thin composite rectangular plates. Accurate frequency ratios for fundamental as well as higher modes of composite plates at various maximum deflections can be determined. The selection of the proper initial conditions for periodic plate motions is presented. Isotropic beam and plate can be treated as special cases of the composite plate. Percentage of participation from each linear mode to the total plate deflection can be obtained, and thus an accurate frequency ratio using a minimum number of linear modes can be assured. Another advantage of the present finite element method is that the procedure for obtaining the modal equations of the general Duffing-type is simple when compared with the classical continuum Galerkin's approach. Accurate frequency ratios for isotropic beams and plates, and composite plates at various amplitudes are presented.

Introduction

Large amplitude vibrations of beams and plates have interested many investigators [1] ever since the first approximate solutions for simply supported beams by Woinowsky-Krieger [2] and for rectangular plates by Chu and Herrmann [3] were presented. Singh *et al.* [4] gave an excellent review of various formulation and assumptions , including the finite element method for large amplitude free vibration of beams. Srirangaraja [5] recently presented two alternative solutions, based on the method of multiple scales (MMS) and the ultraspherical polynomial approximation (UPA) method, for the large amplitude free vibration of a simply supported beam. The frequency ratios for the fundamental mode, ω/ω_L, at the ratio of maximum beam deflection to radius of gyration of 5.0 (W_{max}/r =5.0) are 3.3438 and 3.0914, using the MMS and the UPA method, respectively. Eleven frequency ratios including nine from reference [4] were also given (see Table 1 of reference [5]). It is rather surprising that the frequency ratio for the fundamental mode at W_{max}/r =5.0 for a simply supported beam varied in a such wide range: from the lowest of 2.0310 to the highest of 3.3438, and with the elliptic function solution by Woinowsky-Krieger [2] giving 2.3501. Similar wide spread exists for the vibration of plates. Rao *et al.* [6] presented a finite element method for the large amplitude free flexural vibration of unstiffened plates. For the simply supported square plate,

frequency ratios from six different approaches were reported (see Table 1 of reference [6]). The frequency ratio at $W_{max}/h = 1.0$ varied from a low of 1.2967 to a high of 1.5314, with Chu and Herrmann's analytical solution [3] at 1.4023.

This paper presents a finite element time domain modal formulation for the large amplitude free vibration of composite plates. The formulation is an extension from the isotropic plates [7], and the determination of initial conditions for periodic motions was not employed in reference [7]. The convergence of the fundamental frequency ratio is investigated for a simply supported beam and a simply supported square plate with a varying number of finite elements and a varying number of linear modes. Accurate frequency ratios for fundamental and higher modes at various maximum deflections, and percentages of participation from various linear modes, are obtained for beams and composite plates.

Formulation

Strain-Displacement and Constitutive Relations

The von Karman strain-displacement relations are applied. The strains at any point z through the thickness are the sum of membrane and change of curvature strain components:

$$\{\varepsilon\} = \begin{Bmatrix} \varepsilon_x \\ \varepsilon_y \\ \gamma_{xy} \end{Bmatrix} = \begin{Bmatrix} u_{,x} \\ v_{,y} \\ u_{,y}+v_{,x} \end{Bmatrix} + \begin{Bmatrix} w_{,x}^2/2 \\ w_{,y}^2/2 \\ w_{,x}\, w_{,y} \end{Bmatrix} + z \begin{Bmatrix} -w_{,xx} \\ -w_{,yy} \\ -2w_{,xy} \end{Bmatrix} = \left\{\varepsilon_m^o\right\} + \left\{\varepsilon_b^o\right\} + z\{\kappa\} \tag{1}$$

where $\left\{\varepsilon_m^o\right\}$ and $\left\{\varepsilon_b^o\right\}$ are the membrane strain components due to in-plane displacements u and v and the transverse deflection w, respectively. The stress resultants, membrane force {N} and bending moment {M}, are related to the strain components as follows:

$$\begin{Bmatrix} N \\ M \end{Bmatrix} = \begin{bmatrix} [A] & [B] \\ [B] & [D] \end{bmatrix} \begin{Bmatrix} \varepsilon^o \\ \kappa \end{Bmatrix} \tag{2}$$

where [A] is the elastic extensional matrix, [D] is the flexural rigidity matrix, and [B] is the extension coupling matrix of the laminated plate.

Element Displacements, Matrices and Equations

Proceeding from this point, the displacements in equation (1) are approximated over a typical plate element , e.g. rectangular [8] or triangular [9], using the corresponding interpolation functions. The in-plane displacements and the linear strains are interpolated from nodal values by

$$\begin{Bmatrix} u \\ v \end{Bmatrix} = [H_m]\{w_m\}, \quad \{\varepsilon_m^0\} = [B_m]\{w_m\} \tag{3a,b}$$

where $[H_m]$ and $[B_m]$ denote the displacement and strain interpolation matrices, respectively, and $\{w_m\}$ is the in-plane nodal displacement vector. The transverse displacement, slopes and curvatures are interpolated from the nodal values by

$$w = [H_b]\{w_b\}, \quad \begin{Bmatrix} w,_x \\ w,_y \end{Bmatrix} = [G]\{w_b\}, \quad \{\kappa\} = [B_b]\{w_b\} \tag{4 a, b, c}$$

where $[H_b]$ and $[G]$ and $[B_b]$ denote the bending displacement, slope and curvature interpolation matrices, respectively, and $\{w_b\}$ denotes the nodal transverse displacements and its derivatives. Through the use of Hamilton's principle, the equations of motion for a plate element undergoing large amplitude vibration may be written in the form

$$\begin{bmatrix} [m_b] & 0 \\ 0 & [m_m] \end{bmatrix} \begin{Bmatrix} \{\ddot{w}_b\} \\ \{\ddot{w}_m\} \end{Bmatrix} + \left(\begin{bmatrix} [k_b] & [k_B] \\ [k_B]^T & [k_m] \end{bmatrix} + \begin{bmatrix} [k1_{Nm}]+[k1_{NB}] & [k1_{bm}] \\ [k1_{mb}] & 0 \end{bmatrix} + \begin{bmatrix} [k2_b] & 0 \\ 0 & 0 \end{bmatrix} \right) \begin{Bmatrix} \{w_b\} \\ \{w_m\} \end{Bmatrix} = 0$$

or

$$[m]\{\ddot{w}\} + \{[k] + [k1] + [k2]\}\{w\} = 0 \tag{5}$$

where [m] and [k] are constant matrices representing the element mass and linear stiffness characteristics, respectively; [k1] and [k2] are the first order and second order non-linear stiffness matrices, respectively; $[k1_{Nm}]$ depends linearly on unknown membrane displacement ($\{N_m\} = [A][B_m]\{w_m\}$); $[k1_{NB}]$ depends linearly on the unknown transverse displacement ($\{N_B\} = [B][B_b]\{w_b\}$); $[k1_{bm}]$ depends linearly on the unknown plate slopes and represents coupling between membrane and bending displacements; and $[k2_b]$ depends quadratically on the unknown plate slopes.

SYSTEM EQUATIONS

After assembling the individual finite elements for the complete plate and applying the kinematic boundary conditions, the finite element system equations of motion for the large-amplitude free vibration of a thin laminated composite plate can be expressed as

$$[M]\{\ddot{W}\} + ([K] + [K1(W)] + [K2(W)])\{W\} = 0 \tag{6}$$

where [M] and [K] are constant matrices and represent the system mass and stiffness respectively; and [K1] and [K2] are the first and second order nonlinear stiffness matrices and depend linearly and quadratically on the unknown structural

nodal displacements {W}, respectively. Most of the finite element large amplitude free vibration results for plates and beams in the literature, e.g. references [1,6] and others, were based on eq. (6) using an iterative scheme and various approximate procedures. The system equations are not suitable for direct numerical integration because: a) the nonlinear stiffness matrices [K1] and [K2] are functions of the unknown nodal displacements, and b) the number of degrees of freedom (DOF) of the system nodal displacements {W} is usually too large. Therefore, eq. (6) has to be transformed into modal or generalized coordinates followed by a reduction of the number of DOF. In addition, the general Duffing-type modal equations will have constant nonlinear modal stiffness matrices. This is accomplished by a modal transformation and truncation

$$\{W\} = \sum_{r=1}^{n} q_r(t)\{\phi\}^{(r)} = [\Phi]\{q\} \tag{7}$$

where $\{\phi\}^{(r)}$ and ω_{Lr} are the natural mode (normalized with the maximum component to unity) and linear frequency from the eigen-solution $\omega_{Lr}^2[M]\{\phi\}^{(r)}=[K]\{\phi\}^{(r)}$.

The nonlinear stiffness matrices [K1] and [K2] in eq. (6) can now be expressed as the sum of the products of modal coordinates and nonlinear modal stiffness matrices as

$$[K1] = \sum_{r=1}^{n} q_r(t)\left[K1(\phi^{(r)})\right]^{(r)} \tag{8}$$

$$[K2] = \sum_{r=1}^{n}\sum_{s=1}^{n} q_r(t)q_s(t)\left[K2(\phi^{(r)},\phi^{(s)})\right]^{(rs)} \tag{9}$$

The nonlinear modal stiffness matrices $[K1]^{(r)}$ and $[K2]^{(rs)}$ are assembled from the element nonlinear modal stiffness terms $[k1]^{(r)}$ and $[k2]^{(rs)}$ as

$$\left([K1]^{(r)},[K2]^{(rs)}\right) = \sum_{\substack{\text{all elements}\\ \text{+ bdy. conds.}}}\left([k1]^{(r)},[k2]^{(rs)}\right) \tag{10}$$

where the element nonlinear modal stiffness matrices are evaluated with the known linear mode $\{\phi\}^r$. Thus, the nonlinear modal stiffness $[K1]^{(r)}$ and $[K2]^{(rs)}$ are constant matrices. Equation (6) is thus transformed to the general Duffing-type modal equations as

$$[\overline{M}]\{\ddot{q}\}+\left([\overline{K}]+[K1_q]+[K2_{qq}]\right)\{q\}=0 \tag{11}$$

where the modal mass and linear stiffness matrices are diagonal

$$\left([\overline{M}],[\overline{K}]\right)=[\Phi]^T([M],[K])[\Phi] \tag{12}$$

and the quadratic and cubic terms are

$$[K1_q]\{q\}=[\Phi]^T\left(\sum_{r=1}^{n} q_r[K1]^{(r)}\right)[\Phi]\{q\} \tag{13}$$

$$[K2_{qq}]\{q\}=[\Phi]^T\left(\sum_{r=1}^{n}\sum_{s=1}^{n} q_r q_s[K2]^{(rs)}\right)[\Phi]\{q\} \tag{14}$$

All modal matrices in eq. (11) are constant matrices. With given initial conditions, the modal coordinate responses {q} can be determined from eq. (11) using any direct numerical integration scheme such as the Runge-Kutta or Newmark-β method. Therefore, no updating of the vibration modes is needed [10]. For periodic plate oscillations have the same period T, the response of all modal coordinates should also have the same period T. Since the initial conditions will affect greatly the modal response, the determination of initial conditions for periodic plate oscillations is to relate each of the rest modal coordinates in powers of the dominated coordinate as

$$a_r q_1(t;IC)+b_r q_1^2(t;IC)+c_r q_1^3(t;IC)+\ldots\ldots=q_r(t;IC), \qquad r=2,3,\ \ldots n \tag{15}$$

where the a_r, b_r, c_r , ... are constants to be determined, and IC denotes initial conditions. For a three-mode (n=3) system, it is accurate enough to keep up to the cubic term only in eq. (15) and this leads to two set of equations

$$a_2 q_1(t_p;A,B,C)+b_2 q_1^2(t_p;A,B,C)+c_2 q_1^3(t_p;A,B,C)=q_2(t_p;A,B,C),\ \ p=1,2,3$$
$$a_3 q_1(t_p;A,B,C)+b_3 q_1^2(t_p;A,B,C)+c_3 q_1^3(t_p;A,B,C)=q_3(t_p;A,B,C),\ \ p=1,2,3 \tag{16a,b}$$

in which the modal coordinates q_1, q_2 and q_3 at t_p are known quantities and the initial conditions are $q_1(0)=A$, $q_2(0)=B$, $q_3(0)=C$ and $\dot{q}_1(0)=\dot{q}_2(0)=\dot{q}_3(0)=0$. Practically, only eight equations are needed to determine the eight unknowns a_2, a_3,

b_2, b_3, c_2, c_3, B and C through an iterative scheme. However, the number of equations can be more than the number of unknowns for accurate determination of initial conditions and the least square method is employed in this case.

The time history of the plate maximum deflection can be obtained from eq. (7). The participation value from the r th linear mode to the total deflection is defined as

$$\frac{\max|q_r|}{\sum_{i=1}^{n} \max|q_i|} \tag{17}$$

Thus, the minimum number of the linear modes for an accurate and converged frequency solution can be determined based on the modal participation values.

Results and Discussions

Assessment of Single-Mode Elliptic Function Solution

The fundamental frequency ratio ω/ω_L = 2.3051 at W_{max}/r =5.0 for a simply supported beam obtained by Woinowsky-Krieger [2] using a single-mode and elliptic function is assessed first. The conventional beam element having six (four bending and two axial) DOF is used. A half-beam is modeled with 10, 15, 20 elements, and the lowest four symmetrical linear modes are used in the Duffing modal equations. Table 1 shows that a 20-element and 1-mode model will yield a converged result. The percentages of participation from each mode for various values of W_{max}/r are given in Table 2. The modal participation values demonstrate that a single mode (n=1) will yield an accurate fundamental frequency because the contribution from higher linear modes to the total deflection is negligible (< 0.01 % for W_{max}/r up to 5.0). There is a small difference in frequency ratios between the present finite element and the elliptic integral solutions. This is due to the difference between the axial forces of the two approaches, the finite element method (FEM) gives a non-uniform axial force in each element; however, the average value of the axial force for each element is the same as the one in the classic continuum approach. The lowest (2.0310) and the highest (3.3438) frequency ratios at W_{max}/r =5.0 in reference [5] are not accurate.

Frequency ratios for higher modes of the simply supported beam are obtained next. A model with 40-elements and 3-anti-symmetric modes for the whole beam is employed for the frequency ratio of the second nonlinear mode. The mode participations shown in Table 2 indicate that a single-mode approach will yield accurate frequency results. And the frequency ratios for the second mode are the same as those of the fundamental one. Thus, the present method agrees extremely well with Woinowsky-Krieger's classic single-mode approach.

The time history of the first two symmetric modal coordinates and the beam central displacement, phase plot, and power spectral density (PSD) at maximum beam deflection $W_{max}/r = 5.0$ for the fundamental frequency (or mode) are shown in Fig. 1. The time scale is non-dimensional and T_1 is the period of the fundamental linear resonance. It is noted that although the central displacement response looks like a simple harmonic motion, it does have a small deviation from pure harmonic motion due to the second small peak in the spectrum. This is in agreement with classical solution that the ratio of the frequency of the second small peak to that of the first dominant peak is 3.

Now we are ready to assess the single-mode fundamental frequency of a simply supported square plate obtained by Chu and Herrmann [3]. A quarter of the plate is modeled with 6×6, 7×7, 8×8 and 9×9 mesh sizes and 1, 2, 4 or 5 symmetrical modes are used. The C^1 conforming rectangular plate element with 24 (16 bending and 8 membrane) DOF is used. The in-plane boundary conditions are $u = v = 0$ on all four edges. Table 3 shows that the 8×8 mesh size in a quarter-plate and 4-mode model should be used for a converged and accurate frequency solution. Table 4 shows the frequency ratios and modal participation values for the lowest three modes at various W_{max}/h for a simply supported square plate (8×8 mesh size in a quarter-plate). It indicated that at least two linear modes are needed for an accurate frequency prediction at $W_{max}/h = 1.0$, and the contribution of higher linear modes increase with the increase of plate deflections. The modal participation values also show that the combined modes (1,3)-(3,1) and (2,4)-(4,2) are independent of the large-amplitude vibrations dominated by (1,1) and (2,2) modes, respectively. The time history, phase plot, and PSD at the maximum deflection $W_{max}/h = 1.0$ for the fundamental mode are shown in Fig. 2a, and T_{11} is the period of the fundamental linear resonance. There is one small peak in the spectrum and the frequency ratio of the second small peak to the first dominant one is 3. The low (1.2967) and the high (1.5314) frequency ratios at $W_{max}/h = 1.0$ given in reference [6] are not accurate.

The influence of the initial conditions on periodic motion is demonstrated in Fig. 2a and 2b. In Fig. 2a, the modal coordinates all have the same period, and the initial conditions are determined from eq.(15). They are $q_{11}(0)/h=1.0$, $q_{13+31}(0)/h= -0.0155$, $q_{13-31}(0)/h = 0.0$, $q_{33}(0)/h=0.000813$, and $q_{15+51}(0)/h= 0.00011$, and initial velocities are null, whereas in Fig. 2b, $q_{11}(0)/h=1.0$ and all others are null. The modal coordinates do not have the same period.

CLAMPED BEAM

It is thus curious to find out whether multiple-mode is required for the clamped beam. Convergence study of the fundamental frequency ratios at $W_{max}/r = 3.0$ and 5.0 shown in Table 5 indicates that a 25-element (half-beam) and 4-mode model will yield accurate and converged results. The time history, phase plot and PSD at $W_{max}/r = 5.0$ are shown in Fig. 3. The modal participation values in Table 6 and the PSD in Fig. 3 confirm that at least two modes are needed for accurate frequency results.

SYMMETRIC COMPOSITE PLATE

A simply supported eight-layer symmetrically laminated (0/45/-45/90)s composite plate with an aspect ratio of 2 is investigated. The graphite/epoxy material properties are as follows; Young's moduli E_1 = 155 GPa, E_2 = 8.07 GPa, shear modulus G_{12} = 4.55GPa, Poisson's ratio ν_{12} =0.22, and mass density ρ = 1550 kg/m^3. A 12 × 12 mesh is used to model the plate. The in-plane boundary conditions are fixed (u=v=0) at all four edges. The first seven linear modes are used as the modal coordinates. Table 7 gives the fundamental frequency ratios and mode participation values for the linear modes in increasing frequency order. The modal participation values indicate clearly that four modes are needed in predicting the nonlinear frequency, and other three of the seven are independent of the fundamental nonlinear mode. Figure 4 shows the time-history, phase plot, and PSD at W_{max}/h =1.0.

UNSYMMETRIC COMPOSITE PLATE

A simply supported two-layer laminated (0/90) composite plate of 15 × 12 × 0.048 in. (38 × 30 × 0.12 cm) is investigated. The graphite/epoxy material properties are the same as those of the symmetric composite plate. A 12 × 12 mesh is used to model the plate. The in-plane boundary conditions are fixed at all four edges. The first four linear modes are used as the modal coordinates. Table 8 gives the fundamental frequency ratios and mode participation values for the linear modes in increasing frequency order. From the phase plot, the time histories and PSD shown in Fig. 5, it can be seen that the total displacement response has a non-zero mean (i.e. the positive and negative displacement amplitudes for all modal coordinates are not equal). The quasi-ellipse in the phase plot is not symmetrical about the vertical velocity-axis. In the PSD at W_{max}/h =1.0, it is observed that there are four small peaks in the spectrum and the frequency ratios of the second, third, fourth and fifth peak to the first dominant one are 2, 3, 4 and 5, respectively. This observation indicates that the displacement response includes the superharmonances of orders 2, 3, 4, and 5. The curves, which the positive and negative displacement amplitudes are plotted against the fundamental frequency ratio, are also given in Fig. 5. The difference between the positive and negative amplitudes increases as the frequency ratio increasing.

Conclusions

A multimode time-domain formulation, based on the finite element method, is presented for nonlinear free vibration of composite plates. The use of FEM enables the present formulation to deal with composite plates of complex geometries and boundary conditions, and the use of the modal coordinate transformation enables to reduce the number of ordinary nonlinear differential modal equations to a much smaller one. The present procedure is able to obtain the general Duffing-type modal equations easily. Initial conditions for all modal coordinates having the same time

period are presented. The participation value of the linear mode to the nonlinear deflection is quantified ; they can clearly determine the minimum number of linear modes needed for accurate nonlinear frequency results.

The present fundamental nonlinear frequency ratios have been compared with the single-mode solution obtained by Woinowsky-Krieger for simply supported beams and by Chu and Herrmann for simply supported square plates. The Woinowsky-Krieger's single-mode solution is accurate. For all other solutions, however, two or more modes are needed. The nonlinear frequencies for symmetrically and unsymmetrically laminated rectangular composite plates are also obtained. The phase plot and power spectral density showed that nonlinear displacement responses are no longer harmonic, and multiple modes are required for isotropic clamped beams and isotropic and composite plates.

References

1. M. Sathyamoorthy 1987 Applied Mechanics Review 40, 1553-1561. Nonlinear vibration analysis of plates: A review and survey of current developments.
2. S. Woinowsky-Kreger 1950 Journal of Applied Mechanics 17, 35-36. The effect of an axial force on the vibration of hinged bars.
3. H. N. Chu and G. Herrmann 1956 Journal of Applied Mechanics 23, 523-540. Influence of large amplitudes on free flexural vibrations of rectangular elastic plates.
4. G. Singh, A. k. Sharma and G. V. Rao 1990 Journal of Sound and Vibration 142, 77-85. Large amplitude free vibration of beams-discussion of various formulations and assumptions.
5. H. R. Srirangaraja 1994 Journal of Sound and Vibration 175, 425-427. Nonlinear free vibrations of uniform beams.
6. S. R. Rao, A. H. Sheikh and M. Mukhopadhyay 1993 Journal of the Acoustical Society of America 93 (6), 3250-3257. Large-amplitude finite element flexural vibration of plates/stiffened plates.
7. Y. Shi and C. Mei 1996 Journal Sound and Vibration 193, 453-464. A finite element time domain modal formulation for large amplitude free vibration of beams and plates.
8. K. Bogner, R. L. Fox and L. A. Schmit 1966 Proceeding of Conference on Matrix Methods in Structural Mechanics, AFFDL-TR-66-80, Wright-Patterson Air Force Base, Ohio, October 1965, 397-444. The generation of interelement compatible stiffness and mass matrix using the interpolation formulas.
9. Teseller and T. J. R. Hughes 1985 Computer Methods in Applied Mechanics and Engineering 50, 71-101. A three node Mindlin plate element with improved transverse shear.
10. A. K. Noor 1981 Composites and Structures, 13, 31-44. Recent advances in reduction methods for nonlinear problems.

Table 1. Convergence of the fundamental frequency ratio at W_{max}/r =5.0 for a simply supported beam

No. of elements and 4 modes	$(\omega/\omega_L)_1$	No. of modes and 20 elements	$(\omega/\omega_L)_1$
10	2.3537	1	2.3506
15	2.3511	2	2.3506
20	2.3506	3	2.3506
--	---------	4	2.3506

Table 2 The lowest two frequency ratios and the modal participations for a simply supported beam

	Elliptic integral [2]	FEM			
			Modal Participation %		
W_{max}/r	$(\omega/\omega_L)_1$	$(\omega/\omega_L)_1$	q_1	q_3	q_5
0.2	1.0038	1.0038	100.00	0.000	0.000
0.4	1.0150	1.0149	100.00	0.000	0.000
0.6	1.0331	1.0331	100.00	0.000	0.000
0.8	1.0580	1.0581	100.00	0.000	0.000
1	1.0892	1.0892	100.00	0.000	0.000
2	1.3178	1.3179	100.00	0.002	0.000
3	1.6257	1.6258	100.00	0.004	0.000
4	1.9760	1.9761	99.99	0.005	0.000
5	2.3501	2.3506	99.99	0.009	0.000
W_{max}/r	$(\omega/\omega_L)_2$	$(\omega/\omega_L)_2$	q_2	q_4	q_6
0.2	1.0038	1.0038	100.00	0.000	0.000
0.4	1.0150	1.0149	100.00	0.000	0.000
0.6	1.0331	1.0332	100.00	0.000	0.001
0.8	1.0580	1.0582	100.00	0.000	0.001
1	1.0892	1.0893	100.00	0.000	0.002
2	1.3178	1.3181	99.99	0.000	0.006
3	1.6257	1.6260	99.98	0.000	0.015
4	1.9760	1.9768	99.98	0.000	0.021
5	2.3501	2.3512	99.96	0.000	0.037

Table 3. Convergence of the fundamental frequency ratios for a simply supported square plate (Poisson's ratio=0.3)

Mesh sizes and	$(\omega/\omega_L)_{11}$ at	W_{max}/h	No. of modes and	$(\omega/\omega_L)_{11}$ at	W_{max}/h
4 modes	1.0	1.4	8×8 mesh	1.0	1.4
6×6	1.4174	1.7423	1	1.4058	1.7028
7×7	1.4163	1.7396	2	1.4169	1.7433
8×8	1.4164	1.7403	4	1.4164	1.7403
9×9	1.4164	1.7400	5	1.4163	1.7401

Table 4. The lowest three frequency ratios and the modal participations for a simply supported square plate (Poisson's ratio=0.3)

W_{max}/h	Elliptic integral [3]	FEM					
			Modal Participation %				
	$(\omega/\omega_L)_{11}$	$(\omega/\omega_L)_{11}$	q_{11}	$q_{13}+q_{31}$	$q_{13}-q_{31}$	q_{33}	$q_{15}+q_{51}$
0.2	1.0195	1.0195	99.93	0.07	0.00	0.00	0.00
0.4	1.0757	1.0765	99.72	0.27	0.00	0.01	0.00
0.6	1.1625	1.1658	99.38	0.59	0.00	0.02	0.00
0.8	1.2734	1.2796	98.93	1.02	0.00	0.05	0.01
1.0	1.4024	1.4163	98.34	1.57	0.00	0.08	0.01
1.2	1.5448	1.5659	97.54	2.30	0.00	0.15	0.01
1.4	1.6933	1.7401	96.29	3.42	0.00	0.27	0.02
W_{max}/h		$(\omega/\omega_L)_{21}$	q_{21}	q_{23}	q_{41}	q_{43}	---
0.2	N/A	1.0243	99.93	0.06	0.01	0.00	---
0.4	N/A	1.0976	99.50	0.45	0.03	0.01	---
0.6	N/A	1.2072	98.15	1.28	0.54	0.02	---
0.8	N/A	1.3411	97.54	2.41	0.00	0.05	---
1.0	N/A	1.5126	96.24	3.69	0.00	0.08	---
1.2	N/A	1.6900	94.90	4.92	0.03	0.15	---
1.4	N/A	1.8952	93.54	6.01	0.01	0.44	---
W_{max}/h		$(\omega/\omega_L)_{22}$	q_{22}	$q_{24}+q_{42}$	$q_{24}-q_{42}$	q_{44}	---
0.2	N/A	1.0245	100.00	0.00	0.00	0.00	---
0.4	N/A	1.0751	100.00	0.00	0.00	0.00	---
0.6	N/A	1.1611	99.99	0.00	0.00	0.01	---
0.8	N/A	1.2806	99.98	0.01	0.00	0.01	---
1.0	N/A	1.4041	99.93	0.01	0.00	0.06	---
1.2	N/A	1.5551	99.97	0.01	0.00	0.01	---
1.4	N/A	1.7074	99.98	0.02	0.00	0.00	---

Table 5. Convergence of the fundamental frequency ratios for a clamped beam

No. of elements and 4 modes	$(\omega/\omega_L)_1$ at W_{max}/r = 3.0	$(\omega/\omega_L)_1$ at W_{max}/r = 5.0	No. of modes and 25 elements	$(\omega/\omega_L)_1$ at W_{max}/r = 3.0	$(\omega/\omega_L)_1$ at W_{max}/r = 5.0
10	1.1751	1.4046	1	1.1835	1.4497
15	1.1740	1.4009	2	1.1745	1.4061
20	1.1732	1.3999	3	1.1737	1.4001
25	1.1731	1.3996	4	1.1731	1.3996

Table 6 The fundamental frequency ratios and the modal participations for a clamped beam

W_{max}/r	Elliptic integral	FEM				
			Modal Participation %			
	$(\omega/\omega_L)_1$	$(\omega/\omega_L)_1$	q_1	q_3	q_5	q_7
1.0	1.0222	1.0222	99.78	0.20	0.02	0.00
2.0	1.0857	1.0841	99.33	0.58	0.08	0.02
3.0	1.1831	1.1731	98.35	1.44	0.17	0.04
4.0	1.3064	1.2817	97.37	2.28	0.29	0.07
5.0	1.4488	1.3996	96.26	3.22	0.42	0.11

Table 7 The fundamental frequency ratios and the modal participations for a simply supported rectangular (0/45/-45/90)s composite plate (a/b=2)

W_{max}/h		Modal Participation %						
	$(\omega/\omega_L)_{11}$	q_{11}	q_{12}	q_{21}	q_{13}	q_{22}	q_{23}	q_{31}
0.2	1.0408	99.51	0.00	0.00	0.41	0.07	0.00	0.02
0.4	1.1490	96.57	0.00	0.00	3.01	0.24	0.00	0.17
0.6	1.3484	92.93	0.00	0.00	4.55	0.47	0.00	2.04
0.8	1.5241	98.51	0.00	0.00	0.53	0.94	0.00	0.02
1.0	1.7190	97.43	0.00	0.00	2.39	0.11	0.00	0.07
1.2	1.9258	95.78	0.00	0.00	3.57	0.62	0.00	0.02
1.4	2.1409	94.27	0.00	0.00	4.84	0.77	0.00	0.13

Table 8 The fundamental frequency ratios and the modal participations for a simply supported rectangular (0/90) composite plate

W_{max}/h		Modal Participation %			
	$(\omega/\omega_L)_{11}$	q_{11}	q_{13}	q_{31}	q_{33}
0.2	1.0358	97.83	1.18	0.82	0.18
0.4	1.1432	95.13	2.25	2.24	0.38
0.6	1.2993	94.53	3.86	1.18	0.60
0.8	1.5432	88.56	4.36	4.77	2.31
1.0	1.7880	89.15	3.31	5.06	2.48
1.2	2.0142	92.22	2.89	3.15	1.74
1.4	2.2823	92.01	2.92	2.92	2.15

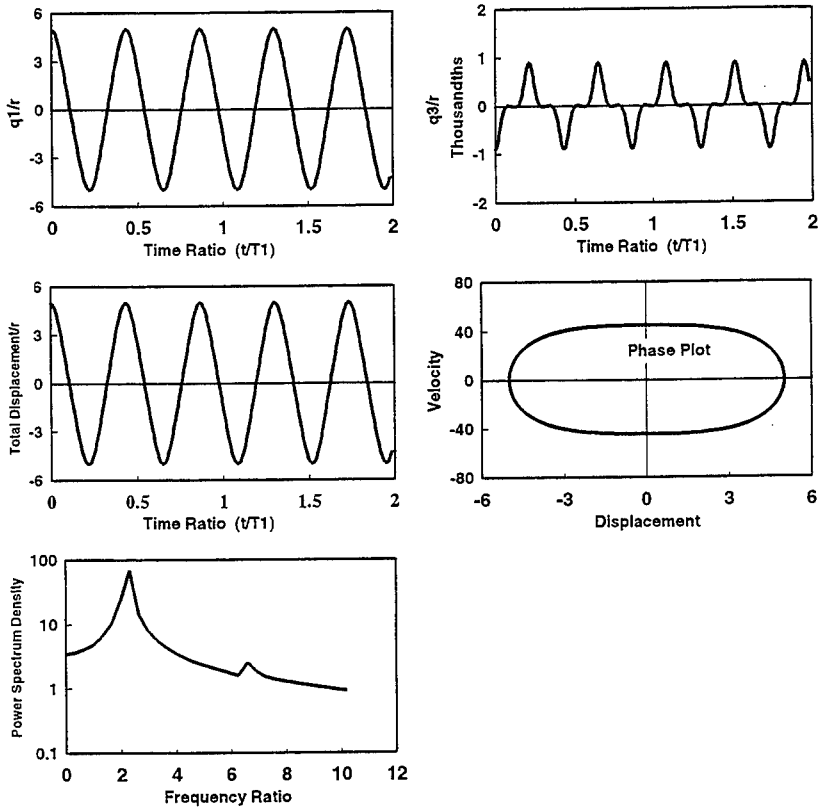

Figure 1. Time histories, phase plot and PSD for the fundamental mode at W_{max}/r =5.0 of a simply supported beam

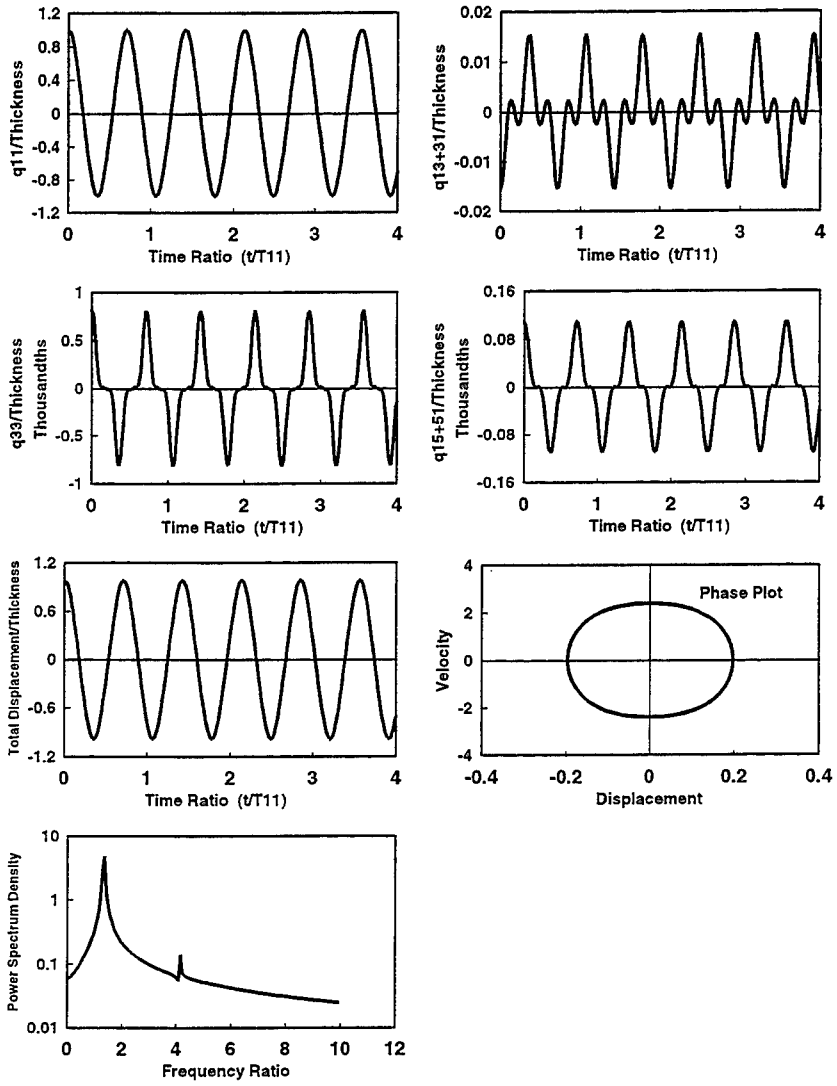

Figure 2a. Time histories, phase plot and PSD for the fundamental mode at W_{max}/h =1.0 of a simply supported square plate

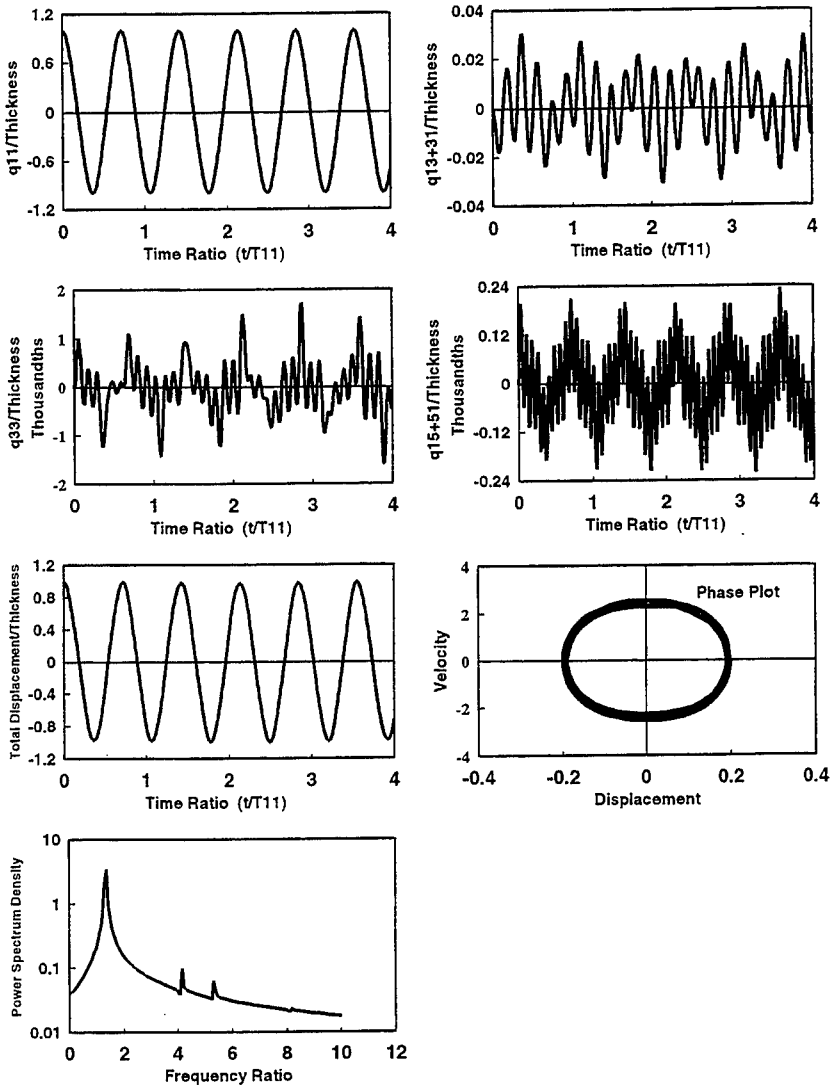

Figure 2b. Time histories, phase plot and PSD for the fundamental mode at W_{max}/h =1.0 of a simply supported square plate with improper initial conditions

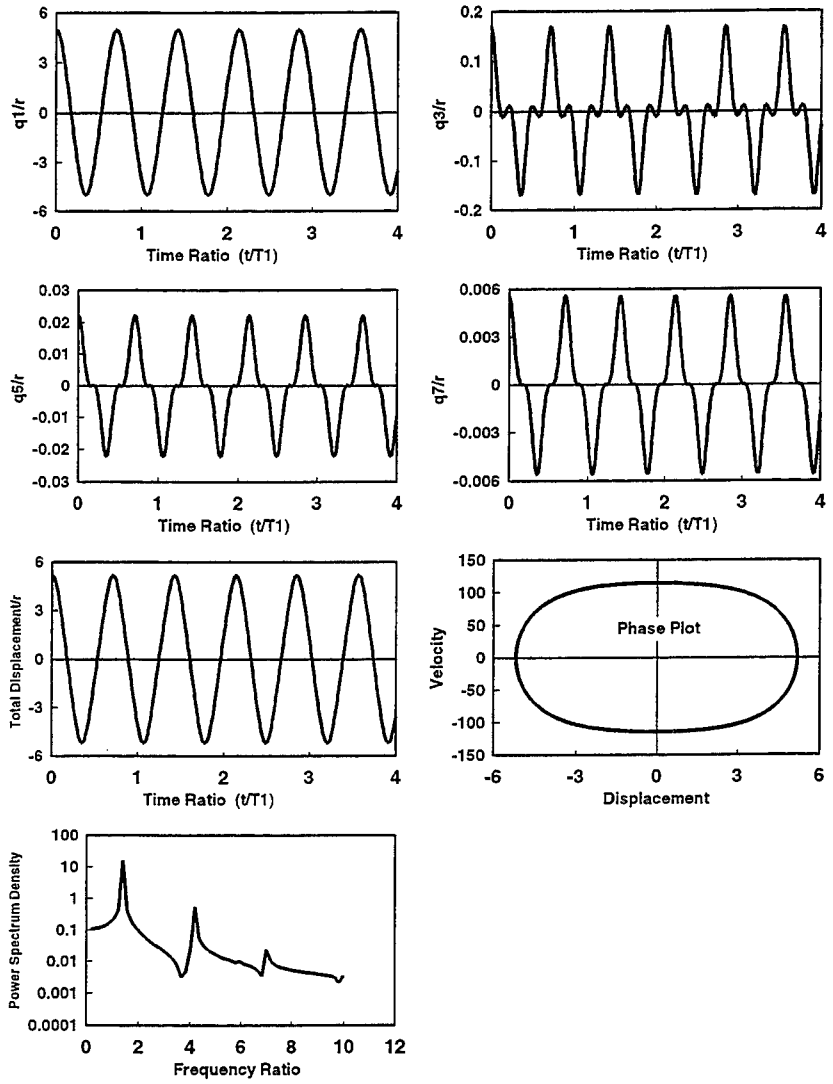

Figure 3. Time histories, phase plot and PSD for the fundamental mode at W_{max}/r =5.0 of a clamped beam

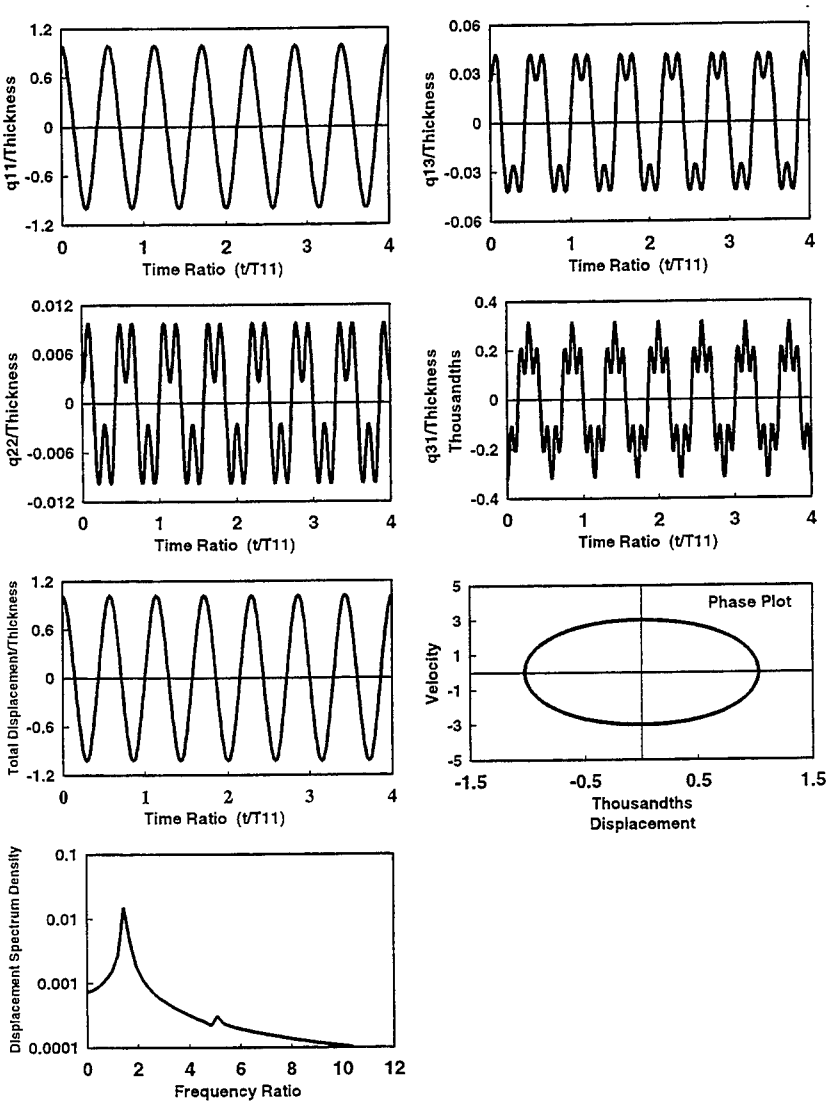

Figure 4. Time histories, plot and PSD for the fundamental mode at Wmax/h =1.0 of a simply supported (0/45/-45/90)s rectangular plate

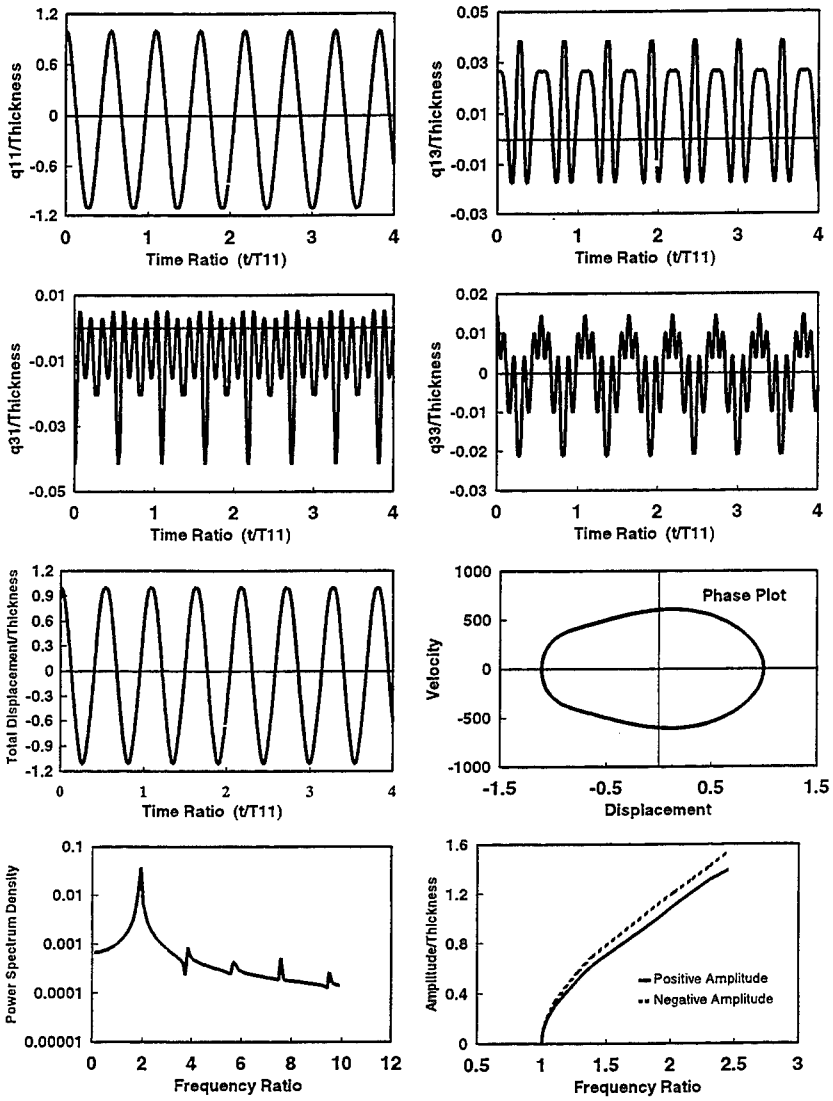

Figure 5. Time histories, phase plot, PSD and amplitude-frequency for the fundamental mode at W_{max}/h =1.0 of a simply supported (0/90)s rectangular plate

NONLINEAR FORCED VIBRATION OF BEAMS BY THE HIERARCHICAL FINITE ELEMENT METHOD

P. Ribeiro and M. Petyt
Institute of Sound and Vibration Research, University of Southampton, Southampton SO17 1BJ, UK

Abstract: The hierarchical finite element (HFEM) and harmonic balance methods are used to derive the equations of motion of beams, in steady-state forced vibration with large amplitude displacements. These equations are solved by the Newton and continuation methods. The stability of the obtained solutions is investigated by studying the evolution of perturbations of the solutions. Additionally, a method that allows a quick examination of the stability of the solution is presented and applied. The convergence properties of the HFEM, the influence of the number of degrees of freedom and of in-plane displacements are discussed. The HFEM results are compared with experimental results. Symbolic computation is used in the derivation of the model.

NOTATION

A - extension coefficient
b - width of the beam
B - coupling coefficient
[C] - damping matrix
D - bending coefficient
[D] - Jacobian of $\{F\}$
$|D|$ - determinant of [D]
E - Young's modulus
[E] - elastic matrix
{f} - vector of out-of plane shape functions
$\{F\}$ - vec. of amplitudes of generalised forces
$\{\bar{F}\}$ - vector of generalised forces
$\{F\}$ - vector of dynamic forces
{g} - vector of in-plane shape functions
h - length of the finite elements
h - thickness of the beam
$[K1_b]$ - linear bending stiffness matrix
$[K1_p]$ - linear stretching stiffness matrix
[K2], [K3] and [K4] - components of nonlinear stiffness matrix
[Knl] - nonlinear stiffness matrix
L - length of the beam
[M] - mass matrix
$[M_b]$ - bending mass matrix
$[M_p]$ - in-plane mass matrix
[N] - matrix of shape functions
$\lfloor N^w(x) \rfloor$ - row matrix of out-of-pl. sh. f.
p_i - number of in-plane shape functions
p_O - number of out-of-plane s. funct.
$\{q_p\}$ - in-plane displacement function
$\{q_w\}$ - transverse displacement function
r - radius of gyration
t - time
u - in-plane displacement
U_r - generalised in-plane displacements
w - transverse displacement
W_r - generalised out-of-pl. displ.
$\{w_c\}$, $\{w_s\}$ - coef. of cosine and sine terms
x - axial coordinate of the beam

α - loss factor
β - damping factor
$\varepsilon_0^p, \varepsilon_0^b$ - linear membrane and bending strains
ε_L^p - geometrically nonlin. membrane strain
$\{\varepsilon_1\}$, $\{\varepsilon_2\}$ - linear and geom. nonl. strains
δW_{ex} - virtual work of the external forces
δW_v - virtual work of the internal forces
δW_{in} - virtual work of the inertia forces
λ - characteristic exponent
ρ - mass density
ω - angular frequency
ω_{0j} - natural frequencies
$\left[\omega_{0j}^2\right]$ - diagonal matrix of squares of natural frequencies
ζ - Viscous damping ratio

1 - INTRODUCTION

In real systems, due to large amplitudes of the excitation, small stiffness or excitation with a frequency in the neighbourhood of resonance frequencies, vibrations with large amplitudes can occur. In this case, the linear theories may not allow a good representation of the dynamic characteristics of the system.

A typical case study of vibrations in the nonlinear regime is the forced vibration of beams, with large displacements. Although a large amount of investigation has been carried out in this field [1, 2, 10, 18 and others], a method that would allow the inclusion of higher order mode contributions and damping, without increasing excessively the number of degrees of freedom (d.o.f.) is desirable. The purpose of this work is to apply and investigate the advantages of a method that satisfies these conditions: the hierarchical finite element method (HFEM).

In the HFEM, to achieve better approximations, higher order shape functions are added to the existing model. Convergence tends to be achieved with far fewer d.o.f. than in the *h*-version of the finite element method [4, 11]. The linear matrices possess the embedding property, meaning that the associated element matrices for a number of shape functions $n=n_1$ are always submatrices for $n=n_2$, $n_2 \geq n_1$. The existing nonlinear matrices of an approximation of lower order, n_1, can be used in the derivation of the nonlinear matrices of the improved approximation, n_2. This makes the construction of a more accurate model, potentially quicker in the HFEM than in the *h*-version.

We are going to consider that the time variation of the solution may be expressed by harmonics and use the harmonic balance method (HBM). Compared with perturbation methods, the main advantages of the HBM are its simplicity, the fact that it is not restricted to weakly non-linear problems and, for smooth systems, the assurance of convergence to the exact solution [5].

In nonlinear vibrations, the frequency response curves can have multi-valued regions, turning and bifurcation points. In these regions, we are going to use a continuation method [8, 14], because, if the Newton method alone is applied, the solution will depend heavily on the initial guess and convergence is very difficult to achieve.

Symbolic computation [15] will be utilised, allowing an easier and more accurate construction of the model.

2 - MATHEMATICAL MODEL

The beam is assumed to be elastic and isotropic, with thin uniform thickness h. The effects of transverse shear deformations and rotatory inertia are neglected. The transverse displacement is large compared with the beam thickness, but is very small compared with the length of the beam (w << L). The slopes are also very small: $(w_{,x})^2 << 1$.

The displacement components u and w may be expressed as the combination of the hierarchical polynomial shape functions,

$$\{d\} = \begin{Bmatrix} u \\ w \end{Bmatrix} = [N]\{q\},\ [N] = \begin{bmatrix} g_1 g_2 \cdots g_{p_i} & 0 \\ 0 & f_1 f_2 \cdots f_{p_o} \end{bmatrix},$$

$$\{q\}^T = \begin{bmatrix} U_1 & \cdots & U_{p_i} & W_1 & \cdots & W_{p_o} \end{bmatrix}. \qquad (2.1)$$

The hierarchical polynomials used in this study were derived from Rodrigue's form of Legendre polynomials [4]. Only one element was used to model the whole beam and only the shape functions that satisfy the boundary conditions were included in the model.

Applying the theory of Bernoulli-Euler, expressing the strain as

$$\{\varepsilon\} = \begin{Bmatrix} u_{,x} \\ -w_{,xx} \end{Bmatrix} + \begin{Bmatrix} (w_{,x})^2/2 \\ 0 \end{Bmatrix} = \begin{Bmatrix} \varepsilon_0^p \\ \varepsilon_0^b \end{Bmatrix} + \begin{Bmatrix} \varepsilon_L^p \\ 0 \end{Bmatrix} = \{\varepsilon_1\} + \{\varepsilon_2\}, \qquad (2.2)$$

and equating the virtual work of the inertia forces (D' Alembert principle) to the virtual work of the external and elastic restoring forces we obtain:

$$\{\delta q\}^T\{\bar{F}\} - b\int_L \left(\{\delta\varepsilon_1\}^T + \{\delta\varepsilon_2\}^T\right)[E]\left(\{\varepsilon_1\} + \{\varepsilon_2\}\right)dL = \{\delta q\}^T[M]\{\ddot{q}\}, \qquad (2.3)$$

$$[E] = \begin{bmatrix} A & 0 \\ 0 & D \end{bmatrix};\ A, D = \int_z (1, z^2)E\,dz;\ [M] = \rho hb\int_L [N]^T[N]dL.$$

The stiffness matrices are defined by:

$$b\int_L \{\delta\varepsilon_1\}^T[E]\{\varepsilon_1\}dL = \{\delta q\}^T[K1]\{q\},\ b\int_L \{\delta\varepsilon_1\}^T[E]\{\varepsilon_2\}dL = \{\delta q\}^T[K2]\{q\},$$
$$b\int_L \{\delta\varepsilon_2\}^T[E]\{\varepsilon_1\}dL = \{\delta q\}^T[K3]\{q\},\ b\int_L \{\delta\varepsilon_2\}^T[E]\{\varepsilon_2\}dL = \{\delta q\}^T[K4]\{q\}. \qquad (2.4)$$

Considering only transverse forces, if $\bar{P}(t)$ represents a concentrated force acting at the point $x=x_j$ and $\bar{P}_d(x,t)$ represents a distributed force, the generalised forces are

$$\{\bar{F}\} = \left(\int_L \bar{P}_d(x,t)\{N^w(x)\}dL + \bar{P}_j(t)\{N^w(x_j)\}\right). \qquad (2.5)$$

In real systems energy is dissipated; consequently, damping should be included in the present model. For a large variety of materials experimental investigations show

that the energy dissipated per cycle is not dependent on the frequency and is proportional to the square of the amplitude of vibration [12, 13]. The corresponding type of damping is called hysteretic. We will represent it by a matrix proportional to the mass matrix and frequency dependent:

$$[C]=\frac{\beta}{\omega}[M] \tag{2.6}$$

Considering that damping in the beam results only from the action of the linear axial and bending strains, we have the following equations of motion:

$$\begin{bmatrix} M_p & 0 \\ 0 & M_b \end{bmatrix}\begin{Bmatrix} \ddot{q}_p \\ \ddot{q}_w \end{Bmatrix}+\begin{bmatrix} \frac{\beta_p}{\omega}M_p & 0 \\ 0 & \frac{\beta}{\omega}M_b \end{bmatrix}\begin{Bmatrix} \dot{q}_p \\ \dot{q}_w \end{Bmatrix}+\left(\begin{bmatrix} K1_p & 0 \\ 0 & K1_b \end{bmatrix}+\begin{bmatrix} 0 & K2 \\ K3 & K4 \end{bmatrix}\right)\begin{Bmatrix} q_p \\ q_w \end{Bmatrix}=\begin{Bmatrix} 0 \\ \overline{F} \end{Bmatrix} \tag{2.7}$$

The in-plane inertia can be neglected for slender beams [3] and the damping contribution due to the axial stress is generally negligible compared to that due to the bending stress [12]. With these approximations and because $[K3]=2[K2]^T$, ref. [4], we can simplify the equations of motion to obtain:

$$[M_b]\{\ddot{q}_w\}+\frac{\beta}{\omega}[M_b]\{\dot{q}_w\}+[K1_b]\{q_w\}+[Knl]\{q_w\}=\{\overline{F}\}, \tag{2.8}$$

$$[Knl]=[K4]-2[K2]^T[K1_p]^{-1}[K2]. \tag{2.9}$$

To integrate exactly terms involving shape functions or its derivatives, present in the stiffness and mass matrices, symbolic computation was employed, using the package *Maple* [15].

If the external excitation is harmonic and if initial conditions are such that no transient response exists, then $\{q_w(t)\}$ may be expressed, in a first approximation, as:

$$\{q_w(t)\}=\{w_c\}\cos(\omega t)+\{w_s\}\sin(\omega t) \tag{2.10}$$

We are going to insert this equation into the equations of motion (2.8) and apply the HBM. This method can be easily implemented in a program written with the symbolic manipulator *Maple*. For that, one defines the command *trign* using the *Maple* library of trigonometric functions, *trig*, in the following way: *trign:=readlib('trig/reduce')* [15, 17]. *trign*, thus defined, replaces all nonlinear trigonometric functions by linear ones[1]. With the command *coeff* one selects the terms in cos(ωt) and sin(ωt). In this way, we obtain equations of motion of the form:

[1] For example $\cos^3(\omega t)$ is replaced by $\frac{3}{4}\cos(\omega t)+\frac{1}{4}\cos(3\omega t)$

$$\{F\}=\left(-\omega^2\begin{bmatrix}M_b & 0\\ 0 & M_b\end{bmatrix}+\begin{bmatrix}0 & \beta M_b\\ -\beta M_b & 0\end{bmatrix}+\begin{bmatrix}K1_b & 0\\ 0 & K1_b\end{bmatrix}\right)\begin{Bmatrix}w_c\\ w_s\end{Bmatrix}+\begin{Bmatrix}F_1\\ F_2\end{Bmatrix}-\begin{Bmatrix}F\\ 0\end{Bmatrix}=\{0\}, \tag{2.11}$$

$$\{F_1\}=\frac{2}{T}\int_0^T[Knl]\{q_w\}\cos(\omega t)\,dt=\left(\frac{3}{4}KNL1+\frac{1}{4}KNL3\right)\{w_c\}+\frac{1}{4}KNL2\{w_s\}, \tag{2.12}$$

$$\{F_2\}=\frac{2}{T}\int_0^T[Knl]\{q_w\}\sin(\omega t)\,dt=\frac{1}{4}KNL2\{w_c\}+\left(\frac{1}{4}KNL1+\frac{3}{4}KNL3\right)\{w_s\}, \tag{2.13}$$

where KNL1 is a function of $\{w_c\}$ only, KNL2 is a function of both $\{w_c\}$ and $\{w_s\}$ and KNL3 is a function of $\{w_s\}$ only[2]. These three matrices are, as well as M_b and $K1_b$, symmetric.

3 - STUDY OF THE STABILITY OF THE SOLUTIONS

We will study the problem of local stability of the harmonic solution by adding a small disturbance to the steady state solution

$$\{\tilde{q}\}=\{q_w\}+\{\delta q_w\} \tag{3.1}$$

and studying how the variation of the solution evolves. If $\{\delta q_w\}$ dies out with time then $\{q_w\}$ is stable, if it grows then $\{q_w\}$ is unstable.

Inserting the disturbed solution (3.1) into equation (2.8), expanding the nonlinear terms into Taylor series around $\{q_w\}$ and ignoring terms of order higher than $\{\delta q_w\}$, we obtain the variational equation:

$$[M_b]\{\delta\ddot{q}_w\}+\frac{\beta}{\omega}[M_b]\{\delta\dot{q}_w\}+[K1_b]\{\delta q_w\}+\frac{\partial([Knl]\{q_w\})}{\partial\{q_w\}}\{\delta q_w\}=\{0\}. \tag{3.2}$$

The coefficients $\frac{\partial([Knl]\{q_w\})}{\partial\{q_w\}}$ are periodic functions of time. With symbolic manipulation, they can easily be expanded in a Fourier series. If $\{q_w\}$ is of the form (2.10) and since $\frac{\partial([Knl]\{q_w\})}{\partial\{q_w\}}$ is quadratic in $\{q_w\}$, we have:

$$\frac{\partial([Knl]\{q_w\})}{\partial\{q_w\}}=\left[[p_1]+[p_2]\cos(2\omega t)+[p_3]\sin(2\omega t)\right]. \tag{3.3}$$

---

[2] With this formulation, KNL2 must be calculated using $2\left[N_x^w\right]\{w_c\}\left[N_x^w\right]\{w_s\}$, otherwise $\frac{1}{2}KNL2$ should be considered instead of $\frac{1}{4}KNL2$.

Simplification (3.14) was possible because the damping matrix is, after transformation into modal coordinates, equal to a scalar matrix.

Now, following Hayashi [7, page 93], we will express the solution of (3.14) in the form:

$$\left\{\delta\bar{\xi}\right\} = e^{\lambda t}\left(\left\{b_1\right\}\cos(\omega t) + \left\{a_1\right\}\sin(\omega t)\right) \tag{3.15}$$

which should allow us to determine, in a first approximation, the first order simple unstable region.

Inserting (3.15) into (3.14) and applying the HBM, we find

$$\left(\lambda^2[I] + \lambda[M_1] + [M_0]\right)\begin{Bmatrix} b_1 \\ a_1 \end{Bmatrix} = \begin{Bmatrix} 0 \\ 0 \end{Bmatrix} \tag{3.16}$$

where

$$[M_1] = \begin{bmatrix} 0 & 2\omega[I] \\ -2\omega[I] & 0 \end{bmatrix} \tag{3.17}$$

$$[M_0] = \begin{bmatrix} [B]^T[D_{11}][B] - \left(\omega^2 + \left(\frac{1}{2}\frac{\beta}{\omega}\right)^2\right)[I] + \left[{\omega_{0j}}^2\right] & [B]^T[D_{12}][B] \\ [B]^T[D_{21}][B] & [B]^T[D_{22}][B] - \left(\omega^2 + \left(\frac{1}{2}\frac{\beta}{\omega}\right)^2\right)[I] + \left[{\omega_{0j}}^2\right] \end{bmatrix} \tag{3.18}$$

To determine the characteristic exponents, λ, we transform this system into [16]

$$\begin{bmatrix} 0 & [I] \\ -[M_0] & -[M_1] \end{bmatrix}\begin{Bmatrix} X \\ \Gamma \end{Bmatrix} = \lambda\begin{Bmatrix} X \\ \Gamma \end{Bmatrix}, \tag{3.19}$$

where $\{X\}$ is a vector formed by $\{b_1\}$, $\{a_1\}$. The values of λ are the eigenvalues of the double size matrix in the previous equation. Bearing in mind that it is the stability of the variable $\{\delta\xi\}$ in which we are interested we substitute equation (3.15) into equation (3.13) to obtain

$$\{\delta\xi\} = e^{\left(\lambda - \frac{1}{2}\frac{\beta}{\omega}\right)t}\left\{\left\{b_1\right\}\cos(\omega t) + \left\{a_1\right\}\sin(\omega t)\right\}. \tag{3.20}$$

If the real part of $\lambda_r - \frac{1}{2}\frac{\beta}{\omega}$ is positive for any λ_r, then the solution is unstable, otherwise it is stable.

For undamped systems, it was demonstrated in [8], that important conclusions about the stability of the solutions can be deducted from the determinant of the Jacobian of $\{F\}$. We are going to extend the demonstration to systems with mass proportional damping.

Applying the derivation rule for composite functions, we obtain the derivatives of $\{F_1\}$ and $\{F_2\}$ with respect to $\{w_c\}$ and $\{w_s\}$ as follows:

$$[D_{11}]=\frac{\partial\{F_1\}}{\partial\{w_c\}}=\frac{2}{T}\int_0^T\frac{\partial}{\partial\{q_w\}}\left([Knl]\{q_w\}\right)\frac{\partial\{q_w\}}{\partial\{w_c\}}\cos(\omega t)\,dt, \tag{3.21}$$

$$[D_{12}]=\frac{\partial\{F_1\}}{\partial\{w_s\}}=\frac{2}{T}\int_0^T\frac{\partial}{\partial\{q_w\}}\left([Knl]\{q_w\}\right)\frac{\partial\{q_w\}}{\partial\{w_s\}}\cos(\omega t)\,dt, \tag{3.22}$$

$$[D_{21}]=\frac{\partial\{F_2\}}{\partial\{w_c\}}=\frac{2}{T}\int_0^T\frac{\partial}{\partial\{q_w\}}\left([Knl]\{q_w\}\right)\frac{\partial\{q_w\}}{\partial\{w_c\}}\sin(\omega t)\,dt, \tag{3.23}$$

$$[D_{22}]=\frac{\partial\{F_2\}}{\partial\{w_s\}}=\frac{2}{T}\int_0^T\frac{\partial}{\partial\{q_w\}}\left([Knl]\{q_w\}\right)\frac{\partial\{q_w\}}{\partial\{w_s\}}\sin(\omega t)\,dt. \tag{3.24}$$

Matrices [I] and $[M_0]$ are symmetric and matrix $[M_1]$ is skew-symmetric. This means that the eigenvalues of equation (3.16) are either purely imaginary or purely real [8]. If λ is imaginary the solution is always stable; if λ is real the stability limit is defined by

$$\mathrm{Re}\left(\lambda-\frac{1}{2}\frac{\beta}{\omega}\right)=0\Leftrightarrow\lambda=\frac{1}{2}\frac{\beta}{\omega}. \tag{3.25}$$

Inserting (3.25) in (3.16) we arrive at

$$\begin{bmatrix}[B]^T[D_{11}][B]-\omega^2[I]+\left[\omega_{0j}{}^2\right] & [B]^T[D_{12}][B]+\beta\\ [B]^T[D_{21}][B]-\beta & [B]^T[D_{22}][B]-\omega^2[I]+\left[\omega_{0j}{}^2\right]\end{bmatrix}\begin{Bmatrix}b_1\\ a_1\end{Bmatrix}=\begin{Bmatrix}0\\ 0\end{Bmatrix}. \tag{3.26}$$

The matrix in the previous equation is $[B]^T[D][B]$, where [D] is the Jacobian of $\{F\}$ with respect to the vector of coefficients of the cosine and sine terms, given by

$$[D]=\partial\{F\}/\partial\begin{Bmatrix}w_c\\ w_s\end{Bmatrix}. \tag{3.27}$$

A non-trivial solution of (3.26) exists if

$$\det\left([B]^T[D][B]\right)=0\Leftrightarrow|B|^2|D|=0\Leftrightarrow|D|=0. \tag{3.28}$$

The last equivalence is true, because [B] is a non-singular matrix. Thus, we proved that in the stability limit, the determinant of the Jacobian of $\{F\}$, $|D|$, is zero.

$|D|$ is a polynomial in the coefficients $\{w_c\}$ and $\{w_s\}$ and in ω; therefore, it is a continuous function in those coefficients. All the experimental and numerical analysis of nonlinear vibration of beams, indicate that the shape of vibration, defined in our model by $\{w_c\}$ and $\{w_s\}$, is a continuous function of the amplitude and the frequency of vibration. Thus, we conclude that $|D|$ varies in a continuous way through the FRF (frequency response function) curve. Hence, if there is a change in its sign between two consecutive points of the FRF curve, then $|D|=0$ for a particular point between these two. In that particular point, the stability limit might have been crossed.

So, a complete study of the first order solution's stability may be carried out by determining only the characteristic exponents of the first solution and when |D| changes sign or when |D| is approximately zero. As |D| is needed in the continuation method and, when the Newton method is applied, can be easily calculated from [D], this results in substantial time savings.

4 - APPLICATIONS

A clamped-clamped beam made in an aluminium alloy with the reference 7075-T6 was analysed. Its material [9] and geometric properties are:
$E = 7.172*10^{10}$ N/m², $\rho = 2800$ kg/m³, h=0.002 m, b=0.02 m, L = 0.405 m [3].

For aluminium, a typical value of the loss factor (which is multiplied by the stiffness matrix) is $\alpha=0.01$ ($\zeta=0.5\%$), but the measured value in reference [18] was approximately equal to 0.038 ($\zeta\cong1.9\%$)[4]. In order to have the same damping coefficient for the first mode of vibration, the value of the damping factor is:

$$\beta = \omega_{01}^{2} \times \alpha . \qquad (4.1)$$

The beam was modelled using the HFEM, as described in section 2. To solve the system of equations (2.11), Newton's method was used in the nonresonant area. In the vicinity of resonance frequencies it is difficult to obtain convergence by the Newton method

[3] Except in the comparison with experimental results, where L=0.406 (value of Wolfe's clamped-clamped beam length).
[4] Wolfe did not think that the measured damping ratio was only due to material damping. He also attributed the obtained value to damping in the joints and to the coil magnet arrangement used to excite the beam.

and a continuation method was applied [8, 14]. The derivation of the Jacobian matrix present in both methods was performed symbolically [15].

Because the excitation force will be applied in the middle of the beam and both the beam and the boundary conditions have symmetric properties, only symmetric out of-plane shape functions and antisymmetric in-plane shape functions will be used[5].

4.1 - Study of convergence with number of shape functions

With four out-of-plane (p_o) and four in-plane shape functions, convergence of the value of the first linear natural frequency is achieved (Table 1). This number of shape functions will be the starting value for our nonlinear analysis. The number of degrees of freedom of the present damped model is equal to $2 \times p_o$.

Table 1 - Natural linear frequencies of the cc beam (rad/s). Mode 1.

Exact [8]	$p_o=2$, $p_i=2$	$p_o=3$, $p_i=3$	$p_o=4$, $p=4_i$	$p_o=5$, $p_i=5$
396.6	396.613 239	396. 605 011	396. 605 008	396. 605 008

In Figures 1, 2 and 3 we can see the FRFs in the vicinity of the first, third and fifth mode, obtained when a force P of 0.03 N was applied. Near the first mode there is no increase in accuracy by using more than four out-of-plane and four in-plane shape functions ($p_o=4$, $p_i=4$). However, for the third mode, as the amplitude of vibration grows, the results obtained with $p_o=4$ and $p_i=4$ depart from the ones obtained with more shape functions. The FRF curve constructed with $p_o=5$ and $p_i=5$ is quite similar to the coincident FRFs obtained with $p_o=6$, $p_i=6$ and with $p_o=7$, $p_i=7$. In the neighbourhood of the fifth mode, convergence seems to be achieved with $p_o=8$ and $p_i=8$.

4.2 - Influence of in-plane displacements

In Figure 4 the FRFs obtained considering and neglecting the in-plane displacements are compared. As in references [1] and [10], we found that the in-plane displacements 'reduce' the non-linearity, in the sense that the non-linearity caused by them is of the soft spring type and counterbalances the hard spring type non-linearity

[5] To check if the nonlinearity introduced any coupling and consequent antisymmetric terms in the response, a model including symmetric and antisymmetric, in- and out-of-plane shape functions was considered. It was confirmed that, with these boundary conditions and with the one harmonic representation of the solution's time dependency, there is no such coupling.

caused by the transverse displacements. This 'reduction' of nonlinearity is due, as the formulation of the nonlinear stiffness matrix - eq. (2.9) - shows, to the effects of in-plane deformation on the stiffness of the structure.

4.3 - Study of stability

In Figures 5 and 6 we can see the stability studies carried out in the neighbourhood of the first and third resonance frequencies, using p_o=6, p_i=6 shape functions and with an excitation force of amplitude P = 0.03 N. In all cases, $|D|$ changed sign when the stability condition of the solutions changed.

4.4 - Comparison with experimental results

In Figures 7 and 8 we can see the comparison between the FRF obtained with the HFEM, using p_o=6, p_i=6 shape functions, and the experimental results [18] when a force P = 0.134 N is applied in the centre of the beam. Two values were used for the damping factor: $\beta=0.01\,\omega_{01}^2$ and $\beta=0.038\,\omega_{01}^2$.

The HFEM provides a FRF with a slope similar to the experimental one around the resonance frequency. This indicates that the nonlinear stiffness is well represented by the model.

The turning point corresponding to the largest amplitude of vibration, where the jump phenomena occurs, obtained with the HFEM, point **B**, does not match the experimental one, point **A**. With the typical value used for the loss factor in aluminium alloys, α=0.01 ($\beta=0.01\,\omega_{01}^2$), the maximum amplitude of vibration was more than double the one measured. However, the HFEM solutions represented in Figure 7 after point **A** are very close. Thus, in a real system, a small perturbation would easily make the shape of vibration change into an unstable one and a change, or jump, to a stable shape of vibration at a lower amplitude could be observed before the largest computed amplitude of vibration was achieved. With the measured loss factor, α=0.038, the largest amplitude of vibration obtained with the HFEM, was around a half of the measured maximum amplitude.

5 - CONCLUSIONS

The HFEM dynamic model of a beam vibrating with large amplitudes was constructed with small time expense. This is due to the small number of degrees of freedom with which convergence is achieved, to the easy way in which the number of d.o.f. are reduced, benefiting from the symmetry properties of the problem, and to the embedding properties[6] of the HFEM.

For the amplitudes of vibration displacement studied, with relatively few d.o.f. the FRF curves were accurately determined until the 5th order mode, inclusive. If modes of order higher than 5th are to be studied, then the inclusion of more elements instead of more shape functions should be considered, as shape functions of excessive high order turn the construction of the matrices quite time consuming. The comparison with experimental results showed a very good prediction of the slope of the FRF by the HFEM. The largest amplitude of vibration and the correspondent turning and jump point, are greatly influenced by the amount of damping used.

Using the flexibility of choosing the shape functions in the HFEM model it was shown that the in-plane displacements cause a softening-type nonlinearity.

With the continuation method the multi-valued regions of the FRF curves were completely and automatically described.

To determine the characteristic exponents that establish the stability of the solution, we solved an eigenvalue problem. Due to the reduced number of degrees of freedom of the HFEM model this was quickly solved. More important, it was proven that in the stability limit the determinant $|D|$ is zero. Thus, we only have to determine the characteristic exponents of the first solution and when there is an indication that $|D|=0$ for a particular point, to check if the stability of the solution changed. This results in significant time savings.

With symbolic computation, the matrices involved in the HFEM model and the Jacobian matrix necessary in the continuation and Newton methods, were easily and exactly derived, thus reducing the numerical errors. Symbolic computation was also helpful in the application of the HBM.

[6] Here we include the HFEM's advantages in the derivation of the nonlinear stiffness matrix.

REFERENCES

[1] - Atluri, S., Nonlinear vibrations of a hinged beam including nonlinear effects. Trans. of the ASME J. of Apl. Mech., 1973, **40**, 121-126.

[2] - Bennet, J. A. and Eisley, J. G., A multiple-degree-of freedom approach to nonlinear beam vibrations. J. of the Am. Inst. of Aeronaut. and Astronaut., 1970, **8**, 734-739.

[3] - Cheung, Y. K. and Lau, S. L., Incremental time-space finite strip method for non-linear structural vibrations. Earthquake Engng. and Struct. Dynamics, 1982, **10**, 239-253.

[4] - Han, W, *The Analysis of isotropic and laminated rectangular plates including geometrical non-linearity using the p-version finite element method*, Ph.D. Thesis, University of Southampton, Southampton, 1993.

[5] - Hamdan, M.N. and Burton, T.D., On the steady state response and stability of non-linear oscillators using harmonic balance. J. of Sound and Vibr., 1993, **166**, 255-266.

[6]- Stokey, W. F., *Shock and Vibration Handbook*, Third edition, ed. C. M. Harris, McGraw-Hill, New York, 1988, p. 7-14.

[7] - Hayashi, C, *Nonlinear Oscillations in Physical Systems*, McGraw-Hill, New York, 1964.

[8] - Lewandowski, R., Non-linear, steady-state analysis of multispan beams by the finite element method. Computers and Struct., 1991, **39**, 83-93.

[9] - ASM Committee on Properties of Aluminium Alloys, *Properties and Selection of Metals*, Metals Handbook, Vol. 1, 8th edition, ed. T. Lyman, Ohio, 1961, p. 948.

[10] - Mei, C and Decha-Umphai, A finite element method for non-linear forced vibrations of beams. J. of Sound and Vibr., 1985, **102**, 369-380.

[11] - Meirovitch, L., *Elements of Vibration Analysis*, McGraw-Hill, Singapore, 1986.

[12] - Mentel, T. J., Vibrational energy dissipation at structural support junctions. In *Colloquium on Struct. Damping*, ed. E. J. Ruzicka, 1959, pp. 89-116.

[13] - Petyt, M, *Introduction to Finite Element Vibration Analysis*, Cambridge University Press, Cambridge, 1990.

[14] - Ribeiro, P. and Petyt, M., Study of nonlinear free vibration of beams by the hierarchical finite element method. ISVR Technical Memorandum No.773, University of Southampton, Southampton, November 1995.

[15] - Redfern, Darren, *The Maple Handbook*, Springer-Verlag, New York, 1994.

[16] - Takahashi, K., A method of stability analysis for non-linear vibration of beams. J. of Sound and Vibr., 1979, **67**, 43-54.

[17] - Wang, S. S. and Huseyn, K., Bifurcations and stability properties of nonlinear systems with symbolic software. Math. Comput. Modelling, 1993, **18**, 21-38.

[18] - Wolfe, Howard, *An experimental investigation of nonlinear behaviour of beams and plates excited to high levels of dynamic response*, Ph.D. Thesis, University of Southampton, Southampton, 1995.

FIGURES

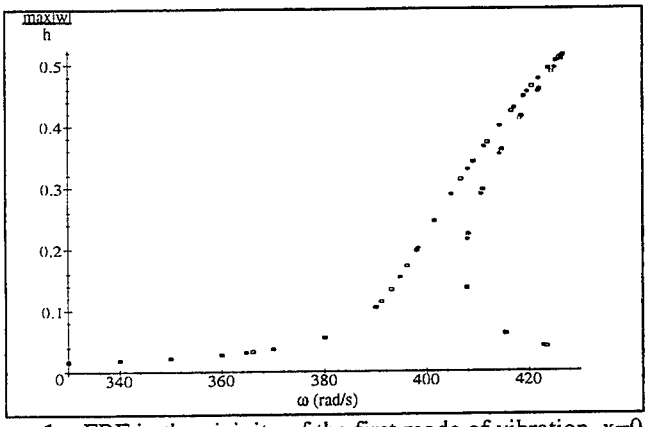

Figure 1 – FRF in the vicinity of the first mode of vibration. x=0.5×L.
o p_o=4, p_i=4; ❑ p_o=5, p_i=5; ◊ p_o=6, p_i=6; + p_o=7, p_i=7.

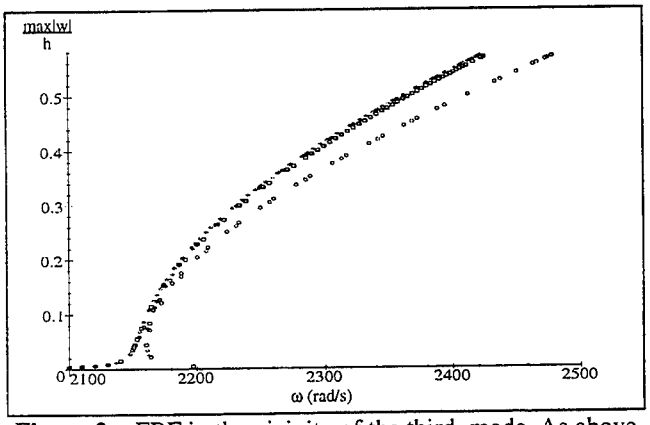

Figure 2 – FRF in the vicinity of the third mode. As above.

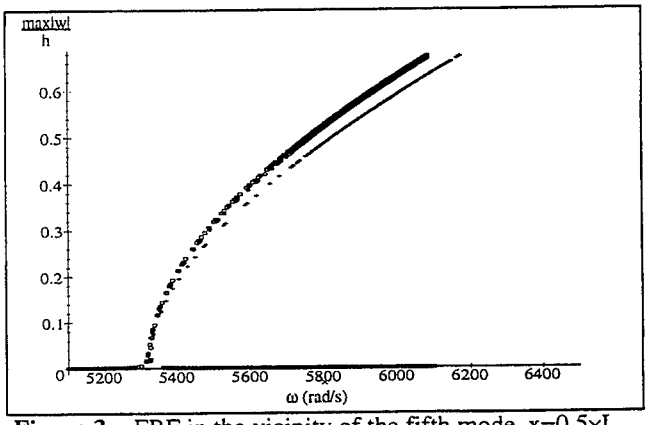

Figure 3 – FRF in the vicinity of the fifth mode. x=0.5×L.
+ p_o=7, p_i=7; o p_o=8, p_i=8; ❑ p_o=9, p_i=9.

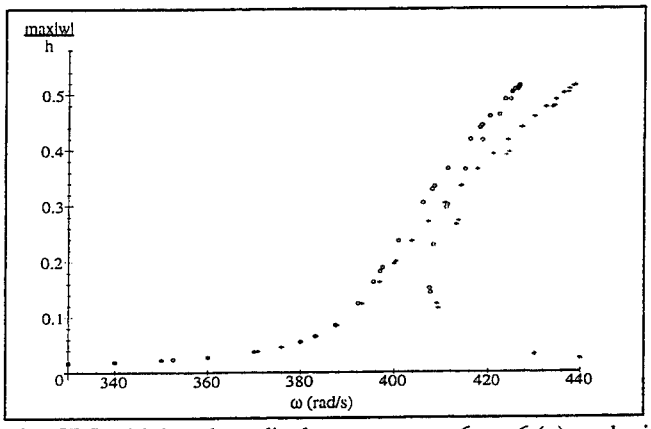

Figure 4 – FRF with in–plane displacements, p_o=6, p_i=6 (o), and without in–plane displacements, p_o=6, p_i=0 (+). x=05×L.

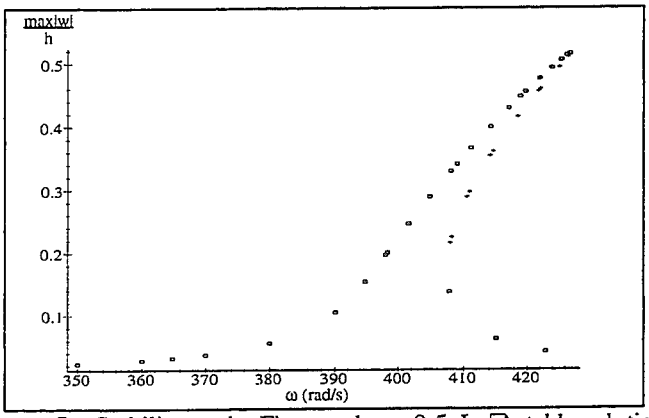

Figure 5 – Stability study. First mode. x=0.5×L. ❑ stable solution; + unstable solution; p_o=6, p_i=6.

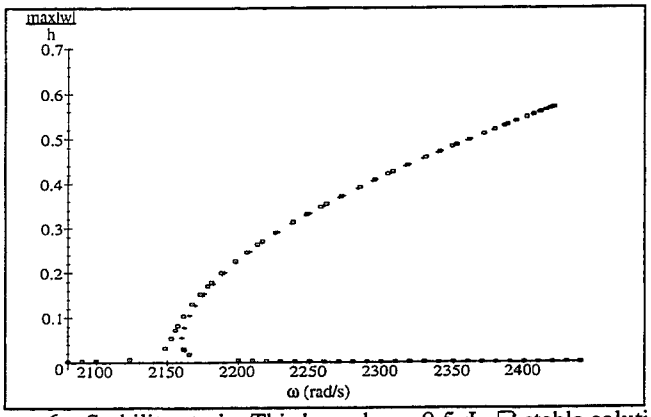

Figure 6 – Stability study. Third mode. x=0.5×L. ❑ stable solution; + unstable solution; p_o=6, p_i=6.

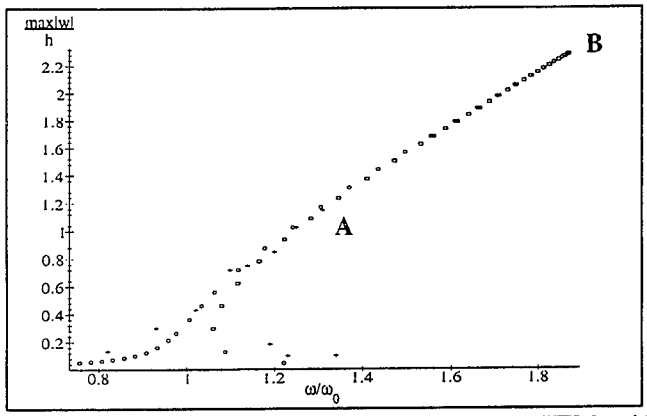

Figure 7 – Comparison with experimental results. o HFEM stable, ❑ HFEM unstable, p_o=6 and p_i=6, β=0.01ω_{0i}^2; + experimental. x=05×L.

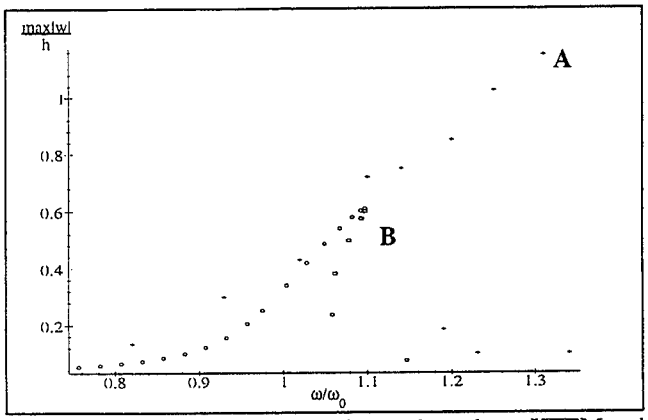

Figure 8 – Comparison with experimental results. o HFEM stable, ❑ HFEM unstable, p_o=6 and p_i=6, β=0.038ω_{0i}^2; + experimental. x=05×L.

GEOMETRICALLY NONLINEAR DYNAMIC ANALYSIS OF 3-D BEAM

Kuo Mo Hsiao and Wen Yi Lin
Department of Mechanical Engineering,
National Chiao Tung University,
Hsinchu, Taiwan, Republic of China

ABSTRACT

A co-rotational finite element formulation for the geometrically nonlinear dynamic analysis of spatial beam with large rotations but small strain is presented. The deformation nodal forces and inertia nodal forces are derived by using the d'Alembert principle and the virtual work principle. The gyroscopic effect is considered here.

The beam element developed here has two nodes with six degrees of freedom per node. Some angular velocity coupling terms, which are so called gyroscopic forces, are obtained in inertia nodal force.

An incremental-iterative method based on the Newmark direct integration method and the Newton-Raphson method is employed here for the solution of the nonlinear dynamic equilibrium equations. Numerical examples are presented to demonstrate the accuracy and efficiency of the proposed method.

INTRODUCTION

In recent years, the nonlinear dynamic behavior of beam structures, e.g., framed structures, flexible mechanisms, and robot arms, has been the subject of considerable research. In [1], Hsiao and Jang presented a co-rotational formulation and numerical procedure for the dynamic analysis of planar beam structures. This formulation and numerical procedure were proven to be very effective by numerical examples studied in [1]. However, it is only limited for planar beam structures. A general formulation for three dimensional beam element is not a simple extension of a two dimensional formulation, because large rotations in three dimensional analysis are not vector quantities; that is, they do not comply with the rules of vector operations. In [2] a motion process of the three dimensional beam element is proposed for the large displacement and rotation analysis of spatial frames. In [3] a co-rotational formulation for three-dimensional beam element is proposed. However, it is only limited for nonlinear static analysis.

The objective of this study is to present a practical formulation for the dynamic analysis of three dimensional Euler beam. The kinematics of the beam element proposed in [3] is adopted here.

The element deformations are determined by the rotation of element cross section coordinates, which are rigidly tied to element cross section, relative to the element coordinate system [2, 3]. The three rotation parameters proposed in [3] are used to determine the orientation of the element cross section coordinates. In order to capture the gyroscopic effect, the relation between the time derivatives of the rotation parameters and the angular velocity and the angular acceleration is derived here. The beam element developed here has two nodes with six degrees of freedom per node. The element nodal forces are conventional forces and moment. The deformation nodal forces and inertia nodal forces are derived by using the d'Alembert principle and the virtual work principle in the current element coordinates. An incremental-iterative method based on the Newmark direct integration method and the Newton-Raphson method is employed here for the solution of the nonlinear dynamic equilibrium equations. Numerical examples are presented to demonstrate effectiveness of the proposed method.

FINITE ELEMENT FORMULATION

Basic assumptions

The following assumptions are made in the derivation of the nonlinear behavior: (1) the beam is prismatic and slender, and the Euler-Bernoulli hypothesis is valid; (2) the centroid and the shear center of the cross section coincide; (3) the unit extension and twist rate of the centroid axis of the beam element are uniform; (4) the cross section of the beam element does not deform in its own plane, and strains within this cross section can be neglected; (5) the out-of-plane warping of the cross section is the product of the twist rate of the beam element and the Saint Venant warping function for a prismatic beam of the same cross section; (6) the deformations of the beam element are small.

Coordinate systems

In this paper, a co-rotational total Lagrangian formulation is adopted. In order to describe the system, following [3], we define three sets of coordinate systems (see Fig. 1):

(1) A fixed global set of coordinates, $X_i\ (i=1,2,3)$; the nodal coordinates, displacements, and rotations, and the stiffness matrix of the system are defined in this coordinates.

(2) Element cross section coordinates, $x_i^s\ (i=1,2,3)$; a set of element cross section coordinates is associated with each cross section of the beam element. The origin of this coordinate system is rigidly tied to

the shear center of the cross section. The x_1^s axes are chosen to coincide with the normal of the corresponding cross section and the x_2^s and x_3^s axes are chosen to be the principal directions of the cross section.

(3) Element coordinates, x_i $(i=1,2,3)$; a set of element coordinates associated with each element. The origin of this coordinate system is located at node 1; the x_1 axis is chosen to pass through two end nodes of the element, and the x_2 and x_2 axes are determined from the orientation of the element cross section coordinates at two end nodes using the way given in [2]. The deformations and stiffness matrices of the elements are defined in terms of this coordinates. In this paper the element deformations are determined by the rotation of element cross section coordinates relative to this coordinate system.

Rotation vector and rotation parameters

For convenience of the later discussion, the term 'rotation vector' is used to represent a finite rotation. Figure 2 shows that a vector $\mathbf{b}$ which as a result of the application of a rotation vector $\phi\mathbf{a}$ is transported to the new position $\mathbf{b}'$. The relation between $\mathbf{b}$ and $\mathbf{b}'$ may be expressed as [4]

$$\mathbf{b}' = \cos\phi\mathbf{b} + (1-\cos\phi)(\mathbf{a}\cdot\mathbf{b}) + \sin\phi(\mathbf{a}\times\mathbf{b}), \tag{1}$$

where ϕ is the angle of counterclockwise rotation, and $\mathbf{a}$ is the unit vector along the axis of rotation.

In this paper, the symbol { } denotes column matrix. Let $\mathbf{e}_i$ and $\mathbf{e}_i^s$ $(i=1,2,3)$ denote the unit vectors associated with the x_i and x_i^s axes, respectively. Here, the traid $\mathbf{e}_i^s$ in the deformed state is assumed to be achieved by the application of the following two rotation vectors to the traid $\mathbf{e}_i$:

$$\theta_n = \theta_n\mathbf{n}, \qquad \theta_t = \theta_1\mathbf{t}, \tag{2, 3}$$

where

$$\begin{aligned}
&\mathbf{n} = \{0,\ \theta_2/(\theta_2^2+\theta_3^2)^{1/2},\ \theta_3/(\theta_2^2+\theta_3^2)^{1/2}\} \\
&\quad = \{0, n_2, n_3\}, \\
&\mathbf{t} = \{\cos\theta_n, \theta_2, \theta_3\}, \\
&\cos\theta_n = (1-\theta_2^2-\theta_3^2)^{1/2}, \\
&\theta_2 = -\frac{dw(s)}{ds}, \qquad \theta_3 = \frac{dv(s)}{ds},
\end{aligned} \tag{4}$$

in which $\mathbf{n}$ is the unit vector perpendicular to the vectors $\mathbf{e}_1$ and $\mathbf{e}_1^s$, and $\mathbf{t}$ is the tangent unit vector of the deformed centroid axis. Note that $\mathbf{e}_1^s$ coincides with $\mathbf{t}$. θ_n is the inverse of $\cos\theta_n$. $v(s)$ and $w(s)$ are the lateral deflections of the centroid axis of the beam element in the x_2 and x_3 directions, respectively, and s is the arc length of the deformed centroid axis.

The rotation vectors θ_n and θ_t are determined by θ_i $(i=1,2,3)$. Thus, θ_i are called rotation parameters in this study.

Using Eqs. (1)-(4), the relation between the vectors $\mathbf{e}_i$ and $\mathbf{e}_i^s$ $(i=1,2,3)$ in the element coordinate system may be obtained as

$$
\begin{aligned}
&\mathbf{e}_i^s = [\mathbf{t}, \mathbf{R}_1, \mathbf{R}_2] = \mathbf{R}\mathbf{e}_i,\\
&\mathbf{R}_1 = \cos\theta_1\mathbf{r}_1 + \sin\theta_1\mathbf{r}_2,\\
&\mathbf{R}_2 = -\sin\theta_1\mathbf{r}_1 + \cos\theta_1\mathbf{r}_2,\\
&\mathbf{r}_1 = \{-\theta_3, \cos\theta_n + (1-\cos\theta_n)n_2^2, (1-\cos\theta_n)n_2n_3\},\\
&\mathbf{r}_2 = \{\theta_2, (1-\cos\theta_n)n_2n_3, \cos\theta_n + (1-\cos\theta_n)n_3^2\},
\end{aligned}
\tag{5}
$$

where $\mathbf{R}$ is the so-called rotation matrix.

Let $\theta = \{\theta_1, \theta_2, \theta_3\}$ be the vector of rotation parameters, $\delta\theta$ be the variation of θ. The traid $\mathbf{e}_i^s$ corresponding to θ may be rotated by a rotation vector $\delta\phi = \{\delta\phi_1, \delta\phi_2, \delta\phi_3\}$ to reach their new positions corresponding to $\theta + \delta\theta$ [3]. When θ_2 and θ_3 are much smaller than unity, the relationship between $\delta\theta$ and $\delta\phi$ may be approximated by

$$
\delta\theta = \begin{bmatrix} 1 & \theta_3/2 & -\theta_2/2 \\ -\theta_3 & 1 & 0 \\ \theta_2 & 0 & 1 \end{bmatrix} \delta\phi = \mathbf{T}^{-1}\delta\phi. \tag{6}
$$

If both sides of Eq. (6) is divided by δt, the first time derivative of θ may be expressed by

$$
\dot{\theta} = \begin{bmatrix} 1 & \theta_3/2 & -\theta_2/2 \\ -\theta_3 & 1 & 0 \\ \theta_2 & 0 & 1 \end{bmatrix} \dot{\phi} = \mathbf{T}^{-1}\dot{\phi}, \tag{7}
$$

where the symbol $\dot{(\,)}$ denotes differentiation with respect to time t.

$\dot{\phi}_i (i = 1,2,3)$ denote the angular velocities about the x_i axes.

From Eq. (7), the second time derivative of θ may be expressed by may be expressed as

$$\ddot{\theta} = \dot{\mathbf{T}}^{-1}\dot{\phi} + \mathbf{T}^{-1}\ddot{\phi}, \tag{8}$$

where $\ddot{\phi}_i (i = 1,2,3)$ denote the angular accelerations about the x_i axes.

Nodal parameters and forces

The global nodal parameters for the system of equations corresponding to the element local nodes j (j = 1, 2) are U_{ij}, the X_i ($i = 1,2,3$) components of the translation vectors $\mathbf{U}_j$ at nodes j, and Φ_{ij}, the X_i ($i = 1,2,3$) components of the rotation vectors Φ_j at nodes j. Here, the values of Φ_j are reset to zero at current configuration. Thus, $\delta\Phi_{ij}$, the variations of Φ_{ij}, represent infinitesimal rotations about the X_i axes [3], $\dot{\Phi}_{ij}$ and $\ddot{\Phi}_{ij}$ represent angular velocities and angular accelerations about the X_i axes, respectively. The generalized nodal forces corresponding to $\delta\Phi_{ij}$ are the conventional moments about the X_i axes. The generalized nodal forces corresponding to δU_{ij}, the variation of U_{ij}, are the forces in the X_i directions.

The element employed here has six degrees of freedom per node. Two sets of element nodal parameters termed 'explicit nodal parameters' and 'implicit nodal parameters' are employed. The explicit nodal parameters of the element are used for the assembly of the system equations from the element equations. Thus, they should be consistent with the global nodal parameters, and are chosen to be u_{ij}, the x_i ($i = 1,2,3$) components of the translation vectors $\mathbf{u}_j$ at nodes j (j = 1, 2) and ϕ_{ij}, the x_i ($i = 1,2,3$) components of the rotation vectors ϕ_j at nodes j. Similarly, the generalized nodal forces corresponding to u_{ij} and $\delta\phi_{ij}$ are f_{ij} and m_{ij}, the forces in the x_i directions and the conventional moments about the x_i axes, respectively.

The implicit nodal parameters of the element are used to determine the deformation of the beam element. They are chosen to be u_{ij}, the x_i ($i = 1,2,3$) components of the translation vectors $\mathbf{u}_j$ at nodes j and θ_{ij}, the nodal values of the rotation parameters θ_i

$(i = 1,2,3)$ at nodes j (j = 1, 2). The generalized nodal forces corresponding to δu_{ij} and $\delta\theta_{ij}$ are f_{ij} and m^{θ}_{ij}, the forces in the x_i directions and the generalized moments, respectively. Note that m^{θ}_{ij} are not conventional moments, because $\delta\theta_{ij}$ are not infinitesimal rotations about the x_i axes.

In view of Eq. (6), the relations between the variation of the implicit and explicit nodal parameters may be expressed as

$$\delta\mathbf{q}^{\theta} = \begin{Bmatrix} \delta\mathbf{u}_1 \\ \delta\theta_1 \\ \delta\mathbf{u}_2 \\ \delta\theta_2 \end{Bmatrix} = \begin{bmatrix} \mathbf{I} & \mathbf{0} & \mathbf{0} & \mathbf{0} \\ \mathbf{0} & \mathbf{T}_1^{-1} & \mathbf{0} & \mathbf{0} \\ \mathbf{0} & \mathbf{0} & \mathbf{I} & \mathbf{0} \\ \mathbf{0} & \mathbf{0} & \mathbf{0} & \mathbf{T}_2^{-1} \end{bmatrix} \begin{Bmatrix} \delta\mathbf{u}_1 \\ \delta\phi_1 \\ \delta\mathbf{u}_2 \\ \delta\phi_2 \end{Bmatrix} = \mathbf{T}_{\theta\phi}\delta\mathbf{q}, \tag{9}$$

where $\delta\mathbf{u}_j = \{\delta u_{1j}, \delta u_{2j}, \delta u_{3j}\}$, $\delta\theta_j = \{\delta\theta_{1j}, \delta\theta_{2j}, \delta\theta_{3j}\}$, and $\delta\phi_j = \{\delta\phi_{1j}, \delta\phi_{2j}, \delta\phi_{3j}\}$, ($j$ = 1, 2). $\mathbf{I}$ and $\mathbf{0}$ are the identity and zero matrices of order 3×3, respectively. $\mathbf{T}_j^{-1}$ (j = 1, 2) are nodal values of $\mathbf{T}^{-1}$.

Let $\mathbf{f} = \{\mathbf{f}_1, \mathbf{m}_1, \mathbf{f}_2, \mathbf{m}_2\}$, $\mathbf{f}^{\theta} = \{\mathbf{f}_1, \mathbf{m}^{\theta}_1, \mathbf{f}_2, \mathbf{m}^{\theta}_2\}$, where $\mathbf{f}_j = \{f_{1j}, f_{2j}, f_{3j}\}$, $\mathbf{m}_j = \{m_{1j}, m_{2j}, m_{3j}\}$ and $\mathbf{m}^{\theta}_j = \{m^{\theta}_{1j}, m^{\theta}_{2j}, m^{\theta}_{3j}\}$ (j = 1, 2), denote the internal nodal force vectors corresponding to the variation of the explicit and implicit nodal parameters, $\delta\mathbf{q}$ and, $\delta\mathbf{q}^{\theta}$, respectively. Using the contragradient law [5] and Eq. (7), the relation between $\mathbf{f}$ and, $\mathbf{f}^{\theta}$ may be given by

$$\mathbf{f} = \mathbf{T}^{T}_{\theta\phi}\mathbf{f}^{\theta}. \tag{10}$$

Kinematics of beam element

The deformations of the beam element are described in the current element coordinate system. From the kinematic assumptions made in this paper, the deformations of the beam element may be determined by the displacements of the centroid axis of the beam element, orientation of the cross section (element cross section coordinates), and the out-of-plane warping of the cross section [3]. Let Q (Fig. 1) be an arbitrary point in the beam element, and P be the point corresponding to Q on the centroid axis. The position vector of point Q in the undeformed and deformed configurations may be expressed as

$$\bar{\mathbf{r}} = x\mathbf{e}_1 + y\mathbf{e}_2 + z\mathbf{e}_3, \tag{11}$$

and

$$\mathbf{r} = x_c(s)\mathbf{e}_1 + v(s)\mathbf{e}_2 + w(s)\mathbf{e}_3 + y\mathbf{e}_2^s + z\mathbf{e}_3^s + \theta_{1,s}\omega\mathbf{e}_1^s, \tag{12}$$

where $x_c(s)$, $v(s)$ and $w(s)$ are the x_1, x_2 and x_3 coordinates of point P, respectively, s is the arc length of the deformed centroid axis measured from node 1 to point P. $x_c(s)$ may be expressed by

$$x_c(s) = u_{11} + \int_0^s \cos\theta_n ds, \tag{13}$$

where u_{11} is the displacement of node 1 in the x_1 direction, and $\cos\theta_n$ is defined in Eq. (4).

Here, $v(s)$ and $w(s)$ in Eq. (12) are assumed to be the Hermitian polynomials of s, and $\theta_1(s)$ in Eq. (12) is assumed to be linear polynomials of s, and may be given by

$$\begin{aligned} v(s) &= \{N_1, N_2, N_3, N_4\}^t \{u_{21}, \theta_{31}, u_{22}, \theta_{32}\} = \mathbf{N}_b^t \mathbf{u}_b, \\ w(s) &= \{N_1, -N_2, N_3 -, N_4\}^t \{u_{31}, \theta_{21}, u_{32}, \theta_{22}\} = \mathbf{N}_c^t \mathbf{u}_c, \\ \theta_1(s) &= \{N_5, N_6\}^t \{\theta_{11}, \theta_{12}\} = \mathbf{N}_d^t \mathbf{u}_d, \end{aligned} \tag{14}$$

$$\begin{aligned} N_1 &= \frac{1}{4}(1-\xi)^2(2+\xi), & N_2 &= \frac{S}{8}(1-\xi^2)(1-\xi), \\ N_3 &= \frac{1}{4}(1+\xi)^2(2-\xi), & N_4 &= \frac{S}{8}(-1+\xi^2)(1+\xi), \\ N_5 &= \frac{1}{2}(1-\xi), & N_6 &= \frac{1}{2}(1+\xi), \end{aligned} \tag{15}$$

$$\xi = -1 + \frac{2s}{S}, \tag{16}$$

where S is the arc length of the centroid axis of the beam element and may be expressed by

$$S = 2\ell \Big/ \int_{-1}^{1} \cos\theta_n d\xi, \tag{17}$$

where ℓ is the chord length of the centroid axis of the beam element, and $\cos\theta_n$ is given in Eq. (4).

The way to determine the current element cross section

coordinates at both ends, element coordinates, and element implicit nodal parameters corresponding to displacement increments is given in [2, 3].

If x, y, and z in Eq. (11) are regarded as the Lagrangian coordinates, the Green strains ε_{11}, ε_{12}, and ε_{13} are given by

$$\varepsilon_{11} = \frac{1}{2}\left[\left(\frac{\partial \mathbf{r}}{\partial x}\right)^t \left(\frac{\partial \mathbf{r}}{\partial x}\right) - 1\right],$$
$$\varepsilon_{12} = \frac{1}{2}\left(\frac{\partial \mathbf{r}}{\partial x}\right)^t \left(\frac{\partial \mathbf{r}}{\partial y}\right),$$
$$\varepsilon_{13} = \frac{1}{2}\left(\frac{\partial \mathbf{r}}{\partial x}\right)^t \left(\frac{\partial \mathbf{r}}{\partial z}\right). \tag{18}$$

Substituting Eqs. (4), (5), (12), and (13) into Eq. (18), ε_{11}, ε_{12}, and ε_{13} can be calculated.

Element nodal force vector

The element nodal force vector $\mathbf{f}^\theta$ (Eq. (10)) corresponding to the implicit nodal parameters are obtained from the d'Alembert principle and the virtual work principle. For convenience, the implicit nodal parameters are divided into four generalized nodal displacement vectors $\mathbf{u}_i$ $(i = a,b,c,d)$, where

$$\mathbf{u}_a = \{u_{11}, u_{12}\}, \tag{19}$$

and $\mathbf{u}_b$, $\mathbf{u}_c$, and $\mathbf{u}_d$ are defined in Eq. (14)..

The generalized force vectors corresponding to $\delta\mathbf{u}_i$, the variation of $\mathbf{u}_i$ $(i = a,b,c,d)$ are

$$\mathbf{f}_a = \mathbf{f}_a^d + \mathbf{f}_a^i = \{f_{11}, f_{12}\},$$
$$\mathbf{f}_b = \mathbf{f}_b^d + \mathbf{f}_b^i = \{f_{21}, m_{31}^\theta, f_{22}, m_{32}^\theta\},$$
$$\mathbf{f}_c = \mathbf{f}_c^d + \mathbf{f}_c^i = \{f_{31}, m_{21}^\theta, f_{32}, m_{22}^\theta\},$$
$$\mathbf{f}_d = \mathbf{f}_d^d + \mathbf{f}_d^i = \{m_{11}^\theta, m_{12}^\theta\}, \tag{20}$$

where $\mathbf{f}_j^d$ and $\mathbf{f}_j^i$ $(j = a,b,c,d)$ are the deformation nodal force vector and the inertia nodal force vector, respectively.

The virtual work principle requires that

$$\delta \mathbf{u}_a^t \mathbf{f}_a + \delta \mathbf{u}_b^t \mathbf{f}_b + \delta \mathbf{u}_c^t \mathbf{f}_c + \delta \mathbf{u}_d^t \mathbf{f}_d = \int_{\overline{V}} (\sigma_{11}\delta\varepsilon_{11} + 2\sigma_{12}\delta\varepsilon_{12} + 2\sigma_{13}\delta\varepsilon_{13} + \rho\delta\mathbf{r}^{\mathrm{T}}\ddot{\mathbf{r}}) d\overline{V}, \tag{21}$$

where $\sigma_{11} = E\varepsilon_{11}$, $\sigma_{12} = 2G\varepsilon_{12}$ and $\sigma_{13} = 2G\varepsilon_{12}$, where E is the Young's modulus and G is shear modulus. ρ is the density, and $\overline{V}$ is the volume of the undeformed beam.

If the element size is properly chosen, the values of the nodal parameters (displacements and rotations) of the element defined in the current element coordinate system, which are the total deformational displacements and rotations, may always be much smaller than unity. Thus only the first order terms of nodal parameters are retained in deformation nodal forces. However, in order to include the effect of axial force on the lateral forces, a second order term of nodal parameters is retained. Because the values of the nodal parameters of the element may always be much smaller than unity, it is reasonable to assume that the coupling between the nodal parameters and their time derivatives are negligible. Thus only zeroth order terms of nodal parameters are retained in inertia nodal forces.

From Eqs. (4), (5), and (12)-(21), the deformation nodal forces and the inertia nodal forces may be expressed as

$$\mathbf{f}_a^d = \frac{AE(S-L)}{L}\{-1,1\}, \qquad \mathbf{f}_b^d = (\mathbf{k}_b + \mathbf{k}_{gb})\mathbf{u}_b, \tag{22, 23}$$

$$\mathbf{f}_c^d = (\mathbf{k}_b + \mathbf{k}_{gc})\mathbf{u}_c, \qquad \mathbf{f}_d^d = \frac{GJ(\theta_{12} - \theta_{11})}{L}\{-1,1\}, \tag{24, 25}$$

$$\mathbf{f}_a^i = \mathbf{m}_a \ddot{\mathbf{u}}_a, \tag{26}$$

$$\mathbf{f}_b^i = (\mathbf{m}_{bt} + \mathbf{m}_{br})\ddot{\mathbf{u}}_b - 2\rho I_z \int \mathbf{N}_b' \dot{\theta}_1 \dot{\theta}_2 ds, \tag{27}$$

$$\mathbf{f}_c^i = (\mathbf{m}_{ct} + \mathbf{m}_{cr})\ddot{\mathbf{u}}_c - 2\rho I_y \int \mathbf{N}_c' \dot{\theta}_1 \dot{\theta}_3 ds, \tag{28}$$

$$\mathbf{f}_d^i = \mathbf{m}_d \ddot{\mathbf{u}}_d - \rho(I_y - I_z)\int \mathbf{N}_d \dot{\theta}_2 \dot{\theta}_3 ds, \tag{29}$$

where A is the cross section area, L is the initial length of the beam element, $\mathbf{k}_i$ and $\mathbf{k}_{gi}$ $(i = b,c)$ are bending and geometric stiffness matrices of conventional beam element [5,6], and J is the torsional constant. ρ is the density, I_y and I_z are the moment of inertia of the beam cross section about the x_2^s and x_3^s axes respectively. $\mathbf{m}_a$ is the consistent mass matrix of bar element for axial translation, $\mathbf{m}_{it}$ and $\mathbf{m}_{ir}$ $(i = b,c)$ are the consistent mass matrices of elementary beam element for lateral translation and rotation, respectively, and $\mathbf{m}_d$ is the consistent mass matrix of bar element for axial rotation. These mass matrices can be found in [5, 6]. The underlined terms in Eqs. (27)-(29) are inertia forces induced by the gyroscopic effect, and are called gyroscopic forces.

Element Matrices

The element stiffness matrices and mass matrices may be obtained by differentiating the element nodal force vectors with respect to nodal parameters, and time derivatives of nodal parameters. However, element matrices are used only to obtain predictors and correctors for incremental solutions of nonlinear equations in this study. Thus, approximate element matrices can meet these requirements. The stiffness matrices and mass matrices of elementary beam element given in [5, 6] are also used here.

Equations of motion

The nonlinear equations of motion may be expressed by

$$\mathbf{F}^R = \mathbf{F}^I + \mathbf{F}^D - \mathbf{P} = 0 \tag{30}$$

where $\mathbf{F}^R$ is the unbalanced force among the inertia nodal force $\mathbf{F}^I$, deformation nodal force $\mathbf{F}^D$, and the external nodal force $\mathbf{P}$. $\mathbf{F}^I$ and $\mathbf{F}^D$ are assembled from the element nodal force vectors in Eq. (10), which are calculated using Eqs. (10) and (22)-(29) first in the current element coordinate system, and then transformed from current element coordinate system to global coordinate system before assemblage using standard procedure.

APPLICATIONS

An incremental iterative method based on the Newmark direct integration method and the Newton-Raphson method is employed here for the solution of the nonlinear dynamic equilibrium equations.

The example considered is a right-angle cantilever beam subjected to an out-of-plane concentrated load as shown in Fig. 3. Four elements are used for discretization. A time step size of $\Delta t = 0.25$ is used. The cantilever undergoes a finite free vibration with combined bending and torsion after the removal of the applied load; the time histories of out-of-plane displacements of the elbow and of the tip are given in Figs. 4 and 5. It is seen that the present results are in excellent agreement with those given in [7] and [8]. However, it should be mentioned that the beam elements used in [7] and [8] are derived using fully nonlinear beam theory and total Lagrangian formulation. Thus, the beam elements used in [7] and [8] are much more complicated than that proposed here.

CONCLUSIONS

A co-rotational finite element formulation for the geometrically nonlinear dynamic analysis of spatial beam with large rotations but small strain is presented. The deformation nodal forces and inertia nodal forces are derived by using the d'Alembert principle and the virtual work principle. The gyroscopic effect are considered here.

The nodal coordinates, displacements, rotations, velocities, accelerations, and the equation of motion of the system are defined in a fixed global set of coordinates. The beam element developed here has two nodes with six degrees of freedom per node. The element nodal forces are conventional forces and moments. All of element deformations and element equations are defined in terms of element coordinates which are constructed at the current configuration of the beam element. The element deformations are determined by the rotation of element cross section coordinates, which are rigidly tied to element cross section, relative to the element coordinate system. In conjunction with the co-rotational formulation, the higher order terms of nodal parameters in element nodal forces are consistently neglected.

An incremental-iterative method based on the Newmark direct integration method and the Newton-Raphson method is employed here for the solution of the nonlinear dynamic equilibrium equations. Numerical examples are presented to demonstrate the accuracy and efficiency of the proposed method

It is believed that the co-rotational formulation for 3-D beam element presented here may represent a valuable engineering tool for the dynamic analysis of spatial beam structures.

ACKNOWLEDGMENT

The research was sponsored by the National Science Council, Republic of China, under contract NSC86-2212-E-009-006.

REFERENCES

1. Hsiao, K.M. and Jang, J.Y., Nonlinear dynamic analysis of elastic frames. *Computers & Structures*, 1991, 33, 769-781.
2. Hsiao, K.M. and Tsay, C.M., A motion process for large displacement analysis of spatial frames. *International Journal of Space Structures*, 1991, 6, 133-139.
3. Hsiao, K.M., Corotational total Lagrangian formulation for three-dimensional beam element. *AIAA Journal*, 1992, 30, 797-804.
4. Goldstein, H., *Classical Mechanics*, Addision-Wesley, Reading, MA,1980.
5. Dawe, D.J., *Matrix and Finite Element Displacement Analysis of Structures*, Oxford Univ. Press, New York, 1984.
6. Hsiao, K.M., A study on the dynamic response of spatial beam structures. NSC 82-0401-E009-081 Report, *National Science Council, Taiwan, Republic of China,*, 1993.
7. Simo, J.C. and Vu-Quoc, L., On the dynamics in space of rods undergoing large motions - A geometrical exact approach, *Computer Methods in Applied Mechanics and Engineering*, 1988, 66, 125-161.
8. Iura, M. and Atluri, S.N., Dynamic analysis of finitely stretched and rotated three-dimensional space-curved beams, *Computers & Structures*, 1988, 29, 875-889.

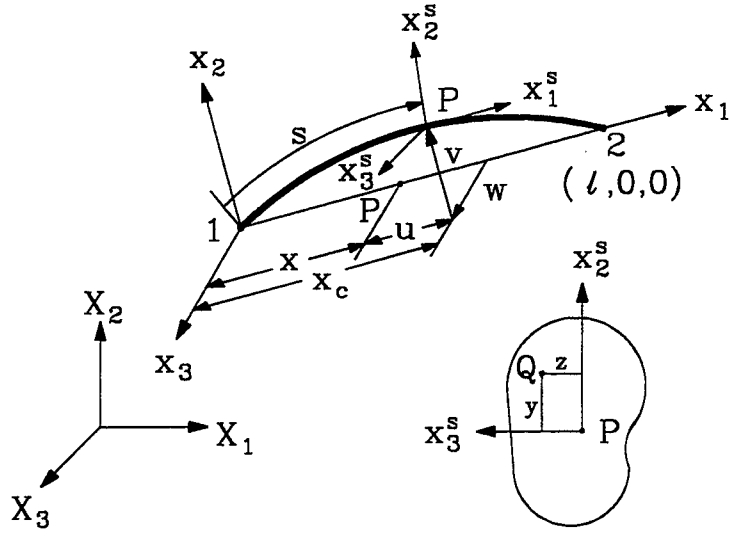

Fig. 1 Coordinate systems.

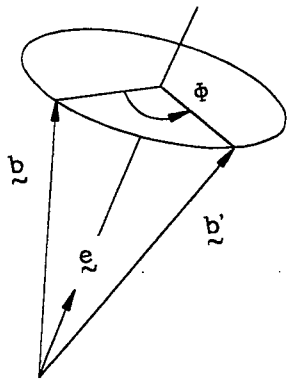

Fig.2 Rotational vecter

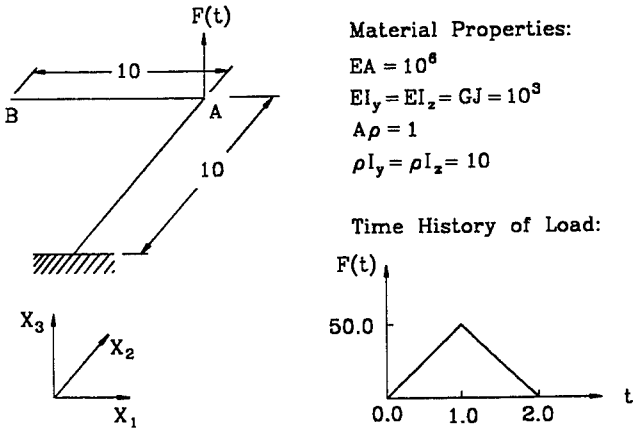

Fig.3 Right-angle Cantilever beam

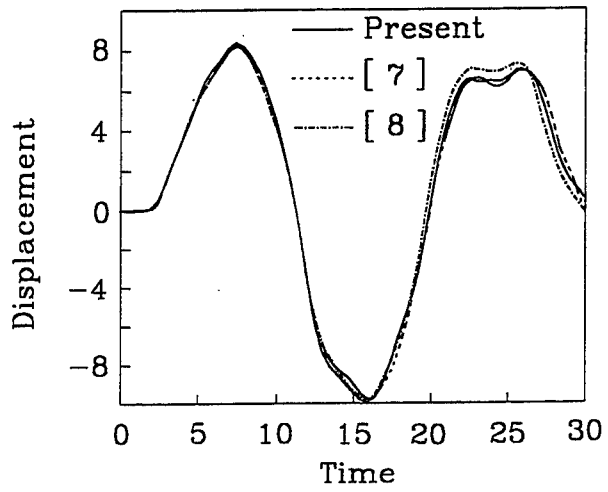

Fig. 4 Displacements in the X_3 direction at point B.

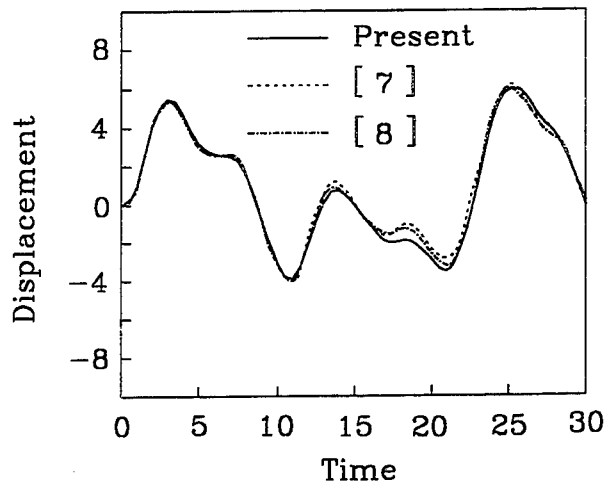

Fig. 5 Displacements in the X_3 direction at point A.

Nonlinear Response of Composite Plates to Harmonic Excitation Using The Finite Element Time Domain Modal Method

Raymond Y. Y. Lee, Yucheng Shi and Chuh Mei
Department of Aerospace Engineering
Old Dominion University, Norfolk, VA 23529-0247

Abstract

A multimode time domain formulation based on the finite element method for large amplitude vibrations of thin composite plates subjected to a combined harmonic excitation and thermal load is presented. By using the modal reduction method, the system equations of motion in physical coordinates are transformed into the linear modal coordinates and the sizes of the system matrices are reduced drastically. The reduced system modal equations can be handled easily with less computational efforts. The frequency-maximum deflection relations of simple harmonic, superharmonic and subharmonic responses are predicted by choosing suitable initial conditions. The procedure for the selection of the initial conditions is also presented. A laminated composite plate is studied in great detail. External loadings considered are harmonic excitations or combined harmonic and thermal loads. The steady state responses of the linear modal coordinates are presented in details at several frequencies. Their phase plots, power spectrums and time domain graphs are given and discussed .

Introduction

The increase use of advanced composites as high performance structural components necessitates accurate prediction methods which reflect their multilayered anisotropic behavior. Thin laminated composite plates subjected to severe harmonic lateral loadings are likely to encounter flexural oscillations having amplitudes of the order a plate thickness. For the prediction of forced vibration response, the multilayered anisotropic behavior, the complex boundary conditions, and the complex loading cases such as the present of the thermal loads make the problem even more difficult. Methods of analysis dealing with large deflections are thus becoming increasingly important.

Whitney and Leissa [1] have formulated the basic governing equations for nonlinear vibrations of heterogeneous anisotropic plates in the sense of von Karman. Based on those equations, a number of classical continuum

approaches exists for the analysis of nonlinear plate behavior. In general, the Galerkin's method is used in the spatial domain, where the plate deflection is expressed in terms of one or more linear vibrational mode shapes; and various techniques in the temporal domain such as the direct numerical integration, harmonic balance, incremental harmonic balance, perturbation, and multiple scales methods, to cite a few, are employed. Excellent collections of classical continuum solutions and reviews on geometrically nonlinear analysis of laminated composite elastic plates are given by Chia [2,3] and Sathyamoothy [4]. The internal resonance of nonlinear systems has been thoroughly investigated using the multiple scales by Nayfeh and Mook [5]. Most recently, Wolfe et al. [6] have reviewed various analytical methods and have obtained experiment data on beams and plates excited sinusoidally or randomly. Most of the classical continuum solutions of composite plates have been limited to single-mode approximation. This is due to the difficulties in obtaining the general Duffing-type multiple-mode equations using the Galerkin's approach especially for arbitrarily (unsymmetrically) laminated composite plates with complex boundary conditions.

The finite element method has proven to be a powerful and versatile approach for structural problems of complex geometries, boundary conditions, and loadings. Reddy [7] has reviewed the application of finite element methods to linear and nonlinear anisotropic composite plate problems. In this paper, the nonlinear steady state periodic responses of thin rectangular arbitrarily laminated composite plates excited sinusoidally with or without the presence of thermal load are presented using the finite element time domain modal method. A rectangular composite plate is studied in detail.

Formulation

The finite element system equations of motion for large amplitude vibrations of a thin laminated composite plate can be expressed as

$$[M]\{\ddot{W}\}+[C]\{\dot{W}\}+([K]-[K_{NT}]+[K1(W)]+[K2(W)])\{W\}=\{P(t)\}+\{P_T\} \tag{1}$$

where [M], [C], [K], $[K_{NT}]$, {P(t)} and $\{P_T\}$ are constant matrices and vectors and represent the system mass, damping, linear stiffness, thermal effort and

loads, respectively; and [K1] and [K2] are the first and second order nonlinear stiffness matrices and depend linearly and quadratically on the unknown structural nodal displacements {W}, respectively. The derivation of the element matrices and load vectors and their explicit expressions are referred to references [8,9].

The system equations of motion presented in eq. (1) are not suitable for direct numerical integration because: a) the nonlinear stiffness matrices [K1] and [K2] are functions of the unknown nodal displacements, and (b) the number of degrees of freedom (DOF) of the system nodal displacements {W} is usually too large. Therefore, eq. (1) has to be transformed into the modal or generalized coordinates of much smaller DOF. Various reduction methods for nonlinear problems have been summarized in an excellent review article by Noor [10]. For nonlinear dynamic problems, the base vectors need updating using the modal methods presented in [10]. In the present formulation, the forced general Duffing-type modal equations will have constant nonlinear modal stiffness matrices, therefore updating of the base vectors is not needed. This is accomplished by a modal transformation and truncation

$$\{W\} = \sum_{r=1}^{n} q_r(t)\{\phi\}^{(r)} = [\Phi]\{q\} \tag{2}$$

where the system mode shapes are the solution from the linear eigen-problem $\omega_r^2[M]\{\phi\}^{(r)} = [K]\{\phi\}^{(r)}$. The nonlinear stiffness matrices [K1] and [K2] in eq. (1) can now be expressed as the sum of the products of modal coordinates and nonlinear modal stiffness matrices as

$$[K1] = \sum_{r=1}^{n} q_r\left[K1(\phi^{(r)})\right]^{(r)} \tag{3}$$

and

$$[K2] = \sum_{r=1}^{n}\sum_{s=1}^{n} q_r q_s\left[K2(\phi^{(r)}\phi^{(s)})\right]^{(rs)} \tag{4}$$

The nonlinear modal stiffness matrices $[K1]^{(r)}$ and $[K2]^{(rs)}$ are assembled from the element nonlinear modal stiffness $[k1]^{(r)}$ and $[k2]^{(rs)}$ as

$$\left([K1]^{(r)},[K2]^{(rs)}\right)=\sum_{\substack{\text{all elements}\\ +\text{ bdy. conds.}}}\left([k1]^{(r)},[k2]^{(rs)}\right) \tag{5}$$

where the element nonlinear modal stiffness matrices are evaluated with known system linear mode $\{\phi\}^r$. Thus, the nonlinear modal stiffness matrices $[K1]^{(r)}$ and $[K2]^{(rs)}$ are constant matrices. Equation (1) is thus transformed to the forced general Duffing-type modal equations as

$$[\overline{M}]\{\ddot{q}\}+[\overline{C}]\{\dot{q}\}+\left([\overline{K}]+[K1_q]+[K2_{qq}]\right)\{q\}=\{F(t)\} \tag{6}$$

where the modal mass, damping, and linear stiffness matrices are

$$\left([\overline{M}],[\overline{C}],[\overline{K}]\right)=[\Phi]^T\left([M],[C],[K]-[K_{NT}]\right)[\Phi] \tag{7}$$

and the quadratic and cubic terms in modal coordinates and the modal force vector are

$$[K1_q]\{q\}=[\Phi]^T\left(\sum_{r=1}^{n}q_r[K1]^{(r)}\right)[\Phi]\{q\} \tag{8}$$

$$[K2_{qq}]\{q\}=[\Phi]^T\left(\sum_{r=1}^{n}\sum_{s=1}^{n}q_rq_s[K2]^{(rs)}\right)[\Phi]\{q\} \tag{9}$$

$$\{F\}=[\Phi]^T\left(\{P(t)\}+\{P_T\}\right) \tag{10}$$

All modal matrices in eq. (6) are constant matrices. With given initial conditions, the response of modal coordinates $\{q\}$ can be determined from eq. (6) with any direct numerical integration scheme such as the Runge-Kutta or Newmark-β method. Therefore, no updating of the vibration modes is needed. The following is the description of the selection of the initial conditions for periodic motions.

With the input of suitable initial conditions, three types of solutions, periodic or nearly simple harmonic, superharmonic and subharmonic solutions, can be obtained. The selection of each type solution is based on the solution of the 1-

DOF Duffing equation obtained by using the modal reduction method described earlier. For example, the system equations of motion of a symmetric composite plate can be reduced to 1-DOF model (Note: the quadratic term is gone because the plate is symmetric) as

$$M_r\ddot{q}_r + C_r\dot{q}_r + K_r q_r + K2_r q_r^3 = F_r \sin(\omega t) \qquad (11)$$

where M_r, C_r, K_r, $K2_r$ and F_r are scalar constants and represent the modal mass, damping, stiffness and force; ω is the forcing frequency and the subscript "r" denotes the linear modal number. The solution of eq. (11) can be assumed as $q_r = A_1\cos(\omega t) + A_3\cos(3\omega t)$ for the simple harmonic and superharmonic solutions, then two sets of A_1 and A_3 can be obtained by the substituting of the assumed q_r into eq.(11). One set is for the simple harmonic solution and the other set is for the superharmonic solution. Based on these solutions, the initial displacement of the r-th modal coordinate in eq. (6) is chosen as A_1+A_3. The initial velocities and all other initial displacements are zero. Similarly, it is assumed that $q_r = A_1\cos(\omega t) + A_{1/3}\cos(\omega t/3)$ for the subharmonic solution. Then, all those initial conditions can be found by repeating the procedure just described.

Results and Discussions

A simply supported eight-layer symmetrically laminated (0/45/-45/90)s composite plate is studied in great details. The plate is of $15 \times 12 \times 0.048$ in. ($38.1 \times 30.5 \times 0.122$ cm). The inplane boundary conditions are immovable, i.e. u=v=0 on all four edges. The graphite-epoxy material properties are : E_1=22.5 Msi (155 GPa), E_2 =1.17 (8.07), G_{12} = 0.66 (4.55), ν_{12} = 0.22 and $\rho = 0.1458 \times 10^{-3}$ lb-s^2/in^4. (1550 kg/m^3). The C^1 conforming rectangular plate element is used in the finite element model and the plate is modeled with 12×12 (144 elements) mesh. The element has a total of 24 DOF (16 bending and 8 membrane). The lowest six natural frequencies (ω_r, r=1,6) and their corresponding mode shapes are : ω_1 = 55.46 Hz for (1,1) mode, ω_2 = 125.736 Hz for (2,1) mode, ω_3 = 151.951 Hz for (1,2) mode, ω_4 = 216.475 Hz for (2,2) mode, ω_5 =250.585 Hz for (1,3) mode and ω_6 = 310.774 Hz for (3,1) mode.

Two load cases considered are uniformly distributed harmonic excitation over the plate with and without the presence of temperature. A constant modal damping factor, $\varsigma_r = C_r/(2M_r\,\omega_r)$, of 0.02 and a four-mode solution are used in the examples (Only the (1,1), (2,2), (1,3) and (3,1) modes are considered because the uniformly distributed excitation cannot induce any response of the (1,2) and (2,1) modes, see Table 7 of [11]).

Harmonic Excitations

A uniformly distributed pressure load of the form $p(x,y,t) = p_o \sin\omega t$ is considered for the forced vibration problem. The force intensity is maintained at $p_o = 0.00438$ psi (30.2 Pa), however, the forcing frequency ω is varying in a wide range from 0 to 4.5 times of the lowest linear natural frequency ω_1. The results are shown in Figs. 1 to 4, where the designations for the total responses are indicated in Fig. 1, while the time-histories, phase plots and power spectra are given in Figs. 2 to 4. To make clear the behavior of the vibration response at particular frequency, each modal coordinate is depicted for understanding the simple harmonic, superharmonic and subharmonic response of the nonlinear system.

Figures 2a-c correspond to the responses of the three forcing frequencies at 0.6, 2.4 and 3.8 times of ω_1 labeled as (1) to (3) in Fig. 1. It can be seen that the total response of the centre of the plate is dominated by the first mode (It should be noted that the centre of the plate has zero contribution from the (2,2) mode). The frequency responses of the four modal coordinates are composed of superharmonic frequency components of order 2, 3, 5 .. etc. , as well as the input driving force frequency. At the frequency of the point (3) in Figs. 2c and 2d, the corresponding time histories of the second, third and fourth modal coordinates are unsymmetric as that of the first modal coordinate is symmetric. Hence, the plate is vibrating with a non-zero equilibrium position due to the unsymmetric responses of the second, third and fourth modes.

In Figs. 3a and 3b, which correspond to the responses of two points (4) and (5) at $\omega = 2.4\ \omega_1$ and $4.2\ \omega_1$ in Fig. 1, the total response of the centre of the plate is almost pure simple harmonic at that particular frequency range.

In Fig. 4a, which corresponds to the response of the point (6) at $\omega = 3.8\ \omega_1$ in Fig 1, the centre of the plate is mainly composed of subharmonic response of order 1/3. In the time histories of the four modal coordinates of Fig. 4b, it can be seen that the subharmonic component in the total response is contributed by

the (1,1) modal coordinate, and the responses of the higher modal coordinates are pesudo harmonic.

Combined Harmonic and Thermal Loads

In addition to the uniform pressure $p_o \sin\omega t$, a steady state temperature change of $2.9T_{cr}$ is also applied to the composite plate (where the buckling temperature T_{cr} =13.79 °F). The forcing frequency is taken as $\omega = 1.45\omega_1$ and it is kept at that constant frequency of excitation, however, three pressure intensities at p_o = 6, 10 and 14 × 10^{-3} psi are considered. The responses are shown in Figs. 5a-c. The results are shown after the transient response being damped out, this is demonstrated by the quasi-steady state time histories in Figs. 5a and 5c.

When the pressure load is small at 0.006 psi (41.3 Pa), the plate exhibits small oscillations about one of the thermally buckled positions (W_{max}/h =1.0237) shown in Fig. 5a. With increase of the pressure loading, the amplitude of vibration increases. Fig. 5b shows the so-called snap-through or oil-canning phenomenon at p_o = 0.010 psi (68.9 Pa), the plate behavior is chaotic and has two potential wells. With the further increase of the pressure loading, the plate exhibits large amplitude oscillations through the two buckled positions as shown in Fig. 5c at p_o = 0.014 psi (96.4 Pa). The plate motion is periodic at low and high pressure loads, however, the plate response composes of superharmonic frequency components of order 2 and 3 at the low pressure and of order 3 and 5 at the high pressure as shown in the PSD plots.

The substance of the transition of the three distinct plate behaviors, from the small oscillations into the chaotic motion then into the large amplitude vibrations with the increase of forcing intensity, is shown in Fig. 6. In the low pressure range, the plate could also vibrate about the another equally possible bifurcation buckled position shown with dotted lines.

Conclusion

Based on the finite element method, a multimode time-domain formulation for nonlinear forced vibration of composite plates is presented. The main advantage of this method is that the system matrix equation derived from the FEM can be transformed into a set of general type Duffing equations with constant system matrices and much smaller DOF. The selections of initial

conditions for the subharmonic, simple harmonic and superharmonic responses are presented. Through detailed descriptions, the frequency response characteristics, phase plots, time histories and the power spectrums have been illustrated for the three types of responses. The responses of a thermally buckled composite plate under harmonic excitation with fixed forcing frequency and various amplitudes are also obtained. Snap-through motion is observed at moderate pressure loads.

References

1. J. M. Whitney and A. W. Leissa 1969 Journal of Applied Mechanics 36, 261-266. Analysis of heterogeneous anisotropic plates.
2. C. Y. Chia 1988 Applied Mechanics Review 41, 439-451. Geometrically nonlinear behavior of composite plate: A review.
3. C. Y. Chia 1980 Nonlinear Analysis of Plates, McGraw-Hill, New York.
4. M. Sathyamoorthy 1987 Applied Mechanics Review 40, 1553-1561. Nonlinear vibration analysis of plates: A review and survey of current developments.
5. A. H. Nayfeh and D. T. Mook 1979 Nonlinear Oscillations, John Wiley, New York.
6. H. F. Wolfe, C. A. Shroyer, D. L. Brown and L. W. Simmons 1995 Technical Report WL-TR-96-3057, Wright Laboratory, Wright Patterson AFB, Ohio. An experimental investigation of nonlinear behavior of beams and plates excited to high levels of dynamic response.
7. J. N. Reddy 1985 Shock and Vibration Digest 17, 3-8. A review of the literature on finite element modeling of laminated composite plates.
8. Y. Shi and C. Mei 1996 Proceedings of the 37th AIAA / ASME / ASCE / AHS / ASC Structures, Structural Dynamics, and Material Conference, Salt Lake City, UT, 1355-1362. Coexisting thermal postbuckling of composite plates with initial imperfections using finite element modal method.
9. C. K. Chiang, C. Mei and C. E. Gray, Jr. 1991 Journal of Vibration and Acoustics 113, 309-315. Finite element large-amplitude free and forced vibrations of rectangular thin composite plates.
10. A. K. Noor 1981 Composites and Structures, 13, 31-44. Recent advances in reduction methods for nonlinear problems.
11. Y. Y. Lee, Y. Shi and C. Mei 1997 Proceedings of the 6th International Conference on Recent Advances in Structural Dynamics, University of Southampton, UK. A finite element time domain multi-mode method for large amplitude free vibration of composite plates.

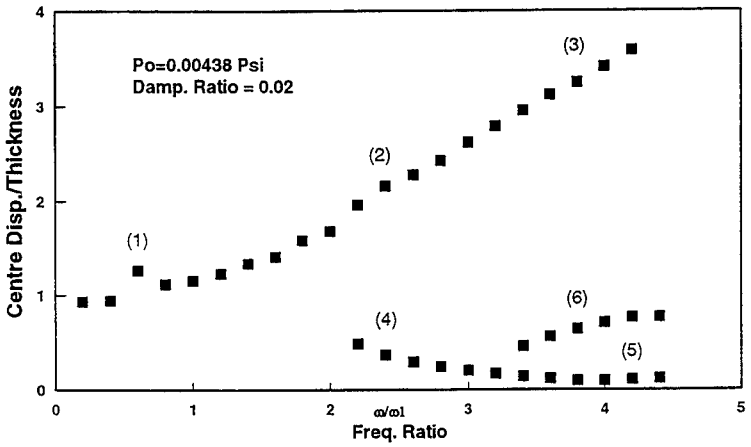

Figure 1. Frequency response of the simply supported (0/45/-45/90)s rectangular plate

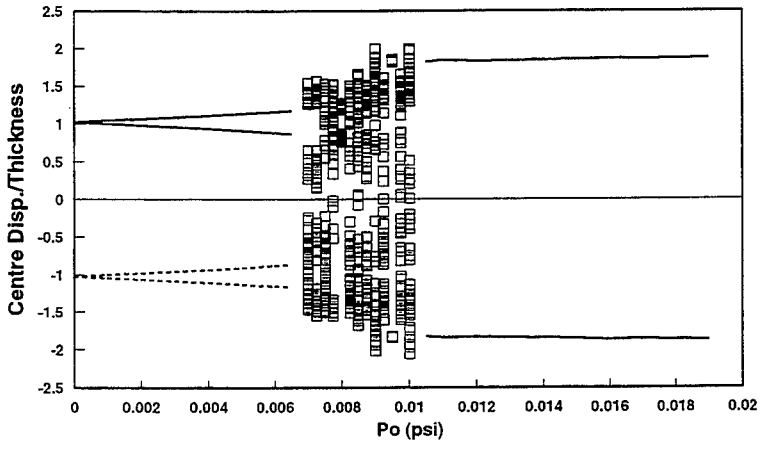

Figure 6. Plate centre response vs force amplitude at $\omega = 1.45\omega_1$ and T = 2.9 Tcr

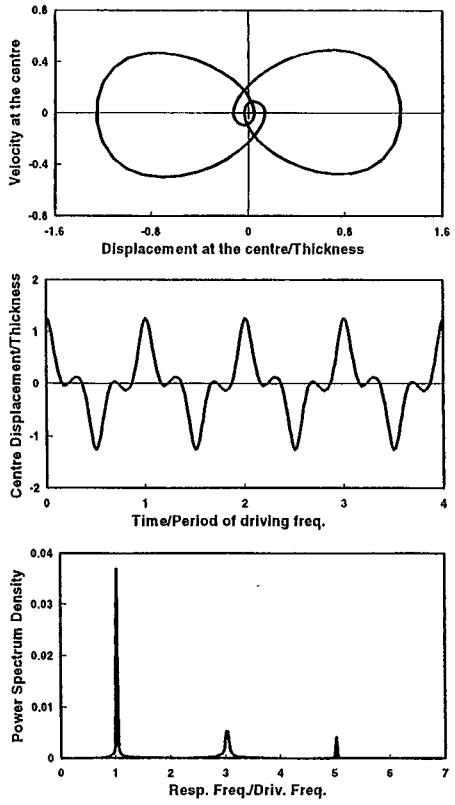

Figure 2a. Phase plot, Time history and PSD at $\omega = 0.6\omega_1$ Point (1)

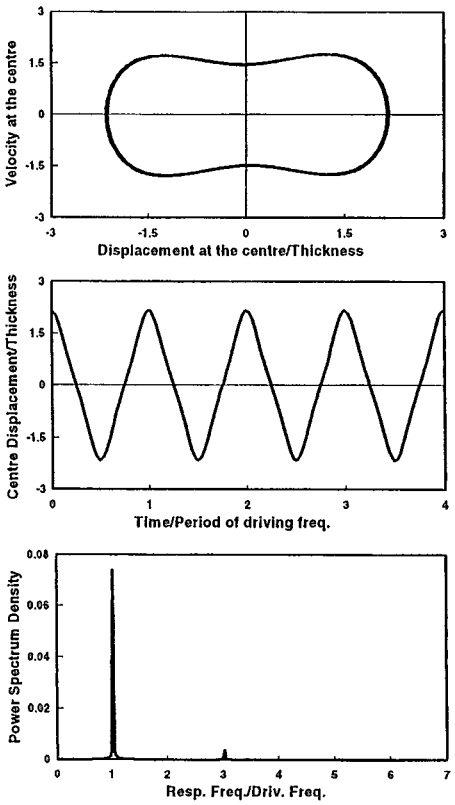

Figure 2b. Phase plot, Time history and PSD at $\omega = 2.4\omega_1$ Point (2)

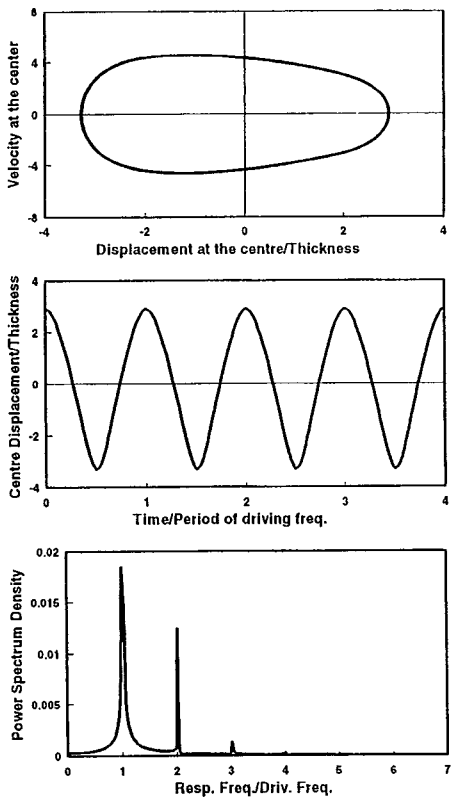

Figure 2c. Phase plot, Time history and PSD at $\omega = 3.8\omega_1$ Point (3)

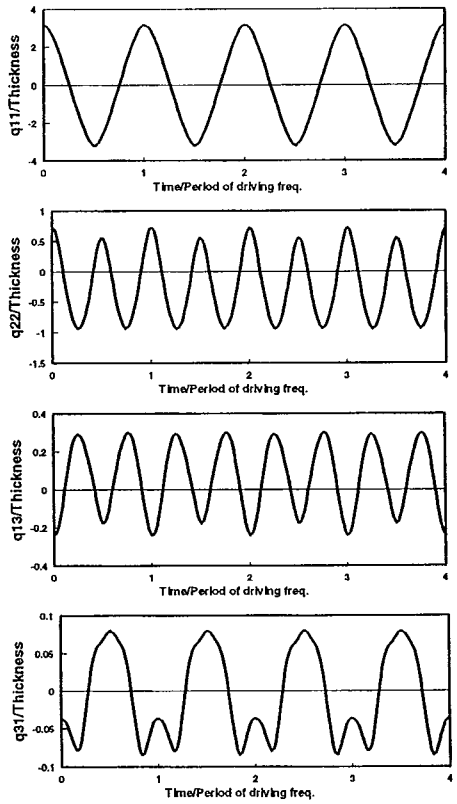

Figure 2d. Modal time histories at $\omega = 3.8\omega_1$ Point (3)

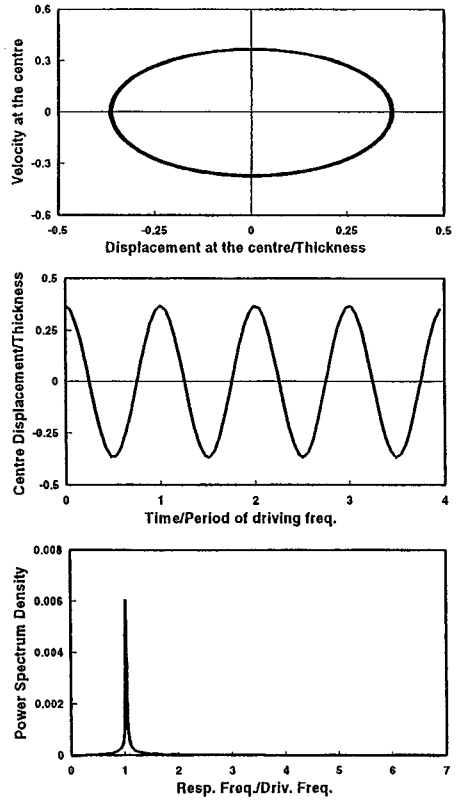

Figure 3a. Phase plot, Time history and PSD at $\omega = 2.4\omega_1$ Point (4)

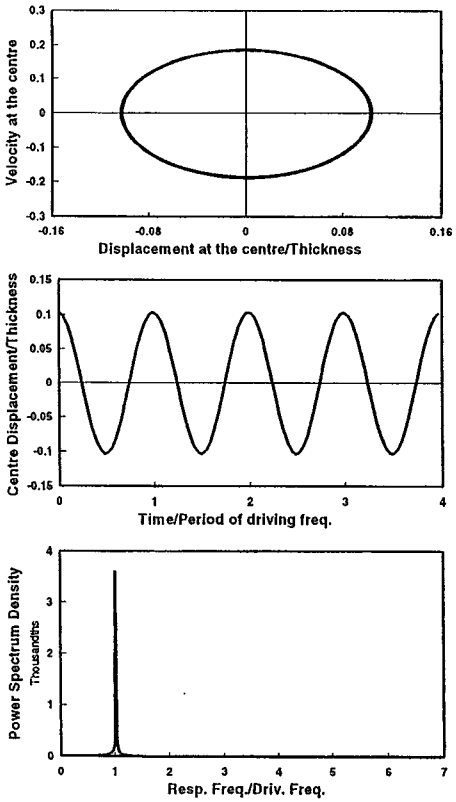

Figure 3b. Phase plot, Time history and PSD at $\omega = 4.2\omega_1$ Point (5)

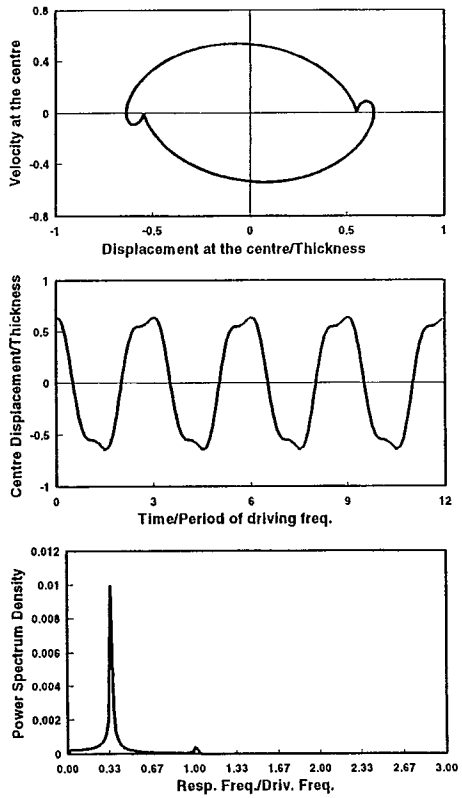

Figure 4a. Phase plot, Time history and PSD at $\omega = 3.8\omega_1$ Point (6)

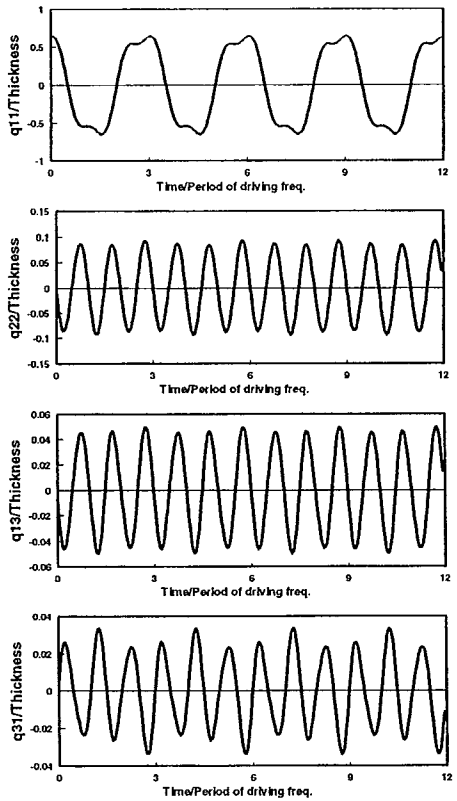

Figure 4b. Modal time histories at $\omega = 3.8\omega_1$ Point (6)

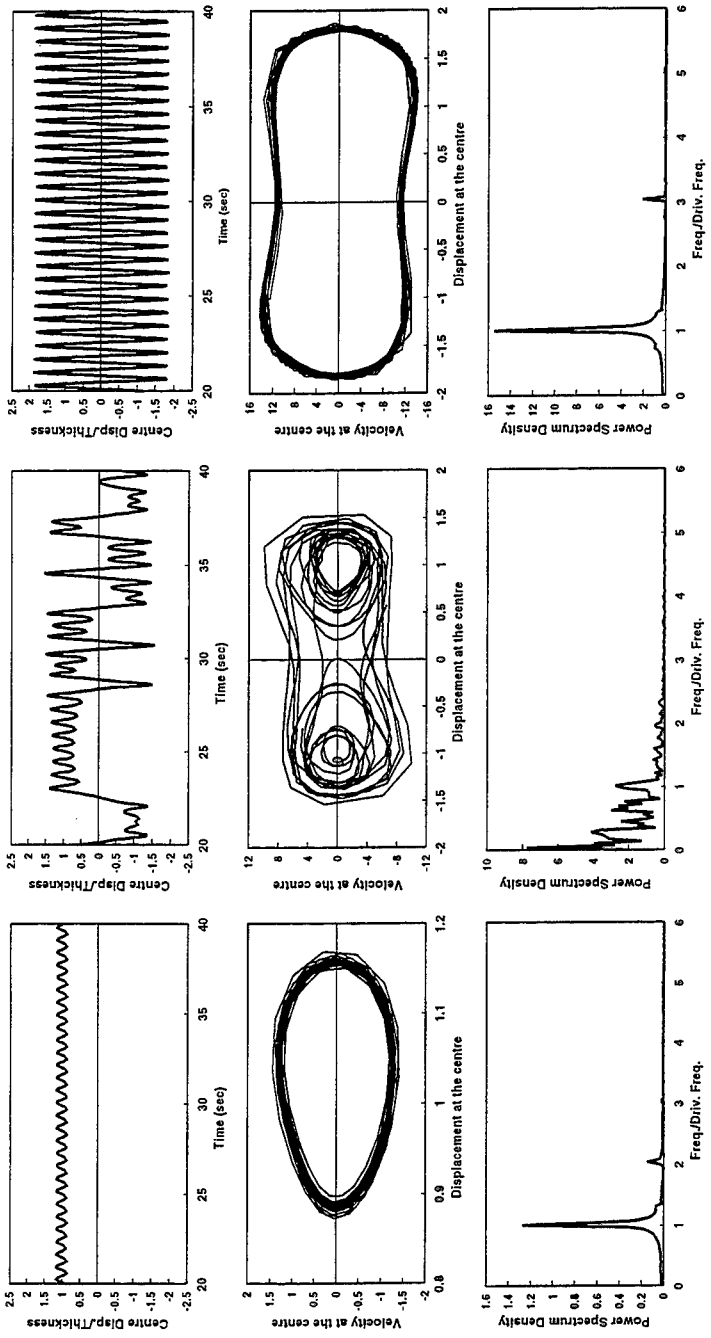

Figure 5a-c. Time history, phase plot and PSD at $\omega = 1.45\omega_1$ and $T = 2.9\ T_{cr}$

GEOMETRICALLY NONLINEAR RESPONSE ANALYSIS OF LAMINATED COMPOSITE PLATES AND SHELLS

C.W.S. To† and **B. Wang‡**
Department of Mechanical Engineering
University of Nebraska
255 Walter Scott Engineering Center
Lincoln, Nebraska 68588-0656
U.S.A.

E-mail: cwsto@unlinfo.unl.edu

Abstract

The investigation reported in this presentation is concerned with the prediction of geometrically large nonlinear responses of laminated composite plate and shell structures under dynamic loads by employing the hybrid strain based flat triangular laminated composite shell finite elements. Large deformation of finite strain and finite rotation are emphasized. The finite element has eighteen degrees of freedom which encompass the important drilling degree of freedom at every node. It is hinged on the first order shear deformable lamination theory. Various typical laminated composite plate and shell structures under dynamic loads have been studied and representative ones are presented and discussed in this paper. Shear locking has not appeared and there is no zero energy mode detected in the problems studied. It is very accurate and efficient. Consequently, it is relatively much more attractive than other elements currently available in the literature for large scale nonlinear dynamic response analysis of laminated composite plate and shell structures.

---

† Professor and corresponding author
‡ Research Associate

1. INTRODUCTION

Many modern structures such as nuclear reactor containment installations, naval and aerospace structures, and their components, must be designed to withstand a variety of intensive dynamic disturbances. Because of their many attractive features over isotropic materials more and more structures or components in the aforementioned systems are made of laminated composite materials. The investigation reported in this paper is therefore concerned with the prediction of geometrically large nonlinear responses of laminated composite plate and shell structures, of complicated geometries, under transient excitations. With complicated geometries analytical solution is impossible and therefore a versatile numerical method, the finite element method has been employed. A hybrid strain based flat triangular laminated composite shell finite element has been developed by the authors [1,2] for the nonlinear analysis of plate and shell structures under static loadings. The present investigation is an extension of [1,2] to cases with the aforementioned dynamic forces. Among various attractive features of the derived element stiffness and consistent element mass matrices five are worthy of listing here for completeness. These are: (a) their ability to deal with large nonlinear elastic response of finite strain and finite rotation, (b) the fact that they are in explicit expressions and therefore no numerical integration is necessary, (c) the obtained results of a relatively comprehensive tests [2, 3] show that the element is free from shear locking, (d) the element gives correctly six rigid body modes, and (e) the finite element has three nodes and eighteen degrees of freedom (dof) which encompass the important drilling degree of freedom (ddof) at every node. It is based on the first order shear deformable lamination theory. It is a generalization of the low-order flat triangular shell element for isotropic materials developed earlier by Liu and To [4].

It is noted that one of the earlier work that employed triangular shell element is due to Noor and Mathers [5]. In the latter a mixed type triangular element was proposed. The element has six nodes, and 78 dof. It was based on the shallow shell theory and was shear deformable. Recently, Lin *et al.* [6] developed a finite element procedure to analyze composite bridges. The finite element procedure was based on small elasto-plastic strains and updated Lagrangian formulation. The element used was flat and constructed by the superposition of a discrete Kirchhoff bending element and a linear strain triangular membrane element. It has six nodes. There are three translational and three rotational dof at its corner nodes and three translational dof at mid-side nodes. In 1994 a flat triangular shell element was presented for static nonlinear analysis by Madenci and Barut [7]. It is based on the so-called free formulation concept for analyzing geometrically nonlinear thin composite shells. A corotation form of the updated Lagrangian formulation is utilized. The theoretical basis was on the geometrically nonlinear Kirchhoff plate theory without considering the effects of transverse shear deformation. The element

is of displacement type. It has three nodes and six dof for each node. While such formulation has some advantageous features computationally the element is relatively less efficient because (a) the linear element stiffness matrix consists of a basic and a higher-order stiffness matrices in the sense of Bergan and Nygard [8] for isotropic materials, and (b) the important effects of transverse shear deformation in the plate component of of this element has been disregarded. A more recent contribution on triangular elements is made by Zhu [9]. The natural approach is used to construct a curved triangular shell element for static analysis of geometrically nonlinear sandwich and composite shell structures. The element has six nodes. There are six dof at each corner node and three dof at each mid-side node. Updated Lagrangian description was adopted in the procedure. In the element formulation the transverse shear deformation was considered by assuming constant transverse shear stress distribution.

In the next section the formulation of element stiffness matrices is outlined. Section 3 deals with the derivation of element matrices. Section 4 is concerned with the application of the derived elements to three example problems of plate and shell structures. The concluding remarks are included in Section 5.

2. FORMULATION OF ELEMENT STIFFNESS MATRICES

Finite element formulation for the derivation of a family of simple three-node, six dof per node, hybrid strain based laminated composite triangular shell finite elements for large scale geometrically nonlinear analysis is briefly outlined in this section. Large deflection of finite strains and finite rotations are included. The first order shear deformation theory and the degenerated three dimensional solid concept are adopted. In particular, element matrices for one member of the family are derived explicitly with the symbolic computer algebra package MACSYMA. To minimize the algebraic manipulation involved in the derivation, updated Lagrangian description is employed in the incremental formulation of the finite element procedure. In essence, the present formulation is an extension of the work by Liu and To [4] for isotropic materials to multi-layer laminated composite shells. Therefore, in the development the present approach follows closely that of the last reference.

2.1 Incremental variational principle

The Hellinger-Reissner functional π_{HR} can be written as

$$\pi_{HR} = \int_{V_e} \left[(e^{\varepsilon})^T C e^{u} - \frac{1}{2}(e^{\varepsilon})^T C (e^{\varepsilon}) \right] dV - W \qquad (1)$$

where,

e^{ε} is the independently assumed strain field;
e^{u} is the strain due to displacement;
C is the material stiffness matrix or elasticity matrix;
W is the work done by external forces,

and the superscripts ε and u indicate that the quantities are from independently assumed strain field and displacement field, respectively. For geometrically nonlinear analysis with incremental formulation and updated Lagrangian description, the static and kinematic variables in current equilibrium configuration at time t are assumed to be known quantities and the objective is to determine their values in the unknown subsequent equilibrium configuration at time t+Δt. For a time increment Δt, that is from time t to (t+Δt), one has

$$\Delta\pi_{HR} = \Delta\pi_{HR}(\Delta u, \Delta e^{\varepsilon}) = \pi_{HR}(t+\Delta t) - \pi_{HR}(t) , \tag{2}$$

or, with reference to equation (1),

$$\Delta\pi_{HR} = \int_{V_e} [(e^{\varepsilon})^T C(\Delta e^{u}) + (\Delta e^{\varepsilon})^T C(\Delta e^{u}) - \frac{1}{2}(\Delta e^{\varepsilon})^T C(\Delta e^{\varepsilon}) - (\Delta e^{\varepsilon})^T C(e^{\varepsilon} - e^{u})] \, dV - \Delta W . \tag{3}$$

where,

Δu is the vector of incremental displacement;
Δe^{ε} is the vector of independently assumed incremental updated Green strains;
Δe^{u} is the vector of incremental updated Green 'geometric' strains or incremental Washizu strains;
ΔW is the work-equivalent term corresponding to prescribed body forces and surface tractions in configuration $\mathbb{C}^{t+\Delta t}$.

Equation (3) is the incremental form of Hellinger-Reissner variational principle. For updated Lagrangian description, the integral is evaluated at the current configuration $\mathbb{C}^{t}$. In the equation, the term

$$\int_{V_e} (\Delta e^{\varepsilon})^T C(e^{\varepsilon} - e^{u}) \, dV$$

is the so-called compatibility-mismatch. Numerical results of Saleeb *et al.* [10] showed that though totally discarding the term resulted in convergence difficulties, while including the term in only the first iteration of every load step yielded essentially the same results as those having the term under all circumstances. However, Liu and To [4] reported no difficulties for convergence when the term was ignored. In the current study, this term is also disregarded. Then equation (3) can be recasted as

$$\Delta\pi_{HR} = \int_{V_e} [\, \sigma^T \Delta e^u + (\Delta e^\varepsilon)^T C(\Delta e^u) - \frac{1}{2}(\Delta e^\varepsilon)^T C(\Delta e^\varepsilon)\,]\, dV - \Delta W\,, \tag{4}$$

where $\sigma^T = (e^\varepsilon)^T C$ is the Cauchy (true) stress vector at the current configuration $\mathbb{C}^t$. In this equation, the incremental Washizu strain Δe^u can be expressed in two parts

$$\Delta e^u_{ij} = \Delta \varepsilon^u_{ij} + \Delta \eta^u_{ij} \tag{5a}$$

and they are related to the incremental displacement by

$$\Delta \varepsilon^u_{ij} = \frac{1}{2}(\Delta u_{i,j} + \Delta u_{j,i})\,, \quad \Delta \eta^u_{ij} = \frac{1}{2}\Delta u_{k,i}\Delta u_{k,j} \tag{5b,c}$$

where the Einstein summation convention for indices has been adopted and the differentiation is with respect to reference co-ordinates at the current configuration $\mathbb{C}^t$.

Substituting equation (5a) into (4) yields

$$\Delta\pi_{HR} = \int_{V_e} [- \frac{1}{2}(\Delta e^\varepsilon)^T C(\Delta e^\varepsilon) + (\Delta e^\varepsilon)^T C(\Delta \varepsilon^u) + \sigma^T \Delta \varepsilon^u + \sigma^T \Delta \eta^u + (\Delta e^\varepsilon)^T C \Delta \eta^u\,]\, dV - \Delta W\,, \tag{6}$$

where σ is the Cauchy stress vector.

Discarding the higher order term, $(\Delta e^\varepsilon)^T C \Delta \eta^u$, results in

$$\Delta\pi_{HR} = \int_{V_e} [- \frac{1}{2}(\Delta e^\varepsilon)^T C(\Delta e^\varepsilon) + (\Delta e^\varepsilon)^T C(\Delta \varepsilon^u) + \sigma^T \Delta \varepsilon^u + \sigma^T \Delta \eta^u]\, dV - \Delta W\,. \tag{7}$$

2.2 Hybrid Strain Formulation

Element stiffness matrices for a hybrid strain based finite element can be derived directly from equation (7). Generally the independently assumed strain field and displacement field can be written as

$$\Delta e^{\varepsilon} = P\,\Delta\alpha\ , \quad \Delta u = \phi\,\Delta q \tag{8a,b}$$

where P is the strain distribution matrix, ϕ is the displacement shape function matrix, $\Delta\alpha$ is the vector of incremental strain parameters and Δq is the incremental nodal displacement. Substituting equations (8a, b) into (7), and defining

$$H = \int_{V_e} P^T C P\, dV_e\ , \qquad G_e = \int_{V_e} P^T C B_L\, dV_e\ ,$$
$$k_{NL} = \int_{V_e} B_{NL}^T \sigma_C^T B_{NL}\, dV_e\ , \qquad F_1 = \int_{V_e} B_L^T \sigma\, dV_e\ , \tag{9}$$

one can show that

$$\Delta\pi_{HR}(\Delta q,\Delta\alpha) = \sum [\, -\frac{1}{2}\Delta\alpha^T H\,\Delta\alpha + \Delta\alpha^T G_e\,\Delta q$$
$$+ F_1^T\Delta q + \frac{1}{2}\Delta q^T k_{NL}\Delta q - F^T\Delta q\,] \tag{10}$$

where F is the external nodal force vector in the neighbour configuration associated with the ΔW term in equation (7); B_L and B_{NL} are the linear and nonlinear strain-displacement matrices, while σ_C is the matrix containing the Cauchy stress components at the current configuration.

Finally, one can show that

$$(k_L' + k_{NL})\,\Delta q = F(t+\Delta t) - F_1\ , \quad k_L' = G_e^T H^{-1} G_e \tag{11a,b}$$

where the expression in equation (11b) is the element "linear" stiffness matrix. The term k_{NL} defined in equation (9) is the "nonlinear" or initial stress stiffness matrix and F_1 is the pseudo-force vector. The right hand side of equation (11a) is the equilibrium imbalance.

3. ELEMENT MATRICES AND THEIR UPDATING

The derivation of nonlinear element stiffness matrices, constitutive equations, mass matrices of the element shown in Figure 1 are outlined here. In addition, updating of configuration and stresses at every time step is considered here for completeness.

3.1 Nonlinear Element Stiffness Matrices

For the assumed displacement field, an arbitrary point within an element is governed by

$$\begin{Bmatrix} r^t \\ s^t \\ t^t \end{Bmatrix} = \sum_{i=1}^{3} \xi_i \begin{Bmatrix} r_i^t \\ s_i^t \\ 0 \end{Bmatrix} + \zeta^t \sum_{i=1}^{3} \xi_i V_i^t \, . \tag{12}$$

The incremental displacements of an arbitrary point within the element are

$$\begin{Bmatrix} \Delta u^t \\ \Delta v^t \\ \Delta w^t \end{Bmatrix} = \sum_{i=1}^{3} \xi_i \begin{Bmatrix} \Delta u_i^t \\ \Delta v_i^t \\ \Delta w_i^t \end{Bmatrix} + \zeta^t \sum_{i=1}^{3} \xi_i \, (\Delta V_i^t) \, . \tag{13}$$

Employing quadratic polynomials for the translational dof and including ddof lead to

$$\begin{Bmatrix} \Delta u^t \\ \Delta v^t \\ \Delta w^t \end{Bmatrix} = \sum_{i=1}^{3} \xi_i \begin{Bmatrix} \Delta u_i^t \\ \Delta v_i^t \\ \Delta w_i^t \end{Bmatrix} + \zeta^t \sum_{i=1}^{3} \xi_i \begin{bmatrix} \Lambda_{i(11)}^t & \Lambda_{i(12)}^t \\ \Lambda_{i(21)}^t & \Lambda_{i(22)}^t \\ \Lambda_{i(31)}^t & \Lambda_{i(32)}^t \end{bmatrix} \begin{Bmatrix} \Delta\theta_{ri}^t \\ \Delta\theta_{si}^t \end{Bmatrix} + \sum_{i=1}^{3} \begin{bmatrix} 0 & 0 & \bar{p}_i \\ 0 & 0 & \bar{q}_i \\ -\bar{p}_i & -\bar{q}_i & 0 \end{bmatrix} \begin{Bmatrix} \Delta\theta_{ri}^t \\ \Delta\theta_{si}^t \\ \Delta\theta_{ti}^t \end{Bmatrix} . \tag{14}$$

In the foregoing,

$$
\begin{aligned}
u &= u_1\xi_1 + u_2\xi_2 + u_3\xi_3 + \bar{p}_1\theta_{t1} + \bar{p}_2\theta_{t2} + \bar{p}_3\theta_{t3} \\
v &= v_1\xi_1 + v_2\xi_2 + v_3\xi_3 + \bar{q}_1\theta_{t1} + \bar{q}_2\theta_{t2} + \bar{q}_3\theta_{t3} \\
w &= w_1\xi_1 + w_2\xi_2 + w_3\xi_3 - \bar{p}_1\theta_{r1} - \bar{p}_2\theta_{r2} - \bar{p}_3\theta_{r3} \\
&\qquad - \bar{q}_1\theta_{s1} - \bar{q}_2\theta_{s2} - \bar{q}_3\theta_{s3} \ ,
\end{aligned}
\tag{15a}
$$

$$
\begin{aligned}
\theta_r &= \theta_{r1}\xi_1 + \theta_{r2}\xi_2 + \theta_{r3}\xi_3 \\
\theta_s &= \theta_{s1}\xi_1 + \theta_{s2}\xi_2 + \theta_{s3}\xi_3 \\
\theta_t &= \theta_{t1}\xi_1 + \theta_{t2}\xi_2 + \theta_{t3}\xi_3
\end{aligned}
\tag{15b}
$$

where

$$
\bar{p}_1 = (a_{31}\xi_3 - a_{12}\xi_2)\xi_1 \ , \quad \bar{q}_1 = (b_{31}\xi_3 - b_{12}\xi_2)\xi_1 \ ,
$$

$$
\bar{p}_2 = (a_{12}\xi_1 - a_{23}\xi_3)\xi_2 \ , \quad \bar{q}_2 = (b_{12}\xi_1 - b_{23}\xi_3)\xi_2 \ ,
$$

$$
\bar{p}_3 = (a_{23}\xi_2 - a_{31}\xi_1)\xi_3 \ , \quad \bar{q}_3 = (b_{23}\xi_2 - b_{31}\xi_1)\xi_3 \ .
$$

The remaining symbols have been defined by Liu and To [4] and are not repeated here for brevity.

For the assumed strain field, the strain vector in equation (8a) may be written as

$$
\Delta e^{\varepsilon} = \begin{Bmatrix} \Delta \varepsilon^{\varepsilon}_{m} \\ \Delta \gamma^{\varepsilon} \end{Bmatrix} + \zeta \begin{Bmatrix} \Delta \chi^{\varepsilon} \\ 0 \end{Bmatrix} \tag{16}
$$

where

$$
\begin{aligned}
\Delta \varepsilon^{\varepsilon}_{m} &= P_m \Delta \alpha_m \ , \quad \Delta \chi^{\varepsilon} = P_b \Delta \alpha_b \\
\Delta \gamma^{\varepsilon} &= P_s \Delta \alpha_s
\end{aligned}
\tag{17a}
$$

with

$$\Delta\alpha_m=\{\Delta\alpha_1\ \Delta\alpha_2\ \Delta\alpha_3\}^T\ ,$$

$$\Delta\alpha_b=\{\Delta\alpha_4\,\Delta\alpha_5\,\Delta\alpha_6\}^T,\ \Delta\alpha_s=\{\Delta\alpha_7\,\Delta\alpha_8\,\Delta\alpha_9\}^T, \tag{17b}$$

and

$$P_m=\begin{bmatrix}1&0&0\\0&1&0\\0&0&1\end{bmatrix},\qquad P_b=\begin{bmatrix}1&0&0\\0&1&0\\0&0&1\end{bmatrix},$$

$$P_s=\begin{bmatrix}-s_3(1-2\xi_2) & s_3(1-2\xi_1) & 0\\ -r_3(1-2\xi_2) & (r_3-r_2)(1-2\xi_1) & r_2(1-2\xi_3)\end{bmatrix},$$

where the subscripts m, b and s denote the membrane, bending and transverse shear components of P in equation (8).

By defining

$$H_{mm}=\int_a P_m^T A' P_m\,da\ ,\quad H_{sm}=\int_a P_s^T C_A^T P_m\,da\ ,$$

$$H_{ms}=\int_a P_m^T C_A P_s\,da\ ,\quad H_{ss}=\int_a P_s^T E' P_s\,da\ ,$$

$$H_{bm}=\int_a P_b^T B' P_m\,da\ ,\quad H_{bs}=\int_a P_b^T C_B^T P_s\,da\ , \tag{18}$$

$$H_{mb}=\int_a P_m^T B' P_b\,da\ ,\quad H_{sb}=\int_a P_s^T C_B^T P_b\,da\ ,$$

$$H_{bb}=\int_a P_b^T D' P_b\,da$$

where a is the area of the triangular shell element and

$$A' = \sum_{k-1}^{n} (C_a)_k (h_k - h_{k-1}),\ B' = \frac{1}{2} \sum_{k-1}^{n} (C_a)_k (h_k^2 - h_{k-1}^2),$$

$$D' = \frac{1}{3} \sum_{k-1}^{n} (C_a)_k (h_k^3 - h_{k-1}^3),\ E' = \kappa_i \kappa_j \sum_{k-1}^{n} (C_b)_k (h_k - h_{k-1}),$$

$$C_A = \sum_{k-1}^{n} (C_{ab})_k (h_k - h_{k-1}),\ C_B = \frac{1}{2} \sum_{k-1}^{n} (C_{ab})_k (h_k^2 - h_{k-1}^2) \tag{19}$$

in which the integer n is the number of laminae in the laminated composite structure. Then the matrix H in equation (9) becomes

$$H = \begin{bmatrix} H_{mm} & H_{mb} & H_{ms} \\ H_{bm} & H_{bb} & H_{bs} \\ H_{sm} & H_{sb} & H_{ss} \end{bmatrix}_{9\times 9} . \tag{20}$$

Similarly by defining

$$G_{mm} = \int_a P_m^T A' B_m \, da,\ G_{sm} = \int_a P_s^T C_A^T B_m \, da,$$

$$G_{ms} = \int_a P_m^T C_A B_s \, da,\ G_{ss} = \int_a P_s^T E' B_s \, da,$$

$$G_{bm} = \int_a P_b^T B' B_m \, da,\ G_{bs} = \int_a P_b^T C_B^T B_s \, da, \tag{21}$$

$$G_{mb} = \int_a P_m^T B' B_b \, da,\ G_{sb} = \int_a P_s^T C_B^T B_b \, da,$$

$$G_{bb} = \int_a P_b^T D' B_b \, da$$

one has the matrix

$$G_e = \left[\begin{array}{c} G_{mm} + G_{mb} + G_{ms} \\ G_{bm} + G_{bb} + G_{bs} \\ G_{sm} + G_{sb} + G_{ss} \end{array} \right]_{9\times 18} . \tag{22}$$

Therefore, with the ddof considered the element stiffness matrix can be shown to be

$$k = k_L' + k_{dd} + k_{NL} \tag{23}$$

where the linear element stiffness matrix k_L' and the "nonlinear" or initial stress stiffness matrix k_{NL} are defined by in equations (9) and (11), while the stiffness matrix associated with the ddof k_{dd} is defined as

$$k_{dd} = \sum_{k=1}^{n} (G_{rs})_k (h_k - h_{k-1}) \int_a \bar{B}_d^T \bar{B}_d \, da , \tag{24}$$

in which

$$\bar{B}_d = \left[\bar{B}_{d1} \; \bar{B}_{d2} \; \bar{B}_{d3} \right]_{1\times 18}$$

and

$$\bar{B}_{di} = \left[\frac{1}{2}\xi_{i,s} \quad -\frac{1}{2}\xi_{i,r} \quad 0 \; 0 \; 0 \quad \xi_i + \frac{1}{2}(\bar{p}_{i,s} - \bar{q}_{i,r}) \right]$$

with i = 1,2,3.

The "nonlinear" or initial stress stiffness matrix k_{NL} can be obtained if the nonlinear strain-displacement matrix B_{NL} and the matrix σ_C which contains the Cauchy stress components at the current configuration are available. The matrix B_{NL} is defined by equation (45) of Liu and To [4].

The matrix σ_C is constructed from the Cauchy stress vector σ and defined as

$$\sigma_C = \left[\begin{array}{ccc} \sigma_{11} I_3 & \sigma_{12} I_3 & \sigma_{31} I_3 \\ \sigma_{12} I_3 & \sigma_{22} I_3 & \sigma_{23} I_3 \\ \sigma_{31} I_3 & \sigma_{23} I_3 & O_3 \end{array} \right] \tag{25}$$

with I_3 being the 3×3 identity matrix and O_3 a 3×3 null matrix. The transverse stress components of σ are considered constant over the thickness, and all components of σ are calculated and updated for each time step at the centroid of each element.

3.2 Constitutive Equations

For finite strain problems in the elastic range, the reduced stiffness matrix is a function of stresses. To incorporate finite strains in the analysis, several approaches can be applied. The following adopted from reference [4] is to add the linear elastic matrix a correction matrix which is a function of Cauchy stress. To begin with, the correction terms in tensor form becomes

$$C'_{ijkl} = -\frac{1}{2}(\sigma_{ik}\delta_{jl} + \sigma_{jk}\delta_{il} + \sigma_{il}\delta_{jk} + \sigma_{jl}\delta_{ik}) \tag{26}$$

where δ_{mn} is the Kronecker delta. Note that this equation comes as a result of transforming the Jaumann stress rate to the incremental second Piola-Kirchhoff stress. If the stress and strain vectors are

$$\begin{aligned} \sigma &= \{\sigma_{11}\ \sigma_{22}\ \sigma_{33}\ \sigma_{12}\ \sigma_{23}\ \sigma_{31}\}^T, \\ e &= \{e_{11}\ e_{22}\ e_{33}\ e_{12}\ e_{23}\ e_{31}\}^T \end{aligned} \tag{27}$$

the matrix form of equation (26) is

$$C' = -\frac{1}{2}\begin{bmatrix} 4\sigma_{11} & 0 & 0 & 2\sigma_{12} & 0 & 2\sigma_{13} \\ 0 & 4\sigma_{22} & 0 & 2\sigma_{12} & 2\sigma_{23} & 0 \\ 0 & 0 & 4\sigma_{33} & 0 & 2\sigma_{23} & 2\sigma_{13} \\ 2\sigma_{12} & 2\sigma_{12} & 0 & \sigma_{11}+\sigma_{22} & \sigma_{13} & \sigma_{23} \\ 0 & 2\sigma_{23} & 2\sigma_{23} & \sigma_{13} & \sigma_{22}+\sigma_{33} & \sigma_{12} \\ 2\sigma_{13} & 0 & 2\sigma_{13} & \sigma_{23} & \sigma_{12} & \sigma_{11}+\sigma_{33} \end{bmatrix} . \tag{28}$$

In present investigation the so-called degenerated concept is adopted and therefore the elastic modulus in the normal direction to the plane of the shell structures is considered zero. Consequently the stress and strain in the transversal direction are ignored. In the linear analysis the constitutive relations for a lamina have been defined as

$$\sigma = \bar{Q}\, e \tag{29}$$

where

$$\sigma = \{\sigma_x\ \sigma_y\ \sigma_{xy}\ \sigma_{yz}\ \sigma_{zx}\}^T,$$
$$e = \{e_x\ e_y\ e_{xy}\ e_{yz}\ e_{zx}\}^T \tag{30}$$

and

$$\bar{Q} = \begin{bmatrix} \bar{Q}_{11} & \bar{Q}_{12} & \bar{Q}_{16} & 0 & 0 \\ \bar{Q}_{12} & \bar{Q}_{22} & \bar{Q}_{26} & 0 & 0 \\ \bar{Q}_{16} & \bar{Q}_{26} & \bar{Q}_{66} & 0 & 0 \\ 0 & 0 & 0 & \bar{Q}_{44} & \bar{Q}_{45} \\ 0 & 0 & 0 & \bar{Q}_{45} & \bar{Q}_{55} \end{bmatrix}. \tag{31}$$

The corresponding matrix from equation (28) is

$$C' = -\frac{1}{2}\begin{bmatrix} 4\sigma_x & 0 & 2\sigma_{xy} & 0 & 2\sigma_{zx} \\ 0 & 4\sigma_y & 2\sigma_{xy} & 2\sigma_{yz} & 0 \\ 2\sigma_{xy} & 2\sigma_{xy} & \sigma_x+\sigma_y & \sigma_{zx} & \sigma_{yz} \\ 0 & 2\sigma_{yz} & \sigma_{zx} & \sigma_y & \sigma_{xy} \\ 2\sigma_{zx} & 0 & \sigma_{yz} & \sigma_{xy} & \sigma_x \end{bmatrix}. \tag{32}$$

The material stiffness matrix for a lamina thus becomes

$$C = \bar{Q} + C' \tag{33}$$

where

$$C = \begin{bmatrix} [C_a]_{3\times3} & [C_{ab}]_{3\times2} \\ [C_{ab}]_{2\times3} & [C_b]_{2\times2} \end{bmatrix}$$

in which C_a, C_b, and $C_{ab} = C_{ba}$ are given in equation (19).

With the consideration of large deformation and finite strain, the constitutive equations for a multilayered structure or laminate can be written as

$$\begin{Bmatrix} N \\ M \\ Q_s \end{Bmatrix} = \begin{bmatrix} A' & B' & C_A \\ B' & D' & C_B \\ C_A^T & C_B^T & E' \end{bmatrix}_{8\times 8} \begin{Bmatrix} \varepsilon_m \\ \chi \\ \gamma \end{Bmatrix}$$

or simply

$$\sigma_N = \bar{C}\, e_N \tag{34}$$

where N, M and Q_s are the vectors of stress resultants corresponding to membrane, bending and transverse shear, respectively. The matrices A', B', D', E', C_A and C_B have been defined in equation (19).

3.3 Element Mass Matrices and Updating of Configurations and Stresses

In the present study, with the updated Lagrangian description, the consistent mass matrix is formulated in the current configuration $\mathbb{C}^t$. The mass matrix is then updated at each time step. The assumptions are that the angular velocities and accelerations are small enough to be discarded. By following the procedures of Liu and To [4] the consistent element mass matrix can be obtained as

$$m = m_{tra} + m_{rot} + m_d \tag{35}$$

in which m_{tra} and m_{rot} are translational and rotational components of the consistent element mass matrix, respectively. Matrix m_d is the part associated with the ddof. When it is used for the incremental formulation with updated Lagrangian description, updating relevant quantities at each incremental step are required before evaluating the mass matrix. All these mass matrices are obtained explicitly with the symbolic computer algebra package MACSYMA.

For each incremental step, the configuration and stresses have to be updated. Details of the steps can be found in the reference by Liu and To [4] and therefore are not included here. However, it may be appropriate to point out that the linear consistent element matrix for multi-layer composites has been employed by the authors [11] for vibration analysis of plates and shells.

4. EXAMPLES OF LAMINATED COMPOSITE PLATE AND SHELL

There are two main objectives in this section. First, accuracy of results obtained by the presently derived element matrices is studied. Second, the validity and conceptual adequacy of the formulation and assumptions made in

the derivation of element matrices are assessed. For brevity, one multi-layer plate, one multi-layer shell structure, and a cantilever panel with free end step moment are included here. More example problems can be found in To and Wang [3], and Wang and To [12].

4.1 Multi-Layer Plate Under Uniformly Distributed Step Disturbance

The square plate considered has two layers. Its geometrical dimensions are: side length a = 2.438 m and total thickness h = 0.00635 m. Each layer of the laminate has equal thickness. The plate stacking scheme is cross-ply (0/90). The layer material properties are: $E_2 = 6.8974 \times 10^{10}$ N/m^2, $E_1 = 25\ E_2$, $G_{12} = G_{13} = 0.5\ E_2$, $G_{23} = 0.2\ E_2$, $\nu_{12} = 0.25$ and density $\rho = 2498.61$ kg/m^3.

It is supported by hinges at its four edges. At these edges U or V (note henceforth upper case of deformation variable refers to global co-ordinate) parallel to the edges are not constrained. These boundary conditions are denoted as BC1 in reference [13]. For the purpose of direct comparison with the results reported in the latter reference, one quarter of the plate is modeled by a 4 × 4 D mesh (see Figure 1 for the definition of D mesh). Thus, the boundary conditions applied are: $V = \Theta_x = 0.0$ at AB, $U = W = \Theta_x = 0.0$ at BC, $V = W = \Theta_y = 0.0$ at CD and $U = \Theta_y = 0.0$ at AD. In addition, all Θ_z are constrained. After application of the boundary conditions there are 158 unknowns in this case.

The uniformly distributed transversal step disturbance with intensity $p_0 = 490.5$ N/m^2 is applied to the plate. In the analysis, the option of inclusion of directors [3, 12] and small strain are selected. The time step size is $\Delta t = 0.001$ seconds. The responses at the centroid obtained by using the HLCTS element are plotted in Figure 2. They are compared with those reported by Reddy [13] in which results were obtained with a nine-node rectangular isoparametric element. In the latter transverse shear was considered. Excellent agreement can be observed. Before leaving this subsection it may be appropriate to mention that the nonlinear element stiffness matrix presented in reference [13] is nonsymmetric while the one derived in the present investigation is symmetric. In fact, when the system is conservative the nonlinear element stiffness matrix can be shown to be symmetric.

4.2 Spherical Shell Segment Under A Uniformly Distributed Step Disturbance

The geometry of the spherical shell is shown in Figure 3 in which the shell is simply supported. The geometrical properties are: radius R = 10.0 m, the side length of the projected plane b = 0.9996 m and the total thickness h = 0.01 m. The spherical shell is considered having two equal thickness layers and they have the (- 45/45) lamination scheme. The pertinent material properties are: $E_1 = 2.5\times10^{11}$ N/m^2, $E_2 = 1.0\times10^{10}$ N/m^2, $G_{12} = G_{13} = 0.5\times10^{10}$ N/m^2, $G_{23} = 0.2\times10^{10}$ N/m^2, Poisson's ratio $\nu_{12} = 0.25$ and density $\rho = 1.0\times10^8$ kg/m^3. For comparison to results available in the literature one quarter of the

shell is modeled by the proposed hybrid strain based shell element (identified as HLCTS for brevity and convenience) with 4 × 4 D mesh. The boundary conditions applied to the finite element model are: $V = \Theta_x = \Theta_z = 0.0$ at line AB, $V = W = \Theta_x = 0.0$ at BC, $U = W = \Theta_y = 0.0$ at DC and $U = \Theta_y = \Theta_z = 0.0$ at AD. The number of equations to be solved after the application of the boundary conditions is 189. A distributed step pressure is applied to its outer surface (pointing toward the outer surface). It has an intensity $p = 2000.0$ N/m^2. The time step used were 0.03 s, 0.01 s and 0.005 s. As there was no significant difference and for efficient reason throughout the computation the time step of 0.03 s was adopted. The nonlinear transient response at the apex (central point A of the shell) is obtained and plotted in Figure 4. The problem has been solved by Wu *et al.* [14] who applied a curved high-order quadrilateral shell element. The latter has 48 dof and was developed based on the classical lamination theory. It is observed that there is a discrepancy of about 8%, with respect to the HLCTS element results, for the amplitudes between the two set of results. However, they have the same vibration period. It is believed that the present results are more accurate as the element used in the present investigation is shear deformable.

4.3 Cantilever Panel With Free End Step Moment

To demonstrate the use of the proposed shell element for structures undergoing large rotation and large deformation a four layer cross-ply cantilever panel is considered here. More computed results for this case can be found in references [3] and [12]. It is symmetrically laminated with the stacking scheme (0/90/90/0). Its geometrical properties are: $L = 1.2$ m, $b = 0.1$ m and $h = 0.01$ m. The material used for this cantilever is the high modulus graphite/epoxy composite. Its properties are: $E_1 = 2.0685\times10^{11}$ N/m^2, $E_2 = 5.1713\times10^9$ N/m^2, $G_{12} = 3.1028\times10^9$ N/m^2, $G_{13} = G_{23} = 2.5856\times10^9$ N/m^2, $\rho = 1605$ kg/m^3 and Poisson's ratio $\nu_{12} = 0.25$. A step moment M about an axis parallel to the width of the panel is applied to the free end. The amplitude of this moment is $m_0 = 1000.00$ N-m.

The panel is discretized by a 12 × 1 A mesh. At the fixed end, all dof are constrained. The finite element model has 144 unknowns.

The time step $\Delta t = 0.001$ s is employed in the trapezoidal rule direct integration. The nonlinear transient responses at the end of the cantilever are solved by selecting the options of director included, small strain and constant thickness in the digital computer program developed. The computed end deflections are plotted in Figure 5. As noted in reference [3,12], the inclusion of directors in the formulation [15] is crucial as the directors are important parameters that constitute the so-called "exact geometry" for large rotation problems.

5. CONCLUDING REMARKS

The hybrid strain based laminated composite flat triangular shell (HLCTS) element for the static analysis of geometrically nonlinear laminated composite plates and shells has been further developed and employed to solve various dynamic problems. A relatively comprehensive study for various plate and shell structures idealized by this element has been performed and three representative examples are included to demonstrate its accuracy, efficiency and conceptual adequacy. It is concluded that the HLCTS element is attractive for large scale finite element analysis and modelling of shell structures undergoing geometrically large deformation of finite strain and finite rotations.

ACKNOWLEDGMENT

The first author gratefully acknowledges the financial support in the form of a research grant from the Natural Sciences and Engineering Research Council of Canada. The results reported above were obtained in the course of the research while the authors were at the University of Western Ontario.

REFERENCES

1. To, C.W.S. and Wang, B., Nonlinear theory and incremental formulation of hybrid strain based composite laminated shell finite elements. *Proc. Second Int. Conf. on Composites Engineering*, August 21-24, 1995, New Orleans, Louisiana, pp. 757-758.

2. Wang, B. and To, C.W.S., Finite element analysis of geometrically nonlinear composite laminated plates and shells. *Proc. Second Int. Conf. on Composites Eng.*, August 21-24, 1995, New Orleans, Louisiana, pp. 791-792.

3. To, C.W.S. and Wang, Hybrid strain based geometrically nonlinear laminated composite triangular shell elements, Part II: Numerical studies. *Comp. and Struct.* (Submitted), 1996.

4. Liu, M.L. and To, C.W.S., Hybrid strain based three node flat triangular shell elements, Part I: Nonlinear theory and incremental formulation. *Comput. Struct.*, 1995, **54**, 1031-1056.

5. Noor, A.K. and Mathers, M.D., Nonlinear finite element analysis of laminated composite shells. In *Computational Methods in Nonlinear Mechanics* (Ed. by J.T. Oden, E.B. Becker, R.R. Craig, R.S. Dunham, C.P. Johnson and W.L. Oberkampf). *Proc. Int. Conf. on Comput. Methods in Nonlinear Mechanics*, Austin, TX, 1974.

6. Lin, J.J., Fafard, M., Beaulieu, D. and Massicotte, B., Nonlinear analysis of composite bridges by the finite element method. *Comput. Struct.*, 1991, **40**, 1151-1167.

7. Madenci, E. and Barut, A., A Free-formulation-based flat shell element for nonlinear analysis of thin composite structures. *Int. J. Numer. Meth. Engng.*, 1994, **37**, 3825-3842.

8. Bergan, P.G., and Nygard, M.K., Nonlinear shell analysis using free formulation finite elements. In *Finite Element Methods for Nonlinear Problems*, (edited by Bergan, P.G., Bathe, K.J., and Wunderlich, W.) Springer-Verlag, 1986.

9. Zhu, J., Application of natural approach to nonlinear analysis of sandwich and composite plates and shells. *Comput. Meth. Appl. Mech. Engng.*, 1995, **120**, 355-388.

10. Saleeb, A.F., Chang, T.Y., Graf, W. and Yingyeunyong, S., A hybrid/mixed model for nonlinear shell analysis and its applications to large-rotation problems, *Int. J. Num.. Meth. Engng.*, 1990 **29**, 407-446.

11. To, C.W.S. and Wang, B., Hybrid strain-based three-node flat triangular laminated composite shell elements for vibration analysis. *J. Sound and Vibration* (submitted), 1996.

12. To, C.W.S. and Wang, B., Transient response analysis of geometrically nonlinear laminated composite shell structures. *Proc. of Design Eng. Conf. and Computers in Eng. Conf.* (edited by McCarthy, J.M.), August 18-22, 1996, Irvine, California, 96-DETC/CIE-1623.

13. Reddy, J.N., Geometrically nonlinear transient analysis of laminated composite plates. *A.I.A.A. J.*, 1987, **21**, 621-629.

14. Wu, C.Y., Yang, T.Y. and Saigal, S., Free and forced nonlinear dynamics of composite shell structures. *J. Comp. Mat.*, 1987, **21**, 898-909.

15. To, C.W.S. and Wang, B., Hybrid strain based geometrically nonlinear laminated composite triangular shell elements, Part I: Theory and element matrices. *Computers and Structures* (submitted), 1996.

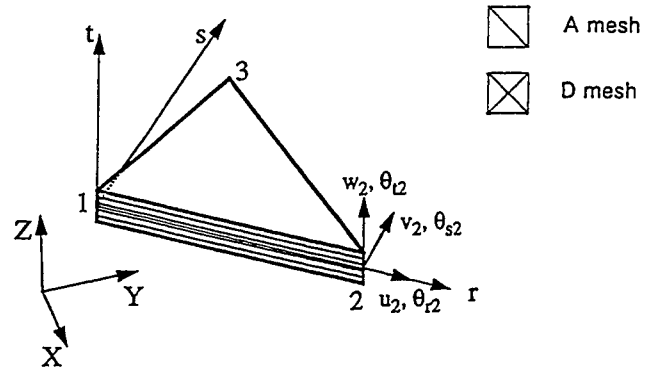

Figure 1 Flat triangular laminated composite shell element

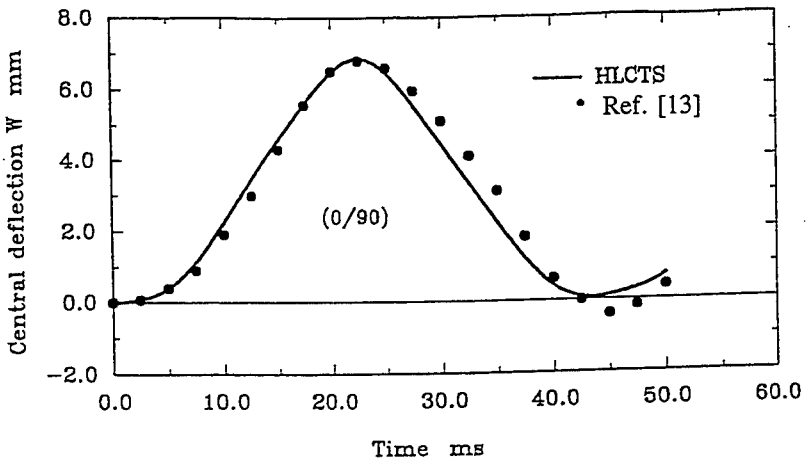

Figure 2 Response of a cross-ply plate

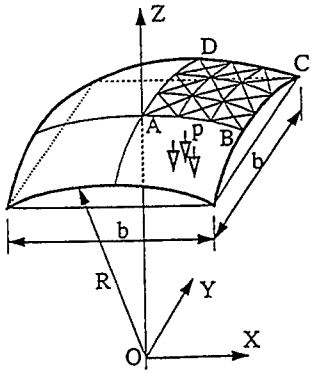

Figure 3 Spherical shell segment under a uniformly distributed load

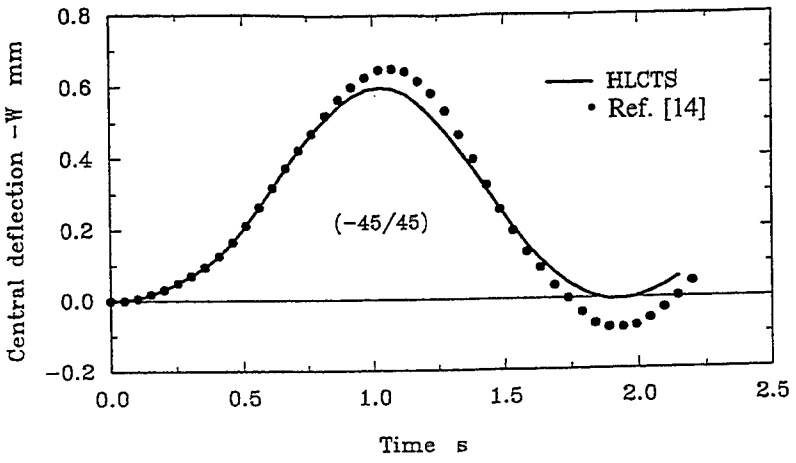

Figure 4 Apex response with quarter shell considered

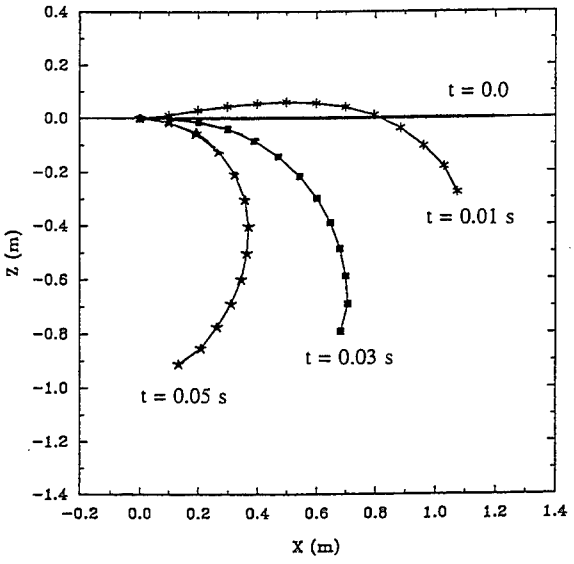

Figure 5 Evolution of cantilever panel with free end step moment

ANALYTICAL METHODS III

THE FREE, IN-PLANE VIBRATION OF CIRCULAR RINGS WITH SMALL THICKNESS VARIATIONS

R S Hwang, C H J Fox and S McWilliam
Department of Mechanical Engineering , University of Nottingham,
University Park, Nottingham NG7 2RD, England

Abstract

Geometric imperfections which cause thickness variations will always exist in nominally circular rings and cylinders due to limitations in manufacturing processes. The effects of circumferential thickness variations on the natural frequencies of in-plane vibration are studied. The circumferential variations in the inner and outer surfaces are described, in a very general way, by means of Fourier series. Novozhilov thin-shell theory is used in conjunction with the Rayleigh-Ritz method to obtain the natural frequencies. Results are presented which show the effects of single-harmonic variations in the inner and outer surface profiles, taking account of the profile amplitude of, and the spatial phasing between, the inner and outer profiles. The frequency factors calculated from the numerical method are in good agreement with those obtained from the Finite Element method.

1. Introduction

The free vibrations of circular rings or shells had been studied by many authors for over a century. The early theoretical works are summarised by Love [1]. Most of these works are restricted to ***perfect*** rings or shells. However, in practice, geometric imperfections (thickness variations and departure from true circularity) are produced in the manufacturing process. These affect the natural frequencies and mode shapes. It is well known that in any truly axisymmetric structure the vibration modes occur in degenerate pairs which have equal natural frequencies and mode shapes which are spatially orthogonal but of indeterminate circumferential location. The main effects of thickness variations are to split the previous equal natural frequencies and remove the positional indeterminacy [2]. Although these effects are often practically unimportant, there are some applications (especially inertial sensors based on vibration rings or cylinders [3]) where the small frequency splits and fixing of the modal positions is of primary practical significance. There is therefore a requirement to be able to predict in detail the effects on vibrational behaviour due to small departures from perfect circularity of the kind produced by manufacturing tolerances.

The vibration of imperfect bells and rings were studied in the general way using group theory [4,5]. In reference [5] the selection rules for frequency splitting of thin circular rings were presented qualitatively. In reference[6] the frequency splitting behaviour of a thin circular ring was investigated both experimentally and analytically by first order perturbation theory. In reference [7], the classical frequency equations, which are generally used to predict the natural frequencies of a thin circular ring, were modified to describe an eccentric ring by using the perturbation method. In reference [8], Fourier series functions were used to represent the circumferential thickness variations of an eccentric cylinder. Love thin-shell theory, which is only strictly suitable for a perfect ring or cylinder, was applied to investigate the free vibration of non-circular shells.

In this paper, the free in-plane vibrations of thin rings of rectangular cross section with circumferential variations in thickness are studied. The circumferential variations in the inner and outer surfaces are described, in a very general way, by means of Fourier series. Novozhilov thin-shell theory [9], in conjunction with the well-known Rayleigh-Ritz method, are applied to analyse the vibration characteristics for in-plane flexural vibration of the ring which is considered as a special case of a thin shell [2,6]. The numerical method is used to investigate the effect of single-harmonic circumferential variations in the inner and outer surface profiles. The effects of harmonic number, amplitude and spatial phasing between the inner and outer profiles are investigated. Some important trends and patterns of effects of profile variations on the splitting of the natural frequencies are observed. The results obtained by using the numerical method developed in the current investigation are validated by comparison with Finite Element predictions.

2. Method of Analysis

2.1 Geometry

Consider a thin ring of mean radius r_a having a rectangular cross-section of mean thickness h ($<< r_a$) and axial length L ($<< r_a$). The inner and outer surface vary along the global circumferential direction (Figure 1). r_P denotes the distance from the centre of the mean radius of the ring to the point P on the middle surface.

Two coordinate systems are used in the formulation of the equation of deformation.

* Global polar coordinates (α', β', ξ'). These are directed along the global axial, circumferential and radial directions. The initial geometry of the undeformed, imperfect ring is defined using this coordinate system.

* Local curvilinear coordinates (α, β, ξ). These are directed along the local axial, tangential and normal directions relative to the true middle surface and coincident with the principal coordinates of the middle surface. This local coordinate system is required for implementation of Novozhilov shell theory which specifies displacements in the local tangential and normal directions.

γ_P is the angle between the global and local coordinate systems at the point P of the middle surface.

All the displacements, thicknesses, and radii in this paper are expressed dimensionlessly by dividing by l_0, where l_0 is the representative length and is defined as the mean radius r_a of the ring.

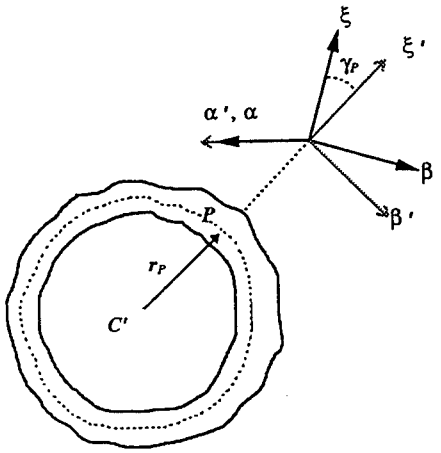

Figure 1. A thin ring having circumferentially arbitrary surfaces

The shape of the middle surface of the ring is determined by the inner and outer surfaces which can be expressed by Fourier series as follows:

$$f^+(\beta') = f_0^+ + \sum_{i=1}^{n} f_i^+ \cos(i\beta') + \sum_{j=1}^{n} f_j^+ \sin(j\beta') \qquad (1)$$

$$f^-(\beta') = f_0^- + \sum_{i=1}^{n} f_i^- \cos(i\beta') + \sum_{j=1}^{n} f_j^- \sin(j\beta') \qquad (2)$$

where $f^{+}(\beta')$ and $f^{-}(\beta')$ denote respectively the outer and inner surface functions with respect to the global circumferential coordinate β' and $f_0^{+}, f_i^{+}, f_j^{+}, f_0^{-}, f_i^{-}$ and f_j^{-} are the Fourier coefficients which are defined in the usual way [10].

The middle surface of a shell or ring is defined as the locus of the points which lie at equal distances, h_ξ^{+} and h_ξ^{-} from the outer and inner surfaces along the direction normal to the mid surface (see Figure 2).

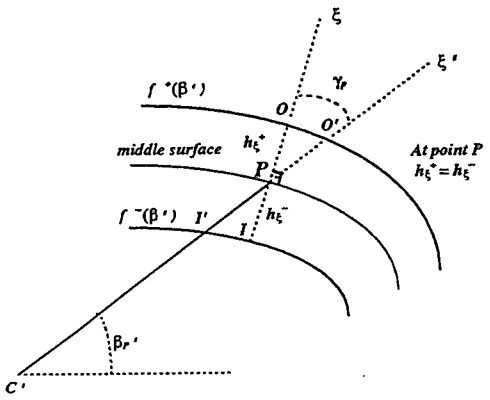

Figure 2. The bounding surfaces and the middle surface

For given inner and outer surfaces, $f^{-}(\beta_P')$ and $f^{+}(\beta_P')$ defined in the global coordinate system, the true middle surface can be determined using an iterative numerical procedure which is fully described in [11]. Once the point P on the true middle surface has been determined, the corresponding h_ξ^{+}, h_ξ^{-}, R_P, γ_P and β_P can be calculated. These will be used in the step-by step integrations which determine the strain energy and kinetic energy of the ring.

2.2 Equations of Motion

The strain energy for a thin ring whose length is much smaller than the mean radius takes the form [2,6]:

$$S = \frac{\ell_o^2 EL}{2} \int_{\beta_1}^{\beta_2} \int_{h_\xi^-}^{h_\xi^+} e_{\beta\beta}^{\ 2} R(1+\xi/R)\, d\beta\, d\xi \qquad (3)$$

Based on Novozhilov thin-shell theory, the normal strain $e_{\beta\beta}$ in equation (3) is given as

$$e_{\beta\beta} = \frac{1}{1+\xi / R}\,(\varepsilon_\beta + \xi\,\kappa_\beta) \tag{4}$$

with

$$\varepsilon_\beta = v,_\beta / R + w / R \tag{5}$$

$$\kappa_\beta = -1/R\ (w,_\beta / R + v/R),_\beta \tag{6}$$

where ε_β, κ_β characterise the deformation of the middle surface of the thin ring and subscript " $,_\beta$ " denotes partial derivatives with respect to β. ε_β is the strain tangential to the middle surface and κ_β is the change of curvature. v, w are the nondimensional local displacement components of the point P on the middle surface along the tangential and normal directions respectively.

Substituting equations (4)-(6) into equation (3), then integrating with respect to the thickness from h_ξ^- to h_ξ^+, neglecting the 4th and higher powers of h_ξ^+ and h_ξ^- and noting that $\int_{\beta_1}^{\beta_2} F(\beta)\,[\,h_\xi^{+2} - h_\xi^{-2}]\,d\beta = 0$ where $F(\beta)$ is an arbitrary function of β, the strain energy of a thin ring can be derived in terms of the local displacements v, w as follows:

$$\begin{aligned} S = \frac{\ell_c^4 EL}{2} \int_{\beta_1}^{\beta_2} \{ & [\,(v,_\beta)^2 + 2w\,v,_\beta + w^2\,](1/R)\,[h_\xi^+ - h_\xi^-] \\ & + [\,w^2 + 2ww,_{\beta\beta} + (w,_{\beta\beta})^2\,]\,\frac{1}{3R^3}\,[\,h_\xi^{+3} - h_\xi^{-3}] \\ & + [\,2ww,_\beta + 2w,_\beta w,_{\beta\beta} - 2v\,w - 2vw,_{\beta\beta}\,]\,\frac{1}{3R^2}(1/R),_\beta\,[\,h_\xi^{+3} - h_\xi^{-3}] \\ & + [\,(w,_\beta)^2 + v^2 - 2vw,_\beta\,]\,\frac{1}{3R}\,((1/R),_\beta)^2\,[\,h_\xi^{+3} - h_\xi^{-3}]\,\}\,d\beta \end{aligned} \tag{7}$$

Similarly, the kinetic energy of a thin ring, based on Novozhilov thin-shell shell theory, can be expressed as follows:

$$\begin{aligned} T = \frac{\ell_0^4 L\rho}{2} \int_{\beta_1}^{\beta_2} \{ & [\,(v,_t)^2 + (w,_t)^2\,]\,R\,[\,h_\xi^+ - h_\xi^-] + \\ & [\,3(v,_t)^2 - 4\,v,_t\,w,_{t\beta} + (w,_{t\beta})^2\,]\,\frac{1}{3R}\,[\,h_\xi^{+3} - h_\xi^{-3}]\,\}\,d\beta \end{aligned} \tag{8}$$

in which ρ is the density of the ring, and the subscript ' $,_t$ ' denotes the partial derivatives with respect to time.

For free vibration the tangential displacement v and the normal displacement w which satisfy the boundary condition can be assumed to take the following forms respectively:

$$v = \sum_n (v_n^s \sin n\beta - v_n^c \cos n\beta) e^{iwt} \tag{9}$$

$$w = \sum_n (w_n^c \cos n\beta + w_n^s \sin n\beta) e^{iwt} \tag{10}$$

where v_n and w_n are the undetermined amplitude coefficients of the tangential and normal displacements of the middle surface respectively. The superscripts "s" and "c" refer to the fact that these coefficients are multiplied by sine and cosine terms respectively.

Substituting equations (9) and (10) into equations (7) and (8), then applying the Rayleigh-Ritz procedure, the general frequency equation of the free vibrations for a thin ring is obtained and can be expressed in the following general matrix form:

$$\left[\begin{bmatrix} K^{ss} & K^{sc} \\ K^{cs} & K^{cc} \end{bmatrix} - \Delta \begin{bmatrix} M^{ss} & M^{sc} \\ M^{cs} & M^{cc} \end{bmatrix}\right]\begin{bmatrix} q_1 \\ q_2 \end{bmatrix} = \begin{bmatrix} 0 \\ 0 \end{bmatrix} \tag{11}$$

where K and M represent stiffness and mass matrices of size **2(N+1)**, and q denotes a vector of generalised coordinates v_n, w_n etc. The matrix elements in equation (11) are given in [11]. Since in the general case the cross-section of the ring will not be symmetric with respect to $\beta = 0$, the classification of the modes as being "symmetric" and "antisymmetric" is meaningless. In the special case of a perfect circular ring, the off-diagonal terms $[K^{sc}]$, $[K^{cs}]$, $[M^{sc}]$ and $[M^{cs}]$ appearing in equation (11) are null matrices, then equation (11) can be uncoupled into two equations: one is for the symmetric modes and the other is for the anti-symmetric modes with respect to $\beta = 0$.

The frequency factors of the ring, Δ_n , are the eigenvalues of equation (11) and are defined by

$$\Delta_n = \frac{\omega_n^2 \ell_0^2 \rho}{E} \tag{12}$$

where ω_n is the natural frequency of the nth radial mode. The frequency factor Δ_n is proportional to the square of natural frequency ω_n .

For a given value of n equation (11) will yield a pair of values of Δ_n. These will be equal in the case of a perfect ring but will be slightly different in

the case of an imperfect ring, giving rise to a higher frequency mode and a lower frequency mode for each value of n.

It should be noted that the matrix elements in equation (11) are expressed as integrals of the functions h_ξ^+, h_ξ^-, R_P, γ_P and β_P with respect to the tangential coordinate β. These functions are expressed in terms of the local coordinates. Hence it is necessary to make a transformation to express these functions and integrals in terms of the global coordinates, so that the integrals can be evaluated over the global circumferential coordinate β' from 0 to 2π.

3. Results and Discussion

By using different combinations of trigonometric functions in equations (1) and (2), it is in principle possible to model any closed thin ring. For the purpose of illustration we will consider a nominally circular ring with a *single* harmonic variation in the inner and outer surfaces, given by

$$f^+(\beta') = r_a^+ + h_f^+ \cos i\beta' \quad (13)$$

$$f^-(\beta') = r_a^- + h_f^- \cos(j\beta' - \phi) \quad (14)$$

where h_f^+ and h_f^- are the amplitudes of the imperfections of the outer surface and the inner surface measured from the mean outer radius r_a^+ and the mean inner radius r_a^- respectively, ϕ is the spatial phase angle between the trigonometric functions of the inner and outer surfaces at $\beta' = 0$, and i, j are the harmonic numbers of the surface variations. Figure 3 illustrates $i = j = 3$ for three values of ϕ.

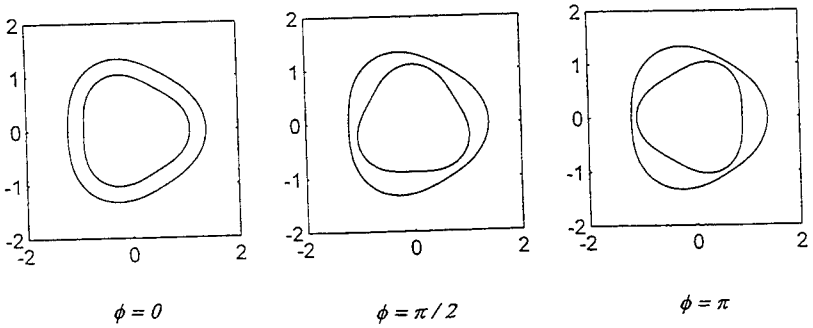

Figure 3. Different spatial phase angles ϕ for i = j = 3

Results for the combinations of the geometric imperfections of $i = j = 2, 3, 4, 5, 6$, $h_f^+ = h_f^- = 0.1h, 0.01h$, and $\phi = 0, \pi/4, \pi/2, 3\pi/4, \pi$ are presented here. The ring dimensions and material properties are as follows: $r_a^+ =$ 40.75mm, $r_a^- = 37.83$mm, $L = 2$ mm, $E = 206.7 \times 10^9$ N/m^2, $\rho = 7850$ kg/m^3.

Note that $h_f = 0.1h$ corresponds to a departure from circular which is much larger than would occur in practice due to imperfection. The results for $h_f = 0.1h$ are presented to highlight the effects. Practically however, $h_f = 0.01h$ represents a more realistic variation in thickness.

Convergence studies indicated that for $h_f^+, h_f^- = 0.1h$ the use of 30 terms in the solution series (equations 9 and 10) gave 4 significant figure accuracy or better for the frequency factors Δ_k for $k = 0, 1, \ldots 6$. This was considered to be acceptable for the purposes of the illustrative examples considered here.

In a parallel Finite Element study, beam elements, and two- and three-dimensional plane stress elements used to model an imperfect ring. In order to get 4 significant figures or better, 120 elements were used to model the complete ring. Comparison of the results obtained from the numerical method and the Finite Element Method shows that

(i) there is good agreement between the curves of frequency factors obtained by the Finite Element method and the numerical method.

(ii) the trends and patterns of frequency splitting are nearly identical irrespective of the analysis methods or the types of finite elements used.

In considering the effect of single harmonic variations of the profile of the inner and outer surfaces on the natural frequencies of different radial modes, the discussion will focus on three aspects:

(a). the effect of the harmonic number of the profile;

(b). the effect of the magnitude of the profile variations; and

(c). the effect of the spatial phasing between the profile variations of the inner and outer surfaces.

The frequency splits shown are often very small (~ 0.001%). Note however that in some inertial sensor applications, such small frequency splits may be of practical significance.

(a) The effect of profile harmonic number

Table 1 compares the frequency factors Δ_n obtained for a perfect ring and an imperfect ring for $\phi = 0, \pi/2, \pi$, $h_f^+ = h_f^- = 0.1h$, and $i = j = 2$ to 6. It is evident from these results that:

For the flexural modes ($n \geq 2$):

(i) When i , j are equal and even (see Table 1), frequency splitting only occurs in the nth mode where $n = ki / 2$ and k is an integer. The maximum frequency splitting occurs in the $n = i / 2$ modes (i.e. $k = 1$) and the splitting decays as k increases.

(ii) When i , j are equal and odd (see Table 1) frequency splitting only occurs in the nth mode where $n = ki$ and k is an integer. The maximum frequency splitting occurs for $k = 1$, and splitting decreases as k increases.

It should be noted here that frequency splitting in the higher modes exists but is very small, e.g., for $\phi = 0$, $i = j = 2$ and $h_f = 0.1h$, frequency splitting occurs in the 2nd and higher radial modes. It can be seen from Table 1 that the splits in frequency factor are 0.019% at the 2nd mode, 0.001% at the 3rd mode, and less than 0.001% at the 4th mode or higher mode. These correspond to actual frequency splits of about 0.01%, 0.0005% and less than 0.0005% respectively (equation (12)).

For the radial extensional mode($n = 0$), no frequency splitting occurs.

It is clear from Table 1 that the trends and patterns of frequency splitting are the same for $\phi = 0, \pi/2$ and π. However, frequency splitting is less for $\phi = 0$ than for $\phi = \pi$ under the same conditions. Frequency splits for ϕ between 0 and π are intermediate between those for $\phi = 0$ and $\phi = \pi$.

The above patterns are in agreement with the qualitative results published in reference [5] in which only the conditions for non-splitting are established.

Table 1. The difference of frequency factors Δ on the radial modes w(n) [the parameters of profile variations are taken as h_f=0.1h, i=j=2 to 6 and (a)ϕ=0; (b)ϕ=π/2; (c)ϕ=π]

(a) ϕ=0

		Δ(0)	Δ(2)	Δ(3)	Δ(4)	Δ(5)	Δ(6)
Perfect		1.0005	0.003313	0.02645	0.09693	0.2525	0.5406
i= 2	high	-0.011%	-0.023%	-0.041%	-0.038%	-0.036%	-0.035%
	low		-0.042%	-0.042%	"	"	"
i= 3	high	0.075%	-0.047%	-0.088%	-0.133%	-0.108%	-0.094%
	low		"	-0.153%	"	"	-0.095%
i= 4	high	0.457%	2.155%	-0.134%	-0.150%	-0.349%	-0.240%
	low		-2.287%	"	-0.594%	"	-0.248%
i= 5	high	1.631%	-0.171%	-0.141%	-0.332%	-0.229%	-0.838%
	low		"	"	"	-1.816%	"
i= 6	high	5.656%	-0.171%	2.406%	-0.267%	-0.715%	-0.302%
	low		"	-2.726%	"	"	-5.624%

(b) ϕ=π/2

		Δ(0)	Δ(2)	Δ(3)	Δ(4)	Δ(5)	Δ(6)
i= 2	high	0.007%	0.336%	-0.595%	-0.971%	-1.169%	-1.272%
	low		-2.427%	-0.676%	-0.972%	"	"
i= 3	high	0.090%	-1.231%	0.336%	-0.721%	-0.869%	-1.038%
	low		"	-2.559%	"	"	-1.040%
i= 4	high	0.382%	14.58%	-1.150%	0.287%	-0.868%	-0.828%
	low		-18.71%	"	-2.871%	"	-0.901%
i= 5	high	1.236%	-5.642%	-1.239%	-1.201%	0.212%	-1.172%
	low		"	"	"	-3.703%	"
i= 6	high	4.111%	-5.620%	13.12%	-1.316%	-1.404%	0.117%
	low		"	-17.59%	"	"	-6.370%

(c) ϕ=π

		Δ(0)	Δ(2)	Δ(3)	Δ(4)	Δ(5)	Δ(6)
i= 2	high	0.026%	0.690%	-1.132%	-1.908%	-2.308%	-2.514%
	low		-4.827%	-1.340%	-1.912%	"	"
i= 3	high	0.106%	-2.469%	0.709%	-1.312%	-1.637%	-1.989%
	low		"	-4.934%	"	"	-1.993%
i= 4	high	0.314%	18.81%	-2.227%	0.528%	-1.388%	-1.447%
	low		-26.96%	"	-4.993%	"	-1.532%
i= 5	high	0.881%	-10.89%	-2.400%	-2.135%	-0.018%	-1.510%
	low		"	"	"	-5.031%	"
i= 6	high	2.808%	-10.81%	16.78%	-2.396%	-2.134%	-1.881%
	low		"	-25.36%	"	"	-5.060%

Note: 1. difference = $[\Delta(n) - \Delta(n)_{perfect}] \times 100\% \; / \; \Delta(n)_{perfect}$

2. $\Delta(n) = \frac{\ell_0^2 \rho}{E} \omega^2(n)$, where $\omega(n)$ is the natural frequency at the nth radial mode.

Table 2. The difference of frequency factors Δ on the radial modes w(n) [the parameters of profile variations are taken as h_f=0.01h, i=j=2 to 6 and (a)ϕ=0; (b)ϕ=π/2; (c)ϕ=π]

(a) ϕ=0

	Δ(0)	Δ(2)	Δ(3)	Δ(4)	Δ(5)	Δ(6)
Perfect	1.0005	0.003313	0.02645	0.09693	0.2525	0.5406
i= 2 high	≈0	≈0	≈0	≈0	≈0	≈0
low		"	"	"	"	"
i= 3 high	0.001%	≈0	-0.001%	-0.001%	-0.001%	-0.001%
low		"	-0.002%	"	"	"
i= 4 high	0.005%	0.222%	-0.001%	-0.001%	-0.004%	-0.002%
low		-0.223%	"	-0.006%	"	"
i= 5 high	0.016%	-0.002%	-0.002%	-0.003%	-0.002%	-0.009%
low		"	"	"	-0.019%	"
i= 6 high	0.060%	-0.002%	0.256%	-0.003%	-0.008%	-0.003%
low		"	-0.260%	"	"	-0.063%

(b) ϕ=π/2

	Δ(0)	Δ(2)	Δ(3)	Δ(4)	Δ(5)	Δ(6)
i= 2 high	≈0	0.004%	-0.006%	-0.010%	-0.012%	-0.013%
low		-0.024%	"	"	"	"
i= 3 high	0.001%	-0.012%	0.003%	-0.007%	-0.009%	-0.010%
low		"	-0.026%	"	"	"
i= 4 high	0.004%	1.684%	-0.011%	0.003%	-0.009%	-0.009%
low		-1.725%	"	-0.029%	"	"
i= 5 high	0.012%	-0.058%	-0.012%	-0.012%	0.002%	-0.012%
low		"	"	"	-0.038%	"
i= 6 high	0.044%	-0.057%	1.550%	-0.013%	-0.014%	0.001%
low		"	-1.595%	"	"	-0.069%

(C) ϕ=π

	Δ(0)	Δ(2)	Δ(3)	Δ(4)	Δ(5)	Δ(6)
i= 2 high	≈0	0.008%	-0.012%	-0.019%	-0.023%	-0.025%
low		-0.048%	"	"	"	"
i= 3 high	0.001%	-0.024%	0.008%	-0.013%	-0.016%	-0.020%
low		"	-0.050%	"	"	"
i= 4 high	0.003%	2.360%	-0.021%	0.006%	-0.014%	-0.015%
low		-2.440%	"	-0.050%	"	"
i= 5 high	0.009%	-0.114%	-0.023%	-0.020%	≈0	-0.015%
low		"	"	"	-0.051%	"
i= 6 high	0.028%	-0.112%	2.165%	-0.023%	-0.020%	-0.018%
low		"	-2.251%	"	"	-0.051%

Note: 1. difference = $[\Delta(n) - \Delta(n)_{perfect}] \times 100\% / \Delta(n)_{perfect}$

2. $\Delta(n) = \frac{\ell_0^2 \rho}{E} \omega^2(n)$, where $\omega(n)$ is the natural frequency of the nth radial mode.

(b) The effect of profile amplitude

The effects of varied profile amplitude ($h_f^+ = h_f^- = 0.1h$ and $0.01h$) upon the frequency factors Δ_n for $\phi = 0, \pi/2, \pi$ and $i = j = 2$ to 6 can be seen by comparing Tables 1 and 2. It may be concluded from these results and others which are presented in [11] that:

(1) When $n = i/2$, frequency factor splitting due to variable profile magnitude compared with the frequency factor of the perfect ring is nearly proportional to the profile amplitudes, h_f^+ and h_f^-.

For example, for $i = j = 4$, $\phi = \pi$ and $h_f^+ = h_f^- = 0.1h, 0.01h$ (see Tables 1 and 2), the magnitude of frequency splitting at the 2nd mode is 45.77% for $h_f = 0.1h$ and 4.80% for $h_f = 0.01h$. These correspond to actual frequency splits of 24% and 2.4% respectively (equation (12))

(2) For modes other than those for which $n = i/2$, splitting of frequency factors is nearly proportional to the square of the profile amplitudes, h_f^+ and h_f^-.

For example, for $i = j = 4$, $\phi = \pi$ and $h_f^+ = h_f^- = 0.1h, 0.01h$ (see Tables 1 and 2), the magnitude of frequency factor splitting at the 4th mode are 5.521% for $h_f = 0.1h$ and 0.056% for $h_f = 0.01h$.

These results shown in Tables 1 and 2 for $\phi = 0$ and $\phi = \pi/2$ show that the general nature of the trends regarding the effect of profile amplitude variations on the frequency factors are the same for all values of ϕ, although the magnitudes of the changes in frequency factors depend on ϕ, as discussed in the following section.

(c) The effect of spatial phase angle variations

The effects of the variations of spatial phase angle ϕ on the frequency factors are shown in Figure 4, from which it is evident that

(1) As frequency splitting occurs (see Figure 4.a-4.d), the maximum frequency splitting is obtained at $\phi = \pi$ and the minimum splitting occurs at $\phi = 0$. It is clear that the maximum frequency splitting occurs in the $n = i/2$ modes.

(2) In modes for which no frequency *splitting* occurs (see Figure 4.e and 4.f), the minimum frequency difference compared with that of the perfect ring is detected at $\phi = 0$ and the maximum at $\phi = \pi$. Irrespective of the value of ϕ, the frequencies of these modes are always less than the corresponding frequencies of the perfect ring.

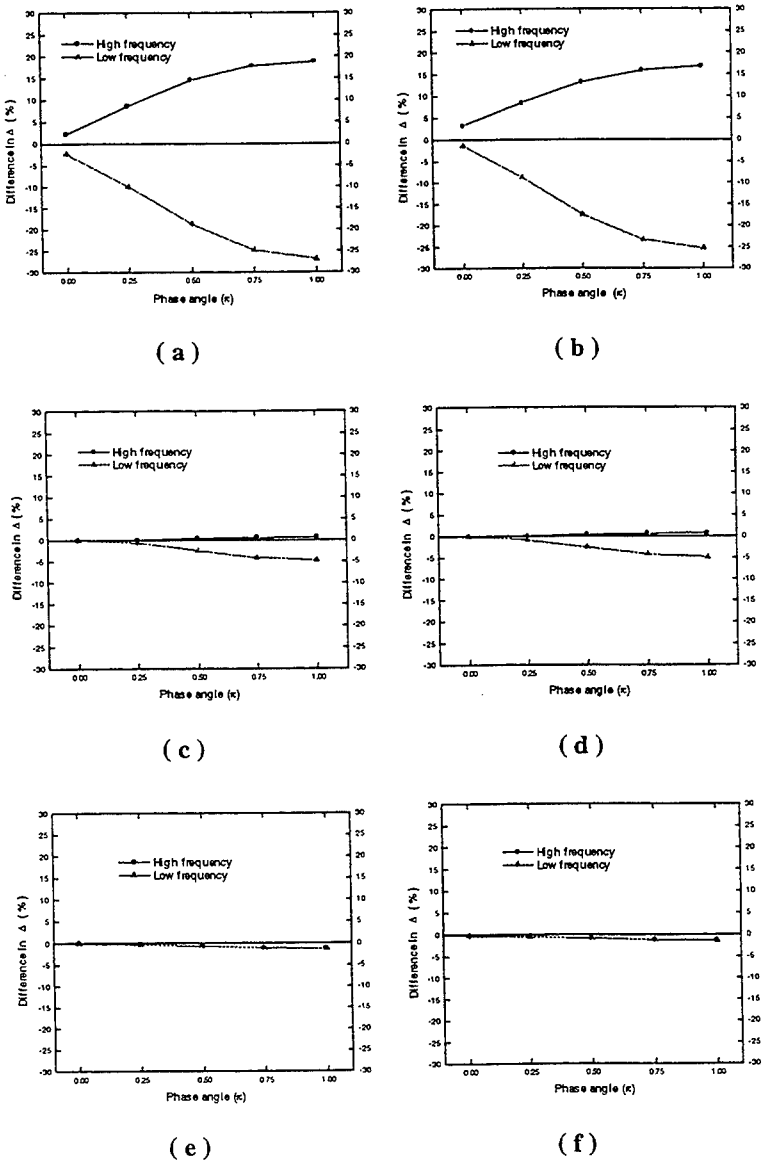

Figure 4. Effect of spatial phasing on frequency factors with $h_f = 0.1h$ and
(a) i=j=4, 2nd mode ; (b) i=j=6, 3rd mode
(c) i=j=2, 2nd mode ; (d) i=j=3, 3rd mode
(e) i=j=3, 4th mode ; (f) i=j=4, 5th mode

4. Conclusions

In this paper, Novozhilov thin-shell theory and the Rayleigh-Ritz procedure have been applied to derive the frequency equations of a thin ring with a rectangular cross-section and a circumferential profile variation. Profile variations are represented, in the general way, by Fourier series functions and the method gives *quantitative* predictions of frequency splitting. The observed frequency splitting patterns are in agreement with previously published *qualitative* results. Numerical results have been presented for example cases in which the inner and outer profiles are nominally circular with superimposed single-harmonic variations in radius. The effects on frequency splitting of the harmonic number of the profile variation, and the amplitude and spatial phasing between the inner and outer surfaces have been investigated.

References

1. Love, A.E.H., ***A Treatise on the Mathematical Theory of Elasticity***, Dover Publications, New York, fourth edition, 1952.
2. Fox, C.H.J., A simple theory for the analysis and correction of frequency splitting in slightly imperfection rings. ***Journal of Sound and Vibration***, 1990, **142(2)**, 227-43.
3. Fox, C.H.J., Vibrating cylinder rate gyro: theory of operation and error analysis. ***Proceeding of DGON Symposium on Gyro Technology,*** Stuttgart, 1988, Chapter 5.
4. Charnley, T. and Perrin, R., Studies with an eccentric bell. ***Journal of Sound and Vibration***, 1978, **58(4)**, 517-25.
5. Perrin, R., Selection rules for the splitting of the degenerate pairs of natural frequencies of thin circular rings. ***Acustica***, 1971, **25**, 69-72.
6. Charnley, T. and Perrin, R., Perturbation studies with a thin circular ring. ***Acustica***, 1973, **28**, 139-46.
7. Valkering, T.P. and Charnley, T., Radial vibrations of eccentric rings. ***Journal of Sound and Vibration***, 1983, **86(3)**, 369-93.
8. Tonin, R.F. and Bies, D.A., Free vibration of circular cylinders of variation thickness. ***Journal of Sound and Vibration***, 1979, **62(2)**, 165-80.
9. Novozhilov, V.V., ***The Theory of Thin Shells***, P. Noordhoff Ltd., The Netherlands, 1959.
10. Kreyszig, E., ***Advanced Engineering Mathematics***, John Wiley & Sons, Inc., Singapore, 1993, pp. 569-71.
11. Hwang, R., Free vibrations of a thin ring having circumferential profile variations. ***Ph.D. Thesis, University of Nottingham, U.K.*** (in preparation)

FREE VIBRATION ANALYSIS OF TRANSVERSE-SHEAR DEFORMABLE RECTANGULAR PLATES RESTING ON UNIFORM LATERAL ELASTIC EDGE SUPPORT

D.J. Gorman
University of Ottawa
770 King Edward Ave.,
Ottawa, Canada K1N 6N5

ABSTRACT

Utilizing the Superposition Method a free vibration analysis is conducted for transverse-shear deformable rectangular plates resting on uniformly distributed lateral elastic edge support. Edges are free of moment. The thick isotropic Mindlin plate is utilized for illustrative purposes. The Mindlin equations are satisfied throughout. Typical computed results are plotted for a square plate.

INTRODUCTION

It is well accepted that classical rectangular plate boundary conditions denoted as simply supported or clamped are often not achieved in real structures. This is because of elasticity in the edge supports. Furthermore, in many rectangular plate installations elastic edge supports may be utilized intentionally. For this reason a number of studies of effects of elasticity in the edge supports on rectangular plate free vibration frequencies have been conducted and results published. Almost all of these studies have been devoted to the free vibration behaviour of thin isotropic plates. Studies by the author, related to this family of vibration problems, have been devoted to situations where elastic stiffness is uniformly distributed along the edges as well as cases where the stiffnesses are arbitrarily distributed. All of his studies have been conducted by means or the Superposition Method and in a fairly recent article he has demonstrated that all of these families are amenable to analytical type solutions [1].

In this paper we exploit the powerful Superposition Method to analyse the free vibration behaviour of transverse-shear deformable plates resting on uniform lateral elastic edge support. This represents a much more complicated problem than the thin isotropic plate problems discussed above. For our purposes we choose the thick shear-deformable Mindlin plate and base our solution on Mindlin theory.

In the interest of keeping the literature review up to date the recent publication

of SAHA, KAR, and DATTA [2] is drawn to the attention of the reader. They report on a study of thick Mindlin plates resting on edge supports with uniform lateral and rotational elasticity. They have employed a Rayleigh-Ritz energy approach. Plate lateral displacement is represented by a rather complicated set of Timoshenko beam functions, each extremity of each beam being attached to a local lateral and torsional spring. It will be seen that no such functions need be selected in the superposition approach adopted here. Another related paper is one by the present author dealing with Mindlin plates where lateral displacement along the plate edges is forbidden but uniform rotational elastic support is provided [3]. This problem is somewhat easier to solve since edge lateral displacement is forbidden and, unlike the present problem, mixed derivatives do not show up in the boundary condition formulation. This latter problem was shown to be amenable to solution by the modified Superposition-Galerkin Method which is extremely easy to use when it is applicable.

MATHEMATICAL PROCEEDURE

A solution to the present problem is obtained through the superposition of the eight edge-driven forced vibration solutions (building blocks) shown schematicaly in Figure 1. All of the non-driven edges have slip-shear support. This type of support, indicated in the figure by two small circles adjacent to the edge, implies that the edge is free of torsional moment and transverse shear forces. Furthermore, rotation of the plate cross-section along the edge is everywhere zero.

We begin by examining the first building block. Its driven edge is free of torsional moment, and rotation of the plate cross-section along this boundary is every where zero. This latter condition is indicated by two solid dots adjacent to the edge. Driving of this edge is accomplished by a distributed harmonic transverse shear force of circular frequency ω. The spatial distribution of the shear force is expressed as,

$$Q_\eta \mid_{\eta=1} = \sum_{m=1,2}^{k} E_m \cos (m-1)\, \pi \xi \qquad (1)$$

where k is the number of terms required in the series.

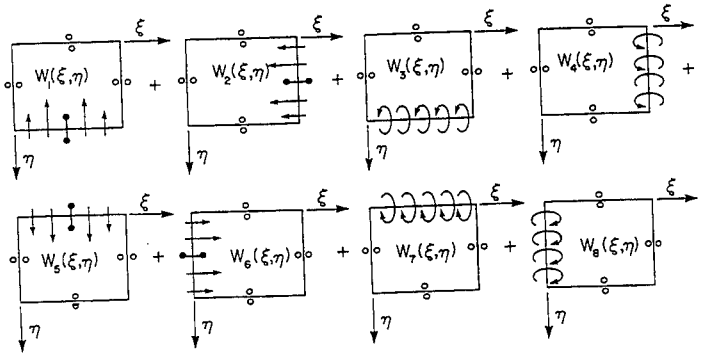

Fig. 1 Schematic representation of building blocks utilised in theoretical analysis.

We now examine the response of the above building block to this harmonic excitation. The proceedure followed is almost identical to that described in an earlier publication [4]. A concise description will be provided here for the sake of completeness.

The governing differential equations which control the response of thick Mindlin plates are written in dimensionless form as,

$$\frac{\partial^2 W}{\partial \xi^2} + \frac{1}{\phi^2}\frac{\partial^2 W}{\partial \eta^2} + \frac{\partial \psi_\xi}{\partial \xi} + \frac{1}{\phi}\frac{\partial \psi_\eta}{\partial \eta} + \frac{\lambda^4 \phi_h^2}{\nu_3} W = 0 \qquad (2)$$

$$\frac{\partial^2 \psi_\xi}{\partial \xi^2} + \frac{\nu_1}{\phi^2}\frac{\partial^2 \psi_\xi}{\partial \eta^2} + \frac{\nu_2}{\phi}\frac{\partial^2 \psi_\eta}{\partial \xi \partial \eta} - \frac{\nu_3}{\phi_h^2}\left(\psi_\xi + \frac{\partial W}{\partial \xi}\right) + \frac{\lambda^4 \phi_h^2}{12} W = 0 \qquad (3)$$

$$\frac{\partial^2 \psi_\eta}{\partial \xi^2} + \frac{1}{\phi^2 \nu_1}\frac{\partial^2 \psi_\eta}{\partial \eta^2} + \frac{\nu_2}{\phi \nu_1}\frac{\partial^2 \psi_\xi}{\partial \xi \partial \eta} - \frac{\nu_3}{\phi_h^2 \nu_1}\left(\psi_\eta + \frac{1}{\phi}\frac{\partial W}{\partial \eta}\right) + \frac{\lambda^4 \phi_h^2}{12 \nu_1} \psi_\eta = 0 \qquad (4)$$

Transverse shear forces, bending moments, etc., are written as,

$$Q_\xi = \psi_\xi + \frac{\partial W}{\partial \xi}, \qquad Q_\eta = \psi_\eta + \frac{1}{\phi}\frac{\partial W}{\partial \eta}$$

$$M_\xi = \frac{\partial \psi_\xi}{\partial \xi} + \frac{\nu}{\phi}\frac{\partial \psi_\eta}{\partial \eta}, \quad M_\eta = \frac{\partial \psi_\eta}{\partial \eta} + \nu\phi\frac{\partial \psi_\xi}{\partial \xi}, \quad M_{\xi\eta} = \frac{\partial \psi_\eta}{\partial \xi} + \frac{1}{\phi}\frac{\partial \psi_\xi}{\partial \eta} \tag{5}$$

When subjected to the first term of the driving force (Eqn 1) the response of the building block will be essentially that of a Timoshenko beam. The governing differential equations reduce to a set of two which may be written as

$$\frac{d^2 W}{d\eta^2} + \phi\frac{d^2 \psi_\eta}{d\eta^2} + \frac{\lambda^4 \phi^2 \phi_h^2 W}{\nu_3} = 0 \tag{6}$$

and

$$\frac{d^2 \psi_\eta}{d\eta^2} - \frac{\nu_3 \phi^2}{\phi_h^2}\left(\psi_\eta + \frac{1}{\phi}\frac{dW}{d\eta}\right) + \frac{\lambda^4 \phi^2 \phi_h^2 \psi_\eta}{12} = 0 \tag{7}$$

It is convenient to represent the lateral displacement W, and plate cross-section rotation as,

$$W(\eta) = X(\eta), \quad \text{and} \quad \psi_\eta(\eta) = Z(\eta)$$

The governing differential equations may then be written as

$$X''(\eta) + a_{m1} Z'(\eta) + b_{m1} X(\eta) = 0 \tag{8}$$

and

$$Z''(\eta) + a_{m3} X'(\eta) + b_{m5} Z(\eta) = 0 \tag{9}$$

where superscripts imply differentiation with respect to η. Coefficients

a_{m1} .... etc., are defined in reference [4].

Applying the appropriate differential operators to this set of equations the parameter X (η) is eliminated and a second order ordinary homogenous differential equation is obtained involving the parameter Z (η). It is found that for our range of interest the roots of the characteristic equation associated with this differential equation are always real. There are then three possible pairs of roots depending on the coefficients in the above differential equation. Designating these pairs of real roots as R_1 and R_2, three possible forms of solution exist as follows,

$$\text{Case 1, } R_1, R_2 < 0{\cdot}0 \quad \text{Case 2, } R_1 < 0{\cdot}0; R_2 > 0{\cdot}0 \quad \text{Case 3, } R_1, R_2 > 0{\cdot}0 \qquad \textbf{(10)}$$

In all work reported here it has been found that only, case 2, has been encountered.

It will be obvious that the functions X (η) and Z (η) must be symmetric with respect to the ξ axis. We may therefore write for case 2,

$$X(\eta) = A_m \cos \alpha\eta + B_m \cosh \beta\eta, \qquad \textbf{(11)}$$

and

$$Z(\eta) = A_m S_{m1} \cos \alpha\eta + B_m S_{m2} \cosh \beta\eta \qquad \textbf{(12)}$$

where $\alpha = \sqrt{|R_1|}$, and $\beta = \sqrt{|R_2|}$

Expressions S_{m1} and S_{m2} are obtained by taking advantage of the coupling of equations 8 and 9, as was done in Reference [4].

We then impose the boundary conditions, $Q_\eta = E_m$, and $\psi_\eta = 0$, at $\eta = 1$, in order to evaluate the unknowns A_m and B_m of Equation (11). Accordingly we obtain,

$$X(\eta) = \frac{E_m}{X2}\{\cos \alpha\eta + X1 \cosh \beta\eta\}, \qquad \textbf{(13)}$$

and

$$Z(\eta) = \frac{E_m}{X2}\left\{S_{m1} \sin \alpha\eta + X1 \; S_{m2} \sinh \beta\eta\right\}, \qquad (14)$$

where X1 and X2 are easily evaluated.

Next we examine the response of the first building block to driving terms where m>1. We follow the proceedure described in Reference [4].

Lévy type solutions for the parameters W, ψ_ξ ..... etc., are written as,

$$W(\xi,\eta) = X_m(\eta) \cos m\pi\xi \qquad (15)$$

$$\psi_\xi(\xi,\eta) = Y_m(\eta) \sin m\pi\xi \qquad (16)$$

$$\psi_\eta(\xi,\eta) = Z_m(\eta) \cos m\pi\xi \qquad (17)$$

It will be noted that all required boundary conditions along the edges, $\xi = 0$, and $\xi = 1$, are satisfied.

Next, the above expressions (Eqns 15, 16, 17) are substituted in the set of governing differential equations. The following set of coupled ordinary differential equations, written in matrix form are obtained

$$\begin{Bmatrix} X_m'' \\ Y_m'' \\ Z_m'' \end{Bmatrix} + \begin{bmatrix} 0 & 0 & a_{m1} \\ 0 & 0 & a_{m2} \\ a_{m3} & a_{m4} & 0 \end{bmatrix} \begin{Bmatrix} X_m' \\ Y_m' \\ Z_m' \end{Bmatrix} + \begin{bmatrix} b_{m1} & b_{m2} & 0 \\ b_{m3} & b_{m4} & 0 \\ 0 & 0 & b_{m5} \end{bmatrix} \begin{Bmatrix} X_m \\ Y_m \\ Z_m \end{Bmatrix} = \begin{Bmatrix} 0 \\ 0 \\ 0 \end{Bmatrix} \qquad (18)$$

Again, the quantities a_{m1} .... etc., are defined in Reference [4].

Applying the appropriate operators on the above equations, as was done in Reference [4] we are able isolate a single homogenous sixth order ordinary differential equation involving the dependent variable $Y_m(\eta)$, only. Because first, third, and fifth order derivates are missing from this equation the associated characteristic equation can be formulated as a cubic algebraic equation. Again it is found that for the range of the

present study all of the roots are real. Designating these roots as R_1, R_2, and R_3, it follows that four solution cases are possible depending on the coefficients of the characteristic equation. They are,

$$\begin{array}{ll} \text{Case 1, } R_1, R_2, \text{ and } R_3 < 0{\cdot}0 & \text{Case 2, } R_1, R_2 < 0{\cdot}0\,;\, R_3 > 0{\cdot}0 \\ \text{Case 3, } R_1 < 0{\cdot}0\,;\, R_2 \text{ and } R_3 > 0{\cdot}0 & \text{Case 4, } R_1, R_2 \text{ and } R_3 > 0{\cdot}0 \end{array} \quad (19)$$

In the present study only case 3, and case 4 are encountered. Introducing $\alpha = \sqrt{|R_1|}$, $\beta = \sqrt{|R_2|}$, and $\gamma = \sqrt{|R_3|}$ and recognizing that $Z_m(\eta)$ must be antisymmetric about the ξ axis while $X_m(\eta)$ and $Y_m(\eta)$ must be symmetric, we are able to write for case 4,

$$Y_m(\eta) = A_m \cosh \alpha\eta + B_m \cosh \beta\eta + C_m \cosh \gamma\eta \quad (20)$$

Utilizing the coupling of the ordinary differential equations, as in Reference [4], it follows that we may write,

$$X_m(\eta) = A_m R_{m1} \cosh \alpha\eta + B_m R_{m2} \cosh \beta\eta + C_m R_{m3} \cosh \gamma\eta \quad (21)$$

and

$$Z_m(\eta) = A_m S_{m1} \cosh \alpha\eta + B_m S_{m2} \cosh \beta\eta + C_m S_{m3} \cosh \gamma\eta \quad (22)$$

The quantities $R_{m1}, \ldots, S_{m1}, \ldots$ etc., are evaluated following steps described in Reference [4]. Expressions for $Y_m(\eta)$, $X_m(\eta)$, etc., for case 3 will differ from the above expressions only in that Cosh $\alpha\eta$ must be replaced by cos $\alpha\eta$.

The unknown constants A_m, B_m, etc., of the above solutions are evaluated by enforcement of boundary conditions along the edge, η=1. These conditions comprise zero torsional moment, zero edge rotation, with transverse shear force $Q_\eta = E_m$. For case 4 we obtain

$$Y_m(\eta) = \frac{E_m}{X3}\{\cosh \alpha\eta + X1 \cosh \beta\eta + X2 \cosh \gamma\eta\} \quad (23)$$

with the functions $X_m(\eta)$ and $Z_m(\eta)$ differing from $Y_m(\eta)$ only in that

R_{ml} and S_{ml}, etc., must be included.

We therefore now have the exact response of the first building block to the imposed driving force components available. It will be observed in Figure 1 that the second, fifth, and sixth building blocks differ from the first only in that they are driven along different edges. Solutions for their response are therefore easily extracted from that of the first.

Focusing our attention on the third building block we find that its driven edge is free of transverse shear forces and torsional moment. It is driven by a distributed cross-section harmonic rotation. The spacial distribution of this imposed driving rotation is also represented by the series of Equation 1.

The reader will appreciate that a solution for the third building block is obtained by following steps identical to those described for the first. Only the imposed boundary conditions along the driven edge differ. Solutions for the quantities W, ψ_ξ, etc., will be identical in form to those already developed for the first building block except that quantities X1, X2, etc., will be slightly different. We designate them as X1P, X2P, etc., for the edge-rotation driven building blocks. Solutions for the remaining four building blocks of Figure 1 are therefore available.

THE EIGENVALUE MATRIX

This matrix is shown schematicaly in Figure 2. It is generated following established practices. Let us first consider the transverse force equilibrium condition along the edge, $\eta = 1$. It is readily shown that this equilibrium condition is written in dimensionless form as,

$$Q_\eta + K_{Ll} W = 0 \qquad (24)$$

The plus sign of this equation must be replaced by a minus sign when we formulate the corresponding equations for the edges, $\eta=0$, and $\xi=0$.

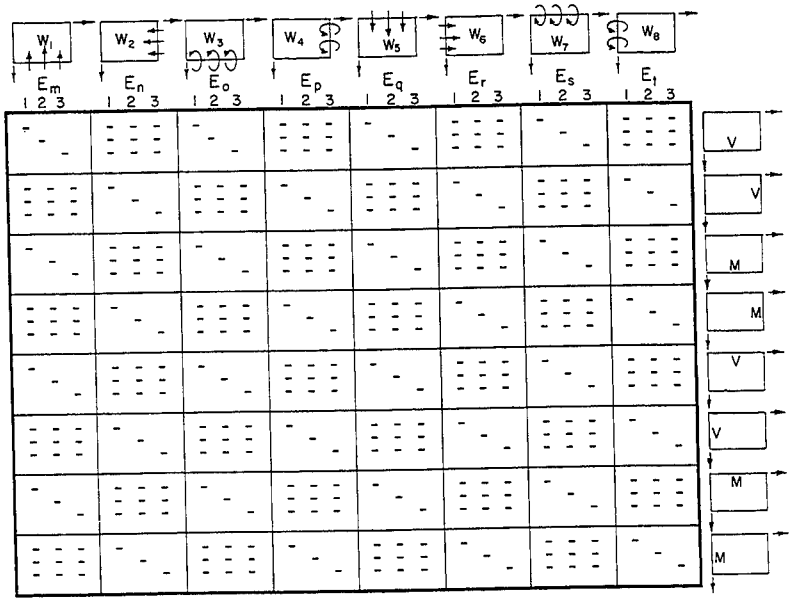

Fig. 2 Schematic representation of Eigenvalue matrix based on three-term function expansions. Short bars indicate non-zero elements. M or V on inserts to right indicate edges along which moment or lateral force equilibrium is enforced.

To construct the first three equations upon which this matrix is based we superimpose all eight building blocks and expand their net contribution to displacement W in a cosine series. The transverse shear force along the edge, η=1, is already available in such a series. We then express the left hand side of equation 24 in series form and require that each net coefficient in this series must vanish. This leads to 3 homogenous algebraic equations relating the 8 k unknowns where, for the illustrative matrix of Figure 2, k equals 3.

A second set of three homogenous algebraic equations is obtained by enforcing the corresponding lateral equilibrium condition along the edge,

$\xi = 1$. Moving down the matrix of Figure 2 it is seen that a third and fourth set of equations are obtained by enforcing the moment equilibrium condition, i.e., net bending moment equals zero along the same edges, in an identical fashion. Finally, it is seen in Figure 2 that four more sets of equations are obtained by enforcing the required equilibrium conditions along the edges, $\eta=0$, and $\xi=0$.

We thus have, in general, 8 k homogenous algebraic equations relating the 8 k unknown driving coefficients. The coefficient matrix of this total set of equations forms our Eigenvalue matrix.

Certain measures can be taken to greatly simplify and expedite generation of the matrix. It will be observed (Fig. 2) that the matrix is composed of 64 natural segments. This array of segments may be referred to through the indices (I, J). It is expedient to first generate the matrix without including contributions related to the driving shear forces along the building block edges (Eqn. 24). The matrix is then completed by adding the quantity 1.0 to diagonal elements of segments (1,1) and (2,2), and subtracting 1.0 from the diagonal elements of segments (5,5) and (6,6).

Physical reasoning leads also to another vast signification. One may begin by generating the elements of the matrix lying below the first four building blocks, only, (Fig. 2). Following a proceedure as discussed in Reference [4], and exercising caution with respect to necessary sign changes, all of the remaining segments of the matrix may be extracted from those already generated.

Eigenvalues are, of course, those values of the dimensionless frequency, λ^2, which cause the determinant of the Eigenvalue matrix to vanish. Mode shapes are obtained after setting one of the non-zero driving coefficients equal to zero and solving for the others.

PRESENTATION OF COMPUTED RESULTS

It will be appreciated that problems involving vast arrays of stiffness coefficients, plate aspect ratios, thickness-to-length ratios, etc. can be resolved by the proceedure described above. Only a single typical problem and its solution will be discussed here, for illustrative purposes.

We consider a square plate with equal dimensionless lateral elastic

stiffness imposed along each edge. Results are presented for two thickness-to-length ratios, 0.01, and 0.1. Two important observations may be made before examining these results. First, for the very thin plate of thickness-to-length ratio, 0.01, we expect the Eigenvalue vs edge-stiffness ratio curves to almost co-inside with those for a thin isotropic plate based on thin plate theory. Secondly, we recall that the Eigenvalue limits for a thin plate will equal 0.0, and 2 π^2, as the elastic stiffnesse approaches natural limits of 0.0, and infinity.

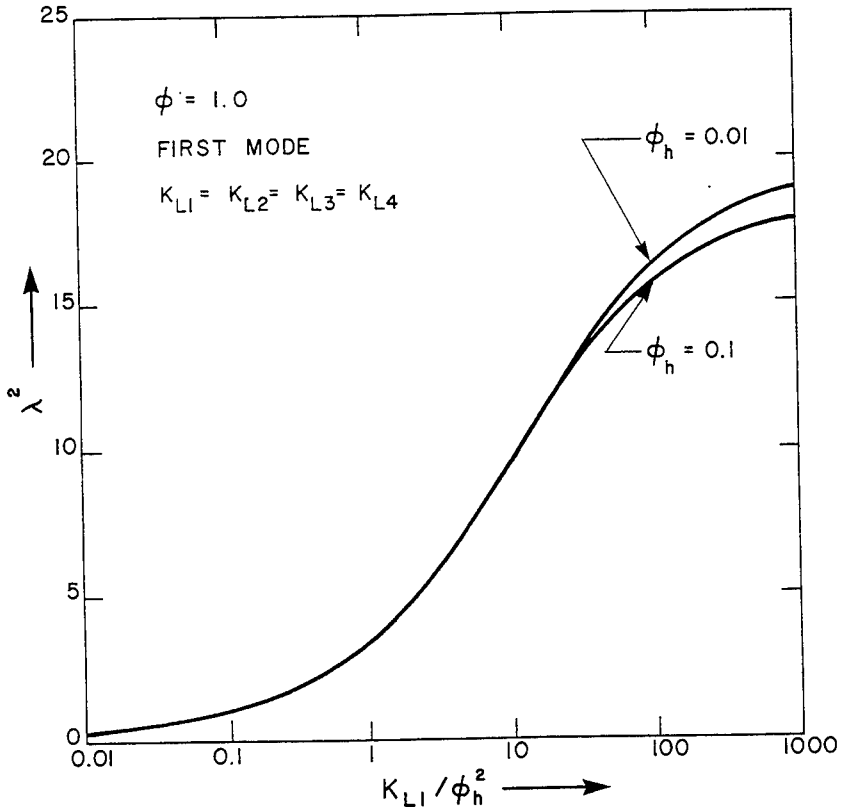

Fig. 3 Eigenvalues vs. Stiffness parameter for square plate first mode vibration with equal elastic support along all edges.

Results of a free vibration study of the above plate are presented in Figure 3. It will be noted that computed Eigenvalues are plotted against the parameter K_{L1} / ϕ_h^2. By presenting data in this manner it is found

that Eigenvalues for both the thick and the thin plate can be plotted on the same Figure. The absissa of the figure appears in five logarithmic decades. This range has been selected with a view to providing information for the reader over the region of greatest interest. It is found that in fact the thin-plate curve approaches the known limits disucssed above. Furthermore, utilizing computing schemes related to Reference [1], it has been shown that this same curve lies extremely close to that obtained for thin plates based on thin plate theory. Because Mindlin theory takes rotary inertia into effect and does not consider resistance to transverse-shear induced deformation to be infinite the thin plate curve of Figure 3 will lie only perceptably below that of its companion curve based on classical thin plate theory. The lower limit for the thicker plate curve of Figure 3 will also equal zero. However, the upper limit, equal to that of a simply supported thick Mindlin plate will lie below the classical value of $2\pi^2$. This is seen to be the case in Figure 3.

DISCUSSION AND CONCLUSIONS

The superposition technique is seen to constitute an accurate, straightforward technique for obtaining analytical type solutions to the problem of analysing free vibration of Mindlin plates resting on uniform lateral elastic edge support. Convergence is found to be rapid. The seven terms utilized here in representing building block solutions are found to be more than sufficient to provide four digit accuracy in computed Eigenvalues.

The reader will appreciate that the analysis described here could easily be modified to handle plates with lateral elastic support along less than four edges. Plates, for example, with two adjacent free edges and the other two given uniform lateral elastic edge support can easily be handled. It is only necessary to set the elastic stiffness coefficients equal to zero for the first two edges. It will also be appreciated that through proper choice of building blocks one can analyse plates with one or more edges resting on elastic support while the others are given various combinations of simply supported, clamped, or free boundary conditions. Natural extensions of the present analysis would lead to the solution of problems involving the same plates resting on arbitrarily distributed elastic edge support and combinations of lateral and rotational elastic support.

LIST OF SYMBOLS

a, b	Plate edge dimensions
D	$= E h^3/(12 (1 - \nu^2))$, Plate flexural rigidity
E	Youngs modulus of plate material
G	Modulus of elasticity in shear of plate material
h	Plate thickness
k_1, k_2, etc.,	Basic lateral spring stiffness along plate edge. Subscript 1 indicates edge, η=1. 2, 3, 4, indicate edges moving counter-clockwise from 1.
K_{L1}, K_{L2}, etc.,	Dimensionless lateral elastic edge coefficients, $= \frac{k_1 a w}{\kappa^2 G h}$, $\frac{k_2 a w}{\kappa^2 G h}$, etc.
M_ξ, M_η	Dimensionless bending moments associated with ξ and η directions, respectively
$M_{\xi\eta}$	Dimensionless twisting moment
Q_ξ, Q_η	Dimensionless shear forces associated with ξ and η directions, respectively.
W	Plate lateral displacement divided by side length a
ξ, η	Distances along plate co-ordinate axes divided by side lengths a, and b, respectively
κ^2	Mindlin shear factor = 0.8601
ν	Poisson ratio of plate material
ν_1	$= (1 - \nu)/2$
ν_2	$= (1 + \nu)/2$
ν_3	$= 6 \kappa^2 (1 - \nu)$
ϕ	Plate aspect ratio = b/a
ϕ_h	Plate thickness ratio = h/a

ψ_ξ, ψ_η	Plate cross-section rotations associated with ξ and η directions, respectively
ω	Circular frequency of plate vibration
λ^2	$= \omega a^2 \sqrt{\rho/D}$, Free Vibration Eigenvalue
ρ	Mass of plate per unit area

REFERENCES

1) Gorman, D.J., "A General Solution for the Free Vibration of Rectangular Plates with Arbitrarily Distributed Lateral and Rotational Elastic Edge Support", *Journal of Sound and Vibration*, 1994, Vol. (174), No. 4, 451-459.

2) Saha, K. N., Kar, R.C. , and Datta, P.K., "Free Vibration Analysis of Rectangular Mindlin Plates with Elastic Restraints Uniformly Distributed Along the Edges", *Journal of Sound and Vibration*, 1996, Vol. (192), No. 4, 885-904.

3) Gorman, D.J., "Accurate Free Vibration Analysis of Shear-Deformable Plates with Torsional Elastic Edge Support", to be published in Journal of Sound & Vibration.

4) Gorman, D.J., "Accurate Free Vibration Analysis of the Completely Free Rectangular Mindlin Plate", *Journal of Sound and Vibration*, 1996, Vol. (189), No. 3, 341-353.

Wave Equation Eigensolutions on Asymmetric Domains

R. G. Parker
Department of Mechanical Engineering
Ohio State University

C. D. Mote, Jr.
Vice Chancellor-University Relations, FANUC Chair in Mechanical Systems
Department of Mechanical Engineering
University of California, Berkeley

Introduction

The wave equation

$$\begin{aligned} -\nabla^2 q + q_{tt} &= f(x,y,t) \qquad \bar{P} \\ q + \beta q_n &= 0 \qquad \partial\bar{P} \end{aligned} \tag{1}$$

is arguably the most widely-studied differential equation in science and engineering. It is used to model physical systems in diverse fields such as acoustics, wave propagation, vibration, electromagnetics, fluid mechanics, heat transfer, and diffusion. Eigensolutions of the two-dimensional wave equation, governed by the Helmholtz equation, are the focus of this paper. We present a perturbation method to analytically calculate eigensolutions when asymmetric perturbations are present in the boundary conditions. The axisymmetric, annular domain case serves as the unperturbed problem. Possible boundary condition perturbations include deviation of the domain P from annular and variation of the parameter β along the boundary ∂P. The eigensolution perturbations are determined *exactly*, and their algebraic simplicity allows extension of the perturbation through fifth order. Both distinct and degenerate eigenvalues of the unperturbed problem are examined. Boundary condition asymmetry splits the degenerate unperturbed eigenvalues. We derive simple rules predicting this splitting at both first and second orders of perturbation. To illustrate the method and quantify its accuracy, the case of domain shape perturbation from circular is addressed in detail and comparisons are made with the exact solutions for elliptical and rectangular domains.

Methods used to analyze eigensolutions of the wave equation on irregular domains have been primarily numerical; for example finite element, finite difference and others. In addition to an extensive summary of theoretical results, Kuttler and Sigillito [1] provide a comprehensive review (142 references) of the application of these and other less popular methods. Mazumdar also reviews approximate methods invoked for this problem [2, 3, 4]. The above methods can be augmented by conformally mapping the irregular domain to a circle [5]. In the spirit of perturbation, Joseph [6] employed a parameter differentiation method to obtain derivatives of the distinct eigenvalues as the domain changes. The requirement of a smooth mapping function from the unperturbed domain to the irregular one and the restriction to distinct eigenvalues of the unperturbed problem limit its applicability. By assuming expressions for the lines of constant deflection in the fundamental eigenfunction, Mazumdar obtained estimates for the fundamental eigenvalue for arbitrarily shaped domains [7]. Accuracy of this method depends on the availability of a good estimate of the lines of constant deflection. Morse and Feshbach [8] used a perturbation analysis different than that presented herein to study the Helmholtz equation on irregular domains. Expansion of the eigenfunction perturbations in infinite series of the unperturbed eigenfunctions leads to a convergence problem restricting the analysis to second order perturbation in the eigenvalue and first order in the eigenfunction. Nayfeh used a perturbation formulation similar to that of this work to calculate the eigenvalue perturbation to first order; no eigenfunction perturbations are presented [9]. This work draws on the results of Parker and Mote [10, 11], where a formal procedure for obtaining exact eigensolution perturbations is developed.

Eigensolution Perturbation Formulation

The eigenvalue problem resulting from separation of the spatial and temporal dependence in (1) by the assumption $q = p(R,\theta)e^{i\Omega t}$ is

$$-\nabla^2 p - \Omega^2 p = 0 \qquad \bar{P} \tag{2a}$$

$$p + \beta p_n = 0 \qquad \partial\bar{P}: \partial\bar{P}_i \cup \partial\bar{P}_o \tag{2b}$$

where subscript n denotes the normal derivative. We examine two classes of asymmetry that normally preclude exact determination of the exact solution to (2): irregular $\bar{P}$ and variation of β along $\partial\bar{P}$. These asymmetries are treated as perturbations of the axisymmetric, annular domain eigenvalue problem.

(i) Irregular Domain Shape: The two-dimensional, doubly-connected domain $\bar{P}$ in Fig. 1 is $\bar{P}$: $\bar{R}_i(\theta) < R < \bar{R}_o(\theta)$, $0 \le \theta < 2\pi$. The deviations of the boundaries $\partial\bar{P}_i$ and $\partial\bar{P}_o$ from circular are

$$\varepsilon\bar{g}_i(\theta) \equiv R_i(\theta) - \bar{R}_i \qquad \varepsilon\bar{g}_o(\theta) \equiv R_o(\theta) - \bar{R}_o \tag{3}$$

where $\bar{R}_i$ and $\bar{R}_o$ are the average radii of the inner and outer boundaries. The variables q, p, and t of (1) and (2) are dimensionless; scaling the domain with the additional dimensionless variables

$$r = \frac{R}{\bar{R}_o} \qquad \gamma = \frac{\bar{R}_i}{\bar{R}_o} \qquad \bar{\omega} = \bar{R}_o\,\Omega \qquad \varepsilon g_o(\theta) = \frac{\varepsilon\bar{g}_o(\theta)}{\bar{R}_o} \qquad \varepsilon g_i(\theta) = \frac{\varepsilon\bar{g}_i(\theta)}{\bar{R}_o} \tag{4}$$

yields the eigenvalue problem for constant $\beta = \beta_o$

$$-\nabla^2 p - \bar{\omega}^2 p = 0 \qquad \hat{P} \tag{5a}$$

$$p + \beta_o p_n = 0 \qquad \partial\hat{P} \tag{5b}$$

where $\hat{P}$: $\gamma + \varepsilon g_i(\theta) < r < 1 + \varepsilon g_o(\theta)$, $0 \le \theta < 2\pi$.

Boundary quantities on $\partial\bar{P}$ are approximated by Taylor series expansion about $r = \gamma, 1$. For example,

$$p\,|_{r=1+\varepsilon g_o} = p\,|_{r=1} + (\varepsilon g_o)p_r\,|_{r=1} + 1/2!\,(\varepsilon g_o)^2 p_{rr}\,|_{r=1} + 1/3!\,(\varepsilon g_o)^3 p_{rrr}\,|_{r=1} + \cdots \tag{6}$$

A similar expansion is developed for $p\,|_{\partial\hat{P}_i}$. The expansions $p_n\,|_{\partial\hat{P}_i,o}$ require asymptotic expansion of p_n in terms of derivatives with respect to the polar coordinates r and θ [12]. Introduction of the expansions for p and p_n on $\partial\bar{P}$ into (5b) yields

$$-\nabla^2 p - \bar{\omega}^2 p = 0 \qquad P: \gamma \le r < 1,\ 0 \le \theta < 2\pi \tag{7a}$$

$$(p - \beta_o p_r) + \varepsilon\bar{C}p + \varepsilon^2\bar{D}p + \varepsilon^3\bar{E}p + \cdots = 0 \qquad r = \gamma \tag{7b}$$

$$(p + \beta_o p_r) + \varepsilon\hat{C}p + \varepsilon^2\hat{D}p + \varepsilon^3\hat{E}p + \cdots = 0 \qquad r = 1 \tag{7c}$$

where $\bar{C}, \bar{D}, \hat{C}, \hat{D}, \cdots$ are linear boundary operators with variable coefficients depending on $g_i(\theta)$ and $g_o(\theta)$.

(ii) Variable β along ∂P: For annular domains with $\beta \to \beta_o + \varepsilon\beta(\theta)$, the eigenvalue problem becomes

$$-\nabla^2 p - \bar{\omega}^2 p = 0 \qquad P: \gamma \le r < 1,\ 0 \le \theta < 2\pi \tag{8a}$$

$$(p - \beta_o p_r) - \varepsilon\beta(\theta)p_r = (p - \beta_o p_r) + \varepsilon\bar{C}p = 0 \qquad r = \gamma \tag{8b}$$

$$(p + \beta_o p_r) + \varepsilon\beta(\theta)p_r = (p + \beta_o p_r) + \varepsilon\hat{C}p = 0 \qquad r = 1 \tag{8c}$$

which is of form identical to (7).

We seek eigensolutions of (7) where the boundary perturbations may result from either or both of the asymmetries discussed above. The eigensolutions are represented as asymptotic series in the small parameter ε

$$\overline{\omega}^2 = \omega^2 + \varepsilon\mu + \varepsilon^2\eta + \varepsilon^3\kappa + \varepsilon^4\chi + \varepsilon^5\sigma + O(\varepsilon^6) \tag{9}$$

$$p = u + \varepsilon v + \varepsilon^2 w + \varepsilon^3 s + \varepsilon^4 t + \varepsilon^5 z + O(\varepsilon^6) \tag{10}$$

Subsequent analysis shows that confinement of the perturbation terms to the boundary conditions ensures that the Bessel and trigonometric forms of the eigenfunction perturbations in (10) do not depend on the boundary perturbations. Only the coefficients of these Bessel and trigonometric functions depend on the boundary condition operators. Because of this essential point, the method presented in the sequel for finding exact solutions for the eigensolution perturbations on irregular domains can be readily applied to find exact eigensolution perturbations for any problem of the form (7).

With the inner product $\langle e, f \rangle = \iint_P ef \, dA$, the normalization $\langle p, p \rangle = 1$ and (10) give

$$\langle u, v \rangle = 0 \quad \langle u, w \rangle = -\tfrac{1}{2}\langle v, v \rangle \quad \langle u, s \rangle = -\langle v, w \rangle$$
$$\langle u, t \rangle = -\langle v, s \rangle - \tfrac{1}{2}\langle w, w \rangle \tag{11}$$

The eigenvalue perturbations μ, η, κ, χ, and σ are determined subsequently in terms of the boundary conjunct $J(e, f)$

$$J(e, f) = \langle -\nabla^2 e, f \rangle - \langle e, -\nabla^2 f \rangle = \int_{\partial P} [ef_n - fe_n] \, d\hat{s} \tag{12}$$

Irregular Domain Eigensolution Perturbation

We demonstrate the solution procedure for eigenvalue problems of the form (7) by examining an irregularly-shaped domain with outer boundary ∂P and boundary condition $p|_{\partial P} = 0$. Use of (4) and (6) yields

$$-\nabla^2 p - \overline{\omega}^2 p = 0 \qquad P: 0 \le r < 1, 0 \le \theta < 2\pi \tag{13a}$$

$$p + \varepsilon g\, p_r + 1/2!(\varepsilon g)^2 p_{rr} + 1/3!(\varepsilon g)^3 p_{rrr} + 1/4!(\varepsilon g)^4 p_{rrrr} + 1/5!(\varepsilon g)^5 p_{rrrrr} = 0 \quad r = 1 \tag{13b}$$

where the subscript o denoting the outer boundary has been omitted. Substitution of (9, 10) into (13) yields the sequence of perturbation problems

$$-\nabla^2 u - \omega^2 u = 0 \qquad P \tag{14a}$$

$$u = 0 \qquad \partial P \tag{14b}$$

$$-\nabla^2 v - \omega^2 v = \mu u \qquad P \tag{15a}$$

$$v = -g\, u_r \qquad \partial P \tag{15b}$$

$$-\nabla^2 w - \omega^2 w = \mu v + \eta u \qquad P \tag{16a}$$

$$w = -gv_r - (1/2) g^2 u_{rr} \qquad \partial P \tag{16b}$$

$$-\nabla^2 s - \omega^2 s = \mu w + \eta v + \kappa u \qquad P \tag{17a}$$

$$s = -gw_r - (1/2) g^2 v_{rr} - (1/6) g^3 u_{rrr} \qquad \partial P \tag{17b}$$

$$-\nabla^2 t - \omega^2 t = \mu s + \eta w + \kappa v + \chi u \qquad P \tag{18a}$$

$$t = -gs_r - (1/2) g^2 w_{rr} - (1/6) g^3 v_{rrr} - (1/24) g^4 u_{rrrr} \qquad \partial P \tag{18b}$$

$$-\nabla^2 z - \omega^2 z = \mu t + \eta s + \kappa w + \chi v + \sigma u \qquad P \qquad (19a)$$

$$z = -gt_r - (1/2)g^2 s_{rr} - (1/6)g^3 w_{rrr} - (1/24)g^4 v_{rrrr} - (1/120)g^5 u_{rrrrr} \qquad \partial P \qquad (19b)$$

Solution of (14) gives the orthonormal unperturbed eigenfunctions

$$u_{m0} = \frac{1}{\pi^{1/2}} \frac{J_0(\omega_{m0} r)}{J_1(\omega_{m0})} = R_{m0}(r) \qquad m \geq 0 \qquad (20)$$

$$u_{mn}^{c,s} = \left[\frac{2}{\pi}\right]^{1/2} \frac{J_n(\omega_{mn} r)}{J_{n+1}(\omega_{mn})} \begin{Bmatrix} \cos n\theta \\ \sin n\theta \end{Bmatrix} = R_{mn}(r) \begin{Bmatrix} \cos n\theta \\ \sin n\theta \end{Bmatrix} \qquad m \geq 0,\ n > 0 \qquad (21)$$

where m and n denote the number of nodal circles and nodal diameters in the eigenfunction. The unperturbed eigenvalue ω_{mn} is the $(m+1)^{th}$ root of the characteristic equation $J_n(\omega) = 0$. ω_{mn} is a distinct eigenvalue for $n = 0$ and a degenerate eigenvalue of multiplicity two for $n \geq 1$. $u_{mn}^{c,s}$ are orthonormal eigenfunctions associated with the degenerate eigenvalues.

For the circular domain P, the boundary conjunct (12) is

$$J(e,f) = \int_0^{2\pi} [ef_r - fe_r]_{r=1}\, d\theta \qquad (22)$$

The following relations are used subsequently

$$R'_{m0}(1) = -\frac{\omega_{m0}}{\pi^{1/2}} \qquad R''_{m0}(1) = \frac{\omega_{m0}}{\pi^{1/2}} \qquad R'_{mn}(1) = -\left[\frac{2}{\pi}\right]^{1/2} \omega_{mn} \qquad R''_{mn}(1) = \left[\frac{2}{\pi}\right]^{1/2} \omega_{mn} \qquad (23)$$

$$g(\theta) = \sum_{j=1}^{\infty} g_j^c \cos j\theta + \sum_{j=1}^{\infty} g_j^s \sin j\theta \qquad (24)$$

$$G(\theta) = g^2(\theta) = G_0 + \sum_{j=1}^{\infty} G_j^c \cos j\theta + \sum_{j=1}^{\infty} G_j^s \sin j\theta \qquad (25)$$

Use of the Fourier representation (24) allows treatment of *arbitrary* boundary shapes, including kinked or discontinuous boundaries. The constant term in (24) vanishes because R is the average radius of the boundary.

Solution of Perturbation Equations

Distinct Eigenvalue Perturbation

Consider perturbation of a distinct unperturbed eigensolution (ω_{m0}, u_{m0}) (the subscript $m0$ will be omitted in the sequel). Using solvability conditions for the perturbation problems (15-19), Parker and Mote present formal expressions for the distinct eigenvalue perturbations in terms of the boundary conjunct [10, 11]

$$\mu = -J(u,v) \qquad \eta = -J(u,w) \qquad \kappa = -\mu\langle u, w\rangle - J(u,s) \qquad (26)$$

$$\chi = -\mu\langle u, s\rangle - \eta\langle u, w\rangle - J(u,t) \qquad \sigma = -\mu\langle u, t\rangle - \eta\langle u, s\rangle - \kappa\langle u, w\rangle - J(u,z)$$

1st Order Perturbation: The first order eigenvalue perturbation μ is evaluated from (26a), (22), (14b), (15b), (20), and (24)

$$\mu = \int_0^{2\pi} [u_r\, v]_{r=1}\, d\theta = -[R'_0(1)]^2 \int_0^{2\pi} g\, d\theta = 0 \qquad (27)$$

The result $\mu = 0$ substantially simplifies subsequent calculations. It results because the radius of the unperturbed circular domain is the mean radius of the irregular domain.

In their treatment of boundary shape perturbation of the Helmholtz equation, Morse and Feshbach [8] noted convergence difficulties when the eigenfunction perturbation is expanded in a series of the unperturbed eigenfunctions. For the similar case of plate boundary shape perturbation, Parker and Mote [12] encountered a divergent series for the second order eigenvalue perturbation when the first order eigenfunction perturbation is expanded in a series of the unperturbed eigenfunctions. These problems do not occur when the exact solution for the eigenfunction perturbation is determined. Furthermore, the exact solution is more accurate, computationally efficient, and notationally convenient than the infinite series expansion. In the sequel, exact eigenfunction perturbation solutions are determined through fourth order perturbation, thereby allowing exact calculation of the fifth order eigenvalue perturbation.

The eigenfunction perturbation $v(r,\theta)$ is decomposed as

$$v = c\,u + v^h + v^p \tag{28}$$

The first term results because u is a non-trivial solution of the homogeneous form of (15a,b); c is a constant to be determined. The second term is the general solution of the homogeneous form of (15a). The third term of (28) is a particular solution of the inhomogeneous equation (15a). Because of (27),

$$v^p = 0 \tag{29}$$

Additionally,

$$v^h = \sum_{j=1}^{\infty} J_j(\omega r)\,[B_j \cos j\theta + C_j \sin j\theta] \tag{30}$$

where the $j = 0$ term is omitted because its contribution is included in the first term of (28). The coefficients in (30) are calculated from (15b)

$$B_j = \frac{\omega\, g_j^c}{\pi^{1/2} J_j(\omega)} \qquad C_j = \frac{\omega\, g_j^s}{\pi^{1/2} J_j(\omega)} \tag{31}$$

where g_j^c and g_j^s are from (24). Substitution of (28) into the normalization condition (11a) yields

$$c = -\langle u, v^h + v^p \rangle = 0 \tag{32}$$

and the solution for v is complete.

2nd Order Perturbation: The second order eigenvalue perturbation η is evaluated from (26b), (22), (14b), (16b), (20), (28-32), (24), and (25)

$$\eta = \int_0^{2\pi} [u_r(-gv_r - \tfrac{1}{2}g^2 u_{rr})]_{r=1}\, d\theta = \omega^2 \left\{ G_0 + \sum_{j=1}^{\infty} [j - \omega \frac{J_{j+1}(\omega)}{J_j(\omega)}]\,[(g_j^c)^2 + (g_j^s)^2] \right\} \tag{33}$$

The solution to (16) is decomposed as

$$w = d\,u + w^h + w^p \tag{34}$$

where the definitions of the terms in (34) are analogous to those in (28), and

$$w^p = -\frac{\eta r}{(4\pi)^{1/2}\omega} \frac{J_1(\omega r)}{J_1(\omega)} \tag{35}$$

$$w^h = \sum_{j=1}^{\infty} J_j(\omega r)\,[E_j \cos j\theta + F_j \sin j\theta] \tag{36}$$

The coefficients E_j and F_j in (36) are determined from (16b)

$$E_j = -\frac{\omega}{(4\pi)^{1/2} J_j(\omega)} \left[G_j^c + \sum_{m=1}^{\infty} [m - \omega \frac{J_{m+1}(\omega)}{J_m(\omega)}] \left\{ \begin{array}{ll} g_m^c(g_{m+j}^c + g_{m-j}^c) + g_m^s(g_{m+j}^s + g_{m-j}^s) & m > j \\ g_m^c(g_{m+j}^c + g_{j-m}^c) + g_m^s(g_{m+j}^s - g_{j-m}^s) & m < j \\ g_m^c\, g_{2m}^c + g_m^s\, g_{2m}^s & m = j \end{array} \right. \right]$$

$$F_j = -\frac{\omega}{(4\pi)^{1/2} J_j(\omega)} \left[G_j^s + \sum_{m=1}^{\infty} [m - \omega \frac{J_{m+1}(\omega)}{J_m(\omega)}] \begin{cases} g_m^c (g_{m+j}^s - g_{m-j}^s) - g_m^s (g_{m+j}^c - g_{m-j}^c) & m > j \\ g_m^c (g_{m+j}^s + g_{j-m}^s) - g_m^s (g_{m+j}^c - g_{j-m}^c) & m < j \\ g_m^c g_{2m}^s - g_m^s g_{2m}^c & m = j \end{cases} \right]$$

From the normalization (11b),

$$d = -\tfrac{1}{2} \langle v, v \rangle - \langle u, w^p \rangle \tag{37}$$

$$= -\frac{\omega^2}{2} \sum_{m=1}^{\infty} \left[1 - \frac{2m}{\omega} \frac{J_{m+1}(\omega)}{J_m(\omega)} + \frac{J_{m+1}^2(\omega)}{J_m^2(\omega)} \right] [(g_m^c)^2 + (g_m^s)^2] - \frac{\eta}{2\omega^2}$$

The particular solution (35) is the critical component of the solution (34). With w^p known, calculation of E_j and F_j is straightforward for any perturbed boundary conditions (7b,c).

Equations (27-37) provide exact, closed-form expressions for both the eigenvalue and eigenfunction perturbations through second order. Their simplicity is remarkable given that they apply for an *arbitrary* deviation in boundary shape.

3rd Order Perturbation: The third order eigenvalue perturbation (26c) is

$$\kappa = -J(u, s) = \int_0^{2\pi} [u_r (-g w_r - \tfrac{1}{2} g^2 v_{rr} - (1/6) g^3 u_{rrr})]_{r=1} d\theta \tag{38}$$

Derivation of a closed-form expression for κ is analogous to (33) and straightforward. The value of the expression is minimal, however, because (38) can be evaluated easily using computer algebra software for a specified $g(\theta)$. Little insight can be gained from the algebraic details at third order perturbation.

The third order eigenfunction perturbation $s(r, \theta)$ is

$$s = e\, u + s^h + s^p \tag{39}$$

A particular solution for the κu term in (17a) is known by analogy with (35)

$$s_1^p = -\frac{\kappa r}{(4\pi)^{1/2} \omega} \frac{J_1(\omega r)}{J_1(\omega)} \tag{40}$$

A particular solution associated with the ηv term of (17a) is

$$s_2^p = -\frac{\eta r}{2\omega} \sum_{j=1}^{\infty} J_{j+1}(\omega r) [B_j \cos j\theta + C_j \sin j\theta] \tag{41}$$

Finally,

$$s^p = s_1^p + s_2^p \tag{42}$$

As in (30) and (36),

$$s^h = \sum_{j=1}^{\infty} J_j(\omega r) [H_j \cos j\theta + L_j \sin j\theta] \tag{43}$$

where numerical evaluation of H_j and L_j for specified $g(\theta)$ is readily achieved. e in (39) is found from (11c)

$$e = -\langle v, w \rangle - \langle u, s^p \rangle \tag{44}$$

4th Order Perturbation: The fourth order eigenvalue perturbation χ is found from (26d)

$$\chi = -\eta d + \frac{\eta^2}{2\omega^2} - J(u, t) \tag{45}$$

The fourth order eigenfunction perturbation $t(r,\theta)$ is

$$t = f\,u + t^h + t^p \tag{46}$$

Expansion of (18a) yields

$$-\nabla^2 t - \omega^2 t = (\chi + \eta d)\,u + \kappa v^h + \eta w^h + \eta w^p \qquad P \tag{47}$$

A particular solution of (47) is

$$t^p = t_1^p + t_2^p + t_3^p + t_4^p \tag{48}$$

$$t_1^p = -\frac{(\chi + \eta d)\,r}{(4\pi)^{1/2}\omega}\,\frac{J_1(\omega r)}{J_1(\omega)} \tag{49}$$

$$t_2^p = -\frac{\kappa r}{2\omega}\sum_{j=1}^{\infty} J_{j+1}(\omega r)\,[B_j \cos j\theta + C_j \sin j\theta] \tag{50}$$

$$t_3^p = -\frac{\eta r}{2\omega}\sum_{j=1}^{\infty} J_{j+1}(\omega r)\,[E_j \cos j\theta + F_j \sin j\theta] \tag{51}$$

$$t_4^p = -\frac{\eta^2 r}{(64\pi)^{1/2}\omega^3 J_1(\omega)}\,[\omega r J_0(\omega r) - 2J_1(\omega)] \tag{52}$$

t_4^p is the only 'new' particular solution not determined by analogy with previous particular solutions. Coefficients of t^h are calculated from (18b). The normalization (11d) gives

$$f = -\tfrac{1}{2}\langle w, w\rangle - \langle v, s\rangle - \langle u, t^p\rangle \tag{53}$$

5th Order Perturbation: From (26e), the fifth order eigenvalue perturbation σ is

$$\sigma = -\eta e - \kappa d + \frac{\eta\kappa}{\omega^2} - J(u,z) \tag{54}$$

Degenerate Eigenvalue Perturbation

Consider perturbation of a degenerate unperturbed eigenvalue ω_{mn} and the associated n nodal diameter orthonormal eigenfunctions $u_{mn}^{c,s}$ (21) (the subscript mn will henceforth be omitted). Because of the eigenvalue degeneracy, the unperturbed eigenfunction u is an element in the linear space spanned by u^c and u^s

$$u = a_c\,u^c + a_s\,u^s \tag{55}$$

a_c and a_s are determined subsequently. The normalization $\langle u, u\rangle = 1$ requires

$$a_c^2 + a_s^2 = 1 \tag{56}$$

Boundary condition asymmetry splits the degenerate unperturbed eigenvalue and fixes the coefficients a_c and a_s in (55). These effects *might* occur at first order perturbation, though, if not, they are predicted at some higher-order perturbation.

Because u^c and u^s are solutions of the homogeneous forms of (15-19), two solvability conditions must be satisfied at each order of perturbation. We follow the method of Parker and Mote [10].

1st Order Perturbation: The solvability conditions for (15) yield

$$a_c\,\mu = -J(u^c, v) \qquad a_s\,\mu = -J(u^s, v) \tag{57}$$

Evaluation of (57) yields a symmetric, algebraic eigenvalue problem

$$-\omega^2 \begin{bmatrix} g^c_{2n} & g^s_{2n} \\ g^s_{2n} & -g^c_{2n} \end{bmatrix} \begin{Bmatrix} a_c \\ a_s \end{Bmatrix} = \mu \begin{Bmatrix} a_c \\ a_s \end{Bmatrix} \quad \rightarrow \quad \mathbf{D}\,\mathbf{a} = \mu\,\mathbf{a}$$

$$\mu_{1,2} = \pm\omega^2 [(g^c_{2n})^2 + (g^s_{2n})^2]^{1/2} \tag{58}$$

The eigenvalues of $\mathbf{D}$ are the first order perturbations of ω. The eigenvectors of $\mathbf{D}$ fix the coefficients in (55). The degenerate eigenvalue splits into distinct eigenvalues as a result of boundary asymmetry if and only if the μ are distinct. The magnitude of μ for an n nodal diameter eigenvalue is proportional to $[(g^c_{2n})^2 + (g^s_{2n})^2]^{1/2}$. This leads to the splitting rule: If either or both of g^c_{2n} and g^s_{2n} are nonzero, the n nodal diameter eigenvalues split at first order perturbation; otherwise the eigenvalues remain degenerate. When no first order splitting occurs, $\mu = 0$ but a_c and a_s remain undetermined.

The eigenfunction perturbation $v(r, \theta)$ is decomposed as

$$v = c_c\, u^c + c_s\, u^s + v^h + v^p \tag{59}$$

where the first two terms result from the two independent solutions of the homogeneous form of (15). Particular and homogeneous solutions of (15a) are

$$v^p = \frac{\mu r}{(2\pi)^{1/2}\omega} \frac{J_{n+1}(\omega r)}{J_{n+1}(\omega)} (a_c \cos n\theta + a_s \sin n\theta) \tag{60}$$

$$v^h = \sum_{j=0, j\neq n}^{\infty} J_j(\omega r)[B_j \cos j\theta + C_j \sin j\theta] \tag{61}$$

where the $j = n$ term of (61) is included in the first terms of (59). Using (15b),

$$B_j = \frac{\omega}{(2\pi)^{1/2} J_j(\omega)} \begin{cases} a_c(g^c_{j+n} + g^c_{j-n}) + a_s(g^s_{j+n} - g^s_{j-n}) & j > n \\ a_c(g^c_{j+n} + g^c_{n-j}) + a_s(g^s_{j+n} + g^s_{n-j}) & j < n \\ a_c\, g^c_n + a_s\, g^s_n & j = 0 \end{cases} \tag{62a}$$

$$C_j = \frac{\omega}{(2\pi)^{1/2} J_j(\omega)} \begin{cases} a_c(g^s_{j+n} + g^s_{j-n}) - a_s(g^c_{j+n} - g^c_{j-n}) & j > n \\ a_c(g^s_{j+n} - g^s_{n-j}) - a_s(g^c_{j+n} - g^c_{n-j}) & j < n \end{cases} \tag{62b}$$

Coefficients c_c and c_s completing the solution (59) are calculated at second order perturbation, just as a_c and a_s of (55) are calculated at first order perturbation.

2nd Order Perturbation: The two solvability conditions for (16) and (11a) yield

$$\begin{bmatrix} \mu + \omega^2 g^c_{2n} & \omega^2 g^s_{2n} & \omega^2 a_c \\ \omega^2 g^s_{2n} & \mu - \omega^2 g^c_{2n} & \omega^2 a_s \\ \omega^2 a_c & \omega^2 a_s & 0 \end{bmatrix} \begin{Bmatrix} c_c \\ c_s \\ \eta/\omega^2 \end{Bmatrix} = \begin{Bmatrix} \dfrac{\mu^2(n+1)}{2\omega^2} a_c - \tilde{J}(u^c, w) \\ \dfrac{\mu^2(n+1)}{2\omega^2} a_s - \tilde{J}(u^s, w) \\ \dfrac{\mu(n+1)}{2} \end{Bmatrix} \tag{63}$$

$$\tilde{J}(u^c,w) = J(u^c,w)|_{c_c=c_s=0} = a_c\left\{ -\frac{\mu n}{2} g^c_{2n} - \omega^2(G_0 + \tfrac{1}{2}G^c_{2n}) - \frac{\omega^2}{2}\sum_{j=0,j\neq n}^{\infty}[j - \omega\frac{J_{j+1}(\omega)}{J_j(\omega)}]\alpha_j \right\} \tag{64a}$$
$$+ a_s\left\{ -\frac{\mu n}{2} g^s_{2n} - \omega^2(\tfrac{1}{2}G^s_{2n}) - \omega^2\sum_{j=0,j\neq n}^{\infty}[j - \omega\frac{J_{j+1}(\omega)}{J_j(\omega)}]\beta_j \right\} = a_c X + a_s Y$$

$$\tilde{J}(u^s,w) = J(u^s,w)|_{c_c=c_s=0} = a_c\left\{ -\frac{\mu n}{2} g^s_{2n} - \omega^2(\tfrac{1}{2}G^s_{2n}) - \omega^2\sum_{j=0,j\neq n}^{\infty}[j - \omega\frac{J_{j+1}(\omega)}{J_j(\omega)}]\beta_j \right\} \tag{64b}$$
$$+ a_s\left\{ -\frac{\mu n}{2} g^c_{2n} - \omega^2(G_0 + \tfrac{1}{2}G^c_{2n}) - \frac{\omega^2}{2}\sum_{j=0,j\neq n}^{\infty}[j - \omega\frac{J_{j+1}(\omega)}{J_j(\omega)}]\Gamma_j \right\} = a_c Y + a_s Z$$

$$\alpha_j = \begin{cases} (g^c_{j+n} + g^c_{j-n})^2 + (g^s_{j+n} + g^s_{j-n})^2 \\ (g^c_{j+n} + g^c_{n-j})^2 + (g^s_{j+n} - g^s_{n-j})^2 \\ 2(g^c_n)^2 \end{cases} \qquad \beta_j = \begin{cases} -g^c_{j+n}g^s_{j-n} + g^c_{j-n}g^s_{j+n} & j>n \\ g^c_{j+n}g^s_{n-j} + g^c_{n-j}g^s_{j+n} & j<n \\ g^c_n g^s_n & j=0 \end{cases}$$

$$\Gamma_j = \begin{cases} (g^c_{j+n} - g^c_{j-n})^2 + (g^s_{j+n} - g^s_{j-n})^2 \\ (g^c_{j+n} - g^c_{n-j})^2 + (g^s_{j+n} + g^s_{n-j})^2 \\ 2(g^s_n)^2 \end{cases} \qquad \delta_j = \begin{cases} g^c_{j+n}g^c_{j-n} + g^s_{j+n}g^s_{j-n} & j>n \\ g^c_{j+n}g^c_{n-j} - g^s_{j+n}g^s_{n-j} & j<n \\ \tfrac{1}{2}[(g^c_n)^2 - (g^s_n)^2] & j=0 \end{cases}$$

$\delta_j = (1/4)(\alpha_j - \Gamma_j)$ is used in (66). The operator in (63) is invertible if and only if the unperturbed eigenvalue splits at first order perturbation; c_c, c_s, and η are calculable from (63). If $g^c_{2n} = g^s_{2n} = 0$, then $\mu = 0$, the operator in (63) is singular, and a_c and a_s are unknown. In this case, the component equations of (63) yield

$$a_c\,\tilde{J}(u^s,w) - a_s\,\tilde{J}(u^c,w) = Y(a_c{}^2 - a_s{}^2) + (Z - X)a_c\,a_s = 0$$
$$\eta = -a_c\,\tilde{J}(u^c,w) - a_s\,\tilde{J}(u^s,w) = -X\,a_c{}^2 - 2Y\,a_c\,a_s - Z\,a_s{}^2 \tag{65}$$

where $X, Y,$ and Z are defined in (64). The first of (65) and (56) can be solved for two unique $\mathbf{a} = (a_c \;\; a_s)^T$ if and only if one or both of the following inequalities hold

$$Y \neq 0 \;\rightarrow\; \tfrac{1}{2}G^s_{2n} + \sum_{j=0,j\neq n}^{\infty}[j - \omega\frac{J_{j+1}(\omega)}{J_j(\omega)}]\beta_j \neq 0$$
$$X \neq Z \;\rightarrow\; \tfrac{1}{2}G^s_{2n} + \sum_{j=0,j\neq n}^{\infty}[j - \omega\frac{J_{j+1}(\omega)}{J_j(\omega)}]\delta_j \neq 0 \tag{66}$$

η is then calculated from (65b). Equations (66) are second order eigenvalue splitting rules: If either or both of (66) are satisfied, the n nodal diameter eigenvalues split at second order; otherwise they do not. When $Y = 0$ and $X = Z$, (65b) and (56) yield $\eta = -X = -Z$ while (65a) is identically satisfied. Thus, η is calculable despite the lack of second order splitting and the continuing indeterminacy of a_c, a_s. In the sequel, we assume the degenerate eigenvalues split at first order. If they do not, the development described by Parker and Mote [11] is required.

The second order eigenfunction perturbation $w(r,\theta)$ is

$$w = d_c\,u^c + d_s\,u^s + w^h + w^p \tag{67}$$

$$w_1^p = -\frac{r}{(2\pi)^{1/2}\omega}\frac{J_{n+1}(\omega r)}{J_{n+1}(\omega)}[(\mu c_c + \eta a_c)\cos n\theta + (\mu c_s + \eta a_s)\sin n\theta] \tag{68}$$

$$w_2^p = -\frac{\mu r}{2\omega}\sum_{j=0,j\neq n}^{\infty} J_{j+1}(\omega r)[B_j \cos j\theta + C_j \sin j\theta] \tag{69}$$

$$w_3^p = -\frac{\mu^2 r}{(32\pi)^{1/2}\omega^3 J_{n+1}(\omega)}[\omega r J_n(\omega r) - 2(n+1)J_{n+1}(\omega r)](a_c \cos n\theta + a_s \sin n\theta) \tag{70}$$

$$w^p = w_1^p + w_2^p + w_3^p \tag{71}$$

$$w^h = \sum_{j=0,j\neq n}^{\infty} J_j(\omega r)[E_j \cos j\theta + F_j \sin j\theta] \tag{72}$$

Components w_i^p are associated with the three inhomogeneities of (16a) resulting from an expansion analogous to (47). The particular solution (71) is the essential element allowing calculation of the E_j and F_j from (16b).

3rd Order Perturbation: The solvability conditions for (17) and (11b) give

$$\begin{bmatrix} \mu + \omega^2 g_{2n}^c & \omega^2 g_{2n}^s & \omega^2 a_c \\ \omega^2 g_{2n}^s & \mu - \omega^2 g_{2n}^c & \omega^2 a_s \\ \omega^2 a_c & \omega^2 a_s & 0 \end{bmatrix} \begin{Bmatrix} d_c \\ d_s \\ \kappa/\omega^2 \end{Bmatrix} = \begin{Bmatrix} -\mu\langle u^c, w^p\rangle - \eta\langle u^c, v\rangle - \tilde{J}(u^c, s) \\ -\mu\langle u^s, w^p\rangle - \eta\langle u^s, v\rangle - \tilde{J}(u^s, s) \\ -\omega^2[\tfrac{1}{2}\langle v, v\rangle + a_c\langle u^c, w^p\rangle + a_s\langle u^s, w^p\rangle] \end{Bmatrix} \tag{73}$$

The operator in (73) is identical to that in (63), and the assumption of first order eigenvalue splitting ensures its invertibility in the calculation of d_c, d_s, and κ.

The third order eigenfunction perturbation $s(r,\theta)$ is

$$s = e_c u^c + e_s u^s + s^h + s^p \tag{74}$$

$$s_1^p = -\frac{r}{(2\pi)^{1/2}\omega}\frac{J_{n+1}(\omega r)}{J_{n+1}(\omega)}[(\mu d_c + \eta c_c + \kappa a_c)\cos n\theta + (\mu d_s + \eta c_s + \kappa a_s)\sin n\theta] \tag{75}$$

$$s_2^p = -\frac{\eta r}{2\omega}\sum_{j=0,j\neq n}^{\infty} J_{j+1}(\omega r)[B_j \cos j\theta + C_j \sin j\theta] \tag{76}$$

$$s_3^p = -\frac{\mu\eta r}{(32\pi)^{1/2}\omega^3 J_{n+1}(\omega)}[\omega r J_n(\omega r) - 2(n+1)J_{n+1}(\omega r)](a_c \cos n\theta + a_s \sin n\theta) \tag{77}$$

$$s_4^p = -\frac{\mu r}{2\omega}\sum_{j=0,j\neq n}^{\infty} J_{j+1}(\omega r)[E_j \cos j\theta + F_j \sin j\theta] \tag{78}$$

$$s_5^p = -\frac{\mu r}{(32\pi)^{1/2}\omega^3 J_{n+1}(\omega)}[\omega r J_n(\omega r) - 2(n+1)J_{n+1}(\omega r)] \\ ((\mu c_c + \eta a_c)\cos n\theta + (\mu c_s + \eta a_s)\sin n\theta) \tag{79}$$

$$s_6^p = -\frac{\mu^2 r}{8\omega^3}\sum_{j=0,j\neq n}^{\infty}[\omega r J_j(\omega r) - 2(j+1)J_{j+1}(\omega r)](B_j \cos j\theta + C_j \sin j\theta) \tag{80}$$

$$s_7^p = \frac{\mu^3 r\,(n+2)}{(288\pi)^{1/2}\omega^4 J_{n+1}(\omega)}[rJ_n(\omega r) + \frac{r^2\omega^2 - 4(n+1)}{2\omega}J_{n+1}(\omega r)](a_c \cos n\theta + a_s \sin n\theta) \quad (81)$$

$$s^p = s_1^p + s_2^p + s_3^p + s_4^p + s_5^p + s_6^p + s_7^p \quad (82)$$

$$s^h = \sum_{j=0, j\neq n}^{\infty} J_j(\omega r)[H_j \cos j\theta + L_j \sin j\theta] \quad (83)$$

where the H_j, L_j follow from (17b).

4th Order Perturbation: From the solvability conditions for (18) and (11c)

$$\begin{bmatrix} \mu + \omega^2 g_{2n}^c & \omega^2 g_{2n}^s & \omega^2 a_c \\ \omega^2 g_{2n}^s & \mu - \omega^2 g_{2n}^c & \omega^2 a_s \\ \omega^2 a_c & \omega^2 a_s & 0 \end{bmatrix} \begin{Bmatrix} e_c \\ e_s \\ \chi/\omega^2 \end{Bmatrix} \quad (84)$$

$$= \begin{Bmatrix} -\mu<u^c, s^p> - \eta<u^c, w> - \kappa<u^c, v> - \tilde{J}(u^c, t) \\ -\mu<u^s, s^p> - \eta<u^s, w> - \kappa<u^s, v> - \tilde{J}(u^s, t) \\ -\omega^2[<v, w> + a_c<u^c, s^p> + a_s<u^s, s^p>] \end{Bmatrix}.$$

The presented boundary perturbation method applies for general boundary conditions of the form (7b,c). For annular domains, the Bessel function $Y_n(\omega_{mn} r)$ is included in (20, 21); particular solutions associated with this additional term are almost identical to those associated with $J_n(\omega_{mn} r)$ [10]. If different unperturbed boundary conditions are considered, the unperturbed eigenfunctions (20, 21) do not change form; only the normalization coefficients change. Consequently, the form of the right-hand side of (15a) is unchanged, and the particular solutions (29, 60) apply except for a change in their leading coefficients. Different first order boundary condition perturbations $\hat{C}$ and $\hat{C}$ change only the values of the coefficients B_j and C_j in (30, 61). Instead of (15b), these coefficients are determined by the general perturbed boundary condition (7c)

$$[v^h + \beta_o v_r^h]_{\partial P} = -\hat{C}u - [v^p + \beta_o v_r^p]_{\partial P} \quad (85)$$

Calculation of B_j and C_j is always possible by Fourier expansion of (85). Thus, the forms of v in (28) and (59) are unaffected by changes in either the perturbed or unperturbed boundary operators. As a result, only coefficients of the particular solutions (35, 71) change for different boundary conditions. This reasoning extends to higher order perturbations, and consequently the presented particular solutions admit exact eigensolution perturbations for general boundary condition perturbations.

Example Problems

The numerical accuracy achievable by the presented method is illustrated by modeling elliptical and rectangular domains with a circle.

Elliptical Domain

An elliptical domain of eccentricity $e = (1 - b^2/a^2)^{1/2}$ is described by

$$R = a\left[\frac{1 - e^2}{1 - e^2\cos^2\theta}\right]^{1/2} \quad (86)$$

where a and b are the semi-major and semi-minor axes, respectively (Fig. 2). The average radius $\bar{R}$ (3b) and the Fourier coefficients of $g(\theta)$ (24) are calculated by quadrature. Though R depends on a and e, $g(\theta)$ depends only on e. For an ellipse, $g_j^c = 0$ for j odd and $g_j^s = 0$ for all j. Eight non-trivial terms through g_{16}^c were used in the calculations.

The dimensionless, fundamental, elliptical domain eigenvalue $\Omega_{00}a$ of (2) evolves from the fundamental circular domain eigenvalue. (We identify the perturbed domain eigensolutions using subscripts mn denoting the number of nodal circles m and nodal diameters n in the circular domain eigensolutions from which the perturbed eigensolutions evolve.) Table 1 compares the fundamental eigenvalue predicted by

perturbation to the exact values computed by Daymond [13]. A maximum error of 0.32% is calculated for eccentricities through $e = 0.9 \rightarrow b/a = 0.4359$. For the extreme eccentricity $e = 0.9611 \rightarrow b/a = 0.28$, the perturbation results degrade substantially. Even without comparison with a known solution, the degradation is evident by the poor convergence of the perturbation with increasing order. For $e = 0.9611$, the asymptotic expansion (9) for the fundamental frequency is

$$\bar{\omega}^2 = 5.7831 + 0 + 5.1154 - 5.3966 + 4.7782 + 1.7258 \qquad (\Omega_{00}a) = \frac{\bar{\omega}}{\bar{R}_{a=1}} = \frac{3.4650}{0.47603} = 7.2790$$

In contrast, for $e = 0.9$

$$\bar{\omega}^2 = 5.7831 + 0 + 1.6774 - 0.6083 + 0.3098 - 0.0005 \qquad (\Omega_{00}a) = \frac{\bar{\omega}}{\bar{R}_{a=1}} = \frac{2.6761}{0.63284} = 4.2287$$

The agreement between perturbation and the exact values is illustrated in Fig. 3. Results for perturbation of the one nodal diameter circular domain eigenvalue are also given in Fig. 3, where the exact values were obtained by optically scanning Fig. 1 of Troesch and Troesch [14] and digitizing points through $e = 0.9$. Differences between the results so obtained and the perturbation values are all less than 3%, which is approximately the precision of the scanned and digitized results. Tabular results for the $(\Omega_{01}a)_{1,2}$ eigenvalues are presented in Table 1.

Rectangular Domain

Consider the rectangular domain of dimension $2a \times 2b$ where $\xi = b/a \leq 1$ (Fig. 4). The average radius R and the Fourier coefficients of $g(\theta)$ are calculated by quadrature. R depends on a and ξ, but $g(\theta)$ depends only on ξ. Also, $g_j^c = 0$ for j odd and $g_j^s = 0$ for all j. Ten non-trivial terms through g_{20}^c were used in the calculations (Fig. 4).

Table 2 compares the fundamental eigenvalue $\Omega_{00}a$ from perturbation to the exact value for $1 \geq \xi \geq 0.3$. Comparisons are shown for first through fifth order perturbation approximations. For a fifth order perturbation approximation, errors in the fundamental frequency are less than 0.5% for $\xi \geq 0.6$, 1.3% for $\xi = 0.5$, and 4.7% for $\xi = 0.4$. For $\xi = 0.3$, the error is 22.% and perturbation is not effective. The behavior of the asymptotic approximation (vertical column of Table 2) reveals a large expected error even in the absence of a known solution.

Substantial improvement in the predicted fundamental eigenvalue results when the perturbation is extended from first to second order. The accuracy obtainable from a second order perturbation is significant because the closed-form expression (33) gives η for an arbitrary shape perturbation. Improved accuracies are achieved with third order and fourth order perturbations. For rectangular domains, fifth order perturbation affords no increase in accuracy. Though the accuracy achieved using fourth or fifth order perturbation may not be needed, the higher order perturbations develop confidence in the convergence of the predicted eigensolutions through the decreased magnitude of the higher order terms.

Comparisons of perturbation predictions and exact eigenvalues are shown in Table 3 for rectangular domains. For square domains, all predicted values differ from the exact values by less than 1%, and the agreement is also excellent for $\xi = 0.95$ and $\xi = 0.9$. The lowest four eigenvalues provide excellent estimates for $\xi = 0.7, 0.8$, as shown in Fig. 5. Where the predicted and exact values differed substantially, the failure of the higher order perturbations to approach zero in the asymptotic expansion is evident.

It is interesting that two distinct circular domain eigenvalues can merge to form a degenerate eigenvalue pair on a square domain. For instance, the $(m,n) = (1,0)$ circular domain eigenvalue and one of the degenerate $(m,n) = (0,2)$ circular domain eigenvalues merge to form the degenerate eigenvalue pair $\Omega a = 4.9673$ in the square domain. In contrast, the degenerate eigenvalue pairs $\Omega a = 3.5124$ and $\Omega a = 5.6636$ in the square domain evolve from the degenerate eigenvalue pairs $(m,n) = (0,1)$ and $(m,n) = (0,3)$ in the circular domain. Perturbation predicts the splitting of the degenerate square domain eigenvalues (Fig. 5).

Conclusions

1. Eigensolutions of the wave equation with perturbations of the boundary conditions are derived by exact solution of the sequence of perturbation problems through fifth order. Perturbations of the domain from circular and variation of boundary condition parameters along the boundary curves are included in the class of perturbations for which the method applies. Exactness of the perturbation solutions means no approximation is introduced other than truncation of the asymptotic series (9, 10).

2. The derived solution offers a combination of analytical and computational advantages:
- exact perturbation through fifth order yields excellent accuracy for perturbations of substantial magnitude (such as the elliptical and rectangular domain perturbation examples);
- Fourier representation of the perturbations allows treatment of general continuous or discontinuous asymmetries;
- algebraic simplicity of the results permits convenient use of the eigensolutions in applications such as inverse and forced response problems;
- admissible functions as required in Ritz-Galerkin analysis are not needed;
- results are easily derived and verified using computer algebra software.

3. Rules governing splitting of the degenerate unperturbed eigenvalues are derived at both first and second orders of perturbation. These rules take simple algebraic forms in terms of the Fourier coefficients of a general asymmetry. The rule for first order eigenvalue splitting is such that it can be applied by inspection.

References

1. J. R. Kuttler and V. G. Sigillito, "Eigenvalues of the Laplacian in Two Dimensions," *SIAM Review*, vol. 26, pp. 163-193, 1984.
2. J. Mazumdar, "A Review of Approximate Methods for Determining the Vibrational Modes of Membranes," *Shock and Vibration Digest*, vol. 7, pp. 75-88, 1975.
3. J. Mazumdar, "A Review of Approximate Methods for Determining the Vibrational Modes of Membranes," *Shock and Vibration Digest*, vol. 11, pp. 25-29, 1979.
4. J. Mazumdar, "A Review of Approximate Methods for Determining the Vibrational Modes of Membranes," *Shock and Vibration Digest*, vol. 14, pp. 11-17, 1982.
5. S. B. Roberts, "The Eigenvalue Problem for Two-Dimensional Regions with Irregular Boundaries," *Journal of Applied Mechanics*, vol. 34, no. 3, pp. 618-622, 1967.
6. D. D. Joseph, "Parameter and Domain Dependence of Eigenvalues of Elliptic Partial Differential Equations," *Arch. Rat. Mech. Anal.*, vol. 24, pp. 325-351, 1967.
7. J. Mazumdar, "Transverse Vibration of Membranes of Arbitrary Shape by the Method of Constant-Deflection Contours," *Journal of Sound and Vibration*, vol. 27, pp. 47-57, 1973.
8. P. M. Morse and H. Feshbach, *Methods of Theoretical Physics*, McGraw-Hill, 1953.
9. A. H. Nayfeh, *Introduction to Perturbation Techniques*, pp. 426-431, J. Wiley & Sons, 1981.
10. R. G. Parker and C. D. Mote, Jr., "Exact Boundary Condition Perturbation Solutions in Eigenvalue Problems," *Journal of Applied Mechanics*, vol. 63, pp. 128-135, March 1996.
11. R. G. Parker and C. D. Mote, Jr., "Exact Higher-order Boundary Condition Perturbation in Eigenvalue Problems," *Journal of Applied Mechanics*, in preparation 1996.
12. R. G. Parker and C. D. Mote, Jr., "Exact Perturbation for the Vibration of Almost Annular or Circular Plates," *Journal of Vibration and Acoustics*, vol. 118, pp. 436-445, July 1996.
13. S. D. Daymond, "The Principal Frequencies of Vibrating Systems with Elliptic Boundaries," *Quart. Journ. Mech. and Applied Math*, vol. VIII, pp. 361-372, 1955.
14. B. A. Troesch and H. R. Troesch, "Eigenfrequencies of an Elliptic Membrane," *Mathematics of Computation*, vol. 27, pp. 755-765, 1973.

		$e=0.4$	$e=0.5$	$e=0.6$	$e=0.7$	$e=0.8$	$e=0.9$	$e=0.9611$
$\Omega_{00}a$	Exact	2.5165	2.5968	2.7202	2.9215	3.2933	4.2151	6.2432
	Pert. (5)	2.5165	2.5968	2.7202	2.9215	3.2936	4.2287	7.2790
	% Error	0.00%	0.00%	0.00%	0.00%	0.01%	0.32%	17.%
$(\Omega_{01}a)_1$	Pert. (4)	3.9212	3.9864	4.0878	4.2559	4.5726	5.3318	
$(\Omega_{01}a)_2$	Pert. (4)	4.0956	4.2822	4.5646	5.0154	5.8259	7.7601	

Table 1: Comparison of the fundamental elliptical domain eigenvaluecomputed using perturbation to the exact solution of Daymond [13]. Perturbed eigenvalues evolving from the 0 nodal circle, 1 nodal diameter circular domain eigenvalues are also presented. e denotes the eccentricity of the ellipse. Numbers in parentheses indicate the order of perturbation.

$\Omega_{00}a$	$\xi=1$	$\xi=0.9$	$\xi=0.8$	$\xi=0.7$	$\xi=0.6$	$\xi=0.5$	$\xi=0.4$	$\xi=0.3$
Exact	2.2214	2.3481	2.5145	2.7391	3.0531	3.5124	4.2295	5.4665
Pert. (5)	2.2243	2.3511	2.5183	2.7460	3.0665	3.5597	4.4293	6.6599
% Error	0.13%	0.13%	0.15%	0.25%	0.44%	1.3%	4.7%	22.%
Pert. (4)	2.2193	2.3455	2.5109	2.7325	3.0409	3.4797	4.1413	4.9888
% Error	-0.10%	-0.11%	-0.14%	-0.24%	-0.40%	-0.93%	-2.1%	-8.7%
Pert. (3)	2.2127	2.3394	2.5027	2.7230	3.0278	3.4672	4.0995	4.9403
% Error	-0.40%	-0.37%	-0.47%	-0.59%	-0.83%	-1.3%	-3.1%	-9.6%
Pert. (2)	2.2479	2.3753	2.5430	2.7700	3.0923	3.5830	4.4038	5.9903
% Error	1.2%	1.2%	1.1%	1.1%	1.3%	2.0%	4.1%	9.6%
Pert. (1)	2.1430	2.2608	2.4049	2.5859	2.8209	3.1400	3.6013	4.3353
% Error	-3.5%	-3.7%	-4.4%	-5.6%	-7.6%	-11.%	-15.%	-21.%

Table 2: Comparison of the fundamental rectangular domain eigenvalue computed using perturbation to exact values. $\xi = b/a$ denotes the aspect ratio of the rectangle. The numbers in parentheses indicate the order of perturbation.

$\Omega_{mn}a$									
(m, n)		$(0, 0)$	$(0, 1)_1$	$(0, 1)_2$	$(0, 2)_2$	$(0, 2)_1$	$(1, 0)$	$(0, 3)_1$	$(0, 3)_2$
$\xi=1$	Exact	2.2214	3.5124	3.5124	4.4429	4.9673	4.9673	5.6636	5.6636
	Pert.	2.2243	3.5081	3.5123	4.4322	4.9679	4.9656	5.7064	5.7071
	% Err.	0.13%	-0.12%	0.00%	-0.24%	0.01%	-0.03%	0.76%	0.76%
$\xi=0.95$	Exact	2.2806	3.5502	3.6610	4.5613	4.9941	5.2032	5.7569	5.8716
	Pert.	2.2836	3.5442	3.6553	4.5499	5.0136	5.2027	5.8693	5.8873
	% Err.	0.13%	-0.17%	-0.16%	-0.25%	0.39%	0.00%	2.0%	0.27%
$\xi=0.9$	Exact	2.3481	3.5939	3.8278	4.6962	5.0252	5.4665	5.8644	6.1062
	Pert.	2.3511	3.5879	3.8218	4.6831	4.9148	5.5454	6.1071	6.1390
	% Err.	0.13%	-0.17%	-0.16%	-0.28%	-2.2%	1.4%	4.1%	0.54%
$\xi=0.8$	Exact	2.5145	3.7047	4.2295	5.0290	5.1051	6.0963	6.1342	6.6759
	Pert.	2.5183	3.6984	4.2219	5.0063	5.0071	3.9446	6.6318	6.7169
	% Err.	0.15%	-0.17%	-0.17%	-0.45%	-1.9%	-35.%	8.1%	0.61%
$\xi=0.7$	Exact	2.7391	3.8607	4.7549	5.4783	5.2194	6.9128	6.5076	7.4289
	Pert.	2.7460	3.8493	4.7478	5.4315	8.7571	imag.	6.1737	7.0269
	% Err.	0.25%	-0.29%	-0.15%	-0.85%	68.%		-5.1%	-5.4%

Table 3: Comparison of rectangular domain eigenvalues from perturbation to exact values. $\xi = b/a$ is the aspect ratio. m and n are the numbers of nodal circles and nodal diameters in the circular domain eigenfunction from which the corresponding rectangular domain eigenfunction evolves.

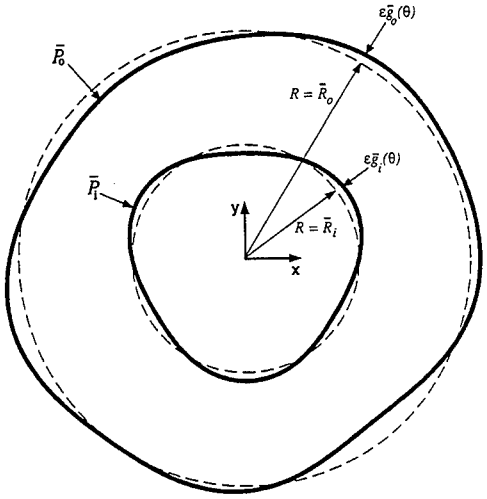

Figure 1: The dashed lines denote the annular domain for perturbation. The radii equal the average radii of the irregular boundaries.

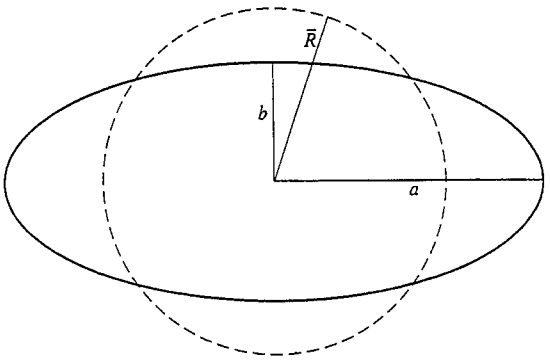

Figure 2: Ellipse of eccentricity e=0.9 (b/a=0.4359). The circle is the base domain for the perturbation. The radius of the circle equals the average radius of the ellipse.

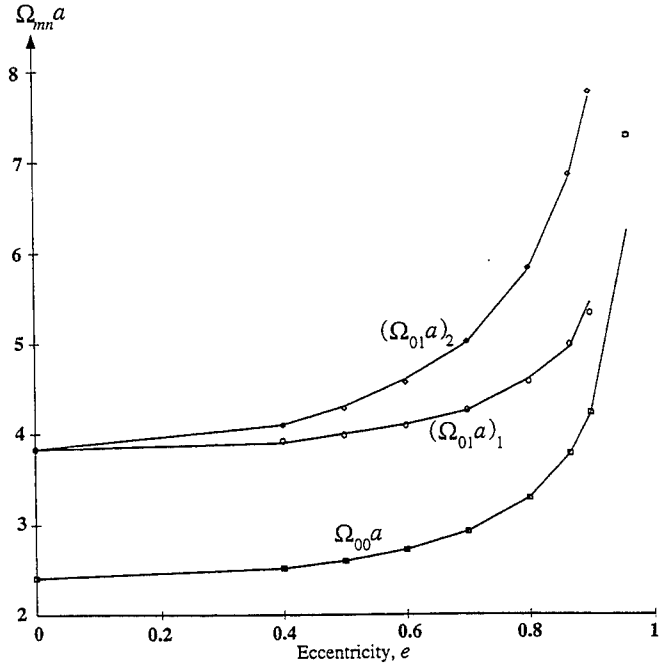

Figure 3: Elliptical domain eigenvalues. The subscript mn denotes the number of nodal circles (m) and nodal diameters (n) in the circular domain eigenvalue. a is the semi-major axis of the ellipse. The solid lines are from the exact solutions of Daymond [13] and Troesch and Troesch [14]. The symbols are values predicted by perturbation.

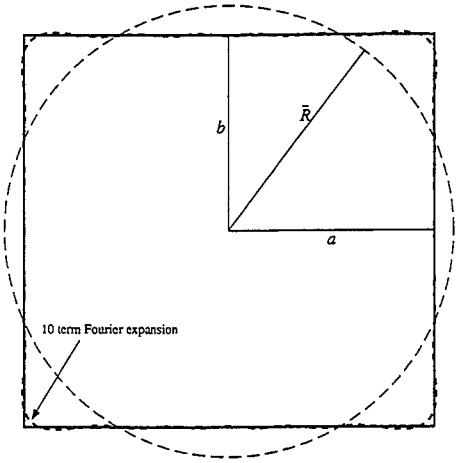

Figure 4: Rectangle of aspect ratio $\xi = 0.9$. The approximate rectangle is a 10 term Fourier approximation. The circle is the domain for perturbation.

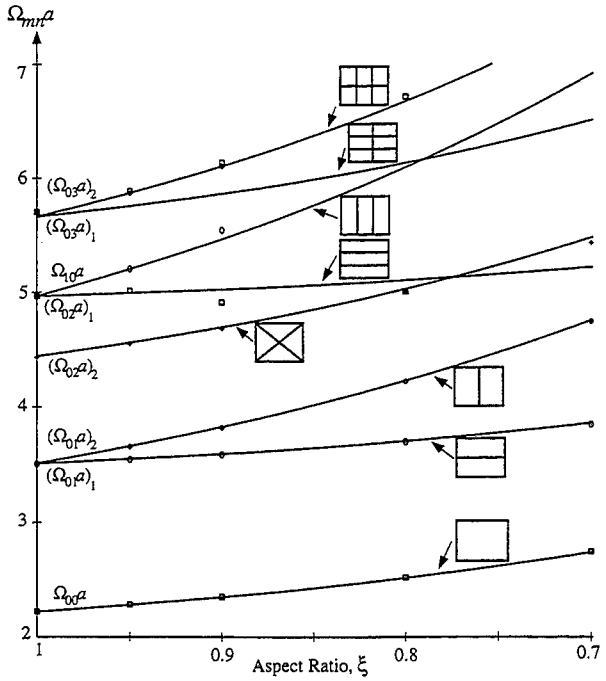

Figure 5: Eigenvalues of a rectangle with aspect ratio $\xi = b/a$. Solid curves denote exact values. Symbols denote values predicted by perturbation.

SUBSTRUCTURING FOR SYMMETRIC SYSTEMS

A.V. Pesterev

State Institute of Physics and Technology
13/7, Prechistenka St., Moscow, 119034 Russia
E-mail: sasha@pesterev.msk.ru

ABSTRACT

It is known that the problem of finding the spectrum of a complex conservative system with interaction of finite rank between its subsystems can be reduced to investigation of some symmetric characteristic matrix. If the system exhibits symmetries of one kind or another, the problem can be further simplified. It is shown how one can decompose the problem for a symmetric system by using results of the representation theory of groups. Considering a group of rigid symmetries of the system and its representation in the interaction space, one can obtain the spectrum of the system by investigating a number of reduced characteristic matrices, the sum of their orders being equal to the rank of the interaction.

1 INTRODUCTION

It is well known that the problem of finding dynamic characteristics of a complex structure consisting of distributed and/or finite-dimensional subsystems which interact at a finite number of points can be reduced to investigation of some matrix of relatively small order (see, e.g., [1–10] and references therein), which is sometimes referred to as the characteristic matrix. If the system exhibits symmetries of one kind or another, the problem can be simplified from the computational standpoint. The aim of this paper is to develop a technique for investigation of such systems. To facilitate discussions, we shall restrict our consideration to conservative systems. To reduce the original spectral problem to the problem of investigation of a characteristic matrix, we will apply the technique used in the structural analysis method [5, 6].

2 FORMULATION OF THE PROBLEM

Let us consider a linear complex mechanical system consisting of a finite number of distributed and/or finite-dimensional subsystems interacting at a finite number of points. Let us write the equation governing small stationary vibrations of jth isolated subsystem in the following operator form

$$A_j(\lambda)X_j = F_j\ ,\ j = 1,\ldots,R\ , \tag{1}$$

where F_j is a vector function of amplitudes of external harmonic generalized forces acting on the subsystem, X_j is an amplitude response vector function, $\lambda = \omega^2$, ω is a circular frequency, $A_j(\lambda)$ is a self-adjoint operator. In the case of a distributed subsystem, $A_j(\lambda)$ is a differential operator; for a finite-dimensional subsystem, it is given by a matrix.

Let the subsystems interact elastically at a finite number of points (e.g., they are connected to each other by means of a finite number of conservative springs). Let us denote by X the R-component vector function of responses of the system, the jth component of X being vector function X_j. Clearly, the interaction forces depend on displacements of only those points that take part in the interaction; i.e., they depend on some finite-dimensional vector $Y \in R^N$ rather than on response vector function X, which, in the general case, belongs to some functional space. Denote by S an operator transforming X into the vector Y: $Y = SX$. Let the interaction be given by a stiffness matrix K such that the amplitude vector of generalized interaction forces $F \in R^N$ is given by the equation: $F = -KY$. As the interaction is assumed to be conservative, the matrix K is positive semidefinite. To transform vector F into the right-hand sides of equations (1), the adjoint operator S^* is used (see [5, 6] for more detail). Assuming zero external forces, one arrives at the following equation governing free stationary vibration of the system under consideration

$$(A(\lambda) + S^*KS)X = 0\ , \tag{2}$$

where $A(\lambda)$ is a diagonal operator matrix $A(\lambda) = \mathrm{diag}[A_j(\lambda)\delta_{jk}]_{j,k=1}^{R}$ governing vibration of the aggregate of the non-interacting subsystems. The discrete spectrum of the system is defined to be the set of numbers λ such that equation (2) has non-trivial solutions. More detailed discussions concerning such a formulation of spectral problems, as well as some examples, are given in [5, 6].

It is well known (e.g., [1, 3–6]) that if operator $A^{-1}(\lambda)$ can be calculated, the problem of finding the spectrum can be reduced to the problem of investigating some characteristic matrix. The matrices can be defined differently, but all of them have an important property: if $A^{-1}(\lambda)$ exists, problem (2) has non-trivial solutions if, and only if, the characteristic matrix is singular.

In this paper, we will take advantage of the definition of the characteristic matrix used in the structural analysis method [5–7]. As the stiffness matrix K is positive semidefinite, it can be factored in the form [11]: $K = \alpha^T \alpha$, where α is $\widetilde{N} \times N$ matrix, and $\widetilde{N}$ is the rank of matrix K. The characteristic matrix of order $\widetilde{N}$ is then defined by the equation

$$Q(\lambda) = I + \alpha S A^{-1}(\lambda) S^* \alpha^T . \tag{3}$$

Properties of eigenvalues and eigenvectors of the matrix that guarantee finding all eigenfrequencies of the system in a given frequency range are discussed in [6]. To save room, we will not discuss here the ways of investigation of those values of λ at which $A^{-1}(\lambda)$ does not exist (detailed discussions of this case as applied to nonsymmetric structures can be found in [8, 9]), as this has no effect on the decomposition discussed.

Let now the subsystems (or part of them) be identical or can be divided into a few groups of identical ones and interact in such a way that the complex system exhibits symmetries of one kind or another. It is reasonable to suggest that these symmetries can be used to simplify the problem and also understand and classify solutions. The technique to be discussed in this paper allows one to decompose matrix (3) into a number of matrices of lesser orders such that the spectrum of the system can be obtained by investigating these matrices separately.

3 DECOMPOSITION OF THE INTERACTION SPACE

Let G be a group of symmetry of the immovable system, elements of the group $g \in G$ being either rotations or reflections that transform the system into itself. Clearly, as we consider systems with a finite number of interaction points, G can be only a finite group. For the same reason, we can consider a representation of the group in a finite-dimensional space. Actually, it follows from the results discussed in [5, 6] that at a given eigenfrequency ω_0 there is one-to-one relationship between eigenfunctions of the system and $\widetilde{N}$-dimensional vectors from the kernel of the matrix $Q(\omega_0^2)$ $\mathrm{Ker}\, Q(\omega_0^2)$. However, as $\widetilde{N}$-dimensional space come into existence as a result of a formal procedure of the factorization of the stiffness matrix K, it may be difficult to build a representation of the group in this space. There are two physical N-dimensional spaces relevant to the problem, namely, the space of displacements of the points at which the subsystems interact with each other and the space of generalized interaction forces. Either of them can be used to build a representation of the group. Let, for definiteness, it be the space of displacements $Y = SX$; we denote it by letter L and will call the "interaction" space. It is evident from general considerations that at a given eigenfrequency there exist one-to-one relationship

between the eigenfunctions of the system and vectors of the corresponding displacements of the connection points.

Let the system free vibrate at some eigenfrequency, and let $Y \in L$ be the corresponding vector of the displacements of the connection points. From this point on, we will call it, for brevity, the "eigenvector" of the system. Any rotation or reflection $g \in G$ transforms the eigenvibration into some, generally speaking, different eigenvibration, the eigenvector Y being transformed into some other eigenvector Y^g. Let us introduce linear operators (matrices) $T(g)$ by the equation: $T(g)Y = Y^g$, $g \in G$. Clearly, $T(g)$ is a real unitary representation of group G and can be constructed for any particular configuration of the interaction points and a given coordinate system.

As will be seen from the next section, the decomposition of the spectral problem can be obtained if we succeed in decomposing the space L into a number of mutually orthogonal real subspaces

$$L = L_1 + \cdots + L_m \tag{4}$$

such that any eigenvector of the system Y could be represented in the form $Y = \sum Y_j$, where $Y_j \in L_j$ is also an eigenvector of the system corresponding to the same eigenfrequency. In other words, we need such a decomposition that either an eigenvector Y belongs to a subspace L_j or (in the case of a multiple eigenfrequency) there exist such elements of the group g_k and real numbers β_k, which are not all zero, that $\sum_k \beta_k T(g_k)Y \in L_j$. Because of lack of room, we restrict our discussions to substantiating reasoning and give the results without proofs.

Let $T_1(g), \ldots, T_q(g)$ be real nonequivalent irreducible unitary representations of the group G and representation $T_j(g)$ of dimension r_j occurs m_j times in $T(g)$. The following lemma is valid.

Lemma 1 *For any given j, there exist such $g_k \in G$ and real numbers β_k, $k = 1, \ldots, r_j + 1$, that $\sum_k \beta_k T_j(g_k) = 0$.*

The proof is based upon application of Cayley–Hamilton theorem [11] to the matrix $T_j(g)$ with g being an element of a cyclic subgroup. It is well known [12] that the space L can be decomposed into $\sum_{i=1}^{q} m_i$ mutually orthogonal invariant subspaces each of which is transformed by one of the irreducible representations. Let us denote by L_j $(j = 1, \ldots, q)$ the direct sum of all invariant subspaces transformed by the representations equivalent to the real representation $T_j(g)$. Using Lemma 1, one can prove the following theorem.

Theorem 1 *For any eigenfrequency, an eigenvector Y either belongs to one of the subspaces L_j or can be represented in the form $Y = \sum Y_j$, where $Y_j \in L_j$ is also an eigenvector of the system. If an eigenvector of the system belongs to a subspace L_j, then the multiplicity of the eigenfrequency is equal to r_j.*

Thus, we have obtained the desired decomposition (4) of space L with m being equal to the number of real nonequivalent irreducible representations of point group G. To take advantage of decomposition (4), one needs projectors P_j onto the subspaces L_j : $P_jL = L_j$. The projector on the subspace L_j is given by the formula [12, Chapter 4]

$$P_j = \frac{r_j}{n} \sum_{g \in G} \chi_j(g) T(g) \,, \tag{5}$$

where n is the order of the group G, and $\chi_j(g)$ is the character of $T_j(g)$.

It turns out that under certain conditions some of subspaces L_j, which are transformed by representations whose dimensions are greater than one, can be decomposed in turn.

Theorem 2 *Let $T_j(g)$ be a real irreducible representation of a group G of dimension $r_j > 1$, and let there exist an element of the group g_0 of order r_j such that the matrix $T_j(g_0)$ has all different complex eigenvalues. Then the subspace L_j can be decomposed into p_j subspaces, where, for even r_j, $p_j = r_j/2 + 1$, and, for odd r_j, $p_j = (r_j + 1)/2$.*

The theorem allows one to obtain more subtle decomposition (4) with m being greater than the number of real irreducible representations.

Let us obtain formulas for projectors onto the subspaces of a decomposable subspace L_j. As mentioned above, L_j is the direct sum of subspaces L_j^k, $k = 1, \ldots, m_j$, transformed by the representations equivalent to $T_j(g)$. Let us consider for a while L_j^k as complex subspaces. It is evident that eigenvalues of the matrix $T_j(g_0)$ are numbers ζ^i, $i = 0, 1, \ldots, r_j - 1$, where ζ is a primitive r_j^{th} root of 1 ($\zeta^{r_j} = 1$). Let e_i^k be the corresponding eigenvectors of matrix $T_j(g_0)$ belonging to the subspace L_j^k. If $r_j > 2$, some vectors e_i^k are complex, and, for each complex vector e_i^k, there is its complex conjugate vector $\overline{e_i^k}$. Denote by $l_{j,i}^k$ ($i = 0, 1, \ldots, p_j - 1$) the subspace of L_j^k spanned either by vector e_i^k, if e_i^k is real, or by two vectors e_i^k and $\overline{e_i^k}$. Denote by $L_{j,i}$ the direct sum of subspaces $l_{j,i}^k$, $k = 1, \ldots, m_j$. It is the decomposition of L_j into p_j real subspaces $L_{j,i}$ that is established in Theorem 2.

Let us take the above eigenvectors e_i^k, $i = 0, 1, \ldots, r_j - 1$ for the orthonormal basis in subspace L_j^k and write the representation $T_j(g)$ in matrix form $T_j(g) = [t_{il}^j(g)]$, $i, l = 0, 1, \ldots, r_j - 1$, which is the same in all subspaces L_j^k, $k = 1, \ldots, m_j$. Using the results of [12, Chapter 4], one can obtain formulas for projectors $P_{j,i}$ on the subspaces $L_{j,i}$

$$P_{j,i} = \frac{r_j}{n} \sum_{g \in G} t_{ii}^j(g) T(g) \,, i = 0 \text{ and } i = p_j - 1 \text{ (for even } r_j) \,, \tag{6}$$

$$P_{j,i} = \frac{r_j}{n} \sum_{g \in G} (t_{ii}^j(g) + \overline{t_{ii}^j(g)}) T(g) \,, \text{otherwise.} \tag{7}$$

Note that the eigenvectors of the system $Y_{j,i} \in L_{j,i}$ exist or do not exist in all subspaces $L_{j,i}$ simultaneously, so that the multiplicity of the corresponding eigenfrequency of the system is equal to r_j as before.

4 DECOMPOSITION OF SPECTRAL PROBLEM

In the previous section, we have decomposed space L of displacements of the connection points. One could take for L the space of generalized interaction forces and obtain the same decomposition. It is not difficult to prove that if the system free vibrates and the corresponding eigenvector Y belongs to a subspace L_j then the corresponding vector of interaction forces $F = -KY$ also belongs to the same subspace L_j. This allows one to introduce matrices $K_j = P_j K P_j$, $j = 1, \ldots, m$, and consider m spectral problems of the form (2) in which the matrix K is replaced by K_j; here projector P_j is given either by formula (5) or by (6)–(7). Matrices K_j can also be presented in the factorized form: $K_j = \alpha_j^T \alpha$, where α_j is $\widetilde{N}_j \times N$ matrix, and $\widetilde{N}_j$ is the rank of K_j. Let us define, analogously to (3), matrices $Q_j(\lambda)$ of orders $\widetilde{N}_j$ by the formula

$$Q_j(\lambda) = I + \alpha_j S A^{-1}(\lambda) S^* \alpha_j^T . \tag{8}$$

It turns out that to obtain the spectrum of the system, one can investigate separately matrices $Q_j(\lambda)$ instead of one matrix $Q(\lambda)$. Let U_j be the set of values of λ such that matrix $Q_j(\lambda)$ exists and is singular. Denote by U the union of the sets U_j, $j = 1, \ldots, m$. If some λ occurs r times in U, we say that it has multiplicity r.

Theorem 3 *1. The sum of orders $\widetilde{N}_j$ of $Q_j(\lambda)$ is equal to the order $\widetilde{N}$ of $Q(\lambda)$.*

2. The set of the eigenvalues of the system different from those of the isolated subsystems coincide with the set U.

The eigenvalues of the isolated subsystems are investigated separately. The approach used in [5, 6, 8, 9] for nonsymmetric systems can be modified and applied to symmetric ones.

Remark. In the general case of a 3D structure consisting of several substructures, the subsystem points that take part in the interaction can be divided into a few independent groups, called "interaction sections," such that the interaction forces acting on the subsystems at the points belonging to a certain interaction section depend on displacements of only those points that belong to this interaction section. This subdivision of the interaction points into independent interaction sections implies a priori decomposition (not connected with the symmetry of the system) of the interaction space and results in a block-diagonal form of the stiffness matrix K (under an appropriate numbering of the interaction points). This

implies also that we can build representations of the group in different interaction sections separately.

5 PROJECTORS FOR THE GROUPS C_n AND C_{nv}

As an illustration, let us decompose the interaction space and calculate projectors for two cases of symmetry. First, consider a system having n-fold axis of symmetry such that rotations about the axis through angles $C_n^k = \frac{2\pi k}{n}$, $k = 0, 1, \ldots, n-1$, transform the system into itself. The rotations C_n^k form the cyclic abelian group C_n of order n. It has [12] n one-dimensional complex irreducible representations. Combining pairs of complex conjugate representations into real two-dimensional representations, one obtains m real irreducible representations, where, for even n, $m = n/2 + 1$, two representations being one-dimensional and the others being two-dimensional; for odd n, $m = (n+1)/2$, with one representation being one-dimensional. Calculating the characters of the representations and applying formula (5), one obtains formulas for the projectors onto the subspaces L_0 and $L_{n/2}$ (for even n) corresponding to the one-dimensional real representations

$$P_0 = \frac{1}{n}\sum_{k=0}^{n-1} T(C_n^k)\ ,\ P_{\frac{n}{2}} = \frac{1}{n}\sum_{k=0}^{n-1}(-1)^k T(C_n^k)\ \ (\text{even } n)\ , \tag{9}$$

and onto the subspaces L_j corresponding to the two-dimensional real representations

$$P_j = \frac{2}{n}\sum_{k=0}^{n-1}\cos(\frac{2\pi kj}{n})T(C_n^k)\ ,\ j = \begin{cases} 1, \ldots, \frac{n}{2}-1, & \text{for even } n, \\ 1, \ldots, \frac{n-1}{2}, & \text{for odd } n. \end{cases} \tag{10}$$

As a second example, let us consider the group of symmetry C_{nv}, which also describes symmetry arrangements with one n-fold axis. But apart from the rotations, there are n reflections transforming the system into itself. The order of the group is equal to $2n$. Let us choose the elements of the group as follows: $C_n^0 = e, C_n^1, \ldots, C_n^{n-1}, \sigma_v, \sigma_v C_n^1, \ldots, \sigma_v C_n^{n-1}$, where σ_v is a reflection in a certain symmetry plane passing through the n-fold symmetry axis. It is known [12] that for odd n this group has two one-dimensional ($T_{0,1}$ and $T_{0,2}$) and $(n-1)/2$ two-dimensional real nonequivalent irreducible representations. For even n, it has four one-dimensional ($T_{0,1}$, $T_{0,2}$, $T_{\frac{n}{2},1}$, and $T_{\frac{n}{2},2}$) and $(n-2)/2$ two-dimensional representations. Calculating the characters of the one-dimensional representations and applying formula (5), one obtains the projectors onto the subspaces corresponding to the one-dimensional representations

$$P_{0,1} = \frac{1}{2n}\sum_{k=0}^{n-1}\left(T(C_n^k) + T(\sigma_v C_n^k)\right), \tag{11}$$

$$P_{0,2} = \frac{1}{2n} \sum_{k=0}^{n-1} \left(T(C_n^k) - T(\sigma_v C_n^k) \right), \tag{12}$$

and (if n is even)

$$P_{\frac{n}{2},1} = \frac{1}{2n} \sum_{k=0}^{n-1} (-1)^k \left(T(C_n^k) + T(\sigma_v C_n^k) \right) , \tag{13}$$

$$P_{\frac{n}{2},2} = \frac{1}{2n} \sum_{k=0}^{n-1} (-1)^k \left(T(C_n^k) - T(\sigma_v C_n^k) \right) . \tag{14}$$

It is not difficult to show that bases in the spaces L_j corresponding to the two-dimensional representations $T_j(g)$ can be chosen in such a way that the matrices $T_j(\sigma_v)$ are diagonal: $T_j(\sigma_v) = \mathrm{diag}[1, -1]$. This means that the two-dimensional representations $T_j(g)$ satisfy the conditions of Theorem 2 with $g_0 = \sigma_v$, and, hence, each of the subspaces L_j can be decomposed into the sum of two real subspaces $L_j = L_{j,0} + L_{j,1}$. Applying formula (6), one obtains the projectors onto the subspaces $L_{j,0}$ and $L_{j,1}$:

$$P_{j,0} = \frac{1}{n} \sum_{k=0}^{n-1} \cos(\frac{2\pi kj}{n}) \left(T(C_n^k) + T(\sigma_v C_n^k) \right) , \tag{15}$$

$$P_{j,1} = \frac{1}{n} \sum_{k=0}^{n-1} \cos(\frac{2\pi kj}{n}) \left(T(C_n^k) - T(\sigma_v C_n^k) \right) , \tag{16}$$

where

$$j = \begin{cases} 1, \ldots, \frac{n-2}{2}, & \text{for even } n, \\ 1, \ldots, \frac{n-1}{2}, & \text{for odd } n. \end{cases}$$

6 AN EXAMPLE OF CONSTRUCTION OF A REPRESENTATION

In the previous section, we obtained formulas (9)–(16) for the projectors for the symmetry groups C_n and C_{nv}. To take advantage of these formulas for a given symmetric structure, it is required only to construct a representation of the group in the corresponding interaction space. The aim of this section is to demonstrate, by way of a simple example, how such a representation can be constructed.

Let a symmetric structure consist of seven interacting subsystems, and let its symmetry be described by the group C_{6v}. Let the 6-fold axis of symmetry be perpendicular to the plane of the sheet. Keeping in mind Remark in Section 4, let us consider one interaction section of the system. Let the interaction points belonging to this section be located at the vertices of a regular hexagon as shown in Fig. 1. Here the circles denote the interaction (connection) points of the subsystems belonging to

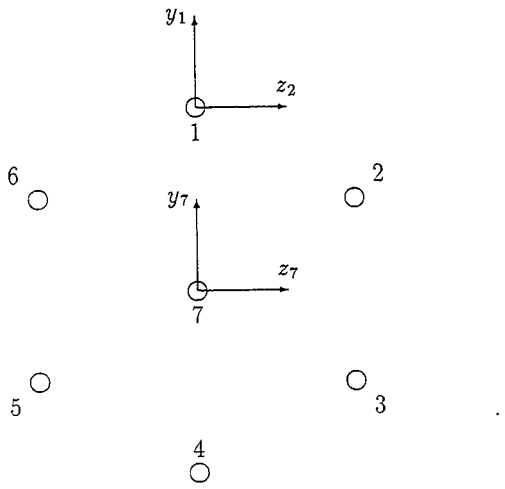

Fig. 1: An interaction section for a system with C_{6v} symmetry group

the considered interaction section. The kind of the subsystems (finite- or infinite-dimensional) is of no concern at this stage, since a representation is constructed in a finite-dimensional interaction space. Note, however, that the configuration shown in Fig. 1 could represent, e.g., a section of a bundle of seven identical 3D beams by a plane perpendicular to the longitudinal axes of the beams.

Let the points be connected to each other through some springs, and the interaction be described by a stiffness matrix of interaction K. To construct a representation, a particular configuration of springs is of no importance. It is required only that this configuration satisfy the same symmetry conditions. That is, the system of springs transforms into itself under any rotations and reflections belonging to the considered group C_{6v}.

To simplify the consideration and to save room, we will assume first that the interaction points are allowed to vibrate only in the plane of the figure, and the interaction forces also belong to this plane. Thus, the interaction space L in this example is 14-dimensional. The construction of the representation is simplified if we represent the displacement of each interaction point in its own coordinate system, the origin of which is placed at the equilibrium state of the point. The coordinate systems associated with point *1* and central point *7* are shown in the figure. The coordinate system of point k ($k = 2, \ldots, 6$) is obtained from that of point *1* by rotation about the symmetry axis x (passing through the central point) through the

angle $C_6^k = \frac{2\pi k}{6}$. The vector of displacements of the interaction points is given by $Y = [y_1, z_1, \ldots, y_7, z_7]^T \in R^{14}$, where y_k and z_k are the coordinates of the displacement of the kth point in its own coordinate system.

As discussed in the previous section, the group C_{6v} consists of 12 elements. Let σ_v be the reflection in the symmetry plane passing through the 6-fold axis x and points *1* and *4*, and C_6^k be the counterclockwise rotation about the 6-fold symmetry axis x through the angle C_6^k. Let the elements of the group be chosen in the same way as in Section 5: $C_6^0 = e, C_6^1, \ldots, C_6^5, \sigma_v, \sigma_v C_6^1, \ldots, \sigma_v C_6^5$. Since $T(g_1 g_2) = T(g_1)T(g_2), \forall g_1, g_2 \in G$ [12], we need to construct only the matrices $T(C_6^k), k = 1, \ldots, 5$, and $T(\sigma_v)$.

It can be checked directly by examining Fig. 1 that the representation T is given by

$$T(\sigma_v) = \begin{bmatrix} E & 0 & 0 & 0 & 0 & 0 & 0 \\ 0 & 0 & 0 & 0 & 0 & E & 0 \\ 0 & 0 & 0 & 0 & E & 0 & 0 \\ 0 & 0 & 0 & E & 0 & 0 & 0 \\ 0 & 0 & E & 0 & 0 & 0 & 0 \\ 0 & E & 0 & 0 & 0 & 0 & 0 \\ 0 & 0 & 0 & 0 & 0 & 0 & E \end{bmatrix}, \quad T(C_6^1) = \begin{bmatrix} 0 & I & 0 & 0 & 0 & 0 & 0 \\ 0 & 0 & I & 0 & 0 & 0 & 0 \\ 0 & 0 & 0 & I & 0 & 0 & 0 \\ 0 & 0 & 0 & 0 & I & 0 & 0 \\ 0 & 0 & 0 & 0 & 0 & I & 0 \\ I & 0 & 0 & 0 & 0 & 0 & 0 \\ 0 & 0 & 0 & 0 & 0 & 0 & \Gamma_1 \end{bmatrix},$$

$$T(C_6^2) = \begin{bmatrix} 0 & 0 & I & 0 & 0 & 0 & 0 \\ 0 & 0 & 0 & I & 0 & 0 & 0 \\ 0 & 0 & 0 & 0 & I & 0 & 0 \\ 0 & 0 & 0 & 0 & 0 & I & 0 \\ I & 0 & 0 & 0 & 0 & 0 & 0 \\ 0 & I & 0 & 0 & 0 & 0 & 0 \\ 0 & 0 & 0 & 0 & 0 & 0 & \Gamma_2 \end{bmatrix}, \ldots, T(C_6^5) = \begin{bmatrix} 0 & 0 & 0 & 0 & 0 & I & 0 \\ I & 0 & 0 & 0 & 0 & 0 & 0 \\ 0 & I & 0 & 0 & 0 & 0 & 0 \\ 0 & 0 & I & 0 & 0 & 0 & 0 \\ 0 & 0 & 0 & I & 0 & 0 & 0 \\ 0 & 0 & 0 & 0 & I & 0 & 0 \\ 0 & 0 & 0 & 0 & 0 & 0 & \Gamma_5 \end{bmatrix},$$

where 0 stands for the 2×2 matrix of zeros, I is the 2×2 identity matrix, E is the diagonal matrix $E = \mathrm{diag}[1, -1]$, and

$$\Gamma_k = \begin{bmatrix} \cos(\frac{2\pi k}{6}) & \sin(\frac{2\pi k}{6}) \\ -\sin(\frac{2\pi k}{6}) & -\cos(\frac{2\pi k}{6}) \end{bmatrix}.$$

Clearly, $T(C_6^0)$ is the identity matrix of order 14, and the other five matrices are obtained by means of the formula $T(\sigma_v C_6^k) = T(\sigma_v)T(C_6^k)$.

Now, whatever is the stiffness matrix corresponding to this interaction section, the interaction space is decomposed into eight subspaces, and the projectors onto these subspaces are easily constructed by means of formulas (11)–(16) at $n = 6$. Repeating this procedure for the other interaction sections and applying the technique discussed in Section 4, we obtain eight characteristic matrices such that the spectrum of the original problem can be obtained by investigating these matrices. The orders of these matrices, in the general case, are different and determined by a particular stiffness

matrix of the interaction. However, according to Theorem 3, the sum of their orders is equal to the order of the characteristic matrix of the system when it is investigated without regard for its symmetry.

Note finally, without going into detail, that the consideration of a more general case, the case of space displacements of the interaction points, presents no additional problem. Let, for example, the vibration of a bundle of seven 3D beams be analyzed. Let the beams be connected to each other through some number of translational and torsional springs located in a plane perpendicular to the longitudinal axes of the beams. Let the interaction section of the bundle be as shown in Fig. 1. In this case, the displacement of each interaction point (which is actually a cross-section of the corresponding beam) is described by six (three linear and three angular) coordinates. Introducing the third axis for each coordinate system and the Eulerian angles, one can construct the representation in the 42-dimensional interaction space. Writing the matrices of the representation in terms of 6×6 matrix blocks, one will obtain them exactly in the same form as in the previous case of plane vibrations. Blocks 0 and I, in this case, are 6×6 zero and identity matrices, respectively; E is a diagonal matrix of ones and minus ones; and Γ_k describes the coordinate transformation under rotation about the 6-fold symmetry axis through the angle C_6^k. A concrete form of matrices E and Γ_k depend on the chosen enumeration of the six coordinates describing the position of the point in the interaction space.

7 NUMERICAL ILLUSTRATIVE EXAMPLE

The aim of this section is to give a simple numerical example of decomposition of the interaction space. Since the result of the decomposition of the interaction space (i.e., the number of nonempty subspaces and their dimensions and, hence, the number of the reduced characteristic matrices and their orders) does not depend on the kind and complexity of the subsystems and is determined only by the symmetry group, the configuration of the interaction points, and the stiffness matrix of the interaction between the subsystems, we will consider a structure consisting of the simplest subsystems—concentrated masses.

We will consider a system possessing the symmetry group C_{6v} and take advantage of the representation constructed in the previous section. Let the free-free spring–mass system shown in Fig. 2 perform plane vibration. Here the circles denote identical masses $m = 1$, and the lines connecting the masses denote linear springs of the stiffness $k = 1$.

The direct analysis results in a conventional matrix formulation of the spectral problem. The eigenvalues (eigenfrequencies squared) are obtained

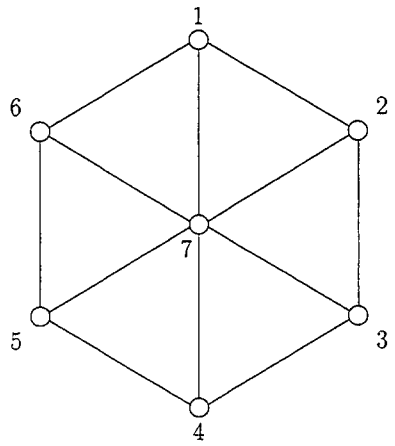

Fig. 2: A spring–mass system of 7 masses and 12 springs

by means of solving the eigenvalue problem

$$(K - \lambda M)h = 0, \tag{17}$$

where M is the identity mass matrix of order 14, and the stiffness matrix K of the same order is easily constructed by means of Fig. 2. The direct computations yield 3 rigid body and 11 elastic modes. The eigenvalues corresponding to elastic modes are 0.849 (2), 1.000 (1), 1.229 (2), 2.000 (1), 2.651 (2), 3.000 (1), and 4.271 (2). The numbers in the parentheses indicate the multiplicities of the eigenvalues.

The interaction space in this degenerate example is also 14-dimensional. Denote $K_j = P_j K P_j$, where P_j is one of the eight projectors defined by equations (11)–(16). As follows from the discussions of Section 4, spectral problem (17) can be decomposed into the eight problems

$$(K_j - \lambda M)h = 0.$$

Factoring the matrices K_j, $K_j = \alpha_j^T \alpha_j$, and applying equation (8), we arrive at the eight characteristic matrices $Q_j(\lambda)$. For this example, $Q_j(\lambda) = I - (1/\lambda)q_j$, where $q_j = \alpha_j \alpha_j^T$, and the nonzero eigenvalues are found as solutions to the eight characteristic problems: $(q_j - \lambda I)z = 0$.

The table below presents the dimensions of the characteristic matrices (the third row) corresponding to each of the projectors defined by equations (11)–(16) and the eigenvalues obtained by solving the corresponding characteristic problems.

j	1	2	3	4	5	6	7	8
Projector	$P_{0,1}$	$P_{0,2}$	$P_{3,1}$	$P_{3,2}$	$P_{1,0}$	$P_{1,1}$	$P_{2,0}$	$P_{2,1}$
$\tilde{N}_j$	1	0	1	1	2	2	2	2
λ	2.000	-	1.000	3.000	1.229 4.271	1.229 4.271	0.849 2.651	0.849 2.651

As can be seen, all the repeated eigenvalues of the original problem are split now; they appear as solutions of different eigenvalue problems (one eigenvalue corresponds to a symmetric vibration with respect to any vertical symmetry plane passing through the 6-fold symmetry axis, and the other corresponds to the antisymmetric vibration). Note also that the dimension of the characteristic matrix corresponding to the projector $P_{0,2}$ is equal to zero. This implies that the system has no eigenvibration such that the corresponding vector of interaction forces belongs to the space $L_{0,2}$.

In conclusion, note that though the decomposition of the spectral problem for this simple example results in no advantages (the time required to factor all the matrices K_j is greater than the time required to solve the original problem (17)), the situation becomes dramatically different in the case where complex subsystems are involved. To make the point clear, let us imagine that Fig. 2 represents the interaction section for a system consisting of seven complex subsystems. Let circles denote the connection points of the subsystems. Assume that the Green's operators of the subsystems are available (e.g., they can be calculated by means of the modal series). If one applies some substructuring method for investigation of such a system, one arrives at the investigation of a certain relatively small matrix (if the structural analysis method [5, 6] is used, the order of the characteristic matrix will be equal to 14), which, however, depends nonlinearly on the spectral parameter λ. The finding of the system spectrum, in this case, will require many iterations involving calculation of the matrix and search for its singularity points (zero determinant). The use of the system symmetry in this case will allow one to reduce the spectral problem to investigation of seven characteristic matrices of orders one or two (see the above table). Since the skeleton factorizations of the matrices K_j are implemented only once (before the iterations), the effect of using the decomposition is evident.

8 CONCLUDING REMARKS

The method of investigation of complex symmetric structures has been presented. The technique is based upon results of the group representation theory. To obtain the decomposition of the spectral problem, the interaction space of the system is decomposed by means of real irreducible representations of the group describing the symmetry of the system. The

projectors onto the subspaces of the interaction space are given for the two symmetry groups.

If the structure under investigation possesses the symmetry described by the group C_n or C_{nv}, in order to decompose the spectral problem, one can take advantage of the results presented in the paper. In this case, one needs only to build a representation of the group in the relevant interaction space. The way of construction of the representation of the group C_{6v} for a particular configuration of the interaction points is presented in Section 6; it can be easily extended to other configurations that fall in the group C_n or C_{nv}.

As to other kinds of symmetry, a general scheme of application of the method discussed in the paper can be briefly summarized as follows:
(i) First, the symmetry group relevant to the investigated structure is determined.
(ii) Second, the connection points of the subsystems are separated mentally from the structure, divided into independent interaction sections, and a representation of the group is built for all interaction sections.
(iii) Then, one should abstract from the structure and to find the decomposition of the interaction space. This is achieved through finding real irreducible representations of the group. For many groups, these representations are available in the literature. Note, however, that they are often complex, and one should combine pairs of complex conjugate irreducible representations to obtain real representations. The case where certain subspaces transformed by representations of order greater than one can be split is more difficult for analysis. To determine whether or not this is possible, one can take advantage of Theorem 2 or try to find other criteria, which may occur more convenient in particular cases. This stage is completed with the construction of the projectors onto the subspaces of the interaction space. The projectors are built by means of formal application of formulas (5) or (6)–(7).
(iv) Finally, the reduced characteristic matrices are constructed by means of the technique described in Section 4.

At last, note that, in the authors' opinion, the approach discussed in the paper can be used to develop a method for analysis of another interesting class of structures—the structures that are not symmetric but consist of identical subsystems (or several sets of identical subsystems). The group relevant to such a class of systems is a subgroup of the permutation group. We suppose that the close examination of this case from the standpoint of the group representation theory may lead to the development of an efficient method for analysis of this important for applications class of structures.

References

1. Bergman, L.A. and McFarland, D.M, On the vibration of a point supported linear distributed structure. *J. Vibr., Acoustics, Stress and Reliability in Design*, 1988, **110,** 485–492.

2. Garvey, S.D., Friswell, M.I. and Penny, J.E.T., Efficient evaluation of composite structure modes. *Proc. of the 5th Int. Conf. on Recent Advances in Structural Dynamics, Southampton*, July 1994, 869–878.

3. Gould, S.H., *Variational Methods for Eigenvalue Problems*, Oxford University Press, London, 1966.

4. Kron, G., *Diakoptics*, MacDonald, London, 1963.

5. Pesterev, A.V. and Tavrizov, G.A., Vibrations of beams with oscillators I: strŭctural analysis method for solving the spectral problem. *J. Sound Vibr.*, 1994, **170,** 521–536.

6. Pesterev, A.V. and Tavrizov, G.A., Structural analysis method for dynamic analysis of conservative structures. *Int. J. Anal. Exper. Modal Analysis*, 1994, **9**, 302–316.

7. Pesterev, A.V and Tavrizov, G.A., Quick inversion of some meromorphic characteristic matrices. *Proc. of the 5th Int. Conf. on Recent Advances in Structural Dynamics, Southampton*, July 1994, 890–899.

8. Pesterev, A.V. and Bergman, L.A., On vibration of a system with an eigenfrequency identical to that of one of its subsystems, *ASME J. Vibr. Acoustics,* 1995, **117,** 482–487.

9. Pesterev, A.V. and Bergman, L.A., On vibration of a system with an eigenfrequency identical to that of one of its subsystems, Part II, *ASME J. Vibr. Acoustics,* 1996, **118,** 414–416.

10. Yee, E.K.L. and Tsuei, Y.G., Direct component modal synthesis technique for system dynamic analysis. *AIAA J.*, 1989, **27**, 1083–1088.

11. Horn, R.A. and Johnson, C.R., *Matrix Analysis*, Cambridge University Press, Cambridge, 1985.

12. Lubarskii, G.Y., *Theory of Groups and its Applications to Physics*, Moscow, 1958, (in Russian).

RANDOM VIBRATION I

ANALYTICAL APPROACH FOR ELASTICALLY SUPPORTED CANTILEVER BEAM SUBJECTED TO MODULATED FILTERED WHITE NOISE

Gongkang Fu and **Juan Peng**
Department of Civil and Environmental Engineering
Wayne State University, Detroit, MI 48202, USA
TEL:(313)577-3842; FAX:(313)577-3881

SUMMARY

For elastically supported cantilever beams, this paper presents an explicit solution of response statistics to seismic input at the base of the beam. The excitation is modeled by modulated filtered white noise. The modulation is described by the sum of exponentially decaying functions, accounting for nonstationarity of strong ground motion. The solution was obtained by analysis in the time domain using the state space approach and impulse response. An example is also included here to demonstrate the application to bridge piers, in developing probabilistic seismic response spectra for design and retrofit of bridge structures.

1. INTRODUCTION

Although various methods have been suggested for random vibration problems, only a few explicit solutions have been reported for random vibration under nonstationary excitations [1,3,7,8,10]. Explicit solutions are often desirable for their advanced abilities of verifying approximation methods and providing insights of the problem. This paper contributes to the knowledge in this area by presenting an explicit solution for the displacement, velocity, and acceleration of a structural system with continuous parameters. It is subjected to strong ground motion modeled by exponentially modulated filtered white noise. The double filter in casecade suggested by Clough and Penzien [4] is included in the excitation. This solution was obtained by analysis in the time domain using the state space approach and the impulse responses.

2. EQUATION OF MOTION

Consider a vertical cantilever beam with constant cross section. Its horizontal displacement V(x,t) at time t and distance x from its base is giverned by the following motion equation, with an assumption of viscous damping:

$$m_c V''(x,t) + c_c V'(x,t) + EI V^{IV}(x,t) = 0 \qquad (1)$$

where the number of primes to V(x,t) indicate the orders of partial derivatives with respect to time t, and the Roman superscript denotes that with respect to location x along the length of the beam. m_c and c_c are constants for mass and damping per unit length, and EI is a constant denoting the flexural stiffness of the beam.

After the displacement V(x,t) is decomposed into pseudo-static and dynamic displacements:

$$V(x,t)=V_s(x,t) + V_d(x,t) ; \qquad V_s(x,t)=f(t)(1-x/L) \qquad (2)$$

Eq.(1) becomes

$$m_c V_d''(x,t) + c_c V_d'(x,t) + EI V_d^{IV}(x,t) = - m_c f''(t)(1-x/L) \qquad (3)$$

It is assumed here that the damping term $C_c f'(t)(1-x/L)$ is negligible. The associated initial and boundary conditions are identified as follows:

$$V_d(x,0) = 0 \qquad V_d'(x,0) = 0 \qquad (4)$$

$$k_t V_d(0,t) + EI V_d^{III}(0,t) = 0$$
$$k_r V_d^{I}(0,t) - EI V_d^{II}(0,t) = 0$$
$$V_d^{III}(L,t) = 0$$
$$V_d^{II}(L,t) = 0 \qquad (5)$$

The boundary condition at the base (x=0) in Eq.(5) describes dynamic equilibrium involving deformations at the base. k_t and k_r denote the elastic stiffness for translation and rocking, respectively. This inclusion is intended to model effects of the foundation. For example, deep pile foundations may be modeled by setting k_t and k_r equal to infinity.

The ground acceleration is modeled by a nonstationary random process, described by the product of a deterministic modulation $\eta(t)$ and a stationary process g(t):

$$f''(t) = \eta(t)\, g(t) \qquad (6)$$

$\eta(t)$ is described by the sum of a series of exponential functions in a general form:

$$\eta(t)= \sum_{i=1,N} a_i \exp(b_i t) \qquad (t\geq 0;\ \eta(0)=0;\ \eta(\infty)=0) \qquad (7)$$

where a_i and b_i are real constants, and b_i must be negative. This general form of modulation is used here for including several popular models and ease of mathematical derivation. g(t) is assumed to be a white noise process with zero mean and filtered by the Clough-Penzien filter [4] modeling soil effects in cascade. Its spectral density function $S_{gg}(\omega)$ and autocorrelation function $R_{gg}(\tau)$ are respectively given by

$$S_{gg}(\omega) = \frac{\omega_{g1}^4 + (2\zeta_{g1}\omega_{g1}\omega)^2}{(\omega_{g1}^2-\omega^2)^2 + (2\zeta_{g1}\omega_{g1}\omega)^2} \frac{\omega^4}{(\omega_{g2}^2-\omega^2)^2 + (2\zeta_{g2}\omega_{g2}\omega)^2} \frac{S}{2\pi} \tag{8}$$

$$R_{gg}(\tau) = -\frac{S}{4} \sum_{k=1,2} \frac{1}{\zeta_{gk}\omega_{gk}} \exp(-\zeta_{gk}\omega_{gk}|\tau|)$$
$$[(C_{ak}+C_{bk})\cos\omega_{gdk}|\tau| + \frac{\zeta_{gk}\omega_{gk}}{\omega_{gdk}} (C_{ak}-C_{bk})\sin\omega_{gdk}|\tau|] \tag{9}$$

where C_{ak} and C_{bk} (k=1,2) are respectively as follows:

$$C_{a1} = -\frac{\omega_{g1}^6}{D}[(1+8\zeta_{g1}^2-16\zeta_{g1}^4)(1-\frac{\omega_{g1}^4}{\omega_{g2}^4}) - 8\zeta_{g1}^2\frac{\omega_{g1}^2}{\omega_{g2}^2}(1-2\zeta_{g2}^2-\frac{\omega_{g1}^2}{\omega_{g2}^2}+2\zeta_{g1}^2\frac{\omega_{g1}^2}{\omega_{g2}^2})]$$

$$C_{b1} = \frac{2\omega_{g1}^6}{D}[(1+8\zeta_{g1}^2-16\zeta_{g1}^4)(1-2\zeta_{g1}^2-\frac{\omega_{g1}^2}{\omega_{g2}^2}+2\zeta_{g2}^2\frac{\omega_{g1}^2}{\omega_{g2}^2})-2\zeta_{g1}^2(1-\frac{\omega_{g1}^4}{\omega_{g2}^4})]$$

$$C_{a2} = \frac{\omega_{g1}^4\omega_{g2}^2}{D}[(1+8\zeta_{g1}^2-16\zeta_{g1}^4)(1-\frac{\omega_{g1}^4}{\omega_{g2}^4}) - 8\zeta_{g1}^2\frac{\omega_{g1}^2}{\omega_{g2}^2}(1-2\zeta_{g2}^2-\frac{\omega_{g1}^2}{\omega_{g2}^2}+2\zeta_{g1}^2\frac{\omega_{g1}^2}{\omega_{g2}^2})]$$

$$C_{b2} = \frac{2\omega_{g1}^2\omega_{g2}^4}{D}[\frac{\omega_{g1}^2}{\omega_{g2}^2}(-\frac{\omega_{g1}^2}{\omega_{g2}^2}-8\zeta_{g1}^2+16\zeta_{g1}^2\zeta_{g2}^2)(1-2\zeta_{g1}^2-\frac{\omega_{g1}^2}{\omega_{g2}^2}+2\zeta_{g2}^2\frac{\omega_{g1}^2}{\omega_{g2}^2})$$
$$+2\zeta_{g1}^2(1-\frac{\omega_{g1}^4}{\omega_{g2}^4})] \tag{10a}$$

and

$$D = -4\omega_{g1}^2\omega_{g2}^2\left(1-2\zeta_{g1}^2-\frac{\omega_{g1}^2}{\omega_{g2}^2}+2\zeta_{g2}^2\frac{\omega_{g1}^2}{\omega_{g2}^2}\right)\left(1-2\zeta_{g2}^2-\frac{\omega_{g1}^2}{\omega_{g2}^2}+2\zeta_{g1}^2\frac{\omega_{g1}^2}{\omega_{g2}^2}\right) + \omega_{g2}^4\left(1-\frac{\omega_{g1}^4}{\omega_{g2}^4}\right)^2 \quad (10b)$$

In Eqs.(8) to (10), ζ_{g1}, ζ_{g2}, ω_{g1}, and ω_{g2} are characteristic damping ratios and frequencies of the respective subfilters indicated by subscript k=1,2. $\omega_{gdk} = \omega_{gk}(1-\zeta_{gk}^2)^{1/2}$ (k=1,2) are their characteristic damped frequencies. $S/2\pi$ is a constant indicating the intensity of white noise.

Note that $R_{gg}(\tau)$ is the Fourier inverse transform of $S_{gg}(\omega)$:

$$R_{gg}(\tau)=\int_{-\infty}^{\infty} S_{gg}(\omega)\exp(i\omega\tau)\,d\omega \quad (11)$$

where $i=(-1)^{1/2}$ is the imaginary unit and $R_{gg}(\tau)$ was obtained by decomposing $S_{gg}(\omega)$ into the sum of two terms:

$$S_{gg}(\omega)=\frac{S}{2\pi}\sum_{k=1,2}\frac{C_{ak}\,\omega_{gk}^2+C_{bk}\omega^2}{(\omega_{g1}^2-\omega^2)^2+(2\zeta_{g1}\omega_{g1}\omega)^2} \quad (12)$$

and performing the inverse Fourier transform individually for each term by the method of residues [12]. Note that the Kanai-Tajimi filter [11,15] can be represented in Eqs.(8) to (10) by setting $\omega_{g2}=0$, leading to $C_{a1}=\omega_{g1}^2$, $C_{b1}=4\zeta_{g1}^2\omega_{g1}^2$, and $C_{a2}=C_{b2}=0$ [6]. On the other hand, $\omega_{g1}\to\infty$ eliminates the effect of the Kanai-Tajimi filter. Note that this seismic excitation model of modulated cascade-filtered white noise covers nonstationarity of intensity, but not that of frequency contents. Either or both of them may be observed in strong motion records.

3. SOLUTION BY STATE SPACE FORMULATION

3.1 Modal Decoupling

Eq.(3) is solved here by separating the two variables x and t, and using modal superposition:

$$V_d(x,t) = \sum_{i=1,2,\ldots}\phi_i(x)\,V_i(t) \quad (13)$$

where $\phi_i(x)$ is the ith mode shape and $V_i(t)$ is the normal coordinate for that

mode. Using modal orthogonality, Eq.(3) becomes a series of decoupled equations of modal motion:

$$V_i''(t) + 2\,\zeta_i\,\omega_i\,V_i'(t) + \omega_i^2\,V_i(t) = S_i\,f''(t) \qquad (14)$$

where

$$\omega_i^2 = a_i^4\,EI/m_e$$
$$\zeta_i = c_e/(2\,\omega_i\,m_e)$$
$$S_i = \int_0^L \phi_i(x)\,(1-x/L)\,dx \,/\, \int_0^t \phi_i^2(x)\,dx \qquad (i=1,2\ldots) \qquad (15)$$

ω_i and ζ_i are respectively modal natural frequency and damping ratio. S_i is a factor indicating the extent of participation of the mode. The mode shapes are given as

$$\phi_i(x) = c_{1,i}\,\sin(a_i x) + c_{2,i}\,\cos(a_i x) + c_{3,i}\,\sinh(a_i x) + c_{4,i}\,\cosh(a_i x) \qquad (16)$$

a_i related to the natural frequency is the solution to the eigen value problem, and the coefficients of $c_{1,i}$ to $c_{4,i}$ are obtained by meeting the boundary condition in Eq.(5) for every mode.

3.2 Modal Solution in State Space

Let the state variables for mode i be denoted by

$$\mathbf{v}_i(t) = (V_i(t),\, V_i'(t),\, V_i''(t))^T \qquad (17)$$

where superscript T denotes transpose of matrix. The inclusion of $V_i''(t)$ is to provide a complete picture of the system behavior, and to be able to describe the maxima of displacement as discussed later.

The solution to Eq.(14) can be shown in the following convolution form:

$$\mathbf{v}_i(t) = -\,S_i\,\mathbf{C}_i \int_0^t \mathbf{z}_i(t-\tau)\,f''(\tau)\,d\tau \qquad (18)$$

where $\mathbf{C}_i$ is a matrix of system parameters for mode i, and $\mathbf{z}_i(t)$ is a time-dependent vector:

$$\mathbf{C}_i = \begin{pmatrix} 0 & 1/\omega_{di} & 0 \\ 1 & -\zeta_i\,\omega_i/\omega_{di} & 0 \\ -2\zeta_i\,\omega_i & (\zeta_i\,\omega_i)^2/\omega_{di}-\omega_{di} & 1 \end{pmatrix} \qquad (19a)$$

$$\mathbf{z}_i(t) = (\exp(-\zeta_i \omega_i t) \cos \omega_{di} t,\ \exp(-\zeta_i \omega_i t) \sin \omega_{di} t,\ \delta(t))^T \qquad (19b)$$

where $\omega_{di} = \omega_i(1-\zeta_i^2)^{1/2}$, and $\delta(t)$ is the Dirac delta function.

Since the ensemble expectation of $\mathbf{v}_i(t)$ is a zero vector due to zero mean of the input process g(t), the covariance matrix of $\mathbf{v}_i(t)$ is

$$\mathbf{R}_{vivi}(t) = E[\mathbf{v}_i(t)\ \mathbf{v}_i^T(t)] = S_i^2\ \mathbf{C}_i\ \mathbf{B}_i(t)\ \mathbf{C}_i^T$$

$$\mathbf{B}_i(t) = \int_0^t\int_0^t \eta(\tau_1)\eta(\tau_2)R_{gg}(|\tau_1-\tau_2|)\mathbf{z}_i(t-\tau_1)\mathbf{z}_i^T(t-\tau_2)d\tau_1 d\tau_2 \qquad (20)$$

where E stands for ensemble expectation. This double integration has been performed as shown in [6] by analysis in the time domain.

It will be seen below that the covariance matrix for two different modes (say m and n) is needed for further analysis. This matrix can be similarly expressed as:

$$\mathbf{R}_{vmvn}(t) = E[\mathbf{v}_m(t)\ \mathbf{v}_n^T(t)] = S_m\ S_n\ \mathbf{C}_m\ \mathbf{B}_{mn}(t)\ \mathbf{C}_n^T$$

$$\mathbf{B}_{mn}(t) = \int_0^t\int_0^t \eta(\tau_1)\eta(\tau_2)R_{gg}(|\tau_1-\tau_2|)\mathbf{z}_m(t-\tau_1)\mathbf{z}_n^T(t-\tau_2)d\tau_1 d\tau_2 \qquad (21)$$

This integration is also carried out in the time domain. The results of $\mathbf{B}_{mn}(t)$ are explicitly given in Appendix. Note that when $m=n=i$, $\mathbf{B}_{mn}(t) = \mathbf{B}_i(t)$. Eqs.(20) and (21) show that the statistics of the nonstationary responses are expressed as product of a stationary part (constant $\mathbf{C}_i$ matrix) and a nonstationary part (matrix $\mathbf{B}_i(t)$ or $\mathbf{B}_{mn}(t)$).

3.3 Mean Square Total Response in State Space

With the elementary terms given, the covariance matrix $\mathbf{R}_{vv}(t)$ of the vector of dynamics state-variables $\mathbf{v}(t)$ can be now formulated as follows:

$$\begin{aligned}\mathbf{v}(x,t) &= (V_d(x,t),\ \dot{V}_d(x,t),\ V_d''(x,t))^T \\ &= (\textstyle\sum_{i=1,2,\ldots}\phi_i(x)\ V_i(t),\ \sum_{i=1,2,\ldots}\phi_i(x)V_i'(t),\ \sum_{i=1,2,\ldots}\phi_i(x)V_i''(t))\end{aligned} \qquad (22)$$

$$\begin{aligned}\mathbf{R}_{vv}(t) &= E[\mathbf{v}(x,t)\ \mathbf{v}^T(x,t)] \\ &= \textstyle\sum_{m=1,2,\ldots}\sum_{n=1,2,\ldots}\phi_m(x)S_m\ \phi_n(x)S_n\ \mathbf{C}_m\ \mathbf{B}_{mn}(t)\ \mathbf{C}_n^T \\ &= \begin{pmatrix} R_{vv,11}(x,t) & R_{vv,12}(x,t) & R_{vv,13}(x,t) \\ R_{vv,21}(x,t) & R_{vv,22}(x,t) & R_{vv,23}(x,t) \\ R_{vv,31}(x,t) & R_{vv,32}(x,t) & R_{vv,33}(x,t) \end{pmatrix}\end{aligned} \qquad (23)$$

Note that the second group of subscripts indicates the physical quantities by

1=displacement, 2=velocity, and 3=acceleration. This system of identification will be used hereafter for variances. Of the summed terms in Eq.(23), the dominant terms are often those referring to the same mode, i.e. $(\phi_n(x)S_n)^2\,\mathbf{C}_n\mathbf{B}_n(t)\mathbf{C}_n^T$ (n=1,2,...).

4. NUMERICAL EXAMPLES

4.1 Unit Step Modulation

The modulation function given in Eq.(7) is in a general form to describe nonstationarity of earthquake excitations. It can be reduced to several commonly used models. For example, the unit step function model of modulation is a special case represented by N=1, $a_1=1$, and $b_1=0$ in Eq.(7). This model is perhaps the earliest modulation envelope for modeling nonstationarity of earthquakes [3]. When effects of the filter is eliminated by setting $\omega_{g1}\to\infty$ and $\omega_{g2}=0$, the solution in Eq.(20) for a mode reduces to the response of an oscillator to white noise modulated by the step function, with natural frequency ω_0, damping ζ_0, and, of course, the modal participation factor $S_0=1$ in Eq.(14):

$$R_{vv,11}(t)=\frac{S}{4\zeta_0\omega_0^3}\{1+\frac{\exp(-2\zeta_0\omega_0 t)}{(1-\zeta_0^2)}[-1+\zeta_0^2\cos2\omega_{d0}t-\zeta_0(1-\zeta_0^2)^{1/2}\sin2\omega_{d0}t]\} \quad (24)$$

$$R_{vv,12}(t)=\frac{S}{4\omega_0^2(1-\zeta_0^2)}\exp(-2\zeta_0\omega_0 t)(1-\cos2\omega_{d0}t)=R_{vv,21}(t) \quad (25)$$

$$R_{vv,22}(t)=\frac{S}{4\zeta_0\omega_0}\{1+\frac{\exp(-2\zeta_0\omega_0 t)}{(1-\zeta_0^2)}[-1+\zeta_0^2\cos2\omega_{d0}t+\zeta_0(1-\zeta_0^2)^{1/2}\sin2\omega_{d0}t]\} \quad (26)$$

$$R_{vv,13}(t)=\frac{S}{4\zeta_0\omega_0}\{-1+\frac{\exp(-2\zeta_0\omega_0 t)}{(1-\zeta_0^2)}[1-2\zeta_0^2+\zeta_0^2\cos2\omega_{d0}t+\zeta_0(1-\zeta_0^2)^{1/2}\sin2\omega_{d0}t]\}$$

$$=R_{vv,31}(t) \quad (27)$$

$$R_{vv,23}(t)=\frac{S}{4(1-\zeta_0^2)}\exp(-2\zeta_0\omega_0 t)[1+(1-2\zeta_0^2)\cos2\omega_{d0}t-2\zeta_0(1-\zeta_0^2)^{1/2}\sin2\omega_{d0}t]$$

$$= R_{vv,32}(t) \tag{28}$$

$$R_{vv,33}(t) \to \infty \tag{29}$$

The first three terms have been given elsewhere [3,10]. The last term is contributed by the white noise acceleration input, representing an impulse of infinite peak at time lag $\tau=0$.

4.2 Shinozuka-Sato Modulation

Another group of modulation models is described by the Shinozuka-Sato model [13], which is a special case of N=2 in Eq.(7). Examples are $a_1=2.32$, $a_2=-2.32$, $b_1=-0.09$, and $b_2=-1.49$ for El Centro earthquake, and $a_1=12.8$, $a_2=-12.8$, $b_1=-0.14$, and $b_2=-0.19$ for Taft earthquake [5]. The latter is used in this example, with $\omega_{g1} = 6.4\pi$ rad/s, $\zeta_{g1} = 0.65$, $\omega_{g2} = 0.32\pi$ rad/s, and $\zeta_{g2} = 0.5$ [16].

For a typical reinforced concrete pier of highway bridges, L=12m, $EI/m_c = 250$ kN/kg-m^3, and $\zeta_i=0.04$ (i=1,2,...) are used here. The constant damping is used because it is felt that the one inversely proportional to the modal frequency as defined in Eq.(15) is not realistic for concrete structures. Three sets of stiffness ratio $r_t=k_tL^3/EI$ and $r_r= k_rL/EI$ are used here: $r_t \to \infty$ and $r_r \to \infty$, $r_t =1$ and $r_r=1$, $r_t=1$ and $r_r=0.1$. The variances of displacement, velocity, and acceleration at the top (free) end of the beam (x=L) are shown in Figs.1 to 3 for the three cases, respectively. Unit intensity is used here. ω_1 is the first natural frequency of the beam. It is seen that decrease of the foundation stiffness causes the response to increase, showing the importance to take into account the foundation stiffness. They also show that the peak responses are slightly delayed by lower foundation stiffness. On the other hand, additional analysis results show that the internal forces (shear and moment) are reduced by lower foundation stiffness.

4.3 Application to Probabilistic Response Spectrum

The mean square response statistics shown here may be used to develop probabilistic seismic response spectra for interested failure modes. An example is given here. Consider a bridge span with one end supported by an abutment with fixed bearings and the other by a pier with expansion bearings. The fixed bearings and the bridge deck (superstructure) are modeled as an SDOF system with mass M, damping C, and stiffness K subjected to the strong motion acceleration f"(t) through the abutment:

$$Mw"(t) + Cw'(t) + Kw(t) = -Mf"(t) \tag{30}$$

where w(t) is the horizontal displacment of the deck relative to the abument. The relative displacment u(t) at the end supported by the pier is focused here:

$$\mathbf{u}(t) = \mathbf{w}(t) - \mathbf{V}(L,t) \tag{31}$$

where $\mathbf{u}(t)=(u(t),u'(t),u''(t))^T$. It is critical to understand the dynamics of the system when designing the bridge to cover the failure mode of span collapse due to excessive relative displacement u(t). The covariance of $\mathbf{u}(t)$ can be readily expressed as

$$\mathbf{R}_{uu}(t) = \mathbf{R}_{ww}(t) - \mathbf{R}_{wv}(t) - \mathbf{R}_{vw}(t) + \mathbf{R}_{vv}(t) \tag{32}$$

$\mathbf{R}_{vv}(t)$ has been given in Eq.(23), $\mathbf{R}_{ww}(t)$ can be expressed using Eq.(20), $\mathbf{R}_{wv}(t)$ and $\mathbf{R}_{vw}(t)$ can be readily formulated using Eq.(21) and taking summation over the significant modes involved in vector $\mathbf{V}(t)$. Note that the length of cantilever beam L in Eq.(31) is omitted in Eq.(32).

Now let us define the failure of excessive relative displacement. Let E[M(-∞,t)] be the mean rate of displacement maxima at time t and E[M(U,t)] be the mean rate of displacement maxima above a given level U, they are respectively [12]:

$$E[M(-\infty,t)] = -\int_{-\infty}^{\infty} du \int_{-\infty}^{0} u'' \, p_{u,u',u''}(u,0,u'',t)\, du'' \tag{33}$$

$$E[M(U,t)] = -\int_{U}^{\infty} du \int_{-\infty}^{0} u'' \, p_{u,u',u''}(u,0,u'',t)\, du'' \tag{34}$$

where $p_{u,u',u''}(.)$ is the joint probability density function for u, u', and u''. If g(t) in Eq.(6) is assumed to be a Gaussian excitation, these state variables are also Gaussian variables. E[M(-∞,t)] and E[M(U,t)] are then derived as:

$$E[M(-\infty,t)] = \frac{\lambda^2(t)}{2\pi} \frac{R_{uu,33}^{1/2}(t)}{R_{uu,22}^{1/2}(t)} \frac{1}{1-\chi^2(t)} \tag{35}$$

$$E[M(U,t)] = E[M(-\infty,t)] \left\{ \Phi\left(-\frac{U}{\lambda(t)\, R_{uu,11}^{1/2}(t)}\right) - \chi(t) \exp\left[-\frac{U^2}{2\lambda^2(t)\, R_{uu,11}(t)} (1-\chi^2(t))\right] \Phi\left(-\frac{\chi(t)\, U}{\lambda(t)\, R_{uu,11}^{1/2}(t)}\right) \right\} \tag{36}$$

where

$$\lambda^2(t) = \frac{|\mathbf{R}(t)|}{R_{uu,11}(t)\, R_{uu,22}(t)\, R_{uu,33}(t)}$$

$$\chi(t) = \gamma_{13}(t) - \gamma_{12}(t)\, \gamma_{23}(t)$$
$$\gamma_{mn}(t) = R_{uu,mn}(t)/[R_{uu,mm}(t)R_{uu,nn}(t)]^{1/2} \qquad (m,n=1,2,3,\ m\ n) \qquad (37)$$

$|\mathbf{R}(t)|$ is the determinant of $\mathbf{R}_{uu}(t)$, and $\Phi(.)$ is the cumulative probability function for the standard normal variable.

Let probability of failure due to excessive displacement be

$$P_f = \text{Probability [maximum } u > U \text{]}$$
$$= \int_0^{T_s} E[M(U,t)]\, dt \,/\, \int_0^{T_s} E[M(-\infty,t)]\, dt \qquad (38)$$

where T_s is the interested time length, being the time interval of significant seismic input. P_f indicates the likelihood that peak displacements exceed a given level U. For a given P_f and seismic input intensity S, variation of the threshold level U as a function of structural system frequency and damping is defined here as probabilistic displacement response spectrum, because it is associated with a probability to be exceeded. This spectrum can be used for design to control displacement. For example, the minimum seat width requirement for highway bridges subjected to seismic hazard may be derived using this approach for risk-based design. For the example of bridge pier discussed above, it is found that when the pier's first natural frequency is close to that of the superstructure-bearing system, U may be significantly lower. This is because the two systems behave very much similarly due to their similar dynamic properties so that their relative displacement u(t) approaches zero. Note that this concept of probabilistic response spectra can be applied to acceleration for force control design.

5. CONCLUSIONS

An explicit solution is presented in this paper for random vibration of elastically supported cantilever beams subjected to the strong ground motion modeled by modulated cascade-filtered white noise. It may be used to develop probabilistic response spectra for risk-based seismic design and retrofit specifications.

REFERENCES

[1] G.Ahmadi and M.A.Satter "Mean-Square Response of Beams to Nonstationary Random Excitation", AIAA Journal, Vol.13, No.8, pp.1097-

1100
[2] C.G.Bucher "Approximate Nonstationary Random Vibration Analysis for MDOF Systems", J.App.Mech. Vol.55, pp.197-200, 1988
[3] T.K.Caughey and H.F.Stumpf "Transit Response of A Dynamic System under Random Excitation, J. Appl. Mech., ASME, Vol.28, pp.563-566, 1961
[4] R.W.Clough and J.Penzien. Dynamics of Structures, McGraw-Hill Book Company, 1975
[5] R.B.Corotis and T.A.Marshall. "Oscillator Response to Modulated Random Excitation," ASCE J.Eng.Mech. Vol.103, EM4 pp.501-513, 1977
[6] G.Fu "Seismic Response Statistics of SDOF System to Exponentially Modulated Coloured Input: An Explicit Solution" Earthquake Engineering and Structural Dynamics, Vol.24, 1995, pp.1355-1370
[7] D.A.Gasparini "Response of MDOF Systems to Nonstationary Random Excitation", ASCE J. of Engg. Mech., Vol.105, No.EM1, Feb. 1979, pp.13-27
[8] D.A.Gasparini and A.DebChaudhury "Dynamic Response to Nonstationary Nonwhite Excitation" ASCE J.Eng.Mech. Vol.106, EM6, pp.1233-1248, 1980
[9] Z.K.Hou "Nonstationary Response of Structures and Its Application to Earthquake Engineering", California Institute of Technology, EERL 90-01, 1990
[10] W.D.Iwan and Z.K.Hou "Explicit Solution for the Response of Simple Systems Subjected to Nonstationary Random Excitation", Structural Safety, Vol.6, 1989, pp.77-86
[11] K. Kanai "Semi-empirical Formula for the Seismic Characteristics of the Ground", Univ. of Tokyo Bull. Earthquake Res. Inst., vol. 35, pp. 309-325, 1957
[12] Y.K.Lin. Probabilistic Theory of Structural Dynamics, R.E.Krieger Publishing Company, 1967
[13] M.Shinozuka and Y.Sato "Simulation of Nonstationary Random Process", ASCE J.Eng.Mech.Div., Vol.93, pp.11-40, 1967
[14] M.Shinozuka and W-F.Wu "On the First Passage Problem and Its Application to Earthquake Engineering", Proc. 9th WCEE, Aug.2-9, 1988, Tokyo-Kyoto, Japan, P.VIII-767
[15] H.Tajimi "A Statistical Method of Determining the Maximum Response of a Building Structure during an Earthquake", Proc. 2nd World Conf. Earthquake Eng. Tokyo and Kyoto, vol.II, pp.781-797, July 1960.
[16] C.-H. Yeh and Y.K.Wen "Modeling of Nonstationary Ground Motion and Analysis of Inelastic Structural Response" Structural Safety, Vol.8, 1990, pp.281-298

Appendix

$$\mathbf{B}_{mn}(t) = \begin{pmatrix} B_{mn,11} & B_{mn,12} & B_{mn,13} \\ B_{mn,21} & B_{mn,22} & B_{mn,23} \\ B_{mn,31} & B_{mn,32} & B_{mn,33} \end{pmatrix} \tag{A1}$$

$$B_{mn,11}(t) = S \exp(-\omega_m\zeta_m-\omega_n\zeta_n)t \sum_{k=1,2} \frac{1}{16\zeta_{gk}\omega_{gk}} \sum_{i=1,N} \sum_{j=1,N} a_i a_j *$$
$$\{(C_{ak}+C_{bk})[g_1(\alpha_{km},\alpha_{kn},\rho_{jkm},\mu_{ikn})-g_2(\alpha_{km},\beta_{kn},\rho_{jkm},\mu_{ikn})$$
$$+g_3(\alpha_{km},\alpha_{kn},\rho_{jkm},\mu_{ikn})-g_4(\alpha_{km},\beta_{kn},\rho_{jkm},\mu_{ikn})$$
$$+g_1(\beta_{km},\beta_{kn},\rho_{jkm},\mu_{ikn})-g_2(\beta_{km},\alpha_{kn},\rho_{jkm},\mu_{ikn})$$
$$+g_3(\beta_{km},\beta_{kn},\rho_{jkm},\mu_{ikn})-g_4(\beta_{km},\alpha_{kn},\rho_{jkm},\mu_{ikn})$$
$$+g_5(\alpha_{km},\alpha_{kn},\mu_{jkm},\rho_{ikn})-g_6(\alpha_{km},\beta_{kn},\mu_{jkm},\rho_{ikn})$$
$$+g_7(\alpha_{km},\alpha_{kn},\mu_{jkm},\rho_{ikn})-g_8(\alpha_{km},\beta_{kn},\mu_{jkm},\rho_{ikn})$$
$$+g_5(\beta_{km},\beta_{kn},\mu_{jkm},\rho_{ikn})-g_6(\beta_{km},\alpha_{kn},\mu_{jkm},\rho_{ikn})$$
$$+g_7(\beta_{km},\beta_{kn},\mu_{jkm},\rho_{ikn})-g_8(\beta_{km},\alpha_{kn},\mu_{jkm},\rho_{ikn})$$
$$+\zeta_{gk}\omega_{gk}/\omega_{gdk}(C_{ak}-C_{bk})\,[g_9(\alpha_{km},\alpha_{kn},\rho_{jkm},\mu_{ikn})-g_{10}(\alpha_{km},\beta_{kn},\rho_{jkm},\mu_{ikn})$$
$$+g_{11}(\alpha_{km},\alpha_{kn},\rho_{jkm},\mu_{ikn})-g_{12}(\alpha_{km},\beta_{kn},\rho_{jkm},\mu_{ikn})$$
$$-g_9(\beta_{km},\beta_{kn},\rho_{jkm},\mu_{ikn})+g_{10}(\beta_{km},\alpha_{kn},\rho_{jkm},\mu_{ikn})$$
$$-g_{11}(\beta_{km},\beta_{kn},\rho_{jkm},\mu_{ikn})+g_{12}(\beta_{km},\alpha_{kn},\rho_{jkm},\mu_{ikn})$$
$$+g_{13}(\alpha_{km},\alpha_{kn},\mu_{jkm},\rho_{ikn})-g_{14}(\alpha_{km},\beta_{kn},\mu_{jkm},\rho_{ikn})$$
$$+g_{15}(\alpha_{km},\alpha_{kn},\mu_{jkm},\rho_{ikn})-g_{16}(\alpha_{km},\beta_{kn},\mu_{jkm},\rho_{ikn})$$
$$-g_{13}(\beta_{km},\beta_{kn},\mu_{jkm},\rho_{ikn})+g_{14}(\beta_{km},\alpha_{kn},\mu_{jkm},\rho_{ikn})$$
$$-g_{15}(\beta_{km},\beta_{kn},\mu_{jkm},\rho_{ikn})+g_{16}(\beta_{km},\alpha_{kn},\mu_{jkm},\rho_{ikn}) \tag{A2}$$

$$B_{mn,12}(t) = B_{nm,21}(t) \tag{A3}$$

$$B_{mn,13}(t) = S\,[\sum_{i=1,N} a_i \exp(b_i t)] \sum_{k=1,2} \frac{1}{8\zeta_{gk}\omega_{gk}} \sum_{j=1,N} a_j \exp(b_j t) *$$
$$\{(C_{ak}+C_{bk})[g_{18}(\alpha_{km},\rho_{jkm})+g_{18}(\beta_{km},\rho_{jkm})]$$
$$+\zeta_{gk}\omega_{gk}/\omega_{gdk}(C_{ak}-C_{bk})[-g_{17}(\alpha_{km},\rho_{jkm})+g_{17}(\beta_{km},\rho_{jkm})]\} \tag{A4}$$

$$B_{mn,21}(t) = S \exp(-\omega_m\zeta_m-\omega_n\zeta_n)t \sum_{k=1,2} \frac{1}{16\zeta_{gk}\omega_{gk}} \sum_{i=1,N} \sum_{j=1,N} a_i a_j *$$
$$\{(C_{ak}+C_{bk})\,[-g_9(\alpha_{km},\alpha_{kn},\rho_{jkm},\mu_{ikn})+g_{10}(\alpha_{km},\beta_{kn},\rho_{jkm},\mu_{ikn})$$
$$-g_{11}(\alpha_{km},\alpha_{kn},\rho_{jkm},\mu_{ikn})+g_{12}(\alpha_{km},\beta_{kn},\rho_{jkm},\mu_{ikn})$$
$$-g_9(\beta_{km},\beta_{kn},\rho_{jkm},\mu_{ikn})+g_{10}(\beta_{km},\alpha_{kn},\rho_{jkm},\mu_{ikn})$$
$$-g_{11}(\beta_{km},\beta_{kn},\rho_{jkm},\mu_{ikn})+g_{12}(\beta_{km},\alpha_{kn},\rho_{jkm},\mu_{ikn})$$
$$+g_{13}(\alpha_{km},\alpha_{kn},\mu_{jkm},\rho_{ikn})-g_{14}(\alpha_{km},\beta_{kn},\mu_{jkm},\rho_{ikn})$$
$$+g_{15}(\alpha_{km},\alpha_{kn},\mu_{jkm},\rho_{ikn})-g_{16}(\alpha_{km},\beta_{kn},\mu_{jkm},\rho_{ikn})$$
$$+g_{13}(\beta_{km},\beta_{kn},\mu_{jkm},\rho_{ikn})-g_{14}(\beta_{km},\alpha_{kn},\mu_{jkm},\rho_{ikn})$$

$$
\begin{aligned}
&+g_{15}(\beta_{km},\beta_{kn},\mu_{jkm},\rho_{ikn})-g_{16}(\beta_{km},\alpha_{kn},\mu_{jkm},\rho_{ikn})\\
&+\zeta_{gk}\omega_{gk}/\omega_{gdk}(C_{ak}-C_{bk})[g_1(\alpha_{km},\alpha_{kn},\rho_{jkm},\mu_{ikn})-g_2(\alpha_{km},\beta_{kn},\rho_{jkm},\mu_{ikn})\\
&+g_3(\alpha_{km},\alpha_{kn},\rho_{jkm},\mu_{ikn})-g_4(\alpha_{km},\beta_{kn},\rho_{jkm},\mu_{ikn})\\
&-g_1(\beta_{km},\beta_{kn},\rho_{jkm},\mu_{ikn})+g_2(\beta_{km},\alpha_{kn},\rho_{jkm},\mu_{ikn})\\
&-g_3(\beta_{km},\beta_{kn},\rho_{jkm},\mu_{ikn})+g_4(\beta_{km},\alpha_{kn},\rho_{jkm},\mu_{ikn})\\
&-g_5(\alpha_{km},\alpha_{kn},\mu_{jkm},\rho_{ikn})+g_6(\alpha_{km},\beta_{kn},\mu_{jkm},\rho_{ikn})\\
&-g_7(\alpha_{km},\alpha_{kn},\mu_{jkm},\rho_{ikn})+g_8(\alpha_{km},\beta_{kn},\mu_{jkm},\rho_{ikn})\\
&+g_5(\beta_{km},\beta_{kn},\mu_{jkm},\rho_{ikn})-g_6(\beta_{km},\alpha_{kn},\mu_{jkm},\rho_{ikn})\\
&+g_7(\beta_{km},\beta_{kn},\mu_{jkm},\rho_{ikn})-g_8(\beta_{km},\alpha_{kn},\mu_{jkm},\rho_{ikn})
\end{aligned}
\tag{A5}
$$

$$
\begin{aligned}
B_{mn,22}(t) = S\exp(-\omega_m\zeta_{\omega m}-\omega_n\zeta_{\omega n})t\sum_{k=1,2}\frac{1}{16\zeta_{gk}\omega_{gk}}\sum_{i=1,N}\sum_{j=1,N}a_ia_j *\\
\{(C_{ak}+C_{bk})[g_1(\alpha_{km},\alpha_{kn},\rho_{jkm},\mu_{ikn})+g_2(\alpha_{km},\beta_{kn},\rho_{jkm},\mu_{ikn})\\
+g_3(\alpha_{km},\alpha_{kn},\rho_{jkm},\mu_{ikn})+g_4(\alpha_{km},\beta_{kn},\rho_{jkm},\mu_{ikn})\\
+g_1(\beta_{km},\beta_{kn},\rho_{jkm},\mu_{ikn})+g_2(\beta_{km},\alpha_{kn},\rho_{jkm},\mu_{ikn})\\
+g_3(\beta_{km},\beta_{kn},\rho_{jkm},\mu_{ikn})+g_4(\beta_{km},\alpha_{kn},\rho_{jkm},\mu_{ikn})\\
+g_5(\alpha_{km},\alpha_{kn},\mu_{jkm},\rho_{ikn})+g_6(\alpha_{km},\beta_{kn},\mu_{jkm},\rho_{ikn})\\
+g_7(\alpha_{km},\alpha_{kn},\mu_{jkm},\rho_{ikn})+g_8(\alpha_{km},\beta_{kn},\mu_{jkm},\rho_{ikn})\\
+g_5(\beta_{km},\beta_{kn},\mu_{jkm},\rho_{ikn})+g_6(\beta_{km},\alpha_{kn},\mu_{jkm},\rho_{ikn})\\
+g_7(\beta_{km},\beta_{kn},\mu_{jkm},\rho_{ikn})+g_8(\beta_{km},\alpha_{kn},\mu_{jkm},\rho_{ikn})]\\
+\zeta_{gk}\omega_{gk}/\omega_{gdk}(C_{ak}-C_{bk})[g_9(\alpha_{km},\alpha_{kn},\rho_{jkm},\mu_{ikn})+g_{10}(\alpha_{km},\beta_{kn},\rho_{jkm},\mu_{ikn})\\
+g_{11}(\alpha_{km},\alpha_{kn},\rho_{jkm},\mu_{ikn})+g_{12}(\alpha_{km},\beta_{kn},\rho_{jkm},\mu_{ikn})\\
-g_9(\beta_{km},\beta_{kn},\rho_{jkm},\mu_{ikn})-g_{10}(\beta_{km},\alpha_{kn},\rho_{jkm},\mu_{ikn})\\
-g_{11}(\beta_{km},\beta_{kn},\rho_{jkm},\mu_{ikn})-g_{12}(\beta_{km},\alpha_{kn},\rho_{jkm},\mu_{ikn})\\
+g_{13}(\alpha_{km},\alpha_{kn},\mu_{jkm},\rho_{ikn})+g_{14}(\alpha_{km},\beta_{kn},\mu_{jkm},\rho_{ikn})\\
+g_{15}(\alpha_{km},\alpha_{kn},\mu_{jkm},\rho_{ikn})+g_{16}(\alpha_{km},\beta_{kn},\mu_{jkm},\rho_{ikn})\\
-g_{13}(\beta_{km},\beta_{kn},\mu_{jkm},\rho_{ikn})-g_{14}(\beta_{km},\alpha_{kn},\mu_{jkm},\rho_{ikn})\\
-g_{15}(\beta_{km},\beta_{kn},\mu_{jkm},\rho_{ikn})-g_{16}(\beta_{km},\alpha_{kn},\mu_{jkm},\rho_{ikn})]
\end{aligned}
\tag{A6}
$$

$$
\begin{aligned}
B_{mn,23}(t) = S[\sum_{i=1,N}a_i\exp(b_it)]\sum_{k=1,2}\frac{1}{8\zeta_{gk}\omega_{gk}}\sum_{j=1,N}a_j\exp(b_jt) *\\
\{(C_{ak}+C_{bk})[g_{17}(\alpha_{km},\rho_{jkm})+g_{17}(\beta_{km},\rho_{jkm})]\\
+\zeta_{gk}\omega_{gk}/\omega_{gdk}(C_{ak}-C_{bk})[g_{18}(\alpha_{km},\rho_{jk})-g_{18}(\beta_{km},\rho_{jkm})]\}
\end{aligned}
\tag{A7}
$$

$$
B_{mn,31}(t) = B_{nm,13}(t) \tag{A8}
$$

$$
B_{mn,32}(t) = B_{nm,13}(t) \tag{A9}
$$

$$
B_{mn,33}(t) = [\sum_{i=1,N}a_i\exp(b_it)]^2R_{gg}(0) \tag{A10}
$$

where α_{km}, β_{kn}, μ_{jkm}, and ρ_{ikn} are functions of system parameters given below:

$$\alpha_{km} = \omega_{dm} - \omega_{gdk}\ ,\quad \beta_{kn} = \omega_{dn} + \omega_{gdk}\ ,$$
$$\rho_{jkm} = b_j + \zeta_{dm}\omega_m + \zeta_{gk}\omega_{gk}\ ,\ \mu_{ikn} = b_i + \zeta_{dn}\omega_n - \zeta_{gk}\omega_{gk} \qquad \text{(A11)}$$
$$(i,j=1,2,\ldots N;\ k=1,2;\ m,n=1,2,\ldots)$$

Note that functions g_1 through g_{18} are not given here due to limited space.

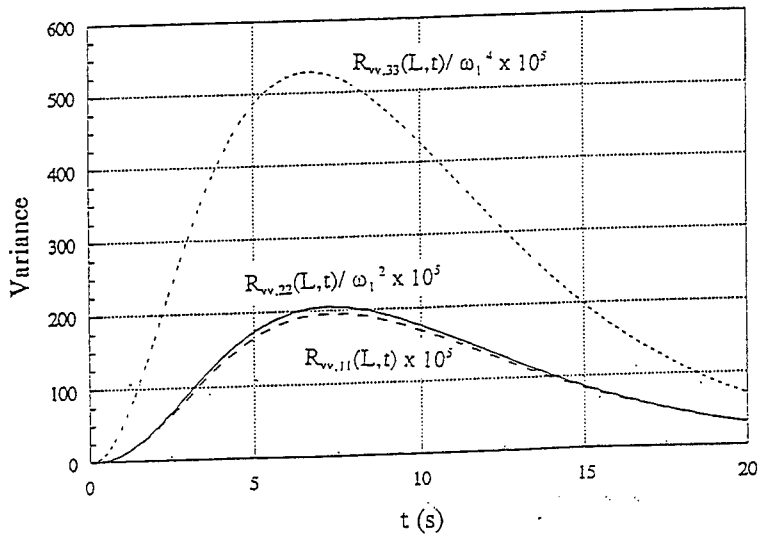

Fig.1 Variance of Top Displacement, velocity, and Acceleration
($S=1$, $r_t \rightarrow \infty$ and $r_r \rightarrow \infty$)

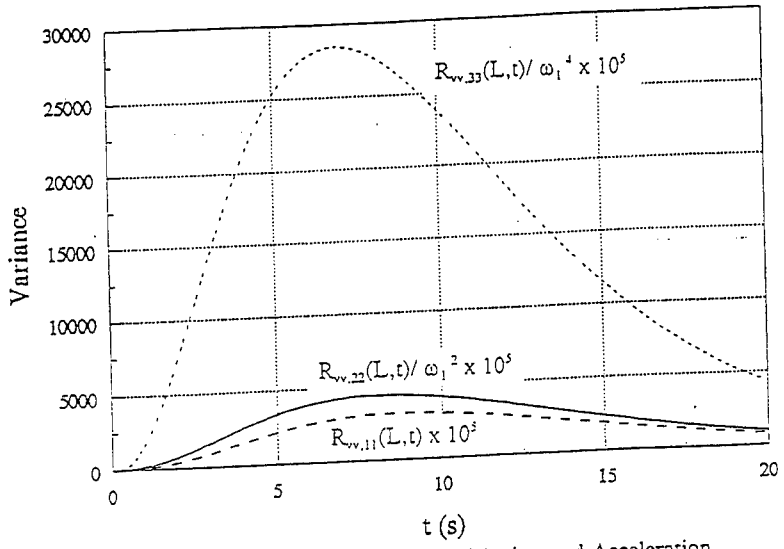

Fig.2 Variance of Top Displacement, Velocity, and Acceleration
($S=1$, $r_t=10$ and $r_r=1$)

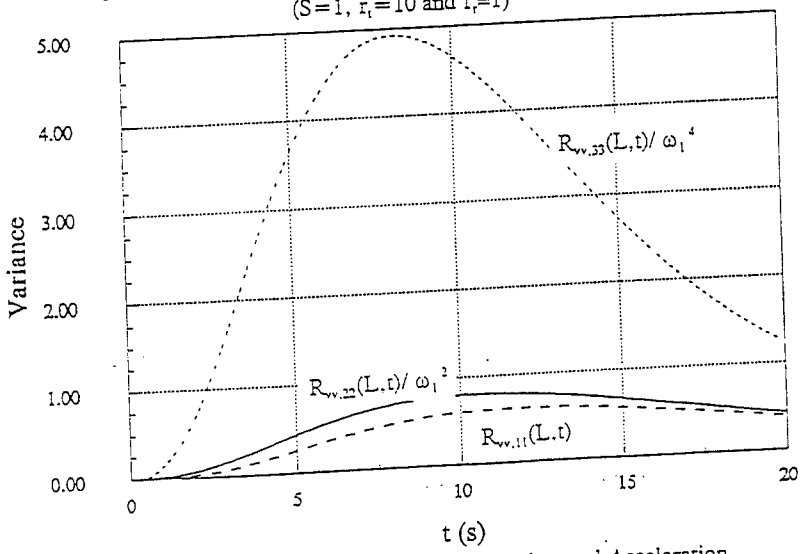

Fig.3 Variance of Top Displacement, Velocity, and Acceleration
($S=1$, $r_t=1$ and $r_r=0.1$)

LINEAR MULTI-STAGE SYNTHESIS OF RANDOM VIBRATION SIGNALS FROM PARTIAL COVARIANCE INFORMATION

S.D. Fassois* *and* K. Denoyer**

*Department of Mechanical & Aeronautics Engineering
University of Patras
GR-265 00 Patras, Greece
E-mail: fassois@mech.upatras.gr

**Department of Mechanical Engineering & Applied Mechanics
The University of Michigan
Ann Arbor, MI 48109-2125, U.S.A.

ABSTRACT

An effective scheme for random vibration signal synthesis from partial covariance information is introduced. The proposed scheme is based upon a Fast Rational Model estimation approach, combined with a discrete ARMA(2n,2n-1) vibration signal representation and a dispersion analysis methodology. Unlike previous approaches, the proposed scheme provides accurate synthesis without resorting on nonlinear operations, and provides the tools for effective representation order determination. Furthermore, it mathematically guarantees the estimated representation stability and invertibility properties, implying that all types of vibration signals, including those characterized by sharp spectral peaks or valleys, can be handled without difficulty. The effectiveness of the scheme is demonstrated via synthesis test cases, through which the benefits of representation overfitting are also presented.

List of Symbols

$\boldsymbol{G}(s)$	:	receptance transfer matrix
G_j	:	j-th term of the Green's function
I_j	:	j-th term of the inverse function
$S(\omega)$	:	power spectral density function
$\gamma(\tau)$	:	continuous time autocovariance function
$\gamma[kT]$	:	discrete time autocovariance function
$\phi(B)$	:	autoregressive polynomial
$\theta(B)$	:	moving average polynomial
ϕ_i	:	i-th autoregressive parameter ($i = 1, 2, \cdots, 2n$)
θ_i	:	i-th moving average parameter ($i = 1, 2, \cdots, 2n-1$)
μ_i	:	i-th continuous pole ($i = 1, 2, \cdots, 2n$)

δ_i : i-th vibration mode dispersion percentage ($i = 1, 2, \cdots, n$)
σ_w^2 : innovations variance
B : backshift operator ($Bx[t] \triangleq x[t-1]$)
R : number of specified autocovariance samples
T : sampling period
p : truncated inverse function order
n_o : number of structural degrees of freedom
n : number of degrees of freedom in the signal representation

Superscript:
^{i} : indicates iteration number.

Conventions:
$[\cdot]$: function of a discrete variable.
$(\cdot)$: function of a continuous variable.
Vector/matrix quantities are indicated in bold-face characters.

1. INTRODUCTION

In this paper the problem of digitally synthesizing stationary random vibration signals from partial (incomplete) covariance information is considered. The problem is important for generating vibration signals to be used in the computer or laboratory based simulation and testing of various types of structural systems, including machine, vehicle, aerospace, and civil engineering structures.

The problem of equi-spaced in time vibration signal synthesis from complete, *analytically* available, covariance information may be tackled via well known spectral factorization techniques [1], which yield an appropriate stochastic realization that may be subsequently used for synthesis purposes. The practically much more important problem of synthesis based upon a *finite* (truncated) number of available covariance samples is equivalent to that of finding an admissible extension of the partially specified covariance sequence, and obtaining an analytical description that can be used for vibration synthesis. A complete analytic description, which automatically implies an admissible extension of a given covariance sequence, as long as the latter corresponds to a rational spectral density, is provided through the AutoRegressive Moving Average (ARMA) representation [2].

Limiting attention to purely AutoRegressive (AR) based vibration synthesis leads to the well-known Yule-Walker equations which are linear in terms of the representation parameters [2]. Unfortunately purely AR based schemes are ineffective for proper synthesis, especially when the partially specified covariance corresponds to relatively sharp valleys in the spectral domain [3,4]. Purely Moving Average (MA) representations, such as the ones advocated by Abdul-Sada and Mahmood [5] in a different context, are also inappropriate for describing the relatively sharp spectral peaks

of vibration signals. These considerations unambiguously lead to mixed Autoregressive Moving Average (ARMA) based vibration signal synthesis.

Unfortunately, ARMA based synthesis is a much less tractable problem, leading to a non-linear mathematical optimization problem [1-3]. To circumvent this difficulty Gersch and Luo [6] proposed a mixed scheme, in which the AR parameters are obtained through the Yule-Walker equations, while the MA parameters are obtained via a non-linear modified Newton-Raphson procedure. In subsequent work, Gersch and co-workers [7,8] utilized proper extensions of the Two Stage Least Squares (2SLS) method introduced in time series analysis by Durbin [9]. The 2SLS method is, nevertheless, known to be characterized by statistical inefficiency and limited achievable accuracy [10]. In related work within a broader context, Georgiou [11] attempted finding an admissible extension of a partially specified covariance sequence via a method that recursively updates ARMA representations of dimension increasing with the sequence length. This method, however, requires a-priori information on the representation's zero locations. For very simple cases, corresponding to low order MA polynomials, this information may be, perhaps, derived from the asymptotic behavior of the partial autocorrelation coefficients. Nevertheless, such a procedure cannot be used with realistic MA polynomials of interest in the vibration synthesis problem.

In this paper an effective scheme for ARMA based vibration signal synthesis is introduced. The scheme is based upon a Fast Rational Model estimation approach [3,4], combined with the covariance invariance principle and a dispersion analysis methodology. The covariance invariance principle [2] is used for relating the continuous and discrete vibration signal representations, and leads to a special ARMA(2n,2n-1) structure for the latter. The Fast Rational Model approach, originally introduced within the context of spectral estimation from available signal samples [3,4], is used for effective parameter estimation, while the dispersion analysis methodology [12] is used as the main tool for representation order determination. The scheme uses the specified autocovariance samples as a pseudo-sufficient statistic, and develops a strongly consistent ARMA representation based upon exclusively linear operations. An additional important property of the proposed scheme is that it is capable of mathematically guaranteeing the stability and invertibility of the obtained ARMA representation; a feature implying that, unlike alternative techniques, it can handle the practically significant classes of vibration signals characterized by sharp spectral peaks or valleys without any difficulty.

The paper is organized as follows: The proposed vibration signal synthesis methodology is presented in Section 2, synthesis test cases are considered in Section 3, and the conclusions of the work are summarized in Section 4.

2. VIBRATION SIGNAL SYNTHESIS METHODOLOGY

2.1 Fundamentals

Consider a linear viscously-damped n_o degree-of-freedom structural

system described by the vector differential equation:

$$\mathbf{M} \cdot \ddot{\mathbf{x}}(t) + \mathbf{C} \cdot \dot{\mathbf{x}}(t) + \mathbf{K} \cdot \mathbf{x}(t) = \mathbf{f}(t) \tag{1}$$

where $\mathbf{M}, \mathbf{C}, \mathbf{K}$ represent the $n_o \times n_o$ mass, viscous damping, and stiffness matrices, respectively, and $\mathbf{f}(t)$, $\mathbf{x}(t)$ the n_o-dimensional force excitation and vibration displacement signals, respectively. Laplace transforming (1) leads to:

$$\mathbf{X}(s) = [\mathbf{M} \cdot s^2 + \mathbf{C} \cdot s + \mathbf{K}]^{-1} \cdot \mathbf{F}(s) \triangleq \mathbf{G}(s) \cdot \mathbf{F}(s) \tag{2}$$

in which s represents the Laplace Transform variable and $\mathbf{G}(s)$ the system's receptance transfer matrix.

Let $G_{ij}(s)$ represent the ij-th element of $\mathbf{G}(s)$, that is the transfer function relating the i-th displacement with the j-th force. Assuming that the force excitation is a stationary zero-mean uncorrelated stochastic signal, that is:

$$E\{f_j(t)\} = 0 \qquad E\{f_j(t_1) \cdot f_j(t_2)\} = \sigma_f^2 \cdot \delta(t_1 - t_2)$$

with $E\{\cdot\}$ indicating statistical expectation and $\delta(\cdot)$ the Dirac delta function, the resulting vibration displacement $x_i(t)$ will, in the steady-state, be a stationary stochastic signal with zero mean and autocovariance [2]:

$$\gamma(\tau) = \sigma_f^2 \cdot \int_0^\infty g(t) \cdot g(t + |\tau|) \cdot dt = \sum_{k=1}^{2n_o} d_k \cdot e^{\mu_k |\tau|} \tag{3}$$

In these expressions (the latter of which assumes distinct poles) $g(t)$ represents the impulse response of the receptance transfer function $G_{ij}(s)$, and μ_k, d_k $(k = 1, 2, \cdots, 2n_o)$ the structural poles and corresponding autocovariance expansion coefficients, respectively.

The uniform instantaneous sampling of the stochastic vibration displacement $x(t)$ (the subscript being, for the sake of simplicity, suppressed) leads to a discrete-time stochastic signal $x[kT]$ $(k = 0, 1, 2, \cdots)$, with T representing the sampling period, which is characterized by an autocovariance function $\gamma[kT]$ satisfying the covariance invariance principle [2]:

$$\gamma[kT] = \gamma(\tau)|_{\tau = kT} \tag{4}$$

Assuming that $x(t)$ is band-limited, and that the conditions of the Nyquist theorem are satisfied, the continuous and discrete spectral densities satisfy the relationship [1]:

$$S^D(\omega) = \frac{1}{T} S^C(\omega) \qquad (-\frac{\pi}{T} < \omega < \frac{\pi}{T}) \tag{5}$$

in which ω represents frequency in $rads/sec$, and $S^C(\omega)$, $S^D(\omega)$ the continuous and discrete densities, respectively.

Denoting the discrete time kT in normalized form as simply k, or t $(t = 0, 1, 2, \cdots)$, the sampled displacement signal may be shown [2] to

admit a stable and invertible AutoRegressive Moving Average (ARMA) representation of orders $(2n_\circ, 2n_\circ - 1)$, that is:

$$x[t] + \sum_{k=1}^{2n_\circ} \phi_k \cdot x[t-k] = w[t] + \sum_{k=1}^{2n_\circ - 1} \theta_k \cdot w[t-k] \Longrightarrow$$
$$\Longrightarrow \quad \phi(B) \cdot x[t] = \theta(B) \cdot w[t] \tag{6}$$

In the above $w[t]$ represents a discrete, zero-mean, uncorrelated (innovations) sequence with variance σ_w^2, and ϕ_k $(k = 1, 2, \cdots, 2n_\circ)$ and θ_k $(k = 1, 2, \cdots, 2n_\circ - 1)$ the autoregressive (AR) and Moving Average (MA) parameters, respectively. The AR and MA polynomials are defined as:

$$\phi(B) \triangleq 1 + \phi_1 \cdot B + \cdots + \phi_{2n_\circ} \cdot B^{2n_\circ} \qquad \theta(B) \triangleq 1 + \theta_1 \cdot B + \cdots + \theta_{2n_\circ - 1} \cdot B^{2n_\circ - 1}$$

with B denoting the backshift operator $(B \cdot x[t] \triangleq x[t-1])$.

Once determined from the specified partial covariance sequence, a proper ARMA representation of the form (6) may be used for vibration signal synthesis.

2.2 The Algorithm

The vibration synthesis problem treated concerns the generation (realization) of discrete random vibration displacement signals with covariance characteristics conforming to a prescribed partial (truncated) autocovariance sequence $\gamma[k]$ $(k = 0, 1, 2, \cdots, R)$.

The vibration signals of interest may be viewed as responses of linear viscously damped structural systems of the form (1) subject to uncorrelated force excitation, and may be synthesized via discrete ARMA(2n,2n-1) representations of the form (6) driven by realizations of pseudo-random uncorrelated sequences characterized by zero mean and variance σ_w^2. Toward this end both the ARMA representation and innovations variance σ_w^2 need to be determined from the given covariance information. This is achieved via the Fast Rational Model estimation approach, which consists of a sequence of stages, with each one based on exclusively linear operations [3,4], as well as the dispersion analysis methodology (see [12] for a treatment of the notion of modal dispersion) for representation order determination. The resulting synthesis algorithm may be outlined as follows:

In *Stage 1* a truncated, p-th order, version of the ARMA representation's inverse function $\{I_j\}_{j=1}^{p}$ $(I_0 \equiv 1)$ $[R > p > 2n$ with p generally selected as $p \approx (2.5 \cdots 5) \times 2n]$ is obtained through the estimator expressions:

$$\sum_{j=1}^{p} I_j \cdot \gamma[k-j] + \gamma[k] = 0 \qquad (k = 1, 2, \cdots, p) \tag{7}$$

□

In *Stage 2* initial MA parameter estimates θ_k° $(k = 1, 2, \cdots, 2n - 1)$

are obtained by solving the set of equations:

$$I_j + \sum_{k=1}^{2n-1} \theta_k^{\circ} \cdot I_{j-k} = 0 \qquad (j = 2n+1, \cdots, 4n-1) \tag{8}$$

□

In *Stage 3* AR parameter estimates ϕ_j^i $(j = 1, 2, \cdots, 2n)$ are obtained via the estimator expressions:

$$\sum_{j=1}^{2n} \phi_j^i \cdot \tilde{\gamma}^{i-1}[k-j] = \tilde{\gamma}^{i-1}[k] \qquad (k = 1, 2, \cdots, 2n) \tag{9}$$

in which the superscript i denotes iteration number and $\tilde{\gamma}^{i-1}[k]$ the autocovariance function of the signal:

$$\tilde{x}^{i-1}[t] \triangleq \frac{x[t]}{\theta^{i-1}(B)} \tag{10}$$

The samples $\tilde{\gamma}^{i-1}[k]$ of this autocovariance are computed by assuming $\tilde{\gamma}^{i-1}[k] \approx 0$ for $|k| > R$. This leads to the following set of equations, which may be solved for $\tilde{\gamma}^{i-1}[k]$ $(k = 0, 1, \cdots, R)$:

$$\sum_{l=0}^{R} A(j,l) \cdot \tilde{\gamma}^{i-1}[l] = \gamma[j] \qquad (j = 0, 1, 2, \cdots, R) \tag{11}$$

in which:

$$A(j,l) \triangleq \begin{cases} a_{j+l} & l = 0 \\ a_{j+l} + a_{|j-l|} & l \neq 0 \end{cases} \tag{12}$$

where $a_j \equiv 0$ for $j \notin [0, 2n-1]$, and:

$$a_j \triangleq \sum_{k=0}^{2n-1-j} \theta_k^{i-1} \cdot \theta_{k+j}^{i-1} \tag{13}$$

□

In *Stage 4* updated MA parameter estimates θ_j^i $(j = 1, 2, \cdots, 2n-1)$ are obtained based upon the expressions:

$$\theta_j^i = -I_j - \sum_{k=1}^{j-1} \theta_k^i \cdot I_{j-k} + \phi_j^i \qquad (j = 1, 2, \cdots, 2n-1) \tag{14}$$

□

In *Stage 5* the innovations variance is estimated as:

$$(\sigma_w^2)^i = \left[\gamma[0] + \sum_{j=1}^{2n} \phi_j^i \cdot \gamma[j]\right] \cdot \left[1 + \sum_{j=1}^{2n-1} \theta_j^i \cdot G_j^i\right]^{-1} \tag{15}$$

with G_j^i representing an estimate, obtained at iteration i, of the j-th sample of the ARMA representation's Green's function [2]. This is achieved through the recursive expressions:

$$G_j^i = \theta_j^i - \sum_{k=1}^{2n} \phi_k^i \cdot G_{j-k}^i \qquad (j = 1, 2, \cdots, 2n-1) \tag{16}$$

with $G_0^i \equiv 1$, $G_j^i \equiv 0$ for $j < 0$. Following this, the representation's autocovariance generating function and spectral density may be obtained as:

$$\gamma^i(B) \triangleq \sum_{k=-\infty}^{\infty} \gamma^i[k] \cdot B^k = \frac{\theta^i(B) \cdot \theta^i(B^{-1})}{\phi^i(B) \cdot \phi^i(B^{-1})} \cdot (\sigma_w^2)^i \qquad S^i(\omega) = \gamma^i(B)|_{B=e^{-j\omega T}} \tag{17}$$

with j denoting the imaginary unit. □

In *Stage 6* the dispersion percentage δ_j $(j = 1, 2, \cdots, n)$ of each vibration mode, expressing the mode's normalized energy contribution in the signal representation, is (in the underdamped case) computed as:

$$\delta_j = (d_{2j-1} + d_{2j}) \cdot \left(\sum_{k=1}^{2n} d_k \right)^{-1} \quad (\%) \qquad (j = 1, 2, \cdots, n) \tag{18}$$

with the quantities d_j $(j = 1, 2, \cdots, 2n)$ being defined by Eq. (3). □

Stages 1 through 6 are repeated for signal representations with successively increasing number of degrees of freedom n, and, in Stage 7, the proper number of degrees of freedom is selected as:

$$n^* = \max\{\, n \mid \quad |\delta_j| > \epsilon \quad \forall j\} \tag{19}$$

with ϵ indicating a small positive threshold value selected in accordance with the desired synthesis accuracy. □

In *Stage 8* the vibration signal is synthesized by exciting the obtained ARMA$(2n^*, 2n^* - 1)$ representation by a simulated zero mean uncorrelated sequence with variance $(\sigma_w^2)^i$. □

Remark 1. For a given signal representation order, stages 3 and 4 of the algorithm are iterated until convergence is achieved. The estimation results of the iteration characterized by minimal innovations variance $(\sigma_w^2)^i$ are selected as best.

Remark 2. The invertibility of an estimated ARMA(2n,2n-1) representation may be mathematically guaranteed via slightly modified MA parameter estimators in stages 2 and 4, that are based upon the stability property of zero-lag least-squares inverses (alternative versions A and B in Fassois [4]). Alternative version B may be used in stage 3 in order to guarantee the representation stability as well. The guaranteed stability and invertibility properties are of primary importance, as they imply that *all* types of vibration signals, including those characterized by sharp spectral peaks or valleys, may be synthesized without difficulty (see section 3).

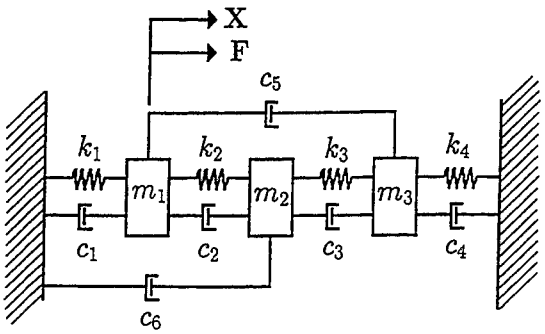

$m_1 = 0.5$ kg	$k_1 = 100$ N/m	$c_1 = 0.5$ N*sec/m
$m_2 = 2.0$ kg	$k_2 = 100$ N/m	$c_2 = 0.5$ N*sec/m
$m_3 = 1.0$ kg	$k_3 = 150$ N/m	$c_3 = 1.5$ N*sec/m
	$k_4 = 100$ N/m	$c_4 = 1.5$ N*sec/m
		$c_5 = 0.6$ N*sec/m
		$c_6 = 0.5$ N*sec/m

Figure 1: Schematic representation of the three degree-of-freedom structural system of Test Case I.

3. SYNTHESIS TEST CASES

Two test cases, in which the scheme is used for the synthesis of signals matching a specified portion of the covariance structure of selected vibration displacements, are presented.

3.1 Test Case I

In Test Case I the synthesis of signals matching part of the covariance structure of the displacement of mass 1 of the three degree-of-freedom system of Figure 1 when excited at that point by a continuous-time uncorrelated force is considered. This type of signal is characterized by spectral peaks at 1.04 and 3.32 Hz, with a spectral valley between them, as well as a much less obvious third peak at 2.68 Hz (solid curve in Figure 2).

The autocovariance function $\gamma[k]$ is specified at lags $k = 0, 1, 2, \cdots$, 50 ($R = 50$), the sampling period is selected as $T = 0.075$ $secs$, the inverse function order as $p = 25$, and the maximum allowable number of iterations as $i_{max} = 25$.

The spectral density of the synthesized, theoretically sufficient, ARMA (6,5) representation is compared to the theoretical spectral density in Figure 2(a), from which very good agreement is observed. A similar remark may be made for the autocovariance function of the synthesized representation (not shown).

Allowing the representation order to be increased to $2n = 8$ [ARMA

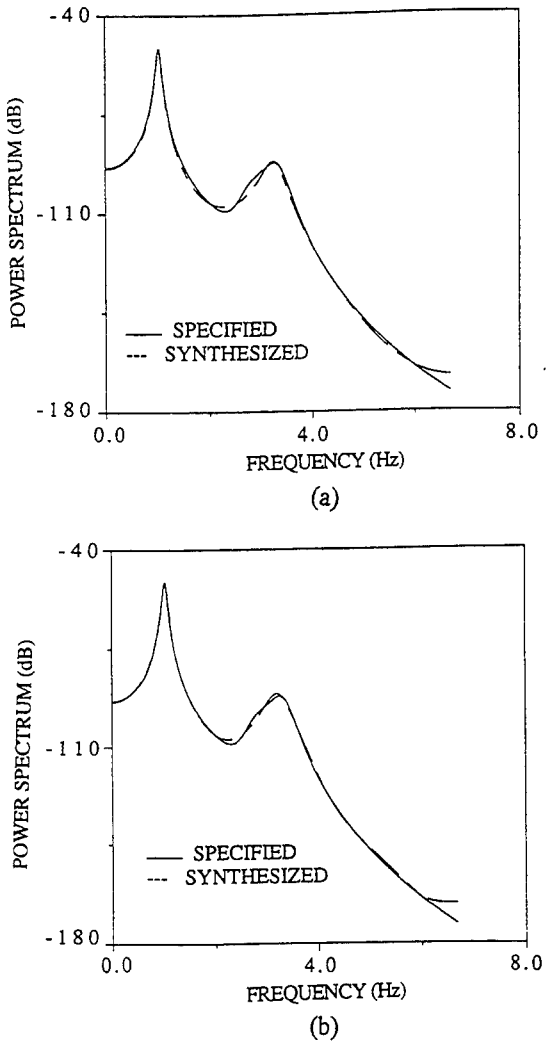

Figure 2: Synthesized (- - -) versus theoretical (—-) spectral density function: (a) ARMA(6,5) based synthesis, (b) ARMA(8,7) based synthesis (Test Case I; $R = 50$).

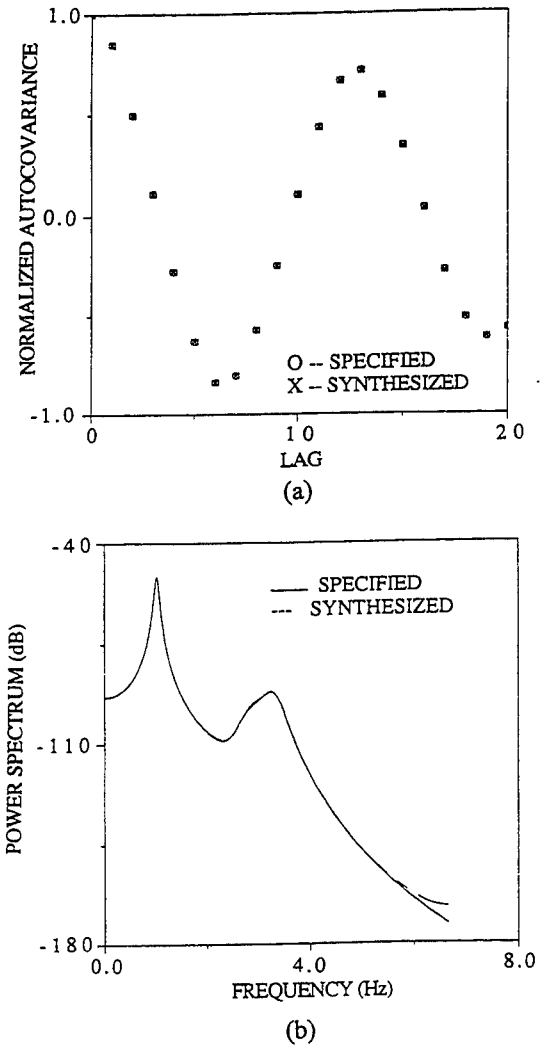

Figure 3: ARMA(10,9) based synthesis results: (a) synthesized (x) versus specified (o) autocovariance function, (b) synthesized (- - -) versus theoretical (—-) spectral density function (Test Case I; $R = 50$).

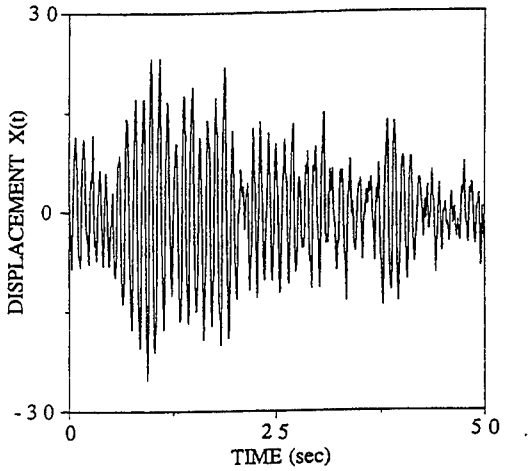

Figure 4: ARMA(10,9) based vibration displacement signal realization (Test Case I; $R = 50$).

(8,7) model] leads to visible improvements in the synthesized representation spectral density [Figure 2(b)], as well as in its autocovariance. These improvements are more evident at autocovariance lags higher than 10, and at frequencies corresponding to the neighborhood of the spectral valley located between the two peaks.

A further increase of the representation order to $2n = 10$ [ARMA(10,9) model] leads to an almost perfect match of both the specified autocovariance and spectral density, as the theoretical and synthesized curves are practically indistinguishable (Figure 3). The extra poles introduced in this case may be grouped into two pairs: a real and a complex conjugate, and are both characterized by small dispersion percentages. These results suggest that, despite the theoretical sufficiency of the ARMA(6,5) representation, which is also confirmed by the Akaike Information Criterion (AIC) [1], overfitting is beneficial in achieving the highest accuracy in matching the specified autocovariance characteristics. Portion of a vibration displacement signal realization obtained by the synthesized ARMA(10,9) representation is depicted in Figure 4.

The effects of the number of lags R, at which the autocovariance function is specified, have been also investigated. Lowering R to 35 (from its current value of 50) does not appreciably change the synthesized representation's spectral density, although it does lead to slight deterioration in the neighborhood of the spectral valley and at the high frequency end. On the other hand, increasing R to 100 produces a spectral density that is essentially identical to that of the $R = 50$ case, and almost indistinguishable from the theoretical.

3.2 Test Case II

In Test Case II the synthesis of signals matching part of the covari-

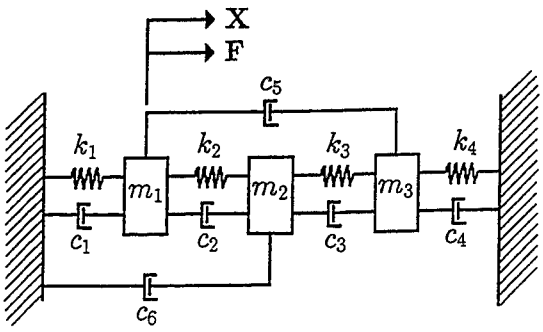

$m_1 = 1.0$ kg	$k_1 = 100$ N/m	$c_1 = 0.6$ N*sec/m
$m_2 = 1.0$ kg	$k_2 = 100$ N/m	$c_2 = 0.5$ N*sec/m
$m_3 = 2.0$ kg	$k_3 = 100$ N/m	$c_3 = 0.6$ N*sec/m
	$k_4 = 100$ N/m	$c_4 = 1.5$ N*sec/m
		$c_5 = 0.5$ N*sec/m
		$c_6 = 0.7$ N*sec/m

Figure 5: Schematic representation of the three degree-of-freedom structural system of Test Case II.

ance structure of the displacement of mass 1 of the three degree-of-freedom system of Figure 5 when excited at that point by a continuous-time uncorrelated force is considered. This type of signal is characterized by three spectral peaks at 1.29, 2.03 and 2.81 Hz, with sharp valleys among them [solid curve in Figure 6(b)] - a case of recognized difficulty.

The autocovariance function $\gamma[k]$ is specified at lags $k = 0, 1, 2, \cdots$, 50 ($R = 50$), the sampling period is selected as $T = 0.0884$ *secs*, the inverse function order as $p = 25$, and the maximum allowable number of iterations as $i_{max} = 25$.

Similarly to the previous case, vibration signal synthesis is based upon an overfitted ARMA(10,9) representation. The extra poles include a real and a complex conjugate pair, and are all characterized by small dispersion percentages. The autocovariance and spectral density of the synthesized ARMA(10,9) representation are compared to those specified in Figures 6(a) and 6(b), respectively. Evidently, the autocovariance function is very close to the specified, and certainly very satisfactory, although the matching is not characterized by the "perfection" of the previous case. This is verified from the representation's spectral density plot as well, which indicates some deviation from the theoretical density, especially in the neighborhood of the first - and sharpest - spectral valley. This is, nevertheless, expected, due to the difficulties associated with signals characterized by sharp spectral valleys. The fact itself that the algorithm operated properly in this case is due to its important inherent stability characteristics. Portion of a vibration displacement signal realization obtained by the estimated ARMA(10,9)

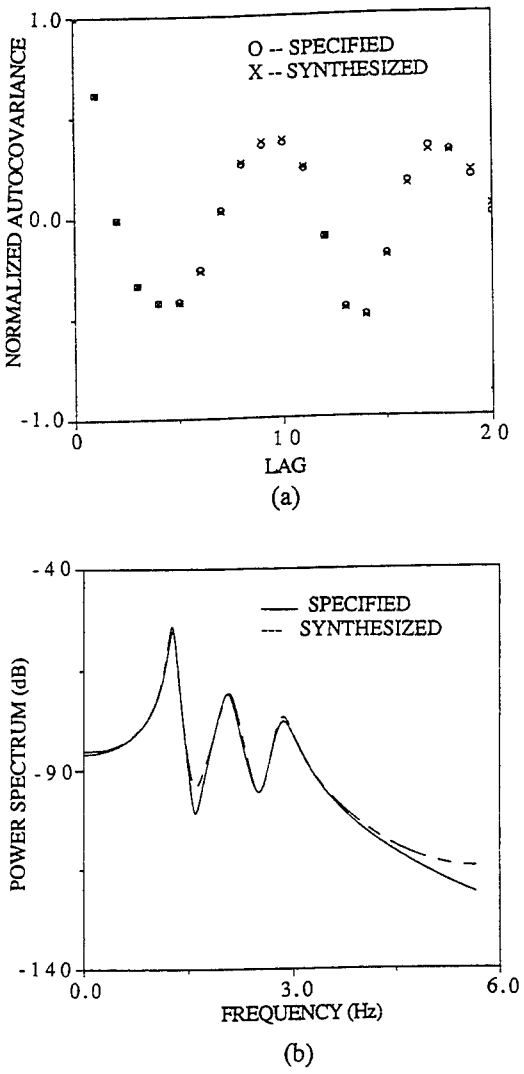

Figure 6: ARMA(10,9) based synthesis results: (a) synthesized (x) versus specified (o) autocovariance function, (b) synthesized (- - -) versus theoretical (—-) spectral density function (Test Case II; $R = 50$).

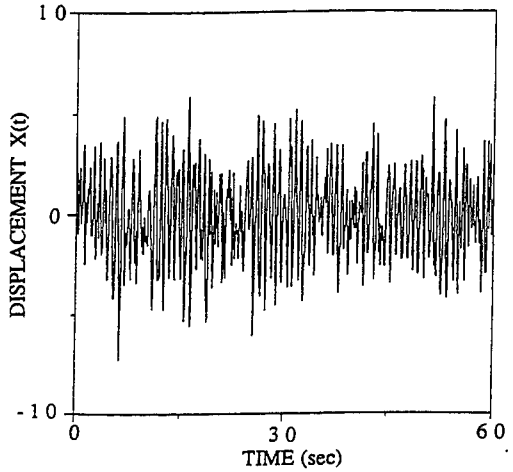

Figure 7: ARMA(10,9) based vibration displacement signal realization (Test Case II; $R = 50$).

representation is presented in Figure 7.

4. CONCLUDING REMARKS

In this paper a linear multi-stage scheme for effective random vibration signal synthesis from partial covariance information was introduced. The scheme was shown to achieve accurate synthesis without resorting on nonlinear operations. Moreover, by providing mathematically guaranteed estimated ARMA representation stability and invertibility, it was shown to be capable of effectively synthesizing all types of vibration signals, including the difficult classes of signals characterized by sharp spectral peaks and/or valleys. In particular:

- Signals characterized by sharp spectral valleys were found to be most difficult to synthesize, with the synthesis accuracy generally lagging in the neighborhood of the spectral valley.
- Representation overfitting, with the additional modes characterized by relatively small dispersion percentages, was shown to be necessary in achieving maximum synthesis accuracy.
- The required minimal number of autocovariance samples for accurate synthesis was found to be about $12n_o$, with n_o denoting the number of structural degrees of freedom. Increasing the proportionality factor to about 16 was shown to lead to some improvement, but further increases were of no significance.

REFERENCES

[1] Kay, S.M. *Modern Spectral Estimation: Theory and Application.* Prentice-Hall, 1988.

[2] Pandit S.M. and Wu, S.M. *Time Series and System Analysis with Applications.* John Wiley and Sons, 1983.

[3] Fassois, S.D. A fast rational model approach to parametric spectral estimation. Part I: the algorithm. *ASME Journal of Vibration and Acoustics*, Vol. 112, 1990, pp. 321-327.

[4] Fassois, S.D. A fast rational model approach to parametric spectral estimation. Part II: properties and performance evaluation. *ASME Journal of Vibration and Acoustics*, Vol. 112, 1990, pp. 328-336.

[5] Abdul-Sada, J.W. and Mahmood, M.K. Generation of gaussian pseudo-random process with specific correlation properties. *International Journal of Systems Science*, Vol. 19, 1988, pp. 2163-2168.

[6] Gersch, W. and Luo, S. Discrete time series synthesis of randomly excited structural system response. *Journal of the Acoustical Society of America*, Vol. 51, 1972, pp. 402-408.

[7] Gersch, W. and Liu, R.S-Z. Time series methods for the synthesis of random vibration systems. *ASME Journal of Applied Mechanics*, Vol. 98, 1976, pp. 159-165.

[8] Gersch, W. and Yonemoto, J. Synthesis of multivariate random vibration systems: a two stage least squares ARMA model approach. *Journal of Sound and Vibration*, Vol. 52, 1977, pp. 553-565.

[9] Durbin, J. The fitting of time series models. *Reviews of the International Institute of Statistics*, Vol. 28, 1960, pp. 233-244.

[10] Mayne, D.Q. and Firoozan, F. Linear identification of ARMA processes. *Automatica*, Vol. 18, 1982, pp. 461-466.

[11] Georgiou, T.T. Realization of power spectra from partial covariance sequences. *IEEE Transactions on Acoustics, Speech, and Signal Processing*, Vol. 35, 1987, pp. 438-449.

[12] Lee, J.E. and Fassois, S.D. On the problem of stochastic experimental modal analysis based on multiple-excitation multiple-response data. Part I: dispersion analysis of continuous-time structural systems. *Journal of Sound and Vibration*, Vol. 161, 1993, pp. 33-56.

FIRST PASSAGE TIME OF MULTI-DEGREES OF FREEDOM NON-LINEAR SYSTEMS UNDER NARROW-BAND NON-STATIONARY RANDOM EXCITATIONS

C.W.S. To† and **Z. Chen**‡
Department of Mechanical Engineering
University of Nebraska
255 Walter Scott Engineering Center
Lincoln, Nebraska 68588-0656
U.S.A.

E-mail: cwsto@unlinfo.unl.edu

Abstract

The study of motion of aerospace systems and buildings, that house sophisticated and expensive electronic equipment under intensive transient disturbances, has in recent years become an important issue in the design and analysis process. Central to the study is the problem of predicting motion and first passage time of the system under such disturbances.

Owing to the intensity and nature of the excitation, and the non-linearity of the deformation of the complex system, techniques available for the response predicting is very limited. To provide a more realistic and accurate prediction of response and assessment of the first passage probability, in this paper the extended stochastic central difference method is proposed. The recursive response statistics and first passage time of a multi-degrees of freedom non-linear system under excitations treated as narrow band non-stationary random excitations are considered. Results of a two degrees of freedom non-linear system indicate that the technique proposed is very efficient and accurate compared with the Monte Carlo simulation data.

---

† Professor and corresponding author
‡ Research Assistant, Department of Mechanical Engineering, The University of Western Ontario, London, Ontario, Canada N6A 5B9

1. INTRODUCTION

The study of motion of aerospace systems and buildings, that house sophisticated and expensive electronic equipment under intensive transient disturbances, has in recent years become an important issue in the design and analysis process. Central to the study is the problem of predicting motion and first passage time of the system under such disturbances.

Owing to the intensity and nature of the excitation, modulated wide band random excitation process is a highly idealization and consequently, even for a two degrees of freedom (dof) linear system it can lead to large differences between the responses of the system under such an excitation process and those using a more realistic representation of narrow band non-stationary random disturbance [1]. For a single dof nonlinear system, the first passage time based on wide band random excitation is very significantly different from that using the narrow-band random excitation process [2]. A survey of the literature seems to suggest that no analytical or computational technique, bar the Monte Carlo simulation (MCS) method, is available for the prediction of motion and first passage time of multi-degrees of freedom (mdof) nonlinear systems under narrow band non-stationary random excitation. When the number of dof is large and the excitation is a narrow band non-stationary process, even the application of the MCS can be difficult if not impossible. The difficulty lies in the choice of centre frequency, bandwidth and amplitude of the response from the filter in order to model the narrow band process that is being approximated and applied to the non-linear system. To provide a more realistic and accurate prediction of response and assessment of the first passage probability, in this paper the extended stochastic central difference (SCD) method is proposed. The recursive response statistics and first passage time of the mdof non-linnear system under excitations treated as narrow band non-stationary random excitations are considered.

The organization of this paper is as follows: a brief introduction to the extended SCD method is given in the next section which is followed by a consideration of the two dof system under narrow band non-stationary random excitation in Section 3. The versatile statistical linearization (SL) or equivalent linearization (EL) technique is applied at every time step to linearize the two dof non-linear system. The scheme adopted here is scheme IV in reference [3]. Section 4 is concerned with the modified adaptive time scheme (ATS) and the first passage probabilities. Computed results are included in Section 5 while remarks are in Section 6.

2. STOCHASTIC CENTRAL DIFFERENCE METHOD FOR NARROW-BAND RANDOM EXCITATIONS

Consider a mdof system under narrow band random excitations, which are obtained from output of a filter perturbed by modulated Gaussian white noise excitations. The governing equations of motion in matrix notation are

$$M_f \ddot{f} + C_f \dot{f} + K_f f = e(t)w(t), \qquad M_y \ddot{Y} + C_y \dot{Y} + K_y Y = f, \tag{1a,b}$$

where M_f, C_f and K_f are the mass, damping and stiffness matrices of the filter while M_y, C_y and K_y are the mass, damping and stiffness matrices of the system respectively; f is the stochastic displacement vector of the filter, and Y is the stochastic displacement vector of the system; e(t) is a vector of time-dependent deterministic modulating functions; the over-dot and double over dot are the first and second derivatives, respectively; w(t) is a zero mean Gaussian white noise process.

Recursive expressions for the mdof filter and mdof system described by equation (1) can be derived [1]. For example, the recursive expression for system responses can be shown as

$$\begin{aligned} R_y(s+1) &= N_{2y} R_y(s) N_{2y}^T + N_{3y} R_y(s-1) N_{3y}^T + \\ &(\Delta t)^4 N_{1y} R_f(s) N_{1y}^T + N_{2y} D_y(s) N_{3y}^T + N_{3y} D_y^T(s) N_{2y}^T \\ &+ (\Delta t)^2 N_{2y} G(s) N_{1y}^T + (\Delta t)^2 N_{1y} G(s)^T N_{2y}^T \\ &+ (\Delta t)^2 N_{3y} H(s) N_{1y}^T + (\Delta t)^2 N_{1y} H(s)^T N_{3y}^T \end{aligned} \tag{2}$$

where $R_f(s) = \langle f_s f_s^T \rangle$; $R_y(s) = \langle Y_s Y_s^T \rangle$; $D_y(s) = \langle Y_s Y_{s-1}^T \rangle = N_{2y} R_y(s-1) + N_{3y} D_y^T(s-1) + (\Delta t)^2 N_{1y} G(s-1)^T$, $G(s) = \langle Y_s f_s^T \rangle$, $H(s) = \langle Y_{s-1} f_s^T \rangle$, $f_s = f(s)$ is f at time step t_s, $\Delta t = t_{s+1} - t_s$, $Y_s = Y(s)$ is Y at time step t_s, the angular brackets denote ensemble average of the enclosing quantity while the superscript T desingates the transpose of the matrix;

$$\begin{aligned} &N_{1y} = [M_y + (\Delta t/2) C_y]^{-1}, \quad N_{2y} = N_{1y} [2M_y - (\Delta t)^2 K_y], \\ &N_{3y} = N_{1y} [(\Delta t/2) C_y - M_y], \\ &G(s) = (\Delta t)^2 N_{1y} D_f^T(s) + N_{2y} H(s) \\ &\qquad + N_{3y} H(s-1) N_{2f}^T + N_{3y} G(s-2) N_{3f}^T, \\ &H(s) = G(s-1) N_{2f}^T + (\Delta t)^2 N_{1y} R_f(s-2) N_{3f}^T \\ &\qquad + N_{2y} G(s-2) N_{3f}^T + N_{3y} H(s-2) N_{3f}^T. \end{aligned}$$

Equation (2) is applicable to systems under multiple narrow band random excitations generated by the filter matrix equation.

In order to provide the required response statistics for the first passage probability computation, the covariance of displacement and velocity responses, and the covariance of velocity response are considered in the following. Starting from the central difference method, the velocity vector at the current time step is given by

$$\dot{Y}(s) = \frac{1}{2\Delta t}\left[Y(s+1) - Y(s-1) \right]$$

which upon post multiplying the transpose of displacement vector Y(s) gives the covariance matrix of velocity and displacement as

$$\left\langle \dot{Y}(s)\, Y^T(s) \right\rangle = \frac{1}{2\,\Delta t}\left[D(s+1) - D^T(s) \right], \tag{3}$$

since $D^T_y(s) = \langle Y_s Y_{s-1}^T \rangle^T = \langle Y_{s-1} Y_s^T \rangle$. Similarly, the covariance matrix of velocity responses becomes

$$\begin{aligned}\left\langle \dot{Y}(s)\, \dot{Y}^T(s) \right\rangle = \frac{1}{4(\Delta t)^2}\Big[& R_y(s+1) + R_y(s-1) - (\Delta t)^2 N_{1y} H^T(s) \\ & - N_{2y} D_y(s) - N_{3y} R_y(s-1) \\ & - (\Delta t)^2 H(s) N_{1y}^T - D_y^T(s) N_{2y}^T \\ & - R_y^T(s-1) N_{3y}^T \Big] .\end{aligned} \tag{4}$$

The foregoing is the so-called extended SCD method. When the excitations are wide band stationary or non-stationary random processes the above equations reduce to those of the SCD method. Equations (2), (3) and (4) can be applied to the response analysis of mdof systems under narrow band non-stationary random excitations. The corresponding first passage probability can be evaluated as in reference [4]. For non-linear systems whose nonlinearities are explicitly defined, however, the following technique is employed in conjunction with the modified ATS before the computation of first passage probabilities can be performed.

3. NON-LINEAR SYSTEMS AND STATISTICAL LINEARIZATION

Consider the two dof system shown in Figure 1. The system is subjected to a narrow band non-stationary random excitation at its base and the restoring force of the spring connecting the two masses M_1 and M_2 has quadratic and cubic nonlinear terms associated with, respectively, parameters

η' and ε'. This two dof system under a modulated white noise excitation was considered by Kimura and Sakata [5], and Liu and To [3, 6]. Practical examples that can be modeled by this system are: (a) soil-structure coupled system, (b) a primary building structure with secondary system representing installed equipment under an earthquake excitation, and (c) an offshore oil platform with a secondary equipment such as the drill string tower under strong wave impact.

If one introduces relative displacements or inter-story drift in the language of earthquake engineering such that $Y_1 = y_1 - y_0$ and $Y_2 = y_2 - y_1$, where y_0, y_1 and y_2 are, respectively, the absolute displacements with respect to the base, the matrix equation of motion can be expressed as [3, 5, 6]

$$\begin{bmatrix} 1 & 0 \\ 0 & 1 \end{bmatrix} \begin{Bmatrix} \ddot{Y}_1 \\ \ddot{Y}_2 \end{Bmatrix} + \begin{bmatrix} 2\zeta_1 W & -2\mu\zeta_2 \\ -2\zeta_1 W & 2(1+\mu)\zeta_2 \end{bmatrix} \begin{Bmatrix} \dot{Y}_1 \\ \dot{Y}_2 \end{Bmatrix} + \begin{bmatrix} W^2 & -\mu \\ -W^2 & 1+\mu \end{bmatrix} \begin{Bmatrix} Y_1 \\ Y_2 \end{Bmatrix} + \begin{Bmatrix} \mu\eta Y_2^2 - \mu\varepsilon Y_2^3 \\ (1-\mu)\eta Y_2^2 + (1+\mu)\varepsilon Y_2^3 \end{Bmatrix} = \begin{Bmatrix} -\ddot{y}_0 \\ 0 \end{Bmatrix} = \begin{Bmatrix} e(\tau)\sqrt{I} \\ 0 \end{Bmatrix} \tag{5}$$

or written in a more compact form

$$M\,\ddot{Y} + C\,\dot{Y} + K_0\,Y + g(Y) = r(\tau) \tag{6}$$

in which

$$M = \begin{bmatrix} 1 & 0 \\ 0 & 1 \end{bmatrix}, \quad C = \begin{bmatrix} 2\zeta_1 W & -2\mu\zeta_2 \\ -2\zeta_1 W & 2(1+\mu)\zeta_2 \end{bmatrix},$$

$$K_0 = \begin{bmatrix} W^2 & -\mu \\ -W^2 & 1+\mu \end{bmatrix}, \quad g(X) = \begin{Bmatrix} \mu\eta Y_2^2 - \mu\varepsilon Y_2^3 \\ (1-\mu)\eta Y_2^2 + (1+\mu)\varepsilon Y_2^3 \end{Bmatrix},$$

$$Y = \begin{Bmatrix} Y_1 \\ Y_2 \end{Bmatrix}, \quad r(\tau) = \begin{Bmatrix} e(\tau)\sqrt{I} \\ 0 \end{Bmatrix},$$

where the over-dot and double over-dot denote, respectively, the first and second derivatives with respect to τ. In equation (6) the non-stationary random excitation is represented as a product of a deterministic amplitude modulating function $e(\tau)$ and a zero mean narrow band random process which is related to the response from the filter. The symbol I is assumed to be constant. Note that the following definitions have been applied in equations (5) and (6)

$$\begin{gathered} \omega_1^2 = K_1/M_1 \ , \quad \omega_2^2 = K_2/M_2 \ , \quad 2\zeta_1\omega_1 = C_1/M_1 \ , \\ 2\zeta_2\omega_2 = C_2/M_2 \ , \quad \eta = \eta'/M_2\omega_2^2 \ , \\ \varepsilon = \varepsilon'/M_2\omega_2^2 \ , \quad \mu = M_2/M_1 \ , \\ W = \omega_1/\omega_2 \ , \quad \tau = \omega_2 t \ . \end{gathered} \tag{7}$$

such that equations (5) and (6) are dimensionless. Therefore, the symbol τ in this section should not be confused with the τ used in the time co-ordinate transformation (TCT) in reference [6].

The discretization of equation (6) in the τ domain leads to

$$M\ \ddot{Y}_s + C\ \dot{Y}_s + K_0\ Y_s + g(Y_s) = r_s \tag{8}$$

where the subscript s is a positive integer denoting the time step τ_s such that $\Delta\tau = \tau_{s+1} - \tau_s$ and $\tau_0 = 0$.

Since this is a non-linear system, the mean of its response will in general be non-zero even though the excitation is of zero mean. It is generally agreed that the assumption of Gaussian response in the linearization technique of Caughey [7] is approximately satisfied for weakly nonlinear systems. In the present investigation the highly nonlinear systems are approximated as a series of weakly nonlinear or linear systems and therefore one can assume that the response at every time step is Gaussian. Experience [3,6] with nonlinear systems under wideband random excitations shows that such an assumption is acceptable as very accurate results were obtained. In spirit similar to references [3,6], equation (8) can thus be represented by the following linearized equation

$$M\ \ddot{Y}_s + C\ \dot{Y}_s + K_{eq}\ Y_s = f_s \tag{9}$$

where K_{eq} is the equivalent stiffness matrix which is time dependent. It is determined by the following equation

$$(K_{eq})_{ij} = \left\langle \frac{\partial g_i(Y(s))}{\partial Y_j(s)} \right\rangle , \qquad i,j = 1,2. \tag{10}$$

Upon substituting the non-linear term g(Y) into equation (10) and carrying out the operation one has

$$K_{eq}(s) = K_0 + \begin{bmatrix} 0 & 2\mu\eta\langle Y_2(s)\rangle - 3\mu\varepsilon\langle Y_2^2(s)\rangle \\ 0 & 2(1-\mu)\eta\langle Y_2(s)\rangle + 3(1+\mu)\varepsilon\langle Y_2^2(s)\rangle \end{bmatrix} . \tag{11}$$

With equation (11), one can then apply the SCD technique to equation (9) and perform the operation to obtain the recursive expression which is identical to that described in Section 2 above. The modified ATS to be introduced in the next section has to be employed with the SCD method to update the K_{eq} at every time step.

As the system is non-linear and therefore ensemble averages of responses are not zero in general, however, the following recursive ensemble average of response vector clearly indicate that it is zero if the system starts from rest

$$m(s+1) = N_{2y}(s)\, m(s) + N_{3y}\, m(s-1) . \tag{12}$$

where m(s+1) is the ensemble average of system response vector at the next time step.

To circumvent this problem, the g(Y) term of equation (6) is moved to the right hand side (RHS) such that

$$M\, \ddot{Y}(s) + C\, \dot{Y}(s) + K_0\, Y(s) = r(s) - g(Y(s)) . \tag{13}$$

As will be seen in the following this equation is applied only for the initial states of the response predictions. Substituting the central difference approximation of velocity and acceleration terms

$$\dot{Y}(s) = \frac{1}{2\,\Delta\tau}[\, Y(s+1) - Y(s-1)\,] ,$$
$$\ddot{Y}(s) = \frac{1}{(\Delta\tau)^2}[\, Y(s+1) - 2\,Y(s) + Y(s-1)\,] , \tag{14}$$

into equation (13) one has

$$Y(s+1) = \bar{N}_{2y}\, Y(s) + N_{3y}\, Y(s-1) + (\Delta\tau)^2 N_{1y}\, r(s) - (\Delta\tau)^2 N_{1y}\, g(Y(s)) \,, \tag{15}$$

where

$$\bar{N}_{2y} = N_{1y} \left[2M - (\Delta\tau)^2 K_0 \right] . \tag{16}$$

Taking the ensemble average of equation (15) one obtains

$$m(s+1) = \bar{N}_{2y}\, m(s) + N_{3y}\, m(s-1) - (\Delta\tau)^2 N_{1y} \langle g(Y(s)) \rangle \,,$$

$$\langle g(Y(s)) \rangle = \begin{Bmatrix} \mu\eta \langle Y_2(s)^2 \rangle - \\ \quad \mu\varepsilon [3 \langle Y_2(s) \rangle \langle Y_2(s)^2 \rangle - 2 \langle Y_2(s) \rangle^3] \\ \\ (1-\mu)\eta \langle Y_2(s)^2 \rangle + \\ \quad (1+\mu)\varepsilon [3 \langle Y_2(s) \rangle \langle Y_2(s)^2 \rangle - 2 \langle Y_2(s) \rangle^3] \end{Bmatrix} . \tag{17}$$

Substituting equation (17) into equations (2) and (13) one can show that

$$R_y(2) = (\Delta\tau)^4 N_{1y} R_f(1) N_{1y}{}^T \,, \quad m(2) = [0 \;\; 0]^T \,,$$
$$m(3) = -(\Delta\tau)^2 \eta \langle Y_2(s)^2 \rangle N_{1y} [\mu \;\; 1-\mu]^T . \tag{18}$$

As soon as the above non-zero ensemble averages are found, one can return to equation (12). For s > 3, equation (12) can be applied to obtain the non-zero ensemble averages. Of course, the recursive mean squares are given by equation (2). Up to this stage, the SCD method with modified ATS technique can be applied to the system to compute its responses to random excitations.

4. MODIFIED ADAPTIVE TIME SCHEME AND FIRST PASSAGE PROBABILITIES

As described by Liu and To [6], the time step size in a non-linear system varies with the variance of displacement response, the time step size has to be updated accordingly. This strategy is known as the adaptive time scheme (ATS). In the present analysis the terms that have to be considered for

the time step updating are R_y(s-1), G(s-2), H(s-2), R_f(s-2), N_{1y}, N_{2y} and N_{3y}. This has become more critical in the extended SCD method because the error would come from not only the system but also the responses of the filter. The interpolation scheme is employed to compute the time step size when it is warranted to do so for the nonlinear system whose natural frequency at every time step is different.

With the variances of displacement and velocity at every time step computed by the extended SCD method, the first passage problem can now be considered. Approximate first passage probabilities based on the modified mean rate of various crossings proposed earlier by the first author [4] are computed. In the latter the trapezoidal rule was employed to evaluate the first passage probabilities and uniform time step was assumed. For nonlinear system employing the SCD or extended SCD method and modified ATS, the time steps are different. Therefore, the interpolation scheme is applied in the present investigation such that the trapezoidal rule can be adopted for the computation of first passage probabilities.

5. NUMERICAL RESULTS

Numerical examples are presented in the following. Parameters of the system in Section 3 are:

$$W = \mu = 1.0 , \quad \zeta_1 = \zeta_2 = 0.1 , \tag{19}$$

such that the two dimensionless natural frequencies of the corresponding linear system, that is when η and ε are both equal to zero, are $\omega_{s1} = 0.618$ and $\omega_{s2} = 1.618$. The amplitude modulating function $e(\tau)$ chosen is

$$e(\tau) = 4(e^{-0.05\tau} - e^{-0.1\tau}) . \tag{20}$$

Numerical results presented in this section include two examples. The first example is the one with the centre frequency of the one dof $\omega_f = 1.0$ and the second is with $\omega_f = 1.618$. Each example has a two dof system described in Section 3 and a single dof filter. The latter equals to one of the two linear dimensionless natural frequencies of the non-linear system. The other is between the two linear dimensionless natural frequencies. Damping ratio of the filter (band width) in the two examples are $\zeta_f = 0.01$, 0.1 and 1.0. The narrow band random excitation to the system is the response taken directly from the filter which is perturbed by a non-stationary zero mean Gaussian white noise. The spectral density of the Gaussian white noise is $S_0 = 0.00012$. The narrow band random excitation to the system is at its base. MCS is also carried out in order to verify the results by the extended SCD method. Other pertinent system parameters are $\eta = -1.0$ and $\varepsilon = 1.5$.

It was observed that the results of the case where $\omega_f = 1.0$ and $\zeta_f = 0.01$ became unstable for both the extended SCD and MCS methods. An attempt was also made to compute responses of the system excited by a narrow band process with $\omega_f = 0.618$. In this case, instability occurs when ζ_f equals to 0.01 and 0.1. Note that the spectral density of the white noise process is one order of magnitude smaller than what was used in reference [6]. This is because when $S_0 = 0.0012$ was used, the response of the system becomes unstable. Representative response statistics for $S_0 = 0.0012$ are present in Figures 2 and 3 in which the covariances of displacement and velocity responses were not included for clarity since they are very close to the variance $\langle Y_2^2 \rangle$. From the figures, one observes that the results by the SCD method has an excellent agreement with those using the MCS. The computational time using a Silicon Graphics Inc. engineering workstation with 64 megabyte random access memory and 60 mega Hz single central processor the extended SCD method is approximately 15 seconds while that for the MCS is about 57 minutes. Consequently, one can conclude that the extended SCD method is very efficient and accurate compared with the MCS data.

For the first passage probabilities, two sets of results were studied. They are: (i) results concerned with narrow band non-stationary random excitations, and (ii) comparison of narrow band non-stationary random responses to wide band non-stationary random responses. It was observed that in term of first passage probability the difference between narrow band non-stationary and narrow band stationary random excitations is insignificant and therefore these results are not presented here. In set (i), results obtained by the MCS technique are included for direct comparison. Some typical results of first passage probability L_D based on the two stage process with allowance for the actual duration of clumps at low threshold levels are presented in Figures 4 and 5. The results for set (ii) are plotted in Figures 6 and 7. In these figures NB designates narrow band, and WB wide band. With reference to the results in Figure 7, one can conclude that the first passage probability of the model with narrow band random excitation is very much different from that with wide band random excitation.

Before leaving this section it may be appropriate to note that although the filter and system parameters for sets (i) and (ii) are identical the corresponding plots in Figures 5 and 7 are different. For the results in set (ii) and plots in Figures 6 and 7 the input to the system is a product of an envelope function and a stationary narrowband random process. However, for the results in set (i) and plots in Figures 4 and 5 the input to the system is the output of the filter whose input is a product of an envelope function and a zero mean stationary white noise process. In other words, in the MCS one is unable to have an absolute control over the exact narrowband nonstationary input to the system. The extended SCD method, however, has no such a restriction and therefore has an added advantage over the MCS in controlling the input to the system.

6. REMARKS

In this paper the extended stochastic central difference method is introduced. The recursive response statistics and first passage time of a multi-degrees of freedom non-linear system under excitations treated as narrow band non-stationary random excitations are considered. Results of a two degrees of freedom non-linear system indicate that the technique proposed is very efficient and accurate compared with the Monte Carlo simulation data.

One also observes that the first passage probability of the two dof model under narrow band random excitation is very much different from that with wide band random excitation. This suggests that correct representation of the excitation process as a wide band or narrow band random process is extremely important if more reliable conclusions are to be drawn and used in the design process.

ACKNOWLEDGEMENT

The investigation reported above was supported in the form of a research grant by the Natural Sciences and Engineering Research Council of Canada awarded to the first author.

REFERENCES

1. To, C.W.S. and Chen, Z., Response analysis of system under narrow band stationary and nonstationary random excitations. In *Proceedings of A.S.M.E. Pressure Vessels and Piping Conference*, Montreal, Canada, July 21-26, 1996, PVP-Vol. 331, pp. 107-114.

2. To, C.W.S. and Chen, Z., First passage time of nonlinear ship rolling in nonstationary random Seas. In *Proceedings of A.S.C.E. 7th Specialty Conference on Probabilistic Mechanics and Structural Reliability*, Worcester, Massachusetts, U.S.A., August 7-9, 1996, pp. 250-253.

3. To, C.W.S. and Liu, M.L., Recursive expressions for time dependent means and mean square responses of a multi-degree-of-freedom nonlinear system. *Comput. Struct.*, 1993, **48** (No. 6), 993-1000.

4. To, C.W.S., Distribution of the first passage time of mast antenna structures to nonstationary random excitation. *J. Sound and Vibration*, 1986, **108**, 11-23.

5. Kimura, K. and Sakata, M., Nonstationary response analysis of a nonsymmetric nonlinear multi-degree-of-freedom system to nonwhite random excitation. *JSME Int. J.*, 1988, **31**(4), 690-697.

6. Liu, M.L. and To, C.W.S., Adaptive time schemes for responses of nonlinear multi-degree-of-freedom systems under random excitations. *Comput. Struct.*, 1994, **52**(No. 3), 563-571.

7. Caughey, T.K., Equivalent linearization techniques. *J. Acoust. Soc. Am.*, 1963, **35**, 1706-1711.

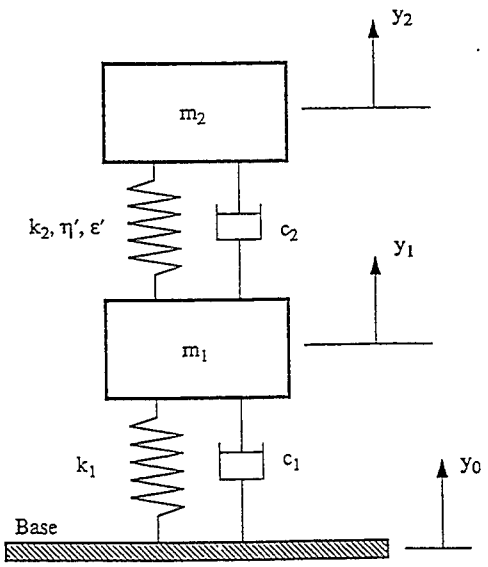

Figure 1. The two dof non-symmetric non-linear system

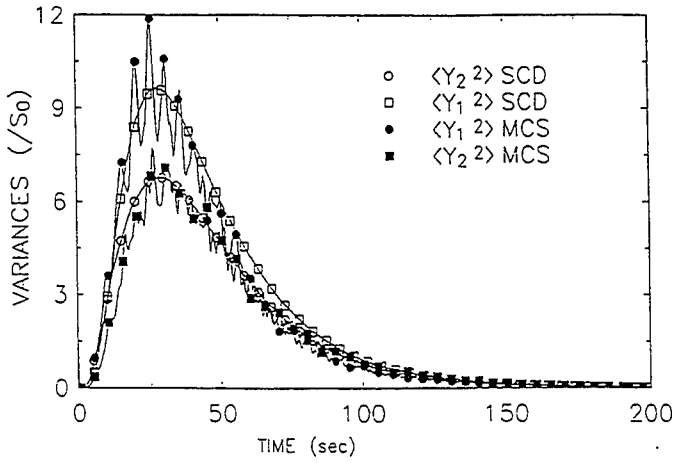

Figure 2. Response variances and covariance of a non-linear two dof system, ω_f = 1.618, ζ_f = 0.01

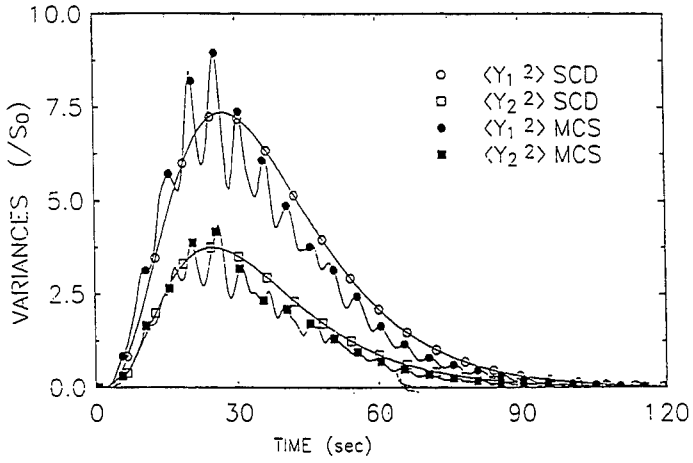

Figure 3. Response variances and covariance of a non-linear two dof system, ω_f = 1.618, ζ_f = 0.1

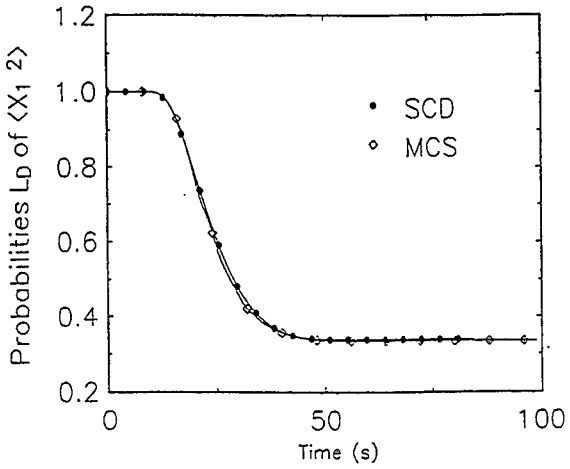

Figure 4. Comparison of first passage probabilities by the extended SCD and MCS, $\omega_f = 1.618$, $\zeta_f = 0.1$

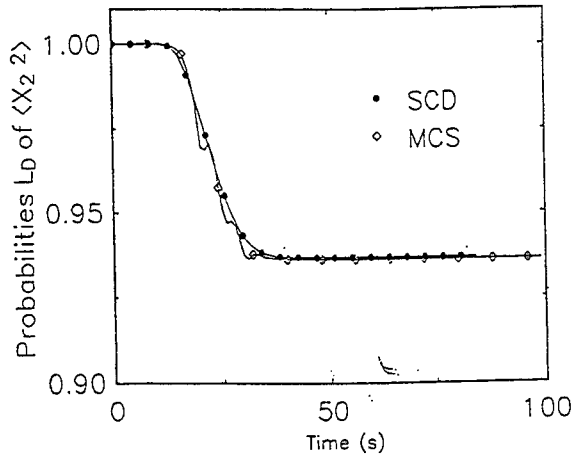

Figure 5. Comparison of first passage probabilities by the extended SCD and MCS, $\omega_f = 1.618$, $\zeta_f = 0.1$

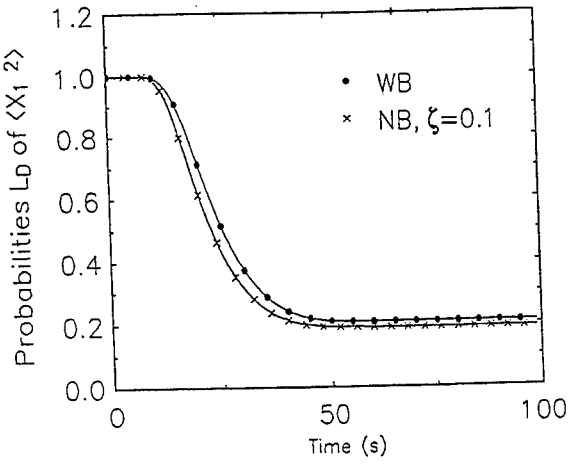

Figure 6. Comparison of first passage probabilities, $\omega_f = 1.618$, $\zeta_f = 0.1$

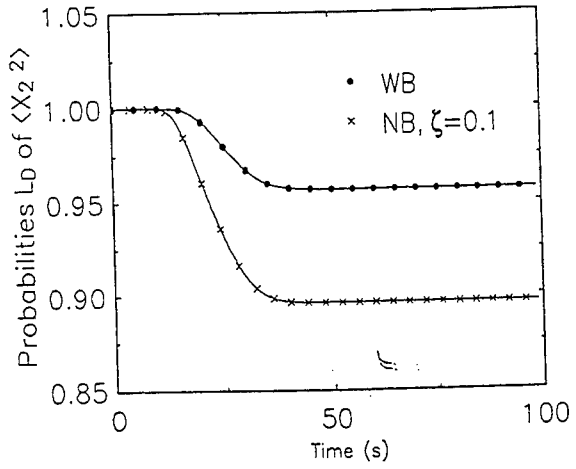

Figure 7. Comparison of first passage probabilities, $\omega_f = 1.618$, $\zeta_f = 0.1$

RANDOM RESPONSE OF DUFFING OSCILLATOR EXCITED BY QUADRATIC POLYNOMIAL OF FILTERED GAUSSIAN NOISE

C. Floris and M.C. Sandrelli

Department of Structural Engineering, Politecnico di Milano, Piazza Leonardo da Vinci 32, I-20133 Milano, Italy

ABSTRACT

The random response of a Duffing oscillator excited by a quadratic polynomial of filtered Gaussian process is considered. The problem is approached by the use of Itô's stochastic differential calculus. Being the system nonlinear, the moment equations (ME) constitute an infinite hierarchy, to close that a procedure different from the classical cumulant-neglect closure method is used. This procedure operates in two phases, in the former of which the system is linearized so that the ME are solved exactly. In the second phase the actual system is considered: the equations for the moments of *m-th* order contain moments of order *m*+2. To solve them an iterative scheme is used, in the first step of which the higher order moments are considered as known quantities and take the values that have been estimated on the linearized system. In the applications the new procedure is shown to converge towards the solution obtained by simulation requiring a charge for calculation considerably lesser than that of cumulant-neglect closure method. Care is taken to detect possible multiple solutions when the excitation is narrow-banded.

1. INTRODUCTION

The study of nonlinear dynamical systems under random excitation of polynomial form is of considerable interest in the theory of random vibration as well as in engineering applications. In fact, important random dynamical agencies can be properly represented as polynomial forms of filtered Gaussian processes. This is the case of gusty wind [1] and random sea waves [2–4]. In this way, both the system and the excitation are nonlinear, which increases the difficulties in characterizing the response statistically. System response is probably well far from Gaussianity, since the non-normality is caused by both the non-

normality of the input (memoryless transformation of normal process) and non-linearity of the response process itself.

Nonlinear random vibration problems can be approached by several ways, such as equivalent linearization, perturbation, quasi-harmonic method, multiple time scales, and Itô's stochastic differential calculus. In this paper the last approach is followed. It is possible since the excitation is idealized as the output of a linear filter excited by a Gaussian white noise. Itô's stochastic calculus provides a straightforward procedure for deriving the differential equations in terms of response moments or in terms of the probability density function [5-9]. Nevertheless, in presence of nonlinearities in both the excitation and the system many difficulties arise. The so-called Fokker- Planck-Kolmogorov (FPK) equation, which gives the probability density function of response, can be solved analitically in very few cases, especially when the transient response is considered (e.g. see [10]). If the moment equation (ME) approach is used, the equations of moments of order k involve higher and lower order moments than k, that is the ME constitute an infinite hierarchy. In order to solve this problem closure schemes have been proposed [9,11,12]. Among the closure schemes the cumulant-neglect closure method is certainly the most popular. However, although this method is generally efficacious, it has some shortcomings. The moments of order higher than k that appear in the equations for the moments of order k are expressed as a function of the lower order moments setting the corresponding cumulants equal to zero. Since these functions are nonlinear, the ME too become nonlinear. In such a way computational difficulties arise. Moreover, a nonlinear system may have more acceptable solutions (it is recalled that a solution is acceptable when all even moments are positive and Cauchy-Schwartz inequality is satisfied). These multiple solutions must be considered with care, possibly determining whether they are stable or not. The significance of multiple solutions in terms of statistical moments of the response of a nonlinear dynamical system is still an open question [13-16]. However, in some cases such as a Duffing oscillator multivalued response moments are expected in the presence of a narrow-band excitation [17]. These different values of variance correspond to different local states around which the system oscillates with abrupt jumps between the different states. Furthermore, the steady-state probability density function (PDF) of response is bimodal or multimodal, even if it is unique, since FPK equation has one solution only. In other cases that have been studied by the writers and Prof. Di Paola [18] the simulated response does not show any jump and the significance of multivalued response is not clear.

In this paper a new closure scheme is adopted. The procedure operates in two phases, in the former of which advantage is taken of the fact that the ME of linear systems excited by polynomial forms of Gaussian processes [2, 19] or delta-correlated processes [20,21] are exactly solvable. Hence, the nonlinear system is replaced by a linear one, whose parameters are chosen in such a way to minimize the error between the original and the linearized system in some statistical sense [22,23]. The statistical moments, which are exact for the latter, are calculated to an order larger than that one chosen for the original system. The reason for this choice will be explained in the next section. In the second phase, the ME of the original system are considered. Now, the procedure operates iteratively: in the first step the higher order moments that appear in the equations for the moments of *k-th* order are considered as known quantities taking the values that have been evaluated for the linearized system. In the generic *i-th* step these moments are set equal to the values obtained in the step *i*-1. The iterations are carried on till the moments do not change appreciably. This procedure is applied to a Duffing oscillator excited by a quadratic polynonial of a filtered Gaussian process. The damping and the nominal vibration period of the oscillator are kept constant, while the bandwidth of the filter is varied in order to ascertain the effects of this quantity on the response. The results of the proposed approach are compared with those of Monte Carlo simulation. When the bandwidth of the filter is narrow, eventual multivalued responses are searched using either the stochastic differential calculus or Monte Carlo simulation.

2. PRELIMINARY CONCEPTS

In the study of nonlinear vibrations the Duffing equation plays a fundamental role. In normalized form it reads as

$$\ddot{x}(t)+\beta_0\dot{x}(t)+\omega_0^2\left[x(t)+\varepsilon x(t)^3\right]=F(t) \qquad (1)$$

in which β_0 is the coefficient of viscous damping, ω_0 is the pulsation of the corresponding linear oscillator ($\varepsilon = 0$), and the term $\varepsilon x(t)^3$ represents the nonlinear restoring force, acting as a hard or soft spring for positive or negative values of ε, respectively. In random vibration studies $F(t)$ is generally assumed to be a Gaussian process, since this type of stochastic process allows the use of analytical methods. When $F(t)$ is a Gaussian white noise, the reduced Fokker-Planck-Kolmogorov equation [10] associated with (1) admits an analytical solution [24] as follows

$$p(x,\dot{x}) = C\,exp\left\{-\frac{2\beta_0}{\pi w_0}\left[\omega_0^2\left(\frac{x^2}{2}+\varepsilon\frac{x^4}{4}\right)+\frac{\dot{x}^2}{2}\right]\right\} \quad (2)$$

in which $p(x,\dot{x})$ is the steady-state joint probability density function (PDF) of $x,\dot{x}$; C is a normalization constant, and w_0 is the strength of white noise, which is expressed as $F(t)=\sqrt{\pi w_0}W(t)$, being $W(t)$ a unit strength Gaussian white noise.

However, not all excitations are so broad-banded that they can be idealized as a white noise. Very narrow-banded excitations can be considered as monochromatic, say

$$F(t) = A(t)\cos\omega_f t + B(t)\sin\omega_f t \quad (3)$$

in which $A(t)$ and $B(t)$ are two slowly varying Gaussian processes. Otherwise, a frequent idealization of $F(t)$ is thinking it as the output of a second order linear filter, say

$$F(t) = y_f(t) \qquad \ddot{y}_f(t)+\beta_f\dot{y}_f(t)+\omega_f^2 y_f(t) = \sqrt{\pi w_0}W(t) \quad (4)$$

where $W(t)$ is a unit strength Gaussian white noise. The steady-state FPK equation associated with the augmented system of (1) and (4) has not an analytical solution, since this system is not amenable to the classes of detailed balance or of generalized stationary potential [10]. However, the primary excitation in (4) is a Gaussian white noise, so that the problem can be suitably framed in the context of Itô's stochastic differential calculus [5-9].

Likewise to the deterministic response of Duffing oscillator subjected to a sinusoidal excitation, in which there appear phenomena such as multiple valued, subharmonic and superharmonic, responses and the associated jumps in response levels, for sufficiently narrow bandwidths of the excitation the random response can exhibit multiple values of the statistical moments, particularly of the variance. This fact was revealed by the analyses performed by some researchers that used different approaches. Some used equivalent linearization technique [13,14,25-27]. Lennox and Kuak [28] faced the problem through a combination of deterministic and stochastic averaging. Other authors preferred the methods of multiple time scaling, quasi-harmonic analysis and harmonic balance [29-31]. More recently, Itô stochastic calculus with a non-Gaussian closure was used in Ref. 16. However, the significance of the multiple solutions generated by equivalent linearization and Itô's calculus is still an open question. The discussions about this subject in Refs. 15, 16 are remarkable.

This paper concerns the response of Duffing oscillator (1) to an excitation of the form

$$F(t) = a_0 + a_1 y_f(t) + a_2 y_f(t)^2 \quad (5)$$

being $y_f(t)$ the output of a filter such as (4). It is recalled that (5) can represent wind excitation by properly choosing the coefficients a_0-a_2. In a literature search made by the writers no theoretical and applied studies have been encountered regarding the response of Duffing oscillator to excitations of the form (5) or of the more general form

$$F(t) = a_0 + a_1 y_f(t) + a_2 y_f(t)^2 + \ldots + a_m y_f(t)^m \quad (6)$$

Clearly, the problem is rendered more difficult by the twofold nonlinearity in both the structure and the excitation. If Itô's calculus is applied, the ME form an infinite hierarchy with many higher order terms arising from the term εx^3 in (1) and the term $a_2 y_f^2$ in (5). In this way, a large number of cumulant-moment relationships must be set equal to zero to close the hierarchy, making the ME highly nonlinear. Furthermore, these last are more than two hundred, if the statistical moments of fourth order are to be computed. Even if the steady-state solution is of concern, and, hence, the ME become algebraic, it is cumbersome to find a solution and more physically realizable solutions may exist. In order to overcome these difficulties, advantage is taken from the fact that the statistical moments of a linear system excited by a polynomial form of a filtered Gaussian process are calculated exactly [2, 19-21]. Therefore, in the first step of the procedure that is here proposed the system (1) is linearized. The statistical moments that are computed in this way constitute a first estimate of the moments of the actual system and are the basis of the algorithm with which the hierarchy of ME is closed.

3. ITERATIVE PROCEDURE

3.1 Linearized system

In the first phase of the iterarive procedure Eq. (1) is substituted by

$$\ddot{x}(t) + \beta_0 \dot{x}(t) + \omega_e^2 x(t) = F(t) \quad (7)$$

in which $F(t)$ is given by (5), and ω_e^2 is the linearization parameter. Making the mean square error between (7) and (1) minimum [22, 23] it is got

$$\omega_e^2 = \omega_0^2 + \varepsilon\omega_0^2 \cdot E\left[x^4\right] / E\left[x^2\right] \quad (8)$$

in which $E[\bullet]$ denotes ensemble average. Since the linearization is confined to the structure, and the excitation holds the nonlinear form (5), $x(t)$ is not a Gaussian process so that the relationship $E[x^4] = 3(E[x^2]\text{-}E[x])^2$ is not valid. Being $E[x^4]$ unknown *a priori*, the equivalent linearization is applied iteratively starting from a tentative value of the

fourth moment of x. The statistical moments are computed to the fourth order, and a new value of ω_e^2 is calculated by using (8). The iterations are terminated when at step n $\left|\omega_{e,n}^2 - \omega_{e,n-1}^2\right| \le \delta_\varepsilon$, being δ_ε of the order 10^{-2}. It is recalled that the non-Gaussianness of the response makes it very difficult to derive an analytical relationship for response variance as it is done in Refs. 25,26. Thus, the search of eventual multiple values of variance is made numerically.

In order to compute the statistical moments of the response, Itô's differential rule is applied [6-9]. The state variables $x_1 = x$, $x_2 = \dot{x}$, $x_3 = y_f$, and $x_4 = \dot{y}_f$ are introduced and Eqs. (4,7) with the excitation (5) are written in incremental form, say

$$dx_1 = x_2 \cdot dt \quad (9a)$$

$$dx_2 = -\beta_0 x_2 \cdot dt - \omega_e^2 x_1 \cdot dt + a_0 \cdot dt + a_1 x_3 \cdot dt + a_2 x_3^2 \cdot dt \quad (9b)$$

$$dx_3 = x_4 \cdot dt \quad (9c)$$

$$dx_4 = -\beta_f x_4 \cdot dt - \omega_f^2 x_3 \cdot dt + \sqrt{\pi w_0} \cdot dB \quad (9d)$$

in which dB is the increment of a unit Wiener process (Brownian motion) that is related to white noise by the formal relationship $dB/dt = W(t)$.

The stationary first order moment (statistical average) of x is

$$E[x] = E[x_1] = \omega_e^{-2}\left\{a_0 + a_2 E\left[x_3^2\right]\right\} \quad (10)$$

$E[x]$ depends on the mean square value $E\left[x_3^2\right] = E\left[y_f^2\right]$, that is known, being y_f a Gaussian process.

The equations for the stationary second order moments read as

$$2E[x_1 x_2] = 0 \quad (11a)$$

$$E\left[x_2^2\right] - \beta_0 E[x_1 x_2] - \omega_e^2 E\left[x_1^2\right] + a_0 E[x_1] + a_1 E[x_1 x_3] + a_2 E\left[x_1 x_3^2\right] = 0 \quad (11b)$$

$$-2\beta_0 E\left[x_2^2\right] - 2\omega_e^2 E[x_1 x_2] + 2a_0 E[x_2] + 2a_1 E[x_2 x_3] + 2a_2 E\left[x_2 x_3^2\right] = 0 \quad (11c)$$

In Eqs. (11) there are moments of order lower and higher than the second. The former, $E[x_1]$ and $E[x_2]$, are known. Viceversa, the moments of the types $E[z_i z_k]$ (i = 1,2; k = 3,4), and $E\left[z_i z_3^r z_4^s\right]$ (i = 1,2; $r+s$ = 2) are unknown. However, Eqs. 11 do not constitute an infinite hierarchy even if there are third order moments. The technique proposed by Muscolino [20] is used to solve the problem. It requires the solution of two linear and uncoupled sets of equations that are written

for the moments $E[z_i z_k]$, and $E[z_i z_3^r z_4^s]$, respectively. Analogously, the evaluation of the moments of third and fourth order of x_1, x_2 requires the solution of five and six linear uncoupled sets of equations, respectively. Once convergence is obtained for ω_e^2, the moments of the linearized system are computed to the sixth order. In this way, a first estimate of the response moments is obtained.

3.2 Nonlinear system

Now we return to the actual system driven by Eq. (1). Eqs. (1,4) are written in incremental form: Eq. (11b) is replaced by

$$dx_2 = -\beta_0 x_2 \cdot dt - \omega_0^2 x_1 \cdot dt - \varepsilon\omega_0^2 x_1^3 \cdot dt + a_0 \cdot dt + a_1 \cdot x_3 \cdot dt + a_2 \cdot x_3^2 \cdot dt \tag{12}$$

The ME of the actual system are written applying Itô's differential rule again. They constitute an infinite hierarchy really, since in the equations for the moments of *k-th* order there are moments of order k+2 because of the term $\varepsilon\omega_0^2 x_1^3$ in (12). In this paper a new technique is used to close the hierarchy profiting by the solution that has been obtained for the linearized sys tem. This technique operates iteratively.

Let us examine some ME of the actual system. The statistical average is given by

$$E[x_1] = E[x] = \omega_0^{-2}\left\{a_0 + a_2 E[x_3^2]\right\} - \varepsilon E[x_1^3] \tag{13}$$

$E[x]$ depends on the third order moment $E[x_1^3]$, which in the first step is assumed to be known and take the value that has been computed for the linearized system. In the other iterations it takes the value of the previous one.

The equation for a moment of order m can be written as

$$\dot{\mu}_{pq} = p\mu_{p-1,q+1} - q\beta_0\mu_{pq} - q\omega_0^2\mu_{p+1,q-1} - q\varepsilon\omega_0^2\mu_{p,q+2} + qa_0\mu_{p,q-1} + \\ + qa_1 E[x_1^p x_2^{q-1} x_3] + qa_2 E[x_1^p x_2^{q-1} x_3^2] \tag{14}$$

in which $p + q = m$ and $\mu_{pq} = E[x_1^p x_2^q]$. If the structure is exposed to a stationary excitation for a sufficiently long time, it reaches the stationarity and the l.h.s. of (14) vanishes. In Eq. (14) there are different types of moments: The fifth addendum has an order lower than m and has been already evaluated, while the first three addenda are of the *m-th* order, and as many equations as these moments can be written.

However, the fourth term and the last two are additional unknowns. The cross-moments among x_1, x_2 and the variables of the filter are evaluated writing the corresponding equations down, as for the linearized system, and the hierarchy is overcome. The fourth addendum $\mu_{p,q+2}$ is an effective hierarchical term. In the first step of the iterative procedure it takes the value that has been computed for the linearized system, while in the generic *i-th* iteration it takes the value of the iteration *i*-1. In this way, the equations for the moments of different order and type are considered separately with an evident computational advantage. Furthermore, the ME remain linear, while in the cumulant-neglect closure method [11, 12] the cumulant-moment relationships introduce non-linearities of degree as higher as the level on which the closure is made. In the case under examination with four state variables, computing the moments to the fourth order, there would arise more than two hundred equations, and this large nonlinear set of equations would be hardly solvable with a personal computer. Viceversa, using the proposed approach the response moments are computed by solving linear systems with a small number of equations. Since the highest order moment appearing in (14) has the order m+2 and the moments of the actual system are computed to the fourth order, the moments of the linearized system are evaluated to the sixth order.

3.3 Search for multiple solutions

Since the writers did not find any study on Duffing oscillator excited by a polynomial form of filtered Gaussian process, it was not possible either to affirm or to exclude the possibility of a multivalued variance in the presence of a narrow-band excitation. Hence, there is need of ascertaining whether the response moments under a given excitation are unique or not. The polynomial form (5) of the excitation does not leave room to a simple expression for the variance as in the case of a filtered Gaussian excitation [13,14,25-27]. Moreover, the bandwidth of the excitation cannot appear explicitly in this case. Thus, an iterative-numerical procedure is used for searching multivalued responses.

The search is made with reference to the linearized system, since it is simpler to be done. From Eqs. (11) we find for the mean square values of x_1 and x_2, respectively

$$E\left[x_1^2\right] = \omega_\varepsilon^{-2}\left\{E\left[x_2^2\right] + a_0 E\left[x_1\right] + a_1 E\left[x_1 x_3\right] + a_2 E\left[x_1 x_3^2\right]\right\} \quad (15a)$$

$$E\left[x_2^2\right] = \beta_0^{-1}\left\{a_1 E[x_2 x_3] + a_2 E\left[x_2 x_3^2\right]\right\} \quad (15b)$$

Eq. (8) giving the linearization parameter is written as $\omega_e^2 = \omega_0^2\left\{1 + \varepsilon k E\left[x_1^2\right]\right\}$. The procedure must accomodate for the possibility of a multivalued variance. After obtaining convergence for ω_e^2 and computing the statistical moments, the ratio $k = E[x_1^4]/E[x_2^2]^2$ is calculated and substituted in the expression of ω_e^2, which at its turn is inserted in Eq. (15a). In Eqs. (15) there are the moments $E[x_1]$, $E[x_i x_3]$, and $E[x_i x_3^2]$ (i=1,2) that obviously depend on ω_e^2: As a first approximation these moments are assumed to take the values obtained at the end of the iterations for finding ω_e^2. In this way (15a) becomes a quadratic equation in the unknown $E[x_1^2]$. Obviously, the two roots must be real, but from a theoretical point of view it cannot be excluded that both result positive. If this were the case, the iterative procedure would be reentered and split into two different searches. The two sets of statistical moments that would be computed would become two different bases for the iterative search operated on the actual system. In this way the iterative computation of the moments of the actual system becomes twofold, but *a priori* it is not possible to affirm whether the convergence is towards two different states or towards the global state corresponding to the unique solution of the FPK equation. The research for a multiple solution is made by simulation too, as will be explained in next section.

4. APPLICATIONS

The procedures outlined in previous sections have been applied to a Duffing oscillator characterized by the following values of the parameters in Eq. (1): β_0 = 0.6283, which corresponds to a ratio of critical damping of a 5 %; $\omega_0 = 2\pi$; ε = 0.5. The coefficients of Eq. (5) are: a_0 = 10, $a_1 = a_2$ = 1. The filter (4) is characterized by $\omega_f = 2\pi$, and w_0 = 5. As regards β_f, it takes the values 0.1257, 0.3770, 1.2567, which correspond to relative dampings of 0.01, 0.03, and 0.10, respectively. The bandwidth parameters associated with these two values are 0.1131, 0.1949, and 0.3386, respectively. The bandwidth parameter is defined as $q = \left[1 - \lambda_1^2/(\lambda_0\lambda_2)\right]^{1/2}$, being λ_i the *i-th* spectral moment [32]. In the case of Eq. (4) the formula $q = (1.16\zeta_f^{0.15} - 0.21)^{2.2}$ gives an accurate estimation [33]. It is remarked that the set of parameters $\omega_f = 2\pi$, β_f = 0.1257,

Table 1: results for Duffing oscillator, $\beta_r = 0.1257$

	$E[x]$	$E[x^2]$	$E[x^3]$	$E[x^4]$
(1)	0.258459	0.105127	0.050338	0.028410
(2)	0.273143	0.073133	0.024813	0.008744
(3)	0.281231	0.080166	0.023150	0.006769

Stochastic differential calculus: (1) linearized system, (2) actual system. (3) Simulation

Table 2: results for Duffing oscillator, $\beta_r = 0.3770$

	$E[x]$	$E[x^2]$	$E[x^3]$	$E[x^4]$
(1)	0.248404	0.078837	0.028604	0.011598
(2)	0.253232	0.073950	0.023958	0.008564
(3)	0.257975	0.067416	0.017316	0.004505

(1)-(3) as in Table 1.

Table 3: results for Duffing oscillator, $\beta_r = 1.2567$

	$E[x]$	$E[x^2]$	$E[x^3]$	$E[x^4]$
(1)	0.246996	0.064276	0.017517	0.004976
(2)	0.248568	0.064627	0.017491	0.004913
(3)	0.254055	0.064595	0.016426	0.004180

(1)-(3) as in Table 1.

and $w_0 = 5$ would cause a multivalued response with a large probability if the filter output were directly applied to the structure. The steady state response only is considered computing the statistical moments to the fourth order.

The results obtained by the use of the procedure proposed in this paper are checked against numerical simulation. It has not been possible to perform a comparison with the standard cumulant-neglect closure method, for both the hardware and the software available to the writers were inadequate for solving a nonlinear algebraic system of more than two hundred equations. Two types of simulations have been performed, the former of which is a standard Monte Carlo simulation. Samples with 10,000 histories of motion starting from zero values of both initial displacement and velocity are constructed and analyzed using ordinary statistical tools. The motion lasts for 30 s and Eq. (1) is solved by applying a fourth order Runge-Kutta scheme. However, the classical simulations cannot reveal multivalued responses, since the averages are performed on a large number of

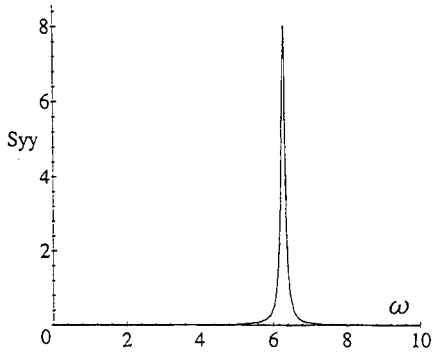

Fig. 1 - Power spectral density of the output of filter (4), $\beta_f = 0.1257$.

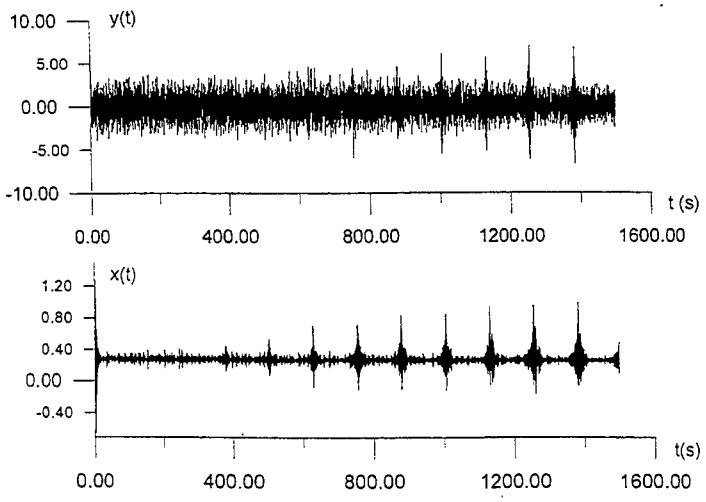

Fig. 2 - Top: typical time history of the output of filter (4). Bottom: response displacement $x(t)$, $\beta_f = 0.1257$.

samples. Roberts [15] suggested another type of simulation, in which a limited number of motion histories is simulated, but each history lasts for a relative long time and is analyzed alone. Recently, Cusumano and Kimble [34] proposed the so-called stochastic interrogation experimen- method, in which, differently from Robert's method, the histories of motion have random initial conditions. Furthermore, Cusumano and Kimble consider large samples and trace the Poincaré maps to reveal the presence of basins of attraction. Due to hardware limitations, these two types of simulation are performed with samples of 10 histories of

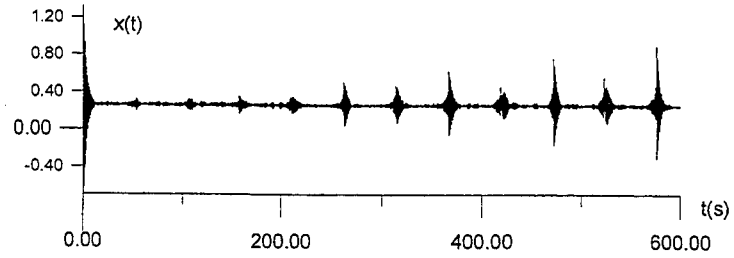

Fig. 3 - Response displacement $x(t)$, $\beta_f = 0.3770$.

motion. When the initial conditions are random, the initial displacecement and velocity are independent normal variates with zero mean and unit variance.

Tables 1-3 show the principal statistical moments obtained by using the three methods, for β_f = 0.1257, 0.3770, and 1.2567, respectively. The statistical linearization fails to yield accurate estimates of the statistical moments for the case β_f = 0.1257. In the other two cases the results for the first two moments are quite acceptable, while the estimates of both the third and fourth moment are too high. In general, the proposed approach for closing the hierarchy of the ME constitutes a substantial improvement over the linearization even if the third and fourth moment of the intermediate case are greatly overestimated (by a 38.4 % for $E[x^3]$ and by a 90 % for $E[x^4]$). Clearly, as higher the order of a moment is, as worse the approximation of the stochastic differential calculus. Using a higher order of closure should improve the accuracy, but this requires the use of more powerful computers.

The performance of the proposed approach is noticeable in the first case, say β_f = 0.1257. This case is characterized by a very narrow-banded output of the filter (4) (Fig. 1), even if the a simulated history of $y_f(t)$ does not resemble a sinusoid (Fig. 2, top). Performing the search for multiple solutions, Eq. (15a) has two real roots, but one of them only is positive. Nevertheless, examining a single motion history lasting for 1,500 s (Fig. 2, bottom) there appears a strange phenomenon. After exposing the system to the excitation for almost 400 s, one can note that evenly spaced peaks rise, whose periodicity is 90-100 s about. During these peak phases the oscillations occur around the unchanged mean value, but their amplitude increases time after time and seems to be unbounded. The writers think that it is improper to define this phenomenon as a multivalued response; rather, this behavior might be assimilated to a kind of instability. An ever increasing amplitude means an increasing mean square value that, perhaps, might be detected by making a non stationary analysis. Thus, the statistical moments that have been calculated with both stochastic differential

calculus and simulation, whose motion histories last for 30 s, are correct for the stationary segment of the response, only. The same trend can be noticed for the case $\beta_f = 0.3770$, but it is slightly faded.

5. CONCLUSIONS

A method is presented to close the hierarchy of the ME of nonlinear systems excited by polynomial forms of filtered Gaussian processes. This method operates in two phases in the former of which resort is made to statistical linearization that yields a first estimate of the moments of the non-Gaussian response. In the second phase the ME of the actual system are considered. They constitute an infinite hierarchy to close which, instead of using the classical cumulant-neglect closure method that may be cumbersome from a computational point of view, an iterative procedure is used. This is based on the estimate of the response moments that has been obtained for the linearized system.

The proposed method is applied to a Duffing oscillator excited by a quadratic polynomial of a filtered Gaussian process. The bandwidth parameter of the filter is varied from a very narrow one to a medium one to ascertain whether the response may be multivalued as in the case of a simple narrow-banded filtered excitation. In the case of a narrow-banded excitation a phenomenon different from those reported in literature occurs. After a certain time system response seems to lose the stationarity and periodically shows peaks with ever increasing amplitude. This phenomenon cannot be detected either by the stochastic differential calculus, if the ME are solved for the steady state, or by the customary simulation in which the histories of motion have a brief duration. In order to reveal this behavior it is necessary to study responses lasting some hundreds of seconds. However, the response moments that are given by the proposed approach are substantially correct for the stationary segment of the response.

ACKNOWLEDGEMENTS

The authors are indebted to Prof. Mario Di Paola of the University of Palermo, Italy, for his continuous advice and encouragement.

REFERENCES

1. Solari, G., Turbulence modeling for gust loading. *J. Struct. Engrg.* ASCE, 1987, **113**(7), 1550-69.
2. Krenk, S., and Gluver, H., An algorithm for moments of response from non normal excitation of linear systems. In *Stochastic Structural Dynamics,* eds. Ariaratnam S. T., Schuëller G. I. and Elishak-

off I., Elsevier Appl. Sc. Publ., London, 1988, 181-195.
3. Li, X.-M., Quek, S.-T., and Koh, C.-G., Stochastic response of offshore platforms by statistical cubicization. *J. Engrg. Mech.* ASCE, 1995, **121**(10), 1056-68.
4. Benfratello,S., and Falsone,G., Non Gaussian approach for stochastic analysis of offshore structures. *J. Engrg. Mech.* ASCE, 1995, **121**(11), 1173-80.
5. Itô, K., On stochastic differential equations. *Mem. Am. Math. Soc.*, 1951, **4**, 289-302.
6. Itô, K., On a formula concerning stochastic differentials. *Nagoya Math. J.*, 1951, **3**, 55-65.
7. Arnold, L., *Stochastic Differential Equations: Theory and Applications*, John Wiley & Sons, New York, 1973.
8. Di Paola, M., Stochastic differential calculus. In *Dynamic Motion: Chaotic and Stochastic Behavior*, CISM Course no. 340, Casciati F. ed. Springer Verlag, Wien, 1993, 29-92.
9 . Soong, T.T., and Grigoriu, M., *Random Vibration of Mechanical and Structural Systems.* Prentice Hall, Englewood Cliffs, 1993.
10. Lin, Y.K., and Cai,G.Q., *Probabilistic Structural Dynamics: Advanced Theory and Applications.* Mc Graw Hill, New York, 1995.
11. Wu, W.F., and Lin, Y.K., Cumulant-neglect closure for non-linear oscillators under random parametric and external excitations. *Int. J. Non-lin. Mech.*, 1984, **19**(4), 349-62.
12. Ibrahim, R.A., Soundararajan, A., and Heo,H., Stochastic response of nonlinear dynamic systems based on a non-Gaussian closure. *J. Appl. Mech.* ASME, 1985, **52**(4), 965-70.
13. Langley, R., An investigation of multiple solutions yielded by the equivalent linearization method. *J. Sound Vibr.*, 1988,**127**(2),271-81. 271-81.
14. Fan, F.-G., and Ahmadi, G., On loss of accuracy and non-uniqueness of solutions generated by equivalent linearization and cumulant-neglect methods. *J. Sound Vibr.*, 1990, **137**(3), 385-401.
15. Roberts, J. B., Multiple solutions generated by statistical linearization and their physical significance. *Int. J. Non-lin. Mech.*, 1991, **26**(6), 945-59.
16. Wojtkiewicz, S.F., Spencer Jr., B.F., and Bergman,L.A., On the cumulant-neglect closure method in stochastic dynamics. *Int. J. Non -lin. Mech.*, 1996, **31**(5), 657-84.
17. Fang,T.,and Dowell,E.H.,Numerical simulations of jump phenomena in stable Duffing systems. *Int. J. Non-lin. Mech.*, 1987, **22**(3), 267-74.
18. Di Paola, M., Floris, C., and Sandrelli, M.C., Quasi-linearization technique of nonlinear sistems under polynomials of normal fil-

tered processes. Submitted for publication.
19. Grigoriu, M., and Ariaratnam, S.T., Response of linear systems to polynomials of Gaussian processes. *J. Appl. Mech.* ASME, 1988, **55** (4), 905-10.
20. Muscolino, G., Linear systems excited by polynomial forms of non -Gaussian filtered processes. *Prob. Engrg. Mech.*, 1995, **10**(1), 35-44.
21. Di Paola, M., Linear systems to polynomials of non-normal processes and quasi-linear systems.*J. Appl. Mech.* ASME,1997, in press.
22. Roberts, J.B., and Spanos, P.D., *Random Vibration and Statistical Linearization*. John Wiley & Sons, Chichester, 1990.
23. Elishakoff, I., and Zhang, X., An appraisal of different stochastic linearization techniques. *J. Sound Vibr.*, 1992, **153**(2), 370-5.
24. Caughey, T.K., Crandall, S.H., and Lyon, R.H., Derivation and application of the Fokker-Planck equation to discrete nonlinear dynamic systems subjected to white random excitation. *J. Acoust. Soc. Am.*, 1963, **35**(11), 1683-92.
25. Davies, H.G., and Nandlall, D., Phase plane for narrow band random excitation of a Duffing oscillator. *J. Sound Vibr.*, 1986, **104**(2), 277-83.
26. Iyengar, R.N., Response of non-linear systems to narrow-band excitation. *Structural Safety*, 1989, **6**, 177-85.
27. Koliopulos, P.K., and Langley, R.S., Improved stability analysis of the response of a Duffing oscillator under filtered white noise. *Int. J. Non- lin. Mech.*, 1993, **28**(2), 145-55.
28. Lennox, W.C., and Kuak, Y.C., Narrow-band excitation of a non-linear oscillator. *J. Appl. Mech.* ASME, 1976, **43**(2), 340-44.
29. Rajan, S., and Davies, H.G., Multiple time scaling of the response of a Duffing oscillator to narrow-band random excitation. *J. Sound Vibr.*, 1988, **123**(3), 497-506.
30. Davies, H.G., and Rajan, S., Random superharmonic and subharmonic response: multiple time scaling of a Duffing oscillator. *J. Sound Vibr.*, 1988, **126**(2), 195-208.
31. Koliopulos, P.K., and Bishop,S.R., Quasi harmonic analysis of the behaviour of a hardening Duffing oscillator subjected to filtered white noise. *Nonlin. Dyn.*, 1993, **4**, 279-88.
32. Vanmarcke,E.H., Properties of spectral moments with application to random vibration. *J. Engrg. Mech. Div.* ASCE,1972,**98**(2),425-46.
33. Der Kiureghian, A., Structural response to stationary excitation. *J. Engrg. Mech. Div.* ASCE, 1980, **106**(6), 1195-1213.
34. Kimble, B.W., and Cusumano, J.P., Theoretical and numerical validation of the stochastic interrogation experimental method. *J. Vibration and Control*, 1996 , **2**(3), 323-348.

EXTREME RESPONSE ANALYSIS OF NON-LINEAR SYSTEMS TO RANDOM VIBRATION

S. McWilliam

Department of Mechanical Engineering, University of Nottingham, Nottingham, NG7 2RD, England.

ABSTRACT

This paper considers the numerical solution of the Fokker-Planck-Kolmogorov (FPK) equation which governs the transition probability density function (pdf) for a certain class of non-linear system. In order to provide a numerical solution for the pdf which is well behaved at its tails (and thus better suited to extreme value problems), the FPK equation is transformed to give an equation for the log-pdf. The resulting non-linear partial differential equation is solved using a weighted-residual approach. This technique is applied to first and second order systems, including the Duffing oscillator. The accuracy of the technique is assessed by comparison with analytic solutions and numerical simulation.

1. INTRODUCTION

Many different types of structure, such as offshore structures, are subjected to random loading. In the design of these structures it is particularly important that the statistics of the response are obtained so that the maximum stresses and fatigue life of the structure can be predicted. For the situation when the system is linear and the excitation is Gaussian the response statistics are well-known. However, most practical engineering structures are non-linear to some extent and the problem of predicting the response statistics is much more difficult.

For systems which are subjected to white-noise excitation, the response is a Markov process and the transitional probability density function (pdf) is governed by the Fokker-Planck-Kolmogorov (FPK) equation. For other systems the FPK equation can be applied provided that the response is a higher order Markov process. In both these cases the problem of predicting the response statistics reduces to solving the FPK equation for the transitional probability density function. The difficulties associated with finding exact solutions to this equation have lead a number of authors to develop approximate solution procedures [1-3]. Although these techniques are limited to the analysis of low order systems, they have been applied to a number of practical engineering problems (e.g.[3,4]).

The most commonly used numerical solution procedures are the Galerkin technique [1], the Finite Element method [2] and the path-integral method [3].

Wen [1] developed a Galerkin method for the solution of the non-stationary FPK equation, in which the joint probability density function was expanded in terms of Hermite polynomials. The disadvantages of this technique are that it tends to have a low-rate of convergence for systems which are strongly non-linear and the accuracy of the tails of the distribution is not guaranteed - yielding negative values . In contrast, the Finite Element method [2] provides a more robust numerical solution procedure which, in principle, has the potential to deal with all types of non-linearity and give an accurate prediction of the tails of the distribution. However, a large number of elements, and hence a large amount of cpu time, are needed to give sufficient resolution over the tails of the distribution in order for it to be used for the prediction of extremes. The path-integral method proposed by Naess [3] has recently been shown to provide an accurate means of estimating the response pdf, including the tails. However, this too requires a substantial amount of cpu time, and is very much at a developmental stage.

In contrast to the above techniques, the primary aim of the present work is to accurately estimate the tails of the response distribution. This is achieved by considering the log-pdf, which has the advantage of ensuring that the resulting probability density function is always positive. This approach has recently been applied by Di Paola et al. [5] in which the log-pdf was expanded as a Taylor series. For the examples considered there, which included various first order systems and the Duffing oscillator, it was shown that this technique gave good agreement over the main body of the pdf, but no results for the tails of the distribution were reported. A disadvantage of the adopted Taylor series solution method is that it can not be used to analyse systems which contain non-linearities whose derivatives are discontinuous at the origin (e.g. $x|x|$).

In this paper an approach similar to that proposed by Di Paola is used in which an orthogonal expansion for the log-pdf is obtained. More specifically, a Hermite polynomial expansion of the log-pdf is obtained by using a weighted-residual approach to solve the governing differential equation for the log-pdf. The main advantage of using this approach compared to a Taylor series solution is that it is reasonably easy to incorporate non-linearities such as $x|x|$ into the analysis. The accuracy of the proposed numerical solution procedure to predict the response statistics of various first and second order systems is investigated by comparison with analytic results or numerical simulation.

2. THE FPK EQUATION AND LOG-PDF EQUATION

Many references (for example [6]) give details of the derivation of the Fokker-Planck-Kolmogorov (FPK) equation for the determination of the transient probability density function (pdf) of non-linear systems subjected to random excitation. Here, the FPK is simply stated and then used to derive the associated

log-pdf equation.

In order to apply the FPK equation it is necessary to write the equations of motion of the system in state-space notation as follows:

$$\dot{z} = g(z) + A w, \tag{1}$$

where z is a vector containing the displacements and velocities of the system, $\boldsymbol{A}$ is a square matrix (assumed here to be constant), $\boldsymbol{g}(z)$ is a general vector function of the variables z, and w is a vector of uncorrelated Gaussian white noise processes, each having a spectral density of unity.

If z constitutes a Markov process, the FPK equation which governs the transitional probability density function $p(z,t)$ is given by [6]:

$$\frac{dp(z,t)}{dt} = \sum_{i=1}^{n} \frac{\partial}{\partial z_i}\left[g_i(z)p(z,t)\right] - \frac{1}{2}\sum_{i=1}^{n}\sum_{j=1}^{n} B_{ij}\frac{\partial^2}{\partial z_i \partial z_j}\left[p(z,t)\right], \tag{2}$$

where n is the dimension of z and $\boldsymbol{B}$ is a matrix given by:

$$\boldsymbol{B} = 2\pi \boldsymbol{A}\boldsymbol{A}^{T}. \tag{3}$$

As mentioned in the introduction, equation (2) can be solved numerically using the Galerkin method, the Finite Element method and the path-integral technique.

In order to obtain an equation which is more suitable for determining the tails of the response distribution (and hence extremes) it is convenient here to express the probability density function (pdf) as follows:

$$p(z,t) = \exp(\rho(z,t)), \tag{4}$$

where ρ is the log-pdf , i.e.:

$$\rho(z,t) = \ln p(z,t). \tag{5}$$

Differentiating equation (5) with respect to t gives:

$$\frac{\partial \rho(z,t)}{\partial t} = \frac{1}{p(z,t)}\frac{\partial p(z,t)}{\partial t}. \tag{6}$$

Using equations (4) and (6), equation (2) can be re-written in terms of the log-pdf $\rho(z,t)$ as follows:

$$\frac{\partial \rho(z,t)}{\partial t} = -\sum_{i=1}^{n}\left[\frac{\partial g_i}{\partial z_i} - g_i\frac{\partial \rho}{\partial z_i}\right] + \frac{1}{2}\sum_{i=1}^{n}\sum_{j=1}^{n} B_{ij}\left[\frac{\partial^2 \rho}{\partial z_i \partial z_j} + \frac{\partial \rho}{\partial z_i}\frac{\partial \rho}{\partial z_j}\right] \qquad (7)$$

Equation (7) is a non-linear partial differential equation governing the transient log-pdf, and forms the basis of the technique proposed here. In what follows a weighted residual procedure for solving this equation is presented.

3 WEIGHTED RESIDUAL SOLUTION FOR THE LOG-PDF

The weighted residual solution of equation (7) is considered for a first order system and then for a second order system.

3.1 First Order Systems

For the case of first order systems equation (7) can be written as follows:

$$\frac{\partial \rho(z,t)}{\partial t} = -\frac{\partial g}{\partial z} - g\frac{\partial \rho(z,t)}{\partial z} + B\left[\frac{\partial^2 \rho(z,t)}{\partial z^2} + \left(\frac{\partial \rho(z,t)}{\partial z}\right)^2\right] \qquad (8)$$

In the weighted residual approach adopted here the log-pdf and the system non-linearity are expressed as the sum of a finite number of weighted Hermite polynomials, such that:

$$\rho(z,t) = \sum_{i=0}^{m} \lambda_i(t)\, H_i(z), \qquad g(z) = \sum_{l=0}^{p} \mu_l H_l(z), \qquad (9,10)$$

where

$$\mu_l = \frac{1}{\sqrt{2\pi}\, l!}\int_{-\infty}^{\infty} g(z) H_l(z) e^{-\frac{z^2}{2}}\, dz, \qquad (11)$$

and $H_i(z)$ is the i'th Hermite polynomial.

Substituting equations (9) and (10) into equation (8) gives:

$$\sum_{i=0}^{m}\dot{\lambda}_i H_i = -\sum_{l=0}^{p}\mu_l\frac{\partial H_l}{\partial z} - \sum_{l=0}^{p}\sum_{i=0}^{m}\mu_l H_i\lambda_i\frac{\partial H_i}{\partial z} + B\left[\sum_{l=0}^{m}\lambda_i\frac{\partial^2 H_l}{\partial z^2} + \sum_{i=0}^{m}\sum_{j=0}^{m}\lambda_i\lambda_j\frac{\partial H_i}{\partial z}\frac{\partial H_j}{\partial z}\right]. \tag{12}$$

Multiplying equation (12) by $H_k\exp(-z^2/2)/\sqrt{2\pi}$, integrating over z from $-\infty$ to ∞ and using the properties of the Hermite polynomials given in Appendix A gives:

$$k!\dot{\lambda}_k = -k!\mu_k - \sum_{i=0}^{m}\sum_{l=0}^{p} i\lambda_i\mu_l I[i-1,l,k] + B\left[(k+2)!\lambda_{k+2} + \sum_{i=0}^{m}\sum_{j=0}^{m} ij\lambda_i\lambda_j I[i-1,j-1,k]\right], \quad k=0,1,\ldots n \tag{13}$$

where $I[i,j,k]$ is an integral of a triple Hermite product which, using the properties given in Appendix A, may be shown to be given by:

$$I[i,j,k] = \int_{-\infty}^{\infty} H_i(x)H_j(x)H_k(x)e^{-\frac{x^2}{2}}dx = \frac{i!j!k!\sqrt{2\pi}}{\left(-\frac{i}{2}+\frac{j}{2}+\frac{k}{2}\right)!\left(\frac{i}{2}-\frac{j}{2}+\frac{k}{2}\right)!\left(\frac{i}{2}+\frac{j}{2}-\frac{k}{2}\right)!}, \tag{14}$$

where k is the smallest of i, j and k.

Equation (13) represents a set of first order, non-linear, differential equations which can be solved numerically for $\lambda_k(t)$ using standard integration techniques. The calculated values can then be substituted back into equation (9) to yield an expression for $p(z)$. To ensure that this is a valid pdf, the coefficient λ_0 is modified to ensure that the normalisation condition is satisfied.

For the situation when the response of the system is stationary (ie. $d\lambda_k/dt=0$ for all k), equation (13) reduces to a set of non-linear algebraic equations. Although the solution of these equations can, in principle, be calculated using standard numerical methods, these methods require a good first estimate of the solution in order to achieve a good rate of convergence. For the systems considered in the numerical examples section, the stationary pdf is calculated by integrating equation (12) until stationary conditions are achieved.

This section has shown how a weighted residual approach can be used to obtain a numerical solution to the log-pdf equation for first order systems. In what

follows this technique is extended to deal with second order systems.

3.2 Second order systems

An identical procedure to that presented for first order systems is now applied to a general second order system.

Let the log-pdf be expressed as follows:

$$\rho(z_1,z_2,t)=\sum_{p=1}^{n}\sum_{q=1}^{m}\lambda_{pq}(t)\,H_p(z_1)H_q(z_2), \tag{15}$$

and the system non-linearity be expressed as:

$$g(z_1,z_2)=\sum_{l=0}^{p}\sum_{m=0}^{q}\mu_{lm}H_l(z_1)H_m(z_2), \tag{16}$$

where

$$\mu_{lm}=\frac{1}{2\pi l!m!}\int_{-\infty}^{\infty}\int_{-\infty}^{\infty}g(z_1,z_2)H_l(z_1)H_m(z_2)\exp(-\frac{z_1^2}{2}-\frac{z_2^2}{2})dz_1dz_2, \tag{17}$$

and H_i is the i'th Hermite polynomial.

A set of non-linear, first order differential equations in terms of λ_{pq} can be obtained by substituting equations (15) and (16) into equation (7), multiplying by $H_p(z_1)H_q(z_2)\exp(-(z_1^2+z_2^2)/2)/(2\pi)$, integrating over z_1 and z_2 from $-\infty$ to ∞, and making use of equation (14). This yields an equation of the form:

$$\dot{\lambda}_{pq}=\sum_{i,j}a_{ij}\lambda_{ij}+\sum_{i,j}\sum_{l,m}b_{ijlm}\lambda_{ij}\lambda_{lm}, \tag{18}$$

where a_{ij} and b_{ijlm} are constant coefficients dependent upon the system considered. As in section 3.1, equation (18) can be solved numerically for λ_{pq} and then the log-pdf can be obtained from equation (15). This procedure is used in the following section to calculate the response statistics of some example systems. In addition, it may be noted that the extension of the weighted residual technique to multi-dimensional systems is straight-forward.

4 NUMERICAL EXAMPLES

The techniques described above are used here to determine the stationary response statistics of: i) first order systems and ii) second order systems. In all cases the initial response conditions are assumed to have a Normal distribution and the stationary response statistics are obtained by integrating the equations governing the Hermite coefficients until stationary conditions are obtained. The response pdf can then be obtained by substituting the Hermite expansion for the log-pdf into equation (4) and applying the normalisation condition (to ensure that it is a valid probability density function).

4.1 First Order Systems

Two first order systems are considered here. The first consists of a system with a polynomial non-linearity, while the second consists of a drag non-linearity. In both cases the results obtained using the proposed technique are compared with the exact analytic solutions available, and both the pdf and log-pdf of the response (z) are plotted.

4.1.1 Polynomial non-linearity

The first order system considered here has the following equation of motion:

$$\dot{x} = -\sum_{i=1}^{5} a_i x^i + f(t) \tag{19}$$

where a_1=0.1, a_2=0.0, a_3=0.05, a_4=0.0, a_5=0.01, and $f(t)$ is a zero mean, Gaussian, white-noise excitation with a constant spectral value $K=1/\pi$. The stationary distribution in this case is given by:

$$p(x) = A\exp\left(-2\int_0^x \sum_{i=1}^{5} a_i z^i dz\right) \tag{20}$$

where A is the normalisation coefficient.

The distribution of x for this case is shown in Figure 1, where Figure 1a) shows the pdf and Figure 1b) shows the log-pdf. In these figures a comparison with the exact result, given by equation (20), is made with the results obtained using the proposed technique with m=4 and m=6 in equation (9), and an equivalent Gaussian distribution. In both cases it is seen that the response statistics are highly non-Gaussian, and the proposed technique gives better agreement with the exact result with m=6 than with m=4. Further, for the case when m≥6 it is found that the proposed technique agrees exactly with the exact result. In many respects

this agreement obtained using the proposed technique is not surprising since the stationary pdf can be expressed exactly in the assumed form when m≥6. However, there is no guarantee that the transient response can be expressed in this assumed form.

4.1.2 Drag non-linearity

The system considered here has the following equation of motion:

$$\dot{x} = -x|x| + f(t), \tag{21}$$

where $f(t)$ is a zero mean, Gaussian, white-noise excitation with a constant spectral value $K=1/\pi$. The exact distribution in this case is given by:

$$p(x) = A\exp(\frac{x^2|x|}{3}), \tag{22}$$

where A is the normalisation coefficient.

Unlike the system considered in section 4.1.1, the drag non-linearity and log-pdf can not be expressed exactly using Hermite polynomials, and is therefore a more difficult system to analyse using the proposed technique.

Figure 2 shows the statistical distribution of x for this situation, where Figure 2a) shows the pdf and Figure 2b) shows the log-pdf. In these figures a comparison with the exact result, given by equation (22), is made with the results obtained using the proposed technique with m=3 and m=7 in equation (9), and an equivalent Gaussian distribution. It is seen that the response statistics are highly non-Gaussian and that using an increased number of Hermite polynomials to represent the log-pdf gives improved agreement with the exact result, especially at the "tails" of the distribution. This is not surprising since the technique proposed here deals with the log-pdf and is therefore well-suited to determining the tails of the distribution.

4.2 Second Order Systems

From a practical point of view it is the response statistics of second (and higher) order systems which are of vital importance to design engineers. In order to demonstrate the performance of the proposed technique, two second order systems are considered. In each case results are obtained for the displacement (z_1) pdf and the velocity (z_2) pdf, and the results are plotted as a pdf's and log-pdf's.

4.2.1 Duffing Oscillator

The equation of motion considered in this case is given by:

$$\dot{z}_1 = -z_2, \quad \dot{z}_2 = -z_2 - z_1 - z_1^3 + f(t), \tag{23}$$

where $f(t)$ is a zero mean, Gaussian, white-noise excitation with a constant spectral value $K=1/\pi$. In this case it is well-known [6] that the displacement and velocity are statistically independent, and exact analytic results are available for the displacement and velocity pdf's, such that:

$$p(z_1) = C_1 \exp(-\frac{1}{2}z_1^2 - \frac{1}{4}z_1^4), \quad p(z_2) = C_2 \exp(-\frac{1}{2}z_2^2), \tag{24,25}$$

where C_1 and C_2 are normalisation constants.

The stationary response statistics for this case are shown in Figure 3, where the analytic results have been compared with those obtained using the proposed technique and an equivalent Gaussian distribution. In this case it is found that the proposed technique gives identical results for the jpdf (and hence displacement and velocity statistics) provided that a sufficient number of Hermite polynomials are used (i.e. $n \geq 4$ and $m \geq 5$ in equation (15)). In some respects this is not surprising since it is known that the stationary jpdf can be expressed exactly in the assumed form given by equation (15), provided a sufficient number of terms are used. However, as in previous examples, it is unlikely that the transient response statistics can be expressed exactly in this form.

4.2.2 Duffing Oscillator with cubic damping non-linearity
The equation of motion considered in this case is given by:

$$\dot{z}_1 = -z_2, \quad \dot{z}_2 = -z_2 - \frac{1}{2}z_2^3 - z_1 - z_1^3 + f(t), \tag{26}$$

where $f(t)$ is a zero mean, Gaussian, white-noise excitation with a constant spectral value $K=1/\pi$. Although there is no exact analytic result available for the displacement distribution in this case, it is shown in Appendix B that there exists an analytic result for the velocity statistics, such that:

$$p(z_2) = A \exp(-\frac{z_2^2}{2} - \frac{z_2^4}{16}), \tag{27}$$

where A is the normalisation constant.

The stationary response statistics for this case are shown in Figure 4, where a

comparison is made with numerical simulation and exact results. In the proposed representation n=4 and m=8 are used in equation (15), and an equivalent Gaussian distribution is shown for comparison. Up to the highest levels obtained by simulation, the proposed method gives excellent agreement.

5 CONCLUSIONS

A numerical method for solving the associated FPK equation governing the response statistics of non-linear systems subjected to random vibration has been presented. The main advantage of this method over alternative techniques is that it ensures that the tails of the response distribution remain positive, suggesting that it well-suited to extreme value prediction. For the numerical examples considered this was shown to be the case, in which excellent agreement with exact analytic solutions and numerical simulation were obtained, especially at the tails of the distribution. Although, in principle, the procedure developed is applicable to an *n*-dimensional system, the computer costs increase rapidly with n. However, the remarkable increases in computer performance over the past decade suggests that the present procedure may, in the near-future, become a viable option for calculating the response statistics of higher order systems.

REFERENCES

1. Wen, Y.K. Approximate method for nonlinear random vibration, *Proceedings of the American Society of Civil Engineers, Journal of the Engineering Mechanics Division,* 1975, **101**, 389-401.

2. Langley, R.S. A finite element method for the statistics of non-linear random vibration, *Journal of Sound and Vibration*, 1985, **101(1)**, 41-54.

3. Naess, A. and Johnsen, J.M. Response statistics of nonlinear, compliant offshore structures by the path integral solution method, *Probabilistic Engineering Mechanics,* 1993, ***8,*** 91-106.

4. Roberts, J.B. A stochastic theory for nonlinear ship rolling in irregular seas, *Journal of Ship Research*, 1982, **26**, 229-245.

5. Di Paola, M., Ricciardi, G., and Vasta, M. A method for the probabilistic analysis of nonlinear systems, *Probabilistic Engineering Mechanics*, 1995, **10(1)**, 1-10.

6. Lin, Y.K. *Probabilistic Theory of Structural Dynamics*, McGraw-Hill, New York, 1967.

APPENDIX A - PROPERTIES OF HERMITE POLYNOMIALS

The following properties of the set of Hermite polynomials are used in section 3.

$$\frac{1}{\sqrt{2\pi}}\int_{-\infty}^{\infty} H_n(z)e^{-\frac{z^2}{2}}dz \quad \begin{matrix} =0 & n=0 \\ =n! & n\neq 0 \end{matrix} \tag{A1}$$

$$\frac{dH_n(z)}{dz} = nH_{n-1}(z). \tag{A2}$$

APPENDIX B - ANALYTIC SOLUTION FOR THE VELOCITY STATISTICS OF A PARTICULAR CLASS OF SECOND ORDER SYSTEM.

For the second order systems considered in the numerical examples section the associated FPK equation (equation (2)) can be written as follows:

$$\frac{\partial p(z_1,z_2)}{\partial t} = z_2\frac{\partial p(z_1,z_2)}{\partial z_1} - \frac{\partial\left[g(z_1,z_2)p(z_1,z_2)\right]}{\partial z_2} - \pi K\frac{\partial^2 p(z_1,z_2)}{\partial z_2^2}, \tag{B1}$$

where

$$g(z_1,z_2) = g_1(z_1) + g_2(z_2). \tag{B2}$$

Substituting equation (B2) into equation (B1) and integrating over z_1 from $-\infty$ to ∞ gives:

$$\frac{\partial p(z_2)}{\partial t} = z_2 p(z_1,z_2)\Big|_{z_1=-\infty}^{z_1=\infty} - g_2(z_2)\frac{\partial p(z_2)}{\partial z_2} - \int_{-\infty}^{\infty} g_1(z_1)\frac{\partial p(z_1,z_2)}{\partial z_2}dz_1 - \frac{\partial g_2}{\partial z_2}p(z_2) - \pi K\frac{\partial^2 p(z_2)}{\partial z_2^2}. \tag{B3}$$

The first term on the right hand side of equation (B3) will reduce to zero since for

it is reasonable to assume that as the displacement (z_1) increases (or decreases) without bound $p(z_1,z_2)$ will tend to zero.

Provided that $p(z_1,z_2)$ is continuous, the third term on the right hand side of equation (B3) can be re-written as:

$$\int_{-\infty}^{\infty} g_1(z_1)\frac{\partial p(z_1,z_2)}{\partial z_2}dz_1 = \frac{\partial}{\partial z_2}\left[\int_{-\infty}^{\infty} g_1(z_1)p(z_1,z_2)dz_1\right] \tag{B4}$$

The term in square brackets on the right hand side of this equation will reduce to zero provided that g_1 is an *odd function* and $p(z_1,z_2)$ is *symmetric* with respect to z_1 for all values of z_2. This condition is satisfied by the systems considered in sections 4.2.1, 4.2.2 when the response is stationary (i.e. $\partial p/\partial t=0$). Consequently, for the examples considered in the numerical examples section the third term appearing in equation (B3) reduces to zero provided that the term on the left hand-side is set to zero (i.e. stationary conditions).

Making use of the above observations and re-arranging, equation (B3) can be written as:

$$\frac{\partial\left[g_2(z_2)p(z_2)\right]}{\partial z_2} - \pi K\frac{\partial^2 p(z_2)}{\partial z_2^2} = 0. \tag{B5}$$

This is the associated stationary FPK equation for the first order system whose equation of motion is:

$$\dot{z}_2 = -g_2(z_2) + f(t). \tag{B6}$$

Thus, it has been shown that the stationary distribution z_2 (alone) is identical to that of a one-dimensional Markov process. Further, the solution of equation (B5) can be written as:

$$p(z_2) = A\exp\left(-\frac{2}{\pi K}\int_0^{z_2} g_2(z)dz\right), \tag{B7}$$

where A is the normalisation constant. Consequently, the velocity statistics of the second order systems considered in the numerical examples section can be obtained analytically. This result is used to validate the accuracy of the results in the numerial examples section.

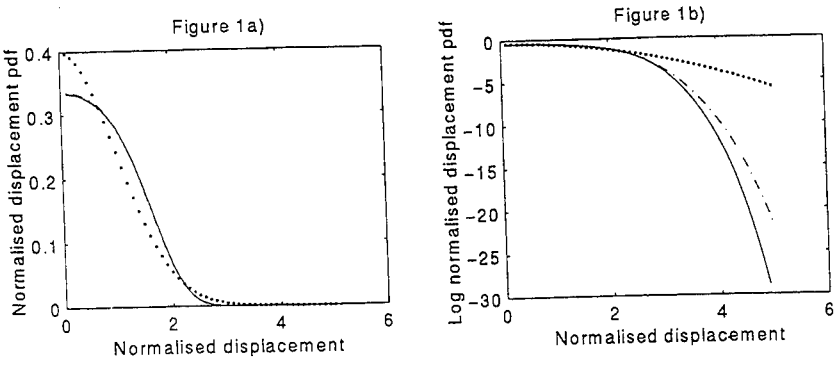

Figure 1. The stationary response statistics of the system given by equation (19): —, exact solution; – · –, proposed technique (m=4); ••••• , equivalent Gaussian distribution. (a) displacement pdf, (b) displacement log-pdf. (Note: *the exact solution and proposed solution* (m=6) *agree exactly in this case.*)

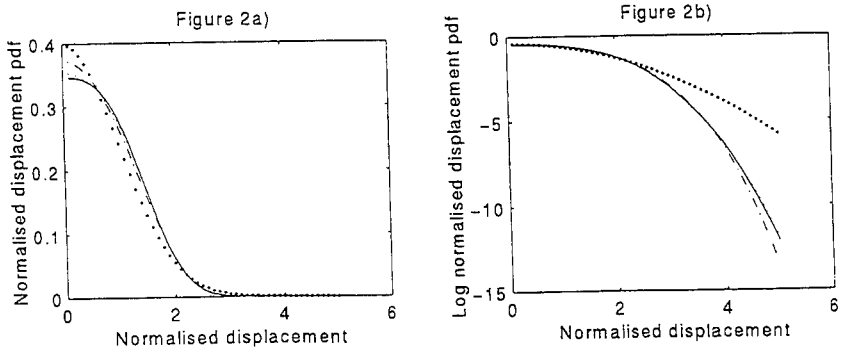

Figure 2. The stationary response statistics for the system given by equation (21): —, exact solution; – · –, proposed technique (m=3); · · ·, proposed technique (m=7); ••••• , equivalent Gaussian distribution. (a) displacement pdf, (b) displacement log-pdf.

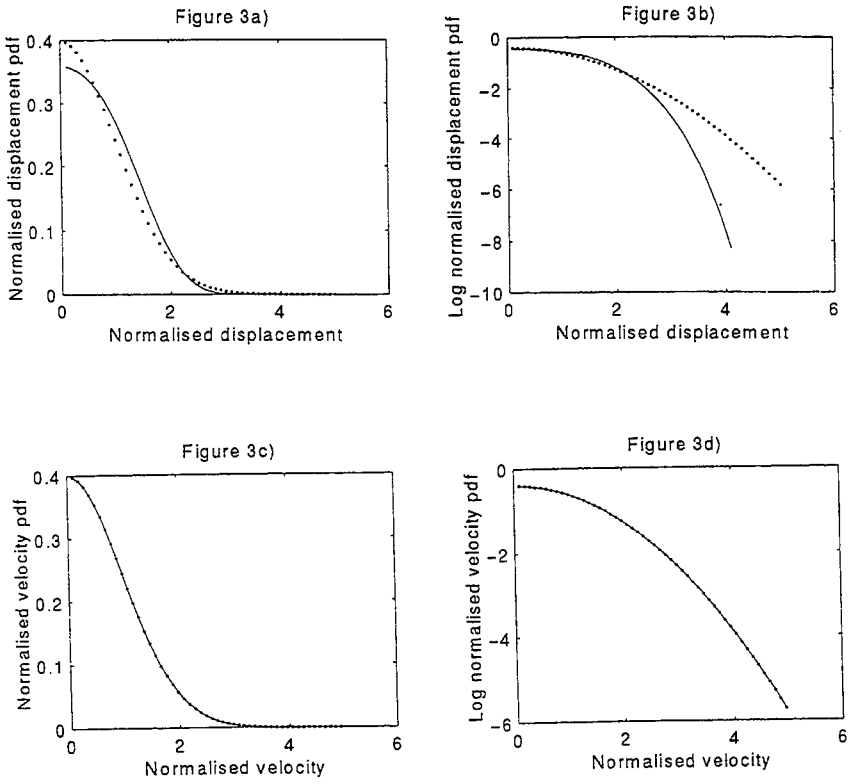

Figure 3. The stationary response statistics for the Duffing Oscillator given by equation (23): ——, exact solution; – · – , proposed technique; ••••• , equivalent Gaussian distribution. (a) displacement pdf, (b) displacement log-pdf, (c) velocity pdf, (d) velocity log-pdf. (Note: *the exact solution and proposed solution agree exactly in this case.*)

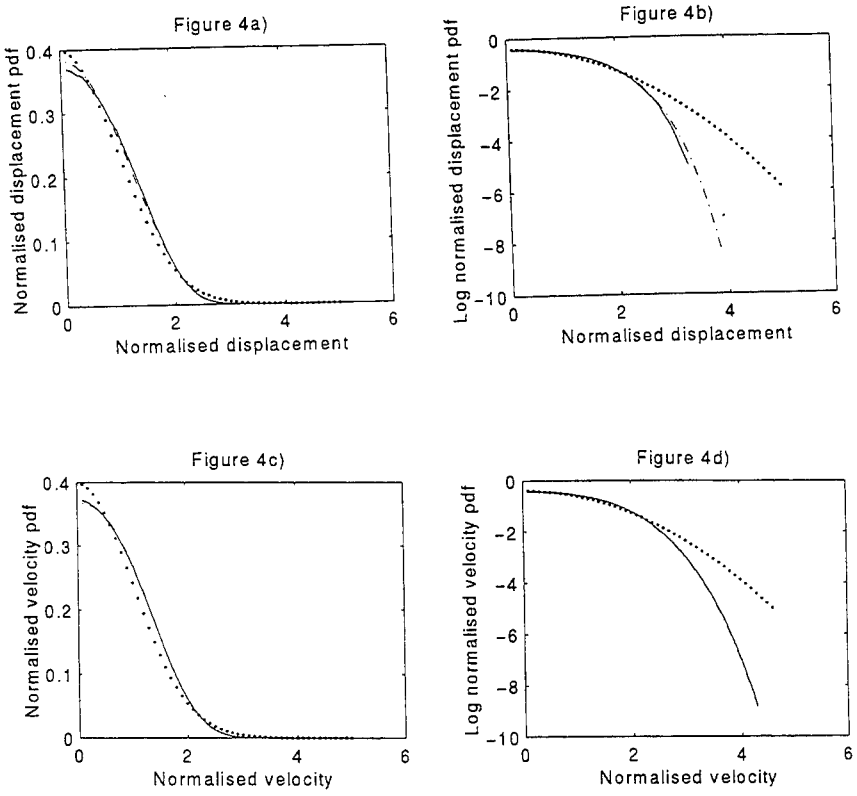

Figure 4. The stationary response statistics for the Duffing Oscillator with cubic damping (see equation (26)): ——, numerical simulation ((a) and (b) only); – · –, proposed technique; – – , exact solution ((c) and (d) only); ••••• , equivalent Gaussian distribution. (a) displacement pdf, (b) displacement log-pdf, (c) velocity pdf, (d) velocity log-pdf.

On the use of Finite Element solutions of the FPK equation for non-linear stochastic oscillator response statistics

M. Ghanbari* **and J. F. Dunne**
School of Engineering, University of Sussex,
Falmer, Brighton, U.K. BN1 9QT.

SUMMARY

Numerical solutions of the stationary Fokker-Planck equation are obtained via Langley's FE method and applied to non-linear oscillators driven externally by Gaussian white-noise. A SDOF model, appropriate to large amplitude random vibration of a clamped-clamped beam excited by band-limited noise, is used to demonstrate convergence of predicted response marginal density functions and extreme-value exceedance probabilities. Experimental verification of this beam model is shown at marginal density level using calibrated FEM-FPK predictions and measured data. Convergence of a 4D FEM-FPK version is also demonstrated at marginal density level, corresponding to a pair of non-linear oscillators. This 4D method is applied up to a practical storage limitation imposed using a systematic FEM node numbering scheme.

1.0 INTRODUCTION

Finite element analysis has now found widespread application in the field of stochastic dynamics for mathematical modelling of structures exposed to random type loading. Applications vary from wave induced response prediction for fixed and compliant offshore structures, seismic response modelling of building structures during earthquakes, wind buffeting problems in aerodynamics, and of course for modelling the effects of roughness on road and rail vehicular motions [1][2].

Predictions of reliability, in the form of appropriate response statistics, can usually be obtained for linear structures from a finite element structural model, combined with linear statistical and normal distribution theory [3]. In cases where significant nonlinearities are present, accurate response statistics cannot be obtained with linear theory, justifying alternatives such as Monte Carlo simulation in the time-domain. Simulations can be very effective in obtaining low-level statistics, for example the first few response moments (even when there are many degrees-of-freedom). But to obtain highly accurate information in the tails of the marginal response amplitude probability density function (pdf), or to obtain accurate low-level extreme-value exceedance probabilities, conventional simulations are impractical owing to the enormously long runs needed to obtain confident probability estimates. Response amplitude probabilities are useful for initial reliability assessment, whereas extreme-value

* Now at: RHP BEARINGS Ltd, Oldends Lane, Stonehouse, Gloucestershire, GL10 3RH UK.

statistics are very important for quantifying the likelihood of dangerously high amplitudes being reached within a specified period of time, since these can often be related directly to risks elsewhere.

Focusing initially on extreme-value statistics, a number of vibration type approaches have been developed using a combination of vibration theory, control techniques and simulation [4-8]. These methods are, under certain conditions, capable of producing highly accurate results, although for broad-band excitation, there is still a need for a direct, accurate, and efficient approach which does not involve complicated intermediate stages or simulation. More generally, within the theory of stochastic processes, there are several important asymptotic routes to extreme-value prediction appropriate for high response amplitude levels or long sample path durations. Local maxima statistics for example, can be used to construct extreme-value statistics, assuming independence of specified response maxima [9] - an approach frequently used for linear structures with Gaussian responses. Another approach [8] uses the asymptotically Poisson character of local maxima at high levels. An alternative route, via threshold crossing statistics, assumes independence of up-crossings, by ignoring 'bandwidth' [5], an effect related to the concentration of energy on response sample paths within a narrow band of frequencies.

Threshold crossing statistics can be approached via the joint pdf for a response amplitude process and its first derivative, which in turn can be obtained for a general class of non-linear systems via Markov process theory using the stationary Fokker-Planck-Kolmogorov (FPK) equation [2][10]. This equation can often be constructed directly from the equations of motion for a stochastic dynamic system, provided the excitation sources can be modelled as broad-band. Although few exact FPK solutions are known, in the past 30 years there have been several types of numerical method proposed (references [11-16] are just some examples of functional-type solutions, not to mention finite difference methods). A good numerical solution opens-up possibilities for obtaining accurate tails of the response amplitude pdf, and accurate extreme-value statistics, thereby avoiding the need for enormously long simulations. Whilst numerical FPK solution methods obviously differ in accuracy and efficiency, there is one school of thought to suggest that finite element structural modelling, followed by FE solution of the FPK equation, offers an attractive and unified approach to structural reliability assessment.

But the accuracy of FEM-FPK predictions depend on the use of a sufficient number of elements in the approximation, and to achieve a certain level of accuracy, this is affected by the dimension of the problem, the strength of nonlinearity in the model, and on the probability levels considered. Computer storage limitations may also prevent the required number of elements from being used. Furthermore stationary FPK solutions contain no 'bandwidth' information at the sample level. Therefore, the assumption of independent up-crossings, intrinsic to all FPK based extreme-value predictions, must be

checked using an alternative such as Monte Carlo simulation. But to justify such lengthy checking, a realistic non-linear model is appropriate, for example a large amplitude model for clamped-clamped beam vibration excited by broad-band noise [17].

In this paper, a SDOF beam model, and a pair of non-linear oscillators, are used to demonstrate use of Langley's FEM-FPK method. In both models, the parameters are known, and only external Gaussian white-noise excitations are assumed. For the SDOF (beam) model, the rate of convergence of the response amplitude pdf via the FEM, is demonstrated as more nodes are used. FEM-FPK based extreme exceedance probabilities are then compared with long Monte Carlo simulations to show convergence with increasing nodes, and to confirm the insensitivity of bandwidth effects at the probability levels considered. The model is justified at the pdf level, by showing calibrated FEM-FPK predictions and experimental measurements. A 4D FEM-FPK version is then applied to a pair of non-linear oscillators. This is to establish the level of convergence reached in the response amplitude pdf, with practical storage limitations imposed using a systematic FEM (global) node numbering system.

2. The FPK Equation and Stationary Response statistics

When the force vector components arising in a structural dynamic model can be treated as broad-band Gaussian processes, Markov process theory allows the (forward) transition probability density function to be modelled using the Fokker-Planck (FPK) equation (and backward transitions via the Backward equation) [2]. From these densities important response statistics can be obtained for use in reliability assessment. Under certain conditions, statistical properties of response trajectories cease to vary with time allowing a simpler (stationary) FPK equation to be constructed. The starting point for constructing the stationary FPK [10] is to express the system of (non-linear) equations of motion:

$$M\underline{\ddot{X}} + F(\underline{X}, \underline{\dot{X}}) = \underline{f}(t) \tag{1}$$

in appropriate state space form as follows:

$$\underline{\dot{z}} = \underline{g}(\underline{z}) + \mathrm{A}\underline{w}(t) \tag{2}$$

where $\underline{z}$ represents an $n\times1$ vector Markov response process, $\underline{w}(t)$ is an assumed $n\times1$ vector of zero-mean uncorrelated Gaussian white-noise processes, whose spectral densities are unity, scaled by a constant square matrix A, and $\underline{g}$ is an $n\times1$ vector of (non-linear) system functions. The stationary FPK equation associated with equation (2), can be obtained by

identifying so called drift and diffusion coefficients [10] and by focusing on steady-state trajectories. This leads to the partial differential equation:

$$\frac{1}{2}\sum_{i=1}^{n}\sum_{j=1}^{n} B_{ij}\frac{\partial^2}{\partial z_i \partial z_j}[p(\underline{z})] - \sum_{i=1}^{n}\frac{\partial}{\partial z_i}[g_i(\underline{z})p(\underline{z})] = 0 \qquad (3)$$

where $B = 2\pi AA^T$ and $p(\underline{z})$ is the stationary joint probability density function (jpdf) associated with the solution trajectories of the dynamic model. Boundary conditions take a variety of forms [2], in addition to the normalisation condition requiring that the total probability must sum to one. Very few exact solutions to equation (3) are known which is one important reason why numerical methods are increasingly used.

2.1 Marginal Densities and Extreme-Value Statistics

From the stationary FPK solution $p(\underline{z})$, marginal density functions, and corresponding moments, can be obtained by successive integration. The joint bi-variate pdf for a response and its first derivative, can be used to obtain the mean threshold crossing rate [10]. If this is accurate, then it offers an approximate route to the distribution of extreme-values for response process z_i. The required bivariate density function is in general obtained by integration as follows:

$$p(z_i, z_{i+1}) = \int_{-\infty}^{+\infty} p(\underline{z})d\underline{z}' \qquad (4)$$

and from equation (4), the mean upcrossing rate is determined from:

$$\upsilon^+(\mathrm{u_T}) = \int_{0}^{+\infty} z_{i+1}\, p(\mathrm{u_T}, z_{i+1})dz_{i+1} \qquad (5)$$

where $\mathrm{u_T}$ refers to the level of interest, and $d\underline{z}'$ corresponds to the reduced state space in which variables z_i and z_{i+1} do not appear. The Poisson assumption of independent upcrossings [6] gives the approximate extreme-value distribution for $z_i(t)$ in the form:

$$F_{\mathrm{M}}(\mathrm{u_T}) = prob\{M(\mathrm{T}) \leq \mathrm{u_T}\} = e^{-\upsilon^+(\mathrm{u_T})T} \qquad (6)$$

where M is the largest value of response process $z_i(t)$ in the interval T. From this, the exceedance probability for extreme-value is defined as:

$$P\{M(T) > u_T\} = 1 - F(u_T) \tag{7}$$

3. Finite Element Solution of the Stationary FPK Equation

There have been several finite element FPK solution methods proposed such as the methods of Langley[12], Bergman[14], Spencer and Bergman[16] (also applied to the Backward equation). These methods are essentially special applications of the weighted residual (WRM) Galerkin-type approximation, using shape functions defined over a finite, rather than infinite region. The Finite element method, for example proposed by Langley, has the additional advantage of being able to deal efficiently with spatial dependence in the FPK equation - a feature which does not normally occur in general structural analysis problems. We do not propose to examine these methods in any detail, except to give a brief outline of Langley's method in the usual context of the WRM appropriate for a stationary multi-dimensional FPK equation since this is used later.

In Langley's method [12], general use is made of piece-wise shape functions to approximate, within a number finite elements, both the solution $P(\underline{z})$, and the non-linear $g_i(\underline{z})$ appearing in equation (3). These elements are usually rectangular for 2D, cuboid for 3D etc., and the total number of nodes for a single n-dimensional element is $m = 2^n$. The solution $P(\underline{z})$ over the entire domain is approximated in terms of the (unknown) nodal values of the pdf as follows:

$$\hat{P}(\underline{z}) = \sum_{i=1}^{m} p_i N_i(\underline{z}) \tag{8}$$

Shape functions $N_i(\underline{z})$ are chosen to take unit values at a specified node, and zero at other nodes within a particular element. For nodes which do not fall within a particular element, the shape function values are zero.

In trial solution (8), the usual far-field boundary conditions are modified to account for use of a finite region, namely that $p(\underline{z}) \to 0$ when $(\underline{z}) \to \pm\underline{a}$ where $\underline{a}$ is some large finite value. Substitution of trial solution (8) for all elements over the entire finite region, allows the FPK equation residual to be formed as follows:

$$\frac{1}{2}\sum_{i=1}^{n}\sum_{j=1}^{n} B_{ij}\frac{\partial^2}{\partial z_i^2}[\hat{p}(\underline{z})] - \sum_{i=1}^{n}\frac{\partial}{\partial z_i}[g_i(\underline{z})\hat{p}(\underline{z})] = R(\underline{z}) \tag{9}$$

Equation (9) gives a measure of how well the entire solution $\hat{p}(\underline{z})$ satisfies equation (2) and if the shape functions are chosen correctly, one hopes that the

residual will reduce uniformly to zero as the number of elements is increased. Weighted residuals are formed as follows:

$$\int\int R(\underline{z})w(\underline{z})d\underline{z} = 0 \tag{10}$$

to provide the basis for selecting the nodal values of the approximate solution. The weight functions $w(\underline{z})$, are chosen appropriately to be the same nodal shape functions $N_i(\underline{z})$ within those elements in which a particular node of interest falls. For all other elements, the weight functions are taken to be zero. This converts the weighted residual statement (10) to a finite number of summations over all elements, which in principle generates the same number of (linear) equations as unknown nodal probability values. This (generally sparse) system of linear equations is in fact singular, but a unique solution can be obtained by imposing the normalisation condition:

$$\int_{-\infty}^{+\infty} p(\underline{z})d\underline{z} = 1 \tag{11}$$

To make best use of finite elements, the simplest type of shape function is used to remove much of the burden in organising the FE code. The simplest choice is indeed a piece-wise linear (Lagrange) function, where n-dimensional shape functions can be constructed using appropriate multiples of the one-dimensional version. However, were a trial solution to be attempted using these Lagrange-type functions directly in equation (10), the FPK equation being second order, would cause the first term to vanish since linear shape functions have only C_0 continuity. This problem was overcome [12] by integrating equation (10), to generate the weak form of weighted residual statement for the FPK equation:

$$\frac{1}{2}\sum_{i=1}^{n}\sum_{j=1}^{n} B_{ij}\int_R \frac{\partial}{\partial z_i}[w(\underline{z})]\frac{\partial}{\partial z_j}[p(\underline{z})]d\underline{z} - \sum_{i=1}^{n}\int_R g_i(\underline{z})p(\underline{z})\frac{\partial}{\partial z_i}[w(\underline{z})]d\underline{z} = 0 \tag{12}$$

Equation(12) applied over all the finite elements will yield a system of linear equations for p_i which can be obtained uniquely by imposing the normalisation condition (11). As mentioned, far-field boundary conditions are applied at a finite, rather than an infinite boundary, determined in practice using equivalent linearization. This boundary is chosen at 5 or 6 standard deviations in all directions where the probability density outside this region is assumed to be zero. The non-linear functions $g_i(\underline{z})$ appearing in equation (3) can also, for reasons of computational efficiency, be approximated within a particular element using the same shape functions as follows:

$$\hat{g}(\underline{z}) = \sum_{i=1}^{m} g_i N_i(\underline{z}) \tag{13}$$

This has the advantage of reducing the amount of pre-processing required to handle the spatial variability in the FPK equation and is therefore useful where parameter or model variations are intended. Once $p(\underline{z})$ is calculated in the above manner, the extreme-value exceedance distribution can be approximated from equations (4)-(7).

A storage problem however arises in the use of the FEM, since the linear coefficient matrix is of dimension $N^n \times N^n$, where N is the number of nodes. This obviously becomes excessive for anything more than the 2-dimensional problem. Iterative solution techniques [18] can be used to solve linear equations without need to store the coefficient matrix. But these methods are suited to sparse matrices with narrow bandwidth, such as arise in structural FEM - the best known being the Frontal solution method. Unfortunately the benefits of using space saving methods in the FEM-FPK are to some extent lost, as it can be shown that even if the theoretical bandwidth is no more than 3^n, the practical bandwidth is significantly more than this when a systematic nodal numbering scheme is used. Therefore for large n (say > 3), unless an extremely sophisticated global node numbering system is used, the bandwidth grows rapidly with the node number and the advantages of space saving methods are not realised. For small n (e.g. n=1 or 2) storage requirements are not so critical, so a good solution can be obtained using standard sparse system solution techniques.

4. Application to SDOF Model

The first application of this FEM-FPK is to a SDOF oscillator model:

$$\ddot{Z} + 2\xi\omega_n \dot{Z} + \alpha_1 \dot{Z} Z^2 + \alpha_2 \dot{Z}|\dot{Z}| + \omega_n^2 Z + k_3 Z^3 = Aw(t) \qquad (14)$$

which represents a system with both linear and non-linear damping, and linear plus cubic stiffness. The excitation $w(t)$ is a unit intensity stationary zero mean Gaussian white noise process, scaled to required level by parameter A. Some evidence will be shown shortly to confirm this as a realistic vibration model for one dimensional large amplitude vibration of clamped-clamped beam, at least in the tails of the response amplitude marginal probability density function [17]. First we intend to show convergence of predicted FEM-FPK pdf solutions with increasing nodes; and then extreme exceedance predictions based on the FEM-FPK using equations (3)-(7), in both cases predictions are compared with Monte Carlo simulations - this includes an assessment of the Poisson assumption using equation(5). To complete the section, pdf predictions using a calibrated form of model (14), are compared with experimental measurements of clamped-clamped beam vibration.

Putting oscillator model (14) into state space form, gives a two-state vector Markov model:

$$\begin{bmatrix} dz_1 \\ dz_2 \end{bmatrix} = \begin{bmatrix} z_2 \\ -2\xi\omega_n z_2 - \alpha_1 z_2 z_1^2 - \alpha_2 z_2 |z_2| - \omega_n^2 z_1 - k_3 z_1^3 \end{bmatrix} dt + \begin{bmatrix} 0 & 0 \\ 0 & A \end{bmatrix} \begin{bmatrix} 0 \\ db(t) \end{bmatrix} \quad (15)$$

and the corresponding stationary FPK equation (3) can then be written as:

$$\pi A^2 \frac{\partial^2 f}{\partial z_2^2} - \frac{\partial}{\partial z_1}\left(z_1 f(\underline{z})\right) + \frac{\partial}{\partial z_2}\left(\left(2\xi\omega_n z_2 + \alpha_1 z_2 z_1^2 + \alpha_2 z_2 |z_2| + \omega_n^2 z_1 + k_3 z_1^3\right) f(\underline{z})\right) = 0 \quad \ldots (16)$$

subject to far-field and normalisation boundary conditions as described in section 2. The parameter values used for the model are : $\xi = 0.0, \alpha_1 = 0.812, \alpha_2 = 0.015$, $\omega_n = 144.34, k_3 = 3021$, $A = 200$. Application of statistical linearization gives $\xi_{eq} = 0.0138$ and simulation reveals a bandwidth parameter value $\varepsilon = 0.97$. Note although explicit parameter values are given here, only damping to intensity ratios appear in the FPK solution, which confirms that bandwidth effects cannot be accounted for, hence the need for an independent check on the accuracy of extreme-value predictions.

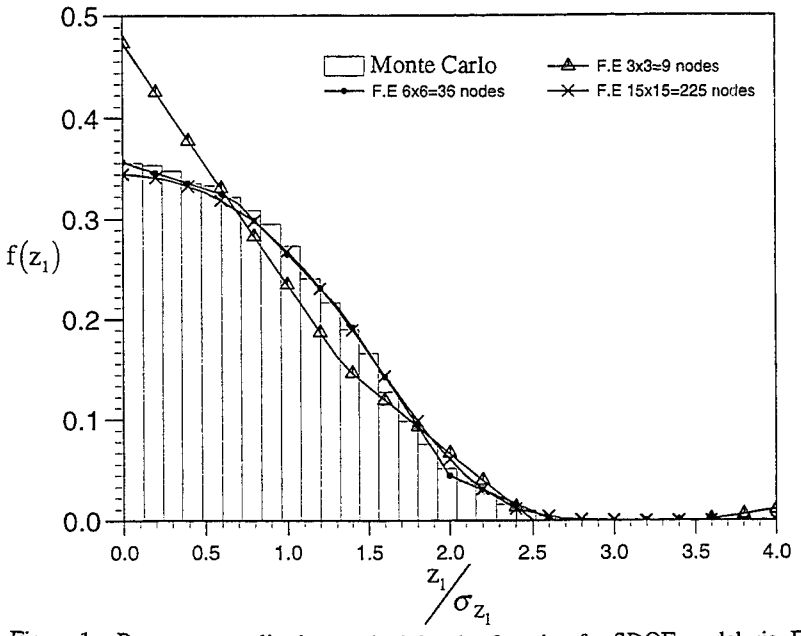

Figure 1. : Response amplitude marginal density function for SDOF model via FEM-FPK solutions and simulation.

To check FEM-FPK predictions, conventional time-domain simulations are used here. These involve three stages : 1) construction of

excitation sample paths ; 2) numerical integration, using a standard 4th order Runge-Kutta scheme; and 3) post-processing, involving transient removal to create a number of output sample paths for estimation of marginal response densities, and for creation of sections of length T, for use in estimation of extreme exceedance probabilities. A truncated Whitaker filter [19] is used to allow convergence of numerical integration using white-noise excitation samples assembled at discrete time intervals of duration Δt, giving a Nyquist bandwidth $f_n = 1/2\Delta t$. In the use of the Whitaker filter Δt is fixed, allowing interpolation to smaller time steps $\Delta\tau$, producing rapid reduction of the truncation error.

Figure 1. shows the response marginal pdf obtained via FEM-FPK and simulation. Using symmetry over 1/4 region, the number of nodes in the FEM is increased as shown, from 9 nodes to a total of 225. This number does not create computational or storage problems using a systematic FEM node numbering scheme, and convergence has clearly occurred by 225 nodes

Figure 2. shows extreme exceedance probabilities using FEM-FPK predictions via the threshold crossing rate equation (5) in equations (6) and (7), compared with very long Monte Carlo simulations. Two durations have been examined: T=1 second, as shown in figure 2a. ; and T=100 seconds in figure 2b. In both figures, convergence of FEM-FPK predictions are compared with converging simulation results for reducing $\Delta\tau$ in the Whitaker filter. Note that the simulations seem to have converged for $\Delta\tau = 0.001$ seconds , and the FEM-FPK predictions seem to similarly converge but only when a total of 961 nodes is used. Results for 225 nodes, which are perfectly adequate for marginal density predictions as shown in figure 1, are clearly not accurate for extreme-value statistics. The final level of agreement between simulation and FEM-FPK predictions would suggest that the Poisson assumption does indeed hold below probabilities of 10^{-1}, justifying use of equation(6).

The statistical variability in extreme exceedance estimates $\hat{p}$ is predicted using the ratio $\sigma_{\hat{p}} / \hat{p} = 1/\sqrt{Np}$, where $\sigma_{\hat{p}}$ is the standard deviation in $\hat{p}$ and N is the sample size. For low probabilities, a large value N=1000 extreme-values was needed for each duration, giving confident estimates of p above 10^{-2}. The CPU time needed here for the simulations varied between 30 and 300 times the FEM-FPK requirement.

Figure 3 shows FEM-FPK predictions, based on a calibrated SDOF model (14), via the parameter estimation method [20], compared with direct measurements of large amplitude beam vibrations [17]. This experimental clamped-clamped beam rig was 1m in length, and 25mm by 3mm section, with density $\rho = 7850 \text{kg/m}^3$ and Young's Modulus $E = 190 \text{GN/m}^2$. Band-limited white noise excitation was applied using a shaker positioned near one

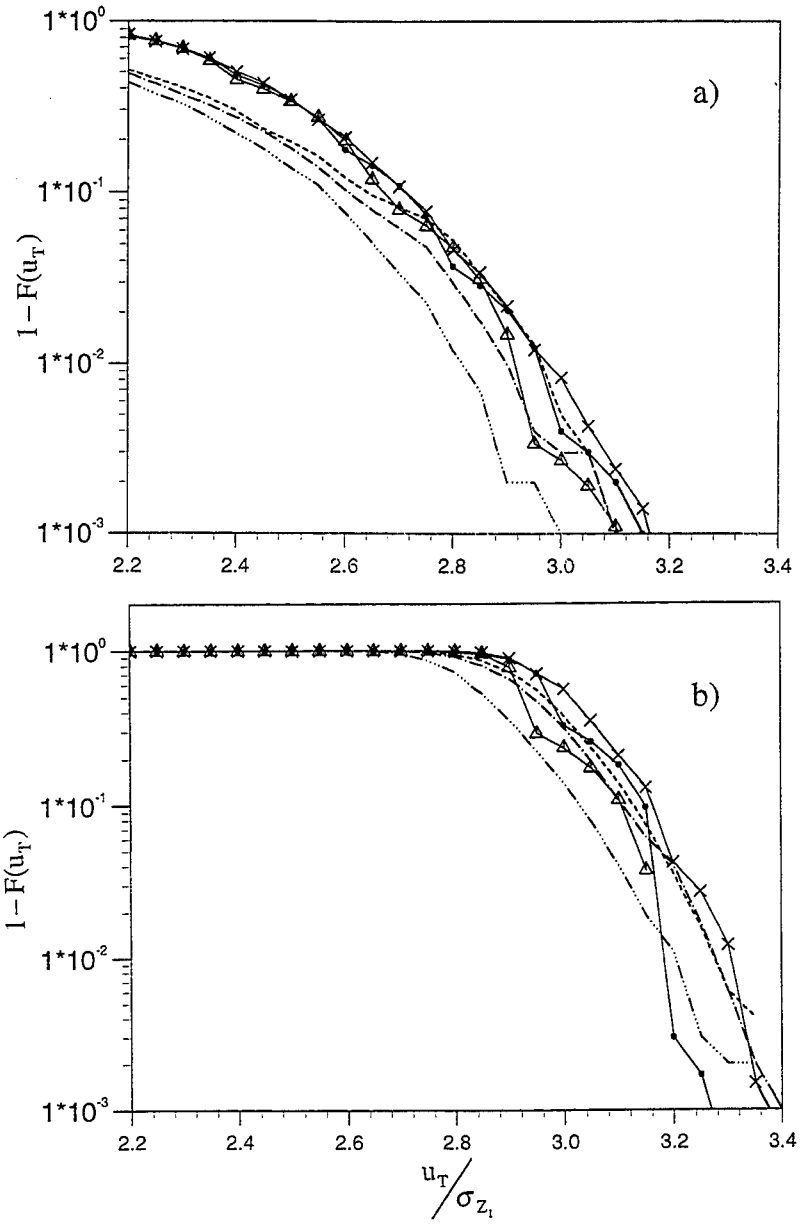

Figure 2. : Extreme Exceedance probabilities for SDOF model. FEM-FPK predictions compared with Monte Carlo simulations: a) T=1 second; b) T=100 seconds.

end of the beam, the central amplitude being measured with an accelerometer. Full details of the rig, instrumentation, and data processing procedure can be

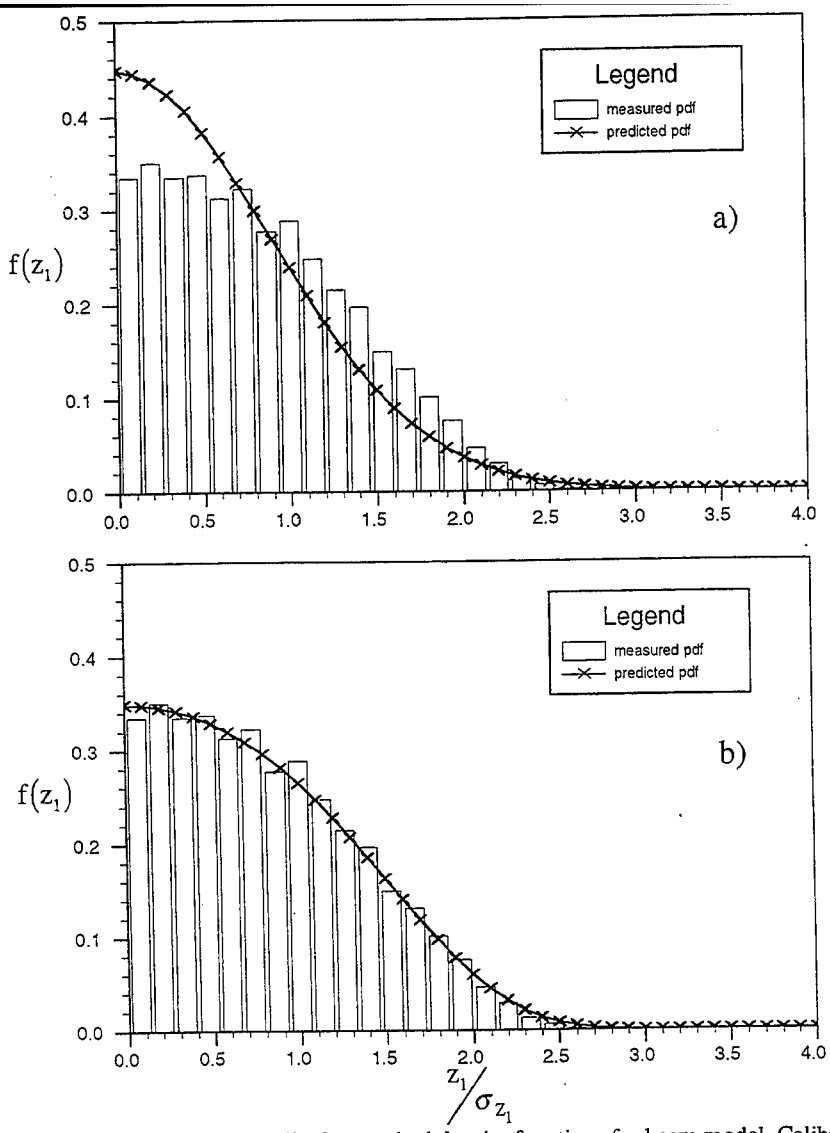

Figure 3. : Response amplitude marginal density functions for beam model. Calibrated SDOF model showing FEM-FPK predictions and experimental measurements: a) linear model; b) non-linear model.

found in [17]. For this beam, linear theory gives the first three small amplitude natural frequencies as 15Hz, 42Hz, and 82Hz respectively, whereas measured large amplitude responses are concentrated around 25Hz in a single-degree-of-freedom type motion without any observed responses above this bandwidth. Figure 3a shows a calibrated linear model, in contrast to figure 3b, which compares a calibrated version of equation (14). The magnitudes of the raw parameter estimates obtained using the moment method [20] are given as : $\xi/A^2 = 5.09\times10^{-8}$, $\alpha_1/A^2 = 18.26\times10^{-6}$, $\alpha_2/A^2 = 0.47\times10^{-6}$, $\omega_n = 132.56$,

and $k_3 = 2322$. Note, the intensity level A need not be known for FEM-FPK predictions at the same excitation level as the measured data. This is advantageous since excitation may in general be difficult to measure.

5. Application to a pair of non-linear oscillators

A 4D FEM-FPK version can be applied for example to an isolating suspension system [21], which in general represents a pair of coupled non-linear equations:

$$\left.\begin{aligned} \ddot{x} + \alpha\dot{x} + K_1 x + K_3 x^3 + \gamma x\theta^2 &= A_1 w_1(t) \\ \ddot{\theta} + \beta\dot{\theta} + G_1\theta + G_3\theta^3 + \gamma\theta x^2 &= A_2 w_2(t) \end{aligned}\right\} \quad (17)$$

By setting $z_1 = x$, $z_2 = \theta$ and $z_3 = \dot{x}$, $z_4 = \dot{\theta}$ the state space model becomes:

$$\begin{pmatrix} \dot{z}_1 \\ \dot{z}_2 \\ \dot{z}_3 \\ \dot{z}_4 \end{pmatrix} = \begin{pmatrix} z_3 \\ -\alpha z_3 - K_1 z_1 - K_3 z_1^3 - \gamma z_1 z_2^2 \\ z_4 \\ -\beta z_4 - G_1 z_2 - G_3 z_2^3 - \gamma z_2 z_1^2 \end{pmatrix} + \begin{pmatrix} 0 & 0 & 0 & 0 \\ 0 & A_1 & 0 & A_{12} \\ 0 & 0 & 0 & 0 \\ 0 & A_{21} & 0 & A_2 \end{pmatrix} \begin{pmatrix} 0 \\ w_1(t) \\ 0 \\ w_2(t) \end{pmatrix} \quad (18)$$

where A_1 and A_2 are white noise intensities; A_{12} and A_{21} are cross-correlations, all scaled by a factor 2π. The FPK equation can be written as follows:

$$2\pi A_1^2 \frac{\partial^2 p}{\partial z_3^2} + 2\pi A_{12} \frac{\partial^2 p}{\partial z_3 \partial z_4} + \pi A_2^2 \frac{\partial^2 p}{\partial z_4} - \frac{\partial}{\partial z_1}(z_3 p) - \frac{\partial}{\partial z_2}(z_4 p)$$
$$+ \frac{\partial}{\partial z_3}\left[\left(\alpha z_3 + K_1 z_1 + K_3 z_1^3 + \gamma z_1 z_2^2\right)p\right] + \frac{\partial}{\partial z_4}\left[\left(\beta z_4 + G_1 z_2 + G_3 z_2 + \gamma z_1 z_2^2\right)p\right] = 0 \quad \ldots (19)$$

Equation (19) can be solved exactly in specific cases, such as when: $A_{12} = A_{21} = 0, \frac{A_1}{\alpha} = \frac{A_2}{\beta} = 2Y$ (a nonzero constant), the solution is then:

$$p(z_1, z_2, z_3, z_4) = C\exp\left[-\frac{1}{2Y}\left\{\frac{1}{2}K_1 z_1^2 + \frac{1}{4}K_3 z_1^4 + \frac{1}{2}G_1 z_2^2 + \frac{1}{4}G_3 z_2^4 + \frac{1}{2}\gamma z_1^2 z_2^2\right\} - \frac{\alpha}{2A_1}z_3^2 - \frac{\beta}{2A_2}z_4^2\right] \quad \ldots (20)$$

To establish the finite region for application of the 4D FEM-FPK, the equivalent linear forms of equations (17) are:

$$\left.\begin{aligned} \ddot{x} + \alpha\dot{x} + (K_1 + 3K_3\sigma_x^2 + \gamma\sigma_\theta^2)x &= A_1 w_1(t) \\ \ddot{\theta} + \beta\dot{\theta} + (G_1 + 3G_3\sigma_\theta^2 + \gamma\sigma_x^2)\theta &= A_2 w_2(t) \end{aligned}\right\} \quad (21)$$

Solving (21) for the amplitude and velocity mean-square values leads to:

$$\sigma_x^2 = \frac{\pi A_1}{\alpha(K_1 + 3K_3\sigma_x^2 + \gamma\sigma_\theta^2)} \quad \text{and} \quad \sigma_{\dot{x}}^2 = \frac{\pi A_1^2}{\alpha} \qquad (22)\ \&\ (23)$$

$$\sigma_\theta^2 = \frac{A_2}{\beta(G_1 + 3G_3\sigma_\theta^2 + \gamma\sigma_x^2)} \quad \text{and} \quad \sigma_{\dot{\theta}}^2 = \frac{\pi A_2^2}{\alpha} \qquad (24)\ \&\ (25)$$

To demonstrate this 4D FEM-FPK, the parameter values were set to: $K_1 = G_1 = 1.0$ and $K_3 = G_3 = 0.5$, with $\gamma = 0.0$ and $A_1 = A_2 = 1/\sqrt{\pi}$. Note, although introducing no change to the FEM-FPK solution method, setting $\gamma = 0.0$ effectively uncouples equations (17) - which can in fact then be solved with a 2D FPK [10]. But from the FEM viewpoint the problem can still be

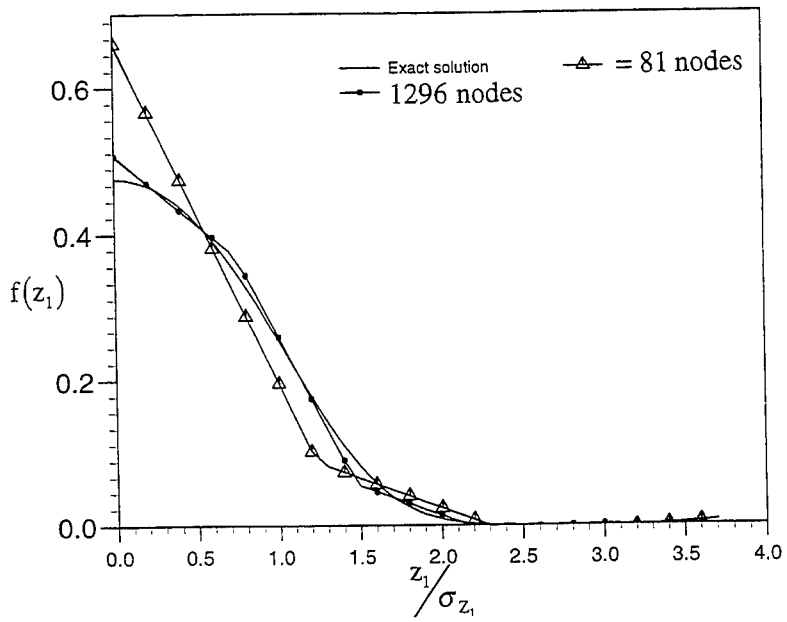

Figure 4. : Response amplitude marginal density function for pair of nonlinear oscillators. 4D FEM-FPK predictions compared with exact solution.

seen as if it were 4D, the advantage being that exact marginal densities can be trivially obtained from the exact jpdf. Use of statistical linearisation [1], gives (after 11 iterations) converged values of $\sigma_x = \sigma_\theta = 0.538$ which are used, along with symmetry, to define the finite FE region: $0 \le z_1 \le 3.7, 0 \le z_2 \le 5.0, 0 \le z_3 \le 3.7, 0 \le z_4 \le 5.0$. This region is made-up of 4D equivalents of cuboid elements, each with 16 nodes. Figure 4 shows response amplitude marginal density predictions obtained with this 4D FEM-

FPK compared with the exact solution. Only two cases are considered, namely $3^4 = 81$ and $6^4 = 1296$ nodes respectively. This second case involves solution of a linear system of equations in 1296 unknowns. But since a systematic node numbering system is used, the bandwidth of the coefficient matrix is very much larger than the minimum value of 81. Although the comparison for the second case, shows good agreement, very many more nodes would clearly be needed to obtain accurate extreme-value statistics. This would not be possible with the present approach owing to computer storage limitations.

6. Conclusions

Accurate stationary response amplitude pdfs are shown to be efficiently obtained using a 2D FEM-FPK approach applied to a realistic non-linear model for SDOF clamped-clamped beam vibration. This model has been corroborated experimentally at the marginal density level. Application of the FEM to extreme-value prediction, via threshold crossing statistics, shows good agreement compared with simulation, for a beam type model. Moreover, application of a 4D FEM-FPK associated with a pair of non-linear oscillators, shows reasonable agreement with the exact solution at the marginal level. But for $n > 2$, use of a systematic FEM node numbering scheme is not suitable for extreme-value prediction owing to the large bandwidth of the FEM coefficient matrices. To circumvent this problem for application to higher dimensions a sophisticated global node numbering scheme is needed to enable space saving linear equation solution techniques to be of benefit.

References

1. Roberts, J.B. and Spanos, P.D., *Random Vibration and Statistical Linearization*, Wiley, Chichester, 1990.
2. Lin, Y.K. and Cai, G.Q., *Probabilistic Structural Dynamics*, Mc-Graw-Hill. 1995.
3. Leadbetter, M.R., Lindgren, G. and Rootzén, H., *Extremes and related properties of random sequences and processes.* New York : Springer - Verlag 1983.
4. Winterstein, S.R. and Ness, O.B., Hermite moment analysis of non-linear random vibration, in *Computational Mechanics of Probabilistic and Reliability Analysis*, Lausanne; Elme Press, 1989,Chapter 21,pp. 452-478.
5. Naess, A., Approximate first-passage and extremes of narrow-band Gaussian and Non-Gaussian random vibration. *Journal of Sound and Vibration*, 1990, 138, pp. 365-380.
6. Naess, A. Galeazzi, F. and Dogliani, M., Extreme Response predictions of non-linear compliant offshore structures by stochastic linearization . *Applied Ocean Research,* 1992,14, pp. 71-81.

7. Winterstein, S. R. and Torhaug, R., Extreme response of Jack-up structures from limited Time-Domain Simulation. *Proceedings of the 12th International Conference of the OMAE-ASME,* 1993, Vol 2, 251-258.
8. Dunne, J.F., An optimal control approach to extreme local maxima for stochastic Duffing-type oscillators. *Journal of Sound and Vibration,* 1996, 193(3), pp. 597-629.
9. Naess, A., On a rational approach to extreme value analysis: Technical note. *Applied Ocean Research*, 1984 ,6(3), pp. 173-174.
10. Soong, T.T., *Random Differential Equations in Science and Engineering*, Academic Press - New York, 1973.
11. Bhandari, R.G. and Sherrer, R.E., , Random vibration in discrete non -linear dynamic systems. *Journal of Mechanical Engineering Science,* 1968, 10, pp. 168-174.
12. Langley, R.S., A finite element method for the statistics of non-linear random vibration. *Journal of Sound and Vibration,* 1985, 101(1), pp. 41 -54.
13. Soize, C., Steady state solution of Fokker-Planck equation for higher dimensions. *Probabilistic Engineering Mechanics,* 1989, 3, pp. 196-206.
14. Bergman, L.A., Numerical solution of the first passage problem in stochastic structural dynamics, in *Computational Mechanics of Probabilistic and Reliability Analysis*; Lausanne; Elme Press 1989, pp. 479-508.
15. Kunert, A., Efficient numerical solution of multidimensional Fokker-Planck equations associated with chaotic and non-linear random vibrations. *Vibration Analysis - Analytical and Computational, ASME DE-37,* 1991, pp. 57-60.
16. Spencer, Jr. B.F. and Bergman, L.A., On the numerical solution of the Fokker Planck equation for nonlinear stochastic system. *Non-linear Dynamics*, 1993, Vol 4 , pp. 357-372.
17. Ghanbari, M., *Extreme response prediction for random vibration of a clamped-clamped beam,* 1996, D.Phil. Dissertation - University of Sussex.
18. Press W.H., Flannery, B. P., Teukolsky, S. A. and Vetterling, W.T., *Numerical Recipes - the art of scientific computing*, Cambridge University Press, 1989.
19. Oppenheim, B.W. and Wilson, P. A., Continuous digital simulation of the second order slowly varying drift force. *Journal of Ship Research,* 1980, 24(3), pp. 181-189.
20. Roberts, J.B., Dunne, J.F. and Debonos, A., Parameter estimation for Randomly excited non-linear systems, in IUTAM symposium on *Advances in Non-linear Stochastic Mechanics*, Kluwer, 1996, pp. 361-372.
21. Ariaratnam, S.T., Random vibrations of non-linear suspensions. Journal of Mechanical Engineering Science, 1960, 2, pp. 195-201.

RANDOM VIBRATION II

SIMULATION OF NONLINEAR RANDOM VIBRATIONS USING ARTIFICIAL NEURAL NETWORKS

Thomas L. Paez*
Susan Tucker
Chris O'Gorman

Sandia National Laboratories
Albuquerque, New Mexico, USA

Abstract

The simulation of mechanical system random vibrations is important in structural dynamics, but it is particularly difficult when the system under consideration is nonlinear. Artificial neural networks provide a useful tool for the modeling of nonlinear systems, however, such modeling may be inefficient or insufficiently accurate when the system under consideration is complex. This paper shows that there are several transformations that can be used to uncouple and simplify the components of motion of a complex nonlinear system, thereby making its modeling and random vibration simulation, via component modeling with artificial neural networks, a much simpler problem. A numerical example is presented.

Introduction

Structural system random vibration simulations are required in a wide variety of applications. Development of techniques that can generate such simulations accurately and efficiently is important, particularly in frameworks where numerous simulations are required, frameworks like Monte Carlo analysis. In practically all situations where the excitation is Gaussian and the system under consideration is nonlinear, the responses will be nonlinear and non-Gaussian, and it is important that simulations preserve the characteristics of the response as accurately as possible.

Artificial neural networks (ANNs) have been applied to the autoregressive modeling of nonlinear system random vibrations. Investigations have shown that nonlinear structures can be modeled with ANNs, at least in the case of simple systems. (See, for example, Yamamoto, [15].) In principle, complicated systems can also be modeled using ANNs. This can be done directly (i.e., without any substantial transformation of the input or output data) using many types of ANNs. As the complexity of the system increases, an ANN that can naturally and efficiently accommodate a large number of inputs must be used for system simulation. When a mechanical system is modeled using an autoregressive ANN to directly simulate motions at a large

* This work was supported by the United States Department of Energy under contract No. DE-AC04-94AL85000. Sandia is a multiprogram laboratory operated by Sandia Corporation, a Lockheed Martin Company, for the United States Department of Energy.

number of degrees of freedom, a very large number of exemplars of motion will be required to train the ANN to accurately represent the system. The reason is that it takes a large number of exemplars to adequately populate a high dimensional input space.

This paper shows how the ANN modeling of nonlinear structures can be made more efficient and accurate when using data measured during experimental, stationary random vibration. There are a number of operations that can be performed on the data to accomplish these goals. Among these are: (1) principal component analysis, (2) localized modal filtering, (3) elimination of statistically dependent components of motion, and (4) transformation of the components of motion to statistically independent, standard normal random signals. These operations are briefly described in the following sections, along with the modeling of the components with two types of ANN - the feed forward back propagation network (BPN) and the connectionist normalized linear spline (CNLS) network. An example is included to assess the random vibration simulation capabilities of the ANNs. The accuracy of the simulations is evaluated in terms of spectral and probabilistic measures.

Data Reduction

It is important to reduce the dimensions of motion of a complex system for the reason listed in the introduction, i.e., the amount of data required to train a very complex system directly is great. Further, because the CNLS net is a local approximation network, it is important to minimize the number of network inputs. The reason is that network size grows rapidly with the number of inputs. To limit the complexity of the input/output mappings required to model a complex system, the system motions can be decomposed into simple components. In general, the ANN modeling of physical systems can often be made more efficient and accurate by preprocessing the training data using any of a number of simplifying transformations. Among these are: (1) principal component analysis, (2) localized modal filtering, (3) elimination of statistically dependent components of motion, and (4) transformation of the components of motion to statistically independent, standard normal random signals. The hopes in using these transformations are that the ANN required to model a component of behavior will be simpler than a model for the entire system, and that a simpler model will be easier to train. Exactly how these transformations fit into the response simulation framework will be discussed more later; the overall framework is described in Figure 4. These operations are briefly described in the following subsections.

Principal Component Analysis - SVD

Principal component analysis of complex structural system motions is aimed at decomposing the motions into their essential constituent parts. A special example of this is the modal decomposition of linear systems, and analogous decompositions can be defined for nonlinear systems using, for example, singular value decomposition (SVD), or a principal component analysis ANN.

SVD is described in detail, for example, in Golub and Van Loan [4]. It can be used to decompose linear or nonlinear structural motions in the following way. Let X be an $n \times N$ matrix representing the motion of a structural system at N transducer locations and at n consecutive times. The form of the SVD is

$$X = UWV^T \cong uwv^T \tag{1}$$

V is an $N \times N$ matrix; its columns describe the characteristic shapes present in the rows of X. W is an $N \times N$ diagonal matrix whose nonnegative elements characterize the amplitudes of the corresponding shapes in V. The elements in W are normally arranged in descending order. Its largest elements correspond to the most important components in the representation. U is an $n \times N$ matrix; its columns are filtered versions of the motions represented by the columns in X. The reason that U is said to be a filtered form of the motions in X is that the columns of both V and U are orthonormal with respect to themselves. Therefore,

$$U = XVW^{-1} \tag{2}$$

and VW^{-1} serves as a filtering coefficient. Because some of the elements of W may be zero or nearly zero, indicating components that do not contribute substantially to the characterization of X, the elements of W^{-1} are taken as the inverses of the diagonal elements in W that are greater than a cutoff level; zero or near zero elements in W are replaced with zeros in W^{-1}. The approximate equality on the right side of Eq. (1) indicates that some components of the representation can be zeroed, and still maintain a good approximation to X. In the experimental framework, the components of W whose ratio to the maximum value is lower than the experiment noise-to-signal ratio are set to zero. The matrices u, w, and v are the matrices U, W, and V with components removed.

The columns of the matrix u are the principal components of the representation. It is the evolution of the system represented in the columns of u which we seek to simulate. Once models are established to simulate system response through simulation of the columns of u, the models can be used along with system initial conditions to predict structural response. The predicted response can be used, along with Eq. (1), to synthesize response predictions in the original measurement space.

Principal Component Analysis - ANN

ANNs can be used in a number of application frameworks, and one of the focuses of this paper is to show how components of a complex system motion can be modeled with ANNs. However, a particular ANN can also be used as a means for decomposing complex system motions into simpler components. This ANN is the principal component ANN (PCANN). (Baldi and Hornik, [2]) The PCANN is simply a multi-layer network of perceptrons like the standard BPN (Freeman and Skapura, [3]), but it has a particular geometry,

shown in Figure 1. Let (x_j) be a row vector of N elements, the jth row of data in the matrix X defined above. Then the collection of all the rows of X provide n exemplars - both input and output - for training the PCANN in Figure 1. Some important features of the ANN in Figure 1 are that (1) it is a BPN with one hidden layer, and (2) the number of neurons, R, in the hidden layer is smaller than N, the number of columns in the measurement matrix. The idea behind the PCANN is that it compresses the information in the input layer into the information present in the hidden layer, then uses this information to reconstruct, as accurately as possible, the original signal on the output layer. To obtain optimal effect from the PCANN, sigmoidal activation functions would normally be used in the hidden and output layer neurons. However, when linear activation functions are used in the hidden and output layer neurons, the ANN weights are related to the components of the SVD, Eq. (1).

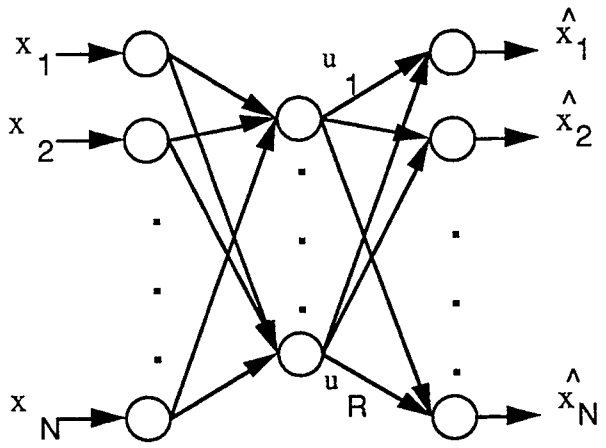

Figure 1. Geometry of the principal component artificial neural network.

Let the jth row of $\boldsymbol{u}$ be the hidden layer outputs, (u_j) in Figure 1. The columns of $\boldsymbol{u}$ are the principal components of the PCANN representation. It is the evolution of the system represented in the columns of $\boldsymbol{u}$ which we seek to simulate. Once models are established to simulate system response through simulation of the columns of $\boldsymbol{u}$, the models can be used along with system initial conditions to predict structural response. The predicted response can be used, along with the portion of the PCANN to the right of the hidden layer, to synthesize response predictions in the original measurement space.

Normally, only one of the principal component analyses described in this and the previous sections would be applied to the data.

Modal Filtering

Modal decomposition of complex system motions is often used for the simplification of mechanical system response when the model for the system is assumed linear or approximately linear. In fact though, data-based modal

decomposition can be used on any collection of data; its purpose is to break the data into simple narrowband components, thereby simplifying system characterization, and perhaps simulation. When such a decomposition is used on nonlinear system or general system data, it is often referred to as modal filtering.

Modal filtering of measured data can be performed in one of two frameworks. First, a single modal analysis can be used to filter measured data into its component parts. The problem with this is that when a system is nonlinear, its characteristics can change with response magnitude, and the number of principal components (modes) also changes. It is difficult for a single model to accurately capture such changes. The second alternative is to specify multiple modal filters, and use each one in a particular range of response amplitudes. A very simple realization of this type of analysis would involve the use of two modal models. One would be applied to data below a particular threshold, and the other would be applied to data above the threshold. A more complicated application creates a linear modal model at each step in a system analysis. Such a model is described in Hunter [7].

The form of a modal filter is similar to the SVD, but the means for obtaining the filter factors is much different. Meirovitch [9] describes the theoretical operations included in the definition and use of a modal filter. Allemang and Brown [1] outline practical means for performing data-based modal analysis. The form of the modal filter can be expressed as

$$X = US\phi^T \cong us\phi^T \tag{3}$$

where X is the same mechanical system motion representation as above. The columns of ϕ represent the characteristic shapes of the system, and the diagonal matrix S contains normalizing factors. When X comes from a linear system the columns of U are the linear modal components of the system motion. As with the SVD, the approximate equality on the right indicates that some components of the representation can be eliminated, and still maintain a good approximation to X. It is the evolution of the columns in u (a reduced form of U) which we seek to simulate. Once models are established to simulate system response through simulation of the columns of u, the models can be used along with system initial conditions to predict structural response. The predicted response can be used, along with Eq. (3), to synthesize response predictions in the original measurement space.

When multiple decompositions are used to filter the motions of a complex system, then multiple expressions like Eq. (3) are used to obtain modal components.

Elimination of Statistically Dependent Components

Although some of the principal component analyses of the previous sections may produce orthogonal components, some of the components may be completely or highly statistically dependent upon others. For example, a structure may have two modes with nearly the same modal frequency. One

modal motion may be nearly a sine wave, and the other may be nearly a cosine. The motions are practically orthogonal, but they are still statistically dependent. Statistical independence of sources implies orthogonality, but orthogonality does not necessarily imply statistical independence. For the sake of efficiency, we seek to eliminate statistically dependent components from the set to be modeled, then reintroduce these components during physical system simulation. In this way, ANN modeling of structural behavior is simplified.

When a dependency exists, it can be characterized using the conditional expected value of the variables in one column of $\boldsymbol{u}$ given values in another column of $\boldsymbol{u}$. This requires approximation of a joint probability density function (pdf) of the data, and this can be obtained using the kernel density estimator. (See Silverman, [13].) The pdf approximation is known as the kernel density estimator (kde). Let $\left(\boldsymbol{u}_j\right)$, $j = 1,...,n$, denote the row vectors of the matrix $\boldsymbol{u}$. The kde of the random source $\boldsymbol{u}$ is given by

$$\hat{f}_u(\alpha) = \frac{1}{nh^N} \sum_{j=1}^{n} K\left(\frac{\alpha - \left(\boldsymbol{u}_j\right)^T}{h} \right) \qquad -\infty < \boldsymbol{u} < \infty \tag{4}$$

where $\boldsymbol{a}$ is an $N \times 1$ variate vector, $K(.)$ is a kernel function, and h is a window width parameter of the kernel function. The kernel function can be any standard probability density function, and often the pdf of a multivariate standard normal random vector is used. That is

$$K(\boldsymbol{x}) = \frac{1}{(2\pi)^{N/2}} \exp\left(-\frac{1}{2} \boldsymbol{x}^T \boldsymbol{x} \right) \tag{5}$$

where $\boldsymbol{x}$ is the $N \times 1$ variate vector. Using the kde in Eq. (4), the estimator for the conditional pdf of elements in one column of $\boldsymbol{u}$ given the values in another column of $\boldsymbol{u}$ can be obtained using the standard formulas. (See, for example, Papoulis [11].)

A statistical dependency between two columns of $\boldsymbol{u}$ can be detected by forming the bivariate pdf estimator of the random source of the two columns using the kde with data from the columns in question, then evaluating and plotting the conditional expected value of one variable, given a range of values of the other variable. At each point where the conditional expected value is evaluated, the conditional variance can also be evaluated. The conditional expected value and variance can be evaluated for situations in which the data in the two columns of $\boldsymbol{u}$ are lagged with respect to one another. If a lag is found where the conditional variance is uniformly small, i.e., small at all locations defined by the conditioning variable, then a statistical dependency has been detected, and the functional form of the dependency is defined by the conditional expected value. The dependent variable can be eliminated from modeling consideration. When modeling has been completed and it is necessary to restore the eliminated component, this can be accomplished using the conditional expected value developed here.

The effect of eliminating components of motion that are completely dependent on other components is to eliminate some columns in the matrix $\boldsymbol{u}$. Denote the reduced matrix $\boldsymbol{u}_r$; our objective is to model the evolution of the columns of $\boldsymbol{u}_r$ with an ANN.

Rosenblatt Transform

The previous step produces a description of the motion of a complex structure in terms of a set of components, none of which is completely statistically dependent on others. We can further transform the components, the columns of $\boldsymbol{u}_r$, into signals that are statistically independent with Gaussian distributions. The transformation that accomplishes this is the Rosenblatt transform. (See Rosenblatt, [12].) The Rosenblatt transform has the following form.

$$
\begin{aligned}
z_1 &= \Phi^{-1}\left(\hat{F}_{u_1}(\alpha_1)\right) \\
z_2 &= \Phi^{-1}\left(\hat{F}_{u_2|u_1}(\alpha_2 \mid \alpha_1)\right) \\
&\cdots \\
z_N &= \Phi^{-1}\left(\hat{F}_{u_N|u_1\ldots u_{N-1}}(\alpha_N \mid \alpha_1,\ldots,\alpha_{N-1})\right)
\end{aligned}
\tag{6}
$$

where the z_i, $i = 1,\ldots,N$, are uncorrelated, standard normal random variables, $\Phi(.)$ is the cumulative distribution function (cdf) of a standard normal random variable, $\Phi^{-1}(.)$ is its inverse, and the $\hat{F}(.)$ are the estimated marginal and conditional cdf's of the random variables that are the sources of the columns of $\boldsymbol{u}$. These approximate cdf's can be obtained by integrating Eq. (4), and this can be accomplished directly when the kernel used in Eq. (4) is Eq. (5).

The Rosenblatt transformation is uniquely invertible because the exact and approximate cdf's used in Eq. (6) are monotone increasing. The data in the matrix $\boldsymbol{u}$ can be transformed to the standard normal space by using it in Eq. (6) in place of the α's. The matrix z is composed of the elements z_i, $i = 1,\ldots,N$, and is the same size as the matrix $\boldsymbol{u}_r$ with the same number of nonzero columns.

It is the evolution of the values in these columns that is to be simulated with ANNs. Because the columns in z are statistically independent, we need only to create ANN models for signals in individual columns. Once models are established to simulate system response through simulation of the columns of z, the models can be used along with system initial conditions to predict structural response. The predicted response can be used, along with the inverse form of Eqs. (6), to synthesize response predictions in the original measurement space.

Modeling of Component Motion with ANNs

Our ultimate objective is to simulate complex system motion, and we aim to do this by simulating the components of system motion obtained using the decompositions and transformations described above. Many ANNs are suitable for this task. The two that we consider in this paper are the feed forward back propagation network (BPN) and the connectionist normalized linear spline (CNLS) network. The BPN is the most widely used ANN and it is described in detail in many texts and papers, for example Freeman and Skapura [3], and Haykin [5]. The BPN is very general in the sense that it can approximate mappings of relatively low or very high input dimension. It has been shown that, given sufficient training data, a BPN with at least one hidden layer and sufficient neurons can approximate a mapping to arbitrary accuracy (Hornik, Stinchcombe, and White, [6]).

The CNLS network is an extension of the radial basis function neural network (Moody and Darken, [10]). It is described in detail in Jones, et.al., [8]. It is designed to approximate a functional mapping by superimposing the effects of basis functions that approximate the mapping in local regions of the input space. Because it is a local approximation neural network, we cannot use the CNLS network to accurately approximate mappings involving a large number of inputs. The CNLS network has not been widely used for the simulation of oscillatory system behavior.

To simulate a column in z using either of the ANNs described above, we configure the net in an autoregressive framework. This configuration uses as inputs previous response values and the independent excitation, and yields on output, the current response. Figure 2 shows such an application schematically. The quantity z_{ji} denotes an element in the ith column of z at the jth time index. The quantity q_j denotes the excitation at the jth time index. L_j denotes a lag index. There are m system response input terms; there are M+2 excitation terms The configuration shown in Figure 2 implies our belief that there is a mapping

$$z_{j+1,i} = g_i\left(z_{ji}, z_{j-L_1,i}, \ldots, z_{j-L_m,i}, q_{j+1}, q_j, \ldots, q_{j-L_M}\right) \tag{7}$$

and that the ANNs can identify that mapping. The subscript i on the function $g(.)$ indicates that the functional mapping varies from one column of z to the next, and a different ANN models each mapping. It is normally anticipated that the time increment, Δt, separating system motion measurements that are the rows of the matrix X is small relative to the period of motion of the highest frequency component we intend to simulate.

We seek to train both types of ANN to model the behavior of the oscillations represented in the columns of z. One ANN of each type (BPN and CNLS net) is used to model each column of z. The inputs to the ANN are current and lagged (past) values of the transformed response and the one-step-into-the-future value, the current value, and lagged values of the excitation. The ANN output is the transformed response one step in the future. Both the

ANNs are trained using the scheme described in Figure 3. The ANN inputs are transformed using a feed forward operation. The ANN output is compared to the desired output, and the error is used to modify the ANN parameters. The BPN uses a back propagation and gradient descent scheme in each training step. The CNLS network uses least mean square (LMS) plus random sampling scheme to identify its parameters. The desired effect of training in both types of ANN is to modify the parameters of the network to diminish the error of representation of the input/output mapping.

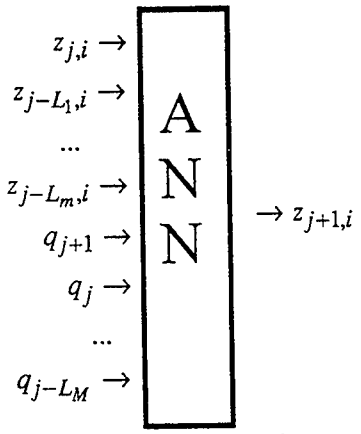

Figure 2. Schematic of ANN in autoregressive configuration.

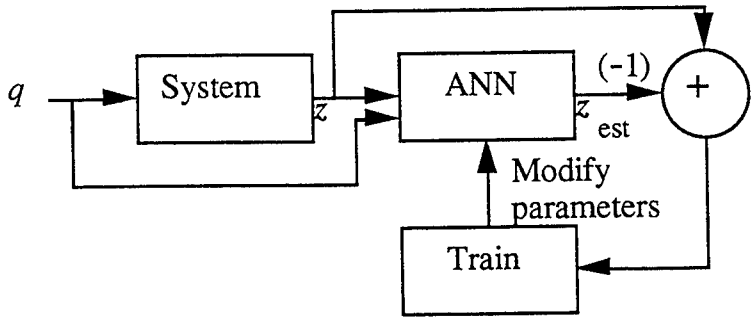

Figure 3. Schematic describing training sequence for ANNs.

Summary

Figure 4 summarizes the decomposition, simulation, and modeling of structural motion described in the previous sections. The principal component analysis in the second box in the top row refers to one of the following: SVD, PCANN, or modal filtering. The synthesis in the fourth box in the second row refers to the corresponding inverse operation - Eq. (1), the right half of Figure 1, or Eq. (3).

In the example that follows, one form of principal component analysis will be combined with ANN simulations to model a nonlinear structure's random vibrations.

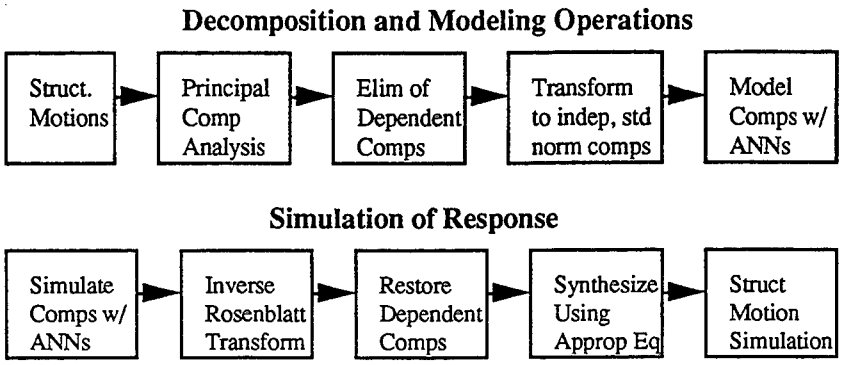

Figure 4. Summary of operations in system simulation.

Numerical Example

We simulate in this example the motion of a simple, nonlinear 10 degree-of-freedom system excited with a Gaussian white noise. Figure 5 shows a schematic of the system. The damping connecting the masses is linear viscous. The springs have a restoring force that is a tangent function. The system physical parameters are summarized in Table 1. Training data for the neural networks were generated by computing response over 8192 time steps (box number one on the top line in Figure 4); excitation and responses at ten locations were recorded. The time increment between response realizations is 0.04 second. Figure 6 shows the displacement response at the 10th mass. This is the location where the simulation-to-experiment comparisons are made in the present example, and where the simulation yielded the poorest match to the experimental results.

The responses were placed in a matrix X as referred to in the previous sections, and its SVD was computed (box number two on the top line of Figure 4). The singular values of the response indicate that accuracy of about 89% should be achieved by simulating the system response with its first four components. The four components were not strongly statistically dependent, so none was removed. The kde of the four components indicate that none is highly non-Gaussian, therefore, the Rosenblatt transform was not used. The first four components of the response were modeled with both BPN and CNLS nets (box number five on the top line in Figure 4).

The entire system was tested in autoregressive operation, as described in Figure 2, using data generated over 1000 steps of response computation. The initial conditions and excitation were used to start then execute a random vibration response simulation with ANNs in the space of $\boldsymbol{u}$ (box number one on the second line of Figure 4). The test was iterated, i.e., the estimated responses at step j were used as initial values for response predictions at time indices greater than j. The first and most significant column of $\boldsymbol{u}$ from the test

data and the first column from the ANN simulated data are compared in Figures 7a and 7b. This is the dominant component of the response. The match is good, particularly in view of the fact that the simulation is iterated. Note that although these and later response predictions remain fairly well in phase with the test responses, this is not usually the case. Typically, we hope that the simulated response amplitudes match the test responses well, and accept the fact that phase will usually be lost. Figures 8a and 8b compare the spectral densities of the signals shown in Figures 7a and 7b. (These were computed using the technique described, for example, in Wirsching, Paez, and Ortiz, [14].) A block size of 256 data points was used, along with a Hanning window, and an overlap factor of 0.55. The first harmonic of motion, at 0.25 Hz, is very well matched. A third harmonic of motion appears to be present in both the test and simulated signals; the BPN provides a better match of the third harmonic than the CNLS net. Figures 9a and 9b compare the kde's of the signals shown in Figures 7a and 7b. The responses are clearly non-Gaussian, as anticipated because of nonlinearity, and to some extent the simulated component responses match the character of the test response. This match needs to be improved to maximize the quality of the simulation. (Some of the mismatch is caused by the limited data - 1000 points - upon which the comparison is based.) However, as will be seen, the simulated synthesized responses have kde's that match test response kde's quite well.

Table 1. Parameters of the test system.

Index	Mass	Tangent Stiffness	Maximum Deformation	Viscous Damping
1	1.0	40	1.0	0.40
2	0.95	38	1.0	0.38
3	0.90	36	1.0	0.36
4	0.85	34	1.0	0.34
5	0.80	32	1.0	0.32
6	0.75	30	1.0	0.30
7	0.70	28	1.0	0.28
8	0.65	26	1.0	0.26
9	0.60	24	1.0	0.24
10	0.55	22	1.0	0.22
11		2	1.0	0.02

The simulated responses are now reconstructed by substituting into Eq. (1) using the simulated $\boldsymbol{u}$ (box number four on the second line of Figure 4), and the results are compared to the test response at mass 10 (box number five on the second line of Figure 4). The result from the BPN simulation is shown in Figure 10a; the result from the CNLS net simulation is shown in Figure 10b. Of course, the matches are quite good since the dominant component is well simulated by both ANNs. Figures 11a and 11b compare the spectral densities of the signals shown in Figures 10a and 10b. The spectral densities estimated from the simulated signals match those of the test signals well up to the frequency where components are no longer simulated; the CNLS net does a slightly better job of matching the test spectral density than the BPN. At mass 10 the rms response of the test signal is 0.45 in, and the rms values of the simulated responses are 0.47 in and 0.40 in for the BPN and CNLS net,

respectively. The corresponding kde's of test and simulated responses were computed and are shown in Figures 12a and 12b. The probabilistic character of the responses appears to be matched well by the ANN simulations.

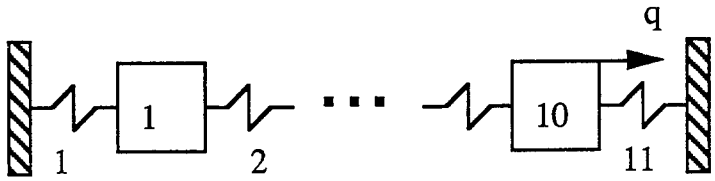

Figure 5. A nonlinear spring-mass system.

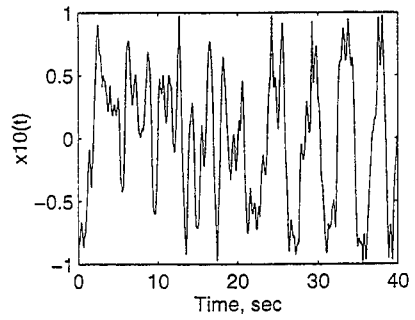

Figures 6. Response at mass 10 to Gaussian white noise input.

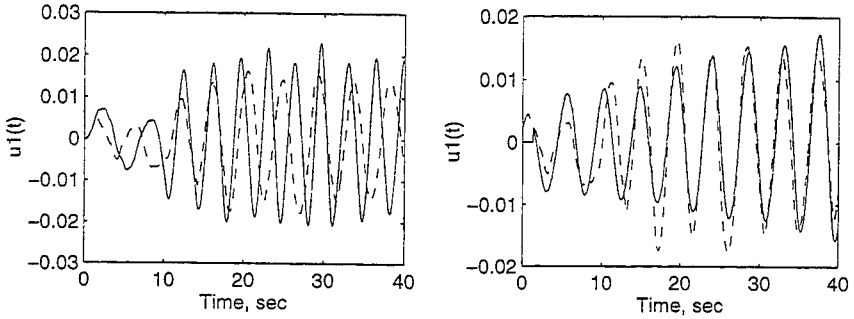

Figures 7a and 7b. Comparison of test and ANN simulated responses - Component 1. BPN simulation on left; CNLS simulation on right. ANN simulation - solid line; test data - dashed line.

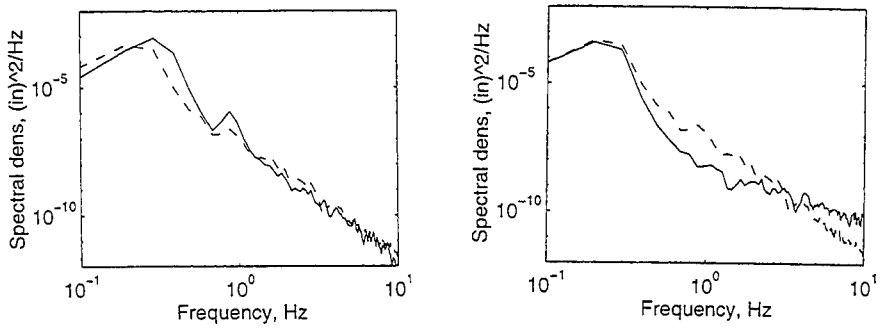

Figures 8a and 8b. Comparison of the spectral density estimates of test and ANN simulated responses - Component 1. BPN simulation on left; CNLS net simulation on right. ANN simulation - solid line; test data - dashed line.

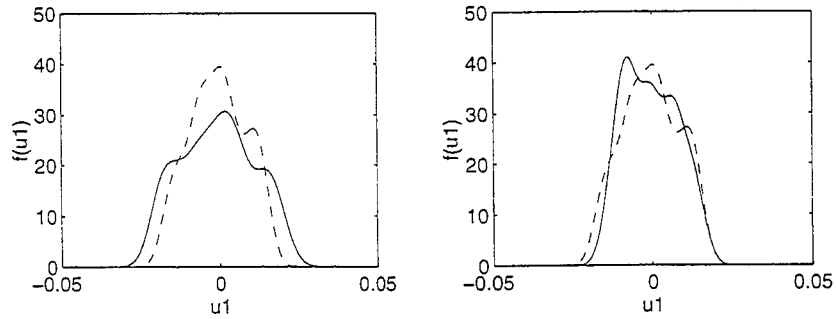

Figures 9a and 9b. Comparison of the kernel density estimators of test and ANN simulated responses - Component 1. BPN simulation on left; CNLS net simulation on right. ANN simulation - solid line; test data - dashed line.

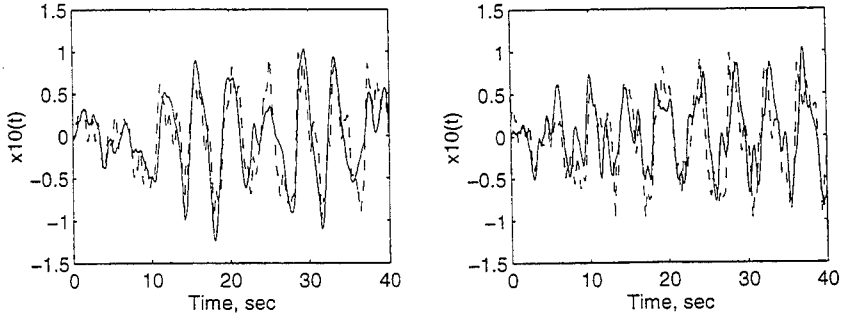

Figures 10a and 10b. Test (dashed) and simulated (solid) responses at a mass 10 in the simple system - BPN (left), CNLS net (right).

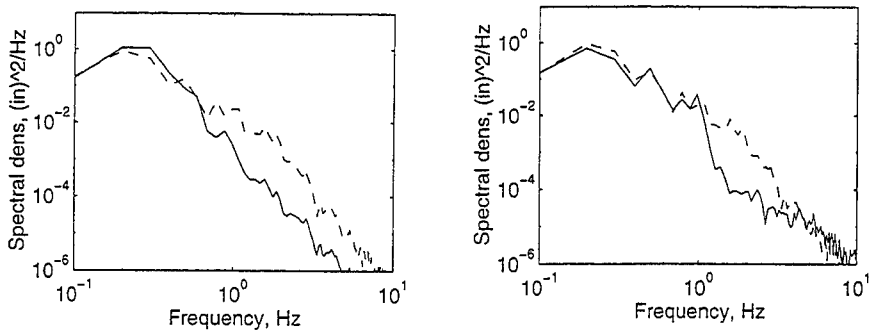

Figures 11a and 11b. Test (dashed) and simulated (solid) estimated response spectral densities at mass 10 in the simple system - BPN (left), CNLS net (right).

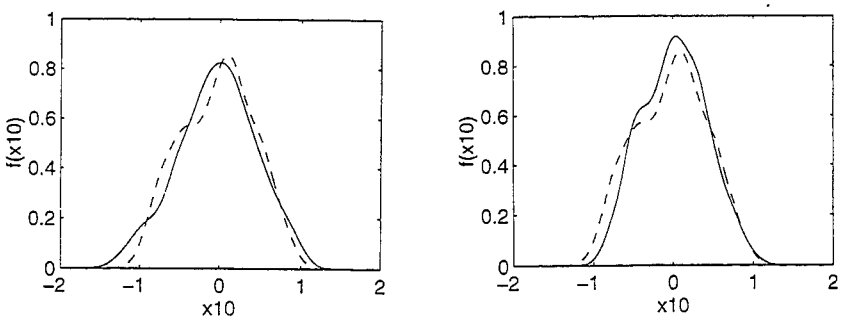

Figures 12a and 12b. Test (dashed) and simulated (solid) response kde's at mass 10 in the simple system - BPN (left), CNLS net (right).

Conclusions

A sequence of operations leading to the simulation of nonlinear structural random vibrations with ANNs is described in this paper. Such simulations are desirable because of their efficiency and relative accuracy. It is argued that if the motions can be decomposed and transformed into simple components, then the simulation will be simpler and more accurate. A numerical example confirms that relatively simple motions can, indeed, be modeled with ANNs - the BPN and CNLS net (a local approximation network) in particular. Given sufficient training data accurate simulations of simple components should always be possible, though obtaining satisfactory accuracy may require substantial effort. Accurate simulations should correctly reflect probabilistic, spectral, and all other characteristics of the simulated component responses. When component responses are correctly modeled then system level responses will be simulated accurately.

References

1. Allemang, R., Brown, D., (1988), "Experimental Modal Analysis," Chapter 21 in *Shock and Vibration Handbook*, Third Edition, Harris, C., editor, McGraw-Hill, New York.
2. Baldi, P., Hornik, K., (1989), "Neural Networks and Principal Component Analysis. Learning from Examples without Local Minima," *Neural Networks*, 2, 53-58.
3. Freeman, J., Skapura, D., (1991), *Neural Networks, Algorithms, Applications, and Programming Techniques*, Addison-Wesley, Reading, Massachusetts.
4. Golub, G. H., Van Loan, C. F., (1983), *Matrix Computations*, Johns Hopkins University Press, Baltimore, Maryland.
5. Haykin, S., (1994), *Neural Networks, A Comprehensive Foundation*, Prentice Hall, Upper Saddle River, New Jersey.
6. Hornik, K., Stinchcombe, M., White, H., (1989), "Multilayer Feedforward Networks are Universal Approximators," *Neural Networks*, V. 2, 359-366.
7. Hunter, N, (1992), "Application of Nonlinear Time Series Models to Driven Systems," *Nonlinear Modeling and Forecasting*, Casdagli, M., Eubank, S., eds., Santa Fe Institute, Addison-Wesley.
8. Jones, R. D., et. al., (1990), "Nonlinear Adaptive Networks: A Little Theory, A Few Applications," *Cognitive Modeling in System Control*, The Santa Fe Institute.
9. Meirovitch, L., (1971), *Analytical Methods in Vibrations*, The Macmillan Company, New York.
10. Moody, J., Darken, C., (1989), "Fast Learning Networks of Locally-Tuned Processing Units," *Neural Computation*, V. 1, 281-294.
11. Papoulis, A., (1965), *Probability, Random Variables, and Stochastic Processes*, McGraw-Hill, New York.
12. Rosenblatt, M., (1952), "Remarks on a Multivariate transformation," *Annals of Mathematical Statistics*, **23**, 3, pp. 470-472.
13. Silverman, B. W.(1986), *Density Estimation for Statistics and Data Analysis*, Chapman and Hall.
14. Wirsching, P., Paez, T., Ortiz, K., (1995), *Random Vibrations - Theory and Practice*, Wiley, New York.
15. Yamamoto, K., (1992), "Modeling of Hysteretic Behavior with Neural Network and its Application to Non-Linear Dynamic Response Analysis," *Applic. Artif. Intell. in Engr., Proc. 7th Conf.*, AING-92, Comp. Mech., UK, pp. 475-486.

Dynamic Properties of Pseudoelastic Shape Memory Alloys

D.Z. Li[a] and Z.C. Feng[b]

[a]Department of Engineering Mechanics
Hunan University, China

[b]Department of Mechanical Engineering
Massachusetts Institute of Technology
Cambridge, Massachusetts 02139 USA

ABSTRACT

In this paper, we report a set of vibration transmission experiments that are conducted to investigate how the pseudoelasticity of shape memory alloys (SMAs) affects the transmissibility characteristics of a spring-mass system, where a shape memory alloy rod is used as a spring. The tests are conducted by subjecting the SMA bar under tension-compression and under bending. The test results indicate that compared with ordinary alloys, SMAs have a much higher damping. Most importantly, the damping property depends on the amplitude of the responses indicating that the spring-mass system is nonlinear. Furthermore, the high damping property persists to the high frequency limit (above 1 KHz) permitted by the equipment setup.

Keywords: Shape memory alloys, Nitinol, vibration damping, hysteresis

1. INTRODUCTION

Shape memory alloys (SMAs) such as Nickel-Titanium (NiTi) and Copper- Zinc-Aluminum (CuZnAl) exhibit nonlinear mechanical properties. Specifically, in a temperature environment which is higher than the phase transformation temperature of the material, when an applied stress exceeds a certain threshold, stress induced phase transformation generates large strains in the material so that the material can accommodate large strain with little change in the applied load. On the unloading cycle, a reverse phase transformation takes place, thus no permanent deformation remains. Moreover, the stress-strain relationship during this loading and unloading cycle shows hysteresis. This phenomenon is called pseudoelasticity. The lower elastic modulus and higher material damping of SMAs are desirable characteristics of passive vibration control systems. Previous investigations show that the damping of SMAs displays a peak and the elastic modulus demonstrates a trough in the vicinity of the phase transformation during the heating and cooling processes [1]-[3]. Some researchers have pointed out that the pseudoelasticity of SMAs can augment passive damping significantly in structural systems and SMAs have potential application in passive vibration control [4]-[5]. Recently, a research study has been undertaken to measure acceleration transmissibility of NiTi shape memory alloy springs [6].

Among all of these studies listed above, the investigators failed to realize that the measurements on the damping coefficient and Young's modulus depend on the specific test methods used. In [7], we have used continuum models of pseudoelastic SMA model to illustrate the nonlinear nature of the dynamic response of SMAs. In this paper, we present experimental evidence on the nonlinear behavior of the materials.

When used as actuators, SMAs typically have a very slow response to thermal actuations unless SMAs are made into very fine filaments. For this reason, SMAs have the perception of being limited to low frequency applications. But when used as a passive vibration damper, the high damping property is not limited to low frequency applications. Here, we demonstrate the high damping property of SMAs to a high frequency permitted by our equipment setup.

(Send correspondence to Z.C.F.)
Z.C.F.: Email: zfeng@mit.edu; Telephone: 617-253-6345; Fax: 617-258-5802

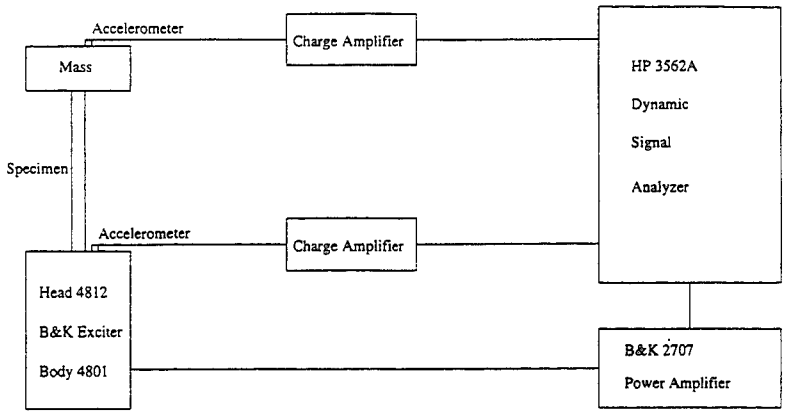

Figure 1. The experimental setup of the tension-compression test.

2. EXPERIMENTAL SETUP AND PROCEDURE

Our vibration tests include tension-compression test and bending test. The experimental setup for these two types of tests are similar. Fig. 1 is a schematic diagram of the tension-compression test setup. A test specimen is mounted vertically by a clamping fixture attached to a shaker. Its top end is fixed to a mass. In bending test, the specimen is fixed horizontally at one end and with a mass of 150g at the other end. The base harmonic motion is generated from HP3562A Dynamic Signal Analyzer, then amplified through B&K Power Amplifier 2707 and finally provided by B&K Exciter body 4801 with general purpose head 4812. Both base excitation and the response at the end of a specimen are picked up by two accelerometers Picomin 22 and PCB 309A respectively. The signals pass through two Kistler 5004 Charge Amplifiers to be feed into an HP 3562A Dynamic Signal Analyzer to obtain transmissibility curves. The transmissibility curves are easily acquired from the frequency response measurement by a sine sweep within the frequency range of interest. During each measurement, the base motion level is kept constant and recorded in voltage for convenience. All test specimens are circular rods, acting as springs in the testing mechanical spring-mass system. The SMA rods are binary NiTi alloys obtained from Shape Memory Applications Inc. of Santa Clara, California. Steel and aluminum rods are also used as our specimens for comparison. For each specimen, the transmissibility properties of the system are investigated under several base motion levels to observe the nonlinearity of the system dynamics. All tests are carried out at room temperature.

3. TENSION-COMPRESSION VIBRATION TRANSMISSIBILITY EXPERIMENT

The parameters of specimens are listed in Table 1. The acceleration transmissibility curves obtained are shown in Fig. 2-Fig. 5, where the mass in the spring-mass system is 250g. It is readily seen that the pseudoelasticity of SMAs does have significant effects on vibration transmissibility characteristics. The NiTi rods behave as nonlinear softening springs. When the base motion level increases, the resonant peak shifts to lower frequency and the peak becomes lower. This indicates that the equivalent elastic modulus of the NiTi rod becomes lower and its material damping becomes higher as the base motion level (measured by the input voltage to the shaker) increases. Higher base motion levels result in larger strains in the rods. For example, the strain amplitudes in the NiTI #2 rod are about 0.001%,

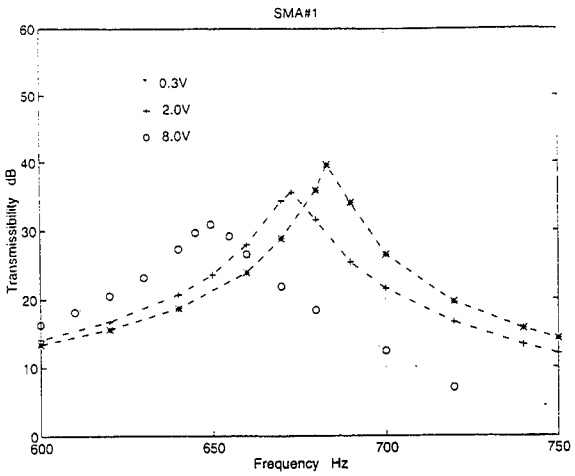

Figure 2. Tension-compression vibration transmissibility curves of NiTi Rod # 1 at different base motion levels.

0.008%, 0.015% and 0.03% corresponding to the base motion levels 0.3V, 2.0V, 4.0V and 8.0V respectively. This amplitude dependence of the elastic and damping properties of the material is significally different from those of conventional alloys. Fig. 4 and Fig. 5 are the transmissibility curves of a steel rod and an aluminum rod. Under two different base motion levels, the transmissibility remains the same. Since the system response at resonances is very big owing to the very low damping of the materials, our experimental setup prevents us to test higher input levels. Quantitative results related to the transmissibility curves are listed in Table 2.

The nonlinearity of the system dynamics is apparent in the amplitude dependence of the damping ratio and the resonance frequency. This is seldom appreciated in the past. Although the damping ratio and the material Young's modulus are often measured using vibration tests, only one excitation level is used in many tests. Thus this nonlinear phenomenon is often not noticed.

Table 1. Parameters of Test Specimens of Tension-Compression Vibration

Specimen	Length (mm)	Diameter (mm)	Mass (g)
NiTi # 1	240	5.86	42.3
NiTi # 2	250	4.96	31.6
Steel	617	4.80	86.9
Aluminum	716	6.36	61.2

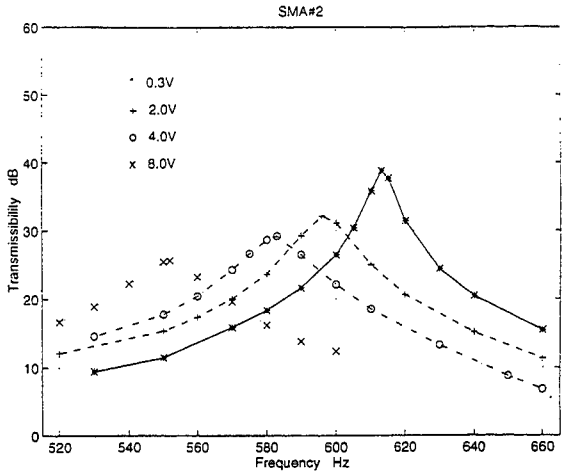

Figure 3. Tension-compression vibration transmissibility curves of NiTi Rod # 2 at different base motion levels.

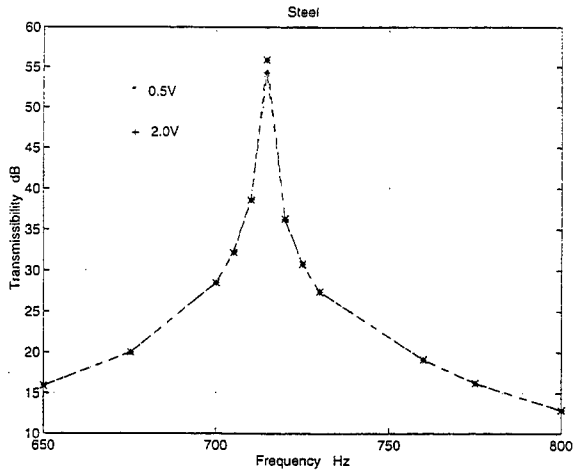

Figure 4. Tension-compression vibration transmissibility curves of steel rod at different base motion levels.

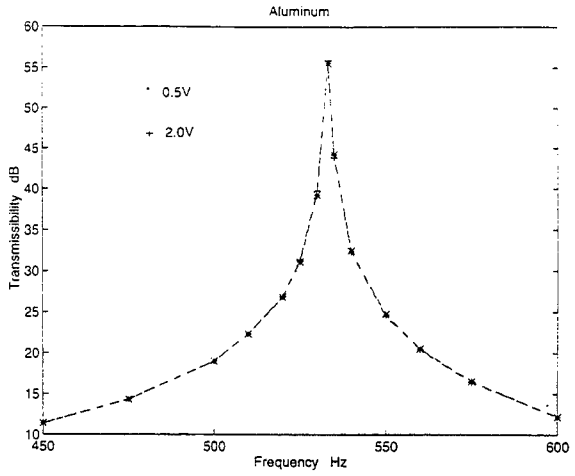

Figure 5. Tension-compression vibration transmissibility curves of the aluminum rod at different base motion levels.

Table 2. Some Experimental Results of Tension-Compression Vibration

Specimen	Base Motion Level (V)	Resonant Frequency (Hz)	Modal Damping Ratio (%)	Resonant Peak Value (dB)
NiTi # 1	0.3	684.2	0.52	39.6
	2.0	673.0	0.83	35.5
	8.0	650.0	1.30	30.9
NiTi # 2	0.3	613.0	0.55	38.8
	2.0	596.5	1.00	32.1
	4.0	583.0	1.10	29.2
	8.0	551.9	1.60	25.6
Steel	0.5	714.6	0.09	55.9
	2.0	714.5	0.10	54.3
Aluminum	0.5	533.3	0.12	55.6
	2.0	533.2	0.10	55.9

Our results listed in Table 2 show that SMAs have higher dampings at a frequency above 500 Hz. This indicates that the pseudoelastic properties of SMAs persist up to reasonably high frequencies relevant to vibration and acoustic control. It is well known that the higher damping of the materials is associated to the movement of the boundaries between different metallurgical phases. It is believed that such movement of interfaces takes place at the speed of sound in the solid. Therefore, the higher damping properties of pseudoelastic SMAs are expected to persist up to even higher frequencies.

To investigate the damping properties of pseudoelastic SMAs at even higher frequencies, we conducted another set of tension-compression tests. To acquire higher resonant frequency of the system, we shorten the specimens and use a smaller mass of 150g. The lengths of the specimens of NiTi # 1, NiTi # 2 and steel rods are 150mm.120mm and 230mm respectively. Fig. 6, Fig. 7 and Fig. 8 are their transmissibility curves measured. It is evident that the SMA

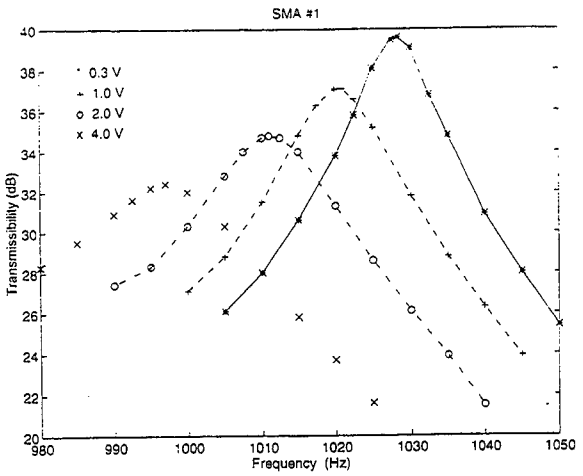

Figure 6. Tension-compression vibration transmissibility curves of NiTi Rod # 1 at higher resonant frequency.

rods are effective as vibration isolators up to a frequency over 1K Hz. The limited power of the shaker prevented us from experimenting with even higher frequencies. Some quantitative measurements related to the transmissibility curves are given in Table 3.

Table 3. Some Experimental Results of Tension-Compression Vibration at Higher Frequency

Specimen	Base Motion Level (V)	Resonant Frequency (Hz)	Modal Damping Ratio (%)	Resonant Peak Value (dB)
NiTi # 1	0.3	1028	0.23	39.6
	1.0	1021	0.51	37.1
	2.0	1011	0.53	34.8
	4.0	997	1.10	32.4
NiTi # 2	0.3	1061	0.39	41.8
	1.0	1052	0.68	37.7
	2.0	1039	0.83	34.5
	4.0	1016	0.96	31.0
Steel	0.3	1504	0.02	70.2
	2.0	1503	0.01	70.9

From Table 2 and Table 3 we can see that the SMA specimens have damping ratios which are an order of magnitude higher than those of steel specimens. When the SMA specimens are subjected to maximum base excitation delivered by the shaker (which has 100 pound maximum force), the peak tension-compression strain remains less than one percent. Since NiTi materials have been shown to have very good fatigue life if the strain is less than 2 percent [8], it is thus safe to say that even higher damping ratio can be achieved in practical usage if the SMA component is designed to operate at close to 2% peak strain. A 2% peak strain seems to be small, but it is nearly an order of magnitude higher than the maximum elastic strain in many conventional metal alloys.

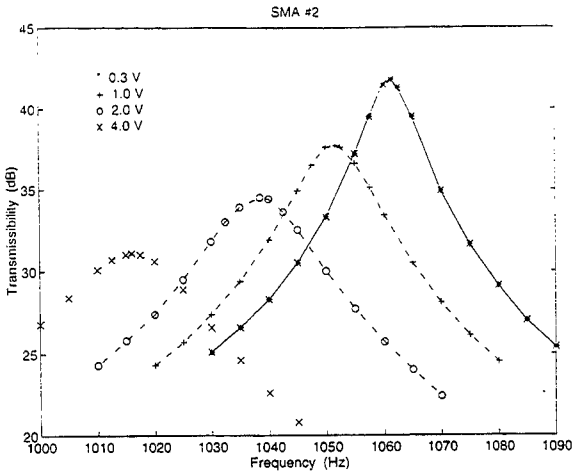

Figure 7. Tension-compression vibration transmissibility curves of NiTi Rod# 2 at higher resonant frequency.

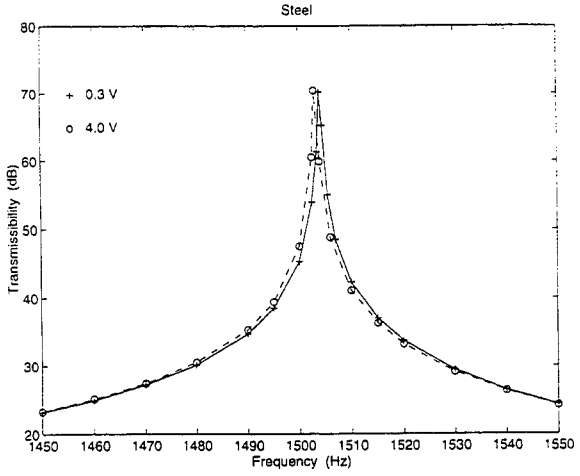

Figure 8. Tension-compression vibration transmissibility curves of the steel rod at higher resonant frequency.

The tension-compression tests at large strains could be conducted using a larger shaker. We point out, however, that in conducting such tests, lateral (bending) vibration must be prevented. Since the base motion is also a source of parametric forcing of the bending modes, the tension-compression tests can be complicated by the onset of parametric instability of the bending modes.

4. BENDING VIBRATION TRANSMISSIBILITY EXPERIMENT

To examine the damping properties of SMAs under larger strains, we conducted bending tests. In the bending tests, the resonance frequency (the fundamental mode) is much lower than the tension-compression mode, thus the shaker can exert a much larger displacement. The parameters of specimens are listed in Table 4. The acceleration transmissibility curves are shown in Fig. 9 - Fig. 12. The same qualitative trend as the tension-compression experiment is seen. As we would expect, the resonant peaks of the system with NiTi rods are more heavily suppressed than the tension-compression tests. For example, the resonant peaks of the systems with specimen NiTi # 1 and NiTi # 2 drop from 35.5 dB to 18.9 dB and from 32.1 dB to 14.4 dB respectively for the same base motion level of 2 V. Since strains generated in bending tests are larger than in tension-compression tests and larger strains lead to larger areas of the hysteresis loop in the stress-strain curve of the NiTi rods, higher damping and lower equivalent elastic modulus occur in the NiTi rod. This indicates that the pseudoelasticity of SMAs makes SMAs more effective particularly in large- amplitude vibration controls. Unlike the tension-compression vibration tests, the acceleration transmissibility curves for the steel and the aluminum rods at different levels of base motion no longer collapse to a single one. This nonlinearity is not caused by the constitutive laws of the material but rather by the geometric and inertial nonlinearity owing to the large amplitude of the vibration. In addition the compliance of the fixture may also contribute to the nonlinearity. Some quantitative measurements related to the transmissibility curves are given in Table 5.

Table 4. Parameters of Test Specimens of Bending Vibration

Specimen	Length (mm)	Diameter (mm)	Mass (g)
NiTi # 1	100	5.86	17.6
NiTi # 2	80	4.97	10.1
Steel	200	4.80	28.2
Aluminum	150	6.36	12.8

Table 5. Some Experimental Results of Bending Vibration

Specimen	Base Motion Level (V)	Resonant Frequency (Hz)	Modal Damping Ratio (%)	Resonant Peak Value (dB)
NiTi # 1	0.1	24.8	2.2	28.0
	0.3	24.1	2.9	26.0
	1.0	22.4	4.4	20.9
	2.0	20.9	4.6	18.9
NiTi # 2	0.1	22.8	3.5	23.2
	0.3	21.9	4.5	20.3
	1.0	19.8	6.8	16.3
	2.0	18.2	7.1	14.4
Steel	0.1	22.2	0.18	51.5
	0.3	22.1	0.34	43.8
Aluminum	0.1	23.1	0.097	47.3
	0.3	23.0	0.17	46.0

Although larger peak strains can be achieved in the bending tests, peak strain occurs only at locations farthest from the neutral axis. Perhaps the more cost effective way of utilizing SMAs in bending vibration control is to place SMAs away from the neutral axis in a composite beam.

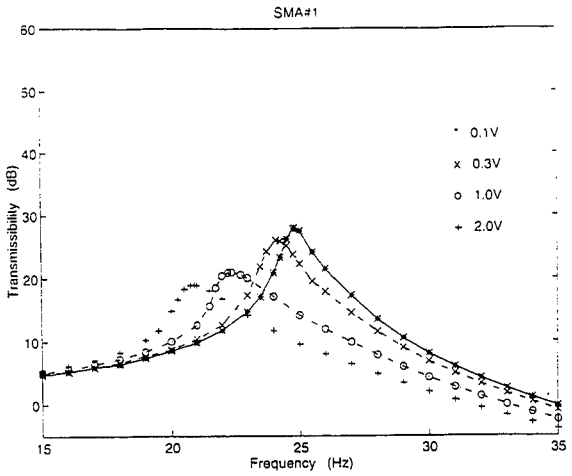

Figure 9. Bending vibration transmissibility curves of NiTi Rod # 1 at different base motion levels

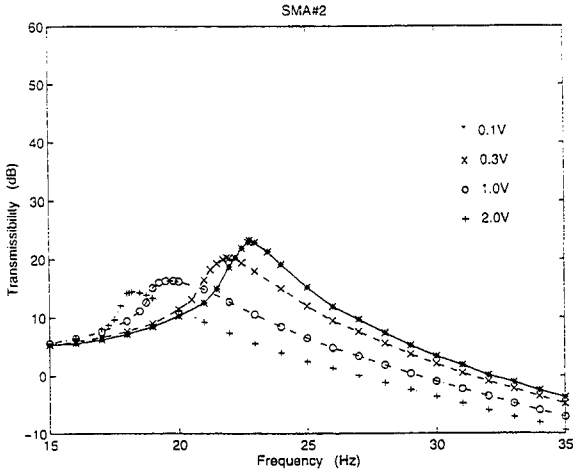

Figure 10. Bending vibration transmissibility curves of NiTi Rod # 2 at different base motion levels

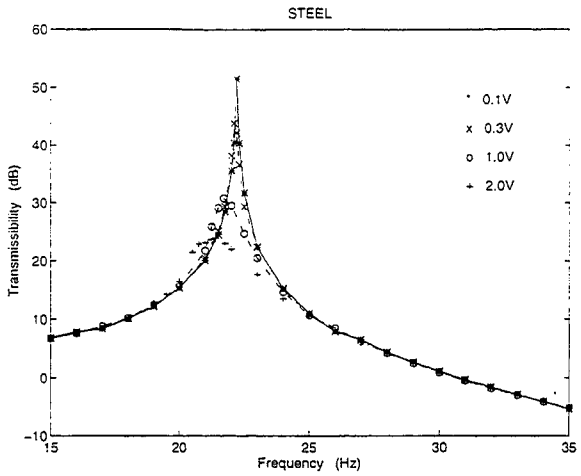

Figure 11. Bending vibration transmissibility curves of the steel rod at different base motion levels

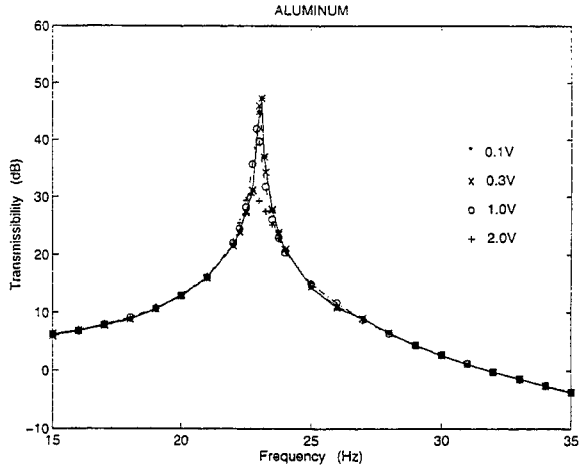

Figure 12. Bending vibration transmissibility curves of the aluminum rod at different base motion levels

5. CONCLUSION

Our test results indicate that compared with conventional alloys, SMA materials have a much higher damping ratio. In fact, the material properties are nonlinear. We observe that the resonance frequencies and the damping ratios are dependent on the excitation levels. When conventional parameters such as the damping ratio and the Young's modulus are used to characterize these nonlinear materials, we must realize that these parameters will be dependent on the test methods and procedures.

As we would expect based on the fact that the stress-induced phase transformation takes place at the speed of the sound, the higher damping associated with pseudoelasticity persists to frequencies high enough for practical vibration and acoustic applications.

BIBLIOGRAPHY

1. S. Ceresara, A. Giarda, G. Tiberi, F.M. Mazzolai, B. Coluzzi and A. Biscarini, Damping characteristics of Cu-Zn-Al shape memory alloys. Journal de Physique IV, Vol.1, C4, 235-240, 1991

2. H.C. Lin, S.K. Wu and M.T. Yeh, Damping characteristics of TiNi shape memory alloys. Metallurgical Transactions A, Vol. 24 A, 2189-2194, 1993

3. C. Li and K.H. Wu, Systematic study of the damping characteristics of shape memory alloys. Smart Material, SPIE Proceedings, Vol. 2189, 314-325, 1994

4. E.J. Graesser and F.A. Cozzarelli, Shape memory alloys as new materials for aseismic isolation. Journal of Engineering Mechanics, Vol.117, No.11, 2590- 2608, 1991

5. P. Thomson, G.J. Balas and P.H. Leo, The use of shape memory alloys for passive structural damping. Smart Mater. Struct., Vol. 4, 36-42, 1995

6. E.J. Graesser, Effect of intrinsic damping on vibration transmissibility of Nickel-Titanium shape memory alloy springs. Metallurgical and Materials Transactions A, Vol. 26A, 2791-2796, 1995

7. Z. C. Feng and D.Z. Li, Dynamics of a mechanical system with a shape memory alloy bar. J. Intell. Mater. Syst. and Struct. Vol. 7, 399-410, 1996.

8. C. Liang and C.A. Rogers, Design of shape memory alloy springs with applications in vibration control. J. of Vibration and Acoustics. Vol. 115, 129- 135, 1993.

INVESTIGATION OF THE REDUCTION IN THERMAL DEFLECTION AND RANDOM RESPONSE OF COMPOSITE PLATES AT ELEVATED TEMPERATURES USING SHAPE MEMORY ALLOYS

Z. W. Zhong and Chuh Mei
Department of Aerospace Engineering
Old Dominion University, Norfolk, VA 23529-0247

ABSTRACT

The reduction in thermal deflection and random response of composite plates with embedded shape memory alloy fibers (SMA) at. elevated temperatures is investigated. The stress-strain relations are developed for a thin composite lamina with embedded SMA fibers. Finite element equations and computational procedures are presented for composite plates with embedded SMA with the consideration of nonlinearities in geometry and material properties. The results demonstrate that SMA can be effective in reduction of thermal deflection and random response of composite plates at elevated temperatures.

INTRODUCTION

For some alloys, a given plastic strain can be completely recovered when the alloy is heated above the characteristic transformation (austenite finish, T_f) temperature. This shape memory effect phenomenon is attributed to the material which undergoes a change in crystal structure known as a reversible austenite to martensite phase transformation. The solid-solid phase transformation also gives an increase in Young's modulus by a factor of three or four and an increase in yielding strength approximately ten times. The transformation temperature can be altered by changing the composition of the alloy. Many alloys are known to exhibit the shape memory effect. They include the copper alloy family of Cu-Zn, Cu-Zn-X (X=Si, Sn, Al, Ga), Cu-Al-Ni, Cu-Au-Zn and the alloys of Ag-Cd, Au-Cd, Ni-Al, Fe-Pt and others [1]. Nickel-Titanium alloys (Ni-Ti or Nitinol) are the most common SMA [2].

SMA has been used as actuators for active control of buckling of beams [3] and shape control of beams [4]. It is also being investigated in active vibration control of beams [5], rotating disk/shaft system [6], large space structures [7] and flow-induced vibration [8]. The design of extended bandwidth SMA actuators was also investigated [9].

Composites with embedded SMA fibers use shape memory alloy fibers as reinforcements which can be stiffened or controlled by the addition of heat.

The concept of active damage control of hybrid material systems using the SMA as embedded induced strain actuators has been proposed [10]. Active vibration control of flexible linkage mechanisms using SMA fiber-reinforced composites has been investigated [11]. Acoustic transmission and radiation control by use of the SMA hybrid composites was presented [12, 13]. Manufacturing of adaptive graphite/epoxy structures with embedded Nitinol wires was recently reported [14]. Detailed formulations of the bending, modal analysis and acoustic transmission of SMA reinforced composite plates have been presented [15, 16].

A limited number of investigations on the thermal postbuckling deflection of SMA fiber-reinforced composite plates exists in the literature. A feasibility study on reduction of thermal buckling and postbuckling deflection of composite plates with embedded SMA fibers was reported [17] and the passive control of random vibrations of SMA embedded composite plates using the analytical continuum method was presented [18]. The finite element analysis of random response suppression of composite panels using SMA was recently proposed [19]. In all those investigations, the material nonlinearities were not considered.

In the present paper, the stress-strain relations for a thin composite lamina with embedded SMA fibers are presented. Governing equations for postbuckling and random vibration of SMA fiber-reinforced composite plates are presented using the finite element method. Solution procedures using the incremental and Newton-Raphson iteration methods are presented. Numerical examples are given.

CONSTITUTIVE AND FINITE ELEMENT FORMULATION

Consider a thin composite lamina; for example, graphite-epoxy, having an arbitrary orientation angle and with SMA fibers embedded in the same direction as the graphite fibers. The stress-strain relations for such a lamina in the principal material directions are derived in Appendix. For a general k-th layer with an orientation angle θ, the stress-strain relations, Eqs. A17 and A18, become

$$\{\sigma\}_k - \{\sigma_o\}_k = \left[\bar{Q}^*\right]_k \begin{Bmatrix} \varepsilon_x \\ \varepsilon_y \\ \gamma_{xy} \end{Bmatrix} + \begin{Bmatrix} \sigma_x^* \\ \sigma_y^* \\ \tau_{xy}^* \end{Bmatrix}_k v_{sk} - \left(\left[\bar{Q}\right]_m \begin{Bmatrix} \alpha_x \\ \alpha_y \\ \alpha_{xy} \end{Bmatrix}_m v_m \right)_k \Delta T, T > T_s \quad (1)$$

and

$$\{\sigma\}_k - \{\sigma_o\}_k = \left[\bar{Q}^*\right]_k \left(\begin{Bmatrix} \varepsilon_x \\ \varepsilon_y \\ \gamma_{xy} \end{Bmatrix} - \begin{Bmatrix} \alpha_x^* \\ \alpha_y^* \\ \alpha_{xy}^* \end{Bmatrix}_k \Delta T \right), \qquad T < T_s \quad (2)$$

where $[\bar{Q}^*]$ and $[\bar{Q}]_m$ are the transformed reduced stiffness matrices of the composite lamina and the composite matrix, Ts is SMA stimulating temperature (austenite start temperature), respectively. The resultant force and moment vectors of the SMA fiber-reinforced composite plate are defined as

$$(\{N\},\{M\}) = \int_{-h/2}^{h/2} \{\sigma\}_k (1,z)dz$$

or

$$\begin{Bmatrix} N \\ M \end{Bmatrix} = \begin{bmatrix} A^* & B^* \\ B^* & D^* \end{bmatrix} \begin{Bmatrix} \varepsilon^o \\ \kappa \end{Bmatrix} + \begin{Bmatrix} N_r^* \\ M_r^* \end{Bmatrix} - \begin{Bmatrix} N_{\Delta T} \\ M_{\Delta T} \end{Bmatrix} + \begin{Bmatrix} N_\sigma \\ M_\sigma \end{Bmatrix} \tag{3}$$

where the laminate stiffness [A*], [B*] and [D*] are all temperature dependent, the recovery inplane force $\{N_r^*\}$ and moment $\{M_r^*\}$ vectors are dependent on temperature and prestrain (see Fig. A2). The vectors $\{N_\sigma\}$ and $\{M_\sigma\}$ are the force and moment vectors due to initial stress $\{\sigma_o\}$. The recovery and the thermal inplane forces and moments due to the SMA recovery stress and the temperature change, respectively, are

$$\left(\{N_r^*\},\{M_r^*\}\right) = \int_{-h/2}^{h/2} \begin{Bmatrix} \sigma_x^* \\ \sigma_y^* \\ \tau_{xy}^* \end{Bmatrix}_k v_{sk}(1,z)dz, \quad T > T_s \text{ and null } T < T_s \tag{4}$$

$$\left(\{N_{\Delta T}\},\{M_{\Delta T}\}\right) = \int_{-h/2}^{h/2} \left(\left[\bar{Q}\right]_m \begin{Bmatrix} \alpha_x \\ \alpha_y \\ \alpha_{xy} \end{Bmatrix}_m v_m \right)_k \Delta T(1,z)dz, \qquad T > T_s \tag{5}$$

$$\left(\{N_{\Delta T}\},\{M_{\Delta T}\}\right) = \int_{-h/2}^{h/2} \left(\left[\bar{Q}^*\right] \begin{Bmatrix} \alpha_x^* \\ \alpha_y^* \\ \alpha_{xy}^* \end{Bmatrix} \right)_k \Delta T(1,z)dz, \qquad T < T_s \tag{6}$$

The inplane strain and curvature vectors, $\{\varepsilon^o\}$ and $\{\kappa\}$, are defined from the von Karman strain-displacement relations as

$$\begin{Bmatrix} \varepsilon_x \\ \varepsilon_y \\ \gamma_{xy} \end{Bmatrix} = \begin{Bmatrix} u_{,x} \\ v_{,y} \\ u_{,y} + v_{,x} \end{Bmatrix} + \begin{Bmatrix} w_{,x}^2/2 \\ w_{,y}^2/2 \\ w_{,x} w_{,y} \end{Bmatrix} + \begin{Bmatrix} w_{,x} w_{o,x} \\ w_{,y} w_{o,y} \\ w_{,x} w_{o,y} + w_{o,x} w_{,y} \end{Bmatrix} + z \begin{Bmatrix} -w_{,xx} \\ -w_{,yy} \\ -2w_{,xy} \end{Bmatrix}$$

$$= \{\varepsilon_m^o\} + \{\varepsilon_b^o\} + \{\varepsilon_o^o\} + z\{\kappa\} \tag{7}$$

$$= \{\varepsilon^o\} + z\{\kappa\}$$

where w_o is the initial deflection (sum of the converged thermal deflections from previous incremental steps) which is necessary for the nonlinear material

properties considered, and u and v are the in-plane displacements and w is the transverse deflection measured from the initial deflection position.

The governing equations for a SMA fiber-reinforced composite plate subjected to a combined thermal and random excitation loads can be derived through the use of a variational principle. The system equations in finite element expression can be written in the form

$$\begin{bmatrix} M_b & 0 \\ 0 & M_m \end{bmatrix}\begin{Bmatrix} \ddot{W}_b \\ \ddot{W}_m \end{Bmatrix}+\left(\begin{bmatrix} K_b & K_B \\ K_B & K_m \end{bmatrix}-\begin{bmatrix} K_{N\Delta T} & 0 \\ 0 & 0 \end{bmatrix}+\begin{bmatrix} K_r^* & 0 \\ 0 & 0 \end{bmatrix}+\begin{bmatrix} K_\sigma & 0 \\ 0 & 0 \end{bmatrix}\right.$$
$$\left.+\begin{bmatrix} K_{bo} & K_{bmo} \\ K_{mbo} & 0 \end{bmatrix}+\frac{1}{2}\begin{bmatrix} N1_{Nm}+N1_{NB} & N1_{bm} \\ N1_{mb} & 0 \end{bmatrix}+\begin{bmatrix} N1_{ob} & 0 \\ 0 & 0 \end{bmatrix}+\frac{1}{3}\begin{bmatrix} N2_b & 0 \\ 0 & 0 \end{bmatrix}\right) \quad (8a)$$
$$=\begin{Bmatrix} P_b(t) \\ 0 \end{Bmatrix}+\begin{Bmatrix} P_{b\Delta T} \\ P_{m\Delta T} \end{Bmatrix}-\begin{Bmatrix} P_{br}^* \\ P_{mr}^* \end{Bmatrix}-\begin{Bmatrix} P_{b\sigma} \\ P_{m\sigma} \end{Bmatrix}+\begin{Bmatrix} P_{\Delta To} \\ 0 \end{Bmatrix}-\begin{Bmatrix} P_{bro}^* \\ P_{mro}^* \end{Bmatrix}-\begin{Bmatrix} P_{\sigma o} \\ 0 \end{Bmatrix}$$

or

$$[M]\{\ddot{W}\}+([K]-[K_{N\Delta T}]+[K_r^*]+[K_\sigma]+[K_o]+\tfrac{1}{2}[N1]+[N1_o]+\tfrac{1}{3}[N2])\{W\}$$
$$=\{P(t)\}+\{P_{\Delta T}\}-\{P_r^*\}-\{P_\sigma\}+\{P_{\Delta To}\}-\{P_{ro}^*\}-\{P_{\sigma o}\} \quad (8b)$$

where [M] is the system mass matrix, [K] and {P} are the system stiffness matrices and the load vector, respectively; $[K_r^*]$ and $[K_{N\Delta T}]$ are geometric stiffness matrices due to the recovery stress σ_r^*(or $\{N_r^*\}$) and thermal inplane force vector $\{N_{\Delta T}\}$, respectively; [K_σ] and [K_o] are the geometric stiffness matrices due to the initial stress {σ_o} and the initial deflection {W_o}, respectively; [N1] and [N2] are the first and second-order nonlinear stiffness matrices which depend linearly and quadratically upon displacement {W}, respectively; [$N1_o$] is the first-order nonlinear stiffness matrix which is linearly dependent on the displacement {W} and the known initial deflection {W_o}. The subscripts b and m denote bending (including rotations) and membrane components, respectively; subscripts r, σ and o represent that the corresponding stiffness matrix or load vector is dependent on the recovery stress σ_r^*, initial stress {σ_o} and initial deflection {W_o}, respectively; and the subscripts B, Nm and NB indicate that the corresponding stiffness matrix is due to the extension-bending coupling laminate stiffness [B], membrane force vectors {N_m} (=[A*]{ε_m^o}) and {N_B} (=[B*]{κ}), respectively. The stiffness matrices [K], [N1], [$N1_o$] and [N2] are also temperature dependent and all the matrices in Eq. (8b) are symmetric. Detailed derivations of the governing equations and expressions for the element matrices and load vectors are referred to [19-21].

SOLUTION PROCEDURES

Equation (8b) is a set of nonlinear ordinary differential equation with respect to time t, and some of the load vectors are independent to time t. The solution for Eq. (8b) consists of a time-dependent solution and a time-independent solution as

$$\{W\} = \{W_s\} + \{W(t)\}_t \tag{9}$$

where $\{W_s\}$ is the time-independent solution and its physical meaning is the large thermal deflection, and $\{W(t)\}_t$ is the time-dependent dynamic solution whose physical meaning is small random oscillations about the static equilibrium deformed position $\{W_s\}$.

Thermal Deflection or Postbuckling

For nonlinear material properties of SMA, the incremental method should be employed. This implies that the material properties are treated as constant within each small increment of temperature. Substituting Eq. (9) into the system equation of motion, Eq. (8b), and neglecting the higher order terms of $\{W(t)\}_t$ for small random response, two sets of equations can be obtained. One is the time-independent nonlinear algebraic equations which yield the thermal postbuckling deflection $\{W_s\}$ and it can be written as

$$\begin{aligned}&([K]-[K_{N\Delta T}]+[K_r^*]+[K_\sigma]+[K_o]+\tfrac{1}{2}[N1]_s+[N1_o]_s+\tfrac{1}{3}[N2]_{ss})\{W_s\}\\&=\{P_{\Delta T}\}-\{P_r^*\}-\{P_\sigma\}+\{P_{\Delta To}\}-\{P_{ro}^*\}-\{P_{\sigma o}\}\end{aligned} \tag{10}$$

where the nonlinear stiffness matrices, $[N1]_s$, $[N1_o]_s$ and $[N2]_{ss}$, linearly and quadratically depend on the thermal displacement $\{W_s\}$. The temperature dependent nonlinear material properties are handled with small temperature increments of ΔT, and the material properties are thus considered to be constants within each small temperature increment. The initial deflection and initial stress are both zero at the first temperature increment. The effects of initial deflection and stress are thus included in the formulation. One effective approach for solving Eq. (10) involves the application of Newton-Raphson iterative method. Thus, the i-th iteration Eq. (10) can be written as

$$[K_{\tan}]_i\{\Delta W\}_{i+1} = \{\Delta P\}_i \tag{11}$$

then $[K_{\tan}]_{i+1}$ and $\{\Delta P\}_{i+1}$ are updated by using

$$\{W_s\}_{i+1} = \{W_s\}_i + \{\Delta W\}_{i+1} \tag{12}$$

The solution process seeks to reduce the imbalance load vector $\{\Delta P\}$, and consequently $\{\Delta W\}$, to a specified small quantity (10^{-5} in this study). The tangent stiffness matrix and the imbalance load vector are

$$[K_{\tan}]_i = [K]-[K_{N\Delta T}]+[K_r^*]+[K_\sigma]+[K_o]+[N1]_{si}+[N1_o]_{si}+[N2]_{ssi} \tag{13}$$

and

$$\{\Delta P\}_i = \{P_{\Delta T}\} - \{P_r^*\} - \{P_\sigma\} + \{P_{\Delta To}\} - \{P_{ro}^*\} - \{P_{\sigma o}\}$$
$$-([K]-[K_{N\Delta T}]+[K_r^*]+[K_\sigma]+[K_o]+\tfrac{1}{2}[N1]_{si}+[N1_o]_{si}+\tfrac{1}{3}[N2]_{ssi})\{W_s\}_i \quad (14)$$

where the nonlinear stiffness matrices $[N1]_{si}$, $[N1_o]_{si}$ and $[N2]_{ssi}$ are evaluated using $\{W_s\}_i$. The total thermal deflection is the sum of the converged $\{W_s\}$ from the many small temperature increments.

Random Response Analysis

The other equation derived from Eqs. (8b) and (9) is a dynamic equation, and it can be written as

$$[M]\{\ddot{W}(t)\}_t$$
$$+([K]-[K_{N\Delta T}]+[K_r^*]+[K_\sigma]+[K_o]+[N1]_s+[N1_o]_s+[N2]_{ss})\{W(t)\}_t \quad (15)$$
$$=\{P(t)\}$$

The sum of stiffness matrices in Eq. (15) is exactly the converged tangent stiffness matrix from Eq. (11). Therefore, there is no need to assemble the system stiffness matrices by considering the effects of SMA recovery stress, thermal stress, and thermal deflection from each element as in the conventional finite element approach. By set $\{P(t)\}=0$, Eq. (15) is a standard linear eigenvalue problem, and the natural frequencies and mode shapes of vibration about the thermally deflected position are obtained.

Substituting a modal transformation and truncation of $\{W\}_t = [\phi]\{q\}$ into Eq. (15) with the consideration of damping, a set of uncoupled modal equations about the thermally deflected or buckled position can be expressed as

$$\ddot{q}_r(t) + 2\zeta_r \varpi_r \dot{q}_r(t) + \varpi_r^2 q_r(t) = f_r / m_r \qquad r=1, 2,\ldots, N \quad (16)$$

where the modal mass, stiffness and force are

$$m_r = \{\phi_r\}^T [M]\{\phi_r\}$$
$$k_r = \{\phi_r\}^T [K_{tan}]\{\phi_r\} \quad (17)$$
$$f_r = \{\phi_r\}^T \{P(t)\}\{\phi_r\}$$

Thus, the root mean square (RMS) of maximum deflections and strains can be easily determined.

RESULTS AND DISCUSSION

The results shown in this study were based on an SMA fiber-reinforced composite laminate, where the graphite-epoxy composite was treated as matrix. The following material properties were used in the analysis:

SMA-Nitinol		Graphite-Epoxy	
T_s	$100°F(37.78°C)$	E_1	22.5(155)
T_f	145(62.78)	E_2	1.17(8.07)

E_s^*	From Reference [2]	G_{12}	0.66(4.55)
σ_s^*	From Reference [2]		
G*	3.604 Msi (24.9 GPa), T<T_s	μ_{12}	0.22
G*	3.712 Msi (25.6 GPa), T>T_s		
μ	0.3	ρ	$0.1458\times10^{-3}(1550.07)$
ρ	$0.6067\times10^{-3} lb-s^2/in^4 (6450 Kg/m^3)$	α_1	$-0.04\times10^{-6}(-0.07\times10^{-6})$
α	$5.7\times10^{-6}/^\circ F(10.26\times10^{-6}/^\circ C)$	α_2	$16.7\times10^{-6}(30.1\times10^{-6})$

The finite element used in this investigation is the three-node Mindlin (MIN3) plate element with improved transverse shear [22]. A reference or ambient temperature $T_o = 70^\circ F$ and a uniform temperature distribution are used in all the examples.

Thermal Deflection

A simply supported 15x12x0.048 in. rectangular $(0/90/90/0)_s$ laminate with or without SMA fibers is studied in detail. The mesh size is 10x8x2 for the full plate. Figures 1 and 2 show the maximum deflections versus temperature for a laminate with no SMA fibers (v_s=0) and with 10%, 20%, 30% SMA fibers and 3% prestrain ($v_s = 10\%, 20\%, 30\%$ *and* $\varepsilon_r = 3\%$), respectively. It is seen that the thermal deflection of the panel without SMA approximately reaches 2 times the plate thickness (W_{max}/h=2) at $200^\circ F$. For the panel with different volume fraction of SMA, Fig. 2 shows that the thermal deflection drops dramatically after the SMA is activated at transformation temperature (T>T_s) and the deflection will increase gradually when the thermal expansion effects become dominant. The most important phenomenon is that although the Young's modulus of SMA is lower than that of the composite matrix material, the thermal deflections of the panel can be reduced because of the effects of recovery stress of SMA. It can be seen that the thermal deflections (W_{max}/h) are less than 1.0 at $200^\circ F$ and less than 1.5 at $300^\circ F$. Figure 3 shows the maximum deflection versus temperature for a laminate with 30% SMA fibers and 3%, 4% and 5% prestrains. Compared to Fig. 2, it is seen that the volume fraction of SMA fibers is more effective than the prestrain of SMA in the reduction of thermal deflection. The thermal deflections versus temperature for a clamped 15x12x0.048 in. rectangular (0/90/90/0)s laminate are shown in Fig. 4. The clamped plate is more stiff than the simply supported. The critical buckling temperature for the clamped laminate without SMA is slightly higher than the SMA transformation temperature T_s. This leads to the postponement of thermal deflection until $300^\circ F$ for the clamped laminate with 10% SMA and 3% prestrain. In this clamped case, this implies that the thermal deflection can be completely eliminated for the highest operating temperature less than $300^\circ F$. The

thermal deflection in the temperature range between the critical buckling temperature and SMA activated temperature for the simply supported case shown in Figs. 2 and 3 can also be suppressed by: 1) selecting the proper percentages of SMA fiber volume fraction and prestrain, and 2) altering the transformation temperature T_s by changing the composition of alloy.

Random Response

For panels with SMA, the dynamic response is affected by the components of stiffness due to SMA ([K]) and due to recovery stress of SMA ($[K_r^*]$). Note that the Young's modulus of SMA is lower than that of the composite matrix, thus the panel becomes less stiff when SMA fibers are embedded. The increase in the dynamic response, observed for some case, is due to the relatively lower modulus and higher mass density of the SMA. On the other hand, large inplane tensile forces are induced by the recovery stress of SMA and this effect will decrease the dynamic response of the panel. Figure 5 shows that the RMS(W_{max}/h) of the panel with 10% SMA fibers and 5% prestrain at $170^\circ F$ is slightly larger than that of the panel without SMA at $170^\circ F$. In this case, the recovery forces induced are not sufficient to overcome the loss of stiffness due to the modulus deficiency of SMA fibers. However, the panel with 20% and 30% SMA fibers and 5% prestrain provide ample recovery forces to significantly reduce the panel dynamic response.

Figure 6 shows the total maximum deflection of panel with no SMA fibers (v_s=0) and for three SMA prestrain values $\varepsilon_r = 3,\ 4$ *and* 5% for each nonzero SMA volume fraction (v_s=10, 20 and 30%) at $170^\circ F$ and SSL=100dB. It clearly indicates that the six graphite/epoxy panels with SMA volume fraction of either 20% or 30% and $\varepsilon_r = 3,\ 4$ *and* 5% are all acceptable designs. Compared to the panel with no SMA fibers, those panels give much small amount of maximum RMS random deflections as well as thermal deflections.

The power spectral density (PSD) of the maximum deflection at 100 dB is shown in Fig. 7 for three cases: no SMA at $70^\circ F$; 10% SMA and 3% prestrain at $170^\circ F$; and 30% SMA and 5% prestrain at $170^\circ F$, respectively. It is seen that the SMA fiber-reinforced plates exhibit significant peak-amplitude reduction and frequency increase at $170^\circ F$.

CONCLUDING REMARKS

The stress-strain relations for a thin composite lamina with embedded SMA fibers have been developed. The finite element method has been successfully implemented to analyze the thermal deflection and random

response of SMA fiber-reinforced composite plates with the consideration of nonlinear material properties of SMA and nonlinearity in geometry.

With the proper percentages of SMA volume fraction and prestrain and also the altering of transformation temperature by changing the alloy composition, the thermal deflection can be dramatically reduced. This reduction in thermal deflection could be useful in practical applications by maintaining optimal aerodynamic configuration for flight vehicles and eliminating snap-through motions.

The RMS maximum deflection can be reduced with some combinations of SMA volume fraction and prestrain. After the SMA is activated and the recovery forces induced are sufficient to overcome the loss of stiffness due to the modulus deficiency of SMA, the dynamic response can be significantly reduced.

ACKNOWLEDGMENTS

The authors would like to acknowledge the support by grant F33615-91-C-3205, AF Wright Laboratory. Dr. Howard F. Wolfe is the technical monitor. The authors would also like to thank Dr. Alex Tessler, NASA Langley Research Center for his assistance on the MIN3 element.

REFERENCES

1. Tadaki, T., Otsuka, K. and Shimizu, K., Shape Memory Alloy. In *Annual Review of Materials Science,* Eds. Huggins, R. A., Giordmaine, J. A. and Wachtmank, J. B., Annual Reviews, Inc., Palo Alto, CA, 1988, Vol. 18, pp. 25-45.
2. Cross, W. B., Kariotis, A. H. and Stimler, F. J., Nitinol Characterization Study, NASA CR-1433, 1970.
3. Baz, A. and Tampe, L., Active Control of Buckling of Flexible Beams.*Proceedings, 18th Biennial Conference on Failure Prevention and Reliability*, Montreal, Canada, 1989, ASME DE-Vol. 16, pp. 211-218.
4. Chaudhry, Z. and Rogers, C. A., Bending and Shape Control of Beams Using SMA Actuators. *Journal of Intelligent Materials Systems and Structures*, 1992, Vol. 2, pp. 581-602.
5. Baz, A., Iman, K. and McCoy, J., Active Vibration Control of Flexible Beams Using Shape Memory Actuators. *Journal of Sound and Vibration*, 1990, Vol. 140, pp. 437-456.
6. Segalman, D. J., Parker, G. G. and Inman, D. J., Vibration Suppression by Modulation of Elastic Modulus Using Shape Memory Alloy. *Intelligent Structures, Materials and Vibrations*, 1993, ASME-DE-Vol. 58, pp. 1-5.
7. Maclean, B. J., Patterson, G. J. and Misra, M. S., Modeling of a Shape Memory Integrated Actuator for Vibration Control of Large Space

Structures. *Journal of Intelligent Materials Systems and Structures*, 1991, Vol. 2, pp. 72-94.

8. Kim, J. H. and Smith, C. R., Control of Flow-Induced Vibrations Using Shape Memory Alloy Wires. *Adaptive Structures and Material Systems*, 1993, ASME AD-Vol. 35, pp. 347-34.
9. Ditman, J., Bergman, L. and Tsao, T., The Design of Extended Bandwidth Shape Memory Alloy Actuators. *Proceedings, AIAA/ASME Adaptive Structures Forum*, Hilton Head, SC, 1994, pp. 210-220.
10. Rogers, C. A., Liang, C. and Li, S., Active Damage Control of Hybrid Material Systems Using Induced Strain Actuator. *Proceedings, 32nd AIAA/ASME/ASCE/AHS/ASC Structure, Structural Dynamics and Materials Conference,* Baltimore, MD, 1991, pp. 1190-1203.
11. Venkatesh, A., Hilborn, J., Bidaux, J. E. and Gotthardt, R., Active Vibration Control of Flexible Linkage Mechanisms Using Shape Memory Alloy Fiber-Reinforced Composites. *Proceedings, 1st European Conference on Smart Structures and Materials,* Glasgow, England, Eds. Culshaw, B., Gardiner, P. T. and McDonach, A., Institute of Physics Publishing, Bristol, England, 1992, pp. 185-188.
12. Anders, W. S., Rogers, C. A. and Fuller, C. R., Vibration and low Frequency Acoustic Analysis of Piecewise-Activated Adaptive Composite Panels. *Journal of Composite Materials*, 1992, Vol. 26, pp. 103-120.
13. Liang, C., Rogers, C. A. and Fuller, C. R., Acoustic Transmission and Radiation Analysis of Adaptive Shape Memory Alloy Reinforced Laminated Plates. *Journal of Sound and Vibration*, 1991, Vol. 145, pp. 72-94.
14. White, S. R., Whitlock, M. E., Ditman, J. B. and Hebda, D. A., Manufacturing of Adaptive Graphite/Epoxy Structures with Embedded Nitinol Wires. *Adaptive Structures and Material Systems,* 1993, ASME AD-Vol. 35, pp.71-79.
15. Jia, J. and Rogers, C. A., Formulation of a Mechanical Model for Composites with Embedded SMA Actuators. *Proceedings, 18th Biennial Conference on Failure Prevention and Reliability*, Montreal, Canada, 1989, ASME DE-Vol. 16, pp. 203-210.
16. Rogers, C. A., Liang, C. and Jia, J., Behavior of Shape Memory Alloy Reinforced Composite Plates, Part 1: Model Formulation and Control Concept. *Proceedings, 30th AIAA/ASME/ASCE/AHS/ASC Structure, Structural Dynamics and Materials Conference,* Mobile, AL, 1989, pp. 2011-2017.
17. Zhong, Z. W., Chen, R., R., Mei, C. and Pates, C. S., III, Buckling and Postbuckling of Shape Memory Alloy Fiber-Reinforced Composite Plates. *Symposium on Buckling and Postbuckling of Composite Structures*, 1994, ASME AD-Vol. 41/PVP-Vol. 293, pp. 115-132.

18. Pates, C. S., III., Zhong, Z. W. and Mei, C., Passive Control of Random Response of Shape Memory Alloy Fiber-Reinforced Composite Plates. *Proceedings, Fifth International Conference on Recent Advances in Structural Dynamics*, eds. Ferguson, N. S. et al. Institute of Sound Vibration Research, Southampton, England, July 18-21, 1994, pp. 423-436.
19. Turner, T. L., Zhong, Z. W. and Mei, C., Finite Element Analysis of the Random Response Suppression of Composite panels at Elevated Temperatures Using Shape Memory Alloy Fibers. Proceedings, 35th *AIAA/ASME/ASCE/AHS/ASC Structure, Structural Dynamics and Materials Conference*, Hilton Head, SC, 1994, pp.136-146.
20. Xue, D. Y. and Mei, C., A Study of the Application of Shape Memory Alloy in Panel Flutter Control. *Proceedings, Fifth International Conference on Recent Advances in Structural Dynamics*, eds. Ferguson, N. S. et al. Institute of Sound Vibration Research, Southampton, England, July 18-21, 1994, pp. 412-422.
21. Chen, R. R. and Mei, C., Thermo-Mechanical Buckling and Postbuckling of Composite Plates Using the MIN3 Elements. *Symposium on Buckling and Postbuckling of Composite Structures*, 1994, ASME AD-Vol. 41/PVP-Vol. 293, pp. 39-53.
22. Tessler, A. and Hughes, T. J. R., A Three-Node Mindlin Plate Element with Improved Transverse Shear. *Computer Methods in Applied Mechanics and Engineering*, 1985, Vol. 50, pp. 71-101.

APPENDIX

Stress-Strain Relations of a SMA Embedded Composite Lamina

A representative volume element of a SMA fiber-reinforced composite lamina is shown in Fig. A1. The element is taken to be in the plane of the plate. The composite matrix, for example graphite/epoxy, has the principal material directions 1 and 2 and the SMA fiber embedded in the 1-direction.

In order to derive the constitutive relation for the 1-direction, it is assumed that a stress σ_1 acts alone on the element ($\sigma_2 = 0$) and that the SMA fiber and composite matrix are strained by the same amount, ε_1 (i.e., plane sections remain plane). The 1-direction stress-strain relation of the SMA fiber can be described as

$$\sigma_{1s} = E_s^* \varepsilon_1 + \sigma_r^*, \qquad T > T_s \tag{A1}$$

or

$$\sigma_{1s} = E_s^* (\varepsilon_1 - \alpha_s \Delta T), \qquad T < T_s \tag{A2}$$

where T_s is the austenite start temperature and α_s is the thermal expansion coefficient. The Young's Modulus E_s^* and the recovery stress σ_r^* are

temperature dependent, indicated by superscript (*). The recovery stress σ_r^* is also dependent on the prestrain ε_r. For Nitinol, σ_r^* and E_s^* can be determined from Figs. A2 and A3, respectively [2]. Similarly, the one-dimensional stress-strain relation in the 1-direction for the composite matrix can be expressed as

$$\sigma_{1m} = E_{1m}(\varepsilon_1 - \alpha_{1m}\Delta T) \tag{A3}$$

The resultant force in the 1-direction ($\sigma_2 = 0$) is distributed over the SMA fiber and composite matrix and can be written as

$$\sigma_1 A_1 = \sigma_{1s} A_s + \sigma_{1m} A_m \tag{A4}$$

where (σ_1, A_1), (σ_{1s}, A_s) *and* (σ_{1m}, A_m) are the (stress, cross section area) of the entire element, SMA fiber, and composite matrix, respectively. Thus, the average stress σ_1 is

$$\sigma_1 = \sigma_{1s} v_s + \sigma_{1m} v_m \tag{A5}$$

where $v_s = A_s / A_1$ and $v_m = A_m / A_1$ are the volume fractions of SMA and composite matrix, respectively. When T>Ts, the SMA effect is activated and the one-dimensional stress-strain relation in the 1-direction becomes

$$\begin{aligned} \sigma_1 &= (E_s^* \varepsilon_1 + \sigma_r^*) v_s + E_{1m}(\varepsilon_1 - \alpha_{1m}\Delta T) v_m \\ &= E_1^* \varepsilon_1 + \sigma_r^* v_s - E_{1m}\alpha_{1m} v_m \Delta T \end{aligned} \tag{A6}$$

where

$$E_1^* = E_{1m} v_m + E_s^* v_s \tag{A7}$$

When T<Ts, the SMA effect is not activated and the stress σ_1 is

$$\begin{aligned} \sigma_1 &= E_1^* \varepsilon_1 - (E_s^* \alpha_s v_s + E_{1m}\alpha_{1m} v_m)\Delta T \\ &= E_1^* (\varepsilon_1 - \alpha_1^* \Delta T) \end{aligned} \tag{A8}$$

where

$$\alpha_1^* = \frac{(E_{1m}\alpha_{1m} v_m + E_s^* \alpha_s v_s)}{E_1^*} \tag{A9}$$

A similar constitutive relation may be derived for the 2-direction by assuming that the applied stress σ_2 acts upon both the fiber and the matrix ($\sigma_1 = 0$). Thus, the one-dimensional stress-strain relations in the 2-direction for the SMA fiber and the composite matrix become

$$\sigma_{2s} = \sigma_2 = E_s^* (\varepsilon_{2s} - \alpha_s \Delta T) \tag{A10}$$

and

$$\sigma_{2m} = \sigma_2 = E_{2m}(\varepsilon_{2m} - \alpha_{2m}\Delta T) \tag{A11}$$

respectively. The recovery stress does not appear in Eq. (A10), since the SMA fiber prestrain ε_r and recovery stress σ_r^* are considered to be a 1-direction effect only.

The total elongation is due to strain in the composite matrix and the SMA fiber and may be written in the form

$$A_1 \varepsilon_2 = A_m \varepsilon_{2m} + A_s \varepsilon_{2s} \tag{A12}$$

Thus, the total strain becomes

$$\varepsilon_2 = \varepsilon_{2m} v_m + \varepsilon_{2s} v_s \tag{A13}$$

Since $\sigma_2 = E_s^*(\varepsilon_{2s} - \alpha_s \Delta T)$, Eqs. (A10) and (A11) may be substituted into Eq. (A13) to give

$$\begin{aligned} \varepsilon_2 &= \frac{\sigma_2}{E_s^*} + \alpha_2 \Delta T \\ &= \frac{\sigma_2 v_s}{E_s^*} + \frac{\sigma_2 v_m}{E_{2m}} + (\alpha_s v_s + \alpha_{2m} v_m)\Delta T \end{aligned} \tag{A14}$$

Therefore, the modulus and thermal expansion coefficient in the 2-direction become

$$E_2^* = \frac{E_{2m} E_s^*}{(E_{2m} v_s + E_s^* v_m)} \tag{A15}$$

and

$$\alpha_2 = \alpha_{2m} v_m + \alpha_s v_s \tag{A16}$$

Expressions for the hybrid composite Poisson's ratios and shear moduli follow from similar derivations.

The constitutive relations for a thin composite lamina with embedded SMA fibers can be derived using a similar engineering approach to give

$$\begin{Bmatrix} \sigma_1 \\ \sigma_2 \\ \tau_{12} \end{Bmatrix} = \begin{bmatrix} Q_{11}^* & Q_{12}^* & 0 \\ Q_{21}^* & Q_{22}^* & 0 \\ 0 & 0 & Q_{66}^* \end{bmatrix} \begin{Bmatrix} \varepsilon_1 \\ \varepsilon_2 \\ \gamma_{12} \end{Bmatrix} + \begin{Bmatrix} \sigma_r^* \\ 0 \\ 0 \end{Bmatrix} v_s - [Q]_m \begin{Bmatrix} \alpha_1 \\ \alpha_2 \\ 0 \end{Bmatrix}_m v_m \Delta T, \quad T > T_s \tag{A17}$$

and

$$\begin{Bmatrix} \sigma_1 \\ \sigma_2 \\ \tau_{12} \end{Bmatrix} = \begin{bmatrix} Q_{11}^* & Q_{12}^* & 0 \\ Q_{21}^* & Q_{22}^* & 0 \\ 0 & 0 & Q_{66}^* \end{bmatrix} \left(\begin{Bmatrix} \varepsilon_1 \\ \varepsilon_2 \\ \gamma_{12} \end{Bmatrix} - \begin{Bmatrix} \alpha_1^* \\ \alpha_2 \\ 0 \end{Bmatrix} \Delta T \right), \qquad T < T_s \tag{A18}$$

where $[Q]_m$ and [Q*] are the reduced stiffness matrices of the composite matrix and the composite lamina, respectively. The [Q*] matrix is temperature dependent and is evaluated using the previously derived relations as

$$(E_1^*, \mu_{12}) = (E_{1m}, \mu_{12m}) v_m + (E_s^*, \mu_s) v_s \tag{A19}$$

and

$$(E_2^*, G_{12}^*) = \frac{(E_{2m} E_s^*,\ G_{12m} G_s^*)}{[(E_{2m}, G_{12m}) v_s + (E_s^*, G_s^*) v_m]} \tag{A20}$$

where the μ's are Poisson's ratios and the G's are the shear moduli. The thermal expansion coefficients α_1^* and α_2 are derived in Eqs. (A9) and (A16).

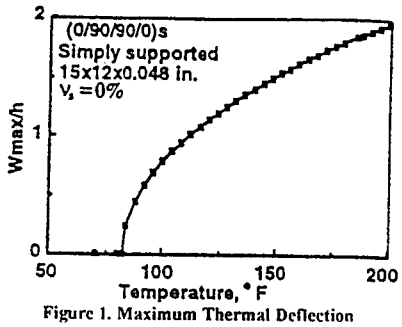

Figure 1. Maximum Thermal Deflection versus Temperature.

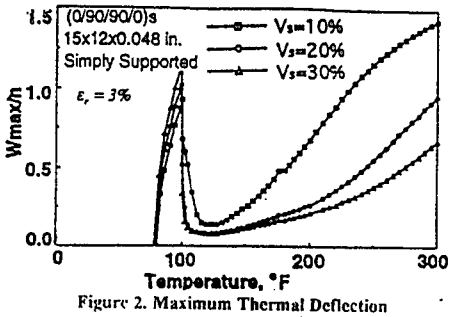

Figure 2. Maximum Thermal Deflection versus Temperature.

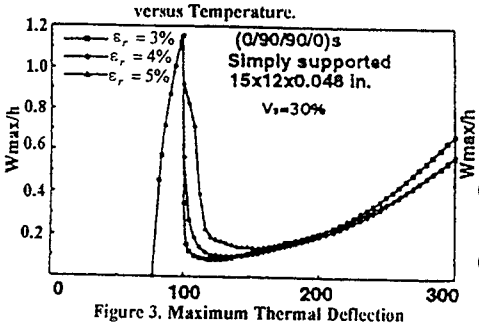

Figure 3. Maximum Thermal Deflection versus Temperature.

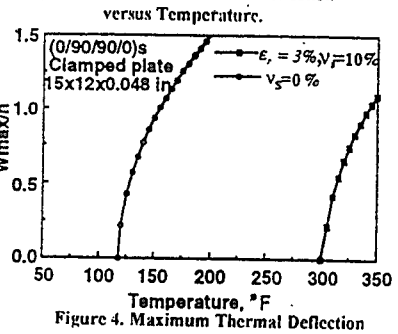

Figure 4. Maximum Thermal Deflection versus Temperature.

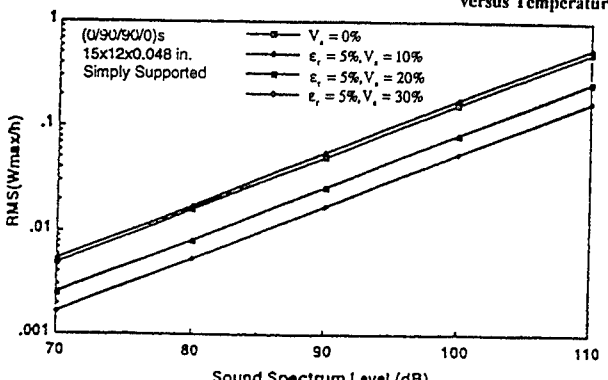

Figure 5. RMS(Wmax/h) vs. Sound Spectrum Level (dB) at 170°F. (Using the lowest 4 Modes)

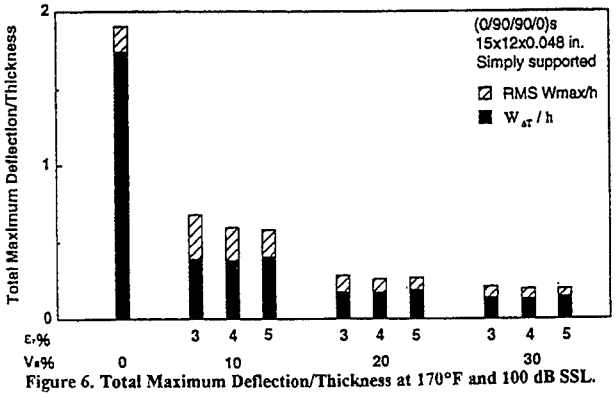

Figure 6. Total Maximum Deflection/Thickness at 170°F and 100 dB SSL.

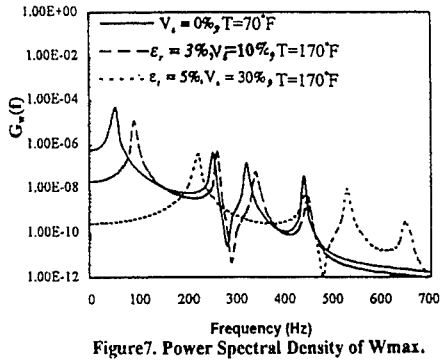

Figure7. Power Spectral Density of Wmax.

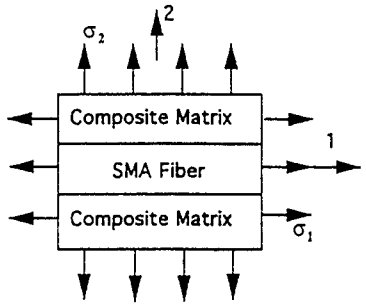

Figure A1 - Representative volume element for SMA fiber-reinforced hybrid composite lamina.

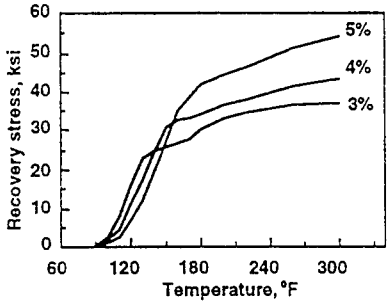

Figure A2 - SMA recovery stress versus temperature and initial strain (Cross et al.,1970).

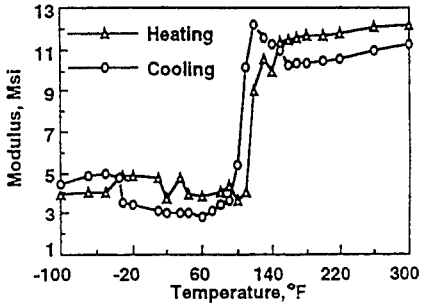

Figure A3 - SMA modulus versus temperature (Cross et al., 1970).

SIGNAL PROCESSING I

DESCRIPTION OF NON-LINEAR CONSERVATIVE SDOF SYSTEMS

Michael Feldman Simon Braun

Faculty of Mechanical Engineering
Technion — Israel Institute of Technology
Haifa, 32000, Israel

1 INTRODUCTION

There are several methods developed for the analysis and identification of non-linear dynamic systems and vibration signals [2, 8, 7, 9]. In the recent past the characterization of the response of non-linear vibration systems has been approached using the Hilbert transform in time domain [4, 3]. The objective was to propose a methodology to identify and classify various types of non-linearity from measured response data. The proposed methodology concentrates on the Hilbert transform signal processing techniques essentially on signal envelope and instantaneous frequency extracting, which enables us to estimate both systems instantaneous dynamic parameters and also elastic (restoring) and friction (damping) force characteristics. When the traditional phase plane $(y, \dot{y})$ of a non-linear system is replaced by the complex plane $(y, \tilde{y})$, the signal envelope, the instantaneous frequency, and the obtained backbone takes an unusual fast oscillation (modulation) form [1]. In addition, the obtained envelope of the signal gains a bias in comparison with the phase plane amplitude [1]. This naturally occurring fast modulation and the bias requires more detail investigation. Further use of the Hilbert methodology for non-linear structures also invites more sophisticated analysis.

2 PHASE PLANE REPRESENTATION

The differential equation of motion for SDOF non-linear conservative vibration system may be written as $m\ddot{y} + K(y) = 0$, where m - the mass, $\ddot{y}$ - the acceleration, and $K(y)$ - the restoring force which is a function of displacement y. The restoring force contains the linear stiffness and also any additional non-linear restoring force component. The second-order differential equation of a conservative system will then take the general form

$$\ddot{y} + k(y) = 0 \tag{1}$$

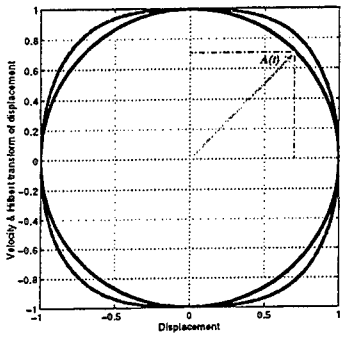

Figure 1: Phase plane (dash line) and Analytic signal (bold line) representation of Duffing equation ($\varepsilon = 5$)

where the term $k(y) = K(y)/m$ represents the restoring force per unit mass as a function of the displacement y.

Traditionally we introduce a new variable $\dot{y}$, which enables us to exclude time from the equation of motion although y and $\dot{y}$ are still time dependent, so $\ddot{y} = \frac{d\dot{y}}{dt} = \frac{d\dot{y}}{dy}\dot{y}$. In the new coordinates Eq.(1) takes the following form: $\frac{d\dot{y}}{dy} = \frac{k(y)}{\dot{y}}$. Using of the new variable $\dot{y}$ is a traditional way of study the motion of an oscillator by representing this motion on the y, $\dot{y}$ plane (Fig. 1), where y and $\dot{y}$ are orthogonal cartesian coordinates [2]. Hence, the time for a full cycle becomes

$$T = 4\int_0^{y_{\max}} \frac{dy}{\sqrt{2\int_y^{y_{\max}} f(\xi)d\xi}} \tag{2}$$

where $y_{\max}$ - the maximum value of the displacement, so the velocity corresponding to $y_{\max}$ in an extreme position is zero, $f(\cdot) \equiv k(\cdot)$. It is a well known fact that the expression obtained for T is a function of $y_{\max}$, thus for non-linear systems the period of oscillation depends on the total stored energy (non-isochronism of oscillation in non-linear system). We shall now divide the angle corresponding to the quarter of a complete circle into n equal small sectors $d\phi = \frac{\pi}{2n}$. Next, we use Eq.(2) to estimate the integral, but separately for each i small interval with new limits: from $l_l = cos[\frac{\pi}{2} - d\phi(i-1)]$ to $l_u = cos(\frac{\pi}{2} - d\phi\, i)$

$$T(i) = 4\int_{l_l}^{l_u} \frac{du}{\sqrt{2\int_y^{y_{\max}} f(\xi)d\xi}} \tag{3}$$

where $u = y/y_{\max}$. In this case only for a linear restoring force the last equation results in a constant value 2π. In general case of non- linear system the current period is a varying function of a phase angle ($T_i(\phi) \neq$ const). An inverse function of the current period will be called an *current angular frequency* $\omega_i(\phi) = \frac{2\pi}{T_i}$. The current angular frequency does not remain constant, but fluctuates between a maximum and a minimum as the radius vector rotates between the y - and $\dot{y}$-axes of the phase plane. Also the radius vector of phase plane $r(\phi)$ becomes to modulate, from its minimum up to the maximum value $r(\phi) =$

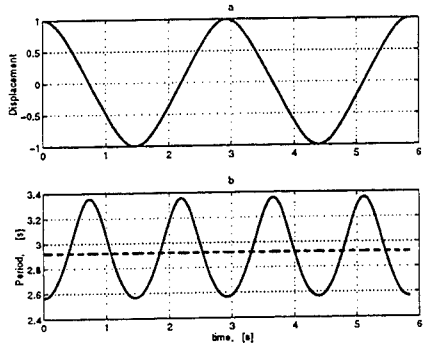

Figure 2: Solution (a) and periods (b) of the Duffing equation ($\varepsilon = 5$, $n = 100$, bold line - the current period, dash line - the mean value of period

$\sqrt{y(\phi)^2 + \dot{y}^2(\phi)} = \sqrt{y(\phi)^2 + 2\int_y^{y_{max}} f(\xi)d\xi}$. To illustrate this interesting phenomena of the current period modulation let us consider an example of Duffing equation.

$$\ddot{y} + (1 + \varepsilon y^2)y = 0 \tag{4}$$

where ε is the non-linear parameter. For the purpose of calculating the current period of free vibration, we substitute expression Eq.(4) into Eq.(3) and obtain $T(i) = 4\int_{l_l}^{l_u} \frac{du}{\sqrt{(1-u^2)(1+\varepsilon(1+u^2)/2))}}$. Figure 2, shows the free vibration signal obtained via numeric integration of the Duffing equation together with the calculated current period of the solution for the total number of small sectors $n = 100$. It is clear that the the current period oscillates two times faster than the non-linear solutions. Now it is clear that the known direct integration for the total period Eq.(2) produces only an average value T which corresponds to the total cycle of the motion.

3 COMPLEX PLANE REPRESENTATION OF ANALYTIC SIGNAL

Let us consider another important technique of representation of vibration process in the time domain on the base of rotating vectors. According the analytic signal theory real vibration process $y(t)$, measured by, say, a transducer, is only one of possible projections (the real part) of some analytic signal $Y(t)$. Then the second projection of the same signal (the imaginary part) $\tilde{y}(t)$ will be conjugated according to the Hilbert transform. Using the traditional representation of analytic signal $Y(t)$ in its complex, trigonometric or exponential form $Y(t) = y(t) + j\tilde{y}(t) = |Y(t)|\,[\,\cos\psi(t) + j\sin\psi(t)\,] = A(t)\,e^{j\psi(t)}$ one can determine its *instantaneous amplitude (envelope, magnitude)*

$$A(t) = |Y(t)| = \sqrt{y^2(t) + \tilde{y}^2(t)} = e^{\mathrm{Re}[\ln Y(t)]} \tag{5}$$

and its *instantaneous phase*

$$\psi(t) = \arctan\frac{\tilde{y}(t)}{y(t)} = \mathrm{Im}[\ln Y(t)] \tag{6}$$

The *instantaneous angular frequency* is the time-derivative of the instantaneous phase:

$$\omega(t) = \dot{\psi}(t) = \frac{y(t)\dot{\tilde{y}}(t) - \dot{y}(t)\tilde{y}(t)}{A^2(t)} = \mathrm{Im}\left[\frac{\dot{Y}(t)}{Y(t)}\right] \tag{7}$$

Each point on complex plane is characterized with the radius vector $A(t)$, and the polar angle ψ (Fig. 1). The analytic signal method is an expedient effective enough to solve general problems of vibration theory, among them – analysis of free and forced nonstationary vibrations (transient processes) and non-linear vibrations.

3.1 The Hilbert transform

The single-value extraction (demodulation) of an envelope and other instantaneous functions of a signal is an issue based on the *Hilbert integral transform* [7]. The Hilbert Transform of a real-valued function $x(t)$ extending from $-\infty$ to $+\infty$ is a real- valued function defined by $\mathbf{H}[y(t)] = \tilde{y}(t) = \frac{1}{\pi}\int_{-\infty}^{\infty}\frac{y(\tau)}{t-\tau}\,d\tau$, where $\tilde{y}(t)$ - the Hilbert transform of the initial process $y(t)$, and meaning of the integral implies its Cauchy principal value. Thus $\tilde{y}(t)$ is the convolution integral of $y(t)$ with $(1/\pi t)$, written as $\tilde{y}(t) = y(t) * (1/\pi t)$. The double Hilbert transform yields the original function with an opposite sign, that's it carries out shifting of the initial signal in $-\pi$. The power (or energy) of a signal and its Hilbert transform are equal. For $n(t)$ lowpass and $y(t)$ highpass signals with nonoverlapping spectra [7],

$$\mathbf{H}[n(t)y(t)] = n(t)\,\tilde{y}(t). \tag{8}$$

3.2 Approximate non-linear system representation

The showning non-linear restoring force $k(y)$ of the second-order conservative system Eq. 1, can be recast into multiplication of varying non-linear natural frequency $\omega_0(y)$ and of the system solution $\ddot{y}+\omega_0^2(y)y = 0$. Let's assume that the varying non-linear natural frequency $\omega_0(y)$ could be separated into two different parts [5]. The first part $\overline{\omega}_0$ is much slower and the second component $\omega_1(y)$ is faster than the system solution, so the equation of motion will be

$$\ddot{y} + [\,\overline{\omega_0^2} + \omega_1^2(y)\,]\,y = 0 \tag{9}$$

The proof of the decomposition of a signal into a sum of low- and high-pass terms, based on Bedrosian's theorem about the Hilbert transform of a product, could be found in [6]. Now according to nonoverlapping property of the Hilbert transform Eq. (8) we use the Hilbert transform for both sides of Eq. 9 $\ddot{\tilde{y}} + \overline{\omega_0^2}\tilde{y} + \widetilde{\omega_1^2}(y)y = 0$. Multiplying each side of the last equation by j and adding it to the corresponded sides of Eq. 9 we get a differential equation in the Analytic signal form $\ddot{Y} + \overline{\omega_0^2}Y + [\,\omega_1^2 + j\widetilde{\omega_1^2}\,]y = 0$, where $Y = y + j\tilde{y}$. This complex equation can be transformed to the commonly accepted form

$$\ddot{Y} + j\delta_{01}Y + \omega_{01}^2 Y = 0 \tag{10}$$

where $\omega_{01}^2 = \overline{\omega_0^2} + \frac{\omega_1^2 y^2 + \widetilde{\omega_1^2} y\tilde{y}}{A^2}$ - the varying natural frequency, $\delta_{01} = \frac{\widetilde{\omega_1^2} y^2 - \omega_1^2 y\tilde{y}}{A^2}$ - the fast varying fictitious friction parameter, and $Y = y + j\tilde{y}$ - is the complex solution.

The obtained equation of the non-linear system has the varying natural frequency, consisting of slow $\overline{\omega_0}$ and fast component, and also has the fast varying fictitious friction parameter δ_{01}. It should be pointed that this non-stationary equation is not a real equation of motion. It is just an artificial fictitious equation which produce the same non-linear vibration signal.

3.3 Non-stationary equation of motion in the analytic signal form

Taking into account the analytic signal representations, enables one to consider this equivalent equation of motion so as to estimate instantaneous natural frequency and instantaneous damping coefficient.
Some general form of a differential equation of motion in the analytic signal form could be written

$$\ddot{Y} + 2h_0(A)\dot{Y} + \omega_0^2(A)Y = 0 \tag{11}$$

where Y - the system solution in the analytic signal form, h_0 - the instantaneous damping coefficient, ω_0 - the instantaneous undamped natural frequency. This equation of motion will have varying coefficients that satisfied the envelope and instantaneous frequency of non-linear oscillated solution.
Solving two equations for real and imaginary parts of Eq.(11), we can write the expression for non-stationary coefficients as functions of a first and a second derivative of the signal envelope and the instantaneous frequency.

$$\begin{aligned} \omega_0^2(t) &= \omega^2 - \frac{\ddot{A}}{A} + \frac{2\dot{A}^2}{A^2} + \frac{\dot{A}\dot{\omega}}{A\omega} \\ h_0(t) &= -\frac{\dot{A}}{A} - \frac{\dot{\omega}}{2\omega}, \end{aligned} \tag{12}$$

where $\omega_0(t)$ - instantaneous undamped natural frequency of the system, $h_0(t)$ - instantaneous damping coefficient of the system, ω, A - instantaneous frequency and envelope (amplitude) of the vibration with their first and second derivatives ($\dot{\omega}$, $\dot{A}$, $\ddot{A}$).

3.4 Two-component signal representation

Let us consider a conservative system having a single degree of freedom that are governed by simple non-linear differential equation having the form Eq. 1 Assuming k can be expanded, one can rewrite Eq. 1 as [8]

$$\ddot{y} + \sum_{n=1}^{N} \alpha_n y^n = 0 \tag{13}$$

where $\alpha_n = \frac{1}{n!}k^{(n)}(y_0)$ and $k^{(n)}$ denotes the nth derivative with respect to the argument. We assume that the solution of Eq. 13 can be represented by an expansion having the form $y(t,\varepsilon) = \varepsilon y_1(t) + \varepsilon^2 y_2(t) + \varepsilon^3 y_3(t) + \ldots$ where the y_n are independent of ε. Retaining

Table 1: Formulas for extreme and mean values of instantaneous frequency and amplitude of biharmonics

Inst. amplitude	Inst. frequency
$A_{\min} = A_1 - A_2$	$\omega_{\min} = \omega_1 - \frac{\omega_2 - \omega_1}{A_1/A_2 - 1}$
$A_{\max} = A_1 + A_2$	$\omega_{\max} = \omega_1 + \frac{\omega_2 - \omega_1}{A_1/A_2 + 1}$
$\bar{A} = A_1\sqrt{1 + A_2^2/A_1^2}$	$\bar{\omega} = \omega_1 + \frac{\omega_2 - \omega_1}{A_1^2/A_2^2 + 1}$

two first main terms of the solution we will get an equation where each of amplitude and frequency is a function of linear and non-linear parameters of the system (Eq. 13).

$$y(t) = y_1 + y_2 = A_1 \cos \omega_1 t + A_2 \cos \omega_2 t \tag{14}$$

Universally known that the more close the frequency of the first term to the precise solution $\omega_1 \rightarrow 2\pi/T$ (Eq. 2) the better approximation.

Consider the non-linear solution that consists of two quasi-harmonics each one with different amplitude and frequency in time domain. In this case, the signal can be modeled as a weighted sum of two monocomponent signals, each one with its own instantaneous frequency and amplitude function. Assuming that each individual signal has a large bandwidth and time duration product (with a purely positive IF), application of the Hilbert transform for both sides of Eq.(14) will produce an analytic signal of the form:

$$Y(t) = A_1 e^{j\omega_1 t} + A_2 e^{j\omega_2 t} \tag{15}$$

The envelope and the instantaneous frequency of double-component vibration signal $Y(t)$ are:

$$A(t) = \{A_1^2 + A_2^2 + 2A_1A_2 \cos[(\omega_2 - \omega_1)t]\}^{1/2}, \tag{16}$$

$$\omega(t) = \omega_1 + \frac{A_2^2 + A_1A_2 \cos[(\omega_2 - \omega_1)t]}{(\omega_2 - \omega_1)^{-1}A^2(t)}. \tag{17}$$

From Eq.(16) it can be seen that signal envelope consists of two different parts, that is a constant part included sum of component amplitudes squared A_1^2, A_2^2 and also a fast varying (oscillating) part, the multiplication of these amplitudes with function *cos* of relative phase angle between two components. The same inference could be made about the instantaneous frequency of the two-terms solution. The obtained formulas for extreme and mean values of instantaneous frequency and amplitude of the biharmonics are shown in Table 1.

It is significant that the mean value of the instantaneous amplitude is very close to the corresponded amplitude of the first harmonics ($\bar{A} \approx A_1$). Also mean value of the instantaneous frequency agrees closely with the frequency of the first harmonics ($\bar{\omega} \approx \omega_1$). Again consider an example of the Duffing equation (Eq. 4). Using for instance the method of the analytic signal representation [9] one can get an equation for the first order approximation of the free vibration frequency

$$\omega_1^2 = 1 + \frac{3\varepsilon a^2}{4} \tag{18}$$

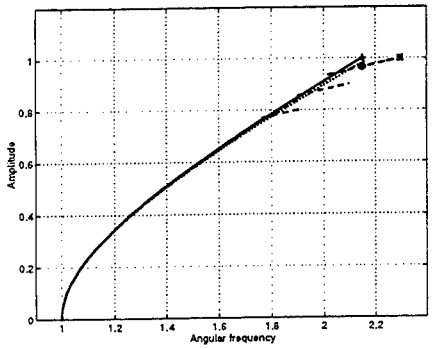

Figure 3: Backbone of the Duffing system ($\varepsilon = 5$)

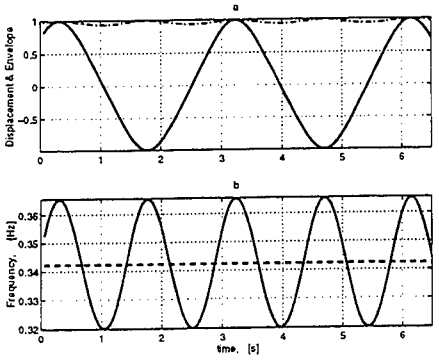

Figure 4: The solution (a) and the instantaneous frequency (b) of the Duffing equation ($\varepsilon = 5$)

where $a = y_{\max}$ is some maximum of the displacement. This approximation of free vibration frequency (dot line on Fig. 3) maps an approximate backbone very close to the traditional precise backbone (bold line on Fig. 3).
Let now an approximate solution be in a form which includes the first two harmonics only

$$y(t) = y_1(t) + y_2(t) = A_1 cos\omega_1 t + A_2 \cos\omega_2 t \tag{19}$$

where $\omega_2 = 3\omega_1$, $A_2 = \frac{\varepsilon a^3}{k_\varepsilon}$, $A_1 = 1 - A_2$, k_ε - numerical coefficient. The instantaneous frequency and the envelope of the solution derived from the Hilbert transform takes the form of oscillated functions with double frequency (Fig. 4). The approximate double component solution ($\varepsilon = 5$, $k_\varepsilon = 156$) coincides very closely with the numerical solution (Fig. 4, a). The corresponded envelope (dash-dot line), and instantaneous frequency (b) of the Duffing equation is also plotted in Figure 4.
Maximum values of the envelope $A(t)$ (Eq. 16) are equal to the chosen maximum of displacement a, but all other points of the envelope (dash-dot line on Fig. 4, a) including the average value of amplitude $\overline{A}$ are smaller than the maximum of displacement a. Now it is clear that for non-linear conservative vibrations two different estimations of amplitude could be suggested. The first estimation is the maximum of displacement $y_{\max}$ which is

equal to the maximum of envelope $y_{max} = A_{max}$. The second estimation is the average value of envelope $\bar{A}$. The difference between the average value of envelope $\bar{A}$ and the maximum of displacement a could be considered as a small bias of amplitude of the solution.

It is vital to note that the mean value of the instantaneous frequency $\bar{\omega}$ obtained through the Hilbert transform is equal to the theoretical value of the free vibration frequency (Eq. 2). On Fig. 4, b the dash line shows these two coincident functions. $\bar{\omega} = 2\pi/T$ This fact indicates that the Hilbert transform is best representation of non-linear vibrations.

3.5 Free vibration frequency and amplitude dependence

Because we considered several different representations of vibration amplitude it is evident that we get some different backbone depictions. A traditional theoretical precise backbone of non-linear system is a dependency between the average free vibration frequency $\bar{\omega}$ (corresponded to the average total cycle of vibration, Eq. 2) and the maximum displacement y_{max} (Fig. 3, bold line). For a conservative system with a chosen maximum displacement, the theoretical backbone is no more than a point (+ on Fig. 3). As far as we can use the mean value of the envelope $\bar{A}$, a dependency between this mean value and the average free vibration frequency $\bar{\omega}$ could be a new kind of the theoretical backbone (dotted line on Fig. 3). But the difference between these two backbone definitions is very small and corresponds to the small bias. According to the traditional vibration system representation, conservative non-linear system has a constant amplitude. It means that vibrations of a conservative Duffing system should map on backbone plot just as a point with a constant amplitude and frequency.

A somewhat different backbone for a conservative system is gained according to the instantaneous frequency and amplitude representation. Eliminating the time dependent oscillating part $cos[(\omega_2 - \omega_1)t]$ from Eq.(16) and Eq.(17), we shall find the equation between signal instantaneous characteristics (envelope and frequency) and initial four parameters of signal components

$$A^2 = \frac{(A_1^2 - A_2^2)(\omega_2 - \omega_1)}{\omega_1 + \omega_2 - 2\omega}, \; A_1 \neq A_2, \omega_1 \neq \omega_2. \tag{20}$$

Equation (20) determines the signal envelope A as a function of instantaneous frequency ω in the form of an hyperbola, whose length and curvature depends on four initial parameters of the biharmonics. So according to the Hilbert transform the instantaneous backbone of a non-linear conservative system stretches to a very short hyperbola (dashline on Fig. 3). This short length of hyperbola is the same for both the numerical solution and the approximate double component solution. The hyperbola goes very close both to the traditional theoretical point of maximum displacement (+) and to the approximate mean value of envelope (Fig. 3, **o**). Figure 3 also includes two additional backbones (short dash lines) corresponding to different maximum values (a) of the displacement.

3.6 Real non-linear force estimation

The proposed direct time domain method based on the Hilbert transform allows a direct extraction of the linear and non-linear parameters of the system $\ddot{y} + \omega_0(y)^2 y = 0$ from the

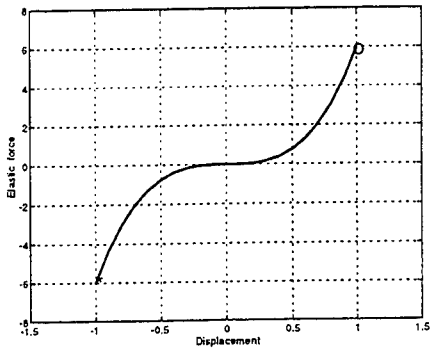

Figure 5: Cubic force characteristics of Duffing model ($\varepsilon = 5$)

measured time signal y of output. The resulting non-linear algebraic equations (Eq.12) are rather simple and do not depend on the type of non-linearity that exists in the structure. When applying this direct method for transient vibration, the instantaneous modal parameters are estimated directly, with the corresponding equation

$$\ddot{y} + \delta_{01}\tilde{y} + \omega_{01}^2 y = 0 \tag{21}$$

where ω_{01}^2 - is the fast varying natural frequency, δ_{01} - is the fast varying fictitious friction parameter, y - is the displacement, and $\tilde{y}$ - is the Hilbert transform of the displacement. With this representation of a non-linear solution we can try to solve an inverse identification problem, namely, the problem of estimation of the initial non-linear elastic force characteristics.

3.6.1 Decomposition technique

Let us consider the case of a conservative system with an initial non-linear spring. According to Eq. 11 this real non-linear elastic force will produce two different fictitious members (elastic and hysteretic damping). The new restoring force, here assumed to be a function of displacement y and its Hilbert transform $\tilde{y}$. This restoring force includes both the fast hysteretic damping $\delta_{01}\tilde{y}$ and the fast elastic force $\omega_{01}^2 y$. It means, that the initial non-linear spring force $\omega_0(y)^2 y$ is split into two terms, and, by summing over the terms, the initial non-linear force characteristics can be extended. Therefore a simple composition of these two members of equation of motion (Eq. 21) will result in the real non-linear force characteristics:

$$k[y(t)] = 2h_0(t)\dot{y} + \omega_0^2(t)y \tag{22}$$

where $k[(y)]$ is the real elastic instantaneous force, $h_0(t)$ is the instantaneous damping coefficient, $\omega_0(t)$ is the instantaneous undamped natural frequency. Fig. 5 shows an example of the instantaneous elastic force identification for the Duffing system (Eq. 4). Fig. 5 includes the results of the identification according to formula Eq. 22 together with the initial cubic force characteristics $k(y) = (1 + 5y^2)y$, but these lines agree so closely that there is no a difference.

3.6.2 Scaling technique

Instead of the previous identification of the detail force characteristics, we can express only the relation between the maximum of elastic force and the maximum of displacement. It can be determined by following consideration. The total energy of a conservative vibration system is constant. During free vibration of the corresponded fictitious model (Eq. 11), for each moment the energy is partly kinetic, partly potential, and partly fictitious alternating positive or negative damping.
To estimate maximum of elastic force we can find time points when all energy is stored in the form of strain energy in elastic deformation and the fictitious damping energy is zero. Using for instance the biharmonics representation of non-linear vibrations (Eq.15) one can show that these time points correspond to the maximum of displacement. This is an important conservative vibration system property, that around every peak point of the displacement the corresponding value of the velocity is equal to zero and vice versa. Therefore around every peak point of the displacement the contribution of the velocity in the varying instantaneous elastic force is negligibly small: $y(t_i) = A(t_i),\ \dot{y}(t_i) = 0$. The number of these peak points is far less than a total number of points of a vibration signal. Therefore it could be recommended to extract the envelope of the fictitious elastic force $\omega_0^2(t)y$ to obtain the average value of the envelope. The obtained average envelope has a small bias relative to maximums of the spring force. Using the Hilbert transform and the obtained expressions we can extract the maximum values of non-linear elastic force corresponded to the maximum of displacement (circle and star point on Fig. 5).

4 CONCLUSIONS

We can draw the following conclusions from the analytic signal representation.
Whatever the method of non-linear vibration representation, both the instantaneous frequency and the amplitude of free vibration is a complicated signal. Non-linear solution could be represented by an expansion of members with different frequencies or by a time varying signal with oscillated instantaneous frequency and envelope.
The instantaneous frequency and envelope of non-linear vibration obtained via the Hilbert transform are time varying fast oscillating functions. For example in the presence of a cubic non-linearity and a threefold high harmonics, the frequency of the instantaneous parameter oscillation is twice that the main frequency of vibration.
The mean value of the instantaneous frequency obtained through the Hilbert transform is equal to the theoretical total cycle average value of the free vibration frequency. The maximum value of vibration envelope is equal to the maximum of displacement. These facts indicates that the Hilbert transform is one of the best representations of non-linear vibrations. Naturally there is a small difference (the bias) between the average value of the envelope and its maximum value.
The dependency between the average envelope and the average instantaneous frequency plots the backbone that practically coincides with the theoretical backbone of non-linear vibrations.
Using the proposed Hilbert transform analysis in time domain we can extract both the instantaneous undamped frequency and also the real non-linear elastic force characteristics.

References

[1] P. Adamopoulos, W. Fong and J.K. Hammond. Envelope and instantaneous phase characterisation of nonlinear system response. Proc. of the VI Int. Modal Analysis Conf., 1988, pp. 1365 - 1371

[2] A.A. Andronov, A.A. Vitt, and S.E. Khaikin. Theory of oscillators. Pergamon Press, 1966, 815 p.

[3] M. Feldman. Non-linear system vibration analysis using Hilbert Transform — I: Free vibration analysis method 'FREEVIB', *Mechanical Systems and Signal Processing*, 1994, 8(2), pp. 119 - 127.

[4] M. Feldman, S. Braun. Analysis of typical non-linear vibration systems by using the Hilbert transform. Proc. of the XI Int. Modal Analysis Conf., Kissimmee, Florida, 1993, pp. 799 - 805.

[5] M. Feldman, S. Braun. Non-linear spring and damping forces estimation during free vibration. Proc. of the ASME Fifteenth Biennial Conference on Mechanical Vibration and Noise Conf., Boston, Massachusetts, 1995, V 3, 1241-1248 pp.

[6] Stefan L. Hahn. The Hilbert Transform of the Product $a(t)cos(\omega_0 t + \phi_0)$. Bulletin of the Polish Academy of Sciences, Technical Sciences, Vol. 44, No 1, 1996, pp.75-80.

[7] Sanjit K. Mitra and James F. Kaiser. Handbook for digital signal processing. Wiley-Interscience, 1993, 1268 p.

[8] Ali H. Nayfeh. Nonlinear oscillations. Wiley-Interscience, 1979, 704 p.

[9] L. Vainshtein, D. Vakman. Frequencies separation in the theory of vibration and waves (in Russian). 1983, Moscow, Nauka, 228 p.

A RATIONAL POLYNOMIAL TECHNIQUE FOR CALCULATING HILBERT TRANSFORMS

N.E.King
Ford Motor Company Ltd.
Research and Engineering Centre
Laindon
Basildon
Essex SS15 6EE
United Kingdom

K.Worden
Dynamics Research Group
Department of Mechanical Engineering
University of Sheffield
Mappin Street
Sheffield S1 3JD
United Kingdom

Abstract

This paper presents a new technique for calculating Hilbert transforms of nonlinear system Frequency Response Functions (FRFs). The method employs rational function and pole-zero decompositions of the FRF. The new method allows Hilbert transforms for zoomed, or generally truncated, data without the use of correction terms. The method is validated using a computer simulation of a Single Degree-Of-Freedom (SDOF) nonlinear oscillator.

INTRODUCTION

It is well-known that the occurrence of nonlinearities in engineering structures can have a significant effect on their behaviour. The most spectacular examples of this can be found in the literature relating to chaotic systems; the response of such a system to a deterministic excitation can be unpredictable beyond a short time scale. Also, any stability analysis for a nonlinear system will depend critically on the type of nonlinearity present. The question of detecting structural nonlinearity is therefore of some importance.

The Hilbert transform is now established as a means of diagnosing structural nonlinearity on the basis of measured Frequency Response Function (FRF) data [8]. It is essentially a mapping on the FRF $G(\omega)$,

$$\mathcal{H}[G(\omega)] = \tilde{G}(\omega) = -\frac{1}{i\pi}\int_{-\infty}^{\infty} d\Omega \frac{G(\Omega)}{\Omega - \omega} \tag{1}$$

(where the integral is to be understood as a principal value). This mapping reduces to the identity on those functions corresponding to linear systems. For nonlinear systems, the Hilbert transform results in a distorted version $\tilde{G}$, of the original FRF, with the form of the distortion often yielding some indication of the type of nonlinearity.

The origin of the distortion is well-known [10]; suppose $G(\omega)$ is decomposed so,

$$G(\omega) = G^+(\omega) + G^-(\omega) \tag{2}$$

where $G^+(\omega)$ (resp. $G^-(\omega)$) has poles only in the upper (resp. lower) half of the complex ω-plane. It is a straightforward exercise in the calculus of residues [9], to show that (with ω on the real line),

$$-\frac{1}{i\pi}\int_{-\infty}^{\infty}\frac{d\Omega}{(\Omega-p)(\Omega-\omega)} = \frac{1}{\omega-p} \tag{3}$$

if p is in the upper half-plane, and,

$$-\frac{1}{i\pi}\int_{-\infty}^{\infty}\frac{d\Omega}{(\Omega-p)(\Omega-\omega)} = -\frac{1}{\omega-p} \tag{4}$$

if p is in the lower-half plane. It follows that,

$$\mathcal{H}[G^{\pm}(\omega)] = \pm G^{\pm}(\omega) \tag{5}$$

The distortion suffered in passing from the FRF to the Hilbert transform will then be given by the simple relation,

$$\Delta G(\omega) = \mathcal{H}[G(\omega)] - G(\omega) = -2G^-(\omega) \tag{6}$$

This relation has already yielded some interesting results [4] and is the basis of the technique presented in this paper. The advantages of the new approach over the standard time- or frequency-domain methods will now be explained.

One of the major problems in using the Hilbert transform on FRF data, occurs when non-baseband (data which does not start at zero frequency) or band-limited data is employed. Practically speaking, all data will fall into one of these categories and the problem of neglecting the contribution of the 'out of band' data always exists. Establishing baseband data is rarely a problem in simulation work, but can be a problem with experimental testing. For example, it is known [5], that the use of random excitation for nonlinear systems produces a FRF which is invariant under the Hilbert transform. This means that other excitation signals must be used. Most commonly, a stepped-sine signal is used, and this is time-consuming due to the need to reach a steady-state condition at each frequency increment. As a consequence, this excitation is usually applied over a limited frequency range, say ω_{min} to ω_{max}.

Unfortunately, the idealised Hilbert transform of (1), is an integral over a doubly-infinite frequency range. In practice, the data over the intervals $(-\infty, \omega_{min})$ and (ω_{max}, ∞) will be unavailable. By making use of the parity

(oddness or eveness) of the real and imaginary parts of the FRF, the Hilbert transform can be cast in the following form,

$$\Re\tilde{G}(\omega) = -\frac{2}{\pi}\int_0^\infty d\Omega\ \frac{\Im G(\Omega)\,\Omega}{\Omega^2-\omega^2} \tag{7}$$

$$\Im\tilde{G}(\omega) = \frac{2\omega}{\pi}\int_0^\infty d\Omega\ \frac{\Re G(\Omega)}{\Omega^2-\omega^2} \tag{8}$$

and now the integrals are over the range 0 to ∞; data will be missing from the intervals $(0, \omega_{min})$ and (ω_{max}, ∞).

The problem of truncated FRF data is usually overcome by adding correction terms to the Hilbert transform evaluated from ω_{min} to ω_{max}. In general, two corrections are needed, one for each of the missing intervals.

In order to display the inconvenience of the procedure, a review of the relevant theory follows. It will later be shown that the method proposed in this paper circumvents the problem of the missing intervals i.e. truncation of the data.

CORRECTION TERMS

There are essentially three methods of correcting Hilbert transforms, they will be described below in order of complexity.

The Fei Correction Method

This approach was developed by Fei [2] for baseband data and is based on the asymptotic behaviour of the FRFs of linear systems. The form of the correction term is entirely dependent on the FRF type; receptance, mobility, or inertance. As each of the correction terms is similar in principle, only the term for mobility will be described.

The general form of the mobility function for a linear system with proportional damping is,

$$G(\omega) = \sum_{k=1}^{N} \frac{i\omega A_k}{\omega_k^2 - \omega^2 + i2\zeta_k\omega_k\omega} \tag{9}$$

where: A_k is the complex modal amplitude of the k^{th} mode; ω_k is the undamped natural frequency of the k^{th} mode and ζ_k is its viscous damping ratio. By assuming that the damping is small and that the truncation frequency, ω_{max} is much higher than the natural frequency of the highest mode, equation (9) can be reduced to (for $\omega > \omega_{max}$),

$$G(\omega) = -i\sum_{k=1}^{N} \frac{A_k}{\omega} \tag{10}$$

which is an approximation to the 'out of band' FRF. This term is purely imaginary and thus provides a correction for the real part of the Hilbert transform via equation (7). No correction term is applied to the imaginary part as the error is assumed to be small under the specified conditions.

The actual correction is the integral in equation (1) over the interval (ω_{max}, ∞). Hence the correction term, denoted $C^R(\omega)$, for the real part of the Hilbert transform is,

$$C^R(\omega) = -\frac{2}{\pi} \int_{\omega_{max}}^{\infty} d\Omega \frac{\Omega \Im(G(\Omega))}{\Omega^2 - \omega^2} = -\frac{2}{\omega} \sum_{k=1}^{N} A_k \int_{\omega_{max}}^{\infty} \frac{d\Omega}{\Omega^2 - \omega^2} \tag{11}$$

which, after a little algebra [2], leads to,

$$C^R(\omega) = \frac{-\omega_{max} \Im(G(\omega_{max}))}{\pi \omega} \ln\left(\frac{\omega_{max} + \omega}{\omega_{max} - \omega}\right) \tag{12}$$

The Haoui Correction Method

The second correction term which again, caters specifically for baseband data, is based on a different approach. The term was developed by Haoui [3], and unlike the Fei correction has a simple expression independent of the type of FRF data used. The correction for the real part of the Hilbert transform is,

$$C^R(\omega) = -\frac{2}{\pi} \int_{\omega_{max}}^{\infty} d\Omega \frac{\Omega \Im(G(\Omega))}{\Omega^2 - \omega^2} \tag{13}$$

The analysis proceeds by assuming a Taylor expansion for $G(\omega)$ about ω_{max} and expanding the term $(1 - \omega^2/\Omega^2)^{-1}$ using the binomial theorem. If it is assumed that ω_{max} is not close to a resonance so that the slope $dG(\omega)/d\omega$ (and higher derivatives) can be neglected, a straightforward calculation yields,

$$C^R(\omega) = C^R(0) - \frac{\Im(G(\omega_{max}))}{\pi} \left[\frac{\omega^2}{\omega_{max}^2} + \frac{\omega^4}{2\omega_{max}^4} + \ldots\right] \tag{14}$$

where $C^R(0)$ is estimated from,

$$C^R(0) = \Re(G(0)) - \left[-\frac{2}{\pi} \int_{0+\epsilon}^{\omega_{max}} d\Omega \frac{\Im(G(\Omega))}{\Omega}\right] \tag{15}$$

Using the same approach, the correction term for the imaginary part, denoted by $C^I(\omega)$, Can be obtained,

$$C^I(\omega_{max}) = \frac{2}{\pi}\Re(G(\omega_{max}))\left[\frac{\omega}{\omega_{max}} + \frac{\omega^3}{3\omega_{max}^3} + \frac{\omega^5}{5\omega_{max}^5} + \ldots\right] \tag{16}$$

The Simon Correction Method

This method of correction was proposed by Simon [7]; it allows for truncation at a low frequency, ω_{min}, and a high frequency ω_{max}. It is therefore suitable for use with zoomed data. This facility makes the method the most versatile of the three. As before, it is based on the behaviour of the linear FRF, say equation (9) for mobility data. Splitting the Hilbert transform over three frequency ranges: $(0, \omega_{min})$, $(\omega_{min}, \omega_{max})$ and (ω_{max}, ∞), the truncation errors on the real part of the Hilbert transform, $B^R(\omega)$ at low frequency and the now familiar $C^R(\omega)$ at high frequency, can be written as,

$$B^R(\omega) = -\frac{2}{\pi}\int_0^{\omega_{min}} d\Omega \frac{\Omega\Im(G(\omega))}{\Omega^2 - \omega^2} \tag{17}$$

and

$$C^R(\omega) = -\frac{2}{\pi}\int_{\omega_{max}}^{\infty} d\Omega \frac{\Omega\Im(G(\omega))}{\Omega^2 - \omega^2} \tag{18}$$

If the damping can be assumed to be small, then rewriting equations (17) and (19) using the mobility form (9), yields,

$$B^R(\omega) = \frac{2}{\pi}\int_0^{\omega_{min}} d\Omega \sum_{k=1}^{N} \frac{\Omega^2 A_k}{(\Omega^2 - \omega_k^2)(\Omega^2 - \omega^2)} \tag{19}$$

and

$$C^R(\omega) = \frac{2}{\pi}\int_{\omega_{max}}^{\infty} d\Omega \sum_{k=1}^{N} \frac{\Omega^2 A_k}{(\Omega^2 - \omega_k^2)(\Omega^2 - \omega^2)} \tag{20}$$

Evaluating these integrals gives,

$$B^R(\omega) + C^R(\omega) = -\sum_{k=1}^{N} \frac{A_k}{\pi(\omega^2 - \omega_k^2)}\left\{\omega_k \ln\left(\frac{(\omega_{max} + \omega_k)(\omega_k - \omega_{min})}{(\omega_{max} - \omega_k)(\omega_k + \omega_{min})}\right)\right.$$
$$\left. + \omega \ln\left(\frac{(\omega + \omega_{min})(\omega_{max} - \omega)}{(\omega - \omega_{min})(\omega_{max} + \omega)}\right)\right\} \tag{21}$$

The values of the modal parameters A_k and ω_k are obtained from an initial modal analysis.

Summary

None of the three correction methods can claim to be faultless; truncation near to a resonance will always give poor results. Considerable care is needed to obtain satisfactory results. The Fei and Haoui techniques are only suitable for use with baseband data and the Simon correction requires a prior modal analysis. The following section proposes an approach to the Hilbert transform which does not require correction terms and thus overcomes these problems.

THE RATIONAL POLYNOMIAL METHOD

The basis of this approach to calculating a Hilbert transform is to establish the position of the FRF poles in the complex plane and thus form the decomposition (2). This is achieved by formulating a Rational Polynomial (RP) model of the FRF over the chosen frequency range and then converting this into the required form via a pole-zero decomposition.

A general FRF may be expressed as the sum of a number of modes, e.g. equation (9) for the mobility form. This 'summation' form is readily expanded into a rational polynomial representation,

$$G(\omega) = \frac{Q(\omega)}{P(\omega)} \tag{22}$$

where,

$$Q(\omega) = \sum_{i=0}^{n_Q} a_i \omega^i \qquad P(\omega) = \sum_{i=0}^{n_P} b_i \omega^i \tag{23}$$

and the polynomial coefficients a_i and b_i, are functions of the natural frequencies, dampings and A_k of the modes. Modal analysis methods in the frequency-domain assume either a summation form (9) or an RP form (22). The coefficients are determined using optimisation schemes which find the parameters which best fit the data. Various methods exist which maximise the numerical conditioning and precision of the resulting coefficients. The RP models fitted for the current work use an 'instrumental variable' approach which minimises the effects of noise and produces unbiased coefficients. The details of the method can be found in [1].

Once the RP model G_{RP} is established, it can be converted into a pole-zero form,

$$G_{RP}(\omega) = \frac{\prod_{i=1}^{n_Q} (\omega - q_i)}{\prod_{i=1}^{n_P} (\omega - p_i)} \tag{24}$$

where q_i and p_i are the (complex) zeroes and poles respectively of the function. The next stage is a long division and partial-fraction analysis in order to produce the decomposition (2). If p_i^+ (resp. p_i^-) are the poles in the upper (resp. lower) half-plane, then,

$$G_{RP}^+(\omega) = \sum_{i=1}^{N_+} \frac{C_i^+}{\omega - p_i^+} \qquad G_{RP}^-(\omega) = \sum_{i=1}^{N_-} \frac{C_i^-}{\omega - p_i^-} \tag{25}$$

where C_i^+ and C_i^- are coefficients fixed by the partial fraction analysis. N_+ (resp. N_-) is the number of poles in the upper (resp. lower) half-plane. Once this decomposition is established, the Hilbert transform follows from (6). (It is assumed here that the RP model has more poles than zeros. If this is not the case, the decomposition (2) is supplemented by a term $G^0(\omega)$ which is analytic. Equation (6) which is used to compute the Hilbert transform is unchanged.)

The procedure described above is demonstrated in the following section using data from numerical simulation.

SIMULATION DATA

A simulated Duffing oscillator system with equation of motion,

$$\ddot{y} + 20\dot{y} + 10000y + 5 \times 10^9 y^3 = X \sin(\omega t) \tag{26}$$

was chosen to test the calculation technique. Data was generated over 256 spectral lines from 0 to 38.4 *Hz* in a simulated stepped-sine test based on a standard fourth-order Runge-Kutta scheme [6]. The data was truncated by removing data above and below the resonance leaving 151 spectral lines in the range 9.25-32.95 *Hz*.

Two simulations were carried out. In the first, the Duffing oscillator was excited with $X = 1.0$ N giving a change in the resonant frequency from the linear conditions of 15.9 *Hz* to 16.35 *Hz* and in amplitude from 503.24×10^{-6} m/N to 483.0×10^{-6}, m/N. The FRF Bode plot is shown in Figure 1, the cursor lines indicate the range of the FRF which was used. The second simulation took $X = 2.5$ N which was a high enough to produce a jump bifurcation in the FRF. In this case the maximum amplitude of 401.26×10^{-6} m/N occurred at a frequency of 19.75 *Hz*. Note that in the case of this nonlinear system the term 'resonance' is being used to indicate the position of maximum gain in the FRF.

RESULTS

The first stage in the calculation process is to establish the RP model of the FRF data. On the first data set with $X = 1$, in order to obtain an accurate model of the FRF, 24 denominator terms and 25 numerator terms

were used. The number of terms in the polynomial required to provide an accurate model of the FRF will depend on several factors including: the number of modes in the frequency range, the level of distortion in the data and the amount of noise present. The accuracy of the RP model is evident from Figure 2 which shows a Nyquist plot of the original FRF, $G(\omega)$ with the model $G_{RP}(\omega)$ overlaid on the frequency range 10 - 30 *Hz*.

The next stage in the calculation is to obtain the pole-zero decomposition (24). This was accomplished here by solving the numerator and denominator polynomials using a computer algebra package. The zeros and poles are given in Tables 1 and 2 respectively. It may not be necessary to obtain the zeroes of the model, this is under investigation. In order to check the stability of the root extraction, the pole-zero model was compared with the measured data, an exact overlay was obtained.

The penultimate stage of the procedure is to establish the decomposition (2). Given the pole-zero form of the model, the individual pole contributions are obtained by carrying out a partial fraction decomposition, because of the complexity of the model, a computer algebra was again used.

Finally, the Hilbert transform is obtained by flipping the sign of $G^{-}(\omega)$, the sum of the pole terms in the lower half-plane. The result of ths calculation for the low excitation data is shown in Figure 3 in a Bode amplitude format. The overlay of the original FRF data and the Hilbert transform calculated by the RP method is given, the frequency range has been limited to 10 - 30 *Hz*.

A simple test of the accuracy of the RP Hilbert transform was carried out. A Hilbert transform of the low excitation data was calculated using a standard FFT based technique [5] on an FRF using a range of 0-50 *Hz* in order to minimise truncation errors in the calculation. Figure 4 shows an overlay of the RP Hilbert transform (from the truncated data) with that calculated from the FFT technique. The Nyquist format is used. The figure shows that a satisfactory level of agreement has been achieved with the new calculation method.

The second, high excitation, FRF used to validate the approach contained a bifurcation or 'jump' and thus offered a more stringent test of the RP curve-fitter. A greater number of terms in the RP model were required to match the FRF. Figure 5 shows the overlay achieved using 32 terms in the denominator and 33 terms in the numerator. There is no discernable difference. Following the same calculation process as above leads to the Hilbert transform shown in Figure 6, shown with the FRF.

CONCLUSIONS

A method of calculating Hilbert transforms from truncated Frequency Response Function (FRF) data is presented which has no need for cor-

rection terms. The rational polynomial (RP) technique operates without needing the functional form of the FRF data, it applies equally well to receptance, mobility and inertance forms.

The main limitation in the method is in the ability of the RP curve-fitter to match the measured FRF. Sensitivity of the method to noise must be investigated. A further problem relates to uniqueness and overfitting of the model. This has already been addressed in the context of modal analysis e.g. through the use of stability plots, and the solutions discovered there should apply.

The implementation of the algorithm used here was based on C code and computer algebra. It is intended to produce a single unified program to carry out the various steps.

ACKNOWLEDGEMENTS

The authors would like to thank Dr. Pete Emmett for providing the rational polynomial curve-fits used in this work.

References

[1] Emmett (P.R.) 1994 *Ph.D Thesis, Department of Mechanical Engineering, Victoria University of Manchester.* Methods of analysis for flight flutter data.

[2] Fei (B.J.) 1984 *Rapport de stage de fin d'etudes, ISMCM, St Ouen, Paris, France.* Transformées de Hilbert numeriques.

[3] Haoui (A.) 1984. *Thèse de Docteur Ingénieur, ISMCM, St Ouen, Paris, France.* Transformées de Hilbert et applications aux systèmes non linéaires.

[4] King (N.) & Worden (K.) 1994 *Proceedings of* 5^{th} *International Conference on Recent Advances in Structural Dynamics.* An expansion technique for calculating Hilbert transforms.

[5] King (N.E.) 1994 *Ph.D Thesis, Department of Engineering, Victoria University of Manchester.* Detection of structural nonlinearity using Hilbert transform procedures.

[6] Press (W.H.), Flannery (B.), Teukolsky (S.), & Vetterling (W.) 1986 *Numerical Recipes, The Art of Scientific Computing.* Cambridge University Press.

[7] Simon (M.) 1983 *Ph.D Thesis, Department of Engineering, Victoria University of Manchester.* Developments in the modal analysis of linear and non-linear structures.

[8] Simon (M.) & Tomlinson (G.R.) 1984 *Journal of Sound and Vibration* **90** pp.275-282. Application of the Hilbert transform in modal analysis of linear and non-linear structures.

[9] Stewart (I.) & Tall (D.) 1992 *Complex Analysis* Cambridge University Press.

[10] Worden (K.) & Tomlinson (G.R.) 1990 *Proceedings of the* 8^{th} *International Modal Analysis Conference, Orlando, Florida* pp.121-127. The high-frequency behaviour of frequency response functions and its effect on their Hilbert transforms.

Numerator Roots
$-1214.211008298219 - 726.1763609509598i$
$-198.1314154141764 + 30.36502191203071i$
$-183.7196601591438 + 0.07476628997601653i$
$-173.0468329728469 - 0.5823124151722738i$
$-167.4159433485794 + 0.2499312686227596i$
$-148.7724514912166 - 0.5776974464158378i$
$-106.029245566151 + 6.329765806548005i$
$-105.755520052376 - 6.440071308643175i$
$-103.9415121027209 - 0.2292638139578766i$
$-100.8868331667942 + 13.96371388356606i$
$-100.3491120108979 - 13.55839223906875i$
$-65.16772266742481 - 0.01242815581475099i$
$-1.161302705005027 \times 10^{-20} + 1357.572389293291i$
$65.16772266742481 - 0.01242815581475099i$
$100.3491120108979 - 13.55839223906875i$
$100.8868331667942 + 13.96371388356606i$
$103.9415121027209 - 0.2292638139578766i$
$105.755520052376 - 6.440071308643175i$
$106.029245566151 + 6.329765806548005i$
$148.7724514912166 - 0.5776974464158373i$
$167.4159433485794 + 0.2499312686227509i$
$173.0468329728468 - 0.5823124151722609i$
$183.7196601591439 + 0.07476628997601194i$
$198.1314154141764 + 30.36502191203071i$
$1214.211008298219 - 726.1763609509598i$

Table 1: Polynomial Numerator Roots for HCS1 data

Denominator Roots
$-198.1567099579465 + 30.40483782876573i$
$-183.7196564899432 + 0.07470973423345939i$
$-173.0468138842385 - 0.5822232400350739i$
$-167.4160993615824 + 0.2497687709924406i$
$-148.7725565604598 - 0.577414017829206i$
$-106.1570440779208 - 5.352981785468519i$
$-105.7091945278726 + 6.50265208908201i$
$-103.941962628465 - 0.2315241290997767i$
$-102.9807367369542 - 9.76073164473401i$
$-100.121488863284 + 14.0251938763936i$
$-97.6024028604877 - 15.11650445816473i$
$-65.16768960663572 - 0.01273266773843805i$
$65.16768960663572 - 0.01273266773843805i$
$97.6024028604877 - 15.11650445816473i$
$100.121488863284 + 14.0251938763936i$
$102.9807367369542 - 9.76073164473401i$
$103.941962628465 - 0.2315241290997704i$
$105.7091945278726 + 6.502652089082006i$
$106.1570440779208 - 5.352981785468523i$
$148.7725565604598 - 0.5774140178292062i$
$167.4160993615824 + 0.2497687709924413i$
$173.0468138842385 - 0.5822232400350746i$
$183.7196564899432 + 0.07470973423345935i$
$198.1567099579465 + 30.40483782876573i$

Table 2: Polynomial Denominator Roots for HCS1 data

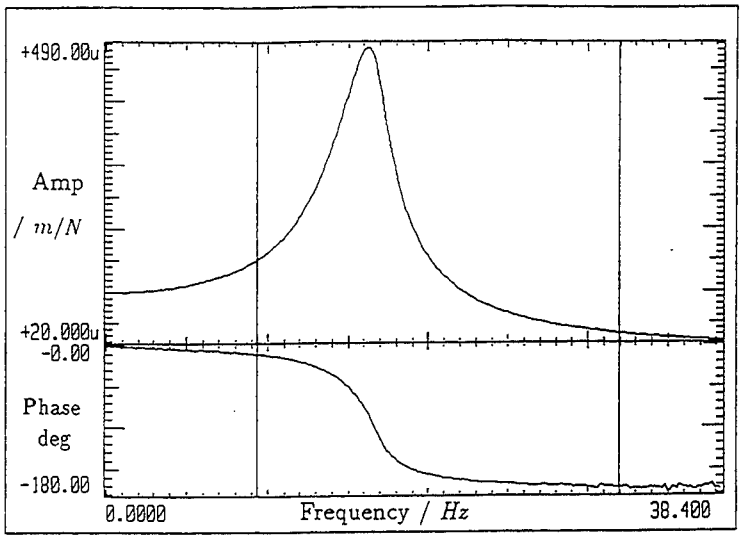

Figure 1: Bode plot of low exitation Duffing oscillator FRF.

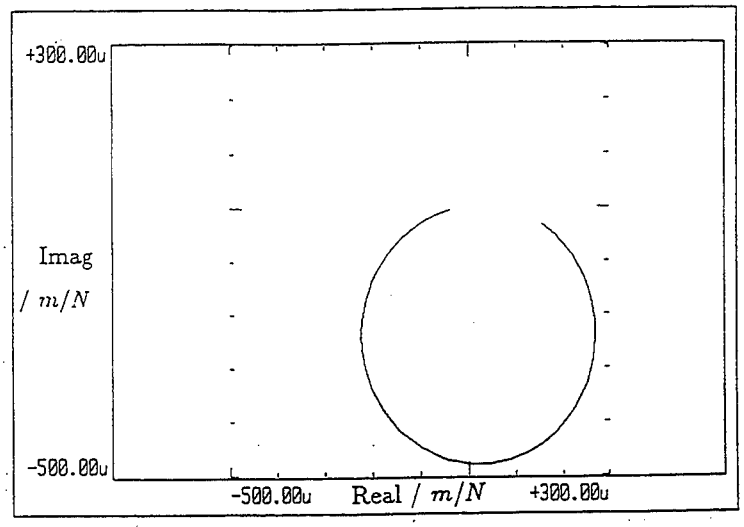

Figure 2: Overlay of RP model $G_{RP}(\omega)$ and original FRF $G(\omega)$ for low excitation Duffing oscillator.

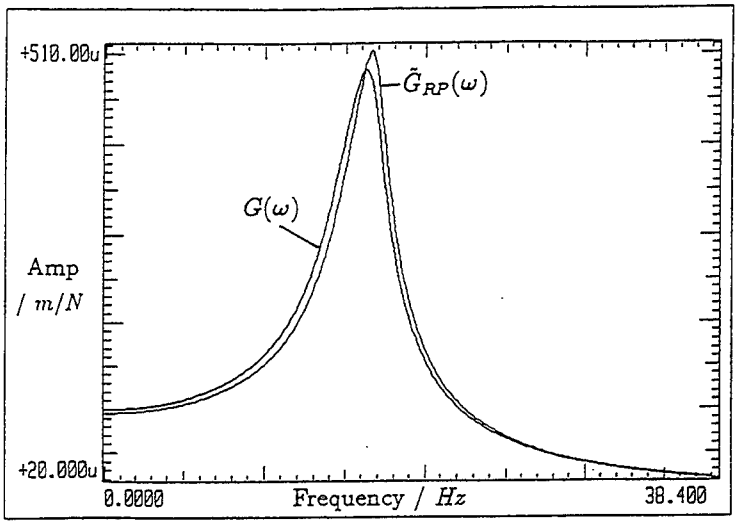

Figure 3: Original $G(\omega)$ and RP Hilbert transform $\tilde{G}_{RP}(\omega)$: Duffing oscillator - low excitation.

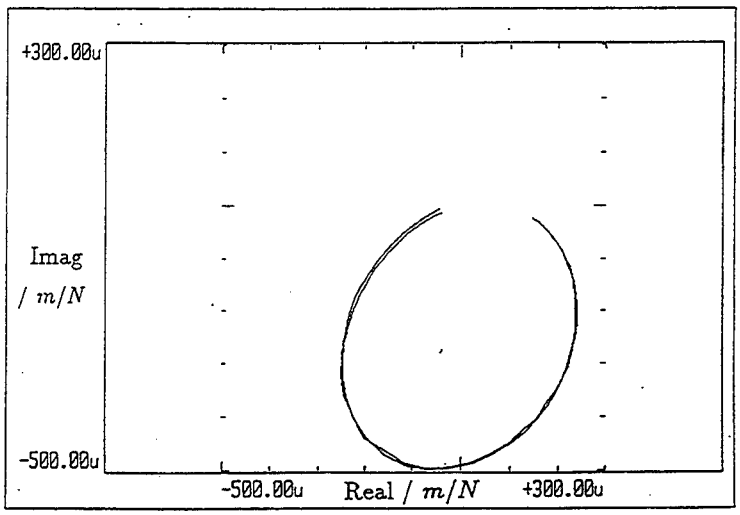

Figure 4: Comparison of RT and FFT Hilbert transforms for low excitation Duffing system.

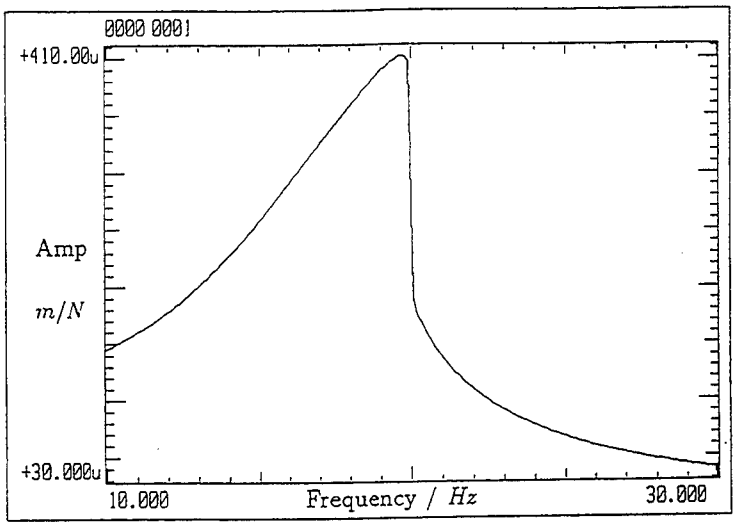

Figure 5: Overlay of RP model $G_{RP}(\omega)$ and original FRF $G(\omega)$ for high excitation Duffing oscillator.

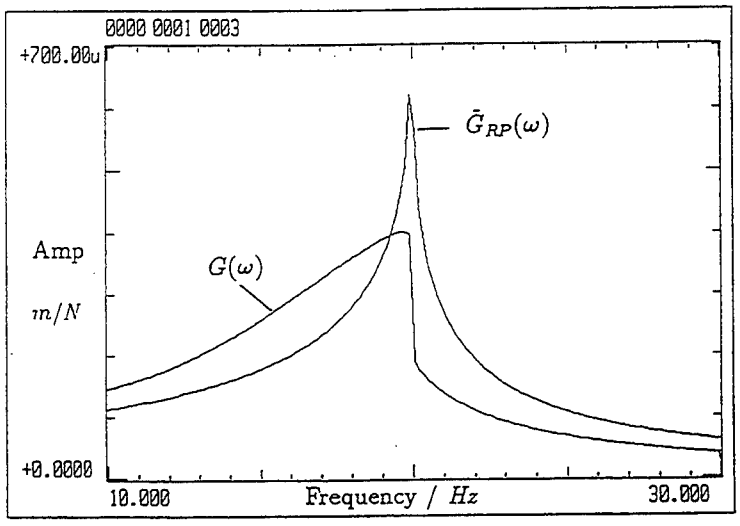

Figure 6: Original $G(\omega)$ and RP Hilbert transform $\tilde{G}_{RP}(\omega)$: Duffing oscillator - low excitation.

Fractional Fourier Transforms and their Interpretation

D.M. Lopes, J.K. Hammond and P.R.White

Institute of Sound and Vibration Research
University of Southampton,
Southampton SO17-1BJ
United Kingdom

Abstract

Fractional Fourier Transforms arise naturally from optical signal processing. However, their interpretation for one-dimensional signals are still to be fully explored. This paper is concerned with fundamental aspects, including :

- Definition and relation to optics
- Interpretation of signal decomposed in terms of 'linear chirps'
- A generalised concept of group delay
- The relationship to time-frequency distributions
- Analytic and computational examples showing the relevance of the decomposition for non-stationary signals occurring commonly in acoustics

Introduction

The Fourier Transform (FT) is perhaps the most widely used tool in the signal processor's armament. It's simple definition, both in the analogue and digital domains enables fast and efficient computation. However, we should sometimes consider whether the information given to us via the FT, could not be better represented in some other form. The Fractional Fourier Transform (FRFT) is a generalisation of the traditional FT, which by changing a given parameter in the transform allows us to continuously move between the time and frequency domains. First used for solving fractional differential equations, the transform later found use in optical physics, and this link is explored in the first section. It can be shown that the FRFT can be viewed as a transform which has a set of basis functions consisting of 'linear chirps'; this is covered in the second section. These are simple harmonic waves, whose frequency changes linearly with

time. In the third section we concern ourselves with the question : 'Given a signal, at what time does linear chirp make its maximum contribution?' This is a generalisation of the work done by Zadeh [9] for the traditional Fourier case. We then investigate the link between the FRFT and Time-Frequency Distributions (TFD). The link between the FRFT and the Wigner Distribution (WD) is explored. We complete the paper by illustrating the above work using an analytical and numerical examples of the manner in which the FRFT decomposes signals.

The FRFT and its Relation to Optical Physics

The simplest way of visualising the form of the FRFT is to consider it in terms of simple optical physics. Figure 1 shows such an example of a simple projector type system. Ozaktas [5] was the first to view the FRFT in this form, and started transition of the transform from pure mathematics into more general usage. Even from this simple system, it is useful to define a few key points. The input image into the system can be considered to be the resultant image produce immediately behind the lens, labelled $\alpha=0$ on the figure. As we move further away from the lens the image converges at the focal plane, this is labelled on the figure as $\alpha=\pi/2$ [1].

At the focal plane the image produced is the 2-D Fourier transform of the input image. If the input image is constant coherent light across the whole of the input image plane, then at the focal plane we would expect to simply see a point of light. This is because the Fourier Transform of a constant is a delta function, as in this case we are dealing in two dimensions it therefore follows that we should see a 'spot' in the centre of the screen.

As we move past the focal plane the image begins to expand once more. At a certain distance we will recover a scaled version of the original image, this point is labelled $\alpha=\pi$. At this point we have applied two Fourier transforms to the input image, resulting in a scaled version of the input. This is as expected from the theory of the Fourier transform. We have therefore seen that the Fourier transform of the input signal is at a distance from the lens of $\alpha=\pi/2$ and that the operation is repeated at a distance of $\alpha=\pi$. At distances from the lens, which are not multiples of $\pi/2$, the resultant image is a fractional Fourier Transform of the input image.

These optical properties are stated in mathematical terms in [2-3]. A given transform (F^{α}) can be considered to be a FRFT, if it

conforms to the a set of properties as outlined in Almeida's paper [4]. (Where **I** is the identity operator)

1. Zero Rotation : $\mathbf{F}^0 = \mathbf{I}$
2. Consistency with the Fourier Transform : $\mathbf{F}^{\pi/2} = \mathrm{FT}$
3. Additivity of Transform : $\mathbf{F}^{\beta}\mathbf{F}^{\alpha} = \mathbf{F}^{\alpha+\beta}$
4. Periodic : $\mathbf{F}^{2\pi} = \mathbf{I}$

Although these properties define the FRFT completely, they do not uniquely define it. However it has been shown that the majority of the definitions given in the literature are consistent.

Figure 1: Propagation of Light through a lens

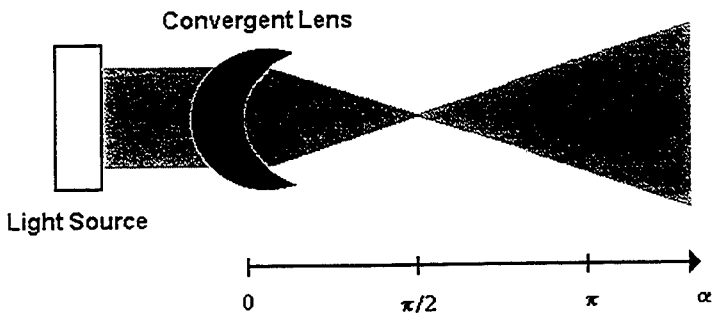

Linear Representation of the FRFT

Almeida [4] defined such a FRFT as follows :

$$X_\alpha(u) = \int_{-\infty}^{\infty} x(t)K_\alpha(t,u)dt \leftrightarrow x(t) = \int_{-\infty}^{\infty} X_\alpha(u)K_{-\alpha}(u,t)du \qquad (1)$$

Were $K_{-\alpha}(t,u)$ is the kernel of the FRFT as is defined as :

$$K_\alpha(t,u) = \begin{cases} \sqrt{\dfrac{1-j\cot(\alpha)}{2\pi}}\, e^{j\left(\frac{t^2+u^2}{2}\right)\cot(\alpha)-jut\csc(\alpha)} & \\ \delta(t-u) & \alpha = 2n\pi \quad n \in Z \\ \delta(t+u) & \alpha+\pi = 2n\pi \end{cases}$$

Where t is the time variable, and u is the generalised frequency axis (i.e. $u \rightarrow \omega$ as $\alpha \rightarrow \pi/2$). Almeida approached the FRFT in much the same manner as other authors on the topic. Starting from the basic properties of the FRFT, he expressed the FRFT in a form similar to that expressed by Ozaktas [5]. Almeida stated that the FRFT consists of expressing $x(t)$ on a basis formed by the set of functions defined by the kernel $B_\alpha(u,t)$. The basis is orthonormal since it can be shown that :

$$\int_{-\infty}^{\infty} B_\alpha(u,t)\, B_\alpha^*(u',t)\, dt = \delta(u-u') \qquad (2)$$

The basis functions are 'chirps', i.e. complex exponentials with linear frequency modulation. The FRFT can now be viewed as the decomposition of the signal in terms of linearly changing harmonic waves or 'chirps', sweeping at a rate dependant upon the parameter α. This can be seen to be consistent with the definition of the FRFT as a generalised FT, since in the limit as the parameter $\alpha \rightarrow \pi/2$, the linear chirps become simple harmonic waves.

We also can consider the FRFT to be a rotation of the TF plane. If $\alpha=0$ then we are along the time axis and thus the input signal remains unchanged. If $\alpha=\pi/2$, then we are on the frequency axis, and thus the FRFT should be precisely the same as the FT. At rotations which are not multiple of $\pi/2$, we are then in a domain which is neither time nor frequency but a mixture of both.

The parameter α can be considered to be the chirp rate, that is the rate at which the swept sine waves of the basis functions increase in frequency. As $\alpha \rightarrow \pi/2$ the basis functions revert to the simple harmonic waves, as α reduces down to zero, the rate at which the chirps change in frequency increases. It can be shown that as $\alpha \rightarrow 0$ that a chirp in Eqn. 1 can be viewed as a Delta function [10, p.99]. The definition of the transform as written in terms of the kernel function as defined by Almeida and Ozaktas then becomes consistent with the viewing the FRFT as a rotation of the FT plane.

Almeida's linear representation of the FRFT as a decomposition of a signal in terms of linearly modulated harmonic waves allows an intuitive hold upon the transform, and can be seen to be of vital importance over the next few pages.

The Generalised Concept of Group Delay

The idea of Group Delay (GD) was well explained by Zadeh, [9, p. 441-444] the core of his idea is as follows. In it's traditional definition GD is the amount by which a given (very small) band of frequencies make their maximum contribution towards a signal. Zadeh was able to show that the GD of a given signal could be expressed as follows :

$$h(t) \cong \frac{\Delta}{\pi}\sum_{n=1}^{\infty} A(\omega_{on})\frac{\sin\left(\Delta/2\right)(t+\phi_n')}{\left(\Delta/2\right)(t+\phi_n')}\cos\left(\omega_{on}t-\phi(\omega_{on})\right) \qquad (3)$$

where Δ is the bandwidth of the group of frequencies under consideration, and $\phi' = \left.\frac{d\phi}{d\omega}\right|_{\omega_{on}}$. This can be viewed as a sum of cosine waves, modulated by a *sinc(x)* type function, which has its centre (and maximum value) at $-\phi'$. This means that by finding ϕ' we can find the time at which a band of frequencies make their maximum contribution to the signal.

A classical example of group delay can be seen if we introduce a pure delay into the input signal. A pure delay of a signal introduces a phase shift in the FT as follows :

$$\mathbf{F}(x(t-\tau))=\mathbf{F}(x(t))e^{-j\omega t}$$

The complex exponential does not change the amplitude of the FT, but introduces a linearly changing phase whose negative gradient, $-\phi'$, is proportional to the delay introduced into the signal. It thus follows that the derivative of the phase, $-\phi'$, is constant, and is the amount by which the signal has been delayed. This serves to reaffirm the definition of group delay, since we defined $-\phi'$ as the time at which a band of frequencies make their maximum contribution, which in this case is the amount by which the signal has been delayed.

We now show that is it possible to extend Zadeh's original definition using the FRFT, to answer the question : At what time does a 'chirp' of rate α, with centre u_{on}, along the u axis make it's maximum contribution to the signal? Starting from our original definition of $X_\alpha(u)$, taking the inverse transform back into the time domain and writing the transform in terms of an modulus and phase it follows that :

$$x(t)=\sqrt{\frac{1-j\cot(\alpha)}{2\pi}}\int A_\alpha(u).e^{j\left(\frac{t^2+u^2}{2}\cot(\alpha)-ut\csc(\alpha)-\phi_\alpha(u)\right)}du \qquad (3)$$

By dividing up the u axis into equal segments of length Δ. Then

$$x(t)=\sqrt{\frac{1-j\cot(\alpha)}{2\pi}}\sum_{n=-\infty}^{\infty}\int_{n\Delta}^{(n+1)\Delta}A_\alpha(u).e^{j\left(\frac{t^2+u^2}{2}\cot(\alpha)-ut\csc(\alpha)-\phi_\alpha(u)\right)}du \qquad (4)$$

If we make Δ sufficiently small so that for all segments A_α is constant, we can make the following re-arrangement, defining the centre of the bandwidth as $u_{on}=\left(n+\frac{1}{2}\right)\Delta$:

$$x(t)\cong\sqrt{\frac{1-j\cot(\alpha)}{2\pi}}\sum_{n=-\infty}^{\infty}A_\alpha(u_{on})\int_{n\Delta}^{(n+1)\Delta}e^{j\left(-\frac{t^2+u^2}{2}\cot(\alpha)+ut\csc(\alpha)-\phi_\alpha(u)\right)}du \qquad (5)$$

Furthermore if we require that Δ be sufficiently small that over each internal $n\Delta...(n+1)\Delta$ we can use the Taylor expansion for $\phi_\alpha(u)$, centred around u_{on}, giving

$$\phi_\alpha(u)\cong\phi_\alpha(u_{on})+(u-u_{on})\left.\frac{d\phi_\alpha}{du}\right|_{u_{on}}$$

By defining $\phi'=\left.\frac{d\phi_\alpha}{du}\right|_{u_{on}}$, and making the above substitution into Eqn. 5 we can write

$$x(t)\cong\sqrt{\frac{1-j\cot(\alpha)}{2\pi}}\sum_{n=-\infty}^{\infty}A_\alpha(u_{on})\int_{u_{on}-\Delta}^{u_{on}+\Delta}e^{j\left(-\frac{t^2+u^2}{2}\cot(\alpha)+ut\csc(\alpha)-\phi_\alpha(u_{on})-(u-u_{on})\phi'\right)}du \qquad (6)$$

After a little manipulation of the exponential it is possible to show :

$$x(t)\cong\sqrt{\frac{1-j\cot(\alpha)}{2\pi}}\sum_{n=-\infty}^{\infty}A_\alpha(u_{on})e^{-j\left(\frac{t^2}{2}\cot(\alpha)+\phi_\alpha(u_{on})-u_{on}t\csc(\alpha)\right)}\int_{u_{on}-\Delta}^{u_{on}+\Delta}e^{j\left(-\frac{u^2}{2}\cot(\alpha)+(t\csc(\alpha)-\phi')(u-u_{on})\right)}du \qquad (7)$$

The integral can be expressed in terms of Error functions, and it is then possible to write Eqn. 7 as follows:

$$x(t) \equiv \sqrt{\frac{1-j\cot(\alpha)}{2\pi}}\frac{\sqrt{2}}{\sqrt{j\cot(\alpha)}}\times$$
$$\sum_{n=-\infty}^{\infty}\left(A_\alpha(u_{on})e^{-j\left(r^2\left(\frac{\cot(\alpha)}{2}+\csc^2(\alpha)\right)+r(-u_{on}\csc(\alpha)-2u_{on}\csc(\alpha)\cot(\alpha)-2\phi'\csc(\alpha))-\phi_{\alpha}(u_{on})+2\phi' u_{on}\cot(\alpha)+\phi'^2\right)}[\text{Erf}[2]-\text{Erf}[1]]\right) \tag{8}$$

Where Erf [1], [2] are defined as :

$$Erf[1] = Erf\left(\frac{j\sqrt{2}\left(-2u_{on}\cot(\alpha)-\Delta\cot(\alpha)+2t\csc(\alpha)-2\phi'\right)}{4\sqrt{j\cot(\alpha)}}\right)$$

$$Erf[2] = Erf\left(\frac{j\sqrt{2}\left(-2u_{on}\cot(\alpha)+\Delta\cot(\alpha)+2t\csc(\alpha)-2\phi'\right)}{4\sqrt{j\cot(\alpha)}}\right)$$

Although somewhat complicated the result can be considered to be a generalisation of Zadeh's result, as $\alpha\rightarrow\pi/2$, the above result simplifies down to Zadeh's result. Loosely the Erf terms can be considered to be the general form of the *sinc* function used in the traditional Fourier case. The parameters u_{on} and ϕ' shift the centre of the function, Δ effects bandwidth, and α tightens the function about the centre. As with the Zadeh definition, we now wish to find the maximum value of the modulating function, to determine when the chirp makes it's maximum contribution. By elementary mathematics this can be found as :

$$t = -\left(u_{on}\cos(\alpha)+\phi'\sin(\alpha)\right) \tag{9}$$

This can be checked against Zadeh's result by setting the sweep rate to $\alpha=\pi/2$. The result is interesting, because of the underlining simplicity hiding the complex mathematics preceding it. Stated again, this can be seen as the maximum time at which a linearly swept sine wave makes its maximum contribution to a given signal.

The FRFT and it's Relation to TFD's

The concept of GD (and instantaneous frequency) allows us to view the internal structure of analytical signals. However, for non-stationary or time-varying signal we need some other method to view

the changing frequency components of a signal (i.e. [1]). The use of Time-Frequency analysis allows us to construct a TF plane, allowing the visualisation of the signal in terms of time and frequency. Almeida's most significant contribution to the field of FRFT was to link the FRFT and Time-Frequency analysis. Almeida viewed the FRFT in terms of a rotation of the Time-Frequency Distribution (TFD) and the application of a Fourier Transform. More important still was the link that Almeida established between the Wigner Distribution (WD) which is one such method of constructing the TFD and the FRFT.

After a little mathematics (see [4]) Almeida's deduced that the WD could be written as :

$$W_x(t,\omega) = 2e^{2ju v} \int_{-\infty}^{\infty} X_\alpha(\xi) X_\alpha^*(2u-\xi)\, e^{-2ju v \xi} d\xi \qquad (10)$$

Where $u = t\cos\alpha + \omega \sin\alpha$, and $v = -t\sin\alpha + \omega\cos\alpha$

The left hand side of this equation is the WD of $X_\alpha(u)$ computed with the arguments (t,ω), and the right is the WD of $x(t)$ computed with arguments (u,v). The equation shows that the WD of X_α is the same as the WD of x if we take into account the rotation due to the change of variables.

" This is equivalent to saying that the WD of X_α is the WD of x, rotated by an angle of $-\alpha$, or that it is simply the WD of x expressed in the new set of co-ordinates (u,v)." Almeida, [4, p. 3088]

Lohmann and Soffer's paper [6] shows essentially the same property, but use the Radon transform to produce the required rotation and projection. Since Almeida published his paper, other authors have established this link not just for the WD, Ozaktas et al. [7] showed that the same properties were true for all members of the Cohen class which are rotationally symmetric about the origin.

Another way of viewing the FRFT is as a rotation and projection of the TF plane. Figure 2 shows this idea. We can assume that a linear chirp is simply a straight line in the TF plane. If we rotate the time and frequency axis by the sweep rate of the chirp, and project along the u axis, we have constructed the FRFT. This is an intuitive representation of the mathematics given by Almeida and Ozatkas. This rotation and projection is called the Radon transform, and in [6] the presentation of the FRFT as a Radon transformed WD was shown.

Figure 2 - FRFT is terms of rotation and projection.

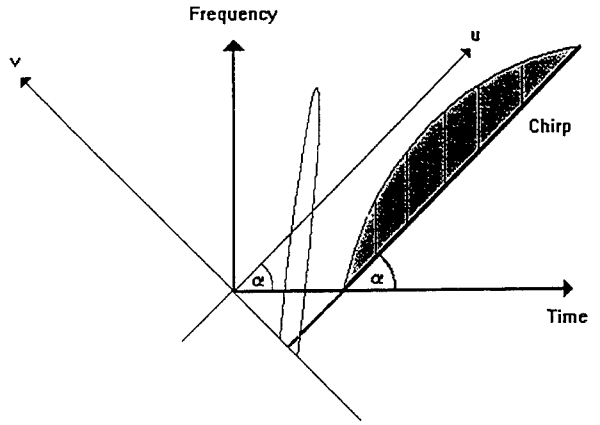

Examples

1. Rectangular Function

The first of our examples, shows the analytical decomposition for a rectangular function. The FRFT can be written in terms of Fresnel integrals, as expressed below :

$$X_\alpha(u) = \sqrt{\frac{1}{2\cot(\alpha)} - \frac{j}{2}}\; e^{j\left(\beta u^2 - \frac{\gamma^2}{4\beta}\right)}\left[K\left(\frac{2b\beta-\gamma}{\sqrt{2\beta\gamma}}\right) - K\left(\frac{2a\beta-\gamma}{\sqrt{2\beta\gamma}}\right)\right] \quad (11)$$

Where K is defined as the Fresnel integral :

$$K(x) = \int_0^x e^{\frac{j\pi\tau^2}{2}}\, d\tau \quad (12)$$

This function is shown in Figure 3. The function can be seen to evolve as the sweep rate is changed. As $\alpha \to 0$ we can seen that the FRFT tends towards the rectangular function as expected. As the sweep rate increases the function develops, with oscillations in the transforms becoming slower. As $\alpha \to \pi/2$ the function develops into the a *sinc* type function, the Fourier transform of a rectangle.

Figure 3 - Modulus of the FRFT of a Rectangular Function.

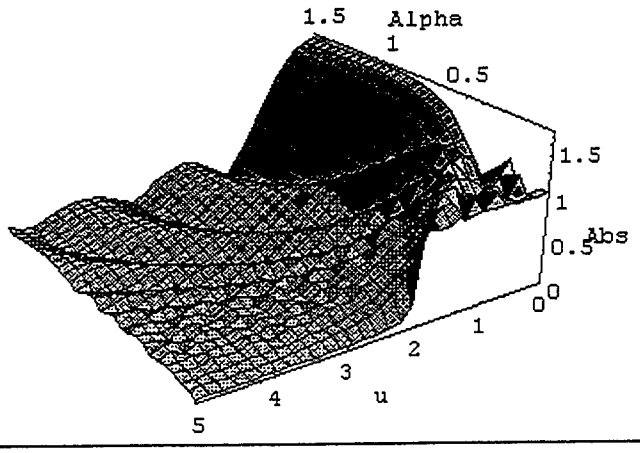

2. Doppler Type Signals

The acoustics of a moving sound source are extremely complicated, both the shift in frequency (Doppler shift) due to the movement of the source, and the propagation delay of the speed of sound must be taken into account. In the following example, we simplify the situation by considering the Doppler shift without propagation delay. In order to simulate the change in level of the sound experienced due to the distance of the vehicle from the microphone, we will use a Gaussian function to reduce the signal to zero at the beginning and end of the signal.

If the source and receiver approach each other at speeds of v and u respectively, and the source emits a tome frequency of f_0 when stationary, then it is possible to show ([8], p. 415) that the receiver will hear a frequency f' where : (c is the speed of sound)

$$f' = f_0 \frac{c+u}{c-v} \tag{13}$$

This change in frequency is known as the Doppler Shift. A schematic of the type of system we are trying to model is shown in Figure 4.

If the microphone is stationary, and the car moves passed it at constant speed, then a modified form of the equations [8] describes the frequency received by the microphone (the signal is shifted in time in order to keep the equations causal) :

$$f' = f_0\left(1+\frac{v\cos(\phi(t))}{c}\right) \tag{14}$$

$$\text{were } \phi(t) = \begin{cases} -\tan\left(\dfrac{x}{v(t-10)}\right) & t < 10 \\ \pi - \tan\left(\dfrac{x}{v(t-10)}\right) & t > 10 \end{cases}$$

Figure 4 - Schematic of the System to be Modelled

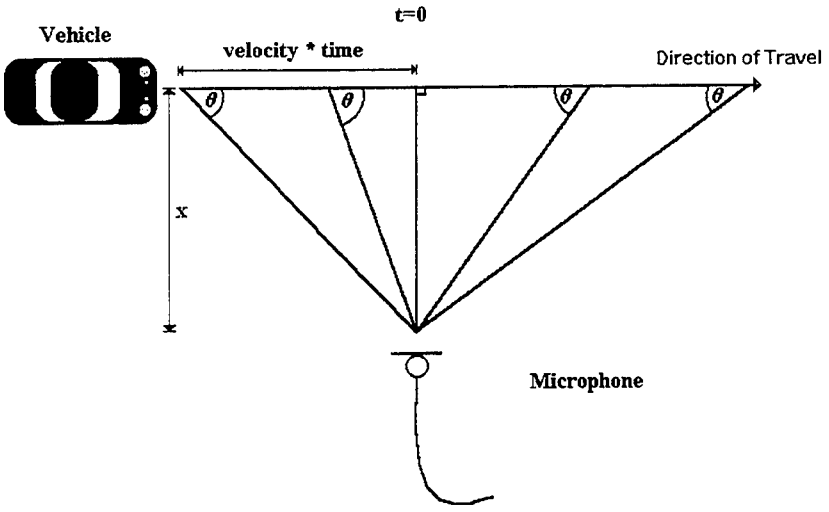

This is a non-linear function; however as the car approaches the microphone, it becomes almost linear. Figure 5 shows the changing frequency component with time for two different (simulated) vehicle speeds. (The curve for the faster speed is marked with '+' signs.) We will assume for the sake of simplicity, that the vehicle emits only one tone, and that it travels at constant velocity.

Figure 5 - Change of Frequency according to Velocity

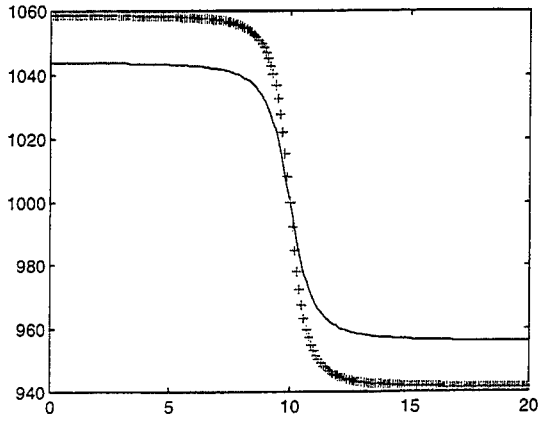

The greater the velocity of the vehicle, the steeper the curve. The angle, θ, varies from $0..\pi$. The rate of decrease of frequency can be found, and is shown to be

$$\frac{df}{dt} = \frac{x f_0 \sin\left(\tan^{-1}\left(\frac{x}{v(t-10)}\right)\right)}{c(t-10)^2\left(1+\frac{x^2}{v^2(t-10)^2}\right)} \tag{15}$$

Since the rate of change of frequency is almost linear at the point when the vehicle passes the microphone, application of the FRFT (at the correct sweep rate setting) will produce a strong spike like distribution. From the knowledge of the sweep rate and thus the rate of change of frequency, it is possible to infer the velocity of the vehicle. Using this simple model of a Doppler shifted signal, and making some basic assumptions (the observation point i.e. microphone is stationary, constant velocity, and single pure tone emission of the source) we simulate the situation. The synthesised signal is shown in Figure 6, and its Spectrogram is depicted in Figure 7.

From the synthetic signal the FRFT is used to find the sweep rate which best matches that of the input. Thus is we pick the right sweep rate, the chirp produced by the vehicle will show up as a spike, or an least a peak in the distribution. In our example case were we know the input parameters,

Figure 6 - Input Synthesised Signal.

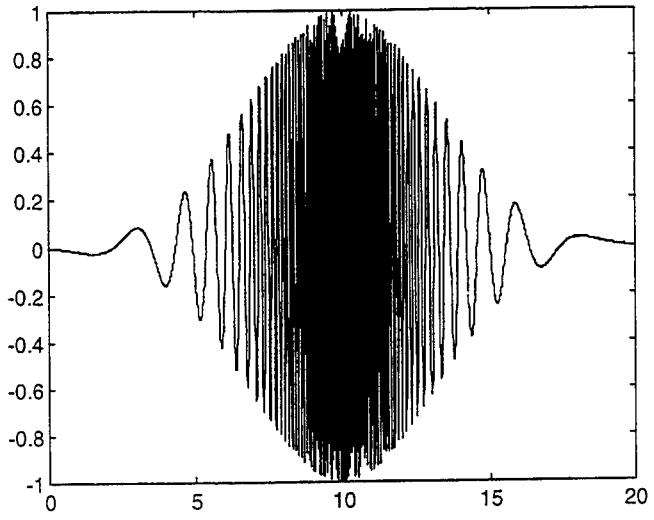

it is possible to predict at what sweep rate, and were on the u domain we expect to see a rise in the distribution. In this example case it has been possible to predict the sweep rate and position of peak on the axis, however in a real situation this would not be the case. Multiple transforms would have to be taken on the data, possibly in some iterative way to find the peak in the distribution. However due to the nature of the delay equations, and the low sweep rate, the location of the peak will not change very much from one velocity to another.

The result of the application of the FRFT can be seen in Figure 8, the peak which was expected does not stand out greatly from the rest of the data because of the way in which the signal changes. Close to the region we are considering to be a linear chirp, other almost linear chirps are also present. These other chirps spread out the distribution into the form seen in Figure 8.

From the knowledge of the rate of change of frequency, it is a simple manner to calculate the passing velocity of the vehicle.

Figure 7 - TF Plane of input signal.

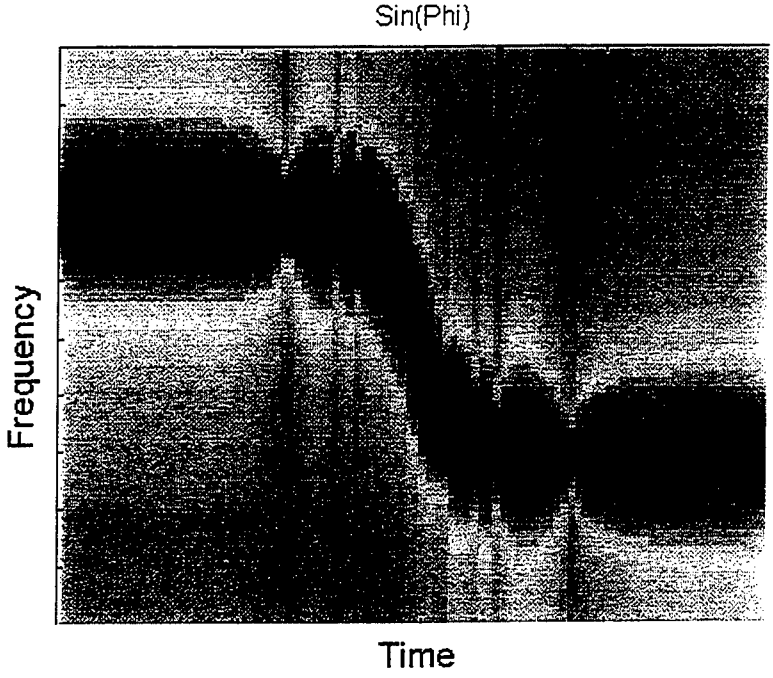

Figure 8 - FRFT of synthesised signal using derived sweep rate

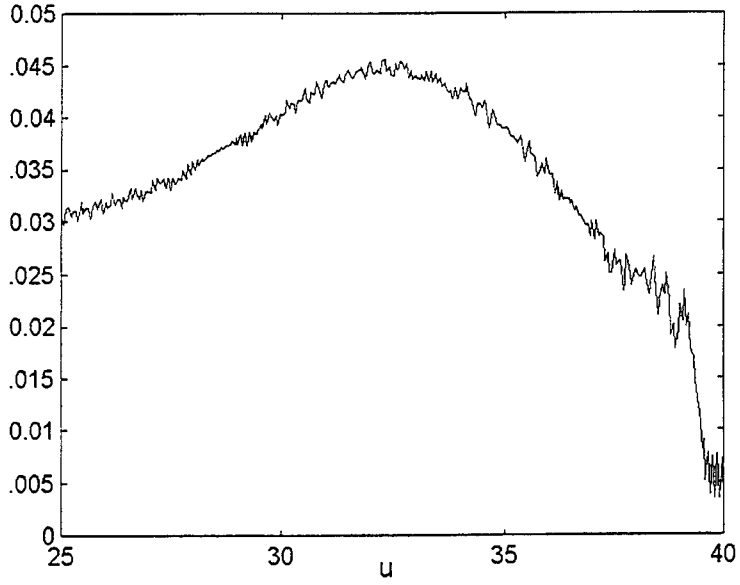

Conclusions

In this paper we have covered some of the theory and applications of the fractional Fourier transform. We have shown that the fractional Fourier transform can be considered to be a generalised version of the Fourier transform, having a basis of swept sine waves rather than harmonic waves. We have considered the notion of 'group delay' as being the time and which a band of frequencies, and generalised this idea to the form where by we can answer the question 'At what time does a chirp, of a given sweep rate make it's maximum contribution to a signal ?' The link between the FRFT and TF has been explored. We have investigated some examples of signal using this technique. Finally we have outlined one application of the FRFT as a way of determining the degree of shift in a Doppler type signal.

References

1) D. Lopes 1996 Disseration submitted as part of an M.Sc. in Sound and Vibration, at ISVR, University of Southampton.

2) A.C. McBride and F.H.Kerr 1985 *IMA Journal of Applied Mathematics* **39**, 159-175. On Namias's Fractional Fourier Transforms

3) S.Abe and J.T.Sheridan 1994 *J. Phys. A: Math. Gen.* **27**, 4179-4187. Generalization of the fractional Fourier transform to an arbitrary linear lossless transform: an operator approach

4) L. B. Almeida 1994 *IEEE Transactions on Signal Processing* **42**(11), 3084-3091. The Fractional Fourier Transform

5) H.M.Ozaktas and B.Barshan 1994 *J. Opt. Soc. Am. A.* **11**(2), 547-561. Colvolution, filtering, and multiplexing in fractional Fourier domain and their relation to chirp and wavelet transforms.

6) A.W.Lohmannm and B.H.Soffer 1995 *J. Opt. Soc. Am. A* **11**(6), 1798-1801. Relationships between the Radon-Wigner and fractional Fourier Transform

7) H.M.Ozaktas, N.Erkaya and M.A.Kutah 1996 *IEEE Signal Processing Letters* **3**(2), 40-41.Effect of Fractional Fourier Transformation on Time-Frequency Distributions Belonging to the Cohen Class

8) L.E.Kinsler and A.R.Frey 1982 *Fundamentals of Acoustics*. New York : John Wiley and Sons Inc.

9) L.A. Zadeh and C.Desoer 1963 *Linear System Theory*. New York : McGraw-Hill.

10) A. Papoulis 1984 *Signal Analysis*. New York : McGraw-Hill.

SYSTEM IDENTIFICATION III

WAVE LOCALIZATION EFFECTS IN DYNAMIC SYSTEMS

J. Dickey
Center for Nondestructive Evaluation,
The Johns Hopkins University, Baltimore, MD 21218, USA

G. Maidanik
David Taylor Research Center, Bethesda, MD 20084, USA

J. M. D'Archangelo
United States Naval Academy, Annapolis, MD 21402, USA

Abstract

Structures with discrete periodic variations in impedance may exhibit pass and stop bands and the related wave localization and delocalization phenomena in their frequency response. Localization, similar to Anderson localization in atomic systems, occurs in the pass-band frequency range when the periodicity is perturbed and waves are thereby inhibited from propagating. Conversely, delocalization occurs in the same systems in the stop-band regions where perturbing the strict periodicity allows for relatively more propagation. Localization and delocalization are demonstrated in several systems: specifically, a beaded string, membranes and plates with periodic stiffeners attached, and a "jungle gym", i.e. a connected beam structure. It is demonstrated that these effects depend on the interactions between discontinuities.

Introduction

A structure with strictly periodic impedance discontinuities exhibits pass and stop bands in its frequency response. The pass bands are frequencies at which waves traverse the structure relatively unimpeded and thus give rise to modes which span the entire structure: i.e. global. Stop bands are frequencies at which waves are impeded from traversing the structure and give rise to modes which are confined near the source: i.e. local. When the strict periodicity of the structure is disturbed by, e.g., randomly varying the distances (or equivalently, the wave propagation speed) between discontinuities, the pass-

and stop-band character in the frequency response is , in some degree, spoiled. The "spoilage" of the strict pass-band behavior results in the long range wave propagation becoming shortened with the attendant localization of the modes. This effect is called localization. Similarly, the "spoilage" of the strict stop-band behavior results in a lengthening of the wave propagation and a delocalization of the modes. This effect is called delocalization. Both localizing and delocalizing cause the long and short range wave propagation, respectively, to tend towards a middle ground, called a "yellow" band (amber to some), where waves are neither short nor long and where modes are neither global nor local. It is proposed that delocalization is as important a phenomena as localization with relevance to practical applications.

These phenomena occur in a wide variety of dynamic systems ranging from atomic lattices to rib-stiffened ship hulls.[1-4] In fact, the phenomenon of localization in atomic systems was popularized by P. W. Anderson in 1958 who characterized it as "absence of diffusion in certain random lattices".[5] Anderson was working with the wave equation describing the electron density in crystalline lattices and noted that randomizing the spacings of an originally regularly spaced crystal tended to inhibit the diffusion of electrons from a point of injection. The analysis here is limited to macroscopic systems obeying linear wave equations since the effects are fundamentally phase interference and, as such, depend on superpositon of wave functions. This is not to say that localization does not exist in non-linear systems, it is just that the model used to describe it here is limited to linear systems. Further, the analysis is limited to one-dimensional systems in the sense that the wave equation for the structure must be separable into functions of a single spatial variable which contains a periodic discontinuity.

Both localization and delocalization depend on a spoiling of the strict periodicity of a system. There are many ways to effect this "spoilage": one which will be used extensively here and which will be used to establish a benchmark for quantification of the phenomena, is to randomize the lengths of the connected 1D systems. The prototypical complex of connected 1D systems is shown in Fig. 1 and it is the length (b) of the constituent systems, enumerated 1-N, which are to be randomized, i.e.

$$\ell_n = b(1 + \alpha R_n) \ , \ 0 \leq \alpha \leq 1 \quad , \qquad (1a)$$

where R_n is a random number between -1 and 1, and α controls the degree of randomization: e.g., $\alpha = 0.1$ is referred to as 10% randomization and the lengths are uniformly distributed, $0.9 < (l_n) < 1.1$. The benchmark from which to quantify localization and delocalization which is proposed here is the limit which is approached when a system is completely randomized. "Complete randomization" as used here means that $\alpha = 1$ and if an ensemble average is taken over a large number of realizations of Fig. 1, each with a different set of R_n's then the oscillatory nature of the phase change in the amplitude of a wave traversing a system will average to zero. With the phase effects averaged, the diminution of a wave traveling through the set of systems will depend on the average propagation loss factor,

$$\eta = \frac{1}{N} \sum_{n=1}^{N} \eta_n \quad , \qquad (1b)$$

and the cumulative transmission coefficient,

$$T_N(\omega) = \prod_{n=1}^{N} T_n(\omega) \quad . \qquad (1c)$$

Without the ensemble averaging over realizations of Fig. 1, each with a different set of R_n, the phase effects must be accounted for. This may be done through the use of an impulse response matrix

$$\underset{\approx}{g}(\underline{x} \mid \underline{x}', \omega) = \left(g_{ji}(x_j \mid x'_i, \omega)\right) \quad , \qquad (2a)$$

in the sense that it relates a response in system j at the coordinate location x_j to an impulse in system i at the coordinate location x'_i. More generally, in linear systems in which wave solutions superpose, Eq. (2a) is the Green function kernel which relates the response at any point in any system, $\underline{v}(\underline{x}, \omega) = \{v_j(x_j, \omega)\}$ to a distributed drive at a particular frequency through the usual relation;

$$\underset{\sim}{v}(\underset{\sim}{x}, \omega) = \int d\underset{\sim}{x}' \underset{\approx}{g}(\underset{\sim}{x} \mid \underset{\sim}{x}', \omega)\ \underset{\sim}{p}_e(\underset{\sim}{x}', \omega) \quad . \qquad (2b)$$

The impulse response matrix, Eq. (2a) is formulated for a connect set of 1-0 systems such as shown in Fig. 1 by following waves as they emanate from the drive position x'_i and propagate with multiple reflections and transmissions at the junctions between systems.(6)

Periodic Complex - Pass and Stop Bands

Equation (2) is used to calculate a response and to demonstrate the phenomena of localization and delocalization in a set of dynamic systems such as shown in Fig. 1. Certain parameters must be specified in order to do this: specifically, the number of systems, their lengths, their impedances, and their manner of attachment to each other. Accordingly, seven systems are assumed, all stationary in time and all supporting a single, non-dispersive wave type which propagates according to:

$$v_j(x_j, \omega) = e^{-ik_j|x_j - x'_j|}\ v(x'_j, \omega) \quad , \qquad (3)$$

The time dependent factor, $e^{i\omega t}$, is implicit in Eq. (3) and

$k_j = k_{0j}(1 - i\eta_j)$

$k_{0j} = \omega/c_j$

c_j = the phase speed of waves propagating in the j^{th} system, generally may depend on frequency (i.e. dispersive) but will be taken to be constant here.

$\eta_j = 10^{-3}$, the propagation loss factor for the j^{th} system

ℓ_j = the length of the j^{th} system, b is the unperturbed length

m_j = the mass of the j^{th} bead.

The response, as calculated by Eq. 2 and Reference 5 for an infinite flexible string with 8 equally spaced point masses (beads) attached is shown in Fig. 2a. For the periodic complex all lengths are the same $\ell_j = b$; also $c_j = c$, $\eta_j = \eta$ and $m_j = m$. The complex is driven in the first bay as indicated and the magnitude of the ratio of the response relative to the response at the drive point x′ is plotted as a function of position in the complex. The drive frequency is $(\omega/\omega_1) = 10$ where ω_1 is the fundamental resonance of the unperturbed bay, i.e. $\omega_1 = \pi b/c$.. The beads are concentrated masses equal to 0.3 times the mass of the string in the unperturbed bay. The standing wave patterns in the bays are evident as is the exponential decrement of the response as the excitation traverses the complex.

Figure 2a illustrates the exponential attenuation characteristic of wave propagation through a cascade of connected one-dimensional systems. The attenuation shown here is due to the combined effect of the propagation loss factors of the individual bays (this is negligible here) and the phase interference due to the reverberation within the bays. The degree of attenuation, i.e. the slope of the log-response vs. distance curve is a function of frequency, and it is this variation with frequency which gives rise to pass/stop band phenomena. Accordingly, a series of responses of the type shown in Fig. (2a) are calculated for a set of increasing frequencies and shown in Fig. (2b). The frequency range encompassed by the calculation is $0 < (\omega/\omega_1) \leq 20$ and the pass and stop bands appear as frequencies where the complex is transparent or opaque respectively to the waves traversing the complex.

An alternate presentation of the response which shows the pass/stop band phenomena more explicitly, is the response at the end of the complex, essentially the transmissibility of the complex, as a function of frequency. The plot in this format which corresponds to the parameters of Fig. (2b) is shown in Fig. (2c). The peaks in the response shown here correspond to the pass bands of the complex and are identical to the pass bands as identified in Fig. (2b) as frequencies where the response shows minimal attenuation in x. The minima in Fig. (2c) are the stop band frequencies which are more difficult to identify in Fig. (2b) because, for clarity, the data shown there is "shadowed" by curves in the foreground. The benchmark attenuation for the

system discussed earlier which delineates between pass and stop band behavior is shown by the dashed line in Fig. (2c)

A-Periodic Complex - Localization and Delocalization

The phenomena of localization and delocalization are demonstrated by calculating the response of the complex where the lengths of the individual systems are randomized. Accordingly, a system response with all parameters the same as in Fig. (2) except that $\alpha = 0.2$ in Eq. (1a) is shown in Fig. (3). Note the disruption of regularity in the decrement as the excitation traverses the systems. The transmissibility shown in Fig. (2c) for the regular complex is repeated for the randomized one and shown in Fig. (3c). It should be kept in mind that the calculations shown in Fig. (3) are for a specific realization of randomized lengths and would not be exactly the same for a different realization of the random number set used to generate the lengths; different realizations, however, show similar behavior. The dashed line in Fig. (3c), again represents the benchmark attenuation.

The demonstration of localization/delocalization lies in the fact that the peaks and valleys, respectively, of the transmissibility shown in Fig. (3c) have moved toward the benchmark value. This is more true at higher frequencies where the length perturbations represent a larger fraction of wavelength.

Special Cases

Two more complex structures are considered. The first is an infinite membrane with an array of 8 stiffeners or ribs attached as shown in Fig. 4a. In the unperturbed case, the rib spacings are all equal and of length b and the ribs are modeled as line impedances. The structure is driven and the response is assessed along lines parallel to the ribs at positions x' and x respectively, as shown. It should be noted that the pass/stop band and localization phenomena do not depend strongly on the magnitude or nature of the rib impedances; i.e. they can be mass-like, resistive, spring-like, resonant, etc. The pass- and stop-band characteristics for this structure where the rib impedances are mass-like with a mass equal to 0.3 times the mass in a bay of length b are shown in Fig. 4b. The solid curve is the transmissibility vs. frequency of the periodic

(unperturbed) case, and the dashed curve is the aperiodic (perturbed) case with $\alpha = 0.2$. Again, the normalizing frequency ω_1 is the fundamental resonance of the system of length b. It should also be noted that if a thin plate were used in place of a membrane, the data shown in Fig. 4b would be similar but show a progressive widening of the frequency separation of adjacent bands with increasing frequency due to the dispersive nature of the plate free-wave propagation. The membrane was given a propagation loss factor of $\eta = 5 \times 10^{-3}$ in the direction of propagation and the slight progressive decrement of the pass-band peaks with frequency reflects this; i.e. the structure would exhibit unity transmission at the center of the pass bands if there were no loss.

A second example of localization/delocalization effects in more complex systems is the planar array of connected one-dimensional systems shown in Fig. 5a. The array dimensions are 13b x 7b where b is the length of the unperturbed system, and, for this example, the bead impedances were taken to be zero. The drive and assessment positions were at $x'_1 = 0.3b$ and $x_{202} = 0.5b$ respectively, as shown. The transmissibility of the regular (unperturbed) complex is shown as a function of (ω/ω_1) by the solid curve in Fig. 5b and one realization of a perturbed case with $\alpha = 0.2$ by the dashed curve.

Conclusions

The phenomena of localization and delocalization is demonstrated in several mechanical systems. The canonical system is an infinite string with a finite array of beads attached in which wave localization and delocalization occur in the pass and stop frequency bands respectively when the strict periodicity of the bead spacing is disturbed. The phenomena are also demonstrated in a membrane with a finite array of attached ribs. The final example is a two dimensional, planar, array of beads connected with wave-bearing elements. Strong localization and delocalization occur in this system also.

References

[1] Hodges, C. H., 1982, *Journal of Sound and Vibration* **82**, 411-424. Confinement of vibration by structural irregularity.

[2] G. Maidanik and J. Dickey 1991 *Acoustica* **73**, 119-128. Localization and delocalization on periodic one-dimensional dynamic systems.

[3] Langley, R. S., 1995, *Journal of Sound and Vibration*, **188** (5), 717-743, Wave transmission through one-dimensional near periodic structures: optimum and random disorder.

[4] D.M. Photiadis, 1996, *Applied Mech. Reviews* **49** (2), 100-125, Fluid loaded structures with one-dimensional disorder.

[5] Anderson, P.W., 1958, *Physical Review* **109**, 1492-1505. Absence of diffusion in certain random lattices.

[6] L. J. Maga and G. Maidanik, 1983, *Journal of Sound and Vibration*, **88**, 473-488. Response of multiple coupled dynamic systems.

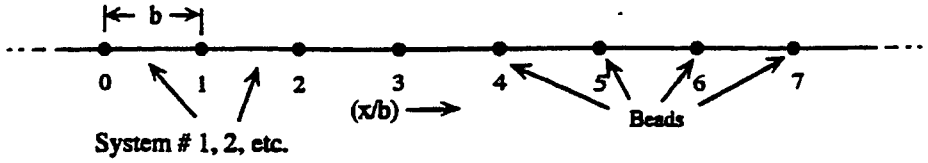

Fig. 1. The prototypical complex of connected one dimensional systems, an infinite string with seven eaually spaced beads attached.

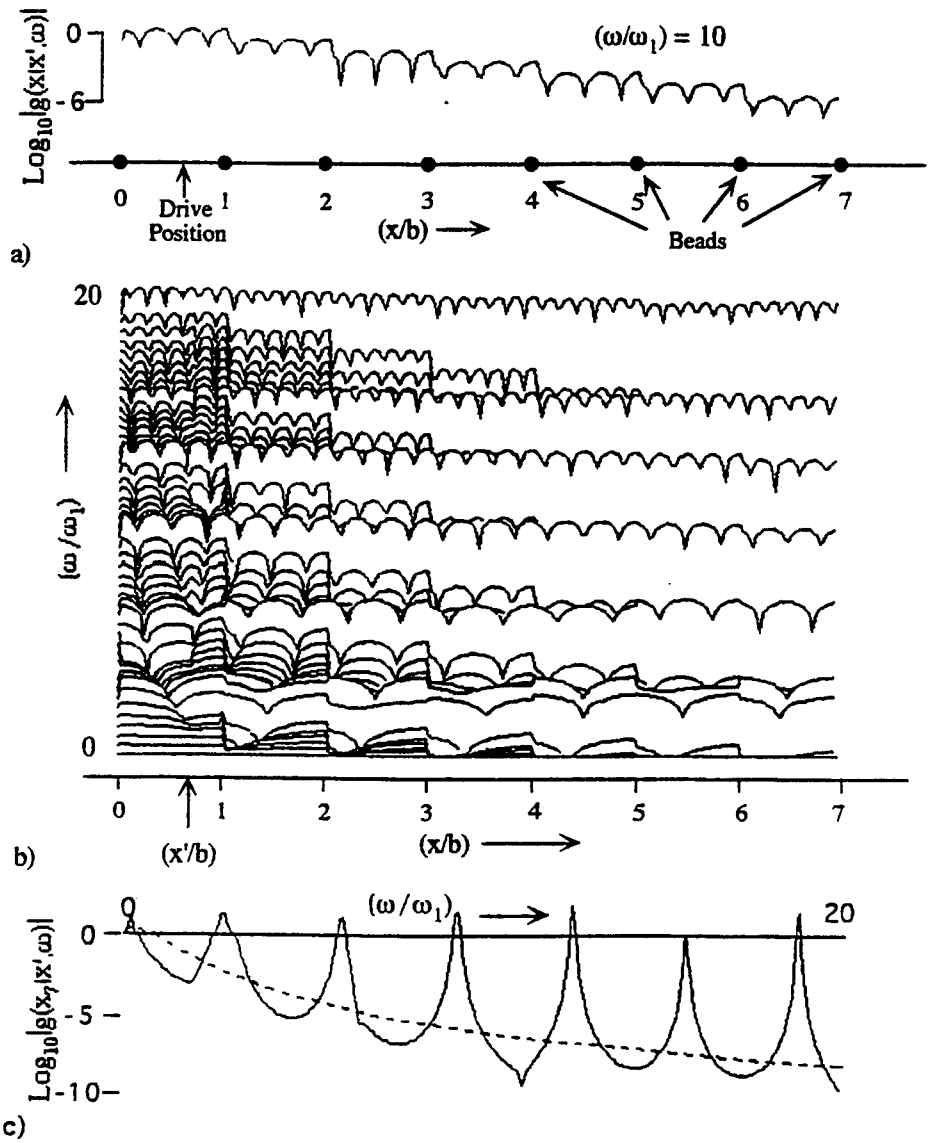

Fig. 2. Periodic bead spaceing; a) the positions of the beads and the response as a function of distance along the string at a single frequency, b) spatial responses as in a) but at a series of frequencies, and c) the response at bead number 7 as a function of frequency, the dashed line is the product sum of the transmission at beads 1 to 7 inclusive and deleniates between pass and stop bands.

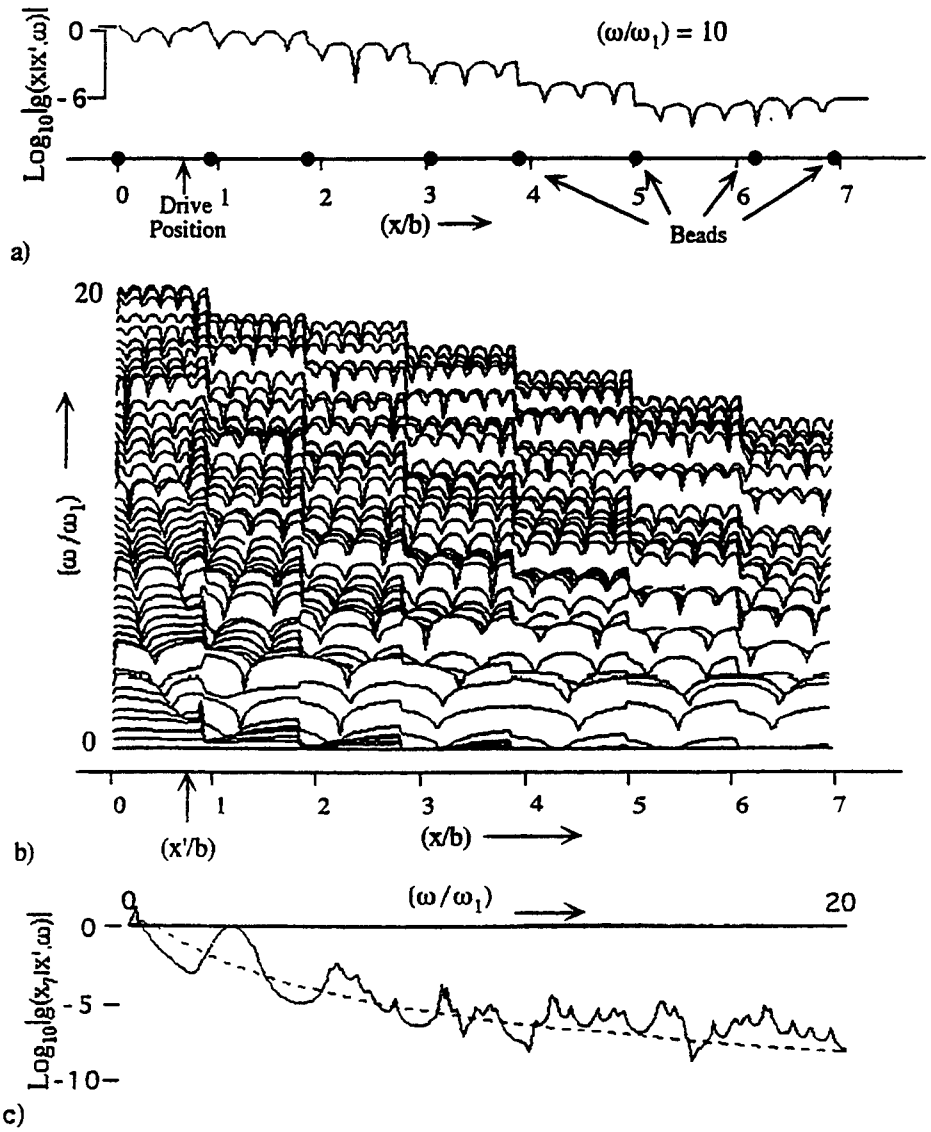

Fig. 3. A-periodic bead spaceing; in the same format as Fig. 2.

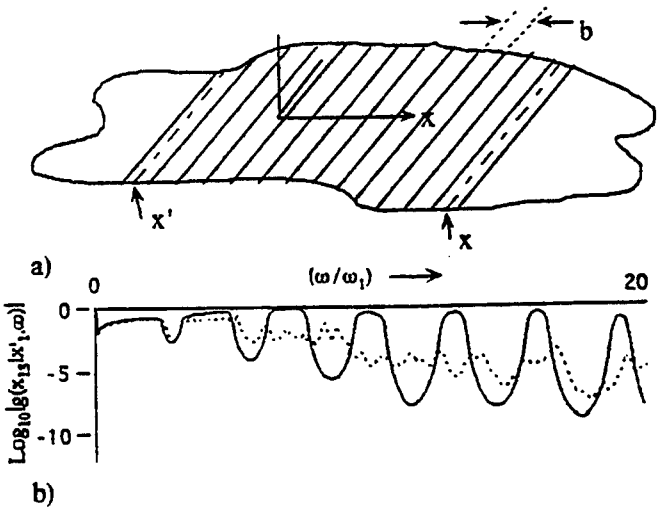

Fig. 4 a) An infinite membrane with 14 ribs attached. b) The transmissibility as a function of frequency for the regularly spaced ribs (solid line) and for one realization of a set with 20% random variation in rib spaceing (dashed line).

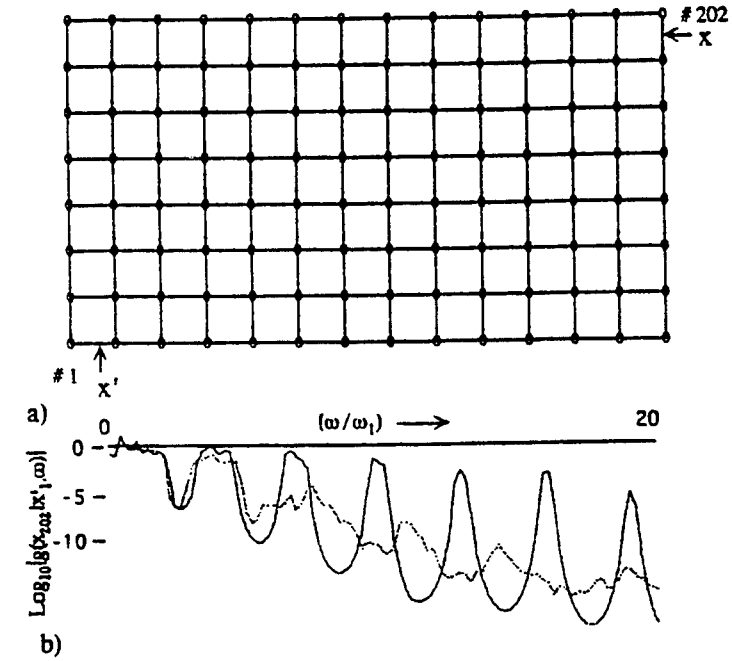

Fig. 5 a) A 13 x 7 planar array of connected 1-D systems driven at x' in system #1; b) the transmissibility as measured in system #202 as a function of frequency for the regular system (solid line) and for one realization of systems with 20% random variation in lengths (dashed line).

Estimated Mass and Stiffness Matrices of Shear Building from Modal Test Data

Ping Yuan, ZhiFeng Wu, and XingRui Ma
Department of Civil Engineering,
Harbin Institute of Technology, Harbin, 150001, P.R.China

ABSTRACT:

A method to estimate mass and stiffness matrices of shear building from modal test data is presented in this paper. The method depends on that measurable points are less than the total structural degrees of freedom, and on first two orders of mode of structure are measured. So it is applicable to most general test. By giving a method to estimate modal data of immeasurable points, global mass and stiffness matrices of structure are obtained by using first two orders of modal data. By use of iteration the optimum global mass and stiffness matrices are gained. Finally an example is studied in this paper. Its result shows that this method is reliable.

1.Introduction:

Measurement of the dynamic characteristics, natural frequencies and mode shapes of structure from modal dates is developed in recent years. Naturally, there is only a finite number of points on the structure for which data can be collected. These points are generally a small subset of the total degrees of freedom(DOF) in a finite element model of the structure. In fact, the number of measurement points may also be less than the total number of vibrational modes identified in the test, specially when utilizing modern instrumentation with high sampling rates and powerful, inexpensive scientific workstations for data for n mode, where $n>l$, there is not a unique model of classical mass and stiffness form with physical DOF that possesses order-n dynamics given only l spatial measurement points.

Much research in recent years has focused on methods for correlation or reconciliation of finite element models that inherently possess very large-order dynamics to the limited sensor and frequency data obtained from modal testing.[1-3]

The primary goal of the present paper is to investigate direct solutions to the inverse vibration problem when the number of sensors l is less than the number of identified modes n. We will show that mass and stiffness matrices of

dimension n, referring to the total DOF, can be found from the l identified modes and the modal dates of the l points.

In this paper, the unmeasured modal dates are evaluated by the measured modal dates. Finally, the mass and stiffness matrices are obtain by first two order modes.

2.Evaluation of unmeasured modal dates

Recent work in the area of structural identification has included the determination of mass and stiffness matrices directly from continuous time system realizations. [4] This approach is that it requires the dimension of the physical mode to be equivalent to the number of second-order states, implying that the number of independent sensors measured are equal to the number of identified modes. A more practical approach is to enrich the computer mass and stiffness matrices with the complete set of measured modes, independent of the number of sensors. This allows the resulting to express contributions of all of the modes observable from the available sensors. We begin by developing the concept of reduced the measured modal dates.

If structure is regard as shear building, we can assume that 1) the total mass of the structure is concentrated at the levels of the floors; 2) the floors are infinitely rigid as compared to the columns; and (3) the deformation of the structure is independent of the axial forces present in the columns. These assumptions transform the problem from a structure with an infinite number of degree of freedom to a structure that has only as many degrees as floor levels. Clearly the stiffness matrix of shear building is a triangular matrix, and the mass matrix is a diagalization matrix. The mass and stiffness matrices of shear building can be written as:

$$K=\begin{bmatrix} k_1+k_2 & -k_2 & \cdots & \cdots & 0 \\ -k_2 & k_2+k_3 & -k_3 & & \vdots \\ \vdots & & \ddots & & \\ & & -k_{n-1} & k_{n-1}+k_n & -k_n \\ 0 & \cdots & \cdots & -k_n & k_n \end{bmatrix} \tag{1}$$

$$M=\begin{bmatrix} m_1 & & \cdots & 0 \\ & m_2 & & \\ \vdots & & \ddots & \vdots \\ & & m_{n-1} & \\ 0 & & \cdots & m_n \end{bmatrix}$$

High building always has standard floor levels. It is to said that these levels have the same mass and stiffness. Assumed that the standard levels are i,

i+1……j, j≤n, i≠1, where n is the total levels of building. In a word there are j-i+1=d standard levels, and the frist level is not standard level. If i-1 and j levels are placed sensors, these two points become measured points. We will use the modal dates of these two points to evaluate the modal dates of unmeasured points.

Suppose that we are given an arbitrary undamped MDOF system. The differential equation of the system is given by:

$$M\ddot{X}+KX=F$$

where M is the structural mass matrix, K is the structural stiffness matrix. X is the vector of generalized modal deflections, $\ddot{X}$ is the vector of generalized modal accelerations. F is the vector of external forces. Considered the corresponding characteristic equation:

$$(K-\lambda_l M)\phi_l=0$$

where λ_l is the lth eigenvalue, and ϕ_l is the lth corresponding mode shape or eigenvector. Eq(1) can be also written as:

$$\left(\begin{bmatrix} k_{aa} & k_{ab} & 0 \\ k_{ba} & k_{bb} & k_{bc} \\ 0 & k_{cb} & k_{cc} \end{bmatrix} - \lambda_l \begin{bmatrix} m_{aa} & 0 & 0 \\ 0 & m_{bb} & 0 \\ 0 & 0 & m_{cc} \end{bmatrix}\right) \begin{Bmatrix} \phi_a \\ \phi_b \\ \phi_c \end{Bmatrix}_l = 0 \tag{2}$$

where a=1,2,……i-1, b=i,i+1,……j-1, c=j,j+1,……n, the mass matrices m_{aa}, m_{bb}, m_{cc} are diaganalization matrices, and the stiffness matrices can be written as:

$$k_{ba}=\begin{bmatrix} 0 & \cdots & -k_i \\ \vdots & \ddots & \vdots \\ 0 & \cdots & 0 \end{bmatrix} = k_{ab}^T$$

$$\text{and } k_{bc}=\begin{bmatrix} 0 & \cdots & 0 \\ \vdots & \ddots & \vdots \\ -k_j & \cdots & 0 \end{bmatrix} = k_{cb}^T \tag{3}$$

Eq.(2) is partition of Eq.(1). The second line of Eq.(2) can be expressed as:

$$k_{ba}\phi_a + k_{bb}\phi_b + k_{bc} - \lambda_l m_{bb}\phi_b = 0 \tag{4}$$

This reduction concept considers the influence of mass. Substituting Eq.(3) into Eq(4), we have:

$$k_{bb}\phi_b - \lambda_l m_{bb}\phi_b = \begin{Bmatrix} k_i\phi_{i-1} \\ 0 \\ \vdots \\ 0 \\ k_j\phi_j \end{Bmatrix}_{d\times 1} \tag{5}$$

Expanding Eq.(5), we have:

$$\begin{aligned}
&(k_i + k_{i+1})\phi_i - k_{i+1}\phi_{i+1} - \lambda_l m_i \phi_i = k_i \phi_{i-1} \\
&-k_{i+1}\phi_i + (k_{i+1} + k_{i+2})\phi_{i+1} - k_{i+2}\phi_{i+2} - \lambda_l m_{+1i}\phi_{i+1} = 0 \\
&\qquad\qquad \cdots \quad \cdots \\
&-k_{j-1}\phi_{j-2} + (k_{j-1} + k_j)\phi_{j-1} - \lambda_l m_{j-1}\phi_{j-1} = k_j \phi_j
\end{aligned} \tag{6}$$

Because from level i to level j are standard level, so their stiffness and mass have following relationships.

$$\begin{aligned}
k &= k_i = k_{i+1} = \cdots = k_j \\
m &= m_i = m_{i+1} = \cdots = m_j
\end{aligned} \tag{7}$$

substituting Eq.(7) into Eq.(6), Eq.(6) can be simplifies to:

$$A\{\phi_b\} = \left(\begin{bmatrix} 2-\lambda_l\alpha & -1 & \cdots & 0 \\ -1 & 2-\lambda_l\alpha & -1 & \vdots \\ \vdots & & \ddots & \\ 0 & \cdots & -1 & 2-\lambda_l\alpha \end{bmatrix} \right) \begin{Bmatrix} \phi_i \\ \phi_{i+1} \\ \vdots \\ \phi_{j-1} \end{Bmatrix} = \begin{Bmatrix} \phi_{i-1} \\ 0 \\ \vdots \\ \phi_j \end{Bmatrix} = D \tag{8}$$

where $\alpha = \dfrac{m}{k}$, $\{\phi_b\} = \{\phi_i, \phi_{i+1}, \cdots, \phi_{j-1}\}^T$, $D = \{\phi_{i-1}, 0, \cdots, \phi_j\}^T$, using least square approach the unmeasured modal shape $\{\phi_b\}$ can be obtained:

$$\{\phi_b\} = (A^T A)^{-1} A^T D \tag{9}$$

By mean of Eq(9) those unmeasured DOF can be expressed by measured DOF. It is to said those modal dates from i to j-1 can be evaluated by (i-1)th and jth level modal dates. In this method the influence between the mass of DOF and level displacement is considered. Using this method measured points can be reduced.

3.The evaluation of mass and stiffness matrices

Expanding Eq(1) we have:

$$\begin{aligned}
&(k_1 + k_2)\phi_{l1} - k_2\phi_{l2} - \lambda_l m_1 \phi_{l1} = 0 \\
&-k_2\phi_{l1} + (k_2 + k_3)\phi_{l2} - k_3\phi_{l3} - \lambda_l m_2 \phi_{l2} = 0 \\
&\qquad \cdots \qquad \cdots \\
&-k_{n-1}\phi_{ln-2} + (k_{n-1} + k_n)\phi_{ln-1} - k_n\phi_{ln} - \lambda_l m_{n-1}\phi_{ln-1} = 0 \\
&-k_n\phi_{ln-1} + k_n\phi_{ln} - \lambda_l m_n \phi_{ln} = 0
\end{aligned} \tag{10}$$

In order to evaluate mass and stiffness of structure, equation (10) can be written as:

$$\begin{bmatrix} \phi_{l1} & -\lambda_l\phi_{l1} & \phi_{l1}-\phi_{l2} & & & \cdots & & & 0 \\ \phi_{r1} & -\lambda_r\phi_{r1} & \phi_{r1}-\phi_{r2} & & & & & & \\ & & \phi_{l2}-\phi_{l1} & \lambda_l\phi_{l2} & \phi_{l2}-\phi_{l3} & & & & \\ & & \phi_{r2}-\phi_{r1} & \lambda_r\phi_{r2} & \phi_{r2}-\phi_{r3} & & & & \\ \vdots & & \cdots & & \ddots & & \cdots & & \vdots \\ & & & & & \phi_{ln-1}-\phi_{ln-2} & \lambda_l\phi_{ln-1} & \phi_{ln-1}-\phi_{ln} & \\ & & & & & \phi_{rn-1}-\phi_{rn-2} & \lambda_r\phi_{rn-1} & \phi_{rn-1}-\phi_{rn} & \\ & & & & & & \phi_{ln}-\phi_{ln-1} & \lambda_l\phi_{ln} & \\ & & & & & & \phi_{rn}-\phi_{rn-1} & \lambda_r\phi_{rn} & \end{bmatrix} \begin{Bmatrix} k_1 \\ m_1 \\ k_2 \\ m_2 \\ \vdots \\ \vdots \\ \vdots \\ k_n \\ m_n \end{Bmatrix} = 0 \quad (11)$$

where r is the rth mode. This equation can be simply written as:

$$B\{b\} = 0 \quad (12)$$

where $\{b\} = \{k_1, m_1, \cdots\cdots k_n, m_n\}^T$. In order to solve this equation the number of equations should equal the number of unknown. Because the number of equation is $2\times$n, so we used two order modes. Clearly matrix B is a singular matrix. In order to assuming m_n=1, the Eq.(12) can be expressed as:

$$B'\{b'\} = \begin{Bmatrix} 0 \\ \vdots \\ \lambda_l\phi_{ln} \\ \lambda_r\phi_{rn} \end{Bmatrix} \quad (13)$$

where B' is the matrix that eliminate the last two lines and last two columns of matrix B. {b'} is the vector that eliminate the last member of vector {b}. Using least square approach {b'} can be obtained.

$$\{b'\} = (B'^T \cdot B')^{-1} B'^T \begin{Bmatrix} 0 \\ \vdots \\ \lambda_l\phi_{ln} \\ \lambda_r\phi_{rn} \end{Bmatrix} \quad (14)$$

The mass and stiffness matrices obtained by Eq.(14) are not the real value. There is a constant rate between evaluate value and real value.

The following procedure has developed for evaluated the global mass and stiffness matrices of shear building.

Step 1: Choose the initial parameter α_o

α is the ratio between the mass and the stiffness of standard levels. We defined the initial parameter $\alpha_o = \frac{1}{\lambda_l}$.

Step 2: Evaluate the mode shapes of unmeasured DOF

In this step Eq.(9) is used to estimated the two order mode shapes $\{\phi\}_l$ and $\{\phi\}_r$. Where $\{\phi\}_l$ and $\{\phi\}_r$ are the *l*th and rth corresponding mode shapes.

Table 2.

	k_1(N/m)	k_2	k_3	k_4	m_1(kg)	m_2	m_3	m_4
Real value	18000×6	18000×3	18000×3	18000×3	18000×5	18000×2	18000×2	18000×2
Evaluation	2.9948	1.4994	1.4994	1.4994	2.4991	0.99896	0.99896	1.0

5. Conclusion

A new method to evaluated mass and stiffness matrices of shear building from modal test dates is presented in this paper. This approach based on the number of measurement points less than the number of total degrees of freedom of structure. In this method only first two order modes are used and the influence of mass is considered. By mean of this method it is possible of using modal test dates to evaluate the global mass and stiffness matrices and the damage of structure.

6. References

1. Kabe,A.M. *Stiffenss Matrix Adjustment Using Mode Data*. AIAA. 1985. Vol 23. №.9. 1431-1436

2. Farhat,C., and Hemez, F., *Updating Finite Element Dynamic Models Using an Element-By-Element Sensitivity Methodology*. AIAA,1993,Vol 31, №.9.1702-1711

3. Yang,C.D., and Yeh,F.B., *Identification, Reduction, and Retinement of model Parameters by the Eigensystem Realization Algorithm*. J. of Guidance, Control and Dynamics, Vol.13,№.6, 1990, 1051-1059

4. Baruch,M., *Optimization Procedure to Correct Stiffness and Flexibility Matrices Using Vibration Tests*, AIAA , Vol.16, 11, 1978, 1209-1210

5. Topole,K.G., and Stubbs,N., *Non-destructive Damage Evaluation of a Structure from Limiten Modal Parameters*, Earthquake eng. struct. dyn., Vol 24, 11, 1995, 1427-1436

THE PROBLEM OF EXPANDING THE VIBRATION FIELD FROM THE MEASUREMENT SURFACE TO THE BODY OF AN ELASTIC STRUCTURE

Yu.I.Bobrovnitskii
Blagonravov Institute of Mechanical Engineering Research of the Russian Academy of Sciences, Moscow 101830, Russia

Introduction

Knowledge of the distribution and magnitude of the dynamic stresses of an engineering structure due to extensive vibration is important for the estimation of the structure reliability and its mean service time. Another practical problem where it is needed is control of the structural vibration: knowledge of the stresses and displacements allows one to compute the vector field of the vibration power flow which makes visible the sources and transmission paths of vibration and thus indicates adequate means to control it [1,2].

Commonly used sensors, e.g., accelerometers or strain gauges, can measure the vibration parameters (acceleration or strains) in discrete points. Some instruments developed in the last decade such as laser interferometers [3] and the vibrometers based on the near field acoustic holography [4], can measure continuous distribution of the vibration amplitudes at a certain surface. Nevertheless in practice, at best only a part of the structure surface is accessible for measuring vibration directly. For most of the interior points of the structure body as well as for some portions of its surface, mounting sensors is impossible or impractical. So, the only way of estimating the stress-strained state of the whole structure is to expand the vibration field from the measurement surface to the structure body.

In this paper, an approach to such expansion is proposed which is applicable to complex elastic structures of which a part of the surface is accessible for direct vibration measurements while the rest of the surface and the body are not. This approach consists of measuring the distribution of the amplitudes for three components of the vibration displacement (or acceleration) on a portion of the accessible surface. For the volume contiguous with this portion, a special boundary-value problem which is called here the problem of field reconstruction (FR-problem) is stated and solved (see Fig.1). As a result, the displacement (and stress) field of this volume is determined (reconstructed) through the measurement data. Then, using the vibration amplitudes measured

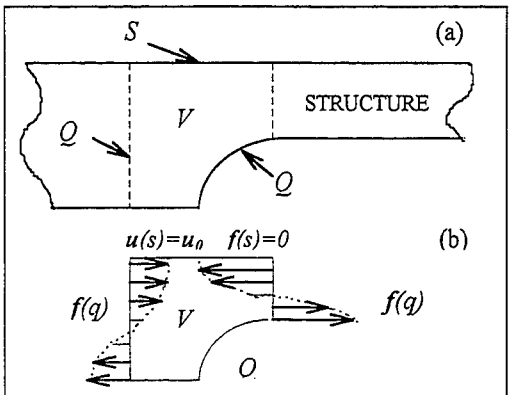

Fig.1.An elastic structure (a) of which only the upper surface S is accessible for vibration measurement; (b) boundary value problem for the chosen volume V: displacements ***u*** *and force f are specified on S.*

on another portion of the accessible surface, one can similarly determine the displacements and stresses in another volume, etc., until the whole structure is investigated.

The idea of reconstructing the general pattern from incomplete or indirect data is not new and is often used in mechanics and structural dynamics. It is used, for example, in the mode shape expansion methods of the model updating techniques, where the responses measured on a part of the DOF's of the FE-model are expanded to the slave (unmeasured) DOF's using the equations of motion [5]. Another example is reconstruction of the time history and localisation of external forces from the measured structural responses [6].

All the cases, where the idea of reconstruction is realised, are distinguished by the statement of the corresponding mathematical problem and by physical peculiarities. In this paper, the key problem is stated as reconstruction of the vibration field in a finite elastic solid from the amplitudes of the displacements of a part of its boundary free of tension. In structural dynamics, such statement was first proposed in Ref. [7] relating to measurement of the vibration power flow in solids. Similar statements are met in a number of papers on the static theory of elasticity (e.g., [8]) for reconstruction of the stresses inside a machine part through the measurement of the strains on its surface.

In what follows, the rigorous mathematical formulation of the FR-problem is given and its general properties are studied. Results of the computer simulation and of the laboratory experiment are presented which prove the practicality of the approach suggested.

Formulation of the problem

For a selected elastic volume V of the structure (Fig.1b), the problem of the harmonic field reconstruction can be formulated as follows (time dependence $exp(-i\omega t)$ is omitted):

find a solution to the homogeneous Lame equations

$$\mu\Delta\boldsymbol{u}(x)+(\lambda+\mu)\,\mathrm{graddiv}\boldsymbol{u}(x)+\rho\omega^2\boldsymbol{u}(x)=0,\quad x\in V, \tag{1}$$

which satisfies the conditions

$$\boldsymbol{u}(s)=\boldsymbol{u}_0(s),\quad \boldsymbol{f}(s)=0,\qquad s\in S, \tag{2}$$

on the upper part S of the surface. Here $x=(x_1, x_2, x_3)$ are the co-ordinates of a point of the volume V, $\boldsymbol{u}=(u_1, u_2, u_3)$ is the displacement vector, $\boldsymbol{f}=(f_1, f_2, f_3)$ is the vector density of the forces acting on the surface, λ and μ are the elastic Lame coefficients, and $\boldsymbol{u}_0(s)$ are the known (measured) displacement amplitudes.

The formulation (1),(2) is not traditional for equations of the elliptic type: the boundary conditions on the part S of the surface are overdetermined, i.e., both the displacements and the forces are specified, whereas no quantities are specified on the rest part Q of the surface.

The boundary-value problem (1),(2) may be formulated as an integral equation. Let $G(x/q)$ be the 3x3 matrix of the Green's functions describing the response (displacement vector) at a point $x\in V$ to a unit force at a point $q\in Q$. Assuming $x=s\in S$, the problem (1),(2) may be rewritten as

$$\boldsymbol{u}_0(s)=\iint_Q G(s/q)\boldsymbol{f}(q)\,dQ. \tag{3}$$

This is a set of three Fredholm equations of the first kind, where the unknowns are the reaction forces $\boldsymbol{f}(q)$ acting on the inaccessible surface Q; the matrix G is assumed to be known. If the forces $\boldsymbol{f}(q)$ are found from Eq.(3), then the displacement field of the volume V can be computed as

$$\boldsymbol{u}(x)=\iint_Q G(x/q)\boldsymbol{f}(q)\,dQ. \tag{4}$$

The formulations (1),(2) and (3),(4) are convenient for investigating the general properties of the problem. In practice, preferable is the formulation based on the expansion of the field in the normal modes of V

$$\boldsymbol{u}(x)=\sum_n a_n\varphi_n(x), \tag{5}$$

where the forms $\varphi_n(x)$ are assumed to be known and the amplitudes a_n must be determined from the first boundary condition (2) on S:

$$\boldsymbol{u}_0(s)=\sum_n a_n\varphi_n(s). \tag{6}$$

Eq.(6) represents an expansion of the known function $u_0(s)$ in terms of the functions $\varphi_n(x)$, non-orthogonal on S, which can be reduced in different ways to a set of linear algebraic equations. In practice, the number of normal modes is taken to be finite, and the number of the unknowns a_n in Eqs.(5),(6) as well as the number of the algebraic equations is finite, too. Discretization of the continuous operators in (1)-(3) also leads to finite systems of linear equations. Thus, in all the above formulations the problem of the field reconstruction reduces to the linear operator equation of the first kind

$$Af = u, \tag{7}$$

where, in theory, the functions $u(s)$ and $f(q)$ are elements of two functional spaces U and F, and A is a linear operator. In practice, u and f are vectors of two Euclidean spaces, and A is a rectangular matrix operator.

General properties and formal solution

The problem of field reconstruction has the following general properties. The problem has a bounded solution if the vector-function $u_0(s)$ is sufficiently smooth -see below. The solution, if it exists, is unique. It means that the absence of information on the inaccessible part Q of the boundary is completely compensated by the overdetermined boundary conditions (2) on the accessible part S. The proof of the uniqueness is based on the Almansi's theorem[9] according to which if on a part (even very small) of the surface of a finite elastic body displacements and stresses are simultaneously equal to zero, then the stresses are zero everywhere and the body is at rest. Almansi proved the theorem for statics; an extension to the dynamic theory of elasticity is given in the paper [7]. One more property: the solution of the FR-problem does not continuously depend on the input data: small variations Δu_0 of the prescribed function may cause large variations Δf of the solution. This can be concluded from the general properties of the Fredholm integral equations of the first kind with continuous kernels (the case of Eq.3). Hence, the problem of field reconstruction belongs to the class of ill-posed in the sense of Hadamard problems of mathematical physics.

Ill-posed problems are often met and solved in various scientific disciplines. For example, the mathematical problem of differentiating functions is ill-posed; the mechanical problem of reconstructing the external forces through the structural response mentioned above is also ill-posed, etc.[10,11]. All the existing methods of treating such problems are principally based on the idea of replacing the ill-posed problem with a well-posed problem appropriately chosen with the aid of an additional information concerning the desired solution. For treating the field reconstruction problem, the most appropriate is

the Singular Value Decomposition (SVD) technique[12]. Below follows the solution of the FR-problem obtained by this technique.

Let $\sigma_1 > \sigma_2 > \ldots$ be the singular values of the operator A in Equation (7), and $\{f_1, f_2, \ldots\}$ and $\{u_1, u_2, \ldots\}$ be the singular pair, i.e. two sets of orthonormal functions (Note that σ_j^2 are the eigen values of the Hermitien operators A^*A and AA^*, while f_j and u_j are their eigen functions). Representing a given function u as a series in terms of u_j and seeking the solution as a series in f_j, one can obtain the following exact formal solution to the problem (7):

$$f = \sum_{j=1}^{\infty} (b_j / \sigma_j) f_j, \quad \text{where} \quad u = \sum_{j=1}^{\infty} b_j u_j. \qquad (8)$$

It is seen from Eq.(8) that a bounded solution to the problem exists (the series converges) if the given function u is sufficiently smooth or, more exactly, if the coefficients b_j of its expansion (8) tend to zero more rapidly than the singular values σ_j. For real structures, the singular values tend to zero very fast (exponentially), therefore the exact functions of distribution of the vibration amplitudes at the accessible part S of the surface should be and actually are very smooth and do not contain components rapidly oscillating along the surface, i.e., addenda in (8) with large numbers j. However, small but finite random errors in u, experimental or due to rounding in a computer, have wide spatial spectra and result in expansions (8) with non-zero coefficients b_j of large numbers which, after enhancing by the small singular values, may cause large errors in the solution f, making it unstable.

The simplest way to overcome the difficulty is to seek an approximate solution which involves a finite number N of terms in the singular value decomposition, i.e. to truncate the series' in (8). With a judicious choice of N this solution does not differ too much from the exact solution (8), because the exact (not contaminated by noise) vibration function u does not contain components with high numbers. On the other hand, this solution cuts off the rapidly oscillating components $j > N$, thereby reducing the inaccuracy due to experimental or computer errors in the input data. Truncating the series (8), we restrict the solution by smooth functions and this is the additional *a priori* information which makes the problem well-posed. However, the choice of the best truncation number N is a difficult and unstudied question, and answering it was one of the objectives of the computer simulation and laboratory experiment.

Results of computer simulation

In computer simulation, two simple structures were studied - a finite longitudinally vibrating rod and a thin elastic strip executing vibrations in its

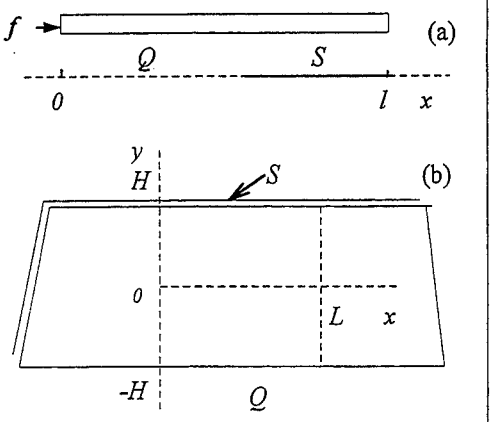

Fig.2. Two simple structures used in computer simulation: a longitudinally vibrating rod (a) and an elastic strip vibrating in its surface(b).

plane(Fig.2).The rod(Fig.2a) is excited by a harmonic force at the left end. The accessible for measurement part is supposed to be the region S at the right end (data region), while the rest part Q of the rod is considered as the reconstruction region. The complex displacement amplitude $u(x)$ satisfies the Bernoulli's equation of longitudinal vibrations [13] with a complex Young modules. This boundary value problem has an analytical solution which has been used for computing the input data "measured" in the region S and for estimating the accuracy of reconstruction in the region Q. In calculations, a modal model was used with the modes corresponding to the free boundary conditions at both ends:

$\{u_n(x) = (\varepsilon_n / l)^{1/2} \cos(\pi(n-1)x/l);\ \varepsilon_1 = 1,\ \varepsilon_n = 2 \text{ for } n = 2,3,...\}$.

The solution (5) has here the form of a finite sum

$$u(x) = \sum_{n=1}^{N} a_n u_n(x) \tag{9}$$

with unknown amplitudes a_n. Equating the representation (9) to M measured values of u at M points of the region S gives a set of M linear algebraic equations with N unknowns that were solved by the SVD-technique.

The elastic strip (Fig.2b) of height $2H$ comparable with the elastic wavelengths vibrates in its plane. It is supposed that only upper surface $y = H$ of the strip is accessible for measurement. It is required to reconstruct the vibration field in the region V with the following dimensions: $l = 3H$. Vibrations of the strip satisfy the dynamic equations of the plane stress state and the boundary conditions of absence of stresses at $y = -H$ and $y = H$. As it is known, they are analogous to vibrations of an elastic layer. Therefore, the field in the strip is represented as a sum of N Lamb's normal modes [13]:

$$\{u_x(x,y);\ u_y(x,y)\} = \sum_{n=1}^{N/2} [\, a_n \{u_{xn}^{+}(y);\ u_{yn}^{+}(y)\} \exp(ik_n x) + b_n \{u_{xn}^{-}(y);\ u_{yn}^{-}(y)\} \exp(ik_n(l-x))], \tag{10}$$

where the k_n are the propagation constants, i.e., the roots of the Rayleigh-Lamb dispersion equation, and the expressions in brackets describe the mode

forms. On the accessible surface $y = H$ of the strip, $M/2$ equidistant points are chosen at which the displacement components, u_x and u_y, are computed using the exact solution. (The exact solution is taken as in an infinite strip excited by a unit y-force applied to the point $(-4H, H)$, i.e., at the distance $4H$ from the region of interest V). Equating the "measured" amplitudes to (10) gives a set of M linear algebraic equations with N unknown mode amplitudes, a_n and b_n, which can be found by the SVD-technique.

The results of computer simulation obtained for the two different structures on Fig.2 (the first structure is one-dimensional and the second is two-dimensional) are similar. They are also similar to those obtained for other structures (the author verified them for an acoustic waveguide and for a circular cylindrical shell). So, they are rather general.

The first and practically most important result is the existence of an optimal model: there is a number N_0 of normal modes (model·parameters) which renders minimum to the reconstruction error. It means that too complicated and exact models containing an excessive number of model parameters $N > N_0$ as well as rough models with a small number of the parameters $N < N_0$, give larger errors of field reconstruction than the optimal model with N_0 parameters. The best number N_0 depends on the structure type, geometry, frequency, etc., but most of all on the accuracy and amount of input data.

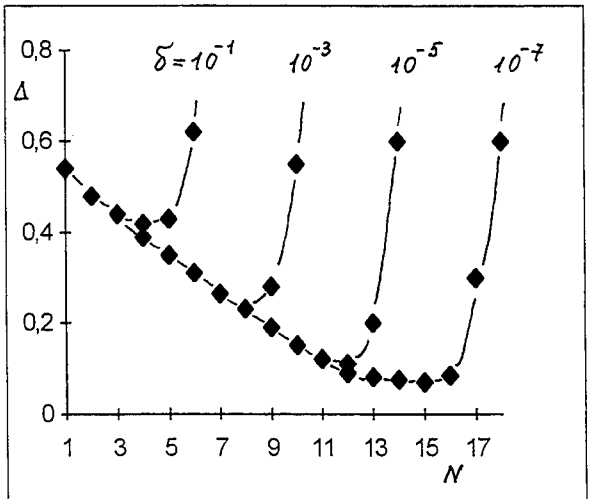

Fig.3 The reconstruction error Δ versus the number of model parameters N for various values of the input error δ.

Fig.3 presents the field reconstruction error Δ versus the number of the model parameters computed for the strip on Fig.2b. The error Δ is defined as relative square module deflection of the reconstructed displacement from the exact one averaged over the reconstruction region V. In computing these plots, a random error of prescribed standard value δ is added to the "measured" data. Four curves in Fig,3 correspond to various values of the

standard error δ. It is seen, that each curve of the field reconstruction error has a pronounced minimum beyond which the error sharply increases reaching arbitrary large values. This result seeming paradoxical has a clear physical explanation. The reason lies in random errors of the input data.

If there were no input errors, i.e., if the input data were known mathematically exactly, the reconstruction error would monotonically decrease with the number of modal parameters N: the more exact is the model the better is the approximation. When input errors are introduced, the decreasing of $\Delta(N)$ holds only to a certain limit since for large N the errors in the input data, enhanced by small singular values (see equation 8), may give an arbitrarily large error in the result of reconstructing the field.

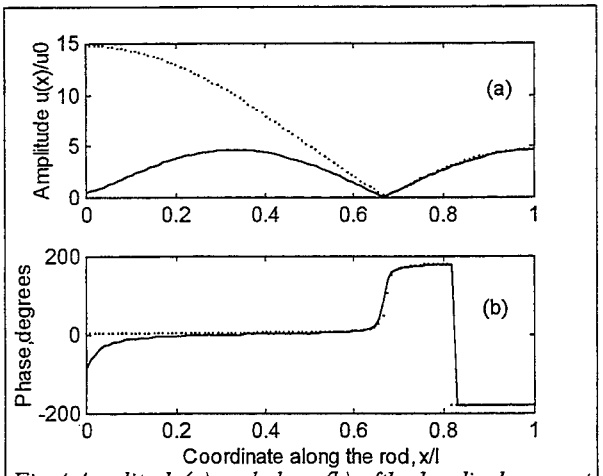

Fig.4.Amplitude(a) and phase(b) ofthe bardisplacement exact -solid lines, reconstructed - dotted lines: kl=4.7; loss factor 0.05; number of modes used N = 2.

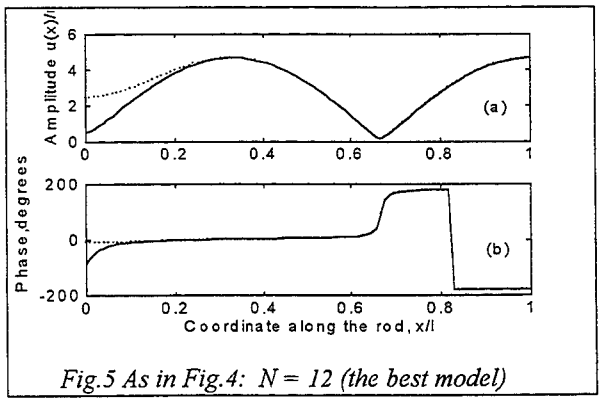

Fig.5 As in Fig.4: N = 12 (the best model)

Thus, for each value of the input error, there exists an optimal number of the model parameters which corresponds to the minimal error in the reconstructed field. Curves, similar to the curves in Fig.3, are obtained also for other structures. For example, when 30% of the bar in Fig.2a are accessible for measurement and the input error is equal to 10^{-7}, the best number of modes is $N_0 = 12$. Fig.4-6 present the displacement amplitude and phase distributions along the rod for a rough model ($N = 2$), the optimal model ($N=12$) and an excessively complicated model

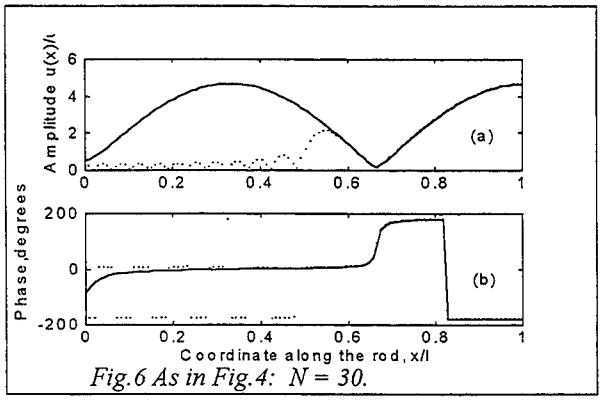

Fig.6 As in Fig.4: N = 30.

(N = 30). It is seen that in all cases the reconstruction error, being small in the measurement region S, increases with distance from S.

Another finding in the computer simulation concerns the amount of input data necessary for obtaining the best solution. Fig.7 presents a typical dependence of the field reconstruction error on the number M of measurement points in the region S for alongitudinally vibrating bar (Fig.2a). It is seen, that the reconstruction error is unstable when the number M is small. With increasing M the error Δ becomes stable and decreases tending to a certain constant value. Similar dependencies take place for the strip and other structures. The optimal amount of the input data correspond to the number of measurements M two or three times the number N of the model parameters involved. A further increase of the amount of data does not improve the results and is, therefore, unjustified.

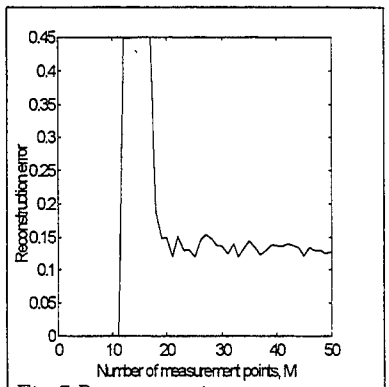

Fig.7 Reconstruction error versus number of measurement points

It should be noted that all components of the prescribed displacement vector are needed in order to obtain the best reconstruction error. This follows from the uniqueness theorem mentioned above: the problem of field reconstruction is uniquely solvable only if the full displacement vector on the accessible surface is available.

Some experimental results

To verify the proposed method, a laboratory experiment has been carried out on a circular cylindrical shell (Fig.8). A finite open shell with dimensions in mm 900x300x3.5 is excited by a shaker with harmonic signals. The amplitudes and phases of vibration are measured at the surface S by a small (2g) 3-component accelerometer, the data are fed into a PC. The

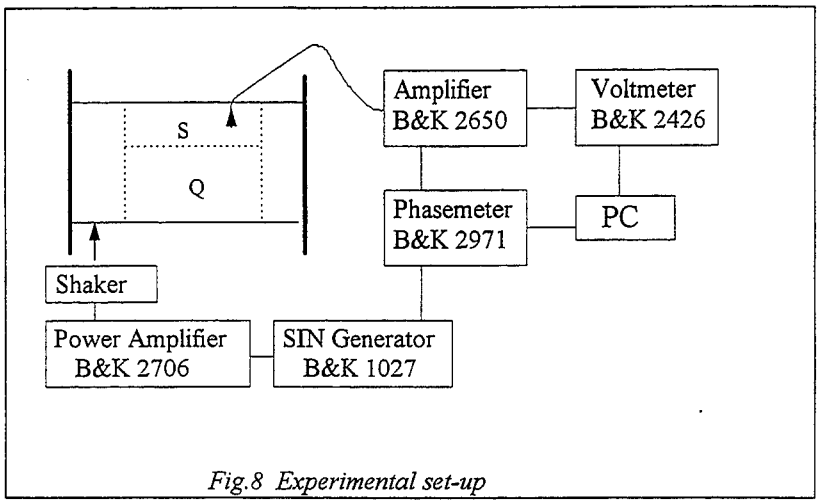

Fig.8 Experimental set-up

amplitudes and phases of vibration in the region Q are reconstructed (by the algorithm described above) and compared with the actual ones. The reconstruction error is computed with respect to the actual field of the region Q. In modelling the vibration field in the shell, the displacement vector is represented by the series of the normal modes which satisfy the simplest shell equations (the Donnel-Mushtari theory [14]). The maximal number of the normal modes used is 52. These modes correspond to the circumferential numbers up to $m = 10$. The evanescent modes decaying more than 40 dB at the distance from the region $S+Q$ to the end of the shell or to the shaker, are excluded from the model. The total error of measuring complex vibration amplitudes is estimated as $0.07 < \delta < 0.08$.

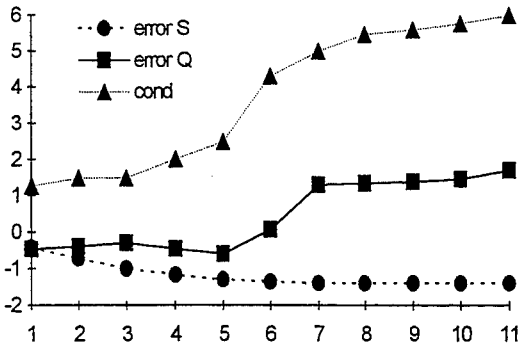

Fig.9 Logarithm of error and condition number vs. model complexity MC (see text); input data 60%.

Fig.9 and 10 show the dependencies of the reconstruction error Δ (solid lines) on the complexity of models used for one of the frequencies (f = 700 Hz) and for two different amount of input data. The curves are obtained as follows.

First, the simplest models containing the normal modes of one single circumferential

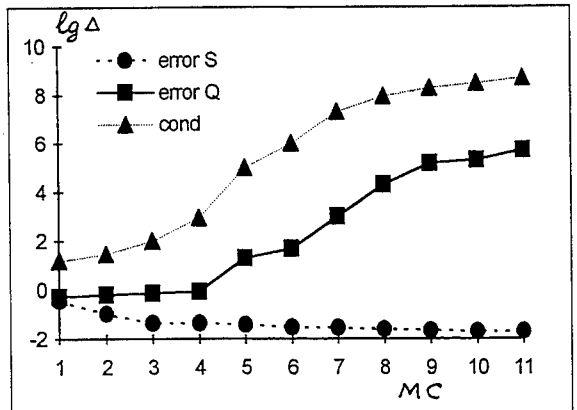

Fig.10 As in Fig.9: input data 40%

number m are tried. Among 11 models with $m = 0,1,...,10$, the best model is chosen which gives the minimal error in describing the measured data (in practice, only these data are actually available). In both cases of Fig.9,10 it is the model with the circumferential number $m = 6$. It corresponds to the model complexity $MC = 1$ in Fig.9,10. Then, all models with two circumferential numbers ($MC = 2$ in Fig.9,10) are considered: one is $m_1 = 6$ and another is chosen among 10 models with $m_2 \neq 6$ which gives the minimal error in describing the input data (It is found that m_2 equals 5 in the case of Fig.9 and $m_2 = 4$ for Fig.10). After that, all models with three circumferential numbers ($MC=3$) are investigated, etc., until all the models are exhausted. Thus, the dashed curves in Fig.9,10 correspond to the best models of various complexity for the measurement region S of the shell. Therefore, these curves decrease monotonically, at least, do not increase, with the number of the model parameters. At the same time, the error of the expansion to the reconstruction region Q (solid curves in Fig.9,10) has tendency to increase with the number of the model parameters. More exactly, they have minima beyond which they increase monotonically. For very complicated models, the reconstruction error may reach hundred of thousand. With these curves, correlate the curves of the condition number (dotted lines).

Now, the question how to choose the optimal model which minimises the reconstruction error in the inaccessible region (i.e., corresponds to the minimum of the solid line curves in Fig.9,10) using only the information about vibration of the measurement (accessible) region (i.e., using the dashed and dotted line curves in Fig.9,10) may be answered as follows. As one can observe from Fig.9 and 10, the error of describing the measured data (dashed lines) first rather rapidly decreases with the model complexity and then becomes almost constant. The best model just corresponds to the transition from the interval of rapid decrease to the interval of stable values of the dashed line curve. Conversely, the curves of the condition number (dotted lines in Fig.9,10) first grow slowly with MC but, after the best model is reached, their growth becomes rather fast.

Thus, it can be concluded that the optimal model can be approximately identified from the behaviour of the curves of the error in the input data and of the condition number. From the physical point of view, this "rule of thumb" is obvious - see explanation of Fig.3. But quantitatively, it is rather uncertain: one can only find an interval of models within which the best model lies. E.g., for the cases of Fig.9,10 the intervals correspond to $MC = \{4,5,6\}$ and $\{2,3,4\}$ where the reconstruction error equals $\{0.35, 0.25, 1.2\}$ and $\{0.64, 0.75, 0.85\}$ while the minimal values in these cases are 0.25 and 0.51. Much more certain identification of the best model can be made if at least one measurement point is taken in the reconstruction region; in other words, if it is possible to place at least one sensor into the needed part of the structure. In this case, however, another procedure of the optimal model identification is required.

Summary

The problem of expanding the vibration field from the measurement surface to the volume of an elastic structure is rigorously posed and studied theoretically and experimentally. When formalised, this problem, also called as the field reconstruction problem, is a non-traditional boundary value problem for differential equations of elliptic type. The conditions for existence of a solution are found and the uniqueness theorem is proven. A general solution based on the generalised singular value decomposition is obtained.

Results of computer simulation with simple structures are presented. Most attention is paid to studying the accuracy of the expansion to unmeasured parts of the structure. Relations between the expansion accuracy, the measurement errors and the complexity of the vibrational model of the structure (number of model parameters) are established. A salient feature of these relations is that, for a given input data accuracy, there is an optimal model which minimises the expansion error.

Results of laboratory experiments with a steel cylindrical shell executing forced harmonic vibration are also presented aiming to verify the obtained relations. Procedures of choosing the optimal models are discussed.

REFERENCES

1. Ramakumar, R., *Reliability engineering. Fundamentals and applications.* Prentice Hall, Allyn & Bacon and Ellis Horwood,1993.
2. *Structural intensity and vibrational energy flow (Proc.4th Int. Congress on intensity technique).* Senlis, France, 1993.
3. Tyrer, J.R., Determination of surface stresses and velocities by optical measurement. *In [2],* 35-45.

4. Maynard, J.D., Williams, E.G. and Lee,Y., Nearfield acoustic holography (NAH). *J.Acoust. Soc. Am.*, 1985, **78**, 1395-1413.
5. To,W.M. and Ewins, D.L., The role of the generalised inverse in structural dynamics. *J.Sound and Vibr.*, 1995, **186**, 185-195.
6. Yen, C.S. and Wu, E., On the inverse problem of rectangular plates subjected to elastic impulse. *J. Appl. Mech., 1995,* **62**, 692-705.
7. Bobrovnitskii, Yu.I., The problem of field reconstruction in structural intensimetry: statement, properties, and numerical aspects. *Acoust. Phys.*, 1994, **40**, 331-9.
8. Preiss, A.K., Evaluation of stress fields by a finite body of experimental information. *Mashinovedenie,* 1984, N2, 77-83.
9. Almansi, E., Un teorema sulle deformazioni elastiche dei solidi isotropi, *Atti R.Accad.Lincei,* 1907, Ser.5, **16**, 865-8.
10. Lavrentiev, M.M., *Some improperly posed problems in mathematical physics.* Springer, Berlin,1967.
11. Tikhonov, A.N. and Arsenin, V.Ya., *Solution of ill-posed problems.* Simon&Schuster, Washington DC, 1977.
12. Golub, G.H. and van Loan, C.F., *Matrix computations.* North Oxford Academic Publishing, Oxford, England, 1983.
13. Graff, K.F., *Wave motion in elastic solids.* Clarendon Press, Oxford, 1975.
14. Leissa, A.W., *Vibration of shells.* US Government Printing Office, Washington DC, 1973.

EVALUATION OF THE EQUIVALENT GEAR ERROR BY VIBRATIONS OF A SPUR GEAR PAIR

M. Amabili (*) and **A. Fregolent** (**)

(*) Dipartimento di Meccanica, Università di Ancona, Ancona, Italy

(**) Dipartimento di Meccanica ed Aeronautica, Università di Roma "La Sapienza", Roma, Italy

ABSTRACT

A new approach based on the measurement of the gear torsional vibrations is proposed to evaluate the equivalent gear error of a spur gear pair and to identify the natural frequency and the damping of the system. The test bench is modelled as a single degree of freedom system and must be realised by using stiff bearings and torsionally compliant shafts. The algorithm is based on the use of the harmonic balance method. Results can be obtained by using a quite simple experimental apparatus. The proposed approach has some advantages with respect to the traditional metrological methods. The effect of measurement errors on the accuracy of the identification is also investigated.

1. INTRODUCTION

In the last decades many papers were published on the effect of gear errors on the dynamic response of gear pairs, *e.g.* references [1-16]. In fact vibrations of gear pairs are largely affected by the amplitude and phase of deviations of the tooth profile from the true involute one. Pitch, pressure angle and mounting (eccentricities and misalignments) errors also are of great importance. Therefore gear errors must be checked to avoid bad working conditions of high speed gears and silent reducers. Moreover profile modifications are introduced to reduce gear vibrations and their accuracy must be verified. Analytical [3, 14, 17-18], numerical [2, 9-13, 15, 19-24] and approximate [6] methods were proposed in the past to simulate the dynamics of a spur gear pair, and single [2-3, 5-12, 21-22], multi [4, 20, 23-24] or infinite [25] degrees of freedom were used by different authors to model the system's behaviours. Multi axes reducers were investigated *e.g.* in references [13-14].

In the present study an approach based on the measurement of the gear torsional vibrations is proposed to evaluate the equivalent gear error of a spur gear pair and to identify the natural frequency and damping of the system. The equivalent error is a function of the gear position and is related to the errors of the driving and the driven gears and to the non-dimensional stiffness of the teeth; its dimension is length. The system is analytically studied by using a single degree of freedom system capable of modelling the experimental test

bench, which therefore must be realised using stiff bearings and torsionally compliant shafts. If gear pairs have different center distances, an appropriate housing or different housings must be built.

The algorithm is based on the use of the harmonic balance method [26]: it is applied to spur gear pairs having low contact ratio ε (*i.e.*, $1 < \varepsilon < 2$) and is suitable to identify pitch, profile, pressure angle and runout errors. Results can be obtained by using a quite simple experimental apparatus requiring only the measurement of vibration response of the driven gear during a revolution for at least three different rotational speeds. The gear pair must be tested with a fixed static load. When testing a single gear this must be coupled with a reference gear.

The proposed approach presents some advantages with respect to the metrological methods used to measure gear errors on driving and driven gears [10]. In fact these methods, that uses control machines, provide the charts of profile errors and cumulative pitch and runout errors for each tooth of the two gears. On the contrary, using the proposed technique, the equivalent error is obtained; it is directly related to the gear vibrations and therefore is particularly appropriate to evaluate the gear accuracy from a dynamic point of view. In fact it is well known that some modifications of the tooth involute profile can provide a reduction of the vibration level, so that the effect of these modifications, the accuracy of gear profiles and mounting can be checked by using the equivalent error.

The effect of noise on the identification of the equivalent error and modal parameters is also investigated. Some simulated tests are performed with noise polluted vibration responses of the gear pair.

2. VIBRATION SIMULATION

A pair of spur gears is modelled with two disks coupled by nonlinear mesh stiffness, mesh damping and excitation due to gear errors. One disk (the driving gear) has radius R_1 and mass moment of inertia I_1, while the other (the driven gear) has radius R_2 and mass moment of inertia I_2; the radii R_1 and R_2 correspond to the radii of the base circles of the two gears, respectively.

The transmission error, defined as the difference between the actual and ideal positions of the driven gear, is expressed as a linear displacement along the line of action. The sign convention used for the transmission error is positive behind the ideal position of the driven gear. Analysing gears with low contact ratio ε (*i.e.*, $1 < \varepsilon < 2$), the nonlinear equation of motion for the dynamic transmission error x can be written as:

$$m\ddot{x} + c\dot{x} + f_1(x,t) + f_2(x,t) = W_0, \tag{1}$$

where

$$x = R_1\theta_1 - R_2\theta_2, \tag{2}$$

being θ_1 and θ_2 the angular displacements of the two gears; the equivalent inertia mass m of the system is:

$$m = I_1 I_2 / (I_1 R_2^2 + I_2 R_1^2); \tag{3}$$

W_0 is the static load given by

$$W_0 = T_1 / R_1 = T_2 / R_2, \tag{4}$$

being T_1 and T_2 the driving and driven torques, respectively; f_j (x, t) are the elastic forces of the meshing tooth pair j, for $j = 1, 2$

$$f_j(x,t) = \begin{cases} k_j(t)\left[x - e_j(t)\right] & \text{when } x - e_j(t) > 0 \\ 0 & \text{when } x - e_j(t) \le 0. \end{cases} \tag{5}$$

Obviously, equation (1) can be easily extended to high contact ratio gears. In equation (5) $k_1(t)$ and $k_2(t)$ are the time-varying meshing stiffness of the two pairs of meshing teeth. The error functions $e_1(t)$ and $e_2(t)$ are the displacement excitations representing the relative gear errors of the meshing teeth; when two pairs of teeth come into contact there will be two separate error functions, each acting on a different spring. It is assumed that positive error functions give a positive transmission error. Error functions represent the sum of pitch, profile, pressure angle and runout errors. Moreover, when separation of tooth pairs occurs, because of the relative vibrations and backlash between the gear teeth, the dynamic forces f_j (x, t) are zero, according to equation (5); these are the nonlinear terms in the equation of motion. In equation (1) a constant viscous damping is assumed.

The total stiffness of the gear pair is given by $k(t) = k_1(t)+k_2(t)$. Let us introduce the meshing circular frequency $\omega = z\Omega$, where Ω is the angular velocity of the driven gear [rad s^{-1}] and z its number of teeth. The stiffness $k_j(t)$, which is a periodic function, has a principal period $T=2\pi/\omega$. The behaviour of $k_j(t)$ and $k(t)$ are discussed, *e.g.*, in references [3, 6, 10] and in section 4.

Now the case when $x\text{-}e_j(t) > 0$ is considered, *i.e.*, when there is contact between the two gears. Therefore the following study is correct when there is no tooth separation between driving and driven gears. The phenomenon of tooth separation is described, *e.g.*, in [13]. The equation of motion (1) can then be written as a second order linear ordinary differential equation:

$$\ddot{x} + 2\zeta\,\omega_0\,\dot{x} + \omega_0^2\,K(t)\,x = F_0 + \omega_0^2\,K_1(t)\,e_1(t) + \omega_0^2\,K_2(t)\,e_2(t), \tag{6}$$

where: $K(t) = k(t)/k_m$, $K_1(t) = k_1(t)/k_m$, $K_2(t) = k_2(t)/k_m$, $F_0 = W_0/m$ and ζ is the damping ratio; K, K_1 and K_2 are non-dimensional functions. Moreover the average value of the mesh stiffness is $k_m = (1/T)\int_0^T k(t)\,\mathrm{d}t$ and $\omega_0 = \sqrt{k_m/m}$ is the natural circular frequency of the undamped system with stiffness equal to its integral average value.

It is useful to introduce the following Fourier expansion of the equivalent error [m]

$$K_1(t)\,e_1(t)+K_2(t)\,e_2(t)=\sum_{n=-\infty}^{\infty}d_n\,e^{in\Omega t}\ , \tag{7}$$

where i is the imaginary unit. The expression on the left side of equation (7) represents the equivalent error of the gear pair; in fact, it is the excitation due to gear errors on the right side of equation (6). It is assumed that this function has a principal period zT, *i.e.* the time revolution of the driven gear, and therefore has principal circular frequency Ω. Strictly the same tooth of the driving and driven gears mesh together only after a period $s_1 zT$, where s_1 and s_2 are the integers that express the gear ratio τ as the rational number $\tau = s_1/s_2$ (usually $\tau \le 1$). In this study the error components having circular frequency lower than Ω are neglected. It is important to observe that in many cases the profile errors can be considered the same for all the teeth of the gear, *i.e.* they all have principal period T; therefore the coefficients d_n for $n = z, 2z, 3z, \ldots$ are due to periodic profile errors, whereas the others are due to pitch, pressure angle and runout errors.

The expansion of the non-dimensional total meshing stiffness is

$$K(t)=\sum_{n=-\infty}^{\infty}\alpha_n\,e^{inz\Omega t}\ . \tag{8}$$

The solution of the equation of motion (6) is obtained by using the harmonic balance method. Therefore the dynamic transmission error x is expanded into a complex Fourier series

$$x(t)=\sum_{n=-\infty}^{\infty}c_n\,e^{in\Omega t}\ . \tag{9}$$

Substituting equations (7-9) into equation (6) the following equation is found

$$\begin{aligned}\sum_{n=-\infty}^{\infty}\left[-n^2\Omega^2 c_n+2in\zeta\,\omega_0\Omega\,c_n+\omega_0^2\sum_{j=-\infty}^{\infty}c_{n-zj}\,\alpha_j\right]e^{in\Omega t}\\ =F_0+\omega_0^2\sum_{n=-\infty}^{\infty}d_n\,e^{in\Omega t}.\end{aligned} \tag{10}$$

Equation (10) gives the following algebraic linear system

$$\mathbf{AC}=\mathbf{F}, \tag{11}$$

where the elements of the matrix **A** are given by

$$A_{n,j}=\left(-n^2\Omega^2+2in\zeta\,\omega_0\Omega\right)\delta_{n,j}+\omega_0^2\,\psi_{n,j}\,\alpha_{(n-j)/z}\ , \tag{12}$$

$\delta_{n,j}$ is the Kronecker delta and $\psi_{n,j}=\begin{cases}1 & \text{if } (n-j)/z \text{ is integer}\\ 0 & \text{otherwise}\end{cases}$. Moreover it is:

$$\mathbf{c}=\begin{Bmatrix} c_N \\ \vdots \\ c_1 \\ c_0 \\ c_{-1} \\ \vdots \\ c_{-N} \end{Bmatrix}, \qquad \mathbf{F}=\begin{Bmatrix} \omega_0^2 d_N \\ \vdots \\ \omega_0^2 d_1 \\ F_0+\omega_0^2 d_0 \\ \omega_0^2 d_{-1} \\ \vdots \\ \omega_0^2 d_{-N} \end{Bmatrix}. \tag{13-14}$$

3. IDENTIFICATION OF MODAL PARAMETERS AND GEAR ERRORS

The aim of this work is to identify the equivalent gear error; therefore the vector **F** in equation (11) is now unknown. On the contrary the contact ratio ε, the shape of the stiffness function $K(t)$ and all the constants α_n of the expansion are known. The transmission error $x(t)$ is then experimentally measured for different rotational speeds Ω of the driven gear; in particular, only rotational speeds where no tooth separation occurs must be chosen. It is obvious that the dynamic transmission error varies according to the speed Ω, so that the constants c_n of the expansion and the vector **C** are functions of Ω. Equation (12) shows that also the matrix **A** is a function of Ω; whereas the vector **F** is independent of it. Therefore it can be written

$$\mathbf{F}=\mathbf{A}(\Omega)\,\mathbf{C}(\Omega). \tag{15}$$

In equation (15) the vector $\mathbf{C}(\Omega)$ is obtained experimentally and the matrix $\mathbf{A}(\Omega)$ theoretically by using equation (12). However in order to compute the matrix **A** the modal parameters ω_0 and ζ of the system must be identified because they appear in equation (12). These parameters can be determined by using the following equation:

$$\mathbf{A}(\Omega_1)\,\mathbf{C}(\Omega_1)=\mathbf{A}(\Omega_2)\,\mathbf{C}(\Omega_2)=\mathbf{A}(\Omega_i)\,\mathbf{C}(\Omega_i)=\text{constant}, \tag{16}$$

where Ω_i are fixed rotational speeds. Then

$$\sum_{n=-\infty}^{\infty}\left[-n^2\Omega^2 c_n+2in\zeta\omega_0\Omega c_n+\omega_0^2\sum_{j=-\infty}^{\infty}c_{n-zj}\alpha_j\right]=\text{constant}. \tag{17}$$

Computing the left hand side of equation (17) for different rotational speeds, e.g. Ω_1, Ω_2, Ω_3, and subtracting first the quantity computed for Ω_2 to the one computed for Ω_1 and then subtracting the quantity computed for Ω_3 to the one computed for Ω_1, one obtains the following linear system

$$\begin{bmatrix} \sum_{n=-\infty}^{\infty} 2ni\left[\Omega_1 c_n(\Omega_1) - \Omega_2 c_n(\Omega_2)\right] & \sum_{n=-\infty}^{\infty}\sum_{j=-\infty}^{\infty} \alpha_j \left[c_{n-zj}(\Omega_1) - c_{n-zj}(\Omega_2)\right] \\ \sum_{n=-\infty}^{\infty} 2ni\left[\Omega_1 c_n(\Omega_1) - \Omega_3 c_n(\Omega_3)\right] & \sum_{n=-\infty}^{\infty}\sum_{j=-\infty}^{\infty} \alpha_j \left[c_{n-zj}(\Omega_1) - c_{n-zj}(\Omega_3)\right] \end{bmatrix} \begin{Bmatrix} \zeta\,\omega_0 \\ \omega_0^2 \end{Bmatrix}$$

$$= \begin{Bmatrix} \sum_{n=-\infty}^{\infty} n^2\left[\Omega_1^2 c_n(\Omega_1) - \Omega_2^2 c_n(\Omega_2)\right] \\ \sum_{n=-\infty}^{\infty} n^2\left[\Omega_1^2 c_n(\Omega_1) - \Omega_3^2 c_n(\Omega_3)\right] \end{Bmatrix}. \qquad (18)$$

The linear system (18) allows to identify the modal parameters ω_0 and ζ and, using equation (15), the vector **F** that gives the equivalent gear error. Considering that usually $\omega_0^2 d_0$ is negligible with respect to F_0, also the ratio W_0/m can be identified; therefore if the static load W_0 is known, the reduced mass m of the system is obtained. Actually all the constant terms of the identified vector **F** can be attributed to the static load, giving to d_0 the zero value. In fact the static load can be easily considered as the mean value of the load during the gear meshing and a non zero coefficient d_0 is equivalent to change the static load.

In system (18) one can substitute the quantity computed for the difference Ω_2-Ω_3 to one of the two differences previously computed. However it is important to observe that with measurements at three different speeds only two linearly independent equations can be obtained for the system (18).

Due to the errors introduced in the experimental measurement of the dynamic transmission error x (errors in **C**) it is preferable to solve an overdetermined system using different velocities to obtain additional equations in system (18). Moreover the problem is ill-conditioned, so that the errors on the known vector **C** are amplified in the solution. In order to overcome this problem, it is necessary to use only the more significant harmonics in the identification when significant measurement errors or differences between the single degree of freedom model and the actual test bench are observed; therefore all the sums involved in system (18) must be stopped at an integer n not too large because higher order harmonics involved in **C** only introduce noise and does not give additional information. This process is similar to the use a low-pass filter on signals coming from sensors used in experiments. A discussion on this phenomenon is deferred to section 5. The natural circular frequency of the system can be evaluated theoretically or experimentally and the damping ratio can be also experimentally determined by an impact test, using the logarithmic decrement, or can be assumed in the range between 0.07 and 0.1, as verified by many authors [6, 10]. Therefore the results of the identification can be compared to data obtained in a different way.

The vector **F** can be also determined by using equation (15) or the following expression:

$$\mathbf{F} = (1/I)\sum_{i=1}^{I} \mathbf{A}(\Omega_i)\mathbf{C}(\Omega_i). \tag{19}$$

This procedure provides a good accuracy in the computation also in presence of measurement errors, and the average reduces the errors that are introduced in the experimental measurement of x (and then in **C**).

4. APPLICATION OF THE METHOD

In the numerical simulations the stiffness function proposed by Cai and Hayashi [6] was used; in particular the following function can be introduced

$$f(t) = \frac{1}{0.85\varepsilon}\cdot\left[\frac{-1.8}{(\varepsilon T)^2}\left[t+((\varepsilon-1)/2)T\right]^2 + \frac{1.8}{\varepsilon T}\left[t+((\varepsilon-1)/2)T\right]+0.55\right]. \tag{20}$$

The two non-dimensional meshing stiffness $K_1(t)$ and $K_2(t)$ are directly obtained by equation (20), *i.e.*:

$$K_1(t) = f(t) \quad \text{for } 0 \le t \le T \tag{21}$$

$$K_2(t) = \left\{\begin{matrix} f(t-T) & \text{if } t > T-((\varepsilon-1)/2)T \\ 0 & \text{if } t \le T-((\varepsilon-1)/2)T \end{matrix}\right\} + \left\{\begin{matrix} f(t+T) & \text{if } t < ((\varepsilon-1)/2)T \\ 0 & \text{if } t \ge ((\varepsilon-1)/2)T \end{matrix}\right\} \text{ for } 0 \le t \le T. \tag{22}$$

The meshing stiffness is therefore a function of the contact ratio ε. The two non-dimensional meshing stiffness $K_1(t)$ and $K_2(t)$ are shown in Figure 1a (ε = 1.8) along the meshing period $T=2\pi/\omega$, and the non-dimensional total meshing stiffness $K(t)$ is plotted in Figure 1b. The integral average stiffness of the pair k_m is related to the maximum stiffness of one pair of teeth k_{MAX} by the following expression: $k_m = 0.85\varepsilon\ k_{MAX}$. The ISO/DIS 6336-1.2 (1990) design code gives a formula to evaluate k_{MAX}.

In order to simplify the experimental measurement of the dynamic transmission error, only a test on the driven gear can be performed. Usually only the acceleration of the driven gear $\ddot{x}_2 = R_2\,\ddot{\theta}_2$ is measured; however the acceleration $\ddot{x}$ can be obtained by using the following relationship

$$\ddot{x}_2 = \frac{m_1}{m_1+m_2}\ddot{x}, \tag{23}$$

where m_1 and m_2 are the reduced masses of the driving and the driven gear, respectively. The measured acceleration, can be related to the coefficients c_n by equation (9), to yield:

$$\ddot{x}_2 = -\frac{m_1}{m_1+m_2}\Omega^2\sum_{n=-\infty}^{\infty} c_n n^2 e^{in\Omega t}. \tag{24}$$

Equation (24) shows that the coefficient c_0 cannot be obtained by vibration measurement; however this coefficient can be easily determined because it is the mean value of the dynamic transmission error x. A good estimation of this value is $c_0 = W_0/k_m$. In the identification process it is very important to use only measured accelerations when no tooth separation occurs. Therefore it is generally necessary to avoid rotational speeds larger than half the main resonance speed ω_0.

The benchmark for gears can be obtained by a variable speed motor and a brake. Torsional flexible shafts, with a natural frequency lower than 1/10 of the natural frequency ω_0 of the gear pair, and stiff bearings must be used in order to well approximate a single degree of freedom system. The rotational speed can be measured by a proximity sensor that counts the number of passing teeth; the load is measured by a dynamometer and the acceleration of the driven gear by accelerometers. In particular two identical accelerometers which are mounted on the gear through two small aluminium blocks are used; they can be placed on opposite sides of a diameter and must have tangential orientation. A summing amplifier sums up the signals from the accelerometers to eliminate the effect of eccentricity. A slip ring is introduced to bring the signals to the amplifier. In alternative a laser rotational vibrometer can be employed to measure vibrations of the driven gear; in this case accelerometers, slip ring and summing amplifier can be eliminated. Lubrication of the meshing teeth must be provided.

5. NUMERICAL RESULTS

To verify the proposed method the gear pair tested by Umezawa *et al.* [10] is studied. The two gears are finished by a MAAG grinding; the characteristics of both the gears are: module = 4, number of teeth = 48, face width = 10 mm, pressure angle = 14.5°, diameter of standard pitch circle = 192 mm; the gear ratio is 1. The contact ratio ε is 1.8, the rotational speed range Ω = 400 ÷ 3000 rpm (41.89 ÷ 314.16 rad s^{-1}), the torque 196 Nm and the teeth have involute profile. The profile errors are about 6μm at the root of the driving gear and at the tip of driven gear; these profile errors are reported in reference [10]. The natural circular frequency is ω_0 = 48×3062 rpm (2450 Hz) and the value of the damping ratio ζ is 0.07.

The response of the gear pair is polluted with noise on the gear data and modal parameters. It is assumed that only profile errors are significant in this case, so that all the other errors are neglected. As a consequence of this hypothesis, the dynamic transmission error has a principal period equal to the meshing period T. The response x is discretized with 201 points in the period. Then the noise is added to the response before computing the vector **C**. In particular the noise is generated using random numbers added to the time response. These random numbers are obtained by a normal distribution having zero mean value and variance $\sigma = lev * max$, where max is the maximum value of the response x in the period and lev is the error level. As a consequence of

the assumed distribution, the 68 % of the points have noise within $\pm\sigma$, the 95 % within $\pm 2\sigma$ and the 99.7 % within $\pm 3\sigma$.

First, equation (18) is used to identify the modal parameters of the system from noise polluted responses. In particular eight responses at rotational speeds Ω = 60, 65, 68, 70, 80, 90, 100, 120 rad s^{-1} with an error level $lev = 0.02$ are employed. This error level gives responses having a difference within ±6% with respect to the true value. In Figure 2a the percent difference between the identified natural frequency ω_0 and the actual value is plotted versus the number of harmonics used in the identification. The range of harmonics of the meshing frequency $\omega = z\Omega$ that gives correct results is $4 \le n \le 8$. In Figure 2b the data relative to the damping ratio ζ are reported. Figure 3 is similar to Figure 2 but it is obtained for an error level $lev = 0.005$ (difference within ±2.5% with respect to the true value). In this case the range of useful harmonics increases. Figure 2 and 3 show that it is not convenient to exceed in the number of harmonics. In fact, for the considered problem, the amplitude of coefficients c_n decreases with n so that higher order harmonics are largely affected by the noise. Being the identification process an ill conditioned problem, it is necessary to employ only harmonics having a good signal to noise ratio.

In Figure 4 the equivalent error obtained by using the profile errors given in reference [10] and equations (7), (20-22) is shown; this one can be called the "actual" equivalent error. In Figure 5 the equivalent error is identified by using a response at Ω = 60 rad s^{-1} without noise. In this case 15 harmonics are used to describe the function. The difference between Figures 4 and 5 can be surely attributed to the truncation error.

Then eight responses at rotational speeds speeds Ω = 60, 65, 68, 70, 80, 90, 100, 120 rad s^{-1} with an error level $lev = 0.005$ are used to identify the equivalent error; the result is given in Figure 6 where the actual modal parameters (ω_0 and ζ) are used. Figures 5 and 6 are very similar and they well describe the "actual" error reported in Figure 4. Also in the case of an error level of $lev = 0.02$ and using the actual modal parameters a quite good evaluation of the equivalent error is reached, as shown in Figure 7.

The effect of an incorrect identification of the modal parameters ω_0 and ζ on the evaluation of the equivalent gear error is then investigated in Figure 8; in this case an error of +10% on the frequency and +40% on the damping ratio is used to evaluate the equivalent error by responses having a noise level $lev = 0.02$. Also in this case a quite good result is obtained.

6. CONCLUSIONS

The reconstruction of the equivalent gear error by acceleration measurement of the driven gear of a spur gear pair is quite good also in the case of measurements affected by noise. In particular the identification of the natural frequency and damping of the system is obtained by an overdetermined

linear system to minimise the error; to obtain correct results only lower order harmonics must be considered. Then these data can be used to evaluate the equivalent gear error that is not largely affected by the inaccuracy in the identification of the natural frequency and damping.

The proposed method seems to have advantages in the quality control of a large production of gears having the same center distance; in this case the same housing can be used. Moreover the gear can be tested together with a reference gear or with the companion gear to check the actual gear pair. As a limitation, the method can be only applied to systems having stiff bearings and torsionally compliant axes, requiring an appropriately designed experimental apparatus.

REFERENCES

1. H. N. ÖZGÜVEN and D. R. HOUSER 1988 *Journal of Sound and Vibration* **121**, 383-411. Mathematical models used in gear dynamics.
2. H. N. ÖZGÜVEN and D. R. HOUSER 1988 *Journal of Sound and Vibration* **125**, 71-83. Dynamic analysis of high speed gears by using loaded static transmission error.
3. M. AMABILI and A. RIVOLA to appear in *Mechanical Systems and Signal Processing*. Dynamic analysis of spur gear pairs: steady state response and stability of the SDOF model with time-varying meshing stiffness.
4. P. VELEX and M. MAATAR 1996 *Journal of Sound and Vibration* **191**, 629-660. A mathematical model for analyzing the influence of shape deviations and mounting errors on gear dynamic behaviour.
5. Y. CAI and T. HAYASHI 1992 *Proceedings of the ASME International Power Transmission and Gearing Conference*, Scottsdale, Arizona **2**, 453-460 (DE - Vol. 43-2). The optimum modification of tooth profile for a pair of spur gears to make its rotational vibration equal zero.
6. Y. CAI and T. HAYASHI 1994 *Transactions of the American Society of Mechanical Engineers, Journal of Mechanical Design* **116**, 558-564. The linear approximated equation of vibration of a pair of spur gears (theory and experiment).
7. Y. CAI 1995 *Transactions of the American Society of Mechanical Engineers, Journal of Mechanical Design* **117**, 460-469. Simulation on the rotational vibration of helical gears in consideration of the tooth separation phenomenon (a new stiffness function of helical involute tooth pair).
8. Y. CAI 1996 *Proceedings of the ASME International Power Transmission and Gearing Conference*, San Diego, CA, 177-184 (DE - Vol. 88). Development of a silent helical gear reducer (vibration simulation and noise measurement).
9. T. SATO, K. UMEZAWA and J. ISHIKAWA 1983 *Bullettin of the Japan Society of Mechanical Engineers* **26**(221), 2010-2016. Effects of contact ratio and profile correction on gear rotational vibration.
10. K. UMEZAWA, T. SATO and J. ISHIKAWA 1984 *Bullettin of the Japan Society of Mechanical Engineers* **27**(223), 102-109. Simulation on rotational vibration of spur gears.
11. K. UMEZAWA, T. SATO and K. KOHNO 1984 *Bullettin of the Japan Society of Mechanical Engineers* **27**(225), 569-575. Influence of gear error on rotational

vibration of power transmission spur gears (1st report, pressure angle error and normal pitch error).
12. K. UMEZAWA and T. SATO 1985 *Bullettin of the Japan Society of Mechanical Engineers* **28**(243), 2143-2148. Influence of gear error on rotational vibration of power transmission spur gears (2nd report, waved form error).
13. K. UMEZAWA, T. AJIMA and H. HOUJOH 1986 *Bullettin of the Japan Society of Mechanical Engineers* **29**(249), 950-957. Vibration of three axes gear system.
14. A. KUBO, S. KIYONO and M. FUJINO 1986 *Bullettin of the Japan Society of Mechanical Engineers* **29**(258), 4424-4429. On analysis and prediction of machine vibration caused by gear meshing (1st report, nature of gear vibration and the total vibrational excitation).
15. R. KASUBA and J. W. EVANS 1981 *Transactions of the American Society of Mechanical Engineers, Journal of Mechanical Design* **103**, 398-409. An extended model for determining dynamic loads in spur gearing.
16. W. D. MARK 1987 *Transactions of the American Society of Mechanical Engineers, Journal of Mechanisms, Transmissions, and Automation in Design* **109**, 268-274. Analytical reconstruction of the running surfaces of gear teeth. Part 2: combining tooth spacing measurements with profile and lead measurements.
17. M. BENTON and A. SEIREG 1978 *Transactions of the American Society of Mechanical Engineers, Journal of Mechanical Design* **100**, 26-32. Simulation of resonances and instability conditions in pinion-gear systems.
18. R. W. CORNELL and W. W. WESTERVELT 1978 *Transactions of the American Society of Mechanical Engineers, Journal of Mechanical Design* **100**, 69-76. Dynamic tooth loads and stressing for high contact ratio spur gears.
19. B. M. BAHGAT, M. O. M. OSMAN AND T. S. SANKAR 1983 *Transactions of the American Society of Mechanical Engineers, Journal of Mechanisms, Transmissions, and Automation in Design* **105**, 302-309. On the spur-gear dynamic tooth-load under consideration of system elasticity and tooth involute profile.
20. A. S. KUMAR, T. S. SANKAR and M. O. M. OSMAN 1985 *Transactions of the American Society of Mechanical Engineers, Journal of Mechanisms, Transmissions, and Automation in Design* **107**, 54-60. On dynamic tooth load and stability of a spur-gear system using the state-space approach.
21. D. C. H. YANG and Z. S. SUN 1985 *Transactions of the American Society of Mechanical Engineers, Journal of Mechanisms, Transmissions, and Automation in Design* **107**, 529-535. A rotary model for spur gears dynamics.
22. D. C. H. YANG and J. Y. LIN 1987 *Transactions of the American Society of Mechanical Engineers, Journal of Mechanisms, Transmissions, and Automation in Design* **109**, 189-196. Hertzian damping, tooth friction and bending elasticity in gear impact dynamics.
23. H-H. LIN, R. L. HUSTON and J. J. COY 1988 *Transactions of the American Society of Mechanical Engineers, Journal of Mechanisms, Transmissions, and Automation in Design* **110**, 221-225. On the dynamic loads in parallel shaft transmissions: Part I - modelling and analysis.
24. H-H. LIN, R. L. HUSTON and J. J. COY 1988 *Transactions of the American Society of Mechanical Engineers, Journal of Mechanisms, Transmissions, and Automation in Design* **110**, 226-229. On the dynamic loads in parallel shaft transmissions: Part II - parameter study.

25. Ö. S. ŞENER and H. N. ÖZGÜVEN 1993 *Journal of Sound and Vibration* **166**, 539-556. Dynamic analysis of geared shaft systems by using a continuous system model.
26. A. H. NAYFEH and D. T. MOOK 1979 *Nonlinear Oscillations*. New York: John Wiley and Sons.

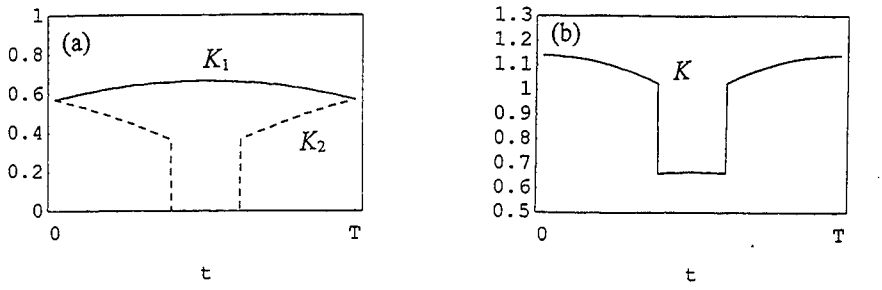

Figure 1. (a) The non-dimensional meshing stiffness $K_1(t)$ and $K_2(t)$. (b) The total meshing stiffness $K(t)$.

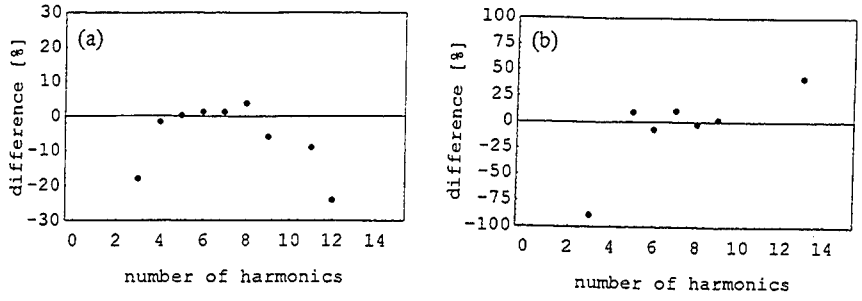

Figure 2. Results of the identification with an error level *lev*=0.02 (a) Percent difference between the identified ω_0 and the actual value *vs.* the number of harmonics used in the identification. (b) Percent difference between the identified ζ and the actual value *vs.* the number of harmonics.

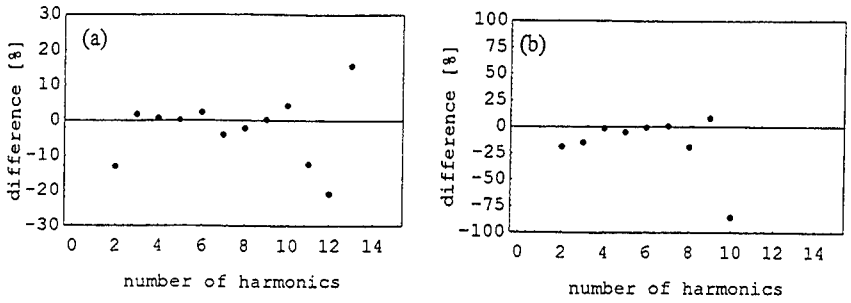

Figure 3. Results of the identification with an error level *lev*=0.005 (à) Percent difference between the identified ω_0 and the actual value. (b) Percent difference between the identified ζ and the actual value.

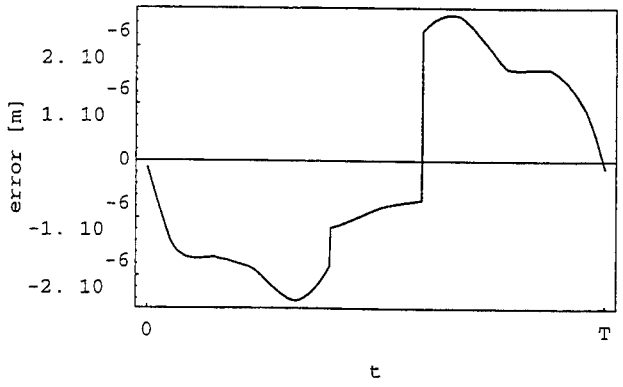

Figure 4. Actual equivalent gear error.

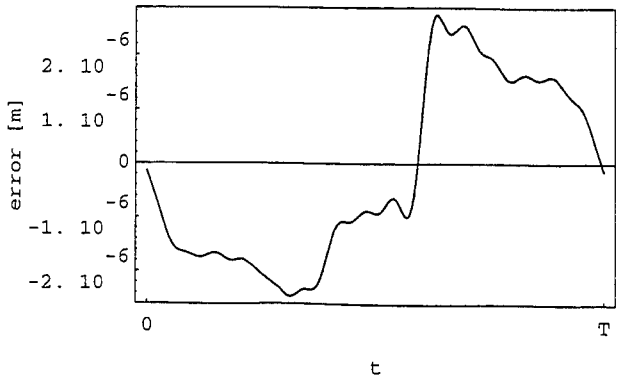

Figure 5. Identified equivalent gear error by response without noise.

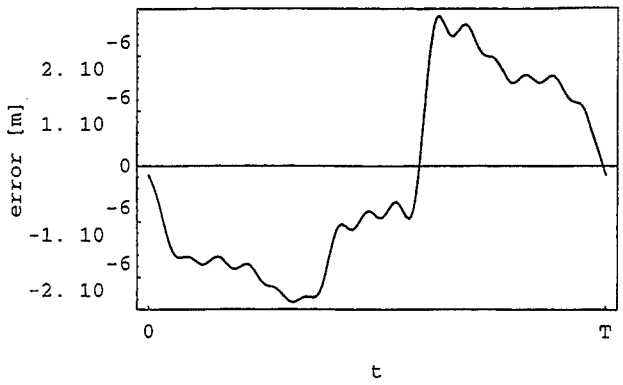

Figure 6. Identified equivalent gear error by responses with a noise level *lev*=0.005; actual modal parameters.

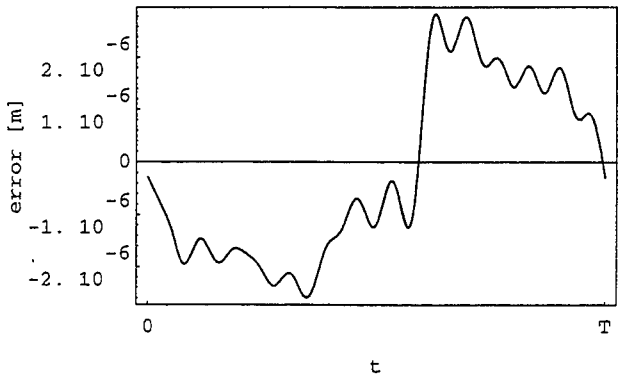

Figure 7. Identified equivalent gear error by responses with a noise level *lev*=0.02; actual modal parameters.

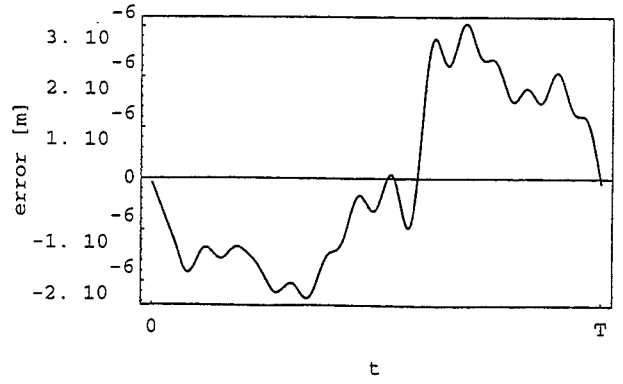

Figure 8. Identified equivalent gear error by responses with a noise level *lev*=0.02; +10% of the actual value of ω_0 and +40% of the actual value of ζ.